

**IAEA-TECDOC-558**

# **STELLARATOR PHYSICS**

PROCEEDINGS OF THE  
SEVENTH INTERNATIONAL WORKSHOP ON STELLARATORS  
ORGANIZED BY THE  
INTERNATIONAL ATOMIC ENERGY AGENCY  
AND HELD IN OAK RIDGE, TENNESSEE, 10-14 APRIL 1989



A TECHNICAL DOCUMENT ISSUED BY THE  
INTERNATIONAL ATOMIC ENERGY AGENCY, VIENNA, 1990

STELLARATOR PHYSICS  
IAEA, VIENNA, 1990  
IAEA-TECDOC-558  
ISSN 1011-4289

Printed by the IAEA in Austria  
July 1990

The IAEA does not normally maintain stocks of reports in this series.  
However, microfiche copies of these reports can be obtained from

INIS Clearinghouse  
International Atomic Energy Agency  
Wagramerstrasse 5  
P.O. Box 100  
A-1400 Vienna, Austria

Orders should be accompanied by prepayment of Austrian Schillings 100,—  
in the form of a cheque or in the form of IAEA microfiche service coupons  
which may be ordered separately from the INIS Clearinghouse.

**PLEASE BE AWARE THAT  
ALL OF THE MISSING PAGES IN THIS DOCUMENT  
WERE ORIGINALLY BLANK**

## FOREWORD

The Seventh International Stellarator Workshop was held as an IAEA Technical Committee Meeting in Oak Ridge, Tennessee, USA, from 10 to 14 April 1989. Oak Ridge National Laboratory acted as the host organization for this meeting. In recent years, workshops have been held in Kyoto, Japan (1986); Lake Tegernsee, Federal Republic of Germany (1984 and 1980); Cape May, United States (1982) and Moscow, USSR (1981). The present workshop was the largest, with 108 papers presented and 127 participants from 25 institutes from Australia, Federal Republic of Germany, Italy, Japan, Spain, USA, UK and USSR.

The purpose of the meeting was to review and discuss the progress into the stellarator approach to nuclear fusion and to test the specific optimization principles on which each device is based.

The programme of the meeting was arranged with reference to the main subjects of stellarator physics:

- overview of experimental results,
- theory: magnetic field configurations, plasma equilibrium and stability, transport,
- plasma diagnostics,
- RF plasma heating,
- new device designs.

Each topic was covered by papers which were either in the nature of a review or were a detailed description of a particular experiment or concept. Discussion periods were held at regular intervals during the meeting. These, together with the informal discussions entered into by the participants, were especially valuable. All contributions were orally presented.

This proceeding contains the manuscripts which have come to hand. They are reproduced directly from the author's copy.

The meeting owed its success to the good interaction of all persons involved. Appreciation is due to the authors for their presentations and to the Organizing Committee for their excellent work. Special thanks must go to Dr. J.F. Lyon (ORNL) for his valuable contribution to the scientific programme and who was also responsible for the technical details of the Workshop and the preparation of this proceeding for publication.

The Workshop has been very successful. It has shown rapid development in stellarator approach to magnetic fusion, which stimulates the progress in the R & D in this field of research. The venue for the next Workshop on Stellarator was proposed to be Yalta, USSR in 1991.

## *EDITORIAL NOTE*

*In preparing this material for the press, staff of the International Atomic Energy Agency have mounted and paginated the original manuscripts as submitted by the authors and given some attention to the presentation.*

*The views expressed in the papers, the statements made and the general style adopted are the responsibility of the named authors. The views do not necessarily reflect those of the governments of the Member States or organizations under whose auspices the manuscripts were produced.*

*The use in this book of particular designations of countries or territories does not imply any judgement by the publisher, the IAEA, as to the legal status of such countries or territories, of their authorities and institutions or of the delimitation of their boundaries.*

*The mention of specific companies or of their products or brand names does not imply any endorsement or recommendation on the part of the IAEA.*

*Authors are themselves responsible for obtaining the necessary permission to reproduce copyright material from other sources.*

## CONTENTS

Summary of presentations .....	11
<i>J.F. Lyon</i>	

### OVERVIEW OF EXPERIMENTAL RESULTS

Status of the advanced stellarator Wendelstein W 7AS: first results and further programme .....	25
<i>H. Renner, W VII-AS Team, NBI Group, ICF Group, ECRH Group</i>	
Overview of the ATF program .....	33
<i>J.F. Lyon, S.C. Aceto, F.S.B. Anderson, G.L. Bell, J.D. Bell, T.S. Bigelow, B.A. Carreras, M.D. Carter, R.J. Colchin, K.A. Connor, E.C. Crume, N. Dominguez, J.L. Dunlap, G.R. Dyer, A.C. England, R.H. Fowler, R.F. Gandy, J.C. Glowienka, R.C. Goldfinger, R.H. Goulding, J.W. Halliwell, J.D. Hanson, J.H. Harris, M.A. Henderson, D.L. Hillis, S. Hiroe, L.D. Horton, H.C. Howe, D.P. Hutchinson, R.C. Isler, T.C. Jernigan, H. Kaneko, R.R. Kindsfather, M. Kwon, R.A. Langley, D.K. Lee, J.N. Leboeuf, V.E. Lynch, C.H. Ma, M.M. Menon, F.W. Meyer, P.K. Mioduszewski, T. Mizuuchi, R.N. Morris, O. Motojima, M. Murakami, G.H. Neilson, V.K. Paré, N.F. Perepelkin, D.A. Rasmussen, R.K. Richards, P.S. Rogers, J.A. Rome, M.J. Saltmarsh, F. Sano, P.L. Shaw, J. Sheffield, T.D. Shepard, J.E. Simpkins, C.M. Simpson, Y. Takeiri, C.E. Thomas, T. Uckan, K.L. Vander Sluis, G.S. Voronov, M.R. Wade, T.L. White, J.B. Wilgen, W.R. Wing, J.J. Zielinski</i>	
Overview of recent Heliotron E experiments .....	45
<i>T. Obiki, A. Iiyoshi, M. Wakatani, O. Motojima, S. Morimoto, K. Kondo, T. Mutoh, M. Sato, S. Sudo, F. Sano, K. Itoh, M. Nakasuga, K. Hanatani, H. Zushi, H. Kaneko, T. Mizuuchi, H. Okada, Y. Nakamura, Y. Takeiri, H. Matsuura, M. Harada, K. Ichiguchi, T. Yamashina, T. Hino, H. Minagawa, T. Oda, K. Muraoka, T. Kajiwara, K. Matsuo, K. Uchino, A. Komori, N. Noda</i>	
Overview of CHS experiment .....	51
<i>K. Matsuoka and the CHS Group</i>	
Overview of the Torsatron/Stellarator Laboratory program at the University of Wisconsin–Madison .....	57
<i>J.L. Shohet</i>	

### TRANSPORT

Neutral gas transport and particle recycling in the W VII-AS stellarator .....	65
<i>F. Sardei, H. Ringler, A. Dodhy, G. Kühner, W VII-AS Team, ECRH Group</i>	
Toroidal and poloidal symmetry studies on neutral and impurities in CHS .....	73
<i>K. Ida and the CHS Group</i>	
Transport modeling of ECH and neutral-beam-heated plasmas in the advanced toroidal facility .....	79
<i>H.C. Howe, L.D. Horton, E.C. Crume, J.H. Harris, R.C. Isler, M.M. Murakami, D.A. Rasmussen, J.B. Wilgen, W.R. Wing</i>	
Convective transport in IMS .....	83
<i>J.N. Talmadge, D.T. Anderson, F.S.B. Anderson, B.J. Peterson, J.L. Shohet</i>	
Experimental studies on drift waves in SHEILA .....	87
<i>B.D. Blackwell, S.M. Hamberger, X.-H. Shi</i>	
Optimization of transport in stellarators .....	93
<i>C.L. Hedrick, C.O. Beasley, W.I. Van Rij</i>	
The role of the radial electric field in enhanced confinement regimes in stellarators .....	97
<i>K.C. Shaing</i>	

How temperature gradients are determined in toroidal plasmas .....	101
<i>S. Yoshikawa</i>	

## IMPURITIES AND DIVERTORS

Divertor biasing experiments in IMS .....	107
<i>D.T. Anderson, F.S.B. Anderson, R.P. Doerner, M.J. Hsieh, W.N.G. Hitchon, P.G. Matthews, J.L. Shohet</i>	
Divertor studies at 6 kG in the interchangeable module stellarator .....	111
<i>P.G. Matthews, D.T. Anderson, F.S.B. Anderson, J.L. Shohet</i>	
The effects of a magnetic field on a collisional presheath .....	117
<i>W.N.G. Hitchon, D.J. Koch, W.D. D'haeseleer</i>	
Edge plasma and divertor studies in the ATF torsatron .....	121
<i>P.K. Mioduszewski, T. Uckan, D.L. Hillis, J.A. Rome, R.H. Fowler, J.C. Glowienka, M. Murakami, G.H. Neilson</i>	
Wall conditioning in ATF .....	127
<i>R.A. Langley, T.L. Clark, J.C. Glowienka, R.H. Goulding, P.K. Mioduszewski, D.A. Rasmussen, T.F. Rayburn, C.R. Schaich, T.D. Shepard, J.E. Simpkins, J.L. Yarber</i>	

## DIAGNOSTICS

Crossed-sightline correlation of Faraday rotation for measurement of perpendicular magnetic fluctuations .....	139
<i>C.E. Thomas, Jr., J.T. Woo, E. Saravia, D.P. Hutchinson</i>	
ECE correlation measurements of magnetic fields and fluctuations .....	147
<i>C.E. Thomas, Jr., G.R. Hanson, R.F. Gandy</i>	
FIR interferometer and scattering measurements on ATF .....	155
<i>C.H. Ma, D.P. Hutchinson, Y. Fockedey, K.L. Vander Sluis, C.A. Bennett</i>	
Recent electron temperature and density results from the ATF Thomson scattering system .....	159
<i>D.A. Rasmussen, A.C. England, M. Murakami, H.C. Howe, T.C. Clark, R.R. Kindsfather, T.M. Rayburn, P.S. Rogers, K.A. Stewart, G.L. Bell, P.L. Shaw, C.E. Thomas</i>	
Bolometric measurements in ATF .....	167
<i>S. Hiroe, R.R. Kindsfather, J.B. Wilgen, D.B. Batchelor, T.S. Bigelow, W.R. Wing, G.L. Bell, R.F. Gandy, R.C. Goldfinger</i>	
Diagnosis of radiation loss asymmetries in TJ-II flexible heliac .....	173
<i>M.A. Ochando, A.P. Navarro</i>	
A diagnostic for 2-D density profiles in heliac H-1 .....	179
<i>J. Howard, L.E. Sharp</i>	
Measurement of attenuation profile of injected neutral beam into a Heliotron E plasma .....	185
<i>K. Kondo, H. Zushi, T. Oda, F. Sano, K. Hanatani, T. Kawabata, H. Kaneko, T. Mizuuchi, H. Okada, S. Sudo, M. Sato, S. Morimoto, T. Obiki, A. Iiyoshi</i>	
Modeling for runaway dynamics in stellarators .....	189
<i>L. Rodríguez, R.L. Vázquez, A.P. Navarro</i>	

## ECH, CONFINEMENT — EXPERIMENTS

First results of electron cyclotron heating on W VII-AS .....	197
<i>W. Kasperek, G.A. Müller, P.G. Schüller, M. Thumm, V. Erckmann, W VII-AS Team</i>	
Electron cyclotron heating experiments in CHS .....	203
<i>H. Iguchi and the CHS Group</i>	

Power balance studies for RF heated plasma in the Uragan-3 torsatron .....	209
<i>V.L. Bereznyj, M.P. Vasil'ev, V.S. Vojtsenya, E.D. Volkov, Yu.V. Gutarev, A.G. Dikij,</i>	
<i>G.V. Zelenin, B.V. Kravchin, S.V. Kovalev, V.G. Konovalov, V.I. Kononenko, V.D. Kotsubanov,</i>	
<i>G.G. Lesnyakov, A.P. Litvinov, Yu.K. Mironov, N.I. Nazarov, I.K. Nokolskij, O.S. Pavlichenko,</i>	
<i>I.I. Patlay, V.K. Pashnev, V.V. Plyusnin, N.F. Perepelkin, A.I. Skibenko, A.S. Slavnyj,</i>	
<i>V.S. Taran, T.O. Tkhoryak, S.I. Fedotov, I.P. Fomin, A.N. Shapoval, O.M. Shvets, V.M. Zalkind</i>	
Experimental studies on the Tohoku University Helicac .....	215
<i>H. Watanabe, S. Kitajima, N. Takeuchi, M. Takayama</i>	

## STABILITY STUDIES

Second stability studies in ATF .....	223
<i>J.H. Harris, M. Murakami, B.A. Carreras, J.D. Bell, G.L. Bell, T.S. Bigelow, L.A. Charlton,</i>	
<i>N. Dominguez, J.L. Dunlap, J.C. Glowienka, H.C. Howe, H. Kaneko, R.R. Kindsfather,</i>	
<i>J.N. LeBoeuf, V.E. Lynch, M.M. Menon, R.N. Morris, G.H. Neilson, V.K. Paré,</i>	
<i>N.F. Perepelkin, D.A. Rasmussen, J.B. Wilgen, W.R. Wing</i>	
Ideal low-n and Mercier mode stability boundaries for $\ell = 2$ torsatrons .....	225
<i>N. Dominguez, J.N. Leboeuf, B.A. Carreras, V.E. Lynch</i>	
MHD instabilities and maximum $\beta$ values in Heliotron DR .....	231
<i>S. Morimoto, N. Yanagi, K. Ichiguchi, S. Kobayashi, M. Iima, S. Besshou, N. Nakamura,</i>	
<i>M. Sato, M. Wakatani, T. Obiki, A. Iiyoshi</i>	

## RF HEATING

ECF heating and current drive in W VII-AS .....	237
<i>U. Gasparino, H. Maassberg, W VII-AS Team, NBI Group, ECRH Group</i>	
Measurements of ECH absorption on ATF using a polarization-controlled beam launcher .....	243
<i>T.S. Bigelow, C.R. Schaich, T.L. White</i>	
ECH experiments in SHEILA .....	247
<i>G.D. Conway, B.D. Blackwell</i>	
Microwave absorption in stellarators (TJ-II) and torsatrons (STORM) .....	251
<i>C. Alejaldre, F. Castejón, V. Krivenski, V. Tribaldos</i>	
Impurity behaviors of ECH and RF plasmas in CHS .....	257
<i>S. Morita and the CHS Group</i>	
Experiment on RF plasma production in CHS .....	265
<i>K. Nishimura, T. Shoji, CHS Group</i>	
ICH system for heliac H1 .....	269
<i>B.D. Blackwell, G.D. Conway</i>	
Plasma production using microwave and radiofrequency sources .....	275
<i>M.D. Carter</i>	
An analytic model for electron cyclotron heating profiles .....	281
<i>R.C. Goldfinger, D.B. Batchelor</i>	

## EQUILIBRIUM AND STABILITY

Averaged equilibrium and stability in low-aspect-ratio stellarators .....	289
<i>L. García, B.A. Carreras, N. Dominguez</i>	
Relation between Mercier criterion and low-n mode stability .....	295
<i>Y. Nakamura, K. Ichiguchi, H. Sugama, M. Wakatani, H. Zushi, J.L. Johnson, G. Rewoldt,</i>	
<i>B.A. Carreras, N. Dominguez, J.N. Leboeuf, J.A. Holmes, V.E. Lynch</i>	
A free boundary algorithm for the BETAS code .....	299
<i>O.L. Betancourt</i>	

Fluctuation studies in ATF .....	307
<i>J.D. Bell, J.H. Harris, J.L. Dunlap, V.K. Paré, M. Murakami, H. Kaneko</i>	
Magnetic fluctuations due to pressure driven instabilities in ATF .....	313
<i>L.A. Charlton, B.A. Carreras, J.N. Leboeuf, V.E. Lynch</i>	
Determination of electron density fluctuations in stellarators by microwave reflectometry .....	317
<i>A.P. Navarro, J. Sánchez, E. Anabitarte, J. Senties, T. Estrada, H.J. Hartfuss, W VII-AS Team</i>	
Tomography analysis of MHD instabilities in W VII-A stellarator .....	323
<i>A.P. Navarro, M.A. Ochando, A. Weller</i>	
Dissipative trapped electron modes in $\ell = 2$ torsatrons .....	329
<i>B.A. Carreras, N. Dominguez, J.N. Leboeuf, V.E. Lynch, P.H. Diamond</i>	
Equilibrium and ideal stability studies for ATF .....	333
<i>V.E. Lynch, B.A. Carreras, N. Dominguez, J.N. Leboeuf</i>	
Stability analysis of free boundary modes for ATF .....	337
<i>F. Bauer, P.R. Garabedian</i>	
Stability studies for TJ-II .....	341
<i>A. Varias, C. Alejaldre, A. López-Fraguas, B.A. Carreras, N. Dominguez, V.E. Lynch</i>	
Techniques for coupling fully three dimensional MHD codes and two dimensional averaged codes for stellarator and tokamak applications .....	347
<i>J.L. Johnson, A.H. Reiman, G. Rewoldt</i>	

## CONFIGURATION EFFECTS, CONFINEMENT

Configurational effects on the confinement in the stellarator Wendelstein W 7AS .....	353
<i>H. Renner, W VII-AS Team, NBI Group, ICF Group, ECRH Group</i>	
Transport and plasma current in W VII-AS .....	359
<i>H. Maassberg, U. Gasparino, G. Kühner, H. Ringler, W VII-AS Team, NBI Group, ECRH Group</i>	
The effects of the magnetic axis shift on transport and MHD stability in Heliotron E .....	363
<i>H. Zushi, F. Sano, K. Itoh, T. Mizuuchi, H. Kaneko, S. Sudo, M. Nakasuga, K. Hanatani, K. Kondo, K. Ichiguchi, M. Harada, W. Wakatani, T. Obiki, A. Iiyoshi</i>	
ATF flux surfaces and related plasma effects .....	369
<i>R.J. Colchin, A.C. England, J.H. Harris, D.L. Hillis, T.C. Jernigan, M. Murakami, G.H. Neilson, J.A. Rome, M.J. Saltmarsh, F.S.B. Anderson, R.F. Gandy, J.D. Hanson, M.A. Henderson, D.K. Lee, V.E. Lynch, C.M. Simpson</i>	
Magnetic field configuration of the modified Uragan-3M torsatron .....	373
<i>V.E. Bykov, E.D. Volkov, V.S. Vojtsenya, A.V. Georgievskij, V.M. Zalkind, Yu.K. Kuznetsov, G.G. Lesnyakov, F.I. Ozherel'ev, O.S. Pavlichenko, D.P. Pogochev, V.S. Taran, K. Schwörer, H. Hailer</i>	

## NEW DEVICE DESIGNS

Heliac physics studies: TJ-II project .....	381
<i>C. Alejaldre, J. Alonso, J. Botija, F. Castejón, J.R. Cepero, J. Guasp, A.L. Fraguas, L. García, V. Krivenski, R. Martín, M. Sorolla, A.P. Navarro, A. Perea, A. Rodríguez-Yunta, A. Varias</i>	

## MAGNETIC SURFACES, ISLANDS

Electron beam mapping of the ATF vacuum magnetic surfaces .....	389
<i>F.S.B. Anderson, A.C. England, R.J. Colchin, J.H. Harris, D.L. Hillis, M. Murakami, G.H. Neilson, J.A. Rome, M.J. Saltmarsh, M.A. Henderson, C.M. Simpson</i>	

Field error modeling studies in the ATF .....	393
<i>D.K. Lee, J.H. Harris, R.J. Colchin, A.C. England, G.S. Lee, V.E. Lynch, G.H. Neilson, M.J. Saltmarsh, F.S.B. Anderson, J.D. Hanson</i>	
Magnetic surface measurement in CHS .....	397
<i>H. Yamada and the CHS Group</i>	
Electron beam measurements in SHEILA using a simple method of image intensification .....	401
<i>B.D. Blackwell, T.Y. Tou</i>	
Vacuum field optimization and the effects of field errors on the flux surfaces of the H-1 heliac .....	405
<i>B.D. Blackwell, T.Y. Tou, D.-F. Zhou, L.E. Sharp</i>	
Configurational effects on plasma confinement in SHEILA .....	409
<i>S.M. Hamberger, B.D. Blackwell, and X.H. Shi</i>	
Simple method for calculating island widths .....	413
<i>J.R. Cary, J.D. Hanson, B.A. Carreras, V.E. Lynch</i>	

## STUDIES OF NEW EXPERIMENTS

Engineering aspects of H-1 .....	419
<i>B.D. Blackwell, S.M. Hamberger, Y.F. Li, L.E. Sharp, B. Shenton</i>	
Experimental equilibria, induced axial currents, and numerical studies of simulated toroidicity in linear high-beta heliacs .....	425
<i>B.A. Nelson, B.G. Miller, G. Spanjers, F.L. Ribe, D.C. Barnes, R. Bishop</i>	
Design of the Compact Auburn Torsatron .....	431
<i>R.F. Gandy, J.D. Hanson, M.A. Henderson, T. Schneider, D.G. Swanson, J.R. Cary</i>	
Analytical field results for stellarator/torsatron configurations .....	437
<i>F. Alladio, P. Batistoni, F. Crisanti, F. De Marco, S. Mancuso</i>	
Configuration studies for TJ-I upgrade .....	447
<i>J. Guasp, C. Alejaldre, A.L. Fraguas, L. García, A. Varias</i>	
R.F. stellarators .....	453
<i>J.L. Shohet</i>	
Ultra-simple stellarators .....	457
<i>T.N. Todd</i>	

## LARGE NEXT-GENERATION EXPERIMENTS

Recent status of the large helical device project .....	467
<i>A. Iiyoshi</i>	
Recent design considerations for the large helical device .....	471
<i>O. Motojima</i>	
Theoretical study of the large helical device .....	475
<i>M. Wakatani, Y. Nakamura, K. Hanatani, T. Kamimura, H. Sanuki, T. Amano, N. Nakajima, M. Okamoto, T. Hayashi, A. Fukuyama, M. Ohnishi, J. Todoroki</i>	
Physics and engineering design for Wendelstein VII-X .....	479
<i>C. Beidler, G. Grieger, F. Herrnegger, E. Harmeyer, J. Kisslinger, H. Maassberg, P. Merkel, J. Nührenberg, F. Rau, J. Sapper, R. Scardovelli, A. Schlüter, H. Wobig</i>	
Optimization of Helias for W VII-X .....	485
<i>W. Lotz, P. Merkel, J. Nührenberg, A. Schlüter, R. Zille</i>	
Low-aspect-ratio optimization studies for ATF-II .....	493
<i>S.P. Hirshman, R.N. Morris, C.L. Hedrick, J.F. Lyon, J.A. Rome, S.L. Painter, W.I. Van Rij</i>	

## NEXT-GENERATION DEVICES AND REACTORS

Divertor design study of the large helical device .....	503
<i>N. Ohyabu</i>	
Coil systems, vacuum fields, and parameter range for Wendelstein VII-X coils .....	507
<i>C. Beidler, E. Harmeyer, J. Kisslinger, P. Merkel, F. Rau, R. Scardovelli, H. Wobig</i>	

An inverse method for expanding about a magnetic axis	521
<i>D A Garren, A H Boozer</i>	
On edge structure and perturbations in a Helias vacuum field	525
<i>C Beidler, E Harmeyer, F Herrnegger, J Kisslinger, F Rau, R Scardovelli, H Wobig</i>	
Neoclassical transport in a modular Helias	535
<i>C D Beidler, E Harmeyer, J Kisslinger, F Rau, R Scardovelli, H Wobig</i>	
Numerical methods for stellarator optimization	539
<i>R N Morris, C L Hedrick, S P Hirshman, J F Lyon, J A Rome</i>	
Coil configurations for low aspect ratio stellarators	545
<i>J A Rome, R N Morris, S P Hirshman, R H Fowler, P Merkel</i>	
High-field, high-current-density, stable superconducting magnets for fusion machines	551
<i>J W Lue, L Dresner, M S Lubell</i>	
Alpha-particle losses in compact torsatron reactors	557
<i>S L Painter, J F Lyon</i>	
Transport survey calculations using the spectral collocation method	567
<i>S L Painter, J F Lyon</i>	

### IMPURITIES, DIVERTORS

Optical measurements of ECRH helium plasma in the L-2 stellarator	579
<i>N P Donskaya, N F Larionova, V I Roshchin, A D Smirnova, G S Voronov</i>	
Investigations of impurity radiation during the initial phase of W VII-AS operation	583
<i>R Brakel, R Burhenn, H Hacker, H J Jackel, A Weller, W VII-AS Team, ECRH Group, NBI Group</i>	
Impurity studies and transport in ATF	589
<i>L D Horton, E C Crume, H C Howe, R C Isler</i>	
Neutral transport and plasma behavior in Heliotron E divertor	593
<i>T Obiki, T Mizuuchi, F Sano, S Sudo, H Zushi, M Sato, H Kaneko, M Nakasuga, K Hanatani, H Okada, M Ima, T Kawabata, H Matsuura, M Harada, M Wakatani, A Iyoshi, K Muraoka, K Uchino</i>	
Impurity studies for the RF heated plasma in the Uragan-3 torsatron	599
<i>V V Vasil'ev, V S Voitsenya, E D Volkov, O S Pavlichenko, G N Polyakova, V G Konovalov, V D Kotsubanov, V V Chechkin, L I Grigor'eva, I K Nikolskiy</i>	

### BOOTSTRAP CURRENTS

Bootstrap current in stellarators	607
<i>A H Boozer, H Gardner</i>	
Bootstrap current control and the effects of the radial electric field in stellarators	611
<i>K C Shaing, B A Carreras, E C Crume, N Dominguez, S P Hirshman, V E Lynch, J S Tolliver, W I Van Rij</i>	
Bootstrap currents in Helias configurations	621
<i>C Beidler, E Harmeyer, F Herrnegger, J Kisslinger, H Maassberg, A Montvai, F Rau, R Scardovelli, H Wobig</i>	
Quasi stationary currents in the RF heated plasma of the Uragan-3 torsatron	627
<i>Yu V Gutarev, Yu K Kuznetsov, O S Pavlichenko, V K Pashnev, O M Shvets</i>	
List of Participants	633

## SUMMARY OF PRESENTATIONS

J.F. Lyon

Oak Ridge National Laboratory  
Oak Ridge, Tennessee  
United States of America

### 1. INTRODUCTION

The material presented at the workshop covered a wide range of topics in current stellarator research, but many of the areas discussed also have wider relevance to toroidal confinement systems.

Most of the papers presented were on experimental results from four major stellarators [Heliotron E, the Advanced Toroidal Facility (ATF), Wendelstein VII-AS (W VII-AS), and the Compact Helical System (CHS)], on design activities for two near-term helical-axis stellarators (H-1 and TJ-II), and on studies for next-generation stellarators [the Large Helical Device (LHD), W VII-X, and ATF-II]. A relatively small number of theoretical papers was presented, in contrast to earlier workshops, and most of these were related to optimization of stellarator performance. This shift is probably due both to a maturing of present stellarator theory and to the need for more definitive tests of theory, and more experimental information to improve theoretical models, from the present generation of experiments.

For this summary of the workshop, the areas covered are summarized under experimental overviews, transport, RF heating, magnetohydrodynamic (MHD) equilibrium and stability, design of new devices, and next-generation experiments.

### 2. MAIN STELLARATOR EXPERIMENTS

Recent results from ten operating stellarator experiments were presented. Device parameters for the larger of these experiments, and for the next-generation devices discussed in Section 7, are given in Table I. These devices fall into two general categories: the helical-winding torsatrons (or heliotrons) with significant shear and a central magnetic well (Heliotron E, ATF, CHS, Uragan-3M, Uragan-2M, LHD, and ATF-II) and the modular-coil devices with low shear and a global magnetic well (W VII-AS, TJ-II, H-1, and W VII-X). The last three of these new devices will have a significant helical-axis component.

Present stellarators have no significant net plasma current, a few kiloamperes at most. Plasma startup is usually accomplished with fundamental or second harmonic ECH, although ICRF has been studied in Uragan-3 and CHS. High-power neutral beam injection (NBI) is oriented perpendicular to the plasma in the older, smaller-access experiments (the earlier W VII-A and Heliotron E) and tangential to the plasma in the newer experiments (ATF, W VII-AS). These devices cover a wide range of magnetic

**TABLE I. PARAMETERS FOR THE LARGER STELLARATOR EXPERIMENTS**

Experiment	Location	$R_0$ (m)	$\bar{a}$ (m)	$V_p$ (m <sup>3</sup> )	$B_0$ (T)	$T_{\text{pulse}}$ (s)	$P_{\text{aux}}$ (MW)
<u>Operating</u>							
W VII-AS	Garching, FRG	2.0	0.2	1.58	3.0	3	5.6
ATF	Oak Ridge, U.S.A.	2.1	0.27	3.02	2.0	5	3
Heliotron E	Kyoto, Japan	2.2	0.2	1.74	2.0	0.5	7
CHS	Nagoya, Japan	1.0	0.2	0.79	1.5	2	4
Uragan-3M	Kharkov, U.S.S.R.	1.0	0.11	0.24	2.0	0.5	1.2
<u>Near-Term</u>							
Uragan-2M	Kharkov, U.S.S.R.	1.7	0.22	1.62	2.4	2	5
TJ-II	Madrid, Spain	1.5	0.22	1.43	1.0	0.5	0.4
H-1	Canberra, Australia	1.0	0.22	0.96	1.0	1	0.2
<u>Next-Generation</u>							
W VII-X	Garching, FRG	6.5	0.65	54	3.0	>10	20–30
LHD	Toki, Japan	4.0	0.5	20	4.0	>5	20
ATF-II	Oak Ridge, U.S.A.	2.0	0.52	11	4–5	$\infty$	10 15

configuration properties (rotational transform, shear, magnetic well extent, cross-section shaping, helical-axis excursion, etc.). The magnetic (or flux) surfaces are inherently non-axisymmetric; the shape of these surfaces throughout a toroidal field period determines the magnetic configuration properties.

W VII-AS at the Max-Planck-Institut für Plasmaphysik (IPP Garching), a modular-coil stellarator successor to the successful W VII-A stellarator, began operation in May 1988. It is designed to test magnetic configurations with reduced secondary parallel (Pfirsch-Schlüter) currents and reduced variation of  $\int dl/B$  on flux surfaces, reduced outward axis (Shafranov) shift with increasing beta, and reduced deviations of passing-particle orbits from flux surfaces. The report of H. Renner on the first year of operation of W VII-AS discussed their magnetic surface mapping studies and initial operation with ECH and NBI at 1.25 T and 2.5 T. Because of the low shear, good magnetic surfaces were obtained except very near low-order rational values of rotational transform ( $t = 1/q$ ). ECH (<400 kW at 70 GHz) was used to produce plasmas with  $n_e < 2 \times 10^{19} \text{ m}^{-3}$ ,  $T_e \geq 1 \text{ keV}$ ,  $T_i \sim 0.2 \text{ keV}$ , and  $\tau_E \sim 5 \text{ ms}$  at  $B_0 = 1.25 \text{ T}$ ; at  $B_0 = 2.5 \text{ T}$ , the plasma parameters could be increased to  $n_e < 4 \times 10^{19} \text{ m}^{-3}$ ,  $T_e \leq 2 \text{ keV}$ ,  $T_i \sim 0.4 \text{ keV}$ , and  $\tau_E = 15 \text{ ms}$ . Discharge durations of 0.5 s with ECH and 0.3 s with NBI alone were obtained; the central beta was limited to 0.5% owing to density limitations. Cyclic, partial collapse-type phenomenon were also observed, but radiation losses were not important in ECH discharges. Compensation for bootstrap and heating-driven currents, which can affect the magnetic configuration, was possible with ECH (variable  $k_{\parallel}$  spectrum), NBI, and a small loop voltage.

ATF at Oak Ridge National Laboratory (ORNL), presently the world's largest stellarator, began operation in January 1988. It is a moderate-aspect-ratio ( $R_0/\bar{a} = 7.8$ ) torsatron designed to access a high-beta second stability region and to explore a wide range of magnetic configurations. J. Lyon (ORNL) reported activities during the first year of ATF operation that included commissioning of the device and its heating and diagnostic systems, electron-beam mapping of the vacuum flux surfaces, analysis and correction of some resonant low-order field perturbations, study of second stability behavior, and confinement studies of ECH and NBI discharges. Typical parameters with 1.4-MW NBI at  $B_0 = 0.95$  T were  $n_{e0} = 5 \times 10^{19} \text{ m}^{-3}$ ,  $T_{e0} = 0.6$  keV,  $T_{i0} = 0.26$  keV,  $\beta_0 \simeq 3\%$ ,  $\tau_E \simeq 5$  ms, and  $Z_{\text{eff}} = 1.5$ -2. Higher values for  $T_{e0}$  (1 keV) and  $\tau_E$  ( $\simeq 15$  ms) were obtained at lower density with ECH alone. Initial (1988) operation showed narrow pressure profiles and second stability behavior at lower beta than expected, and revealed uncompensated dipoles in the leads to the helical windings, which were then made more toroidally symmetric. Energy confinement times obtained with NBI and ECH roughly followed the scaling used in the LHD studies. Although 1-s operation could be obtained with ECH alone, a plasma collapse was observed within 100 ms after the start of NBI. H. Howe (ORNL) reported time-dependent transport modeling of ECH and NBI-heated plasmas for the full three-dimensional (3-D) ATF geometry that reproduced the main features of the discharge, including the radiation-induced temperature collapse.

CHS at Nagoya University Institute of Plasma Physics (IPP Nagoya), now part of the new multi-university National Institute for Fusion Science (NIFS), started operation in June 1988. Its magnetic configuration is similar to that of ATF, but with considerably lower aspect ratio ( $R_0/\bar{a} = 5$ ). K. Matsuoka (IPP Nagoya) reported on a range of experiments in CHS: electron-beam mapping of flux surfaces and plasma production and heating with both ECH and ICRF. Typical parameters for  $B_0 = 0.5$ -1.5 T are  $T_{e0} = 300$ -900 eV and  $\bar{n}_e = (2-6) \times 10^{18} \text{ m}^{-3}$  with 120-kW, 28-GHz ECH and  $T_{e0} = 200$ -300 eV,  $T_{i0} = 200$ -300 eV, and  $n_{e0} = (5-6) \times 10^{18} \text{ m}^{-3}$  with different ICRF plasma production schemes. Hollow density profiles observed with ECH suggest that the drift motion of high-energy electrons with  $v_{\parallel}/v \ll 1$  may play an important role in the particle and energy transport; the transport is enhanced over that from a simple neoclassical model (H. Iguchi, IPP Nagoya), so optimization of particle orbits is important, even for electron confinement, in low-aspect-ratio helical devices. As in ATF, shifting the plasma inward improved the plasma performance, partly because of the improved omnigenicity of the shifted-in configuration.

Heliotron E at Kyoto University Plasma Physics Laboratory (Kyoto PPL), the first of the present generation of heliotron/torsatron experiments, has been in operation since 1980. Recent modifications and research emphasis have been directed toward the design needs of the LHD. T. Obiki (Kyoto PPL) reported on recent experiments in Heliotron E. Magnetic configuration studies (inward and outward shifts of the magnetic axis) indicate that the best operation, which occurs for inward axis shifts of 2-4 cm, depends on both MHD activity and trapped-particle confinement. Divertor plasma properties (with helical divertor baffles along one-fifth of the torus) do not depend on the presence of the baffles, possibly because of the short baffled region and the short connection length from the

baffle throat to the wall. Plasma-wall interaction studies (with carbon tiles in the divertor region) show that hydrogen recycling can be reduced below one only with low-power NBI and helium discharge cleaning and that iron impurities are still of the same order as with an all-metal wall.

The older (1975) L-2 stellarator at the Institute for General Physics (IGP) in Moscow is a conventional stellarator with toroidal field (TF) coils and an Ohmic heating transformer. G. Voronov (IGP Moscow) reported on optical measurement of ECH helium plasmas in L-2. The radiative losses were lower ( $<20\%$  of the absorbed ECH power) and the wall condition had less effect on the plasma with helium plasmas. Typical parameters were  $T_{e0} \simeq 900$  eV at  $\bar{n}_e \simeq 8 \times 10^{18} \text{ m}^{-3}$  with 60- to 70-kW, 37.5-GHz ECH power absorbed.

The Uragan-3M torsatron at the Kharkov Institute of Physics and Technology, a rebuilt version of the earlier (1982) Uragan-3 experiment with improved helical winding accuracy and a more flexible vertical field (VF) coil set, started operation in late 1988. It features three helical windings, rather than the two of other torsatrons, for more shear and more triangularity in the magnetic surfaces. O. Pavlichenko (Kharkov) discussed the power balance for low-density currentless plasmas in Uragan-3 produced by ICRF (0.2-0.3 MW at  $\omega \simeq 0.8\omega_{ci}$ ); the parameters obtained were  $T_i \leq 1.1$  keV,  $\langle\beta\rangle \leq 0.6\%$ ,  $\bar{n}_e = (2-3) \times 10^{18} \text{ m}^{-3}$ , and  $\tau_E = 5$  ms at  $B_0 = 0.44$  T. Most ( $\simeq 90\%$ ) of the ICRF power is absorbed and dissipated by a poorly confined cold plasma mantle that surrounds a hot plasma core. Energy losses from the core are caused by electron heat conduction and radiation.

J. Shohet reviewed the torsatron/stellarator program at the University of Wisconsin [the Proto-Cleo torsatron and stellarator and the Interchangeable Module Stellarator (IMS)]. J. Talmadge described studies of convective transport in IMS plasmas [ $n_e = (0.5-3) \times 10^{17} \text{ m}^{-3}$ ,  $T_e \simeq 10$  eV, and  $T_i = 2-4$  eV]. Diffusive transport cannot explain the steady-state hollow density profiles produced with 2-kW, 7.3-GHz ECH. The measured equipotential contours differ from the measured flux surfaces; the ratio of the calculated  $\mathbf{E} \times \mathbf{B}$  drift velocities for hollow profiles and broader profiles agrees with that calculated for the ratio of convective velocities determined from the equilibrium profiles.

Studies on SHEILA at the Australian National University (ANU) in Canberra were reported by S. Hamberger and B. Blackwell. SHEILA is a small ( $\bar{a} \simeq 3$  cm,  $R_0 = 18.8$  cm), three-field-period heliac, with a small  $\ell = 1$  winding around the central toroidal ring, that produces plasmas with  $n_e \sim 10^{18} \text{ m}^{-3}$  and  $T_e \sim 10$  eV for  $\sim 20$ -ms pulses at  $B_0 \leq 0.25$  T. The helical-axis plasma configuration measured with probes agrees well with the calculated bean-shaped magnetic surfaces. As in other low-shear devices, the magnetic surfaces deteriorate near low-order resonant values of  $\nu$  (1, 3/2). ECH ( $\leq 2$  kW at 2.45 GHz) produces densities up to two orders of magnitude above ordinary-mode (O-mode) cutoff, which may be caused by mode conversion effects or other effects in the evanescent field region. Measurements of coherent fluctuations in SHEILA are generally in good agreement with a linear dispersion theory for electrostatic collisional drift waves in a cylindrical approximation.

Initial results from the small ( $R_0 = 48$  cm,  $\bar{a} = 7$  cm) TU-heliac at Tohoku University in Sendai were presented by H. Watanabe. Measurements of magnetic surfaces with electron beams in vacuum and with probes for an ECH (3-kW, 2.45-GHz, 3-ms) plasma with  $n_e = (0.1-3) \times 10^{16}$  m $^{-3}$  and  $T_e = 2-10$  eV are in good agreement with the calculated surfaces. Heliac behavior at high beta ( $\langle\beta\rangle \sim 50\%$ ) has been studied in the 3-m linear theta pinch High-Beta Q-Machine (HBQM) at the University of Washington (B. Nelson). Studies are under way to eliminate the axial current induced by the fast hard-core current and to simulate toroidicity effects with a shifted hard core.

### 3. TRANSPORT

Roughly one-third of the papers at the workshop dealt with various aspects of confinement in stellarators: magnetic configuration studies, plasma currents, and particle and impurity control and divertors.

#### 3.1. Magnetic configuration studies

Electron-beam measurements of magnetic surfaces were reported for ATF, CHS, Uragan-3M, and SHEILA. The ATF studies (R. Colchin, ORNL, and F. Anderson, U. Wisconsin) revealed a large ( $\approx 6$ -cm-wide) island at the  $\iota = \frac{1}{2}$  radius and smaller islands at other low-order rational  $\iota$  values that were independent of magnetic field, indicating an intrinsic error in the ATF coil system. D. Lee (ORNL) showed that the field perturbation was due to loops in the current feeds to the helical windings; close agreement between the calculations and the experimental data was obtained for both island width and phase for different  $\iota$  values. Adding current loops at other locations to restore the 12-fold toroidal symmetry of the helical field (HF) windings caused all islands, except the central one at  $\iota = \frac{1}{3}$ , to decrease with  $B_0$  and reduced the large  $\iota = \frac{1}{2}$  island width to  $\approx 1$  cm at  $B_0 = 1$  T, in agreement with calculation. J. Cary (U. Colorado) presented a simple, fast method for calculating magnetic island widths that uses only information obtained by integrating along the field line at the center of the island; these calculations reproduced the ATF results with an accuracy of  $\lesssim 30\%$ .

Yu. Kuznetsov (Kharkov) reported that new  $\ell = 3$  helical windings on Uragan-3 (renamed Uragan-3M) increased the average radius of the last closed magnetic surface from  $\approx 8$  cm with the old windings to  $\approx 11$  cm with the new set. A small remaining field perturbation causes islands at the  $\iota = \frac{1}{3}$  surface and introduces a thin ergodic layer between the confinement region and the diverted magnetic flux. Magnetic surface measurements in CHS reported by H. Yamada (IPP Nagoya) showed closed magnetic surfaces out to 95% of the expected radius of the outermost surface. Small magnetic islands caused by the background ambient field decreased with increasing  $B_0$ ; the  $\iota = \frac{1}{2}$  island width extrapolates to  $\approx 5$  mm at  $B_0 = 1$  T. Calculations (B. Blackwell, ANU) indicate that it should be possible to limit the island size in H-1 in the central 75% of the plasma volume to 1 cm.

Plasma confinement in W VII-AS (H. Renner, IPP Garching) exhibits a strong dependence on the edge  $\iota$  value, as in W VII-A. Optimum confinement occurs close to, but not at, low-order rational values of  $\iota$  ( $\frac{1}{4}, \frac{1}{3}, \frac{1}{2}$ ). Small shear is favorable if such resonances

can be avoided. The transport seems to be anomalous in the initial experiments with ECH at low density; the experimental values for  $\chi_e$  are a factor of 3 higher at the center and a factor of 10 higher at half the plasma radius (where  $\chi_e$  is at a minimum) than the calculated neoclassical values, and the experimental values for  $\chi_e$  varied less with plasma parameters ( $T_e$ ) than do the neoclassical values.

H. Zushi (Kyoto PPL) discussed the effects of the magnetic axis shift on transport and MHD stability in Heliotron E. Optimum confinement was found when the magnetic axis was shifted in by  $\sim 10\%$  of the plasma radius, corresponding to the highest fraction of confined trapped particles and the highest shear. An outward axis shift is important for increasing beta because even a small magnetic well stabilizes internal modes in the center. Too large an inward shift creates a magnetic hill configuration in which MHD instabilities affect transport. Combining a magnetic well with improved transport is the aim of current experiments on Heliotron E with an additional toroidal field.

Some theoretical papers were presented on improvement of confinement in stellarators. C. Hedrick (ORNL) related two optimization techniques, that of Mynick ( $\sigma$ -optimization) and that of Nührenberg (quasi-helical field), to single particle orbits and showed that reducing transport in the  $1/\nu$  regime reduces it over a broad range of collisionality. K. Shaing (ORNL) showed that a more negative value of  $E_r$  and/or a more positive value of  $dE_r/dr$  can reduce the fluctuation amplitude associated with pressure-gradient-driven turbulence, which is consistent with results from Heliotron E.

### 3.2. Plasma currents

Although stellarators are designed for net-current-free operation, net toroidal plasma currents can arise from external heating (ECH, NBI, ICRF) and from finite plasma pressure (equilibrium and bootstrap currents). H. Maassberg (IPP Garching) reported that the pressure-driven component of the plasma current in W VII-AS was in rough agreement with that predicted for the neoclassical bootstrap current and that an ECH-driven component was observed. Yu. Kuznetsov (Kharkov) reported that quasi-stationary currents observed in Uragan-3 for RF-heated plasmas could be explained by theory; the toroidal current agrees with the bootstrap current only for low collisionality ( $\nu_e' \simeq 1$ ), and RF-driven currents and inductive currents probably account for the observed collisionality dependence.

A. Boozer (College of William and Mary) reviewed the theory of bootstrap currents in stellarators. H. Wobig (IPP Garching) reported that bootstrap currents calculated for optimized Helias configurations could be a factor of 10 below that in an equivalent axisymmetric (tokamak) case, but these currents depended sensitively on the Fourier spectrum of the magnetic field, the radial electric field, and the collisionality. The effects of the radial electric field on the bootstrap current in ATF-like configurations are weak in the  $\nu_{\text{eff}}/\Omega_E \ll 1$  regime (K. Shaing, ORNL). The bootstrap current can be cancelled or reversed with a poloidal field coil system or addition of a small  $\ell = 1$  field component.

### 3.3. Particle and impurity control, divertors

Particle and impurity control is an important issue for stellarators, and the magnetic geometry of stellarators lends itself to use of a divertor. H. Ringler (IPP Garching) reported  $H_\alpha$  measurements and 3-D DEGAS code simulations for W VII-AS and preliminary estimates of electron fluxes for ECH plasmas that indicated consistency with neoclassical predictions in the high-temperature-gradient region, anomalous fluxes at the edge,  $\chi_i \sim (0.05 - 0.1)\chi_e$ , and recycling (from the limiter) coefficients near one. K. Ida (IPP Nagoya) reported toroidal and poloidal asymmetries in the neutral and impurity particle fluxes in CHS caused by gas puffs, limiters, and RF antennas. R. Langley (ORNL) reported techniques for cleaning and conditioning the ATF vacuum vessel that allowed long-pulse ECH operation and rapid cleanup of a graphite-protected ICRF antenna.

P. Mioduszewski (ORNL) reported on edge plasma and divertor studies in ATF that showed a heat flux of 150–300 W/cm<sup>2</sup> with a decay length of 2 cm at the last closed magnetic surface, 3% (NBI) and 16% (ECH) of the input power on the limiters, and a particle flux of several times 10<sup>17</sup> cm<sup>2</sup>/s with a half-width of 2 cm in the divertor stripes. T. Obiki (Kyoto PPL) reported that neutral transport for a partial divertor baffle in Heliotron E agreed to within a factor of 2 with a simple divertor plasma model. N. Ohya (NIFS) reported on divertor design studies for LHD with different schemes for the divertor baffles. D. Anderson and P. Matthews (U. Wisconsin) reported on divertor experiments with biased targets in IMS. Potentials applied to these plates resulted in a redistribution of the plasma flow to any given divertor bundle caused by  $\mathbf{E} \times \mathbf{B}$  drifts just outside the last closed flux surface. Comparison of the diverted plasma flow in IMS at 2.6 kG and at 5.8 kG showed a poloidally asymmetric flow and an abrupt distribution change when the electron cyclotron resonance moved from inside the magnetic axis to outside it, reflecting a gross change in the transport at the plasma edge.

L. Horton (ORNL) reported transport modeling of multi-charge-state impurities in ATF that reproduces the basic features of the experimental line radiation and predicts a collapse of the plasma temperature and density driven by light impurity radiation. In the experiment, the collapse appears to be initiated by a strong, poloidally asymmetric plasma-wall interaction on the small-major-radius side. S. Morita (IPP Nagoya) reported that an inward plasma shift causes a radiative collapse on CHS because of a strong plasma-wall interaction; limiter-induced collapses are due to an increase of the hydrogen recycling rate at the limiter. Studies of impurity radiation during the initial phase of W VII-AS operation (A. Weller, IPP Garching) showed low radiative power fractions ( $\simeq 20\%$  of the ECH power) at low densities;  $Z_{\text{eff}}$  dropped from  $\simeq 5$  to  $\simeq 2.5$  as the density was increased. Agreement between the measured and calculated total radiation profiles is improved if diffusive spreading, impurity density peaking, and charge-exchange recombination effects are included in the calculations, but a factor of  $\sim 2$  discrepancy remains. Impurity studies for RF-heated plasmas in Uran-3 (O. Pavlichenko, Kharkov) indicate that light impurities played a minor role in the power lost, consistent with neoclassical predictions, and that metal impurities from the helical winding cases were the cause of the radiative losses.

## 4. RF HEATING

Most of the RF heating studies reported at the workshop were on ECH for W VII-AS, CHS, and ATF. G. Müller (Institut für Plasmaforschung, Stuttgart) and H. Maassberg (IPP Garching) reported on ECH and current drive studies in W VII-AS. Initial experiments used 70-GHz ECH at up to 0.6 MW for up to 0.5-s pulse lengths at the fundamental resonance (1.25 T) and the second harmonic (2.5 T). Centrally peaked deposition produced peaked  $T_e$  profiles, and off-axis heating produced flattened profiles. The absorption efficiencies ( $\eta \sim 70\%$  at  $\omega_{ce}$  and  $>90\%$  at  $2\omega_{ce}$ ) agreed with 3-D ray tracing calculations. Changing the toroidal launching angle to vary  $k_{\parallel}$  allowed compensating for the pressure-driven bootstrap plasma current with an ECH-driven current. The dependence of the second harmonic current drive efficiency ( $\leq 20$  A/kW) on the launch angle agreed to within a factor of 2 with theoretical calculations using different simplified models.

T. Bigelow (ORNL) reported on measurements of ECH extraordinary-mode (X-mode) absorption at  $2\omega_{ce}$  on ATF with a polarization-controlled beam launcher that indicate nearly complete absorption under the best conditions. Absorption is small at low density or with a shifted resonance zone, and mode coupling to the perpendicular polarization has been observed, presumably owing to the shear in the ATF field.

An analytic model for ECH profiles derived from ray tracing in a finite-beta plasma was presented by R. Goldfinger (ORNL). The scaled model agrees to within 20% with heating profiles derived from ray-tracing calculations over a wide range of beta and has been applied to calculation of scattering of second harmonic X-mode rays from the ATF vacuum vessel walls. M. Carter (ORNL) reported nonlinear calculations of ECH plasma production at the second harmonic that agreed with experimental results from Uragan-3 (Kharkov). C. Alejaldre of the Centro de Investigaciones Energéticas, Medioambientales, y Tecnológicas (CIEMAT) in Madrid included the effect of a superthermal tail in the electron distribution function in a ray-tracing code and calculated the microwave absorption for TJ-II and for an  $\ell = 1$  torsatron (STORM) under construction at CIEMAT. Strong quasi-linear modification of the wave damping can occur and change the overall power absorption significantly.

A variety of ICRF waves (whistler, slow wave, ion Bernstein wave) were used to produce and heat currentless plasmas in CHS (K. Nishimura, IPP Nagoya). Plasmas with  $n_{e0} = (2-5) \times 10^{18} \text{ m}^{-3}$ ,  $T_{e0} = 100-300 \text{ eV}$ , and  $T_{i0} = 200-300 \text{ eV}$  were produced for a wide range of magnetic fields ( $B_0 = 0.15-1.5 \text{ T}$ ).

## 5. MHD EQUILIBRIUM AND STABILITY

2-D and 3-D MHD equilibrium and stability theories are well-developed areas for stellarators and are used in the design optimization of new experiments. O. Betancourt (City College, City University of New York) described extension of the 3-D spectral code BETAS to include free-boundary calculations with increased resolution and efficiency compared to the finite-difference BETA code. P. Garabedian (New York U.) also reported on a revision of the BETA code (BEFREE) to test the stability of low-order, free-boundary

modes in stellarators. Artificial viscosity was added to improve convergence of the finite-difference calculations, and a spectral representation at the magnetic axis was added for more robust behavior, allowing calculation of the energy to  $\geq 10$  significant figures on any fixed mesh.

M. Wakatani (Kyoto PPL) discussed the relation between the (high- $n$ ) Mercier criterion and low- $n$  mode stability for an ATF-like case and for a cylindrical plasma model. The differences relate to marginal stability, finite Larmor radius effects, and the numerical procedures (mesh size) used. N. Dominguez (ORNL) also studied the relationship between the stability properties of ideal low- $n$  internal modes and the 3-D ideal Mercier criterion for  $\ell = 2$  torsatrons. The critical beta given by the Mercier criterion agreed well with that for the lowest- $n$  unstable mode, even for the global  $n = 1$  modes, showing the usefulness of the usually more pessimistic Mercier criterion as a guide. L. Garcia (U. Complutense, Madrid) reported on averaged equilibrium and stability calculations for low-aspect-ratio stellarators that allowed accurate calculation of the geodesic curvature term in the local Mercier stability criterion. The results agreed well with 3-D calculations for low-aspect-ratio torsatrons but not as well for the more complicated low-aspect-ratio heliacs. C. Alejandre (CIEMAT) reported 3-D Mercier stability for TJ-II up to  $\langle\beta\rangle \simeq 6\%$  and indications of a second stability regime.

A number of papers, both experimental and theoretical, dealt with fluctuations in stellarators. J. Harris and J. Bell (ORNL) reported a decrease of magnetic fluctuations with increasing beta in ATF for  $\beta_0 > 3\%$ , indicating beta self-stabilization and entrance into a second stability regime. V. Lynch (ORNL) reported 3-D Mercier calculations for ATF showing that for the measured profiles, which broadened with beta, ATF was following a marginally stable path into the second stability regime. L. Charlton (ORNL) reported calculations of the nonlinear saturated amplitudes of poloidal magnetic field fluctuations for resistive pressure-gradient-driven interchange modes in cylindrical geometry that showed the same beta dependence and mode structure as observed in ATF.

M. Wakatani (Kyoto PPL) reported a maximum value of beta,  $\langle\beta\rangle \sim 0.5\%$ , for the small Heliotron DR experiment that was limited by an  $m = 1$ ,  $n = 1$  mode localized at  $\varepsilon = 1$  that agreed with calculations of the ideal interchange mode using the free-boundary STEP code. The critical beta increased by  $\sim 50\%$  with addition of a small plasma current and decreased with an inward shift of the magnetic axis.

A. Navarro (CIEMAT) reported application of microwave reflectometry to the determination of electron density fluctuations in W VII-AS. Low fluctuation levels at the edge were correlated with better confinement. He also reported using reconstruction of local soft X-ray emissivity to analyze sawteeth in the previous W VII-A stellarator that revealed the axisymmetric character of the crash and an absence of hollowness afterward.

Studies on proposed fluctuation diagnostics for stellarators were also presented. C. Thomas (Georgia Institute of Technology) proposed cross-sightline correlation of Faraday rotation for measurement of perpendicular magnetic fluctuations and cross-sightline correlation of electron cyclotron emission for measurements of the local magnetic field and its fluctuations parallel to the field. C. Ma (ORNL) discussed a study of a far-infrared scattering system for ATF that could measure density fluctuations with scale lengths from 1 mm up to the plasma radius.

Studies are also being done that have relevance for tokamaks. J. Johnson (PPPL) described application of a stellarator tool to tokamaks, coupling of the 2-D axisymmetric (toroidally averaged) STEP code to the 3-D MHD equilibrium PIES code for study of the effects of plasma currents on the tokamak ripple field. B. Carreras (ORNL) analyzed dissipative trapped-electron modes in  $\ell = 2$  torsatrons using 3-D equilibrium and self-consistent finite-beta effects. For ATF, it was possible to change the localization of the mode and the ratio of helically trapped to toroidally trapped particles, and thus to control this mode, through changing the shear and the confinement of helically trapped particles. This mode is important for both stellarators and tokamaks, but can be studied more easily in stellarators.

## 6. NEW DEVICE DESIGN

Three devices under design or construction were described: the heliacs H-1 and TJ-II, and the small Compact Auburn Torsatron (CAT) at Auburn University. Reports on H-1 at ANU were given by S. Hamberger and B. Blackwell. H-1 is a three-field-period heliac (36 TF coils following a helical path around a linked central toroidal coil) with a small  $\ell = 1$  winding on the central ring for added configuration flexibility (flexible heliac). H-1 will use ICRF (180 kW at 4-26 MHz) for plasma heating; fast wave heating will be used initially, and ion Bernstein and whistler wave heating are being prepared for a second stage of heating. The TJ-II flexible heliac (C. Alejaldre, CIEMAT) is larger than H-1 ( $R_0 = 1.5$  m vs 1 m) and has four instead of three field periods, a larger  $\ell = 1$  winding on its central ring, and a vacuum vessel internal to the TF coils and central ring, rather than the external vacuum tank used for H-1. ECH will be used for plasma heating: 200 kW at 28 GHz initially, 400 kW at 53 GHz later. The toroidal spacing of the 32 TF coils is modulated to minimize the field ripple on the magnetic axis and its associated transport. The TF coils are jointed to allow installation of the highly contoured, one-piece vacuum vessel.

Two small, low-aspect-ratio stellarators are being built. C. Alejaldre (CIEMAT) described the  $\ell = 1$ , six-field-period STORM torsatron with a deep magnetic well, good equilibrium and stability properties, flexibility to study stabilization by fast particles, insensitivity to field errors, and good access for 28-GHz ECH. It should begin operation in 1990. R. Gandy (Auburn) described CAT, which features both  $\ell = 2$  and  $\ell = 1$  helical windings. It will focus on studies of magnetic islands and related plasma effects and is scheduled to start operation in late 1989. Analytic fields and orbit calculations for low-aspect-ratio ( $R_0/\bar{a} < 3$ ) torsatrons were presented by F. Alladio (Frascati). Less conventional stellarator concepts were also presented: an RF multipole stellarator using ponderomotive forces to improve confinement (J. Shohet, U. Wisconsin) and "ultra-simple" low-aspect-ratio, high-transform, single-field-period heliacs featuring just two planar coils (T. Todd, Culham).

## 7. NEXT-GENERATION EXPERIMENTS

Design studies for three large next-generation experiments were reported: LHD at NIFS, W VII-X at IPP Garching, and ATF-II at ORNL. The LHD program is more

advanced than those of W VII-X and ATF-II. O. Motojima (NIFS) reported that a new institute (NIFS), created to build LHD, will be located at Nagoya for the first few years and then moved to Toki. The schedule calls for start of experiments in 1995. The parameter goals for LHD are (1) high  $n\tau T$  at  $B = 4$  T ( $\langle T_i \rangle = 3-4$  keV,  $\langle n_e \rangle = 10^{20}$  m<sup>-3</sup>,  $\tau_E = 0.1-0.3$  s); (2) high  $T_i$  at  $B = 4$  T ( $T_{i0} = 10$  keV,  $\langle n \rangle = 2 \times 10^{19}$  m<sup>-3</sup>,  $\tau_E = 0.05-0.1$  s); and (3) high beta ( $\langle \beta \rangle = 5\%$ ) at  $B = 1-2$  T. M. Wakatani (Kyoto PPL) reported on theoretical studies of MHD equilibrium, stability, neoclassical transport, high-energy particle confinement, and NBI and ICRF for  $\ell = 2$  torsatrons with 14, 12, and 10 toroidal field periods ( $M$ ). Combining an inward magnetic axis shift with a quadrupole shaping field improved particle confinement without deteriorating the good MHD properties of the standard ( $M = 10$ ) case.

H. Wobig (IPP Garching) reported that a five-field-period Helias (Helical Advanced Stellarator) configuration had been chosen for W VII-X. The Helias configuration, with flux surfaces that change from bean-shaped to teardrop-shaped to oval in a field period and with a helical magnetic axis, has a very low Shafranov shift, MHD stability limits up to  $\langle \beta \rangle \sim 5\%$ , and reduced neoclassical transport and bootstrap currents. The aims of W VII-X are to study key issues with  $T > 5$  keV,  $n_e > 10^{20}$  m<sup>-3</sup>, and  $\langle \beta \rangle = 5\%$ . Seven optimization criteria were met simultaneously for the Helias configuration (J. Nührenberg, IPP Garching).  $R_0/\bar{a} \simeq 10$  configurations exist with good magnetic surfaces, small parallel (Pfirsch-Schlüter) currents, small magnetic axis shifts, good collisionless fast-particle orbit confinement, small bootstrap current, and high stability beta limits. Calculations of neoclassical transport in a modular-coil Helias reported by H. Wobig (IPP Garching) showed that transport caused by helical ripple was reduced by more than a factor of 10 over that for a simple  $\ell = 2$  stellarator in the low collisionality ( $\chi \propto 1/\nu$ ) regime; 12 non-planar coils per field period are required to keep the modular-ripple losses less than the helical-ripple losses. F. Rau (IPP Garching) reported on optimization of non-planar coils for W VII-X and on the edge structure (islands and ergodicity) of the magnetic field, which could be used for edge particle control.

A number of papers were presented on the ORNL ATF-II studies. S. Painter reported calculations of alpha-particle losses for compact torsatron reactors with pitch-angle scattering and finite beta; the losses amount to a significant fraction of the helically trapped particles. S. Hirshman and R. Morris reported on an optimization procedure for ATF-II that simultaneously maximizes 3-D equilibrium beta, Mercier MHD stability, and helically trapped energetic-particle orbit confinement. This method is similar to that used in the W VII-X studies, but with different optimization criteria and an assumption of low aspect ratio ( $R_0/\bar{a} \sim 4$ ). The criteria are met for  $\langle \beta \rangle \lesssim 2\%$ , but more studies are needed at  $\langle \beta \rangle \gtrsim 5\%$ . J. Rome used a variation of the Garching approach to calculate quasi-helical and modular coil sets for the finite-beta optimizations in the ATF-II studies. J. Lue reported calculations on forced-flow, cable-in-conduit NbTi/Cu conductors for next-generation stellarators that would increase the space between the plasma edge and the vacuum vessel wall. Windings with high current density (5-15 kA/cm<sup>2</sup> averaged over the winding pack) and high field at the winding (8-12 T) with adequate stability margin ( $\sim 100$  mJ/cm<sup>3</sup>) seem feasible.

## 8. CONCLUSIONS

The new experiments designed to test the principles of stellarator optimization have just come into operation within the last year; they have not yet operated at their full capability in power, density, or configuration flexibility, but preliminary results look encouraging. The primary issue, as in tokamaks, is transport. More work is needed on understanding anomalous transport and ways to improve confinement. Studies of radiative collapse, hollow density (or temperature) profiles, bootstrap currents, electric field effects, turbulence, etc., need to be pursued. The next generation of stellarator experiments is under design, but compromises between high-beta capability, trapped-particle orbit confinement and related transport, and bootstrap currents need to be refined. The proceedings of the workshop will be published by the International Atomic Energy Agency as an IAEA-TECDOC report. The next International Stellarator Workshop is planned for Yalta, USSR, in September 1991.

## ACKNOWLEDGEMENTS

The writing of this summary was supported by the Office of Fusion Energy, United States Department of Energy, under contract DE-AC05-84OR21400 with Martin Marietta Energy Systems, Inc.

## **OVERVIEW OF EXPERIMENTAL RESULTS**

**STATUS OF THE ADVANCED STELLARATOR  
WENDELSTEIN W 7AS: FIRST RESULTS  
AND FURTHER PROGRAMME**

H. RENNER, W VII-AS TEAM, NBI GROUP, ICF GROUP,  
ECRH GROUP

*W VII-AS TEAM*

E. ANABITARTE<sup>1</sup>, E. ASCASIBAR<sup>1</sup>, S. BESSHOU<sup>2</sup>, R. BRAKEL,  
R. BURHENN, G. CATTANEI, A. DODHY, D. DORST, A. ELSNER,  
K. ENGELHARDT, V. ERCKMANN, D. EVANS, U. GASPARINO,  
G. GRIEGER, P. GRIGULL, H. HACKER, H. HAILER<sup>3</sup>, H.J. HARTFUSS,  
H. JÄCKEL, R. JAENICKE, S. JIANG<sup>4</sup>, J. JUNKER, M. KICK,  
H. KROISS, G. KUEHNER, I. LAKICEVIC, H. MAASSBERG, C. MAHN,  
R. MARTIN<sup>1</sup>, G. MÜLLER, H. MÜNCH, A. NAVARRO<sup>1</sup>,  
M. OCHANDO<sup>1</sup>, W. OHLENDORF, M. PETROV<sup>5</sup>, F. RAU, H. RENNER,  
H. RINGLER, J. SAFFERT, J. SANCHEZ<sup>1</sup>, J. SAPPER,  
A.V. SAPOSHNIKOV<sup>6</sup>, F. SARDEI, I.S. SBITNIKOVA<sup>6</sup>,  
I. SCHOENEWOLF, K. SCHWÖRER<sup>3</sup>, F. TABARES<sup>1</sup>, M. TUTTER,  
A. WELLER, H. WOBIG, E. WÜRSCHING, M. ZIPPE

*NBI GROUP*

J.H. FEIST, K. FREUDENBERGER, R.C. KUNZE, W. OTT,  
F.-P. PENNINGSFELD, E. SPETH (Technology Division),  
W. MELKUS (ZTE)

*ICF GROUP*

J. BÄUMLER, W. BECKER, F. BRAUN, R. FRITSCH,  
F. HOFMEISTER, A. MURPHY, J.M. NOTERDAEME, S. PURI,  
F. RYTER, H. WEDLER, F. WESNER (Technology Division)

*ECRH GROUP*

W. KASPAREK, G.A. MÜLLER, P.G. SCHÜLLER, M. THUMM,  
R. WIENECKE (IPF Stuttgart)

EURATOM-IPP Association,  
Max-Planck-Institut für Plasmaphysik,  
Garching  
and  
Institut für Plasmaforschung,  
Universität Stuttgart, Stuttgart  
Federal Republic of Germany

**Abstract**

Beginning October 1988, after magnetic surface mapping, first plasma experiments were conducted in the advanced stellarator W 7AS. The characteristics of the device are described. During the first phase of operation, ECF 70 GHz was used to generate and heat a "currentless" plasma, which was

---

<sup>1</sup> Guest from CIEMAT, Madrid, Spain.

<sup>2</sup> Guest from Kyoto University, Kyoto, Japan.

<sup>3</sup> Guest from IPF, Stuttgart, Fed. Rep. of Germany.

<sup>4</sup> Guest from Southwestern Institute of Physics, Leshan, China.

<sup>5</sup> Guest from Ioffe Institute, Leningrad, USSR.

<sup>6</sup> Guest from General Physics Institute, Moscow, USSR

maintained in quasi-steady state for typical 0.5s. Restricted by the density limitations for ECF-applications central values of  $\beta \leq 0.5\%$  were achieved. Effects of the magnetic configuration on the confinement and measures to deal with the observed plasma current ( bootstrap current ) by ohmic heating and ECF-current drive were investigated. Preliminary results of transport analysis were compared with predictions of transport models.

In future experiments using NBI and ICF-heating towards higher densities detailed investigations of the plasma boundary, the impurity sources and transport are planned. By pressure profile shaping a description of the transport and MHD-stability behaviour of W 7AS will be possible.

## 1. CHARACTERISTICS OF WENDELSTEIN W 7AS

### MAGNETIC FIELD

The configuration of W 7AS ( major radius 2m, effective minor radius 0.15 - 0.2 m ) with  $m=5$  periods, similar to 5 toroidally linked mirrors, is produced by a system of modular coils. Each period consists of 9 individually shaped nonplanar coils / 1 /. A superimposed toroidal field and vertical field are used to modify the magnetic parameters of the configuration for flexibility: rotational transform ( 0.2 - 0.6 ), position of the magnetic axis, separatrix, shear, magnetic ripple, magnetic well etc. otherwise being fixed by the shape and arrangement of the modular coils alone. The  $\beta$ -limit for equilibrium compared with a conventional stellarator is increased to  $\beta(0) \leq 4.5\%$ . A small magnetic well is realized to guarantee stability. The stability limit of W 7AS is expected to be  $\beta \sim 2\%$ .

### HEATING

Three different heating methods are already installed at W 7AS. Figure 1 illustrates the arrangement of the main components and the diagnostics of the first experimental phase. Local power deposition and independent heating of electrons and ions will be applied to perform detailed investigations how the confinement is influenced by the temperature ratio  $T_i/T_e$ , pressure profiles, electric fields and trapped particles under conditions of distorted energy distributions. In addition, the OH transformer of the W 7A survived and is being used with small loop voltages,  $U_L \leq 0.5$  V, to control the plasma current, which is generated by the heating mechanism or by plasma pressure anisotropy.

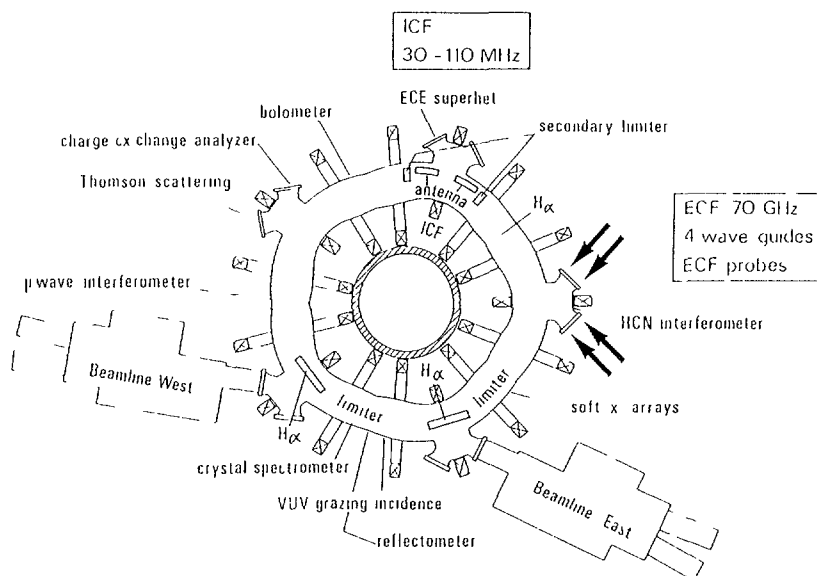


FIG 1 Advanced stellarator Wendelstein W 7AS: heating and diagnostics of the first experimental phase

### ECF at 70 GHz

Starting with neutral gas filling the application of ECF is essential for "currentless operation" of stellarators to replace ohmic heating. At Wendelstein W 7AS the ECF system is designed to feed a power of up to 1 MW ( 4 VARIAN gyrotrons: 200 kW per unit, pulse duration 3 s; 1 VARIAN pulsed gyrotron, pulse duration 0.1 s ) to the plasma. In cooperation with the ECF Group of IPF Stuttgart, a sophisticated transmission line consisting of optimized components: bends, mode converters, filters, k-spectrometer, was realized / 2 /. The plasma is finally irradiated quasioptically by focused and completely polarized beams. The use of moveable mirrors allows the interaction region of the beam with the plasma to be geometrically selected. Thus, in addition to tuning of the magnetic field local power deposition and even local current drive by variation of  $k_{\perp}$  are possible.

The fast modulation of the power allows the excitation of heat waves for investigation of local transport. Within the accessible density range and with the expected electron temperatures  $T_e < 3$  keV ECF heating will be interesting to explore transport at low collisionality. Higher  $\beta$  will be achieved at higher densities  $n \sim 10^{20} \text{ m}^{-3}$ . Gyrotrons at 140 GHz will therefore be used in the future. A pulsed gyrotron ( 140 GHz, 200 kW, 0.1 s, developed by KfK Karlsruhe ) will soon become available.

### NBI

Starting with a target plasma generated by ECF, neutral beam injection and rf at the ion cyclotron frequencies are being used to maintain plasmas at densities exceeding the cut-off densities for ECF. Fast density increase will be achieved by pellet injection. In contrast to W 7A, tangential injection with a power of up to 1.5 MW (  $H^0$  : 45 keV,  $> 1$  s ) is installed at W 7AS / 3,4 /. In view of the long interaction length of 2 m, even at low densities  $n \geq 1 \cdot 10^{19} \text{ m}^{-3}$ , the heating efficiency should be improved.

Two beamlines are used for co and counter injection, and unbalanced injection will be possible for current drive. During the first experiments with unbalanced injection currents of up to 5 kA were already observed at densities  $n \leq 4 \cdot 10^{19} \text{ m}^{-3}$  and  $T_i, T_e \sim 0.2$  keV. At a low field of 1.25 T a power of  $P_N < 750$  kW was applied and the discharge was maintained by NBI alone for 300 ms.

Compensation and control of the current by simultaneous co and counter-injection could be demonstrated.

An increase of the power to 3 MW is already being prepared, but demonstration of successful density and impurity control is a prerequisite.

### ICF

For ion cyclotron heating a flexible experimental antenna system ( 30 - 110 MHz, 1.5 MW, 0.5 s ) is installed at W 7AS. Two classical loops with a Faraday shield allow variation of the k spectra to investigate the coupling to the target plasma in the rather complicated magnetic geometry of W 7AS / 5 /. Depending on the results of the coupling efficiency and impurity handling in a next step, an antenna system developed for high power, 4 MW, and long pulse operation, 3 s, may be used.

## 2. START OF THE W 7AS EXPERIMENT

By May 1988 assembly of the coils and vessel was almost completed. After final tests the existence and quality of the magnetic surfaces of the vacuum field were investigated during the period May 18 to July 7, 1988. This was followed by completion of the components inside the vessel: limiters, carbon tiles, antenna for ECF and ICF, installations for diagnostics followed. Conditioning of the vessel began in September 1988. Baking of the vessel at  $150^\circ \text{C}$ , DC glow discharges with  $\text{H}_2$  and He gas, continuous 50 Hz ohmic discharges at low field  $B_0 \leq 0.4 \text{ T}$  and pulse cleaning with ohmic heating at full field were applied. A base pressure  $p < 4 \cdot 10^{-8}$  mbar is being maintained with a pumping speed of 5000 liters/s at the vessel. First plasma experiments were performed on October 4, 1988 by using 70 GHz ECF at the second harmonic with a field of 1.25 T for plasma generation and heating. Even with He as working gas the recycling coefficient stays below 1, so that density control by external flux using a system of piezoelectric valves operated in a feedback loop related to the line density is being applied. Wall gettering with Ti is being prepared, but has not yet been activated.

## DIAGNOSTICS AND DATA ACQUISITION

The experiment started with an almost complete set of diagnostics, planned for the first phase of experiments:

- mass spectrometer, controllable gas flux
- Thomson scattering system for measurements along a vertical line at the location of an elliptically shaped magnetic surface
- ECE superhet
- reflectometry ( in cooperation with CIEMAT, Madrid )
- ECF probes for monitoring the incident and absorbed  $\mu$ wave power and control of the beam divergence
- bolometers
- soft X-ray cameras
- charge exchange analyzers ( Leningrad )
- $H_{\alpha}$  arrays
- interferometry
- magnetic and electric measurements: Rogowski coils, flux loops, diamagnetic coils
- spectroscopy: crystal spectrometer, VUV grazing incidence spectrometer
- instrumented limiters, Langmuir probes
- targets for deposition of impurities
- CCD cameras, TV monitors

Almost complete information on plasma parameters with temporal and spatial resolution was available from the beginning of the experiments. Data handling is realized on the basis of local  $\mu$ VAX subunits. Relevant data are accumulated by the central VAX 750 computer and transferred to the computer centre at IPP. Synoptical data analysis relating to the whole data file ( presently with a content of 2 Mbyte per shot ) is made possible by the IBM system at the computer centre. Local data of the individual diagnostics can be analyzed on the subunits. These units are also available for control of diagnostics.

### 3. FIRST RESULTS OF WENDELSTEIN W 7AS

#### 3.1 MAGNETIC SURFACE MAPPING

The existence of magnetic surfaces and the approach of the magnetic parameters to those of the design were therefore extensively studied by magnetic surface mapping. Two different methods were applied. Both methods use a directed electron beam source that can be positioned on an arbitrary magnetic surface in the poloidal cross-section. Besides the standard technique, which determines the position of electron transits by the use of a capacitive probe, a faster optical method was developed in cooperation with IPF Stuttgart / 6 /: To detect the beam transits, a fluorescent rod is swept across a poloidal cross-section. An image of the spots, where electrons hit the rod, is taken by a CCD camera and developed by means of an image processor to a picture of one particular magnetic surface associated with the position of the electron gun. Analysis of the different measurements of the vacuum field shows excellent agreement with the magnetic parameters of the design / 7 /, such as rotational transform, shear, position of magnetic axis, formation of a separatrix at higher transform. No corrections of the magnetic field are needed, although small errors ( geometry, uncompensated bus bars ) are indicated by the observed islandization at rational values of the rotational transform:  $1/2$ ,  $1/3$ ,  $2/3$ ,  $2/5$  etc.

#### 3.2 PLASMA EXPERIMENTS

The initial plasma experiments were aimed at exploring the performance of the stellarator and the accessible range of parameters. In a first approach, the confinement as a function of the parameters of the magnetic field, making full use of the flexible ECF launching system, was studied. Owing to the restrictions on the density the maximal achievable  $\beta(0)$  is close to 0.5%. Up to now data from 3400 shots have been accumulated. Activities were concentrated on investigations of plasmas generated by ECF applications. Mostly 2 gyrotrons with an incident power of  $P_N < 400$  kW and a typical pulse duration of 0.5 s were used. The microwave beams are launched at the completely polarized  $HE_{11}$  mode: At the magnetic field of 1.25 T ( 3100 shots ) the polarization is reversed for x-mode irradiation, whereas at 2.5T ( 300 shots ) o-mode irradiation is appropriate. Without any preionization the plasma is generated from a neutral gas filling in the vessel.

### 3.3 RESULTS OF THE PLASMA EXPERIMENTS

#### 3.3.1 PARAMETER RANGE FOR ECF AT 70 GHz

At present, plasma experiments in W 7AS were restricted by the limitations of the power available and the density limits for the application of 70 GHz. Mostly 2 gyrotrons were operated with a power  $P_N < 400$  kW: Irradiating with the second-harmonic extraordinary mode at a main field of 1.25 T, it was possible to maintain plasma in the quasi-steady state with averaged densities  $n < 2 \cdot 10^{19} \text{ m}^{-3} < n_{\text{cutoff}} = 3 \cdot 10^{19} \text{ m}^{-3}$ , with electron temperatures  $T_e \geq 1$  keV and ion temperatures  $T_i \sim 0.2$  keV. The single-path power absorption, as monitored by the ECF probes, approaches 100% during the stationary phase. The high heating efficiency agrees with results from ray-tracing calculations on the basis of experimental density and temperature profiles and is consistent with the transient temperature decay measured by ECE diagnostics after switching off the incident power. The typical energy replacement time for these discharges is about 5 ms and is reduced with increasing temperature. Operating at the fundamental mode with a magnetic field of 2.5 T the parameters can be increased to densities  $n < 4 \cdot 10^{19} \text{ m}^{-3} < n_{\text{cutoff}} = 6 \cdot 10^{19} \text{ m}^{-3}$ ,  $T_e \leq 2$  keV and  $T_i \sim 0.4$  keV. The maximal energy replacement time at high density is evaluated to be 15 ms with slightly reduced heating efficiencies of 0.9. The data base, especially for the case of 2.5 T, is very small and improvements are expected. Suprathermal electrons, at a small fraction with energies about 10 times the thermal energies, are only observed at very low densities:  $n \leq 10^{19} \text{ m}^{-3}$ .

#### 3.3.2 CONFIGURATIONAL EFFECTS AND PLASMA CURRENT

Systematic studies of the confinement as a function of the magnetic configuration for the accessible range of  $\beta \leq 0.5\%$  at field 1.25 T a behaviour was found similar to that observed on W 7A: deterioration of the confinement is associated with the existence of low-order resonant surfaces in the confinement region. Control of the boundary value of the rotational transform, far from resonances, and sufficiently low shear are necessary for optimal confinement. During discharges with long pulse duration,  $>200$  ms, a bootstrap current, strongly dependent on the temperature profiles and additive to the rotational transform of the vacuum field, becomes stationary at values of up to 3 kA. Control of the net current for stationary conditions with good confinement was successfully applied by two different methods: induced voltages by means of OH transformer and ECF current drive. Even fine tuning of the current density profiles by local ECF current drive / 10 / seems possible and may be necessary for approaching higher  $\beta$ .

#### 3.3.3 TRANSPORT

##### BOOTSTRAP CURRENT

The theoretical values of the neoclassical bootstrap current calculated by means of the DKES code ( drift kinetic equation solver by S.P. Hirshman, W.J. Rij ) on the basis of the measured density and temperature profiles were roughly consistent with the experimental observations in W 7AS. The modification of the magnetic configuration by the bootstrap current is especially large at the low field and the high temperature gradients / 10 /. Operation at higher field may be favourable: At higher field, according to the scaling for the bootstrap current the amplitude will be diminished. In addition the contribution of the related poloidal field to the transform scales as  $1/B$ .

##### ELECTRON HEAT CONDUCTION

Some preliminary studies of the electron heat conduction have been discussed. Under conditions of optimal confinement, which were established at particular values of the rotational transform close to  $1/3$  and  $1/2$  by current control, the energy balance was evaluated on the basis of measured density and temperature profiles. For almost all discharges with different heating powers the experimental values of the electron heat conductivity were at the radius  $a/2$  in the range of 0.7 to  $2 \text{ m}^2/\text{s}$ . Towards the centre a slight increase is observed, but a strong increase is seen at the boundary. Especially, at the boundary significant discrepancies in relation to the theoretical predictions of the DKES code occur / 8 /. Additional losses have to be assumed in the boundary region. A destruction of the magnetic surfaces, which become rather fragile at  $T_e < 200$  eV with localized power and particle sources, may be responsible.

## PARTICLE BALANCE

Estimates of the particle confinement based on  $H_{\alpha}$  measurements and DEGAS code simulations / 9 / indicate for some particular discharges consistency with neoclassical predictions for the particle flux in the plasma gradient region and anomalous fluxes at the plasma edge ( $D \sim 1/10 \chi_e$ ).

## RADIATION AND IMPURITIES

Both the measured radiative losses as well as the calculated collisional power transfer to the ions are in the range of less than 40 kW and thus rather small. A first estimate of the impurity content, based on spectroscopic measurements, soft X-ray data, and bolometric measurements, typically leads to concentrations of oxygen and carbon of the order of 2-3%. Iron concentrations seem almost negligible but can increase to 0.03%.

Up to now, in ECF discharges radiation and impurities do not seem to be very important. Control of impurity sources and impurity transport will be studied during the next phase of experimentation and may become problematic for full use of the installed power on W 7AS towards higher densities.

## 4. AIMS OF THE EXPERIMENT AND FUTURE PROGRAMME

So far only a rather restricted parameter range has been accessible during the first experimental phase at W 7AS, mostly at magnetic field 1.25 T.

As preparatory studies for impurity and density control investigations of the boundary and of energy and particle flux to the wall influenced by the magnetic configuration are started. The impurity sources and the impurity transport are being studied by means of impurity doping ( gas flow, laser ablation and pellet injection ).

The observed enhanced losses at the plasma boundary need clarification. The role of fluctuations and the effect of ergodization or destruction of the magnetic surfaces with temperatures  $T_e < 200$  eV will be investigated with improved diagnostics: probes, reflectometry, magnetic probe arrays.

After the necessary improvement of the support of particular coils of the magnetic system planned late summer 1989 operation at magnetic field of 2.5 T will allow to continue ECF experiments in a wider density range. In future experiments the full use of the heating power will achieve higher plasma pressure of  $\beta > 1$  % to investigate the stability limits of W 7AS.

The aims of the experiments on the Wendelstein W 7AS advanced stellarator are the following:

- to produce "currentless" plasma and optimize the heating for three different heating methods: ECF 70 GHz ( 140 GHz ), NBI ( tang. injection ), ICF ( minority, second harmonic, Bernstein waves ).
- to investigate the equilibrium and stability limits of the device as function of the magnetic parameters and pressure profiles
- to describe local transport and determine the effect of magnetic ripple and trapped particles on electric fields
- to study impurity sources and transport as functions of plasma parameters and boundary conditions ( ergodization and island formation ) for possibilities of impurity and density control in stationary operation
- to demonstrate the optimization principle and provide a data base for further development of the advanced stellarator concept.

## REFERENCES

- / 1 / " Engineering problems of Wendelstein W 7AS" Sapper, J. et al. Transactions 8th Int. Conf. Structural Mechanics in Reactor Technology, Amsterdam ( 1985 ), N, p.15
- / 2 / "Microwave technology and tests of the 70 GHz/1 MW long pulse ECRH-system on W 7AS" Kasperek, W., et al., Proc. 15th Symp. on Fusion Techn. ( SOFT ), Utrecht (1988), B19
- / 3 / Lister, G.G., et al., Proc. 11th Europ. Conf. on Contr. Fusion and Plasma Physics, Aachen (1983), vol.II, p.323
- / 4 / Feist, J.H., et al., Proc. 4th Symp. on Heating in Toroidal Plasmas, Rom (1984), EUR 9341 EN, p.1051
- / 5 / Wesner, F., et al., Proc. 5th Symp. on Fusion Technology, Utrecht (1988)
- / 6 / Hailer, H., et al., Contr. Fusion and Plasma Physics, Madrid (1987), Proc. 14th Europ.Conf., Vol. I, p.423

/ 7 / Jaenicke, R., et alt., 16th Europ. Conf. on Controlled Fusion and Plasma Physics, Venedig (1989), P8 B3  
/ 8 / Massberg, H., et alt., 16th Europ. Conf. on Controlled Fusion and Plasma Physics, Venedig (1989), P8 B5  
/ 9 / Sardei, F., et alt., 16th Europ. Conf. on Controlled Fusion and Plasma Physics, Venedig (1989), P8 B6  
/ 10 / Gasparino, U., et alt., 16th Europ. Conf. on Controlled Fusion and Plasma Physics, Venedig (1989), P8 B4

## OVERVIEW OF THE ATF PROGRAM

J.F. LYON, S.C. ACETO<sup>1</sup>, F.S.B. ANDERSON<sup>2</sup>, G.L. BELL<sup>3</sup>,  
J.D. BELL<sup>4</sup>, T.S. BIGELOW, B.A. CARRERAS, M.D. CARTER,  
R.J. COLCHIN, K.A. CONNOR<sup>1</sup>, E.C. CRUME, N. DOMINGUEZ,  
J.L. DUNLAP, G.R. DYER, A.C. ENGLAND, R.H. FOWLER<sup>4</sup>,  
R.F. GANDY<sup>3</sup>, J.C. GLOWIENKA, R.C. GOLDFINGER<sup>4</sup>,  
R.H. GOULDING, J.W. HALLIWELL, J.D. HANSON<sup>3</sup>,  
J.H. HARRIS, M.A. HENDERSON<sup>3</sup>, D.L. HILLIS, S. HIROE,  
L.D. HORTON, H.C. HOWE, D.P. HUTCHINSON, R.C. ISLER,  
T.C. JERNIGAN, H. KANEKO<sup>5</sup>, R.R. KINDSFATHER,  
M. KWON<sup>6</sup>, R.A. LANGLEY, D.K. LEE<sup>4</sup>, J.N. LEOEUF,  
V.E. LYNCH<sup>4</sup>, C.H. MA, M.M. MENON, F.W. MEYER,  
P.K. MIODUSZEWSKI, T. MIZUUCHI<sup>5</sup>, R.N. MORRIS<sup>4</sup>,  
O. MOTOJIMA<sup>5</sup>, M. MURAKAMI, G.H. NEILSON, V.K. PARÉ,  
N.F. PEREPELKIN<sup>7</sup>, D.A. RASMUSSEN, R.K. RICHARDS,  
P.S. ROGERS<sup>6</sup>, J.A. ROME, M.J. SALTMARSH, F. SANO<sup>5</sup>,  
P.L. SHAW<sup>6</sup>, J. SHEFFIELD, T.D. SHEPARD, J.E. SIMPKINS,  
C.M. SIMPSON<sup>8</sup>, Y. TAKEIRI<sup>5</sup>, C.E. THOMAS<sup>6</sup>, T. UCKAN,  
K.L. VANDER SLUIS, G.S. VORONOV<sup>9</sup>, M.R. WADE<sup>6</sup>,  
T.L. WHITE, J.B. WILGEN, W.R. WING, J.J. ZIELINSKI<sup>1</sup>  
Oak Ridge National Laboratory,  
Oak Ridge, Tennessee,  
United States of America

### Abstract

Initial (1988) operation of the Advanced Toroidal Facility (ATF) showed narrow pressure profiles and second stability behavior at lower beta than expected and revealed uncompensated dipoles in the helical winding leads that have since been corrected. Energy confinement times obtained with neutral beam injection (NBI) and electron cyclotron heating roughly follow the LHD scaling. However, a plasma collapse is observed with NBI.

---

<sup>1</sup> Rensselaer Polytechnic Institute, Troy, N.Y., USA.

<sup>2</sup> University of Wisconsin, MD, USA.

<sup>3</sup> Auburn University, Auburn, AL, USA.

<sup>4</sup> Computing and Telecommunications Division, Martin Marietta Energy Systems, Inc., Oak Ridge, TN, USA.

<sup>5</sup> Kyoto University, Kyoto, Japan.

<sup>6</sup> Georgia Institute of Technology, Atlanta, GA, USA.

<sup>7</sup> Institute of Physics and Technology, Khar'kov, USSR.

<sup>8</sup> University of Maryland, College Park, MD, USA.

<sup>9</sup> Institute of General Physics, Moscow, USSR.

## I. INTRODUCTION

The Advanced Toroidal Facility<sup>1</sup> (ATF), shown in Fig. 1, is currently the world's largest stellarator. The main device and heating parameters are listed in Table I. ATF is an  $\ell = 2$  torsatron with constant-pitch helical windings and moderate plasma aspect ratio ( $A = R_0/\bar{a} = 7.8$ ). The main elements of ATF, shown in Fig. 1, are the two independent helical field (HF) windings, the three independent sets of poloidal field coils [the inner, mid-, and outer vertical field (VF) coil sets], the interior vacuum vessel with large side ( $0.6 \times 0.9$  m) and top/bottom (0.5-m diagonal) ports and smaller (0.2-m-diam) inner ports, and the exterior toroidal structural shell.

ATF occupies a position intermediate between Heliotron E and Wendelstein VII-AS in rotational transform  $\iota$  and shear. The nominal ATF magnetic configuration places the  $\iota = 1/3$  resonance near the center and the  $\iota = 1$  resonance at the edge, and it has a central vacuum magnetic well extending out to the  $\iota = 1/2$  surface. A distinguishing feature of the magnetic configuration is a self-stabilization effect<sup>2</sup> that occurs with increasing beta at lower aspect ratio; this should allow access to a second stability region with a higher beta limit and reduced anomalous transport.<sup>3</sup>

The three plasma heating systems on ATF are electron cyclotron heating (ECH) for currentless plasma startup and electron heating, neutral beam injection (NBI) for bulk plasma heating, and ion cyclotron heating (ICH) for development of long-pulse heating. The main parameters of these systems are given in Table I.

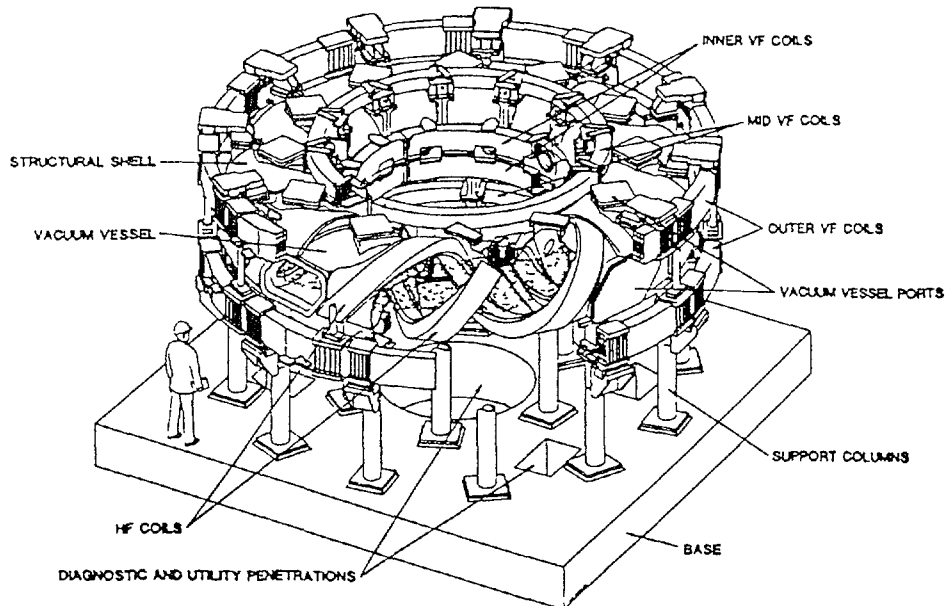


Fig. 1. An artist's sketch of ATF, showing the main components.

Table I. ATF Parameters

---

<u>Magnetic Configuration</u>			
Poloidal multipolarity, $\ell$	2	Standard central transform, $\iota(0)$	0.3
No. of field periods, $M$	12	Standard edge transform, $\iota(\bar{a})$	1.0
<u>Size</u>			
Major radius, $R_0$	2.1 m	Plasma volume, $V_p$	3.0 m <sup>3</sup>
Average minor radius, $\bar{a}$	0.27 m	Vacuum vessel volume	10.5 m <sup>3</sup>
<u>Magnetic Field</u>			
Field on axis, $B_0$	2 T		
Field flattop time	5 s at 2 T	(2.5 s at 1 T)	
<u>Plasma Heating<sup>a</sup></u>			
Electron cyclotron heating		0.4 MW, 53 GHz, steady state (0.2 MW, 53 GHz, 1 s)	
Neutral beam injection		3 MW, 40 kV, 0.3 s (1.4 MW, 30 kV, 0.3 s)	
Ion cyclotron heating		0.3 MW, 5–30 MHz, 30 s (0.1 MW, 29 MHz, 0.1 s)	

---

<sup>a</sup>Near-term (1989–1990) values; 1988 values in parentheses

The ECH power is coupled to ATF with a 6.35-cm-diam quasi-optical waveguide operating in the TE<sub>01</sub> or TE<sub>02</sub> mode. A simple open waveguide with a broad radiation pattern located 1.2 m above the ATF midplane has been used for low-field (top) launch for the 1988 studies. It has been used for second harmonic heating ( $B_0 = 0.94$  T) at the 200-kW level for up to 1-s pulses.

Two neutral beam lines are aimed tangentially 13 cm inside the standard ( $R_0 = 2.1$  m) magnetic axis to minimize beam scrape-off on the vacuum vessel walls. They are aimed in opposing directions to provide balanced injection. During the 1988 run, each beam line was used only up to 0.75 MW at 33 kV.

An uncooled fast-wave ICH antenna has been tested on ATF at the 100-kW level. The antenna uses the compact resonant double loop design developed at Oak Ridge National Laboratory with a two-tier Faraday shield and a 15-cm radial motion capability. Antenna loading experiments in hydrogen plasmas were performed at  $2\omega_{cH}$  (28.8 MHz) in the 1988 run with the magnetic axis shifted in by 5 cm. The results showed an exponential decrease (with an e-folding distance of 5 cm) in the plasma loading with increasing separation between the plasma boundary and the current strap. The maximum loading was 0.6–0.77  $\Omega$  (1.4–1.8  $\Omega\cdot\text{m}^{-1}$ ) at the minimum separation of  $\simeq 12$  cm. The loading resistance also increased linearly with density and frequency.

## II. SUMMARY OF INITIAL ATF OPERATION

The first ATF operating period in January 1988 was chiefly concerned with machine and diagnostic commissioning and with currentless plasma production using 200-kW, 53.2-GHz ECH at 0.95 T. This was followed in March and April 1988 by coil alignment studies and electron-beam mapping of the magnetic surfaces. The coil alignment studies indicated that the HF windings and the VF coil sets were accurately positioned to within 5 mm. However, the magnetic surface mapping indicated a chain of islands extending outward from  $r/\bar{a} \simeq 0.6$  with the largest island (6-cm width) at  $\iota = \frac{1}{2}$ , as shown in Fig. 2. The field errors were later found to be due to uncompensated dipoles at the current feeds to the HF windings and the VF coils.<sup>4</sup>

In the second operating period (May–September 1988), experiments were conducted in the presence of the uncompensated field errors. The plasma was characterized by narrow  $T_e(r)$  profiles, as shown in Fig. 3, and there were sharp reductions in plasma stored energy  $W_p$  and line-averaged density  $\bar{n}_e$  for outward magnetic axis shifts, as shown in Fig. 4. The narrow profiles could be modeled by assuming that  $\chi_i$  and  $\chi_e$  were neoclassical (including ripple effects) in the plasma interior but that  $\chi_e$  was anomalously large for  $r/\bar{a} > 0.5$ , an indication that the observed island structure was degrading confinement. Error field calculations that accurately modeled the amplitude and phase of the magnetic islands also showed that the extent of these islands grew as the magnetic axis was shifted outside  $R_0 = 2.1$  m. The combination of the decreasing radius of the  $\iota = \frac{1}{2}$  surface and the growth of the magnetic island at  $\iota = \frac{1}{2}$  led to the best plasma performance being obtained at  $R_0 = 2.05$  m, 5 cm inside the nominal axis position.

Despite the deterioration associated with the chain of magnetic islands for  $\iota \geq \frac{1}{2}$ , the global ATF confinement is consistent with the scaling for the Large Helical Device (LHD) when the nominal full radius ( $\bar{a} = 0.27$  m) is used to calculate this scaling value for ATF, as shown in Fig. 5 (from Ref. 5). The confinement time  $\tau_E$  in ATF (indicated by the shaded areas) also decreases with neutral beam power, in agreement with the LHD scaling. The uncompensated field errors did not seem to have a major effect on the geometry of the diverted flux outside the nominal last closed flux surface. Langmuir probe measurements of the particle flux in the divertor stripe show a narrow (2-cm) peak.

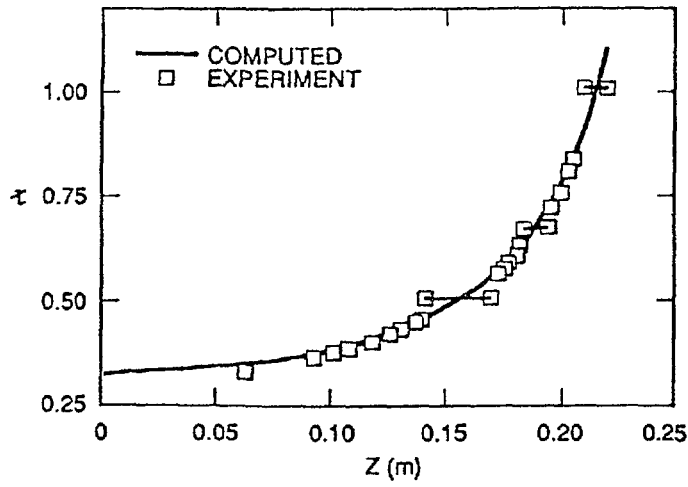


Fig. 2. The rotational transform profile in the vertical ( $Z$ ) direction in the  $\phi = 0$ -deg plane for the standard ATF configuration. Magnetic islands (indicated by the horizontal lines connecting equal values of the measured  $\tau$ ) were created by the original connections of the HF windings and VF coils to their busbars. These connections have since been redone.

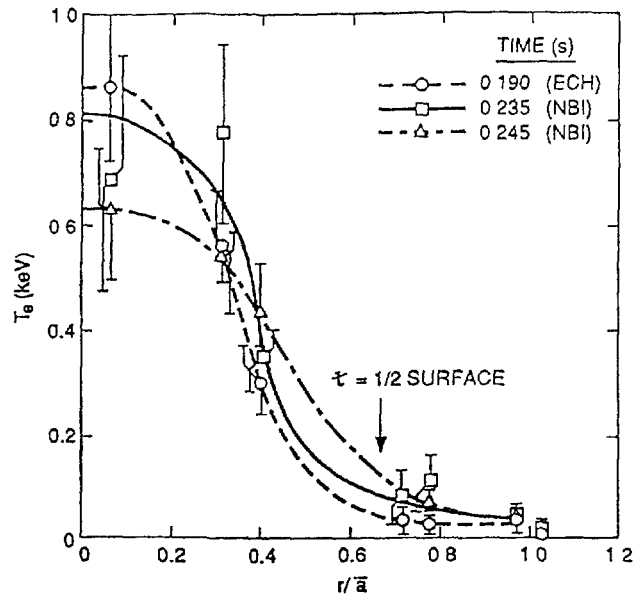


Fig. 3. Peaked electron temperature profiles obtained with both ECH and NBI in ATF, presumably due to the presence of the large magnetic island at  $\tau = \frac{1}{2}$  and the string of islands for  $\tau > \frac{1}{2}$ .

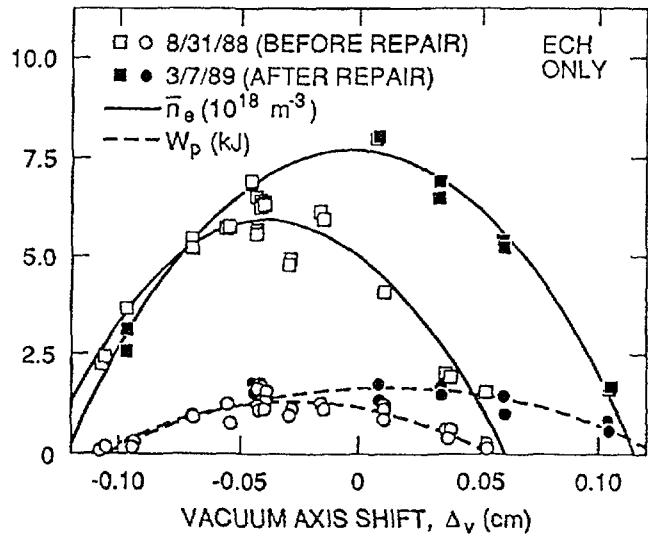


Fig. 4. Stored energy (dashed curves) and central line-averaged density (solid curves) before and after the field error correction. A wider operational range (outward shift of the magnetic axis) is obtained after the field error correction.

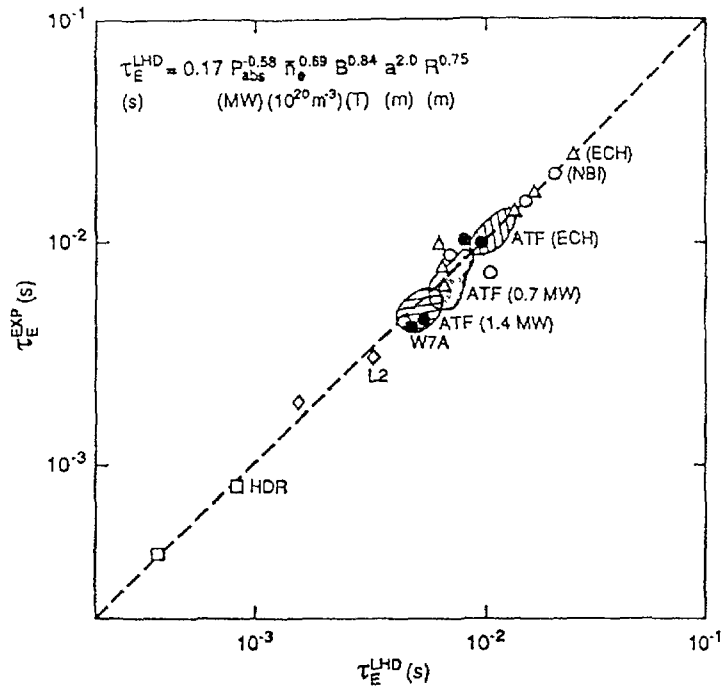


Fig. 5. Global energy confinement times in ATF and in other stellarators vs a scaling expression used in the LHD design studies. The shaded areas indicate ATF data obtained with 0.2-MW ECH, 0.7-MW NBI, and 1.4-MW NBI.

An effect of the narrow pressure profiles was that second stability behavior was obtained<sup>6</sup> at values of  $\beta_0$  less than half that anticipated for the broader (nominal) profiles. In effect, the narrow profiles reduced the edge value of  $\iota$  to  $\frac{1}{2}$  and increased the plasma aspect ratio by a factor  $\sim 1.6$ . This led to a larger Shafranov shift of the magnetic axis ( $\Delta/\bar{a} \simeq \beta_0 A/\iota_{edge}^2$ ) and to a greater deepening of the magnetic well than was anticipated. Experimental evidence for the beta self-stabilization effect on ATF is shown in Fig. 6. The amplitude of the coherent part of the  $n = 1$  fluctuations in the 8- to 40-kHz range, observed on Mirnov loops separated by 180 deg toroidally, is shown as a function of beta. The envelope of the maximum value of the coherent fluctuations first rises with beta and then starts to fall for  $\langle\beta\rangle \gtrsim 0.25\%$ . If beta self-stabilization were not occurring, then the fluctuation amplitude should continue to increase with beta, especially since the axis shift moves the plasma closer to the loops at higher beta. The experimental  $\beta_0$  values obtained (up to 3%) are well above the theoretically predicted transition ( $\beta_0 \simeq 1.3\%$ ) to the second stability regime for the observed profiles. Time-dependent magnetic fluctuation data show a beta dependence during a single shot similar to that seen in Fig. 6. The measured fluctuations are consistent with theoretical predictions for resistive pressure-gradient-driven interchange modes.

Additional evidence for beta self-stabilization is obtained from the broadening of the pressure profile with increasing beta. The beta dependence of the broadness parameter follows the theoretically expected expansion of the magnetic well region ( $V'' < 0$ ) with increasing beta. A sequence of MHD stability calculations using pressure profiles that broaden with beta, as found experimentally, shows that the plasma remains marginally stable along the path to the second stability regime.

Figure 7 shows some of the best data obtained in the May-September 1988 experimental period. Balanced (co- plus counter-injected)  $H^0$  neutral beams (1.4 MW total) were injected tangentially into a hydrogen plasma at  $B_0 = 0.95$  T. The magnetic axis was located at  $R_0 = 2.05$  m. Chromium gettering of about one-third of the vacuum vessel surface was used for this case, resulting in  $Z_{eff}$  between 1.5 and 2. The plasma parameters at  $t = 0.265$  s (the peak of the plasma stored energy) were  $\bar{n}_e = 2.5 \times 10^{19} \text{ m}^{-3}$ ,  $n_e(0) \simeq 5 \times 10^{19} \text{ m}^{-3}$ ,  $T_e(0) \simeq 0.6$  keV,  $T_i(0) \simeq 0.26$  keV,  $W_p \simeq 7$  kJ,  $\langle\beta\rangle \simeq 0.5\%$ ,  $\beta(0) \simeq 3\%$ , and  $\tau_E \simeq 5$  ms. Higher values for  $T_e(0)$  ( $\simeq 1$  keV at lower density) and for  $\tau_E$  ( $\simeq 15$  ms) are obtained in discharges heated only by ECH.

Small net plasma currents are obtained in ATF. The plasma current for the discharge shown in Fig. 7 was less than 1 kA, but higher plasma currents (up to  $\simeq 6$  kA) can be obtained with unbalanced tangential NBI. The plasma current during NBI is probably driven mostly by the neutral beam. The noninductive component of the plasma current during the ECH period (probably bootstrap current) is larger than 1 kA because it must overcome a small negative loop voltage ( $-0.1$  V to  $-0.2$  V) due to a transient in the HF winding current.

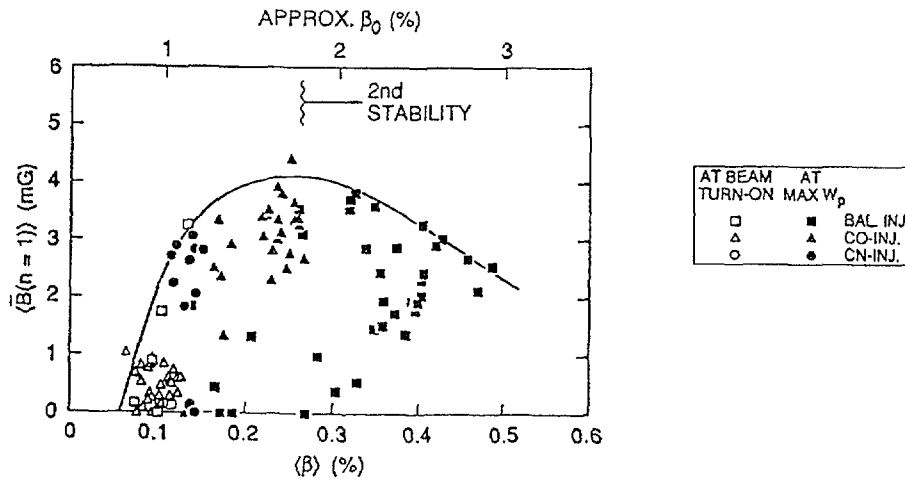


Fig. 6. Variation of the maximum amplitude of coherent  $n = 1$  magnetic oscillations with increasing beta, indicating a beta self-stabilization effect and entrance to a second stability regime.

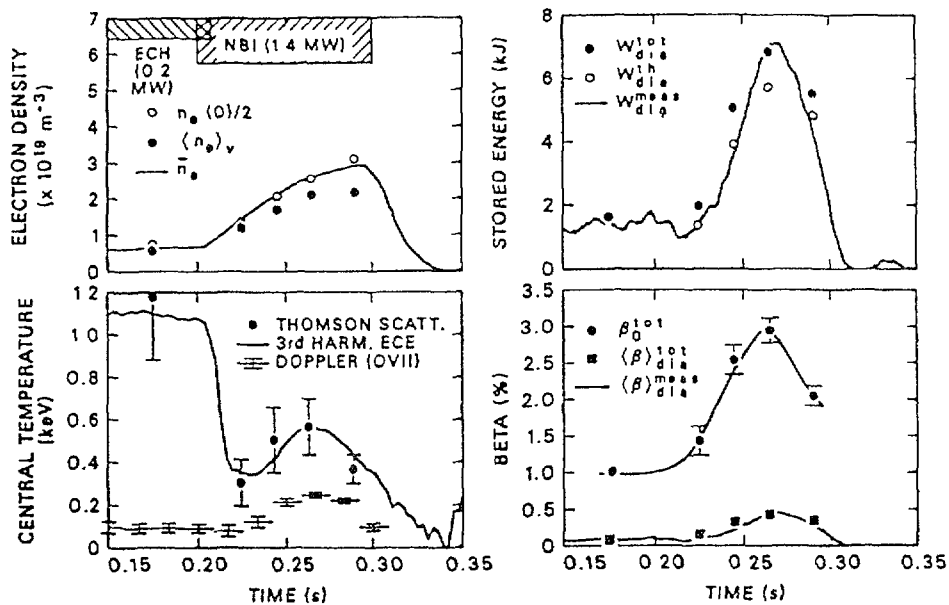


Fig. 7. ATF data obtained at  $B_0 = 0.95$  T during the 1988 experimental operation.

Various wall cleanup procedures were tried in the 1988 experimental period. Electron cyclotron resonance (2.45-GHz) discharge cleaning at  $B_0 = 0.88$  kG and glow discharge cleaning alone were not effective. The ECH plasmas exhibited uncontrollable density increases, eventually approaching cutoff and 100% radiated power, then collapsing to a low-density, low-temperature afterglow plasma. However, within two weeks after a major vacuum opening, simultaneous glow discharge cleaning and baking of the vacuum vessel and its major extensions to temperatures between  $70^\circ\text{C}$  and  $140^\circ\text{C}$  allowed essentially steady-state (1-s) ECH plasma operation. Both spectroscopy and visible bremsstrahlung emission indicated that  $Z_{eff}$  was in the range from 1.5 to 2 during both ECH and NBI operation.

However, NBI-heated plasmas continue to show the collapse phenomena noted in early ECH discharges. In the typical NBI-heated discharge shown in Fig. 8, the plasma stored energy rises rapidly after the start of the neutral beam pulse but then falls, followed later by a rapid decrease in the plasma density. This collapse can be simulated by modeling with the PROCTR code for narrow  $T_e(r)$  profiles under the assumption that  $\chi_e$  and  $\chi_i$  are neoclassical in the center but that  $\chi_e$  is anomalously large outside  $r/\bar{a} \simeq 0.5$ . The narrow  $T_e(r)$  profile allows low ionization stages to penetrate the outer plasma region, resulting in a large radiating volume. The results of the PROCTR code indicate that the combination of the narrow  $T_e(r)$  profile and the observed factor of two rise in the impurity influx during NBI is theoretically sufficient to initiate the thermal collapse, but this point has not been conclusively demonstrated by experiments. Spectroscopic measurements suggest that impurity radiation may drive the collapse, but the development of strong poloidal asymmetries in the emission is an important feature. The stored energy peaks  $\simeq 60$  ms after injection begins, when  $Z_{eff} \simeq 2$  and  $P_{rad}/P_{abs} \simeq 0.37$ . The electron density continues to rise because of fueling from the neutral beams and the influx of cold gas from the beam lines. The edge radiation rises and the electron temperature falls as the density rises. When  $T_e$  falls below  $\simeq 100$  eV, the plasma becomes radiatively unstable and  $P_{rad}/P_{abs}$  rises to  $\simeq 100\%$  while the density collapses.

During the October–December 1988 period, the VF coil connections were modified and compensating current loops were installed in the HF coil system to correct the earlier field errors. The magnetic surfaces were mapped again with the electron-beam probe. The magnitude of the  $\nu = \frac{1}{2}$  island dropped from  $\simeq 6$  cm to  $\simeq 1$  cm at  $B_0 \simeq 1$  T and scaled

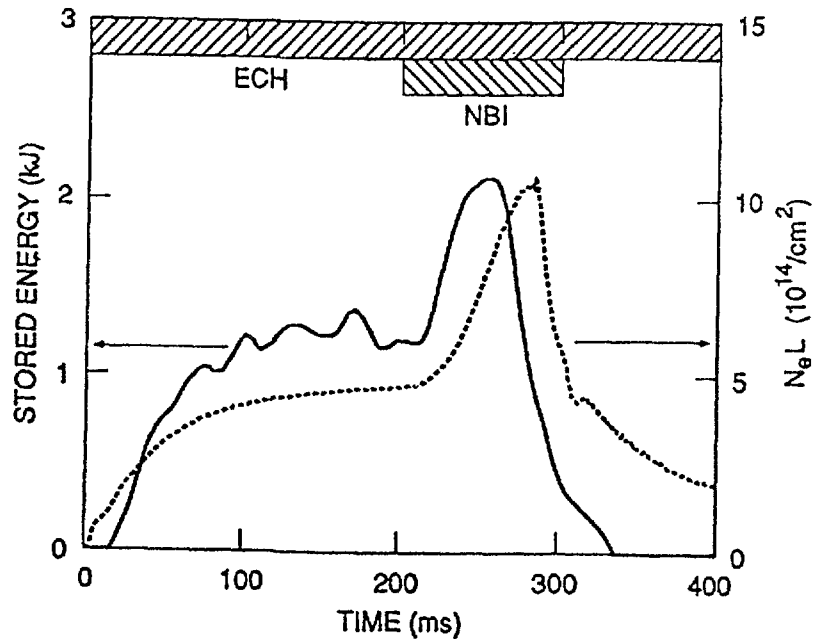


Fig. 8. Collapse of density (central line integral) and stored energy during an NBI-heated discharge in ATF.

inversely with the square root of the helical field strength. This indicated that the small residual field error causing the present  $\iota = \frac{1}{2}$  island arises from a constant resonant stray field component ( $\sim 0.1$  G, smaller than the ambient magnetic field) and not from inaccurate coil alignment or uncompensated dipoles in the bus work. The islands outside the  $\iota = \frac{1}{2}$  surface also decreased in size, but those inside  $\iota = \frac{1}{2}$  increased. All observed islands now decrease with increasing  $B$ , indicating that the bulk of the field perturbation responsible for the islands is not inherent in the magnetic field coils, except for the island at  $\iota = \frac{1}{3}$ , which is independent of  $B$ . The  $\iota = \frac{1}{3}$  island should not have a significant effect because it is in the plasma interior and can be avoided by raising  $\iota(0)$  above  $\frac{1}{3}$ .

Preliminary operation (March 1989) after repair of the field error indicates that the  $T_e(r)$  profiles are broader under some conditions, as shown in Fig. 9, and that a broader range of vacuum axis shifts (toward the outside) is available, as shown in Fig. 4. Long-pulse ECH operation has been recovered with chromium gettering. The stored energy in NBI-heated plasmas now remains high for a longer time before the eventual collapse occurs, but much more work needs to be done in learning to operate ATF in the most effective manner.

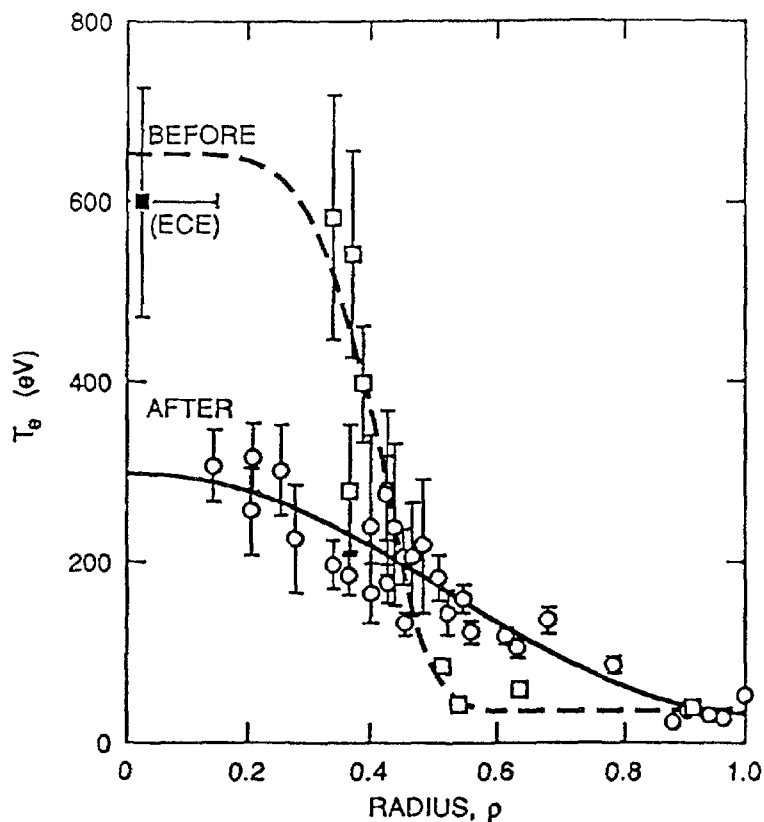


Fig. 9. Electron temperature profiles from Thomson scattering before (1.4-MW balanced NBI, dashed curve and square points) and after (0.65-MW unbalanced NBI, solid curve and round points) the field error correction.

### III. NEAR-TERM STUDIES

A number of additions are planned for ATF through 1990. Operation at 2 T is planned for May 1989. This is expected to improve performance because of the  $B$  dependence of  $\tau_E$ , the higher efficiency of ECH at the electron cyclotron fundamental resonance, and the reduced beta (and effects associated with it). An 8-shot pellet injector is being installed in April 1989 to allow central fueling and peaking of the density profile. An additional 200-kW, 53.2-GHz gyrotron will be added (doubling the ECH power to 400 kW), and the ICH power will be increased from 100 kW to 300 kW. The mid-VF coil power supply will be connected, allowing control of the plasma ellipticity and the value of  $\epsilon(0)$ . A number of diagnostics will be added (15-channel FIR interferometer, 2-D scanning neutral particle analyzer, 200-kV heavy ion beam probe, etc.), and more getters will be added to cover  $\simeq 60\%$  of the vacuum vessel wall (vs  $\simeq 30\%$  at present). The emphasis of the physics studies on ATF during 1989 will be on better understanding of confinement through correlation of fluctuations with local transport coefficients and comparison with theory.

### ACKNOWLEDGMENTS

The authors acknowledge the encouragement of O. B. Morgan and M. W. Rosenthal of Oak Ridge National Laboratory. This research was sponsored by the Office of Fusion Energy, U.S. Department of Energy, under contract DE-AC05-84OR21400 with Martin Marietta Energy Systems, Inc.

### REFERENCES

1. J.F. LYON, B.A. CARRERAS, K.K. CHIPLEY, M.J. COLE, J.H. HARRIS, et al., "The Advanced Toroidal Facility," *Fusion Technol.*, **10**, 179 (1986).
2. L.M. KOVRIZHNYKH and S.V. SHCHEPETOV, "MHD Equilibrium and Stability of Stellarator Plasma," *Nuc. Fusion*, **23**, 859 (1983).
3. B.A. CARRERAS, "Anomalous Transport in the Second Stability Regime," *Comments Plasma Phys. Controlled Fusion*, **12**, 35 (1988).
4. J.H. HARRIS, T.C. JERNIGAN, F.S.B. ANDERSON, R.D. BENSON, R.J. COLCHIN, M.J. COLE, A.C. ENGLAND, et al., "Realization of the ATF Torsatron Magnetic Field," to be published in *Fusion Technol.*

5. DESIGN GROUP FOR THE NEW LARGE HELICAL SYSTEM DEVICE, "New Large Helical System Device—Outline," unpublished (1988).
6. J.H. HARRIS, M. MURAKAMI, B.A. CARRERAS, J.D. BELL, G.L. BELL, T.S. BIGELOW, et al., "Second Stability in the ATF Torsatron," submitted to *Phys. Rev. Lett.* (1989).

## OVERVIEW OF RECENT HELIOTRON E EXPERIMENTS

T. OBIKI, A. IYOSHI, M. WAKATANI, O. MOTOJIMA,  
S. MORIMOTO, K. KONDO, T. MUTOH, M. SATO, S. SUDO,  
F. SANO, K. ITOH, M. NAKASUGA, K. HANATANI, H. ZUSHI,  
H. KANEKO, T. MIZUUCHI, H. OKADA, Y. NAKAMURA,  
Y. TAKEIRI, H. MATSUURA, M. HARADA, K. ICHIGUCHI,  
T. YAMASHINA<sup>1</sup>, T. HINO<sup>1</sup>, H. MINAGAWA<sup>1</sup>, T. ODA<sup>2</sup>,  
K. MURAOKA<sup>3</sup>, T. KAJIWARA<sup>3</sup>, K. MATSUO<sup>3</sup>, K. UCHINO<sup>3</sup>,  
A. KOMORI<sup>3</sup>, N. NODA<sup>4</sup>  
Plasma Physics Laboratory,  
Kyoto University,  
Gokasho, Uji, Kyoto,  
Japan

### Abstract

Results of the recent experiments in Heliotron E are reported. Magnetic configuration studies indicate that the best operation depends on both MHD activity and trapped-particle confinement. Plasma-wall interaction studies show that hydrogen recycling can be reduced but iron impurities are still of the same order as with an all-metal wall.

### I. Introduction

Because of the interest in (i) the improvement of plasma confinement and (ii) the understanding of helical-divertor concept, the Heliotron E experiments in FY1988 placed main emphasis on the magnetic configuration studies and the divertor plasma measurements [1]. The application of the auxiliary vertical field can present a good opportunity for magnetic configuration studies by shifting the magnetic axis outward or inward in the major-radius direction with accompanied changes of configuration parameters (mean plasma radius, rotational transform, shear, well/hill, etc.). In addition, in this case, charged-particle dynamics becomes a key factor for transport with special regard to the loss-cone minimization [2]. The main research objectives were to find out how the magnetic field configuration influences the transport and MHD activity and, as a result, to clarify the roles of configuration parameters in the plasma energy confinement. The fundamental characteristics of the divertor plasma in the throat-baffle installed section ( $\sim 1/5$  toroidal zone) were measured from the viewpoint of "helical divertor action" and compared with those in the other toroidal section without baffles. For Heliotron E plasmas, it seems to be obvious that the edge plasma parameters, both inside and outside the separatrix (or separatrix layer), must play a decisive role as the "boundary condition" for the whole behavior of plasma confinement. The interaction of the edge plasma with the walls (especially on the divertor traces) provides important problems associated with impurity release and particle recycling. In this connection, carbon tiles were attached to the divertor section ( $\sim 1/5$  of the whole vacuum chamber area) and the basic performance of ECH and/or NBI plasma was studied.

<sup>1</sup> Department of Nuclear Engineering, Hokkaido University, Sapporo, Japan.

<sup>2</sup> Department of Applied Physics, Hiroshima University, Hiroshima, Japan.

<sup>3</sup> Interdisciplinary Graduate School of Engineering Sciences, Kyushu University, Kyushu, Japan.

<sup>4</sup> The Institute for Plasma Physics, Nagoya University, Nagoya, Japan.

## II. Configuration control experiments

The characteristics of the global energy confinement time for the Heliotron E plasmas during ECH, NBI, and/or ICRF heretofore have been studied especially as a function of such parameters as density, heating power, and magnetic field. The application of the auxiliary vertical field to those plasmas allows us to experimentally study the effects of configuration variation on plasma confinement. The experiments [3] showed that the best confinement region with regard to the applied vertical field exists in the low collisionality, low- $\beta$  regime and that, for both ECH and NBI plasmas, this region is situated at the almost similar magnetic-axis shift position. An example is shown in Fig.1. Compared

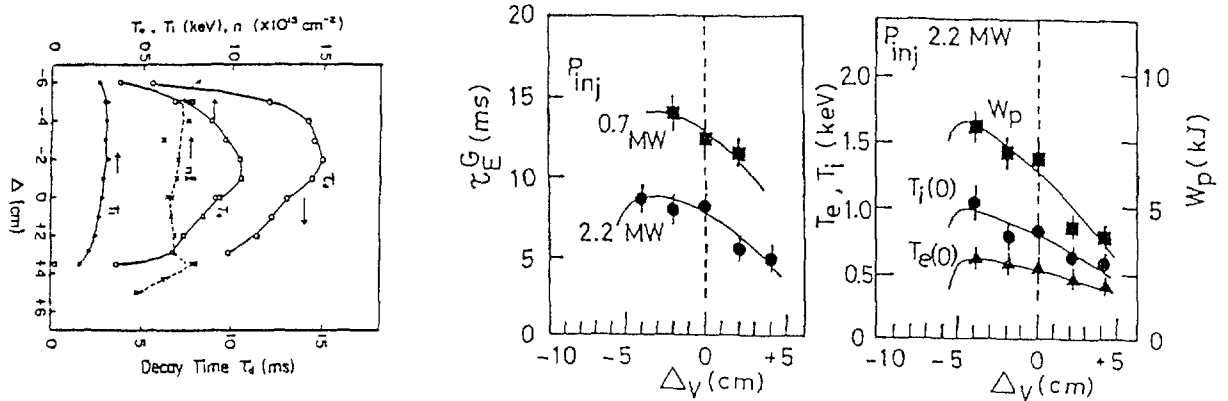


Fig.1 (a) Decay time of the electron temperature after the termination of ECH, central electron and ion temperatures  $T_e$ ,  $T_i$  and the line density  $n_l$  as a function of vacuum magnetic-axis shift  $\Delta_v$  (cm) for ECH plasmas.

(b) Global energy confinement  $\tau_E^G$ , central electron and ion temperatures  $T_e(0)$ ,  $T_i(0)$ , and the plasma internal energy  $W_p$  as a function of vacuum magnetic-axis shift  $\Delta_v$  (cm) for NBI plasmas.

with the confinement characteristics of the standard configuration ( $\Delta_v = 0$ ), the central ion and electron temperatures and the global energy confinement time (accompanied with the electron temperature decay time) were observed to increase by around 20 % at this best position, *i.e.*, at the inward-shift distance ( $\Delta_v$ ) of  $-4 \leq \Delta_v \leq -2$  (cm). The shift positions of  $\Delta_v > 2$  (cm) or  $\Delta_v < -5$  (cm) caused a rapid deterioration of confinement, thus prohibiting the stationary plasma production during NBI. It is not yet clear which factor among the varying configuration properties dominates this improvement and degradation. The characteristic change of confinement seems to be larger than the  $a_p^2$  dependence, where  $a_p$  is the mean plasma radius. Theoretically, the inward-shift permits the helical field ripple to be localized at the inner side of the torus ( $\sigma$ -optimization) and, furthermore, a deeply-trapped particle trajectory to be kept inside the confinement area by minimizing the trajectory departure from the magnetic flux surface ( $B_{min}$ -contours optimization). Experimentally, there seems to be a good confinement window as to the varied shift position and the optimal shift position is consistent with the predicted minimum-loss-cone configuration (and the neoclassical  $\sigma$ -optimization scenario) while the shear stabilization to microstabilities are still candidates for possible interpretations.

MHD activities analysis presents another aspect of confinement behavior and theoretical prospect for the stabilization of MHD instabilities by controlling the magnetic configuration provides a special interest in high-pressure-regime operation. In the standard configuration, the sawtooth relaxation associated with the pressure-driven instabilities at the rational surfaces of  $\iota=1$  and  $\iota=2/3$  was observed so far only in a low-field ( $B=0.94$  T), high- $\beta$  NBI regime with the peaked pressure profiles at central beta values above 2 % (S mode). The configuration change by the auxiliary vertical field was found to cause new MHD instabilities that had not been observed before, as shown in Fig.2, under the conditions where the magnetic axis shift is  $\Delta_v = -2$  (cm), the field strength is 1.9 T, and the plasma  $\beta$ -value is at most 0.7 % at the centre. These instabilities are speculated to be  $(m, n) = (2, 1)$  from (i) the finding that the SX inversion tangency radius is considerably smaller than the  $\iota = 1$  surface ( $r/a \sim 0.7$ ) and (ii) the theoretical prediction that the inward shift in this case causes an appearance of the  $\iota = 1/2$  rational surface near the plasma centre accompanied with the "hill" configuration. The behavior of these MHD instabilities varies with increasing beta by using hydrogen-pellet injection. Pellet injection raises the central beta value ( $\beta_0 \leq 3$  %) and, as a result, the inversion tangency radius of SX signals during both the precursor and the sawtooth phases shifts discretely from the inner radius to the outer radius of the plasma. Since the sawteeth, presumed to be connected with the  $\iota = 1/2$  rational surface, was not observed in the large-size-pellet regime, this phenomenon can be interpreted as being due to the stabilization by the magnetic well generated by a Shafranov shift. On the other hand, the outward shift of the magnetic axis causes an expansion of the vacuum magnetic-well region from the plasma central region. A clear correlation was observed between the expanded well region and the disappeared instabilities, affording another experimental support for "well-stabilization" scenario. As for these MHD activities, the comparison between the experimental results and the theoretical predictions is very interesting. The numerical calculation [4] suggests that the new MHD instabilities due to the hill configuration in the inward shift case

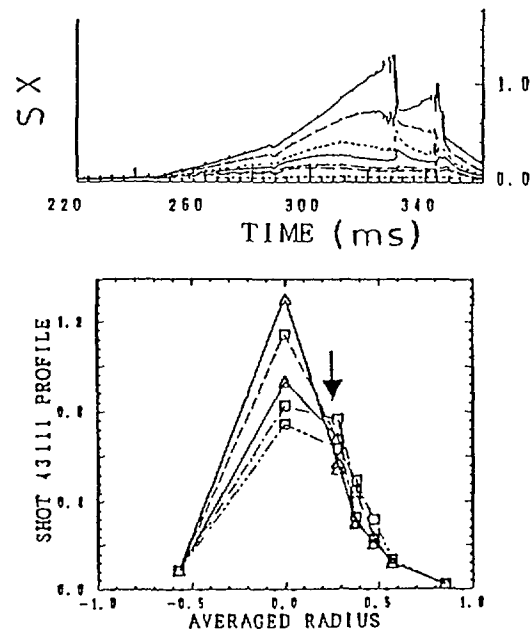


Fig.2 Sawtooth relaxation on SX signals (upper) and time evolutions of the profile (lower), where the top of fluctuations at the centre chord is shown by triangles and bottom by squares. The arrow position shows the SX inversion tangency radius.

(good-confinement regime) are brought about through the resistive modes rather than the ideal modes. The identification of the exact unstable range of a mode by separating the unstable regions of the individual modes or to find out a stability window in  $\beta$ -value remains as a future work and this will be essential for obtaining the reliable experimental evidence of  $\beta$  self-stabilization in Heliotron E. It also should be noted that to find out the compatibility condition between transport and stability in the high- $\beta$  regime is the key issue to be settled in the future work, for example, by applying the additional toroidal field.

### III. Divertor Plasma Measurements

Power balance, confinement, and stability properties are considered to be strongly influenced by the structure of the cooler plasma layers at the edge of the hot plasma column. The edge plasma has to carry off the power released inside the plasma to the divertor region, at least that part of the total power input which is not radiated away. Additionally, all the charged particles leaving the main plasma should be delivered through the edge plasma which determines the recycling conditions necessary to sustain a stationary particle balance. To enhance the ionization of recycling neutrals, the throat-baffle plates were installed in the torus within the 4 helical pitches. The properties of the divertor plasma in the throat-baffle installed section were measured with the calorimeters/Langmuir-probes arrays and compared with those in the other toroidal section without baffles. The divertor plasma parameters such as density  $n_{ed}$  and temperature  $T_{ed}$  (when  $\bar{n}_e = 3 \times 10^{13} \text{ cm}^{-3}$ ,  $n_{ed} \sim 5 \times 10^{11} \text{ cm}^{-3}$  and  $T_{ed} \sim 20 \text{ eV}$ ) showed no clear deviation with or without baffles possibly due to the short baffle-installed toroidal zone and the short connection length from the throat to the walls ( $L_B \sim 0.5 - 1 \text{ [m]}$ ). However, the  $H_\alpha$  emission intensity in the baffle section was generally observed to be greater than that in the other section. The details of the experimental data and some comparisons between the experiment and the computer simulation for the divertor behavior in Heliotron E are discussed in the companion paper [5]. In relation to the configuration control experiments, it was found that the particle and power fluxes in the divertor layer were affected by the applied auxiliary vertical field, providing a change of the in-out ratio of those fluxes as shown in Fig.3 for NBI plasmas of  $\bar{n}_e \sim 3 \times 10^{13} \text{ cm}^{-3}$ ,  $P_{inj} \sim 2 \text{ MW}$ , and  $B = 1.9 \text{ T}$ . The perpendicular neutral beam injection was also observed to cause a high heat-flux flow on the inboard walls of the torus, which may be interpreted in terms of the orbit loss of the injected high-energy trapped particles.

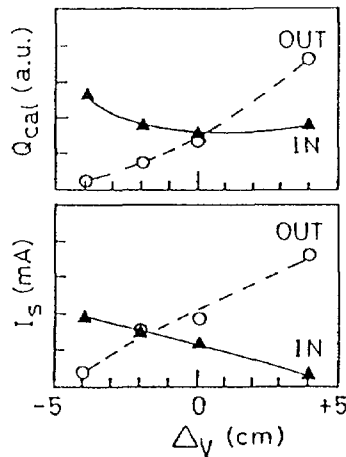


Fig.3 In-out ratio of the heat and particle fluxes as a function of magnetic-axis shift.

#### IV. Plasma-wall Interaction

In Heliotron E, "carbonization" of the torus interior was successful for achieving stationary high-beta plasma production with reducing high-z impurities such as iron. However, the control of hydrogen recycling was a difficult problem in this case, thus restricting the density operation range in medium-and high-density regime. For the purpose of reducing the hydrogen recycling and identifying the source of irons at metal-wall circumstances, the graphite tiles were attached to the divertor section (7.5 m<sup>2</sup>, around 75 % of the total divertor section) and the basic plasma properties were studied with special reference to the edge-plasma behavior. The experiment showed that the hydrogen recycling can be reduced below unity only under low-power NBI conditions with the help of helium discharge cleaning and that the iron impurity contamination is still of the same order of that in the metal-wall cases. In order to clear up the causes of these results, the surface composition of the attached carbon tiles selected toroidally was analyzed by the AES (Auger electron spectroscopic system) [6]. The analysis result indicates that the heavy contamination of irons on the carbon tiles (besides the divertor traces) is restricted only in the neighborhood of the helium-discharge-cleaning electrode ( $\sim 1/3$  toroidal zone). A possible explanation is the importance of the iron sputtering by the charge-exchange neutrals. It is suggested that, while reducing the charge-exchange neutrals, much wider area of the vacuum chamber wall must be covered by the carbon material to effectively reduce the iron impurities.

#### REFERENCES

- [1] T.Obiki, *et al.*, IAEA-CN-50/C-1-1, Nice (1988). [2] K.Hanatani, 44th Meeting of P.S.J., 28aTE10, March 1989, Japan. [3] H.Zushi, *et al.*, this workshop. [4] M.Wakatani, *et al.*, this workshop. [5] T.Obiki, *et al.*, this workshop. [6] H.Minagawa, *et al.*, 6th Meeting of J.S.Plasma Sci. Nucl. Fusion Research, 2aD2, April 1989, Japan.

## OVERVIEW OF CHS EXPERIMENT

K. MATSUOKA and the CHS GROUP<sup>1</sup>

Institute of Plasma Physics,  
Nagoya University,  
Nagoya, Japan

### Abstract

The experiment on confinement and production of a currentless plasma with the low aspect ratio has been started since June 1988. The accuracy of the machine has been confirmed by the measurement of magnetic surfaces using a fluorescent mesh and an electron beam; clean magnetic surfaces are experimentally observed up to 95% of the calculated outermost one, and widths of observed  $m/n=2/1$  islands are proportional to  $B_t^{-0.5}$  for the range of magnetic field strength investigated:  $400G < B_t < 2.4kG$ .

Typical parameters of ECR heated plasmas by use of 28GHz gyrotron are:  $T_e(0)=300\sim 900$  eV and  $n_e=2\sim 6\times 10^{12}cm^{-3}$ . Electron energy decay times after the ECH turn-off range from 1 to 6ms, depending on the temperature and density. Hollow density profiles observed in the ECR plasma suggest an important role of the drift motion of perpendicularly high energy electrons in particle and energy transports. Dependences of plasma parameters on the magnetic axis position have been investigated for three typical positions; parameters are improved as the axis shifts inward. This phenomenon could partly be interpreted by the improved omnigenicity of the magnetic configuration.

ICRF experiments, using Nagoya type-III antenna (7.5~13MHz, ion Bernstein wave and/or slow wave) and poloidal antenna (40MHz, whistler wave), have been made in order to produce a target plasma for neutral injection. Hydrogen plasmas with parameters of  $n_e(0)=5\sim 6\times 10^{12}cm^{-3}$  and  $T_e(0)=200\sim 300eV$  are produced with the type-III antenna at the specific magnetic field strength: 0.6T and 1.1T for 7.5 and 13MHz, respectively. The ion temperature is 200~300eV at  $0.5T < B_t < 1.5T$ .

---

### 1. Introduction

Compact Helical System(CHS), which is an  $l=2$  torsatron type device, has been in operation since the end of June 1988. Its objectives are to study particle and energy transports, MHD characteristics and edge phenomena of currentless plasmas of aspect ratio ( $A_p$ ) as low as 5 [1], which is smaller than those of Heliotron-E( $A_p=11$ ), ATF(7) and WVII-AS(10). Major parameters are the followings:  $R/a_p=1m/0.2m$ ,  $m=8$ ,  $B_t=1.5T$ ,  $\tau(0)/\tau(a_p)\sim 0.3/1.0$ . For ECH and ICRF experiments, 28GHz, 200kW, 75ms gyrotron, and 7.5~13MHz, 800kW, 30ms and 40MHz, 1.5MW, 100ms ICRF power source have been prepared, respectively.

---

<sup>1</sup> A. Ando, J. Fujita, M. Fujiwara, S. Hidekuma, M. Hosokawa, K. Ida, H. Idei, H. Iguchi, O. Kaneko, T. Kawamoto, S. Kubo, K. Masai, K. Matsuoka, S. Morita, K. Nishimura, A. Nishizawa, N. Noda, S. Okamura, H. Sanuki, A. Sagara, T. Shoji, C. Takahashi, Y. Takita, S. Tanahashi, K. Tsuzuki, H. Yamada, K. Yamazaki, D.-G. Bi, S. Sobhanian.

In the near future (June 1989), 53.2GHz, 200kW, 100ms gyrotron and 40kV, 1.2MW (port-through), 1s NI will be operational, which will extend the plasma parameter range and enable further investigation of transport phenomena in the low  $A_p$  configuration.

## 2. Magnetic Surface Measurement

Careful attention has been paid to the design and construction of CHS[2,3], because the fragility of the magnetic surface gets serious as the aspect ratio decreases. Magnetic surface measurements to verify the designed magnetic surface have been done using a fluorescent mesh and an electron beam, in the range of the magnetic field strength from 400G to 2.4kG[4].

Closed magnetic surfaces have been successfully confirmed up to 95% of the expected outermost surface. However, magnetic islands have been observed at the major rational surfaces ( $\iota=1/3, 1/2, 2/3$ ). The dependence of the  $m/n=2/1$  island width  $W$  on the field strength is shown with solid circles in Fig.1, where the island full width scales roughly with  $W \propto B_t^{-0.5}$  indicating that the main cause of the observed island is not intrinsic to the machine itself. Field tracing calculations of the island width which take account of the ambient field in the experimental building, i.e. the horizontal component of 0.9G from south to north, are shown with open circles in the figure. Both results agree fairly well. The island width in the ECH experiment at  $B_t \sim 1T$  is estimated to be below 5mm from the figure.

## 3. ECH Experiment

The  $TE_{01}$  mode with mixed O- and X-waves is injected via a circular waveguide. We adopted the high-field side launching, expecting the high density operation due to the X-mode. The power through the port is up to 120kW. Performances of initial ECR heated plasmas were improved with wall conditionings: vacuum vessel baking at 100°C, and 2.45GHz ECR and helium glow discharge cleanings.

The parameter range of ECR plasmas is shown in Fig.2; plasmas with  $T_e(0)$  of several hundreds eV and  $n_e(0)$  of several  $\times 10^{12} \text{cm}^{-3}$  are produced. The ion temperature is  $\leq 100\text{eV}$ . The electron density profile is hollow with the on-axis heating, while a centrally peaked electron temperature profile is obtained; the electron pressure has a peaked profile. When the off-axis heating is applied, a small dip at the resonance position is observed in the density profile and the electron temperature shows less peaked profile compared with that at the on-axis heating; the pressure profile shows a small hump at the center rather than the flattened profile expected from the power deposition. This may be due to the drift-orbit-originated inward flow of perpendicularly high energy electrons.

The decay time of the electron energy has been measured after the turn-off of ECH power with about 10ms duration. This is to avoid an impurity contamination at relatively early operation periods [5], which leads to a plasma collapse. The time ranges from 1 to 6 msec depending on the plasma parameter [6]. Using the simplified neoclassical transport code which incorporates Kovrizhnykh's theory, we estimate the electron confinement time of ECR plasmas. The decay time is within the factor  $1/2 \sim 1/3$  of the estimated value. Further informations on the power deposition and radiation loss profiles are necessary to discuss the space resolved transport; those are under way and/or preparation.

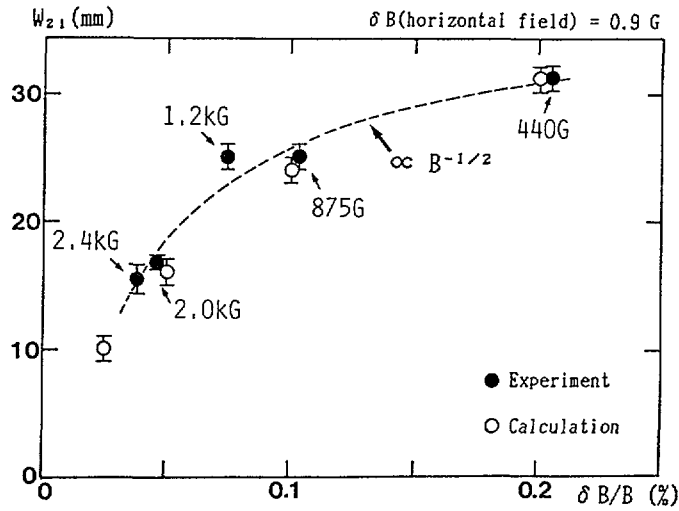


Fig.1. Dependence of  $m/n=2/1$  magnetic island width on the magnetic field strength. Solid and open circles refer to measured and calculated island widths. In the calculation the horizontal field of 0.9G is employed.

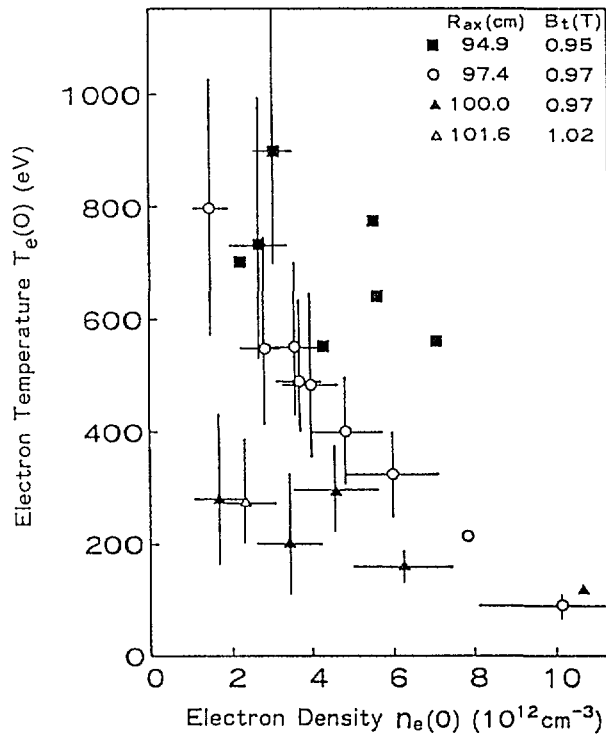


Fig.2. Plasma parameters obtained in ECR heated plasmas. Data are plotted for four cases of the magnetic axis position. Data without an error bar are obtained with one shot.

Experiments on magnetic axis shift have been done to investigate the effect of the omnigenous magnetic surface on plasma parameters:  $R_{axis}=94.9\text{cm}, 97.4\text{cm}, 101.6\text{cm}$  [7,8]. In CHS, the omnigenicity improves as the magnetic axis shifts inward under the present experimental conditions; the central electron temperature and the stored energy from a diamagnetic loop increase as inward shift.

Toroidal and poloidal profiles of hydrogen and light impurities are measured with a space resolved visible spectrograph system [9]. Effects of the limiter on the local recycling have been studied. Informations on a radial electric field are expected to be obtained from this measurement.

#### 4. ICRF Plasma Production

Plasma production experiments, using Nagoya type-III antenna (7.5~13MHz, movable radially) and poloidal antenna (a pair of quarter turn, 40MHz, fixed), have been made to obtain a target plasma for the neutral beam injection [10]. Each antenna has a Faraday shield. The electron density produced is shown in Fig.3 as a function of the magnetic field  $B_t$ .

The production mechanism with the type-III antenna could be the electron Landau damping of ion Bernstein wave and/or the Alfvén resonance of slow wave from the  $B_t$  dependence. Extended efforts are necessary to improve the plasma parameters, on wall conditionings with titanium gettering, a precise control of gas puff (timing and duration), and adjustment of the distance between the outermost magnetic surface and the movable antenna. The electron temperature at the center reaches 200~300eV when the magnetic field strength is 0.6T and 1.1T for the two

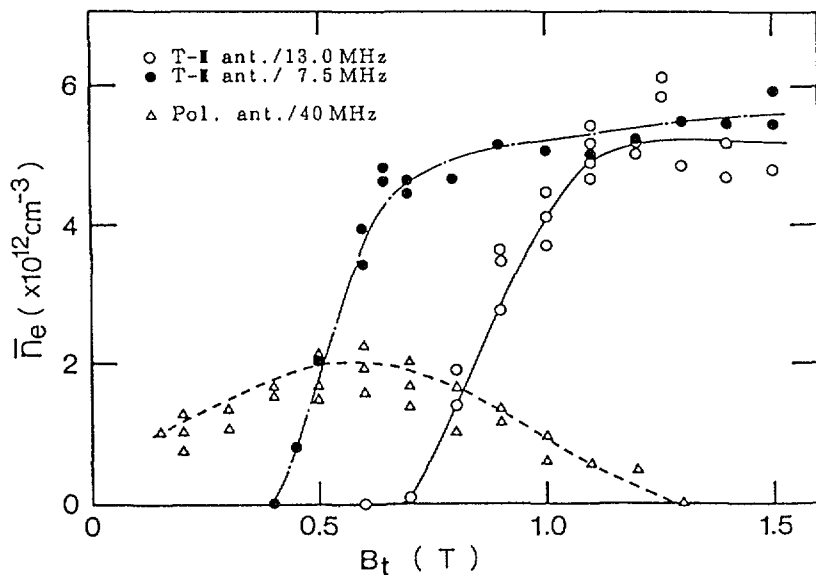


Fig.3. Electron density produced with ICRF as a function of the magnetic field strength. Data are shown for two types of antenna. Plasma production with the type-III antenna is shown for two kinds of frequency.

cases of the frequency studied: 7.5MHz and 13MHz, respectively. The average electron density is  $5\sim 6 \times 10^{12} \text{cm}^{-3}$ . The ion temperature measured tangentially with a TOF neutral particle analyzer is 200~300eV. The electron temperature and electron density from Thomson scattering show rather flattened profiles than peaked ones. The plasma production at a higher magnetic field will be tried at a higher frequency.

The plasma production with the poloidal antenna is ascribed to the whistler wave ( $\omega/\omega_{ce} \lesssim 10$ ). The electron temperature ( $\lesssim 10\text{eV}$ ) and electron density ( $2\sim 3 \times 10^{12} \text{cm}^{-3}$ ) are still low. Simplified estimate based on the toroidal eigen-mode indicates that a higher frequency than 40MHz is necessary for higher densities; such an operation is now under planning.

#### REFERENCES

- [1] M.Fujiwara et al., Proc. 14th EPS Conf.(Madrid 1987), vol.11d, part 1, p404.
- [2] K.Matsuoka et al., Proc. 12th Sympo. Fusion Engineering (Monterey 1987), vol.2, p848. vol.2, p848.
- [3] K.Nishimura et al., Proc. 15th SOFT(Utrecht 1988), A27.
- [4] H.Yamada et al., this workshop.
- [5] S.Morita et al., this workshop.
- [6] K.Matsuoka et al., Proc. 12th IAEA(Nice 1988), IEAE-CN-50/I-I-3.
- [7] S.Okamura et al., Proc. 16th EPS(Venice 1989).
- [8] H.Iguchi et al., this workshop.
- [9] K.Ida et al., this workshop.
- [10] K.Nishimura et al., this workshop.

# OVERVIEW OF THE TORSATRON/STELLARATOR LABORATORY PROGRAM AT THE UNIVERSITY OF WISCONSIN - MADISON

J.L. SHOHEIT

Torsatron/Stellarator Laboratory,  
University of Wisconsin - Madison,  
Madison, Wisconsin,  
United States of America

## Abstract

The paper reviews the experimental programme on stellarator physics provided by the Torsatron/Stellarator Laboratory, and presents the history, state-of-the-art and the plans and prospects for the programme.

---

## Introduction

Since its inception in 1974, the Torsatron/Stellarator Laboratory (TSL) has utilized modest-sized stellarator-type devices (the Proto-Cleo Stellarator, the Proto-Cleo Torsatron, and the IMS modular stellarator) to experimentally investigate basic physics issues related to toroidal confinement. Experimental studies have been augmented and focussed by research into new device concepts, theory and numerical modelling. The program has been guided by the need to understand transport and RF heating in toroidal systems and has been characterized by innovative and useful physics and engineering results.

Initial studies on the Proto-Cleo Torsatron identified the presence of rippling modes and drift waves. The latter have been correlated to transport. Experiments in the Proto-Cleo Stellarator demonstrated the effectiveness of ICRF, Alfvén wave, and alternating current inductive heating. Pfirsch-Schlüter and bootstrap current distributions have been measured in the Proto-Cleo Stellarator in good agreement with neoclassical theory. The role of electron cyclotron heating on plasma electric fields and convective transport in profile formation has been shown on the IMS device and is under continued investigation. The inherent divertor structure in IMS has been utilized to investigate relationships between divertors and the scrape-off-layer. This has become increasingly important because of the need to understand diverted discharges and edge physics in toroidal systems. Control of diverted fluxes through the use of externally applied potentials and magnetic fields has been demonstrated and successfully modeled through  $E \times B$  drifts induced in the scrape-off-layer.

The devices used in the Torsatron/Stellarator Laboratory permit detailed physics studies without prohibitively expensive diagnostic systems. The program allows the flexibility to pursue programmatic needs as well as higher-risk investigations in an expedient and cost-effective manner. Maintaining relevance to the overall program has been guided by collaboration with major programs and active participation in defining important current issues. As an example, the use of optically-thin third harmonic ECE as an electron temperature diagnostic was developed in an exchange visit by a TSL staff member to Heliotron E and is routinely utilized on both Heliotron E and ATF. The recognition of potential reactor difficulties with helical coil systems from joint reactor studies led to the development of the IMS modular stellarator concept and its subsequent construction and operation. This was the first device of its kind. Field mapping techniques and experience gained from IMS formed a basis for an in-depth collaboration with ORNL in the mapping of magnetic surfaces in ATF. The laboratory program has resulted in 15 Ph.D.'s employed throughout the fusion community.

## History and Results

The Torsatron/Stellarator Laboratory at the University of Wisconsin-Madison was formed in 1974 with the acquisition of the Proto-Cleo Stellarator and Proto-Cleo Torsatron from the Culham Laboratory in the United Kingdom with funding provided by the National Science Foundation. These devices operate at 3 kG and each has a major radius of 40 centimeters and an effective plasma radius of 4.5 and 5 centimeters respectively. At that time, they were the only US stellarators in a world-wide field of 23 such devices.

Initial experiments on the Proto-Cleo Stellarator examined both transit-time magnetic pumping (TTMP) and Alfvén wave heating. Some plasma heating coupled with increased plasma loss was observed with the TTMP. Global excitation of Alfvén waves resulted in a doubling of both the electron and ion temperatures. Evidence of the existence of Alfvén-wave resonant surfaces was observed.

Work on the Proto-Cleo Torsatron measured low-frequency fluctuations in the range of  $100 \text{ kHz} < f < 500 \text{ kHz}$  in Ohmic discharges. It was found that broad-band density fluctuations existed that were consistent with drift wave turbulence theory. The power density spectrum dependence on frequency was approximately  $f^{-2.5}$ . The density fluctuation level peaked where the density gradient was maximal. The variation of frequency with perpendicular wavenumber was in agreement with the calculated value of the electron diamagnetic drift velocity both in magnitude and direction. The parallel wavenumbers were coupled proportionally to the shear. Diffusion coefficient estimates agreed with fluctuation induced diffusion. Subsequent investigations in the frequency range below 100 kHz showed evidence of coherent mode structures whose helicity matched the vacuum field. Density fluctuations of  $\sim 15\%$  were found to peak between 20-25 kHz. The poloidal mode number was found to vary linearly from  $m=4$  at 25 kHz to  $m=16$  at 100 kHz. The density fluctuations were coherent with plasma current fluctuations,  $H_\beta$  emission, and x-ray flux. Mirnov loop signals were always in phase and corresponded to a simple plasma current fluctuation  $\Delta I/I \sim 10^{-3}$ . It was concluded that rippling modes driven by gradients in the resistivity were the most likely candidate to explain the fluctuations.

To address the lack of information on transport issues in stellarators, Monté-Carlo codes were applied at MIT, Wisconsin, PPPL and Garching to develop an understanding of low-collisionality transport and the effectiveness of neutral beam injection in stellarators and torsatrons. The results on low-collisionality transport were encouraging showing modest "super-banana plateaus", especially with the inclusion of effects of radial electric fields.

Experimental activities on the Proto-Cleo Stellarator looked at the performance of gun-produced plasma injection with respect to angle to the magnetic field. The results showed a significant improvement in confinement with tangential plasma injection as compared to the "standard" method of cross-field injection. Particle confinement times improved a factor of 2, from 2 ms to 4 ms. Two-dimensional probe measurements of potential contours showed a factor of four increase in the variation of potentials on magnetic surfaces with perpendicular injection and evidence of cell structures. Ion cyclotron heating experiments showed heating of both the electrons and ions, with maximum temperatures of 150 eV for the ions and 15 eV for the electrons. Electron temperature profiles showed electron heating at the ion cyclotron resonance zone. Both the electron and ion temperature scaled as the square root of the coupled power, and the heating per particle was observed to be independent of density (over the range  $10^{10} \text{ cm}^{-3} < n < 10^{13} \text{ cm}^{-3}$ ).

Difficulties envisaged with superconducting joints, anticipated in a stellarator reactor, prompted TSL to take a close look at modular coils for producing stellarator-type fields.

A method of representing modular coils as a natural consequence of a helical-type system was developed by the TSL ( the "ultimate" stellarator ) based upon the twisted-coil concept of Rehker and Wobig at Garching. This work, coupled with the attractive reactor applicability of modular coils and the need to test the concept on a modest scale, led to the Interchangeable Module Stellarator (IMS) device.

During the design of IMS, experimental studies on the Proto-Cleo Torsatron looked at the locations of diverted particle flux, as the need for particle control in any toroidal reactor configuration was becoming apparent. It was observed that the particle flux peaked near the apices of the trefoil shaped separatrix, and was in good agreement with a field-line edge-region model developed. This model was applied to IMS with excellent results. The measurements showed a peaking in flux to the outboard side of the device, as has been observed in other stellarator devices. A runaway instability was also identified in the Proto-Cleo Torsatron and was responsible for the expulsion of 10-20% of the current as well as bursts of microwave and x-ray emission every millisecond. The runaway electrons were found to be localized near the elliptic axis in the upper lobe on an internal separatrix, with the runaway current magnitude in rough agreement with theoretical predictions. Temperature fluctuations of 50% were observed owing to the runaway instability, and a simple calculation of the thermal conductivity was made based upon the propagation of heat pulses.

An experimental investigation of the radial distribution of Pfirsch-Schlüter and bootstrap currents was conducted in the Proto-Cleo Stellarator during this time. The magnitudes, profiles, and directions of the measured currents were consistent with predictions from neoclassical theory. Local currents were measured using small paddle probes and miniature Rogowski coils, with the total plasma current monitored by a conventional Rogowski coil. The measured directed currents were approximately four times smaller than the thermal currents. High-frequency inductive heating was also investigated in the "base" configuration and in a "double-star" configuration with an externally induced internal separatrix. It was shown that power can be effectively coupled to the plasma by a mechanism, described generally as modulation of the geometry of the magnetic surfaces, which circumvents the limitations of the classical skin effect. It was found that the plasma current amplitude was proportional to the amplitude of the local flux changes and to  $(w/V_A)^2$ , where  $V_A$  is the (poloidal) Alfvén speed. In the "base" configuration the current exhibits a characteristic reversal on opposite sides of the magnetic axis. In the "double-star" configuration the current distribution was more uniform due to reconnection of the magnetic flux.

IMS was designed and built entirely at the University of Wisconsin and has the same major and minor plasma radius as the Proto-Cleo Stellarator. The efficient production of magnetic field allows IMS to run at twice the field of the Proto-Cleo devices using the same power supply. As the first modular stellarator built, and the first stellarator built in the United States since the Model C at Princeton, a very complete study of construction field errors was undertaken to ensure good magnetic surfaces in the physical device. Results showed that positioning errors of the coils was more critical than symmetric errors in the coil themselves, and that the current feeds were the most crucial design point. Care was taken in the design to minimize the feed errors, errors resulting from turn-to-turn commutation of coil current, and to require the residual errors to be symmetric with respect to the periodicity of the device. The resulting coil design was fabricated using electrical discharge machining of the coils from toroidal forms. The tooling for the coils won the Grand Prize for Excellence in Design of Design News magazine. Together with Wisconsin's Fusion Technology Institute, the Torsatron/Stellarator Laboratory developed the UWTOR-M modular stellarator reactor design which drew significantly from the IMS design experience.

The first measurements made on the IMS device were to ascertain the actual magnetic structure using electron beam mapping techniques. The results showed a rotational transform profile in agreement with numerical predictions to within experimental

accuracies. The detected locations of the electron beam were in excellent agreement with calculations from a guiding-center code provided that distributed current filaments were used to model the magnetic field production. Particle flux was seen to emerge from the confinement region through the divertor bundles predicted by field-line calculations. Negligible particle flux was observed outside of these regions.

The IMS experimental program has concentrated on transport and divertor issues. Plasmas have been routinely produced in IMS using electron-cyclotron breakdown. The breakdown has been studied by examining the time delay between the beginning of the ECH pulse and the production of a measurable density as a function of puff pressure, magnetic field strength, and RF power. The confinement time of the ionizing electrons was found to scale inversely proportional to the square root of the applied power. It has been shown that when the resonance layer coincides with a saddlepoint in the magnetic field strength, the ionization rate during the breakdown phase is a maximum in agreement with a stochastic heating model. Under this condition, the electron-cyclotron emission during the discharge was an order of magnitude greater than when the resonance coincides with the magnetic axis. Application of approximately 100 W of power in the ion-cyclotron range of frequencies, in conjunction with the ECH, was shown to improve the confinement time of the ionizing electrons by 70%.

Electric fields have been observed to play an important role in profile formation in IMS with electron-cyclotron-resonance produced plasmas. Density profiles vary from almost flat to very hollow ( 10 to 1 peak-to-central density ratio ) as the location of the electron cyclotron resonance layer is moved from the inboard to the outboard side of the torus. Two-dimensional measurements of the space potential obtained using emissive probe techniques show that the density profile is fairly flat when the equipotential surfaces correspond well with the vacuum magnetic surfaces. In the hollow discharges, a large potential island appears on the outboard side of the torus, resulting in poloidal electric fields on the magnetic surfaces. The inclusion of a radially outward convection term in the particle balance equation can reasonably model these hollow profiles. This convection appears to be driven by the poloidal electric fields induced by the ECRH, with the required convection velocities bracketed by the average and local values of the  $E \times B$  drift velocities on the magnetic surfaces.

Correlation of increased electron cyclotron emission and increased potentials with increasingly hollow profiles suggests that non-thermal electrons may be responsible for the poloidal electric field. The confinement time during the ECRH is determined by measuring the particle flux into the divertor regions. The results show that the confinement time of the flat-profile discharges is a factor of two greater than for the hollow-profile discharges, in good agreement with confinement time ratios determined from the equilibrium profile-shape analysis. The IMS Thomson scattering system became operational with useful data from plasma densities of  $4-8 \times 10^{11} \text{ cm}^{-3}$ . Correlations with probe data showed a warm electron component whose location coincided with resonance locations. The density and temperature of the warm electron component were in good agreement with a Monté-Carlo model.

The IMS coil topology naturally produces a set of 63 modular 'bundle' divertors. These divertor bundles have been modelled by tracing magnetic field lines from just outside the last closed magnetic surface to their intersections with a reference torus with a minor radius equal to the coil minor radius. Probe measurements show good correlation with the predicted and experimental diverted flux locations. Ion-acoustic wave propagation experiments and computer modelling show that each divertor bundle connects to a specific region, basically a toroidal 'strip', around the last closed magnetic surface which we call the 'origin' of that diverted bundle.

Experiments have shown the ability to alter diverted flux patterns through the use of externally applied vertical magnetic fields. While external fields will be used in large devices for MHD control and other uses, these results show that these fields need to be

considered when designing particle control/collection schemes for these devices. Electric fields have also been shown to provide a mechanism for redistribution of diverted flux in the IMS divertors. Application of bias potentials, of two to three times the electron temperature, to groups of divertor bundles can reduce particle flux by up to 90% to other divertor bundles. As potentials are applied to a given divertor bundle, the potential in the origin (associated with that bundle) increases with the other origin potentials remaining unchanged. The potential in the biased origin saturates at about the electron temperature. The potential difference between adjacent origins sets up electric fields in the scrape-off layer plasma. An  $E \times B$  drift model qualitatively explains experimentally observed effects with biasing over a large range of configurations. Reversal of the magnetic field direction results in a reversal of the redistribution effects, consistent with this model. Further confirmation is provided by scaling of the biasing results to higher-field ( 5.8 kG compared to 2.6 kG ) operation. In this case, the ratio of  $E \times B$  drift velocity to diverted plasma flow velocity predicts 2/3 of the flow change seen in low field operation. This prediction has been verified within experimental accuracy. Combining the local effects of divertor biasing with global changes which can result from small externally applied vertical magnetic fields allows some tailoring of the diverted particle flux pattern.

The Torsatron/Stellarator Laboratory is continuing to emphasize studies of transport and divertors, especially under ECH, in its experimental program. Configuration studies, with collaboration efforts, are aimed at identification of potential new and innovative concepts which could improve the reactor relevance of toroidal confinement.

## **TRANSPORT**

# NEUTRAL GAS TRANSPORT AND PARTICLE RECYCLING IN THE W VII-AS STELLERATOR

F. SARDEI, H. RINGLER, A. DODHY, G. KÜHNER,  
W VII-AS TEAM<sup>1</sup>

Euratom-IPP Association,  
Max-Planck-Institut für Plasmaphysik,  
Garching

ECRH GROUP<sup>1</sup>  
Institut für Plasmaforschung,  
Universität Stuttgart,  
Stuttgart

Federal Republic of Germany

## Abstract

Neutral gas transport simulations with the 3D DEGAS code were applied to model plasmas before the W VII-AS operation was started. For a source of neutrals due to limiter recycling the calculated neutral density distribution is strongly affected by the asymmetries of the magnetic flux surfaces, limiter and wall structures. For a typical ECF heated deuterium discharge from the first months of W VII-AS operation the time histories of  $H_{\alpha}$  signals at five toroidal positions provide informations about the neutral fluxes due to limiter and wall recycling and to gas puffing. The  $H_{\alpha}$  signals are used to scale the calculated 3D distributions of the neutrals and the radial profiles of the ion sources as obtained from the DEGAS code. By comparing the results for the three different neutral sources the limiter is found to provide more than 80 % of the plasma refuelling, with a recycling coefficient of about 95 %. The calculated total particle fluxes resulting from the integrated ion sources are consistent with neoclassical predictions in the temperature gradient region. Near the plasma edge, however, the fluxes are strongly anomalous. The diffusion coefficient estimated from the fluxes and the measured density gradients (with  $z_{\text{eff}} \approx 3$ ) is about 1/10 - 1/20 of the electron heat conductivity.

---

## Introduction

In the W VII-AS stellarator the global particle and energy balances and the plasma density and temperature in the boundary region are strongly affected by the distribution of neutral particles originating from the plasma-wall interaction processes, similar as in W VII-A [1].

Furthermore, the flux of high-energy charge-exchange neutrals from the bulk plasma can give a significant contribution to thermal loading and impurity sputtering from the wall and the limiters.

---

<sup>1</sup> The members of the W VII-AS Team and ECRH Group are identified in the paper entitled 'Status of the advanced stellarator Wendelstein W 7AS: first results and further programme', these proceedings, p. 25.

## Results for a model plasma

Before the W VII-AS operation was started, model plasmas were used to study the neutral gas transport behaviour with the 3D DEGAS code [2]. In order to investigate to what extent the neutral density distribution is affected by the asymmetries of the flux surfaces and wall structures a simulation was performed for a neutral source due to limiter recycling. The  $T_e$ ,  $T_i$  and  $n_e$  profiles were taken from model calculations with the TEMPL plasma transport code ( $T_e(0) = 1.9$  keV,  $T_i(0) = 500$  eV,  $n_e(0) = 2 \times 10^{13}$  cm $^{-3}$  for an ECF input power of 720 kW) [3].

The typical cross section of the W VII-AS toroidal sector modelled for the neutral transport calculations is shown in Fig. 1. The limiter, the bulge for the NBI ports and the geometry of the magnetic surfaces (see Fig. 1) introduce asymmetries in the torus, which directly affect the neutral density distribution. Figure 2 shows the radial profiles of the neutral density at the poloidal angles  $\theta = 0^\circ, 90^\circ, 180^\circ, 270^\circ$ . As shown by the  $\theta = 90^\circ$  profile, the neutral density has a maximum at the limiter face and drops by 2 orders of magnitude to the plasma centre. In the opposite direction with respect to the limiter,  $\theta = 270^\circ$ , the density is significantly lower, reaching a maximum of 1/3 of the limiter value. Along the horizontal chord,  $\theta = 0^\circ$  and  $\theta = 180^\circ$ , the neutral density profiles are fairly symmetric up to a distance of  $\approx 12$  cm from the magnetic axis. The relatively high gradients of these profiles reflect the smaller plasma radius along this chord, associated with the asymmetry of the magnetic surfaces (see Fig. 1). Due to this asymmetry, the central neutral density is mainly determined by the neutrals penetrating the plasma in the horizontal direction. At  $r > 15$  cm, well inside the scrape-off region, the profiles diverge from each other, reflecting the asymmetry introduced by the bulge. Within the bulge, the neutral density is fairly constant and amounts to roughly 1/4 of the limiter value.

In the following, results from neutral transport simulations are discussed for a typical deuterium discharge from the first months of W VII-AS operation.

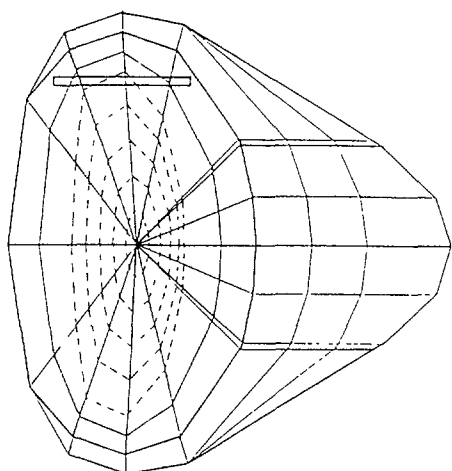


Fig. 1: Vertical cross-section of the modelled W VII-AS torus at the position of the module connecting flanges, including the wall, the bulge for the NBI ports, the flux surfaces and one of the limiters.

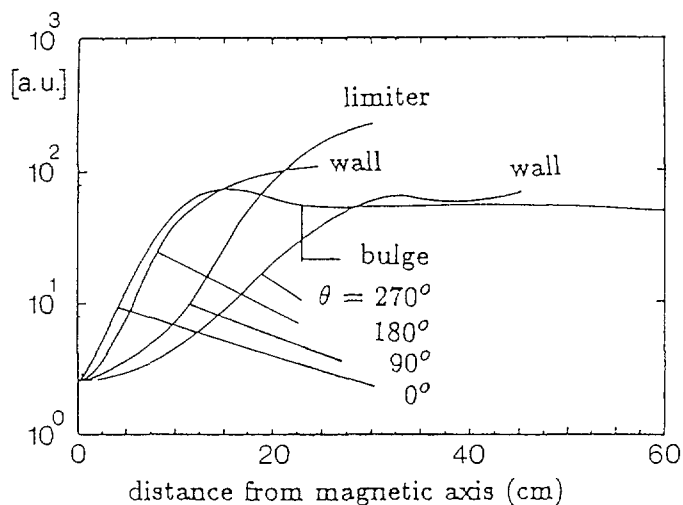


Fig. 2: Radial distributions of the neutral density at the poloidal angles  $\theta = 0^\circ, 90^\circ, 180^\circ, 270^\circ$  in the vertical cross-section shown in Fig. 1.

### Parameters of a selected discharge

The analysis is based on a ECF (70 GHz) heated deuterium discharge at the 2nd harmonic, with 1.25 T at the plasma centre and the external rotational transform  $t \approx 0.53$  at the plasma edge. Electron density and temperature profiles, measured by Thomson scattering, were available at 200 ms (Fig. 3). Stationary plasma conditions were maintained by one gyrotron heating with 150 kW input power and by external gas input linked to a feedback control of the plasma density. A plasma current induced either by ECF and/or by plasma pressure [4] was controlled and kept below  $\approx 500$  A by the OH-transformer. The measured  $T_e$ ,  $n_e$  profiles covered a plasma radius extending up to the separatrix, which was located at  $r_{\text{eff}} = 17.5$  cm, about 2.5 cm outside the last flux surface not intersected by the limiter. The global plasma parameters for the discharge are shown in Fig. 4.

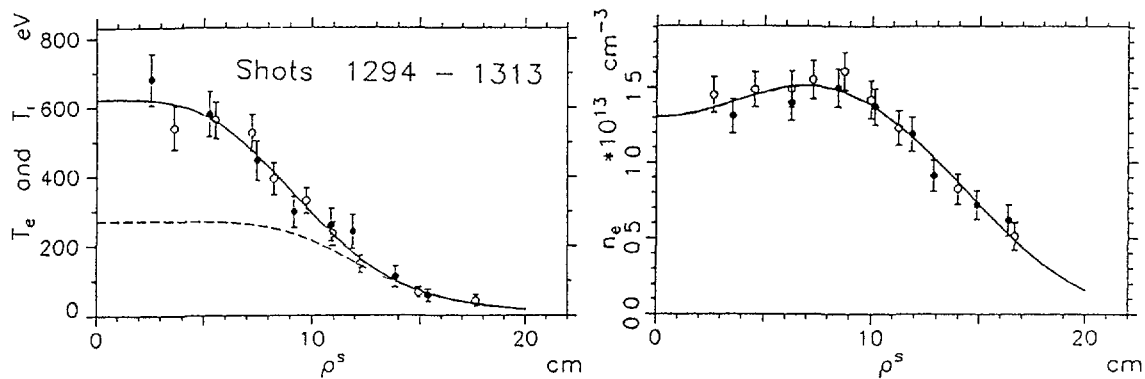


Fig. 3: Radial  $T_e$  and  $n_e$  profiles vs. effective radius at  $\Delta t = 0.2$  s from Thomson scattering. Full circles represent measurements on lh side of the profile.

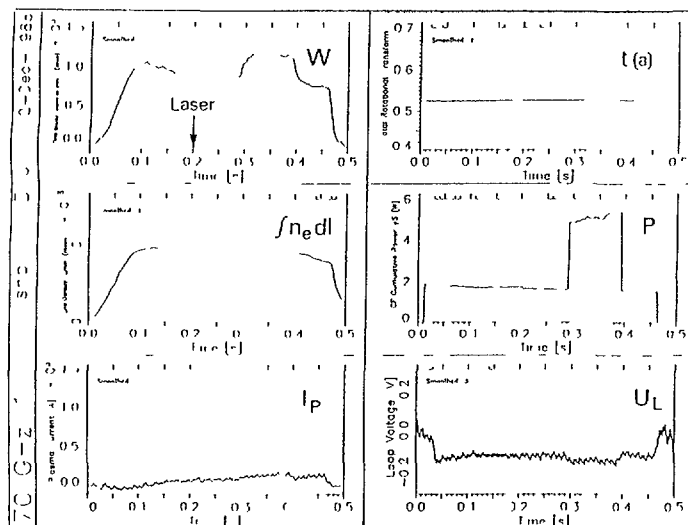


Fig. 4: Global parameters of a discharge, 1294 - 1313 series.

## H $\alpha$ -monitoring systems

An absolutely calibrated H $\alpha$  monitoring system [5] installed at W VII-AS yields information about particle recycling at both limiters (two toroidal positions for the bottom and one for the top limiter) (see Fig. 5a) and at two "triangular" magnetic surface cross sections (see Fig. 5b) close to and far from a gas inlet, respectively.

## Results from experiment and simulations

Three DEGAS simulations were performed for a given discharge according to the three main sources of neutrals (limiter, wall, gaspuff). The toroidal sector used for the limiter source simulation is shown in Fig. 6 and that for the wall and gas puff simulations in Fig. 7.

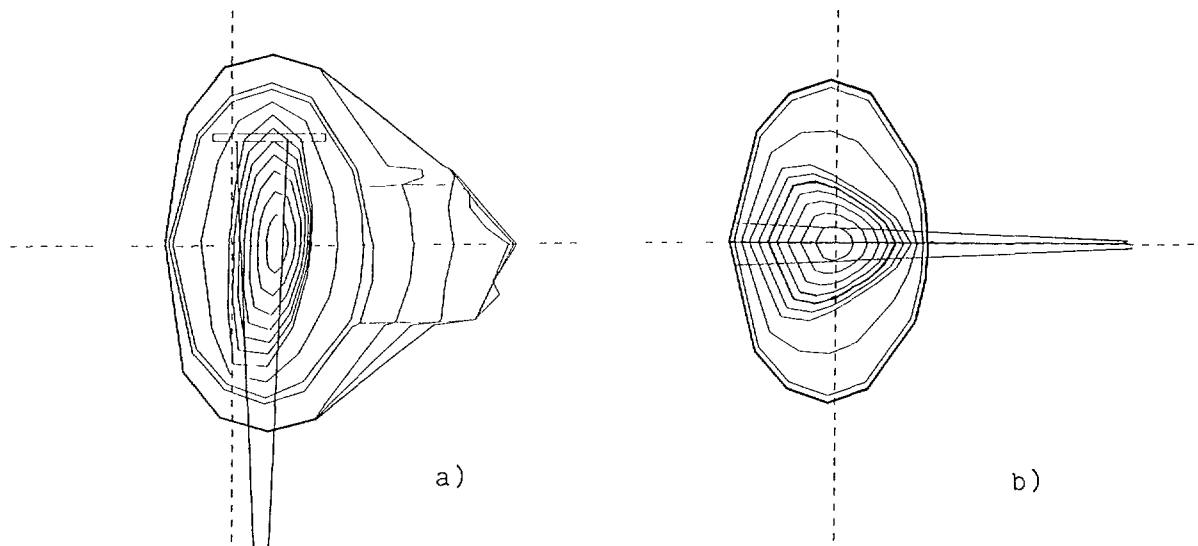


Fig. 5a,b: H $\alpha$ -monitoring systems at the limiter a) and at the triangular plasma cross section b).

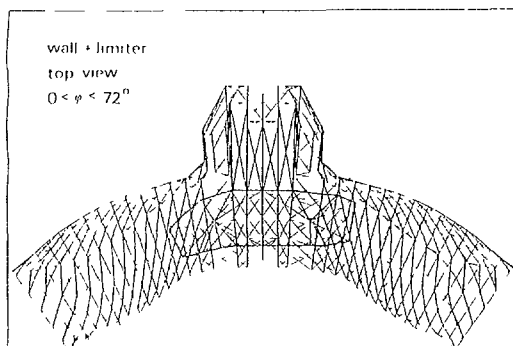
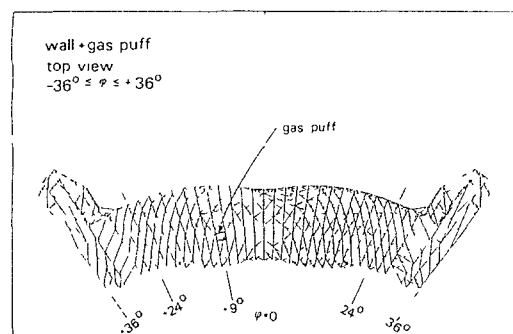


Fig. 6: Toroidal sector for limiter simulation.



The DEGAS code simulation at the "triangular" cross section near the gas inlet was used to find estimates for  $T_e$ ,  $n_e$  between separatrix and wall, which were consistent with both the measured gas input rate and  $H\alpha$  signal close to the gas inlet. These estimates were then used in the limiter and wall recycling simulations. The time histories of the measured  $H\alpha$ -signals from the limiters and the "triangular" cross sections are shown in Fig. 8a,b. The neutral fluxes and densities were estimated by scaling the calculated  $H\alpha$  emission rates to agree with the measured ones. The neutral density distribution in radial, poloidal and toroidal directions for the three neutral sources are shown in Fig. 9. The neutrals are strongly localized near the limiter, with a maximum density of  $2 \times 10^{10} \text{ cm}^{-3}$ , as shown in Fig. 9. At the plasma center, the calculated density due to the limiter source is one order of magnitude higher than that due to the wall and gas puff sources. As expected, no toroidal or poloidal density variations are found for the neutrals originating from wall recycling, if the incident ions are equally distributed along the wall, as assumed in the present case.

The calculated total refuelling rate of the plasma inside the separatrix due to limiter and wall recycling and to external gas feed amounts to  $2.5 \times 10^{20}$  ions/s. 83 % of this ionization source are provided by the limiter, 13 % by the wall and 4 % by the gas puffing. This corresponds to a global recycling coefficient of 0.96. From the calculated refuelling rates and a plasma ion content of  $8.9 \times 10^{18}$  particles inside the separatrix, as resulting from the measured electron densities (Fig. 3) and an assumed  $z_{eff}$  of 3, a global particle confinement time of 36 ms is estimated for this time of the discharge. The plasma refuelling efficiencies as fractions of the neutrals ionizing inside the separatrix are 0.65 for the limiter, 0.44 for the wall and 0.29 for the external gas source. The small values for the wall and gas puff sources are directly related to the large volume of the boundary region between separatrix and wall (more than twice the volume of the confined plasma). On the other hand, this has the advantage of improving the decoupling between the plasma and the wall, thus reducing the wall loading by high energetic charge exchange neutrals.

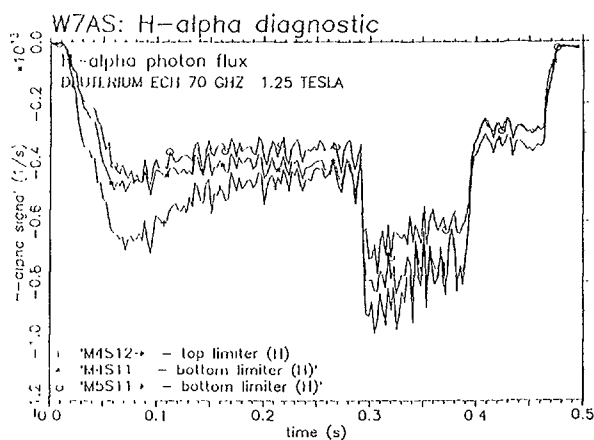


Fig. 8a:  $H\alpha$ -photon fluxes vs. time from ECE discharge looking at top and bottom limiter, plasma cross-section elliptical (a second gyrotron was switched on between 0.3 and 0.4 s).

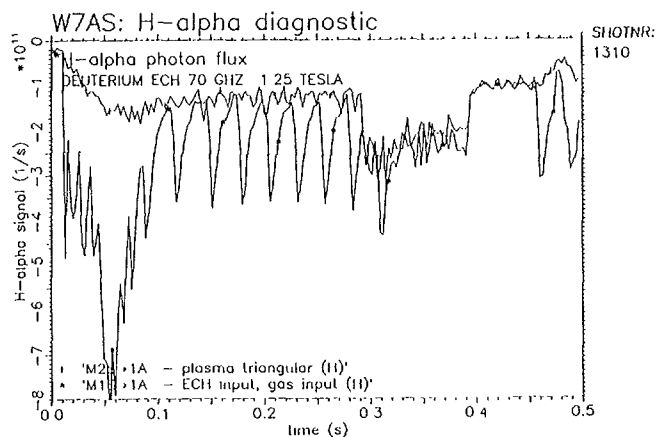


Fig. 8b:  $H\alpha$ -photon fluxes vs. time at two triangular plasma cross-sections, with and without gas inlet. The large spikes reflect the pulse sequence from the gas inlet.

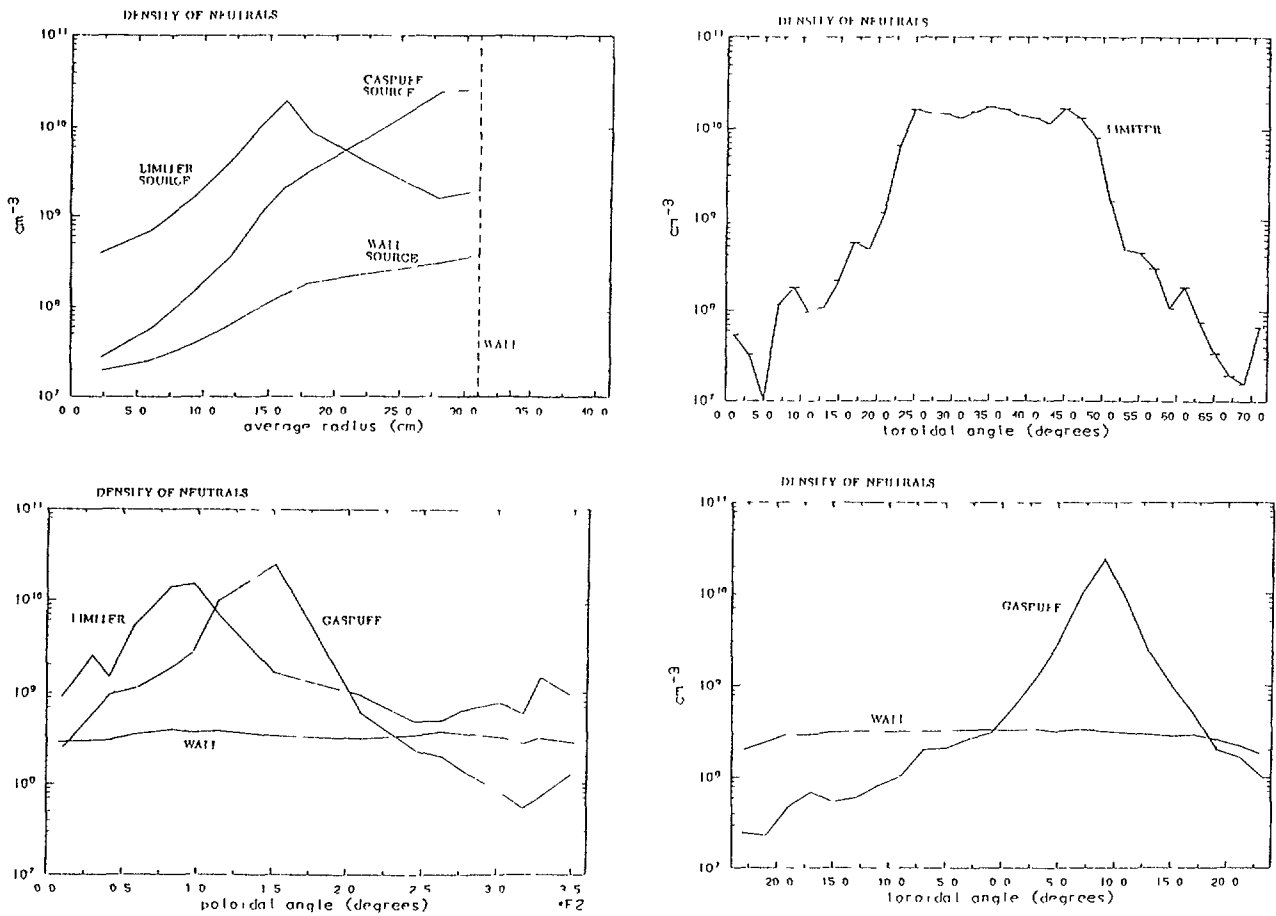


Fig. 9: Neutral density distribution in radial, poloidal and toroidal direction for the three neutral sources.

The radial profile of the ion flux  $\Gamma_i$  is obtained from the magnetic surface averaged ion sources. From  $\Gamma_i$  the electron flux  $\Gamma_e$  is estimated by assuming  $z_{\text{eff}} \approx 3$  for oxygen as main impurity and a confinement time comparable to that of the ions. In the temperature gradient region ( $r \approx 8$  cm) the particle fluxes are consistent with the neoclassical values obtained with the DKES code (Fig. 10). Towards the plasma edge, however, the ion transport becomes strongly anomalous. In this region it can be described by an anomalous diffusion coefficient of about  $1/10 - 1/20$  of the electron heat conductivity, as found earlier in W VII-A [6].

The given refuelling rates and efficiencies from wall recycling and gas puffing may have a considerable error margin due to their sensitivity to the unknown plasma density and temperature in the boundary region. Furthermore, the flux of ions incident on the wall at the position of the H $\alpha$  viewing line may not represent a good average of the ion fluxes over the entire torus wall. However, these uncertainties do not strongly affect the global recycling coefficient and  $\tau_p$ , since recycling from the limiter is the main refuelling mechanism to the bulk plasma.

Experimental indication of a recycling coefficient close to one for the discharge type discussed here is given after a second gyrotron is switched on for about 100 ms (see Fig. 8b). During that time a constant plasma density is maintained without any external gas feed and the H $\alpha$  signals at the triangular cross sections close to and far from the gas inlet coincide (see Fig. 8b). The amplitude of all signals (Figs. 8a,b) is

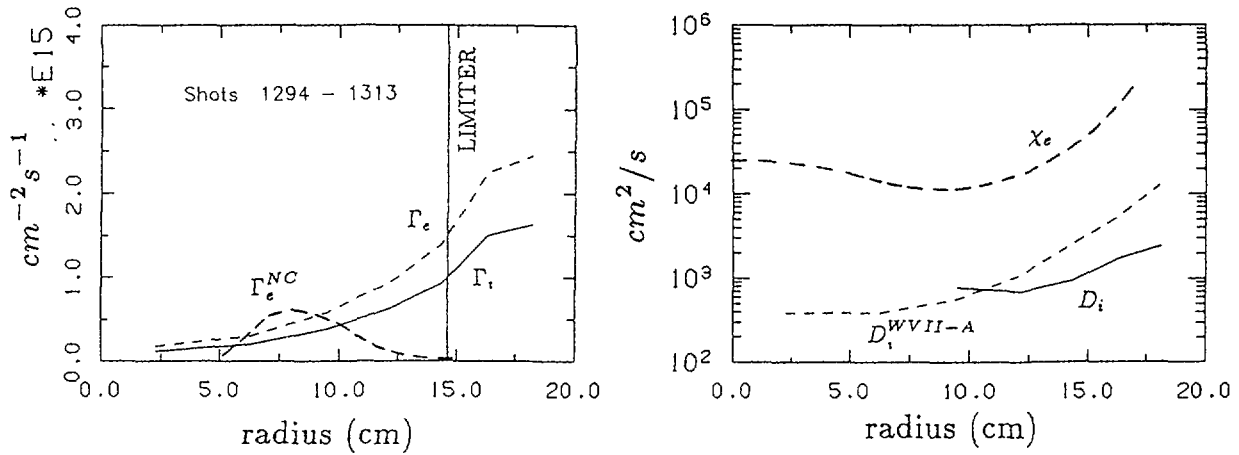


Fig. 10: Comparison of electron and ion fluxes and diffusivities with neoclassical predictions.

considerably higher than before the 2nd gyrotron was added. Considering that for stationary conditions the externally supplied neutral flux equals the fluxes absorbed by the wall and the limiters and that the absorbed fluxes scale linearly with the recycling fluxes, gas puffing proves to be a very efficient density control mechanism for high recycling ECF discharges.

For the same discharge, the calculated average neutral densities at the limiters and the wall due to the recycling sources are  $2.9 \times 10^9 \text{ cm}^{-3}$  and  $3.9 \times 10^8 \text{ cm}^{-3}$ , respectively. The total ion power loss due to charge exchange with all neutrals is 3.1 kW. The total electron power loss due to ionization, excitation and dissociation is 2.0 kW.

### Conclusions

From  $H_\alpha$ -measurements and 3D-DEGAS simulations estimates can be obtained of:

- Distribution of neutral densities
- Radial profiles of ion particle and energy sources
- Particle confinement time and recycling coefficient

However, more information is required about plasma density and temperature in the boundary region and about ion flux distribution on the wall.

Preliminary estimates of electron particle fluxes for ECH deuterium discharges from the first months of W VII-AS operation indicate:

- Consistency with neoclassical predictions in the plasma temperature gradient region ( $r_{\text{eff}} \approx 8 \text{ cm}$ )
- Anomalous particle fluxes at the plasma edge
- Ion diffusion coefficient  $\approx 1/10 - 1/20$  of electron heat conductivity

- Recycling coefficient close to one for all analyzed discharges
- Plasma recycling from the limiter is the main refuelling mechanism to the bulk plasma (large volume of the boundary region may improve screening of high-energy charge-exchange neutrals).

#### REFERENCES

- [1] H. Ringler et al., Plasma Phys. and Contr. Nucl. Fusion, IAEA-CN-47/D-V-1 (1987), Vol. 2, 603
- [2] D.B. Heifetz et al., J. Comput. Phys. 46 (1982), 309
- [3] H. Wobig, Notes on the W VII-A and W VII-AS Stellarators, Ringberg (1986), Internal Report
- [4] U. Gasparino et al., this conference
- [5] T. Uckan, ORNL/TM-10698.
- [6] H. Ringler et al., 9th Europ. Conf. on Contr. Fusion and Plasma Physics, Oxford A 2.4 (1979)

# TOROIDAL AND POLOIDAL SYMMETRY STUDIES ON NEUTRAL AND IMPURITIES IN CHS

K. IDA and the CHS GROUP<sup>1</sup>  
Institute of Plasma Physics,  
Nagoya University,  
Nagoya, Japan

## Abstract

Toroidal and poloidal symmetry of neutral and impurities has been studied for ECH and RF produced plasmas in Compact Helical System (CHS), a torsatron device with  $m=8$ ,  $R=1\text{m}$ ,  $a=0.2\text{m}$ . An eight-channel impurity-monitoring system using a 75 mm visible spectrometer with the band pass of 24 Å has been installed to measure toroidal symmetry of  $H_{\alpha}$  and impurity line intensity. A 34 channel space resolved 1m visible spectrograph system using MCP+CCD camera with a resolution of 0.1 Å /ch (256 spectral channels) has been developed in order to measure spectrum in a poloidal cross section. A neutral influx measured with the toroidal  $H_{\alpha}$  monitor system is localized at the gas puff position when the gas puff is injected during ECH discharge. Local particle recycling is enhanced by a factor of 2 to 3 by inserting one or two movable limiters, while toroidally symmetric  $H_{\alpha}$  radiation is observed for ECH plasma with an intrinsic divertor configuration. Poloidal in-out asymmetry of the oxygen  $O^{4+}$  line radiation is observed, while lower charged state oxygen  $O^{1+}$  shows symmetric profile. Local influxes of oxygen and iron observed in the RF produced plasma are sensitive to the distance between RF antenna and the fundamental ion cyclotron resonance position. The iron influx increases by a factor of ten or more, when the distance is decreased below 9 cm, while the oxygen influx shows weaker dependence.

---

## 1. Introduction

Compact Helical System <sup>1)</sup> (CHS) is an  $m=8$  torsatron device with a major radius of 1m and a minor radius of 0.2m and typical toroidal magnetic field of 1 T. A 28 GHz gyrotron with the injection power of

---

<sup>1</sup> The members of the CHS Group are identified in the paper entitled 'Overview of CHS experiment', these proceedings, p. 51.

100 KW produces ECH plasma with the electron density of  $2-6 \times 10^{12} \text{ cm}^{-3}$  and with the electron temperature of 200 - 900 eV, depending on the electron density<sup>2)</sup> RF plasmas produced by the Nogoya Type -III antenna have the electron density of  $2-6 \times 10^{12} \text{ cm}^{-3}$  in a wide range of magnetic field strength and the electron temperature up to 300 eV at specified magnetic field strength. The objective of CHS experiment is to study the plasma confinement in a low aspect ratio helical system. Toroidal and poloidal symmetry of plasma parameter can not be expected in helical systems, because of their helical and toroidal ripples. The symmetry of plasma parameter in a helical system has not been studied in detail due to a lack of enough ports. In this paper we describe the measurement on toroidal and poloidal symmetry of neutral ( $H_\alpha$ ) and impurity line radiations.

## 2 Spectroscopic Diagnostics for Symmetry Study

We installed two types of visible spectroscopic diagnostics to study both toroidal and poloidal symmetry of neutral and impurities. A toroidally monitoring system has eight channels in the toroidal direction every 45 degrees. A 75 mm visible spectrometer with the band pass of 24 Å is used to measure the intensity of line radiations of impurities and neutral. Four sets of this system can provide four different impurity lines and/or  $H_\alpha$  radiation simultaneously. In order to measure the spectrum width and shift of impurity radiations in a poloidal cross section, a 34 channel space resolved 1m visible spectrograph system using MCP+CCD camera with a resolution of 0.1 Å/ch (256 spectral channels) has been developed<sup>3)</sup>. Although it has a relatively poor time resolution of 16.7 ms, it can provide of radial profiles of ion temperature and poloidal rotation speed radial profile as well as impurity density radial profile.

## 3 Toroidal Symmetry in ECH Plasmas

A neutral influx measured with the toroidal  $H_\alpha$  monitor shows localized recycling at the gas puff position when the gas puff is injected during ECH discharge as shown in Fig 1. Local particle recycling is enhanced by a factor of 2 to 3 by inserting one or two movable limiters, while toroidally symmetric  $H_\alpha$  radiation is observed in an intrinsic divertor configuration. More precise measurement should be done to estimate how this recycling is localized, since the decay length

of the radiation in the toroidal direction is shorter than the spacing of the detector array (45 degrees).

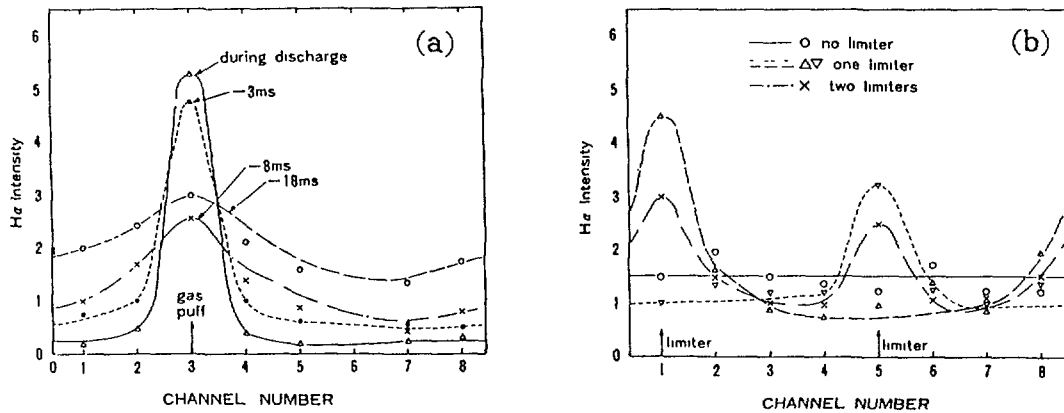


Fig.1 Toroidal distribution of H $\alpha$  radiations (a) effect of gas puff with various timings (b) effect of movable one and two limiters.

#### 4. Poloidal Symmetry in ECH Plasmas

It is one of important issues to study the effect of the magnetic axis shift on an impurity influx and profile, since the shift of the magnetic axis affects the helical field ripple significantly<sup>4</sup>). A plasma nearly touches the inner wall of the vacuum vessel for  $R_{ax} = 94.9$  cm, while there is a large clearance both inside and outside when  $R_{ax} = 101.6$  cm, as shown in Fig. 2. The central electron temperature and the density are 660 eV and  $2.7 \times 10^{12}$  cm $^{-3}$  for inward shifted case ( $R_{ax} = 94.9$  cm), while those are 270 eV and  $2.3 \times 10^{12}$  cm $^{-3}$  for outward shifted case ( $R_{ax} = 101.6$  cm).

Figure 3 shows radial profiles of H $\beta$ , carbon and oxygen line radiations for magnetic axes at 94.9 cm and 101.6 cm. The shift of H $\beta$  intensity peak is consistent to the shift of magnetic axis. CV profile, which represents C $^{4+}$  profile, is observed to be hollow for inward shifted case, while it is peaked at the plasma center for outward shifted case. This is due to the difference of the electron temperature in two cases, since the ionization potential of CV is 392 eV and it is higher than the peak electron temperature for outward shifted case and lower than that for inward shifted case. Oxygen influx estimated from OII (O $^{1+}$ ) line radiation is mainly from the inside wall for inward shifted case, while it shows uniform profile for

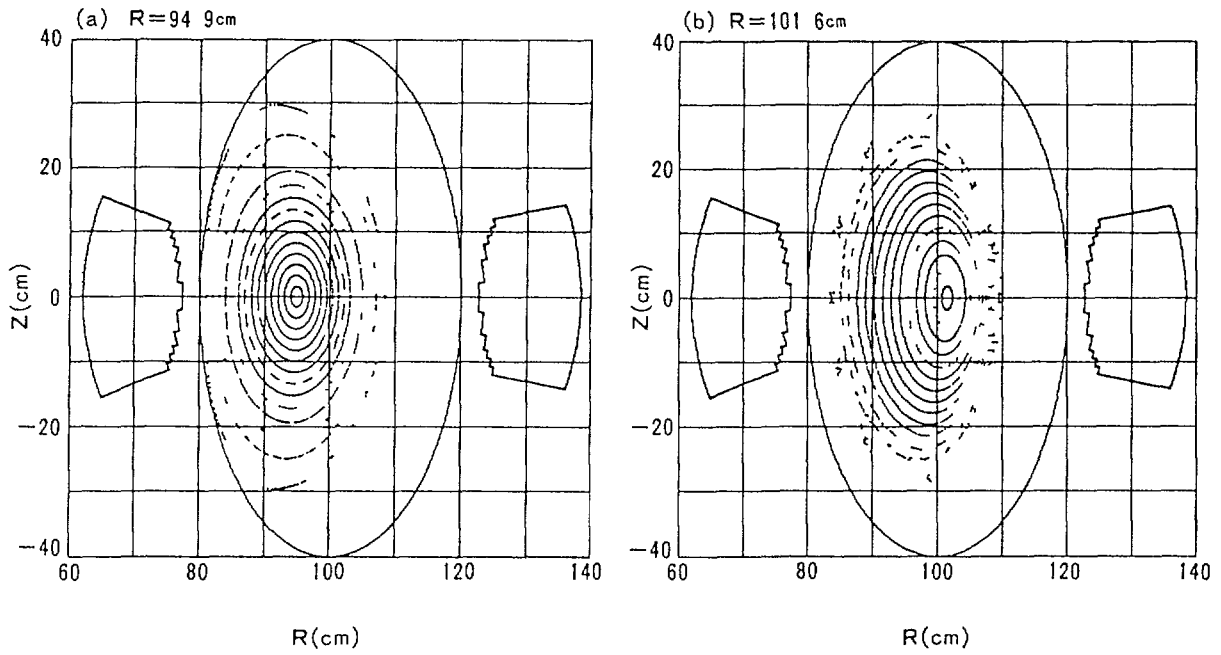


Fig 2 Poloidal cross sections of magnetic surface for  $R_{ax} = 94.9$  cm and 101.6 cm

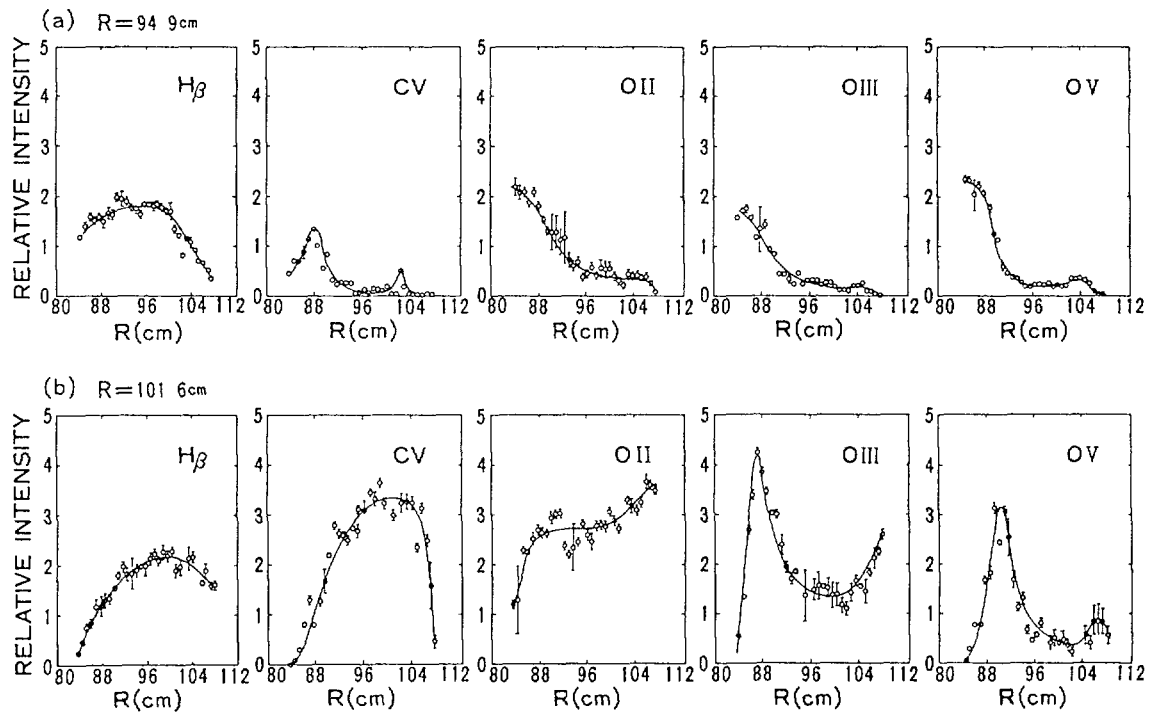


Fig 3  $H_\beta$  and impurity line radiation profiles in a poloidal cross section for two cases of plasma position (a)  $R_{ax} = 94.9$  cm, (b)  $R_{ax} = 101.6$  cm

outward shifted case. Poloidal in-out asymmetry of impurity line radiations of  $O\ III$  and  $O\ V$  ( $O^{2+}$  and  $O^{4+}$ ) is observed for both inward and outward shifted cases. This asymmetry of impurity density is partly due to localized oxygen influx from inside wall for inward shifted case, however it may be mainly due to asymmetry of the impurity transport especially for outward shifted case. The cause of this asymmetric impurity transport has not been well studied yet, however it may be explained by plasma potential and/or particle loss cone

### 5. Impurity Influx in RF Produced Plasmas

The RF antenna becomes the impurity source in RF-produced plasmas, since it is inserted nearly to the plasma boundary to obtain a sufficient coupling with the plasma. The toroidal field was scanned from 0.5 T to 0.9 T to move the fundamental resonance layer from the plasma center to the plasma edge, as shown in Fig. 4. Figure 5 (a) shows the toroidal distribution of oxygen influx in a RF produced plasma at the toroidal magnetic field of 0.65 and 0.75 T. Localized oxygen influx at the antenna is more significant for the toroidal field

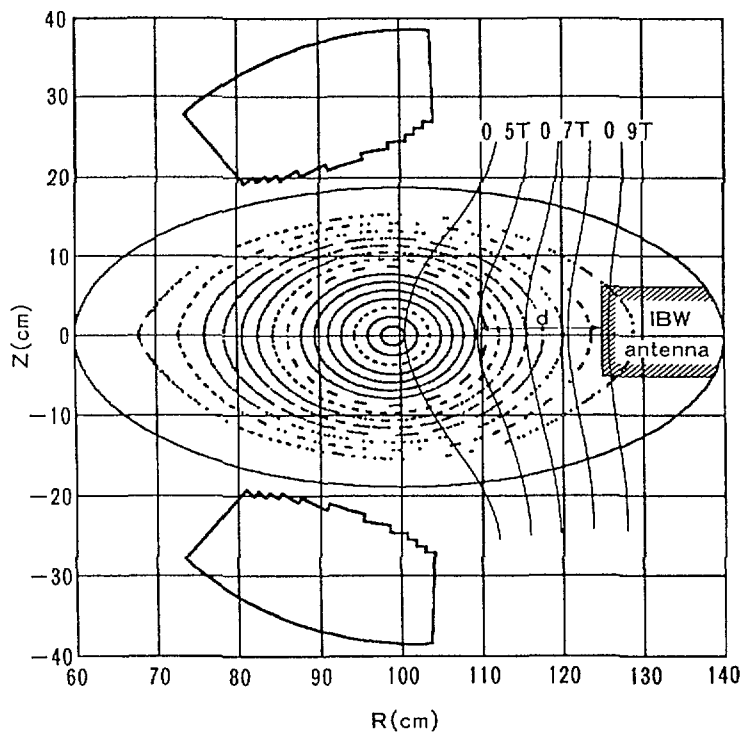


Fig 4 Poloidal cross section of magnetic surfaces and the fundamental ion cyclotron resonance layer

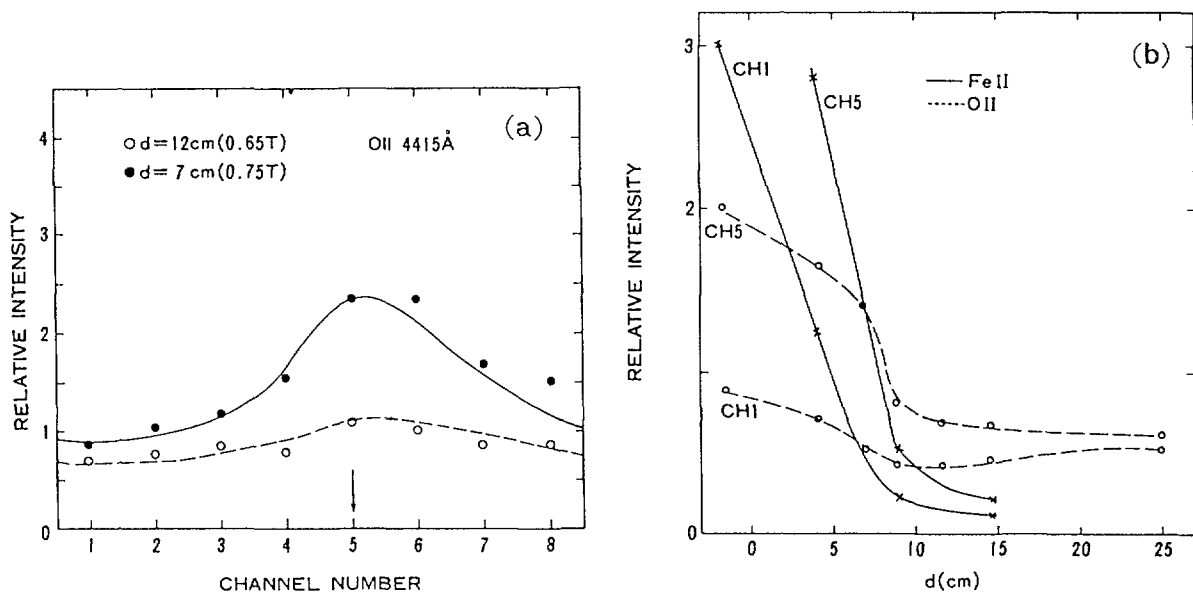


Fig.5 (a) Toroidal distribution of oxygen influx in RF produced plasma at toroidal magnetic fields of 0.65 and 0.75 T. (b) Oxygen and iron impurity influxes as a function of the distance between the RF antenna and the fundamental resonance layer.

of 0.75 T ( $d=7$  cm). This oxygen influx is observed to be sensitive to the distance between the RF antenna and the fundamental resonance position. The iron influx is more sensitive to this distance. This is due that the impurity influx is enhanced by the sputtering due to fast ions heated at the fundamental resonance layer. The iron influx increases by a factor of ten or more, while the oxygen influx increases by a factor of three, when the distance between the antenna and the fundamental resonance layer is decreased below 9 cm as shown in Fig. 5 (b).

#### REFERENCES

- (1) M.Fujiwara et al., in Controlled Fusion and Plasma Physics (Proc. 14th Europ. Conf. Madrid, 1987)
- (2) K.Matsuoka et al, in Plasam Physics and Controlled Nuclear Fusion Research (Proc. 12th IAEA Conf., Nice, 1988) IAEA-CN-50/I-I-3.
- (3) K.Ida and S.Hidekuma, Nagoya Plasma Physics Laboratory Report IPPJ-888 (1989), to be published in Rev. Sci, Instrum.
- (4) S.Okamura et al., Nagoya Plasma Physics Laboratory Report IPPJ (1989).

# TRANSPORT MODELING OF ECH AND NEUTRAL-BEAM-HEATED PLASMAS IN THE ADVANCED TOROIDAL FACILITY

H.C. HOWE, L.D. HORTON, E.C. CRUME, J.H. HARRIS,  
R.C. ISLER, M.M. MURAKAMI, D.A. RASMUSSEN,  
J.B. WILGEN, W.R. WING  
Fusion Energy Division,  
Oak Ridge National Laboratory,  
Oak Ridge, Tennessee,  
United States of America

## Abstract

Results of time-dependent transport modeling of the ATF plasma are compared with a typical ungettered, neutral-beam-heated discharge. For the discharges modeled,  $B_T = 0.95T$  and the plasma was shifted inward 5cm from the standard position resulting in major and average-minor radii of  $R_0 = 205\text{cm}$  and  $a = 27\text{cm}$ . The model is adjusted to give agreement between measured diagnostics signals and the corresponding values inferred from the model plasma. With this agreement, the model reproduces the main features of the discharge, including the radiation-induced temperature collapse.

---

## MODEL

The discharges are modeled with the predictive transport code PROCTR [1], which evolves radial plasma profiles in time in the full 3D ATF geometry. Models are included for the plasma temperatures  $T_e$  and  $T_i$ , the plasma hydrogenic-ion density, and the toroidal current. In addition, a multi-charge-state impurity transport model [2,3], which includes radial transport and ionization and recombination between the various charge states, is used for carbon and oxygen. Neoclassical heat transport including transport due to the helical ripple [4] is assumed for both electrons ( $\chi_e$ ) and ions ( $\chi_i$ ) with a large anomalous enhancement in the outer half of the plasma (in the region  $\epsilon > 1/2$ ) to reproduce the narrow observed  $T_e$  profile shape [5]. This enhancement is partially attributed to magnetic islands due to field errors, the cause of which has been identified and corrected. Hydrogenic-ion and impurity diffusion are treated with a radially constant diffusion coefficient of 0.2–0.5 m<sup>2</sup>/s with a large enhancement for  $\epsilon > 1/2$ . An inward pinch is included in the impurity transport. Electron cyclotron heating (ECH) is treated using a linear-absorption, multi-pass model [6] including cutoff (for  $n_e > 1.8 \times 10^{13}\text{cm}^{-3}$  in ATF). Neutral-injection heating is given by an axisymmetric neutral deposition model plus thermalization governed by a moments solution of the fast-ion Fokker-Planck equation including fast-ion loss due to charge-exchange during slowing down. Thermal neutral transport uses a cylindrical model [7] where the neutral level is determined by recycling and external fueling.

## ECH PLASMA

Approximately steady-state plasmas are obtained with 200 kW of second harmonic ECH in ATF. Measured Thomson scattering  $T_e$  profiles, spectroscopic  $T_i$  values, stored energy, and spectroscopic emission levels may be reproduced using the model described

above when the impurity source rates are adjusted to give impurity levels corresponding to  $Z_{\text{eff}} \simeq 2 - 2.5$ . The power balance for the ECH plasmas indicates that electron (35%) and neoclassical ion (20%) heat conduction are the largest energy losses from the plasma core with neoclassical electron heat conduction accounting for more than 50% of the total electron conduction loss. The total radiated power in the model is approximately 40% to 50% of the heating power, in agreement with spectroscopic estimates, and originates primarily from the outer regions of the plasma.

### NEUTRAL-BEAM-HEATED PLASMA

Neutral-beam-injection (NBI) heated discharges exhibit dynamic behavior and do not reach a steady state in ATF experiments. During NBI heating with 650 kW of co-injection, the density ramps up nearly linearly from the value obtained in the ECH phase of the discharge (see Fig. 1). This ramp is obtained in the model by a combination of beam fueling and an external gas source, which is similar in magnitude to the gas puff introduced in the experiment. At the same time, the stored energy (Fig. 2) and plasma ion temperature rise to a peak and then fall to a low value while the electron temperature decreases monotonically from the ECH-phase value (after a small initial rise in some discharges). These features of the data are all reproduced by the model. Near the end of the stored-energy decrease, the spectroscopic line emission from intermediate charge states of light impurities (C, O, N) disappears due to collapse of the plasma electron temperature. This sudden collapse is reproduced in the model (see Figs. 3 and 4)

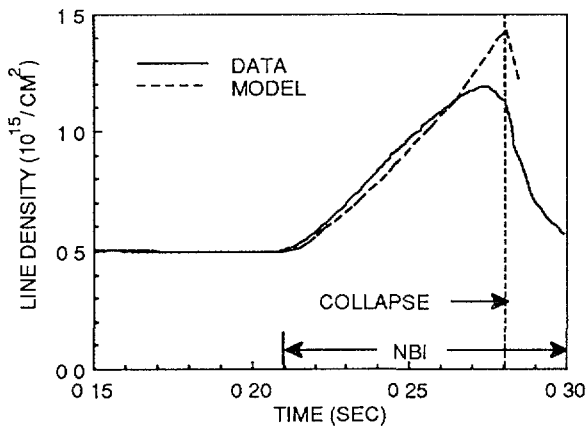


FIGURE 1 LINE-INTEGRATED DENSITY

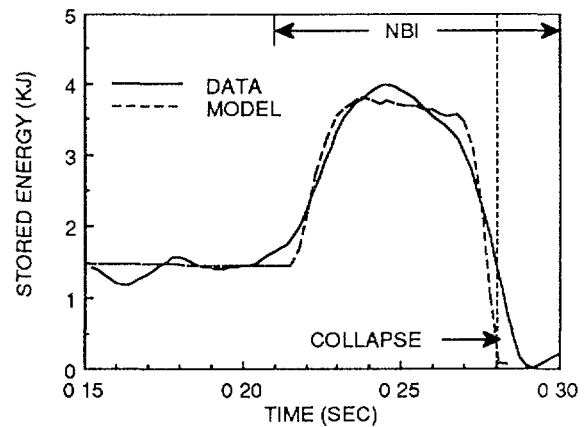


FIGURE 2 DIAMAGNETIC STORED ENERGY

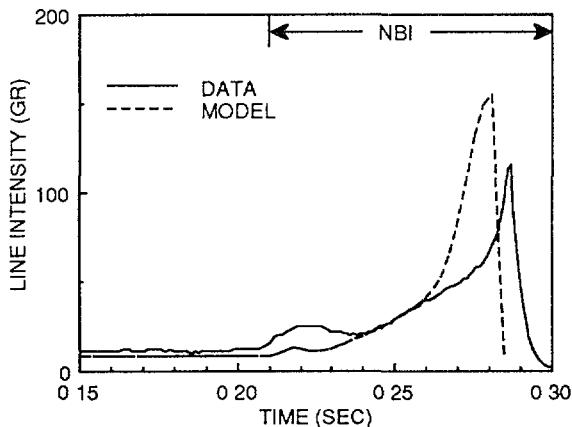


FIGURE 3 LINE INTENSITY FOR OV 760A

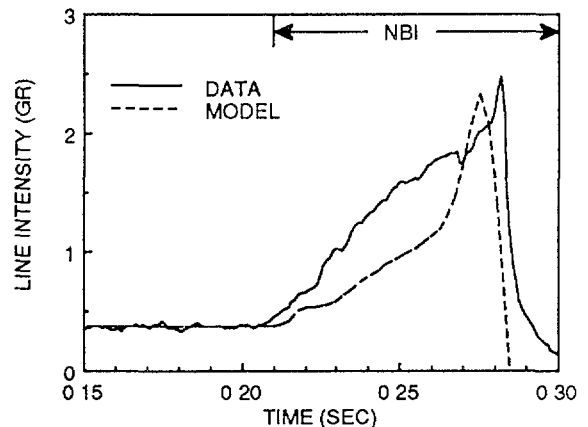


FIGURE 4 LINE INTENSITY FOR CIV 312A

when the impurity source rates are adjusted so that the predicted spectral line-integrated intensities agree with the measured intensities for spectral lines emitted from the plasma interior. This agreement occurs for  $Z_{\text{eff}} \simeq 2$ , indicating a rise in impurity content that is approximately proportional to the rise in electron density. The unstable nature of the collapse is due in the model to the strong increase in impurity line radiation at low plasma electron temperatures ( $T_e < 100\text{eV}$ ). The  $T_e$  profile collapses inward from the edge as large radiation from the outer region of the plasma progressively cools adjacent interior plasma until all the stored energy has been radiated in a brief (5–10ms) burst of radiation. The collapse has been simulated successfully only with the observed narrow  $T_e$  profiles, which allow the lower impurity ionization states to penetrate the outer half of the plasma, resulting in a large radiating volume. The collapse may be initiated in the model either when the plasma density reaches ECH cutoff (in ECH-only discharges) or when the total radiation exceeds the full heating power.

At the time of collapse, the model electron density shows a change in slope from an upward ramp to a slow decrease (Fig. 1). The decrease is due, in the model, to a large reduction in the ionization rate of neutrals by plasma electrons, which results from the low plasma electron temperature. Without an ionization source, the plasma density decays by cross-field diffusion. The saturation of the experimental plasma density just before the collapse is most likely due to a decrease in plasma recycling as the plasma temperature profile contracts and detaches from the wall. A similar reduction in impurity influx just before collapse would also be inferred from the detachment. This effect has not yet been included in the model.

The model time-dependent global power balance (Fig. 5) illustrates the transient nature of neutral-injection-heated discharges. The density of the ECH discharge is adjusted in the experiment so that the central electron density is just below the wave cutoff density; thus, the ECH is cut off almost immediately by the density rise induced by NBI. The neutral-beam electron heating increases continuously during the heating pulse as the shine-through and fast-ion charge-exchange losses decrease due to the rising plasma density. The radiation also rises during injection (as a result of increased impurity influx in the model) and eventually surpasses the heating power, resulting in the temperature collapse. At the peak of the stored energy, the simulation indicates that approximately 50% of the heating power is being radiated (from the outer regions of the plasma) but this ratio is a strongly increasing function of time. The primary energy loss from the plasma core at the time of the stored-energy peak is electron (25%) and neoclassical ion (40%) heat conduction with neoclassical electron heat conduction accounting for less than 50% of the total electron conduction loss. The slow decrease in the measured stored energy (Fig. 2) after the peak and before the collapse may indicate an increase in transport above the model level.

The plasma current also rises to a peak and then decreases to a small value at the time of collapse (see Fig. 6). The small current present during the ECH phase of the discharge may be a bootstrap current, which is not included in the model. The current during the neutral-beam phase is approximately reproduced in the model by the beam-driven current plus the induced plasma current. The current decreases after reaching a peak because of the decreasing plasma electron temperature and resulting decreasing fast-ion slowing-down time.

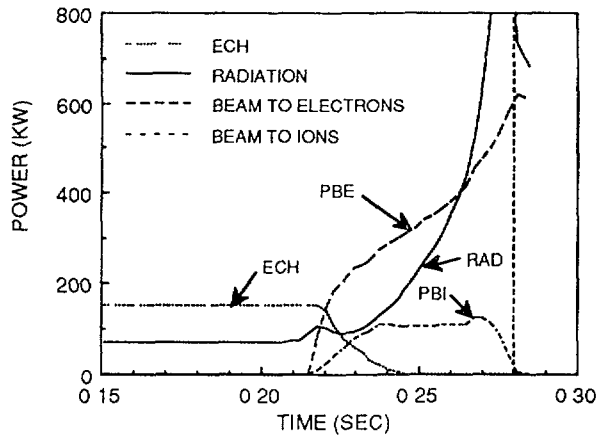


FIGURE 5 SIMULATED POWER BALANCE

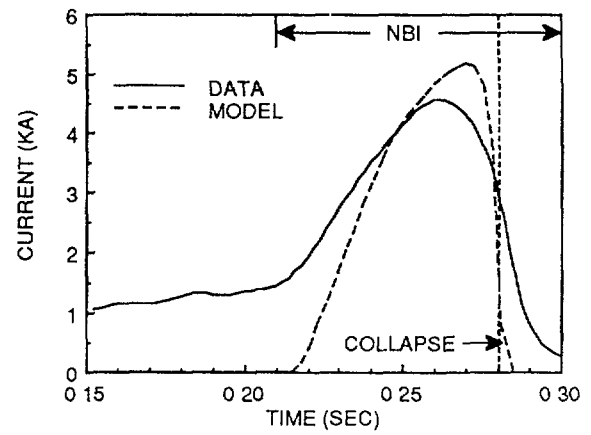


FIGURE 6 TOROIDAL PLASMA CURRENT

### ACKNOWLEDGEMENT

Work sponsored by the Office of Fusion Energy, U. S. Department of Energy, under contract DE-AC05-84OR21400 with Martin Marietta Energy Systems Inc.

### REFERENCES

- [1] H. C. Howe, Technical Report ORNL/TM-9537, Martin Marietta Energy Systems, Oak Ridge Natl. Lab., 1985.
- [2] K. Behringer, Report JET-R(87)08, JET Joint Undertaking, Abingdon, Oxon, UK, 1987.
- [3] L. D. Horton, E. C. Crume, H. C. Howe, and R. C. Isler, paper O5-3 presented at this conference.
- [4] D. E. Hastings, W. A. Houlberg and K. C. Shaing, Nucl. Fusion, **25**, 445, 1985.
- [5] D. A. Rasmussen, A. C. England, M. Murakami, et al., paper 2P-4 presented at this conference.
- [6] R. C. Goldfinger and D. B. Batchelor, in *Applications of radio-frequency power to plasmas*, pages 65-68, American Institute of Physics, 1987.
- [7] K. Burrell, Journal of Comp. Physics, **27**, 88, 1978.

## CONVECTIVE TRANSPORT IN IMS

J.N. TALMADGE, D.T. ANDERSON, F.S.B. ANDERSON,  
B.J. PETERSON, J.L. SHOHEIT  
Torsatron/Stellarator Laboratory,  
University of Wisconsin - Madison,  
Madison, Wisconsin,  
United States of America

### Abstract

Convective transport measurements in IMS device are described. The probes measurements of the ion saturation current were compared with the results of the numerical calculations. Island structures formation has been observed and the explanation of their creation was done.

---

Steady-state plasma density profiles in IMS are hollow during Electron Cyclotron Heating (ECH), with the hollowness increasing as the resonant layer is moved from the inboard side of the torus to the outboard side by increasing the magnetic field strength. The microwave source has a frequency of 7.28 GHz (resonant with  $B=2.6$  kG), power output of 2 kW and pulse length of 10 msec. Plasma densities are in the range of  $0.5-3.0 \times 10^{11} \text{ cm}^{-3}$ , bulk electron temperatures are 10 eV and ion temperatures are 2-4 eV.

Two probes were used to measure the ion saturation current in two-dimensions at two separate toroidal locations. The measurements were made at 5 mm intervals, with about 250 shots needed to record the data. Shown in Figure 1 are the contours of constant ion saturation current normalized to the line-averaged density as measured by a microwave interferometer. Also shown in each figure is the numerical calculation of the magnetic surfaces at the respective probe ports. The regions of greatest ion saturation current are located on the edges of the plasma. Island structures can be observed that are not coincident with the magnetic surfaces.

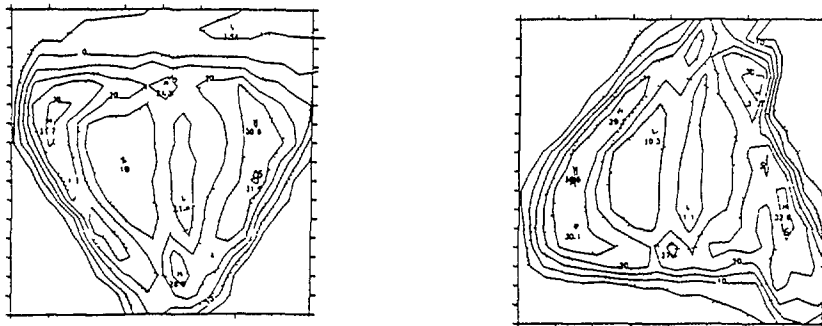


Figure 1 Contours of constant ion saturation current at two toroidal locations.

The density profiles can vary from almost flat to very hollow. Typically, the ratio of the edge peak density to the central density can range from 1.2 to 10.0. In Figure 2a the central magnetic field  $B_0$  is 2.52 kG, which places the resonant layer close to the magnetic axis, about 1 cm inboard from the geometric center. The solid circles are the experimental data points normalized to the peak density. In Figure 2b,  $B_0=2.35$  kG, which places the cyclotron layer on the inboard plasma edge. At this magnetic field the density profile is peaked almost at the center of the plasma.

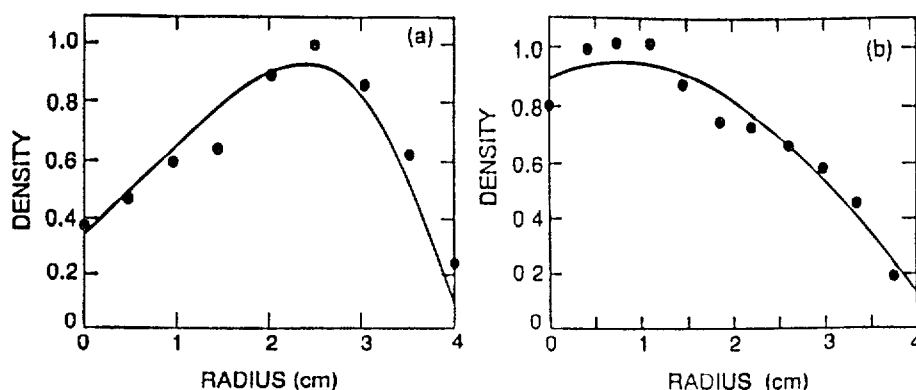


Figure 2 Normalized electron density profiles for (a)  $B_0=2.52$  kG and (b)  $B_0=2.35$  kG

Since diffusion-driven transport alone can not explain steady-state hollow density profiles, a convective term is added to the particle balance equation. If it is assumed that the convective velocity  $V$ , diffusion coefficient  $D$  and ionization rate  $\gamma$  are global averages and independent of radius this equation is,

$$r \frac{\partial^2 n}{\partial r^2} + \left(1 - \frac{V}{D} r\right) \frac{\partial n}{\partial r} + \left(\frac{\gamma r}{D} - \frac{V}{D}\right) n = 0 \quad (1)$$

The solid lines in Figures 2a and 2b are the best fit of Equation (1) to the profiles. This occurs for the hollow profile when  $V/D=0.87$  and  $\gamma/D=0.86$ . For the flatter profile,  $V/D=0.14$  and  $\gamma/D=0.37$ . This implies that the convective velocity would be a factor of 6 less and the confinement time a factor of 2 greater for the flatter profile than for the hollow profile if the diffusion coefficients were the same for the two profiles.

By measuring the particle flux into the divertor regions outside the main plasma confinement volume, an estimate of the confinement time can be made. This is given by  $\tau = qnV_{pI}/I$  where  $n$  is the plasma density,  $V_{pI}$  is the plasma volume and  $I$  is the current to the shields that are mounted on the modular coil support rings. For the flatter profile, the confinement

time was estimated as  $770 \pm 170 \mu\text{sec}$  and for the hollow profile this value was  $360 \pm 110 \mu\text{sec}$ , in reasonable agreement with the factor of two determined from the steady-state profiles.

For both the hollow and flatter profiles, the space potential was measured over the cross-section of the plasma with emissive probes. These measurements were made at 1 cm intervals. In Figure 3a a crescent-shaped contour can be seen on the outboard side of the torus for the hollow profile. This can give rise to an  $E \times B$  drift in the radial direction. In Figure 3b, for the flatter profile, the variation of the potential on a magnetic surface is greatly reduced.

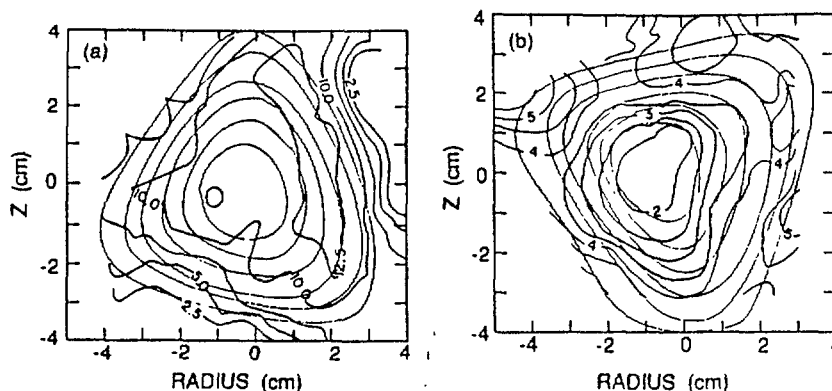


Figure 3 Equipotential contours (bold lines) and flux surfaces for (a) hollow profile (contour interval is 2.5 V) and (b) flatter profile (contour interval is 0.5 V).

The net  $E \times B$  drift on a magnetic surface was calculated by a numerical code which interpolated the potential along a flux surface and as a function of radius. The peak and radially averaged velocity were 500 cm/sec and 170 cm/sec for the hollow profile and 80 cm/sec and 30 cm/sec for the flatter profile. The local  $E \times B$  drift velocities are roughly 2 orders of magnitude greater. The factor of 6 in the ratio of the net  $E \times B$  velocities is in good agreement with the ratio determined by the equilibrium profiles.

Two emissive probes were used to measure the floating potential along a magnetic field line as a function of magnetic field strength. One probe was fixed at  $r=2$  cm from the magnetic axis and biased to -90 V. The other probe, which could be moved in two dimensions and was located at a different toroidal angle, was biased to +90 V to collect electrons and align the two probes in vacuum. Figure 4 shows the locus of signal peaks in the cross-section which traces out a magnetic surface (the dotted line is a numerical calculation of the vacuum magnetic surface).

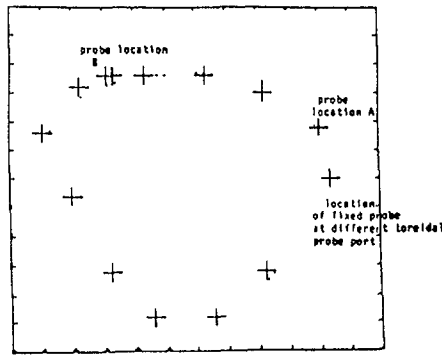


Figure 4. Experimental measurement of the vacuum magnetic surface and numerical calculation (dotted line).

Measurements were made of the difference in floating potential as a function of the magnetic field strength between the moveable probe at point A on the outboard side of the torus and the fixed probe located on the outboard side at a different toroidal angle. Figure 5 shows there is little difference in the potential. Measurements were also made of the difference in potential between the probe at point B on the inboard side and the fixed probe. Substantial changes in the floating potential difference can be observed. The error bars reflect the deviation of the potential difference during the discharge.

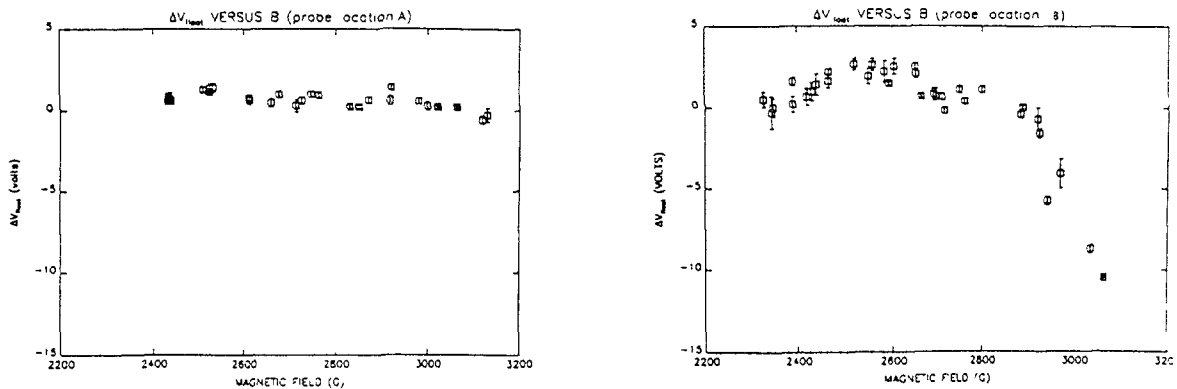


Figure 5. Variation of the difference in floating potential between a moveable probe at positions A and B (see Figure 4) and a fixed probe at a different toroidal angle.

## EXPERIMENTAL STUDIES ON DRIFT WAVES IN SHEILA

B.D. BLACKWELL, S.M. HAMBERGER, X.H. SHI

Plasma Research Laboratory,  
Research School of Physical Sciences,  
Australian National University,  
Canberra, Australia

### Abstract

Detailed studies of coherent fluctuations in several configurations of SHEILA support the view that these are essentially electrostatic collisional drift waves propagating so that the ratio of toroidal to poloidal mode numbers closely matches the rotational transform. The observations are consistent with a linear dispersion theory based on a cylindrical approximation to the helical plasma column in straight-field coordinates.

---

### Mode Structure Measurements

By an appropriate choice of experimental conditions the fluctuation spectrum in SHEILA can be reduced to a single, coherent mode whose eigen-structure is amenable to detailed study, eg. via the ion-saturation current to Langmuir probes. In SHEILA these exist either in the form of fixed arrays which can be pre-set to sample around a given flux surface, or as a pair of one fixed and one articulated probe which can sample throughout a given cross-section. (Fig.1)

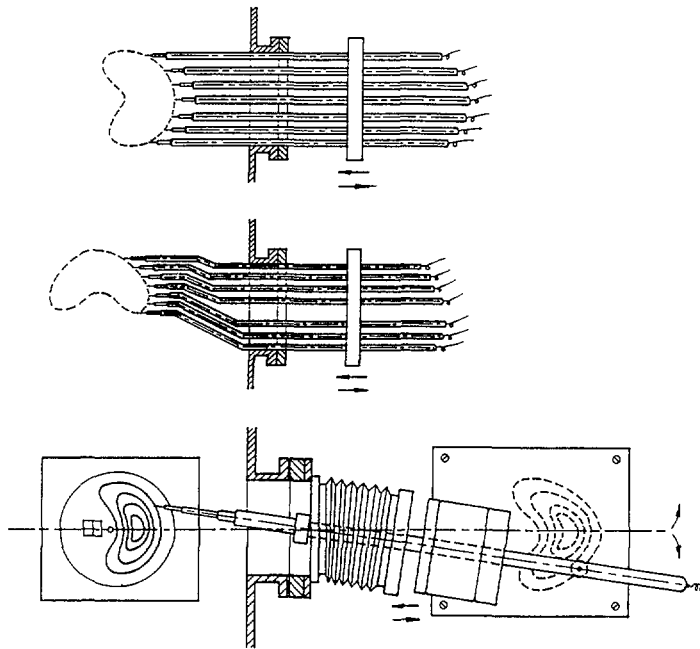


FIG. 1.

Detailed studies have been made for three configurations (I, II, III) characterised by quite different  $\iota$  profiles (Fig.2). Fluctuation data, sampled at 200 kHz, is Fourier analysed in the form,

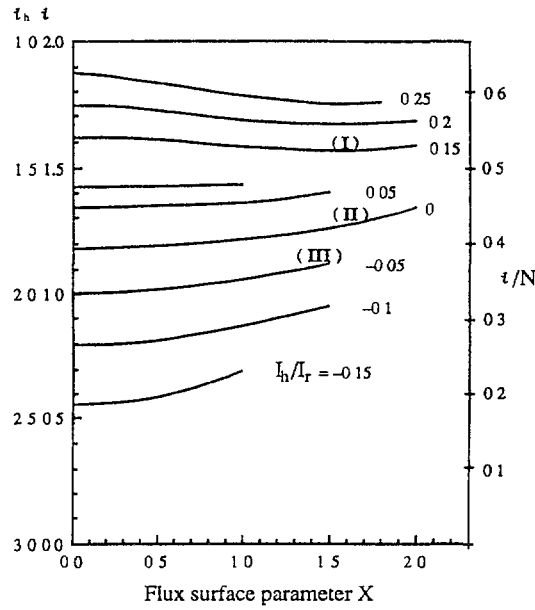


FIG 2

$$\tilde{n}_e = \sum_{m,n} \tilde{n}_e(r) \exp i(m\vartheta - n\phi) \quad (1)$$

where  $m, n$  are the poloidal, toroidal mode numbers, and the flux coordinates are defined as follows:  $r$  is the mean radius of a flux-surface;  $\phi$  is the usual toroidal coordinate; and  $\vartheta$  is a poloidal coordinate chosen to keep the field lines straight (see Fig.3)

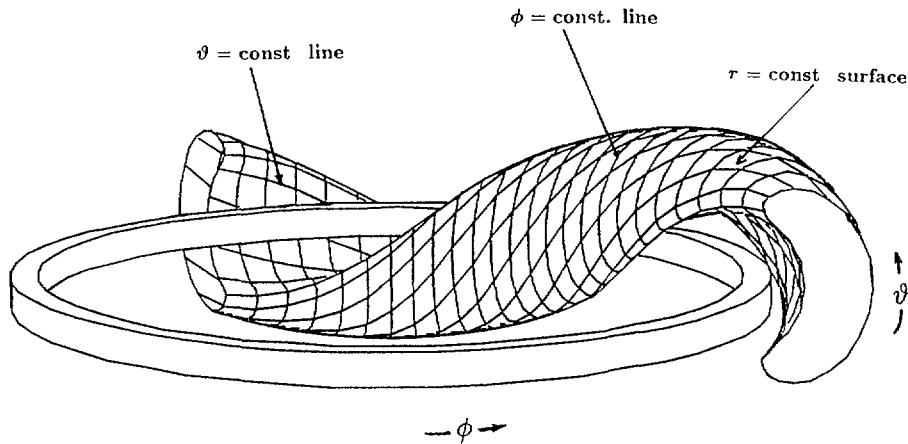


FIG 3

Typical patterns of poloidal fluctuations together with their Fourier decomposition are shown in Fig.4. The radial variation of the dominant components in each configuration are shown in Fig.5.

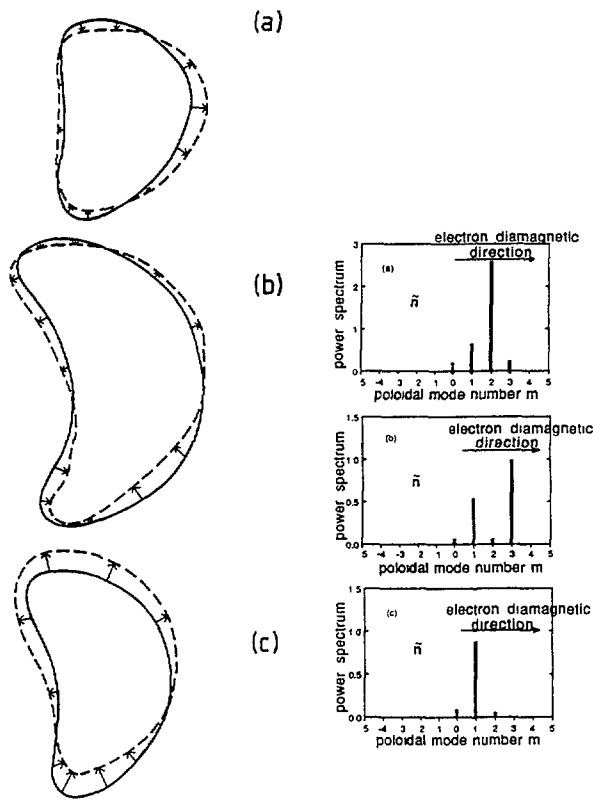


FIG. 4.

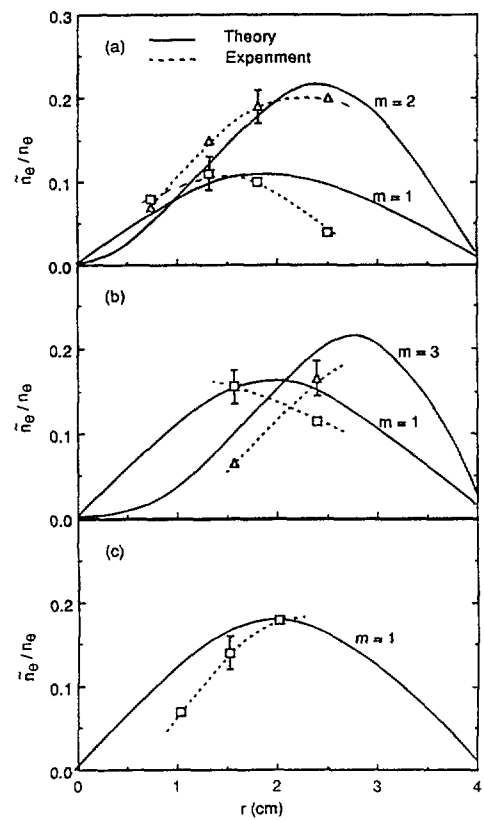


FIG. 5.

Toroidal mode numbers can be obtained from phase differences between probes at fixed toroidal locations on the same  $\vartheta$  coordinate. For example, the dominant mode in configuration II has  $m=3, n=5$ , which is in approximate resonance with the field line ( $k_{\perp} \cdot \underline{B} \approx 0$ ) since  $\iota_h$ , the transform in the helical frame is  $1.71 \approx 5/3 = n/m$ . Since  $k_{\parallel}$  is not precisely zero, it can be measured by following a given fluctuation sufficiently far along a given field line, eg. by measuring the phase differences on the same field line each time it passes through the same vertical plane ( $\phi = \text{const} = 120^\circ$ ), eg. Fig.6 shows the pattern repeating each 9 or 11 toroidal turns respectively for the two surfaces  $r = 1.57 \text{ cm}$  and  $r = 2.39 \text{ cm}$  in configuration II.

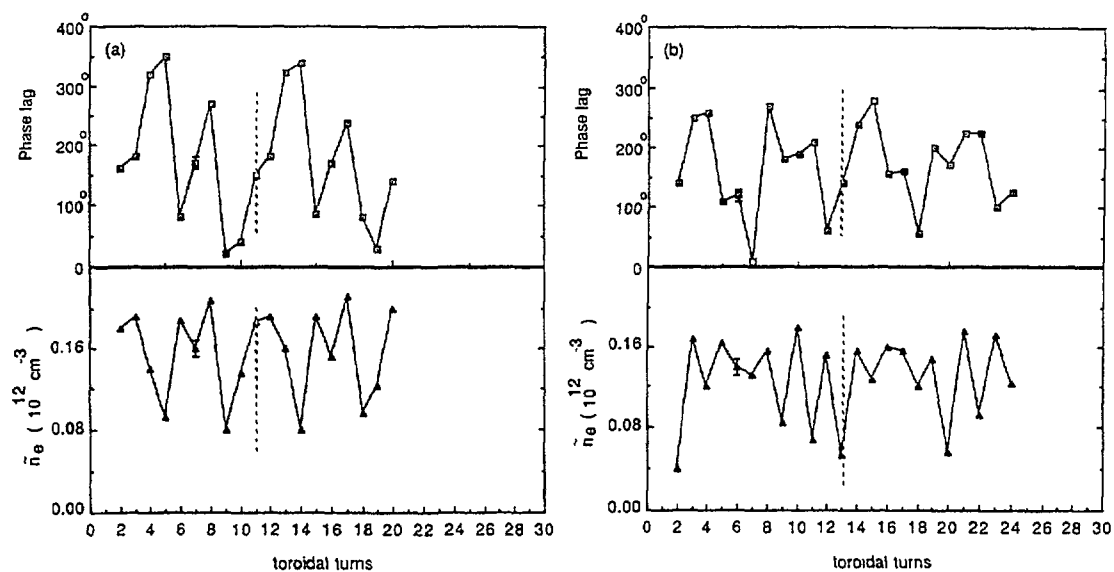


FIG. 6.

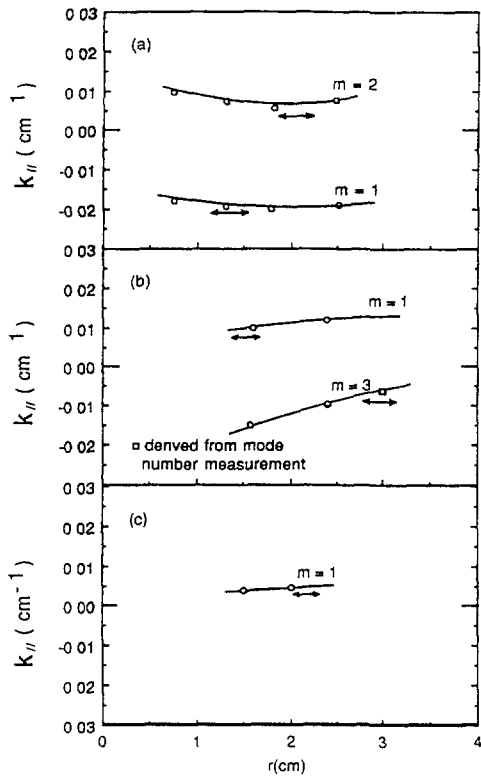


FIG 7

Fig.7 shows plots of the variation of  $k_{||}$  with minor radius for various modes obtained by Fourier analysis of data such as that of Fig.5. (Aliasing possibilities can be eliminated by more direct measurement using toroidally separated fixed probes).

### Dependence on magnetic field strength and collision rate

To aid in the identification of these fluctuations, their amplitude and frequency dependences on  $B$  and total electron collision rate  $\nu = \nu_{e,i} + \nu_{e,n}$  have been measured. An example is given in Figs. 8-9.

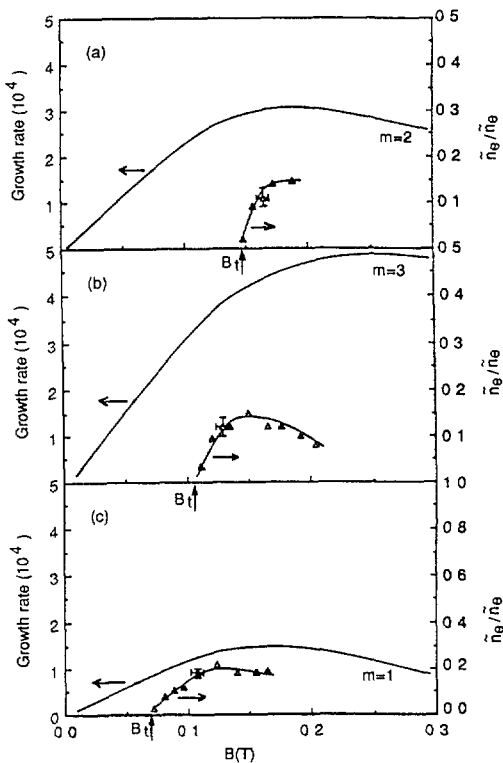


FIG 8

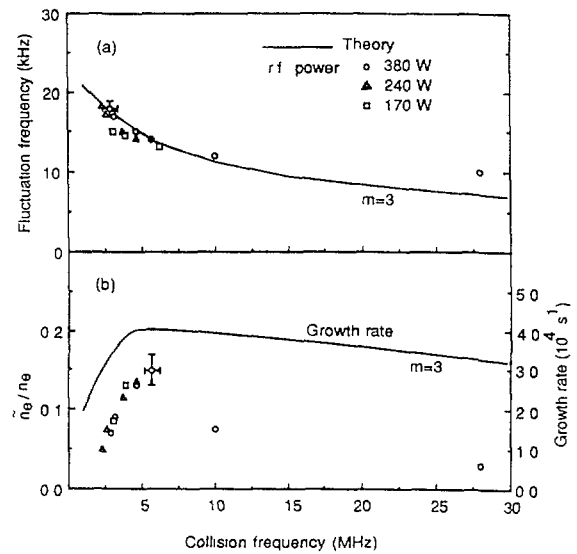


FIG 9

## Comparison with linear dispersion theory

A simplified two-fluid model, based on a periodic cylindrical geometry using the magnetic coordinate and adapted from the work of Fredrickson and Bellan (1985) [1] results in a dispersion relation of the form

$$(1 - i\omega \tau_{||}) \omega k_r^2 \rho_i^2 = (\omega_* - \omega) [1 - (\omega / k_{||} V_A)^2] , \quad (2)$$

where  $k_r \equiv X_j^m / r_a$ ,  $X_j^m$  is the  $j^{\text{th}}$  zero of  $m^{\text{th}}$  Bessel function,  $r_a$  is the plasma radius,  $\omega_*$  is the electron diamagnetic drift frequency,  $\rho_i^2 = T_e / M_i \omega_{ci}^2$ , and  $\tau_{||} = m v / k_{||}^2 T_e$ .

Fig.10 shows the dispersion curve obtained from (1) for the observed mode numbers in each configuration. Also shown in the real frequency plots are the experimentally measured  $\omega_R$  and  $k_{||}$  for each mode. The agreement is close in each case. The parallel wavelength of each dominant mode is shown for comparison with the theoretical dependence of growth rate on  $k_{||}$ : in each case the strongest mode has its  $k_{||}$  close to that for fastest growth.

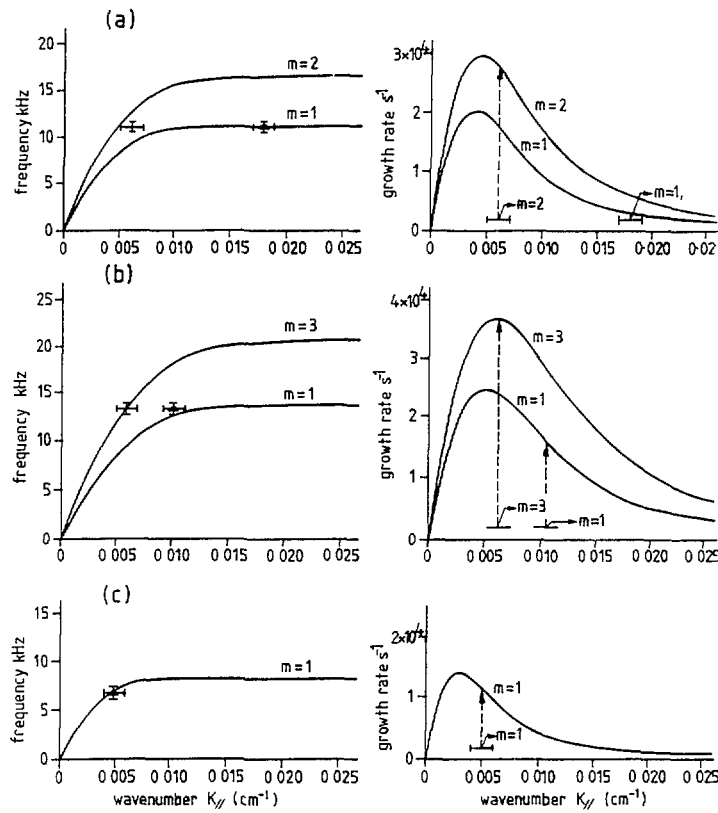


FIG. 10.

[1] Frederickson and Bellan, *Phys. Fluids* **28** (1985) 1866.

The solid line of Fig.5 shows the theoretical radial eigen-functions (normalised to the experimental maxima) which show generally similar behaviour.

The dependence of frequency and linear growth rate calculated for fixed  $k_{||}$  are shown in Fig.9 together with the observed frequency and amplitudes. The agreement is again good, particularly for the lower range of collision frequencies.

The generally good agreement between the theoretical model and the observations supports the view that the oscillations are essentially electrostatic, collisionless drift waves.

## OPTIMIZATION OF TRANSPORT IN STELLARATORS

C.L. HEDRICK, C.O. BEASLEY<sup>1</sup>, W.I. VAN RIJ<sup>2</sup>  
Oak Ridge National Laboratory,  
Oak Ridge, Tennessee,  
United States of America

### Abstract

This paper was devoted to the relation between two stellarator transport optimization schemes to single particle orbits. It is shown that reducing transport in the  $1/\nu$  regime reduces transport over a much broader range of collisionality.

---

Here we relate two stellarator transport optimization schemes to single particle orbits. We also show that reducing transport in the  $1/\nu$  regime reduces transport over a much broader range of collisionality.

In unoptimized stellarators, the orbits of deeply trapped particles usually have the greatest deviation from a flux surface and hence contribute most to diffusive transport losses. Thus it is of interest to focus on these particles. Using the adiabatic invariant  $J'$  [1,2], one can show that the most deeply trapped particles closely follow surfaces given by

$$\mu B_{\min} + e\phi_E = \text{const} \quad (1)$$

Here  $B_{\min}(\Psi, \theta)$  is the minimum of  $B$  with respect to the Boozer toroidal angle,  $\phi$ , at fixed Boozer coordinates  $\Psi$  and  $\theta$ . The electrostatic potential, the magnetic moment, and the charge are  $\phi_E$ ,  $\mu$ , and  $e$ , respectively.

If we make the usual assumption that  $\phi_E$  is independent of poloidal angle,  $\theta$ , then all the poloidal dependence of  $\mu B_{\min} + e\phi_E$  is through  $B_{\min}$ . Indeed, if  $B_{\min}$  were independent of  $\theta$ , then the contours of constant  $\mu B_{\min} + e\phi_E$  would be contours of constant  $\Psi$ , and the bounce-averaged motion of deeply trapped particles would not deviate from the flux surfaces.

We can quantify these ideas by considering a simple model magnetic field of the form

$$B = B_0 \{1 - \epsilon_t \cos(\theta) - [\epsilon_h - \lambda \epsilon_t \cos(\theta)] \cos(M\phi - \ell\theta)\} \quad (2)$$

The minimum value of  $B$  with respect to  $\phi$  is

$$B_{\min} = B_0 [1 - \epsilon_h - \epsilon_t(1 - \lambda) \cos(\theta)] \quad (3)$$

Here we note that the parameter  $\lambda$  is related to  $\sigma$  of Mynick et al. [3] by

$$\lambda = \sigma \epsilon_h / \epsilon_t \quad (4)$$

---

<sup>1</sup> Present address: International Atomic Energy Agency, Vienna.

<sup>2</sup> Computing and Telecommunications Division, Martin Marietta Energy Systems, Inc., Oak Ridge, TN 37831, USA.

From Eq. (3) we see that there are two ways to make  $B_{\min}$  independent of  $\theta$ . One way is to set  $\lambda = 1$ , which is the optimization scheme introduced by Mynick et al [3]. The second way to make  $B_{\min}$  independent of  $\theta$  is to arrange for  $\epsilon_t$  to be equal to zero, i.e. the quasi-helical or “straight” stellarator enunciated by Nührenberg [4]. From  $J'$  one can show that setting  $\epsilon_t = 0$  causes the bounce- and transit-averaged motion of all particles (not just the deeply trapped particles) to follow the flux surfaces. Thus, while one would expect that the  $\epsilon_t$  prescription would be more effective in reducing transport, it is still of interest to examine the  $\lambda$  prescription, since other design considerations may suggest the simultaneous use of both prescriptions.

To examine the dependence of transport on  $\lambda$ , we begin by considering the  $1/\nu$  regime. This regime is formally independent of the magnitude of the electric field and is sufficiently simple that a large amount of magnetic geometric detail can be incorporated analytically. A sequence of analytic approximations has been developed for the  $1/\nu$  regime [5]. For our purposes here, it is sufficient to use an approximation that is usually accurate to a few tens of percent. All the transport coefficients in this approximation have a common geometric factor of the form

$$G = \int d\theta (g_1 - 2g_2\lambda + g_3\lambda^2) \sin^2(\theta) \quad (5)$$

where the  $g_n$  are functions of the single parameter

$$\eta = 2[\epsilon_h - \lambda\epsilon_t \cos(\theta)] / [1 - \epsilon_h - \epsilon_t(1 - \lambda) \cos(\theta)] \quad (6)$$

For  $\epsilon_h \gg \epsilon_t$ ,  $\eta \cong 2\epsilon_h/(1 - \epsilon_h)$ , and the integral in (6) is trivial. Minimizing the transport with respect to  $\lambda$  is then reduced to finding the minimum of the quadratic form

$$R_{1/\nu} = 1 - 2\lambda g_2/g_1 + \lambda^2 g_3/g_1 \quad (7)$$

The normalization of  $R_{1/\nu}$  has been chosen so that it is unity at  $\lambda = 0$ , allowing us to treat it as a “reduction factor” for non-zero  $\lambda$ . Because the factor  $G$  includes the effect of all trapped particles, not just the deeply trapped ones, the minimizing value of  $\lambda$ ,  $g_2/g_3$ , is not precisely equal to unity and varies with  $\epsilon_h$ . For example, when  $\epsilon_h = 0.3$ , the minimizing value of  $\lambda$  is 1.3.

By using the DKES code [6] to calculate the transport flux,  $\Gamma_{11}$ , we have compared its  $1/\nu$  regime dependence on  $\lambda$  with the dependence in other collisionality regimes. At collisionalities just below the  $1/\nu$  regime, a peak in transport occurs as a function of collisionality. The sensitivity of this peak value of transport to  $\lambda$  is of considerable interest. To compare “peak” transport with  $1/\nu$  transport, we define a reduction factor by

$$R_{\text{peak}} = \Gamma_{11}(\lambda)/\Gamma_{11}(\lambda = 0) \quad (8)$$

where both values of  $\Gamma_{11}$  are to be evaluated at the peak in transport as a function of collisionality (which may occur at different collisionalities for different values of  $\lambda$ ).

Figure 1 shows the two reduction factors,  $R_{1/\nu}$  and  $R_{\text{peak}}$ , for three different values of the electric field parameter “EFIELD”  $\equiv E/v$ . (The smallest value corresponds to  $e\phi_E/T_e \simeq 1$ , while the largest value corresponds to  $e\phi_E/T_i \simeq 1$ .) For the cases shown,  $\epsilon_h = 0.3$  and  $\epsilon_t = 0.1$ . Also shown is an estimate of the  $\lambda$  dependence of the loss of high-energy particles due to unconfined drift orbits (proportional to  $\epsilon_t|\lambda - 1|$ ). Notice that

the diffusive transport results for “peak” and  $1/\nu$  are quite similar and that the estimate of direct losses is qualitatively similar.

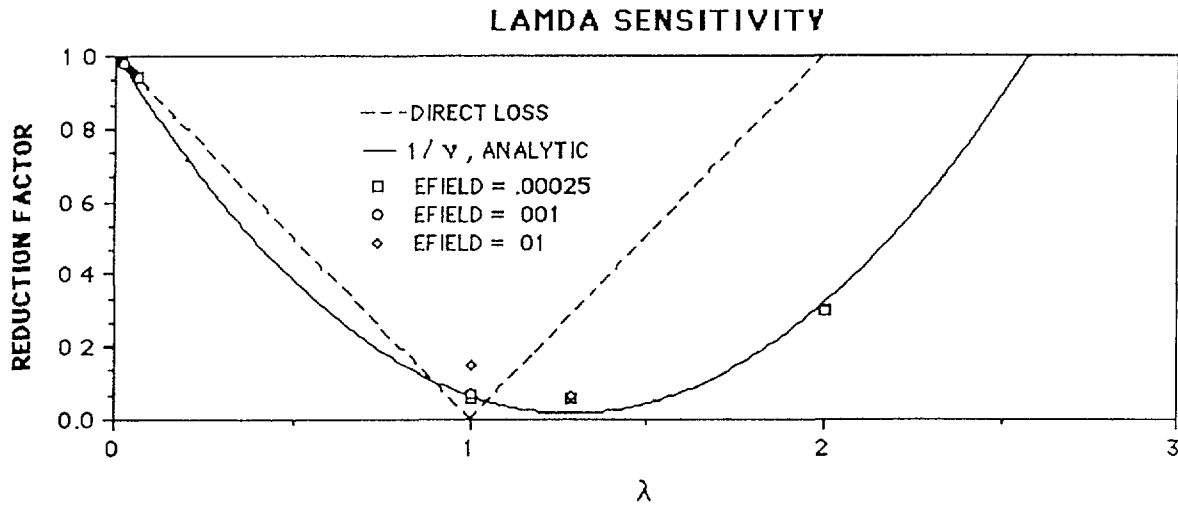


FIG 1

Figure 2 allows comparison of an unoptimized case ( $\lambda = 0$ ) with a  $\lambda$  optimized case ( $\lambda = 1.3$ ) and an  $\epsilon_t$ -optimized case. All three cases have  $\epsilon_h = 0.3$ . The unoptimized and  $\lambda$ -optimized cases have  $\epsilon_t = 0.1$ , while the  $\epsilon_t$ -optimized case has  $\epsilon_t = 0$ . The electric field parameter is  $E/\nu = 0.001$ . Other values of the electric field parameter give similar behavior. Notice that a broad range of collisionality ( $\nu/\nu$ ) is shown, and that both  $\lambda$  and  $\epsilon_t$  optimizations significantly reduce transport over the entire range.

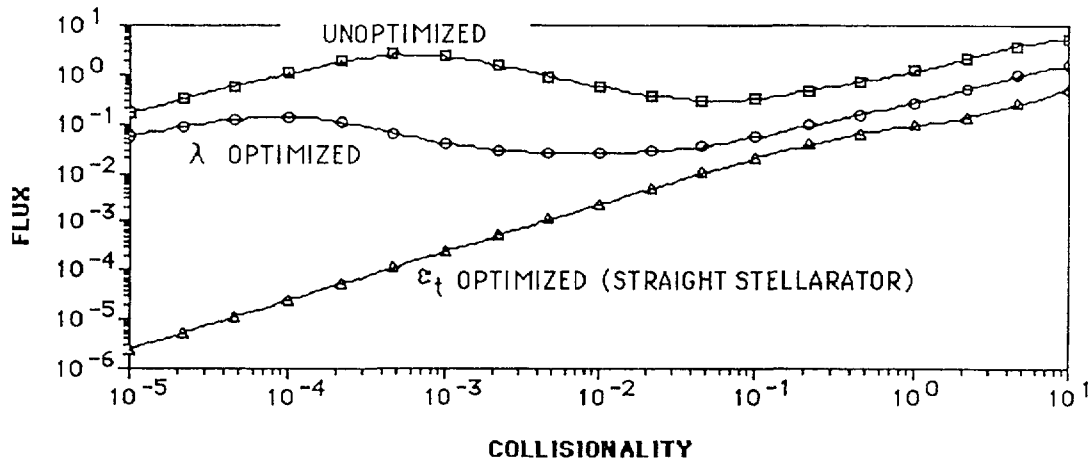


FIG 2

We conclude that both optimization techniques are effective at reducing transport over a broad range of collisionality. This suggests that the two techniques can be used simultaneously to reduce transport, while meeting other design constraints that are outside the purview of transport.

## ACKNOWLEDGEMENT

This research was sponsored by the Office of Fusion Energy, U.S. Department of Energy, under contract DE-AC05-84OR21400 with Martin Marietta Energy Systems, Inc.

## REFERENCES

- [1] CARY, J. R., HEDRICK, C.L., TOLLIVER, J.S., *Phys. Fluids* **31** (1988) 1586.
- [2] HEDRICK, C.L., CARY, J. R., TOLLIVER, J.S., Adiabatic and full guiding center motion in 3-D toroidal systems, to be submitted to *Phys. Fluids*.
- [3] MYNICK, H.E., CHU, T.K., BOOZER, A.H., *Phys. Rev. Lett.* **48** (1982) 322.
- [4] NÜHRENBERG, J., ZILLE, R., *Phys. Lett. A* **114A** (1986) 129.
- [5] HEDRICK, C.L., BEASLEY, C.O., VAN RIJ, W.I., Transport in the  $1/\nu$  regime for stellarators and torsatrons, to be submitted to *Phys. Fluids*.
- [6] VAN RIJ, W.I., HIRSHMAN, S.P., *Phys. Fluids B* **1** (1989) 563.

# THE ROLE OF THE RADIAL ELECTRIC FIELD IN ENHANCED CONFINEMENT REGIMES IN STELLARATORS\*

K.C. SHAING

Oak Ridge National Laboratory,  
Oak Ridge, Tennessee,  
United States of America

## Abstract

The confinement enhancement observed in stellarators could be attributable to the suppression of turbulent fluctuations by the radial electric field  $E_r$ . The pressure-gradient-driven turbulence model is used to illustrate the effects of  $E_r$  on turbulent fluctuations. A more negative value of  $E_r$  and/or a more positive value of  $dE_r/dr$  can reduce the fluctuation amplitudes, if  $dN/dr < 0$ . Here,  $r$  is the local minor radius and  $N$  is the plasma density.

Many confinement enhancement phenomena observed in tokamak experiments could be attributable to the suppression of turbulent fluctuations by a more negative value of the radial electric field,  $E_r$  [1-3]. For example, improved particle confinement with a deeper negative electrostatic potential well has been observed in the UCLA tokamak and TEXT [4,5]. In both ISX-B and ASDEX, better plasma confinement has been found for counter-injected neutral beam cases than for co-injected cases [6,7]. There is also experimental evidence that the onset of the H-mode in DIII-D is triggered by a sudden change of  $E_r$  to a more negative value [8]. Furthermore, the power threshold for the L-H transition is lower in the counter-injected neutral beam cases than in the co-injected cases [8].

There are also some indications that plasma confinement in stellarators is improved with a more negative  $E_r$  when anomalous transport fluxes are the dominant loss mechanism [9]. Global energy confinement times in Heliotron-E seem to increase when  $E_r$  at  $r/a \sim 0.8$  becomes more negative, where  $a$  is the plasma minor radius. The global energy confinement in this case is dominated by anomalous processes.

The effects of  $E_r$  on the fluctuations are demonstrated in a resistivity-gradient-driven turbulence model [3,10]. It is shown that a more negative value of  $E_r$  can indeed reduce the fluctuation level, in agreement with the results of a kinematic argument presented in Refs [2,3]. For stellarator configurations such as Heliotron-E and ATF, pressure-gradient-driven turbulence is a plausible model to describe the edge fluctuations [11,12]. The simplest set of equations that can demonstrate the effects of  $E_r$  on the pressure-gradient-driven turbulence consists of Ohm's law, the density evolution equation, and the vorticity equation [13],

$$\eta_{\parallel} J_{\parallel} = -\nabla_{\parallel} \phi + \frac{T}{Ne} \nabla_{\parallel} N, \quad (1)$$

$$\frac{\partial N}{\partial t} + \mathbf{V}_E \cdot \nabla N = \chi_{\perp} \nabla_{\perp}^2 N + \nabla_{\parallel} \left( \frac{J_{\parallel}}{e} \right) \quad (2)$$

$$NM \left( \frac{\partial}{\partial t} + \mathbf{V}_E \cdot \nabla \right) \nabla_{\perp}^2 \left( \frac{c\phi}{B} \right) = \frac{B}{c} \nabla_{\parallel} J_{\parallel} + T \hat{n} \times \nabla N \cdot \nabla \Omega_0 \\ + NM \mu \nabla_{\perp}^2 \left[ \nabla_{\perp}^2 \left( \frac{c\phi}{B} \right) \right] \quad (3)$$

---

\* Research sponsored by the Office of Fusion Energy, US Department of Energy, under contract DE-AC05-84OR21400 with Martin Marietta Energy Systems, Inc.

where  $T$  is the plasma temperature,  $M$  is the ion mass,  $\phi$  is the electrostatic potential,  $\hat{n} = \mathbf{B}/B$ ,  $\mathbf{V}_E$  is the equilibrium  $\mathbf{E} \times \mathbf{B}$  drift,  $J_{\parallel}$  is the parallel (to the magnetic field) plasma current,  $c$  is the speed of light,  $B$  is the magnetic field strength and  $\nabla\Omega_0$  is the averaged magnetic curvature. The plasma resistivity, perpendicular (to the magnetic field) transport coefficient, and viscosity are denoted by  $\eta_{\parallel}$ ,  $\chi_{\perp}$ , and  $\mu$ , respectively. The turbulence is driven by the averaged bad magnetic curvature with  $d\Omega_0/dr > 0$ .

The density fluctuation spectrum can be calculated from the two point correlation evolution equation by neglecting the dissipation associated with the  $\nabla_{\parallel}J_{\parallel}$  term in Eq (2) for simplicity

$$\begin{aligned} \frac{\partial}{\partial t} \langle \tilde{N}(1)\tilde{N}(2) \rangle - r_{-}\omega' \frac{\partial}{\partial \theta_{-}} \langle \tilde{N}(1)\tilde{N}(2) \rangle - (D_{-} + \chi_{\perp}) \frac{\partial^2}{\partial r^2} \langle \tilde{N}(1)\tilde{N}(2) \rangle \\ = -\frac{c}{Br} \frac{dN}{dr} \frac{cT\eta_{\parallel}}{rB} \frac{d\Omega_0}{dr} \left( \frac{RqL_q}{r-r_s} \right)^2 \sum_{m,n} \tilde{N}_{mn}(1)\tilde{N}_{-m-n}(2) e^{-i(m\theta_1 - n\zeta_1)} \end{aligned} \quad (4)$$

where  $\langle \tilde{N}(1)\tilde{N}(2) \rangle = \sum_{m,n} \tilde{N}_{mn}(1)\tilde{N}_{-m-n}(2) \exp[-i(m\theta_1 - n\zeta_1)]$ ,  $(r, \theta, \zeta)$  is the relative separation of position  $(r_1, \theta_1, \zeta_1)$  and position  $(r_2, \theta_2, \zeta_2)$ ,  $\tilde{N}_{mn}(j)$  is the radial mode amplitude at position  $j$  for the  $(m, n)$  mode,  $R$  is the major radius,  $r_s$  is the mode rational surface,  $q$  is the safety factor,  $L_q = [(dq/dr)/q]^{-1}$ ,  $D_{-}$  is the spatially dependent turbulent diffusion coefficient, and  $\omega' = d\omega/dr$  with  $\omega = (cE_r/Br) + cT(dN/dr)/(NeBr)$ . The angular brackets here denote ensemble average. The fluctuation of a quantity  $A$  is denoted  $\tilde{A}$ . To obtain Eq. (4), we have employed a relationship between  $\tilde{N}$  and  $\tilde{\phi}$ , obtained from Ohm's law and the steady-state vorticity equation without dissipation, namely,

$$\tilde{\phi} = \frac{T}{Ne} \tilde{N} + i \frac{cT\eta_{\parallel}}{rB} \frac{d\Omega_0}{dr} \left( \frac{RqL_q}{r-r_s} \right)^2 \tilde{N}/m \quad (5a)$$

The validity of using this equation to determine  $\tilde{J}_{\parallel}$  in terms of  $\tilde{N}d\Omega_0/dr$  at the saturated state is demonstrated in Ref. [13]. We note that besides the conventional decorrelation mechanism due to turbulent radial diffusion  $D_{-}$ , there is an additional dynamic decorrelation mechanism due to the shear of the angular velocity  $\omega$ . The density fluctuation spectrum  $\langle \hat{N}\hat{N} \rangle_{mn}$  can be obtained from the Fourier transformation of the steady-state solution of Eq. (4) [14]:

$$\begin{aligned} \langle \hat{N}\hat{N} \rangle_{mn} = \frac{1}{(2\pi)^{3/2}} \left( -\frac{c}{Br} \frac{dN}{dr} \frac{d\Omega_0}{dr} \right) \left( \frac{cT\eta_{\parallel}}{rB} \right) \left( \frac{RqL_q}{\Delta_{mn}} \right)^2 \\ \times \frac{I_0}{\Delta_{mn}a_r Z_1} F(m, n) \sum_{m,n} \langle \hat{N}\hat{N} \rangle_{mn} \end{aligned} \quad (5b)$$

where  $\Delta_{mn}$  is the radial mode width for the  $(m, n)$  mode,  $a_r = [k_0^2 + (2m_0\omega'/Z_1)^2]^{1/2} / [(1 + \chi_{\perp}/D)(1 - 2a_0/Z_1^3)]^{1/2}$ . Here  $Z_1$  is the positive real root of a cubic equation

$$Z_1^3 + a_2 Z_1^2 + a_0 = 0, \quad (6)$$

where  $a_2 = -2Dk_0^2$ ,  $a_0 = -4Dm_0^2(\omega')^2$ ,  $k_0$  is the typical radial wave vector,  $m_0$  is the typical poloidal mode number, and  $D$  is the spatially independent turbulent radial diffusion coefficient. The mode number dependence of the spectrum is described by the function  $F(m, n)$  which can be expressed as

$$F(m, n) = \frac{1}{a_\theta a_\zeta} \int_0^{(1-a^2)^{1/2}} dk k J_0(k\ell) \left( \sqrt{1-k^2-a^2} - \sqrt{k^2+a^2} \cos^{-1} \sqrt{k^2+a^2} \right) / I_0$$

where

$$\ell^2 = \frac{m^2}{a_\theta^2} + \frac{\eta^2}{a_\zeta^2},$$

$$a_\theta = \frac{m_0 k_0}{\left[ k_0^2 + (2m_0 \omega' / Z_1)^2 \right]^{1/2} \left[ (1 + \chi_\perp / D) (1 - 2a_0 / Z_1^3) \right]^{1/2}}$$

$$a_\zeta = \frac{n_0}{\left[ (1 + \chi_\perp / D) (1 - 2a_0 / Z_1^3) \right]^{1/2}}$$

$$a = \frac{(\chi_\perp / D)^{1/2}}{\left[ (1 + \chi_\perp / D) (1 - 2a_0 / Z_1^3) \right]^{1/2}} \quad (7)$$

and  $J_0$  is the Bessel function. The normalization constant  $I_0$  is defined as  $F(0, 0) = 1$ .

One of the dominant  $E_r$  dependences in  $\langle \hat{N} \hat{N} \rangle_{mn}$  is from  $\tau_c \propto Z_1^{-1}$  which, in the limit of  $|a_0| \lesssim a_2$ , can be written as

$$Z_1 \simeq 2Dk_0^2 + Dm_0^2(\omega')^2 / (Dk_0^2)^2 \propto \tau_c^{-1} \quad (8)$$

We see from Eq. (8) that in addition to the conventional decorrelation mechanism due to radial turbulent diffusion, there is a novel decorrelation mechanism associated with  $\omega'$ , the radial shear of the  $\mathbf{E} \times \mathbf{B}$  and diamagnetic angular velocities. The decorrelation associated with  $\omega'$  is very similar to that associated with parallel particle speed  $v_\parallel$  and magnetic shear  $q'$  discussed by Hirshman and Molvig [15]. When  $E_r$  becomes more negative and/or  $dE_r/dr$  becomes more positive, the fluctuation level of the pressure-gradient-driven turbulence is reduced for a negative value of  $dN/dr$ . These results are consistent with the improvement of global energy confinement time with a more negative value of  $E_r$  observed in Heliotron-E and in tokamaks.

Of course, the confinement enhancement in tokamaks and stellarators discussed here is attributed to the reduction of the fluctuation level by  $E_r$ , then there must be a wide class of turbulence models besides pressure-gradient-driven turbulence and resistivity-gradient-driven turbulence in which the fluctuation levels can be reduced by a more negative value of  $E_r$  and/or a more positive value of  $dE_r/dr$ , because the plasma parameters of these experiments are very different. However, since the effects of  $E_r$  on the turbulent fluctuations discussed here result from the dynamic decorrelation mechanism associated with  $\omega'$ , which exists in all turbulence models, we can conclude that such effects should occur in other turbulence models as well. Of course, it is also possible that for some turbulence models, a more positive value of  $E_r$  and/or a more negative value of  $dE_r/dr$  may be more beneficial to plasma confinement. However, until such phenomena are observed in experiments, we can probably conclude that these models are unrealistic. It is therefore important to measure and control  $E_r$  profiles in existing devices to test the conclusions drawn here and in Refs [1–3]: that a more negative value of  $E_r$  and/or a more positive  $dE_r/dr$  can reduce the fluctuation level and improve plasma confinement.

We point out that the effects of  $E_r$  on turbulent fluctuations presented here are different from the conventional Kelvin-Helmholtz instability [16] induced by either  $E_r$  or  $dE_r/dr$ . In the conventional Kelvin-Helmholtz instability, the effects of  $E_r$  appear as the free energy source for the instability and turbulent fluctuations and therefore do not exist in other turbulence models. However, the effects of  $E_r$  discussed here appear as the dynamic decorrelation mechanism, which exists in all turbulence models.

On the basis of theory developed here and in Refs [1–3], to improve plasma confinement in stellarators, one needs to make  $E_r$  more negative and/or  $dE_r/dr$  more positive. To make  $E_r$  more negative, we can inject neutral beams perpendicular to the magnetic axis so as

to enhance ion orbit losses. Reducing the edge neutral density could also make  $E_r$  in the edge region more negative by reducing the ion transport associated with plasma-neutral collisions.

In conclusion, we suggest that plasma confinement in stellarators can be improved by making  $E_r$  more negative. Such phenomena may have already been observed in Heliotron-E. We also describe the effects of  $E_r$  on the pressure-gradient-driven turbulence and find that a more negative value of  $E_r$  and/or a more positive value of  $dE_r/dr$  can reduce the fluctuation level, which is consistent with the results from Heliotron-E and with the results of the kinematic argument presented in Refs [2,3].

## REFERENCES

- [1] SHAING, K.C., *Phys. Fluids* **31** (1988) 2249.
- [2] SHAING, K.C., HOULBERG, W.A., CRUME, E.C., *Comments Plasma Phys. Controlled Fusion* **12** (1989) 69.
- [3] SHAING, K.C., LEE, G.S., CARRERAS, B.A., HOULBERG, W.A., CRUME, E.C., in *Plasma Physics and Controlled Nuclear Fusion Research 1988* (Proc. 12th Int. Conf. Nice, 1988) IAEA, Vienna (1989) in press.
- [4] OREN, L., KELLER, L., SCHWIRZKE, F., TALMADGE, S., TAYLOR, R.J., *J. Nucl. Mater.* **111** (1982) 34.
- [5] PHILLIPS, P.E., WOOTTON, A.J., ROWAN, W.L., et al., *J. Nucl. Mater.* **145-147** (1987) 807.
- [6] MURAKAMI, M., EDMONDS, P.H., HALLOCK, G.A., et al., in *Plasma Physics and Controlled Nuclear Fusion Research 1984* (Proc. 10th Int. Conf. London, 1984), Vol. 1, IAEA, Vienna (1985) 87.
- [7] SÖLDNER, F.X., GRUBER, O., MÜLLER, et al., in *Plasma Physics and Controlled Nuclear Fusion Research 1988* (Proc. 12th Int. Conf. Nice, 1988), IAEA, Vienna (1989) in press.
- [8] CARLSTROM, T.N., OHYABU, N., BURRELL, K.H., SHIMADA, M., *Bull. Am. Phys. Soc.* **33** (1988) 1964.
- [9] OBIKI, T., MIZUUCHI, T., ZUSHI, H., et al., in *Plasma Physics and Controlled Nuclear Fusion Research* (Proc. 12th Int. Conf. Nice, 1988) IAEA, Vienna (1989) in press.
- [10] LEE, G.S., CARRERAS, B.A., SHAING, K.C., *Bull. Am. Phys. Soc.* **30** (1988) 2010; to be published.
- [11] SHAING, K.C., CARRERAS, B.A., *Phys. Fluids* **28** (1985) 2027.
- [12] YAGI, M., WAKATANI, M., HASEGAWA, A., *J. Phys. Soc. Jpn.* **56** (1987) 973.
- [13] LEE, G.S., CARRERAS, B.A., GARCIA, L., *Phys. Fluids B* **1** (1989) 119.
- [14] TERRY, P.W., DIAMOND, P.H., SHAING, K.C., GARCIA, L., CARRERAS, B.A., *Phys. Fluids* **29** (1986) 2501.
- [15] HIRSHMAN, S.P., MOLVIG, K.M., *Phys. Rev. Lett.* **42** (1979) 648.
- [16] PERKINS, F.W., JASSBY, D.L., *Phys. Fluids* **14** (1971) 102.

# HOW TEMPERATURE GRADIENTS ARE DETERMINED IN TOROIDAL PLASMAS

S. YOSHIKAWA

Plasma Physics Laboratory,  
Princeton University,  
Princeton, New Jersey,  
United States of America

## Abstract

It is commonly assumed, in toroidal plasmas, that the edge ion or electron temperature is sufficiently low so that the edge temperature can be neglected with respect to the center temperature in modern-day toroidal plasmas. For example, in a detached plasma, where the boundary condition is understood reasonably well, it is both theoretically and experimentally justified to say that the edge temperature can be approximately zero.

Now in a toroidal plasma bounded by the divertor, it is theoretically possible to design a divertor such that each pair of electron and hydrogen ion can carry, on average,  $3/2(kT_e + kT_i)$ . Then, in the absence of recycling, the temperature gradients in the scrape-off layer can be made zero or at least, less than  $1/a$ , where  $a$  is the plasma radius. Under that boundary condition, the temperature gradient inside the plasma vanishes. Realizing this in practice is difficult but not impossible. The problem is discussed in this paper.

---

## 1. Introduction

In a toroidal plasma, usually there exists the scrape-off layer at the edge of the plasma. There the plasma flows along the magnetic field lines to be collected at the limiter plate or end plates in a divertor. The balance of the outward anomalous diffusion,  $D$ , and the parallel flow determines the scrape-off distance, which is given as

$$\lambda \approx \sqrt{DL/v_s} \quad (1)$$

Here  $L$  is the distance measured along the field lines and  $v_s$  is the sound velocity. In the absence of recycling, the density profile inside the scrape-off layer must satisfy the boundary condition at  $r = a$ :

$$-\left(\frac{dn}{dr}\right)/n = \lambda, \quad r = a \quad (2)$$

This condition and  $dn/dr = 0$  at  $r = 0$  is generally sufficient to determine  $n(r)$ , if the expression for  $D$  is given and if the neoclassical or anomalous toroidal pinch effect can be estimated.

The temperature gradient in the scrape-off layer is equally important for determination of the temperature profile within the plasma. If  $(dT/dr)/T$  in the scrape-off layer is  $-\lambda_T$ , the boundary condition

$$-\left(\frac{dT}{dr}\right)/T = \lambda_T \quad \text{as } r \rightarrow a - 0 \quad (3)$$

along with  $dT/dr = 0$  at  $r = 0$  is sufficient. To the author's knowledge, it is customary to assign a fixed (ion or electron) low temperature at  $r = a$  and solve for the temperature distribution. The procedure is justified if  $\lambda_T \gg 1/a$ .

Here we shall estimate  $\lambda_T$  for a toroidal plasma that is bounded by a divertor and is radiation-free within the main plasma. This case is the opposite of the case of a detached plasma.

Then we shall explore the method to reduce  $\lambda_T$ . In particular, if we can reduce  $\lambda_T$  such that  $\lambda_T \leq 1/a$ , we may be able to increase the energy confinement by (i) reducing temperature gradients, (ii) eliminating ion temperature gradient instabilities, and/or (iii) more speculatively generating the H-mode condition.

## 2. The temperature gradient in the scrape-off layer

We shall assume that both ion and electron temperatures are equal in the scrape-off layer. (If not, the problem is still solvable but more complicated). Also, as noted in the introduction, there is no radiation energy loss. Then the equation to determine the temperature gradient may be expressed (similar to the density gradient)<sup>1</sup>

$$\kappa \frac{\partial^2 T}{\partial r^2} = \left(\alpha - \frac{3}{2}\right) T \frac{v_s}{L} \quad (4)$$

Here  $\kappa$  is the perpendicular heat conductivity in the unit of  $m^2/\text{sec}$  and  $2\alpha$  is the average energy of ion-electron pair impinging on the neutralizer plate of a divertor. ( $\alpha$  cannot normally be less than  $3/2$ .)

If the divertor is replaced by a limiter and if the temperature drop along the field line is negligible due to the high parallel electron thermal conductivity,

$$2\alpha = \frac{1}{2} \ln \left(\frac{M}{m}\right) + \frac{5}{2} \quad (\text{for limiter}) \quad (5)$$

Here  $M$  and  $m$  are ion and electron mass respectively.

If on the other hand, in the divertor, there are neutral gas particles which can be excited by plasma electrons, the temperature in the divertor can be lowered with respect to the scrape-off layer temperature in the main chamber. Furthermore, if we assume that the electron heat conductivity (parallel) is small, then  $\alpha \rightarrow 3/2$ .

hence

$$\kappa \frac{\partial^2 T}{\partial r^2} \approx 0 \quad (6)$$

In practice, a divertor with a long throat may approximate this condition.

Thirdly, the magnetic field lines in the divertor section could be made to fan out (as in Doublet type tokamaks). Then the plasmas which flow into the divertor become supersonic. The random thermal energy turns into the directed energy and the plasma temperature in the flow decreases. Under that

---

<sup>1</sup> S. Yoshikawa, W. L. Harries, and R. M. Sinclair, *The Physics of Fluids* 6, 1506 (1963).

circumstance, the parallel heat conduction (in addition to the convected energy by the plasma flow) may approach zero. If so, Eq. (6) is approximately true,  $\lambda_T \ll 1/a$ . Then what kind of consequence can one expect?

### 3. Small temperature gradient in the scrape-off layer

For the sake of simplicity we assume that the temperature gradient is zero in the scrape-off layer. Then provided that the heat conductivity is not infinite at the plasma edge, the heat conduction (in addition to the heat convection) becomes zero. Then the total energy loss is equal to

$$P = \frac{3}{2} (kT_i + kT_e)_{\text{edge}} \Gamma S_p, \quad (7)$$

where  $\Gamma$  is the flux of the particles and  $S_p$  is the surface area of the toroidal plasma.

The solution of  $\lambda_T \approx 0$  is not so obvious, if we suppose that the plasma is heated by the neutral beam injection whose particle has the constant energy  $W$ . As previously, we assume that the plasma can be thermalized so that  $T_e = T_i$ . Then the steady solution exists if

$$T = \frac{1}{3} W = \text{independent of } r \quad (8)$$

To show this, we note that  $T = \text{const.}$  satisfies the boundary conditions at  $r = 0$  and  $r = a$ .

Further, the particle transport equation may be written as

$$- \frac{1}{r} \frac{d}{dr} r(D \frac{dn}{dr} + nV) = \frac{F}{W} \quad (9)$$

where  $V$  is the (inward) velocity due to the pinch effect and  $F$  is the neutral beam energy flux. The boundary condition at  $r = a$  yields  $\Gamma$ , flux defined in Eq. (7). If  $T$  is constant, the energy transport equation is Eq. (9) multiplied by  $T$ . Hence if Eq. (9) is satisfied, the heat transport equation is also satisfied. Since Eq. (7) must be also satisfied,  $T$  is equal to  $W/3$ .

### 4. Conclusions

The ion and electron temperature gradients in the scrape-off layer may be reduced by adequately designing a divertor. If, in the future, recycling-free toroidal plasmas can be produced, the experiments to lengthen the temperature gradient distance may be tried.

Some surprising conclusions can be drawn. A steady solution of the  $\lambda_T \approx 0$  condition has no temperature gradient within the plasma. The plasma temperature reaches 1/3 of the injected neutral energy. In rf or ohmic heating discharges, the plasma density decreases in time. If the rate of decrease is sufficiently small, the plasma temperature confinement time equals to the particle confinement time.

## **IMPURITIES AND DIVERTORS**

## DIVERTOR BIASING EXPERIMENTS IN IMS

D.T. ANDERSON, F.S.B. ANDERSON,  
R.P. DOERNER, M.J. HSIEH, W.N.G. HITCHON,  
P.G. MATTHEWS, J.L. SHOHET  
Torsatron/Stellarator Laboratory,  
University of Wisconsin – Madison,  
Madison, Wisconsin,  
United States of America

### Abstract

An electrostatic method for controlling diverted particle fluxes in a stellarator has been demonstrated. Potentials applied to a defined set of divertor targets (shields) in contact with diverted flux bundles results in redistribution of plasma flow to any given divertor. Examination of the edge magnetic topology shows that  $E \times B$  drifts just outside the last-closed magnetic surface account for the alteration of the diverted particle flows. Divertor models applied to the Proto-Cleo Stellarator show large changes in the expected divertor structure as a function of the scrape-off-layer thickness. Diagnostics recently installed in preparation for experimental investigation will be described.

---

Experimental evidence of divertor structure has been observed in many stellarators<sup>1,2</sup>. Unfortunately, stellarator divertors usually spread the diverted flux over large regions.<sup>3</sup> An externally applied vertical magnetic field has been used to alter the divertor pattern in a stellarator.<sup>4</sup> However, this may conflict with position control using the same fields and provides only a global modification of the divertor pattern. We present here a method using electrostatic fields which provides local control of diverted particle fluxes in the Interchangeable Module Stellarator (IMS) without using magnetic fields.

IMS is an  $l = 3$ , seven field-period modular stellarator with a 40 cm major radius and a 4.5 cm average plasma radius.<sup>5</sup> Outside the last closed magnetic surface (LCMS), is a region of ergodic field lines which extends radially for about 5 mm. Beyond this region, field-line trajectories quickly coalesce to form 63 diverted-flux bundles. This divertor structure has been observed both computationally<sup>6</sup> and experimentally.<sup>7</sup> Electrically-isolated stainless-steel shields are placed at the locations of each of the 63 emergent bundles in IMS and are used to monitor the diverted plasma flow as well as to apply an electrostatic bias to specific divertor bundles. The location of each shield is identified by both the coil support ring on which it is mounted and the poloidal angle at which it is positioned on the coil support ring.

Tracing the magnetic-field lines from a given divertor shield back to a reference surface 5 mm beyond the LCMS gives an origin "map" of the field lines comprising that divertor bundle. It was found that any point on the reference surface is connected by field lines to at most two divertors. By following field lines parallel to the direction of the magnetic field a diagram is generated which indicates the areas of the launch surface that are connected to the various divertors. The field lines connecting to a given divertor originate mainly from a continuous toroidal strip on the reference surface. It has been experimentally confirmed by launching ion-acoustic waves beyond the LCMS and monitoring the divertor shields to detect the wave,<sup>8</sup> that the plasma flows closely follow this mapping in IMS.

Measurements of the floating potential just outside the LCMS were taken during shield-biasing experiments. The regions outside the LCMS which connect to the biased divertor shield exhibited abrupt changes in the floating potential as the d.c. bias voltage on the divertor shield was varied. Abrupt changes in the floating potential of up to  $T_e$ , the electron temperature, were observed. A probe inserted in other origin regions, not connected to the biased shield, showed no appreciable change in floating potential when the same shield's bias was varied. Central plasma parameters also exhibit no changes during divertor-shield biasing. Measurements of the space potential show similar changes to those in the floating potential.

A positive 50-volt potential was applied to the divertor shield in each field period which is located at a poloidal angle of 340 degrees (i.e., the S8-340 shield, see Figure 1). The ion-saturation current to each divertor within one field period was measured. The ion-saturation current to the shield located at a poloidal angle of 300 degrees (the ZS-300 shield) and the shield located at a poloidal angle of zero degrees (the 8Z-0 shield) exhibited changes. The ion-saturation current to the other shields showed no appreciable changes during biasing of the S8-340 shields. The ZS-300 and the 8Z-0 origins flank the biased S8-340 origin. The diverted ion current to the ZS-300 divertor rises abruptly from 10.5 mA to 15.7 mA when the bias is applied to the S8-340 divertor shields. At the same time, the diverted ion current to the 8Z-0 divertor abruptly decreases from 8.0 mA to 2.0 mA when the bias voltage is applied.

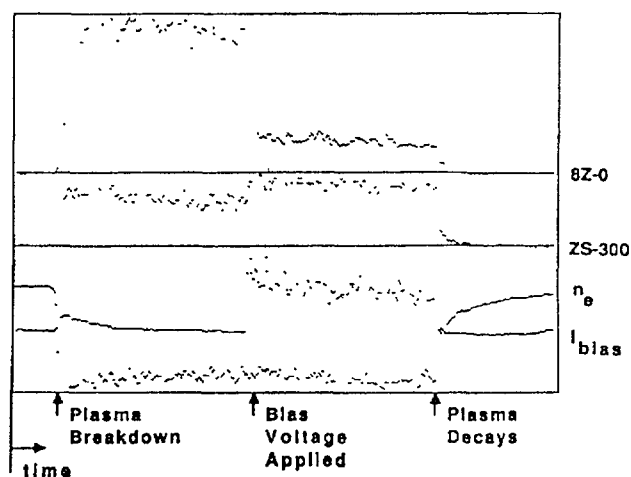


FIG. 1.

Figure 1 shows the experimental data obtained with this shield biasing configuration. The two traces labelled ZS-300 and 8Z-0 monitor the ion-saturation current collected by each of these divertor shields. The current to each divertor clearly exhibits an abrupt change when the bias is applied to the S8-340 shields. The total current collected by the biased shield is the trace labelled  $I_{bias}$ . The bias is switched on half-way through the discharge. The line-averaged density does not change appreciably over the course of the plasma discharge. Particularly, it does not change when the bias is applied.

From this data, the diverted-ion current decreases to the divertor whose origin strip is located on the positive poloidal angle side of the biased origin. The current increases to the divertor whose origin is located on the negative poloidal angle side of the biased origin. This trend persists even when other sets of divertor shields

are biased. Since the decrease in current to one monitored divertor approximately equals the increase in current to the other monitored divertor, and since the currents to remote divertors exhibit only minimal changes, we conclude that the redistribution of flux is predominantly localized to the origin regions bordering the biased origin region.

Reversing the direction of the coil currents leaves the structure of the magnetic field unchanged; only the direction of the magnetic field is reversed. Reversing the direction of the magnetic field should not directly change the electric field structure along a magnetic field line. Thus, one would expect to measure identical alterations to the diverted particle flows (at least to lowest order), if parallel conduction is the dominant mechanism responsible for the alteration of the diverted particle flows. On the other hand, reversing the direction of the magnetic field reverses the direction of any  $E \times B$  drifts. If an  $E \times B$  drift is responsible for the observed alterations, one would expect to see a reversal of the trend described above. That is, with the oppositely directed magnetic field, one could expect the current to decrease to the divertor whose origin is located on the negative poloidal angle side of the biased origin, and increase to the divertor whose origin is located on the positive poloidal angle side. This is shown schematically in Figure 2.

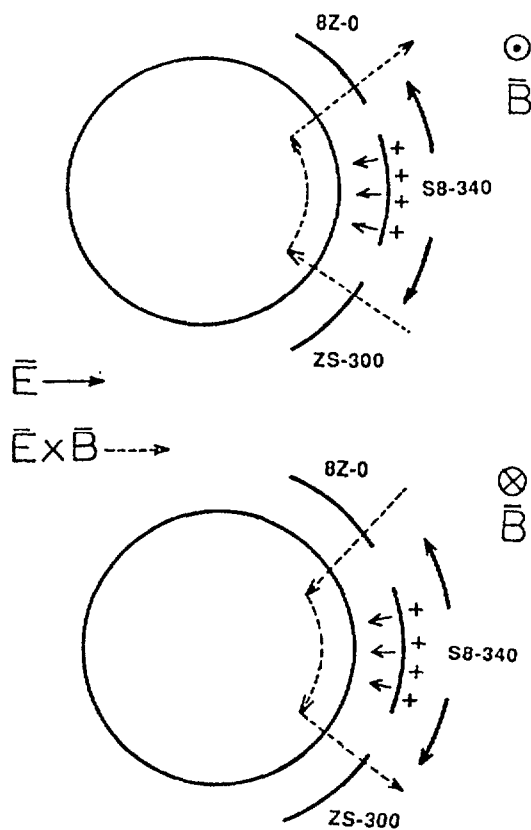


FIG. 2.

The measured potential changes (just outside the LCMS) due to shield biasing indicate the formation of an electric field having both radial and poloidal components. The radial component of the electric field acts to produce a poloidal drift (which pushes plasma poloidally around from one origin to a neighboring origin). The poloidal electric field component results in a radial  $E \times B$  drift. The radial  $E \times B$  drift resulting from shield biasing is the same order of magnitude as the measured plasma flow velocity through the divertors.<sup>8</sup> This radial drift acts

to pull plasma out from near the LCMS on one side of the biased origin (i.e., the drift is outward) and to retard the flow of plasma out of the region near the LCMS on the other side (the drift is inward). The fields thus act in concert, with the poloidal drift channeling plasma from the origin where it was inhibited from flowing through the divertor (by the minor radially inward drift) to the neighboring origin on the other side of the biased origin, where the outward radial drift enhances the probability of the plasma flowing through that particular divertor.

Repeating the measurement with the S8-340 divertor shield biased to +50 volts, but with the oppositely directed (i.e., negative) magnetic field does show a reversal of the change in the diverted ion current to both of the divertors described previously (the ZS-300 and the 8Z-0 divertors). This is consistent with an  $E \times B$  drift acting on the diverted plasma. The diverted ion current to the ZS-300 divertor decreases by 5.2 mA, whereas with a 'positively' directed magnetic field, the current increased by 5.2 mA. The change in the diverted ion current to the 8Z-0 divertor also reversed, increasing by 6.4 mA whereas it had decreased (with a positively directed magnetic field) by 6.0 mA.

This work demonstrates the ability to alter diverted flows through externally applied potentials in IMS. To extend this work to continuous-coil machines, a divertor map was made for the Proto-Cleo Stellarator. It was observed that the shape and location of the emergent flux bundles were a strong function of the scrape-off-layer thickness used for the calculations. With a thin SOL, the divertors were seen to segment in that most of the field lines emerged on the outboard side of the torus. As the SOL was increased, fluxes appeared on the inboard side and formed the classic fishtail appearance. Patterns with small SOL exhibited much longer connection lengths than those with larger SOL thicknesses.

A set of over 100 probe diagnostics have been installed in the divertor regions of the Proto-Cleo Stellarator for a preliminary analysis of the actual divertor structure. These probes are located so that information can be obtained about divertor segmentation, fishtail and divertor stripe widths and appropriate SOL thickness to use for future modelling. Operation of the device with these diagnostics is anticipated in the very near future.

## ACKNOWLEDGEMENT

This work was supported by the U.S. Department of Energy Grant No. DE-FG02-86-ER53216-A004 and Oak Ridge National Laboratory Contract No. 19X-3591-C.

## REFERENCES

- 1 Voitsenya, V.S., Voloshko, A.Y., Latsko, E.M., Solodovchenko, S.I., and Shtan, A.F. Nucl. Fusion **19**, 1241 (1979)
- 2 Motojima, O., Iiyoshi, A., Uo, K., Nucl. Fusion **15**, 985 (1975)
- 3 Gourdon, C., Marty, D., Maschke, E.K., and Touche, J., Nucl. Fusion **11**, 161 (1971)
- 4 Doerner, R.P., Anderson, D.T., Anderson, F.S.B., Matthews, P.G., and Shohet, J.L., Nucl. Fusion, (to be published)
- 5 Anderson, D.T., Derr, J.A., and Shohet, J.L., IEEE Trans. Plasma Sci. **PS-9**, 212 (1981)
- 6 Derr, J.A., and Shohet, J.L., IEEE Trans. Plasma Sci. **PS-9**, 234 (1981)
- 7 Doerner, R.P., Anderson, D.T., Anderson, F.S.B., Shohet, J.L., and Talmadge, J.N., Phys. Fluids **29**, 3807 (1986)
- 8 Doerner, R.P., Ph.D. Thesis, University of Wisconsin-Madison, Department of Electrical and Computer Engineering, (1988)

## **DIVERTOR STUDIES AT 6 kG IN THE INTERCHANGEABLE MODULE STELLARATOR\***

P.G. MATTHEWS, D.T. ANDERSON,  
F.S.B. ANDERSON, J.L. SHOHET  
Torsatron/Stellarator Laboratory,  
University of Wisconsin – Madison,  
Madison, Wisconsin,  
United States of America

### **Abstract**

The Interchangeable Module Stellarator offers a unique opportunity to study various detailed aspects of diverted plasma flow in a stellarator. This report presents measurements showing the structure of the plasma flow exiting the confinement volume for two magnetic field strengths (2.6 kG and 5.8 kG on axis). These patterns of flow, or "footprints" show the relative density of the emerging plasma spatially on the walls of the device. These patterns are compared between the two magnetic field settings.

In addition to measuring the structure of the plasma flux in the individual divertor bundle, a more global picture of the diverted plasma is presented at the two fields. The total diverted flux at all divertor locations within one field period of IMS can be measured simultaneously and shows the poloidal variations of the diverted plasma. These measurements show a poloidally asymmetric flow and a sensitive dependence on the magnetic field. Data is given for magnetic fields within a 15% range around the nominal operating central field strengths of 2.6 and 5.8 kG. Within this range, the diverted plasma is seen to make an abrupt distribution change when the electron cyclotron resonance location is moved from radially inside the magnetic axis to outside. It is postulated that these abrupt changes reflect a gross change in the transport conditions in the edge regions or inside the separatrix, and other experimental observations will be discussed in connection with these phenomena.

---

### **IMS Divertor Experimental Apparatus**

IMS is a 7 field period,  $L=3$  modular stellarator, with a 40 cm major radius and 4.5 cm average plasma radius. The magnetic configuration of IMS produces 63 modular divertors, 9 per field period. Each of these 9 divertors is located at a different poloidal angle which we will use to label them. Electrically-isolated shields are placed at each of the predicted divertor locations, some of which also have semi-permeable screens in front of them. These shields are located between the gaps in the coils and intercept the diverted plasma flow. A schematic diagram of the modular coil configuration and of the shield positions is given in reference [1].

By keeping the screens grounded, the shields may be biased without affecting the bulk plasma. Thus, the shields can be used as Langmuir probes to measure the diverted plasma flux. At three of the divertors, an array of Langmuir probes is imbedded into the shields which allows more detailed measurements of the structure in the diverted plasma flow. It is with these probes that the shape of the flow, or "footprint" pattern, is measured.

All plasmas are produced through ECH sources. For 2.6 kG operation, the source frequency is 7.25 GHz, and the applied RF power is  $\approx 1.2$  kW for 10 ms. For 5.8 kG operation, a different source is used that delivers  $\approx 10$  kW for 1 ms at a frequency of  $\approx 16.5$  GHz.

### **Divertor Footprint Experimental Set up**

The three divertors that contain the probe arrays are located in one field period at 72, 146 and 288 degrees poloidally. One array (at  $\approx 146$ ) consists of an 8x11 grid of probes with a 6 mm by 6 mm spacing, poloidally and toroidally. The other two arrays, which are located in larger coil gaps, each consist of an 8x12 grid of Langmuir probes with a spacing of 8 mm by 6 mm, poloidally and toroidally. Thus, these arrays cover a substantial portion of the area between the coils. More detailed information on these arrays and other divertor diagnostics are presented in R. P. Doerner's PhD thesis [1].

### **Measured "Footprint" Data**

The footprint data is presented as contour plots indicating relative strengths of ion saturation current over the area occupied by the probe tips. The measured current from each of the probes is fitted to a 5th order polynomial in 2-dimensions creating a surface in which the contours drawn. This surface is then normalized to its own peak value, and the contours are drawn in 10% increments revealing the structure of the diverted plasma flow at the radius of the probe array.

---

\* Work supported by the US Department of Energy under grant DE-FG02-86ER53216.A004 and Oak Ridge National Laboratory under contract 19X-9135-C.

Figures 1, 2 and 3 show these contours for the divertors located poloidally at approximately 72, 146 and 288 degrees, respectively. In all the figures, the top contour plot is for 2.6 kG operation and the bottom is for 5.8 kG.

Since each of the contour plots is normalized to its own peak, it would also be useful to present the relative magnitudes of the total current exiting the divertor at each field operation. Table 1 shows this measured divertor current along with the line averaged density measured by a microwave interferometer.

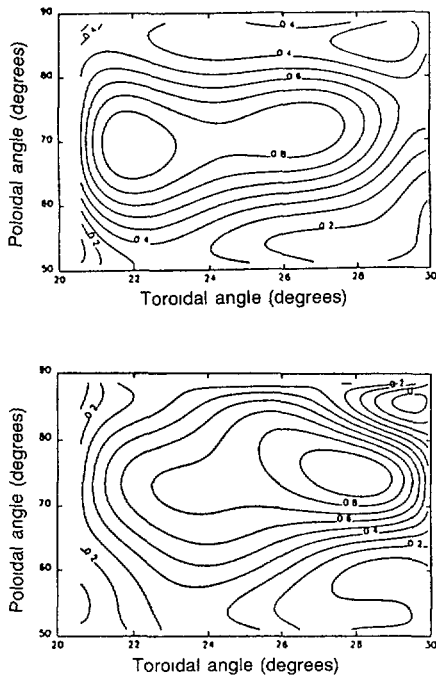


FIG. 1. Ion saturation contours for the 72 degree divertor.

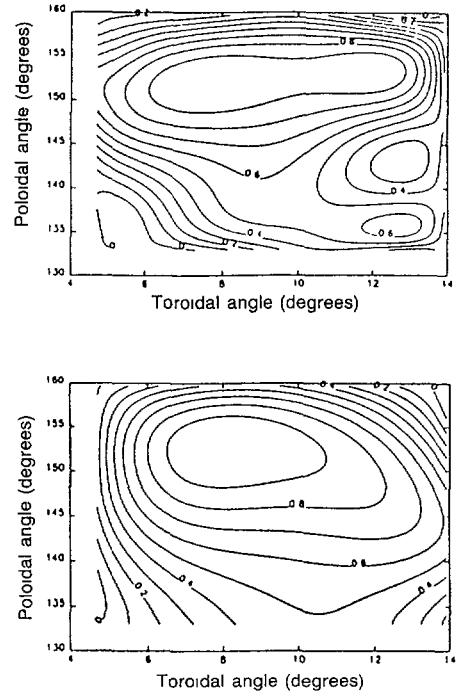


FIG. 2. Ion saturation contours for the 146 degree divertor.

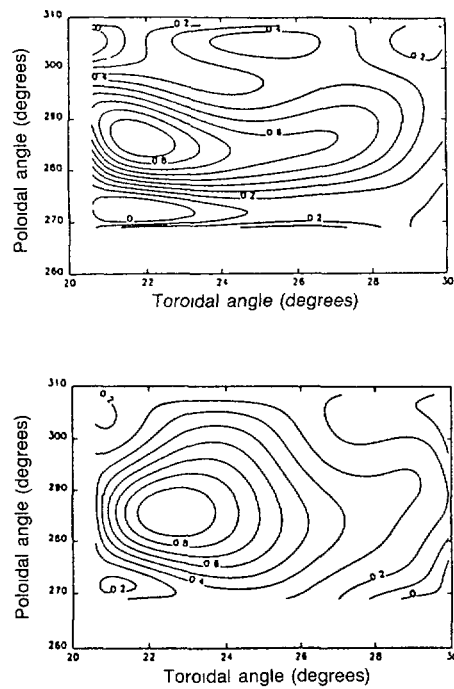


FIG. 3. Ion saturation contours for the 288 degree divertor.

TABLE 1. TOTAL DIVERTOR CURRENT

<u>Magnetic Field Strength (kG)</u>	<u>Line Averaged Density (cm<sup>3</sup>)</u>	<u>72° Divertor Current (mA)</u>	<u>146° Divertor Current (mA)</u>	<u>288° Divertor Current (mA)</u>
2.6	$1.5 \times 10^{11}$	9.35	1.54	13.21
5.8	$4.8 \times 10^{11}$	35.12	2.43	14.28

Observations

In all cases, the contour plots show well defined footprints, and that the majority of the diverted flux is intercepted by the probe array. Their location agrees quite well with the theoretical diverter modeling method used by Doerner [2]. They also show that the flux bundle is found in the same location for both 2.6 kG and 5.8 kG operation which is intuitive since the structure of the magnetic fields should remain constant for both field strengths.

However, referring to the contours in all three figures, one notices that the 2.6 kG contours show the flow to be more concentrated in the poloidal direction than in the 5.8 kG contours. In comparing the half intensity widths between the two contours, one finds approximately 15 to 40 percent increase in the half width of the 5.8 kG footprints. The contours in the 5.8 kG case all seem to be shorter in the toroidal direction.

The total current to the divertors shows an appreciable increase at 5.8 kG operation. This increase should be expected since the density of the plasma is higher at this field. However, these currents do not scale linearly with the plasma density, nor is the relative scaling between individual diverter flows consistent. This implies that the plasma has different transport characteristics at the two field strengths, and also operation at these two magnetic field strengths requires two different RF heating sources, and there may be a redistribution of diverted plasma because of the differences in power, frequency and orientation of the launching antenna. Since these are only three divertors out of a possible nine per field period, one would have to measure all nine to determine how the diverted plasma current is redistributed among the divertors. This redistribution is studied in more detail below.

Poloidal Flow Experiments

By using the whole shield as a Langmuir probe, one can measure the entire flux through a diverter. By measuring all nine types of divertors at in a field period at once, a poloidal distribution of flux can be obtained within a single discharge. This can be accomplished in IMS for all but one of the divertors in a field period. The innermost diverter, located at 180 degrees, lacks enough space to mount a screen in front of the shield. However, it is surmised that the flow out this diverter is much smaller than the divertors on the "out board" side of the machine. The data presented below shows this to be a reasonable assumption.

The shields are biased into ion saturation and the current drawn by the shield is indicative of the plasma density at the shield. This plasma is assumed to be present here only because it has flowed into the diverter from a location near the separatrix.

Measurements of the diverter flux for various magnetic field strengths can be easily accomplished by changing the charging voltage on the capacitor banks that source the IMS coil current. Because the "flat top" (1% variation) of the coil current waveform is  $\approx 1.0$  ms, small variations in B are seen within the 10 ms discharge (about 7.5% variation in B). Thus, the evolution of the diverter flux with magnetic field can be observed within a single discharge.

Measurements of Poloidal Flow Distribution

Figures 4 and 5 show the ion saturation current for each of the eight divertors in one field period versus the magnitude of the magnetic field on the axis of IMS. They show a significant variation of current over the range of magnetic fields. In particular, there is an abrupt change in current, or flow, around the magnetic field values of 2.6 - 2.65 kG. This change in flow is the seen on all the divertors except on the very inside of the device (divertors 146, and 214). Some diverter flows increase, while others decrease, and the pattern is not symmetric with respect to poloidal angle. The net change in density as seen by a microwave interferometer shows no abrupt change in this magnetic field region, as shown in figure 6.

The same experiment was conducted at the higher field operating point, and the results are similar, but the changes are less dramatic. Since the RF power last only 1 ms during these discharges, the data to produce these curves is more sparse than at the lower field. The abrupt change in flow is not seen as clearly on all the divertors, but do is measured at  $\approx 6.0$  kG which is consistent with the characteristics seen at the lower field.

In order to get a feel for the poloidal distribution of the currents, figures 7 and 8 show a histogram of the currents vs. poloidal angle for different values of magnetic field as indicated by the legend to the right. These figures show the poloidal asymmetry of the diverter flows, and how these flows are redistributed by the changing magnetic fields. One of the features to note is that there is much more asymmetry in the higher field operation with respect to top (0-180 degrees) to bottom flows than the lower fields. Much more of the diverter flux exits out the 72 and 112 divertors at high fields. In general, while the abrupt change in flow is consistent between the two regimes of operation, the overall characteristics of the poloidal distribution is not. This supports the earlier assumption that there are different transport mechanisms feeding the divertors between low and high field operation.

Possible mechanisms for observed flows and present and future investigations

I. Local plasma production in the diverted fields outside the separatrix. Local regions outside the separatrix can the correct magnetic field strength for ECH. If this resonance area is large enough, significant plasma production may take place which may feed, or inhibit the flow of plasma to the particular diverter connected to this region.

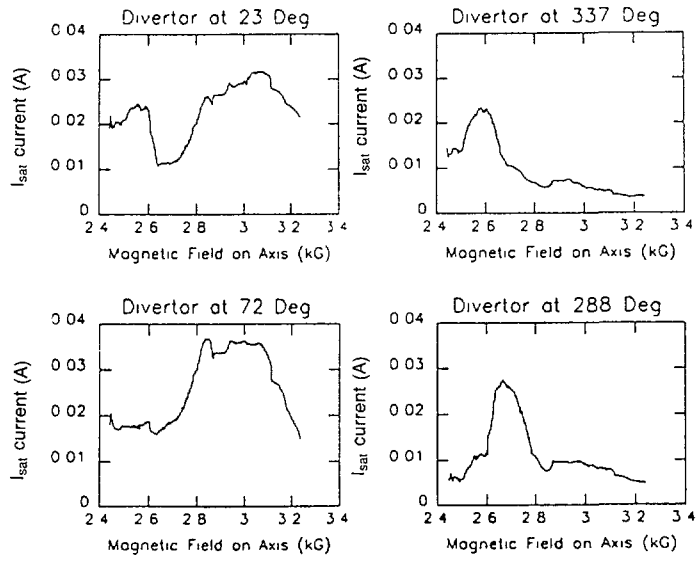


FIG. 4. Divertor currents at low field operation.

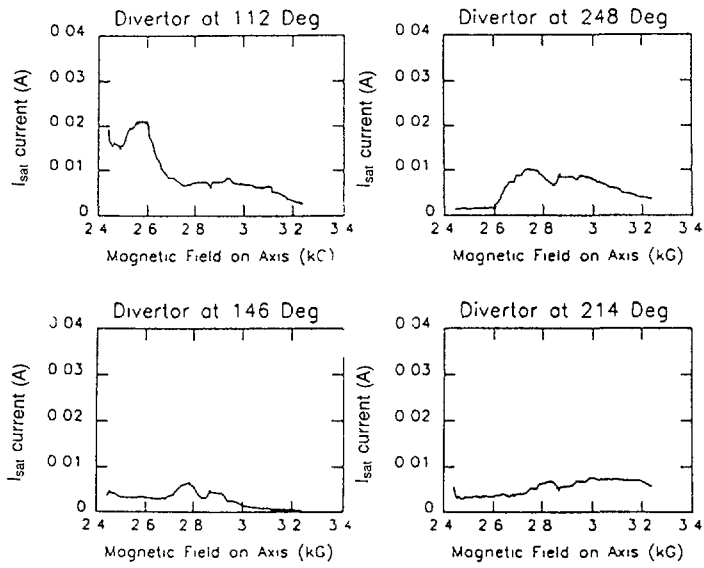


FIG. 5 Divertor currents at low field operation.

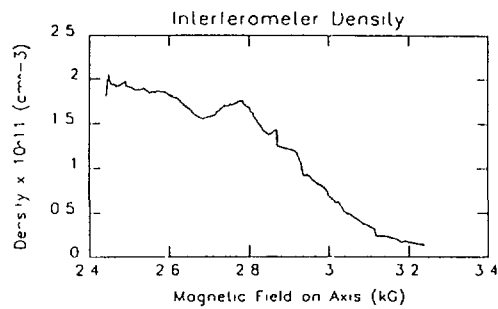


FIG. 6. Interferometer density at low field operation.

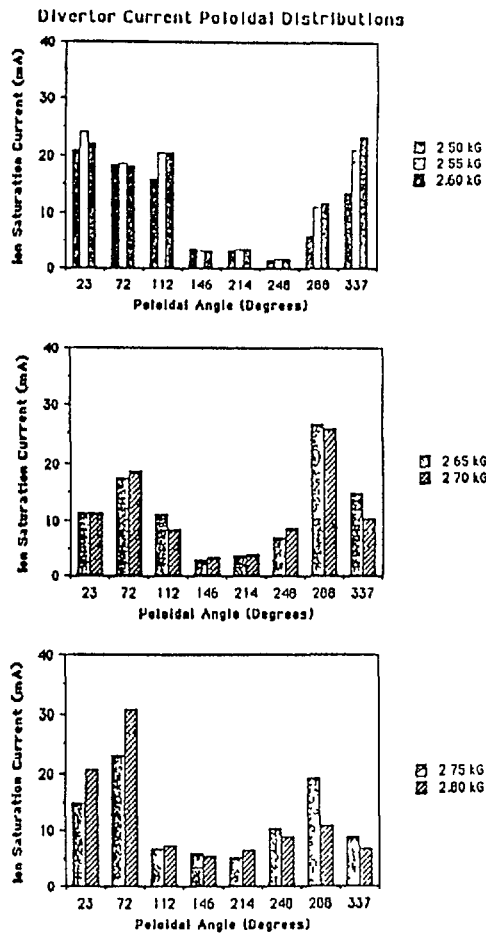


FIG 7 Poloidal variation of divertor flows at low fields

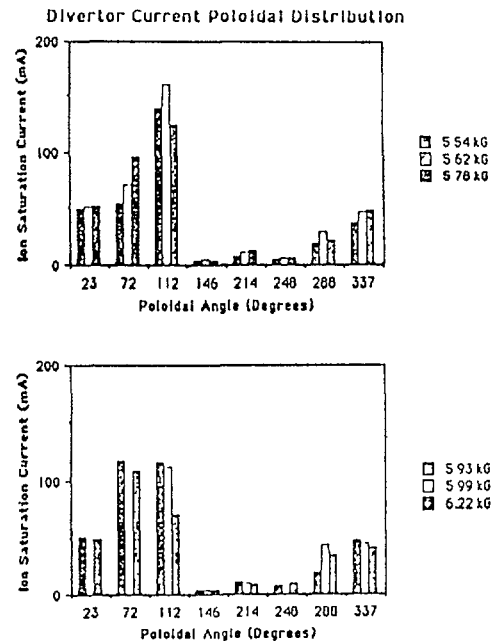


FIG 8 Poloidal variation of divertor flows at high fields

An ordinary Langmuir probe was used to measure density on a major radial cord of IMS during a discharge where the magnetic field was ramped between 2.5 and 2.8 kG. During this discharge, the observed change in divertor flow was seen. Figure 9 shows the density as a function of major radius for 5 different values of magnetic field. The confinement region for this scan is located between 35.5 and 43.0 cm. Note the evolution of density peak located at 44 cm as the magnetic field is increased. This peak is located outside the separatrix, it may be the result of local plasma production there. The location of this density peak corresponds to an area of magnetic flux that is connected to the "out board" divertors (located at 23 and 337 degrees poloidally). If one refers back to figure 6, it is seen that these divertors exhibit a decrease in flow. Thus, this density peak seems to be **inhibiting** the flow, possibly acting like an electrostatic plug. This plug may be formed when the tail of the electron distribution is heated to the point of being lost from the region leaving a net positive space charge. More extensive 3 dimensional measurements of density, electron temperature and space potential in this region, as well as theoretical predictions of electron cyclotron resonance locations, must be made.

**II. Edge Transport is being affected by the changing magnetic field.** It was shown by Doerner [3] that large changes in divertor flux could be achieved by externally applying voltages to the divertor shields which set up electric fields in the scrap-off layer just outside the separatrix. An  $\mathbf{ExB}$  drift model was developed to explain the observed shifts in divertor flux. Assuming electric fields in the scrap off layer due to ECH or other mechanisms, then changing the magnetic fields will alter the  $\mathbf{ExB}$  drifts.

One straight forward way to test this hypothesis would be to repeat the measurement of the evolution of the divertor flux with the direction of  $\mathbf{B}$  reversed. The discharge should be formed in the same manner except that the  $\mathbf{ExB}$  drifts will be in the opposite direction, and the divertor flux evolution should be reversed. This is especially important given the odd symmetry in flows seen between the 72 and 288 divertors. Work is currently in progress to modify the bus structure in the capacitor banks to facilitate changing the direction of current flow in the coils.

Another possible mechanism is that the magnetic fields are affecting the edge fluctuation levels. Thus, the fluctuation induced transport may be responsible for the changes in divertor flow. To investigate this possibility, we have to make direct local plasma parameter measurements in the edge regions, and ascertain the fluctuation levels corresponding to different magnetic field values.

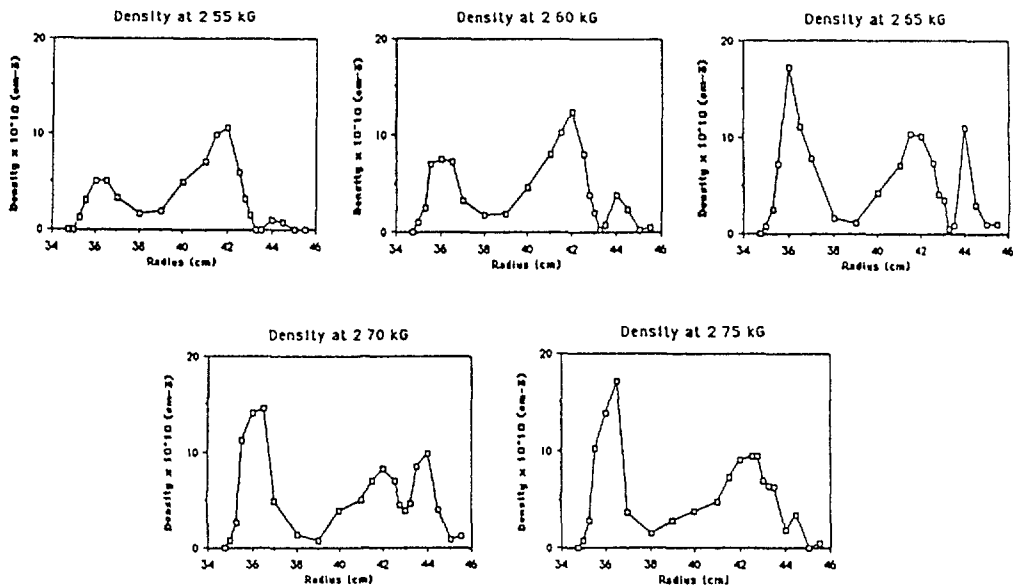


FIG 9 Radial density scans at different magnetic fields

**III. Central plasma transport is being modified by changing magnetic fields.** Again, if there are electric fields inside the separatrix, their effects on transport will depend on the magnetic field. A redistribution of transport in the central plasma will show up in the flows out the divertors.

Also, local density concentrations may feed specific divertors directly, and their movement with magnetic field (possibly through an upper hybrid resonance) will alter the divertor flux. Local density peaks have been observed in an IMS cross-sectional density scan [4]. Other experiments have shown that local areas of high plasma potential exist in IMS and that they are dependent on the ECR location [5]. These high potential areas give rise to convective transport which is dependent on the magnetic field strength.

Another possibility is that trapped particle effects may give rise to a changing electric field structure inside the separatrix, and again  $\mathbf{ExB}$  drifts may account for the redistribution to the divertors.

More detailed measurements will be made on the central plasma, edge plasma and divertor regions to determine plasma behaviour under different magnetic field conditions.

#### Comments

It is evident that there are many questions that need to be answered before one can explain the data presented here. It is probable that more than one of the above mechanisms, and others not mentioned here, are responsible for the divertor poloidal flux distributions. In fact, the data may well contain a wealth of information concerning plasma transport issues. Work will proceed to study this phenomena with the goal that understanding divertor flows will ultimately lead to a better understanding of central plasma transport processes.

#### References

1. Doerner, R. P., Ph.D. Thesis, University of Wisconsin-Madison, Department of Electrical and Computer Engineering, (1988) pp. 33-38
2. Doerner, Ph.D Thesis, pp 39-51
3. Doerner, et. al. "Electrostatic Control of Divertor Flows in a Stellarator", Phys Rev Letters, 62, 159, January, 1989.
4. Peterson, B. J., private communication
5. Talmadge, J. N., "Wisconsin Torsatron/Stellarator Program FY 1989 Final Report"

# THE EFFECTS OF A MAGNETIC FIELD ON A COLLISIONAL PRESHEATH

W.N.G. HITCHON, D.J. KOCH,  
W.D. D'HAESELEER  
Department of Electrical and  
Computer Engineering,  
University of Wisconsin - Madison,  
Madison, Wisconsin,  
United States of America

## Abstract

The numerical method applicable for the solution of the kinetic equation described previously have been used for the investigation of sheath characteristics at a divertor region of the IMS device. The effect of modifying the ripple profile on confinement time and potential profile are described.

## I. Plasma Model

The numerical model has been described previously (Hitchon, Koch and Adams; J. Comp. Phys, to be published), where it was applied to a sheath such as those in the IMS divertors. This numerical method is very effective in solving equations such as the kinetic equation when flow in some sense dominates diffusive processes.

The kinetic equation for the ions is

$$\frac{\partial f}{\partial t} + v \frac{\partial f}{\partial \lambda} + \left\{ \frac{eE}{m} - \frac{\mu}{m} \frac{\partial B}{\partial \lambda} \right\} \frac{\partial f}{\partial v} = C(f) + S, \quad (1)$$

where  $f$  is the ion distribution function,  $E$  the electric field along the diverted field line,  $\mu$  the magnetic moment and other symbols have their usual meanings. Once  $f$  is known, the electrostatic potential  $\phi(\lambda)$  is obtained from the quasineutrality condition, which is appropriate in the presheath, by assuming the electron density obeys the Boltzmann relation  $n_e = n_0 e^{e\phi/kT_e}$ .

## II. Results

In this section, we outline the effects of modifying the ripple profile on  $\tau$ ,  $\phi$  and the fraction of ions going to each plate.

The distribution of ions as a function of distance along the line,  $z$ , and velocity,  $v$ , is shown in Fig. 2. The mean-free-path  $\lambda = 50$  cm.  $\delta = 0.4$ , with  $\delta = 0$  in the source. Only a single bump in the field was used.

The variation of the confinement time  $\tau$  and  $\phi$  with  $\delta$  at a fixed number of ripples,  $N = 4$ , and versus  $N$  at a fixed  $\delta = 0.4$ , is shown in Fig. 3.  $\tau$  varies over a range from about 10-30  $\mu$ s.  $\phi$  varies roughly linearly with both  $\delta$  and  $N$ , in these cases. For  $N = 4$ ,  $\Delta\phi$  is approximately equal to twice  $\mu B\delta$ , for all the  $\delta$  values considered.

The potential drop across the presheath in one of the cases considered above is shown in Fig. 4;  $\delta = 0.4$ ,  $N = 4$ . The potential set up drops to  $-8.4$  V. The 'effective' potential,  $\phi_{\text{eff}} = \phi + \mu B/q$ , is also shown. The effective potential energy gives rise to an energy barrier that traps ions in the source region. This energy barrier ranges from .4 eV for  $\delta = .2$  to 1.3 eV for the  $\delta = .6$  case. The varying height of this energy barrier gives rise to the variation of confinement times. It can be seen that the potentials  $\phi$  and  $\phi_{\text{eff}}$  have maxima and minima which are  $180^\circ$  out of phase with the magnetic field strength. This is due to collided ions that are relaunched with a parallel energy low enough to be trapped in the effective potential wells.

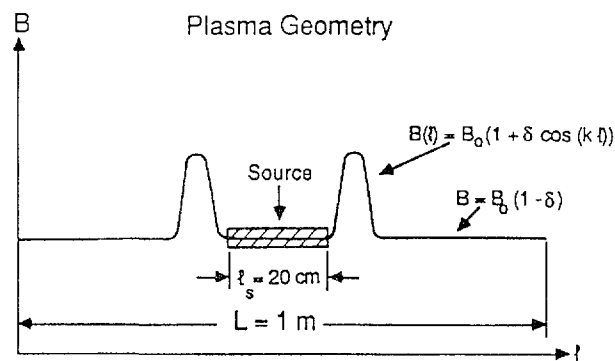


Fig. 1. The geometry of the field line considered. The source is constant throughout a region midway between the plates and zero elsewhere. Various ripple profiles were considered, although most cases had a constant field in the source region.

### Plasma Ion Density

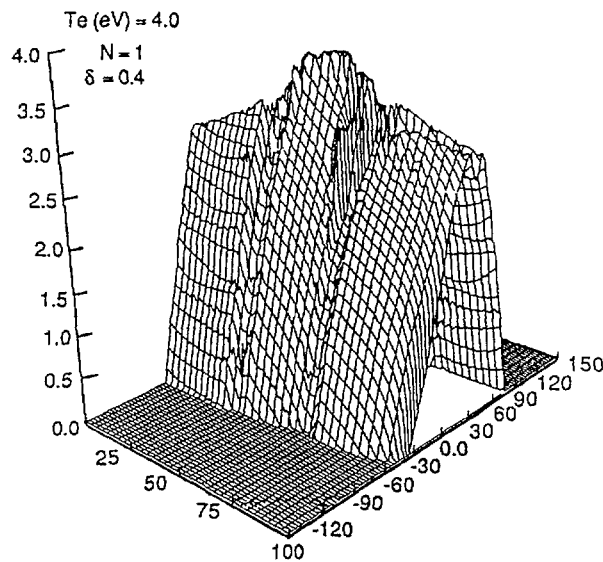


Fig. 2. The distribution function plotted vs.  $(\lambda, \nu)$  for a fixed source rate in the region  $\lambda = 20$  cm. to  $\lambda = 40$  cm.  $T_i = T_e = T_n = 4\text{eV}$ , mean-free path = 0.5 m,  $\delta = 0.4$  and a single bump in the field.

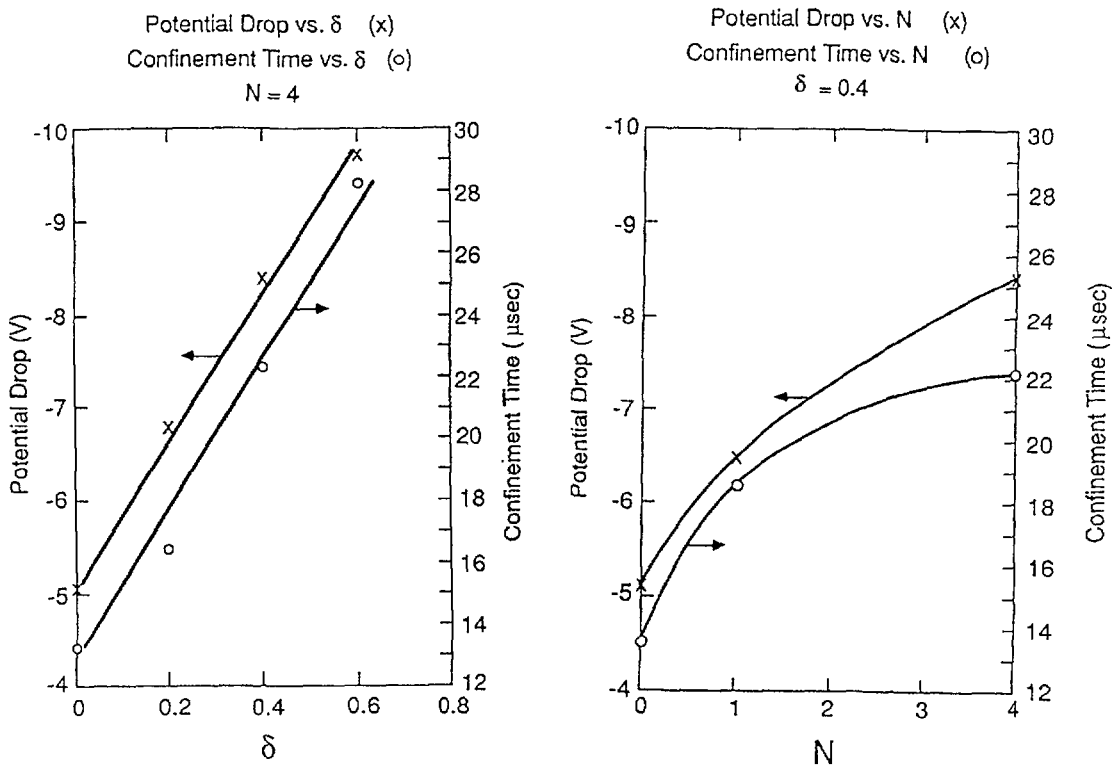


Fig. 3.  $\tau_c$  and  $\phi$  vs  $\delta$  for  $N = 4$ , and vs  $N$ , for  $\delta = 0.4$ .

Plasma Potential vs.  $z$

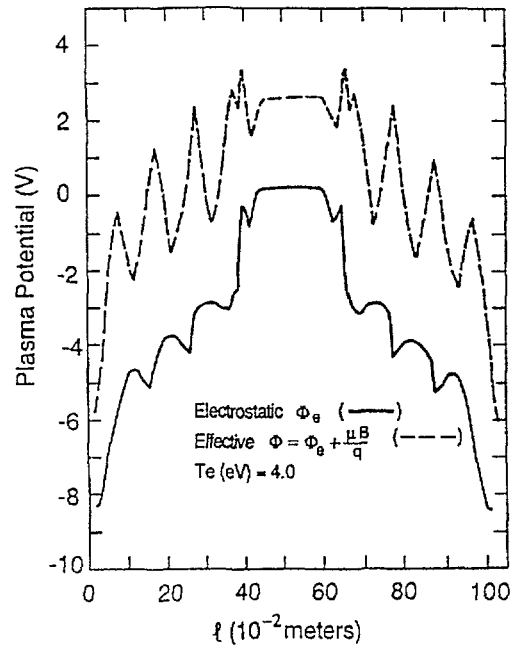


Fig. 4.  $\phi$  and  $\phi_{\text{eff}}$  vs.  $z$  for the case  $N = 4$ ,  $\delta = .4$  as shown in Fig. 3.

## EDGE PLASMA AND DIVERTOR STUDIES IN THE ATF TORSATRON\*

P.K. MIODUSZEWSKI, T. UCKAN, D.L. HILLIS,  
J.A. ROME, R.H. FOWLER, J.C. GLOWIENKA,  
M. MURAKAMI, G.H. NEILSON  
Oak Ridge National Laboratory,  
Oak Ridge, Tennessee,  
United States of America

### Abstract

First plasma edge data have been obtained during the initial operating period of ATF. For discharges with 170 kW of ECH power, 600 kW of NBI power, and line-average densities of  $1.5 \times 10^{19} \text{ m}^{-3}$ , the plasma parameters at the LCFS were:  $n_e = 3 \times 10^{18} \text{ m}^{-3}$ ,  $T_e = 12 \text{ eV}$ ; heat flux  $150 - 300 \text{ W/cm}^2$ , decay length  $\lambda_q = 2 \text{ cm}$ . The fraction of the input power that was deposited on the limiters was 16% in ECH discharges and 3% in NBI discharges. The particle flux in the divertor stripes was several  $10^{17} \text{ cm}^{-2} \text{ s}^{-1}$  with a half-width of 2 cm. Location and width of the stripes did not change when the neutral beam was injected into the ECH plasma.

---

### 1. Introduction

During the first operating period of the Advanced Toroidal Facility (ATF), currentless plasmas have been generated and heated with up to 0.2 MW of electron-cyclotron power (ECH) and up to 1.5 MW of neutral beam injection (NBI) [1]. ATF is an  $l=2$ , 12-field-period torsatron with a major radius  $R_0 = 2.1 \text{ m}$ , an average plasma radius  $a = 0.27 \text{ m}$ , and a mean field of  $B_0 \leq 2 \text{ T}$ . The ECH system consists of one 53.2 GHz, 200 kW, CW gyrotron which provides fundamental heating at  $B_0 = 1.9 \text{ T}$  and second harmonic heating at  $B_0 = 0.95 \text{ T}$ . Two neutral injectors are installed, aligned for tangential injection in opposing directions (co- and counter-injection). Each beam can inject up to 1 MW into the torus at energies up to 40 keV, with pulse lengths up to 0.3 s. For future long pulse or steady state operation, we are investigating options for continuous particle control and edge modifications with a divertor.

### 2. Experimental Arrangement

The poloidal cross-section of the plasma is a function of the toroidal angle. At  $\phi = 0^\circ$  and  $30^\circ$  the plasma is vertically elongated, while halfway in between, at  $\phi = 15^\circ$ , it is horizontally elongated. Toroidal cuts through the vacuum vessel at  $\phi = 0^\circ$  and  $15^\circ$  and the corresponding poloidal cross-sections are shown in Fig. 1. The figure shows the main plasma, limited by the last closed flux surface (LCFS), and the plasma edge. It has been observed in Heliotron-E that

---

\* Research sponsored by the Office of Fusion Energy, US Department of Energy, under contract DE-AC05-84OR21400 with Martin Marietta Energy Systems, Inc.

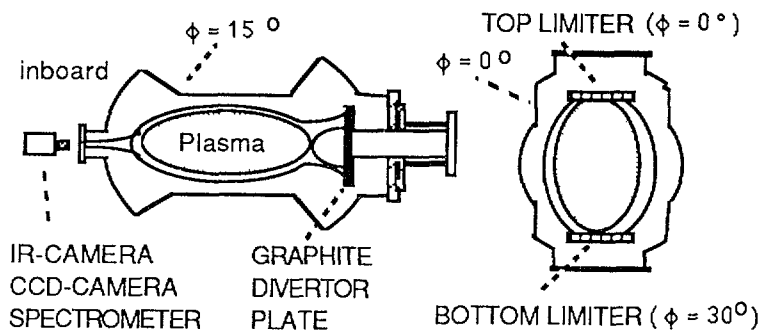


FIG.1 Poloidal cross-section of the plasma at toroidal angles of  $\phi = 0^\circ$  and  $15^\circ$ , showing the plasma edge and the arrangement of limiters and the graphite plate.

the plasma leaves the confinement zone in distinct flux bundles intercepting the wall as "divertor stripes" [2]. As indicated schematically in Fig. 1, two stripes leave the confinement zone towards the outboard wall and one towards the inboard wall. Because of the complicated structure of the plasma edge, the diagnostics system was designed to determine a) the global configuration, i.e. the location and extent of the stripes, and b) the local plasma parameters within the stripes. The main edge diagnostics that have been used so far are the instrumented limiters, the instrumented divertor plate, and an array of  $H_\alpha$ -monitors.

The instrumented limiter system is comprised of one moveable top and bottom module, each with a vertical stroke of 25 cm and a toroidal separation between the two units of one field period. Each module consists of 11 individual graphite tiles, mounted on a water-cooled stainless steel base plate. The tiles form calorimeter arrays for measurements of the energy deposition profile and the total deposited energy. The central tile incorporates Langmuir probes and a gas puff nozzle. The drawing in Fig. 2 shows the schematic arrangement of the top limiter and the central tile.

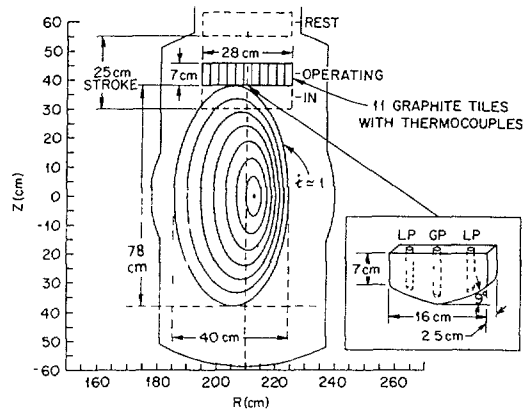


FIG. 2 Location of the top rail limiter in the ATF vessel. The inset shows the central tile.

A system consisting of a graphite divertor plate and an infra-red (IR) or charge-coupled device (CCD) camera is used to study the divertor configuration. Figure 1 indicates the location of the divertor plate; it has a diameter of 50 cm and can be positioned between the wall and the LCFS. The pattern of particle and heat fluxes on the divertor plate can be observed with CCD- or IR-camera respectively. A multi-purpose image processing system has been developed for fast acquisition, display and analysis of these 2-dimensional patterns. For measurements of local plasma parameters, Langmuir probes are imbedded in the graphite plate at three locations. Observing particle fluxes to the divertor plate while scraping off the edge plasma with top and bottom limiters, will allow us to determine the connection lengths in the plasma edge as a function of radial position.

The  $H_{\alpha}$ -monitors view the wall, the gas puff location, the location of neutral beam injection, and the limiter. The observed signals serve as a relative measure of particle fluxes. Because of the complicated structure of the plasma edge, the determination of the integrated global particle flux requires detailed transport modeling of the neutral hydrogen and is in progress.

### 3. Modeling of the Plasma Edge

Particle flow from the confined plasma to the vacuum vessel wall has been studied by following field lines and single particle orbits. A realistic multifilament model for the vacuum magnetic field was combined with a detailed computer model of the ATF vacuum vessel to determine the interception of the field lines with the vacuum vessel. Magnetic field lines as well as 1-keV particles were launched randomly from locations 1 to 3 cm outside the LCFS. The result showed both field lines and particles being funneled to form narrow stripes at the wall. The stripes were similar for the field lines and the 1-keV particles. Modeling the interception of the field lines with the outboard divertor plate showed two distinct stripes with the location depending on the radial position.

### 4. Results

A typical limiter energy profile of a 0.25 s discharge is shown in Fig. 3. The plasma was sustained by 170 kW of ECH with an additional 600 kW of NBI from 0.15 s to 0.25 s; the maximum line-averaged density was  $1.5 \times 10^{19} \text{ m}^{-3}$ . The vertical position of the limiter was at 39 cm which corresponds approximately to the LCFS. The central tile received an energy of 860 J, the total energy deposited on one limiter was 4 kJ. From the width of the energy deposition profile, the scrape-off length of the heat flux was determined to be  $\lambda_q = 2.3 \text{ cm}$ , similar to values obtained in tokamaks. To determine the average power flux as well as the contributions from ECH and NBI, limiter position scans were performed for ECH-only as well as for (ECH+NBI) discharges. The total deposited energy at the top limiter as a function of position is shown in Fig. 4.

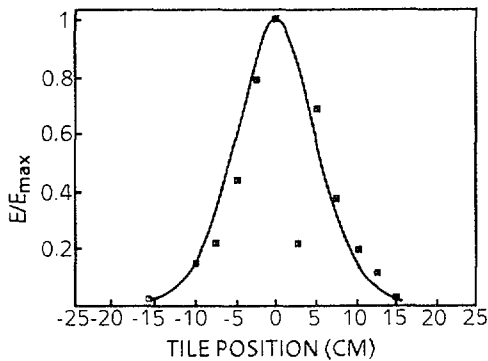


FIG. 3 Energy deposition profile on the top limiter located at  $z = 39 \text{ cm}$

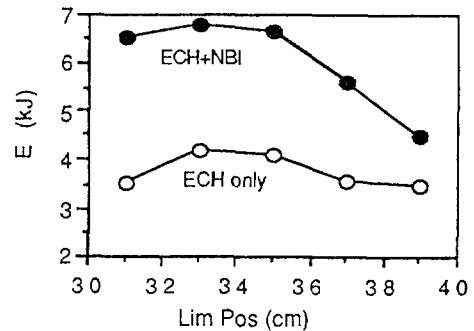


FIG. 4 Total energy deposited on top limiter during 0.25 s discharge as a function of limiter position

The ECH-only discharges are suitable for estimating the power flux. The average ECH input was 170 kW for a duration of 0.25 s. The energy deposition at the LCFS (39 cm) was 3.5 kJ, corresponding to an average limiter power flux of 14 kW. Hence, the total power flux to both limiters was 16.5 % of the input power. Knowing the power to the central tile as well as the e-folding length of the power flux, the power flux density at the LCFS could be calculated and was approximately  $270 \text{ W/cm}^2$ . This is consistent with Langmuir probe measurements which indicate temperatures and densities at the LCFS of 12 eV and  $3 \times 10^{18} \text{ m}^{-3}$  respectively.

The (ECH+NBI) discharges were sustained for 0.25 s by 170 kW of ECH, with an additional 740 kW of NBI for 0.1 s. The total input energy increased by a factor of 2.75. As Fig. 4 shows, the energy on the limiter increased only by a factor of 1.3 at the LCFS and by 1.6 at 33 cm. At the LCFS, an incremental energy of 1 kJ was deposited by NBI, corresponding to a power flux of 10 kW. Accounting for both limiters, the fraction of NBI power that is transported to the limiters, is only about 3 %. Since, on the other hand, the stored energy in the bulk plasma increased typically by a factor of 2.5 with NBI, we conclude that energy transport from the center does not occur by conduction and convection to the plasma edge, but by mechanisms that transport energy directly to the wall such as radiation and charge-exchange processes. This is consistent with measurements of the  $H_{\alpha}$  radiation at the vessel wall. When the limiters were inserted well into the confined plasma, most of the plasma should have been scraped off, causing the particle flux to the wall to vanish. As Fig. 5 shows, this is actually the case for the ECH phase of the discharge while during the NBI phase the particle flux to the wall is hardly influenced by the limiter position. Whether or not these observations can be explained e.g. by charge-exchange processes or by other mechanisms such as orbit losses, will be studied further.

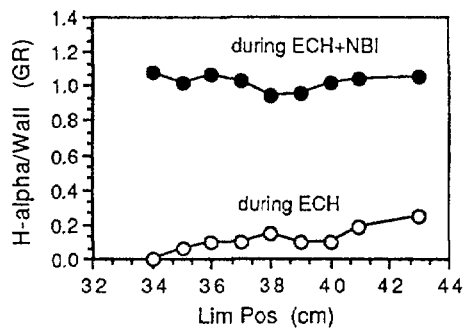


FIG. 5  $H_{\alpha}$ -radiation from the wall at 70 ms (ECH) and 150 ms (ECH+NBI) into the discharge

Some initial experiments with the divertor plate have confirmed modeling results on the "divertor stripes". A position scan of the divertor plate has provided first information on the stripes. The Langmuir probes on the plate were used to measure the ion saturation current as a function of plate position. As a result, three curves were obtained which represent the particle flux in the stripe, each at a different position. Figure 6 shows one example (the zero position corresponds to the plate located at the wall). The figure shows that the stripes were very narrow with only 2 cm half-width and particle fluxes of several times  $10^{17} \text{ cm}^{-2} \text{ s}^{-1}$ . Stripe position and half-width did not change with NBI. The particle flux was three times higher during NBI than during ECH-only which is consistent with the change in line-average density.

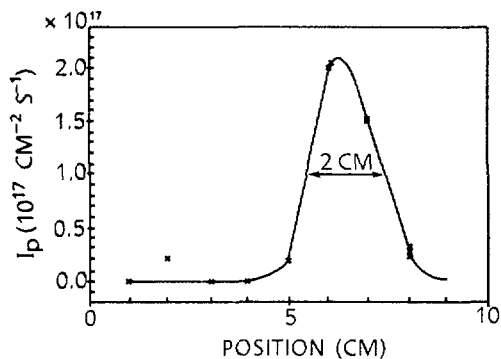


FIG. 6 Particle flux in the "divertor stripe" as a function of the divertor plate position

## 5. Summary

First plasma edge data have been obtained during the initial operating period of ATF. For discharges with 170 kW of ECH power, 600 kW of NBI power, and line-average densities of  $1.5 \times 10^{19} \text{ m}^{-3}$ , the plasma parameters at the LCFS were:  $n_e = 3 \times 10^{18} \text{ m}^{-3}$ ;  $T_e = 12 \text{ eV}$ ; heat flux 150 - 300  $\text{W/cm}^2$ , decay length  $\lambda_{q_0} = 2 \text{ cm}$ . The fraction of the input power that was deposited on the limiters was 16 % in ECH discharges and 3 % in NBI discharges. The particle flux in the divertor stripes was several  $10^{17} \text{ cm}^{-2} \text{ s}^{-1}$  with a half-width of 2 cm. Location and width of the stripes did not change when the neutral beam was injected into the ECH plasma.

## References

- [1] M.J. Saltmarsh et al., IAEA-CN-50/C-1-2, IAEA Conference Nice, France, Oct. 1988
- [2] O. Motojima et al., J. Nucl. Mater. 128 & 129 (1984) 524

## WALL CONDITIONING IN ATF\*

R.A. LANGLEY, T.L. CLARK, J.C. GLOWIENKA,  
R.H. GOULDING, P.K. MIODUSZEWSKI,  
D.A. RASMUSSEN, T.F. RAYBURN, C.R. SCHAICH,  
T.D. SHEPARD, J.E. SIMPKINS, J.L. YARBER  
Oak Ridge National Laboratory,  
Oak Ridge, Tennessee,  
United States of America

### Abstract

Techniques for cleaning and conditioning the vacuum vessel of the Advanced Toroidal Facility (ATF) and its internal components are described. The vacuum vessel cleaning technique combines baking to 150°C and glow discharges with hydrogen gas. Chromium gettering is used to further condition the system. The major internal components are the anodized aluminum baffles in the Thomson scattering system, a graphite-shielded ICRF antenna, two graphite limiters, and a diagnostic graphite plate. Three independent heating systems are used to bake some of the major components of the system. The major characteristics used for assessing cleanliness and conditioning progress are the maximum pressure attained during bakeout, the results of gas analysis, and relevant plasma parameters (e.g., time to radiative decay). Details of the various cleaning and conditioning procedures and results are presented.

---

## 1. INTRODUCTION

The ATF has now gone through three operating periods. The facility and its operational characteristics are described in Ref. [1]; only the vacuum vessel pumping, baking, and glow discharge systems are described here. To ensure an acceptable base vacuum and "clean" walls, cleaning and conditioning of the vacuum vessel and some of the major internal components were incorporated into the initial design.

The initial startup phase of the ATF was dominated by leak checking and leak repair. Plasma operation began with a minimal number of diagnostics. The time before radiative collapse was used as a measure of the system cleanliness, as shown in Fig. 1 for the first 1300 discharges. For discharges 1 through 800 glow discharge cleaning (GDC) alone was used for conditioning the device, while for discharges 800 through 1300 GDC was used in combination with baking to 150°C. Plasma performance, as determined from the time to radiative collapse, improved significantly with the introduction of baking. The third operational period started with discharge 1500.

---

\* Research sponsored by the Office of Fusion Energy, US Department of Energy, under contract DE-AC05-84OR21400 with Martin Marietta Energy Systems, Inc.

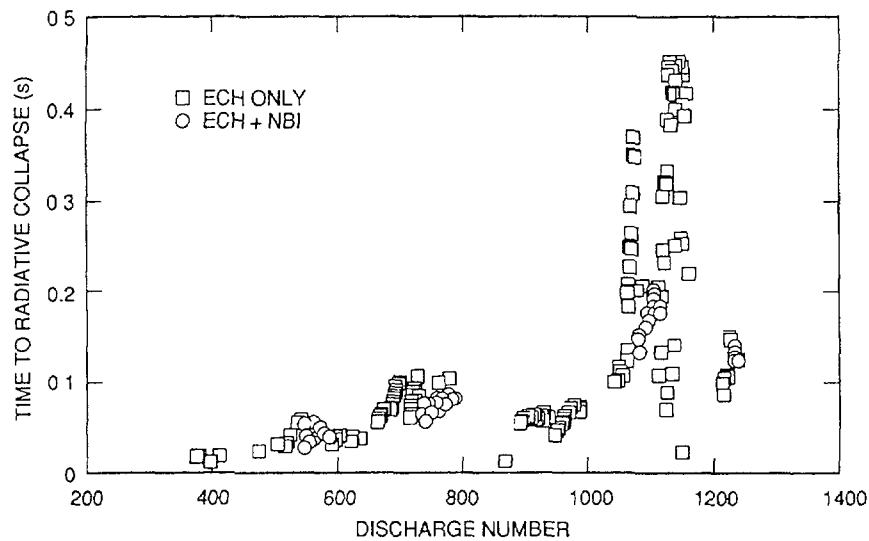


FIG. 1. Time to radiative collapse for the initial and second operational periods of ATF. During the initial period, GDC only was used, whereas during the second period both GDC and baking were used to condition the vessel.

The cleaning systems had been upgraded and several diagnostics added. This paper concentrates on this period, which was dedicated mainly to studying plasma characteristics and installing additional diagnostics. In Section 2, the properties of the vacuum vessel and pumping system are summarized. The vessel bakeout system and the GDC procedure are described in Section 3. In Section 4, we describe procedures for cleaning and conditioning some of the internal components and discuss the results obtained. Chromium gettering is addressed in Section 5. In Section 6, we discuss the effects of the various cleaning and conditioning techniques on plasma performance. Finally, in Section 7, we summarize and draw conclusions from the present results.

## 2. VACUUM VESSEL AND PUMPING SYSTEM

The ATF vacuum vessel is fabricated from nonmagnetic stainless steel plates welded with Inconel filler metal. Heating sources, pumping system components, and diagnostics are coupled to the device through 48 ports of 3 different sizes. Figure 2 shows the vacuum vessel configuration. The complicated shape is designed to accommodate the two helical torsatron windings.

The vacuum vessel consists of the basic torus, including the port throats, and the flanges, each of which is made up of a flange window attached to the port throat and a flange cover (see Fig. 2). Figure 3 is a schematic of the vacuum vessel, the pumping system, and the major internal components. Pertinent surface areas are listed in Table I. The high-vacuum pumping system for the vacuum vessel consists of three 2200-L/s turbopumps in parallel, each backed with a forepump. The effective speed of the pumping station at the vessel was calculated to be 3200 L/s, and the measured pumping speed was 2500 L/s. Two residual gas analyzers (RGAs) are installed in the pumping system for gas analysis. A variable-conductance bypass arm is used for gas analysis during GDC.

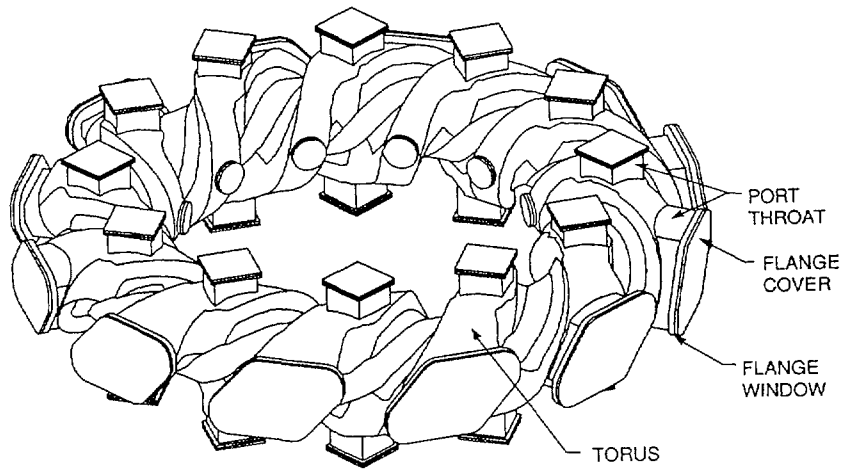


FIG. 2. Geometric configuration of the ATF vacuum vessel.

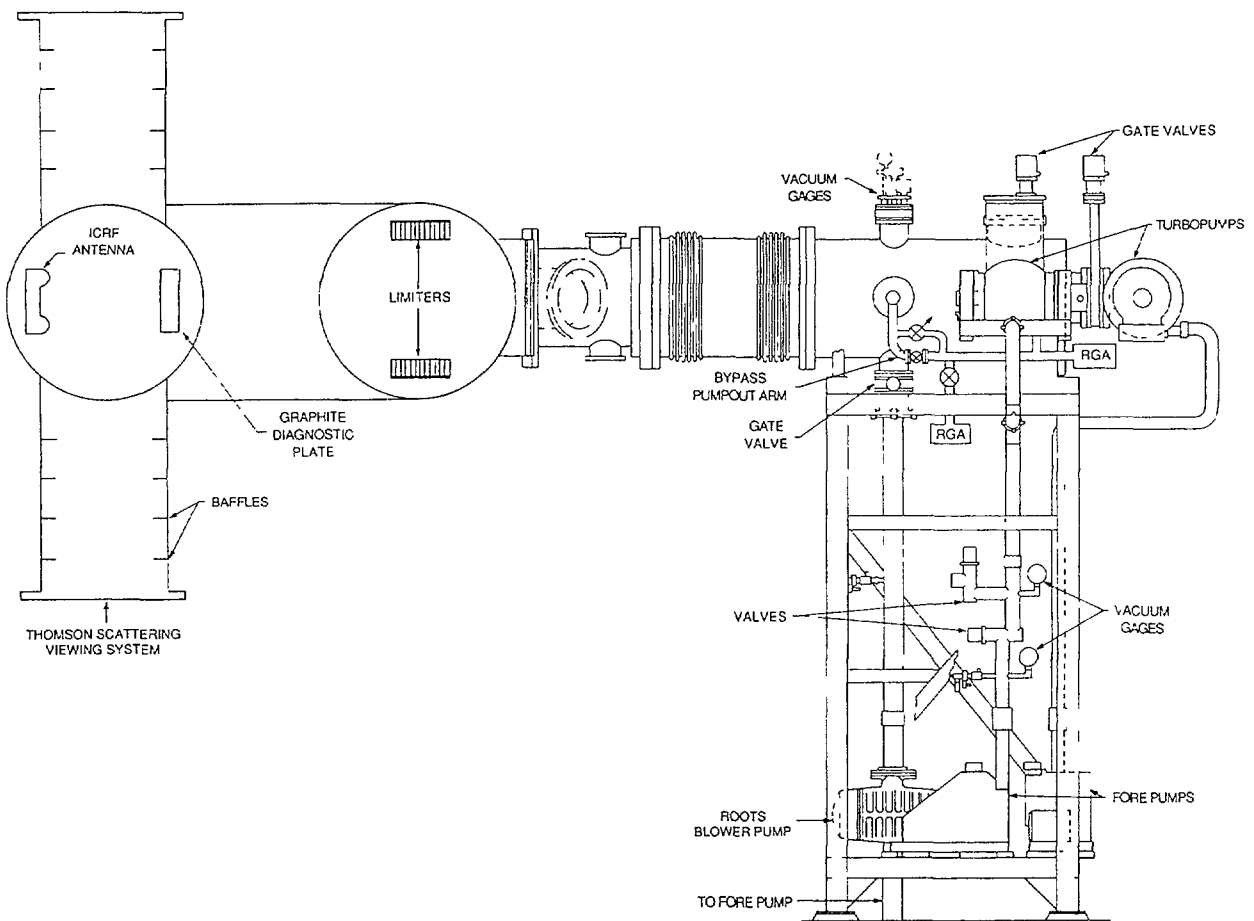


FIG. 3. Schematic of ATF vacuum vessel, major internal components, and pumping system.

Table I. Pertinent surface areas  
(SRF = surface roughness factor)

	Plasma facing area (m <sup>2</sup> )	SRF	Outgassing area (1000 × m <sup>2</sup> )
Vacuum vessel			
Stainless steel	50	10	0.5
Thomson scattering stack			
Anodized aluminum	0	100	3
Stainless steel	0	10	0.1
Limiters			
AXF-5Q	0.2		10
Graphite diagnostic plate			
ATJ	0.06		15
ICRF antenna shield			
AXF-5Q	0.15		1.6

### 3. BAKING AND GDC SYSTEMS

Induction heating of the torus is accomplished by inductive coupling of ac power via excitation of the helical windings. About 20 min is needed to heat the torus to its maximum allowable temperature, 150°C; the maximum heating rate is about 4°C/min, and the cooling rate near 150°C is about 3°C/min. (Earlier estimates [2] were 42 min to heat the torus to 150°C, a heating rate of 3°C/min, and a cooling rate near 150°C of about 1°C/min.) When the maximum temperature is reached, the power is turned off and the temperature is allowed to drop to 140°C before power is re-applied. The cycle time for the induction heating is about 6 min, with 2.5 min on and 3.5 min off. The inductive coupling of the helical coils to the vessel is somewhat nonuniform; when the hottest portion of the vessel is at 150°C, the coolest portion is near 75°C.

Heating tapes are used to heat the torus appendages; each tape is independently controlled using a thermocouple as a sensor. The time to reach the maximum allowable temperature of all appendages heated with tapes, except the Thomson scattering stack, is very long (i.e. many hours). In fact, for a majority of the tapes, the equilibrium temperature is less than 150°C, so these tapes remain on continuously during the heating cycle.

GDC with hydrogen is used extensively in conjunction with baking. Salient features of this widely used technique are described in a recent review by Dylla [3]. For ATF, initial breakdown occurs at about 15 mTorr for a “dirty” vessel and about 40 mTorr for a relatively “clean” vessel at applied voltages near 1 kV. The power supply is limited to 1 kV and 2.5 A. For the geometry of our system, the hydrogen flux to the wall is about  $2 \times 10^{13} \text{ H}_2^+/\text{cm}^2\cdot\text{s}$  at 600 V, 2 A, and an operating pressure

of 2 mTorr. This pressure was chosen because it was the lowest pressure at which a glow discharge could be reliably maintained while still pumping without significant damage to the turbopumps.

We have found an efficient method of operation that permits simultaneous baking and GDC. The magnetic field created when the helical coils are used for induction heating significantly reduces the size of the glow volume, so no effective cleaning takes place during the heating phase, but cleaning does occur during the cooling phase. This provides GDC about 58% of the time.

#### 4. CLEANING AND CONDITIONING OF THE INTERNAL COMPONENTS

The pertinent surface areas of the vessel and major internal components are given in Table I. The plasma-facing areas and the outgassing areas are based on reasonable estimates for the surface roughness factor and the measured area per unit mass for the graphite components.

##### 4.1. Thomson scattering stack

It was thought to be necessary to begin the cleaning process by cleaning the black anodized aluminum apertures in the Thomson scattering stack, since they are somewhat removed from the plasma region. The anodization layer is about 40  $\mu\text{m}$  thick. In addition, it was felt that the remaining parts of the system should be kept hot during this cleaning so that the smallest possible amount of the outgassing constituents would be adsorbed. GDC was not performed during this operation, since the outgassing gases would have been implanted into the surface region of the vessel walls. The maximum pressure reached during a baking operation, starting with the initial cleaning and conditioning operation after a major opening, is shown in Fig. 4. The estimated amount of gas released (mainly water, as determined by RGA) is given in Table II. Figure 5 shows pressure versus time for the second bake cycle. The time for a bake cycle is about  $5 \times 10^4$  s at a temperature of about 150°C. The power for

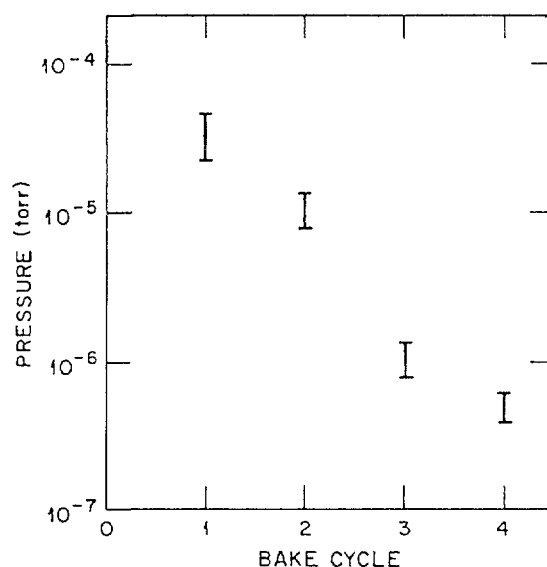


FIG. 4. Maximum pressure reached during baking cycle for ATF.

Table II. Estimated H<sub>2</sub>O released from Thomson scattering stack  
(Bake duration:  $5 \times 10^4$  s, bake temperature: 150°C)

Baking cycle	Gas released (Torr·L)
1	1000
2	300
3	50
4	1

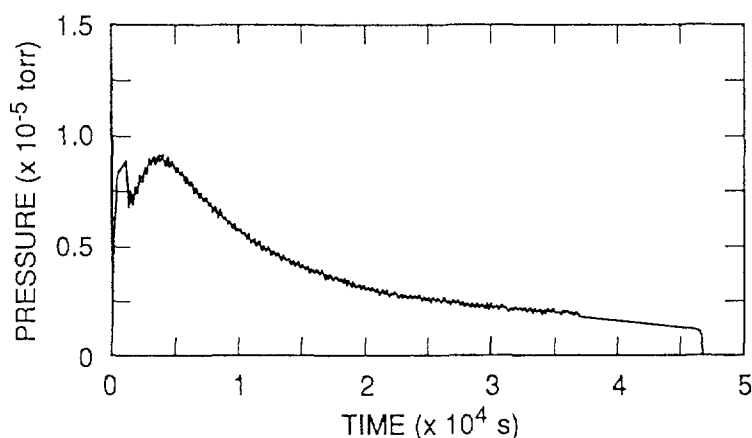


FIG. 5. Pressure response during second baking cycle of Fig. 4.

induction heating and for all heating tapes was started at approximately the same time. The initial rise can be attributed to induction heating of the vessel; the second peak, to gas released from the anodized aluminum. The jagged nature of the pressure response results from the on-off cycling of the induction heating system. After five baking cycles, no detectable release of any gas occurred when the Thomson scattering stack was baked further. This simple procedure appeared to clean this component sufficiently for plasma operation. This component has essentially no plasma-facing surface area; thus, no conclusions can be drawn as to its capability as a plasma-facing surface.

#### 4.2. ICRF antenna

The ICRF antenna is a resonant double loop antenna oriented for fast-wave launch. It operates in the range from 10 to 30 MHz and will launch up to 800 kW in plasma for periods of  $\leq 500$  ms. It has a two-tier, graphite-shielded Faraday shield and graphite armor tiles on its sides. It is movable radially over a 15-cm range. The

launching area is  $21 \times 36$  cm, and the outside dimensions are  $27 \times 42$  cm. The pertinent areas are given in Table I. The antenna was initially conditioned during the bake and GDC procedure described above and further conditioned (both for launching RF power and for preventing vacuum contamination) through operation at increasing power levels, ultimately to 100 kW in vacuum. The residual gas spectrum was monitored during this process. Significant outgassing was observed only when the antenna operated in the multipactor breakdown regime [4], i.e. the 7- to 8-kW power range. Figure 6 shows partial pressure versus time during operation in this regime with 100-ms pulses applied every 10 s. The dominant mass peaks released, 28, 44, and 15, represent CO, CO<sub>2</sub>, and CH<sub>4</sub>. The amount of each gas released is given in Table III. Operation in this regime did not appear to clean or condition the antenna for

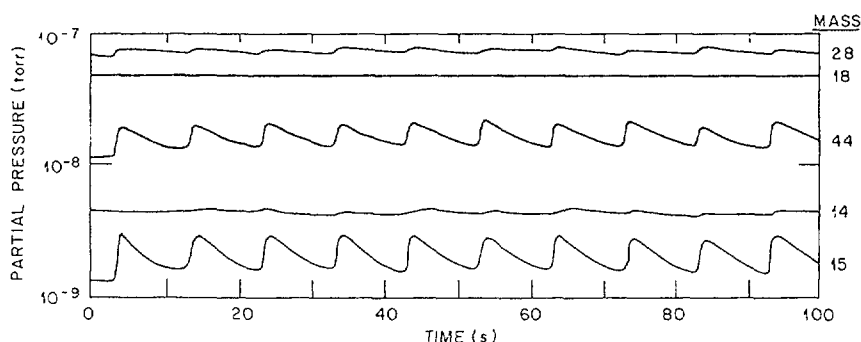


FIG. 6. Partial pressure of five dominant mass peaks vs time during voltage conditioning of ICRF antenna, taken during multipactor breakdown regime (see text).

Table III. ICRF antenna conditioning (operating in multipactor breakdown regime, 7–8 kW and 100-ms pulses)

Major species released	Amount per pulse (Torr-L)
CO	$1.5 \times 10^{-4}$
CO <sub>2</sub>	$1 \times 10^{-4}$
CH <sub>4</sub>	$2.5 \times 10^{-5}$

plasma operation. However, the initial vacuum conditioning accomplished with the bake and GDC procedure allowed very fast conditioning for launching RF power; only a few hours of conditioning were needed, in contrast to previous experience with other antennas that required many days of conditioning.

#### 4.3. Limiters and diagnostic plate

The limiters, which are made of AXF-5Q graphite, are located at the top and the bottom of the torus (see Fig. 3). They are segmented, instrumented, and movable.

They were cleaned and baked before being inserted into the torus but were exposed to air for several weeks after insertion and before pumpdown. The area per unit mass of this type of graphite, as determined by the BET technique [5], is about  $1 \text{ m}^2/\text{g}$ . The diagnostic plate is similar to the limiters in many respects but is made of ATJ graphite. Like the limiters, it was cleaned and baked before insertion in the torus, but it was exposed to air for a few days before pumpdown. No independent method was designed for in situ baking of either the limiters or the diagnostic plate, so these components provide large possible outgassing sources when they are heated and interact with atomic hydrogen.

## 5. GETTERING

Two chromium getter sources that have been installed in ATF provide surface coverage of about 30% of the vessel area. In a typical getter cycle, each source is heated to  $1150^\circ\text{C}$  and yields a sublimation rate of  $0.1 \text{ g/h}$  ( $10^{16} \text{ atoms/cm}^2\cdot\text{s}$ ). The deposition process is continued for 30 min and deposits an average of 5 monolayers of chromium. The results following the small number of getter cycles that have been completed are much better than those obtained when only the bake and GDC procedure was used.

## 6. PLASMA PERFORMANCE

Wall cleanliness influences many plasma properties; those most prominently affected are density, stored energy, and radiative losses. Initial plasma operation after a major opening is characterized by breakdown with no external gas applied and by a large influx of impurities from the wall, due to particle-induced desorption. This leads to radiative collapse terminating the plasma. An unfortunate incident that occurred after a relatively long baking and GDC cycle made it possible to compare the efficacy of the different cleaning and conditioning techniques. A bake and GDC sequence was inadvertently initiated with air instead of hydrogen; this led to a rather "dirty" wall and very poor plasma performance. A sequence of baking and GDC with hydrogen was then carried out; plasma performance following this sequence was significantly better. This was followed by a gettering cycle and plasma operation, during which plasma performance again improved significantly. In Fig. 7, time from the start of neutral beam injection to radiative collapse is shown as a function of discharge number for shots taken during the operating periods following these three "conditioning" sequences. Figure 8 shows the peak stored energy for the same discharges. The plasma parameters improve significantly as the walls are cleaned and conditioned.

## 7. SUMMARY

The procedures used for cleaning and conditioning of ATF have been described. Two significant results were obtained. First, baking to  $150^\circ\text{C}$  can clean anodized aluminum sufficiently for operation in a plasma device but does not address the effect

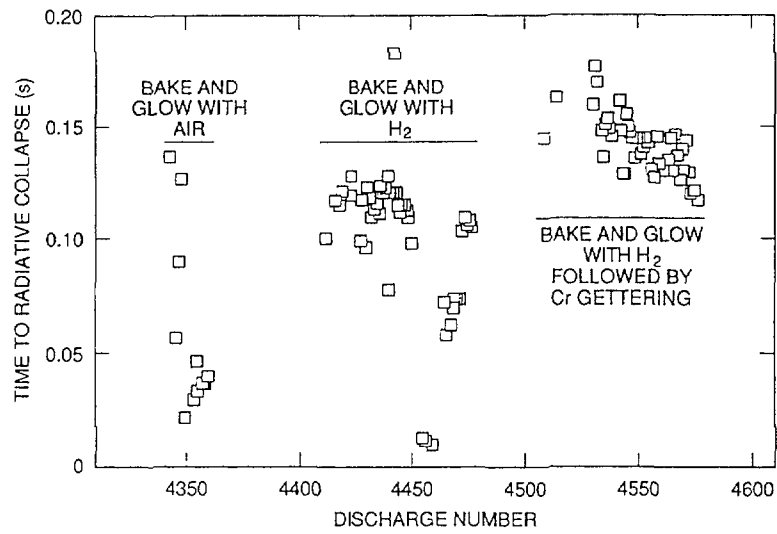


FIG. 7. Time from beginning of neutral beam injection to radiative collapse. Data are from discharges during the operating periods following three conditioning sequences.

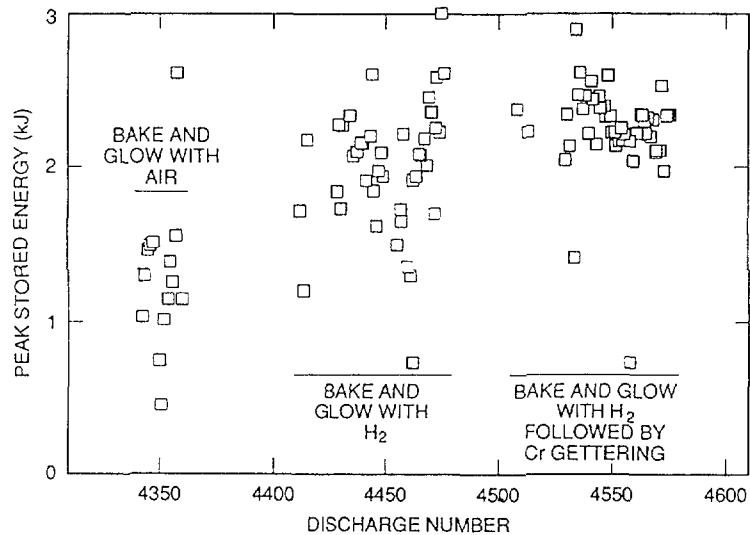


FIG. 8. Peak stored energy in the plasma. Data are from discharges during the operating periods following three conditioning sequences.

of anodized aluminum as a plasma-facing component. Second, the cleaning and conditioning procedure described here can clean a graphite-protected ICRF antenna sufficiently to allow rather rapid conditioning for launching RF power.

## ACKNOWLEDGMENTS

The authors thank the entire ATF team for its cooperation and help. This research was sponsored by the Office of Fusion Energy, U.S. Department of Energy, under contract DE-AC05-84OR21400 with Martin Marietta Energy Systems, Inc.

## REFERENCES

- [1] Lyon, J.F., et al., paper O1-2 presented at this meeting.
- [2] Langley, R.A., et al., *J. Vac. Sci. Technol.* **A6** (1988) 1288.
- [3] Dylla, H.F., *J. Vac. Sci. Technol.* **A6** (1988) 1276.
- [4] Arbez, J., et al., *Fusion Technol.* **1** (1984) 669.
- [5] Causey, R.A., Baskes, M.I., Wilson, K.L., *J. Vac. Sci. Technol.* **A4** (1986) 1189.

## **DIAGNOSTICS**

# CROSSED-SIGHTLINE CORRELATION OF FARADAY ROTATION FOR MEASUREMENT OF PERPENDICULAR MAGNETIC FLUCTUATIONS

C.E. THOMAS, Jr.  
Georgia Institute of Technology,  
Atlanta, Georgia

J.T. WOO, E. SARAVIA  
Interscience, Inc.

D.P. HUTCHINSON  
Oak Ridge National Laboratory,  
Oak Ridge, Tennessee

United States of America

## Abstract

Faraday rotation measurements have been successfully used to measure the poloidal fields on a number of devices (ISX-B, TEXTOR, . . .). It is quite possible that a refinement of this technique, correlation of crossed-sightlines, might be used to measure the fluctuating perpendicular (to  $B_t$  and  $B_p$ ) magnetic fields. Since it is suspected that these fluctuations might be the source of the anomalous cross-field transport in present fusion experiments, this could be an important measurement. Calculations of expected signal levels are presented and compared with possible noise sources. Possible techniques for inferring the poloidal fluctuations from the measured Faraday rotation fluctuations are discussed, and a conceptual design for the diagnostic is given.

## Introduction

It is well known that energy confinement in magnetic fusion experiments is anomalously short compared to the predictions of both classical and neoclassical theory. Magnetic fluctuations perpendicular to the equilibrium magnetic field are a prime suspect as the source of the anomalous transport, with a number of theories available as to why the fluctuations are present. In toroidal devices these perpendicular magnetic fluctuations are necessarily in the "radial" direction, since following an equilibrium magnetic field line forms a toroidal magnetic flux surface.

A method for making radially resolved measurements of the local amplitude and frequency dependence (and possibly correlation length) of radial magnetic fluctuations in a toroidal fusion experiment is suggested. Specifically, it is proposed to study the feasibility of using crossed-sightline correlation of Faraday rotation to measure the radial magnetic fluctuations.

## Physical Basis

A laser beam traversing a magnetized plasma undergoes a number of interactions, any of which, depending on the position of the observer, plasma conditions, laser wavelength, and signal processing electronics, may be important. For simplicity we consider only those interactions which are important at higher frequencies (relative to the plasma frequency and electron cyclotron frequency in the plasma), since we are proposing a high frequency laser system. In decreasing order of magnitude the interactions are:

1. Phase shift of the beam traversing the plasma. The phase of the laser beam is shifted, and the shift is proportional to the integral of electron density along the beam path. The phase shift  $\Delta\phi$  (in radians) is given by:

$$\Delta\phi = (2.82 \times 10^{-15}) \lambda \int_0^L n_e(l) dl \quad , \quad (1)$$

where  $\lambda$  is the laser wavelength,  $n_e(l)$  is the density at position  $l$  along the beam path,  $L$  is the length of the beam path in the plasma, and all units are in MKS.

2. Faraday rotation of the beam traversing the plasma. The electric field vector of the laser beam is rotated, and the rotation is proportional to the integral of electron density times the parallel magnetic field integrated along the path of the laser beam through the plasma. The angle of rotation  $\psi_f$  (in radians) is given by:

$$\psi_f = (2.62 \times 10^{-13}) \lambda^2 \int_0^L n_e(l) B_{\parallel}(l) dl \quad , \quad (2)$$

where  $\lambda, L$ , and  $dl$  are in meters,  $n_e(l)$  is in  $m^{-3}$ , and  $B_{\parallel}(l)$  is the magnetic field parallel to the laser path in Tesla.

## Conceptual Design for a $CO_2$ Laser Based Diagnostic

Figure 1 is a “generic” schematic for a Faraday rotation measurement system based on a  $CO_2$  laser. Note that the system is also designed to measure line-integrated density and density fluctuations. This is almost a free good once the Faraday rotation (polarimeter) system is set up, and will be useful (to be discussed below) when unraveling the local magnetic field fluctuations. It should be noted that our proposal is not only innovative in suggesting correlation of Faraday rotation measurements, but also this (we believe) is the first suggestion of using crossed-sightline correlation of phase measurements to produce local values of the density fluctuation. These local measurements of density fluctuations have been inferred previously from coherent scattering measurements. The alert reader will also notice that not all the elements on our “generic” schematic will be necessary for some of the possible signal processing designs discussed below. They are indicated for completeness in consideration of the possibilities.

A single transverse mode ( $TEM_{00}$ ), single longitudinal mode, linearly polarized, frequency stabilized  $CO_2$  laser, with a power of 1-10 watts will be used as the beam source. It is intended to purchase a commercial unit, and the specifications will be as above. In addition frequency stability of  $1 \times 10^{-9} f^0$  (where  $f^0$  is the nominal laser frequency) over any 100 microsecond period, and amplitude stability of  $1 \times 10^{-4}$  over any 100 microsecond period will be specified. These specifications are not difficult in terms of present  $CO_2$  technology, and insure that laser noise will not be the limiting factor in the proposed fluctuation measurements. Following the laser is an acousto-optic beam splitter. This is a commercially available device, and we intend to drive it at a frequency between forty and one hundred megaHertz (the acoustice wave in the splitter is induced with an RF drive). The acousto-optic device will split the beam into two beams of approximately equal power, and the deflected beam will have it's frequency shifted by the RF frequency applied to the splitter ( $\omega_2 = \omega_1 + \omega_a$ ), where  $\omega_1$  is the laser frequency,  $\omega_a$  is the RF drive frequency to the acousto-optic beam splitter, and  $\omega_2$  is the frequency of the diffracted beam. The frequency drive for the acousto-optic cell will be phase locked to be frequency stable to 1 part in  $10^6$  over any millisecond time period. The nominal choice for  $\omega_a$  is 100 MHz, since this will shift it comfortably away from the polarization modulation frequency. Again this is easily available commercial technology. The purpose of the frequency shift is to provide a reference beam with a shifted frequency so that a phase modulated interferometer can be used to measure the plasma density. The diffracted beam will next have its electric field polarization modulated at a frequency  $\omega_m$  nominally chosen to be 9 MHz. The depth of modulation (rotation angle)  $\theta_m$  is chosen to be about 30 degrees (this is so that twice the angle in radians will correspond to the first maximum of the first order Bessel function of the first kind, see below). The depth of modulation is controlled by the peak voltage of the RF applied to the electro-optic polarization modulator. The modulator crystal itself is commercially available in mounts good to 10 MHz, although it may be necessary to design the frequency and amplitude stabilized 9 MHz RF driver. This would not be too difficult. The frequency  $\omega_m$  is chosen so that after synchronous or lock-in detection, a low-pass filter with a cutoff of 1 MHz can be used, to maintain a 1 MHz bandwidth on the fluctuation measurements. The purpose of the polarization modulation is to provide a signal on top of which the Faraday rotation of the polarization by the plasma can ride as a phase shift. This will make it possible to move the magnetic fluctuation spectrum away from the noise due to low frequency modulations of the laser power or polarization, and detector noise. After passing thru the electro-optic modulator, the “plasma beam” will be split into two parts, and two beams for the reference detectors will be split off from it.

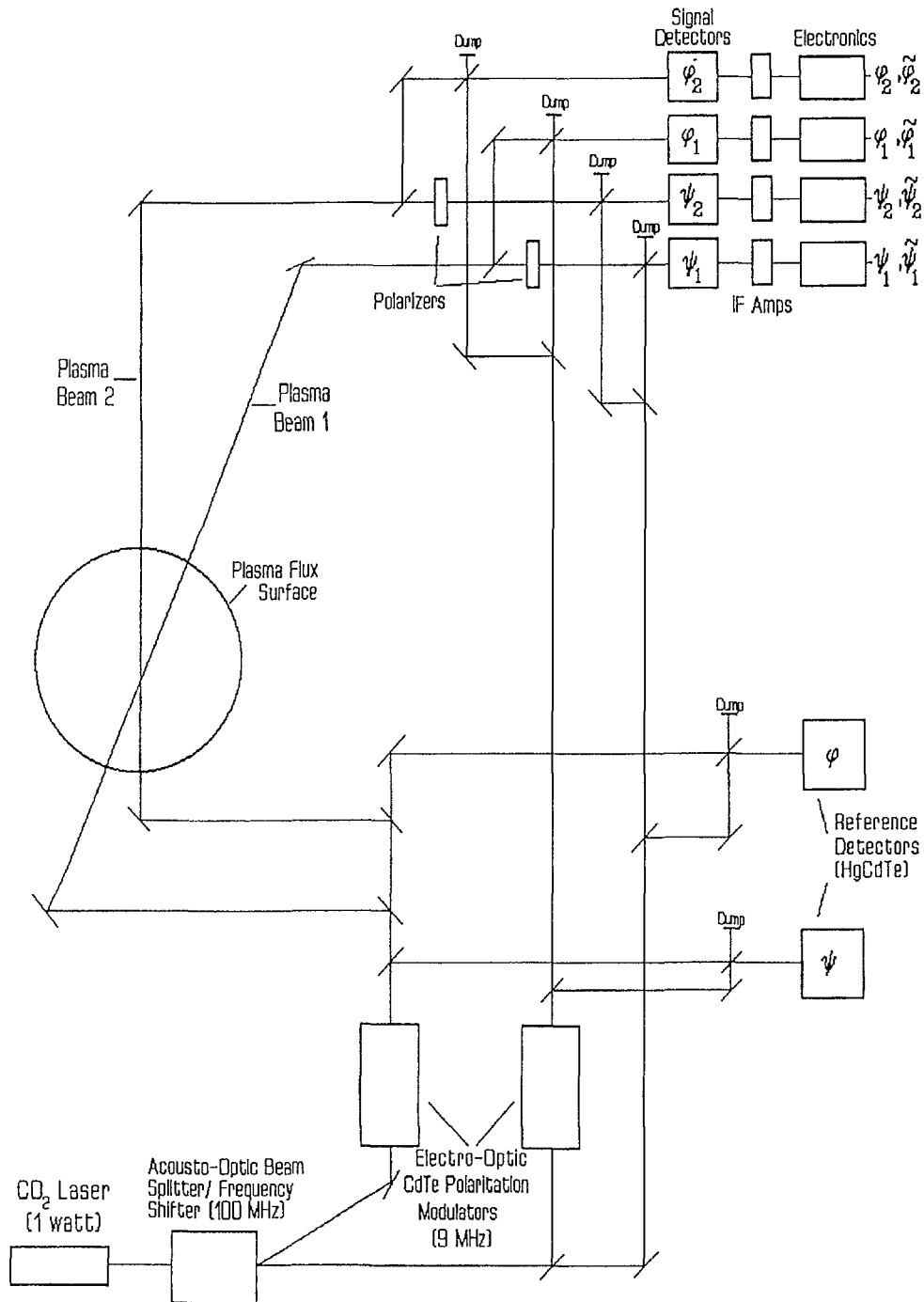


FIG. 1. Faraday rotation correlation system conceptual design.

Still referring to Fig. 1, one of the plasma beams will be passed thru the plasma so that it is "exactly" perpendicular to the toroidal field and the plasma flux surface of interest. Since the flux surfaces shift outward for non-zero plasma pressure, it will be necessary for the mirror directing this beam to be able to translate in and out. The requirement that one beam be exactly perpendicular to the toroidal field and the plasma flux surface will be discussed further below, but the origin of the requirement is easily understood. It is desired to measure radial magnetic fluctuations. The Faraday rotation signal, however, is proportional

to density times magnetic field. Therefore the fluctuations in the Faraday signal will be proportional to the density fluctuations times the steady-state magnetic field, plus the radial magnetic fluctuations times the steady-state density:

$$\tilde{\psi} \propto [\tilde{n}_e B_{||0} + \tilde{B}_{||} n_{e0}] \quad . \quad (3)$$

The proposed method for unraveling the radial magnetic fluctuations becomes more obvious. If  $B_{||0} = 0$ , then the fluctuation in the Faraday rotation angle  $\tilde{\psi}$  is due only to the radial magnetic fluctuations. Of course it is still necessary to time correlate the two sightlines against one another, so that the measurement becomes a local measurement rather than a chord integrated measurement, but the basic idea becomes clear. The second plasma beam must also be exactly perpendicular to the toroidal field, but it is directed at a small angle in the poloidal plane so that it crosses the path of the first beam at the flux surface of interest. The "exactness" of the perpendicularity of the beams with respect to the toroidal and poloidal fields is a question of some considerable interest, but the answer is given by Eq. (3). The angles must be small enough so that the density fluctuation times the steady-state parallel field is small compared to the magnetic fluctuation times the steady-state density,

$$(\tilde{n}_e B_{||0}) \ll (\tilde{B}_{||} n_{e0}) \quad .$$

Several reference beams and two reference detectors are also shown in Fig. 1 above. The undiffracted beam from the acousto-optic splitter is split into two main reference beams. The first of these is passed through another polarization modulator driven by the same signal source as the one for the plasma beams. This beam is then used as the reference beam for the plasma phase shift (density) detectors. The purpose of this is to allow these phase detectors to see only the modulation at the difference frequency  $\omega_a$  between the plasma and reference beams. Since the polarization of both beams is modulated, this modulation doesn't show up at the  $\phi$  detectors. An alternative to this if heterodyne detection is used for the  $\psi$  detectors is not to modulate the polarization of the plasma beam at all, but just to modulate the polarization of the reference beams for the  $\psi$  detectors. This would accomplish the purpose of having the Faraday rotation signal ride on a high frequency modulation, but leave the  $\phi$  detectors unmodulated at this frequency. The reference detectors shown in Fig. 1 may or may not be necessary, depending on exactly how the signal electronics are designed. They are useful for some phase-modulated and lock-in schemes. If some form of quadrature detection is used, then the relevant reference detector would not be necessary.

The Faraday rotation due to radial magnetic fluctuations in TEXT can be estimated from Eq. (2). Using  $n_{e0} = 4 \times 10^{19} m^{-3}$ ,  $B_T = 2 Tesla$ ,  $\tilde{B}_{||} = 1 \times 10^{-4} B_T$ , and  $dl = .01m$  gives:

$$\tilde{\psi} = 3.2 \times 10^{-9} \text{ radians.} \quad (4)$$

This leads to a signal power considerable larger than the detector noise (see below). Also, if the specifications on our laser, and acousto-optic and electro-optic modulators are as advertised, then noise from these devices will not limit our ability to detect  $\tilde{\psi}$  (see below). The other noise source which immediately comes to mind is vibration of the optical components. It can be shown rather easily that the apparent rotation signal due to vibration of an optical component is given by:

$$\psi_v(t) = \frac{l}{c} \omega_m \cos(\omega_v t) \quad . \quad (5)$$

In this equation  $\psi_v(t)$  is the time variation of the polarization angle (in radians) due to an optical component vibrating parallel to the beam path with amplitude  $l$  at frequency  $\omega_v$ , with  $\omega_m$  the electro-optic modulation frequency (as before), and  $c$  is the speed of light. All units are MKS. Then for not unreasonable values ( $l = 10^{-4} m$ ,  $\omega_m = 2\pi \times 10^7 \text{ radians}$ ):

$$\psi_v(t) = (3 \times 10^{-6}) \cos(\omega_v t) \text{ radians.}$$

On the surface this vibration noise looks like the death knell for using a  $CO_2$  laser system, since this adds directly to the apparent Faraday signal. However, there are three causes for hope. First, the natural frequencies of the optical system  $\omega_v$  can be designed to be small compared to the magnetic fluctuation frequencies of interest ( $f \geq 10kHz$ ). Second, with very careful optical design the vibration amplitudes can be greatly reduced. Third, if necessary the vibration frequencies and amplitudes can be measured by passing a higher frequency laser through the same optical chain. It would be preferable not to do this, but it is a standard technique for high-frequency interferometers. It is also important to notice that vibrations are only significant for the beam which has its polarization modulated, the linearly polarized beam suffers no rotation

due to vibrations. If heterodyne detection is used and the reference beam is polarization modulated, rather than the plasma beam, it may be possible to retain the reference beam on a vibration isolated optical table (distant from the Tokamak) so that vibrations are totally negligible.

The work that needs to be done on the  $CO_2$  laser and optical system design follows immediately from the above discussion of the "generic" system. The various choices for the optical layout and detection scheme need to be explored and refined into a final conceptual design. The question of vibrational noise needs to be fully explored and a decision made on how to eliminate it, and calculations done as to the effectiveness of the elimination. Our estimates of the stability of the laser, acousto-optic modulator, and electro-optic modulator need to be checked more fully, and refined calculations made of their effect on the system noise. Present calculations show that, given small fluctuations about a steady-state value, all of these quantities only enter in second order in the expression for the noise in the Faraday rotation signal, but these calculations need to be carefully checked. The optical design needs to be studied carefully for other possible sources of noise. The conceptual design for layout of the optical components, supporting structures, and pointing and translating mounts necessary for alignment needs to be considered carefully and refined, particularly in regards to the importance of and elimination of vibration, and with respect to aligning the laser beams perpendicular to the toroidal and poloidal magnetic fields, as necessary. The desired alignment accuracy with respect to the toroidal field is 100 microradians, and the desired alignment accuracy of the "perpendicular" beam with respect to the poloidal field is about 10 milliradians. This level of alignment is achievable with optical alignment tools, but this may not be necessary. It is likely possible to tune the alignment during plasma shots. Alignment with respect to the toroidal field can be tuned up by varying the angle in the plane parallel to the toroidal field so as to minimize the polarimeter signal. Assuming density fluctuations are present, then alignment of the perpendicular beam with respect to the poloidal field can be tuned up by minimizing the cross-correlation signal between the two beams (this will leave only the signal due to magnetic fluctuations). In addition, the necessity of a second, higher frequency, laser beam co-linear with the interferometer optics should be evaluated. If vibrations cannot be suitably minimized, this may be necessary to measure and eliminate the effect of vibrations on the interferometers. If it is decided to use the interferometers to measure phase fluctuations ( $\tilde{\phi}$ ) only, then the second laser should not be necessary.

**Signal Processing Electronics and Software.** The effort with respect to the signal processing electronics involves evaluating the various possible schemes for deriving phase and polarimetry ( $\phi$  and  $\psi$ ) information, and evaluating the signal to noise ratio and available bandwidth of the signals at the data acquisition hardware. A signal to noise ratio considerably greater than one for the zero order plasma signals is desired, and a signal to noise ratio of at least one for the fluctuating quantities ( $\tilde{\phi}$  and  $\tilde{\psi}$ ) would be nice. Cross-correlation of the fluctuation signals (in software) will greatly increase the signal to noise ratio. The available bandwidth of the signals at the computerized data acquisition hardware (CAMAC) is important. A bandwidth of 1 MHz for the fluctuating quantities is desired, since past experience and theoretical considerations show that the frequency range of these fluctuations may be hundreds of kHz. It is therefore important that the signal bandwidth not be unnecessarily reduced in the electronics.

Figure 2 is a conceptual schematic of one possible design for the signal processing electronics. The upper schematic is for the polarimetry electronics and is based on the work of Ma, Hutchinson, et. al. [International Journal of Infrared and Millimeter Waves, Vol. 3, No. 2, p. 263 (1982)]. If the optical layout is as shown in Fig. 1, then it can be proven that the signal at the polarimeter photoconductive detector (where the plasma and reference beams are combined) is given by:

$$V_s = k(P_p P_r)^{1/2} \cos[\psi_f + \theta_m \sin(\omega_m t)] \cos(\omega_a t + \phi) \quad . \quad (6)$$

Only the difference frequency  $\omega_a$  term has been retained, since the dc and higher frequency terms are filtered out in the first bandpass filter shown on the diagram. The power of the laser beam passing through the plasma is denoted as  $P_p$ , the reference beam as  $P_r$ , and the faraday rotation angle as  $\psi_f$ . The signal is next passed through a diode detector with time constant such that it time averages (demodulates) the  $\omega_a$  term, and then fed to a lock-in amplifier, whose reference signal is derived from the polarization modulator signal. Ma and Hutchinson show that the output of the lock-in  $V_{out}$  is proportional to:

$$V_{out} \propto (P_p P_r) J_1(2\theta_m) \sin(2\psi_f) \quad . \quad (7)$$

Where  $J_1$  is the Bessel function of the first kind of order one, and all the other symbols are previously defined. Examination of this equation shows where all the noise terms from the modulators and laser enter, in the respective amplitudes and frequencies. Note that to first order frequency drift in either modulator

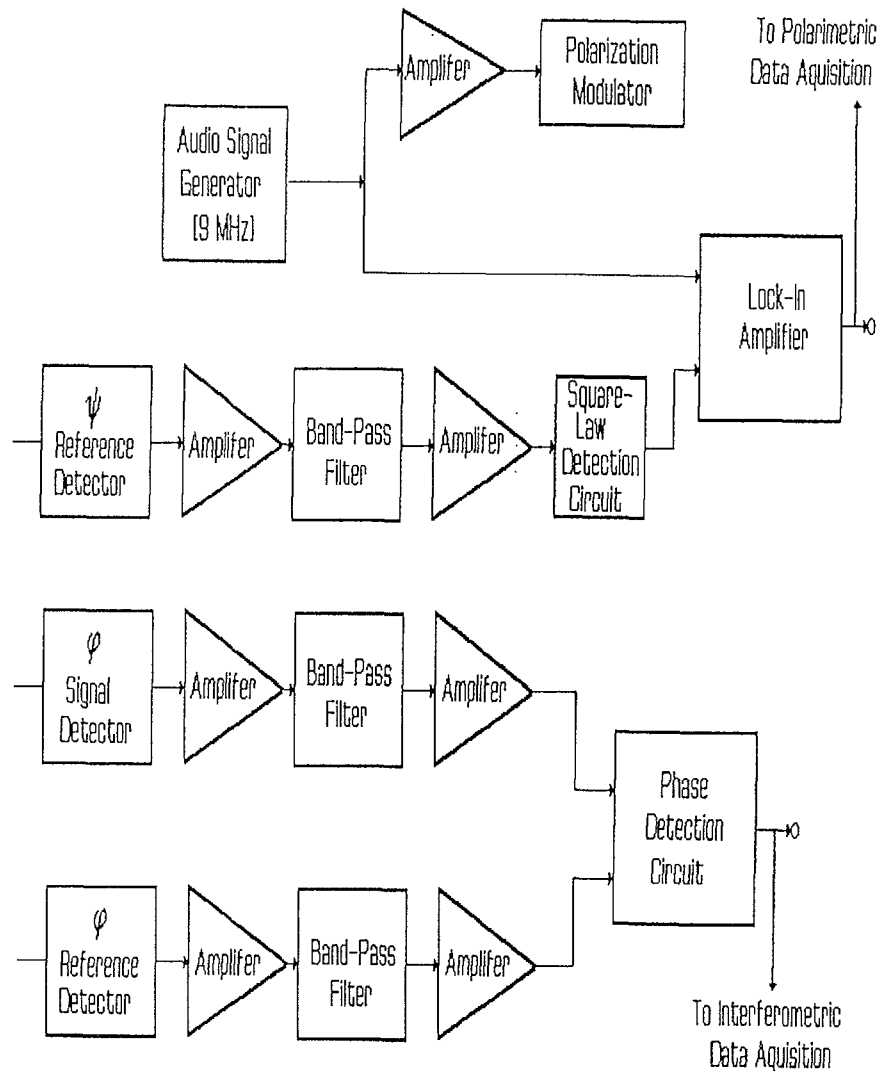


FIG. 2. Possible signal processing scheme of the combined polarimeter/interferometer system.

or the laser does not cause any noise. Errors in the beam splitter modulation amplitude enter through the laser power terms, as does fluctuation in the laser power itself. Errors in the amplitude of the signal to the electro-optic polarization modulator enter through the  $\theta_m$  term. Detector noise at the first detector will dominate the electronically introduced noise, and using Eq. (4) as an estimate of the signal, it can be shown that for heterodyne detection the expected signal to noise ratio (considering detector noise only) at the output of the lock-in is approximately 100, where it is assumed the power in each laser beam is about 10 mW at the detector.

The interferometer electronics scheme shown on Fig. 2 is for a phase-modulated interferometer based on the work of Wolfe, et. al. [Applied Optics, Vol. 15, no. 11, p. 2645 (1976)]. This system may not be stable enough (this is to be determined) for measurement of  $\tilde{\phi}$  fluctuations, but if not then it has been demonstrated by Jacobson [Plasma Physics, Vol. 24, No. 9, p. 1111 (1982)] that a quadrature system [Buchenauer and Jacobson, Review of Scientific Instruments, Vol. 48, No. 7, p. 769 (1977)], is stable enough to make the measurement. A quadrature system would require some additional optics and detectors for the interferometer system.

The  $\phi$  and  $\psi$  signals will be digitized at a rate between 1 and 10 kHz, and the  $\tilde{\phi}$  and  $\tilde{\psi}$  signals will be digitized at about 1 MHz. After the signals are stored in the computer, it is still necessary to process them to determine the value, and frequency dependence of the radial magnetic field signals. Suppose that the system has been calibrated and the signals normalized so that we have  $\tilde{\psi}_1(t)$  and  $\tilde{\psi}_2(t)$ , where the first

is the fluctuation on the polarization signal from the plasma beam at a slight angle to the poloidal plane and the second is the fluctuation on the polarization signal from the plasma beam exactly perpendicular to the poloidal flux surface. Define the time correlation (time averaging) operator  $\langle \tilde{\psi}_1(t)\tilde{\psi}_2(t) \rangle$  as:

$$R_{12}(t) = \frac{1}{T} \int_{-T/2}^{T/2} \tilde{\psi}_1(t + \tau)\tilde{\psi}_2(t + \tau) d\tau \quad . \quad (8)$$

Where  $T$  is the averaging period and the data has been individually filtered so that its time average over  $T$  is zero. Note that if the fluctuations are correlated, the time average of their product is not zero. Using the expression for the Faraday rotation, passing the time integral through the spatial integrals, noting that the correlation function rapidly goes to zero for distances greater than the correlation length in the plasma, and taking the correlation length  $l_c$  to be short compared to the plasma size, it can be shown that:

$$\langle \tilde{\psi}_1(t)\tilde{\psi}_2(t) \rangle = C^2 l_c^2 B_{\parallel 10}(r_x) n_{e0}(r_x) \left[ \left\langle \frac{\tilde{B}_1 \tilde{B}_2}{B_{\parallel 10}} \right\rangle + \left\langle \frac{\tilde{n}_e \tilde{B}_2}{n_{e0}} \right\rangle \right] \quad . \quad (9)$$

Where  $C$  is a constant,  $B_{\parallel 10}(r_x)$  is the magnetic field parallel to sightline 1 at the crossing point  $r_x$  of the two sightlines,  $n_{e0}(r_x)$  is the electron density at the crossing point,  $\tilde{B}_1$  and  $\tilde{B}_2$  are the fluctuating radial magnetic fields at the crossing point, and  $\tilde{n}_e$  is the fluctuating density at the crossing point. This equation was derived assuming, as discussed above, that  $B_{\parallel 20}(r_x)$  the field parallel to sightline 2 at the crossing point is negligible. Examining Eq. (9) it can be seen that if  $\tilde{n}_e$  is known (from cross-sightline correlation of the interferometer signals), or if  $(\tilde{n}_e/n_{e0}) \ll (\tilde{B}_1/B_{\parallel 10})$ , then the equation can be immediately solved for  $\tilde{B}$  (assuming  $\tilde{B}_1 = \tilde{B}_2$ ).

The work to be done concerning software analysis is to verify the derivation given above, and estimate the error implied by doing the cross-correlation with a finite time  $T$ . Note that the fluctuation signal as a function of frequency is found by either band-pass filtering the fluctuation signals (in software), or equivalently by varying the averaging time  $T$ .

**Alcohol and Laser System Designs.** The work discussed above could also be performed for an alcohol laser system ( $\lambda = 119$  microns), and at other wavelengths if it appears necessary to go to longer or intermediate wavelengths to achieve the required amplitude and frequency resolution of the radial magnetic fluctuations.

## Discussion

Local measurement of magnetic fluctuations in high temperature plasma devices is extremely difficult. We have proposed a method which may, or may not work. However, since the understanding of fluctuations and energy transport is so important, we believe that it is worthwhile to pursue the conceptual design and design calculations until some disqualifying fault is found, or until the proposed diagnostic measures the radial magnetic fluctuations (if present).

# ECE CORRELATION MEASUREMENTS OF MAGNETIC FIELDS AND FLUCTUATIONS

C.E. THOMAS, Jr., G.R. HANSON  
Georgia Institute of Technology,  
Atlanta, Georgia

R.F. GANDY  
Auburn University,  
Auburn, Alabama

United States of America

## Abstract

The local value of the magnetic field  $B(r)$  inside the plasma in magnetic fusion experiments is a quantity of considerable interest. Given information about plasma density and temperature it can be used to calculate the poloidal magnetic field, or (for a zero current device) the local value of beta. The time history  $B(r, t)$  can be used to infer the level of magnetic fluctuations in the plasma. These local values are particularly interesting quantities, since they are difficult to measure, and are important for understanding particle and energy transport.

It has been recently suggested that crossed-sightline correlation of electron-cyclotron emission might be used to infer  $B(r_x, t)$  at the crossing point  $r_x$  of the two sightlines. The equations and techniques necessary to simulate this proposed diagnostic are discussed below, and the results of a numerical simulation of the diagnostic resolution for both *TEXT* and *CIT* are presented.

## I Introduction

It has been suggested that crossed-sightline correlation of electron cyclotron emission (ECE) might be used to experimentally measure the absolute value of the local magnetic field and its time variation in a magnetically confined plasma.<sup>[1]</sup> The basic idea is to time correlate the ECE received by two antennas having sightlines which cross in the plasma (see Fig. 1) to obtain the cross-correlation function. This function will represent the ECE near the crossing volume of the two sightlines (for short correlation lengths). By resolving the line center (in frequency space) of this correlated emission and following it in time (at frequencies less than  $1/T$ , where  $T$  is the correlation time), the total magnetic field  $B(t)$  can be measured since the local value of the cyclotron frequency  $\omega_b$  is given by

$$\omega_b = \frac{q B(t)}{m_e}. \quad (1)$$

where  $q$  is the electron charge, and  $m_e$  is the electron mass. References [1], [2], and [3] provide a more detailed discussion of the theory, conceptual design, and resolution of this diagnostic. Figure 2 shows a possible hardware conceptual design for the diagnostic.

The sightlines can be scanned so that a magnetic field profile over a portion of the minor radius can be constructed. If the density and temperature are known, then the poloidal magnetic field can be calculated over this region. In zero current devices, the measurement is a direct measurement of the local value of  $\beta$ , or if the current profile is known or estimated,  $\beta$  can be calculated. If multiple sightlines are used, then a magnetic field profile, and therefore poloidal field or  $\beta$  profiles, across the minor radius can be constructed without scanning.

We have developed a numerical routine which simulates the correlated signal from the crossed-sightline diagnostic and then determines the error in the magnetic field inferred from the simulated data. To obtain this simulated data, the uncertainties in the cross-correlation function are estimated and then used by a Monte Carlo routine to randomize the expected cross-correlation function. A nonlinear curve fitting routine<sup>[4]</sup> is used to fit a function to the randomized data so that the error in the line center due to the expected experimental errors can be calculated.

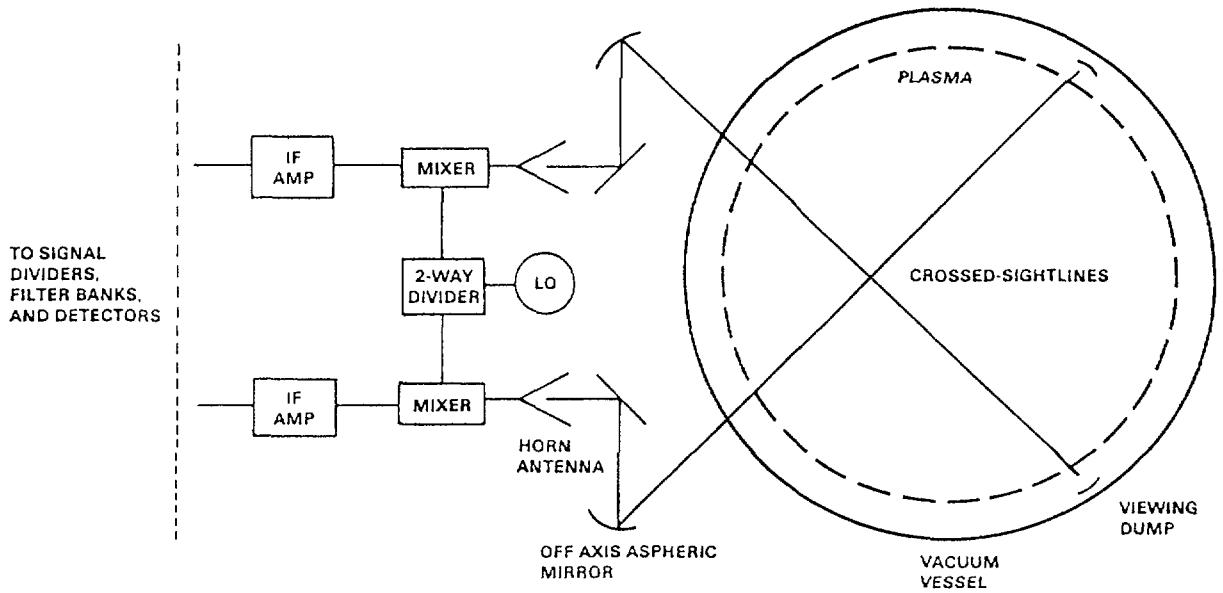


Fig. 1. Conceptual schematic of the antenna system, viewing sightlines and dumps, and mixer, local oscillator (LO), and intermediate frequency (IF) amplifier for crossed-sightline system.

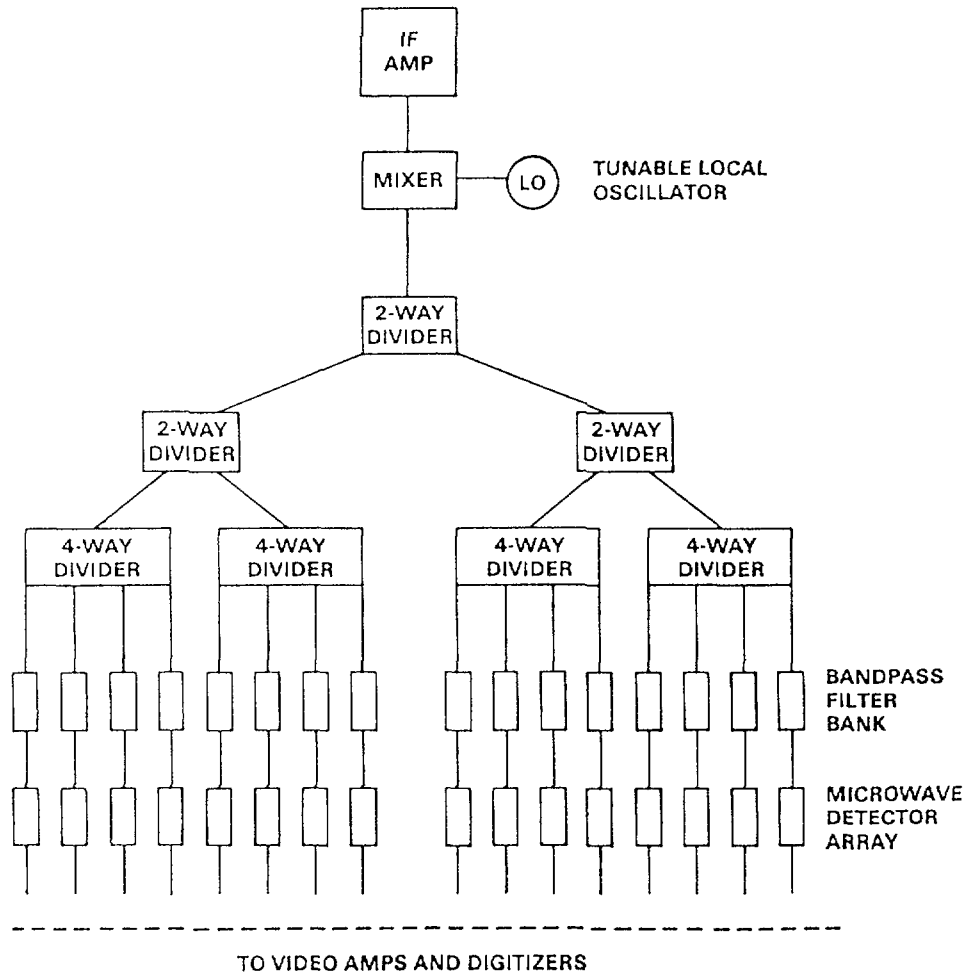


Fig. 2. Conceptual schematic of the balance of the microwave electronics for the crossed-sightline ECE system (see Fig. 1 for the front end).

This numerical routine has been used to perform magnetic fluctuation and absolute magnetic field strength  $|\vec{B}|$  measurement simulations for *TEXT* and *CIT*. We believe the results of these simulations show that the proposed diagnostic will be able to measure perpendicular magnetic fluctuations with an error of the order of 4 % of the toroidal magnetic field and measure the absolute magnetic field strength with an error of the order of 0.1 %. The error in measurement of parallel magnetic fluctuations will also be about 0.1 % of the toroidal magnetic field, the same order as the error in the absolute magnetic field.

A second numerical simulation has been developed to determine the uncertainty in inferring the poloidal magnetic field from the  $|\vec{B}|$  measurement. In this simulation, the uncertainty in the poloidal magnetic field is calculated from the contributing field terms and their uncertainties. Results of this simulation indicate that the poloidal magnetic field can be inferred from the  $|\vec{B}|$  measurement for  $r/a \geq 0.2$  with an uncertainty of less than 10.0 % under many conditions.

The equal time correlation function is estimated as<sup>[6]</sup>

$$\begin{aligned} R_{12}(\omega_i, t) &= \frac{1}{T} \int_{-T/2}^{T/2} i_1(\omega_i, t + \tau) i_2(\omega_i, t + \tau) d\tau \\ &= \langle i_1(\omega_i, t) i_2(\omega_i, t) \rangle \end{aligned} \quad (2)$$

where  $\langle \rangle$  is defined as the equal time correlation function operator, and  $T$  is a finite period.

If  $j_1$  and  $j_2$  are defined as the local values of the fluctuating part of the emission at positions  $s_1$  and  $s_2$  along the two sightlines, that is,

$$j_1(\omega_i, s_1, t) = \frac{di_1}{ds_1} \quad (3)$$

and

$$j_2(\omega_i, s_2, t) = \frac{di_2}{ds_2} \quad (4)$$

where  $s_1$  and  $s_2$  represent respective positions on the two sightlines, then by definition, in regions of a turbulent plasma that are separated by more than a correlation length  $l_c$ , the time-correlation (cross-correlation) function rapidly goes to zero, in which case  $R_{12}$  can be written as

$$R_{12}(\omega_i, t) = \int_{r_x-l_c}^{r_x+l_c} ds_1 \int_{r_x-l_c}^{r_x+l_c} ds_2 \langle j_1(\omega_i, s_1, t) j_2(\omega_i, s_2, t) \rangle \quad (5)$$

where  $r_x$  is the spatial crossing point of the two sightlines, and the time operator has been passed through the two spatial integrals. It can be seen from the above equation that as the correlation length becomes small, the cross-correlation of  $j_1$  and  $j_2$  comes only from the crossing volume of the two antenna sightlines.

## II Possible Measurements

The cross-correlation function  $R_{12}$  can be used to infer several different plasma parameters. From the center frequency of  $R_{12}(\omega, t)$ , the absolute magnetic field strength  $|\vec{B}|$  at the crossing volume of the two sightlines can be calculated, and from  $|\vec{B}|$ , either the poloidal magnetic field or  $\beta$  (for currentless plasmas) can be inferred. By following the peak of  $R_{12}(\omega, t)$  in frequency space, fluctuations in  $|\vec{B}|$  can be measured. The correlation length for fluctuations at the crossing volume can be inferred from the width in frequency space of  $R_{12}(\omega, t)$ . Finally, at optically thick harmonics temperature fluctuations can be inferred from the amplitude of  $R_{12}$ , or at optically thin harmonics a summation of temperature and density fluctuations can be obtained. This assumes that magnetic fluctuations are small compared to temperature and density fluctuations. Below we discuss only magnetic fluctuation measurements, and poloidal magnetic field measurements inferred from  $|\vec{B}|$ .

## III Numerical Simulation of $|\vec{B}|$ Measurement

### III-A Overview

A plot of the predicted cross-correlation function  $R_{12}(\omega_i, t)$  and a typical set of randomized data is shown in Fig. 3. A non-linear curve fitting routine is then used to calculate the line center  $\omega_j$  of this randomized data. Figure 4 shows a plot of the true cross-correlation function  $R_{12}(\omega_i, t)$  and the function fitted to the randomized data. The distance between the line centers of these two functions is the error  $\sigma_\omega$  in the line center  $\omega_o$ .

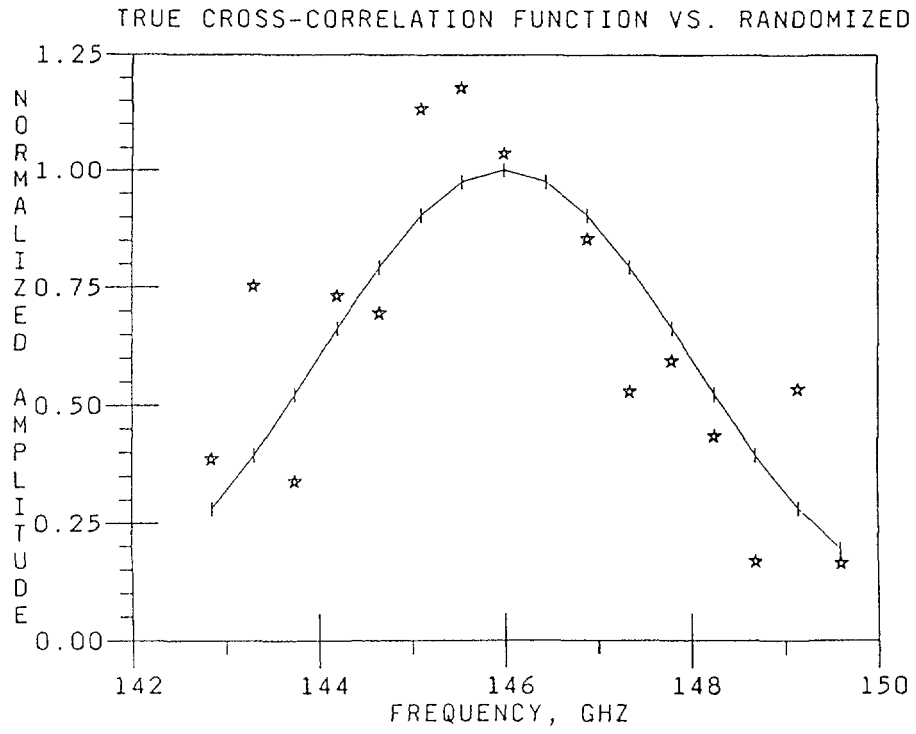


Fig. 3. The predicted cross-correlation function and randomized data versus frequency.

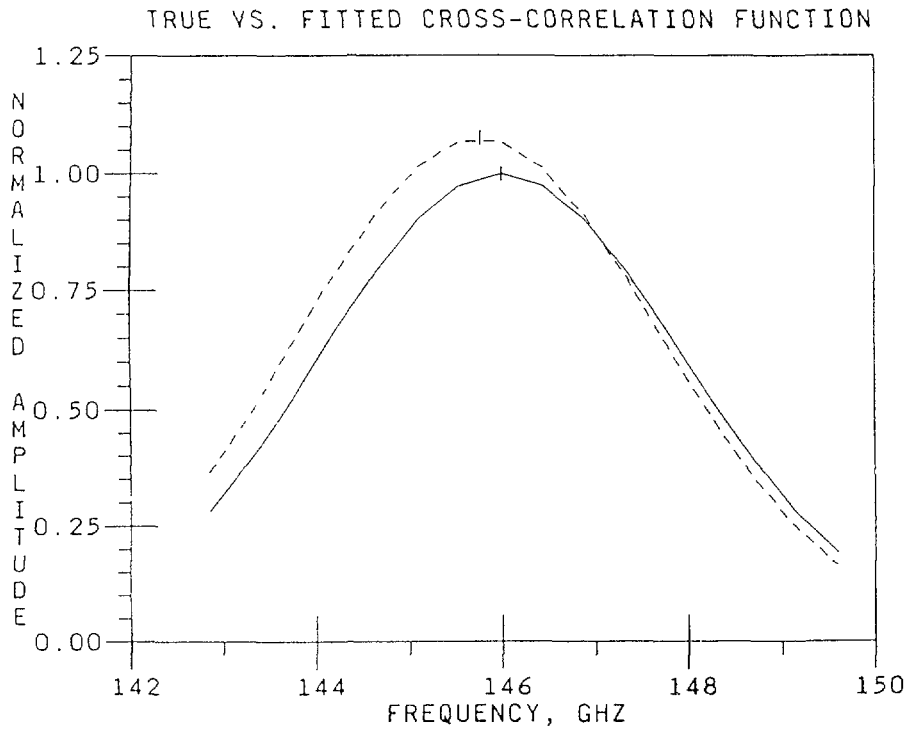


Fig. 4. The predicted cross-correlation function and the function fitted to the randomized data plotted versus frequency. The horizontal separation between the marked line centers is the error in the estimated line center.

The randomization procedure is repeated  $n$  times (typically  $n = 100$ ) for each set of plasma parameters. The predicted error in measurement  $\sigma_\omega$  of the line center  $\omega_o$  is then calculated. For each set of plasma parameters, the calculation is repeated for many possible values of  $A_{fo}$ , the fractional fluctuation in ECE emission due to fluctuations in density, temperature, or magnetic field.

### III-B Results

In running this simulation for a particular plasma device, a set of parameters describing the expected conditions for that device must be established. The important parameters dependent on the plasma device include the expected relative amplitude of the emission fluctuation compared to the amplitude of the cyclotron peak (the fluctuation fraction  $A_{fo}$ ), the electron temperature  $T_e$  at the crossing volume, the correlation length  $l_c$  at the crossing volume, the wall reflectivity  $R_w$ , the viewing dump efficiency  $\eta$ , and the integration time  $T$  over which the correlation is performed. The parameters which are determined by the diagnostic device design include the number of channels of data per sightline, the bandwidth  $\delta\omega_i$  of each channel, the center frequency  $\omega_i$  of each channel, the response time  $\tau$  of the microwave crystal detectors, the angle of intersection of the two sightlines, and the digitization rate of the signals at the detectors.

Figure 5 shows a plot of the fractional error in the magnetic field ( $\delta B/B = \sigma_\omega/\omega_o$ ) versus  $A_{fo}$  for typical TEXT conditions (see Table I for a description of the parameters listed on the figure) Here we assume the amplitude fluctuation  $A_{fo}$  (fluctuation fraction) might be due to density fluctuations for instance.

We have also used our simulation to study the use of this diagnostic on CIT. At  $r/a = 0.5$ , we take the electron temperature as  $5.5 \text{ keV}$  to  $6 \text{ keV}$ . Figure 6 shows that at this location with a correlation time of  $100 \text{ ms}$ , the magnetic field can be measured with an uncertainty of less than  $1 \times 10^{-3}$  of the toroidal field.

## IV Numerical Simulation of the Poloidal Field Measurement

The poloidal magnetic field  $B_\theta$  can be inferred from the  $|\vec{B}|$  measurement. We have performed a numerical simulation to determine the uncertainty in inferring  $B_\theta$  from  $|\vec{B}|$ .

This simulation calculates the uncertainty in the poloidal magnetic field, inferred from a  $|\vec{B}|$  measurement, as a function of radius.

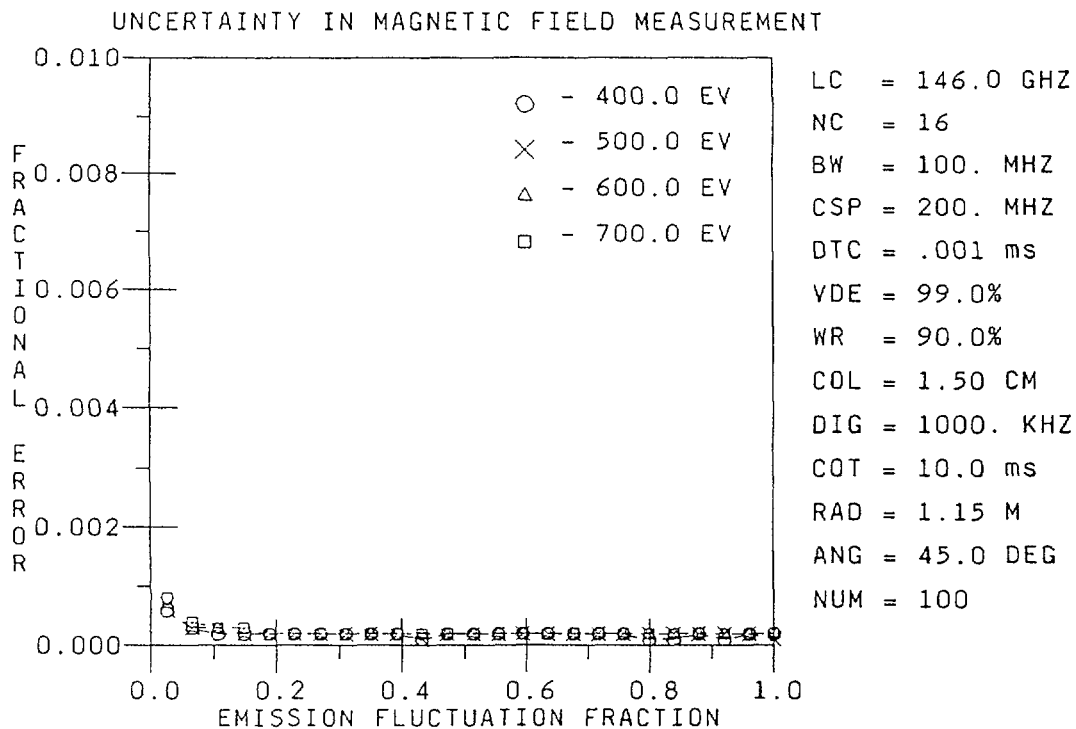


Fig. 5. Uncertainty in the magnetic field measurement on TEXT The correlation integration time has been set to  $10 \text{ ms}$  to emphasize the low uncertainty that can be obtained.

TABLE I

Description of Parameter List for Figures 5 and 6

- 
- LC** The center frequency of the ECE Line Center at the sightline crossing point,  $\omega_o$ .
  - NC** The Number of data Channels per sightline.
  - BW** The frequency BandWidth of each channel,  $\delta\omega_i/2\pi$ .
  - CSP** The frequency spacing between channel centers, (Channel SPacing).
  - DTC** The response time  $\tau$  of the microwave crystal detectors, (Detector Time Constant).
  - VDE** The Viewing Dump Efficiency,  $\eta$ .
  - WR** The vacuum vessel Wall Reflectivity,  $R_w$ .
  - COL** The assumed COrrrelation Length  $l_c$  of the plasma fluctuations.
  - DIG** The DIGitization frequency of the ADC's.
  - COT** The COrrrelation Time  $T$  of the cross correlation integral.
  - RAD** The sightline crossing point on the major RADius,  $R$ .
  - ANG** The ANGLE of intersection of the two sightlines.
  - NUM** The NUMber of random data sets to be averaged over per set of input parameters.
- 

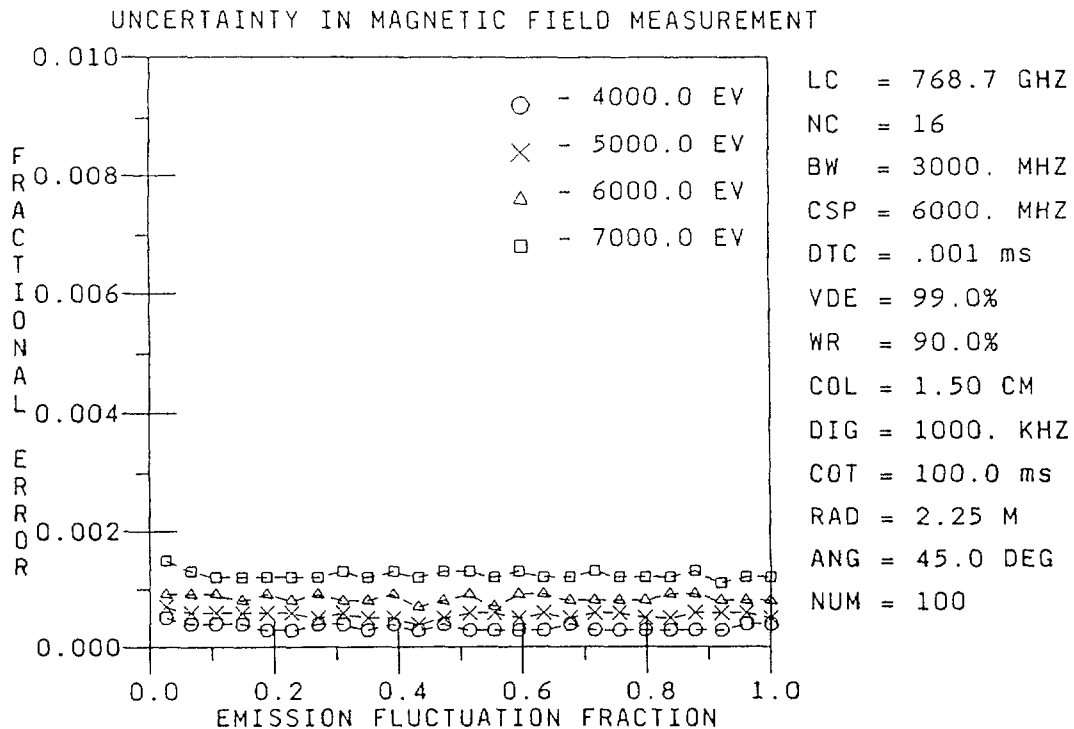


Fig. 6. Uncertainty in the magnetic field measurement on CIT at  $r/a = 0.5$  for correlation times of 100 ms.

For *CIT* this simulation demonstrates that we can hope to make  $B_\theta$  measurements for  $r/a \geq 0.2$  with an uncertainty of less than 15% and for  $r/a \geq 0.4$  with an uncertainty of less than 5%. Figure 7 shows a plot of this uncertainty for our *CIT* reference parameter set:  $a = .5\text{ m}$ ,  $R_o = 2.0\text{ m}$ ,  $B_o = 7.0\text{ T}$ ,  $I_T = 7.0\text{ MA}$ ,  $\beta_o = 5\%$ ,  $n = 2$ ,  $m = 2$ ,  $\epsilon_B = .1\%$ ,  $\epsilon_v = .05\%$ ,  $\epsilon_{\phi p} = 5\%$ ,  $\epsilon_\beta = 5\%$ .

## V Discussion

We believe that the calculations above indicate that the potential of this diagnostic is excellent. With careful design and construction, it has a very good chance of measuring parallel fluctuations in  $|\vec{B}|$  as small as  $1 \times 10^{-3}$  of the toroidal field at  $10\text{ KHz}$  or even smaller fluctuations at lower frequencies on both *TEXT* and *CIT*. Our results also indicate that the absolute magnetic field strength can be measured with an uncertainty of less than 0.10% on both devices. For a stellarator, the  $|\vec{B}|$  measurement gives  $\beta$  directly. With  $\beta$  measurements from another source, we should be able to infer the poloidal magnetic field with an uncertainty of less than 10% for  $r/a$  greater than about 0.2. The diagnostic also has the potential of measuring electron temperature and density fluctuations.

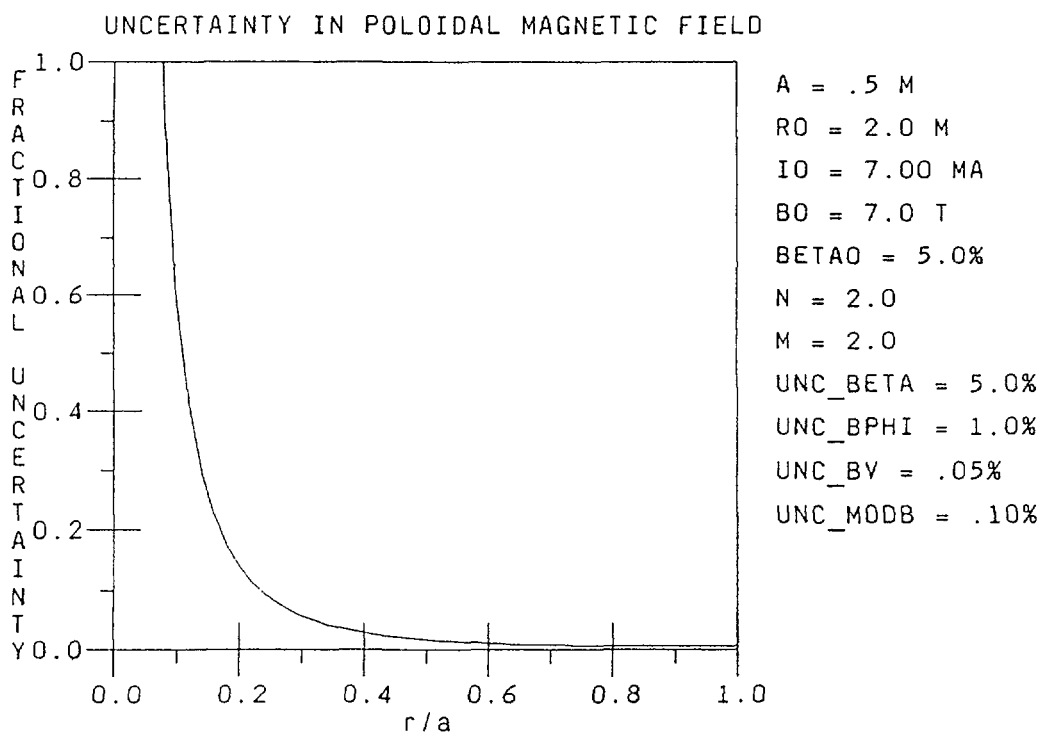


Fig. 7. Uncertainty in the poloidal magnetic field inferred from the  $|\vec{B}|$  measurement on *CIT* for a low field, low current configuration.

## Acknowledgments

Work leading to the conceptual design and numerical simulation of this proposed diagnostic was supported by the United States Department of Energy, Office of Fusion Energy, under contract DE-FG05-87ER53253, and by the Georgia Institute of Technology. We also owe considerable thanks to our colleagues Pete Politzer, John Wilgen, Rex Gandy, Dave Rasmussen, and Jim Callen for useful discussions.

## References

- [1] C. E. Thomas Jr., "Using Crossed-Sightline Correlation of Electron Cyclotron Emission to Measure Magnetic Fluctuations in Plasmas", EC6 — Joint Workshop on ECE and ECRH, Sept. 16–17, 1987, Oxford, U.K., proceedings.
- [2] C. E. Thomas Jr., G. R. Hanson, R. F. Gandy, D. B. Batchelor, and R. C. Goldfinger, *Rev. Sci. Instr.*, 59, no. 9, p. 1990, (1988).
- [3] G.R. Hanson and C.E. Thomas, Jr., "Analysis of the Expected Resolution of the ECE Crossed-Sightline Magnetic Field Diagnostic", submitted to *Rev. Sci. Instr.*, March, 1989.
- [4] P. R. Bevington, *Data Reduction and Error Analysis for the Physical Sciences*, McGraw-Hill, New York, 1969.
- [5] G. L. Bell, R. F. Gandy, J. B. Wilgen, and D. A. Rasmussen, "ECE Radiation Path Design for ATF", Auburn University Physics Report PR21, Technical Report MMESI-19x-5596V-2, October, 1987.
- [6] J. S. Bendat and A. G. Piersol, *Random Data: Analysis and Measurement Procedures*, 2nd edition, Wiley Interscience, New York, 1986.

## FIR INTERFEROMETER AND SCATTERING MEASUREMENTS ON ATF\*

C.H. MA, D.P. HUTCHINSON, Y. FOCKEDEY,  
K.L. VANDER SLUIS  
Oak Ridge National Laboratory,  
Oak Ridge, Tennessee

C.A. BENNETT  
North Carolina University,  
Asheville, North Carolina  
  
United States of America

### Abstract

A 15-channel far-infrared (FIR) interferometer system has been constructed to measure the electron densities on the ATF plasmas. The system consists of a pair of cw 214- $\mu\text{m}$  difluoromethane ( $\text{CH}_2\text{F}_2$ ) lasers, optically pumped by separate  $\text{CO}_2$  lasers. The large number of channels is achieved by the use of reflective beam expansion optics to create a beam of 2 cm  $\times$  45 cm. After passing through the plasma discharge, the elongated beam produced by the cylindrical mirrors is dissected by an array of 15 off-axis paraboloid reflectors, each of which illuminates a single Schottky-diode detector. The use of the beam expanding optics system reduces the number of optical elements required for the interferometer to approximately 2-3 per channel. The FIR laser beams are transported from the laser room to the experimental area by 25 mm i.d. dielectric waveguides purged with dry nitrogen. The system can also be operated at a wavelength of 119- $\mu\text{m}$  by changing the gas in FIR laser cavities to methanol for high density experiments. Details of the system are described.

A study is underway to determine the optimum design of a FIR scattering system for the ATF. This scattering system will be used to investigate density fluctuations with scale lengths from 0.1 cm to the plasma radius. The laser for this scattering system may be operated at wavelengths of 447, 307, 214, 184, and 119  $\mu\text{m}$  with power levels of 100 to 500 mW. A summary of the study is presented.

---

### FIR Interferometer System

The interferometer system is configured to measure the line-integrated electron density along 15 vertical chords on the  $\phi = 0$  plane of the ATF plasma. The system is a modification of the FIR interferometer system that was used on the ISX-B tokamak [1]. However, instead of using separate probing beams, a phase image technique [2] is used to improve the spatial resolution of the measurement. A schematic diagram of the interferometer system is shown in Fig. 1. Briefly, the system employs a pair of cw  $\text{CH}_2\text{F}_2$

---

\* Research sponsored by the Office of Fusion Energy, US Department of Energy, under contract DE-AC05-84OR21400 with Martin Marietta Energy Systems, Inc.

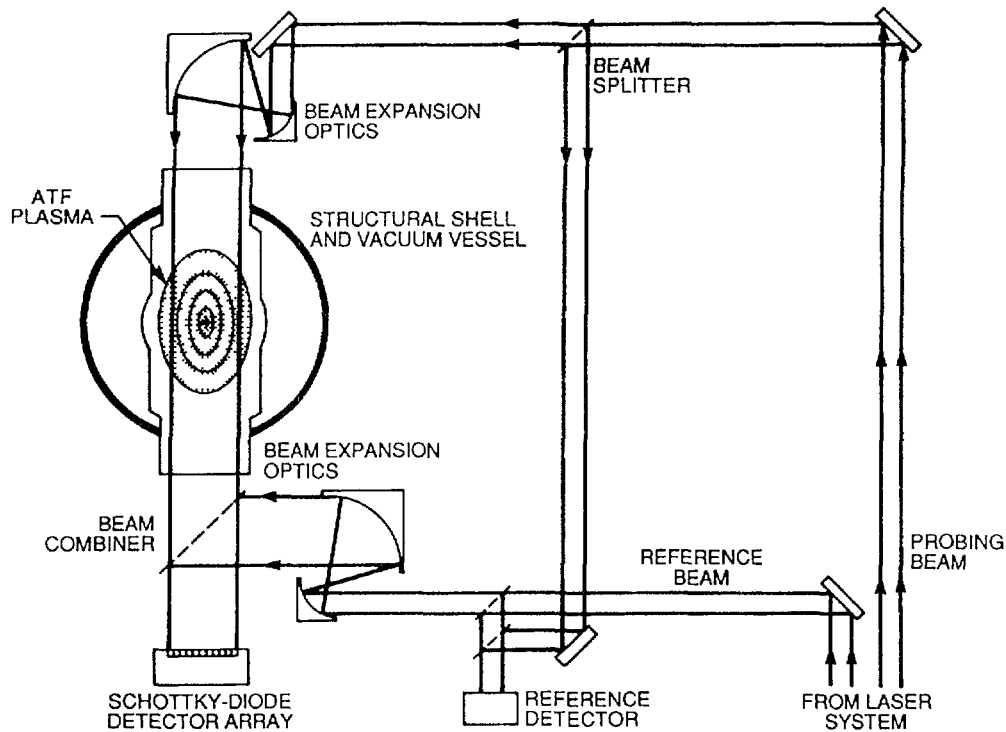


Fig. 1. Schematic of the 15-channel FIR interferometer system on ATF.

lasers, optically pumped by separate CO<sub>2</sub> lasers. The FIR cavities are tuned such that the two oscillate at frequencies differing by  $\Delta f$  of the order of 1 MHz. As shown in the figure, cylindrical mirrors and mirrors shaped parabolically in one direction are used to create a slab-like probing beam of 2 cm  $\times$  45 cm. The beam is transmitted through almost the whole cross section of the plasma. After passing through the plasma, the probing beam is dissected at the focal plane of the optics system by an array of 15 off-axis paraboloid reflectors, each of which illuminates a signal detector. Part of the beam from the reference laser is mixed first in a reference detector with a portion of the probing laser, which is split off before passing through the beam expansion optics, and the remainder is also expanded and is guided to the signal detectors to mix with the probing beam. Schottky diodes are utilized for all detectors. The detector signals are filtered, amplified, and fed into a digital phase detection circuit to extract the phase shift between the output of the signal detector and the reference signal, which is proportional to the line-integrated electron density. The outputs of the phase detectors are displayed on oscilloscopes for photographic recording and are digitized for computer storage and processing.

The pump laser is a 80-W invar-stabilized waveguide CO<sub>2</sub> laser, grating tuned to the 9R34 line. The resonator is formed by a grating of 150 lines/inch and a piezoelectric tunable ZnSe output mirror with radii of curvature  $R = 20$  m and reflectivity  $r = 69\%$  and two sections of 1.1 cm i.d. correlated Pyrex tube. The discharge length is approximately 215 cm. The FIR laser, also invar-stabilized, produce about 200 mW power on the 214- $\mu$ m line. Each resonant cavity consists of a 1-in. i.d. Pyrex waveguide and two flat reflectors which are separated by 240 cm. The input reflector is a 2-in.-diam gold-coated copper mirror with a 4-mm hole. The input end is sealed by a ZnSe Brewster window.

The output reflector is a gold-coated Si mirror with a 1-cm hole, and is attached to a motorized translation stage. The output end is sealed by a Z-cut crystalline quartz window. Each reflector is set between two bellows in order to be free from atmospheric pressure changes.  $\text{CH}_2\text{F}_2$  is used as the active gas in the cavity and is sealed off at a pressure near 200 m Torr. The laser is operated at the waveguide  $\text{EH}_{11}$  mode. The frequency difference between two FIR lasers is obtained by slightly detuning the two cavities by mechanically changing their lengths. The entire laser system is mounted on an optical table of 2 ft  $\times$  12 ft, and is enclosed in a Plexiglas shield. The enclosure is slightly pressurized with breathing air to eliminate the water vapor absorption.

Because the electron density is measured interferometrically, vibrations must be reduced to the lowest possible level. Therefore, all the optical elements and waveguides are mounted on a single frame which is independent from the ATF. The frame is constructed of 1 ft  $\times$  1 ft fiberglass I beam to eliminate the effects of eddy currents. The frame consists of three vertical mounts, an upper shelf and a lower I beam. The structure stands approximately 5.5 meters tall. The waveguides are made of 1-in. i.d. Plexiglas tubing. Water vapor absorption is eliminated by slightly pressurizing the waveguide with dry nitrogen. Emerging from the FIR laser, the beam is immediately passed into the waveguide where it is directed vertically to the ATF area. In the waveguide, the FIR laser beam assumes an  $\text{EH}_{11}$  high-order waveguide mode and is transmitted without the need for relay lenses to maintain a uniform beam size. Transparent pellicles of mylar are used to seal the ends of the waveguide against the atmosphere. The waveguide system consists of ten 90° bends and two 60° bends. The total beam pathlength is approximately 30 meters.

Because stray magnetic field levels at the interferometer can exceed 500 Gauss, it is necessary that all components be nonmagnetic, hence all optical mounts are constructed of stainless steel while the frames of beam splitters and the joints of waveguides are constructed of Plexiglas. All mirrors are made of first surface gold-coated glass. The beam splitters are made of quartz which exhibits the double advantage of having a low absorption coefficient for  $\text{CH}_2\text{F}_2$  radiation and being transparent to visible light for easy alignment. The vacuum windows on ATF consist of six 2-in.  $\times$  6-in.  $\times$  0.25-in. Z-cut crystalline quartz. To reduce absorption, the windows are made as thin as possible, consistent with their size, which is the minimum needed to pass the FIR beam through the vacuum vessel. Shutters are installed to minimize window coating which could occur during discharge cleaning or other similar operation. The beam combiner is a free-standing wire grid with the electric field of the FIR beams parallel to the wires. The wire grids are made of 10- $\mu\text{m}$ -diam copper wires with 70- $\mu\text{m}$  spacing.

Sixteen Farran Technology quasi-optical Schottky diode detectors are utilized: fifteen are configured in an array to detect the probing beams, and one is used for the reference detector. Each detector has a corner cube wire antenna mixer with a whisker contacted Schottky barrier diode. This type of detector was chosen because it is fast enough to respond to the 1 MHz interferometer modulation signals and sensitive enough so as not to require cryogenic cooling with all the attendant complications. An off-axis paraboloid is used to focus the FIR beams into the antenna pattern of the diode. Parabolic reflectors work well with corner cubes since the relatively small effective waist radius at the apex of the mirror ensures that one is operating in the far field. Each mirror and mixer is pre-assembled and tested in a right angle bracket, with the mirror oriented so that the input beam is vertical. This unit is held in place by fixing screws and compressed against a ball pivot so that angular adjustment of the unit with respect to the input beam is possible.

Five of these units are stacked closely together and are held in place on two sliding rails with locking screws. The signal processing circuitry consists of a phase comparator, a fringe counter, and low-pass filters. The heart of the phase comparator is a phase-locked tracking filter. The output of the phase comparator is sampled by the fringe counter which stacks the individual fringes in real time. A digital-to-analog convertor then samples the output of the fringe counter so that the output of this circuitry is proportional to the line density. The analog voltages are displayed on oscilloscopes and are digitized at typically a 10 kHz sampling rate. The data are read by the CAMAC acquisition system and are archived for data analysis.

### FIR Scattering System

Collective Thomson scattering of FIR laser radiation has been successfully used to measure the electron density fluctuations in tokamak plasmas [3-5]. However, to our knowledge, this powerful technique has not been utilized on stellarators. Fluctuations in ATF plasmas have been investigated using soft X-ray detectors and Mirnov coils [6]. A study is carried out to determine the optimum design of a FIR scattering system for the measurements of spatial and temporal fluctuations in ATF plasma. The system may be operated at wavelengths from 447  $\mu\text{m}$  to 119  $\mu\text{m}$ . Lasers operated at these wavelengths have been designed, constructed, and tested. Output power levels from 100 to 500 mW have been achieved. A pair of crystal quartz windows 38 mm  $\times$  300 mm located adjacent to the multichannel FIR interferometer windows will allow scattering angles of  $\pm 15^\circ$  from the incident beam. A single FIR laser beam will be split to provide both the scattering beam and local oscillator beam in a 3 to 5 channel detector array. The detector is designed to observe scattering from a single point at 3 to 5 different angles or several points at the same angle. Storage of the scattered signals will be accomplished by a PC-based CAMAC data acquisition system.

### References

- [1] C. H. Ma, D. P. Hutchinson, P. A. Staats, and K. L. Vander Sluis, *Int. J. Infrared Millimeter Waves* 3, 263 (1982).
- [2] C.A.J. Hugenholtz and B.J.H. Meddens, *Rev. Sci. Instrum.* 53, 171 (1982).
- [3] H. Park, C. X. Yu, W. A. Peebles, N. C. Luhmann, Jr., and R. Savage, *Rev. Sci. Instrum.* 53, 1535 (1982).
- [4] T. Saito, Y. Hamada, T. Yamashita, M. Ikeda, M. Nakamura, and S. Tanaka, *Nucl. Fusion* 21, 1005 (1981).
- [5] D. L. Brower, W. A. Peebles, and N. C. Luhmann, Jr., *Nucl. Fusion* 27, 2055 (1987).
- [6] J. H. Harris, J. D. Bell, J. L. Dunlap, H. Kaneko, and V. K. Pare, *Bull. Am. Phys. Soc.* 33, 2070 (1988).

## RECENT ELECTRON TEMPERATURE AND DENSITY RESULTS FROM THE ATF THOMSON SCATTERING SYSTEM

D.A. RASMUSSEN, A.C. ENGLAND, M. MURAKAMI,  
H.C. HOWE, T.C. CLARK, R.R. KINDSFATHER<sup>1</sup>,  
T.M. RAYBURN, P.S. ROGERS, K.A. STEWART  
Oak Ridge National Laboratory,  
Oak Ridge, Tennessee

G.L. BELL  
Auburn University,  
Auburn, Alabama

P.L. SHAW, C.E. THOMAS  
Georgia Institute of Technology,  
Atlanta, Georgia

United States of America

### Abstract

A spatial multipoint Thomson scattering system has been developed for the Advanced Toroidal Facility (ATF) torsatron. The system measures temperature and density at 15 vertical locations on a vertical chord for each laser shot (one per plasma discharge). By remotely relocating the laser beam and reconfiguring the viewing optics during a series of ATF discharges, a two-dimensional (2-D) electron temperature and density map of the plasma cross section can be obtained. Results obtained with this system during ATF operation in 1988 and early 1989 are presented.

---

### INTRODUCTION

The Thomson scattering system for the ATF [1] can provide a 2-D profile of the electron temperature and density by shot-to-shot horizontal translation of the vertically directed ruby laser beam coupled with a repointing of the viewing optics [2]. A sketch of the Thomson scattering system is shown in Fig. 1. The source light for Thomson scattering is provided by a single-pulse ruby laser (made by Quantel Inc.). The maximum output energy is 25 J. Typical laser shots deliver 13 J to the scattering volume with a pulse width of 40 ns (FWHM). Laser energy is measured on each shot. To obtain  $T_e$  and  $n_e$  scans, the laser beam is

---

<sup>1</sup> Present address: Igen Inc., Rockville, MD 20852, USA.

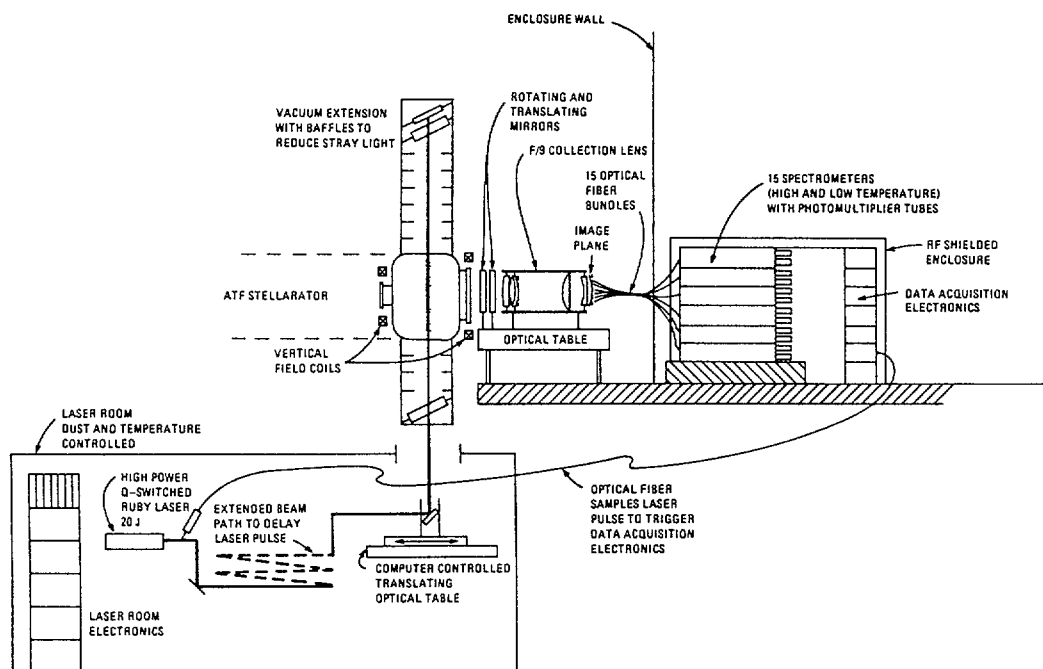


FIG 1. The ATF Thomson scattering system outline.

translated along a major radius ( $\phi = 0$  plane) between plasma discharges. The beam is focused with a 7-m focal length lens to a diameter of 2.1 mm at the ATF midplane. The scattered light is viewed through a toroidally offset port at the ATF midplane (Fig. 2). The viewing optics relay the scattered laser light onto a vertical image plane, which is coupled via fiber-optic bundles to a maximum of 15 spectrometers. The fibers receive light from a 24-mm segment of the laser beam in the plasma. Each spectrometer has from five to eight output channels, depending on the particular grating used. The output of the spectrometer channels is coupled via optical fibers to an array of approximately 105 photomultiplier tubes. The viewing optics track the laser beam by means of the set of rotating and translating mirrors shown in Fig. 2. The complex shape of the ATF vacuum vessel means that the different scattering positions in the plasma have varying levels of reflected stray laser light and plasma radiation light. The restricted viewing angle, limited access to the ATF device, and measurement on the red side of the spectrum result in an overall collection efficiency (detected photoelectrons) for scattered light of 0.24% for our arrangement.

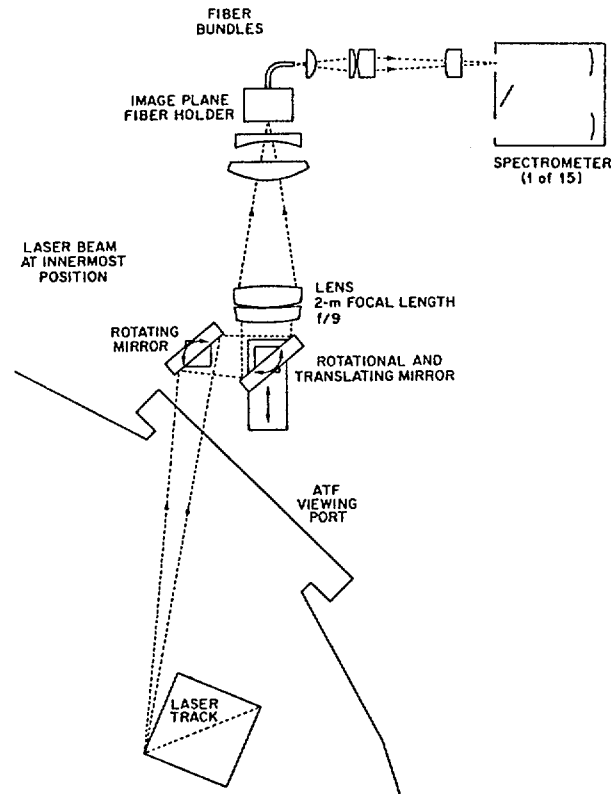


FIG. 2. Viewing optics layout.

## PHASE II RESULTS (MAY–SEPTEMBER 1988)

During this phase of ATF operations, the Thomson scattering system could obtain data from only one vertical chord and from seven vertical scattering volumes. ATF was operated during this period with known field errors [3, 4]. The largest magnetic field islands ( $\sim 6$  cm wide) were present at the  $\iota = 1/2$  surface ( $r/a \sim 0.6$ ). Figure 3 shows electron temperature data obtained during second harmonic electron cyclotron heating (ECH) operation of ATF (53 GHz, 0.2 MW at 0.95 T). The temperature profile represents the average of data obtained at  $t = 0.190$  s from 28 identical discharges. The laser chord was located at 210 cm for these discharges. The data are mapped to flux coordinates ( $\rho$ ) using a finite- $\beta$  equilibrium [5, 6] ( $\beta(0) \sim 1\%$ ). For this narrow temperature profile, the central flux surface shifts approximately 4 cm outward from its vacuum field location ( $R = 205$  cm). The central temperature and profile shape are representative of other times during the quasi-steady-state phase of ECH pulses.

Data were also obtained during 1.4 MW balanced neutral beam injection (NBI) operation [4] for the phase II operating period. The temperature profile shown in Fig. 4(a) is from measurements made at

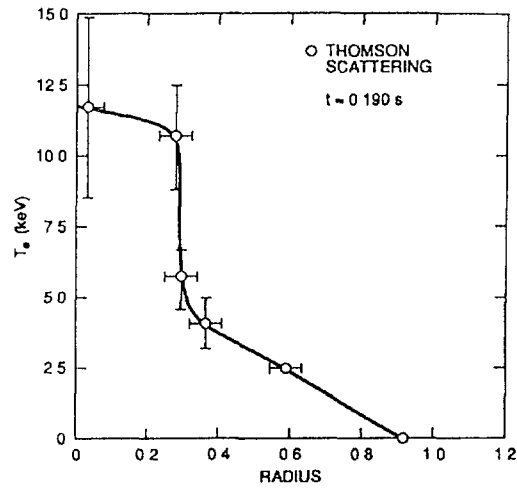


FIG. 3. Electron temperature profile obtained at  $t = 0.190$  s for 200 kW, 53 GHz ECH operation. Data are averaged from 28 identical discharges. Data are mapped to flux surfaces using a finite- $\beta$  equilibrium with  $\beta(0) = 1\%$

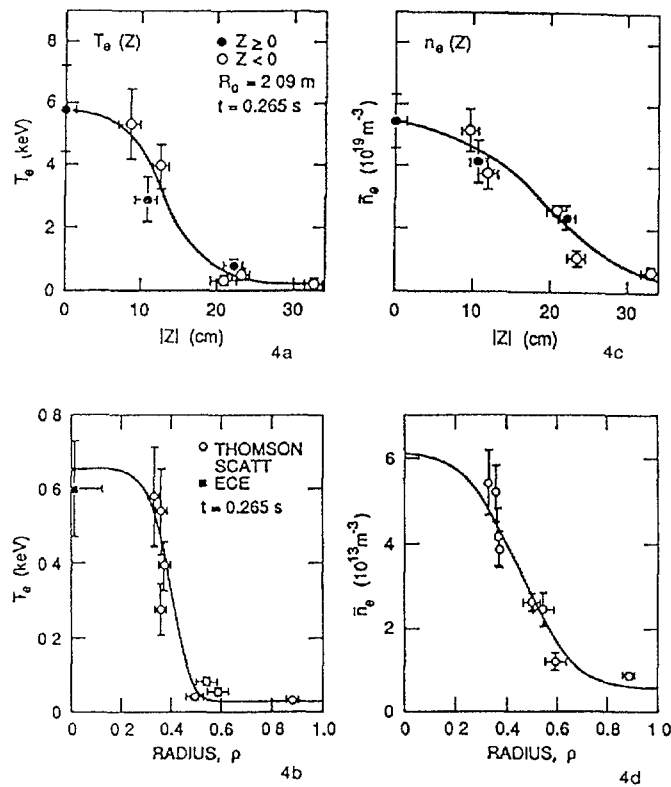


FIG. 4 Electron temperature measured (a) along a vertical chord ( $|Z|$ ) and (b) as a function of flux coordinate ( $\rho$ ), and electron density measured (c) along a vertical chord ( $|Z|$ ) and (d) as a function of flux coordinate ( $\rho$ ). All plots are for 1.4 MW NBI at  $t = 0.265$  s.

$t = 0.265$  s along a chord at  $R = 209$  cm. Figure 4(b) shows the data plotted in a flux coordinate system based on a finite- $\beta$  equilibrium [5, 6] of  $\beta(0) = 3\%$ . The vacuum and the finite- $\beta$  equilibrium used to obtain the flux surfaces are shown in Fig. 5. The central flux surface shifts approximately 11 cm outward from its vacuum field location ( $R = 205$  cm). This narrow profile shape was obtained during all NBI discharges. The time evolution of the electron temperature for a typical 1.4 MW NBI discharge is shown in Fig. 6(a). The data points were obtained from averages of multiple discharges of the central channel of Thomson scattering. The solid line is derived from measurements of the central third harmonic electron cyclotron emission [7] (ECE) normalized to a Thomson scattering value at one time. The line-averaged density, central and volume-averaged  $\beta$ , and input power (ECH and NBI) for these discharges are shown in Fig. 6(b). The density rises with application of NBI and the electron temperature, after an initial drop, increases until approximately 0.265 s, at which time the diamagnetic stored energy reaches a peak. The plasma undergoes a radiative collapse at  $t = 0.300$  s, as indicated by the sudden decrease in the line-averaged density.

Electron density measurements were made during this period of operation. Density calibration was obtained by the standard technique of Rayleigh scattering. For both ECH and NBI operation, the density profile was slightly broader than the electron temperature profile. The density profile for the 1.4 MW NBI case discussed above is plotted in real space and flux coordinates in Figs 4(c) and 4(d). Good agreement was obtained when the line-integrated density ( $n_e \ell$ ) from 2 mm interferometry was compared to the integrated density from Thomson scattering.

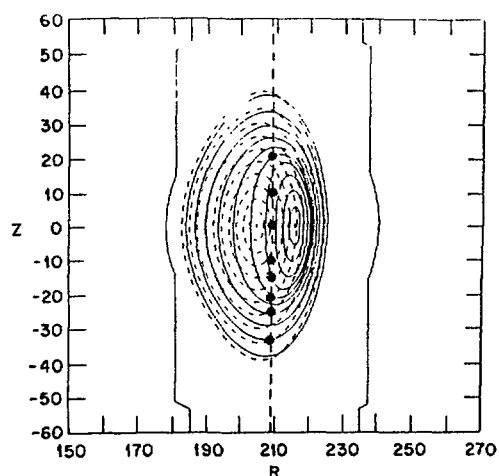
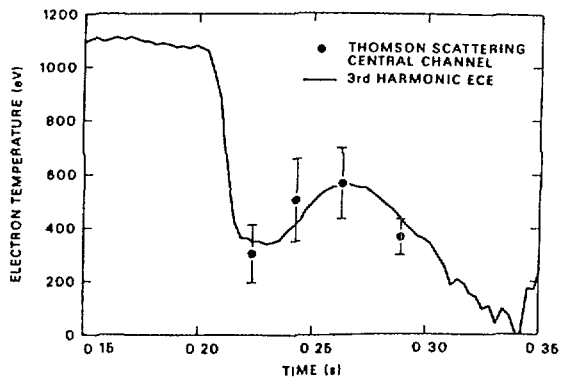
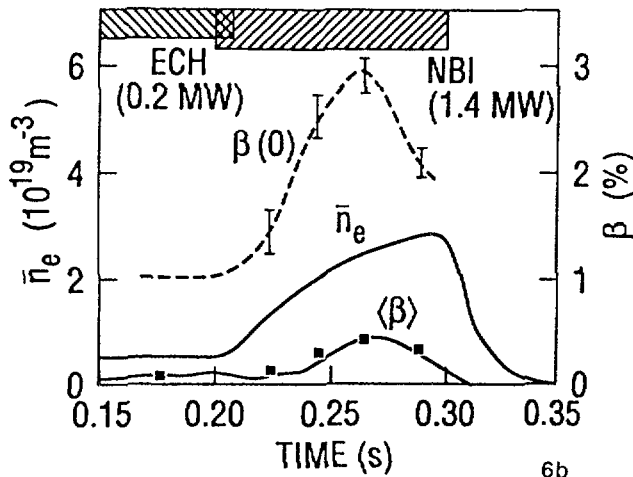


FIG. 5. The vacuum (dashed) and finite- $\beta$  (solid) equilibrium [5, 6] for the data of Figs 4 and 6 at  $t = 0.265$  s. The laser chord and the viewed scattering volumes are also indicated.



6a



6b

FIG 6 (a) Time evolution of the electron temperature during 1.4 MW balanced NBI. The data points are obtained from Thomson scattering, the solid line is from third harmonic ECE [7]. The ECE signal is normalized to Thomson scattering at  $t = 0.265$  s. (b) Line-averaged density, central and volume-averaged  $\beta$ , and input power (ECH and NBI) for 1.4 MW balanced NBI discharges.

### EARLY PHASE III RESULTS (FEBRUARY–MARCH 1989)

Prior to phase III operation of ATF, the current feeds were modified in order to reduce the field errors. As of the date of this meeting, the Thomson scattering system can obtain data from 13 vertical scattering volumes at 5 vertical chords. Alignment measurements now in progress will allow data collection from an arbitrary number of vertical chords.

At this writing, plasma operation for phase III has been with only one NBI source. Because of the limited time of operation, optimized plasma conditions have not yet been obtained. Preliminary results from this period of operation indicate broader electron temperature and density profiles. The maximum electron temperatures remain lower than for equivalent phase II operation. Absolute density calibration for this operating period has not yet been obtained.

## ACKNOWLEDGEMENTS

The authors acknowledge valuable discussions with E.A. Lazarus, J.B. Wilgen, and W.R. Wing. We thank the ATF operations and data acquisition groups for their cooperation. We also thank J.L. Dunlap, R.C. Isler, J.F. Lyon, and G.H. Neilson for their encouragement and support.

This work was sponsored by the Office of Fusion Energy, U.S. Department of Energy, under contract DE-AC05-84OR21400 with Martin Marietta Energy Systems, Inc.

## REFERENCES

- [1] LYON, J.F., CARRERAS, B.A., CHIPLEY, K.K., et al., Fusion Technol. **10**, (1986) 179.
- [2] KINDSFATHER, R.R., RASMUSSEN, D.A., MURAKAMI, M., et al., Rev. Sci. Instrum. **57**, (1986) 1816.
- [3] COLCHIN, R.J., HARRIS, J.H., ANDERSON, F.S.B., et. al., Controlled Fusion and Plasma Physics (Proc. 16th Eur. Conf., Venice, 1989), Vol. 13B, Part II, European Physical Society (1989) 615..
- [4] MURAKAMI, M., CARRERAS, B.A., HARRIS, J.H., et. al., *ibid.*, p. 575; HARRIS, J.H., MURAKAMI, M., CARRERAS, B.A., et. al., submitted to Phys. Rev. Lett..
- [5] HIRSHMAN, S.P., WHITSON, J.C.,, Phys. Fluids **26**, (1983) 3553,
- [6] HOWE, H.C., HORTON, L.D., CRUME, E.C., et. al., Transport modeling of ECH and neutral-beam-heated plasmas in the Advanced Toroidal Facility, paper 1P-3 presented at this conference.
- [7] BELL, G.L., GANDY, R.F., WILGEN, J.B., RASMUSSEN, D.A., Rev. Sci. Instrum. **59**, (1988) 1614.

## BOLOMETRIC MEASUREMENTS IN ATF

S. HIROE, R.R. KINDSFATHER<sup>1</sup>, J.B. WILGEN,  
D.B. BATCHELOR, T.S. BIGELOW, W.R. WING  
Oak Ridge National Laboratory,  
Oak Ridge, Tennessee

G.L. BELL, R.F. GANDY  
Auburn University,  
Auburn, Alabama

R.C. GOLDFINGER  
Computing and Telecommunications Division,  
Martin Marietta Energy Systems, Inc.,  
Oak Ridge, Tennessee

United States of America

### Abstract

Bolometer measurements are made under various plasma conditions in ATF. Each bolometer module includes four pairs of detectors; each pair consists of a sensor and a reference detector. Two or three detector pairs in each module were installed with various types of aperture masks to serve as radiation detectors. The rest were completely shielded from plasma emissions and used as blind detectors to measure background levels. When electron cyclotron heating (ECH) power was applied to ATF, the radiation signal was more than 10 times higher than that expected for 100 kW of radiated power. Surprisingly, similar signal levels were observed on the blind detectors. It is hypothesized that the bolometers are sensitive to ECH power at 53 GHz. (This problem may be general in near-term fusion experiments, in which microwave power will be an important tool for plasma heating.) In this paper, experiments aimed at proving this hypothesis are reported; bolometric signals before and after chromium gettering are discussed; and measurements of the microwave power deposition profile around the torus, made by using the observed microwave interference with the blind detectors, are presented.

## 1. INTRODUCTION

In near-term fusion experiments, microwave power will be used for both plasma heating and current drive. With higher magnetic fields, an increase in the microwave frequency allows microwaves to penetrate diagnostic systems. The result is interference of ECH power with diagnostics. Interference of this type has been observed in the bolometers on the Advanced Toroidal Facility (ATF). We identify the problems, report the results of experiments aimed at solving these problems, and discuss the present status.

The target plasma for neutral beam injection (NBI) in ATF is produced by ECH at 53 GHz. During the first phase of ATF operation, the magnetic field strength was limited to 1 T. Consequently, target plasmas were produced by second harmonic ECH. Such plasmas are reported to have lower densities and temperatures than those generated by fundamental ECH [1]. In addition, the vessel wall was not well conditioned at first (there was no baking during the early phase of operation), and the plasmas produced had poor parameters. These limitations resulted in poor single-pass absorption of microwaves [2]. When single-pass absorption is poor, microwave power can be reflected many times before being absorbed by the plasma or the wall or escaping from the plasma. This multiple reflection is a potential source of microwave interference.

---

<sup>1</sup> Present address: Igen, Inc., Rockville, MD 20852, USA.

The bolometer system on ATF uses detector module and signal processing electronics designed at Princeton Plasma Physics Laboratory [3]. Two or three of the four detector pairs (sensor and reference detectors) mounted in a bolometer module were installed with various types of aperture masks and used as radiation detectors. The rest were completely shielded from most other plasma emissions and used as blind detectors to measure background levels.

## 2. MICROWAVE INTERFERENCE FROM ECH POWER

When ECH power was launched into ATF, the radiation detector signal was more than 10 times larger than the anticipated level for 100 kW radiated power. This surprising result was obtained simultaneously in the blind detectors. The critical issue to be resolved was the interpretation of the signals from the blind detectors.

As noted in Section 1, the poor plasma parameters resulting from second harmonic ECH and poor wall conditioning result in poor single-pass microwave absorption. When  $\bar{n} = 5 \times 10^{18} \text{ m}^{-3}$  and  $T_e = 0.6 \text{ keV}$ , then the single-pass absorption coefficient  $\alpha = 0.1$  [2]. Thus, microwave power is reflected 22 times before 90% of the input power is absorbed. This is a potential source of strong microwave interference, since the bolometers can absorb power each time the microwaves are reflected toward them.

Figure 1 shows blind detector signals for several cases, in which the ECH power was about 200 kW. Case 1 is for a signal with extremely low plasma density ( $n_e l \sim 2 \times 10^{20} \text{ m}^{-2}$ ). The signal level for this plasma was similar to that obtained when ECH is launched into vacuum (no plasma).

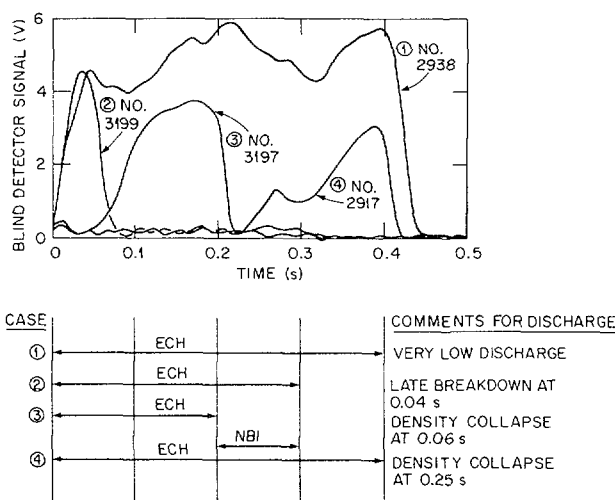


FIG. 1. Signals in blind detectors. Plasma conditions for each trace are given at bottom of figure.

The blind detector also receives an extremely high signal when ECH breakdown is delayed (case 2 for  $t < 0.04 \text{ s}$ ), after the density collapses during the ECH pulse (case 3 for  $t > 0.06 \text{ s}$ ), and after the density collapses during the ECH pulse with simultaneous NBI heating (case 4). The signal level in case 2 is essentially the same as that in case 1. When ECH breakdown occurs soon after  $t = 0$ , this high signal level is not observed (see cases 3 and 4).

When the density collapses, ECH power cannot sustain the plasma; electron cyclotron emission (ECE) signals (third harmonic) indicate low electron temperatures after a collapse. The single-pass microwave absorption is lower for lower-temperature plasmas; thus, the blind detector signal remains high after a collapse.

When a neutral beam is injected into an ECH target plasma (case 4 of Fig. 1), the ECE signal starts to decline at  $t \sim 0.22$  s, and the signal on the blind detector increases until  $t = 0.27$  s, when the neutral beam cannot sustain the plasma. This increase results from the poor single-pass absorption of microwave power when the plasma density reaches the cutoff value for electron cyclotron transmission. For this case, the plasma collapsed at  $t = 0.27$  s and was no longer sustained; thus, the unabsorbed ECH power appeared at the blind detector, whose signal level became similar to that for case 3 at  $t = 0.06$  s.

From these observations, we conclude that the blind detector signals are high when single-pass absorption is poor, as it is for ECH launch into vacuum, for low-density plasmas, for low-temperature plasmas, and for plasmas in which the cutoff density is attained. It appears that the blind detector signals might result from microwave interference with the bolometer system.

To confirm this possibility, several experiments were conducted. First, a bolometer was mounted outside the ATF vacuum vessel so that it viewed the plasma through a shuttered glass port. When closed, the shutter blocked most plasma emissions but did not seal tightly enough to block ECH power. When ECH power was injected into vacuum, the signal level in this detector with the shutter closed was similar to that in the radiation detector. Covering the module with aluminum foil reduced the signal to a low level, thus confirming that cable pickup was not the source of the interference.

Plasma parameters have been improved by wall conditioning, and ATF plasmas can now be sustained by NBI without ECH power. The microwave interference in the bolometer system that occurs with ECH power has been confirmed by comparing the signals from the blind detectors with and without ECH power during NBI. The data in Fig. 2 were taken for a discharge with simultaneous ECH and NBI; those in Fig. 3, for a discharge with ECH power removed during NBI. The signal from the blind detector during NBI increases in Fig. 2 but is reduced in Fig. 3, confirming that the source of the blind detector signal in Fig. 2 is the ECH power. To strengthen this confirmation, the blind detector signals of Figs. 2 and 3 were compared with measurements of microwave power leakage made through a glass window with a 53-GHz microwave horn. The behavior of the blind detector signals was qualitatively equivalent to that of the microwave leakage signal.

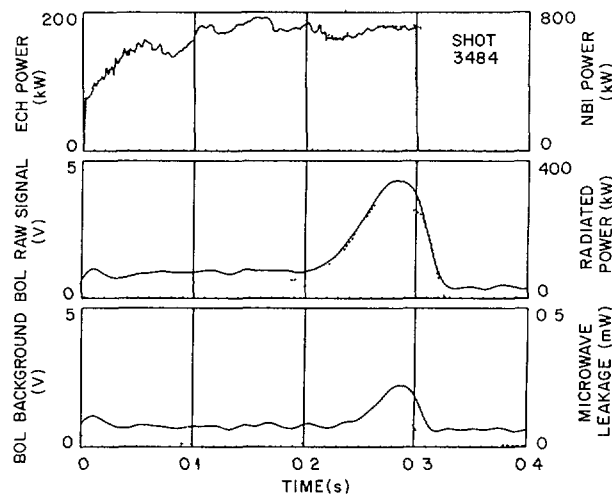


FIG. 2. Plasma discharge with simultaneous ECH and NBI. Top: ECH power (solid line), NBI power (dashed line). Center: Signal from radiation detector (solid line), radiated power (dashed line). Bottom: Signal from blind detector (solid line), signal from microwave leakage detector (dashed line).

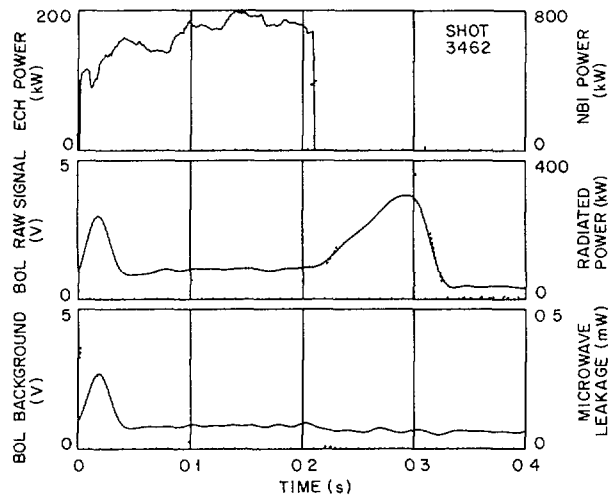


FIG. 3. Plasma discharge with ECH removed during NBI. Top: ECH power (solid line), NBI power (dashed line). Center: Signal from radiation detector (solid line), radiated power (dashed line). Bottom: Signal from blind detector (solid line), signal from microwave leakage detector (dashed line)

### 3. PLASMA RADIATIVE POWER MEASUREMENTS

The signal level on the blind detector has continuously declined from 5 V when initially measured to 0.2 V. This decrease appears to be related to wall conditioning; unfortunately, the bolometric power was not measured during the early phase of operation because of the microwave interference. At this point, it is reasonable to assume that the same quantity of ECH power observed by the blind detector should reach the radiation detector. Thus, a “radiated power” is calculated by subtracting the signal of the blind detector from the signal of the radiation detector. This difference is proportional to the bolometric power. By applying the geometric constant and the conversion constant from output voltage to power (kW), the bolometric power can be determined. The traces identified as “radiative power” in Figs. 2 and 3 were obtained in this way. Note that, at the moment, this quantity consists of both radiation power and charge exchange power. The “radiative power” is 50 kW during ECH (200 kW) and  $\sim 300$ –450 kW during NBI (1.4 MW). The bolometric power constitutes around 25% of the total input power for both ECH and NBI plasmas.

To determine the effect of wall conditioning on bolometric power, we analyzed the radiative power for a series of discharges that began immediately after a vacuum opening. Figure 4 shows the fraction of input power radiated as a function of shot number. To minimize the charge exchange contribution, the “radiative power” was analyzed during the ECH phase of the discharge; in the figure, the data are averaged arithmetically from 0.1 s to 0.2 s. The vacuum vessel was closed just before shot 2743. From shot 2743 to shot 3104, simultaneous baking and glow discharge cleaning with  $H_2$  gas were carried out. Chromium gettering started after shot 3104. The long arrows in Fig. 4 indicate occasions when chromium gettering was carried out after and before a day’s operation; the short arrows; occasions when chromium gettering was carried out in the middle of the day’s operation. The fractional radiation from ECH plasmas decreased continuously from 45% immediately after the vacuum vessel was closed to 25%. There is no significant change in the fractional radiation after gettering. The fractional radiation divided by  $n_e l$  was also evaluated, but no distinguishing effects on the radiative power are associated with gettering, in contrast to the results for ISX [4].

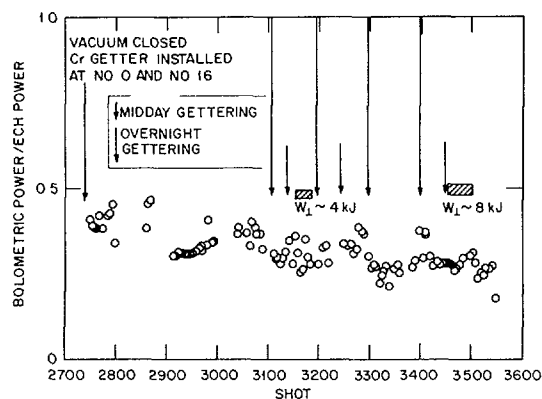


FIG. 4. Fraction of total ECH power that appears as bolometric power, as a function of shot number. Chromium gettering does not have a significant effect on the ratio of bolometric power and total ECH power.

#### 4. ELECTRON CYCLOTRON ABSORPTION PROFILES

The blind detector signal resulting from microwave interference can be used to evaluate the power absorption profile around the torus. The ratio of the signal from the blind detector with plasma to that when ECH power is launched into a vacuum was measured for six bolometers and one microwave leakage detector distributed around the torus. This ratio is roughly similar to the ratio of the blind detector signal at  $t \sim 0.15$  s for trace 2 or 4 in Fig. 1 to that for trace 1. This ratio is peaked near the ECH launcher; that is, it is about 0.65 at the sector adjacent to the ECH launcher (toroidal angle of  $15^\circ$ ) and 0.05 at  $180^\circ$  in toroidal angle from the ECH launcher, indicating that the microwaves are strongly absorbed near the launcher.

#### ACKNOWLEDGEMENTS

This research was sponsored by the Office of Fusion Energy, U.S. Department of Energy, under contract DE-AC05-84OR21400 with Martin Marietta Energy Systems, Inc.

#### REFERENCES

- [1] IIYOSHI, A., HELIOTRON GROUP, in Plasma Physics and Controlled Nuclear Fusion Research (Proc. 10th Int. Conf. London, 1984), Vol. 1, IAEA, Vienna (1985) 453.
- [2] GOLDFINGER, R.C., BATCHELOR, D.B., submitted to Nuclear Fusion.
- [3] SCHIVELL, J., et al., Rev. Sci. Instrum. **53** (1982) 1527.
- [4] WOOTTON, A.J., MIODUSZEWSKI, P.K., et al., J. Nucl. Mater. **128-129** (1984) 886.

# DIAGNOSIS OF RADIATION LOSS ASYMMETRIES IN TJ-II FLEXIBLE HELIAC

M.A. OCHANDO, A.P. NAVARRO  
Asociación Euratom/CIEMAT,  
Madrid, Spain

## Abstract

In this paper the designs of special collimators for single detectors and simulations of their use in TJ-II installation are presented. The numerical iterative tomographic technique is applied to determine the local emissivity distributions.

---

## INTRODUCTION

Even in absence of local accumulations, strong asymmetries in radiation losses are expected in TJ-II device (1) due to the toroidal dependence of the plasma shape. Detailed plasma confinement studies in this helical magnetic axis experiment would require the use of a great number of detector arrays, located at different poloidal and toroidal positions, and adequate tomographic techniques to reconstruct the local plasma emissivity from chord measurements.

When possible, the use of single detectors to obtain array-like information in diagnostics such as bolometry or soft-X-ray, would be very convenient because of the reduction of channels devoted to these diagnostics and the much easier attachment of single detectors to vessel ports.

On the other hand, tomographic techniques that allow to detect local perturbations with few poloidal views in any plasma shape, and able to analyze data from conventional arrays and array-like detectors would be required.

In this paper we are presenting designs of special collimators for single detectors and simulations of their use in TJ-II. Besides, the numerical iterative tomographic technique EBITA (2) is applied to determine local emissivity distributions even in the case of hollow profiles or very localized perturbations in the emission.

## TVCD's

In slowly variable plasmas, array like information can be obtained with only one detector, whenever is possible to associate signals to well defined plasma regions. Depending on the shot length, spatial information of the emission is drawn when modifying the plasma volume viewed by the detector along a shot or from shot to shot.

Among the ways for practical performance of this method, we have already used movable detectors in repetitive discharges in the TJ-I tokamak (3) and now we discuss the capability of some kinds of time variable collimated detectors, TVCD, in TJ-II to provide spatially resolved signals.

### a) Shutter collimator

Fig. 1 shows a detector, D, looking at a plasma poloidal section through a slit that is shut with an absorbing foil, S. When collimator shuts down, the plasma volume viewed

by the detector decreases and the difference in signals obtained every two selected times is associated to the plasma chord defined by the volume difference. The signals expected from integral detectors, such as bolometers, are shown in fig.2a and line integrals deduced from them are represented in fig. 2b. T, the time necessary to define the upper plasma chords, is fixed depending on the plasma emissivity level and the number of chords resolved is chosen depending on detector sensitivity. Lower chords are defined when shutter goes from positions 3 to 5, according to the scheme shown in fig. 1.

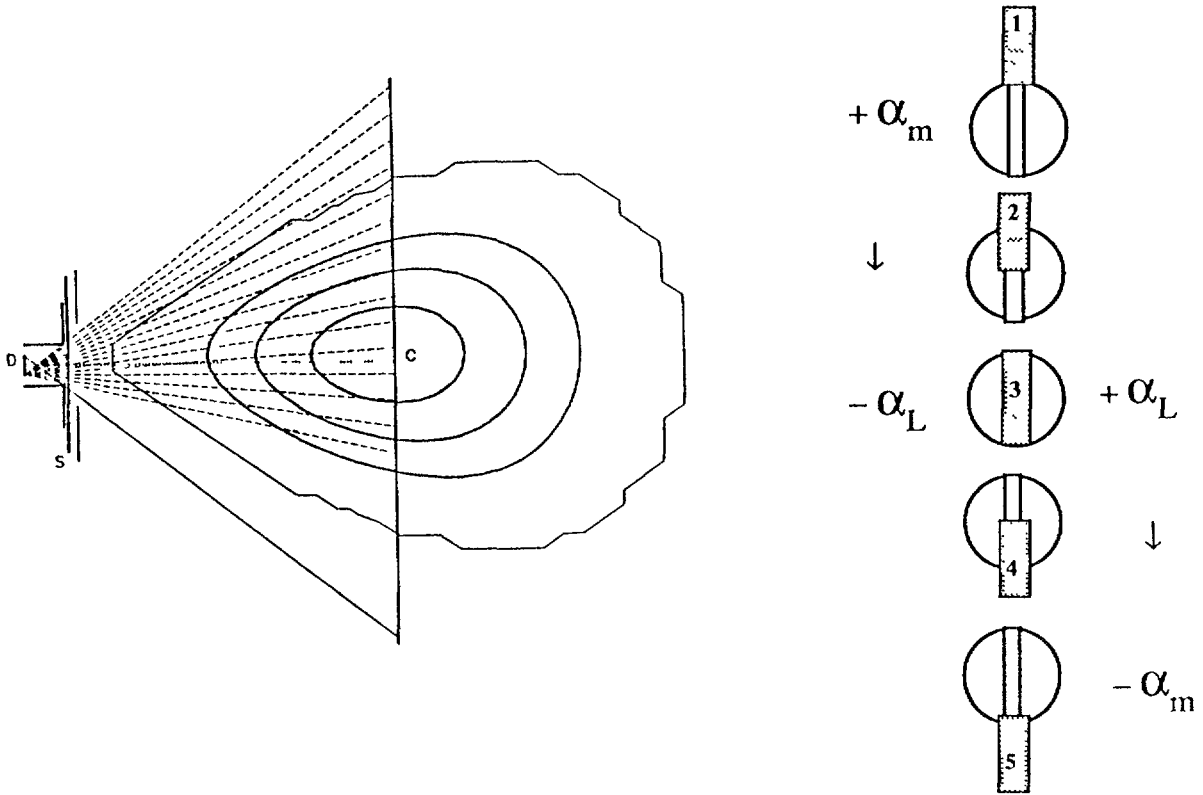


Figure 1. Shutter collimator scheme (---) represents the detector limit of view for successive shutter positions.

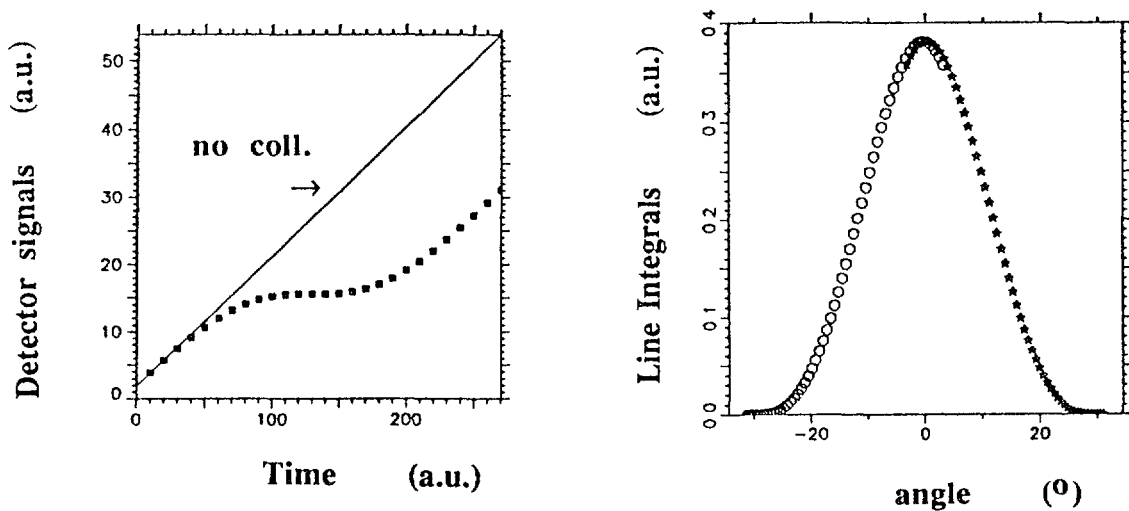


Figure 2. a) Time evolution of the bolometer signal when shutter operates. b) Deduced line integrals emissivities when shutter goes from 1 to 5.

b) Chopper

A rotary disk with holes at different radii chops the radiation passing through a fixed slit paced in front of the detector. Now the signals are directly related to the plasma chords (see fig. 3).

As above, number of chords and angular velocity of the disk, depend on detector sensitivity and plasma emissivity levels.

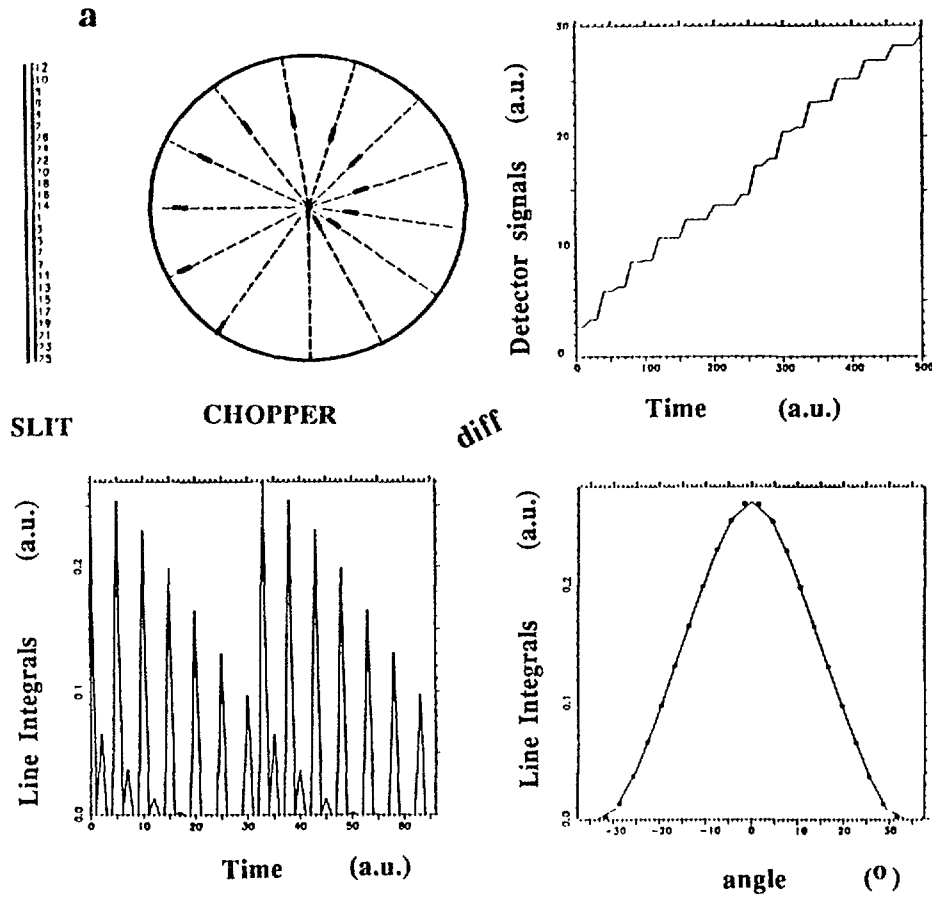


Figure 3. Chopper collimator scheme. One turn of the wheel scans a complete poloidal section and resolves 26 plasma chords in the order indicated at **a**.

Table I	
Input power	$P_{in} = 400 \text{ kw}$
Electron density	$n_{e0} = 1.6 \times 10^{-19} \text{ m}^{-3}$
Electron temperature	$T_{e0} = 700 \text{ eV}$
Toroidal field	$B_0 = 1 \text{ T}$
Discharge length	$t_0 \approx 500 \text{ ms}$

In TJ-II, under the normal operational conditions (shown in Table I) expected and supposing detectors being Ge bolometers, it will be possible to obtain between 10 and 20 line integral profiles by any of the proposed methods.

## TOMOGRAPHIC RECONSTRUCTION

Equilibrium Based Iterative Tomography Algorithm (EBITA) is a tomographic technique that reconstructs the local emissivity distribution of any plasma shape from line integral data provided by a low number of arrays.

For a plasma emissivity  $E_0(x,y)$ , array signals are given by:

$$S(\delta_n, \rho_i) = \sum_{j=1}^{NX} \sum_{k=1}^{NY} E_0(x_j, y_k) M(n, i, j, k)$$

$M$  is the **contribution matrix** of each grid cell  $(i,j)$  to detector signals (calculated once for a particular array geometry),  $\delta_i$  is the array angular position and  $\rho_i$  is the detector impact parameter.

EBITA deduces the local emissivity as:

$$E(x_j, y_k) = \frac{W(j, k)}{NC(j, k)} \sum_{n=1}^{NA} \sum_{i=1}^{ND} S(\delta_n, \rho_i) \frac{M(n, i, j, k)}{WN(n, i)}$$

$W$  is the weight matrix for signal distribution,  $WN$  the weight normalization factor matrix and  $NC$  the number of contributions of each cell to detector signals.

Array signals are calculated with this emissivity:

$$SR(\delta_n, \rho_i) = \sum_{j=1}^{NX} \sum_{k=1}^{NY} E(x_j, y_k) M(n, i, j, k)$$

Reconstruction error evaluated as:

$$Er(it) = \frac{1}{ST} \left[ \sum_{n=1}^{NA} \sum_{i=1}^{ND} (S(\delta_n, \rho_i) - SR(\delta_n, \rho_i))^2 \right]^{\frac{1}{2}}$$

with

$$ST = \sum_{n=1}^{NA} \sum_{i=1}^{ND} (S(\delta_n, \rho_i))^2$$

Convergence is analyzed by following  $E_r(it)$  evolution.

After each iteration, deduced local emissivity values are used as new weights :

$$W_{it}(j, k) = E_{it-1}(x_j, y_k)$$

## TWO ARRAYS RECONSTRUCTION

With adequate weights, deduced from flux distributions obtained in equilibrium calculations, TJ-II local emissivity distributions can be determined even with few arrays. Complicated structures, such as hollow profiles or local perturbations, can be also determined using this technique in spite of they are not assumed in the initial weight functions. As an example, results are presented in figure 4 for the local perturbation case. Using 2 TVCD at the top and outer sides of the device, the local accumulation is detected after a few iterations. Same behaviour appears in the case of the hollow profile.

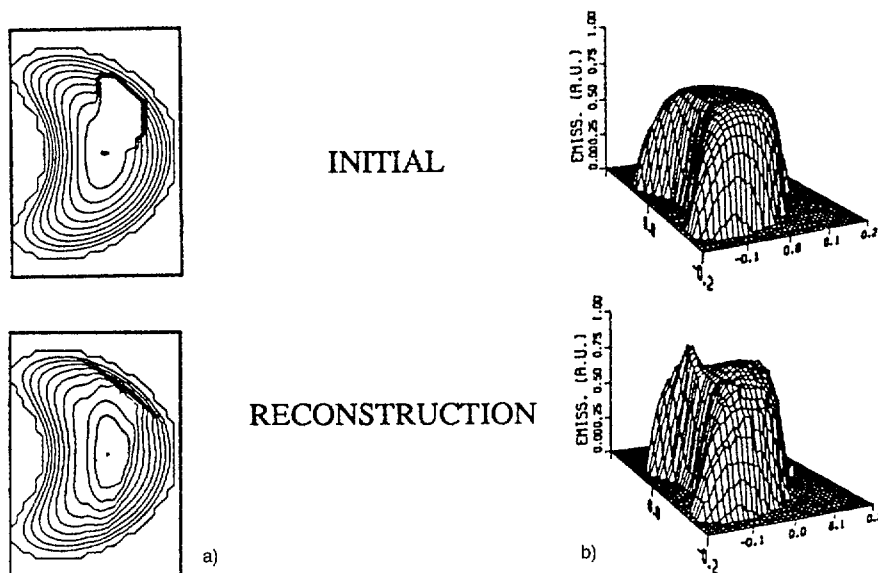


Figure 4. Two arrays TJ-II emissivity reconstruction. a) local perturbation after 6 iterations; b) hollow profile (1 iteration).

## CONCLUSIONS

Study of very asymmetric emissivity distributions would be affordable if single detectors could provide array like information. This is possible by using movable ones or adequately designed collimators or choppers, as those presented in this paper. In addition, a tomography technique able to deal directly with information from this kind of detectors has been developed. Based in the use of algebraical iterative techniques, it enables to study strong asymmetrical distributions with a reduced number of arrays. The standard drawbacks of these techniques have been avoided by using as initial weights in the reconstruction process, the flux distributions deduced from equilibrium calculations.

## REFERENCES

- [1] A.P. Navarro et al., Proc. IAEA Meeting on Plasma Confinement and Heating on Stellarators, EUR 9618 EN, Vol. II, 563, 1984.
- [2] A.P. Navarro et al., Proc. 16th Eur. Conf. Cont. Fusion and Plasma Phys., Vol. II, 687, 1989.
- [3] M.A. Ochando et al., IEEE Trans. on Plasma Science, April, 1989.

# A DIAGNOSTIC FOR 2-D DENSITY PROFILES IN HELIAC H-1

J. HOWARD, L.E. SHARP  
Plasma Research Laboratory,  
Research School of Physical Sciences,  
Australian National University,  
Canberra, Australia

## Abstract

A novel multi-view scanning interferometer is described. An air turbine driven scanning rotating grating wheel is used to produce  $\geq 30$  distinct spatial channels in four equi-spaced views of the H-1 plasma. The interferometer signals, derived from just three detectors, are multiplexed in time with a temporal resolution of  $\sim 1$  ms.

---

## 1. INTRODUCTION

Here is described a novel scanning, heterodyne interferometer which employs a rotating disc grating as the scanning and frequency shifting element [1]. The probing laser beam is reflected through a fan of discrete scan angles from the grating surface allowing sampling of the plasma over a range of different impact angles and impact radii. Signals from different positions are multiplexed in time so that spatial resolution is obtained at the expense of time resolution.

The H-1 flexible heliac currently under construction at the A.N.U. is a helical axis stellarator offering almost unhindered viewing access to the poloidal cross section of the plasma. This feature has motivated the design of an interferometer system which, within the anticipated resource constraints, possesses a truly tomographic capability. This is most important given the distorted "bean" shaped plasma cross-sections typically produced in such a device and the large range of magnetic configurations accessible. The scanning rotating grating is ideally suited to this application, offering high scan rates and excellent spatial resolution at low cost in detector and hardware resources. The design and performance of the grating/turbine assembly are discussed in [1].

## 2. THE INTERFEROMETER

Figure 1 shows one of several conceptual arrangements for the interferometer which are currently being assessed. The optical system has been modelled using a geometric ray trace code. The optics, including grating/turbine are to be mounted in a vertical plane on a solid granite slab. A finite elements analysis confirms the excellent mechanical and thermal properties of the granite table. Both horizontal and vertical views are of Michelson configuration, with the probing beams in each case executing a double pass of the rotating grating (twice the Doppler shift). The incident and return beams are separated using polarizing optics [2]. To minimize losses, reflecting components are used wherever possible.

A reference signal for the horizontal arm is taken from a point on the grating diametrically opposite the horizontal source position. A similar reference for the vertical arm is not shown, though, in principle, it is necessary only if the wheel rotation speed  $\Omega$  changes significantly in a wheel rotation. Also not shown in the diagram are the local oscillator arms derived from the unshifted laser radiation.

The return optics (curved reflecting mirrors) inside the vacuum vessel must be mounted on the magnetic coil support structure (CSS) independent of the main interferometer and so are a possible source of spurious phase shift. This may necessitate the installation of a vibration monitor. However, computer models of the electromagnetic deflections in the CSS indicate maximum displacements of  $\leq 0.3$  mm [3]. These movements

are expected to be reproducible and of low frequency and so could be subtracted in the post processing of the interferometer signals. Note that the internal, curved reflecting mirrors shown in Fig. 1 could be replaced by an array of corner cube reflectors. This would significantly reduce alignment difficulties but at the expense of power received by the detector.

Two diagonal views bisecting the vertical and horizontal scans are generated using optics mounted on a separate rigid support surrounding the plasma and attached to the CSS. The source radiation is obtained by sampling some portion of the vertical beam power. These views form Mach-Zehnder interferometers (single pass) and so require a separate reference detector not shown in Fig. 1. The entire probe beam is collected by each detector (rather than shared by an array) ensuring adequate signal to noise even for many more than four distinct views. The number of attainable views of the plasma is limited only by the logistics of positioning and maintaining alignment of the various optical components.

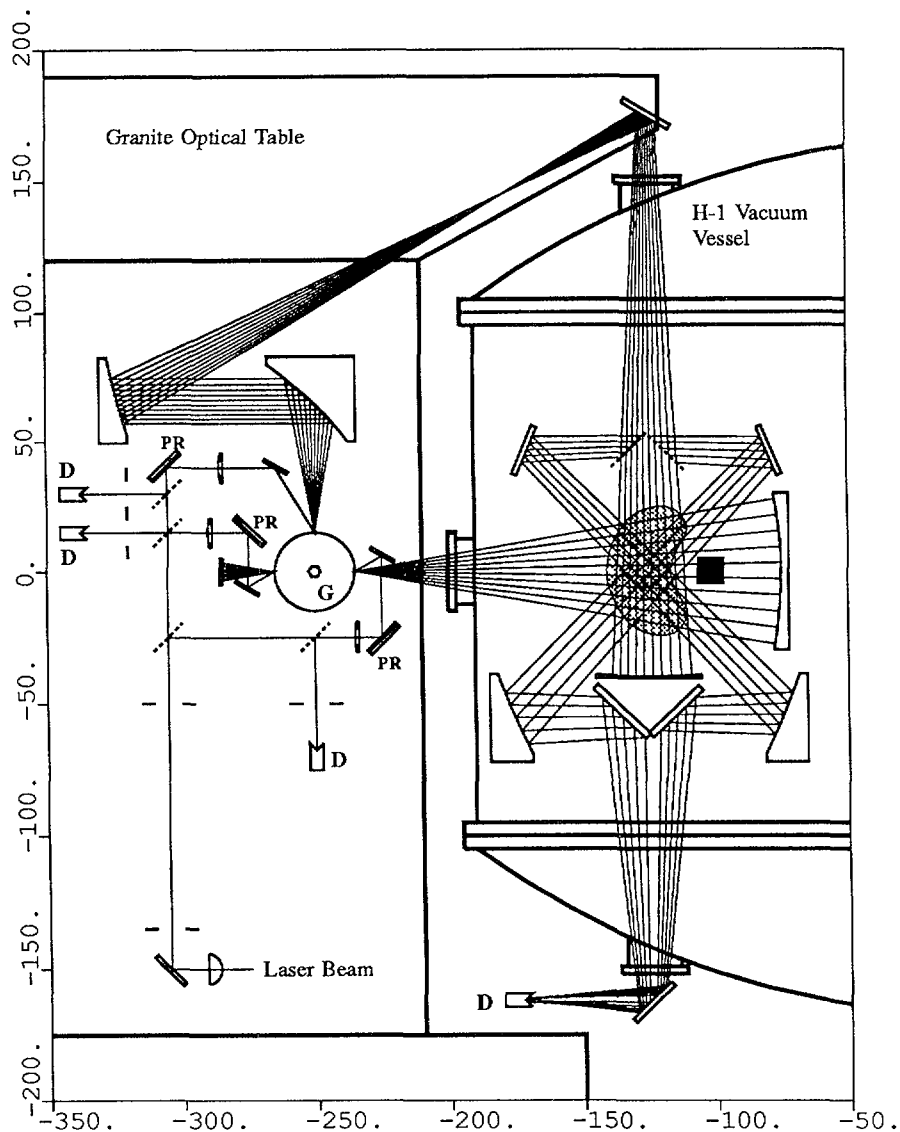


Figure 1: Proposed interferometer arrangement for the H-1 heliac. Local oscillator arms are not shown. The axes are marked in centimetres and the origin is the centre of the vacuum vessel. The solid square represents the main poloidal field coil and the shaded "bean" the plasma region. Key: D – detectors; PR – polarization transforming reflectors; G – rotating scanning grating.

### 3. TOMOGRAPHIC CAPABILITY

Constant density surfaces in the low beta, current-free H-1 plasmas should conform closely with the shape of computed vacuum magnetic flux surfaces. This has already been confirmed using Langmuir probes on the prototype heliac device SHEILA [4]. An analytically invertible transformation between “straight field line” or flux coordinates and laboratory coordinates has been invented [5] to allow testing of the proposed interferometer tomographic capability. The transformation in its simplest form has four adjustable parameters which can be extracted from a least squares fit to the computed magnetic surfaces. Using this transformation, a two-dimensional Gaussian density distribution  $\Psi(R, \Theta) = \exp(-R^2/\sigma^2)$  ( $\sigma = 0.6$ ) in the flux coordinate domain  $|R| \leq 1$  maps onto the distribution  $\psi(r, \theta)$  ( $|r| \leq 1$ ) computed for the standard H-1 configuration and shown in the line contour plot of Fig. 2. This type of density distribution models well the measured equilibrium density profiles in the SHEILA device [6].

Expanding  $\psi$  as a Fourier series

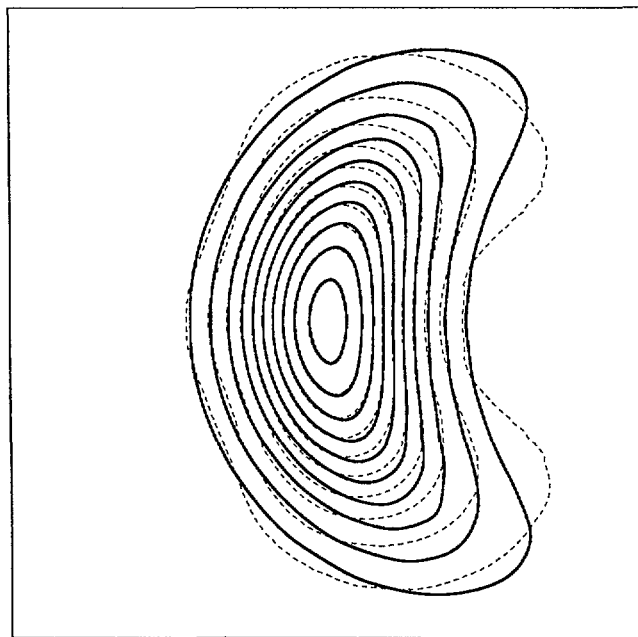


Figure 2: Contour plot of the source distribution  $\psi$  described in the text (solid lines). The broken contours represent the approximation to  $\psi$  obtained by removing all higher angular harmonics than  $l = 4$ .

$$\psi(r, \theta) = \sum_{l=-\infty}^{\infty} f_l(r) \exp(il\theta) \quad (1)$$

allows retrieval of the angular harmonic components  $f_l(r)$  and hence an estimate of the relative energy content  $E_l/E_\psi$  where

$$E_l = \int_{-\infty}^{\infty} |f_l(r)|^2 r dr \quad (2)$$

and  $E_\psi$  is the total energy. This ratio has been computed for the distribution  $\psi$  and is plotted in Fig. 3 in histogram form for  $l = 1$  to  $l = 7$ .

The energy in components  $l \geq 4$  is quite small, suggesting that a four view tomography system should be capable of encoding  $\psi$  without serious loss of definition or risk of aliasing contamination [7]. Note that the  $l = 4$  component is retrievable by the H-1 four view system due to its favourable orientation with respect to the chosen viewing angles.

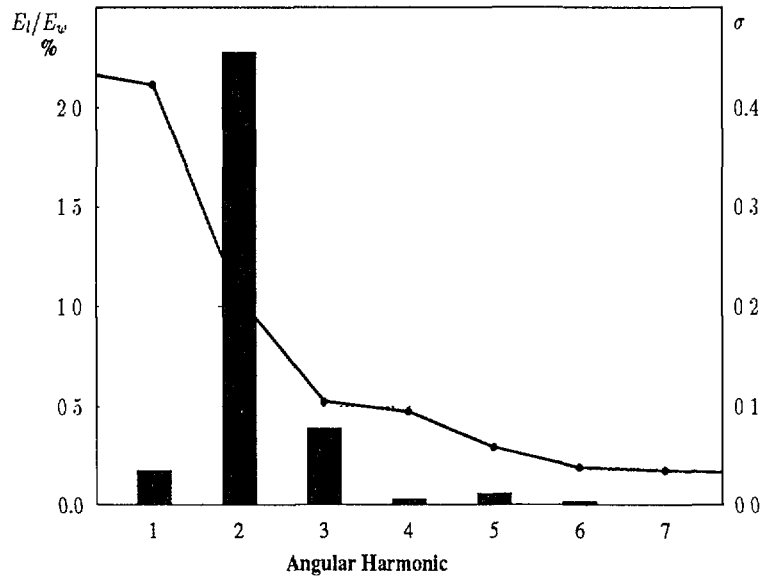


Figure 3: Histogram of the relative energies  $E_l$  of angular components of the plasma distribution  $\psi$  shown as percentages of the total energy  $E_\psi$ . The plotted line shows the improvement in image fidelity  $\sigma$  (right hand scale) with number of included angular harmonics.

Unfortunately, however, the higher angular harmonics significantly influence the shape of the outer, lower density contours. This can be seen upon comparing  $\psi$  with its filtered ( $l \leq 4$ ) approximation shown as the dashed set of contours in Fig. 3. In terms of the measure

$$\sigma = \frac{\left\{ \sum_{i,j} [\psi_F(i,j) - \psi(i,j)]^2 \right\}^{1/2}}{\left\{ \sum_{i,j} [\psi(i,j) - \bar{\psi}]^2 \right\}^{1/2}} \quad (3)$$

where  $\psi_F$  is the filtered  $\psi$  and  $\bar{\psi}$  is the mean of the distribution  $\psi$ , significant improvements in image fidelity can be obtained by increasing the number of views to six. The relative improvement thereafter, however, becomes increasingly less significant.

Initially only the vertical and horizontal arms of the interferometer system will be installed on H-1. In this case,  $l > 2$  features will alias contaminate the reconstruction unless strong *a priori* constraints are imposed. One possible approach for the extraction of 2-D information in this case is to use maximum entropy techniques to recover an image on a pixel grid which conforms to the shape of the vacuum flux surfaces. This technique is currently being investigated. Another possibility is to use the abovementioned transformation to perform an Abel inversion of the now distorted line integrals for a density distribution which is assumed circularly symmetric in flux coordinates.

Adequate sampling within a view is also of importance for the fidelity of the tomographic reconstruction. Assume that  $\psi$  is effectively bandlimited in the sense that energy in the spectrum above some spatial cutoff frequency or wavenumber  $K_0$  can be neglected. Adjacent channels within a view should then be sufficiently close (separation  $\Delta s$ ) to satisfy the Nyquist criterion  $\Delta s = \pi/K_0$ . Unfortunately, it is not always possible to anticipate  $K_0$  or indeed to provide sufficient channels in the event that  $K_0$  is known.

A major feature of the proposed interferometer is that the views obtained are naturally bandlimited by diffraction to approximately half the sampling frequency within the view, irrespective of the natural bandlimit  $K_0$ . Aliasing contamination is then avoided even when  $\Delta s > \pi/K_0$ . To see this, note that wavefront

perturbations of wavenumber  $K = 2\pi/\Lambda$  diffract at a rate greater than the natural Gaussian beam divergence  $\delta\theta_R$  whenever  $\Lambda \lesssim W$  where  $W$  is the probing beam diameter. For propagation distances greater than a Rayleigh length  $z \gtrsim z_R$  from the density perturbation, wavefront irregularities for which  $K \equiv K_{\max} \geq 2/W$  have been effectively lost from the beam. Propagation has caused the density information encoded by the beam to be low pass filtered. When certain grating design criteria are satisfied [1], the spacing between the probing beams at  $z = z_R$  is  $\Delta s = z_R \Delta\theta_R \lesssim \pi/K_{\max}$  and the Nyquist condition is satisfied for the bandlimited information.

## REFERENCES

- [1] HOWARD, J., *A Novel Scanning Interferometer for the H-1 Helicac*, To be submitted to J. Phys. E. (1989)
- [2] HOWARD, J., PEEBLES, W.A. and LUHMANN, N.C., Jr., *The Use of Polarization Transforming Reflectors for Far-infrared and Millimeter Waves*, Int. J. Infrared and Millim. Waves, 7 (1986) 1591
- [3] GRESHAM, R., LI, Y.F. and SHENTON, D.B., *Finite Element Analysis and Optimization of the Coil Support Structure of the H-1 Helicac Facility*, ANU-PRL TR 88/10 (1988)
- [4] SHI, X.H., HAMBERGER, S.M. and BLACKWELL, B.D., *Experimental Investigations of Different Configurations in a Flexible Helicac*, Nucl. Fus. 28, (1988) 859
- [5] HOWARD, J., *A Simple Invertible Model for the Shape of Magnetic Flux Contours in the H-1 and SHIELA Helicacs*. ANU-PRL TR 89/?? (1989)
- [6] SHI, X.H., BLACKWELL, B.D., and HAMBERGER, S.M., *Studies of Drift Waves in a Toroidal Helicac*, Submitted to Plasma Physics Contr. Fusion. (1989)
- [7] HOWARD, J., *Tomography and Reliable Information* J. Opt. Soc. Am. 5, (1988) 999

# MEASUREMENT OF ATTENUATION PROFILE OF INJECTED NEUTRAL BEAM INTO A HELIOTRON E PLASMA

K. KONDO, H. ZUSHI, T. ODA<sup>1</sup>, F. SANO,  
K. HANATANI, T. KAWABATA, H. KANEKO,  
T. MIZUUCHI, H. OKADA, S. SUDO, M. SATO,  
S. MORIMOTO, T. OBIKI, A. IYOSHI

Plasma Physics Laboratory,  
Kyoto University,  
Gokasho, Uji, Kyoto,  
Japan

## Abstract

Attenuation profile of the injected neutral beam into a Heliotron E plasma was measured using the Doppler-shifted  $H_{\alpha}$  emissions of beam particles, which were excited by collisions with electrons and protons.

---

## §1. Introduction

High power neutral beam injection has been recognized as a promising method to heat plasmas confined in tokamaks [1], stellarator [2], and Heliotron [3]. It is an important task to measure the attenuation profile of the injected neutral beam into a plasma in order to understand the heating processes. Attenuation or ionization profiles of the injected neutral beams are usually analyzed with Monte Carlo simulations and up to now there was not a direct measurement. Recently the Doppler-shifted  $H_{\alpha}$  emissions have been observed in the plasma [4,5], which are excited by electron and proton collisions with the injected beam particles. The wavelength of this emission shifts by the Doppler effect if the beam line and the sightline is not perpendicular, because of high speed of the injected beam particles. The  $H_{\alpha}$  emission from the injected neutral beams is distinguished from the unshifted  $H_{\alpha}$  emission which is localized in the periphery of the plasma. The beam density is estimated by the intensity of these Doppler-shifted  $H_{\alpha}$  emissions.

In this report, the attenuation profile of the injected neutral beam was obtained by the space-resolved measurements of the Doppler-shifted  $H_{\alpha}$  emissions.

## §2. Experimental Setup

The neutral beam injectors, BL-2,3 and 5, are installed on Heliotron E. The bucket type ion sources are used and the maximum extracted ion current is 55 A, and the acceleration voltage is varied from 10 keV to 30 keV. The injection angles are 90 degrees to the minor axis for both BL-3 and the half of the ion sources of BL-5. The other three ion sources of

---

<sup>1</sup> Faculty of Engineering, Hiroshima University, Higashi-Hiroshima, Japan.

BL-5 have an angle of 79 degree and BL-2 has 62 degree to the minor axis. The diameter of the beam was 20 cm. These neutral beams were injected into a plasma, which was initiated by high power gyrotrons with a frequency of 53.2 GHz.

The Doppler-shifted  $H_\alpha$  emissions were measured at the two beam lines, BL-3 and BL-5. The collecting optics, consisting of quartz lens and fiber optics, bring the emissions into two spectrometers (SPEX 1269) equipped with 512-channel detectors (Tracor Northan, TN-6133). The diameter of the sightline was 3 cm. The angle between the sightline and BL-5 beam line is fixed at 45 degree, but that of BL-3 can be varied from 76 degree to 63 degree, and we can observe the Doppler-shifted  $H_\alpha$  emissions from near the half way to the edge of the plasma of the inner side.

### §3. Intensity of the Doppler-shifted $H_\alpha$ Emissions from the Injected Neutral Beam

Figure 1 shows the typical spectrum observed from the BL-5 beam line. The integration time was 20 msec. The average electron density was  $2 \times 10^{13} \text{cm}^{-3}$ , and the electron and ion temperatures were about 300 eV. The magnetic field was 0.94 T. Near the unshifted  $H_\alpha$  emission, there are three peaks designated E, E/2 and E/3, and E was 23 keV. These lines are due to beam neutrals originated from  $H^+$ ,  $H_2^+$  and  $H_3^+$  ions in the ion sources, since they appeared only during beam injection and their wavelengths shift according to the Doppler effect.

The intensities of these three emissions are described as

$$I(E/k) = \{n_e n_b(E/k) \langle \sigma_{ex} v_e \rangle + n_p n_b(E/k) (\sigma(E/k) v(E/k))\} (\Omega/4\pi) V_{bs} \quad (k = 1, 2, 3) \quad (1)$$

$$= n_e n_b(E/k) \langle \sigma_{ex} v_e \rangle g(E/k, n_p/n_e) (\Omega/4\pi) V_{bs} \quad (2)$$

$$g(E/k) = 1 + \frac{(\sigma(E/k) v(E/k)) n_p}{\langle \sigma_{ex} v_e \rangle n_e} \quad (3)$$

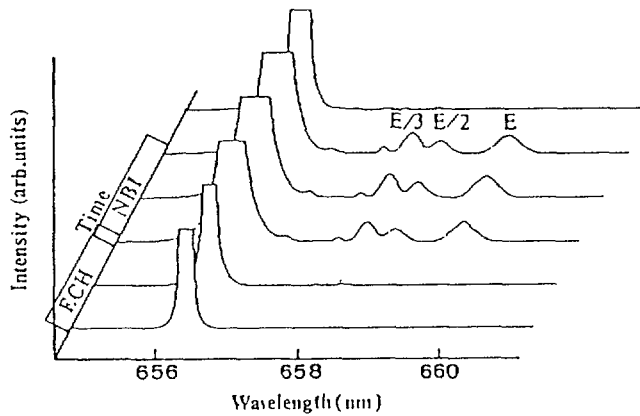


Fig.1 The spectra of the unshifted and the Doppler-shifted  $H_\alpha$  emissions. The vertical axis is the intensity and it is expanded to show the Doppler-shifted  $H_\alpha$  emissions from the beam particles. Three peaks, designated by E, E/2, and E/3 originate from  $H^+$ ,  $H_2^+$ , and  $H_3^+$ .

where  $n_e$ ,  $n_p$  and  $n_b$  are electron, proton and beam densities,  $\langle \sigma_{ex} v_e \rangle$  is electron excitation rate and  $\sigma(E/k)$  is cross section of proton excitation and  $v(E/k)$  is beam velocity,  $\Omega$  is solid angle and  $V_{b_s}$  is the emission volume defined as the intersection by the beam path and the sightline of the optics. The contribution of proton excitation is included by a function  $g(E/k, n_p/n_e)$  [5]. The electron excitation cross section by Morrison and Rudge [6] was used. The proton excitation cross sections were used from the references by Franco and Thomas [7], and Bhadra and Ghosh [8].

To estimate the intensity of the Doppler-shifted  $H_\alpha$  emissions, it is necessary to measure proton density, but the function  $g(E/k, n_p/n_e)$  has a weak dependence on the proton to electron density ratio. The typical acceleration energy of our neutral beam injection is less than 30 keV, and correction from the proton collision is small.

#### §4. Attenuation Profile of the Injected Neutral Beam

The beam attenuation profile was measured along the BL-3 beam line. Figure 2 shows the intensities of the Doppler-shifted  $H_\alpha$  emissions. The average electron density was  $3 \times 10^{13} \text{ cm}^{-3}$  and the electron temperature was about 300 eV. The magnetic field was 0.94 T. The acceleration voltage for the primary beam was 23.5 keV and 28 keV, respectively. The input power of BL-3 was 200 kW, and BL-5 and BL-2 provide another 1 MW power into the plasma. There were no differences in the electron density and temperature in both acceleration energies. Figure 3 shows the beam densities estimated from the  $H_\alpha$  intensities in Fig.2. The vertical axis is the beam density in arbitrary scale, and the horizontal axis is the length measured along the beam line. Converting to the beam density from the  $H_\alpha$  emission intensity, the electron density profile is assumed as a parabolic one. The beam density in the case of 28 keV injection is smaller than the case of 23.5 keV injection, since the input power of both cases were 200 kW, and the beam neutral density is proportional to  $E^{-3/2}$ .

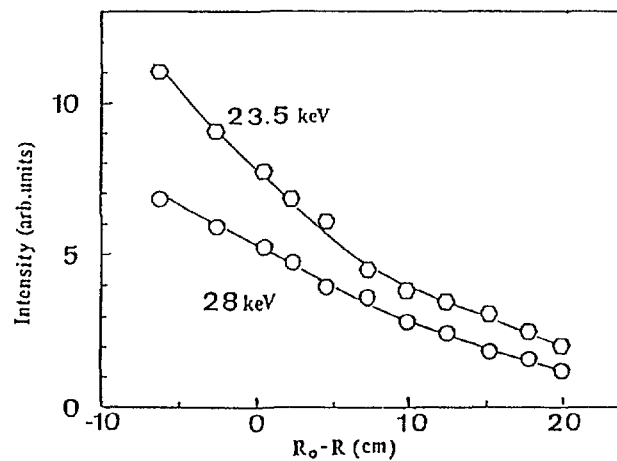


**Fig.2** The intensities of the Doppler-shifted  $H_\alpha$  emissions along the BL-3 beam line.

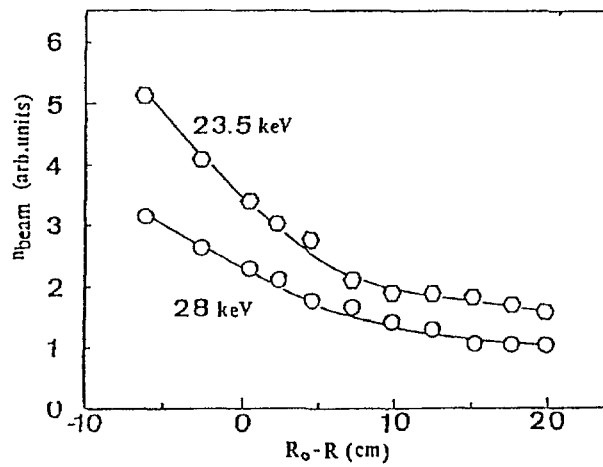


Fig.3 The attenuation profiles of the injected neutral beams with 23.5 keV and 28 keV.

### §5. Conclusion

It was demonstrated that the attenuation profile of the injected neutral beam was obtained using the Doppler-shifted  $H_{\alpha}$  emissions. The higher energy beam attenuates slower than the lower energy beam, and in the high density plasmas the attenuation was strong. These measurements are important for understanding the heating processes by the neutral beam injection because the birth profiles are given.

### References

- [1] JET Team: Proc. 11th Conf. of Plasma Physics and Controlled Nuclear Fusion Research, Kyoto., Nucl. Fusion Suppl. (1987) vol.1, p.31.
- [2] H.Wobig, H.Maassberg, H.Renner, *et al.*: *ibid.* vol.2, p.369.
- [3] F.Sano, T.Obiki, O.Motojima, A.Sasaki, K.Hanatani, H.Zushi, S.Sudo, S.Besshou, M.Sato, T.Mutoh, H.Kaneko, T.Mizuuchi, K.Kondo, M.Nakasuga, Y.Nakashima, N.Nishino, A.Iiyoshi, and K.Uo: Nucl. Fusion, 24 (1984) 1103.
- [4] B.W.Sleaford, G.A.Cottrell, and J.Kim: Nucl. Fusion, 28 (1988) 523.
- [5] K.Kondo, H.Zushi, F.Sano, T.Kawabata, T.Mizuuchi, H.Kaneko, S.Sudo, M.Sato, T.Obiki, and A.Iiyoshi: PPLK-29 (1988) Plasma Physics Laboratory, Kyoto University
- [6] D.J.T.Morrison and M.R.H.Rudge: Proc. Phys. Soc., 89 (1966) 45.
- [7] V.Franco and B.K.Thomas: Phys. Rev., A 4 (1971) 945.
- [8] K.Bhaadra and A.S.Ghosh: Phys. Rev. Lett., 26 (1971) 737.

# MODELING FOR RUNAWAY DYNAMICS IN STELLARATORS

L. RODRÍGUEZ, R.L. VÁZQUEZ, A.P. NAVARRO  
Asociación Euratom/CIEMAT,  
Madrid, Spain

## Abstract

A 2D model for runaway electron dynamics in tokamaks have been developed based on the solution of a conservative numerical scheme. The bidimensional character of the model enables to study the situations where other component, in addition to the toroidal one, is important.

---

## INTRODUCTION

Plasma soft and hard-X-ray spectra, as is well known, present slopes that are usually related to its electron temperature. In the case of H-X-R it has being shown [1] that the denomination of "suprathermal temperature" is not correct since there is not a maxwellian in the tail of the distribution. We have then correlated the slope of H-X-R spectra with the electron confinement time of runaway electrons  $\tau_r$ .

In [2] we used a 2D model to describe the dynamics of the runaway electrons and we obtained a correlation between the slope of the H-X-R spectra and the confinement time of runaway electrons in tokomaks. Our numerical scheme shows a discrete analogy with the underlying continuous equation conservation laws, symmetries and stability properties. Otherwise, the scheme can show numerical chaos and solutions would exhibit unphysical properties [3]. Experimentally we can then obtain from the H-X-R spectra electron confinement time and then deduce the electron distribution function in the plasma; that takes few minutes in a VAX-11/785 computer. Here we discuss the application of this model to stellarators determine from H-X-R spectra the electron distribution function, in an attempt to relate this distribution with the ECH absorption in these devices. In the application of this model to stellarators, we have to considerate the following features : a) Electrostatics fields and b) Fields due to the application of ECH. As it was done in [5] for the one dimensional case, we apply our single particle two dimensional model to an electron population with a maxwellian energetic distribution function. We consider that the tail of the maxwellian distribution losses e times runaway electrons in a time  $\tau_r$ , defined as runaway electron confinement time, and the initial maxwellian distribution is restored in the thermal equilibration time given by:

$$\tau_{eq} = \frac{\sqrt{m_0 T_e^3}}{\sqrt{2} \pi n_i e^4 \ln \lambda}$$

With this approach we obtain the electron distribution function, in the phase space, shown at figure 1. In figure 2, we represent the distribution function along axis  $v_x$ . For each electron distribution function we obtain the hard-x-ray intensity spectrum  $P(k)$ , using as cross section the expression given in [4]. In figure 3, we represent hard-X-ray photon and intensity spectra for the conditions of figure 1. For different values of the runaway confinement time we obtain intensity spectra with different slope  $\alpha$ . In figure 4, the relation between  $\alpha$  and  $\tau_r$  is shown.

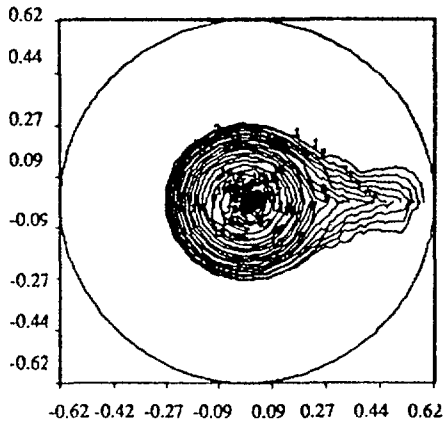


Fig 1: Electron distribution for  $T_e=600\text{eV}$ ,  $Z_{\text{eff}}=1$ ,  $E_x=2\text{ V/m}$ ,  $E_y=1.e-3\text{ V/m}$  and  $\tau_r=1.e-4\text{ s}$ .

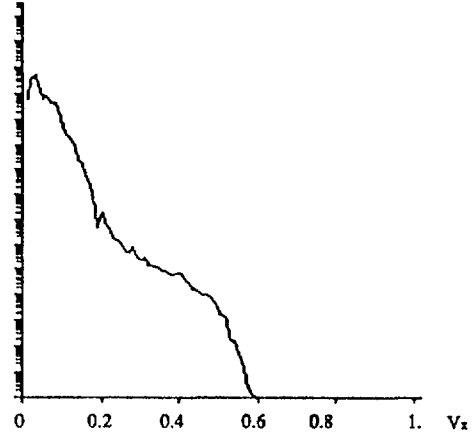


Fig 2: Distribution function along axis  $v_x$

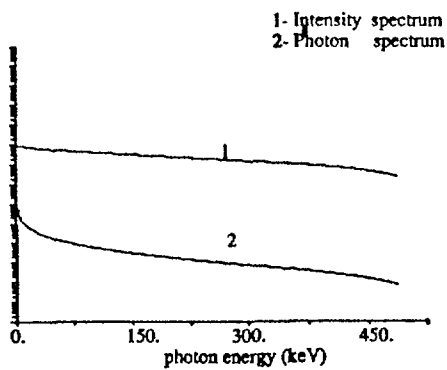


Fig. 3 : H-X-R photon and intensity spectra.

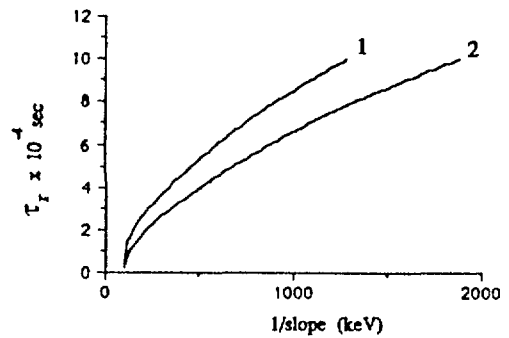


Fig 4: Runaway confinement time versus slope of intensity spectra.

## TWO DIMENSIONAL MODEL

Motion equations for a single electron in a fully ionized plasma for a force field with Coulomb collisions can be expressed as:

$$\left\{ \begin{array}{l} \dot{x} = \frac{p_x}{\sqrt{m_0^2 + \vec{p}^2}} \quad ; \quad \dot{y} = \frac{p_y}{\sqrt{m_0^2 + \vec{p}^2}} \\ \dot{p}_x = -\frac{\partial U}{\partial x} - \alpha v_x \quad ; \quad \dot{p}_y = -\frac{\partial U}{\partial y} - \alpha v_y \end{array} \right.$$

where, (we use the natural units  $c=1$ ),  $m_0$  is the rest mass of the particle and,  $\vec{p}$  the momentum,  $U(x)$  the potential energy of the particle and  $\alpha$  the total electron momentum loss collision frequency with relativistic corrections and:

$$U = -e\vec{E}\vec{x}, \quad \vec{E} = (E_x, E_y, 0)$$

To solve this system we apply a two dimensional conservative scheme [5] to the following modified discrete equations:

$$\left\{ \begin{array}{l} \frac{x_{n+1} - x_n}{\tau} = \frac{\sqrt{m_0^2 + (p_x^2)_{n+1} + (p_y^2)_n} - \sqrt{m_0^2 + (p_x^2)_n + (p_y^2)_n}}{(p_x)_{n+1} - (p_x)_n} \\ \frac{y_{n+1} - y_n}{\tau} = \frac{\sqrt{m_0^2 + (p_y^2)_{n+1} + (p_x^2)_{n+1}} - \sqrt{m_0^2 + (p_y^2)_n + (p_x^2)_{n+1}}}{(p_y)_{n+1} - (p_y)_n} \\ \frac{(p_x)_{n+1} - (p_x)_n}{\tau} = -\frac{U(x_{n+1}, y_n) - U(x_n, y_n)}{x_{n+1} - x_n} + \alpha \frac{(x_{n+1} - x_n) / \tau}{v_n^3} \\ \frac{(p_y)_{n+1} - (p_y)_n}{\tau} = -\frac{U(x_{n+1}, y_{n+1}) - U(x_{n+1}, y_n)}{y_{n+1} - y_n} + \alpha \frac{(y_{n+1} - y_n) / \tau}{v_n^3} \end{array} \right.$$

where:

$$v_n = \frac{\sqrt{(p_x^2)_n + (p_y^2)_n}}{\sqrt{m_0^2 + (p_x^2)_n + (p_y^2)_n}}$$

The electric field has a main component  $E_x$  parallel to  $v_x$  and to the magnetic field lines. As initial conditions we take  $-1 < (v_x)_0 < 1$ , and  $(v_y)_0 = 0$ . All calculations are normalized for  $p$  using  $p = p/p_t$ , where  $p_t$  is the

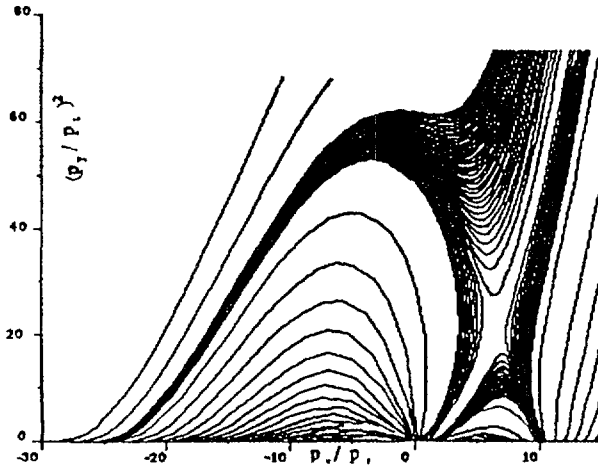


Fig 5: Momentum-space plot for  $E_x = E_y = 2$   
 $V/m, Z_{eff} = 1$

momentum for the electron temperature  $T_e$ . For different values of  $T_e, Z_{eff}$  and electric fields  $E_x$  and  $E_y$  we obtain momentum-space trajectories as is shown at figure 5. We can define two regions in the momentum-space plot, delimited by a separatrix  $S$ . With our scheme we can approximate qualitatively the trajectory corresponding to  $S$ , calculating trajectories above and below it. The value of the intersection of  $S$  with axis  $x$  is called  $p_T$ . An electron lying on a trajectory above  $S$  will gain energy, then runaway, and an electron lying on a trajectory inside  $S$  will lose energy and stay thermal. Therefore  $S$

represents a trajectory of constant energy. Electrons with negative momentum can become runaway, when their trajectory is above  $S$ .

## SCHEME FOR ECH ON STELLARATORS

This model can be extended to stellarator by considering three different phases in the usual case of ECH star-up and heated plasmas in these devices. In the first phase, when the coils are energized, we can apply the model as it was developed for tokamak considering an adequate set of values for the parameter group,  $(E_x, E_y, T_e, n_e$  and  $\alpha)$ .

During the heating phase, two different approaches can be taken. In the first one, the 2D model is enough by considering only those electrons with the resonance energy for the applied wave (6). In this case the main limitation is coming from the grid precision when defining the resonance population. Only the center guide trajectory is considered for the electrons. The second approach considers the full movement of the electrons in the device magnetic field and the wave fields. In this case, displacements due to cyclotron effect are considered and a 3D model must be invoked. In both approaches the step time in the calculation must be very short due to the high frequency range involved, in the order of GHz; and, because  $T_e$  changes along the process,  $\alpha$  must be change accordingly. Out of the spatial region where the wave is launched, the standard model that was applied in the preheating phase can be applied, with the adequate set of parameters.

## CONCLUSIONS

A 2D model for runaway electron dynamics in tokamaks have been developed based in the solution of a conservative numerical scheme. The bidimensional character of the model enables to study situations where other component in addition to the toroidal one can be important such as ECR heated or stellarator plasmas. The application to stellarators can made possible the determination of the runaway distribution function and its influence on the ECH absorption. Nevertheless a detailed study of this phenomena would require a 3D model to take into account the electron cyclotron displacements.

## REFERENCES

1. L.Rodríguez R., and A.P. Navarro, Proc. 13<sup>th</sup> Conf. on Contr. on Contr. Fusion and Plasma Physics, 10D, I, 272, 1986.
2. L. Rodríguez R., A.P. Navarro, L. Vázquez, Proc 16<sup>th</sup> Conf. on Contr. Fusion and Plasma Physics, 13B, I, 311, 1989.
3. W.A. Strauss and L.Vázquez, J. Comp. Phys. 28 (1978) 271.
4. E. Hisdal, Phys. Review, 105, (1957) 1821.
5. L. Rodriguez, R., L. Vazquez and A.P. Navarro “2-D model for runaway dynamics in tokomaks. Using a conservatrive numerical scheme”. Submitted for publication to J. Comp. Phys.
6. I. Fidone, G. Granata, R. L. Meyer, Phys. Fluids 25 (2), (1982), 2249.

## **ECH, CONFINEMENT — EXPERIMENTS**

# FIRST RESULTS OF ELECTRON CYCLOTRON HEATING ON W VII-AS

W. KASPAREK, G.A. MÜLLER,  
P.G. SCHÜLLER, M. THUMM  
Institut für Plasmaforschung,  
Universität Stuttgart,  
Stuttgart

V. ERCKMANN, W VII-AS TEAM<sup>1</sup>  
Euratom-IPP Association,  
Max-Planck-Institut für Plasmaphysik,  
Garching

Federal Republic of Germany

## Abstract

During the first period of 70 GHz ECRH experiments on W VII-AS electron heating at second harmonic and fundamental resonance has been investigated. Plasma build-up from neutral gas and electron heating with quasi-stationary plasma behaviour at microwave pulse lengths up to 500 ms with a power level up to 0,5 MW could be attained. Owing to the flexibility of the quasi-optical microwave beam injection antenna, different energy deposition profiles were realized. For central energy deposition peaked  $T_e$  profiles ( $T_{e0} = 1.2$  keV,  $n_{e0} = 3 \cdot 10^{19} \text{ m}^{-3}$  at  $B = 2.5$  T with  $P_{rf} = 380$  kW) were measured, whereas with off-axis heating flattened  $T_e$  profiles were observed. The microwave absorption efficiency was deduced from single-pass absorption measurements. The measured values at fundamental ( $\sim 70\%$ ) and second harmonic resonance ( $> 90\%$ ) are in good agreement with theoretical calculations. Experiments with EC current drive were successful in compensating the pressure driven bootstrap plasma current. With the variation of the  $k_{\parallel}$  value of the wave by change of the toroidal launching angle different current drive scenarios could be verified.

---

## 1. Introduction

One of the requirements for the stellarator approach to plasma magnetic confinement is a non-ohmic electron heating avoiding disturbances of the toroidal magnetic configuration by a toroidal plasma current. Electron cyclotron resonance heating (ECRH) by wave particle resonant interaction at the gyrofrequency of the electrons or at their harmonics is a direct way of energy transfer from an electromagnetic wave launched from the outside into the plasma. Owing to the resonance effect the energy transfer is localized in the inhomogeneous toroidal magnetic field. This localization of the energy deposition allows the programming of a well defined heating profile for modelling of the temperature distribution, as well as the generation of heat waves used for transport diagnostics by temporal modulation of the wave power. In addition the localized absorption of wave energy is con-

---

<sup>1</sup> The members of the W VII-AS Team are identified in the paper entitled 'Status of the advanced stellarator Wendelstein W 7AS: first results and further programme', these proceedings, p. 25.

nected with the localized parallel momentum transfer from the wave to the electrons, a method for toroidal current drive when the wave is launched with some wavenumber  $k_{\parallel}$  parallel to the magnetic field. This localized current drive is a means of counteracting the pressure driven bootstrap current to maintain net current free configurations. In addition this current drive can be used to modify slightly the  $t$ -profile by introducing some additional shear to the magnetic field.

All these types of wave plasma interaction at ECR were tested in the first period of experiments on the newly installed W VII-AS stellarator. Some typical results are presented in the following sections.

## 2. Wave launching and detection

The magnetic field configuration of the W VII-AS stellarator is of the linked mirror type. The magnetic surfaces at the five toroidal positions of the magnetic field maxima on the magnetic axis have the shape of nested upstanding ellipses [1]. Electron heating by ECR at this position offers several advantages: The gradient of  $|B|$  in radial direction has a maximum in this plane which localizes absorption. Owing to the elongation of the magnetic surfaces which determine the equidensity contours of the plasma, the irradiating RF-beams are nearly normal to these surfaces if they are launched radially inwards. This minimizes the effect of ray bending due to density gradients allowing central plasma densities near the cut-off value.

To meet the requirements for programmable energy deposition profiles and RF-current drive, up to 4 microwave beams with Gaussian shape are launched from circular waveguide antennas via focusing ellipsoidal mirrors into the plasma from the low magnetic field side. The angle of injection with respect to the toroidal and poloidal direction can be varied by tilting the mirrors. The beam diameter at the plasma center is approx. 6 cm. Each launcher is supplied by a 70 GHz CW gyrotron via a transmission line of about 60 m length containing elements for power monitoring and controlled mode conversion from the circular symmetric  $TE_{02}$  gyrotron output mode to the linearly polarized  $HE_{11}$  mode in the launching antenna [2]. Up to 200 kW microwave power at 70 GHz with a pulse length of up to 3 s is radiated in one beam. The polarization of the beam can be changed from linear to right- or left-handed elliptical polarization to meet the accessibility condition for plasma wave penetration without reflection for different launching angles with respect to the direction of the magnetic field.

For enhanced wave absorption the nonabsorbed part of the beam is reflected back into the plasma in a controlled polarization state from a graphite mirror installed at the inner wall of the plasma chamber, opposite to the launching system. This mirror is equipped with an array of polarization sensitive coupling holes (monomode waveguides) which allow the monitoring of the beams which have passed the plasma. The beam quality without plasma as well as beam absorption and deflection by the plasma can be measured.

## 3. Experimental results

Up to now 3400 shots with ECRH were explored on W VII-AS. Up to 3 beamlines with total injected power of 560 kW were in operation. Most of the experiments were performed with one or two beamlines at pulse lengths up to 500 ms. Plasma breakdown and build-up from neutral gas to temperatures above 200 eV can be achieved by one microwave beam with a power of 150 kW whenever the resonance layer is within the confinement region.

### 3.1. Plasma parameters with ECRH at 70 GHz

#### 3.1.1. Second harmonic heating

Most of the experiments up to now were performed at a magnetic field of  $B = 1.25$  T. The wave is absorbed at the resonance layer where  $\omega = 2 \cdot \omega_{ce}$ . The wave is polarized perpendicular to the magnetic field (X-mode) thus it is absorbed in the first pass through the plasma with high efficiency. Plasmas with central densities of just below  $n_{ec} = 3 \cdot 10^{19} \text{ m}^{-3}$ , the cut-off density for wave propagation, could be produced.

In long pulse (0.4 s) quasi-stationary operation, at optimal  $\tau$  value of 0.53, a central electron temperature of  $T_{eo} = 1$  keV was obtained at an axial density of  $n_{eo} = 1.5 \cdot 10^{19} \text{ m}^{-3}$  with 200 kW injected microwave power.

#### 3.1.2. First harmonic heating

About 300 discharges were investigated at fundamental resonance with  $B = 2.5$  T. In this case the wave, polarized parallel to  $B$  (O-mode), launched from the low magnetic field side can penetrate into the plasma whereas an X-mode is reflected at the outer plasma edge. In this case for O-mode propagation the cut-off density is  $n_{ec} = 6 \cdot 10^{19} \text{ m}^{-3}$ . With 200 kW microwave power  $T_{eo} = 1.5$  keV was obtained at  $n_{eo} = 1.5 \cdot 10^{19} \text{ m}^{-3}$  in long pulse quasi-stationary conditions at  $\tau = 0.34$ . With 370 kW power at the same conditions but with increased gas puffing an axial density of  $3 \cdot 10^{19} \text{ m}^{-3}$  was achieved with  $T_{eo} = 1.3$  keV.

### 3.2 Measurements of wave absorption

One of the main parameters for the evaluation of the energy balance in the plasma is the fraction of absorbed microwave power. This fraction is measured by the wave absorption in one transit through the plasma. If the single-pass absorption is about 70% or higher, the second pass via reflection from the inside mirror leads to more than 90% total absorption in the plasma core. Less than 10% of the power is absorbed in an uncontrolled way. The single-pass absorption is measured at the monitor coupling hole array in the surface of the inner reflector. These measurements are compared with the results of a 3 D ray code [3]. This code moreover calculates the energy deposition profile required for transport codes [4].

In the case of second harmonic heating nearly full single-pass absorption is observed.

The O-mode absorption at fundamental resonance shows a temperature and density dependence as predicted by theoretical calculations. At  $T_{eo} = 1.5$  keV and  $n_{eo} = 1.5 \cdot 10^{19} \text{ m}^{-3}$  70% single-pass absorption was found experimentally in agreement with the numerical code.

### 3.3 Temperature profile shaping

The microwave beams illuminating the plasma can be moved in poloidal direction by pivoting a pair of the mirror antennas. If the resonance layer is crossing the plasma center the energy deposition will be concentrated there when both beams are crossing the center. If the beams are moved up and down, respectively, the energy deposition moves to the outer magnetic surfaces. Fig. 1 shows temperature and density profiles with on-axis and off-axis deposition at  $r_{eff} = 8$  cm. In Fig. 2 the numerical simulation with the ray code of the off-axis deposition is shown. Even in this case the X-mode is fully absorbed in the first pass.

### 3.4 EC current drive experiments

By moving the mirror antennas in toroidal direction the  $k_{||}$  value of the wave can be varied. Therefore a momentum parallel to the magnetic field can

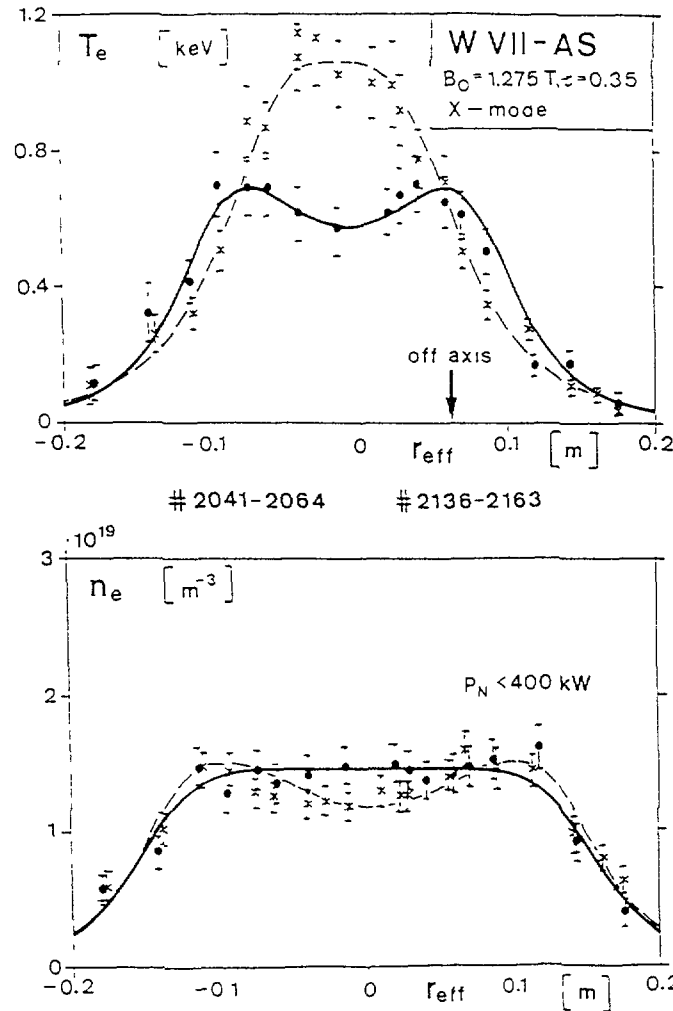


Fig.1: Temperature and density profiles with on-axis and off-axis ( $r_{\text{eff}} = 8$  cm) energy deposition.

be transferred to the electrons when the wave is absorbed, which means that a toroidal current will be generated. This current has a density distribution which depends on the absorption profile changing the internal  $\psi$  profile. In a first step of investigation concerning this RF current drive method the loop voltage generated by the wave was measured. This voltage in the OH circuit of the stellarator used in a feed back loop holds the net toroidal current to zero [5]. Fig. 3 shows the change in the loop voltage induced by the wave as a function of the wave injection angle with respect to the radial launch. The measurements were performed with RF-current drive in co- and counter-direction to the bootstrap current. In the analysed experimental case a maximum of the induced voltage appears at a launching angle in toroidal direction of about  $10^\circ$ . Without feedback circuit this voltage induces a current of about 4 kA which means an RF current drive efficiency of 20 A/kW. These results are also theoretically analysed with the ray code and a kinetic particle code [3].

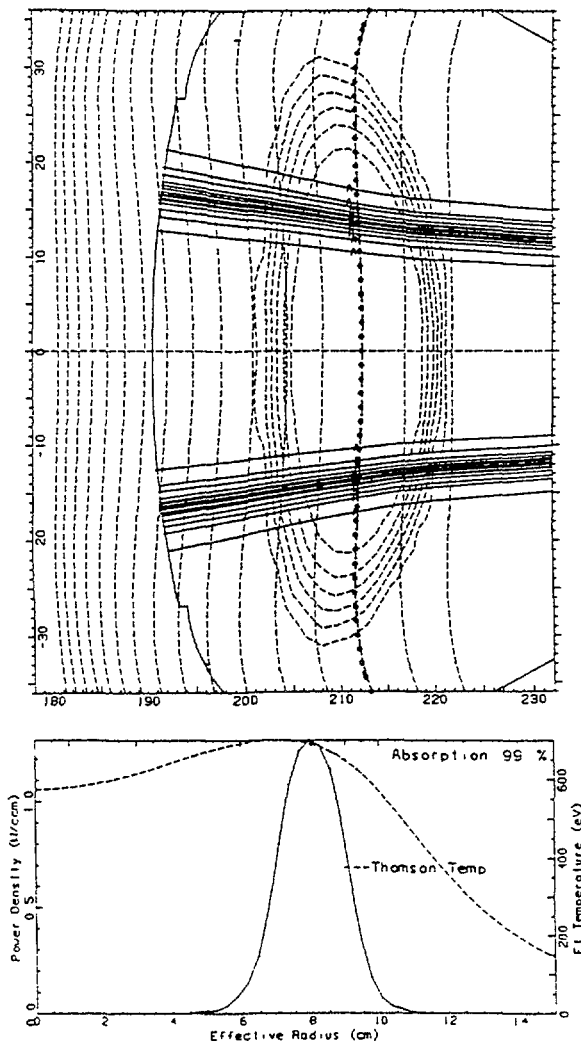


Fig.2: Numerical simulation of the off-axis deposition with the ray code.

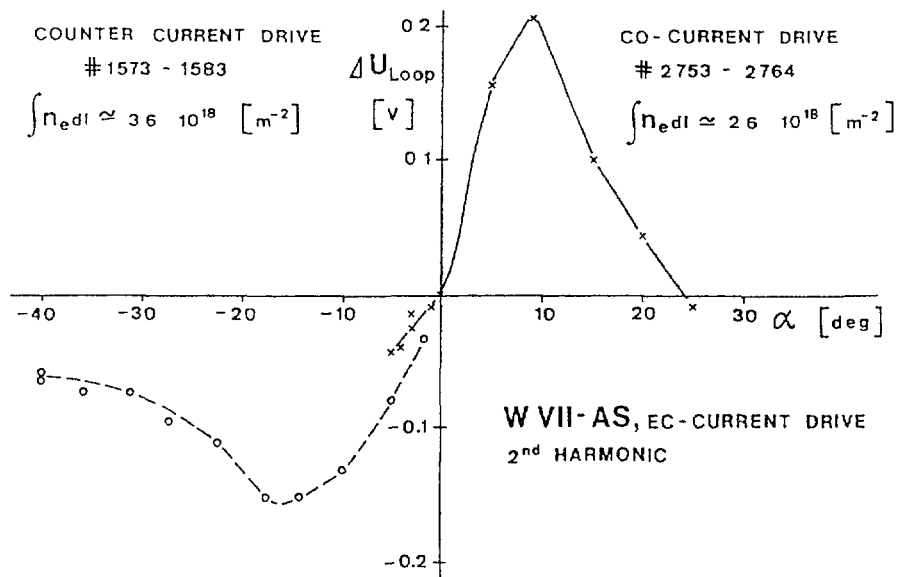


Fig.3: Induced loop voltage by ECR absorbed waves (X-mode) as a function of wave launching angle. ( $0^\circ$  means perpendicular to B).

## References

- [1] Brossmann, U., Dommaschk, W. et al., Plasma Physics and Controlled Nuclear Fusion Research (Proc. 9th Conf. Baltimore 1982) Vol. 3, IAEA, Vienna (1983), p. 141.
- [2] Kasperek, W. et al., Proc. 15th Symp. on Fusion Techn. (SOFT), Utrecht (1988), B 19.
- [3] U. Gasparino et al., this workshop
- [4] H. Maaßberg et al., this workshop
- [5] H. Renner et al., this workshop

# ELECTRON CYCLOTRON HEATING EXPERIMENTS IN CHS

H. IGUCHI and the CHS GROUP<sup>1</sup>

Institute of Plasma Physics,  
Nagoya University,  
Nagoya, Japan

## Abstract

Electron cyclotron heating with 28 GHz gyrotron has been carried out in a low-aspect-ratio helical system CHS. Spatial profiles of electron density and temperature are measured in various heating and magnetic configurations. It is shown that the drift motion of the trapped particles across the magnetic surfaces play an important role in the energy transport in electron cyclotron heated currentless plasmas, especially in a low collisionality regime. It is concluded that optimization of particle orbit is of primary importance even for electron confinement in low aspect ratio helical systems like CHS.

---

## 1. Introduction

In the Compact Helical System(CHS), plasma aspect ratio as low as 5 is achieved by introducing the pitch modulation  $\alpha^* = 0.3$ , where the loss cone is enlarged in comparison with normal winding. CHS is designed to study on the optimum magnetic field configuration by changing magnetic shear, magnetic well, helical ripple and so on, which can be done through magnetic axis shift by vertical field control. Main purpose of ECH experiments in CHS is a radially resolved transport study of a currentless plasma in a low-aspect-ratio helical system, especially in a low collisionality regime. Here we report the experimental results on the electron cyclotron heating with 28 GHz gyrotron at the power level around 100 kW, in which plasma parameters range:  $n_e = (2 - 6) \times 10^{12} \text{ cm}^{-3}$  and  $T_e = 200 - 900 \text{ eV}$ . Experiments have been performed in various heating (on axis and off axis) and magnetic configurations (magnetic axis shift).

## 2. Global Confinement

Microwave is injected from an inside port of the torus with a typical pulse duration of 40 ms. Hydrogen plasma is produced and heated, and its density is controlled by gas puffing combined with a small amount of prefill which is introduced to suppress hard X-rays at the start-up of the

---

<sup>1</sup> The members of the CHS Group are identified in the paper entitled 'Overview of CHS experiment', these proceedings, p. 51.

main helical field. In the standard operation, the magnetic axis is located at  $R_{ax} = 97.4$  cm and the average plasma radius is 20 cm. Plasmas reach quasi-steady state within 10 ms from the initiation of ECH and most of the data point in the experiments are taken at 12 - 16 ms. Figure 1 shows the ECH power dependence of the central electron temperature and the density (left), the line averaged electron density and the pyroelectric detector signal which is a measure of total radiation loss power(right). At power levels below 50 kW the line averaged electron density increases with increasing the ECH power but the electron temperature remains low. The radiation loss increases in proportion to the ECH power. The data indicate that the radiation power is comparable to the input microwave power.

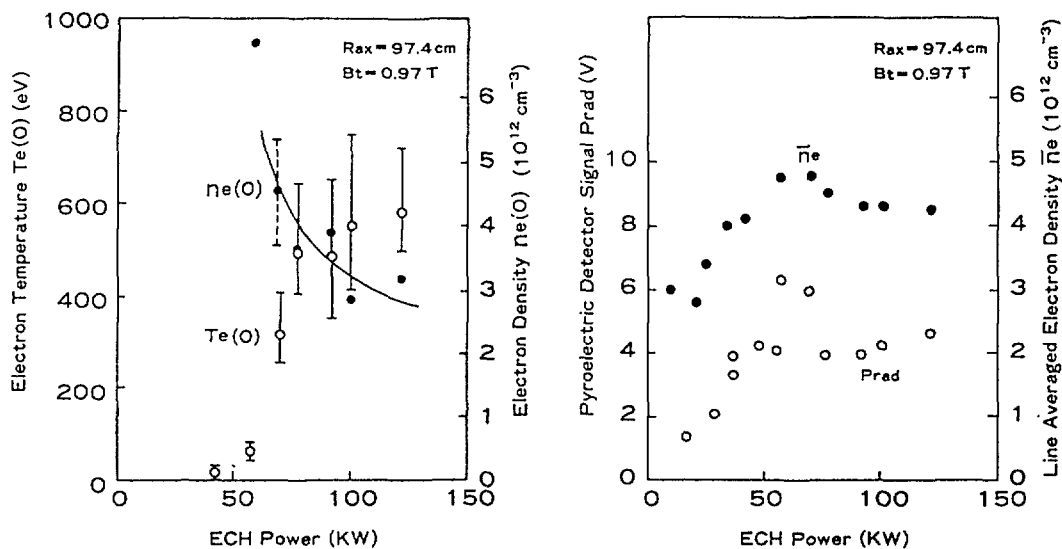


Fig. 1 ECH Power dependence of central electron temperature and density measured by Thomson scattering (left) and ECH power dependence of line averaged electron density and pyroelectric detector signal which is the measure of the total radiation loss(right).

Above the threshold power the electron temperature abruptly increases up to 600 eV at the ECH power of 100 kW. The line averaged density remains almost constant in this range while the central density decreases with increasing the ECH power. From the behavior of the pyroelectric detector signal, we estimate the power lost through impurity radiation to be about 40 % at 100 kW injection. This estimate is consistent with that from the results of soft X-ray spectrum analysis<sup>1)</sup>, which indicates the oxygen concentration of a few percent before radiation collapse. The electron density and the temperature profiles are measured by Thomson scattering. Total electron kinetic energy is calculated from the profile data

to be about 90 Joule, while the total stored energy measured by a diamagnetic coil is 120 Joule. Thus the global confinement time is about 2 ms. A simple neoclassical estimate with Kovrizhnykh's formula evaluated at half plasma radius gives a confinement time of several milliseconds for a flat density and the measured temperature profile. The effect of pitch modulation is not taken into account in the estimate. Although the transport in the central region is most likely dominated by neoclassical process, there is a discrepancy between the experiment and the simple neoclassical estimate.

### 3. Hollow Density Profile

In low density and high temperature operation, the electron density profile exhibits a hollow profile <sup>1)</sup>, and the hollowness defined by  $n_e(\text{center})/n_e(\text{peak})$  is enhanced with less collisionality and is sometimes up to 40 %. Now they are measured in off axis heating case with the same microwave power and the same magnetic field configuration except slightly reduced magnetic field strength. The results are compared in Figure 2. The data with on axis heating are the same as reported previously<sup>1)</sup>, but the density scale is readjusted with help of the data from

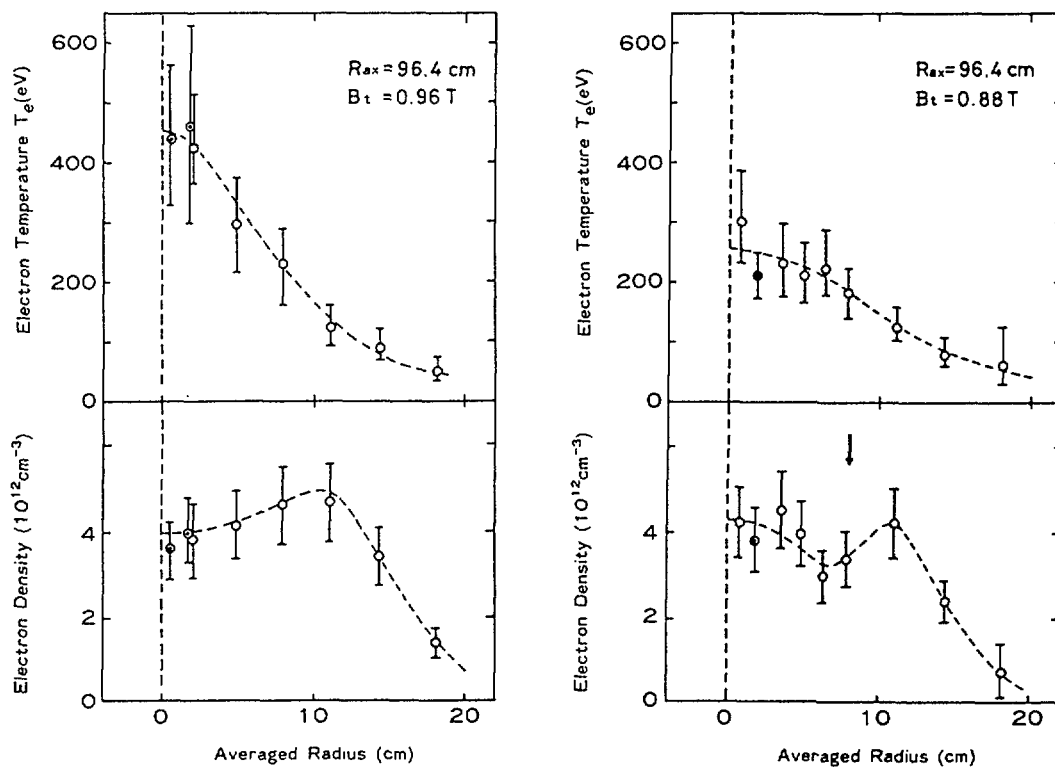


Fig. 2 Spatial profiles of electron temperature and density for on axis and off axis electron cyclotron heating. The arrow indicates the inner-most electron cyclotron resonance zone for off axis heating.

a 4 mm microwave interferometer. Furthermore, three data points are eliminated because they are concerned with the discharges where 28 GHz klystron(2 kW) for pre-ionization was accidentally turned off. Data points are re-plotted as a function of averaged radius and double circles are data at opposite side with respect to the magnetic axis. In the case of on axis heating, the electron collision frequency is on the boundary between plateau and  $1/\nu$  regime within half plasma radius. It is observed that the electron density is depressed near the electron cyclotron resonance zone, that is, with off axis heating the density dip appears near the inner most electron cyclotron resonance zone where the microwave power absorption seems to be maximum, and the central electron density recovers. The electron pressure profiles are compared between two cases in Fig. 3. It should be noticed that the electron kinetic energy has a centrally peaked profile in spite of no resonance zone in the central region for off axis heating, although the profile is not so strongly peaked as in the on axis heating. The hollow density profile has been observed in Heliotron-E at high power electron cyclotron heating, and it is discussed as a density clamping phenomena commonly observed in ECH experiments<sup>2)</sup>. In CHS, the density hollowness is more conspicuous in spite of lower microwave power density (The plasma volume is about one half of that in Heliotron-E). Those results indicate that direct energy and particle flow associated with particle drift motions across the magnetic surfaces cannot be ignored in comparison with diffusion processes.

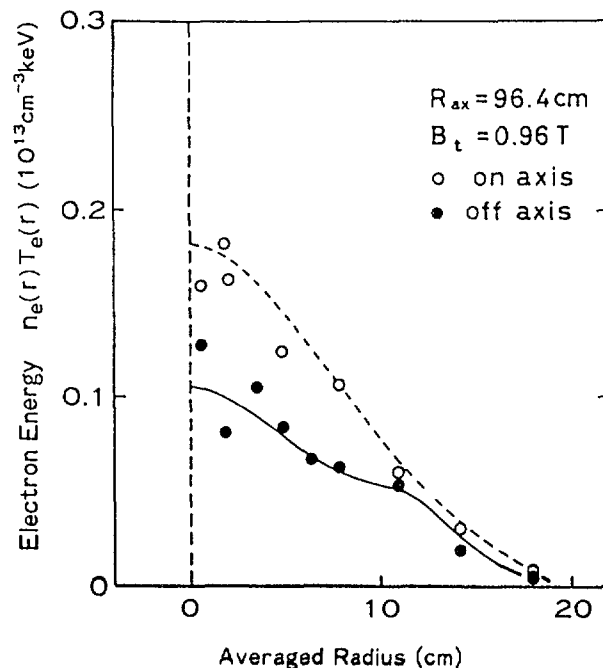


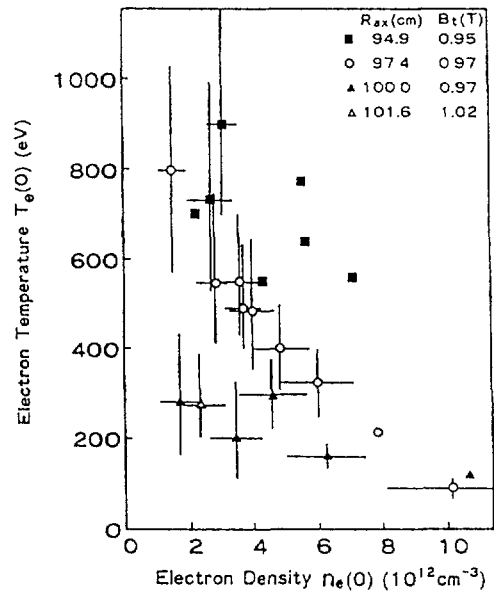
Fig. 3 The electron pressure profiles for on-axis and off-axis electron cyclotron heating calculated from  $n_e$  and  $T_e$  data in Fig.2.

Qualitative explanation for the hollow density profile is possible with the theory by K. Itoh et.al.<sup>3)</sup>. It is pointed out that enhanced transition from passing particle to trapped particle by electron cyclotron heating causes particle pump out from the central region. This effect is more serious in a low aspect ratio helical system like CHS. Centrally peaked electron pressure profile observed with off axis heating comes from the same process but the opposite direction of the energy flow. Electron cyclotron heating gives perpendicular energy to electrons near the resonance and those energetic electrons can drift into the central region across the magnetic surfaces and deposit their energy there. Even if the fraction of those power is rather small, good confinement in the central region may support peaked pressure profile. Discrepancy of the experimental results from the simple neoclassical estimate might partially be explained by this process, for which detailed analysis by computer code with CHS magnetic field configuration is necessary. Information on the power absorption profile and radiation loss profile is required there, and those diagnostics are under preparation.

#### 4. Magnetic Axis Shift

Intending to optimize magnetic field configuration in low-aspect-ratio helical systems, we tried to vary the position of the magnetic axis by vertical field control. Several parameters characterizing the confinement magnetic field structure such as magnetic shear, magnetic well, plasma wall clearance and so on are changed with the shift of the magnetic axis as discussed in Ref.4. Spatial profiles of the electron temperature and the density and the total electron kinetic energy calculated from them are compared among three different magnetic axis positions ( $R_{ax} = 94.9$  cm, 97.4 cm, 101.6 cm). It is noted that the total electron kinetic energy as well as the central electron temperature has the highest value for inward shift ( $R_{ax} = 94.9$  cm). The total stored energy measured by the diamagnetic coil shows similar tendency<sup>4)</sup>. Figure 4 shows the central electron temperature versus the central density measured by Thomson scattering for typical four positions of the magnetic axis. Each data point with an error bar is an average over several to ten shots. In the two cases of the outward shift of the magnetic axis with slightly different resonance locations, the central temperature is limited at around 300 eV, while it reaches up to 900 eV for inward shift ( $R_{ax} = 94.9$  cm). The data point without error bar is taken every shot for different amount of gas puffing, and the plasmas are transient at high densities above  $5 \times 10^{12}$  cm<sup>-3</sup>. It is clear again that higher central electron temperature is attained with inward shift of the magnetic axis. Two possible explanations have been discussed. Firstly, the power deposition profile is more peaked with inward shift, because the magnetic field ripple on the magnetic axis becomes small with inward shift and vanishes at  $R_{ax} = 94.9$  cm. Secondly,

Fig. 4 Central electron temperature and density diagram for four different positions of the magnetic axis. Data points with error bars are taken by averaging over several shots in steady states. Data points without error bar are taken by one shot measurement for different amount of gas puffing and plasmas at high densities are in transient state.



shift of the drift axis for trapped particles from the magnetic axis becomes small with inward shift, which reduces the radial transport. In view of particle confinement, the latter effect seems to be important, because the loss cone is reduced with inward shift. However, measurements of power deposition profiles are necessary again in order to get the final conclusion on the magnetic axis shift.

## 5. Summary

The electron cyclotron heating with 28 GHz gyrotron has been carried out in the low aspect ratio helical system CHS. In order to study the electron transport, especially in a low collisionality regime, spatial profiles of electron density and temperature are measured for various heating and magnetic configurations. It is shown that the direct energy transport across the magnetic surfaces through drift motions of trapped electrons with higher energy than thermal ones plays an important role and thus the transport is enhanced from the simple neoclassical model. It is concluded that optimization of particle orbit is of primary importance even for electron confinement in low-aspect-ratio helical systems like CHS.

## REFERENCES

- 1) K. Matsuoka, et. al., in Proc. 12th Intern. Conf. Plasma Physics and Controlled Fusion Research (Nice, 1988) IAEA-CN-50/I-I-3.
- 2) H. Zushi, et. al., Research Report of Plasma Physics Laboratory, Kyoto University, PPLK-R-27(August, 1988).
- 3) K. Itoh, et. al., *ibid.* PPLK-R-25(May 1988).
- 4) S. Okamura, et. al., in Proc. 16th European Conf. Controlled Fusion and Plasma Physics (Venice, 1989) and Research Report of Institute of Plasma Physics, Nagoya University, IPPJ-

## POWER BALANCE STUDIES FOR RF HEATED PLASMA IN THE URAGAN-3 TORSATRON

V.L. BEREZHNYJ, M.P. VASIL'EV, V.S. VOJTSENYA,  
E.D. VOLKOV, Yu.V. GUTAREV, A.G. DIKIJ,  
G.V. ZELENIN, B.V. KRAVCHIN, S.V. KOVALEV,  
V.G. KONOVALOV, V.I. KONONENKO, V.D. KOTSUBANOV,  
G.G. LESNYAKOV, A.P. LITVINOV, Yu.K. MIRONOV,  
N.I. NAZAROV, I.K. NIKOLSKIJ, O.S. PAVLICHENKO,  
I.I. PATLAY, V.K. PASHNEV, V.V. PLYUSNIN,  
N.F. PEREPEL'KIN, A.I. SKIBENKO, A.S. SLAVNYJ,  
V.S. TARAN, T.O. TKHORYAK, S.I. FEDOTOV, I.P. FOMIN,  
A.N. SHAPOVAL, O.M. SHVETS, V.M. ZALKIND

Institute of Physics and Technology,  
Ukrainian Academy of Sciences,  
Khar'kov, Union of Soviet Socialist Republics

### Abstract

Power balance of RF heated currentless plasma in the Uragan-3 torsatron has been studied for low density quasi-stationary discharges ( Q-discharges [1] ). It was shown that the most part of RF power is absorbed and dissipated by a cold plasma mantle surrounding a hot plasma core. In the hot core energy losses are determined by electron heat conductivity and radiation.

### 1. INTRODUCTION

Studies of currentless plasma production and heating by RF waves in the  $\omega \approx \omega_{ce}$  frequency range in the Uragan-3 torsatron resulted in a revelation of regime of quasi-stationary discharges with ion temperature up to 1,1 KeV and average beta up to 0,6% [1]. Highest ion temperature and plasma energy content realized at low electron density ( $\bar{n}_e = (2+3) \cdot 10^{12} \text{cm}^{-3}$ ). The electron density increase resulted in the decrease of the ion temperature and energy content of plasma as well.

To understand the reason of this degradation of plasma energy it is necessary to analyze the power balance of RF plasma.

This report presents the results of the power balance studies in low density Q-discharges performed for the Uragan-3 torsatron before device shutdown in March 1988.

### 2. THE EXPERIMENT

The Uragan-3 torsatron has been operated with a confining field 4,4 KG. Hydrogen RF discharges were produced by one antenna which radiated the power of 0,2-0,3 MW at  $\omega \approx 0,8 \cdot \omega_{ce}$ .

Principal diagnostics were described in a paper [1]. In this experiment electron density profiles were reconstructed from multichord interferometer data ( $\lambda = 8; 2; 1; 0,337 \text{ mm}$ ).

The NPA with a vertical line-of-sight scanning was used for the ion temperature profile studies. Electron temperature profiles were reconstructed from a single-point Thomson scattering data ( at the plasma axis), spectroscopic data ("carbon thermometer" at  $r = 0.7a$  ) and electric probe data ( at the plasma edge). Hydrogen atom density profiles were determined from the  $H_{\beta}$ - line profiles. Radiation and charge exchange loss power  $P_{rad}$  was measured by a collimated pyroelectric detector. Total plasma energy content  $W_T$  was measured by a saddle-type magnetic coil.

### 3. RESULTS AND DISCUSSION

Figure 1 shows the time behaviour of the plasma parameters in the studied Q-discharges. Figure 2 shows  $T_e, T_i, n_e$  profiles measured at the time moment shown by an arrow at Fig.1. Electron temperature and density profiles were narrower than ion temperature one. Hydrogen atom density profile was rather flat inside of  $r < 0,8a$  ( $n_H = 1,7 \cdot 10^9 \text{ cm}^{-3}$  ). Volume averaged loss power measured by the pyroelectric detector is equal 5 kW. Saddle coil plasma energy content evaluation agrees (within an error of 30%) with data obtained from  $T, n$  profile measurements.

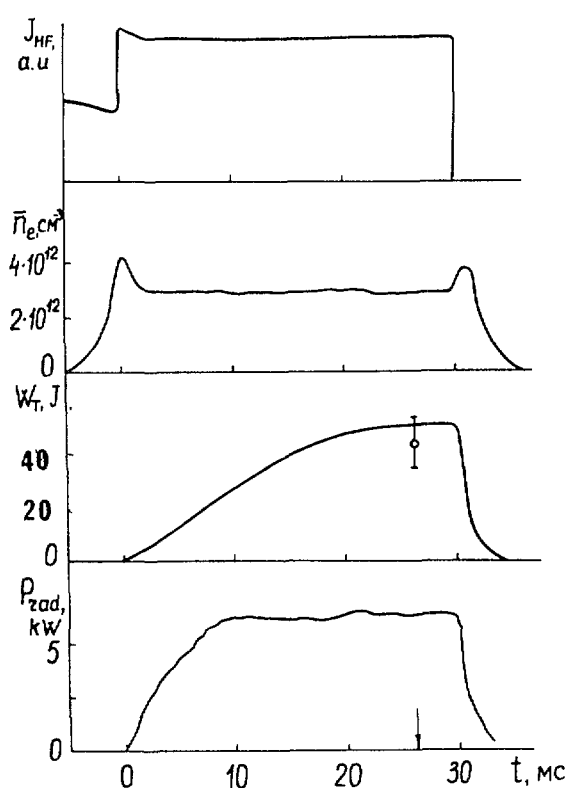


FIG. 1. The time behaviour of parameters ( $J_{HF}$ : antenna current,  $\bar{n}_e$ : electron density,  $W_T$ : total plasma energy,  $P_{rad}$ : radiated power).

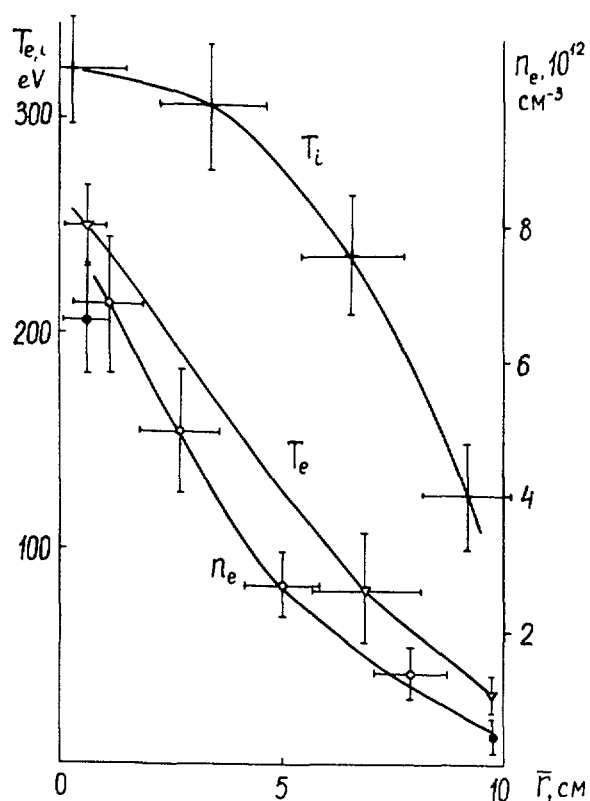


FIG. 2. Profiles of  $n_e, T_i, T_e$ . Black points on the  $n_e$ -profile: data obtained by Thomson scattering and by electric probes.

The RF power deposition profiles for electrons and ions are necessary for power balance calculations. Until now we don't have a reliable data on power deposition profiles. Therefore we have limited the power balance calculations for the decaying plasma ( $\Delta t \leq 0,5$  ms after RF power switch-off).

Figure 3 shows the time behavior of total plasma energy  $W_T$ ,  $W_{e+i}$  and ion and electron  $W_e$  energy after RF switch-off ( $W_{e+i} = W_e + W_i$ ).

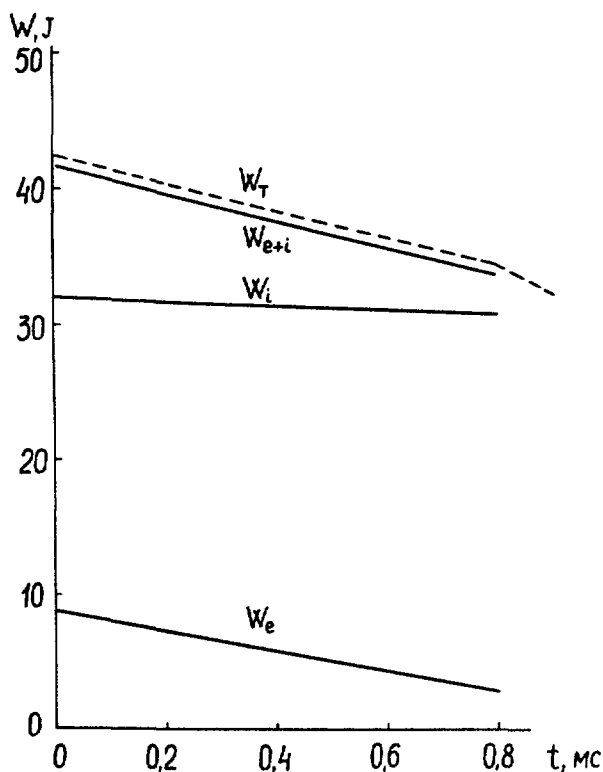


FIG. 3. Decay of energy after RF switch-off.

One can see that the total plasma energy decay rate is governed by a rapid electron cooling inspite of their minor role ( $\approx 20\%$ ) in the total energy content. The electron cooling is determined by the heat conductivity ( $P_{hc} = 5$  KW) and radiation ( $P_{rad} \approx 6$  KW) and slow ion cooling is determined by a charge-exchange losses ( $P_{cx} = 1$  KW). Ion-electron collisional heating is negligible ( $P_{ie} \approx 0,2$  KW).

In this regime the global energy confinement time  $\tau_E^*$  equals 5 ms, the electron heat conductivity time  $\tau_{hc}^e$  equals 1,5 ms. As the ion cooling time is governed by charge exchange mostly, one can have only minor estimate for the ion heat conductivity time  $\tau_{hc}^i \approx 30$  ms.

This power balance analysis showed that in this Q-discharges a small part of antenna radiated power ( $\approx 10\%$ ) is absorbed by a plasma core and ions and electrons are heated independently. High ion temperature is the result of a small power losses by ions.

It's worthwhile to compare estimates of ion and electron energy confinement times with the theory predicted ones [2].

In the studied regime the ions are in a banana regime ( $\nu_i^* \ll 0,5; \epsilon_H \ll \epsilon_t$ ), the electrons are in a plateau regime ( $\nu_e^* \approx 1$ ).

The ion energy confinement time estimate taking into account the profile data gives a value of  $\tau_{pe}^i \approx 20 \pm 65$  ms which doesn't contradict to experimental data. Electron heat losses are of the order of neoclassical value in the near-axis region, but two orders of value higher at the plasma edge ( $Z \approx 0,7a$ ), (Fig.4).

Strong hydrogen atoms "burning-out" in the plasma created in the large vacuum chamber ( $V = 70 \text{ m}^3$ ) filled by the hydrogen with a molecule density of  $2 \cdot 10^{18} \text{ cm}^{-3}$

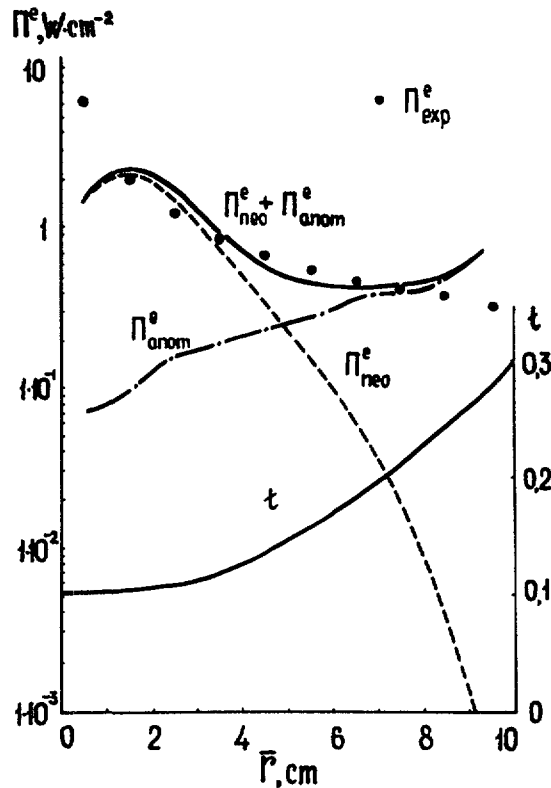


FIG. 4. Radial profiles of electron energy flux  $\Pi^e$ .  $\Pi_{neo}^e$ : neoclassical one [2],  $\Pi_{anom}^e$ : corresponding to

$$\chi_e = \frac{1 \cdot 10^{18}}{n_e \cdot T_e^{3/2}} \text{ cm}^2 \cdot \text{sec}^{-1}$$

needs an explanation. This "burning-out" may be the result of the plasma core screening by a plasma in an ergodic layer (target density  $f_{ped} \ell = 1 \cdot 10^{13} \text{ cm}^{-2}$ ,  $T_e = 15 \text{ eV}$ ) and a plasma mantle ( $n_e \approx 1 \cdot 10^{11} \text{ cm}^{-3}$ ,  $T_e \approx 5 \pm 10 \text{ eV}$ ) existing in the whole vacuum chamber ( $r = 2,5 \text{ m}$ ). Nearly 90% of RF power is absorbed and lost by this cold plasma mantle.

#### 4. CONCLUSION

The power balance studies for RF produced Q-discharges in the Uragan-3 toratron showed that the main part of RF power ( 90%) is absorbed by a non-confined plasma which is screening a hot plasma core hydrogen atoms coming from a vacuum chamber. The rest of power ( $\approx 10\%$ ) is lost from a hot plasma core mostly by electrons.

#### REFERENCES

1. V.L.Berezhnyi, N.T.Besedin, M.P.Vasil'ev, et al., Plasma Physics and Controlled Nuclear Fusion Research 1986, v.2, 497 ( 1987).
2. K.C.Djabilin, L.M.Kovrizhnykh, Fizika Plasmy (Sov.) 13, 515 ( 1987).

# EXPERIMENTAL STUDIES ON THE TOHOKU UNIVERSITY HELIAC

H. WATANABE, S. KITAJIMA,  
N. TAKEUCHI, M. TAKAYAMA  
Department of Nuclear Engineering,  
Faculty of Engineering,  
Tohoku University,  
Sendai, Japan

## Abstract

Recent experimental results on TU-Heliac are presented. This device is a small-size heliac without an inner  $l = 1$  helical winding around the central conductor. Measurements of magnetic surfaces have been done by electron beam method. Plasma is produced by ECRH. The enhanced diffusion due to the trapped particles was observed.

Interest in the helical axis stellarators such as heliacs, has been growing in the recent years due to many advantageous characteristics for plasma confinement<sup>(1-6)</sup>.

We present recent experimental results on Tohoku University Heliac (TU-Heliac). TU-Heliac is a small size heliac without an inner  $l=1$  helical winding around the central conductor. This conductor is installed inside the helically deformed vacuum vessel (Fig.1). The machine started operation in July 1988. The main device parameters are listed in Table I.

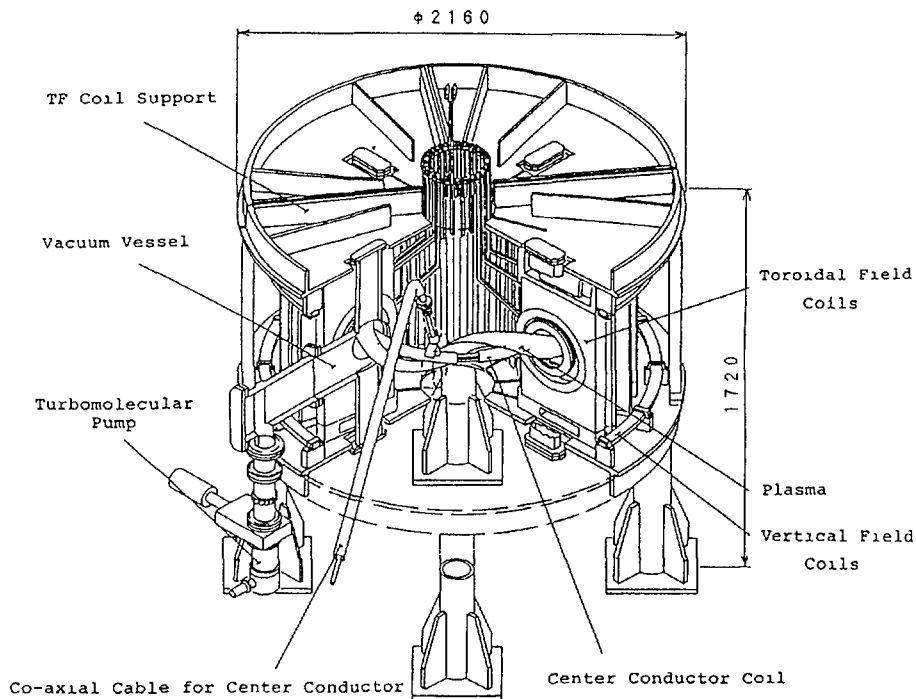


Fig. 1. Bird's eye view of Tohoku University Heliac (TU-Heliac).

TABLE I MACHINE PARAMETERS

No. of field periods	4
Major radius (m)	0.48
No. of TF coil	32
Mean TF coil radius (m)	0.19
TF coil swing radius (m)	0.08
VF coil location (m)	R= 0.9 z=±0.3
Max. Central ring current (kAT)	100
Flat top of CR current (ms)	12
Flat top of VF coil current (ms)	12
Flat top of TF coil current (ms)	20

### I. Magnetic Configuration

The magnetic coil systems of TU-Heliac consist of the toroidal field coils, the center conductor and the vertical field coils. Typical magnetic surfaces produced by these coil systems are shown in Fig. 2.

Figure 3 illustrates the variation with average radius, of the rotational transform  $\iota$  and of the specific volume  $V'$ .

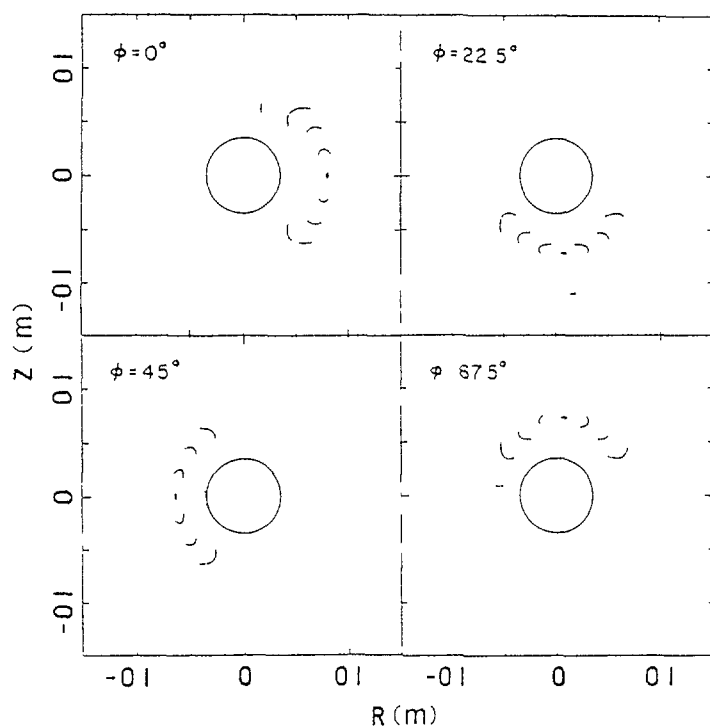


Fig. 2. Typical magnetic surfaces in constant toroidal angle planes shown for  $\phi=0^\circ, 22.5^\circ, 45^\circ$  and  $67.5^\circ$  with  $\chi_0=1.54$ ,  $I_c/(RH_0)=0.4$  and  $B_V/B_0=0.08$ .

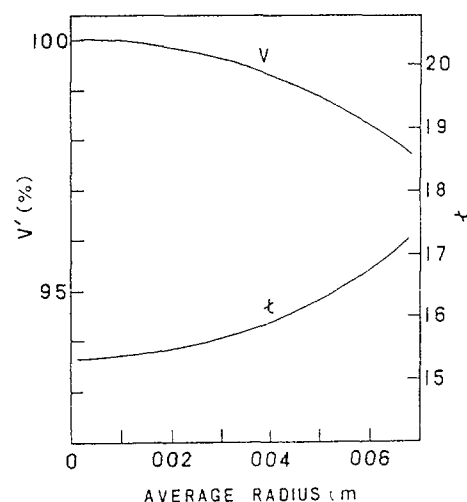


Fig. 3. Typical rotational transform profile  $\iota$  and specific volume  $V'$  for the same configuration of Fig 2

## II. Measurement of Magnetic Configuration Parameters

The broad predictions of the magnetic surfaces and the rotational transform computations have been experimentally confirmed by two methods of using a low energy electron beam. One is the resistance-capacitance method (R-C method) with the electron beam energy of 15.0 eV, a pulse length 2.0 ms and the other is the electron beam mapping method with 7.5 eV, 1.0  $\mu$ s pulse.

Principle of measurement by R-C method is as follows. The injected electrons accumulate on some magnetic surface. There appears capacitance  $C$  between electron cloud and the vacuum vessel and also there is a leakage resistance  $R$  illustrated in Fig. 4.

By moving the electron gun two-dimensionally on a meridian plane, one can get  $C$  and  $R$  corresponding to the location of the gun.

Plotting the contour lines of equi-resistance or equi-capacitance, we can get the approximate shape of the magnetic surfaces. One example of the surface measured by this method is shown in Fig.5. The shape of the experimentally obtained surfaces shows good agreement with the computed ones.

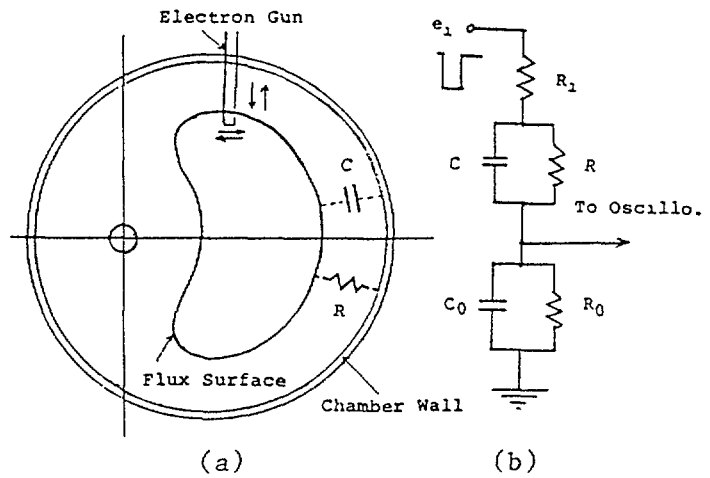


Fig. 4. (a); The injected electrons by the gun form  $C$  and  $R$  to chamber wall. (b); Equivalent circuit of the R-C method:  $R_1$ ; internal resistance of the gun,  $R_0$ ,  $C_0$ ; external resistance and capacitance.

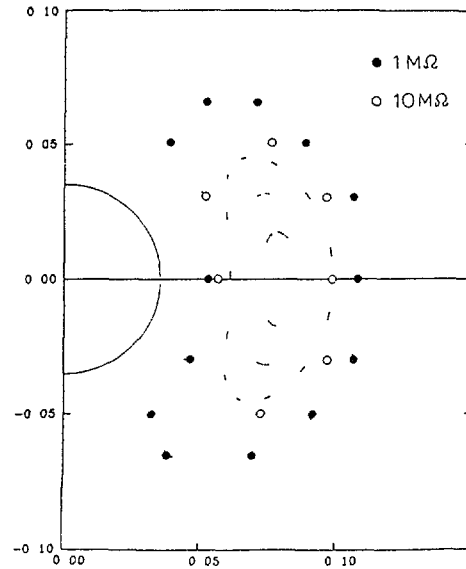


Fig. 5. Plots of constant equivalent resistance which is measured by R-C method. The computed magnetic surfaces are shown corresponding to the experimental results.

### III. Plasma Production by ECRH

Plasma is produced using ECRH of 2.45 GHz microwave source with 3 ms pulse of 3 kW peak power. The density and temperature are measured by Langmuir probe. The densities are  $n_e = 1 \times 10^9 \sim 3 \times 10^{10} \text{ cm}^{-3}$  and temperatures are  $T_e = 2 \sim 10 \text{ eV}$ . Working gas is argon at a pressure of  $5 \times 10^{-3} \text{ Pa}$ . In Fig.6, we show the radial profiles through the horizontal mid-plane, of ion saturation current by Langmuir probe for the case of  $I_c / (RH_o) = 0.4$ ,  $B_v / B_o = 0.09$  after 2.0 ms and 4.6 ms of microwave turned on and also show the computed magnetic surfaces under the same experimental conditions. Measurements of two-dimensional isolines of ion saturation current have been made to verify more clearly the existence of the bean shape equilibrium surface. Figure 7(a) corresponds to contour lines of ion saturation current after 2.0 ms of microwave on and (b) after 1.6 ms off with the same conditions of Fig.6. These shapes of contour lines clearly reflect those of the predicted magnetic surfaces.

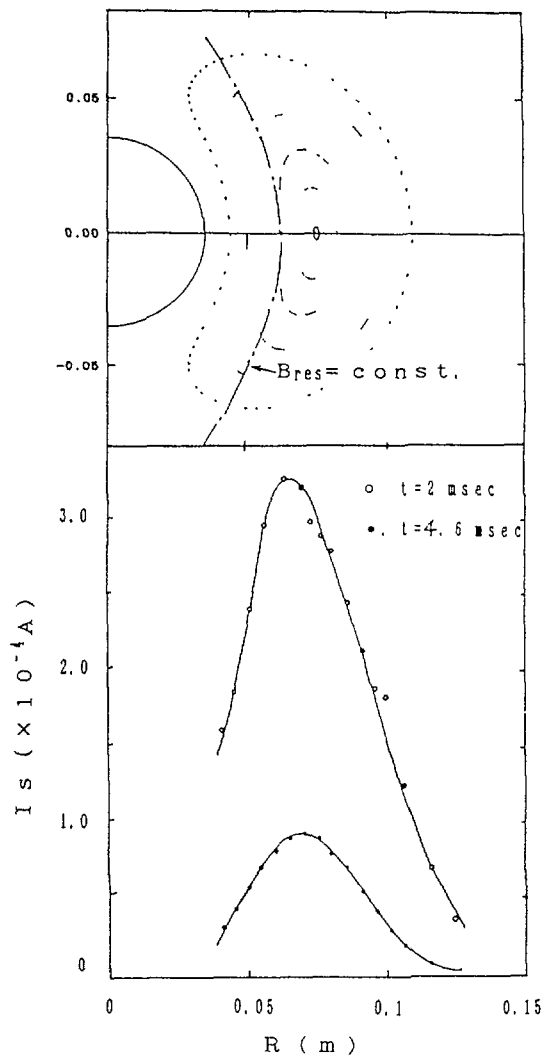


Fig. 6. The radial profiles of ion saturation currents after 2.0 ms and 4.6 ms of microwave on. The predicted magnetic surfaces under the same experimental conditions are also shown.

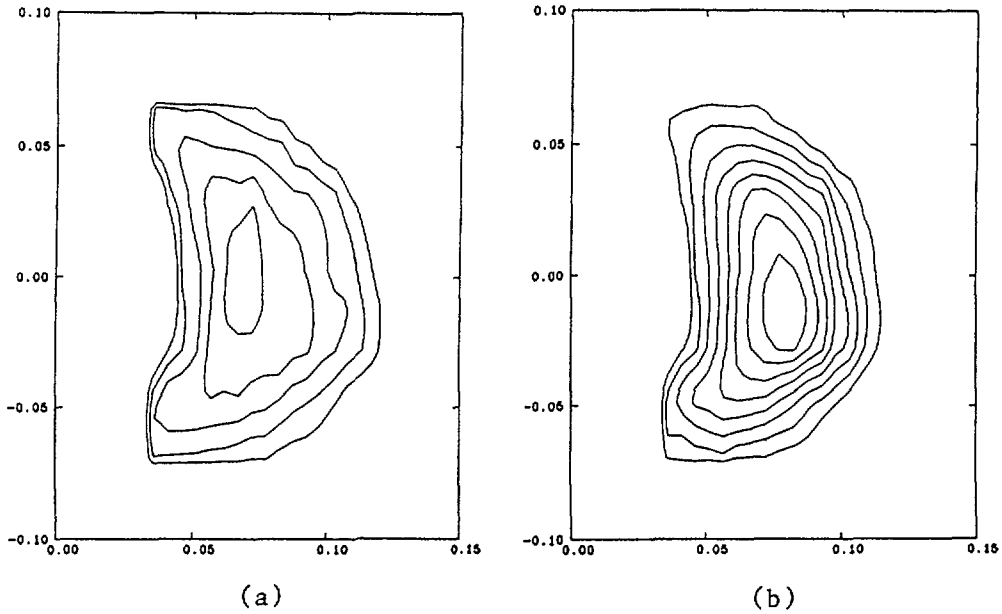


Fig. 7. Contour lines of ion saturation current after 2.0 ms of microwave on (a) and after 1.6 ms off (b) with the same conditions of Fig. 6.

Figure 8 shows the decay of the electron density and temperature of the afterglow plasma. Soon after ECRH is turned off, recombination which is proportional to  $n^2$  is dominant. After the density has reached a low value, diffusion becomes dominant and the decay is exponential. The observed diffusion coefficient is  $2.6 \times 10^3 \text{ cm}^2/\text{s}$  for  $B_0 = 0.9 \text{ kG}$ . This value is comparable with that of the enhanced helical ripple diffusion of the neoclassical theory.

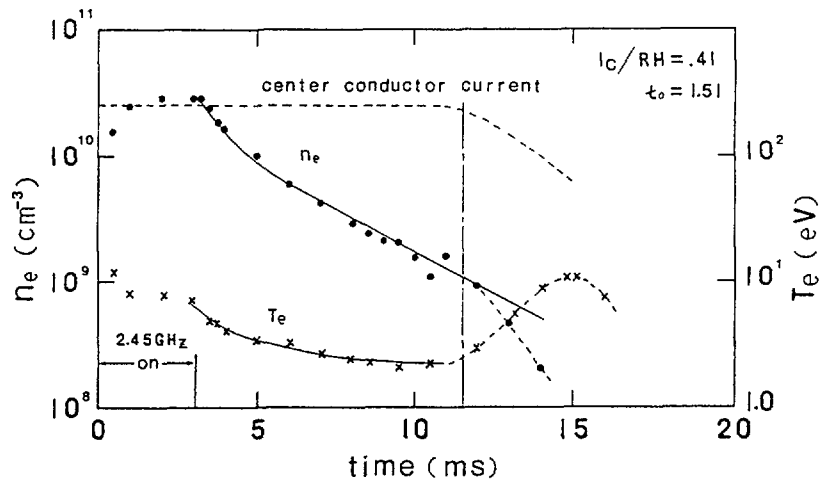


Fig. 8. The electron density vs time in the afterglow plasma produced by ECRH. The decay of electron temperature is also shown.

#### IV. Summary and Conclusions

(1) We have constructed a small size conventional heliac to study the many advantageous characteristics of the helical axis stellarators.

(2) Measurements of magnetic surfaces have been done by electron beam methods. The shapes of magnetic surfaces experimentally obtained show good agreement with the computed ones.

(3) Plasma is produced by ECRH of 2.45 GHz. Measurements of 2D isolines of ion saturation current have also shown the existence of the equilibrium surfaces in a heliac.

(4) The enhanced diffusion due to the particles trapped in the helical ripple of the field was observed.

#### ACKNOWLEDGEMENTS

The authors are indebted to Prof. N.Sato and Prof. M.Fujiwara for helpful suggestions and encouragement. Thanks are also due to Messrs. T.Zama, K.Takaya, T.Ando and T.Sugiura for experimental support in these studies. This work was supported by the Grant-in-Aid for Scientific Research from the Ministry of Education of Japan, No.63050005 and in part by the Grant from A & D Engineering Inc. (Tokyo, Japan).

#### REFERENCES

- (1) BOOZER, A.H., et al., in Plasma Physics and Controlled Nuclear Fusion Research 1982 (Proc. 9th Int. Conf. Baltimore, 1982), Vol.3, IAEA, Vienna (1983) 129.
- (2) YOSHIKAWA, S., Nucl. Fusion **23** (1983) 667.
- (3) BLACKWELL, B.D., et al., Nucl. Fusion **25** (1985) 1485.
- (4) HARRIS, J.H., et al., Nucl. Fusion **25** (1985) 623.
- (5) GUASP, J. and FABREGAS, J.A., Nucl. Fusion **26** (1986) 231.
- (6) SHI, X.H., et al., Nucl. Fusion **28** (1988) 859.

## **STABILITY STUDIES**

## SECOND STABILITY STUDIES IN ATF\*

J.H. HARRIS, M. MURAKAMI, B.A. CARRERAS,  
J.D. BELL<sup>1</sup>, G.L. BELL<sup>2</sup>, T.S. BIGELOW,  
L.A. CHARLTON<sup>1</sup>, N. DOMINGUEZ, J.L. DUNLAP,  
J.C. GLOWIENKA, H.C. HOWE, H. KANEKO<sup>3</sup>,  
R.R. KINDSFATHER<sup>4</sup>, J.N. LEBOEUF, V.E. LYNCH<sup>1</sup>,  
M.M. MENON, R.N. MORRIS<sup>1</sup>, G.H. NEILSON,  
V.K. PARÉ, N.F. PEREPELKIN<sup>5</sup>, D.A. RASMUSSEN,  
J.B. WILGEN, W.R. WING  
Oak Ridge National Laboratory,  
Oak Ridge, Tennessee,  
United States of America

### Abstract

Soft X-ray detectors and Mirnov coils were used to measure fluctuations in ATF plasmas. The beta-stabilization of the ideal MHD-modes permits the transition to second stability region at low value of the average plasma pressure.

The ATF torsatron was designed to study the physics of the ideal MHD second-stability regime, wherein the magnetic well produced by the outward Shafranov shift at finite- $\beta$  stabilizes interchange modes driven by unfavorable field-line curvature, which are the dominant instabilities for stellarators. As a result, the plasma is expected to become more stable as  $\beta$  increases (" $\beta$  self-stabilization"), with a potential reduction in the anomalous transport induced by the curvature-driven instabilities.

For the original ATF design assumptions (plasma aspect ratio  $A=7$ , central rotational transform  $\kappa_0 \approx 0.3$ , and edge transform  $\kappa_a \approx 1$ ), the  $\beta$  self-stabilization effect should dominate at  $\beta_0 \approx 5\%$ . Initial studies in early 1988 using electron-beam field mapping revealed substantial magnetic islands (now corrected) that acted as a magnetic limiter and effectively reduced the plasma radius to  $r_p \approx 0.6\bar{a}$  (increasing  $A$  to 10) and the effective transform to  $\kappa_a \approx 0.5$ . This led to a large increase in Shafranov shift ( $\delta/a \propto \beta_0 A / \kappa_a^2$ ) that enhanced the self-stabilization effect, making it possible to access the second-stability regime at modest values of  $\langle \beta \rangle < 0.5\%$ .

Soft X-ray detectors and Mirnov coils  $\sim 30$  cm outside the plasma were used to measure fluctuations in ATF plasmas produced by ECH ( $\leq 200$  kW) and NBI ( $\leq 1.4$  MW) with  $\langle \beta \rangle \leq 0.5\%$ . The soft X-ray signals show no evidence of instabilities. Spectral correlation analysis of the magnetic fluctuation signal ( $\tilde{B}_\theta$ ) reveals bands of high-coherence fluctuations in the frequency range 5-60 kHz with amplitudes  $\sim 10^{-3}$  G. The fluctuations show predominantly  $n=1$  toroidal mode symmetry, with a poloidal spectrum containing principally  $m=2$  and  $m=3$  components.

\* Research sponsored by the Office of Fusion Energy, US Department of Energy, under contract DE-AC05-84OR21400 with Martin Marietta Energy Systems, Inc.

<sup>1</sup> Computing and Telecommunications Division, Martin Marietta Energy Systems, Inc., Oak Ridge, TN, USA.

<sup>2</sup> Auburn University, Auburn, AL, USA.

<sup>3</sup> Plasma Physics Laboratory, Kyoto University, Kyoto, Japan.

<sup>4</sup> Present address: Igen, Inc., Rockville, MD 20852, USA.

<sup>5</sup> Institute of Physics and Technology, Khar'kov, USSR.

The amplitudes of the  $n=1$  component of  $\tilde{B}_\theta$  rise with  $\beta$  for  $\langle\beta\rangle \leq 0.2\%$ , but then saturate and decrease as  $\langle\beta\rangle$  exceeds  $0.3\%$  (Figure 1). This behavior can also be observed in the time history of individual discharges. The pressure profiles broaden substantially as  $\langle\beta\rangle$  increases to  $\sim 0.2\%$  (Figure 2).

Theoretical studies of the ideal Mercier stability of the reduced-radius ATF configuration show that the transition to second stability occurs at  $\langle\beta\rangle=0.3\%$ . While the plasma remains resistively unstable,  $\beta$  self-stabilization is found to decrease the saturation amplitude of these resistive modes. Multiple helicity calculations of resistive-interchange turbulence show that the magnetic fluctuation spectrum is dominated by  $(n, m) = (1, 2)$  and  $(1, 3)$  modes. These features are very similar to those observed in the experiment. The  $\beta$  self-stabilization of these instabilities results from the radial expansion of the region with magnetic well (Figure 2). When the pressure profile is allowed to broaden as  $\beta$  increases (as in the experiment), the calculations show that the plasma remains marginally stable along the path to second stability.

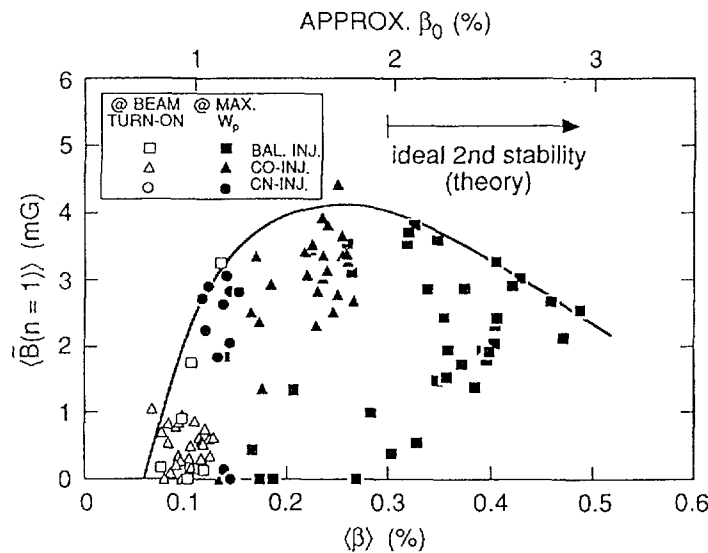


Figure 1. Dependence of rms (5-60 kHz) coherent  $n=1$  poloidal magnetic fluctuation amplitude ( $\langle\tilde{B}(n=1)\rangle$ ) on  $\langle\beta\rangle$ .

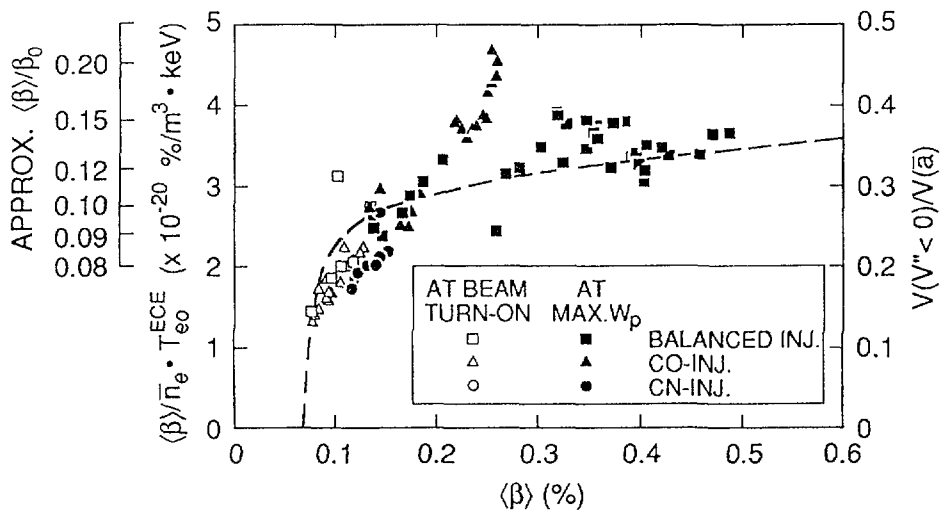


Figure 2. Profile broadening parameter ( $\langle\beta\rangle/\bar{n}_e T_{e0}^{ECE}$ ) versus  $\langle\beta\rangle$  for the same discharges shown in figure 1, and calculated plasma volume with  $V'' < 0$  (magnetic well)

# IDEAL LOW- $n$ AND MERCIER MODE STABILITY BOUNDARIES FOR $\ell = 2$ TORSATRONS\*

N. DOMINGUEZ, J.N. LEBOEUF,  
B.A. CARRERAS, V.E. LYNCH<sup>1</sup>  
Oak Ridge National Laboratory,  
Oak Ridge, Tennessee,  
United States of America

## Abstract

We studied the relationship between the stability properties of ideal low- $n$  internal modes and the three-dimensional (3-D) ideal Mercier criterion for  $\ell = 2$  torsatron configurations. For the low- $n$  stability studies, we used the stellarator expansion as implemented in the FAR code. The 3-D Mercier criterion was applied to equilibria calculated with the VMEC code. We found that (1) low- $n$  modes with singular surfaces lying in a Mercier region are, in general, unstable and (2) the critical beta given by the Mercier criterion agrees well with the critical beta for the lowest- $n$  unstable mode. This is verified even in the case of global  $n = 1$  modes. Therefore, the 3-D Mercier criterion is a useful guide in mapping the ideal stability beta limits for these torsatron configurations.

---

## INTRODUCTION

Gruber et al. [1] and Merkel et al. [2] compared the unstable regions and equilibrium beta limits for low- $n$  Mercier modes and high- $n$  ballooning modes for a helically symmetric equilibrium. We compared stability limits for ideal low- $n$  modes and Mercier modes for more general equilibria using different techniques.

## CONFIGURATIONS UNDER STUDY

The vacuum magnetic flux surfaces were generated from a magnetic field produced by currents in axisymmetric coils and  $\ell = 2$  helical coils having the winding law  $\phi = \phi_0 + \Theta/M$ , where  $\phi$  and  $\Theta$  are the geometric toroidal and poloidal angles.

---

\* Research sponsored by the Office of Fusion Energy, US Department of Energy, under contract DE-AC05-84OR21400 with Martin Marietta Energy Systems, Inc.

<sup>1</sup> Computing and Telecommunications Division, Martin Marietta Energy Systems, Inc., Oak Ridge, TN 37831, USA.

We studied torsatron configurations with different average plasma minor radius  $a_p$  and coil minor radius  $a_c$ , different numbers of field periods  $M$ , and different values of the rotational transform at the axis  $\iota_0$  and at the boundary  $\iota_a$ . These configurations had the following parameters:

$M$	$A_p$	$p_c$	$\iota_0$	$\iota_a$
10	7.6	1.27	0.45	0.95
12	7.8	1.44	0.33	0.98
14	9.2	1.31	0.52	1.45
19	10.0	1.38	0.50	2.3

Here  $A_p$  is the aspect ratio of the configuration and  $p_c = a_c M / R_0 \ell$  is the coil pitch parameter, with  $R_0$  the major radius.

## NUMERICAL METHODS

### 2-D equilibrium and low- $n$ modes

For the two-dimensional (2-D) equilibria and low- $n$  stability, we used the stellarator expansion as implemented in the FAR code [3]. In this code, a perturbed potential  $\Xi$  is expanded as

$$\Xi(\rho, \theta, \zeta, n) = \sum_{mn} \xi_{mn}(\rho) \cos(m\theta + n\zeta) + \sum_{mn} \tau_{mn}(\rho) \sin(m\theta + n\zeta)$$

where  $n$  and  $m$  denote the toroidal and poloidal mode numbers. In this initial value code, a component with helicity  $q$  ( $= 1/\iota = m/n$ ) is initially perturbed. In this study, we considered  $n$  between 1 and 6. We used 800 radial grid points in the numerical calculation, with convergence studies using 200 and 400 points. The growth rate is interpolated to zero radial grid spacing. The higher the value of  $n$ , the more localized the mode and the more resolution needed.

### 3-D equilibrium and Mercier modes

For Mercier modes, only equilibrium quantities are needed. For this part of the study we used the VMEC code [4]. Closed flux surfaces were assumed and expressed in the inverse coordinate representation:

$$R = \sum_{mn} R_{mn}(s) \cos(m\alpha - n\phi)$$

$$Z = \sum_{mn} Z_{mn}(s) \sin(m\alpha - n\phi)$$

Here  $\alpha$  is a poloidal-like angle and the flux label  $s$  is proportional to the toroidal magnetic flux. In calculating the VMEC equilibrium we used the set of modes  $n = (-3M, -2M, -M, M, 2M, 3M)$  and  $m = (0, 1, 2, 3, 4, 5, 6)$ . A radial grid of 61 points is considered.

The Mercier criterion is a necessary condition for stability that must be evaluated on each flux surface. The ideal stability analysis is based on the energy principle. We write the condition for stability à la Bauer, Betancourt, and Garabedian [5] as  $D_M = D_S + D_W + D_I + D_G > 0$ , where

$$D_S = \frac{(\chi''\Phi')^2}{4} \quad \text{shear}$$

$$D_W = \left\langle \frac{gB^2}{g^{ss}} \right\rangle P'V'' - (P')^2 \left\langle \frac{g}{B^2} \right\rangle \left\langle \frac{B^2g}{g^{ss}} \right\rangle \quad \text{well}$$

$$D_I = \left\langle \frac{gB^2}{g^{ss}} \left( \chi''I' - \chi''\Phi' \frac{\mathbf{J} \cdot \mathbf{B}}{B^2} \right) \right\rangle \quad \text{net currents}$$

$$D_G = - \left\langle \frac{(\mathbf{J} \cdot \mathbf{B})^2}{B^2} \frac{g}{g^{ss}} \right\rangle \left\langle \frac{B^2g}{g^{ss}} \right\rangle + \left\langle \frac{g \mathbf{J} \cdot \mathbf{B}}{g^{ss}} \right\rangle^2 \quad \text{geodesic curvature}$$

with  $g$  the Jacobian. The prime indicates the derivative with respect to the flux label  $s$ ,  $V'$  is the magnetic well,  $I$  is the toroidal net current enclosed in the flux surface,  $\Phi$  is the toroidal flux, and  $\chi$  is the poloidal flux;  $g^{ss} = \nabla s \cdot \nabla s$ , and the angle brackets indicate the operation  $\langle(x)\rangle = \int \int d\alpha d\phi (x)$ .

## NUMERICAL RESULTS OF THE STABILITY ANALYSIS

Our results on stability for low- $n$  and Mercier modes for the configurations with  $M = 10, 14,$  and  $19$  are presented in Figs. 1-3, which shows the unstable regions and the positions at which the dominant component of the low- $n$  modes is localized (thick lines). The helicities of the most dominant modes are also indicated. Figure 1 shows the results for two flux conserving  $M = 10$  configurations, one unshifted and the other with an inward shift in magnetic axis of 2.5% of the major radius. Figure 2 shows the flux-conserving and zero-current modes of operation for the  $M = 14$  configuration. Figure 3 shows the unstable regions for the zero-current  $M = 19$  torsatron.

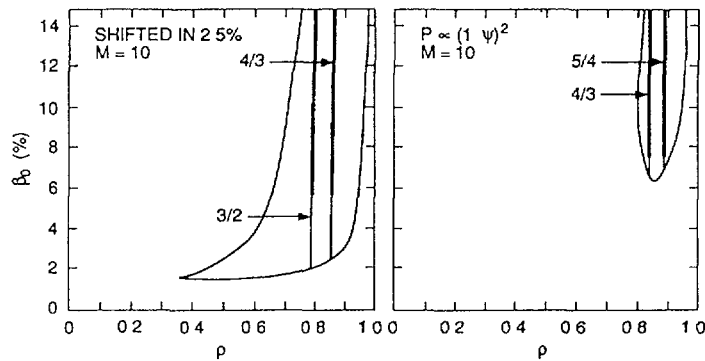


FIG 1

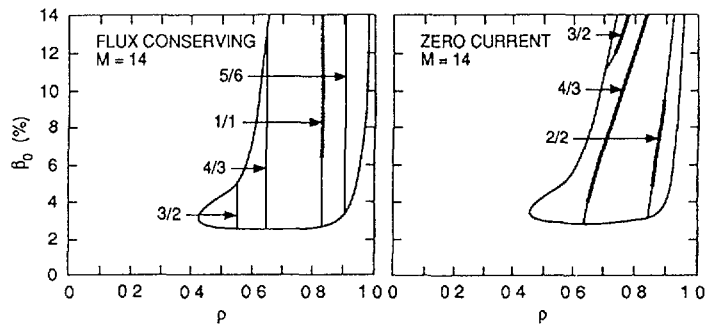


FIG 2

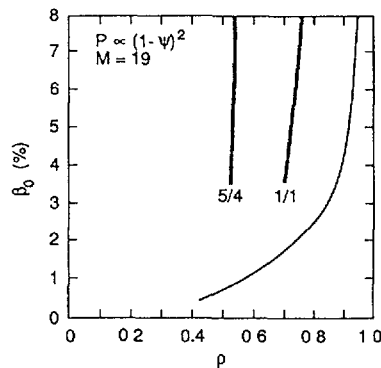


FIG. 3.

## CONCLUSIONS

The Mercier criterion usually yields a more pessimistic stability beta limit. However, the unstable low- $n$  modes map out the radial boundaries of the Mercier unstable region quite closely. There is good agreement between the 3-D low- $n$  calculations made using a 2-D equilibrium and the 3-D Mercier stability calculations for the full 3-D equilibrium, even for  $\ell = 2$  torsatrons with fairly low aspect ratio. Therefore, the similarity in stability with respect to low- $n$  perturbations and Mercier modes that was found for helically symmetric configurations by Gruber, Merkel, and others still holds for the more general  $\ell = 2$  configurations studied here. The practical application of our calculations is that we can perform a stability analysis for the ideal pressure-driven modes by studying either the low- $n$  or the Mercier modes.

## ACKNOWLEDGEMENTS

We are indebted to S. P. Hirshman for allowing us to use his VMEC code.

## REFERENCES

- [1] GRUBER, R., KERNER, W., MERKEL, P., NÜHRENBURG, J., SCHNEIDER, W., TROYON, F., *Comput. Phys. Commun.* **24** (1981) 389.
- [2] MERKEL, P., NÜHRENBURG, J., GRUBER, R., TROYON, F., *Nucl. Fusion* **23** (1983) 1061.
- [3] CHARLTON, L.A., et al., *J. Comput. Phys.* **63** (1986) 107; LYNCH, V.E., *J. Comput. Phys.* **66** (1986) 441.
- [4] HIRSHMAN, S.P., et al., *Phys. Fluids* **26** (1983) 3553; HIRSHMAN, S.P., et al., *Comput. Phys. Commun.* **43** (1986) 143.
- [5] BAUER, F. BETANCOURT, O., GARABEDIAN, P., *Magnetohydrodynamic Equilibrium and Stability of Stellarators*, Springer-Verlag, New York (1984).

# MHD INSTABILITIES AND MAXIMUM $\beta$ VALUES IN HELIOTRON DR

S. MORIMOTO, N. YANAGI, K. ICHIGUCHI,  
S. KOBAYASHI, M. IIMA, S. BESSHOU,  
H. NAKAMURA, M. SATO, M. WAKATANI,  
T. OBIKI, A. IIYOSHI  
Plasma Physics Laboratory,  
Kyoto University,  
Gokasho, Uji, Kyoto,  
Japan

## Abstract

The MHD stability and the maximum ( $\beta$ ) values were investigated in Heliotron DR. Small plasma current drastically improves the critical ( $\beta$ ) value. By shifting the magnetic axis inward new mode of instability was observed and the maximum ( $\beta$ ) values become lower. The experimental results are well explained by the numerical calculation based on the STEP code for the ideal interchange mode.

---

## 1 Introduction

The pressure driven MHD instability and the maximum beta value have been studied both experimentally and theoretically for the currentless ECH plasmas ( $\bar{n}_e = (2 - 3) \times 10^{13}/\text{cm}^3$ ,  $T_{eo} = (300 - 400) \text{ eV}$ ,  $\langle\beta\rangle \lesssim 0.5 \%$ ) in Heliotron DR ( $R = 90 \text{ cm}$ ,  $a_p \sim 7 \text{ cm}$ ,  $B \sim 5 \text{ KG}$ ).

The plasmas are produced through the second harmonic electron cyclotron heating by using a 28 GHz, 200 kW gyrotron. Efficient heating has been observed at the electron densities above the cut-off value for the ordinary mode ( $n_e = 1 \times 10^{13}/\text{cm}^3$ ). The achievable  $\langle\beta\rangle$  value is limited to  $\sim 0.5 \%$  by onset of the MHD instability which has an  $m=1/n=1$  mode and are localized around the  $\iota=1$  magnetic surface [1].

The analysis of the MHD stability has been performed by using the STEP code under the free boundary condition [2]. The calculated  $\langle\beta\rangle$  limit for the ideal interchange mode agrees well with the experimentally observed one [1].

## 2 Effects of Toroidal Plasma current on the MHD stability

Toroidal plasma current changes the rotational transform and therefore the MHD stability of the Heliotron DR plasma. A small current which decreases the rotational transform ( $t_p(a) \sim 0.05$ ) suppresses drastically the low frequency ( $f \sim 3 \text{ kHz}$ ) MHD instability as is seen in the magnetic probe ( $\tilde{B}_p$ ) and the soft-X ray (SX) signals in Fig.1. The maximum  $\langle\beta\rangle$  value is increased by  $\sim 50 \%$  according to the suppression of the instability. However, the high frequency ( $f \sim 100 \text{ kHz}$ ) fluctuations are not stabilized by the plasma current and they seem to determine the maximum  $\langle\beta\rangle$  value. Figure 2 shows experimentally observed and calculated  $\langle\beta\rangle$  limits as a function of the edge rotational transform  $t_p(a)$ , where

pressure profile is assumed to be  $(1 - \Psi)^2$  according to the experimental result [3]. The calculation shows that the stability is drastically improved by the current with  $t_p > 0$  ("sub" case) but spoiled in the  $t_p < 0$  ("add") case in consistent with the experimental result. By increasing  $t_p (> 0)$ , the rotational transform is lowered and the rational magnetic surfaces with  $\iota = 0.8$  and  $0.75$  appear in the central part of the plasma where  $m=5/n=4$  and  $m=4/n=3$  modes can be unstable. The calculation, however, shows the rather high  $\langle \beta \rangle$  limits for these modes. This is because the lowered  $\iota$  leads to an enhanced outward axis shift of plasma and therefore to a deeper magnetic well [4].

### 3 Magnetic Axis Shift Experiment

The MHD stability of plasma has also been investigated by changing the location of magnetic axis (and the vacuum magnetic configuration) with the additional vertical field.

As shifting the magnetic axis inward, critical  $\langle \beta \rangle$  value is predicted to become lower due to the  $m = 5/n = 4$  mode instability. This mode becomes unstable because of the appearance of  $\iota = 0.8$  surface in the central region of plasma and also of the magnetic hill configuration. On the other hand, as shifting the magnetic axis outward, magnetic well tends to be produced at lower  $\langle \beta \rangle$  value. However in Heliotron DR, the  $\iota = 1$  surface shifts into the central region of plasma and the critical  $\langle \beta \rangle$  value is not improved as a result.

Figure 3 shows the experimentally obtained maximum  $\langle \beta \rangle$  values against the shift of magnetic axis  $\Delta$ . Toroidal plasma currents are kept below  $\sim 500A$  ( $t_p(a) \sim 0.04$ ). Critical  $\langle \beta \rangle$  values calculated by the STEP code are also shown. As seen in this figure, the experimentally obtained maximum  $\langle \beta \rangle$  values well coincide with the calculated ones.

In the case of inward magnetic axis shift ( $\Delta \lesssim -0.2cm$ ), different type of instability (as compared to  $m = 1/n = 1$  mode) is observed and the maximum  $\langle \beta \rangle$  values are limited to be much lower than in the standard case. Signals of the magnetic probes show the oscillation with the frequency around  $10 \sim 15kHz$ , which is several times higher than that of  $m = 1/n = 1$  mode. As seen in Fig.4, signals of the soft X-ray diode array show that the inversion radius of the instability fairly coincides with the mode rational surface of  $\iota = 0.8$  in the central region of plasma. Although the mode numbers have not yet been identified, these results indicate that this instability is likely to be  $m = 5/n = 4$  mode as predicted by the STEP code [4].

In the case of outward shift, the characteristics of instabilities are almost the same as in the case of standard configuration. Signals of the magnetic probes and the soft X-ray diode array (Fig.4) indicate that the mode numbers are  $m = 1/n = 1$  and the instabilities are localized around the  $\iota = 1$  surface.

It is to be noted that as in the standard case, small plasma current in the subtractive direction stabilizes the MHD instability in both cases of inward and outward shift of magnetic axis. It is especially drastic in the inward shift case (maximum  $\langle \beta \rangle$  values are improved by the factor  $\sim 2$ ), and this condition is favorable for good confinement together with good stability.

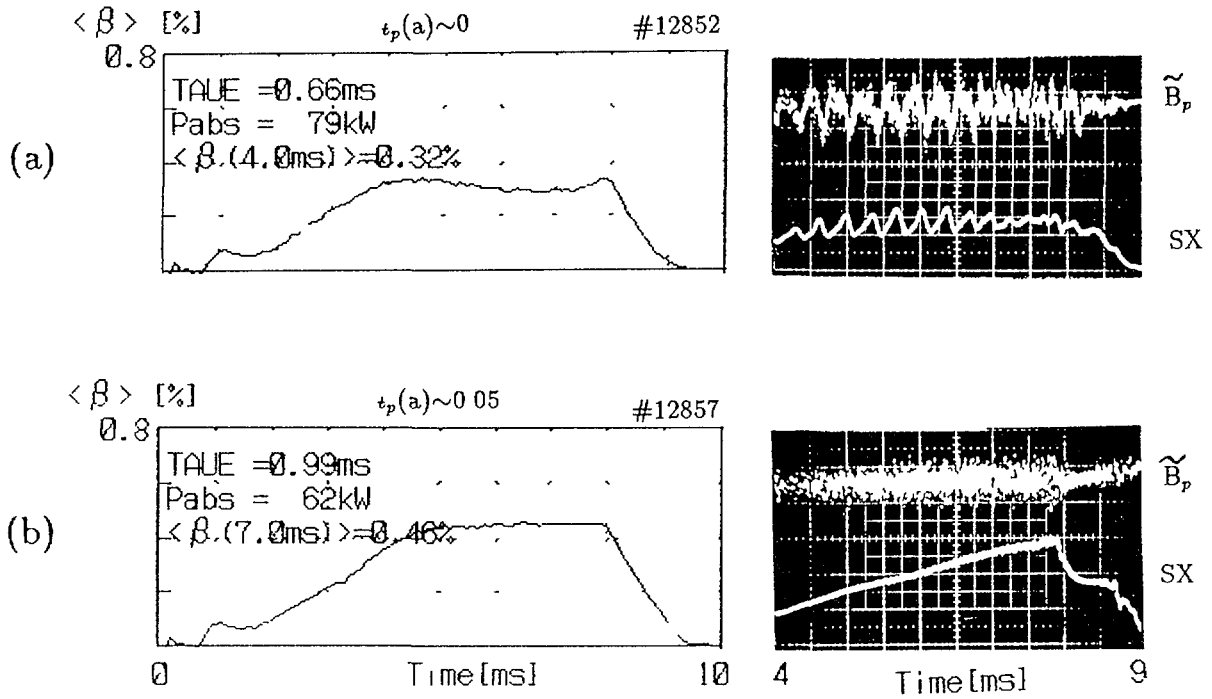


Fig 1 Time evolutions of  $\langle \beta \rangle$  (diamagnetic),  $B_p$  (magnetic probe) and SX (soft X-ray) signals in the discharges (a) without and (b) with a small toroidal plasma current

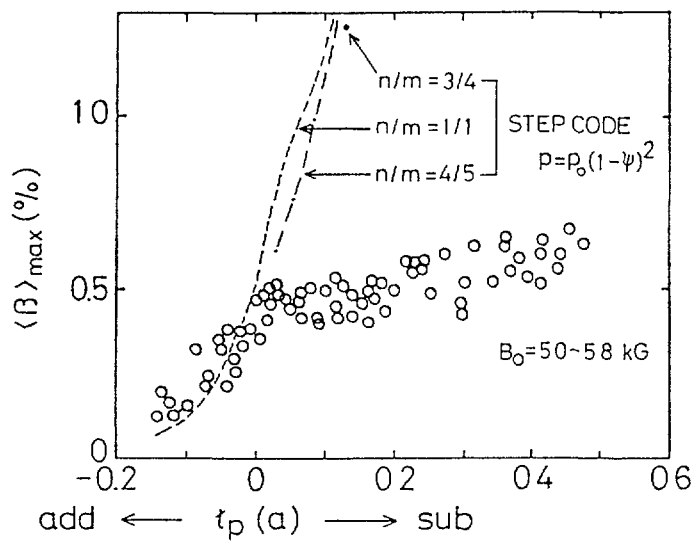


Fig 2 Maximum  $\langle \beta \rangle$  value versus edge rotational transform produced by the plasma current  $t_p(a)$ . The net rotational transform is decreased for  $t_p > 0$  and increased for  $t_p < 0$ . The calculated (STEP code)  $\langle \beta \rangle$  limits are also shown for the  $(1-\psi)^2$  pressure profile.

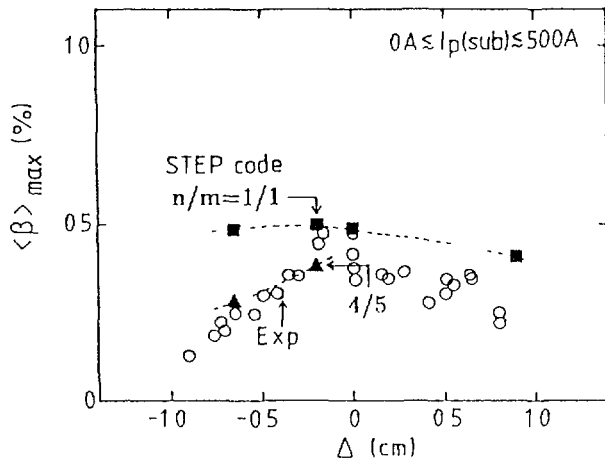


Fig 3 Maximum  $\langle \beta \rangle$  values versus magnetic axis shift  $\Delta$   $\Delta > 0$ : outward,  $\Delta < 0$  inward. Calculated  $\langle \beta \rangle$  limits are also shown in the figure for  $n/m=1/1$  and  $4/5$  modes.

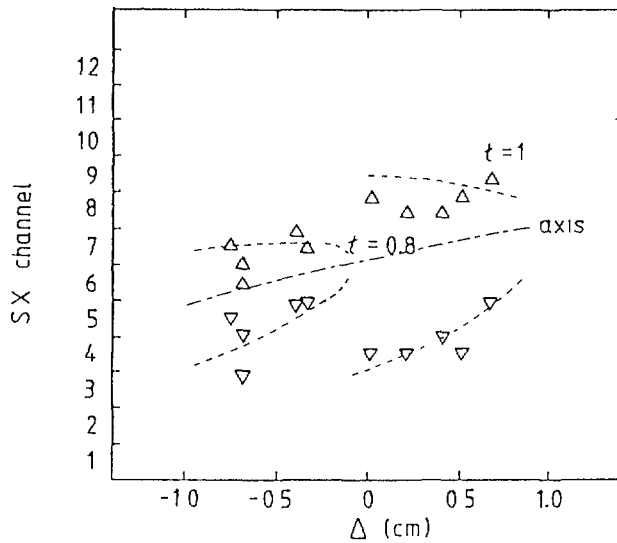


Fig 4 Inversion radius of the soft X-ray fluctuations versus magnetic axis shift  $\Delta$ . The magnetic surface with  $\epsilon=0.8$  appears for  $\Delta < 0$ .

## 4 Conclusion

The MHD stability and the maximum  $\langle \beta \rangle$  values were investigated in Heliotron DR. Small plasma current drastically improves the critical  $\langle \beta \rangle$  value. By shifting the magnetic axis inward new mode of instability was observed and the maximum  $\langle \beta \rangle$  values become lower. The experimental results are well explained by the numerical calculation based on the STEP code for the ideal interchange mode.

## REFERENCES

- [1] MOTOJIMA, O., et al., IAEA-CN-50/E-I-4(1988)
- [2] NAKAMURA, Y., ICHIGUCHI, K., WAKATANI, M., JOHNSON, J.L., PPLK-R-34, Plasma Physics Laboratory, Kyoto Univ., Kyoto(1988)
- [3] MORIMOTO, S., YANAGI, N., et al., Nucl. Fusion 28(1988)1491.
- [4] ICHIGUCHI, K., NAKAMURA, Y., et al., submitted to Nucl. Fusion

## **RF HEATING**

## ECF HEATING AND CURRENT DRIVE IN W VII-AS

U. GASPARINO, H. MAASSBERG,  
W VII-AS TEAM<sup>1</sup>, NBI GROUP<sup>1</sup>  
Euratom-IPP Association,  
Max-Planck-Institut für Plasmaphysik,  
Garching

ECRH GROUP<sup>1</sup>  
Institut für Plasmaforschung,  
Universität Stuttgart,  
Stuttgart

Federal Republic of Germany

### Abstract

ECH generated and sustained plasmas at an ECF power level up to 600 kW at mainly 2nd harmonic ( $B_0 \simeq 1.25$  T) are analyzed. Electron temperature profiles depend sensitively on the radial position of the resonance zone. The ECF power absorption profiles were estimated using a 3-D Hamiltonian ray tracing code with global heating efficiencies in agreement with the experimental findings. ECF current drive at 2nd harmonic was clearly demonstrated by changing the injection angle with respect to the magnetic field direction (corresponding to a change of  $k_{\parallel}$ -spectrum) with maximum efficiencies of typically 20 A/kW. The theoretical current drive efficiency based on the quasi-linear diffusion tensor (computed by the ray tracing code) in combination with a Fokker-Planck solution or with a simple Spitzer function convolution agrees fairly well with the experimental findings. The dependence of ECH current drive efficiency on both the electron parallel momentum confinement and the power loss mechanism (electron heat conduction) is theoretically discussed.

### Introduction

The possibility of plasma heating and current drive with RF waves became very important in the last years. While the estimation of wave propagation and absorption is very complex for lower hybrid waves, it is much simpler for waves in the electron cyclotron frequency range (ECF). For ECH in the old W VII-A stellarator, good agreement was obtained between experimental data of power absorption for both fundamental and 2nd harmonic heating and theoretical predictions based on ray tracing calculations [1, 2]. As ECF power deposition profiles are rather close to the resonance zone, ECH current drive is a natural candidate for current profile control.

In the nearly shearless W VII-AS stellarator as well as in the predecessor W VII-A, a strong correlation between the global energy confinement properties and the edge value of the rotational transform has been observed in "net current-free" discharges. Strong degradation of energy confinement was found at low order rational values of the rotational transform. Additionally, extended magnetic islands were measured in the W VII-AS vacuum field at values of  $\iota \simeq 5/m/3$ . The pressure driven bootstrap current which is clearly confirmed in W VII-AS significantly affects the  $\iota$ -profile, up to few kA were observed. Operation in the narrow  $\iota$  regimes with optimum confinement during the whole duration of the discharge required external current control, in most cases by a small loop voltage. The W VII-AS ECRH system consists of four 200 kW, 70 GHz, 3 ns pulse-length gyrotrons, highly oversized circular waveguide transmission lines and quasi-optical wave launch antenna. Before reaching the plasma the Gaussian beams are reflected by focusing mirrors which can be tilted in both toroidal and poloidal directions. With this launching system, the  $k_{\parallel}$ -spectrum and the radial power deposition profile can be varied over a wide range.

---

<sup>1</sup> The members of the W VII-AS Team, NBI Group and ECRH Group are identified in the paper entitled 'Status of the advanced stellarator Wendelstein W 7AS: first results and further programme', these proceedings, p. 25.

## Theoretical Models

The ECF power deposition is estimated by means of a 3-D Hamiltonian ray tracing code in the rather complex topology of the W VII-AS magnetic field. The cold plasma dispersion relation and an absorption coefficient for general angle of propagation (relativistic Doppler shifted resonance condition) based on a Maxwellian distribution function are used. The ECF power deposition is estimated in full configuration space.

In principle, ECH current drive must be described by a drift kinetic Fokker-Planck equation (FPE) in full phase space with particle, parallel momentum and energy conservation. For axi-symmetric configurations, velocity space can be transformed to the adiabatic invariants of motion which are given analytically. This approach is unqualified for configurations as W VII-AS stellarator where, similar as in neoclassical theory, a full numerical treatment is necessary for a full selfconsistent solution. As this solution of the nonlinear FPE in full phase space is not available, two independent approaches are used and stationary conditions are assumed. The neoclassical transport problem is treated numerically by the DKES code /4/ without parallel momentum conservation in the collision operator and without additional particle and energy sources. By this approach, the neoclassical transport and the bootstrap current are calculated. For the other approach, the configuration space dependence is strongly simplified: a dependence of the electron distribution function of poloidal and toroidal angle is neglected. Radial transport, trapped particle effects and connected damping of parallel momentum are outside of this model. Consequently, the condition of energy conservation requires an additional loss term in the simplified FPE.

With the local power deposition and  $k_{\parallel}$ -spectrum from the ray tracing calculations, the flux surface averaged quasi-linear tensor in velocity space is calculated for different radii. As the electron energy balance can not be described by neoclassical transport /5/ and radiative losses are unimportant for the type of discharges reported here, a simple convective loss term (proportional to the electron distribution function) which conserves particle and parallel momentum is additionally used in the FPE. The collision operator is linearized with respect to the deviation of the electron distribution function from the Maxwellian. The collisional interaction with the background ions, modelled by an unshifted Maxwellian, represents a sink for electron parallel momentum and energy. The simplified FPE is iteratively solved using Legendre polynomial expansion, numerical differencing in the quasi-linear operator and straight forward integration of the collision term. The electron distribution function is calculated for each radius separately leading to the ECH driven current density profile.

For low levels of ECF power absorption ( $< 0.1 \text{ W/cm}^3$ ), these simplified Fokker-Planck calculations are in very good agreement with a much simpler approach which is also used within the ray tracing code: the current densities are estimated by convolution of the quasi-linear operator where a Maxwellian is used with Spitzer's function (self-adjoint method). This procedure leads to an upper limit of the ECH current drive efficiency. At higher power levels, however, the simplified Fokker-Planck calculations show a degradation of the current drive efficiency due to quasi-linear effects. Analogous to more realistic calculations for an axisymmetric case /6/, parallel momentum damping due to trapped particles will result in a significantly reduced current drive efficiency. Furthermore, the parallel momentum loss due to transport is linked to the obscure problem of global electron energy transport. On the other hand, the deviation of the distribution function from the Maxwellian driven by the ECH, especially a suprathermal tail at small parallel velocities (neoclassical ripple losses), can significantly increase the neoclassical transport and affect the bootstrap current.

### ECF Heating Efficiency

At half field operation, nearly full single path absorption of the 2nd harmonic ECF waves was obtained. At fundamental heating, efficiencies of 70 to 80% were found. The absorption efficiencies were estimated from the remaining ECF power measured on the inner side of the vacuum vessel (ECF wave launch from low field side) and agreed very well with predictions of the ray tracing code /7/. Up to now, the diamagnetic loop data indicate a rather long time constant leading to an underestimate of absorbed power in the ECH switch-off phase. The ECE system is optimized for full field operation (12 frequency channels covering a half profile), however, no information close to the resonance zone is available. Up to now, no separation of power deposition and heat propagation after ECH switch-off is possible. With the heat wave propagation technique (ECH power modulation), both the electron heat conductivity profile as well as the power deposition profile can be estimated /8/, this will be done in future.

### ECH Current Drive

In discharges with very small ECH current drive (ECF wave launch perpendicular to the magnetic field), the bootstrap current could be clearly identified. The estimates from the neoclassical

DKES code which were based on measured electron temperature and density profiles were smaller by a factor of typically up to 2 than the measured value /5/ (some uncertainty is related with Spitzer's conductivity in case of small loop voltages being applied to stabilize the discharges). In one series of discharges with 2nd harmonic on-axis ECH, one gyrotron with wave launch perpendicular to the magnetic field was used to generate and sustain the plasma. Using an additional ECH pulse, the launching mirror was toroidally tilted leading to ECH current drive. In the discharges of Figure 1, no external loop voltage was applied. The bootstrap current evolution is damped (L/R time constant) in the initial phase of the discharges. The additional bootstrap current driven by the 2nd gyrotron with a wave launch angle of  $14^\circ$  from the perpendicular is mainly compensated by the ECH current drive. Furthermore, the injection angle of the 2nd gyrotron was scanned ( $k_{\parallel}$ -scan) where current control ( $I_{pl} \approx 0$ ) by external loop voltage was used in order to fix the edge value of  $\epsilon$  and to have comparable confinement conditions. As the plasma parameters were nearly independent from the launching angle, the change in loop voltage was directly related to ECH current drive (Figures 2 and 3). The bootstrap current driven by the total ECH cannot be compensated by the 2nd gyrotron also when the launching angle corresponds to optimal current drive efficiency ( $\approx 14^\circ$ ).

The dependence of the observed loop voltage on the launching angle is that expected from ECH current drive theory (Figure 3). For comparison, the scan of launching angle was simulated by means of the 3-D ray tracing code in combination with the Spitzer convolution (self-adjoint method) leading to an upper limit of the current drive efficiency. For a quantitative comparison, the experimental electron temperatures and densities must be used, however, Thomson data are not available for this scan. Profiles of temperature ( $T_e(0) \approx 1.2$  keV) supported by ECE and X-ray signals and density ( $n_e(0) \approx 1.4 \cdot 10^{13} \text{ cm}^{-3}$ ) reproducing the observed line density and in agreement with the diamagnetic energy were assumed. With these profiles, nearly full absorption of injected X-mode polarized waves was found by the ray tracing code. Passing from

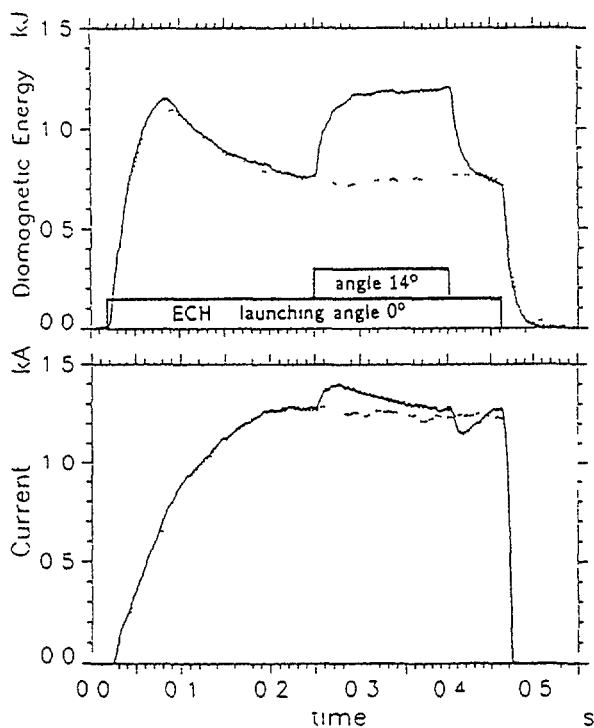


Fig. 1  
Diamagnetic energy and plasma current vs time for 2 discharges with 2nd harmonic ECH by 1 gyrotron (dotted lines) and by an additional gyrotron (solid lines). The 1st gyrotron beam was launched perpendicular to the magnetic field, the launching angle of the 2nd was  $14^\circ$  to the perpendicular.

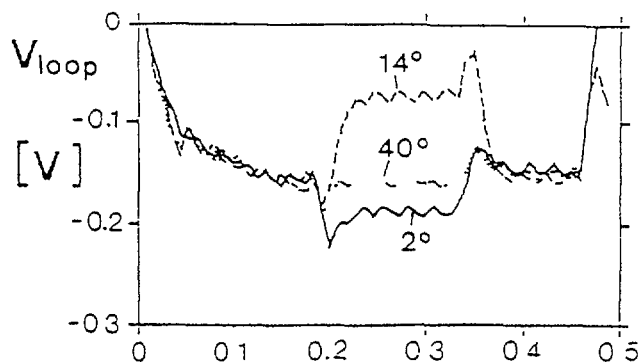


Fig. 2  
External loop voltage for current control vs. time where a 2nd gyrotron with different angles of the ECH beam to the perpendicular is added. Diamagnetic energy is similar to the case of Fig. 1 (solid line).

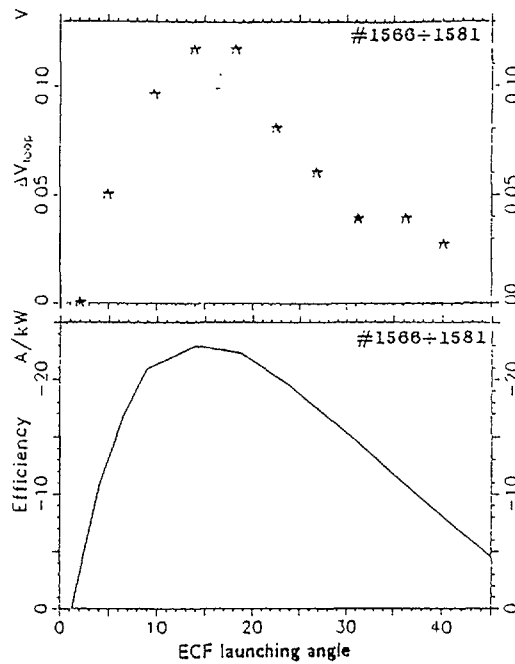


Fig. 3

Change of external loop voltage (upper part, comp. Fig. 2) and theoretical estimate of ECH current drive efficiency (lower part) versus the ECF wave launching angle to the perpendicular.

perpendicular to oblique launching, the degree of X-mode polarization as well as the single path absorption were slightly decreased (10% effect). A maximum current drive efficiency 23 A/kW at an launching angle of  $\approx 15^\circ$  to the perpendicular was estimated. Neglecting trapped particle effect and using Spitzer's resistivity, the observed change of loop voltage due to current drive is consistent with a  $Z_{\text{eff}}$  value of about 4.

The ECH current drive is concentrated to the power absorption region which is very narrow for the usual launching conditions in W VII-AS, typically of the order of about 3 cm in effective radius (broadness of the focused Gaussian beam). Consequently, in case of ECH current drive, the resultant current density profile can lead to a very strong deviation from the nearly shearless vacuum magnetic field configuration even in the case of net current-free operation. In Figure 4, the ECF power deposition and current density profiles (estimated by the simplified Fokker-Planck code in combination with the ray tracing code) are shown together with the bootstrap current density profile (from neoclassical DKES code). In this series of nearly net current-free discharges without external loop voltage, the resonance was slightly off-axis. Current drive with absorbed ECF power of about 370 kW was obtained with a launching angle of  $10^\circ$ . During these discharges, the current compensation was also maintained for three different ECH power levels. Based on measured Thomson profiles, the calculated total bootstrap currents were within a factor of about 3 smaller than the estimates for the ECH driven component. For the case shown in Figure 4, the ECH driven component was scaled to the bootstrap value in order to get vanishing total current. The rotational transform contribution,  $\Delta t$ , shown in the lower part of Figure 4 resulted from this current density profile. This example shows that, although the boundary value of the rotational transform remains fixed, very high local disturbances can be present for ECH current drive close to the magnetic axis.

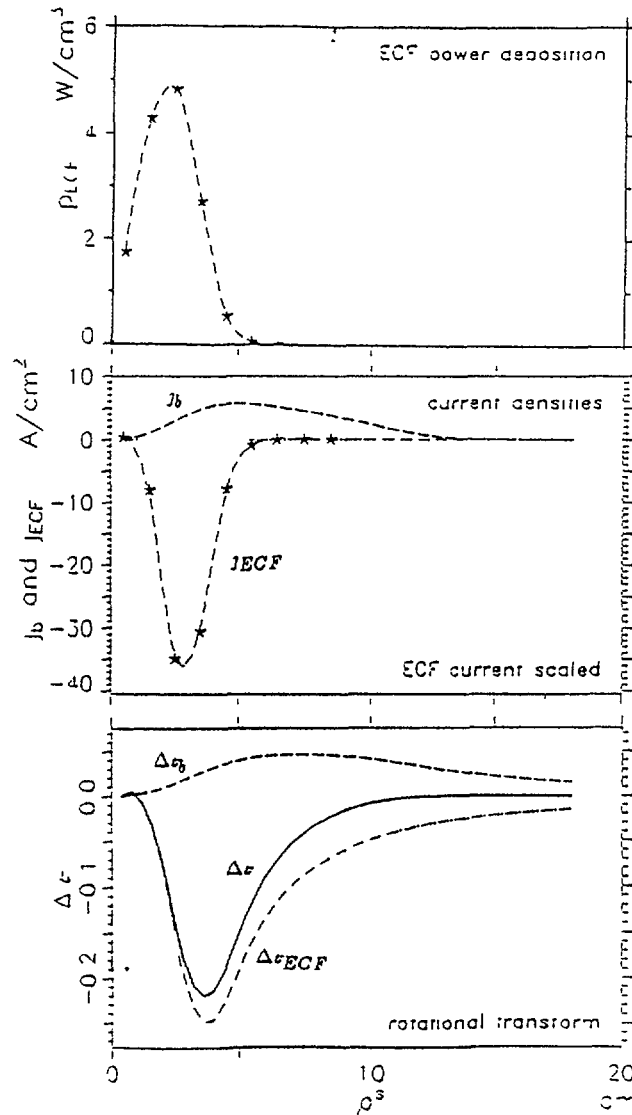


Fig. 4

Theoretical estimates of ECF power deposition, ECH driven and bootstrap current and contributions to the rotational transform for 2nd harmonic ECH slightly off-axis with a power level of about 370 kW. The ECF wave launching angle is  $10^\circ$  to the perpendicular.

### Conclusions

The absorption of ECF wave power described by the 3-D ray tracing code is in good agreement with the experimental findings in the W VII-AS stellarator. For the discharges of the initial phase of plasma operation mainly at 2nd harmonic ECF heating, no significant degradation of heating efficiency depending on the ECH power densities was found. Neoclassical bootstrap current and ECH driven current had been identified. In particular, the theoretically predicted dependence of the electron cyclotron current drive efficiency on the angle of the launched ECF waves with respect to the magnetic field has been experimentally verified. A maximum current drive efficiency up to 20 A/kW was derived, however, the value of  $Z_{eff}$  was not directly measured.

ECH current drive was demonstrated to be an appropriate candidate for net current control which is of importance due to the dependence of the energy confinement on the edge value of the rotational transform. However, the highly localized ECH driven current densities can also lead to strong local contributions to the rotational transform so that low order rational values of  $\iota$  can exist within the confinement region. All these experimental findings are described fairly well by the different simplified models, the quantitative agreement was typically within a factor of two. Considering the complexity of all these phenomena, where transport, quasi-linear and trapped particle effects are strongly linked together in the magnetic field topology of W VII-AS stellarator, this result is fairly satisfactory.

#### REFERENCES

- /1/ V. Erckmann et. al., Plasma Phys. Contr. Fusion, **28**, (1986), 1277
- /2/ U. Gasparino et. al., Plasma Phys. and Contr. Fusion, **30** (1988), 283
- /3/ H. Renner et. al., this workshop
- /4/ S.P. Hirshman et al., Phys. Fluids **29** (1986), 2951
- /5/ H. Maaßberg et. al., this workshop
- /6/ G. Giruzzi, Phys. Fluids **31** (1988), 3305
- /7/ G.A. Müller et al., this workshop
- /8/ H.J. Hartfuß et al., Nucl. Fusion **26** (1986), 678

## MEASUREMENTS OF ECH ABSORPTION ON ATF USING A POLARIZATION-CONTROLLED BEAM LAUNCHER\*

T.S. BIGELOW, C.R. SCHAICH, T.L. WHITE  
Oak Ridge National Laboratory,  
Oak Ridge, Tennessee,  
United States of America

### Abstract

Electron cyclotron heating (ECH) is used on the Advanced Toroidal Facility[1] (ATF) experiment at ORNL for plasma formation and heating. A 53.2 GHz gyrotron generates 200 kW cw which is transported to ATF in 6.35 cm evacuated waveguide. Power is launched into ATF using a recently completed polarization controlled beam launcher which can launch a linear polarized beam with a -20 dB diameter of 12 cm at the plasma center. The launcher consists of a Vlasov mode converting antenna, a Teflon-copper laminate polarization rotating grating, and a spherical focusing mirror. The plane of polarization can be remotely adjusted by rotating the grating with a motorized vacuum feedthrough. First pass plasma absorption is monitored in two planes of polarization using a dual-polarized detector looking through a dome shaped scattering cut-off screen. During plasma operation, the detected signals indicate that absorption under ideal conditions is nearly complete. With low density or a shifted resonance zone, absorption is small and there are cases where there is mode coupling to the perpendicular polarization. This is presumably due to shear in the ATF magnetic field.

---

### Introduction

The ATF experiment will be operated at both 0.95 and 1.9 Tesla central magnetic field so that ECH power can be absorbed at either second harmonic or fundamental resonance. Ray tracing results by Goldfinger and Batchelor[2] show that for second harmonic heating nearly complete first pass absorption of a microwave beam can occur. There are several requirements for this absorption efficiency. The beam must be narrow enough (10 cm) to pass inside the saddle point that occurs near the magnetic axis of the ATF fields. The beam must be linearly polarized in the extraordinary mode ( $E_{rf}$  perpendicular to  $B_0$ ). Plasma density must be slightly below cutoff ( $1.8 \times 10^{13} \text{ cm}^{-3}$ ) and temperature should be at least 200 - 300 eV. For 1.9 T operation, similar beam requirements exist however the polarization must be ordinary mode, and plasma density can be up to  $3 \times 10^{13} \text{ cm}^{-3}$ . ATF vacuum vessel ports allow power to be launched either from the outside in a horizontal plane or vertically. In the vertical plane, the saddle point is several cm closer to the magnetic axis which is desirable for maximizing the central power deposition. This plane was chosen for the beam launch for this reason, however in this plane the magnetic axis and saddle point move away from the beam during operation with a shifted plasma configuration.

---

\* Research sponsored by the Office of Fusion Energy, US Department of Energy, under contract DE-AC05-84OR21400 with Martin Marietta Energy Systems, Inc.

Due to shear in the magnetic field along a chord into the center of the plasma, the local orientation of ordinary and extraordinary mode polarization plane will vary with respect to launch point and resonance zone coordinates. This implies that a wave launched in a particular polarization will, at certain points in the path toward the center, be coupled into both ordinary and extraordinary modes and then back into the desired mode at the center. Since the phase velocity of these two modes are not equal at higher plasma densities, it is possible that there will be net rotation of the polarization at the plasma center due to the shear.

The ECH beam launcher was designed to have a continuously rotatable linear polarized beam with as narrow a beamwidth as practical. The adjustable polarization allows optimization of absorption for either fundamental or second harmonic operation and also allows experimental studies of the polarization rotation caused by the shear. Due to the beam pointing capabilities of the launcher mirror it is also possible to aim the beam away from the plasma either at a high field reflector for improved density operation or just to spoil the first-pass absorption to compare non-optimized launch performance.

### ECH Launcher Design

Figure 1 shows the launcher recently installed on ATF. A vacuum shroud encloses the entire device and serves as support for the various components. This vacuum shroud is modular which allows reconfiguration of the launcher so that it could be mounted either on a side or top port of ATF. The launcher has been installed above ATF with the output beam pointing downward. The weight of the launcher is supported by the ATF structural shell.

Input power from the gyrotron is primarily in the  $TE_{01}$  mode in a 6.35-cm diameter waveguide. This diameter is reduced to 3.83 cm in an optimized down taper which feeds a square-cut Vlasov mode converting antenna. This down taper is used to reduce the effective waist size of the input beam and also to significantly shorten the length of the Vlasov device. From the Vlasov device, a linearly polarized beam radiates at an angle of about 9 degrees from vertical which is set by the wave bounce angle for the  $TE_{01}$  mode in the 3.83 cm waveguide at 53 GHz. This expanding beam hits a flat polarization rotating grating tilted to bring the beam to a horizontal plane. The grating is a pure Teflon substrate 0.078-cm thick with copper lines 0.1-cm wide on the surface. The substrate is attached to a 33-cm diameter copper plate connected to a vacuum rotary feedthrough. The output polarization can be rotated from 0 to 180 degrees by rotating the grating 90 degrees. A 33-cm diameter spherical focusing mirror directs and focuses the beam down to a -20 dB beamwidth at the plasma center of about 12 cm. This beamwidth is in the radial direction of ATF where the magnetic field saddle point width is about 10 cm. Low power testing of the launcher with the entire waveguide run included has been performed. The launcher performance was very similar to laboratory measurements with some evidence of effects from vessel wall scattering.

To measure the absorption efficiency of the launcher, a diagnostic is located on the bottom port of ATF in line with the beam. This diagnostic consists of a 30 cm glass vacuum window with a dome shaped cutoff screen that scatters most of the power away but permits a small amount of the beam (-35 dB attenuation) to pass. Holes in the screen are uniform and round so polarization and beam shape are preserved. A dual polarized receiver which consists of an ortho-mode transducer and two detectors is located below the glass. The transducer is oriented so that the detectors receive O- and X-mode. Extra attenuation is necessary to reduce the signal levels about 30 db to keep the detectors linear.

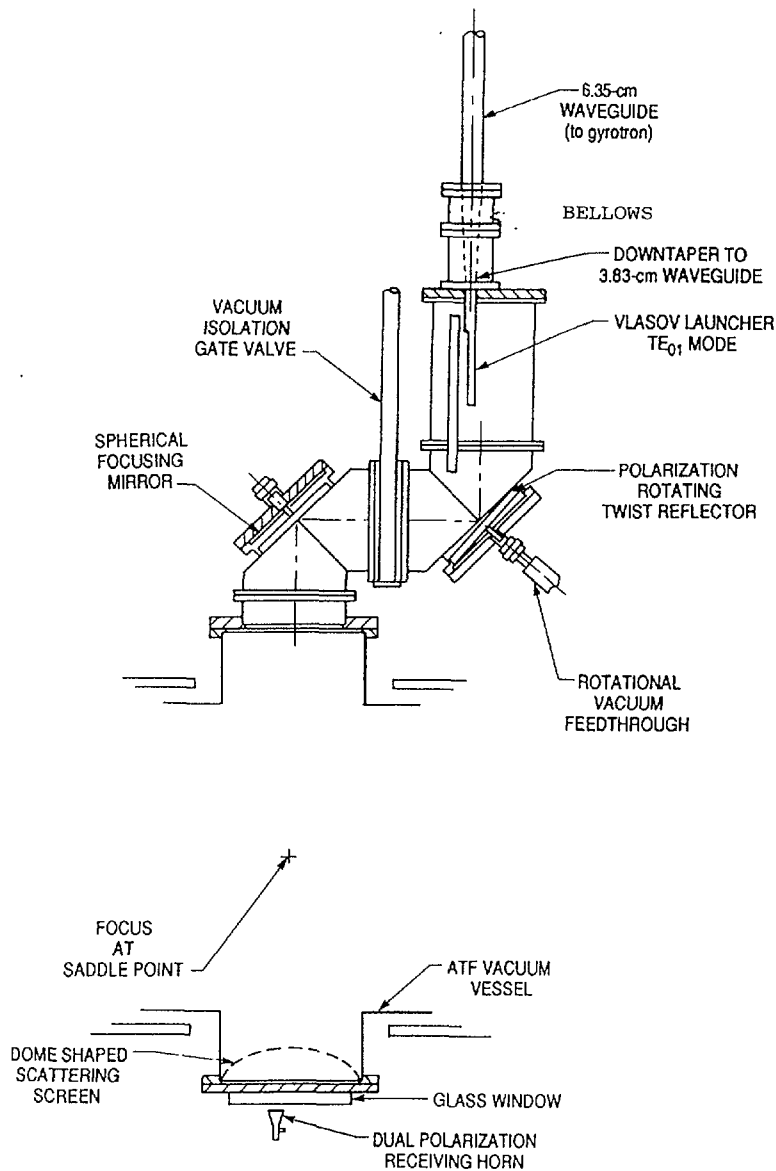


FIG. 1. Configuration of the ATF ECH beam launcher and absorption diagnostics.

### Measured Results

Several phenomenon have been observed using the absorption diagnostic during ATF operation. Since ATF has only operated at 0.95 T to date, X-mode launch has mainly been used. On a typical plasma shot, the plasma forms rapidly after a 10 to 40 ms delay. As shown in Fig. 2, the X-mode detector will show a large signal which falls rapidly to zero as the plasma density rises. There is usually very little signal on the O-mode detector except for cross-polarization coupling due to misalignment and lack of mode purity in the transmission system. In cases where the plasma density is low and is slowly rising, coupling between the X-mode launch and O-mode detector is observed as shown in Fig. 3. It is thought that this occurs due to the magnetic shear in ATF near the edge of the plasma. On some experiments, the plasma is deliberately shifted in or out from the centerline which moves the resonance zone saddle point away from the beam. With this configuration, only partial absorption of the beam occurs and a large noisy signal is observed in both X- and O-mode detectors.

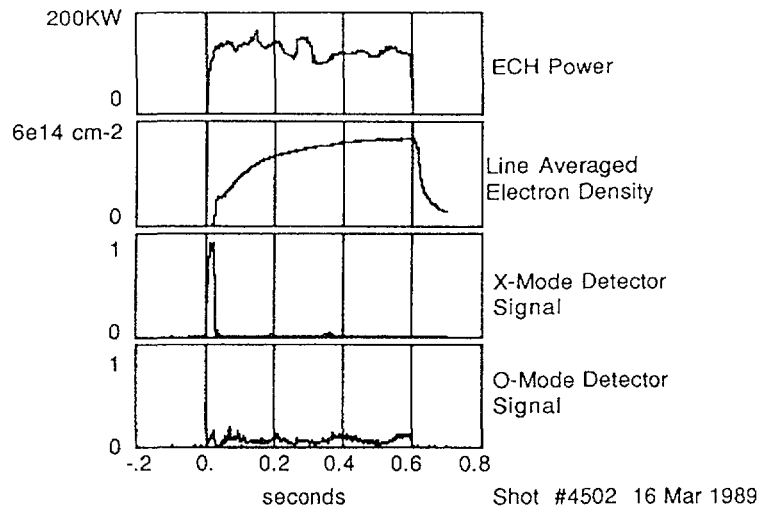


FIG. 2. Typical detector waveforms with plasma.

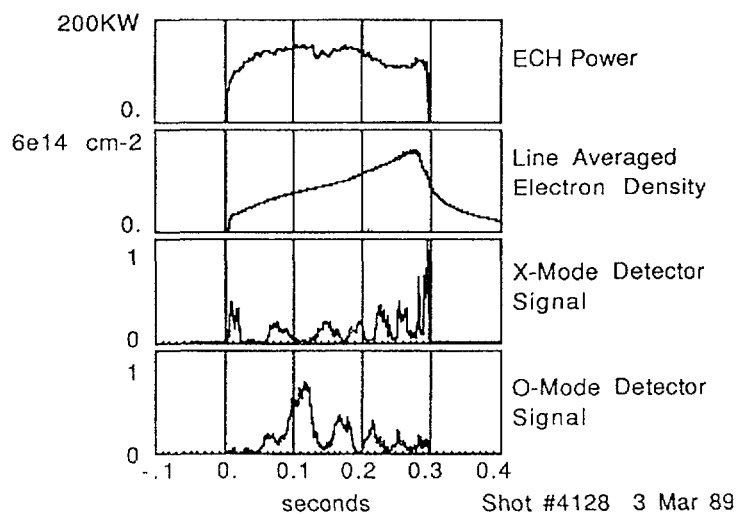


FIG. 3. Detector waveforms with slowly varying plasma density.

### Planned Experiments

In the near future improvements to the absorption diagnostic and launcher are planned. Beam profile and plasma diffraction can be measured by the addition of several detectors in a radial line below the plasma. Since a large window is used for viewing, it is possible to add more detectors at arbitrary locations without affecting the ATF vacuum condition.

### REFERENCES

- [1] Lyon, J.F., et.al., Fusion Tech. v.10 p179-226 (1986)
- [2] Goldfinger, R.C., Batchelor, D.B., Nuc. Fusion. Vol 27, no. 1 (1987)

## ECH EXPERIMENTS IN SHEILA

G.D. CONWAY, B.D. BLACKWELL

Plasma Research Laboratory,  
Research School of Physical Sciences,  
Australian National University,  
Canberra, Australia

### Abstract

We present preliminary experimental results of the first application of ECH power to plasmas confined in the heliac geometry. Employing up to 2 kW at 2.45 GHz we have observed strong absorption at both the fundamental and second harmonic with either a helical or a shaped dipole antenna. Either peaked or broad radial density profiles were obtained, depending on the location of the resonant field layers. Breakdown at the second harmonic appears to require seeding by a fundamental produced plasma. Densities up to two orders of magnitude above O-mode cut-off are observed.

---

### 1. Introduction

We have applied 2 kW (10 ms pulse) of ECH power at 2.45 GHz [1] to both H<sub>2</sub> and Ar plasmas confined in the SHEILA heliac. Strong absorption has been observed at both the fundamental ( $\omega = \omega_{ce}$ ) and the second harmonic ( $\omega = 2\omega_{ce}$ ) under a variety of operational conditions. Depending on the position of the resonant field layer and other parameters, either peaked or broad density profiles are observed. Recent theoretical studies [2] have predicted good ECH absorption profiles in a flexible heliac which are independent of the density profile. Breakdown at the second harmonic appears to require seeding by a fundamental produced plasma. We present cases in which this is achieved through variation in  $|B|$  with time or by exploitation of the spatial variation of  $|B|$ . Densities up to cut-off ( $n_e = 7.4 \times 10^{10} \text{ cm}^{-3}$ ) are easily achieved with a helical launching antenna positioned on the low field side. A conforming profile dipole antenna in contact with the plasma can produce overdense plasmas approximately two orders of magnitude above cut-off [3].

### 2. SHEILA

The SHEILA heliac is a toroidal device of major radius ( $R_o$ ) 18.75 cm and minor radius ( $a$ ) of about 3 cm. 24 toroidal field coils (TFC) are displaced 2.5 cm about  $R_o$  to form a  $N = 3$  period helix. A centre ring coil and 2 vertical field coil pairs complete the configuration. An additional 3 period helical winding about the ring coil allows optimization of the heliac field. Fig.1 is a plan view of SHEILA showing the coil layout and the location of the diagnostic ports and ECH antenna. The device is described more fully in ref. [4] and in accompanying papers this conference. The vacuum field forms a set of nested flux surfaces with a bean shaped cross section. Fig.2 shows a cross section of the flux surfaces at  $\phi = 0^\circ$  together with contours of constant  $|B|$ . The ratio of helical winding current to ring current is adjustable, but for all the results presented here a field configuration with  $I_h/I_r = +0.16$  was employed.

### 3. Microwave source

The ECH power is produced by a 2.45 GHz pulsed 2 kW peak magnetron [1] which is coupled to a coaxial transmission line (TEM mode) by a tunable cavity. A directional coupler monitors the incident and reflected powers prior to a double stub tuner which matches the antenna and vacuum feeder. Of the several types of antenna tested, two have proved most successful; i.e. highest densities and lowest antenna VSWR. The first is a non-resonant dipole shaped to conform to the flux surfaces at  $\phi = 150^\circ$ . The direction of  $\underline{k}$  is unrestricted relative to  $\underline{B}$ , but  $\underline{E}$  has components both perpendicular and parallel to  $\underline{B}$ . The second is an end-fire helix antenna located at a side port outside the TFCs with  $\underline{k} \perp \underline{B}$  (nearly transverse) and  $\underline{E}$  right circularly polarized. In the far-field the radiation would couple into both the O- and X-mode. However for both antennas, but

particularly the dipole, the plasma is in the near-field region (evanescent fields) and the plasma scale length is small compared to the wavelength ( $a/\lambda < 1$ ), which makes it inappropriate to consider coupling to the various plasma modes.

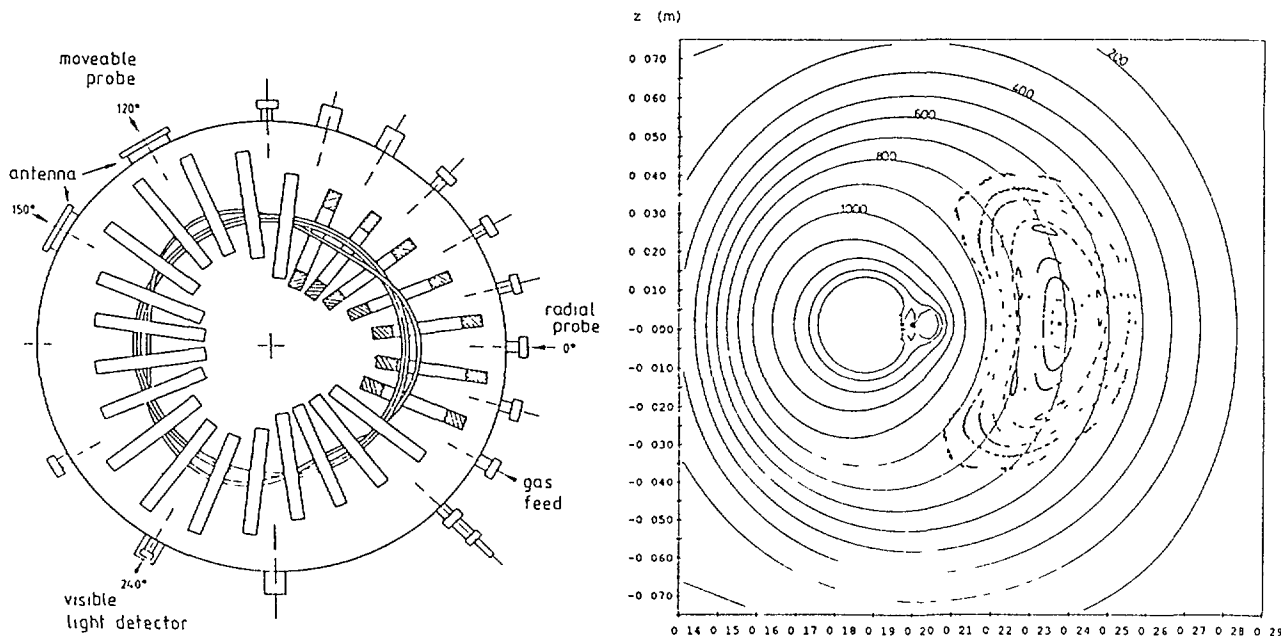


fig.1: Plan view of SHEILA showing toroidal location of antenna and probes relative to coils.

fig.2: Puncture plot of flux surfaces and  $|B|$  contours at  $\phi = 120^\circ$

#### 4. Results

A typical SHEILA shot with microwave only breakdown is shown in fig.3. The toroidal field pulse (ring current  $I_r$ ) lasts approximately 45 ms during which two ECH pulses occur. The pulses are 10 ms wide with a separation of 10 ms. The relative delay between the field pulse and the microwave pulses can be varied in 1 ms steps, but under normal operating conditions the centre of the first ECH pulse is timed to coincide with the field maximum. The density trace (Langmuir probe) and ionization rate (visible light emission) show breakdown at both the field maximum (fundamental) and at half the field strength (2nd harmonic). For most operating conditions the amplitude of the 2nd density pulse is at least twice that of the 1st.

The radial density profile at  $\phi = 0^\circ$  for the 1st and 2nd pulses are plotted in fig.4. The 1st pulse (fundamental) ECH profile is much broader and flatter than that obtained with the previous RF/ohmic breakdown (400 W at 96 kHz) [4], but the 2nd pulse profile is strongly peaked around the second harmonic resonant layer. The resonant field layers can be spatially positioned by varying the maximum current in the coil set  $I_r$ . Increasing  $I_r$  moves the fundamental resonant layer outward and transforms the 1st pulse profile from a low density flat profile to a high density peaked profile, fig.5.

In fig.6 the central density (magnetic axis) of the 1st and 2nd pulses are plotted as a function of  $I_r$ . For  $I_r > 10$  kAt, for which the fundamental resonant layer lies outside the last closed flux surface, no plasma is formed. With decreasing  $I_r$  the  $\omega = \omega_{ce}$  resonant layer enters the plasma confinement region and the 1st pulse density rises. The density maximum corresponds to the resonant layer roughly coincident with the magnetic axis. As the resonant layer continues to move inward the volume of intersection of the resonant layer decreases and the density falls, until at  $I_r \approx 6$  kAt the  $\omega = 2\omega_{ce}$  resonant layer enters the outside of the configuration and the density recovers. The density continues to rise until at  $I_r \approx 4.5$  kAt the  $\omega = \omega_{ce}$  resonant layer exits from the inside of the configuration. At this point the fundamental resonant layer no longer provides a seed plasma for the second harmonic absorption and there is no plasma.

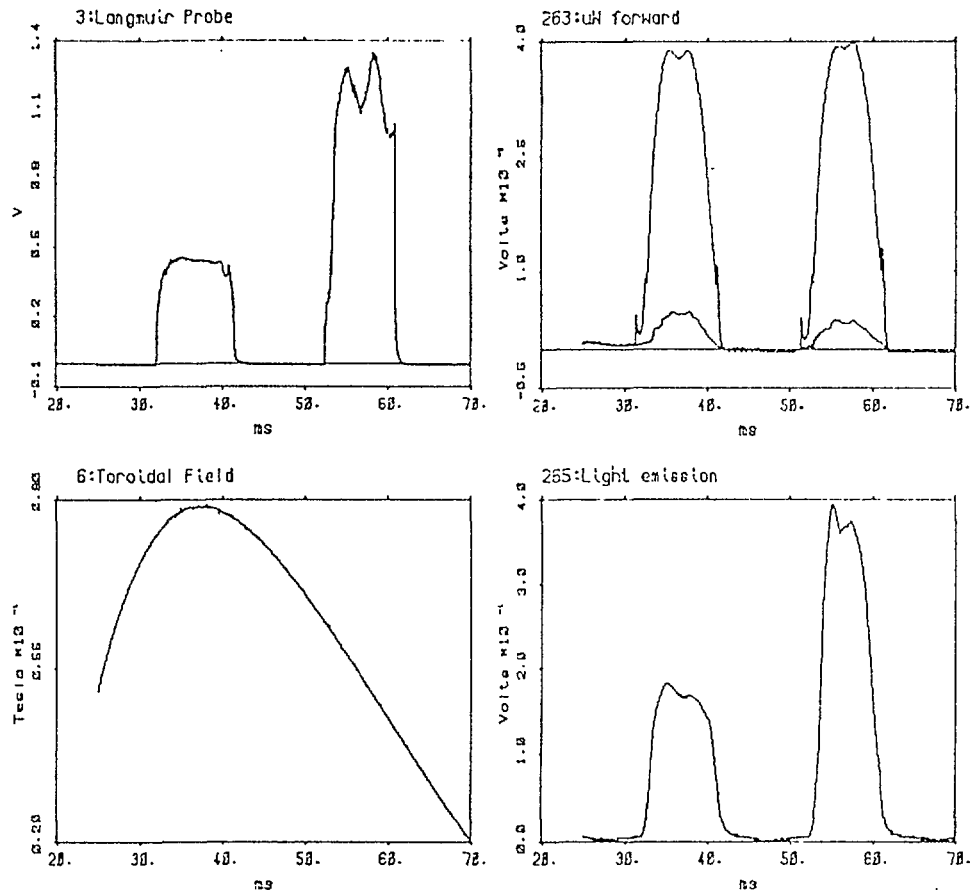


fig.3: SHEILA microwave shot,  
a) Density,  
b) Toroidal field,  
c) Incident and reflected power,  
d) Light emission (ionization rate).

Shot no. 15455  
taken on 5-Dec-88

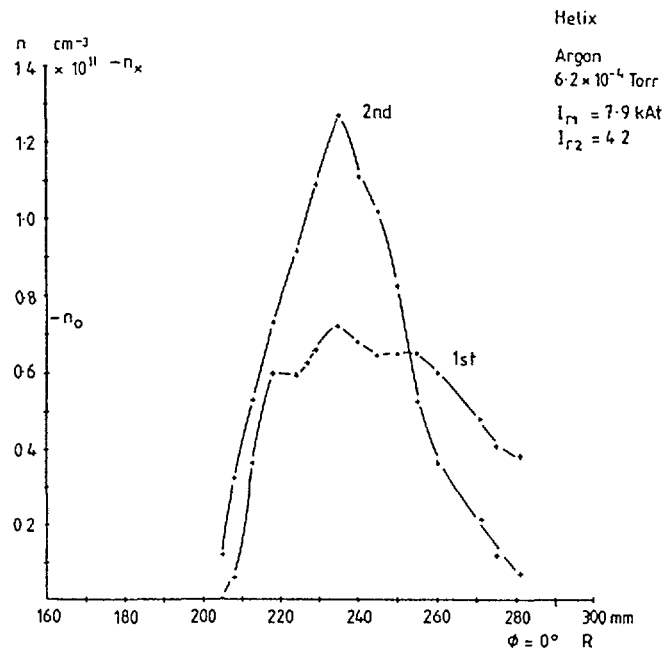


fig.4: Radial density profile for fundamental and second harmonic at  $\phi = 0^\circ$ .

For the more complicated case of the 2nd ECH pulse the magnetic field strength decays rapidly during the 10 ms pulse (fig.3). The density variation with  $I_r(t)$  is plotted for several shots with different maximum  $I_r$  values. As  $I_r$  decays the density rises and falls for each shot with the maxima tracing out a sharp peak around the second harmonic resonant layer. However, if  $I_r$  is less than  $\approx 4.5$  kAt at the start of the pulse, then again there is no  $\omega = \omega_{ce}$  resonant layer to initiate the plasma.

### 5. Discussion

In figs.5 & 6 the core density is well above the cut-off for the X-mode at fundamental resonance. This suggests the possibility of mode conversion ( $O \rightarrow X \rightarrow$  Electron Bernstein) or that the concept of mode cut-offs is not relevant in the evanescent field region. Localized microwave breakdown at the antenna is unlikely, since, as seen in fig.6, the presence of a resonant field is required to sustain the plasma.

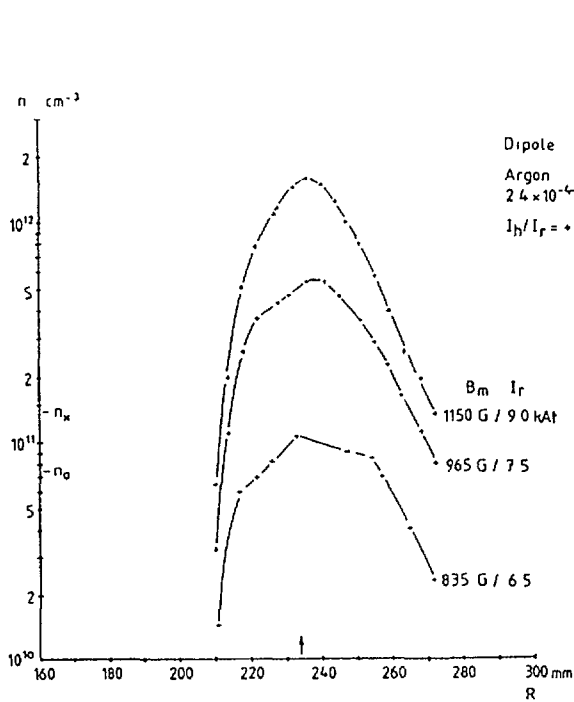


fig.5: Variation of radial profile with toroidal field strength  $B_m$ .

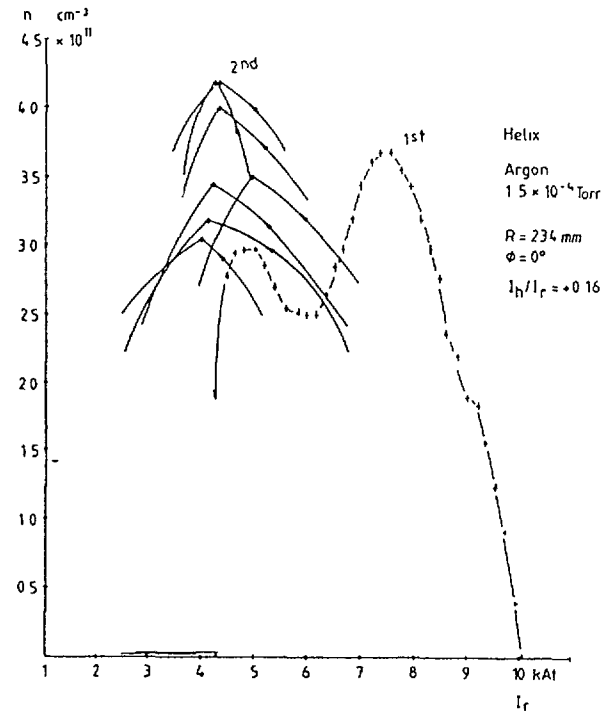


fig.6: 1st and 2nd pulse core density as a function of ring current (toroidal field strength).

### REFERENCES

- [1] G.D.Conway (1988), Design report, ANU-PRL-TR 88/2. Available on request.
- [2] C.Alejalde & J.Guasp (1987), Nucl. Fusion, 27, 2153.
- [3] G.D.Conway, B.D.Blackwell & S.M.Hamberger (1989), 17th AINSE Plasma Phys. Conf., Lucas Heights, Australia, Feb. 1989.
- [4] B.D.Blackwell *et al.* (1989), Aust. J. Phys. 42, 73.

## MICROWAVE ABSORPTION IN STELLARATORS (TJ-II) AND TORSATRONS (STORM)

C. ALEJALDRE, F. CASTEJÓN,  
V. KRIVENSKI, V. TRIBALDOS  
Asociación Euratom/CIEMAT,  
Madrid, Spain

### Abstract

Numerical simulation of the electron cyclotron wave power absorption by stellarator-like plasma has been performed and applied to the TJ-II and STORM installations to be built at CIEMAT. It is shown that the part of electrons from the tail of distribution function plays a crucial role in the absorption processes through the efficiency decrease and change of the absorbed power radial distribution profile.

Recent ECH experiments on stellarators and tokamaks show the existence of a superthermal tail in the electron distribution function and at the same time a disagreement between the linear theory of microwave absorption and the experimental values is usually reported<sup>1</sup>. To account for the effect upon microwave power absorption of a superthermal tail in the electron distribution function, an absorption module that takes into account the existence of a superthermal tail has been added to the ray-tracing code RAYS<sup>2</sup>. Then, an study has been conducted to determine the optimum launching position, including the more realistic simulation module, and the influence upon profile deposition and power absorption of the tail distribution, for waves propagating in the first (28 GHz.) and near second harmonic (53.2 GHz) of the electron cyclotron frequency in the flexible heliac TJ-II<sup>3</sup> and the l=1 torsatron STORM<sup>4</sup> to be built at the CIEMAT site in Madrid .

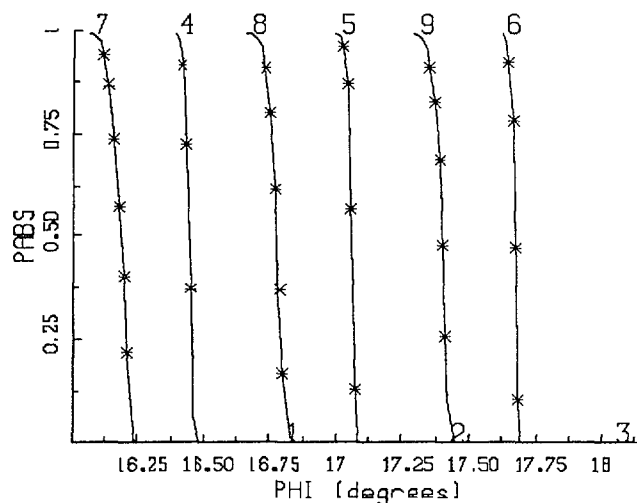


**Figure 1**

Fractional power absorbed in one-pass.  $f = 53.2$  GHz.  
 $n_e(0) = 1.5 \times 10^{13} \text{ cm}^{-3}$ ,  $T_e(0) = 1 \text{ keV}$

## TJ-II

Nine rays, located in a 3x3 rectangular array of  $\approx 5 \times 5$  cm. to simulate a five cm. radius beam, are launched into the plasma at the toroidal angle  $\phi = 16.875^\circ$ , chosen to be the illuminating point after this study.

The plasma parameters are :  $n_e(0) = 1.5 \times 10^{13} \text{ cm}^{-3}$ ,  $T_e(0) = 1 \text{ keV}$  and a parabolic profile is assumed for both magnitudes. The rays were launched into a plasma with a 10 keV tail temperature and a tail population of  $10^{-3}$  [5,6]. It is observed that the region of absorption increases sensibly with respect to the pure Maxwellian case in agreement with experimental observations, no appreciable differ-

ence can be observed in the absolute value of the absorbed power in the second harmonic, figure 1, since in both cases 100% of the power emitted is absorbed in one pass. Figure 2 shows a degradation in power with an increasing value of the tail population for propagation in the first harmonic, 28 GHz that depending on the ray direction can be of significance.

Quasilinear effects can play a major role during Electron Cyclotron heating if the RF diffusion coefficient is sufficiently large. If this is the case the distribution function presents non-thermal features in the resonant range of velocities; the modification of the distribution function results in a modification of the wave damping and therefore of the absorption profile and of the total power absorbed during a single transit of the microwaves across the plasma.

The strong absorption near the second harmonic results in a strong quasilinear effect. The initial deviation of the wave damping from the Maxwellian value can be obtained following Ref. 7. For the conditions used, we found a strong quasilinear modification of the wave damping, especially for the on-axis heating where the radius of the magnetic surfaces is smaller by a factor of 5. The overall power absorption decreases from the Maxwellian value (99%) to 90% ( $\tau = 1.8$ ) and 30% ( $\tau = 9.3$ ), the parameter  $\tau$  is the time normalized to the collision frequency.

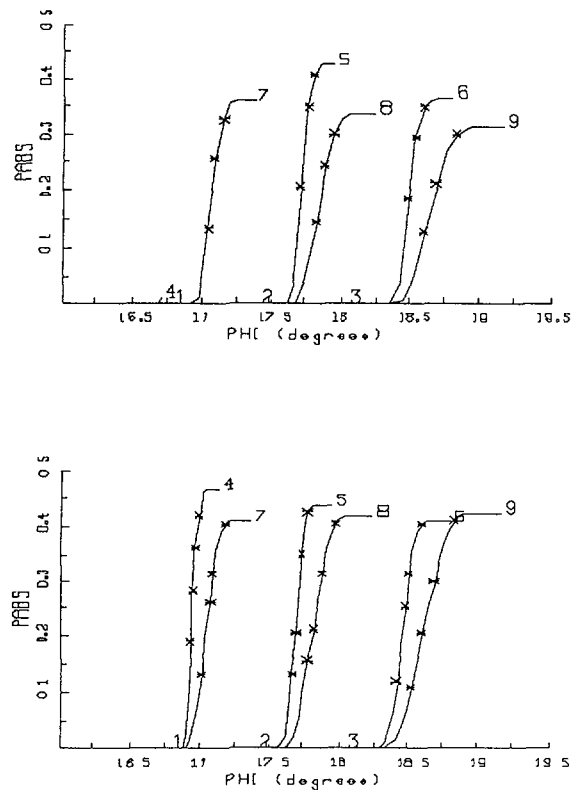


**Figure 2**

Fractional power absorbed in one pass for waves propagating at 28 GHz, using the non-Maxwellian model (a) and the pure Maxwellian one (b)

The modification of the wave damping is due to the quasilinear flattening of the distribution function, and therefore a compromise must be found between the launching angle and microwave absorption properties.

## STORM

The small  $l=1$  toroidal STORM<sup>3</sup> will be heated by an ECRH system. Given the availability of a 28 GHz gyrotron in our laboratory, the machine was designed for .5 Teslas of magnetic field

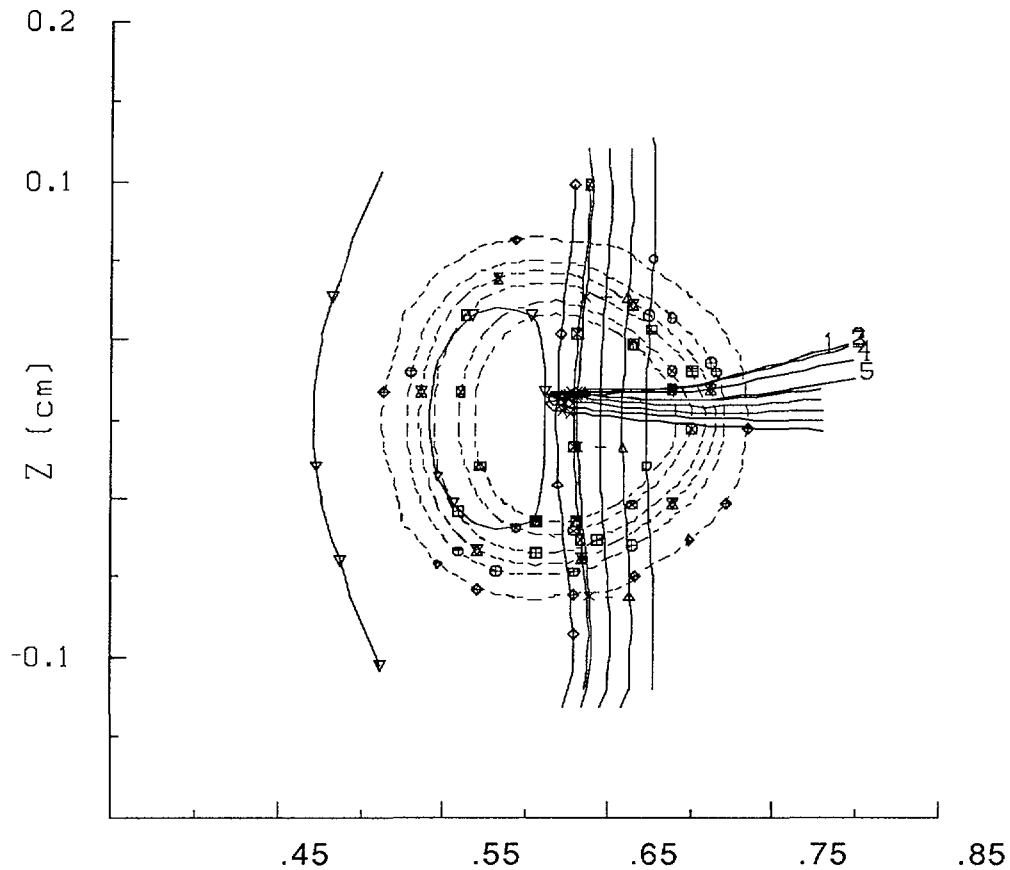


Figure 3

at the magnetic axis, to use  $2c^d$  harmonic heating in the X-mode. Microwave launching was simulated using five rays separated one cm. each. After considering the limitations imposed by the building, the diagnostic ports and the results from the code, the toroidal position of  $30^\circ$  was chosen as the optimum for microwave heating. Figure 3 shows the ray tracing of five rays

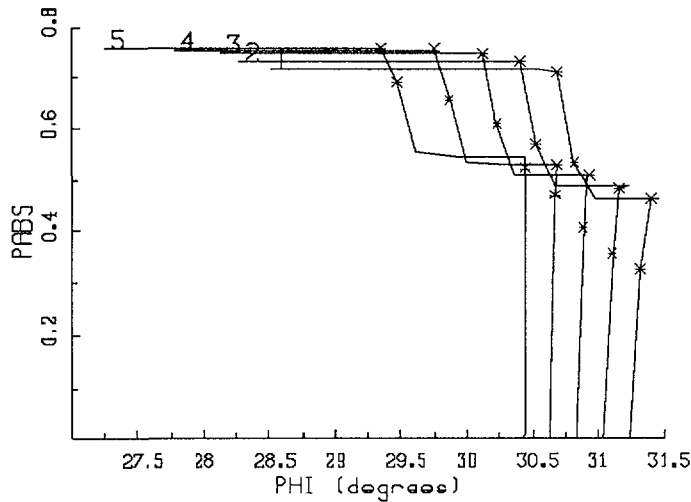


Figure 4

launched horizontally (equatorial plane) at  $\phi=30^\circ$ . At this position the passing through the resonance layer at high densities is guaranteed not only for the reference configuration used but also for the alternative configurations considered, see ref. 3, even if a considerable displacement of the plasma occurs. At the density

used,  $n_e(0)=.45 \times 10^{13} \text{ cm}^{-3}$ , the density cut-off already covers part of the plasma, although it actually helps to the microwave absorption by forcing the waves to pass twice through the resonance layer. Figure 4 shows the power absorption obtained, close to an 80% of the launched power.

A low density case  $n_e(0)=.3 \times 10^{13} \text{ cm}^{-3}$  shows that the one-pass power absorption value

is close to 45%, although, in this case the waves are reflected at the low density cut-off, and again due to the low density of the plasma refraction is low and the waves are able to cross over the resonance layer for a second time, see figure 5.

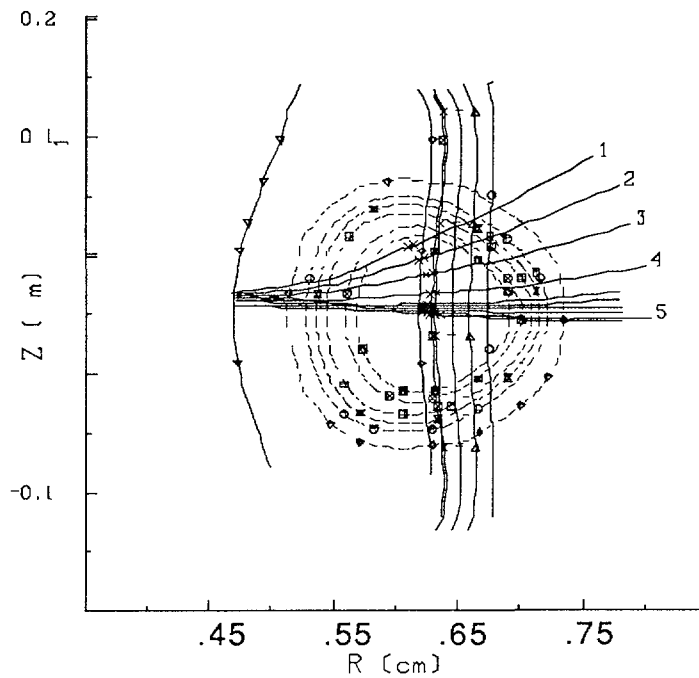


Figure 5

## REFERENCES

1. L.M.Kovrizhnykh, IAEA meeting, Nice, France, October 1988
2. R. C. Goldfinger and D. B. Batchelor, Nucl. Fusion **27**, 31 (1987)
3. C. Alejaldre et al. , this conference
4. J. Guasp et al. , this conference
5. C. Alejaldre and F. Castejon, *Microwave Absorption on Stellarators with a non-Maxwellian Electron Distribution Function*, Submitted for publication to Physics of Fluids
6. C. Alejaldre , Nucl. Fusion **28**, 849 (1988)
- 7 V. Krivenski, I. Fidone, G. Giruzzi, R. L. Meyer, L. F. Ziebell, Phys. Fluids **30**, 438 (1987).

# IMPURITY BEHAVIORS OF ECH AND RF PLASMAS IN CHS

S. MORITA and the CHS GROUP<sup>1</sup>

Institute of Plasma Physics,  
Nagoya University,  
Nagoya, Japan

## Abstract

Spectroscopic measurements have been carried out for ECH and ICRF currentless plasmas. The results from the ECH plasmas are described for typical three operations of magnetic axis shift, limiter insertion and gas puff control. From the spectroscopy it is observed that the inward shift causes radiation collapse because of the severe contact with vacuum wall. Although the limiter insertion also causes the radiation collapse at the end of the 35ms discharge, it is due to the increase of the hydrogen recycling rate on the limiter surface. The discharge without gas puffing realizes a low-density and low-impurity concentration plasma ( $n_e=2 \times 10^{12} \text{cm}^{-3}$ ,  $T_e=800 \text{eV}$ ) indicating no buildup of the impurity. The ICRF plasma is produced with Ti gettering. The Ti gettering drastically suppressed a large amount of the oxygen influx. As a result, relatively long discharges of 12ms are obtained with parameters of  $n_e=3.5 \times 10^{12} \text{cm}^{-3}$  and  $T_e=200\text{--}300 \text{eV}$ .

## I. Introduction

Compact Helical System (CHS) is an  $l=2$ ,  $m=8$  torsatron device with  $R=1\text{m}$ ,  $\langle r \rangle=20\text{cm}$ , and it is characterized by a low aspect ratio of 5. The first plasma of the CHS torsatron was obtained on last June (1988) with ECH pulse after magnetic surface measurements using an electron gun. The electron temperature, however, was still low because of the electron density rise arising from a rapid increase in impurity concentration.  $\text{H}_2$  ECR (2.45GHz) and He glow discharges were carried out for wall conditioning with simultaneous  $100^\circ\text{C}$  baking of the device. The quantities of light impurities and hydrogen recycling rate could be successfully suppressed to a permitted level. As a result, high-temperature ECH plasmas with an injection power of 100kW were obtained after a few months, although the electron temperature decreased at the latter half of the ECH pulse during 50ms. The plasma parameters obtained are ranging in  $1 \leq n_e \leq 10 \times 10^{12} \text{cm}^{-3}$  and  $T_e \leq 800 \text{eV}$ .

As the CHS device is a low aspect ratio torsatron, the plasma-wall distance is relatively small. For example it has only a distance between 0 and 2cm in usually used magnetic configurations. Then, it becomes important to investigate the impurity behaviors, in addition to the realization of good wall condition and of clearly defined scrap-off layer. One of studies of the ECH plasma is carried out along these purposes. The results are obtained on (i) variation of the plasma-wall distance, (ii) limiter insertion and (iii) gas puff control.

---

<sup>1</sup> The members of the CHS Group are identified in the paper entitled 'Overview of CHS experiment', these proceedings, p. 51.

On the other hand, ICRF plasmas could not be sustained without using Ti gettering because of the rapid increase in radiation loss due to a lot of oxygen influx from antennas and simultaneous density rise. For the experiment of the ICRF plasma production the large effort was made on extension of the discharge length. Consequently plasmas with the electron temperature of 200–300eV have been sustained during 12ms by the ICRF wave injection only, when the Ti gettering was applied shot by shot. The impurity behaviors of the ICRF plasmas are roughly described in relation with the Ti gettering.

## II. ECH Plasmas

ECH hydrogen plasmas have been produced with a 28GHz gyrotron under a magnetic field of around 1T. The input power of the ECH is about 100kW.

The measurements of the impurity VUV lines were done by a 1m normal incidence vacuum monochromator with an osmium-coated 1200g/mm grating. The VUV lines of hydrogen, carbon, oxygen and chromium are routinely monitored. From the observations of these lines over three months in CHS the dominant impurity making electron densities increased is understood to be oxygen.

Figure 1 shows the results of the magnetic axis shift experiment. The plasma-wall distance for the inward shift of the plasma at  $R_{ax}=94.9\text{cm}$  is smaller than the standard case at  $R_{ax}=97.4\text{cm}$ . In the case of the inward shift the electron density is linearly increasing until just before the ECH pulse off (see Fig 2). The radiation loss observed from the pyro-electric detector is higher compared with the standard case and the peak value exceeds the input power of

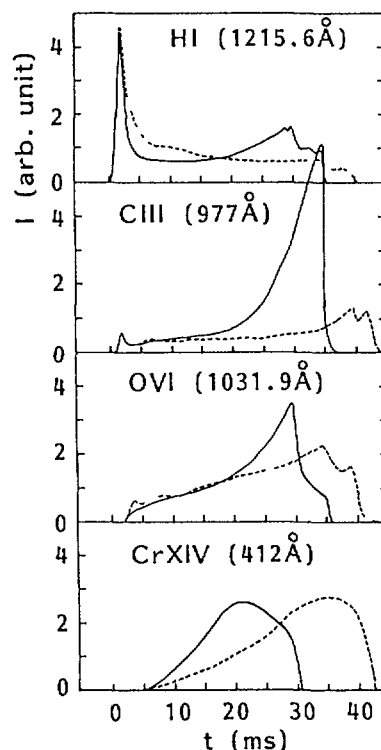


Fig.1 Impurity behaviors of magnetic axis shift experiment  
Solid lines and dotted lines indicate inward shift ( $R_{ax}=94.9\text{cm}$ )  
and standard ( $R_{ax}=97.4\text{cm}$ ), respectively

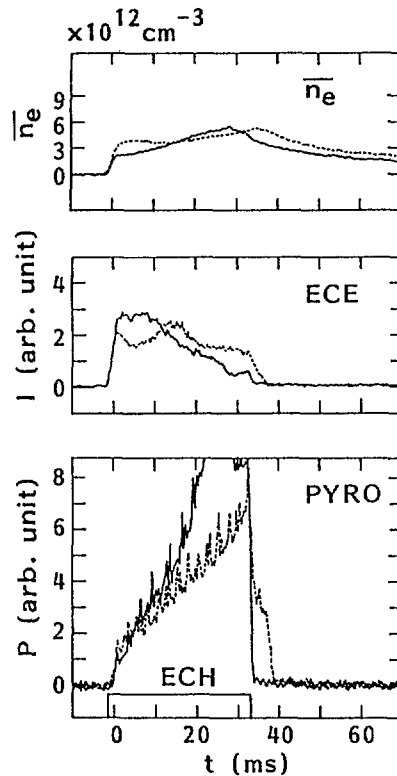


Fig.2 Plasma behaviors of magnetic axis shift experiment.  
Line indications are the same as Fig.1.

the ECH. The impurity lines, especially carbon and oxygen, increase in the inward shift case. In addition, the hydrogen recycling suggested from the HI emission also increases in the middle phase of the ECH pulse. According to it, the electron temperature decreases and finally the radiation collapse happens. On the contrary in the standard case the plasma is sustained without the radiation collapse. These phenomena clearly depend on the plasma-wall distance and/or plasma-wall interaction.

The limiter insertion experiment of Mo material is carried out as shown in Figs.3 and 4. It is easily noticed that Mo and Cr ions increase in the limiter insertion. The enhancement of the Cr ions is coming from the material (stainless steel) of the limiter support bar. The hydrogen recycling is relatively large in the limiter experiment, although it is located at the limiter section. Moreover, the recycling increases at the later phase of the plasma and the radiation from the light impurities is enhanced. This increase leads to the radiation collapse. At present the radiation from the limiter material of Mo is not dominant in CHS. It is probably important to reduce the recycling rate from the limiter using some method such as a limiter baking.

The electron temperature of the ECH plasma strongly depends on the electron density. The lower density of  $2 \times 10^{12} \text{cm}^{-3}$  is obtained in the case of without gas puffing. At that time the maximum electron temperature of 800eV is established. In this case the impurity levels become low and the recycling rate decreases drastically as shown in Fig.5. The total radiation loss is saturated at a middle of the ECH pulse (see Fig.6). This behavior is in contrast to that of the discharge with gas puff. These phenomena are limited to the

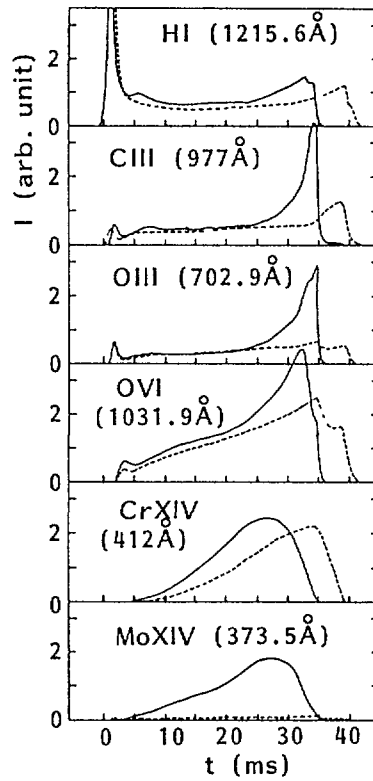


Fig.3 Impurity behaviors of Mo limiter insertion experiment  
 Solid lines and dotted lines indicate limiter-on  
 and limiter-off cases, respectively.

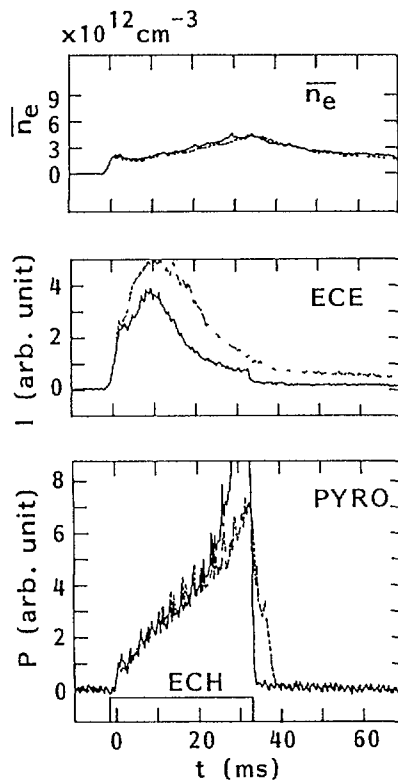


Fig.4 Plasma behaviors of Mo limiter insertion experiment  
 Line indications are the same as Fig 3.

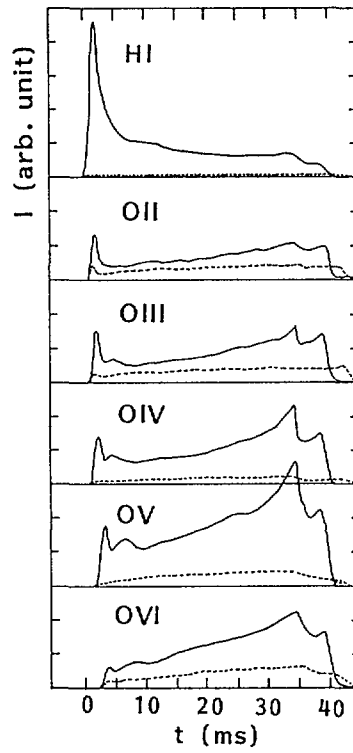


Fig.5 Impurity behaviors of gas puff control experiment. Solid lines and dotted lines indicate gas-puff-on and gas-puff-off cases, respectively.

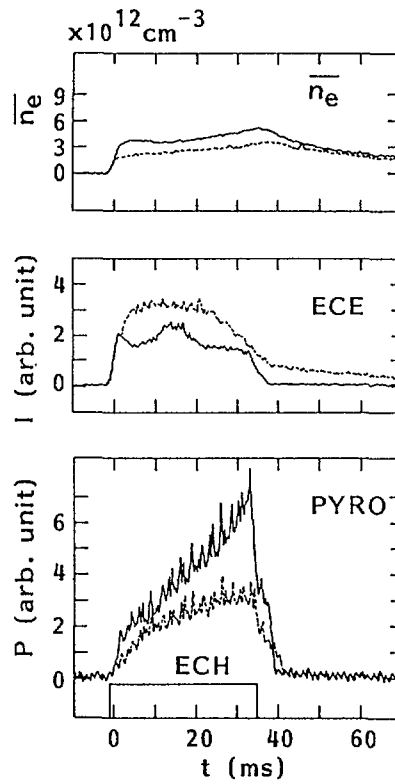


Fig.6 Plasma behaviors of gas puff control experiment. Line indications are the same as Fig.5.

discharges of reduced hydrogen recycling rate, and the saturation of the radiation loss and impurity levels might be considered in relation with the plasma electric potential

### III. ICRF Plasma

ICRF plasma production has been made by injecting only the ICRF wave under various magnetic fields. In this report the results are described on the ICRF plasma using Nagoya type-III antenna (500kW, 75MHz,  $B_t=0.6T$ )

The discharge length of the ICRF plasmas was limited to less than 5ms because of the radiation loss and the density rise caused by the intense oxygen influx, although the accumulation of the discharges reduced the oxygen level a little, as shown in Fig 7 (shot 3473, shot 4690). The use of T<sub>1</sub> gettering, however, extremely improved such a condition. The flashing of a T<sub>1</sub> ball facing to the antenna and two more T<sub>1</sub> balls at other locations covers 10% of the total vacuum wall area. Especially, the pulse length reached 12ms in carrying out shot-by-shot-based T<sub>1</sub> gettering (shot 5988). Thus, the oxygen level becomes comparable to that of the ECH plasma.

Figure 8 shows an effect of single flash of T<sub>1</sub> gettering on the discharge length. It indicates that the duration of the effect is less than 10 discharges. So, the shot-by-shot-based T<sub>1</sub> gettering controls the oxygen influx also, and it leads to the improvement of the reliability of the ICRF plasma (see Fig 9).

The electron density and the impurity line behaviors of the typical discharge in the ICRF plasma production are shown in Figs 10 and 11, respectively. The averaged electron density obtained is  $3.5 \times 10^{12} \text{cm}^{-3}$  at the flat top. The rapid rise at the initial phase of the discharge in the HI emission disappears because of the intense T<sub>1</sub> flashing. The TiXII having an ionization potential of 292eV appears gradually in proportion to the discharge summation with the T<sub>1</sub> gettering. From the Fig 11 it is estimated that the electron temperature is 200-300eV. Further wall conditioning including the antenna will give a potentiality to get longer discharge length.

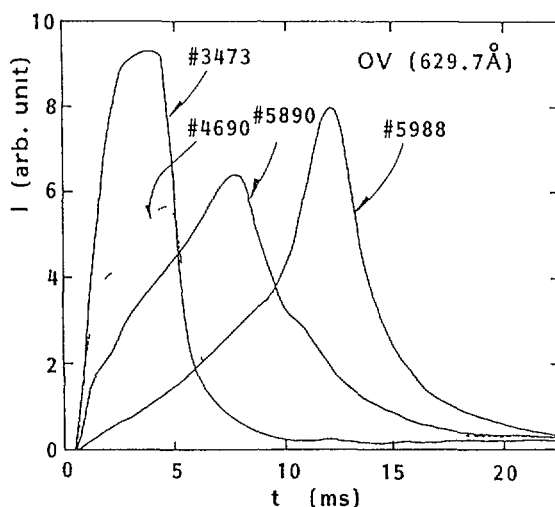


Fig.7 Time behaviors of OV line  
 Numerals indicate shot number of the ICRF plasma production  
 shot 3473 and 4690 (without T<sub>1</sub> gettering), shot 5890 (after T<sub>1</sub>  
 gettering of a few times), shot 5988 (shot by shot gettering)

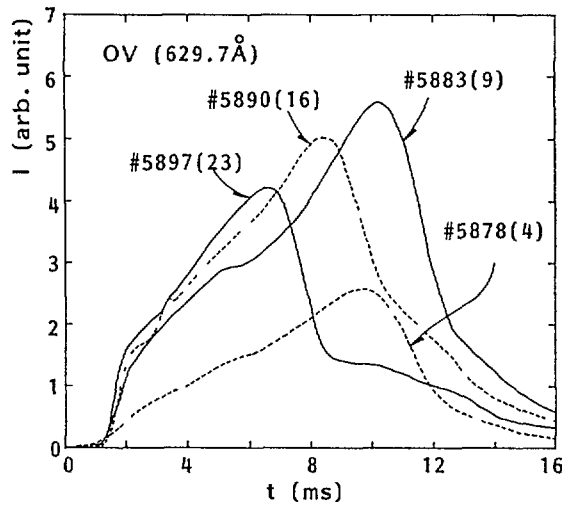


Fig.8 Effect of single flash of T<sub>1</sub> gettering  
 Single T<sub>1</sub> gettering is done between shot 5874 and 5875  
 Numerals in bracket indicate shot summation after the T<sub>1</sub> gettering

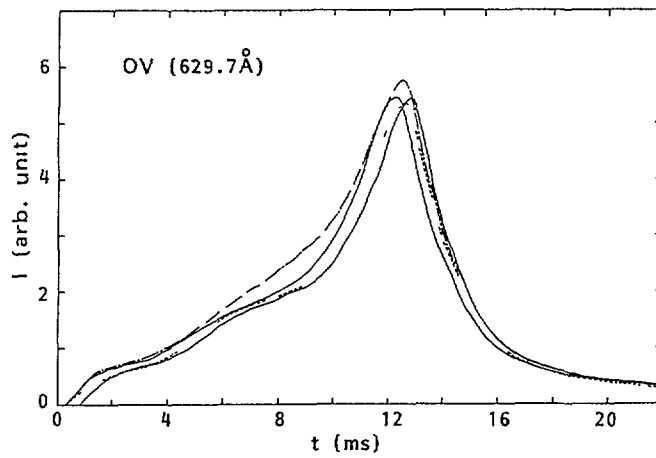


Fig.9 Reliability of ICRF plasmas with shot-by-shot-based  
 T<sub>1</sub> gettering

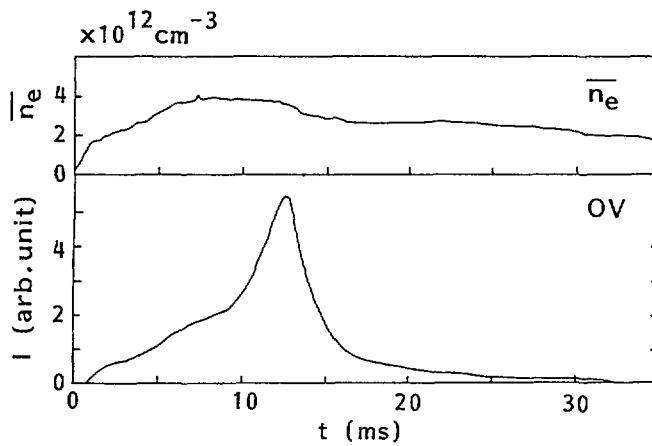


Fig.10 Time behaviors of typical ICRF plasma

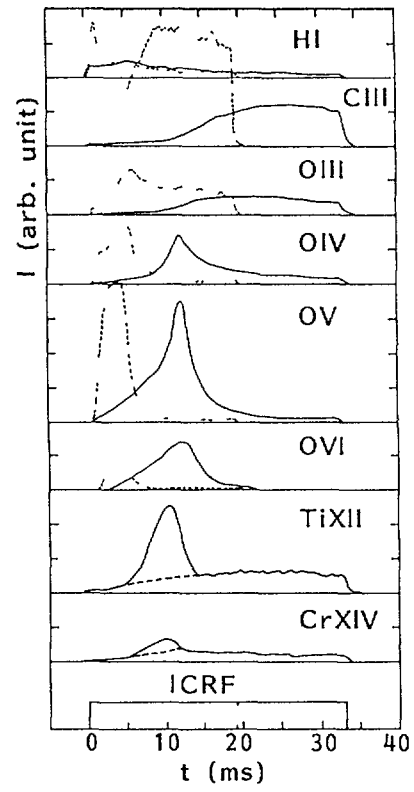


Fig.11 Impurity behaviors of typical ICRF plasma

# EXPERIMENT ON RF PLASMA PRODUCTION IN CHS

K. NISHIMURA, T. SHOJI, CHS GROUP<sup>1</sup>

Institute of Plasma Physics,  
Nagoya University,  
Nagoya, Japan

## Abstract

ICRF waves are applied to produce and heat a currentless plasma. Three waves (a whistler wave, a slow wave and an ion Bernstein wave) have been chosen for the plasma production. Two different type antennas are used to excite these waves. One is a pair of quarter turn antennas for the whistler wave excitation and another is the Nagoya Type-III antenna [1] for excitation of the slow and ion Bernstein waves. Both antennas have Faraday shields. These antennas were designed to fit the plasma boundary. Plasma of  $n_{e0} = 2-5 \times 10^{12} \text{ cm}^{-3}$ ,  $T_e(0) = 100-300 \text{ eV}$  and  $T_i(0) = 200-300 \text{ eV}$  was produced and sustained with the RF only.

---

## 1. Introduction

ECR discharge has been used to produce plasma in a helical system. However, the operating frequency of the Gyrotron is fixed, and a usable magnetic field range is narrow. It is inconvenient for the confinement studies in a wide range of the magnetic field. ICRF plasma production is a suitable method, because it is easy to change the operating frequency. Moreover, the cost of ICRF system is cheaper than that of ECRH system.

This paper describes the ICRF plasma production in Compact Helical System (CHS) [2]. Objectives of the ICRF plasma production in CHS are as follows; development of antenna system for plasma production in a helical system, research of plasma confinement in a wide range of the magnetic field, and research of equilibrium and stability of high beta plasma.

## 2. ICRF plasma production

Usually a slow wave propagates in lower frequency range than the ion cyclotron frequency. However, it is known that a complex magnetic field configuration like a helical system leads to a local Alfvén resonance and

---

<sup>1</sup> The members of the CHS Group are identified in the paper entitled 'Overview of CHS experiment', these proceedings, p. 51.

wave components of  $B_\theta$  and  $E_\parallel$  become strong. This component of  $E_\parallel$  gives the energy to electrons by the Landau damping and these electrons are expected to produce a plasma.

On the other hand, the ion Bernstein wave is an electrostatic wave which propagates in the region of  $n\omega_{ci} < \omega < (n+1)\omega_{ci}$  ( $n \geq 1$ ). The propagating direction of this wave is perpendicular to the magnetic field lines of force, and this wave is also expected to give the energy to electrons by the Landau damping. The propagation region of the ion Bernstein wave is a peripheral region ( $\omega/\omega_{ci} > 1$ ).

The whistler wave is an electromagnetic wave with right-hand circular polarization which propagates in the region of  $\omega_{ci} \leq \omega \leq \omega_{ce}$ . Since the phase velocity of this wave is slow, this wave is expected to couple with low energy electrons of the bulk plasma which is expected to sustain the ionization.

By use of these waves with suitable frequency, it is possible to produce a plasma in a wide range of the magnetic field.

### 3. Experimental results

A pair of quarter turn antennas (poloidal antenna), shown in Fig. 1, is used with 40MHz/1.5MW/100msec for the excitation of the whistler wave. The dependence of the line averaged electron density on the magnetic field strength is shown in Fig. 2. Abscissa is the normalized frequency by the ion cyclotron frequency on axis of the hydrogen ( $\omega_{CH}$ ). Decrease of the electron density near the ion cyclotron frequency ( $\omega/\omega_{CH} \sim 1$ ) shows that these frequency region is not effective for the whistler wave excitation.

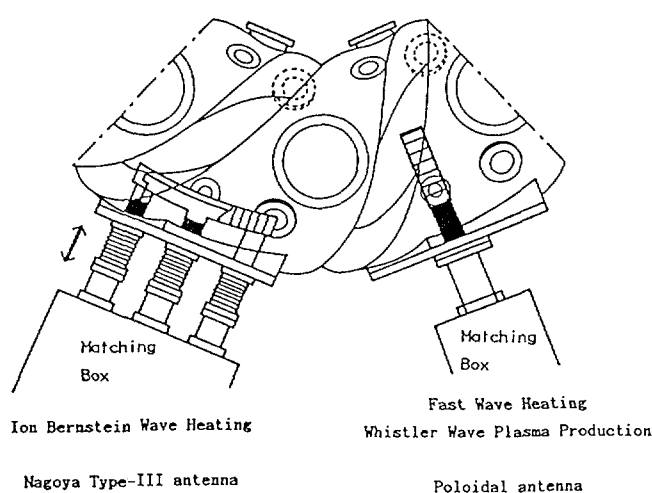


Fig. 1. RF antennas used in the experiment.

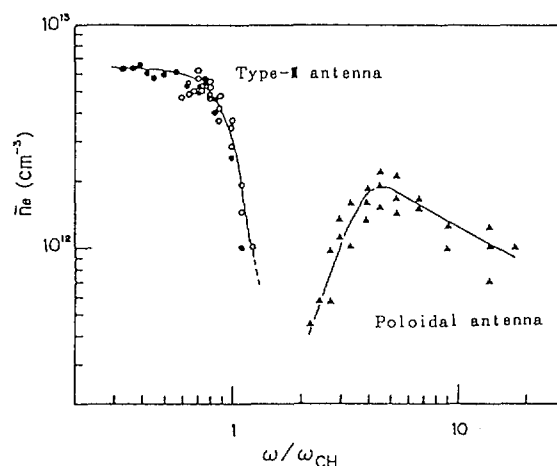


Fig. 2. Dependence of the line averaged electron density on the magnetic field strength for two type antennas. The magnetic field strength is normalized by the ion cyclotron frequency of hydrogen ( $\omega/\omega_{CH}$ ).

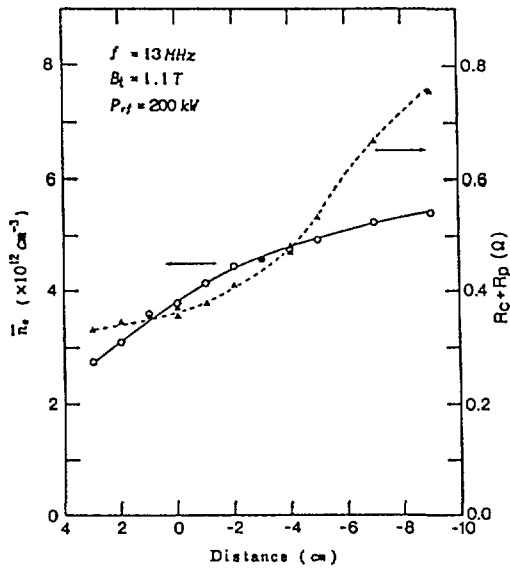


Fig. 3. The line averaged electron density and the loading resistance. Abscissa is the distance between the antenna and the plasma boundary.

The ion Bernstein and slow waves are excited in the range of the ion cyclotron frequency by the Nagoya Type-III antenna, shown in Fig 1. This antenna is movable radially by 15cm. Production efficiency is sensitive to the distance between the antenna and the plasma boundary. Figure 3 shows the line averaged electron density and the loading resistance as a function of the distance between the antenna and the plasma boundary. When the antenna position is inside the plasma boundary, which is indicated with the negative sign in this figure, the loading resistance becomes larger and

the electron density higher. In these experiments, the ion Bernstein wave is expected to be excited, because the region between plasma center and the antenna satisfies the condition of  $2 > \omega/\omega_{ci} > 1$ .

Figure 4 shows the dependence of the line averaged electron density on the magnetic field strength with two frequencies. When the magnetic field strength is high ( $> 1.5T$  for 13MHz and  $> 0.9T$  for 7.5MHz), there is no region of  $\omega/\omega_{ci} > 1$  inside the plasma. In such cases, the slow wave is thought to play the main role in the plasma production, because the ion Bernstein wave can not propagate into the plasma region. The ion temperature measured with the time of flight particle energy analyzer is about 150 eV in all range of the magnetic field.

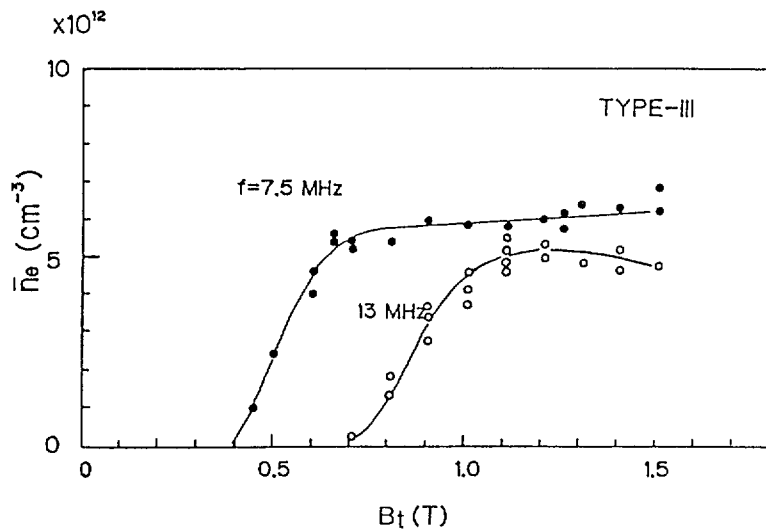


Fig. 4. The line averaged electron density produced by the Type-III antenna as a function of the magnetic field strength.

This shows the possibility of the ion heating at the ion cyclotron resonance layer ( $\omega/\omega_{ci} = 1$ ) in the plasma.

The profiles of the electron density and temperature measured with Thomson scattering system are shown in Fig. 5. Plasma of  $n_{e0} = 2-4 \times 10^{12} \text{ cm}^{-3}$  and  $T_{e0} = 200-300 \text{ eV}$  has been produced and sustained for 10-15 msec.

This experiment has been done under the following conditions: RF 7.5MHz with Type-III antenna, position of the magnetic axis  $R_{axis} = 93.6 \text{ cm}$ ,  $B_t = 0.59 \text{ T}$  ( $\omega/\omega_{ci} \sim 0.8$ ), titanium gettering and careful control of gas fuelling. This magnetic field configuration is suitable for the ion Bernstein wave excitation and the slow wave heating. Titanium gettering is effective to suppress the oxygen impurity and to prolong the discharge with the high temperature.

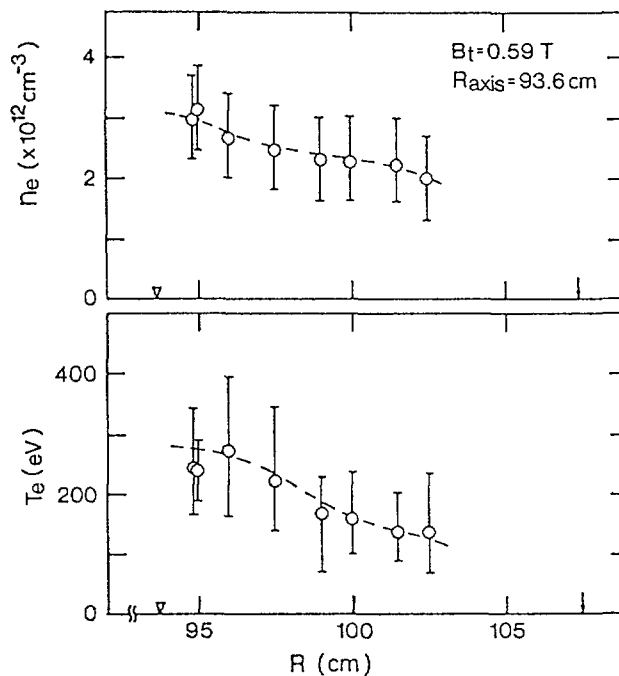


Fig. 5. Profiles of the electron density and temperature with Thomson scattering. This experiment is done with the Type-III antenna (7.5MHz).

#### 4. Summary

Plasma of  $n_{e0} = 2-5 \times 10^{12} \text{ cm}^{-3}$  is produced and sustained with the ICRF waves only in a wide range of the magnetic field strength (0.15T ~ 1.5T). The electron temperature of 100-300 eV and the ion temperature of 200-300 eV are achieved with careful control of gas fuelling and titanium gettering.

#### REFERENCES

- [1] T.Watari, et al., Phys. Fluids, 21 (1978) 2079.
- [2] M.Fujiwara, et al., Proc. 14th European Conf. Controlled Fusion and Plasma Physics, Madrid, 1987, Vol.11d, Part 1, p404.

# ICH SYSTEM FOR HELIAC H1

B.D. BLACKWELL, G.D. CONWAY  
Plasma Research Laboratory,  
Research School of Physical Sciences,  
Australian National University,  
Canberra, Australia

## Abstract

An Ion Cyclotron Heating system for the H1 heliac has been defined. Stage 1 (1987-90) has concentrated on the construction and optimization of a fast wave (15 MHz – 180 kW) antenna system. Stage 2 of operation (1990-92) will investigate heating by ion Bernstein and whistler waves.

---

## 1. Introduction

For the initial operation of the H1 heliac, the plasma will be heated by RF power in the ion cyclotron range of frequencies. The heliac geometry provides a challenge for ICRF heating: the ring conductor causes the magnetic field strength to vary considerably in a poloidal cross-section, and the helical axis makes toroidal variation quite significant. Several wave modes - fast and slow modes, ion Bernstein and the whistler modes [1] are being considered in view of requirements for the RF - plasma formation, plasma density buildup and plasma heating.

## 2. Fast mode heating

A prototype antenna for hydrogen minority fast wave heating has been constructed [2], and will shortly be tested at high reactive powers in a vacuum test stand. The antenna consists of two sections of shorted strip line with an array of electrostatic shields. Each antenna half (top and bottom) is in the same poloidal plane with its own coaxial current feeder. The antenna is of all-metal construction (stainless steel) and is curved in the poloidal direction with two radii chosen to conform to the plasma boundary on the low field side at  $\phi = 135^\circ$  (fig.1). The 40 mm wide active conductor (silver plated) is 20 mm above the backplane and is surrounded by a double layer of shields 80 mm wide (fig.2) The top antenna is 564 mm long and the bottom 449 mm. The antenna design calls for water cooling and side limiters, but the prototype antenna omits these features to allow easily dismantling for repairs and modifications. This simple, proven geometry will provide experience in construction techniques, high voltage standoff and surface coatings in the H1 environment, and will ensure that a tested antenna will be available for the first plasma experiments.

## 3. ICRF System

The ICH power system consists of six 30 kW (continuous) transmitters, installed below the machine room. The transmitters have an operational frequency range of 4–26 MHz and are externally synchronized. A lumped element two channel tuning circuit, with a high degree of flexibility, has been designed to accommodate the various antennas (fig.3). A twin  $6\frac{1}{8}$  inch dia rigid coaxial transmission line connects the tuning circuits to the vacuum feedthroughs. The matching box will also house the transmitter power combiners and the DC-breaks. Directional couplers are located in both the rigid line sections and at each of the transmitter outputs. The RF cabling and dummy load have been installed, and the first transmitter is ready for power tests. H1 will operate in either of two modes, pulsed with  $B_o = 1$  T, or quasi-continuous with  $B_o = 0.25$  T. However, even for dc field operation the RF system will be pulsed (typically 10 Hz with a 10 ms pulse length) to reduce unnecessary heat loads on the transmitters and antennas.

## 4. Numerical modelling

Analysis of the ICH system falls into three distinct parts: a) the antenna – evaluation of the plasma loaded antenna impedance; b) the transmission line – calculation of the voltage distribution along the line and the

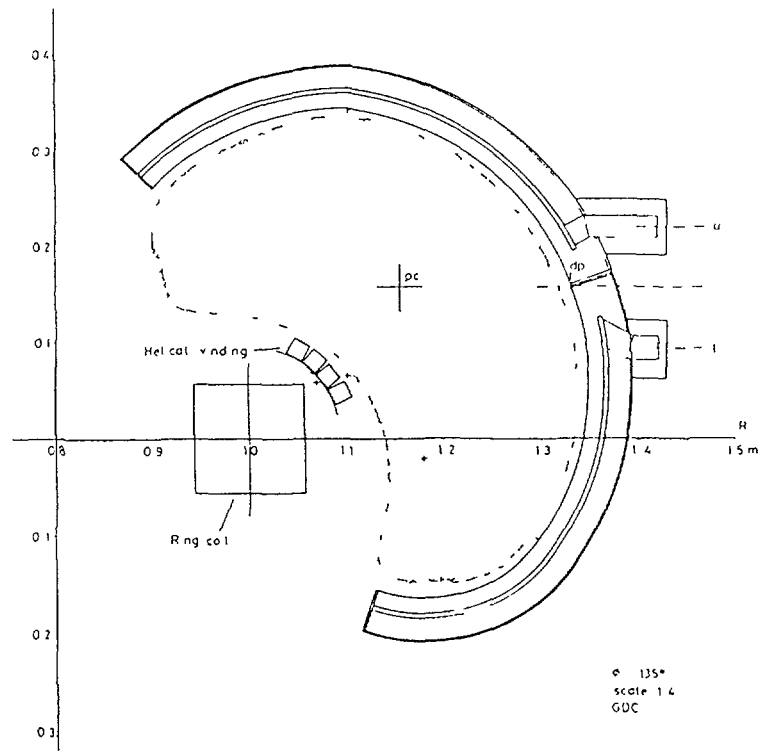


fig.1 ICRF antenna and plasma boundary at  $\phi = 135^\circ$ .

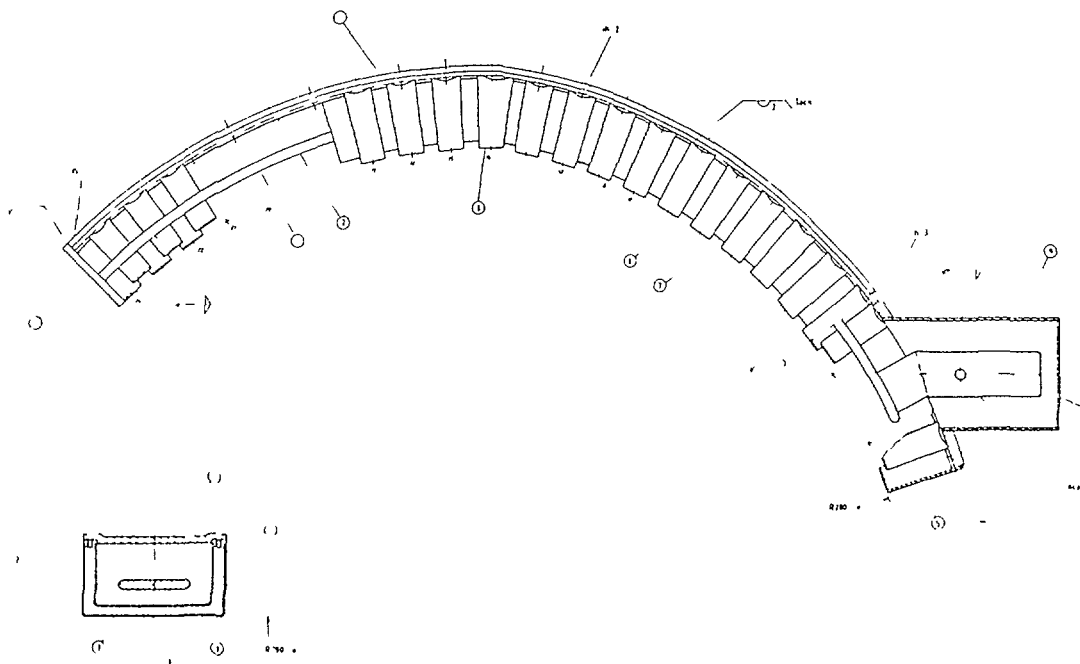


fig 2: Detail of top half of antenna & shields.

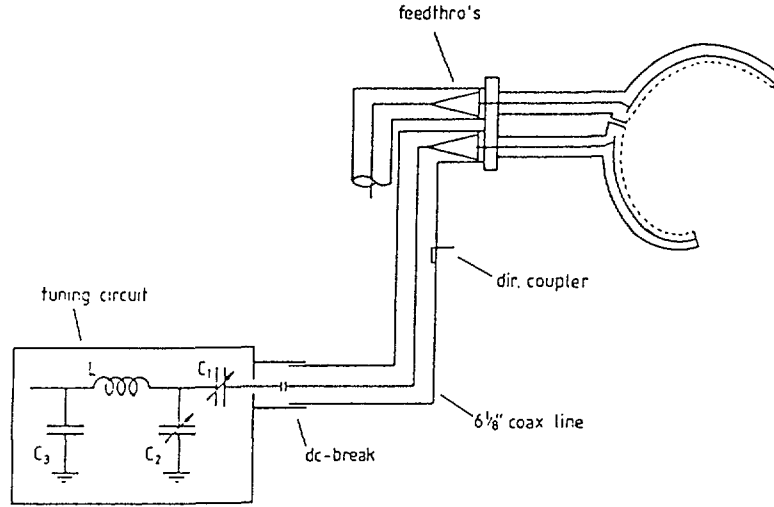


fig.3: Layout of transmission line system & tuning circuit.

transformation of the antenna impedance; c) the matching circuit – determination of the optimum component values and operational limits.

**a) Antenna.** The antenna design has been analysed with a code based on the 2D model developed by the Brussels group [3], [4]. Their EMF method uses a cold plasma description, retaining only the magnetosonic wave, a uniform magnetic field with single pass absorption (no reflection beyond cut-off). We retain the linear radial  $k_{\perp}^2$  profile and have scaled the density gradient from experimental results from SHEILA [5].

The specific resistance  $R$  and reactance  $L$  are related to the resistive and reactive spectra  $g'(k_{\parallel})$  and  $h'(k_{\parallel})$  by:

$$R - i\omega L = -\frac{\omega\mu_0}{2\pi} \int_{-\infty}^{\infty} (g' - ih') \frac{|J(k_{\parallel})|^2}{|I|^2} dk_{\parallel}$$

The (toroidal) width of our antenna is narrow compared to  $\pi/|k_{\parallel}|$  which requires us to calculate fully  $g'(k_{\parallel})$  and  $h'(k_{\parallel})$  using fractional order Bessel functions before integrating through  $k_{\parallel}$ . Fig.4 shows the  $g'$  and  $h'$  spectra multiplied by a flat antenna current profile  $J^2(k_{\parallel})/I^2$  (gp1 & hp1) and a profile peaked at the antenna edges (gp2 & hp2). Fig.5 compares the antenna spectra for two core densities (gp1)  $1 \times 10^{18} \text{ m}^{-3}$  and (gp2)  $5 \times 10^{19} \text{ m}^{-3}$ .

The antenna impedance is calculated from the specific resistance, capacitance and inductance using the transmission line equation. Fig.6 & 7 show the impedance computed as a function of the core density for a)  $f = 15.2 \text{ MHz}$ ,  $B = 1 \text{ T}$  (pulsed operation) and b)  $f = 3.8 \text{ MHz}$ ,  $B = 0.25 \text{ T}$  (quasi continuous operation). For the expected operating density  $n_e = 5 \times 10^{19} \text{ m}^{-3}$   $R_a$  is approximately 0.8 ohms and  $L_a$  is 8.3 ohms at  $f = f_{cH} = 15.2 \text{ MHz}$ . The results shown are for the top half of the antenna alone.

**b) Transmission line.** From the standard transmission line equations the standing wave voltage  $|V_y|$  and the transformed resistance  $R_y$  and reactance  $X_y$  were computed as a function of the distance from the antenna input. Fig.8 shows a typical distribution for the antenna parameters in fig.6. The attenuation factor  $\alpha$  is determined primarily by the conductivity and dimensions of the copper coax line.

**c) Tuning circuit.** An impedance matching circuit with four elements was chosen for maximum flexibility (fig.3).  $X_y$  is compensated by the equal and opposite reactance of the variable vacuum capacitor  $C_1$ ; while  $R_y$  is transformed to  $Z_o = 50 \text{ ohms}$  by the pi-network formed from  $L$ ,  $C_3$  and the variable capacitor  $C_2$ . Fine tuning is through  $C_1$  and  $C_2$ , whilst  $L$  and  $C_3$  are replaced for different operating frequencies.

Design work is also in progress on the breakdown antenna (a short unshielded stripline antenna) and the ion Bernstein antenna (a twisted 1–2 m long shielded antenna conforming to the last flux surface but parallel to  $B$ ).

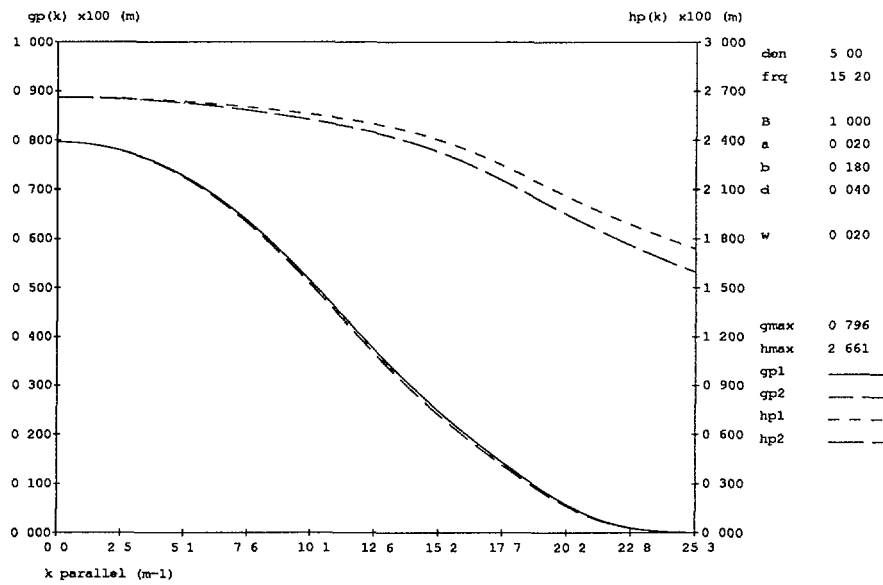


fig.4: gp(k) & hp(k) spectra

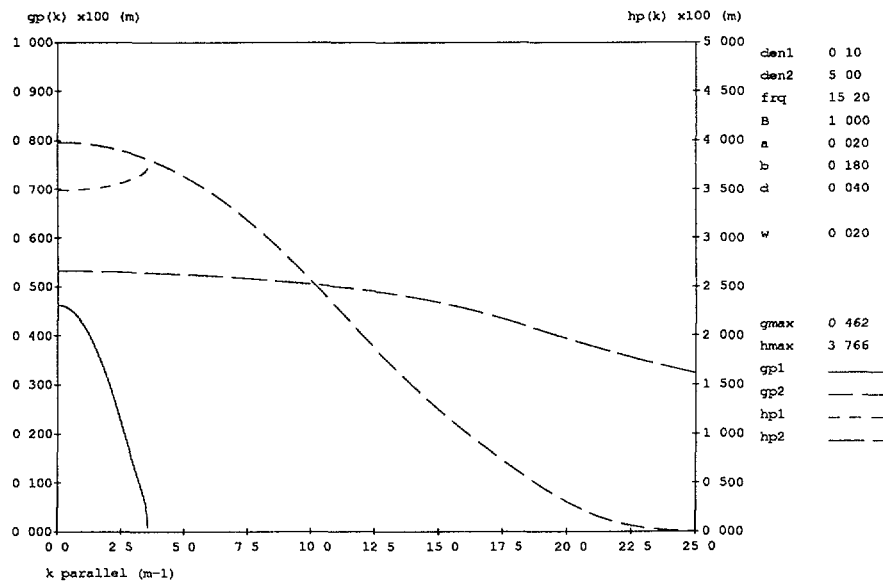


fig.5: gp(k) & hp(k) spectra

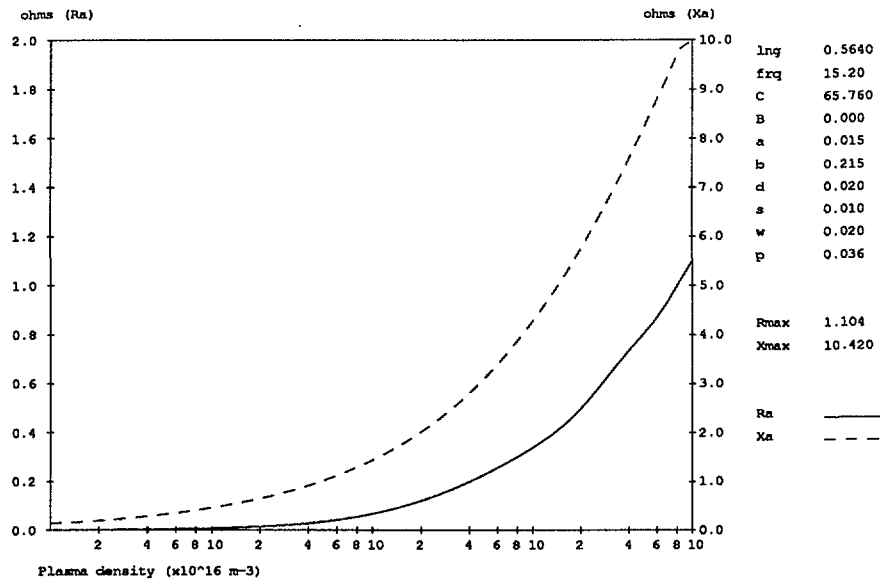


fig.6: Antenna impedance B=1.00T

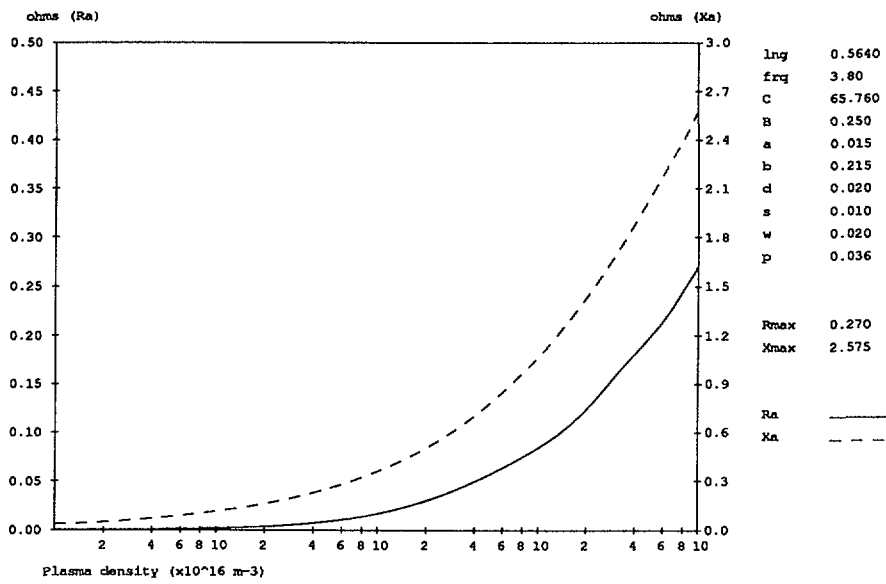


fig.7: Antenna impedance B=0.25T

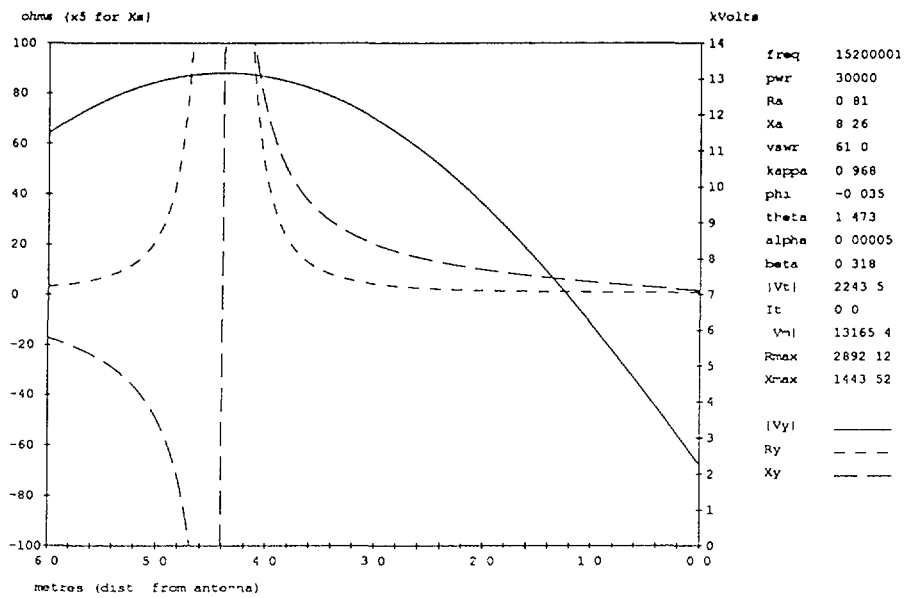


fig.8: Voltage distribution on transmission line.

### References

- [1] R.W.Boswell (1985), Plasma Phys. 10, p1147.
- [2] G.D.Conway & B.D.Blackwell (1989), 'An ICRF Fast-wave antenna design for the H1 Helic', report no. ANU-PRL-TR 89/3.
- [3] A.M.Messiaen, R.Meynart & R.R.Weynants (1981), LPP-ERM/KMS report no. 76, Brussels.
- [4] A.M.Messiaen *et al.* (1982), in 'Heating in Toroidal Plasmas III' vol.1, p243; and (1980) 'H in TP II' vol.1, p487, CEC Pergamon.
- [5] B.D.Blackwell *et al.* (1989), Aust. J. Phys. 43, 73.

# PLASMA PRODUCTION USING MICROWAVE AND RADIOFREQUENCY SOURCES\*

M.D. CARTER  
Oak Ridge National Laboratory,  
Oak Ridge, Tennessee,  
United States of America

## Abstract

This paper is devoted to the plasma production by microwave and RF sources in magnetic traps. It is shown that microwaves with frequencies at the fundamental electron cyclotron resonance can be used for this purpose. Waves with frequencies of a few megahertz have been used to produce plasmas at the Uragan-3 device at KFTI. Qualitative agreement was found between the results of these experiments and the analytic predictions were presented in this paper.

---

## 1. INTRODUCTION

The initial breakdown of neutral fill gas is an important issue for stellarators where ionization of the neutral gas prefill is necessary before other auxiliary power can be coupled to the system. Microwaves with frequencies at the fundamental electron cyclotron resonance can be used for this purpose because they couple to electrons through linear wave-particle interactions. In addition, microwave applications at twice the electron cyclotron frequency typically have a strong enough nonlinear coupling to initiate breakdown with reasonable agreement between theory and experiment [1,2]. Nonlinear couplings at higher harmonics are progressively weaker, and the possibilities of using the third harmonic are discussed in Section 2.

A difficulty can arise when microwave sources are used for plasma production because it is often too expensive to support the frequency ranges needed to obtain breakdown at arbitrary static magnetic field values. Thus, devices that rely exclusively on microwave sources to obtain target plasmas may be limited in their operational range by their microwave source frequencies. Alternatively, RF sources possessing a broad band of tunable frequencies are often available in the megahertz frequency range. The use of these types of power sources to produce target plasmas could add to the operational limits of many devices.

Waves with frequencies of a few megahertz (well below the frequency for vacuum cavity modes) have been used to produce plasmas at the Institute of Physics and Technology at Kharkov (KFTI) for many years [3,4]. The technique and mechanism by which the neutral gas is broken down in the very early phases of these discharge are presented in Section 3. A summary and conclusions are presented in Section 4.

## 2. MICROWAVE PLASMA PRODUCTION

When considering the interaction of microwaves with frequencies equal to a localized value of the electron gyrofrequency, the linear interaction of particles with waves having polarization in the same sense as the electron gyration is strong regardless of the electron's initial energy. Thus, any free electrons can be excited and breakdown can easily occur if power balance requirements are satisfied.

---

\* Research sponsored by the Office of Fusion Energy, US Department of Energy, under contract DE-AC05-84OR21400 with Martin Marietta Energy Systems, Inc.

For waves that are resonant at higher integer multiples of the electron cyclotron frequency, the linear interaction becomes negligibly small for low initial electron energies and nonlinear wave-particle interactions must be considered. When multiples of the cyclotron resonance occur in regions of broad magnetic scale lengths, the gyrophase of the electron can be “locked” by the waves so that energy can be added over many gyroperiods until relativistic or finite gyroradius detuning effects become comparable to the nonlinear “locking” effect. When the resonance becomes detuned because of the energy change, the electron energy decreases so that a periodic energy excursion occurs [1]. The change in  $\mu = (v_{\perp}/c)^2$ ,  $\Delta\mu$ , that produces a phase slippage comparable to the phase “locking” effect for a precisely tuned resonance is given roughly by

$$\Delta\mu \approx \epsilon\bar{\mu}^{(\ell/2-1)} \quad (1)$$

and the approximate frequency of the energy excursion is

$$\nu_{\text{rf}} \approx \epsilon\omega\bar{\mu}^{(\ell/2-1)} \quad (2)$$

where  $\ell$  is the harmonic number,  $\epsilon = (2e|E_{-}|)/(mc\omega)$  is a very small parameter typically of order a few  $\times 10^{-5}$ ,  $e$  is the electron charge,  $|E_{-}|$  is the right-hand circular component of the microwave field,  $m$  is the electron rest mass,  $c$  is the speed of light in vacuum,  $\omega$  is the microwave frequency, and  $\bar{\mu}$  is roughly the average value of  $\mu$ . Efficient ionization of the surrounding neutral gas can then occur if  $mc^2\Delta\mu$  is greater than or of the order of the ionization potential,  $I_p$ , and  $\nu_{\text{rf}}$  is greater than or of the order of the electron-neutral collision frequency,  $\nu_{\text{en}}$ .

Note that for  $\ell = 2$  (second harmonic) the change in  $\mu$  giving rise to the phase slippage depends only on the microwave field strength and frequency, so that a strong nonlinear coupling occurs even if the initial electron energy is very low ( $\sim 1$  eV). The resulting energy excursions for  $\ell = 2$  can then take place with frequencies of the order of megahertz and amplitudes of the order of several times  $I_p$  for typical parameters found in present experiments. The marginal requirements for plasma production at the second harmonic ( $\ell = 2$ ) can then be summarized by [2]:

$$|E_{-}| \gtrsim 3fI_p \quad \text{V/m}$$

and

$$\nu_{\text{en}} \lesssim 500|E_{-}| \text{ s}^{-1} \quad (3)$$

where  $f$  is the microwave frequency in GHz,  $I_p$  is in eV, and  $|E_{-}|$  is in V/m.

For the case of a third harmonic interaction ( $\ell = 3$ ), Eqs (1) and (2) show that the  $\Delta\mu$  required for significant phase slippage is smaller by a factor of order  $v/c$  such that only a very small nonlinear coupling can occur over a very long time scale for electrons with low initial energies. Thus, one would expect that the enhancement in the electric field strength required to achieve a nonlinear interaction comparable to that at the second harmonic is of the order of several hundred for 1 eV electrons. Such an enhancement could be obtained only by providing extremely high microwave power levels, greatly increasing the cavity  $Q$ , or strongly focusing the microwaves directly on the resonance region. Alternatively, some linear microwave coupling for  $\ell = 3$  might occur with tenuous, very hot ( $\sim$  keV) electrons produced by some other source.

### 3. LOW FREQUENCY PLASMA PRODUCTION

The method by which plasmas are produced using low frequency RF sources ( $\sim$  MHz) in the Uragan-3 device at KFTI is illustrated in Fig. 1. Figure 1 shows that the process occurs in two stages, a “preionization” phase where there is no wave propagation as shown by RF pickup loops located roughly half way around the torus, and a “build-up” phase ( $t > \Delta t$ ) where waves propagate and heat the plasma by various damping mechanisms [3,4]. The antennas used are frame-type antennas that are contoured to fit around the last closed flux surface of the stellarator plasma with the longest elements separated poloidally

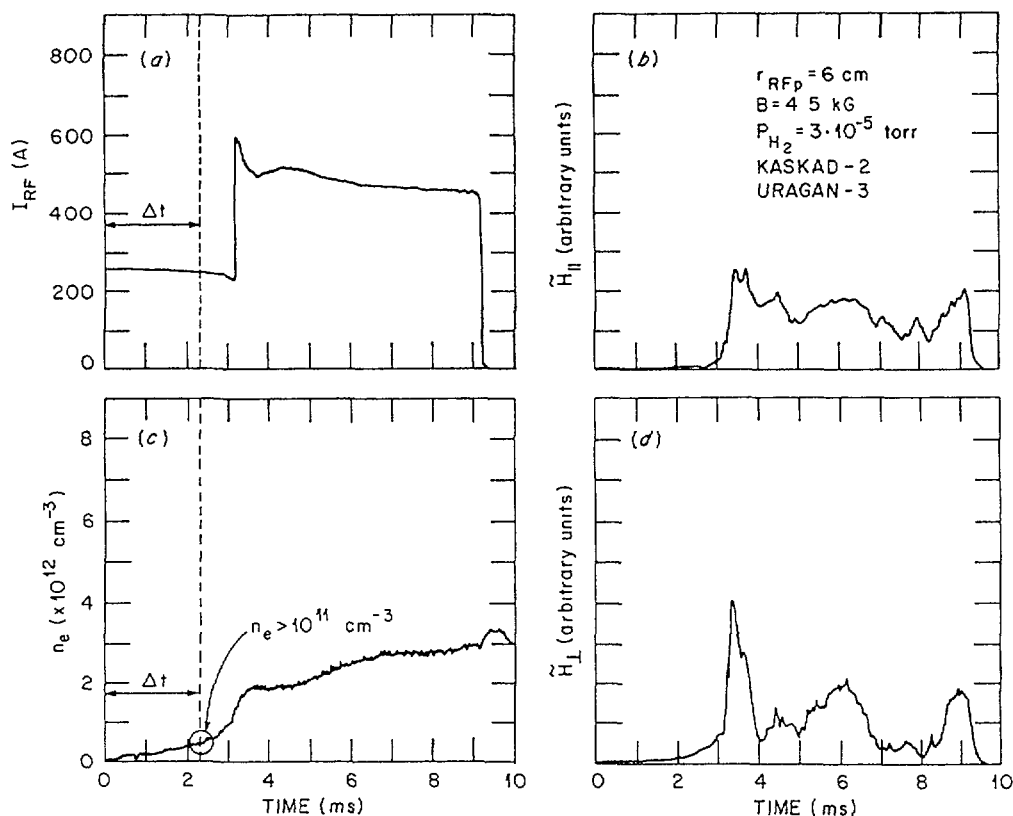


FIG 1

by roughly one-third of the plasma poloidal extent and having a length of roughly 70 cm along the static magnetic field. These longest current elements are at an angle to the toroidal magnetic axis.

A window in the applied RF antenna voltage (current) is observed experimentally such that if the RF current is either *too low* or *too high* the “preionization” phase is never completed. The low-current limit is expected on the basis of the electron oscillation energy requirements to cause ionization driven by RF electric fields parallel to the static magnetic field. The high-current limit is not intuitively expected, but can be understood in terms of the ponderomotive trapping effect by the RF near fields. By looking at the RF near-field patterns from a rectangular loop of RF current, it is found that the electric field along a field line can be approximated by

$$|E_z| \approx -E_0 \frac{z}{\lambda}; |z| < \lambda \quad (4)$$

giving rise to Mathieu’s equation for the parallel electron motion:

$$\frac{d^2 z}{d\tau^2} + (2\xi^2 + 2\xi \cos \tau) z - 0 \quad (5)$$

where  $\xi = eE_0/(2m\lambda\omega^2)$  and only the largest slowly varying and oscillatory terms have been retained. The concept of a ponderomotive force on the electrons (first term in parentheses in Eq. (5)) remains valid so long as the solutions to Eq. (5) remain stable for many RF periods. The condition for the existence of stable solutions to Eq. (5) is that  $\xi < (\sqrt{3} - 1)/4 \approx 0.183$  [5]. Electrons will remain confined in the exciting region and

produce more electrons in the region if their oscillation energy is sufficient to ionize neutral atoms and if the electron is not expelled from the exciting region on the RF period time scale. Note that if an electron is expelled because its orbit is unstable, it may produce more electrons in the region away from the antenna, but these electrons will be born in a region of low excitation and will be repelled from the exciting region by the ponderomotive force; thus, the efficiency of the "preionization" phase is greatly reduced if the electron orbits are unstable in the RF near field region.

The criterion for efficient "preionization" by low frequency waves can be summarized in terms of the dimensionless parameters,  $\alpha = |eE_0\lambda|/I_p$ , and  $\beta = m\lambda^2\omega^2/I_p$ , by

$$\sqrt{2\beta} < \alpha < \left(\frac{\sqrt{3}-1}{2}\right)\beta \quad (6)$$

In Fig. 2 the regions satisfying Eq. (6) in front of a planar loop antenna are shown superimposed over the confining flux surface regions of the Uragan 3 device for several different RF currents for a frequency of 5.4 MHz, an angle of  $16^\circ$  to the static magnetic field, and with the length of the loop along the static field equal to 70 cm. Although effects caused by the helical geometry are not included in the calculation, the movement of the breakdown region with antenna current strongly indicates that the experimental preionization phase in Uragan 3 was governed by the existence of a "ponderomotive" potential electron trap in the antenna region. In fact, the window in RF current for this calculation is in very good quantitative agreement with the experimental measurements.

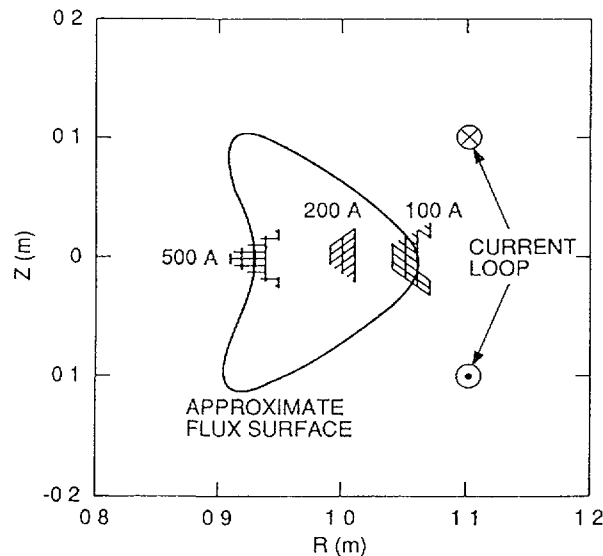


FIG 2

#### 4. CONCLUSIONS

The efficient breakdown of a neutral gas using microwaves with frequencies that are resonant at the electron gyrofrequency can be understood from power balance considerations alone because of strong linear wave-particle interactions. For microwave frequencies that are resonant at twice the electron gyrofrequency, a strong nonlinear interaction can take place with cold electrons if the resonance is located near a region of broad static magnetic field scale length, and breakdown requirements for this process can be identified in terms of the frequency and electric field strength. Microwaves that are resonant at three times the electron gyrofrequency have an extremely weak nonlinear interaction with cold

electrons such that a very strong focusing on resonance, or extremely high power levels, or extremely high cavity  $Q$  would be required to initiate an unassisted breakdown of the neutral gas.

Qualitative and reasonably close quantitative agreement is found between the experimental results for Uragan-3 showing a window in the applied RF current and the analytic breakdown criterion given by Eq. (6) and illustrated in Fig. 2. This agreement strongly suggests that the successful "preionization" of a neutral gas requires the existence of a "ponderomotive trap" along with an RF electric field parallel to the static magnetic field. However, if the RF electric field parallel to  $B$  is too strong, the concept of a "ponderomotive force" becomes meaningless because the electron orbits become unstable and electrons are expelled from the exciting region along a field line in a time scale on the order of an RF period. When the "ponderomotive force" does provide a trapping effect in front of the frame antenna, the oscillation energy of the trapped electrons can ionize the surrounding neutral gas and build up to a density that begins to support plasma waves. The linear and nonlinear damping of these waves can then heat the plasma [3,4] so that the "build-up" phase of the production process can continue, resulting in good target plasmas for nuclear fusion experiments.

#### ACKNOWLEDGEMENTS

The author thanks D.L. Grekov, A.I. Lysojvan, V.Ye. Moisyenko, N.I. Nazarov, O.M. Shvets, and K.N. Stepanov for many useful discussions concerning low frequency plasma production and for providing experimental data and information.

#### REFERENCES

- [1] CARTER, M.D., CALLEN, J.D., BATCHELOR, D.B., GOLDFINGER, R.C., *Phys. Fluids* **29** (1986) 100.
- [2] CARTER, M.D., BATCHELOR, D.B., ENGLAND, A.C., *Nucl. Fusion* **27** (1987) 985.
- [3] SHVETS, O.M., DIKIJ, A.G., DIKIJ, I.A., et al., in *Heating in Toroidal Plasmas* (Proc. 4th Int. Symp., Rome, 1984), Vol. 1, Int. School of Plasma Physics, Varenna (1984) 513.
- [4] SHVETS, O.M., DIKIJ, I.A., KALINICHENKO, S.S., et al., *Nucl. Fusion* **26** (1986) 23.
- [5] BENDER, C.M., ORSZAG, S.A., *Advanced Mathematical Methods for Scientists and Engineers*, McGraw-Hill, New York (1978).

# AN ANALYTICAL MODEL FOR ELECTRON CYCLOTRON HEATING PROFILES\*

R.C. GOLDFINGER, D.B. BATCHELOR  
Oak Ridge National Laboratory,  
Oak Ridge, Tennessee,  
United States of America

## Abstract

A model is described which scales electron cyclotron heating (ECH) profiles derived from ray tracing over a range of plasma beta. The model includes terms that incorporate the magnetic geometry and the local dependence on density and temperature. With this model, a heating profile generated from ray tracing is calculated once for a given magnetic field and used to predict new heating profiles for arbitrary beta without any need for further ray tracing. The current level of sophistication allows realistic prediction of heating profiles (agreement of 20% between the integrated power predicted from ray tracing and the scaling model) over several orders of magnitude in plasma beta. Since temperature and density dependence is incorporated in the model, sensitivity to different profile shapes can also be predicted. This model is applied to the laborious calculation of treating the second harmonic extraordinary mode rays that scatter from the vacuum chamber walls of the Advanced Toroidal Facility (ATF) device.

---

## ANALYTIC MODEL FOR ECH PROFILES

The heating profile calculated by the RAYS code [1,2,3],  $P(\psi)$ , is a histogram of the fraction of power  $\Delta P(\psi)$  deposited into the flux-surface-averaged volume  $\Delta\psi$  located at  $\psi$ . This profile is calculated in RAYS by taking output data along the ray trajectory and allocating the power decrement into bins of  $\Delta\psi$ . Figure 1 shows a cross section of ATF [4] where  $B(0)$  has been adjusted to make the second harmonic electron cyclotron resonance fall on the the magnetic axis. The volume lying between two adjacent flux surfaces, located at  $\psi$ , is indicated by cross-hatching. Since the deposition of power into this flux bin will occur near the regions where the resonance surface intersects the flux volume, the model takes  $\Delta P(\psi)$  to be proportional to the number of times a given ensemble of rays hits the resonance surface in  $\Delta\psi$ . This factor is multiplied by a second term that models an average absorption profile per ray:

$$P(\psi) = (\text{Number of resonance hits } (\psi)) \times (\text{Average absorption } (\psi) \text{ per ray}) \quad (1)$$

These two factors are expanded to give

$$\text{Number of resonance hits } (\psi) = (\text{ray flux } (\psi)) \times (A(\psi) \times G(n_e(\psi)/n_c)) \quad (2)$$

$$(\text{Average absorption } (\psi) \text{ per ray}) = 1 - \exp(-n_e(\psi) \times T_e(\psi) \times F(\psi)) \quad (3)$$

---

\* Research sponsored by the Office of Fusion Energy, US Department of Energy, under contract DE-AC05-84OR21400 with Martin Marietta Energy Systems, Inc.

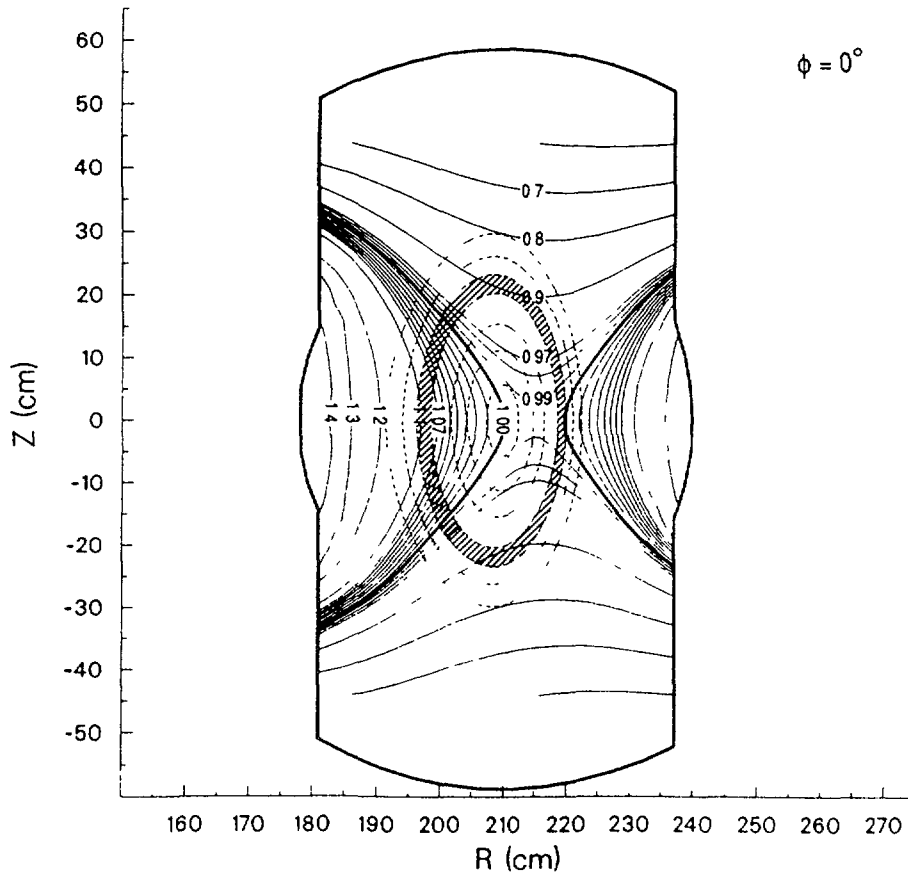


FIG. 1. Intersection of the second harmonic resonance surface (indicated by bold lines) with a flux tube in the  $\phi = 0^\circ$  plane. The volume lying between two adjacent flux surfaces is indicated by cross-hatching.

Here  $n_e$  and  $T_e$  are the electron density and temperature and are assumed to be constant on a flux surface, and  $n_c$  is the cutoff density.

The term (ray flux ( $\psi$ )  $\times$   $A(\psi)$ ) is a measure of how much of the surface area of the cyclotron resonance lies in the given flux bin. It is approximated by doing a ray tracing calculation for the set of rays that is to be modelled with the desired value of  $B(0)$  and counting the number of times that the resonance is crossed in each flux bin. The quantity  $G(n_e/n_c)$  models the refractive effect, which tends to direct rays outward as the local cutoff density is approached. The form that has been empirically determined to best fit the model is

$$G = \begin{cases} (1 - n_e(\psi)/n_c)^{0.7}, & n_e(\psi) < n_c \\ 0, & n_e(\psi) \geq n_c \end{cases} \quad (4)$$

This function has zero effect on the heating profile at low density (minimal refraction at low density) and gives zero heating on flux surfaces when the local density is above cutoff.

The factor “average absorption ( $\psi$ ) per ray” serves to model the scaling of the heating profile as a function of density and temperature. The motivation for this is the fractional absorption of wave energy for a ray,

$$f(s) = 1 - \exp(-2 \int \vec{K}_i \cdot d\vec{s}) \quad (5)$$

where  $\vec{K}_i$  is the imaginary part of the wave vector along the ray trajectory,  $s$ . At this point, all the terms in Eq. (1) have been defined with the exception of  $F(\psi)$ .  $F(\psi)$  is obtained by doing a run with RAYS and using the resulting heating profile on the left-hand side of Eq. (1) to permit solving for  $F(\psi)$ . The full equation is written as

$$P(\psi) = A(\psi) \times G(n_e(\psi)/n_c) \times \{1 - \exp[-n_e(\psi) \times T_e(\psi) \times F(\psi)]\}. \quad (6)$$

This analytic model can now be applied to the case of second harmonic wall-reflected rays in ATF, where  $B(0) = 0.95$  T and  $f_\mu = 53.0$  GHz. For other values of  $B(0)$ , new calculations are needed to determine the  $A(\psi)$  and  $F(\psi)$  profiles. The assumption of a uniformly illuminated wall is approximated by choosing four toroidal launch angles covering half a field period in ATF and four poloidal launch angles at a constant minor radius of 40.0 cm. At each of these 16 launch points, 96 rays are launched at various angles toward the plasma. Figure 2 shows  $A(\psi)$  and  $F(\psi)$  functions derived from a low-density, low-temperature ray tracing

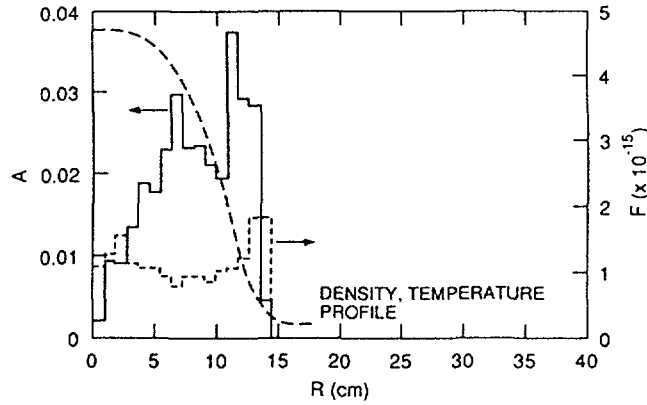


FIG. 2. Calculated forms for the  $F(\psi)$  and  $A(\psi)$  functions as described in the text.

run ( $n_e(0) = 3.5 \times 10^{11}$  cm $^{-3}$ ,  $T_e(0) = 50$  eV), with  $B(0)$  adjusted to make the second harmonic resonance pass through the magnetic axis corresponding to Fig. 1. The histogram runs from the magnetic axis,  $\psi = 0$ , out to the plasma edge, with  $\sim 20$  bins spanning the range. The  $A(\psi)$  function varies approximately linearly from the axis. Inspection of Fig. 1 reveals that the intersection of the resonance surface with the flux surface volume qualitatively displays this dependence. The  $F(\psi)$  profile, derived from the same RAYS calculation, turns out to be nearly constant across the plasma. In Fig. 3 the model is used to predict a heating profile for  $T_e(0) = 1000$  eV,  $n_e(0) = 1 \times 10^{13}$  cm $^{-3}$ , with the same profile shape used to define  $A(\psi)$  and  $F(\psi)$ . To test the accuracy of the model, the RAYS code was also run for these parameters. It is seen that the heating profile shapes are in good agreement and the total power deposited ( $= \Sigma P(\psi)$ ) is 17.9% with RAYS versus 17.0% with the analytic model. Considering that the plasma beta is nearly three orders of magnitude greater than in the case used to derive the model, this agreement is remarkable.

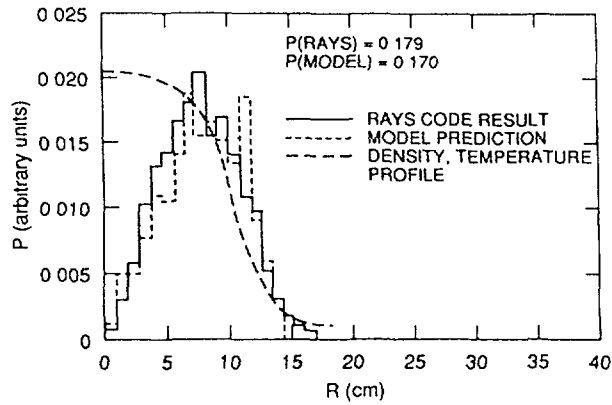


FIG. 3. Comparison of heating profiles predicted by the analytic model and calculated by the RAYS code. The central density is  $1 \times 10^{13} \text{ cm}^{-3}$ . The central temperature is 1000 eV.

Since the density dependence is incorporated in the model for both the ray propagation (through the  $G(n_e(\psi)/n_c)$  function) and absorption (through  $\exp[-n_e(\psi) \times T_e(\psi) \times F(\psi)]$ ), the model should be able to test the effect of different  $n_e$  and  $T_e$  profiles. Figure 4 shows a comparison for a case with density and temperature profiles about half of the width of those in the previous case. The model predicts 7.1% total absorption with a narrow profile, compared with a RAYS calculation of 9.5%.

A striking demonstration of the predictive capabilities of the model over a wide range of parameters is seen in Figure 5, in which total absorption is plotted as a function of peak density for peak temperatures of 100, 500, and 1000 eV (all done with the standard-width profile and the same model parameters). The solid curves are the analytic model predictions, while individual symbols denote selected RAYS runs.

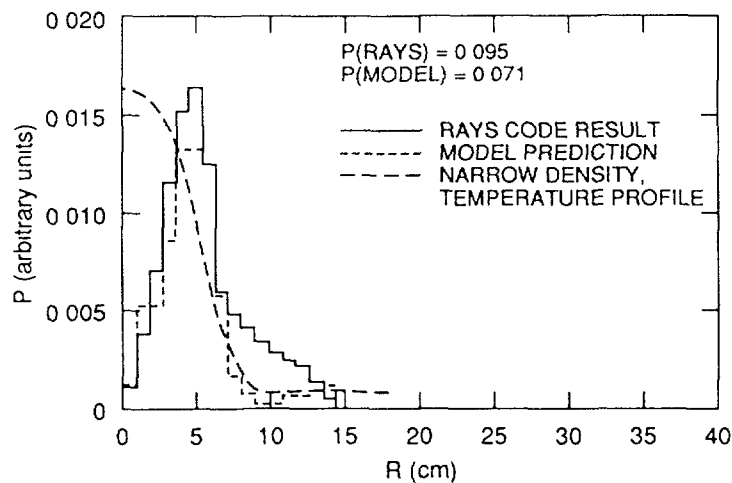


FIG. 4. Heating profiles generated with the RAYS code and with the analytic model for narrow density and temperature profiles.

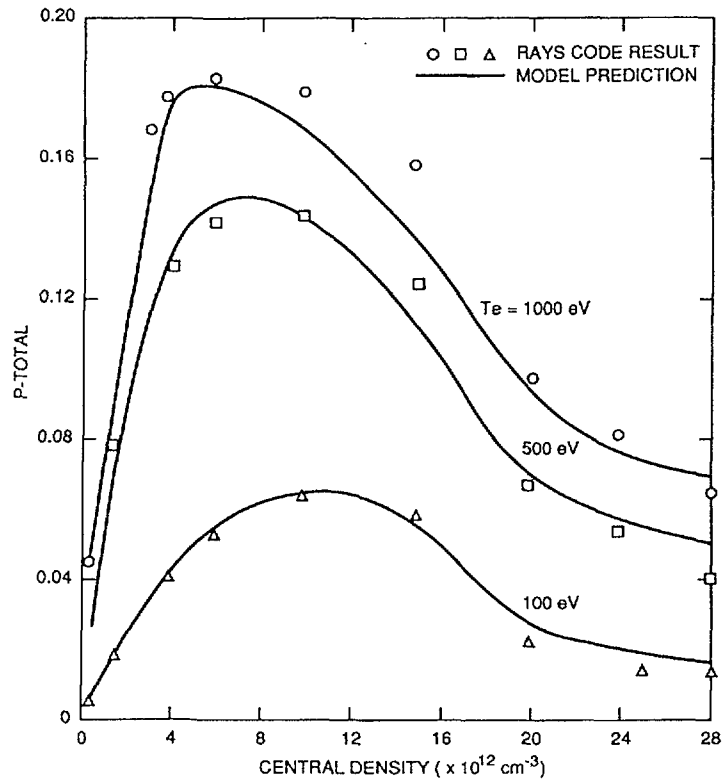


FIG. 5. Total absorption over a wide range of density and temperature.

## CONCLUSION

A heuristic model has been developed to scale ECH profiles generated from ray tracing calculations over a wide range of density and temperature. Most of the important features of ray absorption and propagation are phenomenologically incorporated in the model, including the refraction of rays as the density approaches cutoff, the fraction of resonance surface lying between flux surfaces for the device of interest, and the dependence on density and temperature of the local absorption rate. These features model the scaling of the ECH profiles surprisingly well. The model is applied to the laborious calculation of the wall reflections in the ATF torsatron. Agreement between the scaling model prediction and ray tracing runs is usually within 20% when the plasma beta is varied over several orders of magnitude.

## REFERENCES

1. Batchelor, D.B., Goldfinger, R.C., RAYS: A Geometrical Optics Code for EBT, Rep. ORNL/TM-6844, Oak Ridge National Laboratory, Oak Ridge, TN (1982).
2. Batchelor, D.B., Goldfinger, R.C., Rasmussen, D. A., Phys. Fluids **27** (1984) 948.
3. Goldfinger, R.C., Batchelor, D.B., Nucl. Fusion **27** (1987) 31.
4. Lyon, J.F., Carreras, B.A., Chipley, K.K., et al., Fusion Technol. **10** (1986) 179.

## **EQUILIBRIUM AND STABILITY**

# AVERAGED EQUILIBRIUM AND STABILITY IN LOW-ASPECT-RATIO STELLARATORS

L. GARCÍA

Universidad Complutense  
and Asociación Euratom/CIEMAT,  
Madrid, Spain

B.A. CARRERAS, N. DOMINGUEZ

Oak Ridge National Laboratory,  
Oak Ridge, Tennessee,  
United States of America

## Abstract

In this paper the results of the numerical calculations of local stability properties in low-aspect-ratio stellarators are presented. The results for the magnetic axis shift with beta and for the magnetic wall depth agree well with those obtained using 3D codes.

---

## INTRODUCTION

The MHD equilibrium and stability calculations for stellarators are complex because of the intrinsic three-dimensional (3-D) character of these configurations. The stellarator expansion [1] simplifies the equilibrium calculation by reducing it to a two-dimensional (2-D) problem. The classical stellarator expansion includes terms up to order  $\epsilon^2$ , and the vacuum magnetic field is also included up to this order. For large-aspect-ratio configurations, the results of the stellarator expansion agree well with 3-D numerical equilibrium results [2]. But for low-aspect-ratio configurations, there are significant discrepancies with 3-D equilibrium calculations [3]. The main reason for these discrepancies is the approximation in the vacuum field contributions. This problem can be avoided by applying the average method in a vacuum flux coordinate system [4]. In this way, the exact vacuum magnetic field contribution is included and the results agree well with 3-D equilibrium calculations, even for low-aspect-ratio configurations [5].

Using the average method in a vacuum flux coordinate system also permits the accurate calculation of local stability properties with the Mercier criterion. The main improvement is in the accurate calculation of the geodesic curvature term. In this paper, we discuss the application of the average method in flux coordinates to the calculation of the Mercier criterion [6] for low-aspect-ratio stellarator configurations.

## METHOD

The vacuum flux coordinates used are those described by Boozer [7]. For a vacuum configuration, the magnetic field may be written as  $\vec{B}_v = B_0 \vec{\nabla} \rho \times \vec{\nabla}(\theta - \epsilon_v \phi) - g_B \vec{\nabla} \phi$ , where  $\epsilon_v(\rho)$  is the vacuum rotational transform,  $g_B$  is a constant, and  $B_0 \pi \rho^2 = \Phi$  is the toroidal flux. To do the stellarator expansion, we assume the standard ordering of the basic stellarator parameters:  $\beta \sim \epsilon \sim 1/N \sim \delta^2$ , where  $\epsilon = a/R_0$  is the inverse aspect

ratio,  $a$  is the value of  $\rho$  at the edge,  $N$  is the number of toroidal field periods,  $R_0 = g_B/B_0$  is the major radius, and  $\delta$  is the strength of the helical field. To lowest order, the averaged equilibrium equations yield a Grad-Shafranov-type equation for the averaged poloidal flux [4]:

$$\begin{aligned} & \frac{1}{\rho} \frac{\partial}{\partial \rho} \left[ \rho \left( \langle g^{\rho\rho} \rangle \frac{\partial \Psi}{\partial \rho} + \langle g^{\rho\theta} \rangle \frac{1}{\rho} \frac{\partial \Psi}{\partial \theta} \right) \right] + \frac{1}{\rho} \frac{\partial}{\partial \theta} \left( \langle g^{\rho\theta} \rangle \frac{\partial \Psi}{\partial \rho} + \langle g^{\theta\theta} \rangle \frac{1}{\rho} \frac{\partial \Psi}{\partial \theta} \right) \\ & = -\frac{B_0 F}{g_B} \left[ \frac{1}{\rho} \frac{\partial}{\partial \rho} (\rho^2 \iota_v \langle g^{\rho\rho} \rangle) + \frac{1}{\rho^2} \frac{\partial}{\partial \theta} (\rho^2 \iota_v \langle g^{\rho\theta} \rangle) \right] - \mu_0 g_B^2 \left\langle \frac{1}{B_v^2} \right\rangle \frac{dp}{d\Psi} - F \frac{dF}{d\Psi} \end{aligned}$$

The CHAV code [5] is used to solve this equation. The average pressure  $p$  is an analytical function of the average poloidal flux  $\Psi$  or the toroidal flux  $\Phi$ . The dependence  $F(\Psi)$  is obtained by requiring either flux conservation ( $\iota = \iota_v$ ) or zero net current within each flux surface.

The equilibrium solution can be used as input to evaluate the 3-D Mercier criterion [6] for local instabilities,

$$D_M = D_S + D_W + D_I + D_G \geq 0$$

Here,  $D_S$  gives the stabilizing contribution of the shear,  $D_W$  is the contribution of the magnetic well,  $D_I$  is the contribution of the net currents, and  $D_G$  gives the contribution of the geodesic curvature. Up to order  $\epsilon$ , these contributions are

$$\begin{aligned} D_S &= \frac{s}{64\pi^2 \iota^2} \left( \frac{d\iota}{ds} \right)^2 \\ D_W &= \frac{\mu_0 B_0 g_B}{2\pi \iota^2 \Phi_e^4} s \frac{dp}{ds} \frac{d}{ds} \int \int \left\langle \frac{B^2}{B_v^2} \frac{1}{|\nabla s|^2} \right\rangle \rho \, d\rho \, d\theta \left[ \frac{d^2 V}{ds^2} \right. \\ & \quad \left. - 2\pi \mu_0 B_0 g_B \frac{dp}{ds} \frac{d}{ds} \int \int \left\langle \frac{1}{B^2 B_v^2} \right\rangle \rho \, d\rho \, d\theta \right] \\ D_I &= \frac{\mu_0 B_0 g_B}{8\pi \iota^2 \Phi_e^4} s \frac{d\iota}{ds} \left( \frac{1}{\Phi_e} \frac{dI}{ds} \frac{d}{ds} \int \int \left\langle \frac{B^2}{B_v^2} \frac{1}{|\nabla s|^2} \right\rangle \rho \, d\rho \, d\theta - \frac{d}{ds} \int \int \left\langle \frac{\vec{J} \cdot \vec{B}}{B_v^2} \frac{1}{|\nabla s|^2} \right\rangle \rho \, d\rho \, d\theta \right) \\ D_G &= \left( \frac{\mu_0 B_0 g_B}{2\iota \Phi_e^2} \right)^2 s \left[ \left( \frac{d}{ds} \int \int \left\langle \frac{\vec{J} \cdot \vec{B}}{B_v^2} \frac{1}{|\nabla s|^2} \right\rangle \rho \, d\rho \, d\theta \right)^2 \right. \\ & \quad \left. - \frac{d}{ds} \int \int \left\langle \frac{(\vec{J} \cdot \vec{B})^2}{B_v^2} \frac{1}{|\nabla s|^2} \right\rangle \rho \, d\rho \, d\theta \cdot \frac{d}{ds} \int \int \left\langle \frac{B^2}{B_v^2} \frac{1}{|\nabla s|^2} \right\rangle \rho \, d\rho \, d\theta \right] \end{aligned}$$

where  $s = \Phi/\Phi_e$ , with  $\Phi_e$  the toroidal flux at the plasma edge.

The 2-D integrals can be written in terms of the average and toroidally varying contributions to the parallel plasma current,  $\langle (\vec{J} \cdot \vec{B})/B^2 \rangle$  and  $\left( \widetilde{(\vec{J} \cdot \vec{B})}/B^2 \right)$ , respectively. They can be calculated from the condition  $\vec{\nabla} \cdot \vec{J} = 0$ ; that is,

$$\vec{B} \cdot \vec{\nabla} \left( \frac{\widetilde{(\vec{J} \cdot \vec{B})}}{B^2} \right) = -\vec{\nabla} \cdot \left( \frac{\vec{B} \times \vec{\nabla} p}{B^2} \right)$$

At lowest order in  $\epsilon$  and for zero net current equilibrium, we have

$$\left\langle \frac{\vec{J} \cdot \vec{B}}{B^2} \right\rangle = F \frac{dp}{d\Psi} \left( \left\langle \frac{1}{B^2} \right\rangle - \left\{ \frac{1}{B^2} \right\} \right)$$

$$\left( \widetilde{\frac{J \cdot B}{B^2}} \right) = R_0 \frac{dp}{d\Psi} \left[ \frac{1}{\rho} \frac{\partial \Psi}{\partial \theta} \frac{\partial}{\partial \rho} \left( \widehat{\frac{1}{B^2}} \right) - \frac{\partial \Psi}{\partial \rho} \frac{1}{\rho} \frac{\partial}{\partial \theta} \left( \widehat{\frac{1}{B^2}} \right) \right]$$

The braces  $\{ \}$  denote average over the flux surface, and

$$\left( \widehat{\frac{1}{B^2}} \right) = \int_0^\phi \left( \widetilde{\frac{1}{B^2}} \right) d\phi - \left\langle \int_0^\phi \left( \frac{1}{B^2} \right) d\phi \right\rangle$$

## NUMERICAL RESULTS

In this section, we compare the results of equilibrium and Mercier stability calculations obtained with the average method in vacuum flux coordinates, 3-D calculations using the VMEC code [8], and 2-D calculations from the classical stellarator expansion (RSTEQ) [9]. First, we consider the results for a low-aspect-ratio torsatron configuration, CT6 [3]. The CT6 is a 6-field-period,  $\ell = 2$  torsatron with a plasma aspect ratio of 3.8 and rotational transform ranging from 0.32 at the magnetic axis to 0.95 at the edge. The equilibrium calculations assume flux conservation and pressure proportional to  $(1 - s)^2$ . The value for the magnetic axis shift obtained with CHAV is better than the results obtained with the standard average method (Fig. 1). The Mercier criterion contributions for the CT6 configuration calculated with VMEC and with CHAV are compared in Fig. 2. The equilibrium input for these calculations assumes zero net current within each flux surface, and the pressure is proportional to  $\Psi^2$ . The agreement is good and shows the usefulness of the average method approach for low-aspect-ratio torsatron configurations when the vacuum magnetic field is taken exactly to all orders.

We have also studied the 4-field-period flexible heliac TJ-II [10,11]. The vacuum rotational transform ranges from 1.46 at the magnetic axis to 1.48 at the edge, and the

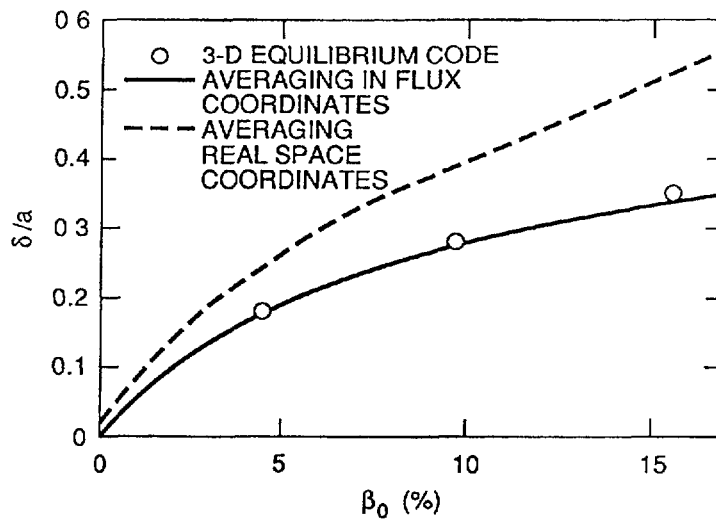


FIG. 1.

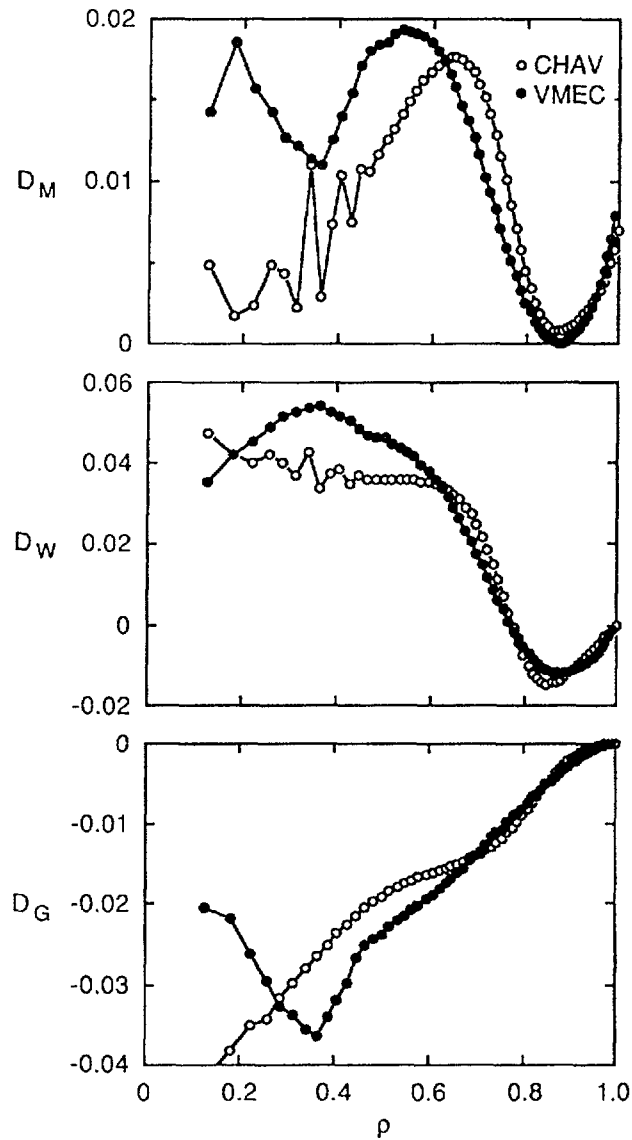


FIG. 2.

vacuum magnetic well depth is 2%. Although this configuration does not fulfill the ordering assumptions of the method, some features of the equilibrium can be described by this method. The reason is that the total magnetic axis shift is clearly dominated by the toroidal shift, due to the low aspect ratio. For these calculations, the pressure profile is  $(1 - s)^2$ , and the equilibrium is calculated with the assumption of zero net current within each flux surface. This configuration has been studied in detail with the VMEC code [12]. The results of the average method for the toroidal shift agree well with 3-D results. However, the magnetic well is deeper for the 3-D calculations. The magnetic surfaces reconstructed with the average method calculation do not show the strong helical deformations at high beta found in the 3-D numerical results. We would need to include the helical corrections to the average equilibrium to improve the reconstruction of the magnetic surfaces. When we use this equilibrium as input for the Mercier criterion, we find that the results do not give an accurate description of the stability properties of this configuration. The Mercier criterion contributions for the TJ-II configuration calculated with VMEC [12]

and with CHAV are compared in Fig. 3. The differences in the geodesic curvature term are important. They are caused by the finite-beta contribution to the helical curvature, which has not been taken into account in the average method calculation.

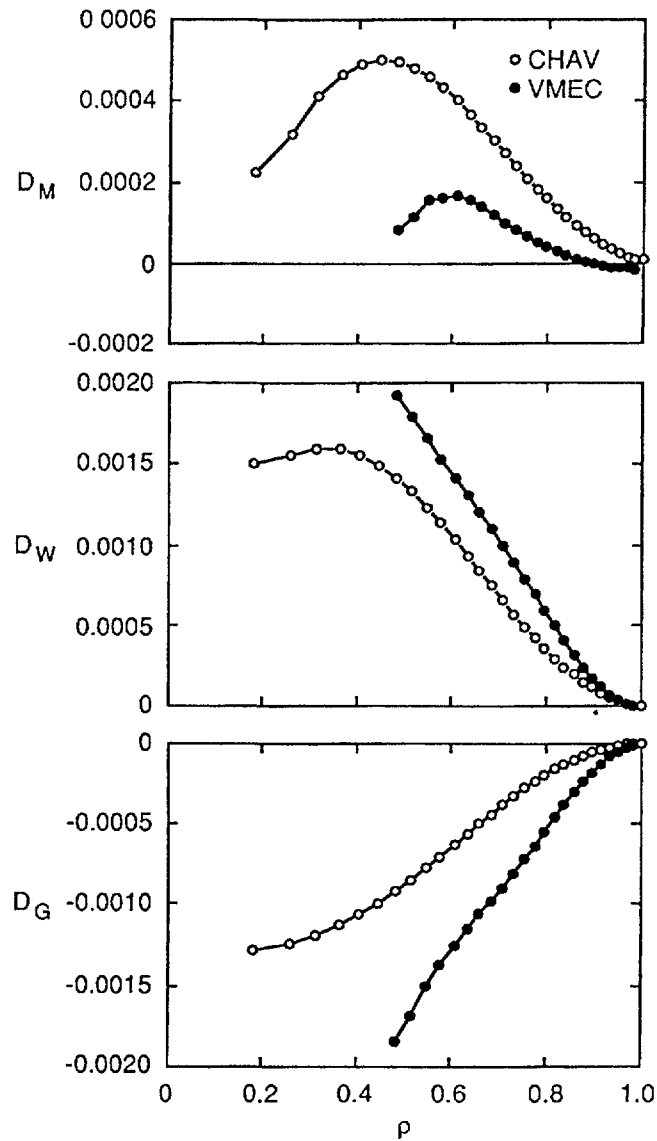


FIG 3

## CONCLUSIONS

The results for the magnetic axis shift with beta and for the magnetic well depth agree well with those obtained using 3-D codes, and they represent a major improvement over the results obtained with the classical stellarator expansion in low-aspect-ratio configurations.

The Mercier criterion is calculated accurately for low-aspect-ratio torsatrons. However, that is not the case for low-aspect-ratio heliacs. The main reason is the differences in the geodesic curvature term.

## ACKNOWLEDGEMENT

This research was sponsored by the Office of Fusion Energy, U.S. Department of Energy, under contract DE-AC05-84OR21400 with Martin Marietta Energy Systems, Inc.

## REFERENCES

- [1] GREENE, J.M., JOHNSON, J.L., *Phys. Fluids* **4** (1961) 875.
- [2] CARRERAS, B.A., HICKS, H.R., HOLMES, J.A., LYNCH, V.E., GARCIA, L., HARRIS, J.H., HENDER, T.C., MASDEN, B.F., *Phys. Fluids* **26** (1983) 3569.
- [3] CARRERAS, B.A., DOMINGUEZ, N., GARCIA, L., LYNCH, V.E., LYON, J.F., CARY, J.R., HANSON, J.D., NAVARRO, A.P., *Nucl. Fusion* **28** (1988) 1195.
- [4] HENDER, T.C., CARRERAS, B.A., *Phys. Fluids* **27** (1984) 2101.
- [5] GARCIA, L., et al., in *Plasma Physics and Controlled Nuclear Fusion Research* (Proc. 12th Int. Conf. Nice, 1988), IAEA, Vienna (1989) paper C-1-5-1.
- [6] MERCIER, C., *Nucl Fusion* **1** (1960) 47.
- [7] BOOZER, A.H., *Phys. Fluids* **25** (1982) 520.
- [8] HIRSHMAN, S.P., VAN RIJ, W., MERKEL, P., *Comput. Phys. Commun.* **43** (1986) 143.
- [9] HOLMES, J.A., PENG, Y-K.M., LYNCH, S.J., *J. Comput. Phys.* **36** (1980) 35.
- [10] HENDER, T.C., et al., *Fusion Technol.* **13** (1988) 521.
- [11] ALEJALDRE, C., *Heliac physics studies: the TJ-II project*, paper O3-6 presented at this meeting.
- [12] VARIAS, A., et al., *Stability studies for TJ-II*, paper 4P-12 presented at this meeting.

## RELATION BETWEEN MERCIER CRITERION AND LOW- $n$ MODE STABILITY

Y. NAKAMURA, K. ICHIGUCHI, H. SUGAMA,  
M. WAKATANI, H. ZUSHI  
Plasma Physics Laboratory,  
Kyoto University,  
Gokasho, Uji, Kyoto,  
Japan

J.L. JOHNSON, G. REWOLDT  
Plasma Physics Laboratory,  
Princeton University,  
Princeton, New Jersey,  
United States of America

B.A. CARRERAS, N. DOMINGUEZ, J.N. LEBOEUF,  
J.A. HOLMES, V.E. LYNCH<sup>1</sup>  
Oak Ridge National Laboratory,  
Oak Ridge, Tennessee,  
United States of America

### Abstract

In the present paper the relation between the beta limit by Mercier criterion and that by low- $n$  mode stability have been established.

---

It has been pointed out that aspect ratio, plasma shift by the vertical field and plasma shaping by the poloidal field coils are important ingredients to get high beta plasmas in heliotron/torsatron plasmas. Ideal MHD stability is investigated from various points of view. In the present study, we pay attention to the relation between the beta limit by Mercier criterion and that by low- $n$  mode stability, where  $n$  is a toroidal mode number.

The vacuum configuration shown in Fig.1 has a major radius at the center of the helical coils  $R_0=4\text{m}$ , an averaged plasma minor radius  $\bar{a} \sim 42\text{cm}$  ( $A = R_0/\bar{a} \sim 9.5$ ) and the rotational transforms,  $t(0) \sim 0.5$  at the magnetic axis and  $t(\bar{a}) \sim 1.3$  at the plasma boundary. Here the major radius of the magnetic axis,  $R_{axis}$  is equal to  $R_0$ . This configuration more slender than the ATF Torsatron is chosen arbitrarily and is not optimized with respect to the MHD stabilities. Figure 2 shows constant  $D_I$  contours in the plane of normalized poloidal flux  $\psi$  and the axis beta value  $\beta_{axis}$  by the STEP code<sup>[1,2]</sup>. Localized ideal interchange modes or Mercier modes become unstable inside the  $D_I = 0$  line or  $D_I > 0$  region. It is found that Mercier modes give the beta limit at  $\beta_{axis} \simeq 2\%$ . This result is consistent with that by the three-dimensional VMEC code<sup>[4]</sup>. Dashed lines in Fig.2 show the positions of low mode

---

<sup>1</sup> Computing and Telecommunications Division, Martin Marietta Energy Systems, Inc., Oak Ridge, TN 37831, USA.

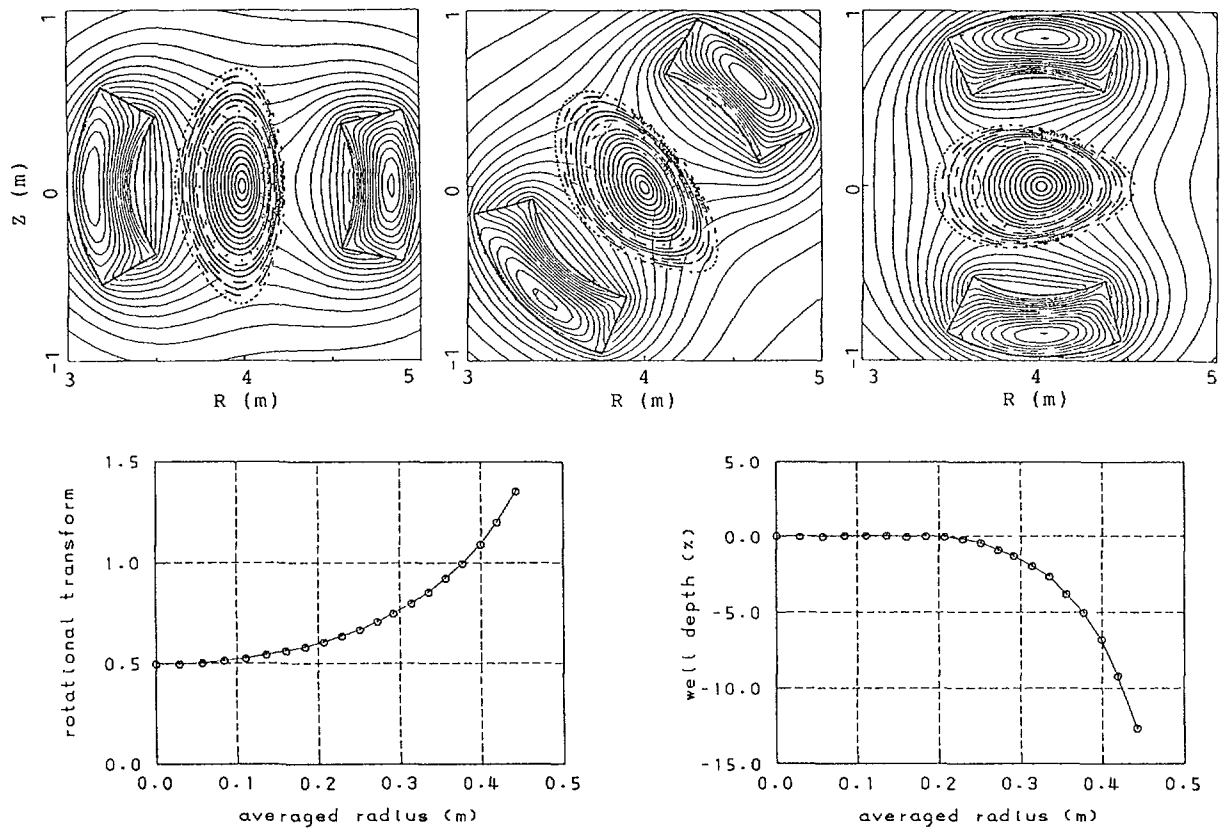


FIG. 1.

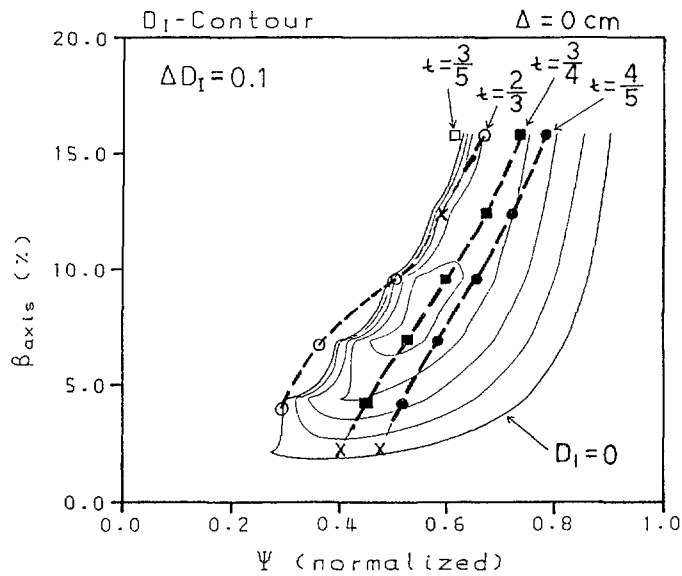


FIG. 2.

rational surfaces and thick dashed line regions denote that the corresponding low- $n$  ideal modes analysed by the STEP stability code<sup>[3]</sup> are unstable. Here we used 193 radial grid points and placed a conducting wall at the plasma boundary in the

STEP stability calculation. It is found that dominant unstable eigenmodes are ideal interchange modes in this case. Marks of square and circle denote the unstable  $n = 3$  and  $n = 4$  modes at the specific  $\beta_{axis}$  value by the STEPcode, respectively, and the black square or circle means that the corresponding mode have dominant contribution to the unstable eigenmode. In the present calculations, low- $n$  mode stability was investigated against  $n = 1$  to 4, but here we showed only results for  $n = 3$  and  $n = 4$  because  $n = 1$  and 2 modes are less unstable than  $n = 3$  or  $n = 4$  modes in this case.

Stability beta limit against low- $n$  ideal modes of the configuration in Fig.2 is  $\beta_{axis} \simeq 3\%$  and this axis beta value corresponds to the lower bound of  $D_I > 0.1 \sim 0.2$  region. There is a gap between the low- $n$  stability limit and the Mercier stability limit. For beta values between these two limits, the interchange mode is considered to be marginally unstable with a highly localized eigenfunction and a very small growth rate as discussed later. Note that almost all low- $n$  mode unstable lines (thick dashed lines) are within  $D_I = 0.1 \sim 0.2$  line except near the lefthand side boundary of  $D_I \geq 0$  region in Fig.2. Thus, there is a correlation between the low- $n$  mode unstable region and  $D_I > 0.1 \sim 0.2$  region. In the lefthand side boundary of  $D_I = 0$ , which is close to the boundary between the inner magnetic well region ( $V'' < 0$ ) and the outer magnetic hill region ( $V'' > 0$ ), the small difference between the  $V'$  value estimated by the standard stellarator expansion ordering used in the low- $n$  stability analysis<sup>[3]</sup> and that by the improved stellarator expansion ordering<sup>[2]</sup> used to derive the Mercier criterion would make an appreciable difference of  $V''$  value and change the MHD stability result. However, the disagreement between low- $n$  mode unstable region and  $D_I > 0.1 \sim 0.2$  region caused by the difference of the expansion ordering is usually small and it does not affect on the correlation between the low- $n$  stability beta limit and the  $D_I = 0.1 \sim 0.2$  contour.

In order to elucidate the relation between the Mercier criterion and the low- $n$  mode stability, we examine it in the cylindrical plasma model. Growth rates and eigenfunctions of global modes were obtained by applying the shooting method to the linearized reduced MHD equations<sup>[5]</sup>. In Fig.3, growth rates,  $\gamma$ , of  $m=1/n=1$ ,  $m=2/n=2$ , and  $m=3/n=3$  modes are shown as functions of the central beta value  $\beta(0)$ . They have the same mode resonant surface at  $t=1$ . Here we used 10,000 meshes equally divided in the radial direction to keep sufficient accuracy in the numerical calculations. The Suydam mode growth rate is also given in Fig.3. Figure 4 shows radial profiles of the stream function ( or electrostatic potential ) for  $m=1/n=1$  mode at  $\beta(0) = 4\%$  and  $\beta(0) = 2.5\%$ . It is clearly seen that the more localized is the mode for the lower beta value. The ratio of the mode width around the resonant surface to the plasma minor radius  $a$  is characterized by  $(R_0\gamma/v_A)/m$ , where  $v_A$  and  $R_0$  are the Alfvén velocity and the major radius, respectively. Its value becomes about  $10^{-4}$  for  $m=1$  and  $\beta(0) \simeq 2\%$ , which is the lower limit of beta that our numerical method can resolve the mode structure. In the beta limit analysis on the STEP, the critical beta has been obtained by extrapolating linearly growth rates calculated numerically in the higher beta region than  $\beta_c(0)$  to the zero growth rate. The resultant critical beta value is not rigorous since the beta dependence of growth rate obeys the exponential scaling,  $\gamma \propto \exp(-const./\sqrt{\beta(0)/\beta_c(0) - 1})$ <sup>[6]</sup>.

The gap between the Mercier limit or the Suydam limit and that by the global mode stability depends on the numerical procedures and particularly radial mesh number,  $N$ . The gap may disappear when  $N \rightarrow \infty$ ; however, this is not practical in realistic numerical calculations. It is better to understand that the gap region

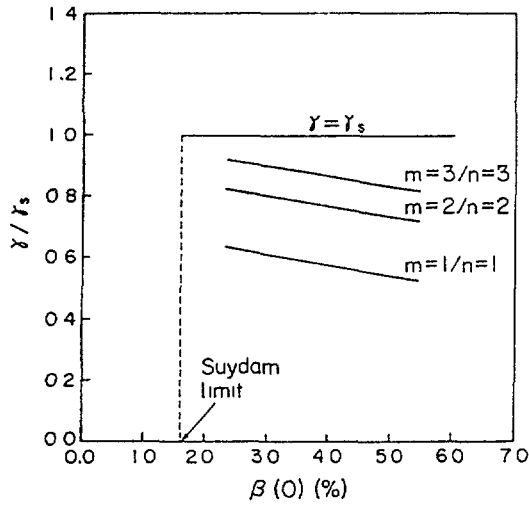


FIG. 3.

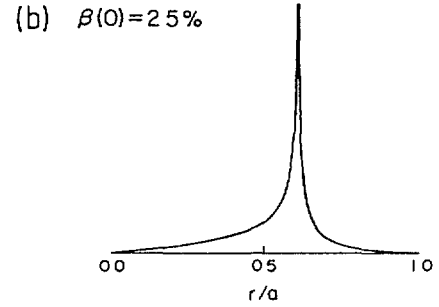
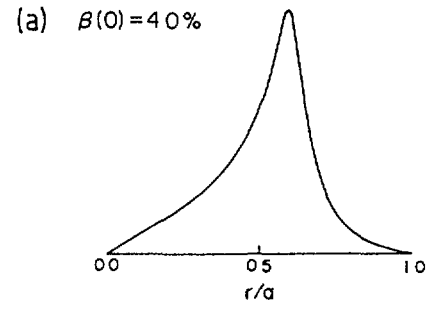


FIG. 4.

corresponds to marginal stability because the growth rates are negligibly small in this region. From this point of view,  $\sigma$ -stability<sup>[7]</sup> is useful in the beta limit determined by the interchange modes. When finite Larmor radius (FLR) effect is included, the linear growth rate is given by<sup>[6]</sup>  $\gamma = \sqrt{\gamma_s^2 - (\omega_{*i}/2)^2}$ , where  $\omega_{*i}$  is the ion diamagnetic drift frequency. Even if the FLR effect is small, it completely stabilizes the mode for  $\beta_c(0) < \beta(0) < \beta_{FLR}$  and the gap region disappears, where  $\beta_{FLR}$  denotes the central beta value determined by  $\gamma_s = |\omega_{*i}/2|$ .

### References

- [1] G.Anania, J.L.Johnson, and K.E.Weimer: Phys. Fluids **26** (1983) 2210.
- [2] Y.Nakamura, K.Ichiguchi, M.Wakatani and J.L.Johnson: Research Report of Plasma Phys. Lab., Kyoto Univ., PPLK-R-31 (October, 1988).
- [3] G.Anania and J.L.Johnson: Phys. Fluids **26** (1983) 3070.
- [4] S.P.Hirshman, W.I.van Rij, and P.Merkel: Comput. Phys. Commun. **43** (1986) 143.
- [5] M.Wakatani: IEEE Trans.on Plasma Science **PS-9** (1981) 243.
- [6] H.Sugama and M.Wakatani: J. Phys. Soc. Jpn. **58** (1989) 1128.
- [7] J.P.Goedbloed and P.H.Sakanaka, Phys. Fluids **17** (1974) 908.

## A FREE BOUNDARY ALGORITHM FOR THE BETAS CODE\*

O.L. BETANCOURT  
Computer Sciences Department,  
New York University,  
New York, N.Y.,  
United States of America

### Abstract

The three-dimensional spectral code BETAS is extended to include free boundary calculations. The formulation is the same as that of the finite difference code BETA, where the free boundary condition is obtained from minimization of the Hamiltonian and can therefore be used in free boundary stability analysis. The coils are represented by a boundary condition for the vacuum potential which approximates a given winding law. Earlier spectral versions have been developed using a Green's function technique.

---

### 1. Variational Principle

The variational formulation is analogous to that in the finite difference BETA [1] code, which allows for free boundary stability as well as equilibrium studies. For a given position of the free boundary  $\Gamma$ , we assume that the magnetic field in the plasma  $B_p$  and the vacuum magnetic field  $B_v$  satisfy the equilibrium equations

$$\nabla \cdot B_p = 0, \quad J \times B_p = \nabla p, \quad J = \nabla \times B_p \text{ in the plasma region,}$$

and  $\nabla \cdot B_v = \nabla \times B_v = 0$  in the vacuum region, with the boundary condition  $B_p \cdot n = B_v \cdot n = 0$  on the free surface  $\Gamma$ . The vacuum field is expressed in terms of a potential  $B_v = \nabla \phi$ , which has prescribed boundary values  $\phi = \phi(u, v)$  on an outer control surface, representing coils with a given winding law.

The free boundary  $\Gamma$  is found by minimizing the Hamiltonian

$$\min_{\Gamma} H(\Gamma) = \min_{\Gamma} \left( \int_p \left( \frac{1}{2} B_p^2 + p \right) dV - \int_v \frac{1}{2} B_v^2 dV \right)$$

---

\* Work supported by the US Department of Energy under grant DE-FG02-89ER53285.

with respect to variations of the free boundary  $\Gamma$ . The boundary condition for  $\phi$  implies that it is the periods of  $\phi$ , corresponding to currents, which are prescribed. For the magnetic field on the plasma  $B_p$ , the constraint is of zero net current in the stellarator case and a given rotational transform in the Tokamak case.

The first variation of the Hamiltonian is then given by

$$\delta H = - \int_{\Gamma} \left( \frac{1}{2} B_p^2 + p - \frac{1}{2} B_v^2 \right) \delta \nu \, dS ,$$

where  $\delta \nu$  is an arbitrary displacement of the normal to the free surface  $\Gamma$ . The requirement that the first variation vanishes yields the free boundary condition

$$G = \frac{1}{2} B_p^2 + p - \frac{1}{2} B_v^2 = 0$$

which determines the position of the free boundary  $\Gamma$ .

We consider modified cylindrical coordinates  $a + r$ ,  $\phi = 2\pi v$ ,  $z$  where  $a$  is the major radius of the torus and  $\phi$  the toroidal angle. The location of the free boundary  $\Gamma$  is represented by

$$r_B = r_0(v) + g(u, v)(r_c(u, v) - r_0(v))$$

$$z_B = z_0(v) + g(u, v)(z_c(u, v) - z_0(v))$$

where  $r_c$ ,  $z_c$  are equations for the outer control surface,  $r_0$ ,  $z_0$  are the equations for the magnetic axis and  $u$  is the poloidal angle.

The free boundary condition reduces to a first order, nonlinear, partial differential equation for the radial function  $g(u, v)$ ,

$$G(g, g_u, g_v) = 0 .$$

The coefficients of this P.D.E. are nonlinear functions of the values of the vacuum and plasma fields on the free surface  $\Gamma$ .

The vacuum region is described by the mapping

$$r = r_B + s(r_c - r_B)$$

$$z = z_B + s(z_c - z_B)$$

with  $0 \leq s \leq 1$ . The equation for the vacuum potential is given by

$$\Delta \phi = \frac{\partial}{\partial s} (a\phi_s + d\phi_u + e\phi_v) + \frac{\partial}{\partial u} (b\phi_u + d\phi_s + f\phi_v) + \frac{\partial}{\partial v} (c\phi_v + e\phi_u + f\phi_s) = 0$$

where the coefficients  $a, b, c, d, e$  and  $f$  are functions of the mapping  $r(s, u, v)$ ,  $z(s, u, v)$  and its derivatives.

The boundary condition on  $\Gamma$  ( $s = 0$ ) is

$$a\phi_s + d\phi_u + e\phi_v = 0$$

corresponding to  $B_v \cdot n = 0$ . At the outer control surface ( $s = 1$ ), we prescribe

$$\phi(1, u, v) = Vz + \frac{c_1}{2\pi} \operatorname{Re} \int \frac{\zeta_u du}{i(\zeta - \zeta_0)} + c_2v + AR_0 \tan^{-1} \left( \frac{\sin \Theta}{R_0 - \cos \Theta} \right)$$

where  $\zeta = r_c + iz_c$ ,  $\zeta_0 = r_0 + iz_0$ ,  $\Theta = 2\pi[Lu - Mv]$ . Here  $\Theta = 0$  represents the winding law for the helical coils,  $V$  is the vertical field and  $c_1, c_2$  are the toroidal and poloidal currents respectively. For stellarator cases  $c_1$  is equal to zero, and in Tokamak cases the term changes with the magnetic axis location, representing the influence of the plasma current in the vacuum magnetic field at the control surface.

## 2. Numerical Method [2, 3].

Details of the numerical method for the plasma region have been presented in [2]. We use a spectral collocation method in the two angles  $u$  and  $v$ , and finite difference in the  $s$  direction. The Hamiltonian is a minimum with respect to the free boundary variation but a maximum with respect to variations of the vacuum potential. In practice this requires that the solution of the vacuum equation be quite accurate for each position of the free boundary, with the residuals well below that of the free boundary condition. To achieve this we have implemented a fast solver analogous to that of the plasma region, with an approximation to the inverse Laplacian used as a preconditioner in the accelerated steepest descent method.

We define the approximation  $\Delta^*$  to the Laplacian  $\Delta$  by

$$\Delta^* \phi = \frac{\partial}{\partial s} (\langle a \rangle \phi_s) + \frac{\partial}{\partial u} (\langle b \rangle \phi_u + \langle f \rangle \phi_v) + \frac{\partial}{\partial v} (\langle c \rangle \phi_v + \langle f \rangle \phi_u)$$

where  $\langle a \rangle$  represents the average of  $a(s, u, v)$  on  $s = \text{constant}$ . Since the coefficients are functions of  $s$  alone, evaluation of the inverse  $(\Delta^*)^{-1}$  for the spectral representation reduces to solving a simple tridiagonal system. We then define accelerated path of steepest descent given by the artificial time differential equation

$$(\phi_{m,n})_{tt} + e(t) (\phi_{m,n})_t = -(\Delta^*)^{-1}(\Delta\phi)_{m,n}$$

where  $\phi_{m,n}$  is the Fourier coefficient of  $\phi$ ,  $e(t)$  is optimized automatically to maximize the convergence rate. The resulting scheme converges in a number of iterations independent of the mesh size, instead of being proportional to the number of mesh points as it would be if we do not use  $(\Delta^*)^{-1}$  as a preconditioner.

Steepest descent for the free boundary equation is given by

$$e_B g_t = G(g, g_u, g_v)$$

and the corresponding iterative scheme

$$(\delta g)_{m,n} = \frac{\Delta t}{e_B} \frac{(G^*)_{m,n}}{1 + \alpha(m^2 + n^2)}$$

where  $g_{m,n}$  is the Fourier coefficient of  $g$ ,  $e_B$  and  $\alpha$  are empirically chosen and  $G^*$  is defined by

$$G^* = G + \nu_B h^2 (g_{uu} + g_{vv}) .$$

Here  $\nu_B$  is an artificial viscosity coefficient and  $h$  is the mesh size for the collocation points.

### 3. Some preliminary results

We have computed free boundary equilibria for ATF-like stellarator configurations. We choose  $L = 2$ ,  $M = 12$  to represent the winding law for the helical coils, with  $A = -0.5$  and  $R_0 = 1.5$  for the helical field amplitude and coil radius respectively. In these units the control surface corresponds to  $R_0 = 1$  and the plasma surface is at  $R = 0.45$ . The plasma aspect ratio is chosen to correspond to that of ATF.

Figure 1 shows the convergence to the solution of the plasma region equation, zero net current condition, free surface Fourier coefficients, free boundary and vacuum equations respectively (clockwise from the top) as a function of the artificial time parameter. Residuals shown are maximum residuals over the whole region, rather than the average of the square of the pointwise residual as is sometimes customary. For example, the plasma region residuals have converged to  $10^{-6}$ , which correspond to residuals less than  $10^{-12}$  for the average of the square. The number of iterations is about 1000 and the plasma pressure corresponds to  $\beta$  on axis of 4%.

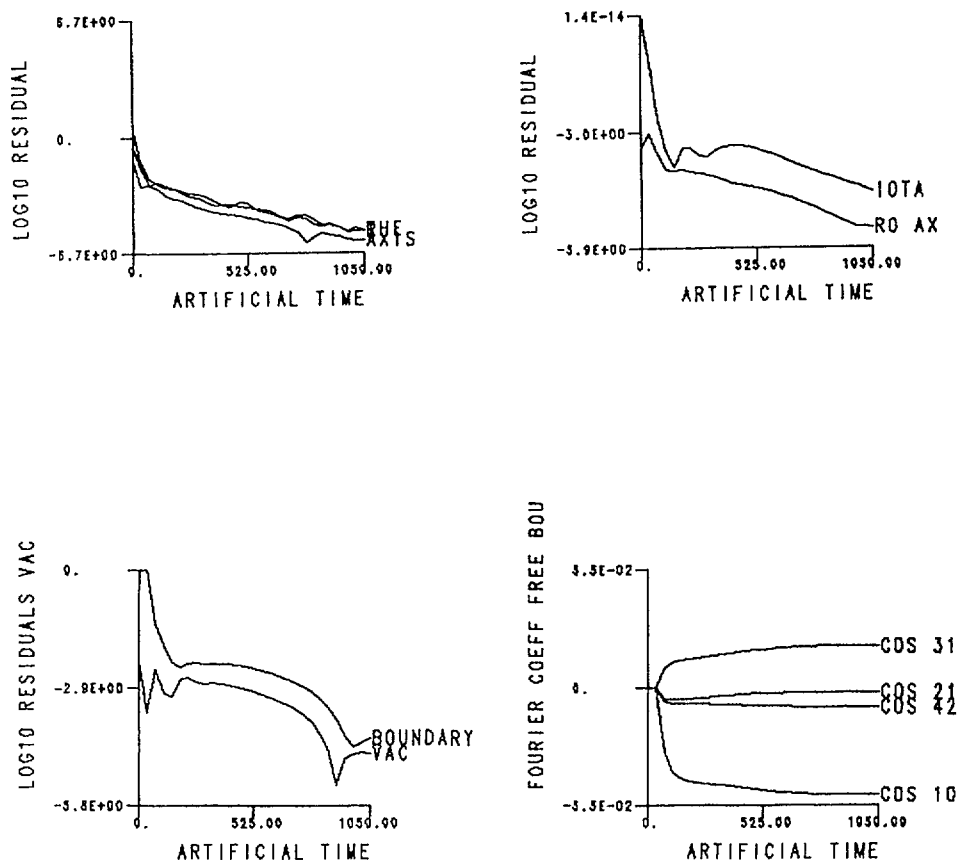


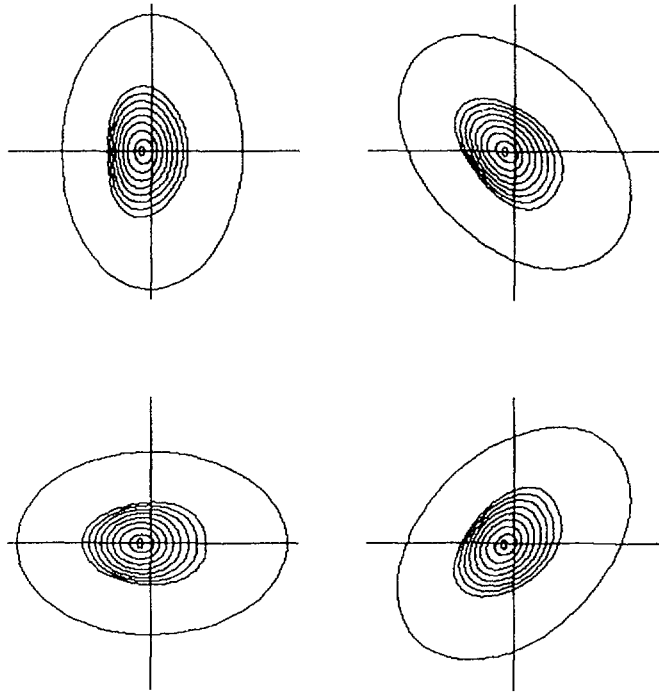
FIGURE 1. CONVERGENCE OF THE ITERATIVE METHOD.

Figures 2 and 3 show the free surface and the outer control surface as  $\beta$  on axis increases from 0 to 4%, with a fixed vertical field  $V = 0.08$ . As expected the free boundary moves outwards, with the magnetic axis shifting by a larger amount creating a shift of the axis relative to the free surface resulting in crowding of the flux surfaces on the outside.

Figure 4 shows the corresponding pressure and rotational transform profiles for the same cases, showing a flattening of the iota profile as the pressure is increased.

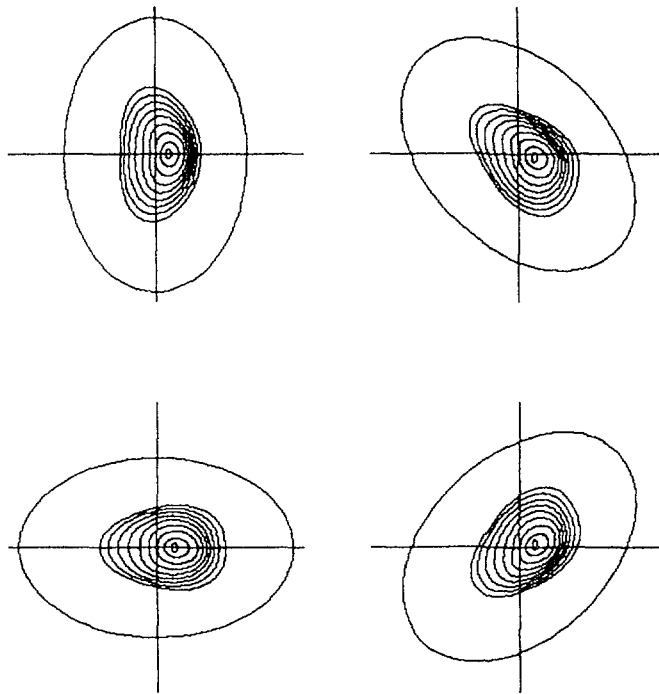
Additional runs show that as pressure increases further, the free boundary can be shifted back to the center by an increasing vertical field, but that this results in a distortion of some of the middle flux surfaces into a bean shape and a rather uncharacteristic iota profile.

As a conclusion, we have a working free boundary algorithm, which has an increased resolution and efficiency as compared to the finite difference version. Equilibrium and stability properties of stellarator configurations are strongly dependent on the shape of



CROSS SECTIONS IN PARAMETER SPACE, ASPECT RATIO= 0.26  
 MAJOR RADIUS= 3.12 MINOR RADIUS= 1.00

FIGURE 2. FREE BOUNDARY EQUILIBRIA WITH  $\beta_0 = 0.0$ ,  $\nu = 0.08$ .



CROSS SECTIONS IN PARAMETER SPACE, ASPECT RATIO= 0.26  
 MAJOR RADIUS= 3.12 MINOR RADIUS= 1.00

FIGURE 3. FREE BOUNDARY EQUILIBRIA WITH  $\beta_0 = 0.04$ ,  $\nu = 0.08$ .

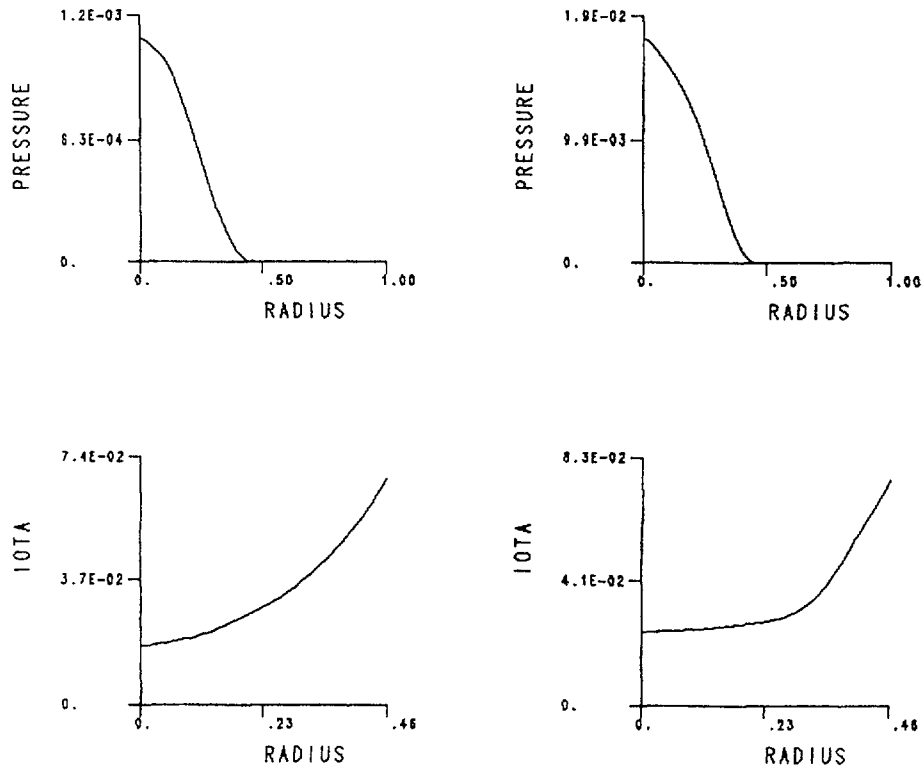


FIGURE 4. PRESSURE AND IOTA PROFILES FOR  $\beta_0 = 0.0$  AND  $\beta_0 = 0.04$ .

the boundary, and since in ATF like configurations this shape changes appreciably with increasing pressure we think it is important to compute the effects of these changes on iota profiles, Mercier criteria and transport coefficients. This will be the subject of future work.

#### REFERENCES

- [1] F. Bauer, O. Betancourt and P. Garabedian, *Magnetohydrodynamic Equilibrium and Stability of Stellarators*, Springer-Verlag, 1984.
- [2] O. Betancourt, "BETAS, a spectral code for three dimensional magnetohydrodynamic equilibrium and nonlinear stability calculations", *Comm. Pure Appl. Math.*, Vol. XLI (1988).
- [3] S. Hirshman and W. I. Rij, "Three dimensional free boundary calculations using a spectral Green's function method", *Computer Physics Comm.* (1986).

## FLUCTUATION STUDIES IN ATF

J.D. BELL

Computing and Telecommunications Division,  
Martin Marietta Energy Systems, Inc.,  
Oak Ridge, Tennessee,  
United States of America

J.H. HARRIS, J.L. DUNLAP,  
V.K. PARÉ, M. MURAKAMI  
Oak Ridge National Laboratory,  
Oak Ridge, Tennessee,  
United States of America

H. KANEKO  
Kyoto University,  
Gokasho, Uji, Kyoto,  
Japan

### Abstract

Detailed measurements of plasma fluctuations and ATF torsatron are described using Mirnov coil system and a soft X-ray detector array. Soft X-ray signals from the central region of the plasma show no gross instabilities. Coherent oscillations in magnetic probes signals are seen.

---

The ATF torsatron was designed to study the physics of the ideal MHD second stability regime, wherein the magnetic well produced by the outward Shafranov shift at finite  $\beta$  stabilizes interchange modes driven by unfavorable field line curvature, which are the dominant instabilities for stellarators. As a result, the plasma is expected to become more stable as  $\beta$  increases (" $\beta$  self-stabilization"), with a potential reduction in the anomalous transport induced by the curvature-driven instabilities. This paper details our measurements of plasma fluctuations in ATF. The companion paper by J. H. Harris et al. discusses the observations in the context of second stability.

The ATF Mirnov coil system presently consists of five "monitor" assemblies, each with three pickup coils mounted as shown in Fig. 1. The frequency response, with and without anti-alias filters, is shown in Fig. 2.

A soft X-ray detector array, from the Heliotron-E group at Kyoto University, was installed on an inner port on ATF, viewing a "horizontal" section of the ATF plasma. Vacuum and mechanical pieces restrict the usable detectors to those whose lines of sight cross  $R = 2.10$  m (the vessel center) at  $|Z| < 13.4$  cm.

After anti-alias filtering, signals from these sensors were connected to a CAMAC-based data acquisition system operating at digitizing frequencies of 256 or 163.84 kHz for Mirnov loops, and 10 kHz for the soft X-ray signals. For each signal, 8K or 16K samples were

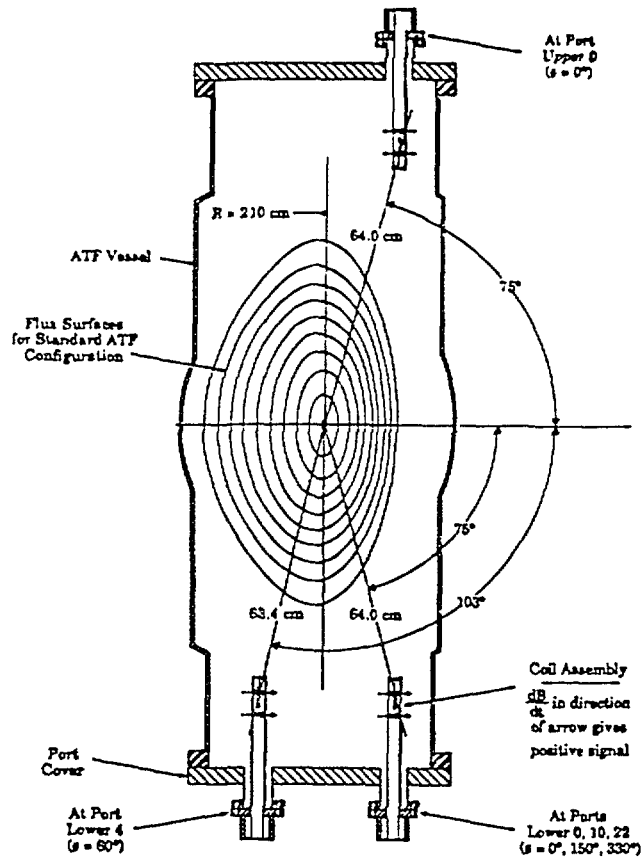


FIG. 1. Locations of Mirnov coils

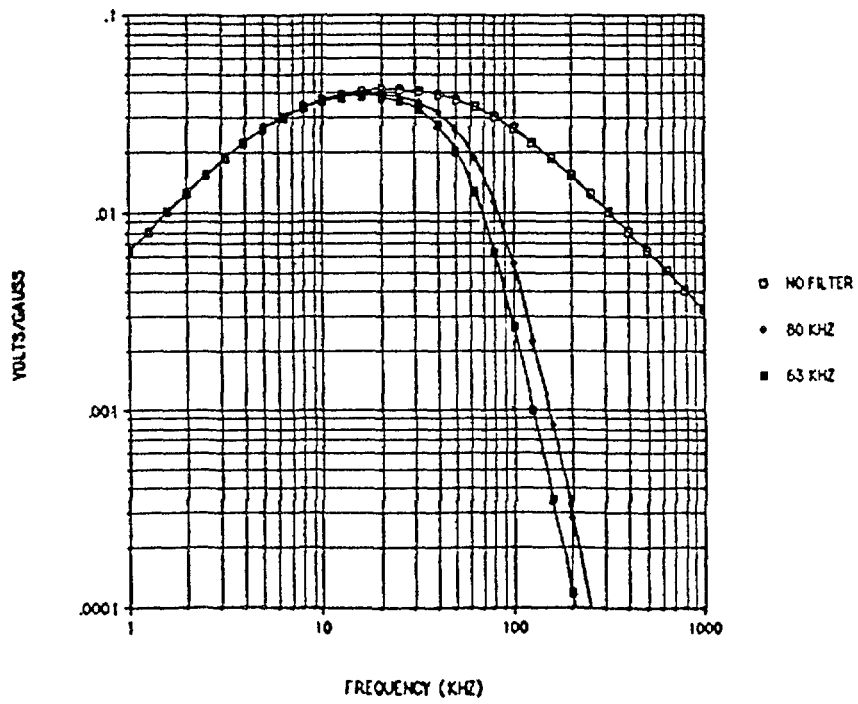


FIG. 2. Frequency response

recorded per shot, and the signal processing code used 256 points per FFT segment, giving an FFT frequency resolution of 0.64 kHz at 163.84 kHz.

To describe our analysis of fluctuation signals, we will use the following standard frequency-domain terms:

- (a)  $F_1, F_2$  = Fourier transform of a segment of data from signal 1 and 2.
- (b)  $G_{11} = \langle (F_1)(F_1^*) \rangle$  = auto-power spectral density (APSD).
- (c)  $G_{12} = \langle (F_1)(F_2^*) \rangle$  = cross-power spectral density (CPSD), which gives the frequency component common to the two signals, and the phase shift of that component between the two signal sources.
- (d)  $\gamma = \sqrt{(G_{12})(G_{12}^*) / (G_{11})(G_{22})}$  = the coherence, a measure (0 to 1) of the extent to which the two signals are correlated at each frequency.

The heart of our frequency-based analysis is a computer program which allows users to compute APSDs, CPSDs, and  $\gamma$  for two signals. Given the signals to process, the code applies the following algorithm to a selected time interval:

- (a) Load a segment of data for signal 1 and 2.
- (b) Compute the FFT and apply a Hanning (cosine-squared) window.
- (c) Compute APSD for each signal, and CPSD amplitude and phase for that data segment.
- (d) Advance one-half segment and repeat.

When all segments are completed, the code computes average APSD and CPSD, and  $\gamma$  for the selected interval and corrects for the Mirnov coil transfer functions, the amplifier transfer functions, and windowing.

We have investigated the influence of electromagnetic interference (EMI) on our data. EMI dominates the X-ray signals (above 300 Hz). For the Mirnov coils, the interference is large at 360 Hz but negligible in the frequency range (5–60 kHz) of the plasma fluctuations reported here.

Studies of the soft X-ray waveforms show no gross instabilities (no sawteeth, no disruptions). We see no plasma-induced fluctuations on the X-rays, and coherence between X-ray and Mirnov signals is low, except for EMI.

To illustrate the magnetic fluctuation analysis, we have applied the signal processing code to the high- $W_{\perp}$  phase of shot 3819, for a pair of Mirnov coils 180° apart toroidally. The CPSD amplitude and phase and the coherence are shown in Fig. 3.

The signal processing code can also write out selected results from its analysis. We have chosen to examine [two-coil] CPSD frequency components for which  $\gamma$  is  $\geq 0.7$ , since at present we are interested in coherent fluctuations. The results obtained include:

1. Plots of electrical phase difference for two pairs of coils which have different toroidal spacing show predominantly  $n = 1$  symmetry, with fragmentary evidence of other  $n$  values.

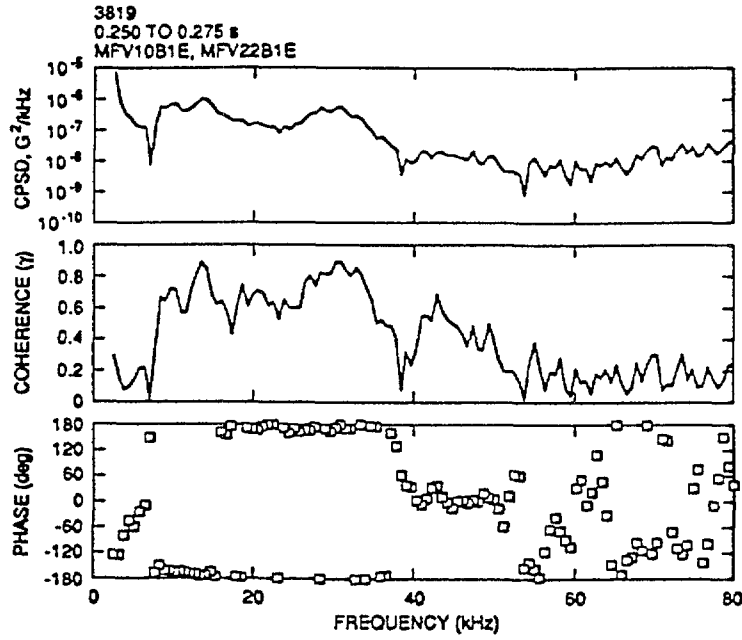


FIG. 3. Signal processing results for S-3819

2. Plots of electrical phase difference for two pairs of coils which have different poloidal and toroidal spacing show predominantly  $(n = 1, m = 2)$  and  $(n = 1, m = 3)$ . The cases assigned  $m = 2$  and  $m = 3$  also clump together in frequency (8–20 kHz for  $m = 2$ , 20–45 kHz for  $m = 3$ ) when  $\tilde{B}$  is plotted against frequency.
3. A plot of  $\langle \tilde{B}(n = 1) \rangle$  versus  $\langle \beta \rangle$  (where  $\langle \tilde{B}(n = 1) \rangle$  is defined as the square root of the sum of amplitudes of  $n = 1$  components in the CPSD, from 5 to 60 kHz) shows an envelope with  $\tilde{B}$  increasing as  $\langle \beta \rangle$  goes from 0 to 0.25% and decreasing thereafter. The behavior of  $\tilde{B}$  does not obviously correlate with plasma current.
4. Time histories of  $\langle \tilde{B}(\text{all coherent modes}) \rangle$ ,  $\langle \tilde{B}(n = 1) \rangle$ ,  $\langle \tilde{B}(n = 1, m = 2) \rangle$ , and  $\langle \tilde{B}(n = 1, m = 3) \rangle$  can be computed for a single shot, as shown in Fig. 4; note how  $\langle \tilde{B}(\text{coherent}) \rangle$  rises, dips when  $\langle \beta \rangle \simeq 0.3\%$ , and then rises again as  $\langle \beta \rangle$  drops below 0.3%.

In summary, soft X-ray signals from the central region of the plasma ( $< \bar{a}/2$ ) show no gross instabilities. Coherent oscillations in  $B_\theta$  are seen. Spectral analysis of the  $\tilde{B}_\theta$  oscillations shows that they have amplitudes of  $\sim 10^{-3}$  G in the frequency range  $\sim 5$ –60 kHz, with low poloidal mode numbers ( $m = 2$  and 3) and toroidal mode number  $n = 1$ . Trend analysis of  $\tilde{B}$  amplitude data from a variety of discharges shows that the  $n = 1$  mode amplitude initially rises with  $\langle \beta \rangle$ , but saturates and may decrease as  $\langle \beta \rangle$  exceeds 0.3%.

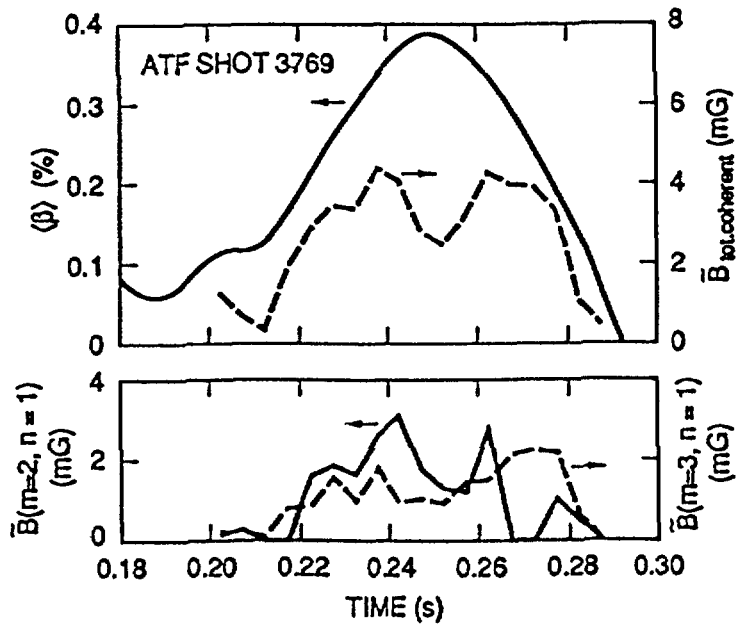


FIG. 4. Time histories

#### ACKNOWLEDGEMENT

Research sponsored by the Office of Fusion Energy, U.S. Department of Energy, under contract DE-AC05-84OR21400 with the Martin Marietta Energy Systems, Inc.

## MAGNETIC FLUCTUATIONS DUE TO PRESSURE DRIVEN INSTABILITIES IN ATF\*

L.A. CHARLTON, B.A. CARRERAS,  
J.N. LEBOEUF, V.E. LYNCH<sup>1</sup>  
Oak Ridge National Laboratory,  
Oak Ridge, Tennessee,  
United States of America

### Abstract

In this paper the results of the numerical simulation of the poloidal magnetic field fluctuations based on the resistive pressure-gradient-driven model are presented.

---

**INTRODUCTION.** The Advanced Toroidal Facility (ATF) was designed to have stable access to the second stability regime.<sup>1</sup> For the design conditions, this should occur at beta values near  $\beta_0 \approx 5\%$ . In its initial phase of operation, the ATF plasma minor radius and the edge rotational transform,  $\tau_a$ , were reduced by field errors,<sup>2</sup> which have now been repaired. This reduction in radius and  $\tau_a$  caused a large increase in the Shafranov shifts, and as a consequence a reduction in the beta value needed to access the second stability regime. From the low-n and high-n stability analysis using the experimentally measured profiles, the threshold to second stability was found<sup>3</sup> to be as low as  $\beta_0 \approx 1.0\%$ . The beta values reached in the experiment, up to  $\beta_0 \approx 3.0\%$ , are well above this threshold value. The magnetic fluctuation measurements showed a reduction in the fluctuation level for  $\beta_0 \geq 2\%$ .<sup>4</sup> In this paper, we discuss the results of simulations of the poloidal magnetic field fluctuations based on the resistive pressure-gradient-driven model.

**MODEL.** To model the observed fluctuations, we assume that the cause is the resistive interchange instability. We can apply the reduced set of MHD equations<sup>5</sup> for stellarator configurations. This set of equations can be derived using the stellarator expansion.<sup>6</sup> They contain the main physics of the resistive interchange. The equations are

---

\* Research sponsored by the Office of Fusion Energy, US Department of Energy, under contract DE-AC05-84OR21400 with Martin Marietta Energy Systems, Inc.

<sup>1</sup> Computing and Telecommunications Division, Martin Marietta Energy Systems, Inc., Oak Ridge, TN 37831, USA.

$$\begin{aligned}\frac{\partial \psi}{\partial t} &= -R_0 \nabla_{\parallel} \phi + R_0 \eta J_{\zeta} \\ \frac{\partial U}{\partial t} &= -\frac{1}{\rho_m} \nabla_{\parallel} J_{\zeta} + \frac{1}{\rho_m} \bar{z} \cdot (\bar{\nabla} \Omega \times \bar{\nabla} p) + \mu \nabla_{\perp}^2 U \\ \frac{dp}{dt} &= \chi_{\perp} \nabla_{\perp}^2 p - V_r \frac{dp_0}{dr}\end{aligned}$$

Here  $\psi$  is the poloidal flux,  $\phi$  the velocity stream function,  $p$  the pressure,  $U$  the toroidal component of the vorticity, and  $J_{\zeta}$  the current density in the  $\zeta$  direction. The  $\bar{\nabla} \Omega$  is the toroidally averaged curvature. At zero beta, this term includes only the average helical curvature, but the deepening of the magnetic well with increasing beta modifies this term, and is the cause of the self stabilization effect.

**NUMERICAL RESULTS.** Numerical studies of these magnetic fluctuations were done using the reduced set of MHD equations implemented in the 3-D nonlinear codes KITE,<sup>7</sup> for the cylindrical geometry approximation, and FAR,<sup>8</sup> for toroidal geometry. The linear resistive stability properties have been investigated in toroidal geometry. For the lowest  $n$  modes the dominant components were the  $(m;n) = (3;1), (5;2)$  and  $(8;3)$ . These components have their resonant surfaces in regions which are Mercier unstable at low  $\beta$  values. The resistive interchange character of these modes is well established from the scaling of the linear growth rate as  $S^{1/3}$ . Even though the linear growth rates keep increasing with  $\beta$ , the poloidal magnetic field fluctuations at the edge calculated from the linear eigenmodes decrease sharply for  $\beta_0 > 1.0\%$ . This is caused by the shift of the dominant component to a higher  $m$  value as the magnetic well broadens in the inner part of the plasma. This is an indication of the beta self stabilization effect.

The first estimates of the resistive interchange modes nonlinear saturation level has been done in cylindrical geometry, allowing for pressure profile relaxation, using KITE. Single helicity calculations show the spectrum peaks at low  $n$ 's even though higher  $n$ 's are linearly the most unstable modes. In particular, for the 5/2 helicity, modes from  $(m = 5; n = 2)$  to the  $(m = 95; n = 38)$  have been included in the calculation. A radial grid of  $\Delta r = 10^{-3}$  was used. At saturation most of the energy content was in the  $(m = 5; n = 2)$  component. The saturation level as a function of  $\beta$  shows a sharp increase at low  $\beta$ , levels off and it is followed by a strong reduction of the saturation level for  $\langle \beta \rangle \approx 0.25\%$ . This is illustrated in Fig.1 for the 5/2 helicity. Multiple helicity calculations in cylindrical and toroidal geometry show the same effect. They further indicate (Fig. 2) that  $n = 1$  modes achieve the highest level of magnetic fluctuations through nonlinear coupling, consistent with experimental observation.

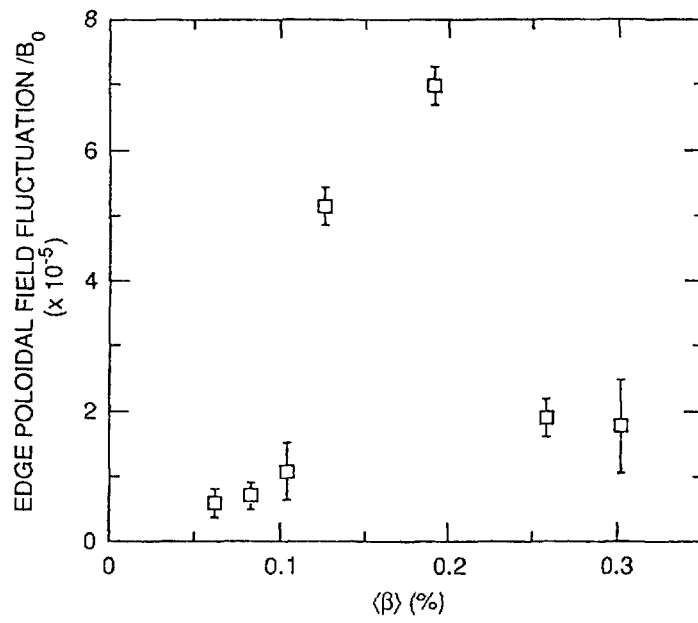


FIG. 1.

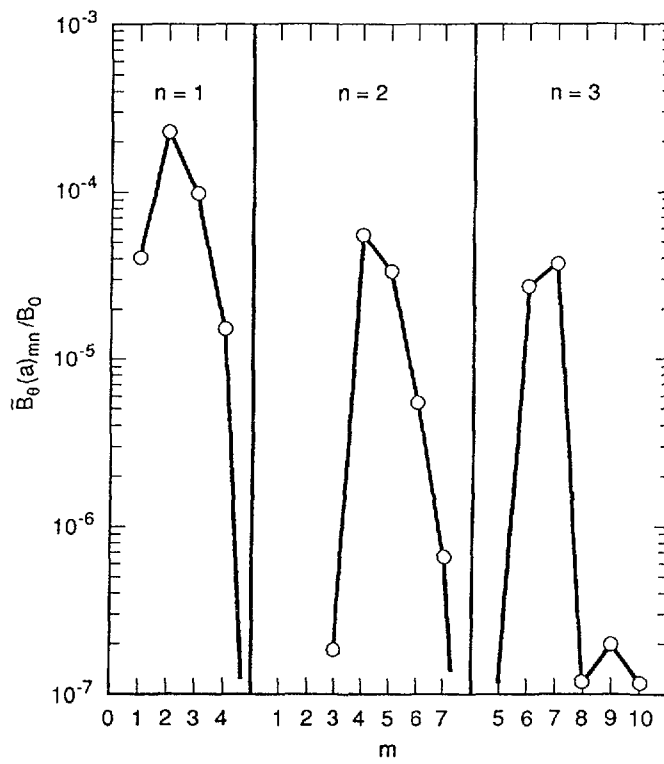


FIG. 2.

## REFERENCES

1. Carreras, B. A., Hicks, H. R., Holmes, J. A., Lynch, V. E., Garcia, L., Harris, J. H., Hender, T. C., Masden, B. F., *Phys. Fluids* **26** (1983) 3569.
2. R. J. Colchin, et al., "ATF Flux Surfaces and Related Plasma Effects," paper O3-4 presented at this meeting.
3. V. E. Lynch, B. A. Carreras, N. Dominguez, and J. N. Leboeuf, "Equilibrium and Ideal Stability studies for ATF," paper 4P-10 presented at this meeting.
4. J. H. Harris, et al., "Second Stability Studies in ATF," paper O2-5 presented at this meeting.
5. H. Strauss, *Plasma Phys.* **22**, 633 (1980).
6. J. M. Greene, and J. L. Johnson, *Phys. Fluids* **4** (1961) 875.
7. L. Garcia, H. R. Hicks, B. A. Carreras, L. A. Charlton and J. A. Holmes, *J. of Comp. Phys.* **65**, 253 (1986).
8. L. A. Charlton, J. A. Holmes, H. R. Hicks, V. E. Lynch and B. A. Carreras, *J. Comp. Phys.* **63**, 107 (1986).

## DETERMINATION OF ELECTRON DENSITY FLUCTUATIONS IN STELLARATORS BY MICROWAVE REFLECTOMETRY

A.P. NAVARRO, J. SÁNCHEZ, E. ANABITARTE,  
J. SENTÍES<sup>1</sup>, T. ESTRADA  
Asociación Euratom/CIEMAT,  
Madrid, Spain

H.J. HARTFUSS, W VII-AS TEAM<sup>2</sup>  
Euratom-IPP Association,  
Max-Planck-Institut für Plasmaphysik,  
Garching, Federal Republic of Germany

### Abstract

Application of microwave reflectometry to the determination of electron density fluctuations is presented in this paper. Data obtained in the W7AS stellarator, with an homodyne system working in the V band, have enabled to correlate these fluctuations with different discharge parameters. Improvements of the system to get fluctuation absolute values are also discussed.

---

## INTRODUCTION

Experimental determination of electron density fluctuations in stellarator plasmas is an important task, not only because of the intrinsic interest of characterization of this phenomena, but due to the possible influence of turbulence on plasma confinement [1] and the expected relationship between the level of these fluctuations and the access to the second stability regime [2].

Microwave reflectometry [3], based on the measurement of the phase difference between an incident wave in the plasma and the reflected one at the cutoff layer, has the potential to determine electron density [4] and its fluctuations [5, 6] with good time and spatial resolution. In the TJ-I tokamak this technique, using an homodyne detection system, has provided qualitative indication of the existence of big density fluctuations for MHD dominated discharges with a radial profile that peaks around the singular surface radius [7]. Figure 1 summarizes these results.

---

<sup>1</sup> Facultad de Ciencias, Universidad Cantabria, 39005 Santander, Spain.

<sup>2</sup> The members of the W VII-AS Team are identified in the paper entitled 'Status of the advanced stellarator Wendelstein W 7AS: first results and further programme', these proceedings, p. 25.

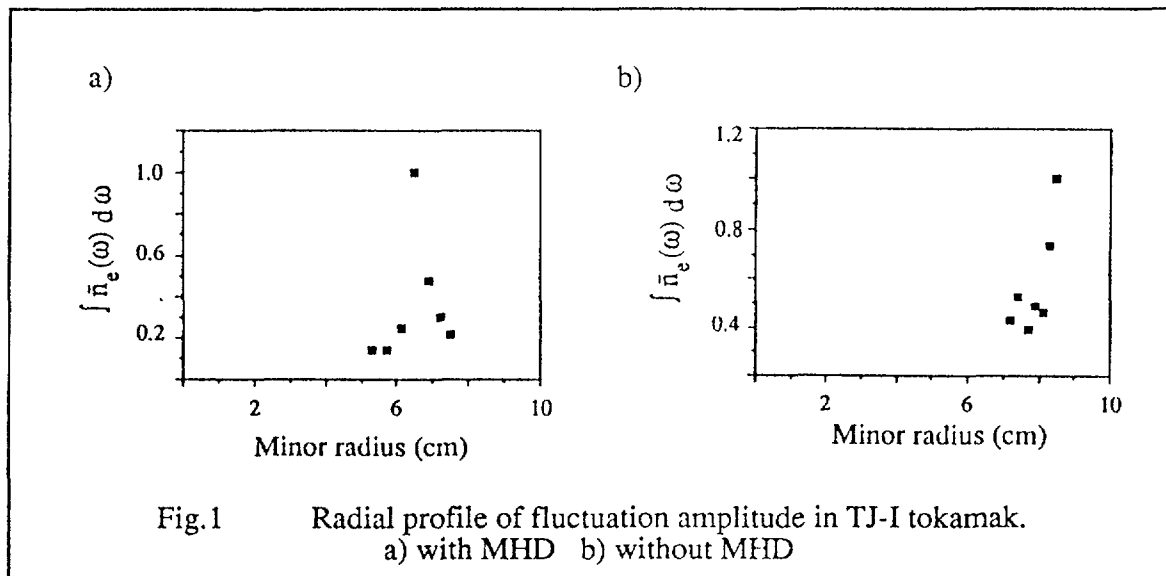


Fig.1 Radial profile of fluctuation amplitude in TJ-I tokamak.  
a) with MHD b) without MHD

Results from the application for the first time of this technique to the study of density fluctuations in Stellarators are presented in this paper, together with possible methods to improve this diagnostics to make possible the determination of absolute values of density fluctuations.

#### APPLICATION TO W7AS STELLARATOR

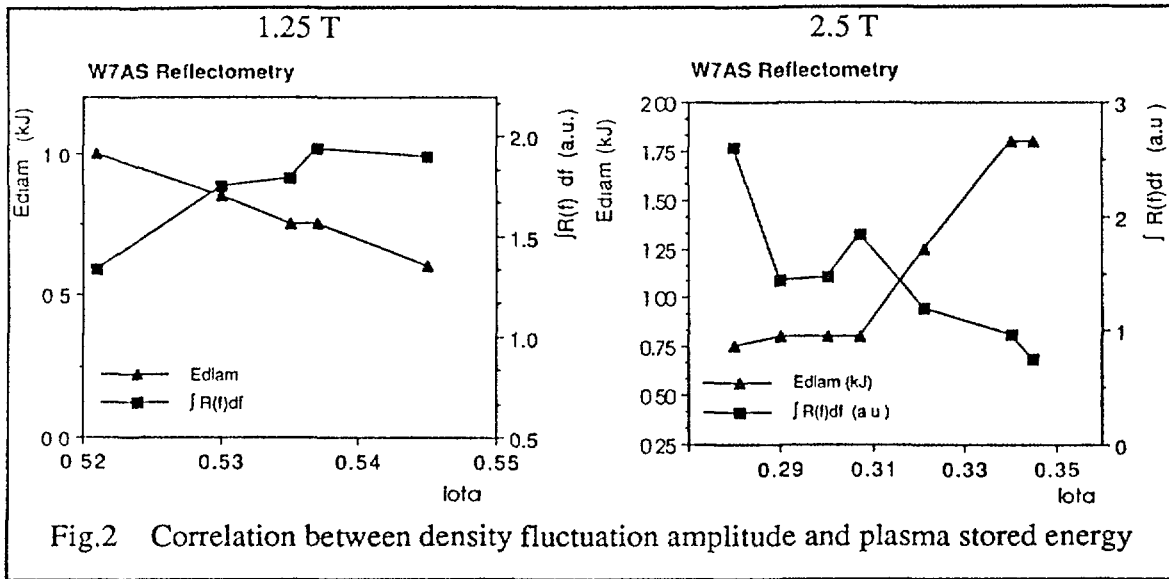
A single antenna reflectometer has been installed in the outer side of the equatorial midplane of the W7AS stellarator [8], looking at the plasma through a 28 mm diameter port. It is basically an homodyne system working in the 50 - 75 GHz V band, that can cover most of the density profile gradient part, when working with a toroidal field of 1.25 T, and only the plasma edge if the field is increased to 2.5 T. The spatial resolution for fluctuation determination, in both cases, is better than 5 mm, as deduced from [3] :

$$\Delta = \left[ \frac{\lambda}{2\pi} \left( \frac{d\epsilon}{dr} \right)^{-\frac{1}{2}} \right]^3$$

where the standard density profile for W7AS was assumed.

##### a) Correlation between density fluctuations and plasma confinement.

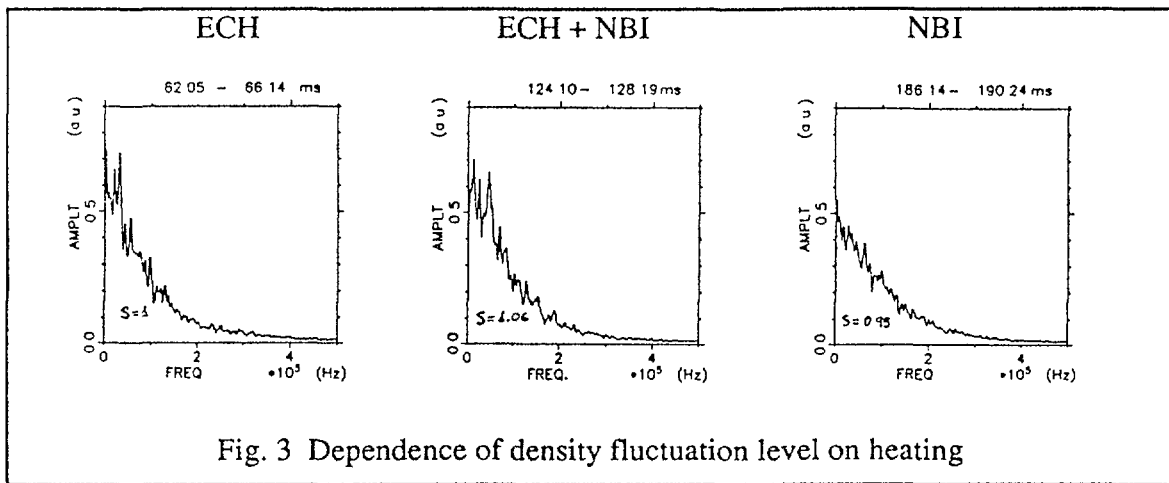
Total fluctuation level was measured by the integrated reflectometer signal spectrum. This level was compared with the total plasma stored energy, deduced from the diamagnetic loop signal, for series of discharges with the same density and heating power, during an iota scan. The reflectometer frequency was chosen to measure around  $r/a = 0.6$ , by using the information from Thomson Scattering on density profile. As can be seen at figure 2, a clear correlation between fluctuation level and plasma energy appears, with the fluctuations decreasing when the plasma confinement improves. This behavior seems



to be independent of the range of Iota values scanned, because the same correlation appears when the scan is made around  $\iota = .3$  with 2.5 T .

b) Dependence on heating power.

Keeping the density constant along the discharge, density fluctuations were measured at different times, when the heating power level was different due to the change from ECH at the beginning to NBI at the end. The analysis results are presented at figure 3. They seem to indicate that Neutral Beam heated plasmas have a wider density fluctua-



tion spectrum than ECH ones and that increases in the injected power in the order of 50% do not introduce a big change in the fluctuation level.

c) Fluctuation radial dependence

A radial scan, in the range accessible to the available frequency span in the reflectometer, was made for different experimental conditions in W7AS. Results are shown at figure 4. These results indicates the total fluctuation level, normalized to the density

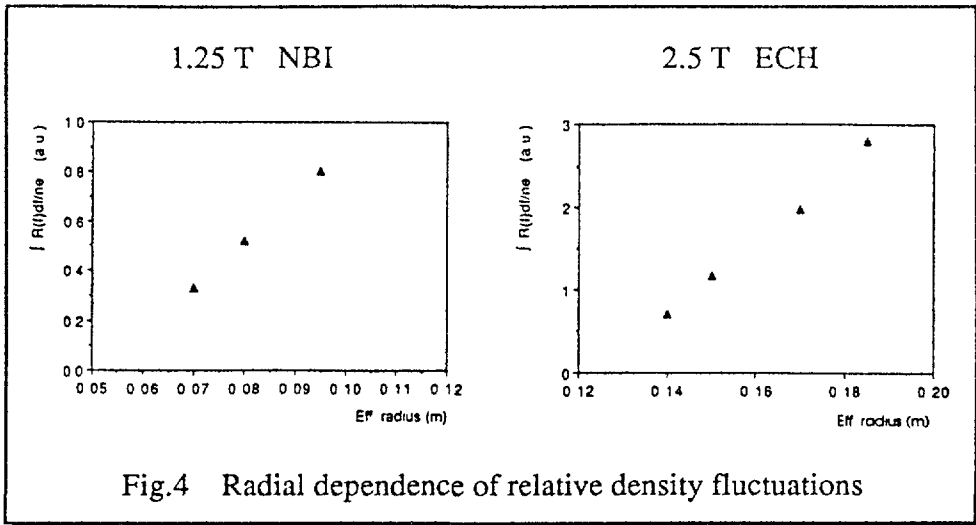


Fig.4 Radial dependence of relative density fluctuations

value at the considered point (deduced from Thomson Scattering profile), decreases when moving inside the plasma. This effect

appears for both values of the toroidal field and for ECH and NBI plasmas.

### SYSTEM IMPROVEMENTS

The absolute magnitude of the plasma reflecting layer displacement and hence of the density fluctuations can be only determined by coherent phase measurements. With this aim, several approaches are under test in our system. First, Frequency Modulated Reflectometry is being tried by introducing sawtooth modulation in the BWO tube and, by digital filtering and fringe counting, direct determination of the phase is obtained. The

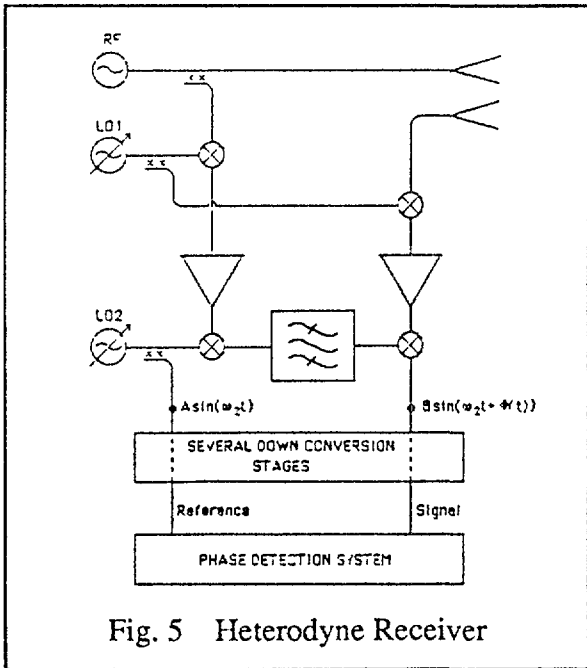


Fig. 5 Heterodyne Receiver

system has been checked and calibrated in the laboratory and it is now installed in W7AS. A second approach is Broadband Heterodyne Reflectometry. By heterodyne techniques the millimeter wave is down-converted to a 50 MHz signal carrying the phase information. Figure 5 shows a block diagram of the system being assembled. Since BWO tubes do not have high frequency stability, an IF system with tolerance to RF and local oscillator drift has been constructed.

## CONCLUSIONS

Preliminary results from microwave reflectometry on W7AS stellarator probes the capabilities of this diagnostic technique for electron density fluctuation determination in these devices. Indications of correlation between the level of fluctuations at the plasma edge and plasma confinement have been obtained. Better confinement seems to be correlated with lower fluctuation levels. Radial dependence of the relative fluctuation level decreases when going inside the plasma, that could be an indication of a turbulence layer at the plasma edge. System improvements are in progress to make possible to determine the absolute value of the density fluctuation.

## REFERENCES

- [1] P. Liewer, Nucl. Fusion 25, 543, 1985.
- [2] M. Murakami et al., Proc. 16th European Conf. on Cont. Fusion and Plasma Physics, II, 575, 1989.
- [3] A. Cavallo and R. Cano, EUR-CEA-FC-1137, 1982.
- [4] F. Simonet, Rev. Sci. Instrum., 56, 5, 1985.
- [5] TFR Group, Plasma Physics, 27, 1299, 1985
- [6] E. Anabitarte et al., Bull. Am. Phys. Soc., 32, 1938, 1987.
- [7] J. M. Senties et al., Proc. 16th European Conf. on Cont. Fusion and Plasma Physics, I, 51, 1989.
- [8] H. Renner, 16th European Conf. on Cont. Fusion and Plasma Physics, (invited talk), to be published on Plasma Physics.

# TOMOGRAPHY ANALYSIS OF MHD INSTABILITIES IN W VII-A STELLARATOR

A.P. NAVARRO, M.A. OCHANDO  
Asociación Euratom/CIEMAT,  
Madrid, Spain

A. WELLER  
Euratom-IPP Association,  
Max-Planck-Institut für Plasmaphysik,  
Garching, Federal Republic of Germany

## Abstract

Reconstruction of local Soft-X-ray emissivity in W7A stellarator during MHD phenomena is made using an algebraical technique that enables to study very distorted distribution using single array data. This technique is also applied to finite  $\beta$  discharges deducing from this analysis the distortion of emissivity contour due to high pressure and the Shafranov shift.

## INTRODUCTION

MHD instabilities can play an important role on energy and particle confinement in any plasma device. Experimental study of these perturbations can be made by analyzing plasma soft-X-ray signals, looking for magnetic island structures and their behavior during the instability evolution. To determine the local distribution of plasma emissivity from line integral measurements, as it is case for these signals in tokamaks and stellarators, tomography techniques are required due to the marked non circularity of those distributions during MHD phenomena. In this paper an iterative algebraical method, that uses as initial weights the fluxes deduced from equilibrium calculations for the used plasma configuration, has been applied [1]. The most important feature of this technique is the possibility to deduce complicated structures, such as local accumulations or very distorted distributions, with an small number of detector arrays. Even one single array data can be inverted using this method, by imposing the shape of the equal emissivity contours. Local emissivity is deduced as:

$$E(x_j, y_k) = \frac{W(j, k)}{NC(j, k)} \sum_{n=1}^{NA} \sum_{i=1}^{ND} S(\delta_n, \rho_i) \cdot \frac{M(n, i, j, k)}{WN(n, i)}$$

---

[1] A.P. Navarro, M.A. Ochando and A. Weller, "Equilibrium Based Iterative Tomography Technique for Soft-X-Ray in W VII-A Stellarator", XVI EPS Conference, Venice, 1989.

where  $E(x_j, y_k)$  is the local emissivity value of cell  $(j, k)$  and  $M(n, i, j, k)$  gives the contribution from that cell to the signal of detector  $i$  at array  $n$ . ( $NX, NY$  are the grid dimensions,  $W$  is the weight matrix,  $WN$  is the weight normalization factor for each line of sight and  $NC$  the number of contributions of each cell to different detector signals.  $NA$  is the number of arrays, each one with  $ND$  detectors). After each iteration new weights are defined by calculating the average emissivity on each assumed contour. Chi-squared evaluation after each iteration measures the method convergence.

### W7A STELLARATOR DATA ANALYSIS

Using the signals from a single array with 30 soft-X-ray detectors, located at a bottom port in the W7A stellarator as it is shown at figure 1, different types of discharges with OH have been analyzed. Results are summarized below. In this figure the shape of the vacuum magnetic flux surfaces are also displayed.

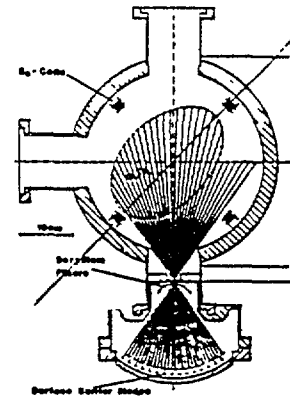


Fig.1  
W7A Array Location

#### a) Sawtooth analysis

Many discharges present a sawtoothing behavior. In all the analyzed discharges no hollow profiles appear after the sawtooth crash, for a  $500 \mu s$ . time resolution, as shown at figure 2a. Besides, the loss of energy from the plasma center due to this internal disruptions appears as an axisymmetrical mode. This is deduced from the determination of the increase in radiation between successive reconstructions, that is obtained by subtracting them, and that for the crash it is really a decrease for the center of the plasma and an increase at the outer part as can be seen at figure 2b.

a) Emissivity before and after crash

b) Loss of energy during crash

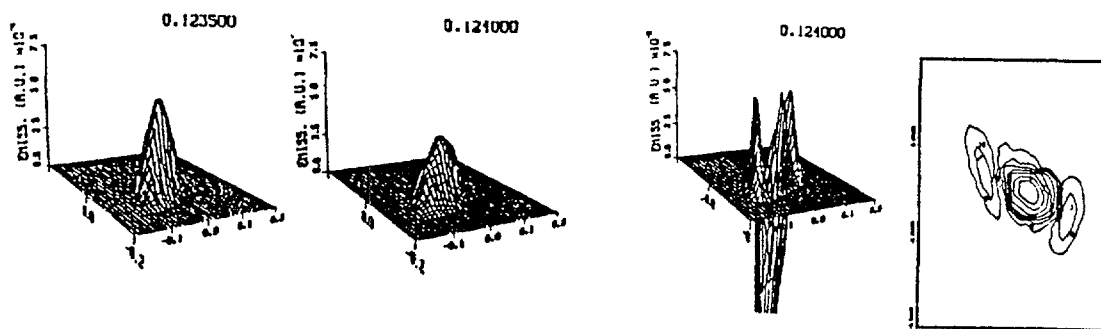


Fig.2 Sawtooth Analysis

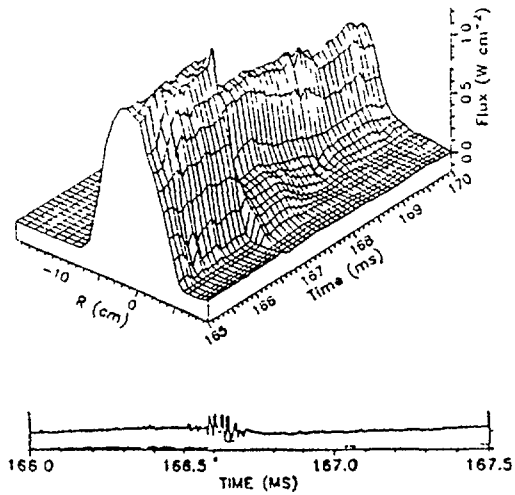


Fig. 3 Signal evolution during soft disruption

## b) Soft disruption analysis

Soft disruptions often appear during NBI in W7A plasmas when OH current is present. Figure 3 displays the array signal evolution around one of these disruptions. Signal at the central detector is also presented. It can be seen that, after the disruption, no activity is detected.

Reconstructions of local emissivity distributions deduced from these profiles are presented at figure 4. After several cycles of perturbation, the disruption occurs at 166.7 ms. In the reconstructions the contour structure shows a big

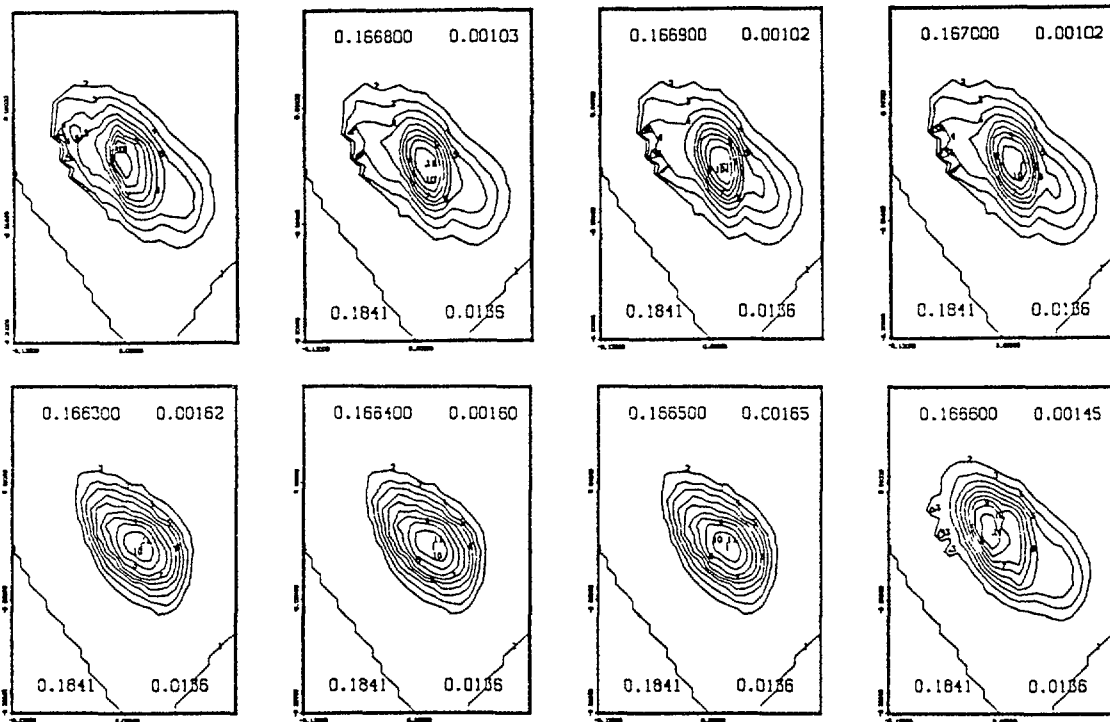


Fig.4 Reconstruction for soft disruption

distortion, that can be identified as an odd mode, at 166.6 ms. This feature last for about 200  $\mu$ s and disappears at the time of the soft disruption. But after this the contour distribution remains distorted, in an even structure, for a long period of time. In summary, there is some indication about soft disruptions being produced by the interaction between an even ( $m=1$ ) and odd mode ( $m=2$ ), with this last one remaining after the disruption but in a locked mode.

c) Finite  $\beta$  effects study

Using Neutral Beam Injection as additional heating, plasmas with  $\beta$  in the order of 1 % were obtained in W7A. Figure 5 shows the array signal evolution during a discharge with injection taking place during the interval 140 to 170 ms. Reconstructed local emissivity contours, deduced from these signals each 10 ms., are shown at figure 6. In spite of the assumed shape for these contours is  $45^\circ$  inclined ellipses, deduced from the vacuum calculation for the toroidal position of the array, a different structure appears when NBI is on. Basically they become less elliptical inclined at the plasma center.

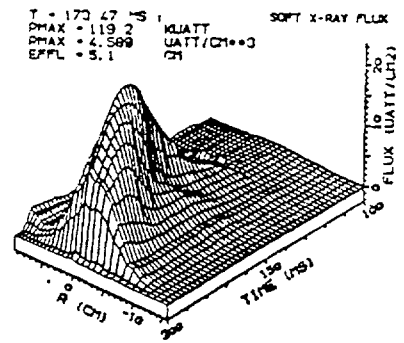


Fig. 5 Array signals for NBI discharge

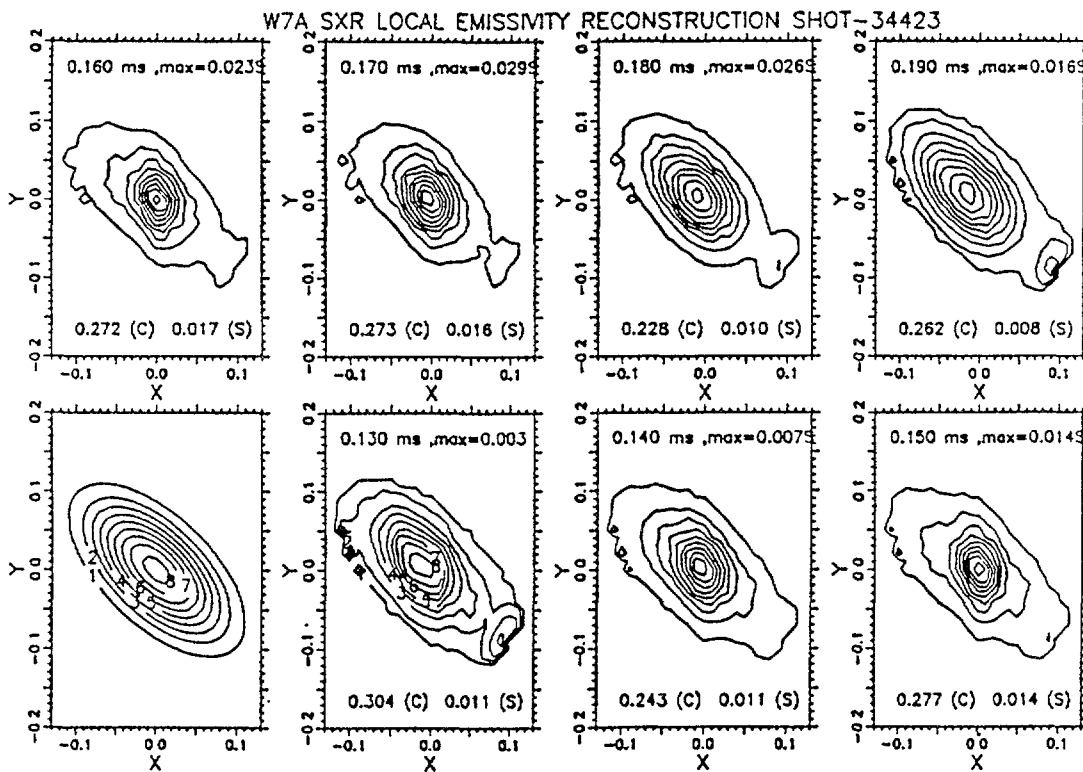
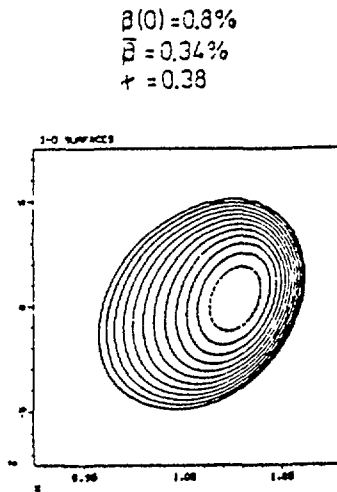


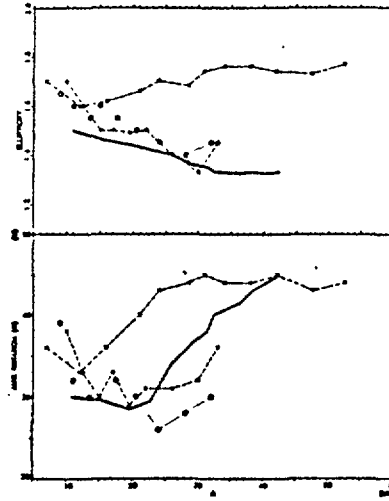
Fig. 6 Emissivity reconstructions for NBI plasmas in W7A

These results are in qualitative agreement with equilibrium calculations for finite  $\beta$ , as shown at figure 7, where the theoretical values for ellipticity and inclination of each contour (solid lines) are compared with those obtained from these analysis (dots). This agreement does not occur when same analysis is applied to reconstructions when NBI is off.

a) Flux contours



b) Ellipticity and inclination



c) Displacement

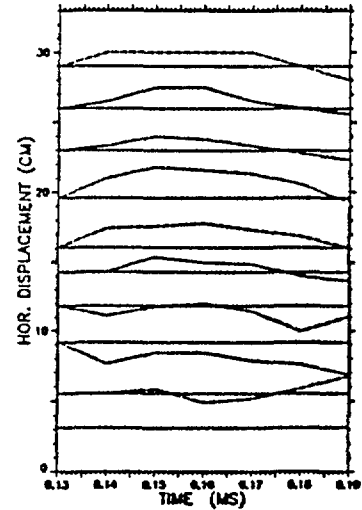


Fig. 7 Comparison with equilibrium calculation

Emissivity contour displacements has been also analyzed, obtaining no vertical displacement but a noticeable one for the the horizontal one, in the order of 1 cm, for the inner contours and no displacement for the outer ones. These displacements agree with Shafranov shifts for these plasma conditions.

## CONCLUSIONS

Tomography studies for Soft-X-ray signals in W7A stellarator, using an iterative algebraical technique, enable to deduce some characteristics of different phenomena such as the axisymmetrical character of sawtooth crash and the no hollowness of emissivity after those crash. There are also indication of the presence of even and odd mode simultaneously during soft disruptions with the even mode remaining locked after that. Finally application to NBI plasma enables to study the deformation and the displacement of emissivity contour due to finite b effects. These results are in good agreement with theoretical calculations and show clear Shafranov shift, in the order of 1 cm, for the central part of the plasma.

# DISSIPATIVE TRAPPED ELECTRON MODES IN $\ell = 2$ TORSATRONS

B.A. CARRERAS, N. DOMINGUEZ,  
J.N. LEBOEUF, V.E. LYNCH<sup>1</sup>  
Oak Ridge National Laboratory,  
Oak Ridge, Tennessee

P.H. DIAMOND  
University of California at San Diego,  
La Jolla, California  
United States of America

## Abstract

Trapped electron modes can play an important role in enhancing losses in a toroidal magnetic traps. It could be one cause of the deterioration of the confinement with beta increase in tokamaks. The helical ripple and short connection lengths in stellarators could serve as a basis for suggestion that trapped electron modes for those traps can be more unstable than in tokamaks. In this paper this problem is theoretically investigated for a realistic 3D stellarator.

---

Trapped electron modes [1] can play an important role in enhancing losses in a toroidal confinement device. They could be one cause of the deterioration of confinement with beta in tokamaks. For straight stellarators and for a model field, it has been shown [2] that the helical ripple and short connection lengths allow for strongly localized solutions to the drift wave equation. Therefore, it is suggested that trapped electron modes in stellarators can be more unstable than in tokamaks. This is particularly the case for low-shear configurations. In this paper, we consider this problem for a realistic 3-D stellarator. We use as input a 3-D equilibrium and include the finite-beta effects self-consistently.

In contrast to tokamaks, stellarators have the advantage that the magnetic field can be changed substantially by modifying the currents in the vertical field (VF) coils. In ATF [3], for example, changing the quadrupolar moment of the VF coils changes the rotational transform at the magnetic axis and, as a consequence, the shear. The change in quadrupole field also changes  $|B|$  along the field lines, allowing the trapping regions to change independently of the average curvature. This presents the opportunity for substantially changing the properties of these instabilities. We are exploring ways to devise experiments in ATF that will permit us to study trapped electron modes and evaluate their role in plasma confinement.

Guided by the results of Ref. [2], which show that stellarator drift waves are more localized in shearless configurations, we have studied two ATF configurations: one that is practically shearless in the inner half of the plasma radius and another for which the shear

---

<sup>1</sup> Computing and Telecommunications Division, Martin Marietta Energy Systems, Inc., Oak Ridge, TN 37831, USA.

is strong over most of the radius. We expect that in the first case the mode will be localized and that in the second case it will be extended along the field lines. The dissipative trapped electron mode will be more dangerous in the first configuration, because of the localization of the drift wave. The numerical results indicate that in the ATF experiment it could be possible to control this dissipative mode and study its implications for confinement of toroidal plasmas.

We obtain the 3-D equilibrium with the VMEC code [4]. To solve the drift wave equation along magnetic field lines, the equilibrium is transformed to Boozer coordinates [5]. In this coordinate system the magnetic field lines are straight,

$$\mathbf{B} = (\nabla s \times \nabla \theta) \Phi' + (\nabla \zeta \times \nabla s) \chi'$$

Here,  $(s, \theta, \zeta)$  are the Boozer coordinates,  $\Phi$  is the toroidal flux, and  $\chi$  is the poloidal flux. After the transformation [6] to Boozer coordinates, the flux surfaces are represented as

$$\begin{aligned} R &= \sum_{mn} R_{mn} \cos(m\theta - n\zeta) \\ Z &= \sum_{mn} Z_{mn} \sin(m\theta - n\zeta) \\ \phi &= \zeta + \sum_{mn} \phi_{mn} \sin(m\theta - n\zeta) \end{aligned}$$

The  $(R, Z, \phi)$  are the usual cylindrical coordinates in real space.

Zero-current equilibria have been considered, with the plasma pressure profile  $P = P(0)[1 - (\chi/\chi_a)]^2$ . Here  $\chi_a$  is the poloidal magnetic flux at the plasma boundary.

The dissipative trapped electron modes can be studied following the formalism of Antonson and Lane [7]. Here, we present only the results for the electrostatic drift wave model. The model is based on fluid ions and adiabatic electrons (i.e. we consider collisionless electrons without their non-adiabatic response). The eigenmode equation, using an eikonal representation for the perturbation, can be written in Boozer coordinates as

$$\begin{aligned} \partial^2 \Psi / \partial^2 \zeta &= \{ -\Omega^2 F |\nabla \alpha|^2 / |\nabla \alpha|_0^2 \chi^2 \\ &\quad - \Omega F [-1 - (2p\mathbf{B} \times \boldsymbol{\kappa} \cdot \nabla \alpha / p' B^2)] - F \Omega^2 \\ &\quad + (1/2B) \partial^2 B / \partial^2 \zeta - (1/4B^2) (\partial B / \partial \zeta)^2 \} \Psi \end{aligned}$$

where

$$|\nabla \alpha|^2 = |\nabla(\zeta - q\theta)|^2 = (B^2 / \chi'^2 g^{ss}) \left\{ 1 + [(g^{ss}/B) \int \Sigma dl / B]^2 \right\}$$

is the perpendicular wave vector,  $g^{ss} = |\nabla s|^2$  is the metric element,  $(g)^{1/2} = (J\chi' - I\Phi')/B^2$  is the Jacobian,  $\boldsymbol{\kappa} = (1/B^2)\nabla(p + B^2/2) - (\mathbf{B}/2B^4)\mathbf{B} \cdot \nabla B^2$  is the curvature vector,

$$\begin{aligned} \Sigma &= (1/g^{ss})(\nabla s \times \mathbf{B}/g^{ss}) \cdot [\nabla \times (\nabla s \times \mathbf{B})] \\ &= \Phi'^2 t' / (g)^{1/2} + \mathbf{B} \cdot \nabla [(-g_{\theta s} I - g_{s\zeta} J) / (g)^{1/2} g^{ss}] \end{aligned}$$

is the local shear, and  $\iota = \chi'/\Phi'$  is the rotational transform.

The drift wave equation is essentially a Schrödinger-type equation, which, when written in dimensionless form, depends on three parameters:  $\lambda = m\rho_s|\nabla\alpha|_0$ ,  $\omega_n = \omega'/\omega_s$ , and  $k_0$ . To solve the drift wave equation, we have used a Numerov shooting code [8] with outgoing wave boundary conditions.

We have looked only for even modes localized in the outer region of the configuration. We have found that these modes localize where the potential has a minimum. Typical eigenfunctions for ATF configurations (for  $\omega_n \sim 1$ ,  $\lambda_0 \sim 1$ ) are plotted in Figs 1 and 2. Figures 1 and 2 correspond to ATF configurations with negative and positive quadrupolar field [3], respectively. The configuration with a negative quadrupolar component has a flat rotational transform over most of the radius, in contrast to the one with a positive component, which has very strong shear. Thus, we have found that we can change the localization of the modes by changing the external quadrupolar field of the configuration. Because the ratio of helically trapped to toroidally trapped particles is also changed, this presents a very interesting scenario to be tested experimentally.

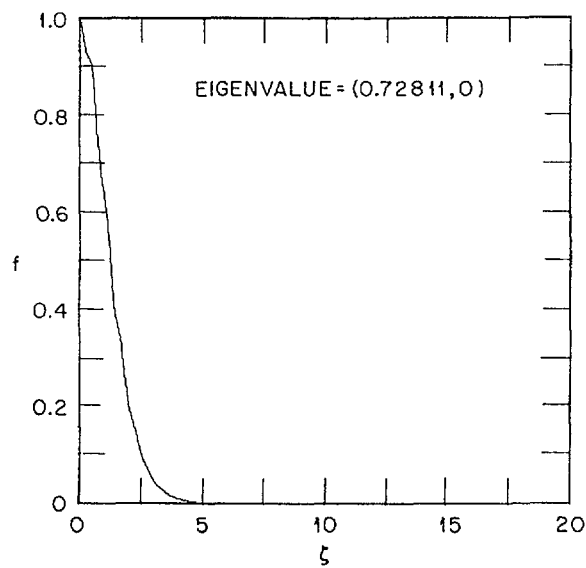


FIG. 1.

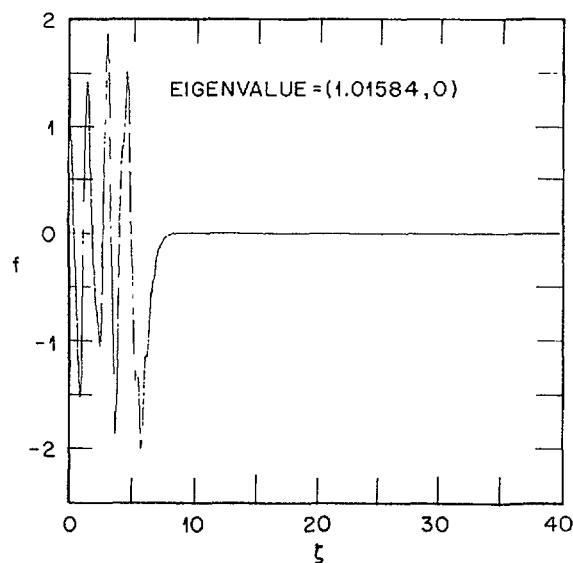


FIG. 2.

## ACKNOWLEDGEMENT

This research was sponsored by the Office of Fusion Energy, U.S. Department of Energy, under contract DE-AC05-84OR21400 with Martin Marietta Energy Systems, Inc.

## REFERENCES

- [1] KADOMTSEV, B.B., POGUTSE, O.P., *Sov. Phys. Dokl.* **14** (1979) 420.
- [2] BHATTACHARJEE, A., et al., *Phys. Fluids* **26** (1983) 880.
- [3] LYON, J.F., CARRERAS, B.A., CHIPLEY, K.K., et al., *Fusion Technol.* **10** (1986) 179.
- [4] HIRSHMAN, S.P., VAN RIJ, W.I., MERKEL, P., *Comput. Phys. Commun.* **43** (1986) 143.
- [5] BOOZER, A.H., *Phys. Fluids* **26** (1981) 2616.
- [6] NÜHRENBERG, J., ZILLE, R., in *Theory of Fusion Plasmas* (Proc. Workshop Varenna, 1987), Editrice Compositori, Bologna (1988) 3.
- [7] ANTONSEN, T., LANE, B., *Phys. Fluids* **23** (1980).
- [8] WHITE, R.B., *J. Comput. Phys.* **31** (1979) 409.

## EQUILIBRIUM AND IDEAL STABILITY STUDIES FOR ATF

V.E. LYNCH<sup>1</sup>, B.A. CARRERAS,  
N. DOMINGUEZ, J.N. LEBOEUF  
Oak Ridge National Laboratory,  
Oak Ridge, Tennessee,  
United States of America

### Abstract

The results of the theoretical calculations of the ATF equilibrium and stability analysis are presented. Two sequences of equilibria with different plasma pressure profiles have been analyzed. It is shown that the equilibria with pressure profiles broadening with beta as the experiment are stable for all beta values.

---

The Advanced Toroidal Facility (ATF) [1] was designed to have stable access to the second stability regime. For the design conditions, this access should occur at beta values of about  $\beta_0 \approx 5\%$ . The electron-beam mapping experiment in March 1988 revealed the presence of magnetic islands [2]. In particular, an  $\iota \equiv 1/q = 1/2$  island, the largest (width of  $\approx 6$  cm, and chains of islands outside  $q = 2$  were found. The initial operation in ATF (June-September 1988) proceeded with the field errors that created these islands. The cause of field errors was identified as buswork for the HF and outer VF coils. It was corrected in January 1989. A consequence of these field errors was that the pressure profiles measured in the experiment were narrow. The  $q = 2$  island acted as a stochastic limiter for the discharges. Such narrow pressure profiles cause an effective reduction of the edge rotational transform,  $\iota_{\text{edge}}$ , and an increase of the plasma aspect ratio,  $A$ . As a result, the finite-beta magnetic axis shifts were large,

$$\frac{\Delta_p}{a} \approx \beta_0 \frac{A}{\iota_{\text{edge}}^2}$$

which caused a reduction in the beta value needed to access the second stability regime, as discussed below.

Another result from the experiment was that the pressure profiles broadened with increasing beta. To understand the stability properties of the experiment, two sequences of equilibria with different profiles have been analyzed: (1) equilibria with constant pressure profile shape and varying  $\beta_0$ , and (2) equilibria with pressure profile width changing with beta (Fig. 1), as given by the experiment.

The ideal MHD stability analysis based on the stellarator expansion approach shows stability for  $n = 1, 2$ , and 3 modes. They are close to marginal stability at low beta values,  $\beta_0 < 2\%$ .

---

<sup>1</sup> Computing and Telecommunications Division, Martin Marietta Energy Systems, Inc., Oak Ridge, TN 37831, USA

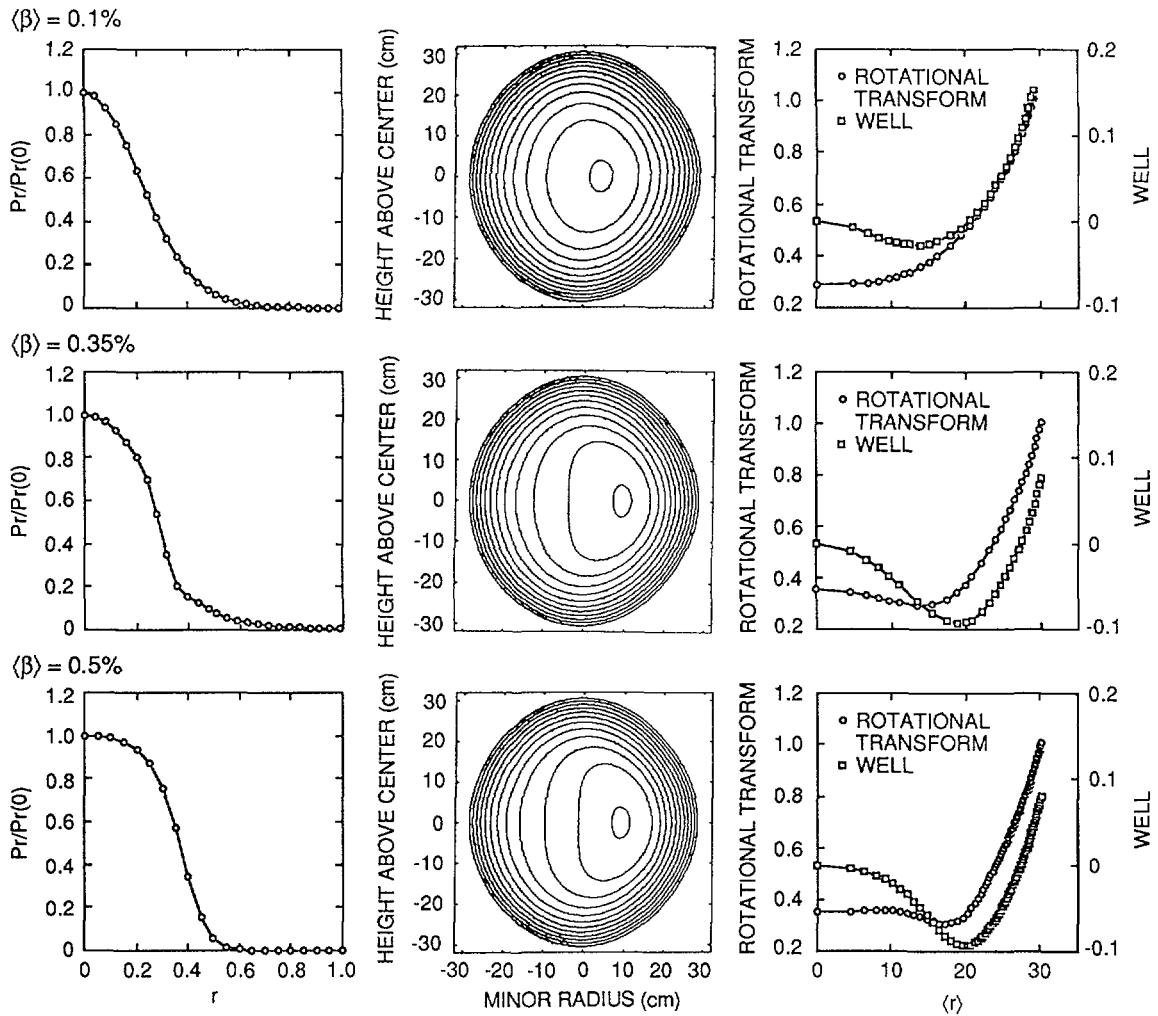


FIG. 1. Pressure profiles, average magnetic surfaces derived from stellarator expansion equilibria calculations with zero current, and  $\iota$  and  $V''$  versus average radius for equilibria with pressure profile width broadening with beta

The results of the 3-D Mercier criterion ( $D_m > 0$  for stability) calculation for the constant pressure profile scan are shown in Fig. 2. The only region of instability is for  $0.25\% < \beta_0 < 1.1\%$ . The transition to the second stability regime is at a value of  $\beta_0 \approx 0.6\%$ . The Mercier criterion results also show clear evidence of beta self-stabilization effects (Fig. 3). The equilibria with pressure profiles broadening with beta as the experiment are stable for all beta values. Therefore, for the highest beta values obtained in the experiment,  $\beta_0 \approx 3\%$ , the plasma is in the second stability regime [3].

The magnetic fluctuation measurements showed reduction in the fluctuation level for  $\beta_0 \geq 1\%$  [4]. These fluctuation levels are in reasonable agreement with the theoretical calculations based on the resistive pressure-gradient-driven turbulence and support the evidence that ATF has already operated in the second stability regime.

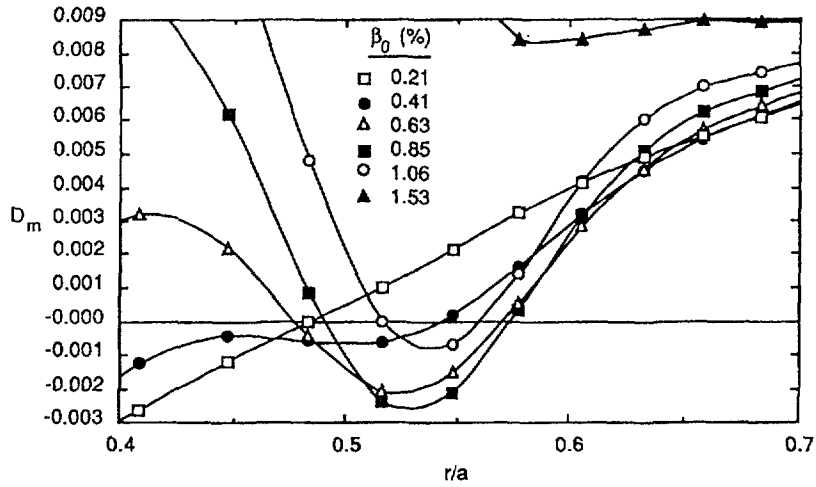


FIG. 2. 3-D Mercier criterion  $D_m$  versus average radius for zero-current equilibria with the constant pressure profile and different values of beta.

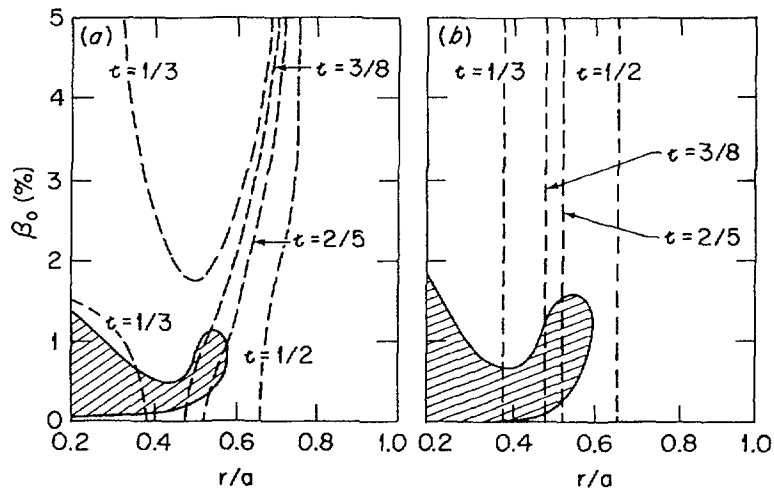


FIG. 3. 3-D Mercier unstable region (hatched) in the  $(\beta, r/a)$  plane for (a) zero-current and (b) flux-conserving equilibria. The positions of the most relevant low- $n$  singular surfaces are also plotted. The constant pressure profile is used with the vacuum magnetic axis at  $R = 2.05$  m.

### ACKNOWLEDGEMENT

This research was sponsored by the Office of Fusion Energy, U.S. Department of Energy, under contract DE-AC05-84OR21400 with Martin Marietta Energy Systems, Inc.

## REFERENCES

- [1] LYON, J.F., CARRERAS, B.A., CHIPLEY, K.K., et al., Fusion Technol. **10** (1986) 179.
- [2] COLCHIN, R.J., et al., ATF flux surfaces and related plasma effects, paper 03-4 presented at this meeting.
- [3] CARRERAS, B.A., DOMINGUEZ, N., LEBOEUF, J.N., LYNCH, V.E., CHARLTON, L.A., A First Glance at the Initial ATF Experimental Results, ORNL/TM-11102, Oak Ridge National Laboratory (1989).
- [4] HARRIS, J.H., Second stability studies in ATF, paper 02-5 presented at this meeting.

## STABILITY ANALYSIS OF FREE BOUNDARY MODES FOR ATF\*

F. BAUER, P.R. GARABEDIAN  
Courant Institute of Mathematical Sciences,  
New York University,  
New York, N.Y.,  
United States of America

### Abstract

A new MHD code called BE FREE has been developed to test the stability of low order free boundary modes in stellarator. This code has been used particularly for the stability analysis of free boundary modes for ATF and Helias devices.

---

By thorough revision of the BETA code a new MHD code called BEFREE has been developed to test the stability of low order free boundary modes in stellarators. Artificial viscosity has been added to the free boundary condition to assure adequate convergence of the finite difference method, and a spectral representation has been applied to the equations at the magnetic axis that produces a robust algorithm. The energy can now be calculated to ten or more significant figures on any fixed mesh, and convergence studies provide reliable growth rates from the usual second minimization associated with a trial mode.

As predicted by two-dimensional theory, the free boundary modes of three-dimensional stellarators are found to be generally more stable than internal modes of higher order. However, the  $m = 1, n = 0$  free boundary mode of a two-dimensional ATF configuration is only stable for average  $\beta$  below 5%. Comparable modes for a Helias of moderate aspect ratio have  $\beta$  limits exceeding 7%. Runs of the new code suggest that while ATF and Helias equilibria can be stabilized by shifting the magnetic axis outwards, there is then a risk that the magnetic surfaces deteriorate.

---

\* Work supported by US Department of Energy grant DE-FG02-86ER53223 and NSF grant DMS-8701258.

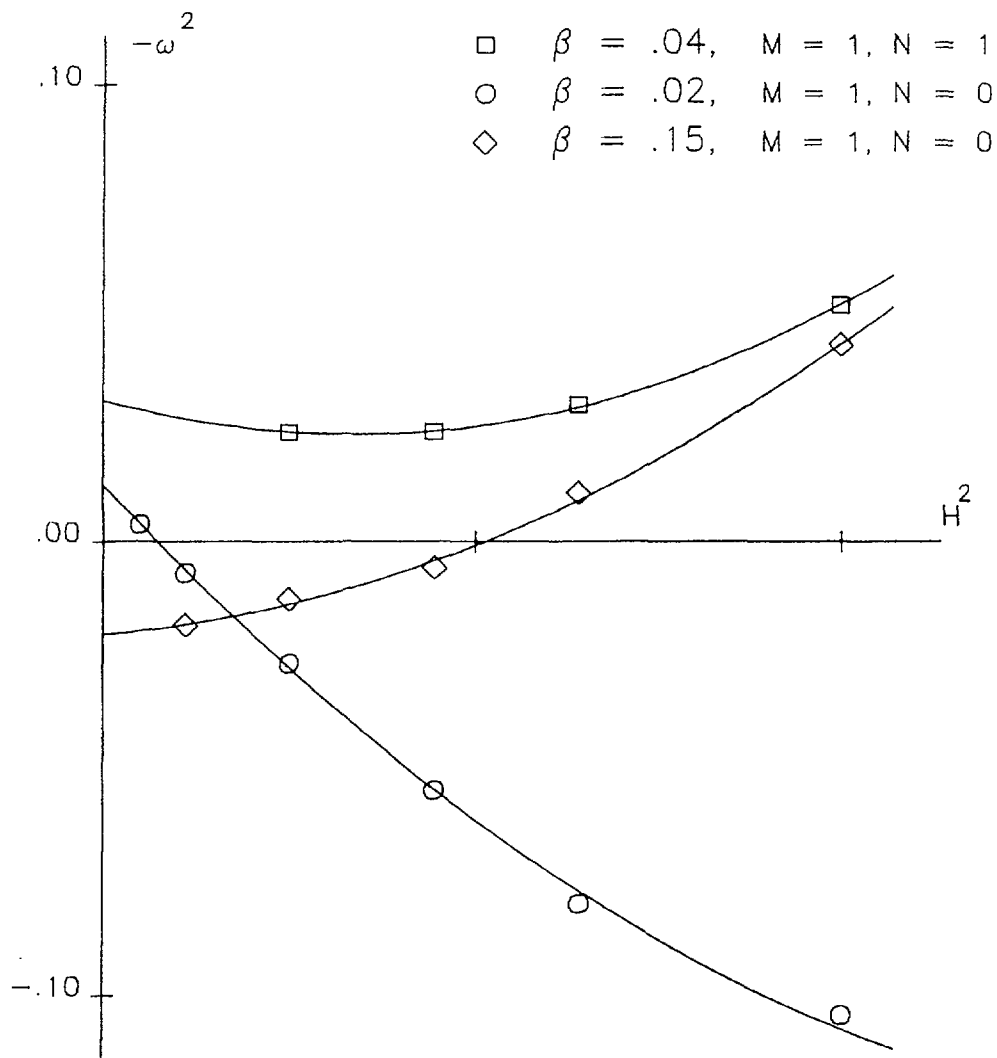


Fig. 1. Convergence study of nonlinear stability for free boundary modes of ATF configurations comparing the growth rate  $\omega$  with the mesh size  $h$ . Second minimization of the energy for the  $n = 1$  mode was performed over 12 field periods of a three-dimensional equilibrium that had been calculated in one field period to begin with. Second minimization for the  $n = 0$  modes was done more economically over just one field period of two-dimensional equilibria that were first calculated with the magnetic axis at the origin. A standard pressure distribution of the form  $p = p_0(1 - s)$  was used in the cases with  $\beta = 0.04$  and  $\beta = 0.15$ , where  $s$  is the normalized toroidal flux; but for  $\beta = 0.02$  the pressure distribution was adjusted to become nearly constant so that a sharp boundary mode could be tested.

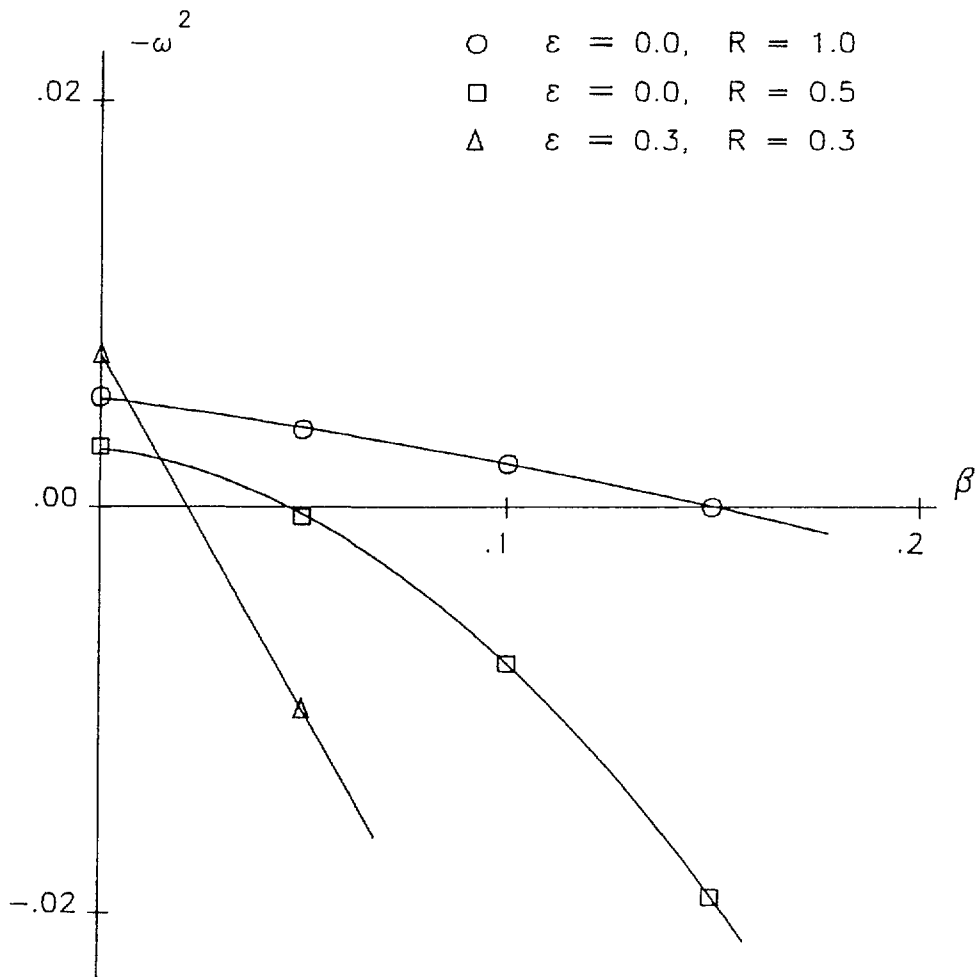


Fig. 2. Graphs of the transformed growth rate  $-\omega^2$  versus average  $\beta$  for the  $m = 1, n = 0$  mode of ATF with  $p = p_0(1 - s)$ .  $R$  is the ratio of the plasma radius to the radius of an outer control surface on which the boundary values of the magnetic potential are prescribed, and  $\epsilon$  is the inverse aspect ratio of that control surface. The case  $R = 1$  refers to a fixed boundary calculation, and the equilibria with  $\epsilon = 0$  were two-dimensional. The example with  $R = 0.3$  is three-dimensional and has plasma aspect ratio 10; this is supposed to model the ATF when there is a significant  $m = 2, n = 1$  island defining a separatrix at  $\iota = 1/2$ . The computed  $\beta$  limit of 2% agrees more or less with what has been achieved experimentally.

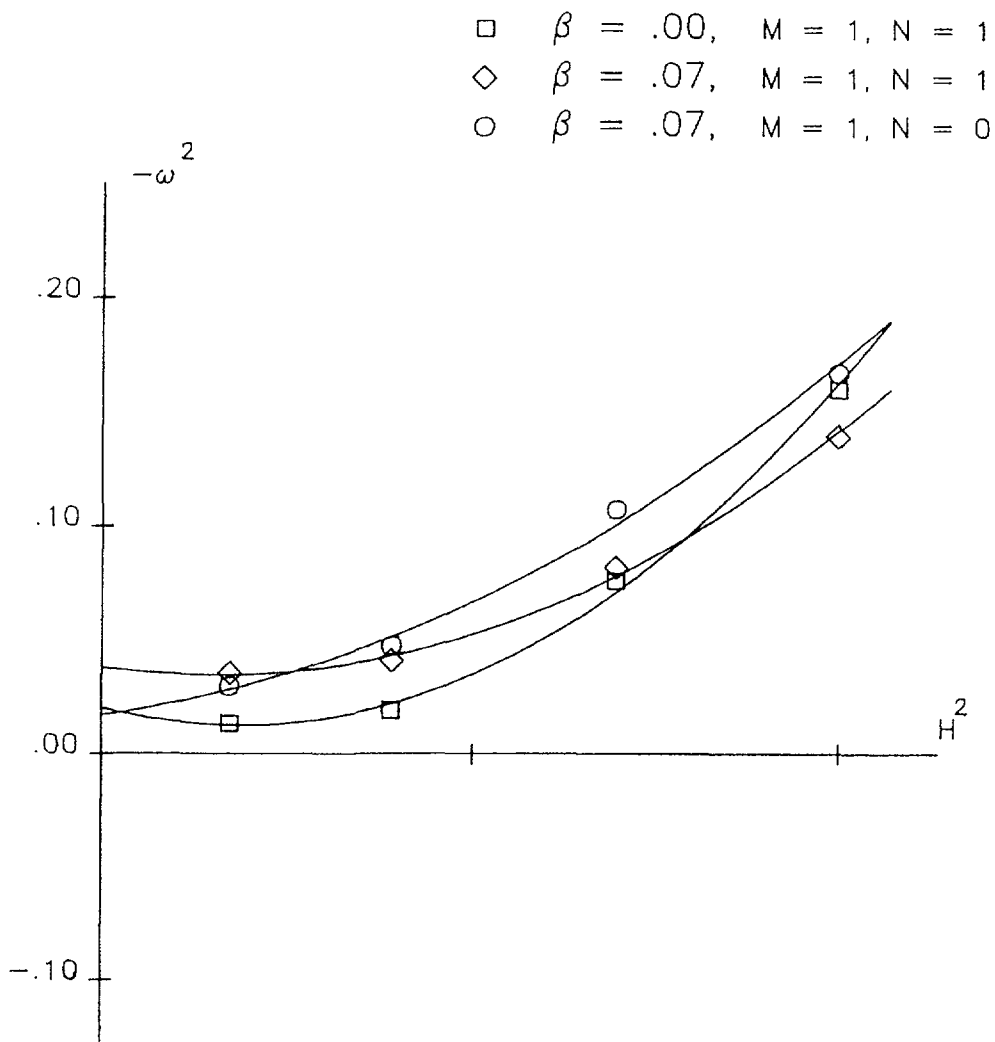


Fig. 3. Convergence study of the free boundary modes for a Helic with 6 field periods, plasma aspect ratio  $A = 11$ , and rotational transform  $\iota$  in the range  $1.5 < \iota < 2$ . The pressure distribution was of the form  $p = p_0(1 - s)^2$ , and the finest mesh had  $24 \times 24 \times 48$  points in each field period. The stability of the free boundary modes is consistent with a global magnetic well that appears to prevail in the vacuum region surrounding the plasma. Stability of the  $m = 1, n = 0$  mode seems to depend on the ratio  $\iota/A$  of rotational transform  $\iota$  to aspect ratio  $A$ .

## STABILITY STUDIES FOR TJ-II\*

A. VARIAS, C. ALEJALDRE, A. LÓPEZ-FRAGUAS  
Asociación Euratom/CIEMAT,  
Madrid, Spain

B.A. CARRERAS, N. DOMINGUEZ,  
V.E. LYNCH<sup>1</sup>  
Oak Ridge National Laboratory,  
Oak Ridge, Tennessee,  
United States of America

### Abstract

The hard core winding of the four period heliac TJ-II, to be built at CIEMAT site in Madrid, is composed of a circular coil and a helical winding with separately controllable currents<sup>1</sup>. This makes the TJ-II a very attractive flexible heliac with a broad range of controllable rotational transform and magnetic well. This flexibility will permit to experimentally explore regimes with stability average beta limit to Mercier modes, ranging from near zero to  $\approx 6\%$  in an almost continuous manner. Furthermore, configurations with second stability regime behaviour have been found.

---

### Introduction

In this paper we study this flexibility by studying a set of configurations having equal rotational transform and different magnetic well, to observe the effect of the magnetic well upon the MHD properties of the configurations.

We have studied four configurations having equal rotational transform at the axis and different magnetic well. The parameters that describe the configurations are summarized in table I. Figure 1 shows the two extreme configurations (A) and (D) at the toroidal angle  $0^\circ$ , it is clearly seen how the increase in the magnetic well is obtained through an increase in the indentation of the flux surfaces. Vacuum field configurations are determined with fixed TF coil line currents, fixed VF coil line currents and various circular coil,  $I_{cc}$  and helical coil  $I_{hc}$  line currents.

---

\* Research sponsored by the Office of Fusion Energy, US Department of Energy, under contract DE-AC05-84OR21400 with Martin Marietta Energy Systems, Inc.

<sup>1</sup> Computing and Telecommunications Division, Martin Marietta Energy Systems, Inc., Oak Ridge, TN 37831, USA.

Table I				
	$\iota_0/M$	$-I_{cc}$ (kA)	$-I_{hc}$ (kA)	Well
Configuration A	0.36	290	92	1%
Configuration B (Standard)	0.36	219	95	2%
Configuration C	0.36	105	82.5	3%
Configuration D	0.36	65	55	4%

The boundary of the confinement region is Fourier analyzed in a form suitable as input for the VMEC equilibrium code. The selected modes are distributed in a rectangle ( $0 \leq m \leq 5$ ,  $-12 \leq n \leq 12$ ). We needed 138 Fourier amplitudes to satisfactorily characterize the boundary of the confinement region in terms of the vacuum rotational transform and magnetic well<sup>2</sup>.

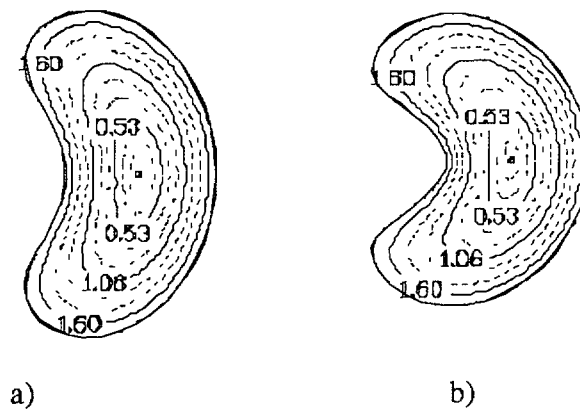


Figure 1

Two vacuum configurations with magnetic well a) 1% b) 4%

The fixed boundary equilibria for the four configurations were obtained using the 3-D equilibrium code VMEC<sup>3</sup> with a radial mesh of 31 points. The total average force for the equilibrium configurations was less than  $10^{-9}$ . Convergence studies were done with a radial mesh of 61 pts. and average force of  $10^{-11}$ . Typical CPU times in a CRAY-II machine range from 80 minutes for low values of  $\beta$  ( $< 2\%$ ) and  $> 300$  minutes for higher values of  $\beta$ . We considered a sequence of zero current equilibria with two pressure profiles  $p \propto (1 - \Phi)$  and  $p \propto (1 - \Phi)^2$  where  $\Phi$  is the normalized toroidal flux.

## Conclusions

The results from applying a 3-D Mercier criterion to the equilibria described previously is shown in figure 2. The value of the Mercier criterion at the fixed normalized radius 0.97 is plotted versus the averaged  $\beta$  of the configuration. A linear pressure profile was used. It is seen that the configuration with a shallow well (A) is Mercier unstable for any value of  $\beta$ . The standard configuration (B), reaches its  $\beta$  limit at  $\approx 2\%$ , well in agreement with that found in reference 2. When we increased the magnetic well, the configuration becomes more stable and for a value of the magnetic well of 3% (C), the  $\beta$ -limit with this pressure profile is almost 4%. The last configuration studied (D) shows positive values of the Mercier criteria for  $\beta$ -values of the order of 6% .

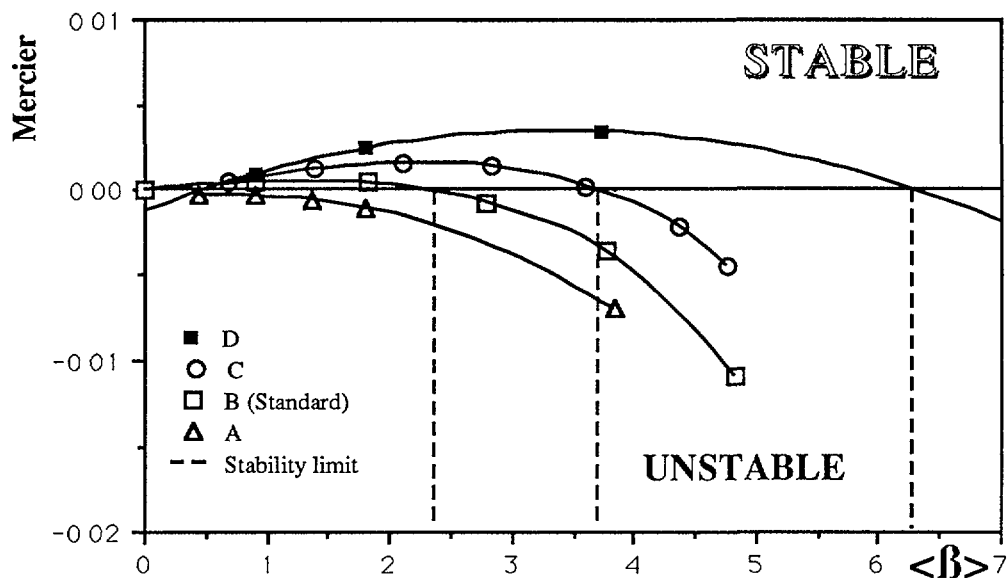


**Figure 2**  
The Mercier criterion for the four configurations vs.  $\langle\beta\rangle$  for a fixed normalized radius = 0.97

The influence of the pressure profile on the stability can be clearly seen in figure 3 where the averaged  $\beta$  is plotted vs. the normalized radius for the configuration (C). The stable region sensibly increases when one changes from a parabolic to a linear pressure profile. This increase occurs in all the configurations studied.

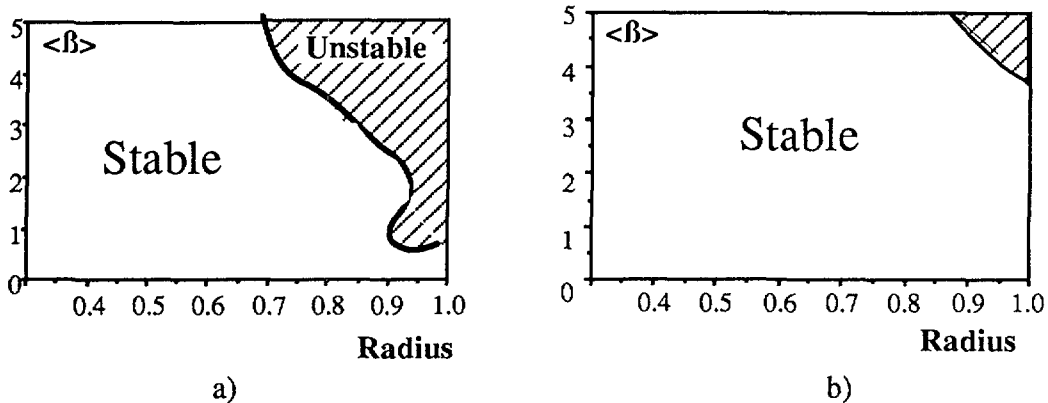


**Figure 3**  
The stable regions for the configuration (C) with two pressure profiles a) Parabolic b) Linear

### Self-stabilization

We studied a fifth configuration with a lower value of the rotational transform at the axis ( $\approx 0.30$ ) and a magnetic well of  $\approx 2\%$ . This configuration is also characterized for having a smaller average radius  $\approx 12$  cm and therefore having an effective aspect ratio greater than the previous set. Figure 4a

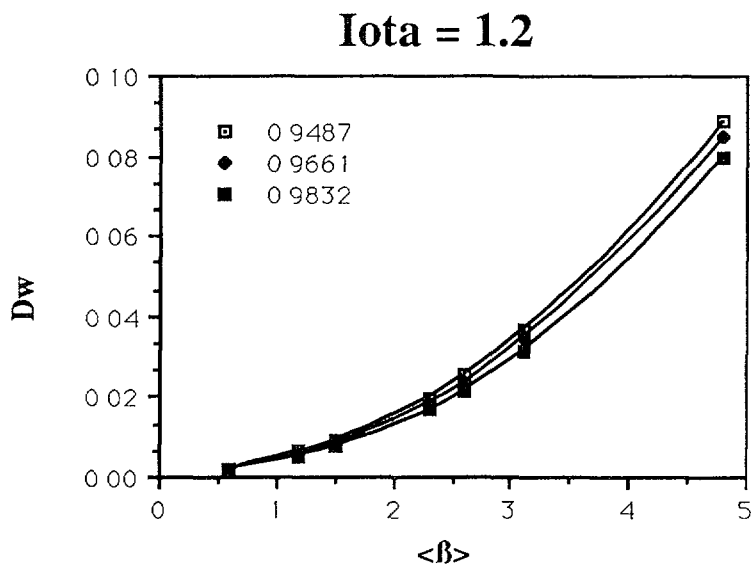


**Figure 4 a**

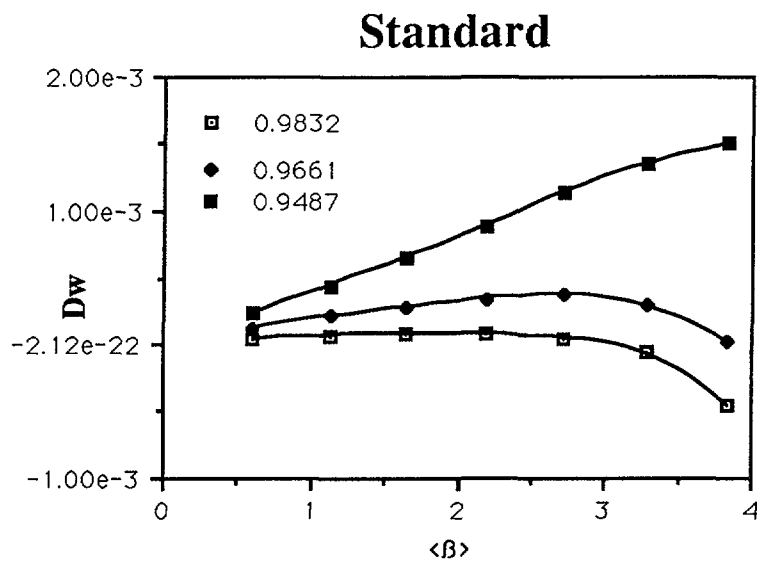


Figure 4 b

shows the positive contribution to the Mercier criteria for this configuration and fig. 4b for the standard one as  $\langle \beta \rangle$  is increased. It is seen the quite different behaviour of this configuration, clearly showing a  $\beta^2$  dependence for high values of  $\beta$  characteristic of a second stability regime, suggesting the possibility that higher stability limits can be found in configuration space. Work is under way to study configurations with higher effective aspect ratios and high rotational transform/period  $\approx 0.6$ .

### References

- 1.- Alejaldre C. et al., this conference
- 2.- Varias et al., 16 th. Eur. Conf. on Controlled Fusion and Plasma Physics, Venice 1989
- 3.- Hirshman, S.P. et al. Comp. Phys. Comm. **39**, 546 (1989)
- 4.- Nührenberg J., Zille R. and Hirshman S.P., 14th Eur. Conf. on Contr. Fusion and Plasma Physics, Madrid 1987, ECA **11d**, part I, 415 (1987)

# TECHNIQUES FOR COUPLING FULLY THREE DIMENSIONAL MHD CODES AND TWO DIMENSIONAL AVERAGED CODES FOR STELLARATOR AND TOKAMAK APPLICATIONS\*

J.L. JOHNSON, A.H. REIMAN, G. REWOLDT  
Plasma Physics Laboratory,  
Princeton University,  
Princeton, New Jersey,  
United States of America

## Abstract

The recently developed PIES code can be used to study three dimensional MHD equilibrium problems associated with both stellarators and tokamaks. We have worked out techniques for studying the effect of plasma currents on the tokamak ripple field by carrying through most of the calculation as if the tokamak were an axisymmetric configuration and then adding the ripple field before doing the final iterations. Then the difficult part of the program only needs a few further iterations. This modification enables us to use a true vacuum ripple field in the studies, rather than to impose the nonaxisymmetry by introducing the previously used approximate distortion of the shape of the plasma surface. The ideas that were developed in this application have led to a technique for converting the output of the axisymmetric toroidally averaged STEP code into a form that can be used directly as input for the PIES code. The coupling of these codes has the additional feature that it provides good line following techniques for analysis of the output of the STEP code and enables one to use its output as the initial values for a fully three dimensional study. It is especially useful for the PIES code in that it makes it easy to determine free boundary equilibria. A combination of this ability to transform from two dimensional to three dimensional models with an inverse coupling from three dimensional calculations to the STEP code should improve our tools for analysis of the equilibrium and linear stability properties of both stellarators and tokamaks. These techniques could easily be adapted for other codes.

---

## I. INTRODUCTION

The need for calculation of three-dimensional configurations, including stellarators and the nonaxisymmetric properties of tokamaks, has increased. Fortunately, the capabilities of computer hardware and numerical algorithms have been expanded so that it is now possible to carry through elaborate calculations for fully three-dimensional systems. Codes such as PIES [1], VMEC [2], BETAS [3], and MH3D [4] have been developed for this purpose. These are still being complemented with results from two-dimensional averaged codes like STEP [5,6], NAV [7], and H-APPOLO [8]. Three-dimensional codes by their very nature are time-consuming and require careful monitoring in their execution. It is the purpose of this note to show how two-dimensional and three-dimensional codes can be coupled so as to improve the situation.

---

\* Work supported by the US Department of Energy under contract DE-AC02-76-CHO3073 with Princeton University.

In the next section we describe some modifications that we have incorporated into the PIES code [1] to provide the flexibility of modifying the magnetic field after several iterations have been carried through. The studies that were done in connection with these modifications of the PIES code led to the idea that it would not be difficult to convert the output of the STEP code into a form that could be used as input for the PIES code. Thus a reasonably good approximation to a desired equilibrium could be obtained quickly and then the fully three-dimensional code could be used for further refinement. This is discussed in Sect. III. It has been proposed previously [10] that the output of a three-dimensional code could be used as input for the STEP stability studies. This idea is described in Sect. IV. Finally, some comments about the possible improvements and applications that have been suggested here are given in Sect. V.

## II. MAGNETIC FIELD MODIFICATION IN THE PIES CODE

The particular application that we have in mind is the study of the effect of currents in a tokamak plasma on the magnitude of the magnetic field ripple associated with having a finite number of toroidal coils. Such a study was done previously [9] by calculating the shape of the plasma boundary and specifying it as an initial condition for the calculation. The model used for the fields produced by the toroidal field coils was

$$\mathbf{B} = R_0 B_0 \nabla \{ \phi + [(R/b)^N / 2N] \cos N\phi \}, \quad (1)$$

corresponding to a sinusoidal vertical sheet current at a major radius  $R = b$ . An approximation to this field ripple was inserted into the PIES code by distorting the plasma boundary into the form

$$R = R_a \{ 1 - [(R_a/b)^N / 2N] \cos N\phi \}, \quad Z = Z_a. \quad (2)$$

This had to be done at the beginning of the calculation. Although the final solution can be regarded as a small perturbation of an axisymmetric equilibrium, this approach required that the full three-dimensional coupling be computed at each iteration of the equilibrium algorithm.

We have recently written a program to modify the output of an axisymmetric calculation to add the field of Eq. (1) directly so that we can then proceed to the answer. It will be simple to modify the form of the added nonaxisymmetric field so that this program is quite versatile.

## III. CONVERSION OF OUTPUT FROM THE STEP CODE INTO INPUT FOR THE PIES CODE

The work that was done in the previous section led to the realization that it is straightforward to convert the output of the STEP code into a form that can be used directly as input for the PIES code. The basic idea is that what is needed is a subroutine which is capable of giving the magnetic field at any point, together with the specification of the pressure profile and a profile of the net current inside a magnetic surface as functions of the toroidal flux. We have the pressure  $p(\Psi)$  and the net current  $I(\Psi)$  available at the end of a STEP run. A simple spline fit can provide these values at the desired surfaces. Furthermore, we have the magnetic field,

$$\mathbf{B}(R, \phi, Z) = R_0 B_0 (1 - p(\Psi)/B_0) \nabla \phi + \nabla \phi \times \nabla A^\sigma(R, Z) + \mathbf{B}^\delta(R, \phi, Z), \quad (3)$$

with the stream function associated with axisymmetric currents in the plasma,  $A^\sigma$ , given on an  $(X, Z)$  array and a nonaxisymmetric vacuum field,  $\mathbf{B}^\delta$ , prescribed. It is useful to compute it in a divergence free form; for example the field of Eq. (1) should be written as

$$\mathbf{B} = \nabla Z \times \nabla R_0 B_0 (R/b)^N / 2N \sin N\phi, \quad (4)$$

so that the field is intrinsically divergence free. A two-dimensional cubic spline provides the necessary interpolation. The PIES code then follows field lines so as to establish magnetic coordinates, determine the Fourier decomposition of the different field components, and obtain the shape of the plasma boundary.

This conversion is useful for the STEP code as it enables the output to be studied with powerful line-following techniques [11]. It should enable the PIES code to start with field and position values which are close to the desired equilibrium so that the necessary calculations are greatly shortened and simplified. It has the added feature that it provides a technique to work with a free plasma-vacuum interface, rather than keeping the interface fixed as is presently being done.

#### IV. CONVERSION OF OUTPUT FROM THREE-DIMENSIONAL CODES FOR INPUT INTO THE STEP STABILITY CODE

Since the physics restrictions on the unstable modes that were introduced by the stellarator expansion are quite reasonable even for fully three-dimensional configurations, it would be useful to average the results from codes like PIES, VMEC or BETAS over the magnetic field periods to obtain the necessary input for the STEP code. These codes provide a description of the magnetic surfaces and fields in terms of a Fourier decomposition in the poloidal and toroidal angle variables  $u$  and  $v$ ,

$$B_R(\Psi, u, v) = \sum_n \sum_m B_{R,m,n}(\Psi) \sin(mu) \cos(nv), \quad (5)$$

etc. We can easily average over the toroidal angle  $v$  to obtain the shapes of the averaged magnetic surfaces,

$$\bar{R}(\Psi, u) = \sum_m R_{m,0} \cos(mu), \quad \bar{Z}(\Psi, u) = \sum_m Z_{m,0} \sin(mu), \quad (6)$$

and the associated Jacobian and metric elements. Averaging over  $v$  gives expressions for the necessary input about the nonaxisymmetric fields: its contribution to the poloidal flux,

$$\Psi_{\text{vac}}^{(0)} = \frac{1}{R_0 B_0} \int_0^{2\pi} [R^3 \tilde{B}_Z \int_0^\phi \tilde{B}_R d\phi] d\phi, \quad (7)$$

and the average field line curvature,

$$\Omega(\bar{R}, \bar{Z}) = \left\langle \frac{\bar{R}^2(\Psi, U)}{R_0^2} + \frac{\bar{B}^2(\Psi, u, v)}{B_0^2} \right\rangle. \quad (8)$$

#### V. COMMENTS

The techniques for modifying the plasma and magnetic field properties during the course of a series of iterations towards a three-dimensional equilibrium should improve the versatility of the PIES code significantly. Determination of the input parameters for this code by making a preliminary two-dimensional STEP run should provide even more flexibility,

both by providing an easy way to incorporate free boundary conditions and by decreasing the number of iterations necessary. Construction of the averaged properties of three-dimensional equilibria obtained from PIES and then utilization of the stability code STEP should provide a reasonable way of determining the linear stability properties. These ideas could be incorporated equally well into other two- and three-dimensional codes.

#### REFERENCES

- [1] A. H. Reiman and H. S. Greenside, *Comput. Phys. Commun.* **43**, 157 (1986).
- [2] H. P. Hirshman *et al.*, *Comput. Phys. Commun.* **43**, 143 (1986).
- [3] O. Betancourt, *Communications on Pure and Applied Mathematics* (John Wiley & Sons, Inc., New York, 1988) Vol. XLI, p. 551.
- [4] R. Izzo, D. A. Monticello, W. Park, J. Manickam, H. R. Strauss, R. Grimm, and K. McGuire, *Phys. Fluids* **26**, 2240 (1983).
- [5] G. Anania, J. L. Johnson, and K. E. Weimer, *Phys. Fluids* **26**, 2210 (1983).
- [6] G. Anania and J. L. Johnson, *Phys. Fluids* **26**, 3070 (1983).
- [7] T. C. Hender and B. A. Carreras, *Phys. Fluids* **27**, 2101 (1984).
- [8] J. Todoroki, *J. Phys. Soc. Japan* **56**, 128 (1987).
- [9] J. L. Johnson and A. H. Reiman, *Nucl. Fusion* **28**, 1116 (1988).
- [10] J. L. Johnson, G. Rewoldt, Y. Nakamura, and M. Wakatani, *Bull. Am. Phys. Soc.* **33**, 1928 (1988).
- [11] A. H. Reiman and H. S. Greenside, *J. Comput. Phys.* **75**, 423 (1988).

**CONFIGURATION EFFECTS,  
CONFINEMENT**

# CONFIGURATIONAL EFFECTS ON THE CONFINEMENT IN THE STELLARATOR WENDELSTEIN W 7AS

H. RENNER, W VII-AS TEAM<sup>1</sup>, NBI GROUP<sup>1</sup>,  
ICF GROUP<sup>1</sup>

Euratom-IPP Association,  
Max-Planck-Institut für Plasmaphysik,  
Garching

ECRH GROUP<sup>1</sup>  
Institut für Plasmaforschung,  
Universität Stuttgart,  
Stuttgart

Federal Republic of Germany

## Abstract

The plasma containment of W 7AS exhibits a strong dependence on characteristics of the magnetic configuration: rotational transform, shear and remaining plasma current. During the first experiments by application of ECF 70 GHz in the accessible range for  $\beta(0) \leq 0.5\%$  optimal confinement is found operating close to, but not at rational values of the rotational transform:  $\iota = 1/4, 1/3, 1/2, 2/3$ . Small shear is beneficial, if such "resonances" can be excluded from the entire plasma column.

---

## INTRODUCTION

The measurements of magnetic surfaces in Wendelstein W 7AS showed an excellent agreement of the magnetic parameters with the values of the design. / 1,2 / Without the need for corrections of the vacuum configuration extensive studies of the plasma confinement depending on **rotational transform, shear and the remaining plasma current** were started. The parameters of the magnetic configuration are widely variable by the adjustment of currents in the modular coils, the toroidal field coils and the vertical field coils. Furthermore, nonhomogeneous current distributions in the plasma with finite  $\beta$  modify the profiles of rotational transform. Such currents are associated with the plasma pressure in the case of equilibrium with secondary currents and bootstrap currents, and are related to the heating method.

During the first phase of experimental work in W 7AS / 3 / detailed studies on the confinement were performed to find optimal operational conditions. ECF generated plasmas could be maintained with sufficient long pulse duration ( typically 0.5s ) to establish quasistationary conditions with respect to the plasma parameters as density, temperature and remaining current , with time constants of the order of 100 ms. A plasma current up to 3 kA is being observed dependent on the energy content and strongly on the electron temperature, as expected for the bootstrap current. To control the boundary value of the rotational transform the plasma current could be influenced either by induced loop voltages or by ECF current drive launching the microwave power with variable  $k_{II}$  components: The contribution of the plasma current at field 1.25 T to the boundary value of the transform is  $\Delta \iota = 0.014 I_p$  (kA). In a more sophisticated way by ECF applications even local current control is possible. The modification of the power deposition profiles by tuning of the magnetic field or by geometrical adjustment of the plasma-beam interaction and by varying the angle of incidence allow to shape current density profiles.

---

<sup>1</sup> The members of the W VII-AS Team, NBI Group, ICF Group and ECRH Group are identified in the paper entitled 'Status of the advanced stellarator Wendelstein W 7AS: first results and further programme'. these proceedings, p.25.

## CONFIGURATIONAL EFFECTS ON THE CONFINEMENT EFFECT OF ROTATIONAL TRANSFORM

The low-shear Wendelstein W 7A / 4,5 / exhibited a strong influence of the magnetic configuration on the confinement. Therefore systematic studies of the global confinement properties of W 7AS as a function of the magnetic parameters were initiated.

To minimize the contribution of currents generated by the heating method to the magnetic configuration almost perpendicular injection of the  $\mu$ wave power with central power deposition was chosen. The rotational transform was varied shot by shot by changing the currents fed to the modular coils and the toroidal field coils. Figure 1 presents the energy content obtained versus the boundary value of the transform, which was calculated for the last closed magnetic surface, either being determined by the position of the limiter ( $z_L = 0.275$  m) at low transform or by the separatrix at high transform. In the investigated range of the rotational transform between 0.24 and 0.65 the effective plasma radius is slightly reduced from  $a = 0.18$  m to 0.15 m. The energy content is derived from the diamagnetic signals during the quasistationary phase of the discharge with a pulse duration of 400 ms. Because of an almost constant absorbed heating power of  $P_N \leq 200$  kW (1.25 T) the energy replacement time is proportional to the given energy content. The line density is being fixed at  $1.5 \cdot 10^{19} \text{ m}^{-3}$  by gas feed.

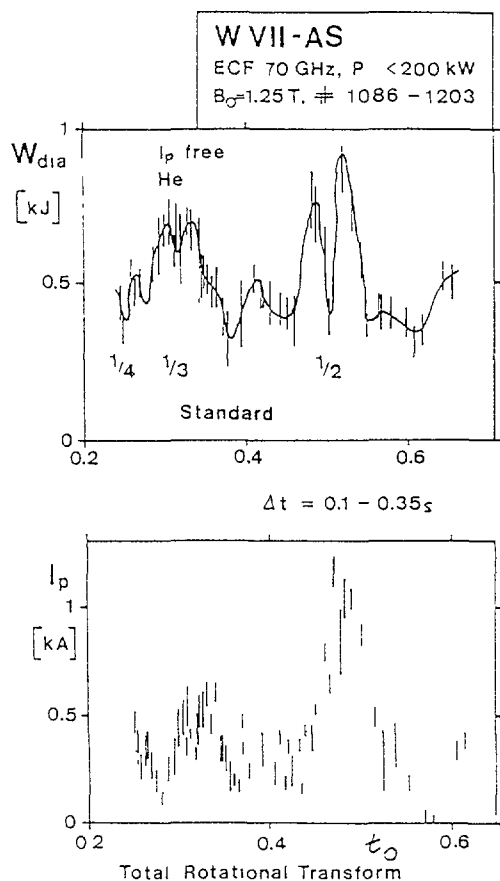


Fig.1: Energy content versus boundary value of the rotational transform: the line density is kept constant to  $4.5 \cdot 10^{18} \text{ m}^{-2}$ . The observed stationary currents are correlated with the energy content. Time window: 0.1 - 0.35 s.

Similarly to the results from W 7A the confinement of W 7AS is also strongly dependent on the particular value of the transform: Reduced confinement is observed to be associated with low-order rational values of the transform  $\iota = 1/4, 1/3, 1/2, 2/3$ , at the plasma edge. The values  $5/n$  should also be avoided. Close to these "resonances" optimal confinement is found. As has been shown by the vacuum field measurements, the system of nested magnetic surfaces can easily be destroyed even by small error fields of the order of  $10^{-3}$  at rational values of the transform, it appears to be robust apart from rational ones. The formation of magnetic islands, ergodic regions, and the onset of convective cells consequently enhances the transport. Convection becomes particularly important if islands are localized at the plasma edge, with low temperature.

### EFFECT OF PLASMA CURRENT

Relatively large plasma currents are observed which appear to be correlated to the energy content and become almost stationary after several 100 ms. The current density distribution modifies the profile of the rotational transform and contributes additive to the boundary value. The observed plasma current is found to be in agreement with the expected bootstrap current and changes the direction with inverse magnetic fields. Parameter studies based on measured profiles support this conclusion. Figure 2 shows the temporal development of discharges at 2.5 T. In addition to the global parameters: line density, energy content and plasma current, temperature profiles measured by ECE diagnostics are being presented for two different cases: "free current" and controlled current ( $I_p = 0$ ), using the ohmic transformer at  $U_L \sim -0.1$  V. The transient behaviour of the discharge, with relatively long time constants as expected on the resistive time scale, is demonstrated by varying the net current and the perturbations of the temperature profiles. The vacuum field has been adjusted to a rotational transform close to  $1/3$  and small negative shear. The perturbations may be associated with resonant magnetic surfaces and the shift of their position across the plasma radius with varying plasma current. Good confinement can be maintained by controlling the plasma current and adjusting the rotational transform.

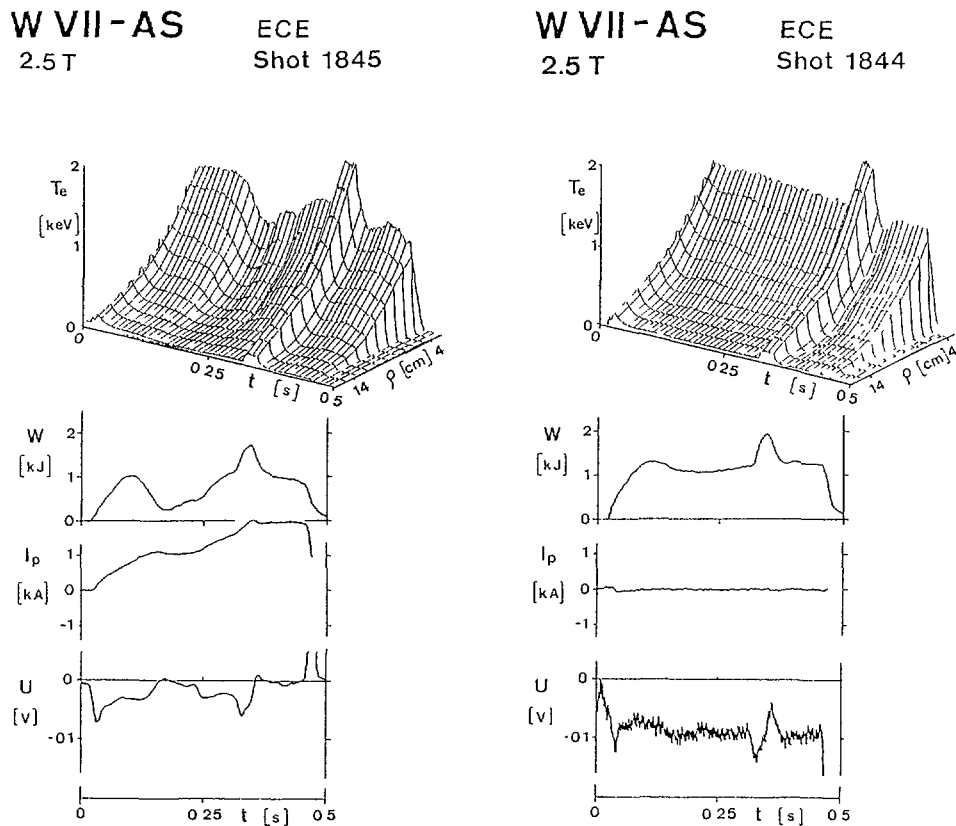


Fig.2: Electron temperature profiles by means of ECE and global parameters: energy content, plasma current, and the measured loop voltage during discharges with free current and with current control by the ohmic transformer. A second gyrotron is switched on for a short pulse at time  $\Delta t = 0.32$  s. Controlled line density with  $5 \text{ E}18 \text{ m}^{-2}$ .

Experiments with induced currents of up to 5 kA were performed to introduce shear by shaping the current density profiles. Figure 3, like fig. 1, presents data from discharges at  $-1.25 \text{ T}$  in the vicinity of the transform close to  $1/2$ . Three cases were considered with induced currents  $-5 \text{ kA}$ ,  $0$ , and  $+5 \text{ kA}$ . For the bootstrap current distribution a maximal current density is expected at the pressure gradients, especially at the temperature gradients. The current distribution of the induced current is determined by the conductivity profile. The case with  $+5 \text{ kA}$  introduces a current in the direction opposite to the bootstrap current, so that by overcompensating the local current densities a strong positive shear will be established.

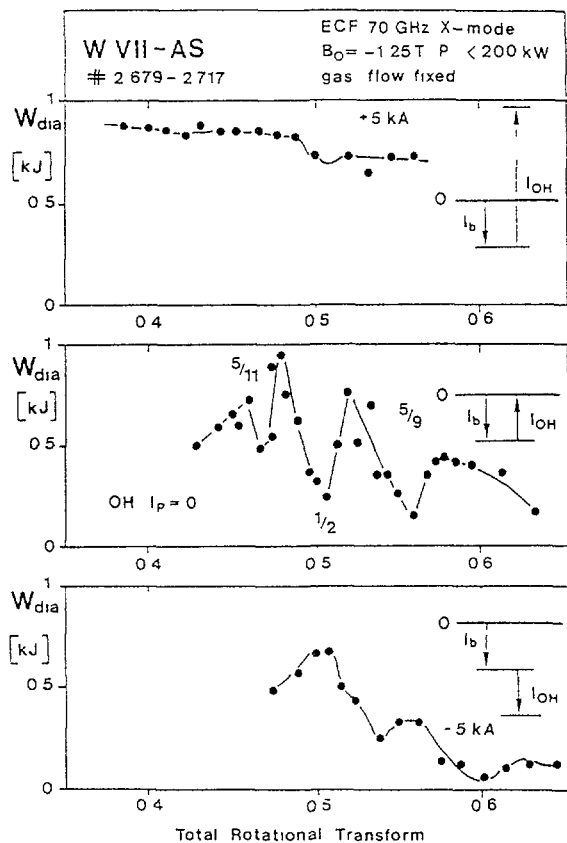


Fig.3: Energy content versus rotational transform with induced currents:  $I_p = +5 \text{ kA}$  ( subtractive to the transform ),  $I_p = 0$ ,  $I_p = -5 \text{ kA}$  (additive to the transform )  
Note: the inverted magnetic field.

The energy content now shows a rather weak dependence on the boundary value. Probably as a consequence of the increased shear and the reduced extent of the associated island, the discharge can be maintained even at  $\iota = 1/2$ . Maximum confinement is being obtained in the case of low shear with  $I_p = 0$  close to  $1/2$ . A critical influence of the current density distribution on the confinement is indicated for the last case, where with  $-5 \text{ kA}$  additive to the bootstrap current the shear may become negative.

## SUMMARY AND CONCLUSIONS

For plasma conditions in the investigated range with  $\beta_0 \leq 0.5\%$  the confinement appears strongly dependent on the boundary value of the rotational transform:

\*At "resonances", rational values of the transform  $\iota = 1/2, 1/4, 1/3, 2/3$  a deterioration of the confinement is observed. Rational values  $\iota = 5/n$  are also important. Together with the reduced

confinement for cases with low shear and resonances at the boundary strong particle losses are observed. Perturbations correlated to resonant surfaces at the plasma core flatten the temperature profiles as indicated from measured temperature profiles.

The destruction of the confinement seems related to a loss of equilibrium by island formation at resonant magnetic surfaces.

**\* Optimum confinement is being found close to these "resonances".**

**\* Small shear is being favourable**, if such "resonances" can be excluded from the plasma column. In the case of W 7AS slight shear can be introduced into the vacuum configuration, but plasma pressure effects, the bootstrap current and currents associated with the different heating schemes modify the profile of the transform significantly.

**\* By proper processing of the plasma, adjustment of the magnetic configuration optimal confinement can be maintained.**

These experiments clearly demonstrate the influence of resonances, and for improved confinement the need for configurations which exclude resonances from the confinement region. The destruction of the confinement so far seems caused by loss of equilibrium rather than by MHD instabilities. In practice, the control of the boundary conditions is mandatory. Effects due to internal resonances are also visible and therefore internal resonances should be excluded. In W 7AS such perturbations should be controlled by local current density shaping using OH, ECF current drive / 6 / or unbalanced NBI, especially at higher  $\beta > 0.5\%$ , when finite  $\beta$ -effects will become important.

## REFERENCES

- / 1 / Hailer, H., et al., Contr. Fusion and Plasma Physics, Madrid (1987), Proc. 14th Europ.Conf., Vol. I, p.423
- / 2 / Jaenicke, R., et al., 16th Europ. Conf. on Controlled Fusion and Plasma Physics, Venedig (1989), P8 B3
- / 3 / Renner, H., et al., Contr. Fusion and Plasma Physics, Proc. of 16th Europ. Conf., Venedig ( 1989 ), to be published
- / 4 / Renner, H., Proc. Workshop on Basic Physical Processes of Toroidal Fusion Plasmas, Varena (1985), EUR 10418 EN, Brüssel (1986), Vol.II, p.479
- / 5 / Grieger, G., et al., Plasma Physics and Contr. Fusion, 28 1A (1986), p.43
- / 6 / Gasparino, U., et al., 16th Europ. Conf. on Controlled Fusion and Plasma Physics, Venedig (1989), P8 B4

## TRANSPORT AND PLASMA CURRENT IN W VII-AS

H. MAASSBERG, U. GASPARINO, G. KÜHNER, H. RINGLER,  
W VII-AS TEAM<sup>1</sup>, NBI GROUP<sup>1</sup>

Euratom-IPP Association,  
Max-Planck-Institut für Plasmaphysik,  
Garching

ECRH GROUP<sup>1</sup>  
Institut für Plasmaforschung,  
Universität Stuttgart,  
Stuttgart

Federal Republic of Germany

### Abstract

For the rather complex magnetic field topology of W VII-AS stellarator, the full neoclassical transport matrix with radial electric field included in both the plateau and long mean free path regimes was calculated using the DKES code. Electron temperature and density profiles measured by the Thomson scattering diagnostic for ECF heated discharges (at both fundamental and 2<sup>nd</sup> harmonic heating) were analyzed, the electron heat conductivity coefficient was estimated and compared with the neoclassical prediction. Based on the measured profiles, the neoclassical bootstrap current was calculated. To the net toroidal current contribute a pressure driven component, an ECH generated and a component induced by a small loop voltage. The pressure driven component was in rough agreement with the prediction for the neoclassical bootstrap current.

### Introduction

For stellarators as well as for tokamaks, the energy confinement depends sensitively on the electron heat conduction which is not understood at present time (*anomalous transport* is only another word for this fact). Typical values of the electron heat conductivity,  $\chi_e$ , found experimentally in all larger devices are of the order of  $10^4 \text{ cm}^2/\text{s}$ , much larger than predictions based on neoclassical theory. Only for collisionalities in the long mean free path (LMFP) regime ( $1/\nu$ -regime), the neoclassical ripple loss in stellarators leads to similar poor confinement properties. Since the optimization of neoclassical confinement is one important aim of the advanced stellarator concept, the examination of the neoclassical transport predictions is a main topic of the W VII-AS experiment.

The new W VII-AS stellarator is characterized by a rather complex magnetic field topology [1]. Particles being trapped in the minima of magnetic field strength on a flux surface contribute significantly to the neoclassical transport in the LMFP-regime. The neoclassical transport coefficients were calculated using the DKES code (developed by S.P. Hirshman and W.I. van Rij [2]). Together with Monte-Carlo simulations, the DKES code is probably the best instrument for estimating the neoclassical transport properties of W VII-AS. One advantage for using DKES is that also the bootstrap current densities and the neoclassical parallel conductivity are easily obtained.

Only ECH generated and sustained discharges of the initial phase of plasma operation in W VII-AS both at 2nd harmonic ( $B_0 \simeq 1.25 \text{ T}$ ) and fundamental ( $B_0 \simeq 2.5 \text{ T}$ ) with an injected ECF power up to 600 kW (3 gyrotrons at 70 GHz) are reported here. Electron temperature and density were measured by the Thomson scattering diagnostic with the old W VII-A system (a new single shot system being under construction). About 10 to 30 single shots are necessary to get one

---

<sup>1</sup> The members of the W VII-AS Team, NBI Group and ECRH Group are identified in the paper entitled 'Status of the advanced stellarator Wendelstein W 7AS: first results and further programme', these proceedings, p. 25.

profile, in most cases, the reproducibility of the discharges was very high and only nearly identical discharges were used. The estimation of the experimental electron heat conductivity is based on these profiles. Modeling the energy source and loss terms with regard to the experimental conditions, the energy balance equation is used to fit the electron temperature profile yielding the experimental electron heat conductivity coefficient.

### Neoclassical Transport Code

The DKES code (Drift Kinetic Equation Solver /2/) is based on the linearized monoenergetic drift kinetic equation in magnetic flux coordinates with radial electric field included for each particle species. As the poloidal component of the  $\nabla B$ -drift is neglected, the solution depends only on the  $|\mathbf{B}|$  Fourier spectrum independently for each magnetic surface. For the complex topology of W VII-AS magnetic field, typically more than 20 Fourier coefficients in the  $|\mathbf{B}|$ -representation were necessary for each flux surface (e.g., with only 7 Fourier coefficients at half plasma radius, the particle transport coefficient was decreased by a factor of about 2). About 200 Fourier harmonics in poloidal and toroidal angle and up to 150 Legendre polynomials in pitch angle were used to represent the neoclassical deviation of the distribution function from the Maxwellian. Especially in the LMFP with moderate radial electric fields, this large number of basis functions was necessary for the estimation of the non-diagonal term in the monoenergetic Onsager transport matrix which is related to the bootstrap current and the Ware pinch. For each magnetic surface, the 3 monoenergetic transport coefficients were computed for varying collisionality and radial electric field (more than 200 values with up to 10 min. CPU on the CRAY 1 for each run). On this grid of stored monoenergetic transport coefficients, the energy convolution was performed based on bi-cubic interpolation resulting in the full neoclassical transport matrix,  $D_{ij}$ . For a fixed magnetic configuration (defined by rotational transform,  $\iota$ , vertical field,  $B_z$ , and pressure profile,  $\beta(r)$ ) the monoenergetic transport coefficients were computed for different minor radii, cubic interpolation in  $r$  was applied in connection with the energy convolution algorithm. For larger values of radial electric field, high resolution was necessary close to the toroidal resonance,  $E_r = \nu r B_0 / R$ , strongly affecting the ion transport coefficients in both the plateau and the LMFP regimes.

Due to this toroidal resonance, several roots of the ambipolarity condition (up to 7 values for radial electric field) can exist in the LMFP regime. This result is contrary to the picture of radial electric field based on the Shaing-Houlberg transport model /3/ (only 2 stable and 1 unstable root possible). In principle, however, with the condition of ambipolarity, the radial electric field, particle and energy flux and the bootstrap current can be calculated for given profiles of density and electron and ion temperature. For an axisymmetric field, DKES computations were compared with Monte Carlo simulations /4/, nearly identical particle and energy transport coefficients were found. Furthermore, the bootstrap coefficient was tested for symmetric configurations using a relation to the particle transport /5/ where reliable agreement was found. For the W VII-AS configuration, the particle and energy transport coefficients in the plateau regime are comparable to those of an equivalent axisymmetric model showing some improvement due to the advanced stellarator concept. However, with exception of the innermost flux surfaces, one deep strongly localized minimum in  $|\mathbf{B}|$  exists leading to a rather large fraction of trapped particles with mainly radial  $\nabla B$ -drift. By an additional  $B_z$ -field of  $\pm 300$  G, the magnetic configuration was modified in such a way that the neoclassical particle and energy transport coefficients were changed by a factor of about 2, the bootstrap current coefficients, however, were nearly unaffected. The electron energy transport coefficient related to the temperature gradient,  $D_{22}$  (called heat conductivity  $\chi_e$ ), was typically by a factor of 3 larger than the coefficient  $D_{21}$  with is related to density gradient and radial electric field. Furthermore, the density profiles were found to be much broader than the electron temperature profiles justifying a simple diffusive ansatz for the electron energy flux. At present time, DKES results with radial electric field included are available for only one W VII-AS vacuum field configuration at  $\iota \simeq 0.51$ , all DKES results reported here are based on this magnetic field configuration.

### Local Electron Heat Conductivity

Electron temperature and density profiles were measured by the Thomson scattering diagnostic in a series of nearly identical discharges. After transformation of the real space positions along the laser chord to magnetic coordinates, the symmetry of the measured profiles was analyzed: in most cases, only the pressure profile was found to be highly symmetric (Figure 1) which is consistent with the ideal MHD condition,  $p = p(r)$ . While the electron temperature profiles were strongly peaked for central heating, the much broader density profiles were mainly hollow and asymmetric: above the equatorial plane, the densities were typically up to 10 % higher

independent on magnetic field direction. At higher densities (e.g. NBI heated discharges), also highly symmetric density profiles were measured, but an adjustment problem of the Thomson scattering system cannot be fully excluded at present time. Correlations to an external particle source (e.g. neutral gas valve located at the top of the vacuum vessel close to the Thomson diagnostic) must be analyzed in future. As a consequence, symmetric least squares fits to the pressure profiles were used to define an experimental origin for the profile analysis. The electron energy balance equation with the ansatz  $-n_e \chi_e \cdot dT_e/dr$  for the electron energy flux density is integrated with simplified models for ECH power deposition (adjusted to ray tracing calculations) and for power losses (radiative cooling and collisional ion heating). By means of a least squares fit to the measured electron temperature profile, the energy balance integration leads to the electron conductivity,  $\chi_e(r)$  (Figure 2).

For almost all types of ECH discharges in W VII-AS, the electron heat conductivity,  $\chi_e$ , found experimentally is minimum at about half plasma radius, slightly increasing for smaller radii, but strongly increasing towards the plasma edge (Figure 3). Only little variation of  $\chi_e$  at about half plasma radius was found for the quite different discharges, whereas the corresponding neoclassical values estimated using the DKES code were more than one order of magnitude smaller showing a strong variation mainly depending on the local temperature. At outer radii, the behaviour of

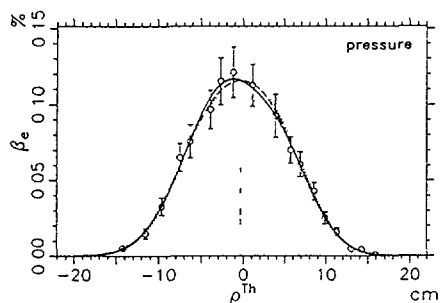


**Fig. 1:** Electron pressure profile versus radius derived from the transform of laser chord positions on magnetic coordinate (same series of discharges as in Fig. 2). The dashed line is the symmetric fit, the dotted lines represent the functional variance of the asymmetric pressure fit (bold line).

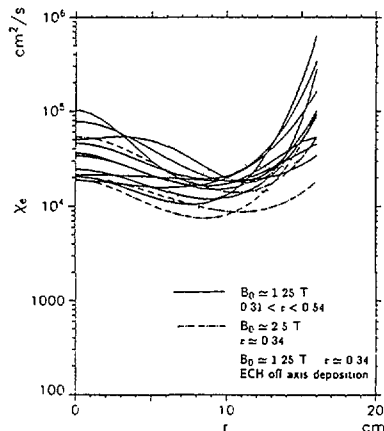


**Fig. 3:** Electron heat conductivity profiles of the initial phase of W VII-AS operation.

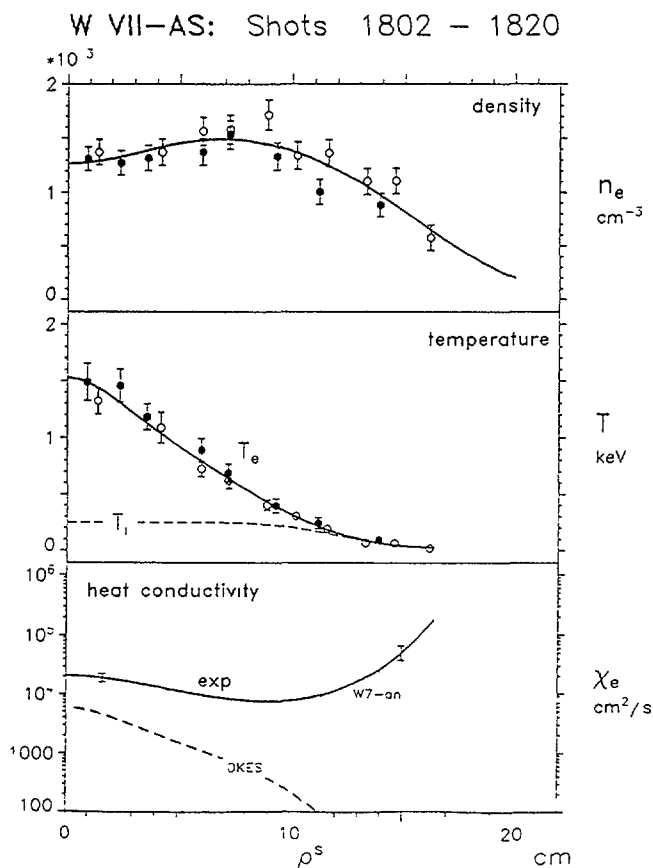


**Fig. 2:** Profiles of density and temperature and the resultant electron heat conductivity (with neoclassical and anomalous values) versus symmetrized radius (origin from pressure fit),  $B_0 = 2.5 \text{ T}$ ,  $t \approx 0.34$ ,  $P_{ECF} = 140 \text{ kW}$

the experimental  $\chi_e$  is close to the old W VII-A scaling ( $\chi_e \propto n_e^{-1} \cdot T_e^{-0.67}$ ). Furthermore,  $\chi_e$  decreases with increasing magnetic field, but less than expected from neoclassical theory ( $\chi_e \propto B^{-2}$ ). For strong off-axis ECF power deposition, hollow pressure and even hollow electron temperature profiles were found, the central radiative and collisional cooling is too small to explain these hollow profiles. As a consequence, the diffusive ansatz for the electron energy transport leads to very small values of heat conductivity in the region with positive temperature gradients indicating that the electron energy flux cannot be described only by a simple diffusive term related to the temperature gradient.

On the basis of the measured electron temperature and density profiles, also the neoclassical particle flux was estimated, the influence of radial electric field was disregarded. The particle flux was maximum at about 5 cm, at larger radii strongly decreasing. For the hollow electron temperature profiles, the neoclassical particle flux was negative in the center. Consequently, these radial dependences of the neoclassical particle flux on the basis of measured profiles are inconsistent with the particle balance condition.

### Plasma Current

Most discharges of the initial phase were stabilized by a small loop voltage induced by the transformer to control the plasma current and to avoid critical rational values of the rotational transform at the plasma edge. Also by ECH current drive, net current-free conditions ( $I_{pl}$  less than some 100 A) could be obtained, ECH current drive was clearly demonstrated /6/. As all current sources are linked together, the quantitative estimation of the pressure driven component, the bootstrap current, depends on the reliability of the models for the other current components. Furthermore, the value of  $Z_{eff}$  was rather uncertain /7/. The experimental database without additional loop voltage nor ECH current drive is very small up to now. In these discharges with higher electron temperatures, the bootstrap current component found experimentally was up to a factor of 2 larger than the neoclassical prediction (electrons only, the ion contribution was neglected due to the small  $T_i$  values) based on the DKES code. This finding was also confirmed by discharges controlled by small loop voltages. In some discharges with low electron temperatures, however, rather large currents (up to 4 kA) were found in disagreement to the neoclassical predictions.

### Conclusions

The pressure profiles derived from the experimental data of electron temperature and density are highly symmetric in magnetic coordinates. For the ECH discharges under consideration, mostly hollow density profiles were found. Additionally, Thomson scattering data indicate a slight asymmetry in electron density and temperature independent on magnetic field direction. For central ECF power absorption, strongly peaked pressure and temperature profiles were found. In case of off-axis ECH deposition, hollow pressure and even hollow electron temperature profiles were measured.

Almost all electron heat conductivity profiles were minimum at about half plasma radius with  $\chi_e$  values between 0.7 and  $2 \cdot 10^4$  cm<sup>2</sup>/s for the quite different types of ECH discharges, but lowest for  $B_0 \approx 2.5$  T. Here, the neoclassical heat conductivities estimated using the DKES code were more than one order of magnitude lower than the experimental values, in the central part more than a factor of 3. Furthermore, the variation of the neoclassical  $\chi_e$ , mainly dependent on electron temperature, was much larger than the one found experimentally for the different discharges. All the ECF heated discharges of the initial phase of plasma operation in the W VII-AS stellarator with rather low densities were not dominated by neoclassical electron energy transport. Neoclassical bootstrap current and ECH current drive had been clearly identified. For most discharges, the experimental estimate of the bootstrap current was in rough agreement with the neoclassical prediction. Future experiments at higher heating power levels (ECH, NBI and ICH) and with higher densities will extend the range for a more detailed parameter analysis of both the experimental electron heat conductivity and the plasma currents.

### References

- /1/ J. Kisslinger, F. Rau and H. Wobig, *Fusion Tech. (Proc. 12th Symp. 1982)*, Pergamon (1983), 1051
- /2/ S.P. Hirshman et al., *Phys. Fluids* **29** (1986), 2951
- /3/ K.C. Shaing et al., *Plasma Phys. and Contr. Nucl. Fusion Res.*, **2**, IAEA Vienna (1984), 189
- /4/ W. Lotz and J. Nührenberg, *Phys. Fluids*, **31** (1988), 2984
- /5/ H. Wobig, *Report IPP 2/297* (1988)
- /6/ U. Gasparino et al., *this workshop*
- /7/ A. Weller et al., *this workshop*

# THE EFFECTS OF THE MAGNETIC AXIS SHIFT ON TRANSPORT AND MHD STABILITY IN HELIOTRON E

H. ZUSHI, F. SANO, K. ITOH, T. MIZUUCHI,  
H. KANEKO, S. SUDO, M. NAKASUGA, K. HANATANI,  
K. KONDO, K. ICHIGUCHI, M. HARADA, M. WAKATANI,  
T. OBIKI, A. IYOSHI  
Plasma Physics Laboratory,  
Kyoto University,  
Gokasho, Uji, Kyoto,  
Japan

## Abstract

The effects of the magnetic axis shift on the transport and stability in Heliotron-E device have been studied by varying an auxiliary vertical field. The optimum confinement condition was found when the magnetic axis was shifted inward. It was also found that even small it is effective to stabilize the internal modes near the central region.

## I. Introduction

It has been considered that the global energy confinement is dominated by an anomalous transport even in a currentless stellarator/heliotron plasma [1]. Therefore the reduction of an anomalous transport should have a high priority in order to improve the global transport. Although a mechanism of the anomalous transport has not yet been clarified, the toroidally (or helically) trapped particle instabilities may be one of the most probable candidates as in tokamaks. The condition for the shear stabilization of the collisionless toroidally trapped particle instability has been given by  $d\ln l/d\ln r > 3/2$  [2]. This condition is favorable to the heliotron configuration with positive shear, in contrast to a tokamak with negative shear. In the low collisional regime the direct orbit loss should be also reduced in a sense of the absolute particle trapping [3]. Since the orbit trajectory of the deeply trapped particles is shifted inward by  $\varepsilon_{ta}/2\varepsilon_{ha} \times \bar{a}$  from the magnetic surfaces, the inward axis shift will increase the trapping efficiency [4]. The shear is the highest around this position because the increased last closed magnetic surface leads to the higher edge rotational transform and the inward axis shift reduces the central rotational transform. However, this inward shift is unfavorable from the viewpoint of MHD stability because of the magnetic hill configuration [5]. In this paper, the effects of the magnetic axis shift on transport and stability are studied by varying an auxiliary vertical field.

## II. Transport improvement by inward axis shift

Experiments have been done in currentless plasmas heated by electron cyclotron resonance heating (ECRH) and neutral beam injection (NBI). The parameter range is as follows;  $0.7 \leq \bar{n}_e \leq 4 \times 10^{13} \text{ cm}^{-3}$ ,  $0.4 < T_e < 1.3 \text{ keV}$ ,  $0.2 < T_i < 1 \text{ keV}$ ,  $B_0 = 1.9 \text{ T}$  and  $\beta(0) \leq 1 \%$ . In ECRH ( $T_e \gg T_i$ , collisionality of electrons (ions) is deeply (shallowly) in the  $1/\nu$  regime (trapped particle regime), and in NBI ( $T_i \gtrsim T_e$ ) ions are deeply in the  $1/\nu$  regime. Therefore these plasmas could be affected by

the above mentioned orbit effect. Figure 1 shows the  $\Delta_v$  - dependences of  $T_e$ ,  $T_i$ ,  $n_e l$ , and electron temperature decay time  $\tau_{de}^{ECH}$  in ECRH plasmas. The line density  $n_e l$  was kept almost constant around  $7 \times 10^{14} \text{ cm}^{-2}$  with the constant gas puffing rate and constant RF power of 320 kW. When  $\Delta_v = -2 \text{ cm}$  ( $\Delta_v/\bar{a} \sim 0.1$ ),  $T_e$  and  $T_i$  increased by  $\sim 15\%$ . For  $-4 \text{ cm} < \Delta_v < 0$ , these parameters were improved, but at  $\Delta_v \sim -5 \text{ cm}$  they started to decrease, and then for  $\Delta_v < -6 \text{ cm}$  a hot plasma state could not be sustained at this power level. For  $\Delta_v > 0$ , both temperatures decreased monotonically, and then for  $\Delta_v > 4 \text{ cm}$  it was also difficult to maintain a hot plasma state. To indicate the improvement of confinement in the central region,  $\tau_{de}^{ECH}$  within  $r/a \leq 0.2$  are also plotted. It was the longest at  $\Delta_v = -2 \text{ cm}$ , being improved by  $\sim 20\%$  than the case of  $\Delta_v = 0 \text{ cm}$ . Thus, a plasma with higher temperatures and longer confinement time was obtained by shifting the magnetic axis inward [6].

Similar improvement was also found in low  $\beta$  NBI plasmas, in which a change in the beam deposition profile seemed not to be serious compared with ECRH. Under the

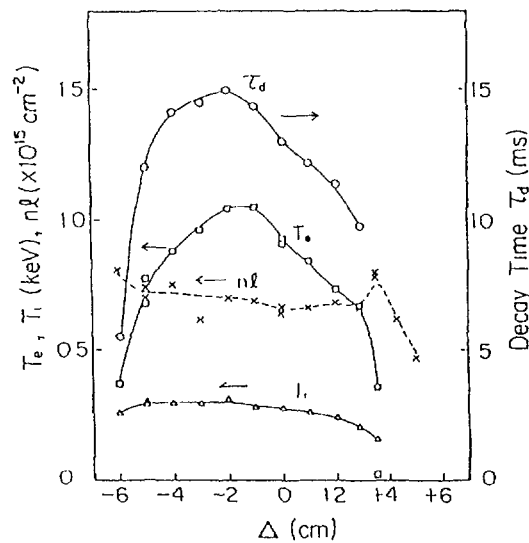


Fig.1  $T_e$ ,  $T_i$  and  $n_l$  versus  $\Delta_v$  in ECRH. The electron temperature decay time  $\tau_{de}^{ECH}$  in the central region is also plotted.

same gas condition, the density increased by  $\sim 20\%$  with the inward shift. Generally speaking, temperatures decrease with increasing  $\bar{n}_e$ . In this case, however, both  $T_e$  and  $T_i$  increased by  $\sim 20\%$ . Here  $T_e$  on axis was measured by varying the laser scattering viewing chord along the major radius. It was clearly seen that  $T_e(0)$  at  $\Delta_v = -4 \text{ cm}$  was almost twice as high as  $T_e(0)$  at  $\Delta_v = +3.5 \text{ cm}$ . The electron temperature decay time  $\tau_{de}^{NBI}$  was also found to be the longest at  $\Delta_v = -2 \text{ cm}$ . However, sawtooth oscillations and internal disruptions occurred and they significantly affected  $\tau_{de}^{NBI}$ , especially at  $\Delta_v = -4 \text{ cm}$ , as will be discussed later. For  $\Delta_v > 0$ , in which there were no MHD activities,  $\tau_{de}^{NBI}$  decreased drastically. In NBI plasmas, the electron energy transport is considered to be anomalous. Therefore, it could be deduced that the inward axis shift was effective to reduce an anomalous transport. Magnetic fluctuations were investigated by a pick up coil located outside the torus. Although the frequency spectrum was studied up to 100 KHz, the power spectrum between 15 - 50 KHz was found to be most sensitive to the axis shift as shown in

Fig.2.  $\tilde{B}_\theta$  was enhanced for  $\Delta_v > 0$  and was reduced for  $-2 \text{ cm} \leq \Delta_v \leq 0 \text{ cm}$ . It was also increased for  $\Delta_v < -4 \text{ cm}$ . This variation suggests that  $\tilde{B}_\theta$  is not simply correlated with a distance between the coil and the outermost surface. For  $\Delta_v < -4 \text{ cm}$  toroidally trapped particles are confined in the bad curvature region, which will enhance trapped particle instabilities [7]. The  $\Delta_v$  variation in  $\bar{n}_e \tau_{de}^{NBI} T_e$  and  $\tilde{B}_\theta$  seems to correspond to the change in shear.

In order to study the effects of the axis shift on the fast ion confinement the following experiment has been carried out. Two beam lines were used. One (BL-5) produced helically trapped particles with the pitch angle between  $65^\circ$  and  $90^\circ$  at the injection energy of  $22 \text{ keV}$  and was pulsed for  $20 \text{ ms}$  into a target plasma maintained by the other one (BL-2), which produced passing particles. A neutral particle energy analyzer was set only to detect trapped particles with pitch angle of  $70^\circ - 90^\circ$  along its sight line and was located along the torus by  $\sim 45^\circ$  from BL-5. The decay time  $\tau_d^{cx}$  of the charge exchange flux was measured after switching-off of BL-5 for  $-5 \text{ cm} < \Delta_v < 4 \text{ cm}$  and it was found that  $\tau_d^{cx}$  at  $E = 21.5 \pm 1.1 \text{ keV}$  was  $\sim 1.3 \text{ ms}$ , being the longest at  $\Delta_v = -2 \text{ cm}$ , and the variation of  $\tau_d^{cx}$  was similar to that for bulk plasma parameters, as shown in Fig. 3. The results in the outward shift suggests the enhancement of the direct orbit loss due to the outward localized  $\varepsilon_h$ . Thus the axis shift effects the bulk transport and the fast ion confinement in low collisional regime.

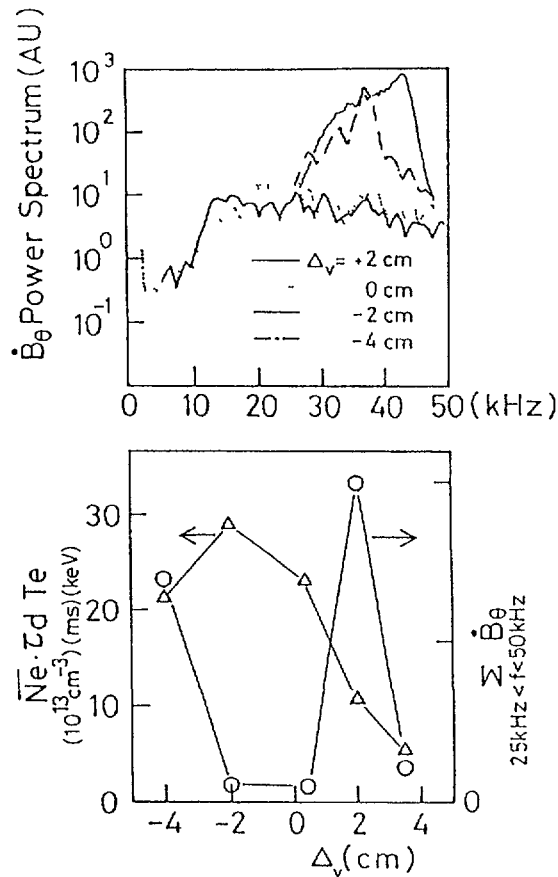


Fig.2 (a) Frequency spectrum of  $B_\theta$ .  
 (b)  $\bar{n}_e \tau_{de}(0) T_e(0)$  and  $\tilde{B}_\theta$  ( $25 < f < 50 \text{ kHz}$ )

### III. MHD activities and well-stabilization

The effects of shift on MHD activities were studied in NBI plasmas by gas puffing and pellet injection. The parameter range as follows;  $2 < \bar{n}_e < 20 \times 10^{13} \text{ cm}^{-3}$ ,  $300 < T_e < 1000 \text{ eV}$ ,  $0.4 < \beta_o \leq 3\%$ , and  $P_{NBI} \leq 4 \text{ MW}$ . For the inward shifted case ( $-5 \text{ cm} < \Delta_v \leq -1 \text{ cm}$ ) at which the transport was improved, it was clearly observed that MHD activities appeared at  $\beta(o) \sim 0.5\text{-}0.7\%$ , as shown in Fig.3. The amplitude of fluctuations grew at  $\Delta_v \sim -1 \text{ cm}$  and then an internal disruption was found around  $\Delta_v \sim -2 \text{ cm}$ . At  $\Delta_v = -4 \text{ cm}$ , the sawtooth oscillations appeared with the amplitude  $\Delta A/A$  of 10 % and the repetition time of 2-5 ms. When the magnetic axis was further shifted inward ( $\Delta_v \leq -5 \text{ cm}$ ), it was difficult to sustain the hot plasma. There were no visible oscillations for  $0 \leq \Delta \leq 4 \text{ cm}$ . The vertical field can change the rotational transform depending on the direction of the axis shift. When the magnetic axis is shifted inward, the central rotational transform  $\iota(0)$  becomes below 0.5, which means the new rational surface  $\iota = 1/2$  appears near the central region where the magnetic hill is created. The phase inversion radius for these oscillations (SX, ECE, and  $n_e$ ) was found to be around  $r/a = 0.2$  to 0.4. The density profile becomes rather slightly broad and the temperature profile seems to be peaked since the central electron and ion temperatures increase for inward shift. Therefore a change in the pressure gradient

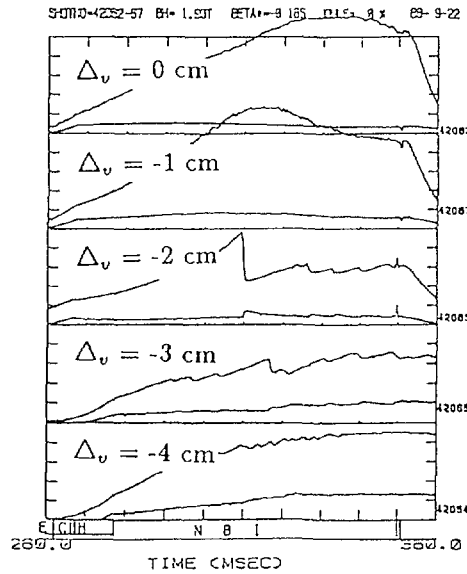


Fig.3 Soft X-ray traces at different magnetic axis positions.

may be small. The global shear ( $\equiv \iota(a) - \iota(0)/\iota(0)$ ) increases from  $\sim 4$  for  $\Delta_v = 0 \text{ cm}$  to 5 for  $\Delta_v = -2 \text{ cm}$ . Therefore, it is considered that these newly observed MHD instabilities are mainly caused by a change of the magnetic configuration from the small well at standard to the hill in the inward shift case.

It has been pointed out in Ref.[8] that self-stabilization of these MHD instabilities is possible by the deep magnetic well due to Shafranov shift  $\Delta_\beta (> 0)$ . Here we studied the beta effect on the phase inversion radii  $r_{inv}$  of observed instabilities, as shown in Fig.4. From horizontally viewing eight-chord soft X ray signals and the calculated vacuum magnetic surfaces the phase inversion tangency radius was determined. For  $\Delta_v = 0$ , there were no or weak instabilities below  $\beta(0) < 1.5\%$  and  $r_{inv}$  was around  $r/a = 0.5 - 0.7$  above 1.5 %. Since the magnetic well region expands from interior

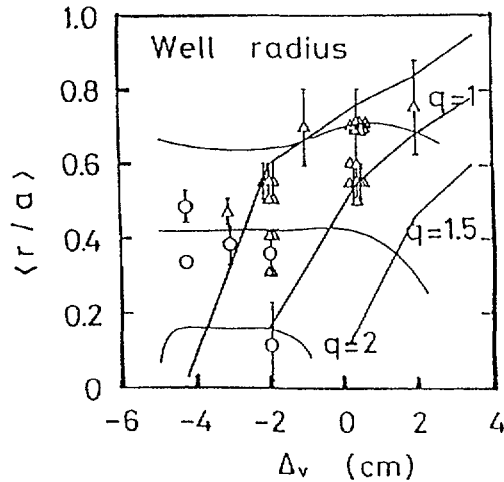


Fig.4 The phase inversion radius of the soft X ray line integrated signal at the saw-tooth oscillations versus  $\Delta_v$ . Rational surfaces and well radius are show.

with increasing beta, instabilities associated with the internal rational surfaces may be stabilized. For  $\Delta_v = -2$  or  $-4$  cm,  $r_{inv}$  was found to be interior of plasma above  $\beta(0) = 0.5\%$ . From calculations the magnetic well is only formed when  $\beta(0) > 0.8 - 1.5\%$ . Since shear is weak near the central region, these unfavorable effects destabilize internal MHD modes associated with  $\iota = 1/2$  and  $2/3$  surfaces. At high  $\beta(0)$   $r_{inv}$  moved outward, which was considered to be an evidence of well-stabilization effect. For  $\Delta_v = +2$  cm, instabilities were also found in pellet discharge and their phase inversion radii were at  $r/a = 0.6$  and almost the same as those for  $\Delta_v = 0$  cm. However, after instabilities occurred, a plasma was rapidly cooled down and the high  $\beta$  state was not sustained during the beam pulse length. It was difficult to produce a high beta plasma by pellet injection for  $\Delta_v > 2$  cm. Thus, it should be noted that the outward shift by  $B_v$  is limited by enhanced orbit loss, enhanced transport, reduced heating efficiency and decreasing shear.

#### IV. Summary and Discussion

The optimum confinement condition (electron and ion energy decay time, trapped fast ion decay time, and particle confinement time) was found when the magnetic axis was shifted inward by  $\Delta_v/\bar{a} \sim 10\%$ . This optimum position corresponds to the configuration with the maximum efficiency of the absolute trapping of helical trapped particles and the highest shear. It is found that even the small well is effective to stabilize the internal modes near the central region but in the hill configuration MHD instabilities affect the improved transport by inward shift. The outward shift by  $B_v$  seems to be impertinent to increase  $\beta$  value. Thus, we must find a configuration with the deep well at the optimized position. One solution may be given by adding the strong toroidal field [9]. The effect of toroidal field is now being studied in Heliotron E.

## References

- [1] B.A.Carreras, G.Grieger, J.H.Harris, J.L.Johnson, *et al.*, Nucl. Fusion 28 (1988) 1613. [2] B.B.Kadomtsev and O.P.Pogutse, in Reviews of Plasma Physics, edited by M.A.Leontovich (Consultants Bureau, New York, 1970), Vol.5, p.249. [3] S.-I.Itoh, Comments on Plasma Phys. Controlled Fusion 12 (1989) 133. [4] K.Hanatani, "Fast ion confinement in Heliotron E-Effects of magnetic axis shift," P.S.J. (28aTE10) March 1989. [5] O.Motojima, T.Mutoh, M.Sato, H.Zushi, *et al.*, IAEA-CN-50/E-1-4 (1988). [6] M.Wakatani, K.Ichiguchi, F.Bauer, O.Betancourt, P.R.Garabedian, Nucl. Fusion 26 (1986) 1359. [7] M.Okabayashi, R.Freeman, Phys. Fluids 15 (1972) 359. [8] V.D.Shafranov, Phys. Fluids 26 (1983) 357. [9] K.Uo, A.Iiyoshi, Sh.Yoshioka, T.Ishida, Sh.Konoshima, M.Sato, IAEA-CN-28/H-8 (1974).

## ATF FLUX SURFACES AND RELATED PLASMA EFFECTS

R.J. COLCHIN, A.C. ENGLAND, J.H. HARRIS,  
D.L. HILLIS, T.C. JERNIGAN, M. MURAKAMI,  
G.H. NEILSON, J.A. ROME, M.J. SALTMARSH  
Oak Ridge National Laboratory,  
Oak Ridge, Tennessee

F.S.B. ANDERSON  
Torsatron/Stellarator Laboratory,  
University of Wisconsin - Madison,  
Madison, Wisconsin

R.F. GANDY, J.D. HANSON, M.A. HENDERSON  
Auburn University,  
Auburn, Alabama

D.K. LEE, V.E. LYNCH  
Computing and Telecommunications Division,  
Martin Marietta Energy Systems, Inc.,  
Oak Ridge, Tennessee

C.M. SIMPSON  
University of Maryland,  
College Park, Maryland  
  
United States of America

### Abstract

Flux surfaces in the Advanced Toroidal Facility (ATF) were mapped using an electron beam which was incident on a fluorescent screen. Islands were found at  $r/a \geq 0.6$ , indicating the existence of field errors. Failure of the island size to scale with magnetic field indicated that the islands were intrinsic to the coils. The source of the field errors was found to be uncompensated dipoles in the helical coil feeds. The electron temperature was observed to be very low in the vicinity of the islands.

Modifications were made to the helical field buswork to eliminate the field errors, and the flux surfaces were again checked using an electron beam. Islands at  $r/a \geq 0.6$  were found to be greatly reduced in size, with the residual island at  $\epsilon = 1/2$  scaling to 1 cm at  $B = 1$  T. Initial experiments indicate that the plasma operating space has been extended since the buswork modifications.

---

### INITIAL FLUX SURFACE MAPPING EXPERIMENT

During the commissioning of the ATF torsatron (March 1988), experiments were performed to determine if field errors were present. The experiments were run with steady-state magnetic fields of 1 kG (decreasing to 125 G during scaling experiments). An electron beam was used to trace out flux surfaces. It was detected when it impinged on a phosphor-coated wire screen. Pictures of the flux surfaces were taken with a light-intensified CCD camera and recorded on a VCR. The electron gun was driven by a X-Y probe drive which was capable of scanning all of the contained flux surfaces in  $\sim 4$  min.

Flux surface scans revealed the existence of islands located from  $r/a \approx 0.6$  outward. The most prominent islands were located at  $\iota = 1/2, 2/3,$  and  $1$ . The largest island was located at  $\iota = 1/2$  and was 6 cm wide (for  $B = 1$  kG) at its widest extent. Theory indicates that island size ( $\Delta$ ) should scale as  $\Delta \sim (\tilde{B}/B_0)^{1/2}$ , where  $B_0$  is the applied field and  $\tilde{B}$  is the error field. Scaling experiments (see Fig. 1) showed that the width of the  $\iota = 1/2$  island did not appreciably change as the applied magnetic field was lowered from 1 kG to 125 G. This implied that  $\tilde{B}/B_0 = \text{const}$ , indicating an intrinsic error in the magnetic field coil system.

A small misalignment ( $\sim 1-2$  cm) of one of the vertical field coils was first suspected as the cause of the field error. A probe capable of measuring the  $B_r$  and  $B_z$  fields of individual coil pairs was used to determine the alignment of the coils. No misalignments large enough to cause the observed islands were found. Subsequently, detailed modeling of the buswork revealed the presence of four uncompensated dipoles of  $\sim 600$  cm<sup>2</sup> each in the current feeds to the helical field coils. The size and phase of the islands calculated using these field errors agreed with those observed. Details of the initial phase of this work are given in Refs. [1] and [2].

### INITIAL PLASMA RESULTS IN THE PRESENCE OF FIELD ERRORS

The first extensive plasma experiments were performed in ATF from May to September 1988. Electron temperature profiles [3], as determined by Thomson scattering, were peaked near the center, and temperatures were less than 100 eV outside  $r/a \approx 0.6$  in the region of the islands (see Fig. 2). These profiles may have resulted from rapid energy loss due to efficient heat conduction across the islands.

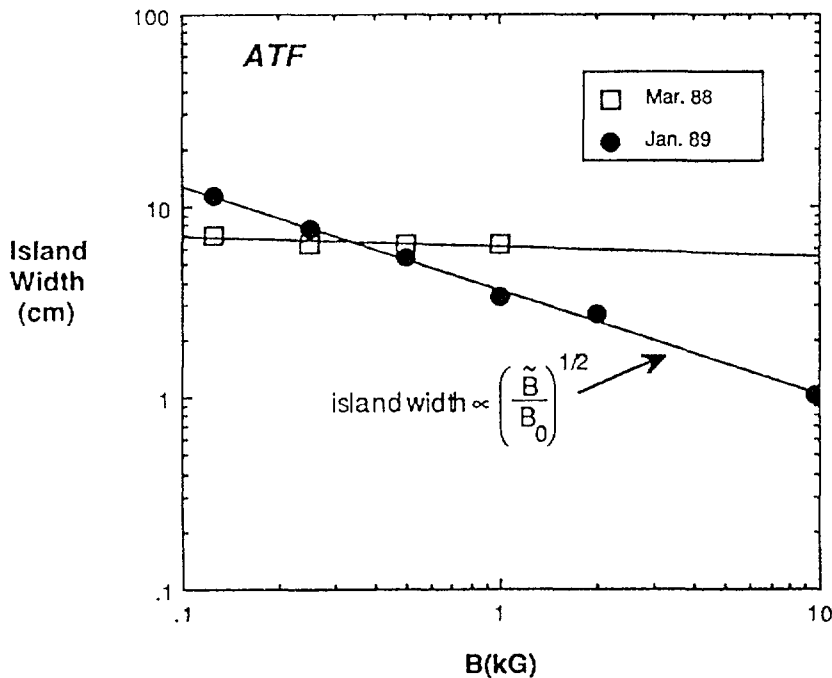


FIG. 1. Size of the  $\iota = 1/2$  island before and after the buswork repairs.

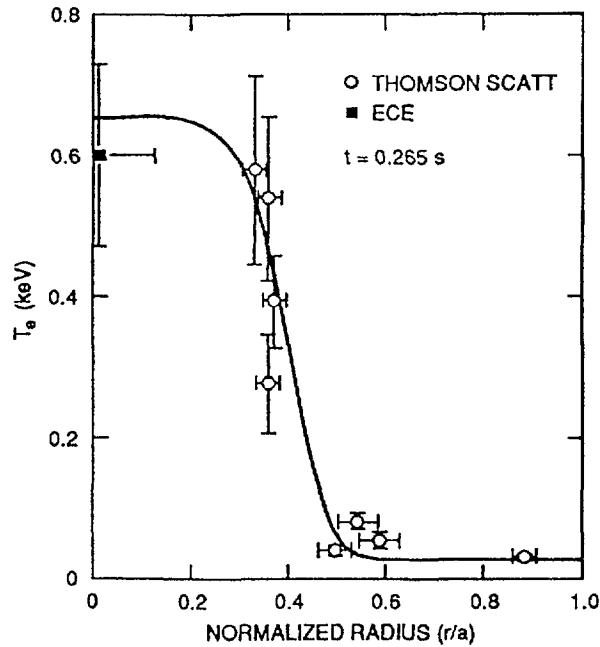


FIG. 2. Electron temperature as a function of radius before the buswork repairs.

## BUSWORK MODIFICATIONS

Islands can be avoided in stellarators and torsatrons by eliminating all magnetic field asymmetries. Thus, the islands observed during the initial flux surface mapping experiments could have been eliminated either by removing the four uncompensated dipoles or by adding eight more dipoles to produce the 12-fold symmetry of the helical fields. The latter course was taken since elimination of the original four dipoles would have involved modifications to the structural supports of ATF. The necessary bus work modifications were carried out from October to December 1988. Changes were also made in the outer vertical field buswork to reduce smaller uncompensated dipoles and to strengthen the coils in the area of the current feeds.

## FINAL FLUX SURFACE MAPPING EXPERIMENTS

The electron gun and the fluorescent screen were reinstalled in ATF immediately after the buswork modifications were completed. The islands originally seen from  $r/a \approx 0.6$  outward were found to either be small or absent. The  $\iota = 1/2$  island size was reduced by a factor of three at  $B = 1$  kG. Scaling experiments were performed over almost two orders of magnitude in magnetic field (from 125 G to 9600 G); the results are shown in Fig. 1. The island size scales as  $\Delta \sim 1/\sqrt{B_0}$ , implying that  $\tilde{B} \approx \text{const}$ . The size and magnetic field scaling of the remaining islands are discussed in detail in Ref. [4].

## PLASMA RESULTS AFTER BUS WORK MODIFICATIONS

At this writing, only preliminary data are available concerning plasma parameter changes after the buswork modifications. However, initial indications are that the operating range of the plasma axis positions has been extended, as shown in Fig. 3. The stored energy and the density remain high over a much larger range of plasma positions than before the modifications, allowing operation with the plasma positioned outboard of the center. There are also initial indications that the radial electron temperature profile is much broader.

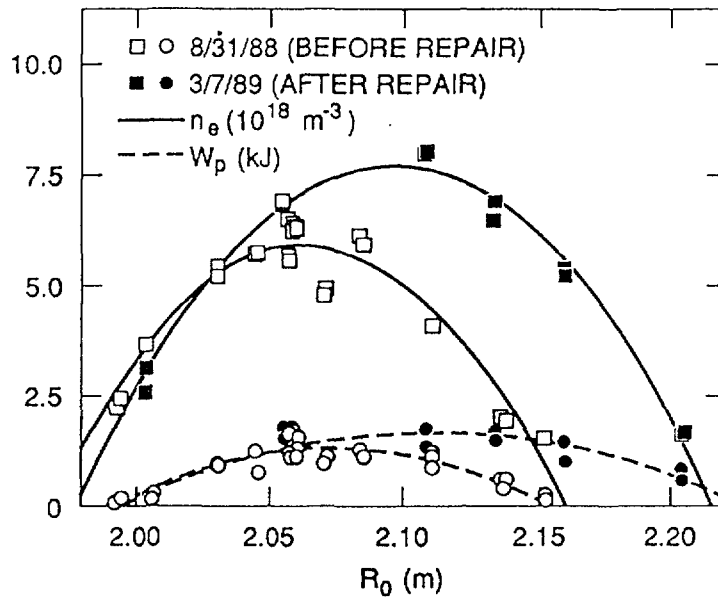


FIG. 3. Stored energy and average density before and after the buswork repairs.

#### ACKNOWLEDGEMENT

This research was sponsored by the Office of Fusion Energy, U.S. Department of Energy, under contract DE-AC05-84OR21400 with Martin Marietta Energy Systems, Inc.

#### REFERENCES

- [1] COLCHIN, R.J., ANDERSON, F.S.B., ENGLAND, A.C., et al., Electron Beam and Magnetic Field Mapping Techniques used to Determine Field Errors in the ATF Toratron, accepted for publication in Rev. Sci. Instrum.
- [2] COLCHIN, R.J., HARRIS, J.H., ANDERSON, F.S.B., et al., Controlled Fusion and Plasma Physics (Proc. 16th Eur. Conf., Venice 1989), Vol. 13B, Part II, European Physical Society (1989) 615.
- [3] MURAKAMI, M, CARRERAS, B.A., HARRIS, J.H., et al., *ibid.*, p. 575.
- [4] ANDERSON, F.S.B., ENGLAND, A.C., COLCHIN, R.J., et al., Electron Beam Mapping of ATF Vacuum Magnetic Surfaces, paper 5P-1, these proceedings.

## MAGNETIC FIELD CONFIGURATION OF THE MODIFIED URAGAN-3M TORSATRON

V.E. BYKOV, E.D. VOLKOV, V.S. VOJTSENYA,  
A.V. GEORGIEVSKIJ, V.M. ZALKIND,  
Yu.K. KUZNETSOV, G.G. LESNYAKOV,  
F.I. OZHEREL'EV, O.S. PAVLICHENKO,  
D.P. POGOZHEV, V.S. TARAN

Institute of Physics and Technology,  
Ukrainian Academy of Sciences,  
Khar'kov, Union of Soviet Socialist Republics

K. SCHWÖRER, H. HAILER  
Institut für Plasmaforschung,  
Universität Stuttgart,  
Stuttgart, Federal Republic of Germany

### Abstract

Magnetic field configuration has been studied for the modified URAGAN-3M Torsatron. Flux mapping was performed for the vertical field range of  $\pm 1,5 \cdot 10^{-2}$   $B_0$  by means of "electron emitter + grid" and linear fluorescent detector methods. It is shown that for optimal conditions the last closed magnetic surface radius  $a$  is equal of 11 cm and limited by island formation at  $t = \frac{1}{3}$  rational magnetic surface.

### 1. INTRODUCTION

The Uragan-3 has been operated in Kh PTI with magnetic field up to 1T since 1981. This magnetic field limit was established due to the increasing risk of the helical coil insulation damage.

The new magnetic system (URAGAN-3M) aiming to increase the magnetic field up to 2T has been designed and manufactured in Kh PTI during 1987 ÷ 88. Essentially the new  $l=3$ ,  $m=9$  helical winding has the same design parameters as the URAGAN-3 winding. Major change in the helical coil support system was an inclusion of 9 ring bandages welded to helical coil in each coil period. Two inner vertical field coils were put in the system also.

The magnetic system has been tested with the magnetic field up to 1.6 T. The stress measurements confirmed a conclusion coming from the stress calculations that the highest achievable magnetic field in the URAGAN-3M is limited by the thermal expansion forces due to the helical coil heating during the current pulse. An extrapolation of experimental data allowed to conclude that the magnetic system can be operated with the magnetic field up to 2T and the current pulse flat top time up to 0.5 s.

The magnetic alignment studies has been performed by the method developed earlier [1-3]. These studies showed that all coils are centered within an error of 1 mm.

In this report the results of calculation and experimental studies of the magnetic flux surfaces in the URAGAN-3M torsatron are presented.

## 2. CALCULATED FLUX SURFACES IN URAGAN-3M

URAGAN-3M is  $l=3, m=9$  torsatron with the coil configuration shown in Figure 1. It has a major radius of  $R_0=1,0m$ , a minor radius of 26 cm, and a winding law

$$\phi = -\frac{3}{9}(\theta - 0.2 \cdot \sin\theta + 0.01 \cdot \sin 2\theta)$$

where  $\theta$  and  $\phi$  are the poloidal and toroidal angles, respectively. All coils are powered in series from flywheel generator, with shunts provided to vary the relative currents in the VF and trim coils.

For flux surface calculations, each of helical coils is modelled with filaments, and each of VF coils is represented by a single filament.

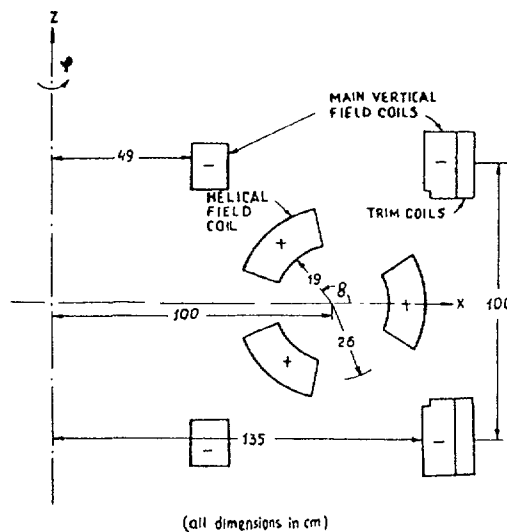


Fig. 1 Cross-sectional view of the URAGAN-3 coil system.

Figure 2 shows closed flux surfaces calculated for URAGAN-3 and URAGAN-3M coil configurations. Larger area of given  $\mathcal{X}$ -value flux surfaces in URAGAN-3M is a result of improved vertical field homogeneity after inclusion of inner VF coils. In URAGAN-3M the closed flux surfaces existed for wider range of the vertical field  $B_{\perp}$  change ( $-1.5\% < \frac{B_{\perp}}{B_0} < +1.5\%$ ). In this range parameter  $\Delta V'/V_0'$  changed from +0.1 ("hill") to -0.1 ("well").

## 3. MAGNETIC FLUX SURFACE MEASUREMENTS

Two methods: "electron emitter + grid" (EEG) [1] and linear fluorescent detector (LFD) [2] were used for flux surface mapping.

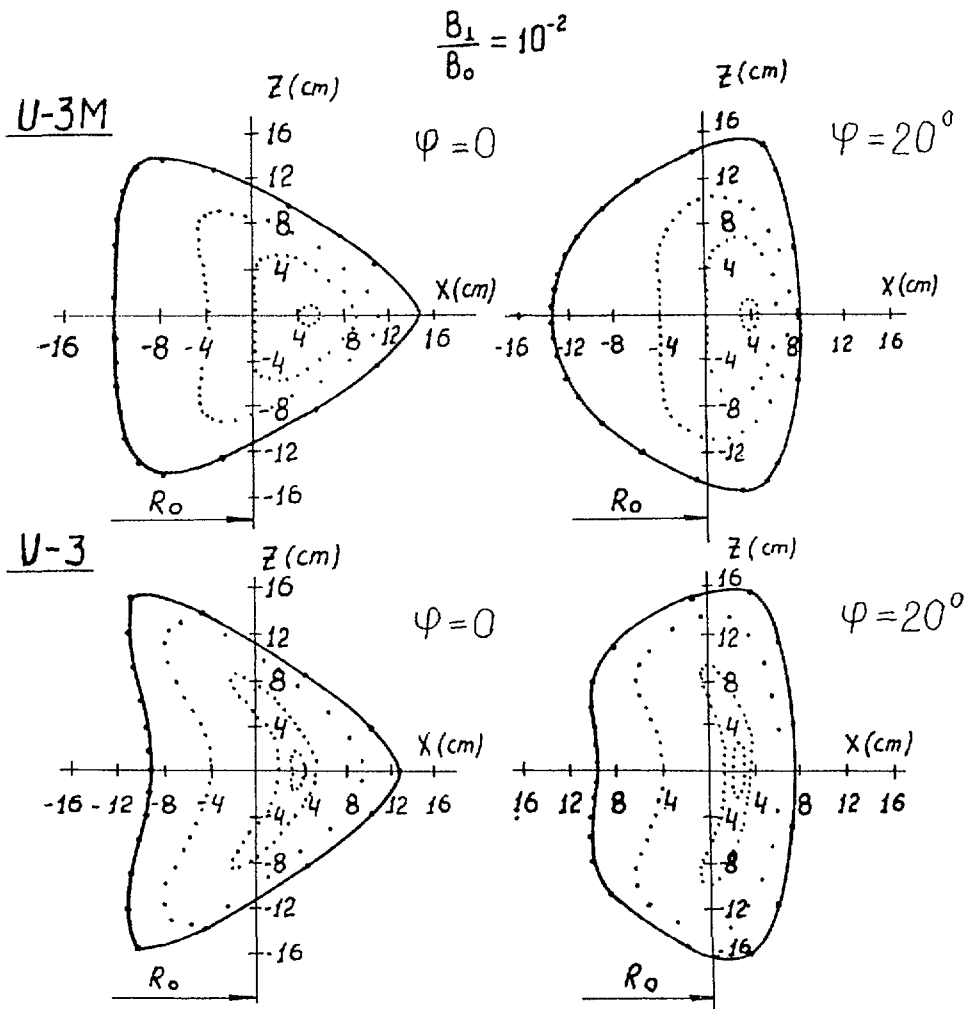


Fig.2 Flux surfaces in URAGAN-3 and URAGAN-3M.

In the first method the emitter with size of 1 mm scanned  $\phi = 0^\circ$  cross section and the grid with a transparency of  $K=0,985$  was put in  $\phi = 120^\circ$  cross section. A computerized measurement system allowed to scan the emitter position by steps of 5 mm, to measure the emitter coordinates, emitter ( $J_{em}$ ) and grid ( $J_g$ ) currents and to calculate "magnetic field line transit number"  $N = \ln \left( 1 - \frac{J_g}{J_{em}} \right) / \ln K$  [1]. The emitter position was displayed at TV screen, colour of each point depended on value of  $N$ .

In the second method a fluorescent rod with a diameter of 1mm scanned  $\phi = 160^\circ$  cross section, an electron gun (electron energy -  $40 \div 100$  eV, beam current -  $5 \div 10 \mu A$ , beam diameter  $\approx 1$  mm) could be put in any point of  $\phi = 0$  cross section. The lumination of detector hit by the electron beam was photographed by a "Polaroid" camera through the tangential port. Unfortunately, part of cross section view was shadowed by the helical winding.

The first experiments with EEG method (magnetic field of  $B_0 = 0,1 T$ ) showed that magnetic flux surfaces were up-shifted ( $\Delta z \approx 8$  cm). This shift was eliminated by imbalance of current in one of outer vertical field coils and flux mapping was

performed for wide range of vertical field  $B_z$  change ( $-0,015 < \frac{B_z}{B_0} < +0,015$ ). A qualitative improvement of magnetic field configuration in URAGAN-3M illustrates Figure 3. For URAGAN-3M the value of  $N$  in near axis region reached of  $N_{max} = 300$  ( $I_g / I_{em} = 0,99$ ) while for URAGAN-3 this value was not more than 100 ( $I_g / I_{em} \leq 0,78$ ).

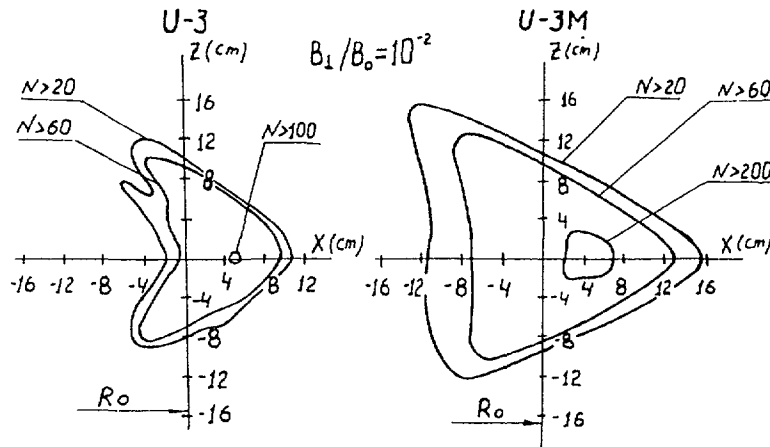


Fig.3 BEEG map of flux surfaces in URAGAN-3 and URAGAN-3M.

More data on magnetic flux surface structure were obtained with LFD method (magnetic field of  $B_0 = 0,5T$ ). In the studied range of vertical field magnetic islands at rational surfaces with  $t = \frac{1}{5}, \frac{1}{4}, \frac{1}{3}$  were observed. For low shear configurations maximum width of  $t = \frac{1}{3}$  islands reached value of  $\frac{\Delta r}{r} \approx 0,1$ . For higher shear configurations the islands at  $t = \frac{1}{4}, \frac{1}{3}$  ( $\frac{\Delta r}{r} \leq 5 \cdot 10^{-2}$ ) were observed also. No nested surfaces were observed out of  $t = \frac{1}{3}$  surface. The last closed surface shape observed by LFD method is similar to  $N = 60$  surface obtained by BEEG method. Comparison of data obtained by both methods is illustrated in Figure 4. The radial position of islands is in a good agreement with the calculated  $t(r)$  profile.

#### 4. CONCLUSION

Studies of magnetic field configuration for the URAGAN-3M torsatron showed a considerable improvement as compared with URAGAN-3 configuration. For optimal VF value the last closed magnetic surface ( $t \approx 0,3$ ) has an average radius of  $a \approx 11$  cm rather than of  $a \approx 8$  cm for URAGAN-3 [4]. Nevertheless the magnetic field perturbations  $\bar{B}$  of unknown nature ( $\frac{\bar{B}}{B} \approx 1 \cdot 10^{-4}$  at  $r \approx 10$  cm) destroyed the outer magnetic surfaces and brought the ergodic magnetic layer ( $\Delta a \approx 2$  cm,  $N = 10 \pm 1$ ) between the confinement region and diverted magnetic flux. This ergodic magnetic layer is beneficial for a plasma core screening against an impurity influx.

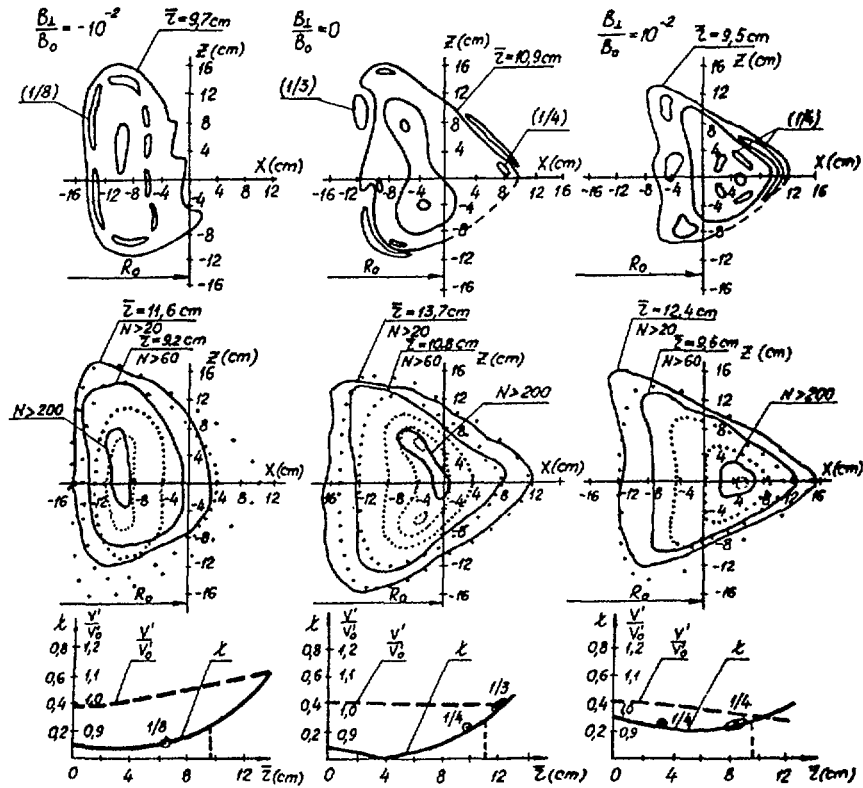


Fig. 4 Electron beam map of flux surfaces in URAGAN-3M. Upper row-LFD measurements (dashed line -helical winding shadowing). Middle row-EEG measurements and calculation(...). Lower row- calculated  $\lambda(\bar{z})$  and  $V'/V_0(\bar{z})$  profiles ( $\bullet$  - magnetic island position).

Operational VF range allows to study the influence of parameter  $V''$  on a high beta plasma stability. These experiments are planned for RF heated plasma in the URAGAN-3M torsatron in future.

#### REFERENCES

1. Дикий А.Г., Залкинд В.М., Лесняков Г.Г. и др., Физика плазмы, 14, 279 (1988).
2. M.Hailer, J. Massig, F. Schuler, K. Schworer, H. Zwicker. 14 Europ. Conference on Control. Fusion and Plasma Phys.. Madrid, Pt.1, 423 (1987).
3. R.J.Colchin, S.S.Fedotov, J.H.Harris et al., Rev.Sci.Instr. 57, 1233 (1986).
4. Н.Т.Беседин, В.Е.Быков, А.В.Георгиевский и др. Сб. Вопросы атомной науки и техники. Сер.:Термоядерный синтез, вып.4, 7 (1987).

## **NEW DEVICE DESIGNS**

## HELIAIC PHYSICS STUDIES: TJ-II PROJECT

C. ALEJALDRE, J. ALONSON, J. BOTIJA, F. CASTEJÓN,  
J.R. CEPERO, J. GUASP, A.L. FRAGUAS, L. GARCÍA,  
V. KRIVENSKI, R. MARTÍN, M. SOROLLA, A.P. NAVARRO,  
A. PEREA, A. RODRÍGUEZ-YUNTA, A. VARIAS  
Asociación Euratom/CIEMAT,  
Madrid, Spain

### Abstract

The paper is devoted to the analytical and numerical analysis of the confinement properties of the Heliac TJ-II device to be built at CIEMAT, Madrid. The ECRF power absorption has been calculated using RAYS numerical code. The method of transport losses reduction was found through spatial modulation of the toroidal field coil location. The stability of the TJ-II plasma of high pressure has been studied.

The TJ-II configuration consists of 32 toroidal field coils centered around a toroidal helix of major radius  $R_0 = 1.5$  m., minor radius  $r_{sw} = 0.28$  m., and pitch law  $\theta = -4\Phi$ , where  $\theta$  and  $\Phi$  are the usual poloidal and toroidal angles. The hard core is made of two components, a circular coil located at the major axis, 1.5 m., and a helical winding wrapped around the circular one following the same winding law as the toroidal coils, see figure 1. These separately controllable currents in the hard core windings give the device its unique flexibility and differentiate it from the original heliac design. Two circular vertical field coils complete the coil configuration<sup>1</sup>. In this paper, it is shown our latest understanding of TJ-II physics in the fields of ECH, Transport and MHD, and the engineering changes introduced in its final design.

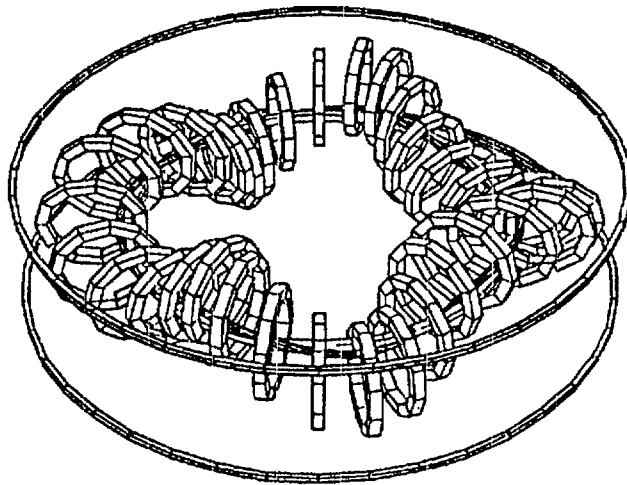


Figure 1  
The TJ-II coil configuration

### I. Electron Cyclotron Resonance Heating

In a first stage, plasma breakdown and heating will be based upon an electron cyclotron resonance heating (ECRH) system. Preliminary experiments will be done with a 200 kW, 28 GHz. gyrotron. Due to the density dependent cut-offs in the wave propagation frequency and to obtain

more relevant plasmas in the TJ-II, an ECRH system based upon two gyrotrons, 200 kW each, working at 53.2 GHz. will be provided.

To take into account the three dimensional TJ-II geometry, the ray-tracing code RAYS<sup>2</sup> has been adapted to the geometry of TJ-II and a new absorption module has been introduced that permits to calculate power absorption when a non-maxwellian electron distribution is present<sup>3</sup>. Using RAYS a study ,taking into consideration the limitations of the actual vacuum chamber for access to the plasma, has been conducted to obtain the optimum position of ray launching from the point of view of maximizing power deposition and controlling the temperature profile. The power absorbed by the plasma in "one-pass" has maximum values of the order of 40% for first harmonic propagation in the O-mode and in excess of 99% for X-mode propagation in the 2<sup>nd</sup> Harmonic. The strong absorption near the second harmonic induces strong quasilinear effects that degrade power absorption to about 90% at  $\tau=1.8$  and 30% when  $\tau=14$ . ( $\tau$  is the time normalized to the collision time). Work is continuing to find the optimum incidence angle to minimize quasi-linear effects.

## II. Transport

To minimize the magnetic field ripple at the magnetic axis and therefore optimize the transport properties in TJ-II we will spatially modulate the toroidal field coil location. The harmonic content of the magnetic field diminishes globally and in particular, the corner ripple term (0,1), due to the "square" shape of the TJ-II, almost disappears.

Figure 2 shows the normalized diffusion coefficient  $D^*$  as a function of the normalized

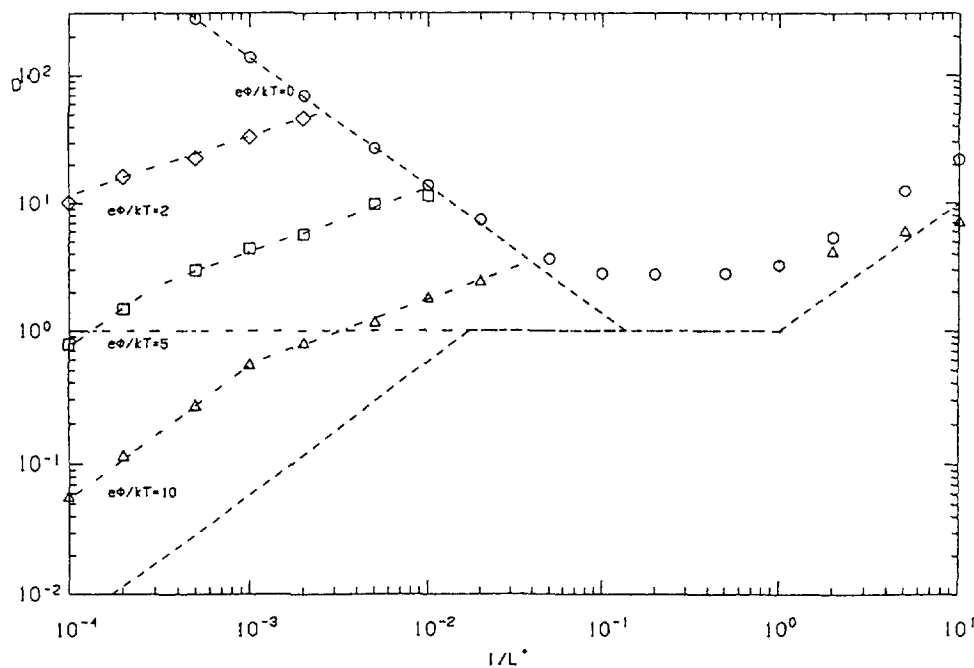


**Figure 2**  
The mono-energetic normalized diffusion coefficient for the  $a/2$  surface and several values of the radial electric field. The dotted line correspond to the diffusion coefficient of the equivalent tokamak.

frequency  $\nu^*$  for the magnetic surface located at  $a/2$ . For comparison purposes the values corresponding to the equivalent Tokamak are included. The influence of a radial electric field upon transport can be clearly seen in the figure. For electric fields strong enough the  $1/\nu$  regime can disappear, particles going from "plateau" to the  $\nu^{1/2}$  regime directly. Table I shows the confinement times obtained from the ambipolarity condition  $\Gamma_i(\Phi)=\Gamma_e(\Phi)$ .

Table I  
 Confinement times in ms  
 $n_e = 1.65 \times 10^{19} \text{ m}^{-3}$ ,  $T_e = 620 \text{ eV}$ ,  $T_i = 170 \text{ eV}$

Pot(V)/ $T_e$	$\tau_c$	$\tau_{ee}$	$\tau_{ei}$	$\tau_e$
+1.7	13.5	3.8	7.5	4.3
+1.6	13.8	3.9	7.7	4.4
+1.3	15.6	4.5	8.7	5.0

where  $\tau_c$  is the particle confinement time,  $\tau_{ee}, \tau_{ei}$  the electron, ion energy confinement time and  $\tau_e$  the global energy confinement time.

### III. Stability

The high degree of flexibility of TJ-II makes it a very attractive device to study the stability properties of helical axis plasmas with a broad range of rotational transform and

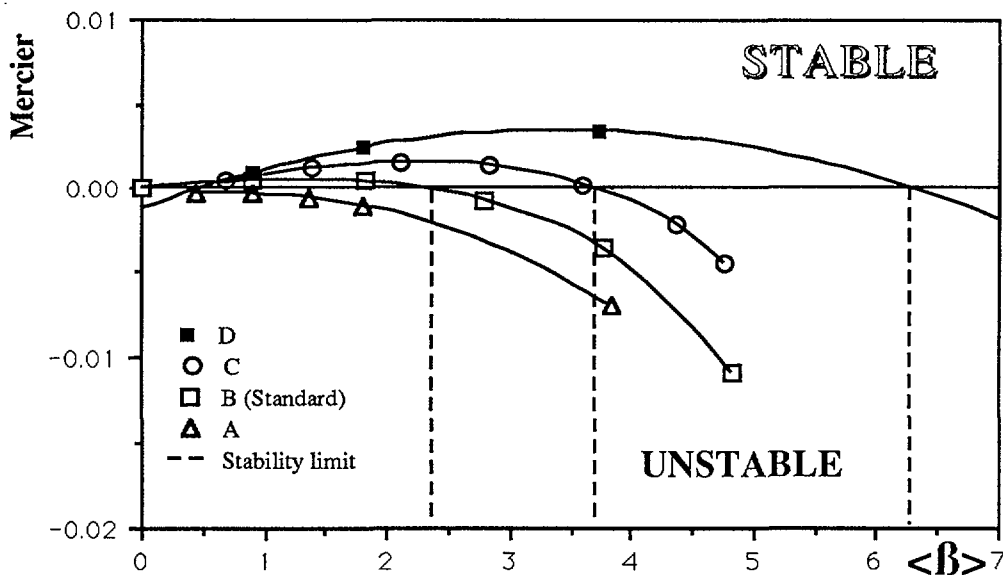


Figure 3  
 The Mercier criterion for the four configurations vs.  $\langle \beta \rangle$  for a fixed normalized radius = 0.97

magnetic well. This flexibility will permit to experimentally explore regimes with stability average beta limit ranging from near zero to 5% in an almost continuous manner<sup>7</sup>.

We have studied four configurations having equal rotational transform at the axis and different magnetic well. The parameters that describe the configurations are summarized in table II.

Table II

	$t_0/M$	$-I_{cc}$ (kA)	$-I_{hc}$ (kA)	Well
Configuration A	0.36	290	92	1%
Configuration B (Standard)	0.36	219	95	2%
Configuration C	0.36	105	82.5	3%
Configuration D	0.36	65	55	4%

The fixed boundary equilibria for the four configurations were obtained using the 3-D equilibrium code VMEC<sup>8</sup> with a radial mesh of 31 points. We needed 138 Fourier amplitudes to satisfactorily characterize the boundary of the confinement region. The total average force for the equilibrium configurations was less than  $10^{-9}$ . We considered a sequence of zero current equilibria with a pressure profile  $p \propto (1-\Phi)$  where  $\Phi$  is the normalized toroidal flux. We found that the configuration with a shallow well depth (A) is unstable to Mercier modes even at small values of beta but when the vacuum well becomes deeper, its stability increases until for the extreme case (D) the beta limit is  $\approx 6\%$ . And this change comes without changing the value of the rotational transform, therefore suggesting the possibility that higher stability limits can be found in configuration space. Work is under way to study configurations with higher effective aspect ratios and high rotational transform/period  $\approx 0.6$ .

#### IV. Engineering Studies

A detailed design for TJ-II is under way at the Italian company ANSALDO.

To maintain the hard core conductors outside the vacuum and therefore relaxing the requirements on feasibility for these coils, the chamber will be almost circular with an helical indentation to accommodate the hard core coils. Nevertheless, even with this restriction it is possible to build the chamber by octants. These octants will be joined by flanges which will help to achieve the geometrical accuracy required for this device.

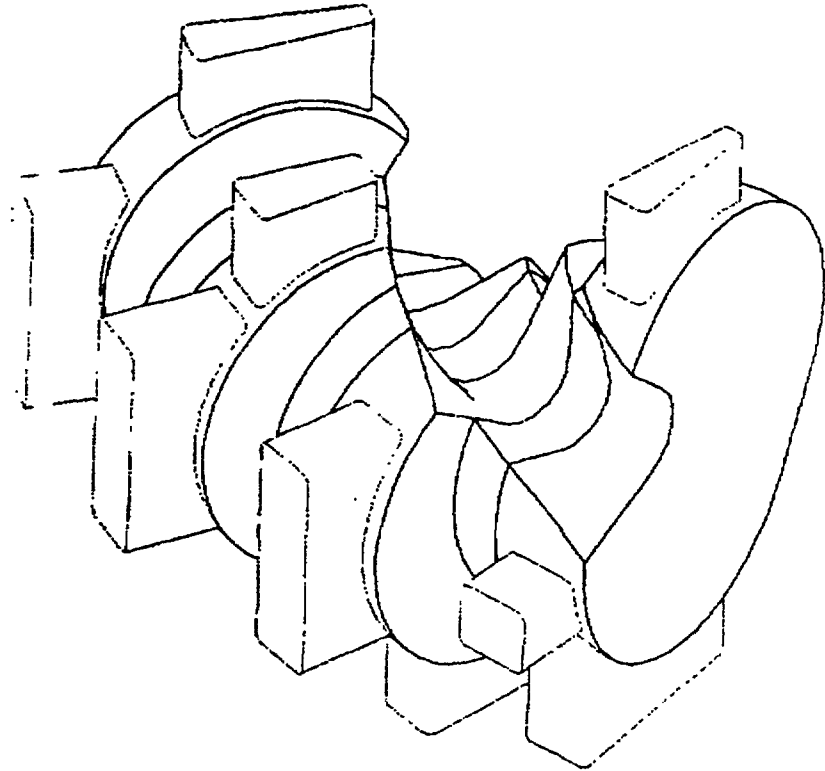


Figure 4

Schematic drawing of an octant of the vacuum chamber

Figure 4 shows an octant of this design. Special protections for energy and particle deposition have been designed. They are basically a toroidal shield for thinnest part of the chamber, all along the hard core position, and nine poloidal ones, covering the welding between consecutive sectors.

A high degree of access to the plasma is guaranteed through 3 windows per sector, located at the top, external and bottom side of the device.

Demontable coils have been chosen for the toroidal field coils. This design, together with the vacuum chamber described above, enable to build independently the main components of the device and assemble them later in the experimental hall. This water cooled coils are made in copper and work with a current density around  $5 \text{ kA/cm}^2$

The design for the hard core coils is based in copper conductors with a high density current,  $J=10\text{kA/cm}^2$ , to accommodate them in the small available space. Cooling will be made by water, hollow conductors have been chosen for the circular coil. The helix will be indirectly cooled from water flowing at both sides of the package. Feeders have been calculated to test they have no influence on the vacuum magnetic surface structure.

## REFERENCES

- 1.- Guasp,J.et al. Proc.12th Europ.Conf.Controlled Fusion and Plasma Physics, Budapest (1985) 441
- 2.- Batchelor,D.B.,et al., RAYS:A Geometrical Optics Code for EBT, Oak Ridge National Lab., Rep. ORNL/TM-6844(1982)
- 3.- Alejaldre, C., Nucl. Fusion, May (1988)
- 4.- Krivenski, V. et al Phys. Fluids **30** , 438 (1987)
- 5.- R.H. Fowler, J.A. Rome and J.F. Lyon, Phys. Fluids **28**, 851, (1981)
- 6.- Lotz,W. , Nürenberg J. and Schlüter, A. , J. Comput. Phys. **73**, 73, (1987)
- 7.- Varias, A. , Alejaldre , C., and Fraguas ,A.L. ,1989 IAEA Workshop on Stellarators, Oak Ridge, U.S.A.
- 8.- Hirshman, S.P. et al. Comp. Phys. Comm. **39**, 546 (1989)

## **MAGNETIC SURFACES, ISLANDS**

## ELECTRON BEAM MAPPING OF THE ATF VACUUM MAGNETIC SURFACES

F.S.B. ANDERSON

Torsatron/Stellarator Laboratory,  
University of Wisconsin - Madison,  
Madison, Wisconsin

A.C. ENGLAND, R.J. COLCHIN, J.H. HARRIS,  
D.L. HILLIS, M. MURAKAMI, G.H. NEILSON,  
J.A. ROME, M.J. SALTMARSH  
Oak Ridge National Laboratory,  
Oak Ridge, Tennessee

M.A. HENDERSON  
Auburn University,  
Auburn, Alabama

C.M. SIMPSON  
University of Maryland,  
College Park, Maryland

United States of America

### Abstract

The results of the ATF magnetic surface structure checking by electron beam magnetic surface mapping techniques are reported.

---

The Advanced Toroidal Facility (ATF) torsatron was designed as a high field plasma confinement device which produces the plasma confining magnetic surfaces using helical and vertical field coils. Inherent device flexibility was incorporated into the ATF design through additional vertical field coil sets which permit a wide range of magnetic surface topologies and rotational transform profile control. To check the magnetic surface structure after construction, electron beam magnetic surface mapping techniques were implemented which permitted easy evaluation of any magnetic configuration.

The use of a highly transparent screen, which fluoresced on electron impact, permitted a complete record of an entire magnetic surface cross-section to be stored on video tape for subsequent data analysis; the entire surface structure could be scanned with the electron gun in approximately four minutes. Computer frame-grabbing, and subsequent image distortion compensation, enabled real-space analysis of any desired magnetic surface to obtain information on island widths, island phasing, island scaling with magnetic fields, magnetic axis location, or any other desired surface data. Computer control of the electron gun drive unit enabled accurate electron beam scanning of the magnetic surfaces. The identification of rational surfaces, together with the accurate electron gun location, enabled an accurate determination of the rotational transform profile to be made.

Initial surface mapping experiments demonstrated the existence of broad magnetic islands in the outer half of the ATF magnetic surfaces; low-order rational surfaces from

$\iota = 1/2$  out to the  $\iota = 1.0$  surface were all found to have islands which maintained a constant width under magnetic field scaling. Measurements of the rotational transform profile confirmed that the overall magnet coil construction was close to the design specifications (Fig. 1), but the island scaling data indicated the presence of an intrinsic error field (later determined to arise from uncompensated helical field coil feed dipoles). Implementation of the auxiliary vertical field coils also demonstrated the design flexibility of the device, and the magnetic configuration of various rotational transform profile configurations was determined.

A second phase of magnetic surface mapping experiments was instigated subsequent to symmetrization of the helical feed error, implemented to remove the low-order error fields causing the outer surface islation. As predicted by computer models, the outer surfaces were measured to have a greatly reduced island width, with the  $\iota = 1/2$  surface island being reduced from 6 cm to under 3 cm for toroidal field strengths of 0.1 T. Rational magnetic surfaces internal to the  $\iota = 1/2$  surface were found, however, to now have significant islands. In particular, the  $\iota = 1/3$  surface was seen to have a 6 cm island at 1 kG fields, which did not reduce in width significantly as the magnetic field strength was increased. The rotational transform profile or the repaired magnetic configuration is shown in Fig. 2. The reduction in the outer island widths is clearly evidenced, as is the significant increase in the internal surface islation.

♣ PROFILE BEFORE FIELD ERROR REPAIRS

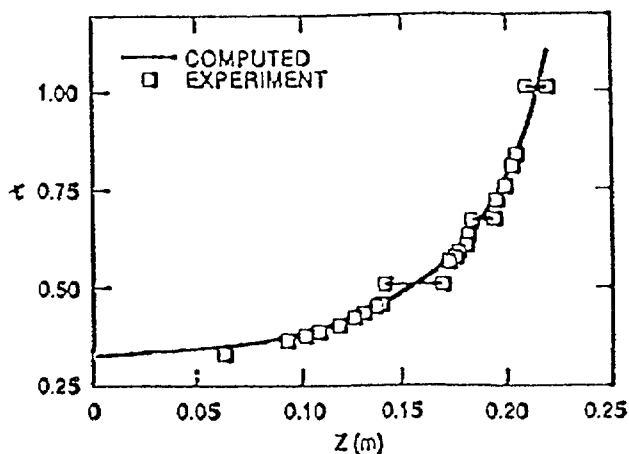


FIG. 1.

♣ PROFILE AFTER FIELD ERROR REPAIRS

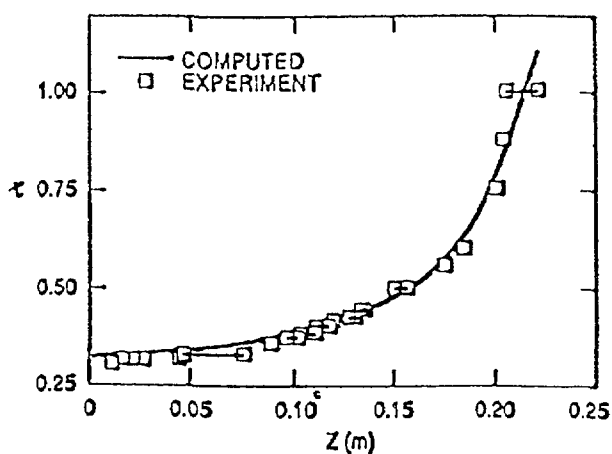


FIG. 2.

Mapping of the vacuum magnetic surface structure was also performed when a large billet of iron (1 m long and 0.6 m dia.) was placed at various locations about ATF to simulate the effects of the implementation of plasma diagnostics on the ATF magnetic surfaces. This iron was placed either on the equatorial midplane, to simulate the charge exchange diagnostic, or directly above the vacuum vessel to simulate the heavy-ion beam probe diagnostic. Unless the iron was placed extremely close to the vacuum vessel, closer than anticipated for any diagnostic implementation, no significant magnetic surface deformation or islation could be measured. When placed close to the vacuum vessel, the iron billet was found to actually reduce the width of the  $\iota = 1/2$  island for each of the toroidal locations at which the iron was placed. This island width reduction is shown in Fig. 3 for

the  $\iota = 1/2$  surface, which also clearly shows the island width reduction as the toroidal magnetic field was increased. Figure 4 shows that the iron billet increased the size of the  $\iota = 1/3$  island.

The final phase of the electron beam mapping experiments involved mapping the magnetic surfaces when a controlled low-order error field had been introduced. Two 1/2 m diameter coils were placed 180 degrees toroidally apart and directly above the vacuum vessel, and energized along with the standard ATF magnetic coils. The current phasing of these error-coils was chosen to intentionally add a 2-1 harmonic to the ATF magnetics. The electron beam mapping of this magnetic configuration clearly demonstrated the ability to significantly increase the low-order rational surface isolation (Figs 3 and 4). Maintaining a constant current in these coils while the main ATF fields were scaled clearly demonstrated a  $(1/\sqrt{B})$  scaling of the island width. The electron beam mapping experiments determined the entire magnetic surface configuration of both the optimal ATF magnetic configuration as well as the configuration under intentional error field surface isolation. Thus, ATF has now the opportunity to directly investigate the effects on plasma transport of the introduction of a known field error and surface isolation.

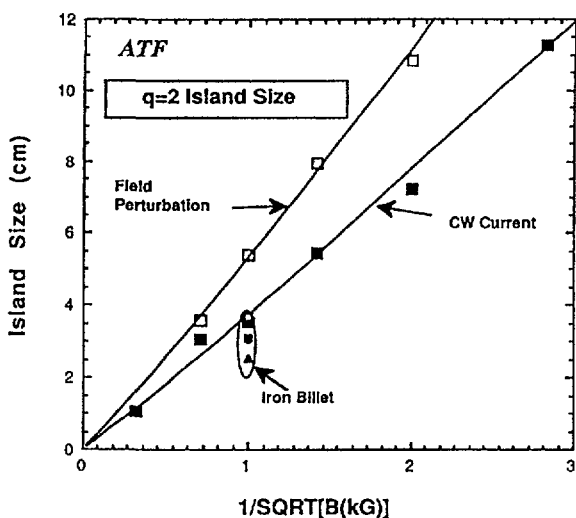


FIG. 3.

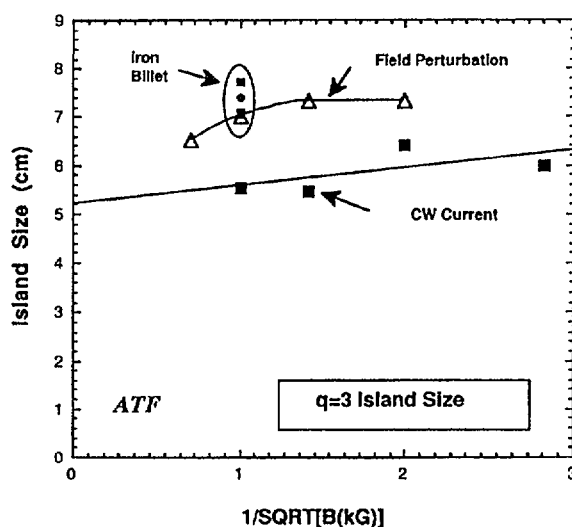


FIG. 4.

#### ACKNOWLEDGEMENTS

This research was supported by the United States Department of Energy under Grant Number DE-FG02-86ER53216.A004 and the Oak Ridge National Laboratory under contract number 19X-9135-C.

## FIELD ERROR MODELING STUDIES IN THE ATF\*

D.K. LEE<sup>1</sup>, J.H. HARRIS, R.J. COLCHIN,  
A.C. ENGLAND, G.S. LEE, V.E. LYNCH<sup>1</sup>,  
G.H. NEILSON, M.J. SALTMARSH  
Oak Ridge National Laboratory,  
Oak Ridge, Tennessee

F.S.B. ANDERSON  
Torsatron/Stellarator Laboratory,  
University of Wisconsin — Madison,  
Madison, Wisconsin

J.D. HANSON  
Department of Physics,  
Auburn University,  
Auburn, Alabama

United States of America

### Abstract

Initial flux surface measurements on the ATF torsatron revealed the presence of a large magnetic island of width  $\sim 6$  cm on the  $\nu = 1/2$  surface and smaller islands on other rational surfaces. Modeling studies of a large number of possible field error sources were carried out by considering various coil misalignments, current feeds to the helical (HF) and vertical field (VF) coils, and ferromagnetic materials. The results of extensive calculations showed that the magnetic dipoles due to the HF current feeds were the most likely cause of the islands, while the VF coils contributed a smaller additional perturbation. The buswork was redesigned to "symmetrize" the perturbations, and extensive optimization studies were done to find an arrangement of feeds resulting in minimum island widths at the  $\nu = 1/2$  and the other rational surfaces. The buswork modifications based on these studies have been installed on ATF, and flux surface measurements have been completed. The results are rather surprising: the  $\nu = 1/2$  island was essentially eliminated without the final optimization step envisioned in the design studies, but the  $\nu = 1/3$  island increased in size.

---

## THEORETICAL BACKGROUND

Toroidal confinement devices having rotational transform are highly sensitive to perturbing magnetic fields that resonate with rational values of the rotational transform to produce magnetic islands that break up the closed flux surfaces. There are various sources for the error fields, which include coil misalignments during installation, imperfections in coil windings, perturbations by fields from busworks and leads, and the presence of ferromagnetic materials in the vicinity.

---

\* Research sponsored by the Office of Fusion Energy, US Department of Energy, under contract DE-AC05-84OR21400 with Martin Marietta Energy Systems, Inc.

<sup>1</sup> Computing and Telecommunications Division, Martin Marietta Energy Systems, Inc., Oak Ridge, TN 37831, USA.

A perturbation field with helical harmonics of the type

$$B_{mn} = b_{mn}(r) \cos(m\theta - n\phi) \quad (1)$$

produces magnetic islands at the resonant rational surface  $\iota = n/m$  with the maximum island size (width) [1]

$$d_0 = 4 \left( \frac{b_{mn} R_0}{m B_0 \iota'} \right)^{1/2}, \quad (2)$$

where  $R_0$  is the major radius,  $\iota' = d\iota/dr$  is the shear at the rational surface, and  $B_0$  is the average toroidal component of the magnetic field.

## CONTRIBUTIONS FROM NON-RESONANT ERRORS

Although the dominant contribution to the formation of an island at the surface of  $\iota = n/m$  comes from the resonant harmonics of the perturbation field given by Eq. (1), error fields of the form

$$B_{m\pm 1, n} = b_{m\pm 1, n}(r) \cos(m\theta - n\phi) \quad (3)$$

can also generate islands at the  $n/m$  surface with a width

$$d_{\pm 1} = 4 \left( \frac{a_1 b_{m\pm 1, n} R_0}{2m B_0 \iota'} \right)^{1/2}, \quad (4)$$

where  $a_1$  is the ( $m = 1, n = 0$ ) Fourier coefficient in the expansion of  $R/B_\phi$ :

$$\frac{R}{B_\phi} = \frac{R_0}{B_0} (1 + a_1 \cos \theta + \dots), \quad (5)$$

For a closed flux surface with an average radius of  $r$ , we have  $a_1 \simeq r/R_0$ . Thus, if  $b_{m\pm 1, n} = b_{mn}$ , then  $d_{\pm 1}/d_0 = (a_1/2)^{1/2}$ . In the case of the  $\iota = 1/2$  flux surface of the ATF,  $r = 17.2$  cm,  $R_0 = 210$  cm, and hence the non-resonant error fields  $B_{11}$  and  $B_{31}$  would produce islands whose sizes are about 29% of  $d_0$ .

## MODELING STUDIES AND BUSWORK MODIFICATIONS

Initial flux surface measurements on the ATF torsatron showed that there are magnetic islands present on the  $\iota = 1/2$  and other rational surfaces [2]. The largest island, at  $\iota = 1/2$  surface, had a maximum width of about 6 cm; shown in Fig. 1(c). Smaller islands were observed at the  $\iota = 1/3$  and  $2/3$  rational surfaces, as shown in Figs. 1(b) and 1(d), respectively. To determine field error sources responsible for these islands, we carried out quite extensive modeling studies by considering various types of misalignments for the helical field (HF) and vertical field (VF) coils, perturbations due to current feeds to the HF and VF coils, and dipole field contributions from ferromagnetic materials in the vicinity of the ATF. The results of these studies revealed that the four current feeds to the HF coils at  $0 \leq \phi \leq 90^\circ$  [Fig. 2(a)] produce islands at surfaces of  $\iota = 1/2, 1/3,$  and  $2/3$  in close agreement with the experimental observations, as shown by Figs. 1(a)-(d).

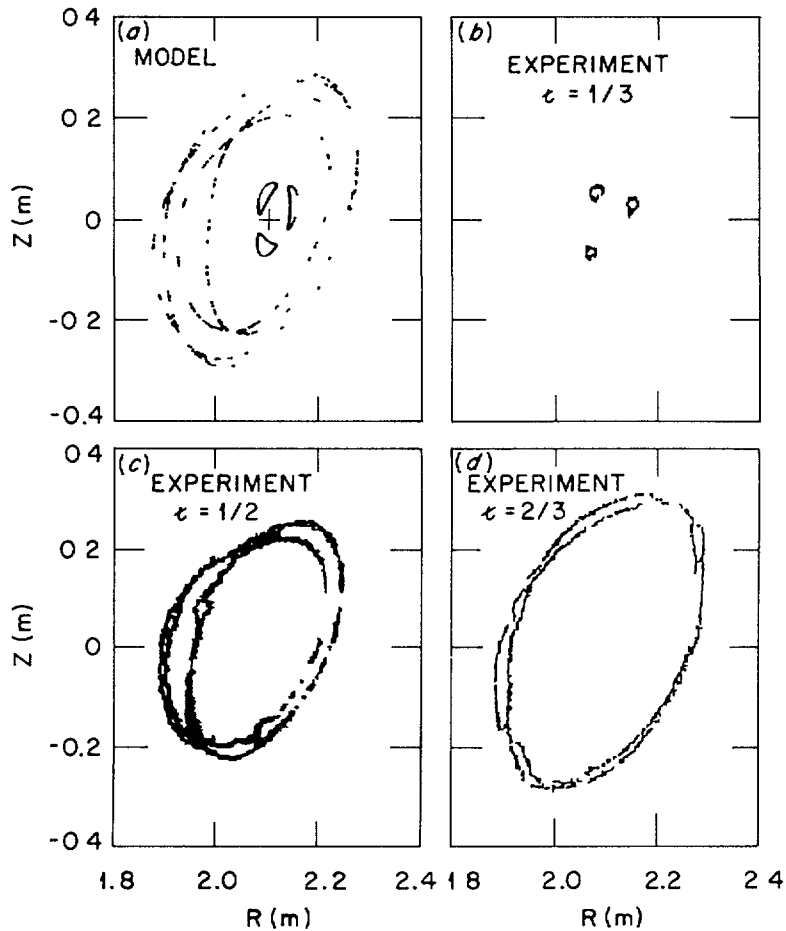


FIG. 1. (a) Computed islands at surfaces of  $\tau = 1/3, 1/2,$  and  $2/3$ , assuming field errors due to uncompensated currents in HF and VF coil feeds shown in Fig. 2(a). (b)-(d) Corresponding measured flux surfaces

An obvious solution to this imbalance was to “symmetrize” the perturbations by adding eight additional loops as shown in Fig. 2(b). This modification reduced the  $\tau = 1/2$  island to 2.9 cm. A further fine tuning to compensate the current feeds to the VF coils was carried out by moving the “trombone” sections 15 cm radially outward at  $\phi = 150^\circ, 180^\circ, 270^\circ,$  and  $300^\circ$ , as shown in Fig. 2(c). This final optimization reduces the  $\tau = 1/2$  island to 1.1 cm. The buswork modifications shown in Fig. 2(b) have been completed. The results of flux surface measurements now show that the size of the  $\tau = 1/2$  island is quite small [3] and hence the final optimization step shown in Fig. 2(c) has not been implemented. On the otherhand, the  $\tau = 1/3$  island size has increased. Further studies are in progress to find possible explanations.

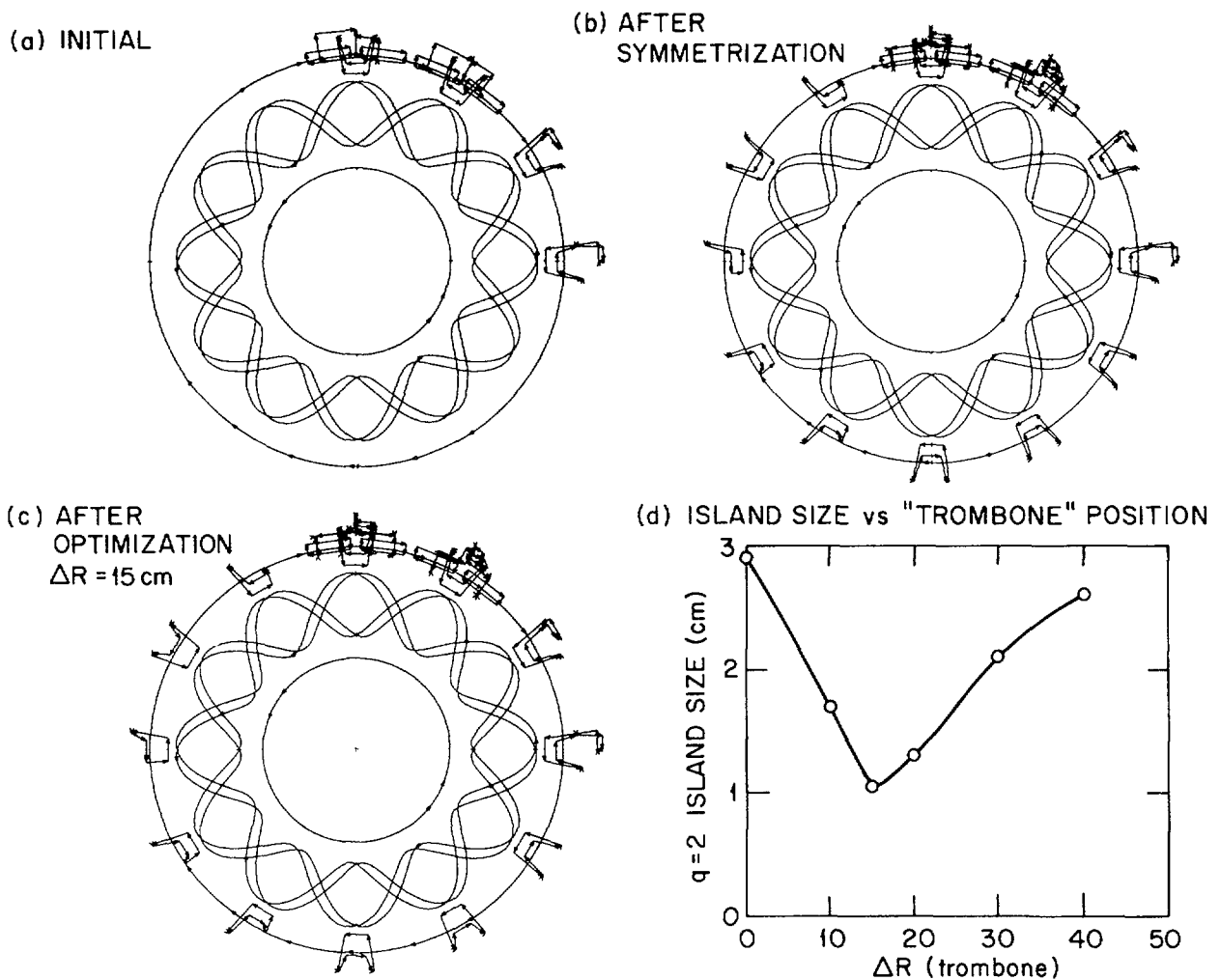


FIG. 2. (a) Initial coil configuration (before modification), showing un-compensated feed coils, (b) Symmetrized coil configuration, (c) Optimized configuration with "trombone" sections shifted 15 cm radially outward at  $\phi = 150^\circ, 180^\circ, 270^\circ,$  and  $300^\circ$ , (d) Reduction in island size as a function of "trombone" positions at  $\phi = 150^\circ, 180^\circ, 270^\circ,$  and  $300^\circ$ .

## REFERENCES

- [1] S. Matsuda, M. Yoshikawa, Jpn. J. Appl. Phys. 14, (1975) 87.
- [2] R. J. Colchin, J. H. Harris, F. S. B. Anderson, A. C. England, R. F. Gandy, J. D. Hanson, M. A. Henderson, D. L. Hillis, T. C. Jernigan, D. K. Lee, V. E. Lynch, M. Murakami, G. H. Neilson, J. A. Rome, M. J. Saltmarsh, and C. M. Simpson, Plasma Physics and Controlled Nuclear Fusion Research (Proc. 16th Int. Conf. Venice 1989) European Phys. Soc. Vol. 13B, Part II (1989) 615.
- [3] R. J. Colchin, F. S. B. Anderson, A. C. England, R. F. Gandy, J. H. Harris, M. A. Henderson, D. L. Hillis, R. R. Kindsfather, D. K. Lee, D. L. Million, M. Murakami, G. H. Neilson, M. J. Saltmarsh, and C. M. Simpson, "Electron Beam and Magnetic Field Mapping Techniques used to Determine Field Errors in the ATF Torsatron," to be published in Rev. Sci. Instrum.

# MAGNETIC SURFACE MEASUREMENT IN CHS

H. YAMADA and the CHS GROUP<sup>1</sup>

Institute of Plasma Physics,  
Nagoya University,  
Nagoya, Japan

## Abstract

The magnetic-field-mapping experiment has been done in CHS. Closed magnetic surfaces have been successfully confirmed up to 95 % of the expected outermost surface and coincided with computed ones within the experimental resolution. Magnetic-island structures seen at the major rational surface ( $\tau = 1/3, 1/2, \text{ and } 2/3$ ) tend to shrink with the increase of  $B_t$ . The experimental results and the computed analyses consistently explain that the error field is the ambient field due to magnetization of the building structure. The  $m = 2$  island width is estimated around 5 mm in ECH experiment at  $B_t = 1\text{T}$ .

---

## 1. INTRODUCTION

Compact Helical System (CHS) is characterized by small aspect ratio <sup>1)</sup>, which leads to fragility of magnetic surfaces in general. Therefore, the strict execution of the engineering design is prerequisite for physics study. During the construction of the machine, extended efforts have been devoted to suppressing error fields in order to realize requisite magnetic field configurations. In particular, choice of small cross-section conductor and employment of the vacuum vessel as frames of the helical-coil windings enable adequate tolerance to electro-magnetic and thermal stresses, highly accurate winding and significant reduction of error fields due to the crossovers and the bus-works<sup>2,3)</sup>. Engineering mission of the accuracy of fields is realization of  $\delta B/B_t \sim 10^{-4}$  in the plasma-confining volume. The dimension and the magnetic-field measurements suggest that the coil alignment is within the tolerable scale ( $\pm 0.5$  mm for the helical coil and  $\pm 3$  mm for the outer two sets of poloidal coils)<sup>4)</sup>. In order to verify designed magnetic surfaces, we have done the magnetic-field-mapping experiment and analyzed the results.

## 2. MAGNETIC SURFACE MAPPING

Magnetic-surface measurement has been done utilizing a fluorescent mesh coated with ZnO and a movable electron gun with acceleration voltage of 200 V. They are away by 150 degree in the toroidal direction. The size of the meshes, which determines our experimental resolution, is 6 mm  $\times$  6 mm and the transmittance is estimated around 90 %. Images of magnetic surfaces on the mesh are observed through CCD TV-camera connected with a micro-channel-plate image intensifier with gain of  $10^4$ . Data are stored on VCR and transferred through the video digitizer with 256  $\times$  256 space to the

---

<sup>1</sup> The members of the CHS Group are identified in the paper entitled 'Overview of CHS experiment', these proceedings, p. 51.

computer, where the pictures are regenerated and analyzed. We have conducted the magnetic field mapping under the steady state field up to 2.4 kG of  $B_t$ . Since two of four sets of poloidal field coils can be energized stationarily, magnetic configurations in the present experiment are limited and the obtainable largest closed surface is expected to be  $\bar{a} \sim 18$  cm while closed surfaces up to  $\bar{a} \sim 21$  cm are expected in the regular operation.

### 3. RESULTS AND DISCUSSIONS

Closed magnetic surfaces are observed apart from major rational surfaces and coincide with computed magnetic surfaces within the experimental resolution (see Fig.1). Although the fragile  $\tau = 1$  surface does not exist in the present experimental condition ( $\tau_a \sim 0.9$ ), fine surface structure is observed up to 95 % ( $\bar{a} \sim 17$  cm) of the outermost surface. The outer periphery is unfortunately out of the sight since clearance between the vacuum-vessel wall and the outermost surface is not sufficiently large in CHS because of introducing pitch modulation.

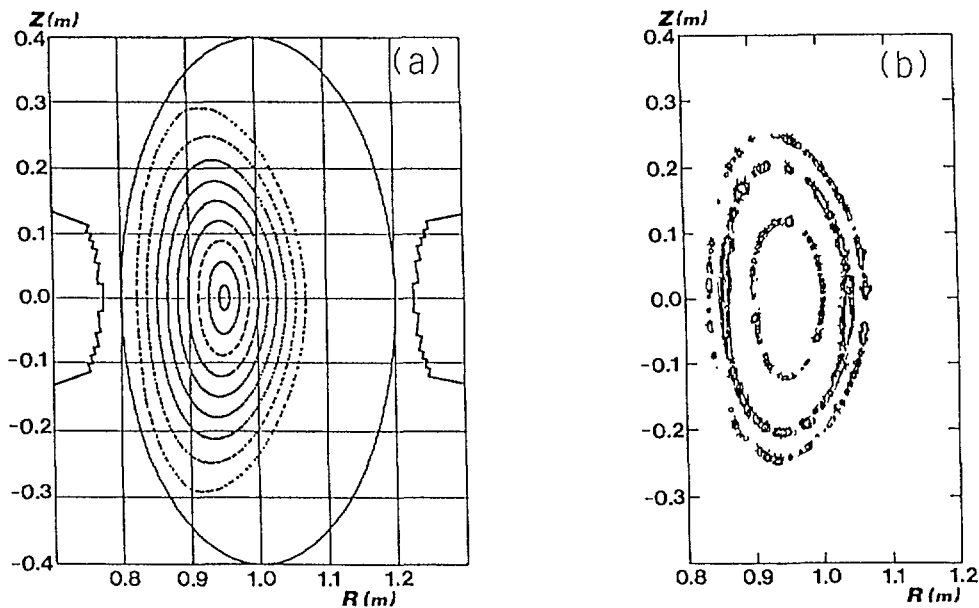


Fig.1 Magnetic surfaces in CHS. (a) Computed surfaces, (b) Experimentally observed surfaces apart from major rational surfaces.

At major rational surfaces ( $\tau = 1/3, 1/2$  and  $2/3$ ), island structures corresponding to the rational numbers are observed (see Fig.2(a)). The width of the  $m = 2$  island at  $\tau = 1/2$  is 3 cm when  $B_t = 440$  G. Figure 2 (b) shows the computed island due to the horizontal error field with 0.2 % of  $B_t$ , which is consistent with the measured ambient field  $\sim 0.9$  G when the coils are not energized. Modeling calculation gives good agreement with the experiment in both the size and the phase of the island. Computational analyses also prove that other possible perturbed fields due to misalignment of the poloidal coils and magnetization of the welded part of the vacuum vessel do not lead to significant macroscopic destruction of magnetic-surface structure. The phase of the  $m = 2$  island does not change for the reversal of  $B_t$  although it should change by 90 degree depending on the direction of  $B_t$  if a fixed

uniform perturbation in the horizontal direction exists. The width of the island, however, tends to shrink with the increase of  $B_t$ . Since the power dependence of the island size on the main field clearly shows proportion to  $B_t^{-1/2}$  in the investigated range of  $0.4 \text{ kG} < B_t < 2.4 \text{ kG}$  (see Fig.3), the error field generating the islands is caused by a factor other than the CHS machine itself. These two observations, immutability of the phase and dependence on the main field strength, are attributed to the reversal of the perturbed field due to the direction of stray flux from CHS. The experimental results and the computed analyses consistently explain that the error field is the ambient field due to magnetization of the building structure. From the present study, we estimated that the  $m = 2$  island, which has the largest width among the observed islands, is around 5 mm in our ECH experiments at  $B_t = 1\text{T}$ .

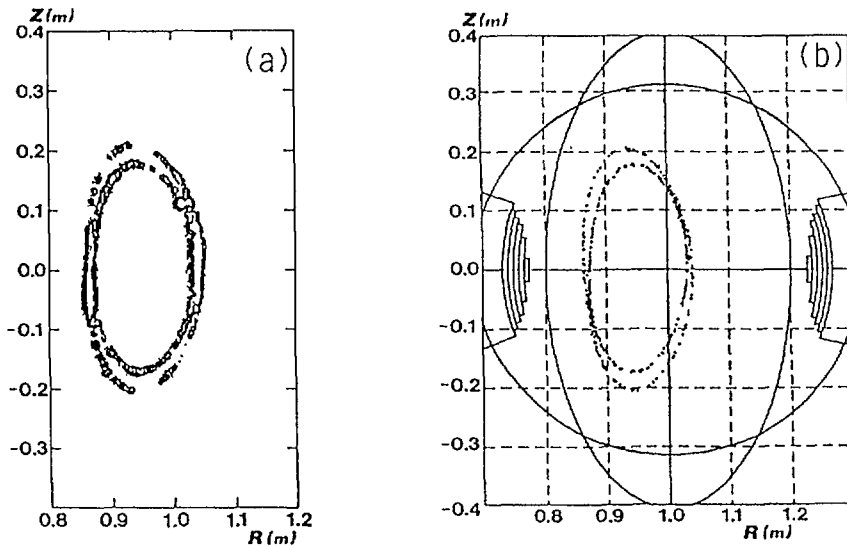


Fig.2  $m = 2$  island structure. (a) Experiment at  $B_t = 440 \text{ G}$ , (b) Computation including the ambient horizontal field  $\delta B/B_t = 0.2 \%$  as an error field.

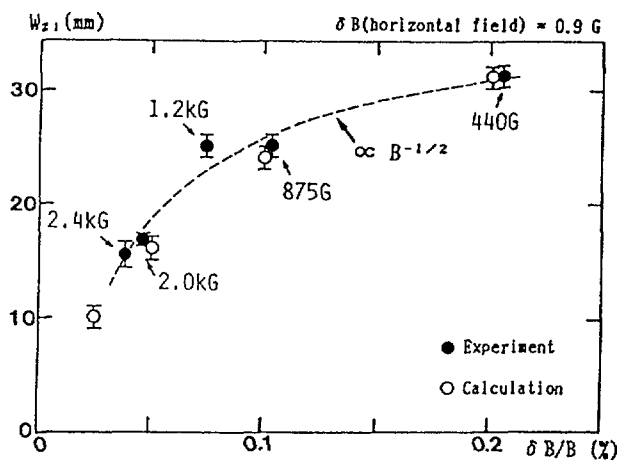


Fig.3 Dependence of the width of the  $m = 2$  island on the strength of the main field. Open circles show the calculated results and closed circles the experiment.

## ACKNOWLEDGEMENT

The authors would like to thank Dr.J.H.Harris at ORNL for useful discussions.

## REFERENCES

- 1) M.Fujiwara et al., in Proc.14th EPS, Madrid, 1987, Vol.2, 404.
- 2) K.Matsuoka et al., in 12th Symp.on Fusion Engr., Monterey 1987.
- 3) S.Imagawa et al., in Proc.15th SOFT, Utrecht, 1988.
- 4) K.Nishimura et al., in Proc.15th SOFT, Utrecht, 1988.

## ELECTRON BEAM MEASUREMENTS IN SHEILA USING A SIMPLE METHOD OF IMAGE INTENSIFICATION

B.D. BLACKWELL, T.Y. TOU  
Plasma Research Laboratory,  
Research School of Physical Sciences,  
Australian National University,  
Canberra, Australia

### Abstract

A simple, cost-effective image-intensifying fluorescent probe and subminiature two-element electron gun have been developed and used in the heliac SHEILA to map its magnetic surfaces. A  $128 \times 128$  pixel CCD camera records the visible image which is accumulated digitally as the fluorescent rod is moved through the magnetic surface. Image-intensification allows the use of a low velocity beam, minimizing drift errors. The gain characteristic and resolution of the intensifier are examined, and result for typical closed and open magnetic surfaces are given.

---

The image intensifying fluorescent rod was developed for the SHEILA heliac allows multiple toroidal circuits of the device without obstruction [1] and then accelerates electrons as they are collected to produce enhanced light output. A phosphor coated stainless steel strip is placed in a 1.7 mm U-channel, and a bias voltage applied. Electrons are launched from a 1.6mm cross-section gun with a 0.7 mm aperture with an energy of typically 8eV. The electron energy remains low in flight (provided that the toroidal EMF is kept small) so that the electron orbit closely approximates a magnetic field line. Because of the high rotational transform ( $\iota$ ) on axis in heliacs, the main deviation of drift surfaces from magnetic surfaces is a distortion in the surface shape, rather than a gross shift. The departure from the true magnetic surfaces in SHEILA has been measured to be <1mm for 8eV, 1200 G. The image intensifier allows a beam of this energy to be used without experiencing energy threshold effects in the phosphor, and allowing enhancements of more than two orders of magnitude over the intensity produced by a 100eV beam if the intensifier accelerating voltage is raised to 1kV (fig. 2).

There are two effects which limit the resolution of this intensifier at high accelerating voltage: a de-focussing of the electron spot at voltages above 300 V, and the leakage of the accelerating field outside the U channel which shields the rod. The fringing electric field can deflect and attract the electron beam slightly and increase the effective collection cross-section for the gun. This effect is used to advantage in SHEILA as a resolution control: when a quick scan of gross features is required, the accelerating voltage can be set high (200-500V) and bright images can be found without the need to set the position of the probe precisely. Fig. 3 show the effect of moderate voltages on the effective resolution. Precise mapping is performed with accelerating voltages  $\sim 50$  V.

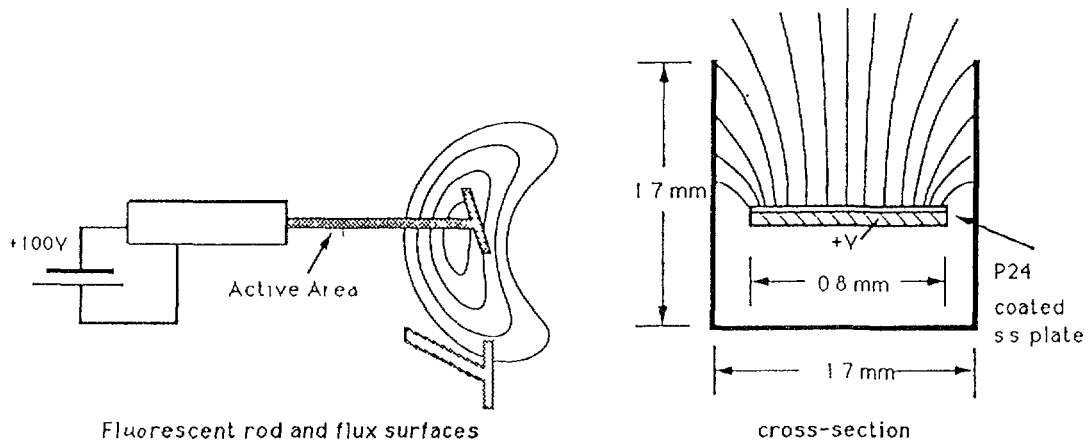


Fig. 1. A schematic and cross-sectional view of the image intensifying fluorescent probe.

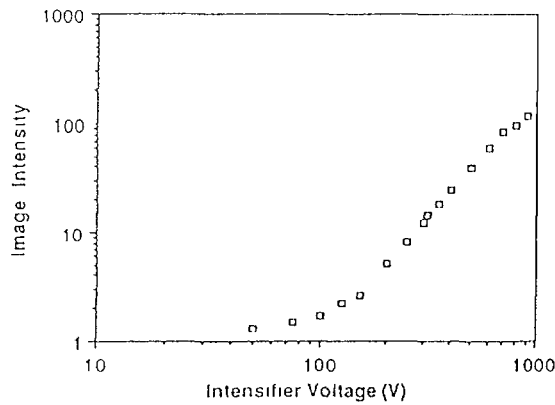


Fig. 2. The dependence of image intensification on applied voltage for a 100eV beam.

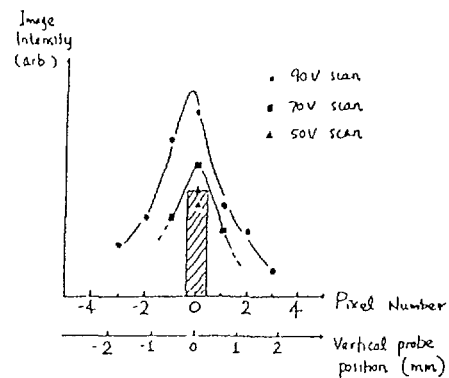


Fig. 3. The defocussing effect for high intensifier voltages.

Time-of-flight measurements are carried out with some slight variations to the experimental setup. The time-resolved information, together with the spatial distribution of the visible electron-beam images, enables calculation of the rotational transform of the magnetic field line.

Figure 4 shows a typical "good" surface mapped by the fluorescent rod. The agreement with the shape computed surface is excellent. Owing to a small horizontal displacement of the centre conductor and the helical winding, error fields are produced which produce some islands and displace the magnetic axis[2]. The position of the surface shown in fig 4, slightly above the median plane, and other surfaces is in agreement with numerical calculations that include the known deviations in the geometry. The agreement degrades as the helical core current is increased; the source of this error is under investigation.

This mapping technique can also be applied to poor surfaces such as those shown in Figure 5, which are close to being open or ergodic because the transform is near the resonance  $\iota = 3/2$ . Some difficulty was experienced mapping the surfaces in the centre of the scan, close to the  $\iota = 3/2$  resonance. A gradual transition can be seen from a closed configuration to a bifurcated configuration and back. Dramatic changes in surface shape can be seen for small changes in current (0.6%), and the changes for 0.2% increments are quite apparent.

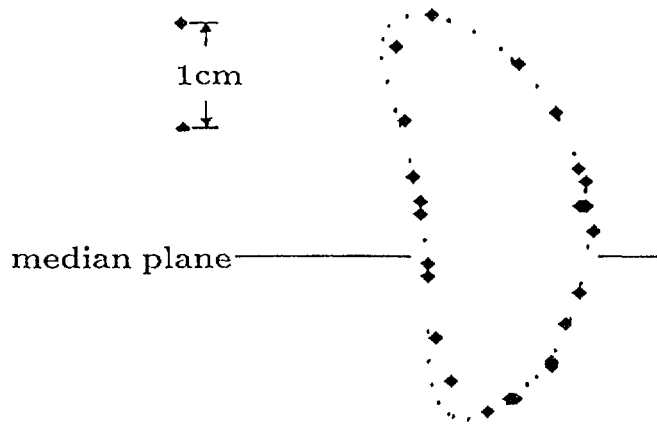


Fig. 4. A measured magnetic surface ( $\bullet$ ) near mid-radius shown in comparison with the corresponding computed surface ( $\circ$ ).  $I_h/I_r=0.029$ ,  $B_0=1200$  G,  $0.6\text{mm}/\text{pixel}$ .

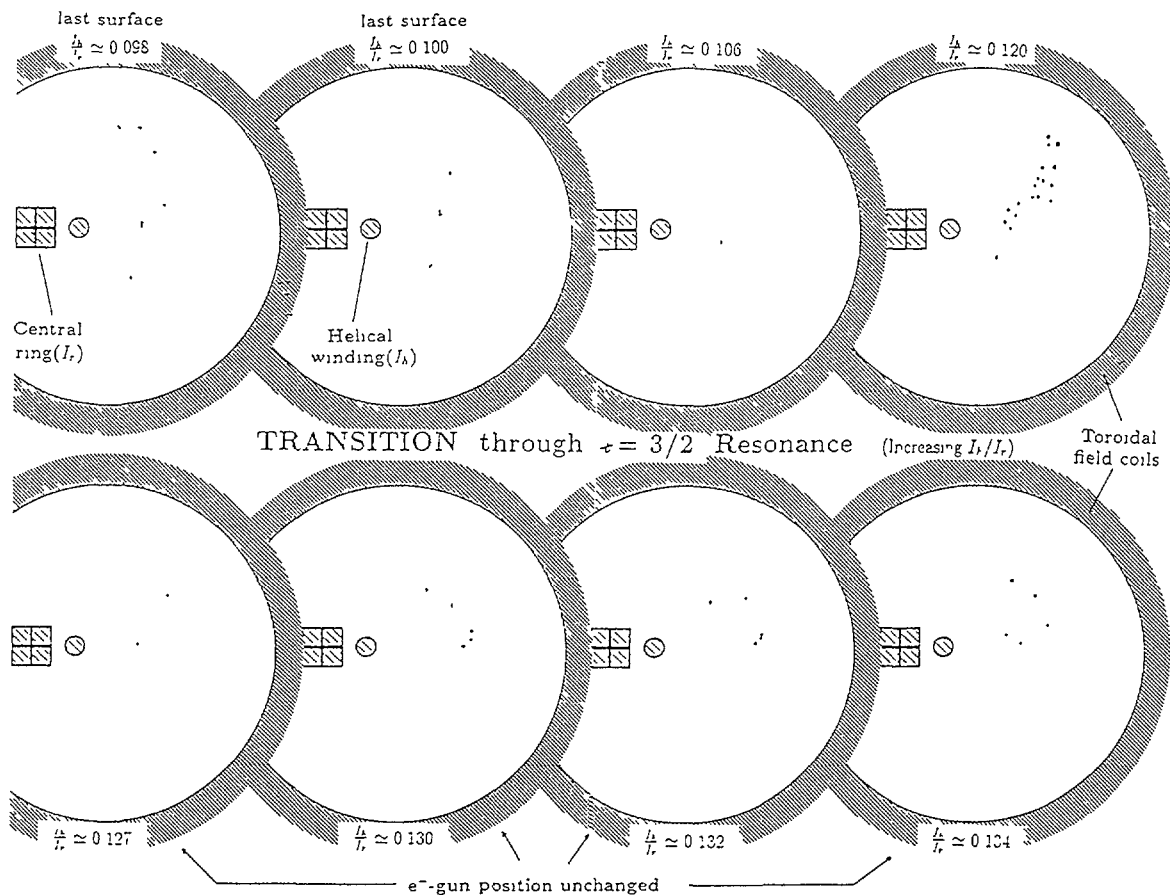


Fig. 5. Flux surfaces showing a transition from closed to open to closed as the helical core current is adjusted in very fine increments to take the rotational transform through the  $\iota = 3/2$  resonance.

## REFERENCES

- [1] H. Hailer, J. Massig, F. Schuler, K. Schworer and H. Zwicker, 14th European Conf. on Controlled Fusion and Plasma Physics, Madrid (1987).
- [2] X. H. Shi, S. M. Hamberger, and B. D. Blackwell, Nucl. Fusion **28**, (1988) 859.

# VACUUM FIELD OPTIMIZATION AND THE EFFECTS OF FIELD ERRORS ON THE FLUX SURFACES OF THE H-1 HELIAC

B.D. BLACKWELL, T.Y. TOU, D.F. ZHOU, L.E. SHARP  
 Plasma Research Laboratory,  
 Research School of Physical Sciences,  
 Australian National University,  
 Canberra, Australia

## Abstract

The H-1 heliac configuration has been optimized for low aspect ratio and minimum |B| ripple by modulation of the toroidal spacing of the toroidal field coils, and by optimization of the vertical field magnitude and index. Two numerical studies of symmetry breaking error configurations are presented, a displacement of the central conductor and a stray field modelled by a dipole. The rate of growth of island size with the error magnitude  $\Delta x$  is found to increase from the expected  $(\Delta x)^{1/2}$  scaling to  $\Delta x$  scaling within the range of errors to be expected for H-1. It is expected that the island size in the central 75% of the plasma volume can be limited to 10mm. We present a preliminary investigation of compensation of the toroidal coil position errors by adjustment of the position of the ring conductor.

## Magnetic Design of H-1

The large number of TF coils per period (12) was chosen to minimize ripple in the outer plasma regions to aid particle confinement. A large swing radius  $\rho_h$  optimizes the plasma size. The resulting small aspect ratio ( $A \sim 5$ ), introduces strong toroidal effects which are partially compensated by modulating the angular spacing of the TF coils. A choice of 3 field periods ( $N=3$ ) allows a practical number of coils ( $N_T = 36$ ).

This design complements that of TJ-II ( $N=4$ , 8 coils/period) in which more emphasis is placed on optimizing the configuration for high  $\beta$ -limits through reducing toroidal effects with a larger aspect ratio and using more field periods to obtain the required rotational transform.

The toroidal angle  $\Phi$  of the TF coils is described by the winding parameter  $\alpha$  as follows

$$\Phi = \Phi' - \alpha \frac{\sin N\Phi'}{N} \quad \text{where} \quad \Phi' = \frac{2\pi(j - \frac{1}{2})}{N_T}, \quad j = 1, 2, \dots, N_T$$

If  $\alpha \sim$  inverse aspect ratio (0.2), then the TF spacing is approximately constant in units of distance. Typical values are  $\alpha = 0.3$ , (design 1), and  $\alpha = 0.35$  (design 2). The primary effect of this modulation is to reduce the toroidal ripple  $\delta_{3,0}$ , by a factor of 5 or more. The overall ripple at the magnetic axis typically falls by a factor of 2-4, or more for a special case discussed later. The secondary effect is to reduce higher order toroidal effects, such as beating between the  $\delta_{3,0}$  component and the basic heliac shape component  $\delta_{3,1}$  to produce the toroidal  $\delta_{0,1}$  component. While this appears effective at very high aspect ratio, the effect in H-1 has been less obvious. The radial variation of these Boozer Fourier components is shown in Fig. 1. Unless otherwise specified, the coil currents have been approximated by circular current filaments distributed as follows: for the toroidal coil set by a filamentary current (at radius 383 mm) in each of the 36 toroidal coils; the poloidal ring by one filament at the centre of the ring core, radius 1m; the helical winding by a single filament of winding law  $R = R_0 + \rho_h \cos(N\phi)$ ,  $z = \rho_h \sin(N\phi)$ , where  $\rho_h$  is the swing radius with respect to the minor axis; and an analytic vertical field  $B_v = B_{v0}(R_0/R)^Y$ .

The vertical field index and value can be adjusted to reduce the magnetic field ripple, particularly at the magnetic axis (Fig 2). The lowest value obtained (0.8%) is at the expense of magnetic well depth.

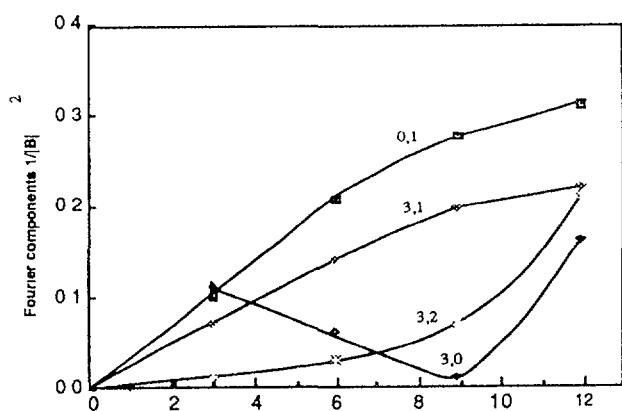


Fig 1: Flux surface parameter x (cm) from MA

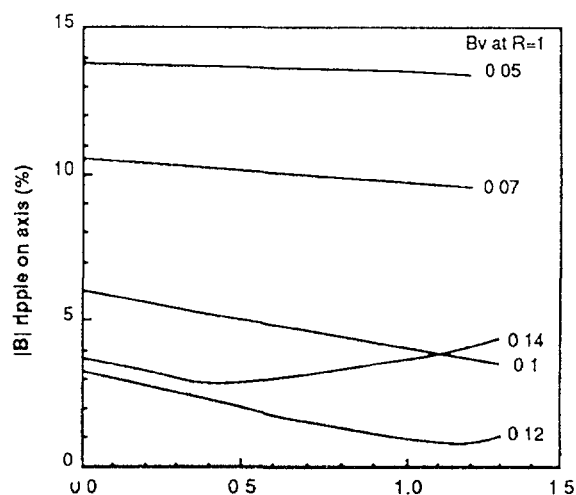


Fig 2 Vertical field index

### Analysis of Error Fields

The presence of perturbations  $\Delta B$  in the magnetic configuration will in general cause small deviations from the ideal shape and position of the surfaces, and introduce small magnetic islands on rational surfaces (Fig. 3). Numerical studies of the effect of such errors have been performed on the ANU Fujitsu VP-100 supercomputer, using a version of the HELIAC computer code [1].

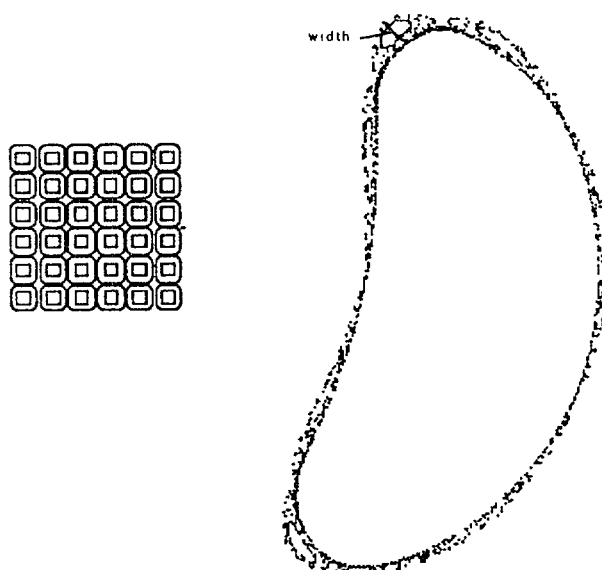


Fig 3 Example of the magnetic islands produced when the central circular conductor is displaced in the y direction by 10 mm

The island size for a given error field grows rapidly with minor radius, and the islands are wider (in cartesian space) near the tips of the heliac bean-shape. For this study, the island width is defined as the maximum width measured in mm, normal to the local direction of the flux surfaces. Fig. 3 shows a set of islands near the outer surface of the plasma with poloidal mode number  $m = 6$ , and toroidal mode number  $n = 7$  (resonant at  $\iota = 7/6$ ), for the standard

[1] Ehrhardt, A.B. "Optimization of the Magnetic Design of Helic", 5th International Workshop on Stellarators, Proc. IAEA Tech. Comm. on Plasma Confinement and Heating in Stellarators, Schloss Ringberg, FRG, II, p717-728, Sept. 1984.  
Ehrhardt, A.B., "Helic User's Guide", Jan 1985 (contact author at PPPL, or B.D.Blackwell)

case of H-1, with error fields introduced by a 10mm displacement of the axis of the ring coil. In this case the surfaces have been displaced downwards at this particular location as a result of the error in ring core position. This displacement of the surfaces, provided it is recognized and allowed for when interpreting measurements, is usually less important experimentally than the islands produced. An exception is when  $t \sim 1$ , where the surface displacement can become very large.

Two cases have been studied in detail. The effect of iron reinforcements in the floor of the H-1 experimental area is simulated by a magnetic dipole located 2m below the midplane of the coil set, at various radial distances (0,1,2 m) from the major axis and at various angles in the plane of the floor. The results are found to depend primarily on the magnetic field strength at a point on the magnetic axis of the machine closest to the error source.

Fig. 4 shows the expected  $\sqrt{\Delta B}$  dependence of the magnetic island size on the dipole strength for error fields much larger than those indicated by measurements of the actual magnetic field near the floor. If these results are extrapolated to the measured field strength, (0.5G - pessimistically assuming all the field measured is due to dipoles), islands no larger than 2mm are expected. This prediction ignores the effect of magnetization induced by the relatively large external magnetic fields produced by H-1 itself (>50G), and of changes in the remanent magnetization.

Results for the second type of error are shown in Fig. 5: here the ring conductor is assumed to be displaced from the major axis of the TF coils. The rate of growth of island size with the error field magnitude  $\Delta B$  is found to increase from the expected  $(\Delta x)^{1/2}$  scaling to  $\Delta x$  scaling within the range of errors to be expected for H-1.

Fig. 6 summarizes the results of the calculations. Once again, the magnitude of the errors has been chosen to be considerably larger than that expected to aid in the identification of the islands. The simulations showed that random displacements and tilts of the TF coils, even when applied to all 36 coils will be a factor of at least 3 times less significant than ring core displacements or tilts. The sensitivity of the configuration to small tilts of the axis of the ring core is about the same as for displacements of the ring of the same magnitude as the greatest

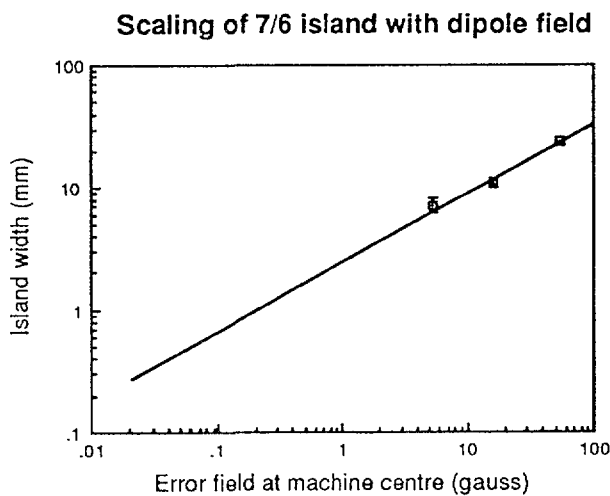


Fig. 4: 7/6 island width plotted against error dipole strength. The solid line shows a  $\sqrt{B_{dip}}$  dependence

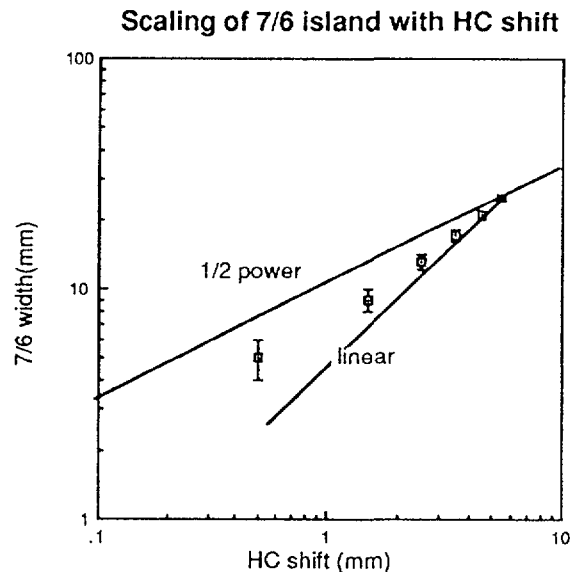


Fig. 5: Scaling of the width of the 7/6 island with central conductor offset. For large offsets, the island grows almost linearly with offset.

vertical displacement caused by the tilt. These calculations have shown that the tolerances for ring tilt and displacement are the most severe: avoidance of islands wider than 5 mm requires accuracies of better than 0.5 mm.

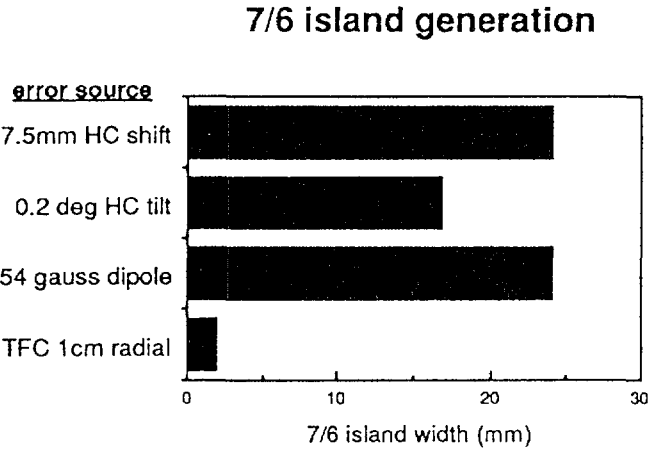


Fig. 6: Summary of the effects of error fields on the 7/6 island.

# CONFIGURATIONAL EFFECTS ON PLASMA CONFINEMENT IN SHEILA

S.M. HAMBERGER, B.D. BLACKWELL, X.H. SHI  
Plasma Research Laboratory,  
Research School of Physical Sciences,  
Australian National University,  
Canberra, Australia

## Abstract

Comparison between the measured plasma configurations and those computed from the coil currents show excellent agreement provided known field errors are taken into account. Low order resonances in a configuration have a strongly adverse affect on plasma confinement. Direct experimental evidence of island formation is seen when  $\iota \sim 3/2$ .

SHEILA is a three-field period heliac (Fig.1) in which 24 two-turn coils, mean radius 6.25 cm, are helically disposed with a swing radius 2.5 cm about a four-turn poloidal field ring conductor ( $R_0 = 19\text{cm}$ ) around which is a single-turn,  $l=1$  helical control conductor wound in phase with the toroidal coil centres and radius 1.4 cm. These, together with vertical field windings are operated in series at  $I \leq 4\text{kA}$ , with the helical current adjusted by means of a shunt between  $\pm 0.25I$ . The coil set is immersed in a stainless steel vacuum vessel (base pressure  $\sim 10^{-6}$  torr). Plasma is generated by gas breakdown ( $\text{H}_2, \text{He}, \text{Ar}, p \sim 10^{-4}$  torr), either by a weak oscillatory ohmic discharge ( $< 100 \text{ A @ } 100 \text{ kHz}$ ) or by an ECRH pulse ( $\leq \text{kW @ } 2.45 \text{ GHz}$ ).

Pulsed plasmas with typical parameters  $n_e \sim 10^{12}\text{cm}^{-3}$ ,  $T_e \sim 10\text{eV}$ , lasting  $\sim 20 \text{ ms}$ , are generated in fields up to 2.5 kG. Fig.2 shows some rotational transform profiles, varied by changing the helical winding current, for configurations in which reproducible plasma can be formed. Articulated probe mechanisms enable the interior bean-shaped flux surfaces to be explored, and quantities such as  $n_e, T_e, n_e, \phi$  to be measured at many known

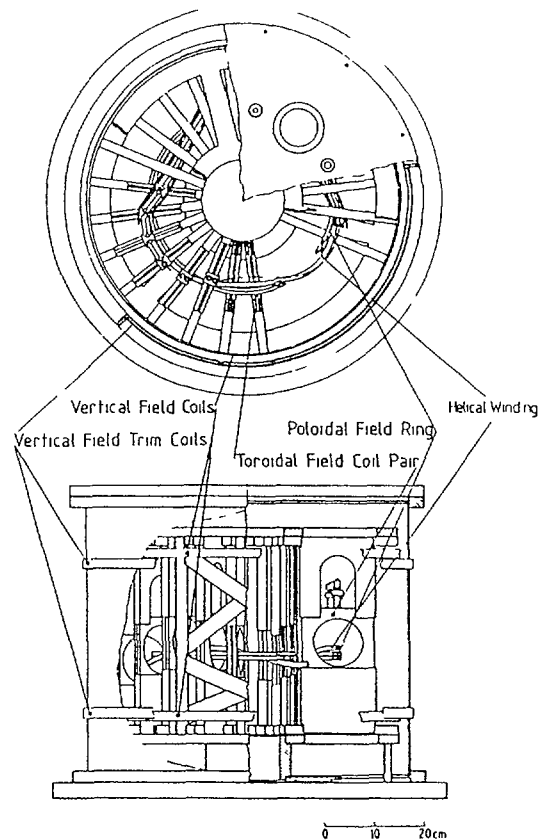


FIG. 1.

locations within the confinement volume. These locations can be referred to appropriate flux coordinates via numerical computation of the vacuum field.

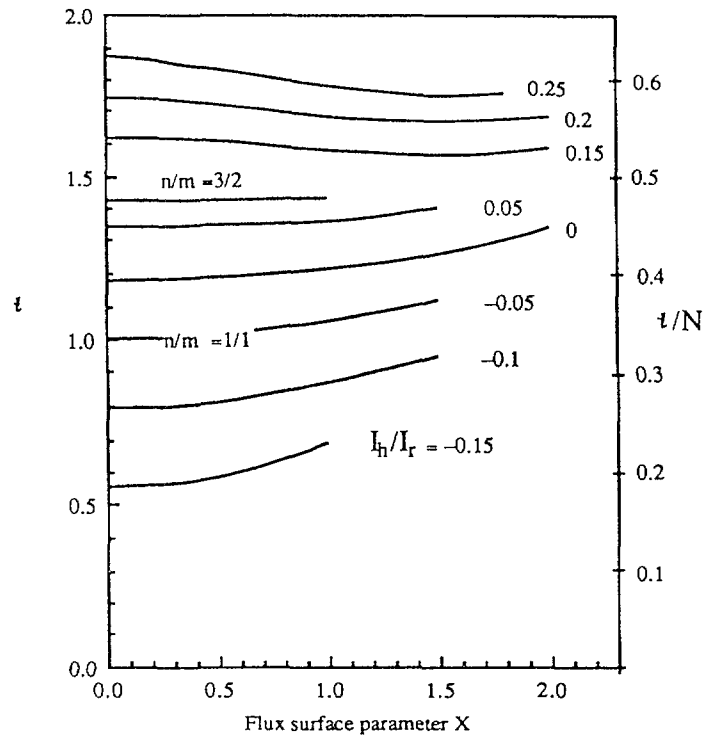


FIG. 2.

In all cases studied, the observed peak plasma pressure occurs at the calculated magnetic axis,  $\Psi = 0$ , (computed to include a known ring positional error) to within an absolute uncertainty (in probe position)  $\sim \pm$  mm.

If probe positions are calibrated by assuming  $(n_e T_e)_{\max}$  occurs at  $\Psi = 0$ , then all measurements show plasma pressure is constant on each computed closed flux surface  $X$ . Some examples are shown in Fig.3 for various configurations.

Fig.4 shows the effect of changing the configuration in the range  $0.5 < \iota < 2$  on both the electric field required for breakdown and on the central plasma density achieved for otherwise constant conditions. The 'worst' conditions for plasma formation clearly correspond to the presence of the low order resonances  $\iota = 1$  and  $\iota = 3/2$ . The case,  $\iota = 3/2$  corresponds to the breaking up of the confinement region into two main islands, while loss of confinement when  $\iota \sim 1$  is related to the complete absence of closed flux surfaces found when the symmetry breaking error is included in the computation. Results from both RF and ECR produced plasmas are essentially the same.

Figs.5 and 6 show density and floating potential profiles obtained for cases ( $\iota \approx 3/2$ ) where island formation is predicted: the discontinuities in both measured profiles occur at places which agree well with the calculated boundaries of the islands.

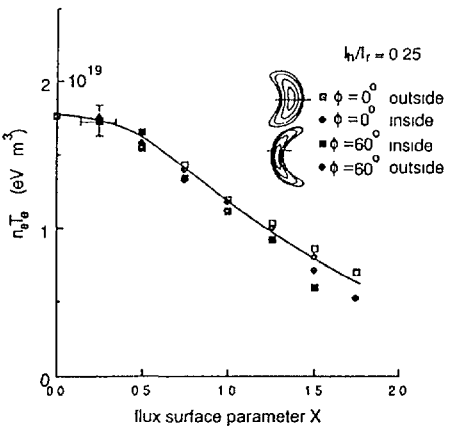
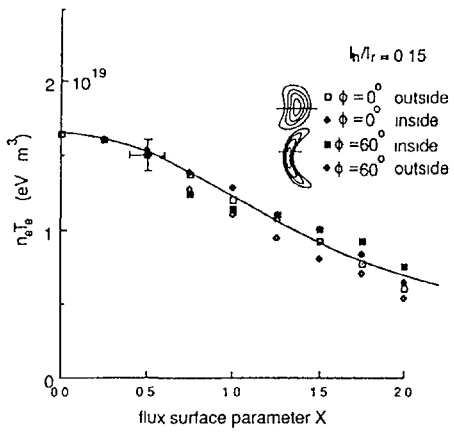
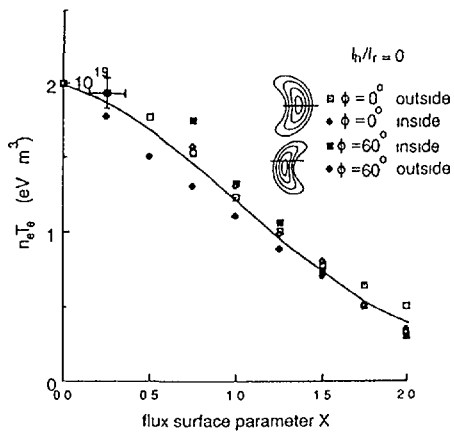


FIG 3

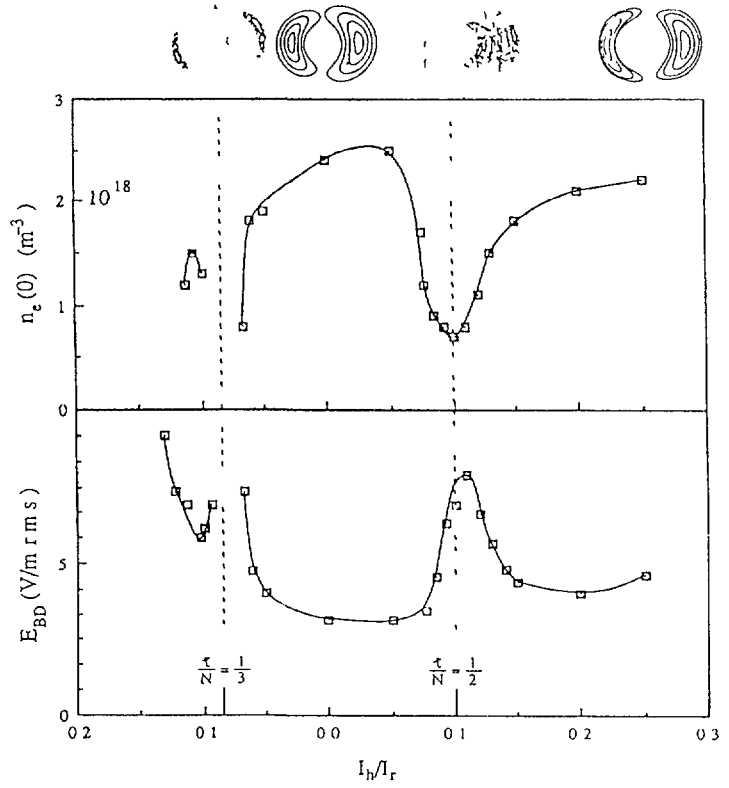


FIG 4

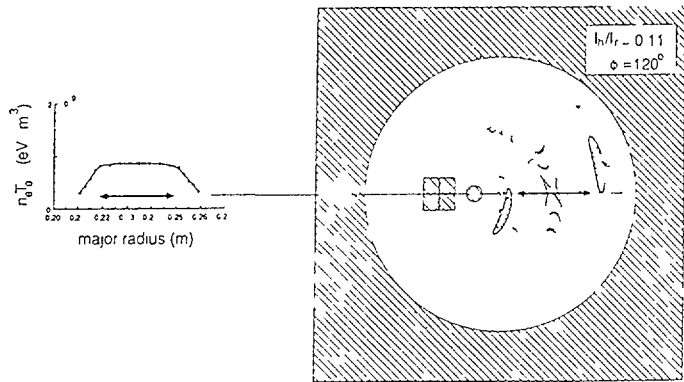


FIG 5

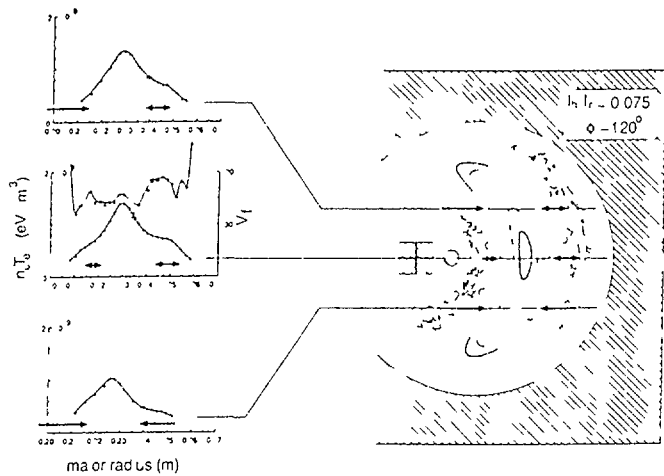


FIG 6.

# SIMPLE METHOD FOR CALCULATING ISLAND WIDTHS

J.R. CARY

Department of Astrophysical, Planetary,  
and Atmospheric Sciences and  
Department of Physics,  
University of Colorado,  
Boulder, Colorado

J.D. HANSON

Department of Physics,  
Auburn University,  
Auburn, Alabama

B.A. CARRERAS, V.E. LYNCH<sup>1</sup>

Fusion Energy Division,  
Oak Ridge National Laboratory,  
Oak Ridge, Tennessee

United States of America

## Abstract

A simple method for calculating magnetic island widths has been developed. This method uses only information obtained from integrating along the closed field line at the island center. Thus, this method is computationally less intensive than the usual method of producing surfaces of section of sufficient detail to locate and resolve the island separatrix. This method has been implemented numerically and used to analyze the buss work islands of ATF. In this case the method proves to be accurate to at least within 30%.

---

## I. Introduction

In the design of helical magnetic confinement systems, it is desirable to obtain a system with nested flux surfaces. That is, one would like there to be neither chaotic regions nor islands. The Cary-Hanson technique<sup>1</sup> allows one to reduce systematically the size of islands while preserving other desirable features of the system, such as reasonable rotational transform, shear, and magnetic well. However, practical constraints, such as power supplies and available space for coil locations, may pre-

clude the complete elimination of islands. Thus, one must calculate the island widths for a given design in order to determine whether it is acceptable. Such calculations are also necessary for comparisons of theory with experimentally observed islands to due, e.g., error fields.

Determination of island widths using standard methods is computationally intensive. Standard methods require the generation of puncture plots with sufficient detail to find a field line just inside, but close to

---

<sup>1</sup> Computing and Telecommunications Division, Martin Marietta Energy Systems, Inc., Oak Ridge, TN 37831, USA.

the island boundary. Then, this field line must be integrated for a sufficiently long time for the points in the surface of section to sample the island boundary well enough that the width can be measured. We have developed a new, computationally less intensive method for calculating the island width. Our method uses only information obtained from integrating along the closed field line at the center of the island.

The method works as follows. Fixed points of the return map, the map of a poloidal plane onto itself obtained by following a field line, are found. Such fixed points are the intersection of a closed field line and the surface of section. The map is linearized about this fixed point. This linearized map, or tangent map, describes the motion of points near the fixed point. The trace of the matrix representing the tangent map determines the eigenvalues of the linearized motion. Complex, unit-magnitude eigenvalues imply that the fixed point is elliptical, and the argument of these eigenvalues determines the rotation rate about the island center. In the small-island approximation, this rotation rate depends on the island width and the shear of the underlying integrable system. The off-diagonal elements of the tangent map, suitably averaged over the iterates of the fixed point, give the shear. Thus, from the tangent map we are able to deduce the island width.

This method has been implemented in the stellarator design code, IFT (Integrable-Field Torsatron). This method was used to analyze the buss work<sup>2</sup> islands of ATF.<sup>3</sup> These islands are moderately well separated. This comparison shows that this method of calculation is accurate to approximately 20% for this case.

## II. Return map and fixed points

The systems we are considering are assumed to be  $m_0$ -fold symmetric in the

toroidal angle to lowest order. Breaking of this symmetry is due to small effects such as coil errors and the ambient magnetic field. The magnetic field-line map is generated as follows. One begins at some point  $\mathbf{X} \equiv (R, Z)$  in a particular poloidal plane defined to be  $\varphi = 0$ . From this point, a field line is followed by numerically integrating the field line equations until  $\varphi = 2\pi/m_0$ . At this value of  $\varphi$ , the poloidal position is  $\mathbf{F}_0 = (F_{0R}(R, Z), F_{0Z}(R, Z))$ . This defines the map for the first period of the torus. There are  $m_0$  such maps, one for each of the periods of the torus. If the periodic symmetry is exact, then these maps are identical.

A fixed point of the map is the intersection of a closed field line with the surface  $\varphi = 0$ . To find fixed points we first introduce the composed map,

$$\mathbf{F}^n(\mathbf{X}) \equiv \mathbf{F}_{n-1}(\mathbf{F}_{n-2}(\dots \mathbf{F}_0(\mathbf{X}) \dots)),$$

in which the convention,  $\mathbf{F}_{i+m_0} = \mathbf{F}_i$ , is used. In the  $m_0$ -symmetric systems, a  $k^{\text{th}}$ -order fixed point,  $\mathbf{X}_0$ , is a solution to  $\mathbf{F}^n(\mathbf{X}_0) = \mathbf{X}_0$  with  $n = k$ . In the nonsymmetric systems, a  $k^{\text{th}}$ -order fixed point is a solution to  $\mathbf{F}^n(\mathbf{X}_0) = \mathbf{X}_0$  with  $n = km_0$ . (Note that symmetry breaking may change the order of a fixed point.) In either case such fixed points may be found by Newton's method. Once the fixed point is found, its iterates, defined by  $\mathbf{X}_{i+1} \equiv \mathbf{F}_i(\mathbf{X}_i)$  may be obtained.

Motion of points near the fixed point is governed by the tangent map,

$$\mathbf{T}_i \equiv \begin{pmatrix} \frac{\partial F_{iR}}{\partial R} & \frac{\partial F_{iR}}{\partial Z} \\ \frac{\partial F_{iZ}}{\partial R} & \frac{\partial F_{iZ}}{\partial Z} \end{pmatrix}.$$

We define the partial composition of the tangent maps via  $\mathbf{T}^0 \equiv \mathbf{I}$ , the identity, and  $\mathbf{T}^k \equiv \mathbf{T}_k \mathbf{T}^{k-1}$ . Composing the tangent

maps,  $M_0 = T_{n-1} \cdot T_{n-2} \cdot \dots \cdot T_0$ , for the entire closed field line yields the motion of nearby points around the initial point of the closed field line.

This tangent map has been extensively studied. (See, e.g., Ref. 4.) When islands are small, the residue,  $\mathcal{R} = [2 - \text{Tr}(M_0)]/4$ , is small. This provides the basis for elimination of islands in three-dimensional systems. The angular rotation about the elliptic fixed points, those with  $0 < \mathcal{R} < 1$ , per  $n$  mappings is given by

$$\delta = \arccos(1 - 2\mathcal{R}). \quad (1)$$

The motion of points near the fixed point has a quadratic invariant,<sup>5</sup>  $\delta X \cdot W_0 \cdot \delta X$ , where  $W_{0ij} = \frac{1}{2}[(M_0 \cdot J)_{ij} + (M_0 \cdot J)_{ji}]$ , and  $J$  is the fundamental symplectic matrix,  $J = \begin{pmatrix} 0 & 1 \\ -1 & 0 \end{pmatrix}$ . Diagonalization of  $W_0$  yields the principal axes of the elliptical invariant curves. The corresponding eigenvalues are  $w_{0\perp}$  and  $w_{0\parallel}$  with  $w_{0\perp}$  being the larger in magnitude. (In the limit of vanishing island the perpendicular direction is perpendicular to the flux surfaces.) We denote the corresponding unit vectors by  $e_{0\perp}$  and  $e_{0\parallel}$ .

### III. Single-resonance model

Field line flow is a Hamiltonian system.<sup>6</sup> Thus, to understand the perturbation of flux surfaces away from the ideal nested case, it is sufficient to study perturbed Hamiltonian systems. The single-resonance model for perturbation of a Hamiltonian provides an accurate description of the major islands in a perturbed Hamiltonian system when the neighboring islands are far from overlapping the island being considered. In this model, the Hamiltonian is

$$H = H_0(\psi) + \varepsilon(\psi) \cos(\theta - m\phi - \zeta(I)), \quad (2)$$

where  $\psi$  is the momentum variable,  $\theta$  is the angle variable, and  $\phi$  is the time. The first term in this Hamiltonian is the integrable

piece, which corresponds to the system with perfect flux surfaces. The second piece induces islands. [In general, the cosine in (2) may be some other periodic function. However, typically the lowest harmonic is dominant, so that only the cosine is needed.] This Hamiltonian (2) has been extensively analyzed.<sup>7</sup> Given the limitations of space we simply state the results of this analysis.

Because the Hamiltonian depends on the angles only through the combination,  $\eta = \theta - m\phi/\ell$ , phase-space structures, such as the island, must have this same dependence. This implies that such structures move ( $\theta = \tau_r \phi + \theta_0$ ) with the velocity,  $\tau_r \equiv m/\ell$ . The resonant value of the momentum (or flux) variable,  $\psi_r$ , is the value at which the unperturbed motion is in resonance with the perturbation, i.e.,  $\tau(\psi_r) \equiv \frac{dH_0}{dI}(\psi_r) = \tau_r$ . Without loss of generality it is assumed that  $\varepsilon(\psi_r) > 0$ .

The width of the island for the Hamiltonian (2) is found by calculating the width of the separatrix. The standard calculation yields the full-width,  $\Delta\psi = 4|\varepsilon/\tau'|^{1/2}$ , the extent of the separatrix at the o-point, in terms of the resonance amplitude and the shear,  $\tau'(I_r)$ . The frequency of rotation about the o-point is found by linearizing the motion near the o-point, and diagonalizing the appropriate matrix. This procedure give a frequency,  $\delta = \ell |\varepsilon(\psi_r) \tau'(\psi_r)|^{1/2}$ , for oscillation about the o-point. From this relation and its predecessor, the amplitude of the perturbation may be eliminated to give  $\Delta\psi = 4 \delta / \ell |\tau'(\psi_r)|$ . This is the width in the flux variable  $\psi$ . To obtain the width,  $s$ , in distance, we use must divide by the gradient of  $\psi$ . This gives

$$s = \Delta\psi / |\nabla\psi| = 4 \delta / \ell |\nabla\tau| \quad (3)$$

Thus, we have the island width in terms of

the shear and the rotation  $\delta$ , which can be calculated from the residue via Eq. (1).

#### IV. Calculation of the shear

The basic idea of the shear calculation is that the tangent map has the form,

$$\mathbf{M}_0 = |\nabla\psi|^2 \mathbf{e}_{0\perp} \mathbf{e}_{0\perp} + |\nabla\psi||\nabla\theta| \mathbf{e}_{0\parallel} \mathbf{e}_{0\perp} + |\nabla\theta|^2 \mathbf{e}_{0\parallel} \mathbf{e}_{0\parallel},$$

to lowest order in the perturbation. Thus, by taking the appropriate element of the tangent map and averaging to obtain the angle gradients, one finds the shear. The averaging over the surface is replaced by averaging over the iterates of the fixed point, which to lowest order are equally spaced in the flux angle. (This approximation assumes that the order of the fixed point is large.) Here we present only the result,

$$|\nabla\psi| = \frac{\mathbf{e}_{0\parallel} \cdot \mathbf{M}_0 \cdot \mathbf{e}_{0\perp}}{C} \left[ 1 + \sum_{k=1}^n \frac{B_{T0}}{B_{Tk} \sqrt{(\mathbf{T}^k \cdot \mathbf{e}_{0\perp}) \cdot \mathbf{W}_k \cdot \mathbf{T}^k \cdot \mathbf{e}_{0\perp}}} \right], \quad (4)$$

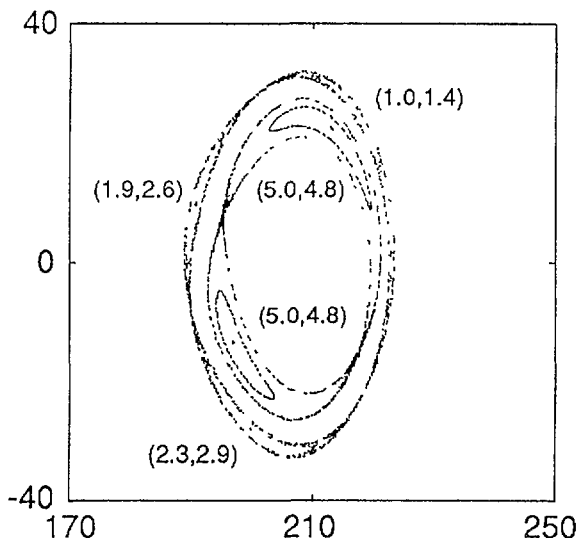
in which  $C$  is the circumference of the polygon defined by the iterates of the map and  $B_{Tk}$  is the toroidal field at iterate  $k$ . Combination of Eq. (2-4) yields the island width in terms of the tangent map.

#### V. Comparison with the buss work islands of ATF

A surface of section for the buss work islands of ATF is shown in the figure below. We have calculated the island widths using two methods. The results of these two methods are the ordered pairs in the figure. The first of the pair was obtained by the direct method of measuring the width of the island across the o-point from the surface of section. The second was obtained via the calculation outlined here.

This comparison shows that the larger, second-order islands are obtained to within 5% by this method, while the smaller, third-order islands are obtained to within 30%.

Likely, the calculation of the third-order islands is less accurate because the presence of the large second-order islands is beginning to make the single-resonance approximation invalid. Conversely, the smaller third-order islands do not affect the second-order islands significantly.



#### VI. Conclusions

We have presented a method for calculating island widths using only that information obtained by integrating along the closed magnetic field line at the center of the island. Thus, our method is much less computationally intensive than the standard method. Our calculation predicts the island widths produced by the buss work of ATF to at least within 30% accuracy even though these islands are within a factor of two of overlapping.

#### References

- 1 J. D. Hanson and J. R. Cary, *Phys. Fluids* **27**, 767 (1984); J. R. Cary and J. D. Hanson, *Phys. Fluids* **29**, 2464 (1986).
- 2 D. K. Lec *et al*, *Bull. Am Phys. Soc.* **33**, 2069 (1988).
- 3 J.F. Lyon *et al*, *Fusion Technol.* **10**, 179 (1986).
- 4 J. M. Greene, *J. Math. Phys.* **20**, 1183 (1979).
- 5 A. J. Lichtenberg and M. A. Lieberman, *Regular and Stochastic Motion* (Springer-Verlag, New York, 1983).
- 6 J. R. Cary and R. G. Littlejohn, *Ann. Phys. (NY)* **151**, 1 (1983).
- 7 B. V. Chirikov, *Phys. Rep.* **52**, 263 (1979).

## **STUDIES OF NEW EXPERIMENTS**

## ENGINEERING ASPECTS OF H-1

B.D. BLACKWELL, S.M. HAMBERGER,  
Y.F. LI, L.E. SHARP, B. SHENTON  
Plasma Research Laboratory,  
Research School of Physical Sciences,  
Australian National University,  
Canberra, Australia

### Abstract

The flexible heliac H-1 has its coil assembly and support structure located inside a vacuum baked chamber. The position of the toroidal field coils have limited adjustment while the poloidal field coil can be remotely adjusted in angle and position during final alignment before being locked into place. The maximum deflection of any coil is  $<1.8\text{mm}$  at  $B=1\text{T}$ . The device can also operate continuously at  $B=0.25\text{T}$ .

H-1 is a medium sized, three period heliac:  $R_0/a = 1.0/0.22\text{m}$ ,  $B \leq 1\text{T}$  (pulsed),  $0.25\text{T}$  (dc). The thirty-six toroidal field coil assembly located on a helix of  $R_0=1.0\text{m}$  with a swing radius  $\rho=0.22\text{m}$ , is mounted inside a  $4\text{m}$  high stainless steel vacuum chamber comprising a central cylindrical section ( $2\text{m}$  high,  $3.8\text{m}$  diameter) and spherically domed ends. (Fig 1). The  $11$  tonne coil and support structure rests on three tubular pillars which transmit the weight through the vacuum vessel to the floor and support the tank.

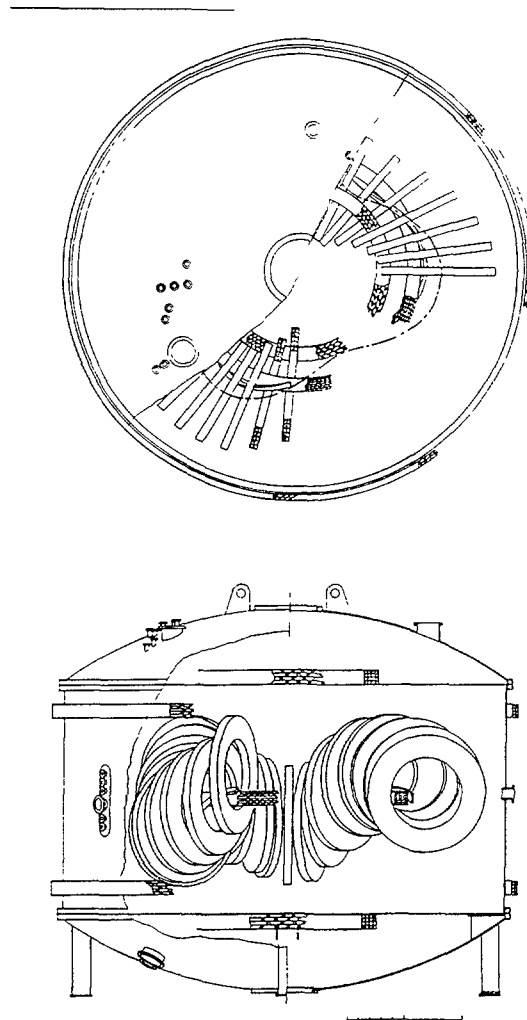


Fig 1. H-1 experimental assembly

Each toroidal field coil (Figs 2 and 3) consists of a double pancake of  $10$  turns of  $30\text{mm}$  square copper with a  $6\text{mm}$  cooling hole, wound with a mean radius of  $0.38\text{m}$ . The coil is sheathed in a  $1.2\text{mm}$  thick stainless steel, fully

welded canister whose inner clear radius is 0.28m and (toroidal) thickness is 65mm. Glass tape and Nomex provide primary insulation and the whole can is vacuum filled with Dow Corning Sylgard 701.

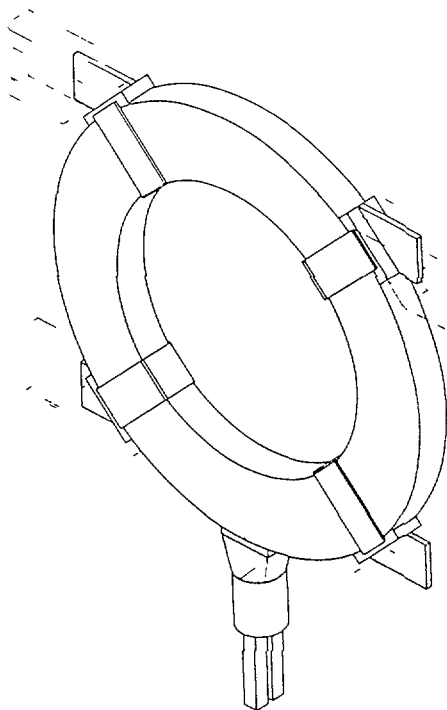


Fig 2 Toroidal field coil.

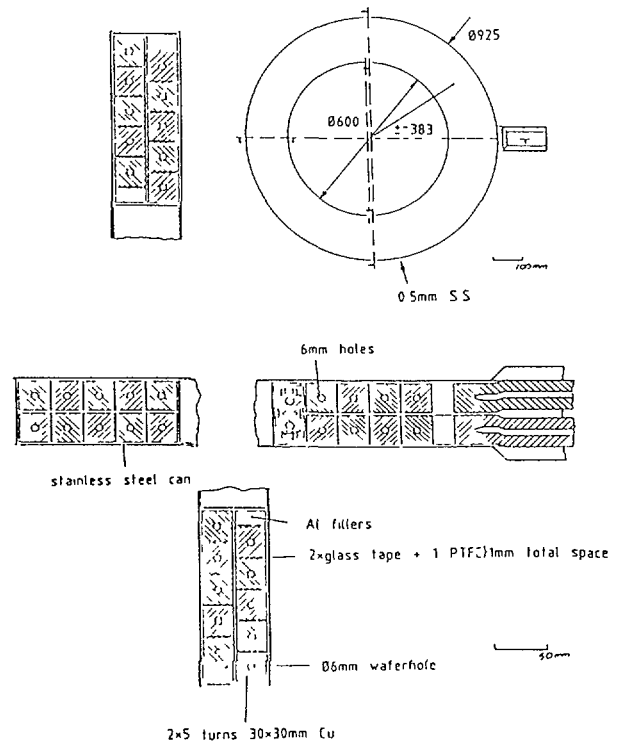


Fig 3 Construction of toroidal field coil.

The poloidal field coil is wound horizontally in situ inside the toroidal coil assembly (see Fig1). and consists of 36 turns of 17.5mm square copper with a coolant hole. The 36 turns are grouped into 3 double pancakes assembled horizontally side by side with each group having a separate current feeder, allowing coarse control of the poloidal field coil current (Fig.4). The principal insulation is Kapton with Nomex sheet separating each 6 turn layer. The whole coil assembly is again sheathed in stainless steel and vacuum filled as before. A four turn helical control winding surrounds the poloidal field coil at a radius of 98mm.

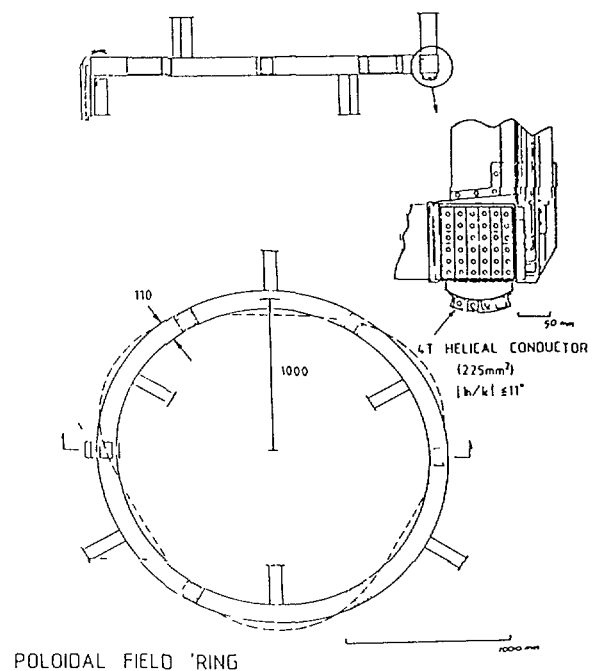


Fig 4 Construction of poloidal field coil.

Two four-turn vertical field coils (mean diameter 1.4m) made with the same fabrication technique as the toroidal coils, are located inside the tank with two four-turn coils outside at a mean diameter of 4.0m. (Fig 1).

A rigid space frame structure constructed from tubular section stainless steel supports all internal coils and allows limited spatial adjustment in the vertical and radial planes (Fig 5). The space frame consists of a central triangular column welded to a box section base, and an outer frame connected by horizontal webs to the upper part of the central structure (Fig 6).

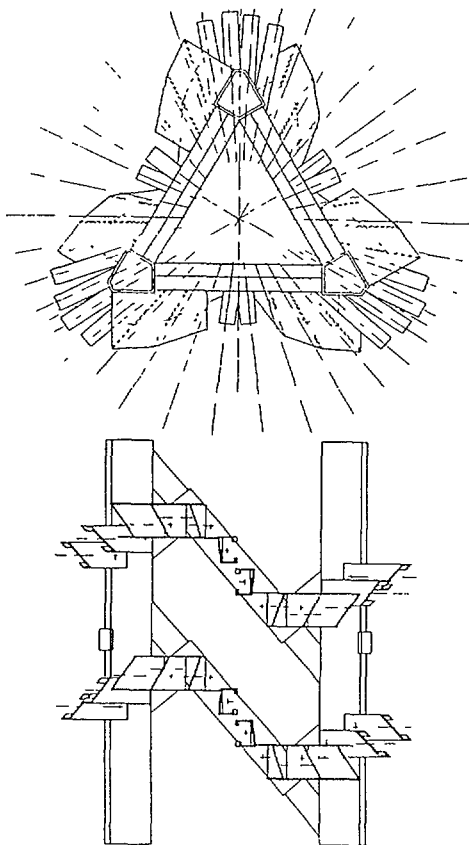


Fig 5 Central support column

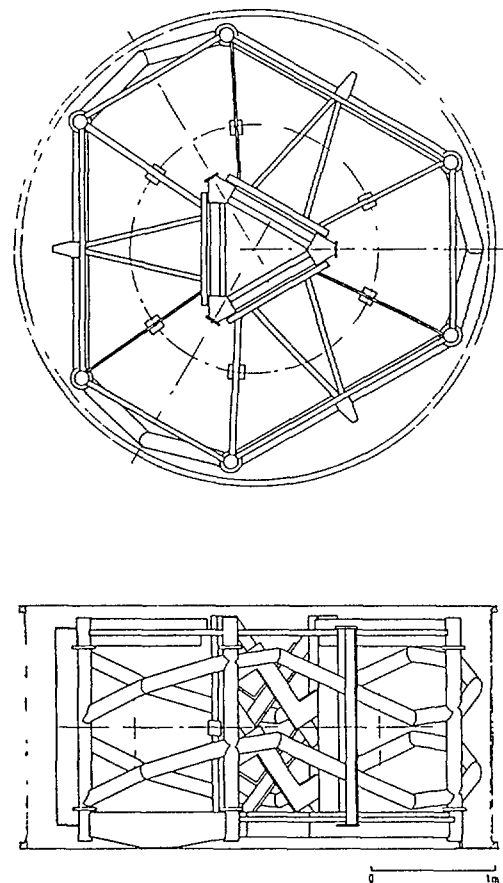


Fig 6. Coil support structure

Finite element stress analysis of the total system including the toroidal and poloidal field coils (Fig 7) has been used to determine the deflections of the various components due to electromagnetic forces and to gravity. These are tabulated in Table 1 and indicate a maximum coil deflection due to electromagnetic forces of less than 2mm.

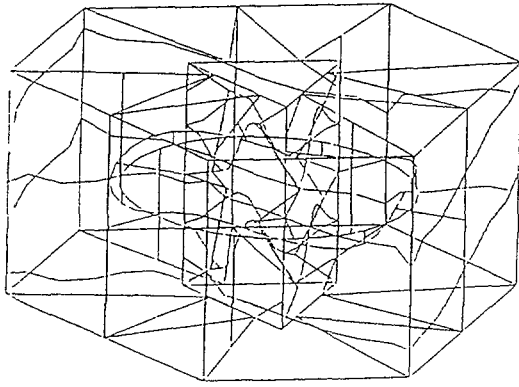


Fig 7a Finite element model of support structure

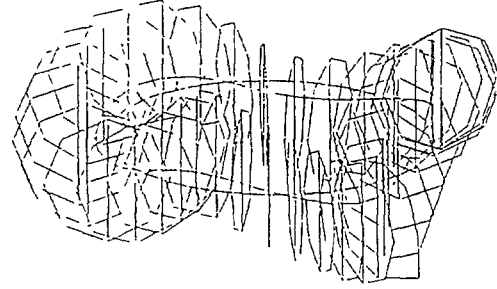


Fig 7b Finite element model of coil system

TABLE I  
Deformations in mm

Load Case	Gravity only		Electromagnet Forces only		Combined Gravity and electromagnenc	
	Vertical	Horizontal	Vertical	Horizontal	Vertical	
IF Coils						
Smallest value	Coil 11, -0.56	Coil 9, 0.08	Coil 9, 0.001	Coil 7, 0.14	Coil 7, 0.65	
Greatest value	Coil 7, -0.65	Coil 2, 1.53	Coil 7, -0.28	Coil 2, 1.53	Coil 2, 0.84	
PF Coils						
Upper support	-0.58	0.18	-0.86	0.18	-1.43	
Lower support	-0.54	0.14	0.72	0.14	0.19	
Inner support	-0.52	0.22	-0.11	0.22	-0.63	
Outer support	-0.62	0.27	-0.02	0.27	0.63	
Maximum Deflection between supports	-0.52	0.16	0.30	0.17	0.22	
Helical winding	-0.59	0.64	0.40	0.64	-0.20	
CSS						
Outer vertical column	-0.60	0.06	-0.01	0.04	-0.61	
Outer diagonal beam	-0.55	0.29	0.05	0.26	-0.50	
Inner vertical column	0.64	0.09	-0.03	0.09	-0.66	
Inner diagonal beam	0.65	0.19	0.006	0.19	-0.64	

The forces on the toroidal coils are diagrammatically shown in Fig 8 for a representative set of 8 coils.

The 9.4MW power required for 1T pulsed operation is provided from the mains using 4 six-phase grid controlled arc rectifiers which supply 13.5 kA through all coils connected in series. Continuous operation at reduced field can also be obtained using a 1MW motor generator. The vacuum tank reached a base pressure of  $1.2 \times 10^{-8}$  torr without bake-out using two 2,200 l/s turbo pumps. All exposed surfaces are mechanically polished to approximately  $0.6 \mu\text{m}$ . The whole device can be baked up to  $150^\circ\text{C}$  using pressurized hot water in the coils and heating pipes on the outer surface of the tank.

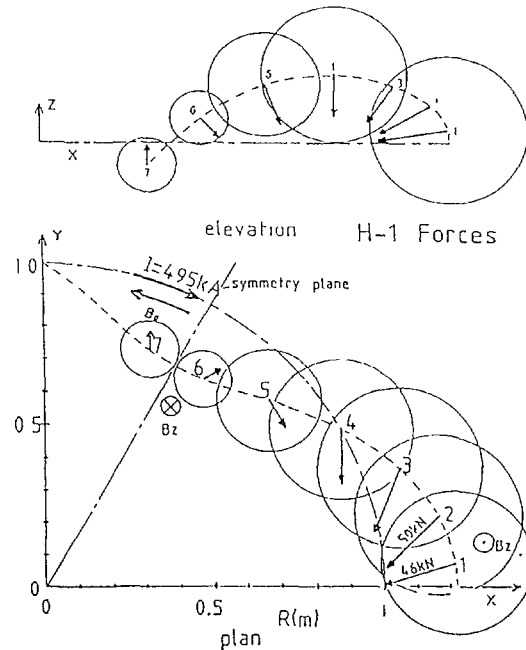


Fig 8 .The resultant electromagnetic forces on 8 coils.

At present Viton A O-rings seal the main two joints. We have the option of replacing the O-rings with sacrificial welds if it is found necessary.

The machine control system is based on IBM -AT personal computers with touch screen monitors ( Fig 9). The computers are interfaced through CAMAC by an opto -isolated parallel ring system which delivers the latched instruction set between machine discharges to up to 16 remote data handing stations. Each station can handle up to 32 function modules with differing tasks. eg, A-D converters, D-A converters, input/output opto-isolated relays. In addition to controlling the machine parameters eg .peak magnetic field, timing sequences, gas pressure, etc. the control system monitors the parameters which effect the safety of the machine , eg coil water flow and temperature, vacuum integrity, power supply voltage and current, and can initiate shut down procedures in the case of emergencies. In parallel with this computer control system is a simple manual system which will allow the machine to operate in a limited operational range.

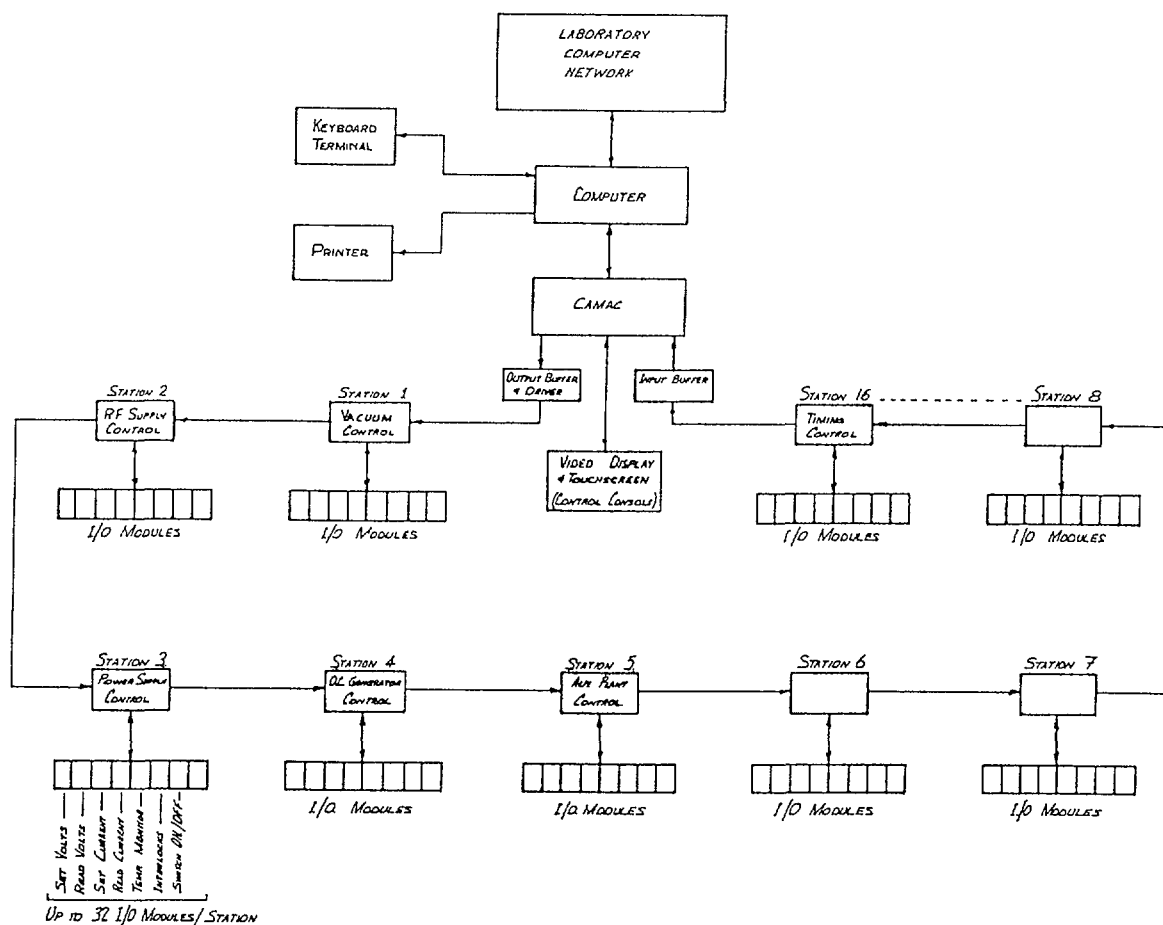


Fig 9 Block diagram of H-1 control system.

# EXPERIMENTAL EQUILIBRIA, INDUCED AXIAL CURRENTS, AND NUMERICAL STUDIES OF SIMULATED TOROIDICITY IN LINEAR HIGH-BETA HELIACS\*

B.A. NELSON, B.G. MILLER, G. SPANJERS,  
F.L. RIBE, D.C. BARNES<sup>1</sup>, R. BISHOP<sup>1</sup>  
University of Washington,  
Seattle, Washington,  
United States of America

## Abstract

A 3 m linear high-beta ( $\langle\beta\rangle = 0.3$ ) heliac equilibrium is produced in the High Beta Q Machine (HBQM) theta pinch when the hardcore center conductor current rise time is within a factor of two of that of the main  $l = 1$  compression coil. However, this fast-rising hardcore current is found to induce an oppositely directed net longitudinal current in the heliac plasma, which presumably returns along an outer resistive plasma layer on the inside of the discharge tube.

This induced current and its effect on the rotational transform have been studied in an induced-current experiment on a cylindrical hardcore  $\theta$ -pinch (no  $l = 1$  fields). The axial current and its return are measured with internal  $B_\theta$  magnetic probes. In future linear heliac experiments on the HBQM, the heliac plasma formation will utilize a programmed (or "notched") hardcore current circuit to eliminate the return current.

Simulation of a toroidal heliac is proposed by offsetting (shifting) the hardcore from the geometrical  $l = 1$  stellarator axis. This represents the helical symmetry breaking effect of a large aspect ratio torus. Numerical studies have been performed to investigate the shifted-hardcore vacuum magnetic field lines, as well as the finite-beta plasma build-up on these flux surfaces. Future numerical studies are aimed at determining the time scale of magnetic-island formation in the shifted-hardcore linear heliac plasmas.

---

## 1. MACHINE DESCRIPTION

The High Beta Q Machine[1] is a 3 m low compression  $\theta$ -pinch with two available segmented coils sets: A cylindrical  $\theta$ -pinch set with coil radius  $r_c = 0.11$  m, and an  $l = 1$  stellarator set with  $r_c = 0.1$  m, helical axis radius  $r_{ha} = 0.02$  m, and helical period  $L = 0.4064$  m. The current for these compression coil sets (main bank current) is produced by a  $9 \times 0.4 \mu\text{F}$  capacitor bank, charged to 85 kV, and switched through LANL staged  $\theta$ -pinch cylindrical rail gaps (the current start time defined as time  $t = 0$ ). The current rises to 850 kA with a quarter-period risetime of  $\tau_{1/4} = 500 \mu\text{s}$ , and is then crowbarred with parallel gaps, producing an axial vacuum magnetic field of 0.35 T.

An axial hardcore conductor (5 m long, 9.5 mm diameter Al rod) was used for the experiments described here, carrying a current of  $I_{HC} \sim 15 - 20$  kA,  $\tau_{1/4} = 1.1 - 1.3 \mu\text{s}$ , switched by  $2 \times 1.8 \mu\text{F}$  capacitors with Syllac gaps through a 5:1 turn bitter plate trans-

---

\* Work supported by the US Department of Energy under grant DE-FG06-87-ER53242.

<sup>1</sup> SAIC, Inc., Austin, Texas, USA.

former and crowbarred at maximum current. The hardcore when operated in conjunction with the  $l = 1$  or the  $\theta$ -pinch coils, produced vacuum magnetic fields with a heliac geometry or a screw-pinch like geometry, respectively.

Plasmas were produced by 260 kHz ringing preionization (PI) of deuterium filling pressures of  $4 \text{ mT} < P_o < 15 \text{ mT}$ . The 3.4 m long compression coil set matching quartz discharge tube used (0.2 m ID cylindrical for the  $\theta$ -pinch coils, 0.22 ID helical for the  $l = 1$  coils) was evacuated to  $5 \times 10^{-8} \text{ T}$  by a turbomolecular pump.

### 1.1. Diagnostics

Miniature three-dimensional internal magnetic field probes (6 mm OD quartz jacket protruding radially 4 – 6 cm into the plasma) were used to locally measure  $B$ . Probe perturbation effects were checked with external flux loops and external field probes and were found to be minimal. The raw signals were passively integrated,  $\tau_{RC} = 0.25 \text{ ms}$ , and mapped onto a single plane (from several axial locations) using helical symmetry ( $u = \theta + hz$ ,  $h = 2\pi/L$ ) in the heliac, and onto a single radius (from several probe angles) using axisymmetry in the hardcore  $\theta$ -pinch. Local plasma currents were deduced from the  $B$  measurements by using  $\oint \mathbf{B} \cdot d\mathbf{l}$  around a flux surface, bean shaped in the heliac and circular in the hardcore  $\theta$ -pinch.

Global plasma parameters were provided by axial heterodyne quadrature laser interferometry, flux loops, and external magnetic field probes. Typical plasma parameters were  $n \sim 0.5 - 1.0 \times 10^{21} \text{ m}^{-3}$ ,  $T_e + T_i \sim 80 - 100 \text{ eV}$ , and plasma lifetimes on the order of  $10 - 15 \mu\text{s}$ .

## 2. HELIAC EQUILIBRIUM

A fast risetime hardcore current rising concurrently with the main bank current was found necessary to produce a high  $\beta$  heliac equilibrium,[1] Fig. 1. (A slower rising hardcore current, initiated earlier than the main bank current, trapped an axisymmetric plasma around the hardcore itself.) The peak beta was  $\beta \sim 0.5$  with the magnetic axis located at  $r_{ma} = 0.035 \text{ m}$ . A Shafranov shift of  $\Delta_s = 0.005 \text{ m}$ , relative to the vacuum magnetic axis, was observed.

### 2.1. Induced axial current

The hardcore current was found to induce an axial current in the heliac plasma. The preionization of the deuterium filling gas provided a helical plasma conductor to allow an axial Faraday's law current to be produced during the hardcore current risetime. The induced plasma current was in the opposite direction to the hardcore current, and had an initial peak of approximately 12 kA.

The induced current was found to flow in one direction through the heliac bean, as seen in Fig. 2-a. The return current was presumed to be along the inner wall of the discharge tube. The induced plasma current decayed away more quickly than the hardcore current circuit decay time, consistent with the presumed resistive return path through the low temperature plasma near the discharge tube wall. The induced axial current modified the heliac's rotational transform profile, Fig. 2-b, from nearly shearless in vacuum to highly sheared in plasma.

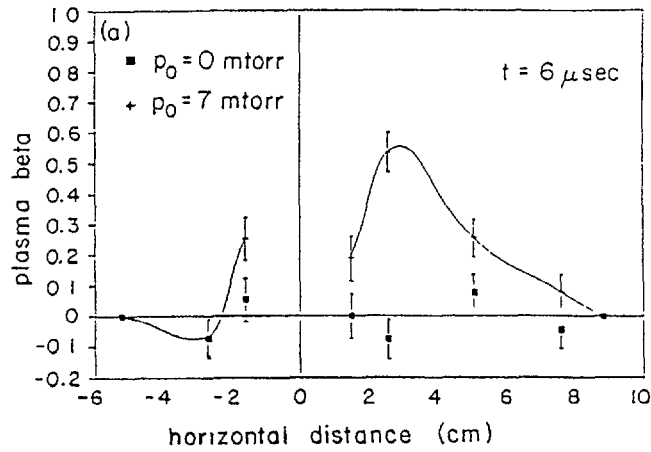


Figure 1. Linear Heliac plasma beta vs. distance from the hardcore center conductor.

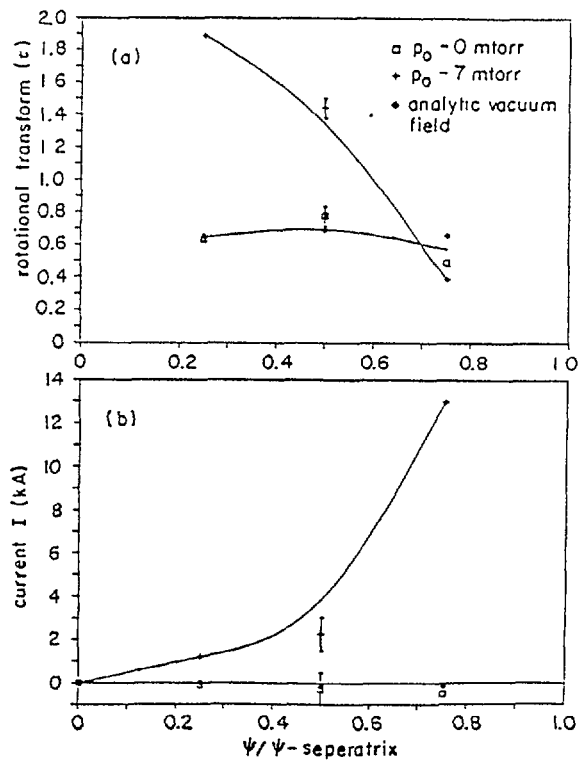


Figure 2. a) Rotational transform, vacuum and plasma.  
b) Induced axial current in linear Heliac.

### 3. HARDCORE $\theta$ -PINCH EXPERIMENT

To study the nature of the induced axial current and test a proposed method of eliminating it, a hardcore  $\theta$ -pinch experiment was performed. The measured plasma equilibrium was an annulus with peak pressure at  $r \sim 0.02 - 0.03$  m.

### 3.1. Induced current measurements

Using the assumption of axisymmetry, the  $B_\theta$  probe measurements were multiplied by  $2\pi$  times their radius to give the total normal current piercing a loop of the probe radius. Subtraction of the hardcore current from this total normal current yielded the net induced plasma current within the probe radius. These  $B_\theta$  measurements were made at several radii 0.4 m inside of the end of the coil set (Fig. 3) and show the induced plasma current to be small near the hardcore, increase to 6 kA at  $r = 0.045$  m, ( $I_{HC} = 11$  kA at this time,  $t = 5 \mu\text{s}$ ) then decrease back to low values at larger radii. The net current density (also in Fig. 3) derived from this total net current shows the induced current and its return to flow through the plasma annulus itself (*i.e.* not returning at the wall as was the case in the heliac).

Measurements of  $B_\theta$  at several axial locations showed the induced current to decrease near the end of the coil, and to be completely gone 0.1 m outside the coil.

### 3.2. Proposed elimination of induced axial current

To produce a currentless heliac on the HBQM, it is proposed to use a slow risetime hardcore current (using ignitron switches) in series with the fast hardcore transformer circuit. The slow circuit would be initiated before the main bank current, using the fast circuit to: 1) reduce the current to zero, inducing an axial current in the PI plasma, then 2) bring the hardcore current back up simultaneously with the main bank current, producing both pressure in the heliac bean *and* removing the already induced plasma current. The hardware for the notched hardcore experiment is presently under development.

## 4. SIMULATED TORIODICITY STUDIES

A vacuum magnetic field line solving program, HELIK,[2] found the field line structure and Boozer harmonic structure to be quite similar between a large aspect ratio toroidal heliac, Fig. 4-a, (without a helically wound ring conductor) and a linear heliac with a "shifted" hardcore, Fig. 4-b, (*i.e.* the hardcore is translated off center from but parallel to the  $l = 1$

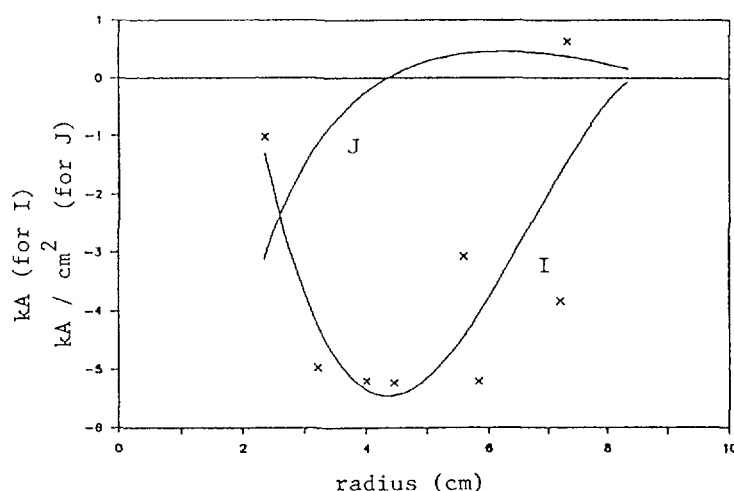


Figure 3. Induced axial current,  $I$ , and current density,  $J$ , for the hardcore theta-pinch.

coil geometrical axis). The similar loss of helical symmetry for both of these cases can be seen from the partial recovery of flux surfaces *via* an inward shift of the toroidal hardcore, Fig. 4-c. The empirical relationship between the major radius,  $R$ , of the toroidal heliac and the shift,  $\delta$ , of the hardcore in the linear heliac is  $R\delta = 0.371 \text{ m}^2$ . It is proposed to study island formation and evolution in a toroidal heliac by simulating the toroidicity in a shifted-hardcore experiment on the HBQM.

#### 4.1. Desired currentless heliac equilibrium

The characterization and elimination of the induced plasma currents are deemed crucial for the simulated toroidicity experiments on the HBQM. It is desired to produce islands in the heliac plasma by the helical symmetry breaking, but these islands are predicted to produce axial currents and grow[3], thus we wish to study them in an initially currentless heliac. The notched hardcore  $\theta$ -pinch study will provide the basis of induced current elimination in the shifted hardcore heliac experiment.

#### 4.2. ISLE code results

The ISLE code is under development to study the build-up of pressure in the shifted hardcore heliac experiment. A helically symmetric pressure profile is loaded onto the shifted hardcore vacuum magnetic field lines. Using the finite-pressure resistive MHD equations:

$$\frac{\partial \mathbf{A}}{\partial t} = \mathbf{u} \times \mathbf{B} - \eta \mathbf{J}, \quad \rho \frac{\partial \mathbf{u}}{\partial t} = \mathbf{J} \times \mathbf{B} - \nabla P, \quad \frac{\partial P}{\partial t} = -\nabla \cdot P\mathbf{u} + H$$

$$H = \begin{cases} P_o(\mathbf{r})/\tau_\eta & \text{inside separatrix} \\ -P/\tau_\eta & \text{outside separatrix} \end{cases}$$

where  $\mathbf{A}$  is the vector magnetic potential,  $\mathbf{B}$  the magnetic flux density,  $\mathbf{J}$  the current density,  $\mathbf{u}$  the MHD fluid velocity,  $P$  the plasma pressure,  $P_o(\mathbf{r})$  is the initial helically symmetric pressure,  $\rho$  and  $\eta$  are the plasma mass and resistivity (both held constant), and  $H$  is a source or sink term, depending on the location in a constant  $z$  plane. The profiles are Fourier analyzed in  $\theta$  and  $z$ , and finite differenced in  $r$ . The vector potential  $\mathbf{A}$  is advanced using a semi-implicit time difference method.

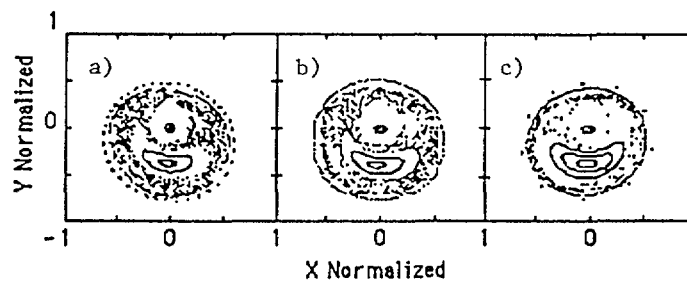


Figure 4. HELIK vacuum flux surfaces for a) 2 cm hardcore shift linear heliac, b) toroidal heliac,  $R = 1.86 \text{ m}$ , and c)  $R = 1.86 \text{ m}$  toroidal heliac with 2 cm inward hardcore shift.

Initial results show the evolution of constant pressure contours from the symmetrically loaded pressure at time  $t = 0$ , Fig. 5-a, to quasi-equilibria 200 Alfvén times later,<sup>1</sup> for no hardcore shift, Fig. 5-b, and a 1 cm hardcore shift, Fig. 5-c. Note the asymmetry in Fig. 5-c, resulting from helical symmetry breaking. These results are planned to guide magnetic probe data taking strategies, as the previous method of using helical symmetry to map data at several axial locations to one plane cannot be used.

ISLE is presently being modified to specifically study island formation and evolution. Helically symmetric fields near the hardcore will be interpolated onto shifted fields near the  $l = 1$  windings, allowing islands to form and evolve near this boundary.

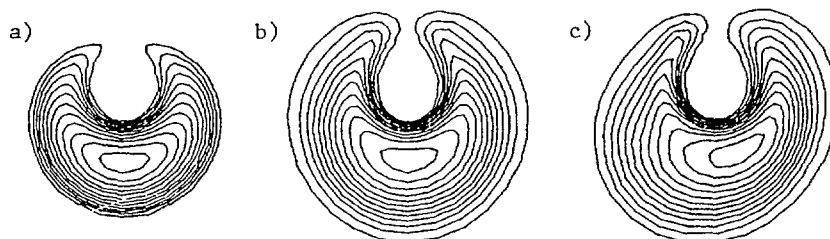


Figure 5. ISLE pressure contours for a)  $t=0$  and b)  $t=200 t_A$ , no hardcore shift, and c)  $t=200 t_A$ , 1 cm hardcore shift.

## 5. SUMMARY

- Heliac equilibrium experiments show a fast hardcore risetime is necessary to place plasma pressure in the heliac bean, which unfortunately induces an axial current
- Fast-rising hardcore  $\theta$ -pinch experiments show induced axial plasma currents that confirm the return mechanism (though through a different path) presumed for the heliac experiments.
- The proposed shifted hardcore/simulated toroidicity experiments are proceeding in the experimental and theoretical areas.
  - Hardware for the shifted hardcore experiment has been designed and is undergoing preliminary testing.
  - Numerical modelling of the shifted hardcore heliac experiments include finite  $\beta$  build-up and island formation studies

## REFERENCES

- [1] C. M. Greenfield, M. E. Koepke, and F. L. Ribe. Experimental Studies of Linear High Beta Helic Plasma Configurations. 1989. Submitted to *Physics of Fluids*.
- [2] D. C. Barnes. Science Applications International Corporation Report: APPAT-88, Science Applications International Corporation, Austin TX 78746, January 1986.
- [3] A. H. Reiman and A. H. Boozer. Island Formation and Destruction of Flux Surfaces in Three-dimensional MHD Equilibria. *Physics of Fluids*, **27**(10):2446–2454, October 1984.

<sup>1</sup> $t_A \sim 1 \mu\text{s}$ , making this long on HBQM time scales, but computationally necessary.

## DESIGN OF THE COMPACT AUBURN TORSATRON\*

R.F. GANDY, J.D. HANSON, M.A. HENDERSON,  
T. SCHNEIDER, D.G. SWANSON  
Auburn University,  
Auburn, Alabama

J.R. CARY  
Department of Astrophysical, Planetary  
and Atmospheric Sciences and  
Department of Physics,  
University of Colorado,  
Boulder, Colorado  
  
United States of America

### Abstract

A detailed description of the Compact Auburn Torsatron are presented. The optimization of the torsatron magnetic surfaces configuration was done by new optimization technique which serves as a basis for Integrable Field Stellarator code.

---

The Compact Auburn Torsatron (CAT) is currently under construction at Auburn University, and is scheduled for completion in October 1989. The machine will replace the Auburn Torsatron which has been operating since 1984. The design of CAT was done using the Cary-Hanson Optimization technique. CAT will have two helical field(HF) coils. The main component of the HF is from an  $\ell=2$ ,  $m=5(A=1.9)$  coil. The second component of the HF comes from an  $\ell=1$ ,  $m=5(A=2.6)$  coil. Since the CAT vacuum vessel has a circular cross section, effort was taken to force the magnetic axis to be nearly circular. The role of the  $\ell=1$  HF coil is to keep the magnetic axis close to the vacuum vessel axis. The various parameters of CAT can be seen in Table 1. Figure 1 shows the vacuum magnetic surfaces as well as the coil locations at  $\psi=0^\circ$ . Note that there is a large distance between the plasma and the  $\ell=2$  coil. CAT will have moderate shear(see Figure 2) and a magnetic well.

Recent theoretical work by Cary and Hanson[1,2] allows optimization of torsatron and stellarator magnetic surfaces based on minimizing stochasticity of magnetic field line flow, and thereby

---

\* Work supported by the US Department of Energy under grant DEFG605-85ER53192C.

maximizing the enclosed plasma volume. It was realized that the same principles used in this optimization method could be applied to designing a new machine. The machine design was done with the Integrable Field Stellarator (IFS) code. The coils are represented as a collection of connected straight line filaments(multi-filament option). The filament endpoints lie on a continuous curve called the winding law. A convenient parameterization for the helical coil winding law is

$$\psi = \pm\pi/m + l\theta/m + \psi_0 + \sum \alpha_n \sin(n\theta)$$

where  $\psi(\theta)$  is the toroidal (poloidal) angle, and the  $\pm$  refer to the two components of the main helical coil. The machine is then optimized(using certain fixed constraints such as rotational transform on axis) with the  $\alpha_n$ s as parameters.

The approach described has relevance to a stellarator or torsatron reactor for several reasons. One impediment to building a reactor is the high precision requirements placed on the windings.

Table 1: Machine Parameters for CAT

<b>CAT Parameters</b>			
SIZE		MAGNETICS	
Major Radius	53.3 cm	Multipole Order	2 (1)
Avg. Minor Radius	11 cm	No. of Field Periods	5
Vacuum Vessel Rad.	16.8 cm	Winding Law:	
Avg. Hel. Coil Rad.		l=2	
l=1	27.4 cm	$\phi \approx 2\theta/5 - 0.21 \sin\theta + 0.043 \sin 2\theta$	
l=2	20.6 cm	- 0.021 sin 3 $\theta$	
Number of turns		l=1	
l=1 Coil	150	$\phi \approx \theta/5 - 0.1 \sin\theta$	
l=2 Coil	64	Rotational Transform	
VF per	60	$t(0) \approx 0.25$	
Plasma Volume	0.12 m <sup>3</sup>	$t(\text{edge}) \approx 0.6$	
Vac. Vessel Volume	0.29 m <sup>3</sup>	Magnetic Field, B	1kG
Vac. V. Surface Area	3.5 m <sup>2</sup>	Vacuum Mag. Well	
Port Surface Area	0.7 m <sup>2</sup>		
POWER SUPPLIES			
Main Coil Set	177V/500A(2)	DC	
ECH Power	1kW CW		
	2.45 GHz		
ICH Power	5kW CW		
1-30 MHz	50 kW Pulsed		

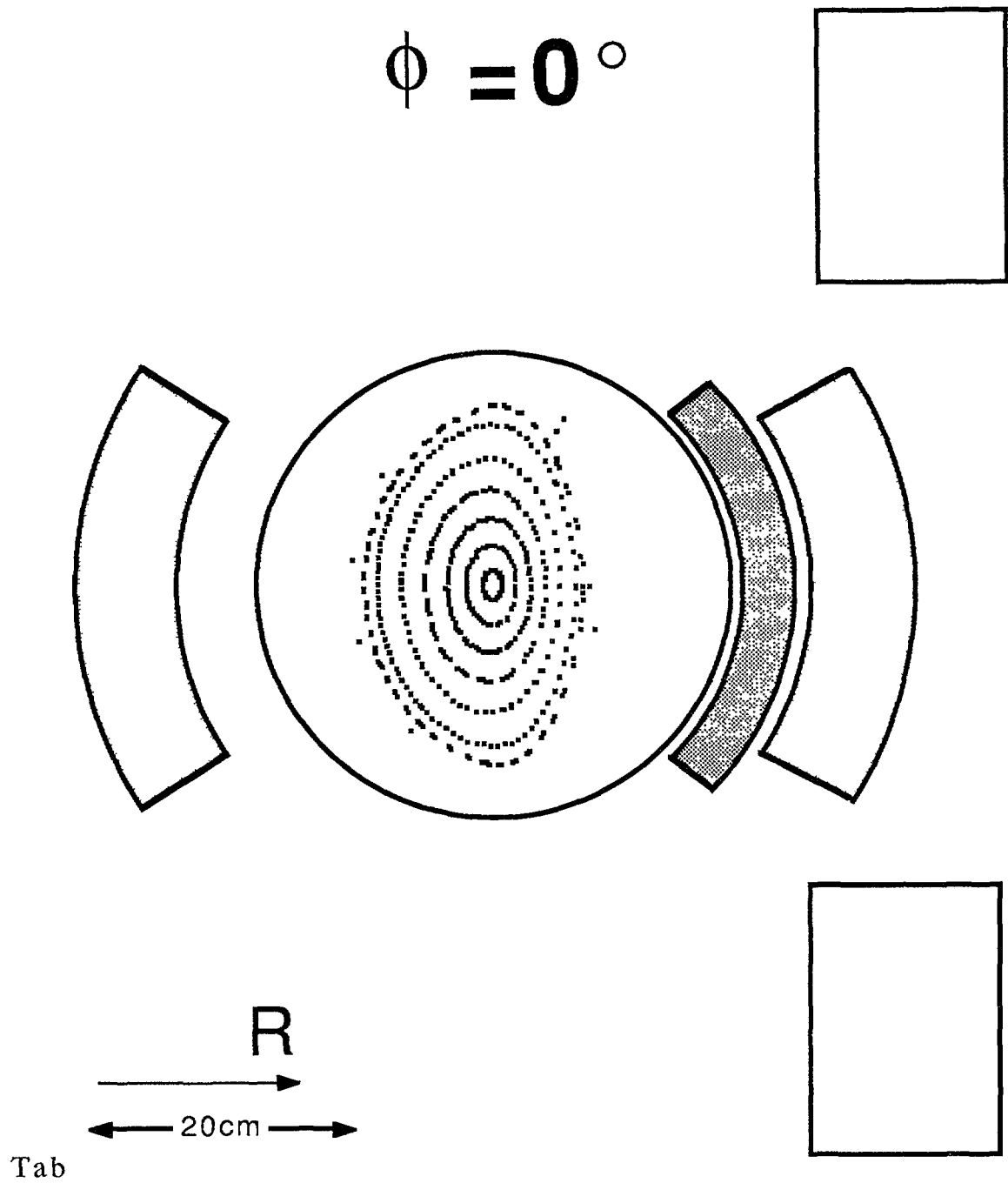


Figure 1 : Magnetic Surface of Section for CAT.

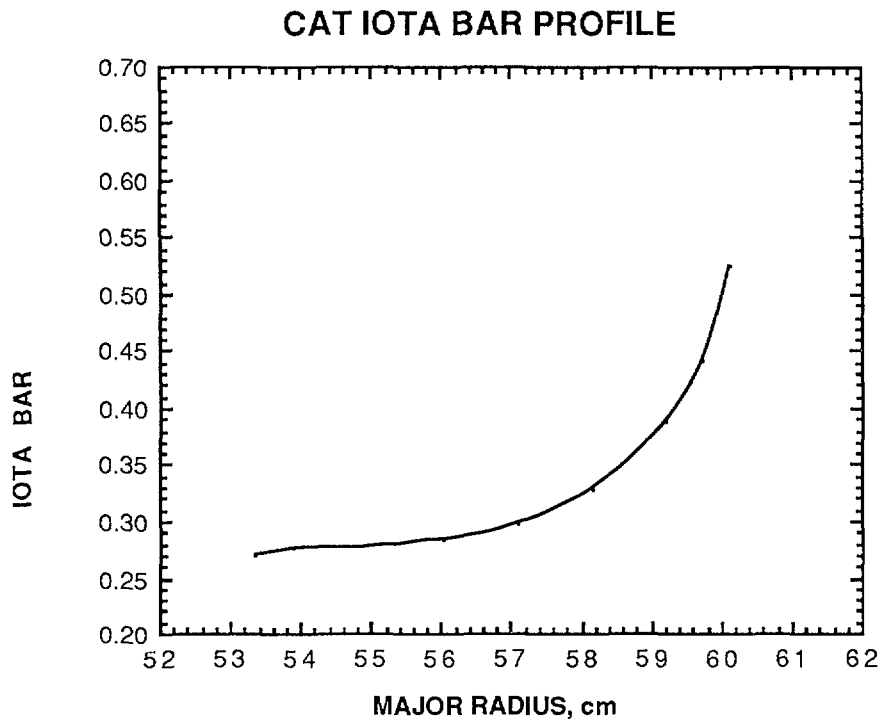


Figure 2: Rotational Transform for CAT.

Using the techniques described above, currents in a set of trim coils can be adjusted to produce an optimum configuration despite small errors in the main windings. This would certainly reduce the precision requirements and probably lower the cost of the reactor.

Another area of relevance to reactor plasmas concerns the ability to tune the magnetic island structure near the plasma boundary. A set of trim coils should give this capability. Control of the plasma boundary region in a reactor may be crucial for impurity control and divertor action. The method has application with regard to its original intent, that is to optimize the vacuum closed-surface volume. This certainly constitutes one criterion for optimization of future machine design studies.

Much of the work on CAT will be devoted to the study of islands and the related plasma effects. The diagnostics for the island studies (vacuum magnetic fields) include the diode and phosphor screen techniques of magnetic surface mapping. During plasma operation the diagnostics include: microwave interferometers, Langmuir probes (1D & 2D), microwave emission (ECE), magnetic probes, and visible spectroscopy. To

enhance the island studies on CAT, there is a large flexibility built into the machine to alter the magnetic fields. For example, both the  $\ell=1$  and the  $\ell=2$  coil packs are divided into four layers of windings. Each layer can be powered separately. Thus the coil aspect ratio can be changed by shifting the HF current centers. Another adjustment to the HF can be made through a  $\sin\theta$  trim coil which can change the winding law by increasing or decreasing the  $\sin\theta$  modulation on the current center of the  $\ell=2$  coil. The outer VF coil current centers will also be very flexible with four degrees of freedom(see Table 2). In addition to the outer VF, we will have a set of inner VF coils which will be used as an auxiliary VF or as part of a quadrupole field.

Table 2: Planned studies to determine island size dependency on various error fields and coil adjustments.

<b>ISLAND SIZE DEPENDENCE ON:</b>		
<b>RESIDUAL FIELDS</b>	<b>WINDING LAW ADJ.</b>	<b>VFCOILS</b>
EARTH'S FIELD	Change aspect ratio of coil center ( $l=1, l=2$ )  Modulated trim coils	XZ tilts
BUS WORK/LOCAL DIPOLES		$\Delta R$ shifts
IRON		$\Delta Z$ shifts
		XY shifts
		Inner VF

#### REFERENCES

- [1] Hanson, J.D., Cary, J.R., Phys. Fluids **27** (1984) 767.
- [2] Cary, J.R., Hanson, J.D., Phys. Fluids **29** (1986) 2464.

# ANALYTICAL FIELD RESULTS FOR STELLARATOR/ TORSATRON CONFIGURATIONS

F. ALLADIO, P. BATISTONI, F. CRISANTI,  
F. DE MARCO, S. MANCUSO  
Associazione Euratom-ENEA sulla Fusione,  
Centro Ricerche Energia Frascati,  
Frascati, Rome, Italy

## Abstract

The analytical calculations for the vacuum magnetic configurations in non-axisymmetric toroidal systems are described with the use of the "toroidal harmonic functions".

The existence of nonergodic vacuum magnetic configurations for non-axisymmetric toroidal systems is an open theoretical problem [1,2]; one of the ways used to explore this problem is the use of the well known "toroidal harmonic functions" [3]. The Laplace equation, in toroidal coordinates  $(\theta, \tilde{\omega}, \phi)$  with the concentration locus at  $R=R_0$ , admits the well known quasi-separable solution [4] for the magnetic scalar potential

$$\Phi_M = \sum_{q=0}^{\infty} \sum_{p=0}^{\infty} \left( L_{pc}^{e,qc} \phi_{pc}^{e,qc} + L_{pc}^{e,q\tilde{s}} \phi_{pc}^{e,q\tilde{s}} + L_{ps}^{e,qc} \phi_{ps}^{e,qc} + L_{ps}^{e,q\tilde{s}} \phi_{ps}^{e,q\tilde{s}} \right) \quad (1)$$

where  $L_{ps}^{e,q\left\{ \begin{smallmatrix} c \\ \tilde{s} \end{smallmatrix} \right.}$  are the scalar external multipolar moments,

$$\phi_{ps}^{e,q\left\{ \begin{smallmatrix} c \\ \tilde{s} \end{smallmatrix} \right.} = \sqrt{\text{ch}\theta - \cos\tilde{\omega}} Q_{p-1/2}^q(\text{ch}\theta) \begin{Bmatrix} \cos \\ \sin \end{Bmatrix} (p\tilde{\omega}) \begin{Bmatrix} \cos \\ \sin \end{Bmatrix} (q\phi) \quad (2)$$

are the toroidal multipolar harmonics and  $Q_{p-1/2}^q(\text{ch}\theta)$  is the second-kind Legendre function [4].

The problem of connecting the scalar multipolar expansion to the current distribution flowing on the surface of a torus  $\theta=\theta_*$  can be solved in the following way: i) given the current  $\mathbf{J}$  flowing on the surface we can replace it by an equivalent magnetization density  $\mathbf{M}$  outside the torus ( $\theta < \theta_*$ ) such that  $\nabla \wedge \mathbf{M} = \mathbf{J}$ . ii) we then evaluate  $\nabla \cdot \mathbf{M}$  outside the torus. iii) we finally solve by Green's function technique the Laplace-Poisson scalar problem  $\nabla^2 \Phi_M = \nabla \cdot \mathbf{M}$ . iv) the field inside the torus ( $\theta > \theta_*$ ) can then be evaluated as  $\mathbf{B} = -\mu_0 \nabla \Phi_M$ .

Among the various winding laws that we can try for a helicoidal surface current flowing on the torus  $\theta=\theta_*$ , a simple choice is the one of constant pitch in toroidal coordinates.

$$\begin{cases} j_\phi = \frac{mI}{2R_0^2} (\text{ch}\theta_0 - \cos\tilde{\omega}_0)^2 \delta(\theta_0 - \theta_*) \cos(m\tilde{\omega}_0 + n\phi_0) \\ j_{\tilde{\omega}} = \frac{nI}{2R_0^2 \text{sh}\theta_0} (\text{ch}\theta_0 - \cos\tilde{\omega}_0)^2 \delta(\theta_0 - \theta_*) \cos(m\tilde{\omega}_0 + n\phi_0) \end{cases} \quad (3)$$

where  $I$  is the modulus of the total current flowing between two lines of null current ( $m\tilde{\omega}_0 + n\phi_0 = \pi/2, 3\pi/2, \dots$ )  $m$  is the poloidal winding number and  $n$  the toroidal one. With this particular current we have been able to obtain a fully analytical solution for the multipolar moments that have a pure  $q=n$  toroidal number, but contain all the  $p$  poloidal numbers. The expression for these moments is

$$\begin{cases} L_{pc}^{e,ns} = \frac{I}{2\sqrt{2}\pi} (2 - \delta_{p0})(-i)^n \frac{\Gamma(p-n+1/2)}{\Gamma(p+n+1/2)} \left\{ -P_{p-1/2}^n(\text{ch}\theta_*) \left[ g_{lm+p}(\text{ch}\theta_*) + g_{lm-p}(\text{ch}\theta_*) \right] \right. \\ \left. + \left[ (p+n-1/2) P_{|p-1|-1/2}^n(\text{ch}\theta_*) - \text{ch}\theta_* (p-1/2) P_{p-1/2}^n(\text{ch}\theta_*) \right] \left[ Q_{lm+p-1/2}^0(\text{ch}\theta_*) + Q_{lm-p-1/2}^0(\text{ch}\theta_*) \right] \right\} \\ L_{ps}^{e,nc} = \frac{I}{2\sqrt{2}\pi} (2 - \delta_{p0})(-i)^n \frac{\Gamma(p-n+1/2)}{\Gamma(p+n+1/2)} \left\{ P_{p-1/2}^n(\text{ch}\theta_*) \left[ g_{lm+p}(\text{ch}\theta_*) - g_{lm-p}(\text{ch}\theta_*) \right] \right. \\ \left. - \left[ (p+n-1/2) P_{|p-1|-1/2}^n(\text{ch}\theta_*) - \text{ch}\theta_* (p-1/2) P_{p-1/2}^n(\text{ch}\theta_*) \right] \left[ Q_{lm+p-1/2}^0(\text{ch}\theta_*) - Q_{lm-p-1/2}^0(\text{ch}\theta_*) \right] \right\} \end{cases} \quad (4)$$

where  $P_{p-1/2}^q(\text{ch}\theta)$  is the first-kind Legendre function and  $f_m(\text{ch}\theta), g_m(\text{ch}\theta)$

are the first and second-kind Fock functions [3]. When we consider the configurations with  $m=1,2,3$  (i.e. the ones of practical interest for a stellarator design) a truncation of the expansion to  $p=12$  is computationally accurate. An idealized stellarator configuration is produced as  $\mathbf{B} = -\mu_0 \nabla \Phi_M + \mathbf{B}_T^\circ (\text{ch}\theta - \cos\omega)/(\text{sh}\theta) * \mathbf{e}_\phi - \mu_0 \nabla \Phi_M^v$

where a pure toroidal field with value  $\mathbf{B}_T^\circ$  at the concentration locus  $R=R_0$  is added and furthermore a vertical axisymmetric field is superposed to the toroidal-helicoidal field. A possible choice for the vertical field is produced by an axisymmetric surface current flowing on the torus  $\theta=\theta_*$  with distribution

$$j_\phi = f_v \frac{B_0^T}{R_0 \mu_0} \frac{m}{n \text{sh}^2 \theta_* \sqrt{m^2 \text{sh}^2 \theta_* + n^2}} (\text{ch}\theta_0 - \cos\tilde{\omega}_0)^2 \delta(\theta_0 - \theta_*) \quad (5)$$

where  $f_v$  is a constant of order unity that has to be chosen in order to maximize the rotational transform  $i$  at the edge of the configuration. The main interesting feature of such vacuum configurations is that they do not show any internal magnetic island formation at any aspect ratio and are able to provide extremely low aspect ratio  $A = \langle R \rangle / \langle a \rangle$  with  $i_{\text{edge}} > 1$  when  $A > 3.5$ . Even at  $A = 2.7$  (see Fig.1) we can achieve  $i_{\text{edge}} = 2/3$  (see Fig.4) and separatrix-like features at the edge of the configuration.

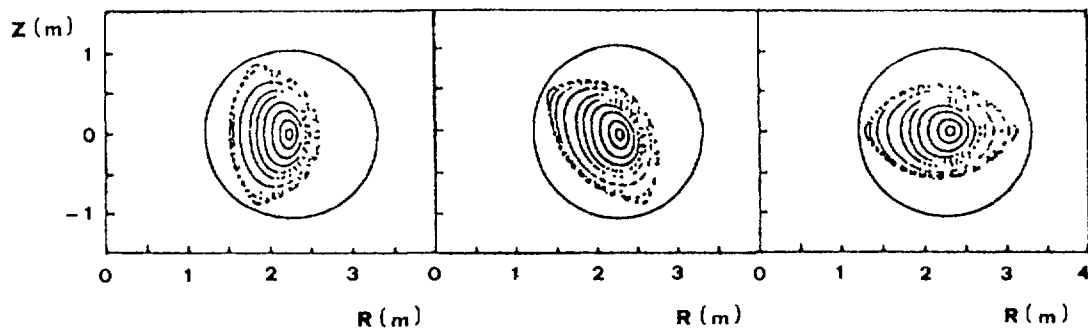


Fig 1 Idealized surface current stellarator configuration with  $m=2$  poloidal and  $n=6$  toroidal number with aspect ratio  $A=2.7$  at  $\phi = 0, -2\pi/4n$  and  $-2\pi/2n$

The main parameters of the configuration of Fig.1 are as follows: the helicoidal current is distributed on the surface of a torus with  $R=2.26$  m,  $a=1.05$  m ( $\theta_0=1.4$ ,  $R_0=2$  m) with  $m=2$ ,  $n=6$  winding numbers and  $I=4.17$  MA, the toroidal field is  $B_T^0=5$  T and the vertical field has  $f_v=1.5$  which means a total net toroidal current of 0.97 MA to produce it. A possible torsatron configuration, designed to be as similar as possible to the ideal configuration of Fig.1 is shown in Fig.2.

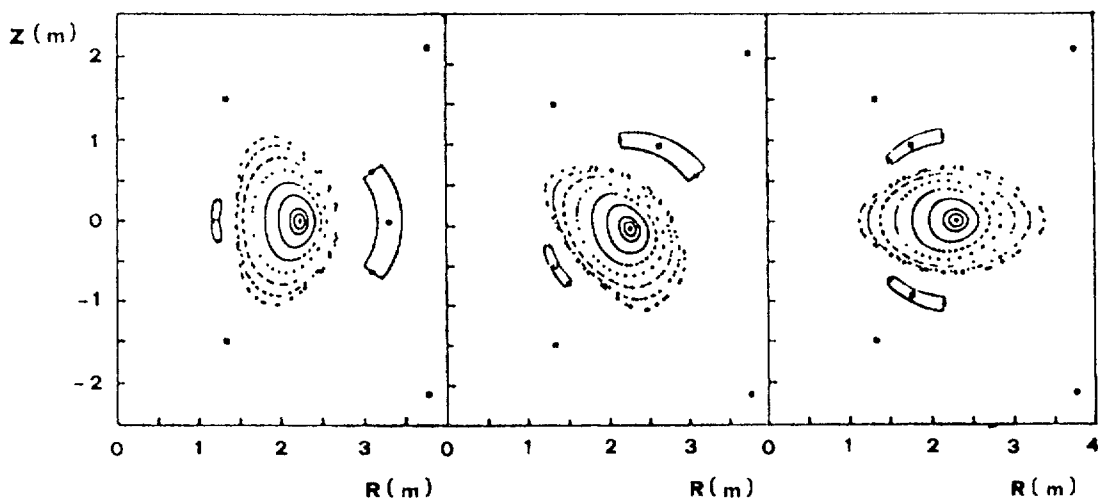


Fig 2 Torsatron configuration with same winding numbers and aspect ratio  $A=2.3$  at  $\phi = 0, -2\pi/4n$  and  $-2\pi/2n$

Its main features are  $I=8.33$  MA for each of the two helical coils, a return current  $I_{\perp}=-2.37$  MA for the inner vertical coil and  $I_{\perp}=-4.49$  MA for the outer coil (see Fig 3)

The main difference with respect to the idealized stellarator is that the volume of the configuration becomes even larger ( $A=2.3$ ) keeping the same value of rotational transform at the edge (see Fig.4) but the sharp separatrix-like features are lost.

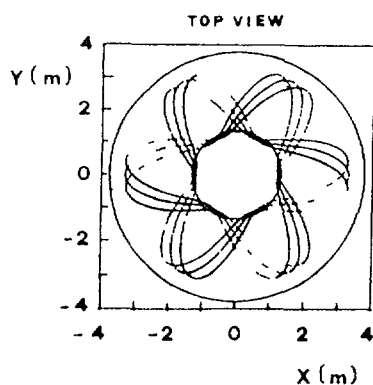


Fig 3 Top view of helical and vertical field coils filaments for the torsatron configuration

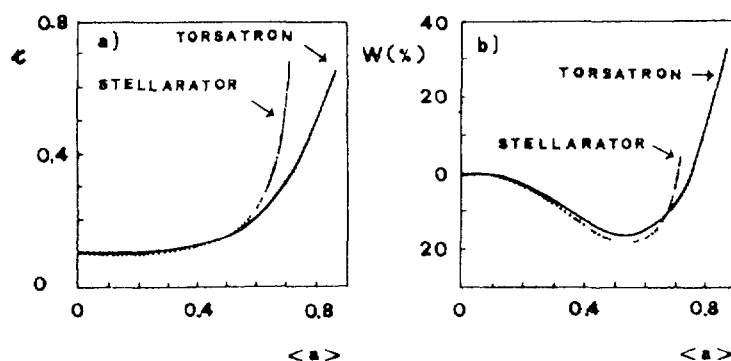


Fig 4 Comparison between the idealized stellarator and the torsatron configuration a) Rotational transform  $\epsilon$  vs average minor radius  $\langle a \rangle$ , b) magnetic well depth vs  $\langle a \rangle$

The advantages of compact torsatron configurations, apart from the lower cost of small aspect ratio machines, are the high equilibrium and stability  $\beta$  limits. This fact was explored, in the case of the torsatron configuration of Fig.2, by the code VMEC [5]. The equilibrium result is quite encouraging as the  $\beta$  limit, defined by the averaged magnetic axis displacement equal to half averaged minor radius ( $\delta/\langle a \rangle = 0.5$ ), is found at  $\langle \beta \rangle_{vol} = 8\%$ . The fixed boundary equilibrium as calculated from VMEC is shown in Fig.5 where  $\langle \beta \rangle_{vol} = 6.9\%$ ,  $\beta_{axis} = 10.6\%$ .

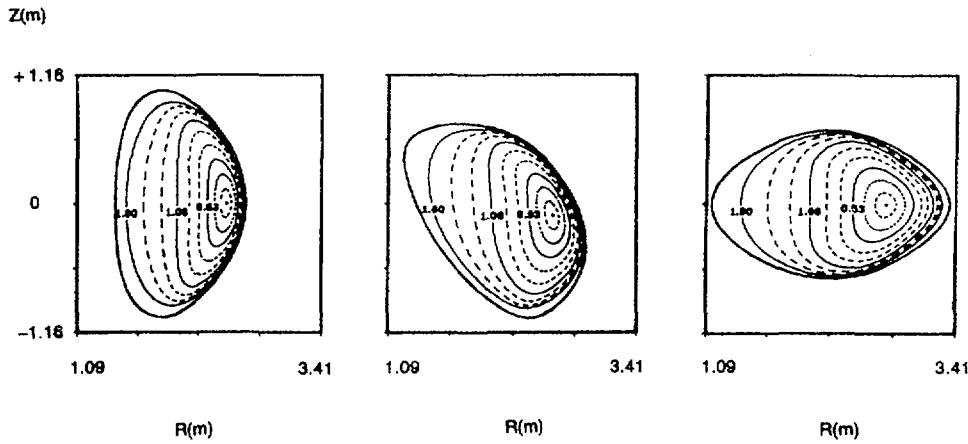


Fig 5 Torsatron magnetic flux surfaces at  $\phi = 0, -2\pi/4n,$  and  $-2\pi/2n$  as calculated from the VMEC code in fixed boundary configuration with  $\langle\beta\rangle_{vol} = 6.9 \%$ ,  $\beta_{axis} = 10.6 \%$

The main effect of such  $\beta$  value on the rotational transform profile is to make it hollow, increasing the value  $\tilde{k}_{axis}$  to 0.33 ( from 0.1 in vacuum ) and decreasing it halfway to a minimum  $\tilde{k}=0.07$ , whereas the boundary value  $\tilde{k}_{edge}$  decreases slightly to 0.61 ( from 0.66 in the vacuum ) .

The magnetic well depth is increased to 60 % ( from 20 % in vacuum ) . The Mercier stability criterion is investigated on the equilibrium calculated by the VMEC code with a parabolic pressure profile  $p(\psi) \propto (\psi_{edge} - \psi)^2$  . The main result is that the central part of the plasma column, from  $\tilde{k}=0.33$  down to  $\tilde{k}=0.25$  is found to be unstable. This fact could be exploited in an experiment to avoid impurity accumulation in the center of the plasma. The most troublesome points in the design of compact torsatron are the  $\alpha$ -particle containment capabilities of such configurations and their resilience to flux surface breaking due to field errors and beta effects. A collisionless  $\alpha$ -particle orbit calculation based on the Boozer formalism [6] has been performed using the ORBIT code [7]. The evaluation of the magnetic coordinates  $(\psi, \theta_\psi, \phi_\psi)$  for the idealized stellarator analytical field produced by the winding law (3) is particularly simple. The Boozer coordinates [8]  $\chi_0$  is simply the known analytical magnetic scalar potential  $\chi_0 = -\mu_0 \Phi_M$  ; then, knowing the  $\psi = \Phi_{Tor} / 2\pi$  coordinate by a few turns field line tracing, we can evaluate  $\theta_0$  by integrating

$$\nabla\theta_0 = \frac{\nabla\chi_0 \wedge \nabla\psi}{|\nabla\psi|^2} \quad (6)$$

Then the magnetic coordinates are calculated as

$$\begin{cases} \phi_\psi = \frac{1}{R_0 B_T^0} \chi_0 \\ \theta_\psi = \theta_0 + \frac{\tau(\psi)}{R_0 B_T^0} \chi_0 \end{cases} \quad (7)$$

A new equally spaced mesh in  $\theta_\psi, \phi_\psi$  is set up on a  $\psi$  surface and the Fourier coefficients of the various quantities such as

$$|B| = \sum_{p,q} \delta_{pq}^{|\mathbf{B}|}(\psi) \cos(p\theta_\psi - q\phi_\psi) \quad (8)$$

are easily evaluated

The spectrum of the most relevant Fourier coefficients as a function of  $\psi$  ( $0 < \psi < 1.07$ ) for the idealized stellarator configuration of Fig 1 is shown in Fig 6, it is interesting to observe that the toroidal coefficients  $\delta_{1,0}(\psi)$  is always dominant with respect to the main helical coefficient  $\delta_{2,6}(\psi)$ .

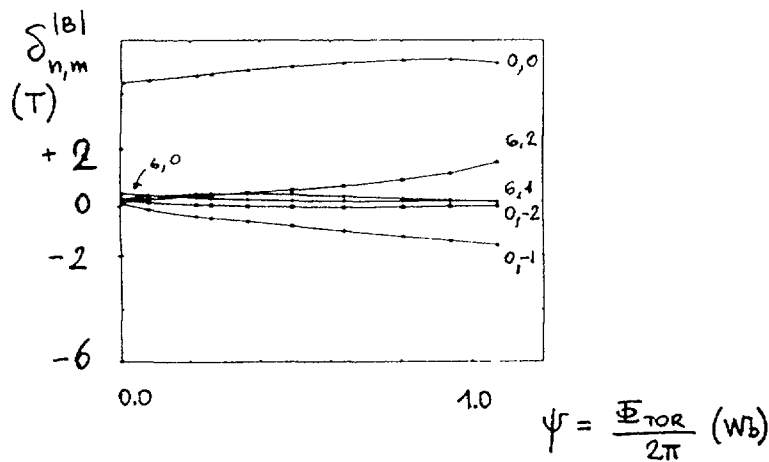


Fig 6 Radial behaviour of the most relevant Fourier coefficients  $\delta_{n,m}$  as a function of the radial flux variable  $\psi = \Phi_{\text{Tor}} / 2\pi$

The plot of the minimum of  $|B|$  along  $\phi_\psi$  as a function of  $((\langle r \rangle / a = \sqrt{\psi / \psi_{\text{edge}}})$ ,  $\theta_\psi$ ) is shown in Fig 7. It suggests [9] that roughly 40% of the trapped particles should not be promptly lost. A rough estimate of the  $\alpha$  particle contained fraction can be obtained as

$$f_{\text{CONT}} = \left(1 - \frac{1}{\sqrt{A}}\right) + 0.4 \frac{1}{\sqrt{A}} \sim 64\%$$

To obtain a reactor relevant estimate of the  $\alpha$  particle confinement capabilities of this configuration the product  $B_T^0 \cdot \langle a \rangle$  has been rescaled by a factor of 4; this reduces the Larmor radius of the  $\alpha$  particle from 8% to 2% of the minor radius. A preliminary calculation based on the orbits of 200  $\alpha$  particles (some of which are shown in the ( $\langle r \rangle/a = \sqrt{\psi/\psi_{\text{edge}}}$ ),  $\theta_\psi$ ) circle representation of Fig.7) gives  $f_{\text{cont}}=66\%$  at all radii investigated up to  $\langle r \rangle/a=0.8$ . The fact that  $f_{\text{cont}}$  does not increase toward the magnetic axis is presumably due to the relevant ( $\pm 5$  cm)  $m=1, n=6$  helical wobbling of the magnetic axis. Moreover the promptly lost  $\alpha$  particles escape in two narrow helical strips roughly coincident with the separatrix-like features of the configuration and no particles are observed to escape in the innerside of the torus in the poloidal angle range  $\pi - \arcsin(1/A) < \theta_\psi < \pi + \arcsin(1/A)$ .

That would mean that presumably in a torsatron configuration the promptly lost  $\alpha$  particles should escape far from the helical coils and should not hit them. However a complete study of the containment and of the prompt losses in the torsatron configuration of Fig.2 remains to be done.

The resilience to flux surface breaking of the torsatron configuration due to field errors has been partly assessed. A rigid displacement of 5mm between the two helical fields coils, both in horizontal as well as in vertical direction (+2.5 and -2.5mm opposite displacement with respect to fixed vertical field coils) does not break up the internal magnetic flux surface neither does decrease below 0.6 the rotational transform at the edge. A horizontal displacement of 5mm of a single vertical field coil produces as well unnoticeable effects.

The problem of magnetic surface breaking due to finite  $\beta$  effects has simply not been yet studied as it would require iterative equilibrium codes that, at the moment, are not available to us.

The main feature and the main risk of the low aspect ratio torsatron approach turns out to be the high shear region at the edge of the magnetic configuration. An advantage of the torsatron approach versus the stellarator one is that such high shear region becomes more large and less steep (see Fig.4) in the torsatron case and so maybe less prone to destruction.

The advantages of high shear at the edge are quite clear; from the equilibrium point of view raising up the  $\epsilon_{\text{edge}}$  raises up the  $\beta$  limit; from the ideal stability point of view it strongly stabilizes the edge of the configuration leaving the possibility on an unstable centre that could prevent impurity accumulation; from the  $\alpha$  particles containment point of

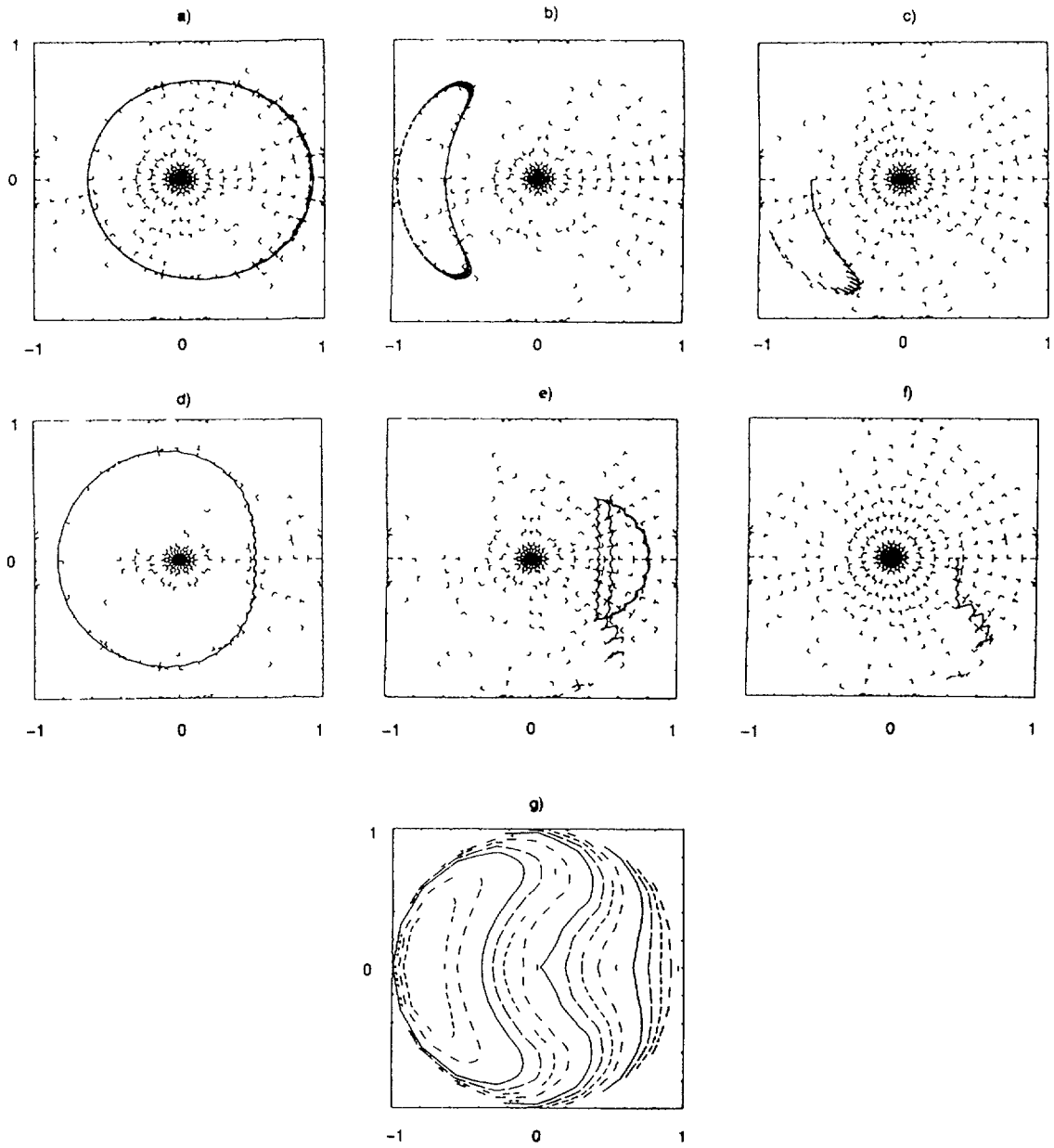


Fig 7 Orbits of  $\alpha$  particles in the stellarator configuration of Fig 1 with  $\langle a \rangle \cdot B_T^{\circ}$  increased by a factor 4 (so that  $\rho_{L\alpha} / \langle a \rangle = 2\%$ ) in the  $(\sqrt{\psi/\psi_{edge}}, \theta_{\psi})$  polar representation  
 Internally born a) circulating, b) trapped contained, c) lost orbits  
 Externally born d) circulating, e) trapped lost, f) lost orbits  
 g) plot of mean  $|B|$  over  $0 < \phi_{\psi} < 2\pi/n$  in the same  $(\sqrt{\psi/\psi_{edge}}, \theta_{\psi})$  polar representation

view it allows a good containment in the edge region and channels the prompt  $\alpha$  particles losses in the in the separatrix-like region far from the helical coils.

However the high shear region remains in our view the main risk in a possible low aspect ratio ( $A < 3$ ) torsatron experiment as its destruction could be due to field errors or to finite  $\beta$  effects (the strong compression toward the outside of the magnetic flux surfaces at high  $\beta$ , obtained from the Lagrangian equilibrium codes (see Fig.5), is yet a warning). Should such high shear region be destroyed then the experiment would reduce to a higher effective A configuration with the disadvantage of far away helical coils, that would mean a low shear and a low rotational transform. So we think that much more work is needed to asses whether a low aspect ratio ( $A < 3$ ) torsatron could become a reasonable experimental proposal for a machine with  $R \simeq 2$  m and  $B_T^0 \simeq 5$  T.

#### ACKNOWLEDGEMENTS

The authors of this paper would like to express their gratitude to the ORNL Group (in particular B. Carreras, S. Hirshman, N. Dominguez, and V. Lynch) for helpful suggestions and discussions and for allowing an extensive comparison with their computational codes. Moreover we want to thank R. White for the use of the ORBIT code.

#### REFERENCES

- [1] L.M. Kovrizhnykh: Sov. Phys. Techn. Phys. **8**, 281 (1963)
- [2] J.R. Cary: Phys. Rev. Lett. **49**, 276 (1982)
- [3] F. Alladio and F. Crisanti: Nucl. Fusion **26**, 1143 (1986)
- [4] Morse & Feshbach: Methods of Theoretical Physics, Mac Graw-Hill, New York (1953)
- [5] S.P. Hirshman, J.C. Whitson: Phys. Fluids **26**, 3553 (1983)
- [6] A.H. Boozer: Phys. Fluids **23**, 904 (1980)
- [7] R.B. White, M.S. Chance: Phys. Fluids **27**, 2455 (1984)
- [8] A.H. Boozer: Phys. Fluids **24**, 1999 (1981)
- [9] S.L. Painter, J.F. Lyon: ORNL/TM 10792 (1988)

## CONFIGURATION STUDIES FOR TJ-I UPGRADE

J. GUASP, C. ALEJALDRE, A.L. FRAGUAS,  
L. GARCÍA<sup>1</sup>, A. VARIAS  
Asociación Euratom/CIEMAT,  
Madrid, Spain

### Abstract

The main characteristics of the new TJ-I Upgrade installation are reported. It is shown that  $l=1/ m=6$  configuration fulfills all the TJ1 Upgrade requirements. It has a deep magnetic well, good stability, sufficient microwave launching conditions and is rather insensitive to field errors.

---

### 1. Introduction.

In order to fill up the temporal gap until TJ-II completion (1992) and to acquire expertise on ECRH with the available 28 GHz gyrotron, a new small Stellarator has been planned at CIEMAT. It will share with the present TJ-I Tokamak, site, power supplies, data acquisition systems and diagnostics.

By necessity it shall be of easy construction ( no extreme currents or accuracy), small size and cost but with, at least, 10 cm of average radius and the most similar as possible to TJ-II magnetic configuration.

### 2. Coil structure.

After many trials and optimisation the chosen configuration is an  $\ell =1 / m=6$  Torsatron ( Figs. 1-2). It has an  $\ell=1$ , six turn, helical coil with winding modulation given by  $\phi = 1/6 (\theta + 0.4 \sin \theta )$  and with a major radius of 0.6 m and a minor one of 0.24 m. Two couples of vertical field coils provide dipolar and quadrupolar vertical field components. That modulation is opposite to the usual in "ultimate" torsatrons and is essential to achieve deep magnetic well, it makes the helix direction more closer to the vertical on the inner side of the torus than on the outer one.

### 3. Configuration properties.

For the "reference" current settings (  $I_{hc} = 280$  kA,  $I_{vf1} = -122$  kA,  $I_{vf2} = -49$  kA ) the magnetic surface cross sections are shown at Figs. 3-4, the average plasma radius is 10 cm, rotational transform at axis 0.30, with shearless radial profile, the magnetic axis,

---

<sup>1</sup> Departamento de Física Fundamental, Facultad de Ciencias, Universidad Complutense, Madrid, Spain.

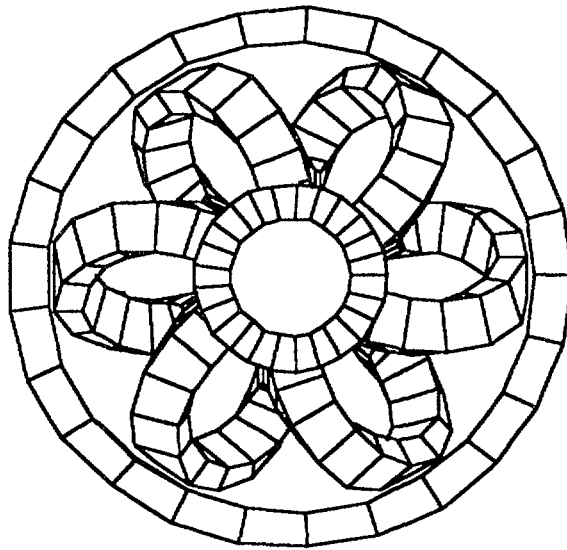


FIG. 1.

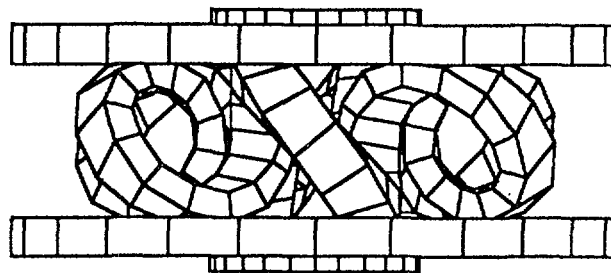


FIG. 2.

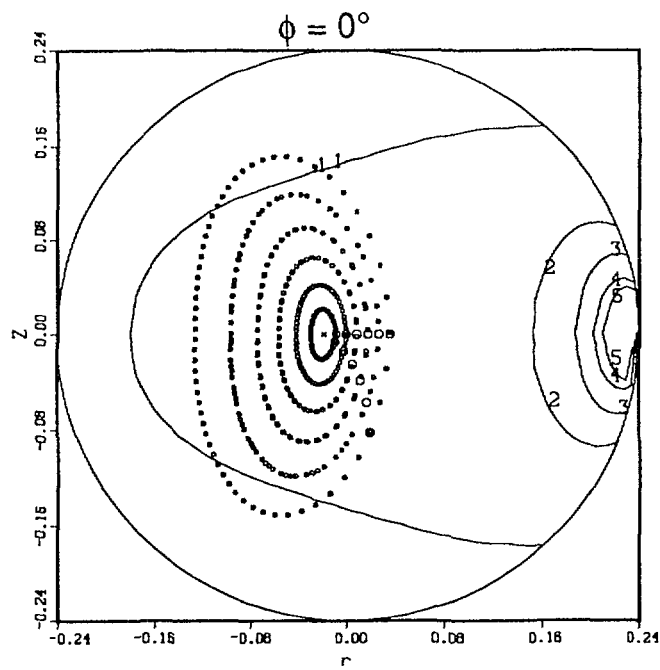


FIG. 3.

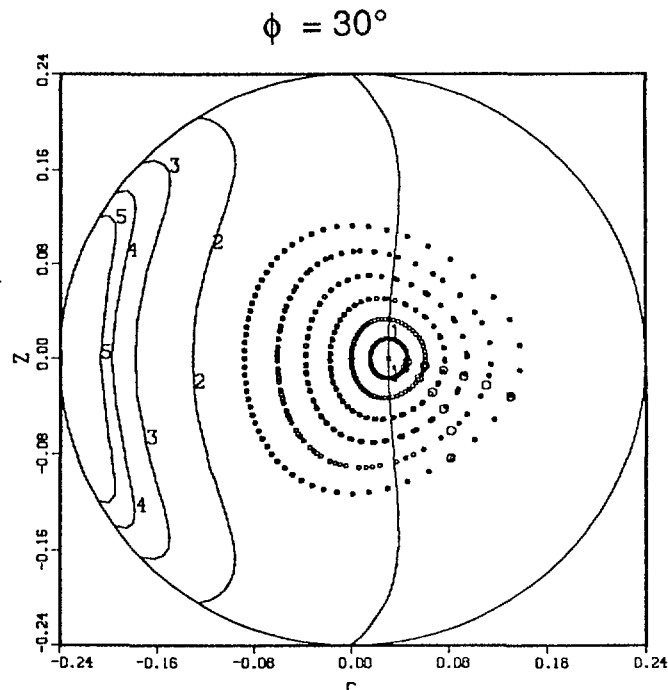


FIG. 4.

placed at  $R_{ax}=0.58$  cm for  $\phi = 0^\circ$ , has a slight helicity ( $\approx \pm 2.5$  cm) and, most important, a deep magnetic well of 6.9% depth exists. Magnetic field intensity at axis for  $\phi = 30^\circ$  is just 0.5 T suitable for 2<sup>nd</sup> harmonic ECR heating at 28 GHz.

The VF coils allow some configuration flexibility by means of magnetic axis shift, it can be positioned between 0.61 and 0.52 m, in this way the rotational transform can be varied between 0.14 and 0.4 maintaining always an average radius greater than 7 cm, magnetic well is optimal for the reference case, disappearing gradually for extreme shift-ings (Fig.5).

An extensive field error analysis has been done, as well for periodic perturbations as for symmetry breaking errors, in no case the accuracy requirements are finer than 1%, the most dangerous case is a tilting of one of the external VF coils. The configuration shows a remarkable robustness against any kind of errors. The effect of finite coils and current leads has been analysed also.

#### 4.Microwave heating.

Ray tracing analysis shows that the optimal launching position for 2<sup>nd</sup> harmonic in X-mode at 28 GHz appears at  $\phi = 30^\circ$ , horizontally, along the equatorial plane. Below and near the density cut-off ( $n_e(0) = 0.45 \times 10^{13} \text{ cm}^{-3}$ ) the absorption can attain 80%

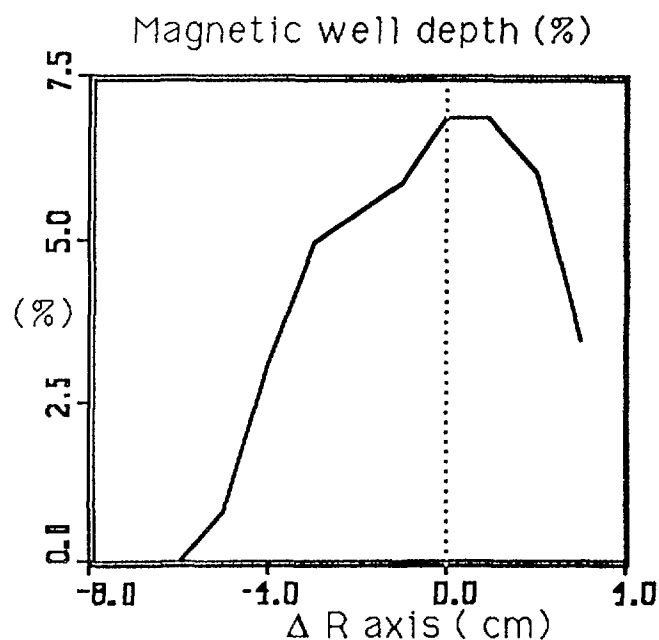


FIG. 5.

while for lesser densities ( $0.3 \times 10^{13} \text{ cm}^{-3}$ ) single pass absorption is about 45% but the total reflexion produced on the cut-off can occasionate a second pass over the resonant layer.

#### 5. Equilibrium and Stability.

Equilibrium studies using the 3-D code VMEC have been done obtaining equilibria, at least, up to  $\langle \beta \rangle = 1.16\%$  and showing 3-D Mercier stability against local modes for the whole range of  $\beta$  considered.

#### 6. Drift particle trajectories.

Drift particle trajectories have been studied showing that for strong inner shifting of the magnetic axis ( $\Delta R_{ax} \leq -5 \text{ cm}$ ) these trajectories remain inside the magnetic surfaces for almost all the plasma volume. This fact is shown at Fig. 6 where the projection on a meridian plane ( $\phi = \text{Cte}$ ), in flux coordinates, of the magnetic surfaces (circles) and the drift trajectories are shown.

As for these inner axis shiftings the magnetic well disappears, this fact suggest the possibility to realise on this device experiments on stabilisation by fast particles, produced either by the ECRH system or by additional RF sources.

## B-min Contours TJ1-Up

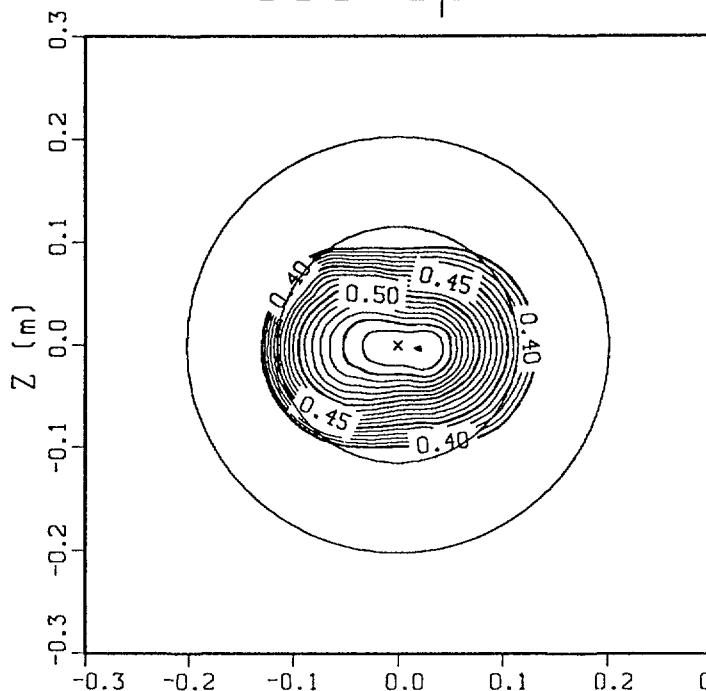


FIG. 6.

### 7. Transport estimations.

Transport simulations by means of a 1-D flux coordinates code, with a model including neoclassical and helical ripple losses as well as anomalous electron thermal conductivity, give a central electron temperature of about 435 eV for 100 kW ECRH and  $n_e(0)=0.5 \times 10^{13} \text{ cm}^{-3}$ , this corresponds to  $\langle \beta \rangle = 0.14\%$  (well inside the stability region), and a global energy confinement time  $\tau_E = 0.33 \text{ ms}$ . The radial profiles are rather rounded, almost parabolic for  $T_e$ , and slightly dependent of the beam spread ( $\approx 8 \text{ cm}$ ).

### 8. Conclusions.

In conclusion the present  $\ell=1 / m=6$  configuration fulfills all the TJ-I Upgrade requirements, it has a deep magnetic well, some flexibility that could allow the study of stabilisation by fast particles, it shows good stability and microwave launching conditions and is rather insensitive to field errors.

The engineering design of the device is now well under way and the machine is expected to start working at the beginning of 1990.

## R.F. STELLARATORS\*

J.L. SHOHEET

Torsatron/Stellarator Laboratory,  
University of Wisconsin - Madison,  
Madison, Wisconsin,  
United States of America

### Abstract

Conventional stellarators utilize twisted d.c. multipole fields for confinement. This paper contains new proposals to either supplement or replace the stellarator magnetic confining field with that produced by RF multipole field. Combined RF and d.c. magnetic field multipole fields can be used for either injection of charged particles into a magnetic stellarator or improving the confinement properties of conventional stellarator.

### I. Introduction

R.F. multipole fields may be used as both a mass filter<sup>1</sup> and a means to inject ions into a region of a strong magnetic field<sup>2</sup>. If the multipole field is strong enough to outweigh the d.c. magnetic field, then charged particles may be confined with the multipole field alone. An approximate expression for the r.f. fields from a quadrupole is:

$$v(x,y) = [(x^2 - y^2)/r_0^2]V_T \quad (1)$$

where  $v$  is the electrostatic potential inside the quadrupole region,  $x$  and  $y$  are the coordinates perpendicular to the direction of the quadrupole rods,  $r_0$  is the radius from the axis of the quadrupole to the rods and  $V_T$  is the r.f. potential applied to the rods.

In effect, if the frequency of the r.f. is high enough, the r.f. fields reverse before a charged particle can be accelerated outside of the quadrupole region and a ponderomotive force<sup>3</sup>, as in radio frequency plasma confinement exists. If the charged particle moves fast enough to leave the confined region before the r.f. fields reverse in sign, then confinement will not occur. The result is that the quadrupole can then act as a mass filter.

If the r.f. quadrupole is twisted to form a helix and then bent into a torus, an r.f. stellarator configuration can be generated. In addition, a combination of stellarator d.c. magnetic fields together with superimposed r.f. multipole fields offers the potential of improved confinement, especially under the conditions which might result in direct orbit losses in pure d.c. magnetic field stellarators.

---

\* Work supported by the US Department of Energy under grant DE-FG02-86ER53216.A004.

## II. R.F. Multipole Confinement

Conventional stellarators utilize twisted d.c. multipole fields for confinement. The work here proposes to either supplement or replace the stellarator magnetic confining field with that produced by a r.f. multipole field. Combined r.f. and d.c. magnetic field multipole fields can be used advantageously for either injection of charged particles into a magnetic stellarator or improving the confinement properties of magnetic stellarators.

In the example used here, we assume that an r.f. quadrupole field, as produced by the rods shown in Figure 1, is established. The r.f. quadrupole is a set of rods which can be straight as shown or wound into a helix. There is no explicit requirement, however, that the pitch of the r.f. multipole helix match that of the stellarator helix. The electrostatic field produced from an r.f. source applied in quadrature between the rods is that shown in equation (1). By finding the electric field from the potential and finding its time average, we can obtain the ponderomotive potential

$$\phi_p = q^2 \langle E_0^2 \rangle / (2m^2 \omega_{rf}^2) \quad (2)$$

provided that  $\omega_{rf} \gg \omega_c$ . The gradient of the ponderomotive potential is the net time-averaged body force on a particular charged particle. Note that it is inversely proportional to the mass and to the r.f. frequency. Thus, higher mass particles have a smaller ponderomotive body force than lighter ones. It can be seen from equations (1) and (2) that the force acts perpendicular to the z direction (axis of the multipole rods), but varies sinusoidally with azimuthal angle. It is a maximum in the direction going directly to the rods, and a minimum half way between them.

If a particle moves fast enough to leave the confined region before the r.f. fields reverse, confinement does not occur, and thus a mass filtering action can be accomplished.

Similar confining fields can be found with waveguide modes, as shown in Figure 2. Here the square region in the center of the cavity is a ponderomotive potential well in which particles are confined provided that their energies are less than the maximum height of the well as given by equation (2).

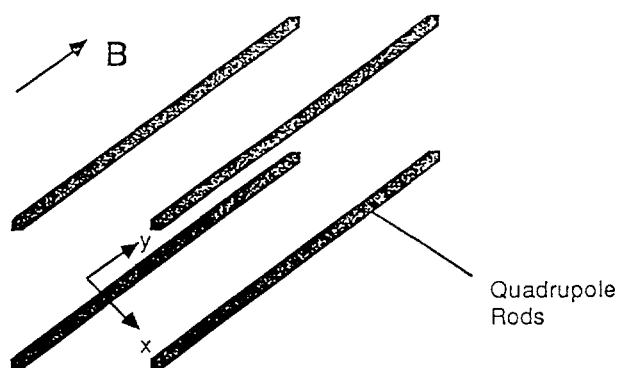


FIG. 1.

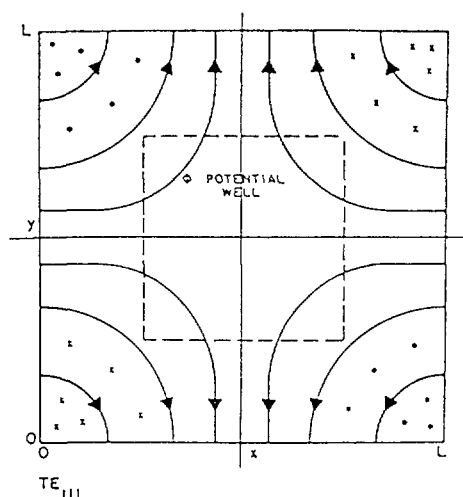


FIG. 2.

### III. R.F. Multipoles in d.c. Magnetic Fields

The problem to be solved here is to determine the effectiveness of the quadrupole field in the presence of a d.c. magnetic field. We show this by showing the effects of the r.f. quadrupole on a particle entering a solenoidal d.c. magnetic field. Figure 3 shows the particle trajectory without the use of the quadrupole. The magnetic field is 100 times smaller at the left hand edge of the figure compared with its maximum which is at the center. Note that the particle is reflected, just as would be expected. Figure 4 is the projection of the trajectory in a plane perpendicular to the magnetic axis.

Figures 5 and 6 show the orbit of the same particle, but with an r.f. quadrupole field set up between the left hand edge of Figure 5 and the midplane. Figure 5 shows that the particle is not reflected and passes through the center of the solenoid. The

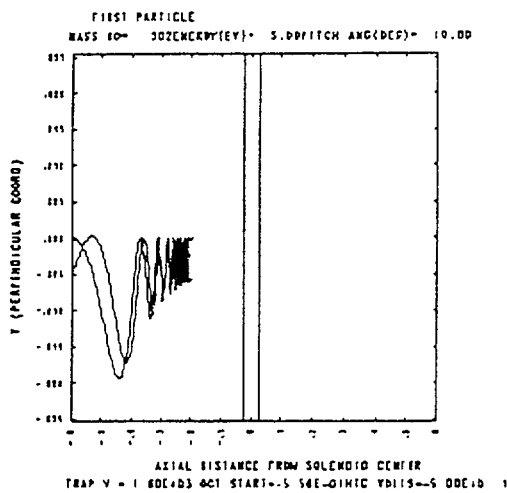


FIG. 3.

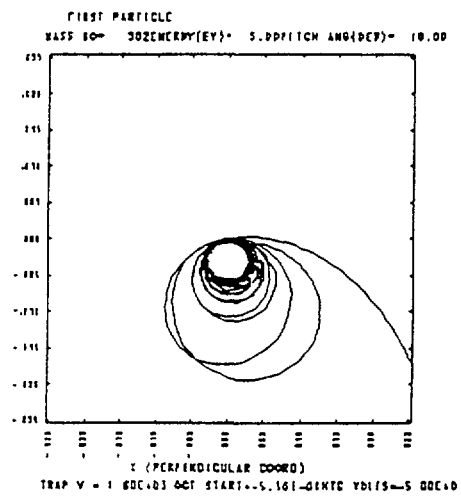


FIG. 4.

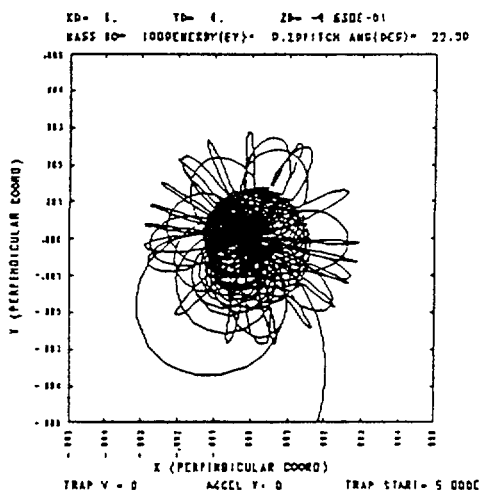


FIG. 5.

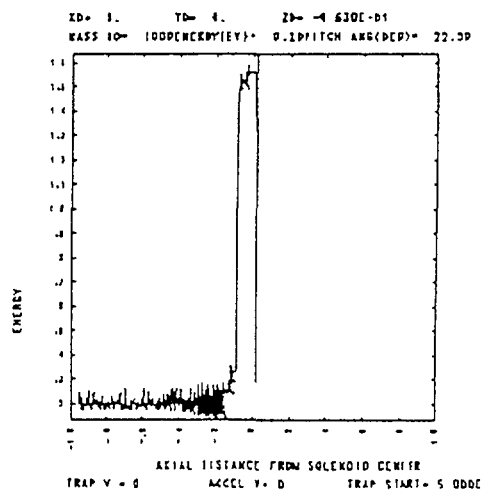


FIG. 6.

magnitude of the electrostatic field is such that it is greater than the magnetic force at the boundary of the figure, but, because the magnetic field increases toward the mid plane, the magnetic force outweighs the electrostatic force at the mid plane region. Figure 6 shows the effects. Near the outer edge, the orbit oscillates up and down in following the r.f. field. As the particle travels toward the midplane, the orbit begins to precess and then "open", finally reaching a full circular orbit when it enters the mid-plane region.

Direct applications to stellarators can be used to improve confinement, especially since the ponderomotive force acts in the opposite direction to the motion of particles that are drifting out along the minor radial direction. It might also result in particle "de-trapping" which can improve confinement as well.

#### REFERENCES

- 1 H. Wollnik, Optics of Charged Particles, Academic Press (New York), (1987), Ch. 3.
- 2 J. E. Campana, J. Shabanowitz and J.L. Shohet, Ion Injection into a Fourier Transform Mass Spectrometer, Proc. Am. Soc. for Mass Spectrometry Conference (1989).
- 3 G. Schmidt, Physics of High Temperature Plasmas, 2nd ed., Academic Press (New York), (1979), p. 49.

## ULTRA-SIMPLE STELLARATORS

T.N. TODD

Culham Laboratory,  
Euratam–UKAEA Fusion Association,  
Abingdon, Oxfordshire,  
United Kingdom

### Abstract

An ultra-simple approach to achieving a high rotational transform, low aspect ratio toroidal magnetic confinement system is presented, featuring just two planar coils, optionally interlinked. The effect of the principle free parameters on the vacuum magnetic topology of the configuration is explored, suggesting a compromise between minimising magnetic field ripple and plasma aspect ratio. It appears that an attractively simple, magnetically robust design can be achieved, with the possibility of further improvements by more sophisticated optimisation of the coil shapes.

Magnetic confinement fusion is presently undergoing a revival of interest in stellarators, with a number of new devices recently commissioned and others in advanced stages of planning. The majority of these devices feature a daunting level of technology, whether of the classical helical winding types such as ATF, U2-M and LHS or the more recent modular and heliac [1] types exemplified by W7AS, H-1 and TJ-II. As such they are beyond the resource capability of all but the relatively well-endowed plasma physics institutions, unless built more on the scale of Shatlet-M, IMS or Sheila. Some other institutions e.g. universities in developing countries, would pursue the physics of plasmas in stellarator configurations if they were as easy to build as the small tokamaks or plasma focus experiments commonly favoured, thus broadening the stellarator community to the benefit of all concerned.

So what is the simplest possible geometry for a stellarator? Since helical or severely non-planar coils are inevitably prone to engineering difficulties, it would seem reasonable that a heliac constructed from planar coils might be preferred. Such devices typically feature several field periods, each consisting of several toroidal field coils, but there is no reason in principle why the number of field periods and coils per period should not be reduced to one. This is equivalent to constructing a global  $q = 1$  surface and then resonantly perturbing it with the stray field from the return limb of the single toroidal field coil employed. Besides reducing the number of field periods, the choice of  $q = 1$  for the global structure has the advantage of producing the minimum density of neighbouring low-mode-number rational surfaces, enhancing the immunity to satellite perturbations from harmonics of the vacuum fields, constructional errors or pressure-driven plasma currents. The basic structure of the proposed configuration is accordingly a single large rectangular TF coil with a hardcore ring arranged axisymmetrically around one long limb, as shown in Fig 1.

When the TF coil is extremely large ( $200R \times 200R$ ,  $R$  being the ring radius) the structure of the magnetic surfaces is broadly consistent with simple linear theory for the structure of an island in the gradient of global rotational transform,  $\nabla\bar{i}$ , i.e.

$$(r - r_o) = \pm(w/2\sqrt{2})\sqrt{\cos(m\theta_1) + f}$$

and

$$\frac{1}{\bar{i}_{private}} \equiv q_{private} = \frac{4\sqrt{2}}{m\pi w \nabla\bar{i}} \int_0^{\cos^{-1}(-f)} \frac{d(m\theta_1)}{\sqrt{f + \cos(m\theta_1)}}$$

Here  $r_o$  is the radius of the resonant surface,  $m$  is the resonant poloidal mode number,  $w$  is the full island width, given by

$$\frac{w}{2} = \sqrt{\frac{-4Rb_{r_o}}{mB_\phi \nabla\bar{i}}}$$

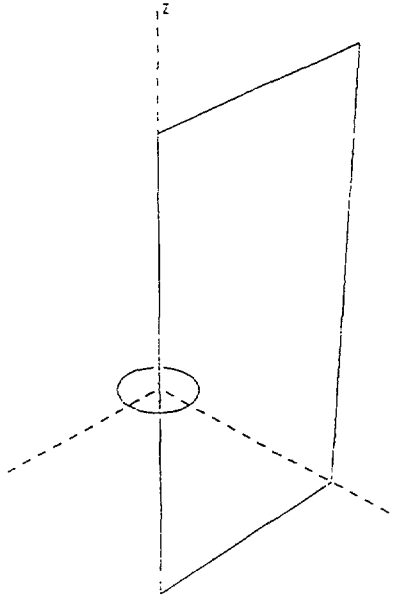


Figure 1. Coil layout of ultrasimple, single field period heliac.

(where  $R$  is the major radius of the resonant surface,  $b_{r_0}$  is the amplitude of the perturbing field and  $B_\phi$  is the toroidal field),  $\theta_1$  is the poloidal angle subtended between the o-point and a point in the island, and  $f$  is the nesting parameter, varying between  $-1$  (representing the o-point) and  $+1$  (corresponding to the separatrix). The value of the integral is  $\pi/\sqrt{2} \approx 2.22$  at  $f = -1$ , rising slowly to  $\approx 4.1$  at  $f = 0.9$  and diverging to  $\infty$  at  $f = +1$ .

Clearly as the size of the TF coil is reduced towards more manageable proportions, the field from the return limb rises, eventually becoming too large for clean island generation and creating stochasticity. However the field from the return limb can be compensated by tilting and/or outwardly shifting the hardcore, until some optimum is reached where the magnitude of the satellite perturbation spectrum (and hence the degree of magnetic surface destruction) arising from the various non-axisymmetries is just tolerable. A wide range of such configurations has been found by simple field line tracing, featuring various ratios of ring current to TF coil current and TF dimensions.

A natural property of simple heliacs is that the magnetic field strength explored by the field lines includes the global variation with major radius, so that the field ripple rises with the inverse aspect ratio of the original resonant surfaces, i.e. the ratio of ring to TF current. The achievement of good surfaces when this ratio was low, however, was possible only with a moderately large toroidal field coil, so that for a given plasma volume a compromise between machine size and trapped particle losses due to field ripple seems to be necessary. Figure 2 shows a sequence of surface cross-sections at the outboard midplane for various ratios of  $I_{ring}/I_{TF}$  with TF dimensions  $10R \times 16R$ , the longer dimension being directed along the axis of (global) symmetry. All of these cases feature a monotonic rotational transform profile falling from  $\leq 2/3$  at the centre to  $\geq 1/2$  at the surface. Sliding the ring too far away from the return limb causes private  $m=2$  ( $\bar{\nu} = 1/2$ ) islands to appear at the edge, while sliding it the other way creates an  $m=3$  ( $\bar{\nu} = 2/3$ ) island chain near the magnetic axis. These effects are due to the whole rotational transform profile shifting downwards as the compensation of the return limb field is increased, consistent with the linear theory above. Another class of configurations with  $\bar{\nu}(r) \leq 1/2$  (as found in the 200 m square TFC case) can only be preserved for modest reductions in the size of the TFC, down to  $\approx 20R \times 40R$ , without becoming ergodic.

Very tight aspect ratio configurations are possible with this approach, as shown at various toroidal angles in Fig 3 for a case with  $I_{ring}/I_{TF} = 0.15$  (hence very large field ripple) and TF dimensions of  $7R \times 14R$ . This achieves a ratio of mean major radius to mean minor radius (volumetrically averaged)

of 2.74, while the equivalent current of the outermost surface ( $I_{eq} = I_{TF}\bar{u}(\bar{a}/\bar{R})^2$ ) is 49% of the ring current. Fig 4 shows the profiles of rotational transform, magnetic field ripple and specific volume  $V' = \frac{1}{\phi} \int_0^\phi \frac{d\ell}{|B|}$  for this case and another at  $I_{ring} = 0.05$ , TF size 10R x 16R. Evidently although the achievable aspect ratios and rotational transform profiles of this configuration class are (serendipitously) very favourable, the ripple and well depth (or rather, hill height) leave much to be desired.

The presence of a magnetic hill is theoretically expected to destabilise modes such as the resistive interchange [2] but the non-linear effects of such activity on energy transport etc are not easily predicted and could perhaps be acceptable, as suggested in ref [3] for modest hills. Devices such as asperators [4], bumpy tori [5,6,7] and levitrons [8,9] have been operated successfully at low  $\beta$  with magnetic hills, so that plasma initiation is not in question. The equilibrium currents associated with finite plasma pressure will, particularly at tight aspect ratio, cause an outward shift of the inner magnetic surfaces, reducing the vacuum hill, while the strong shear of the configuration will exert a stabilising influence, but the necessary equilibrium and stability analyses to quantify these effects are beyond the scope of this study.

Adding a uniform vertical field or single extra circular coil alters the shape of the surfaces considerably but has no significant effect on the profile of specific volume. Various shapes and/or winding elongations for either or both of the coils have been tried, preserving their planarity, but the principle effect was to introduce strong splitting of the magnetic surfaces. It may be that the addi-

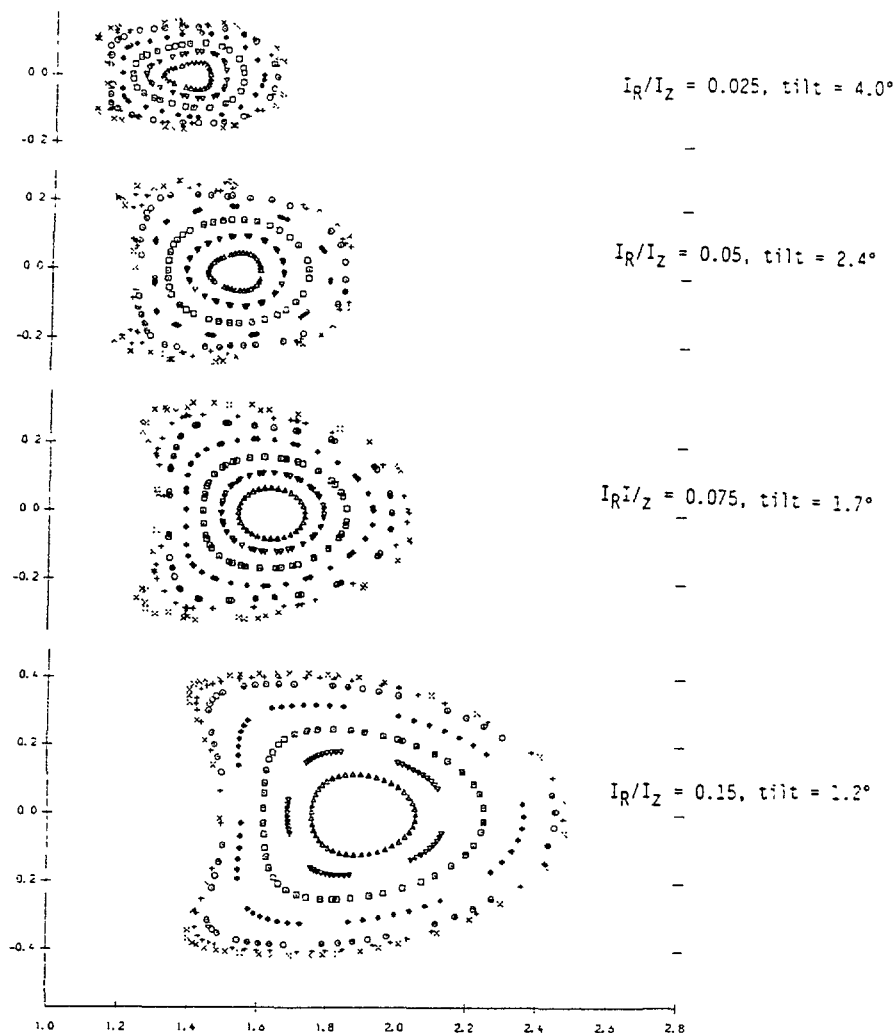


Figure 2. Effect of varying  $I_{ring}/I_{TF}(I_R/I_Z)$  with optimum ring tilt, for TF size = 10R x 16R

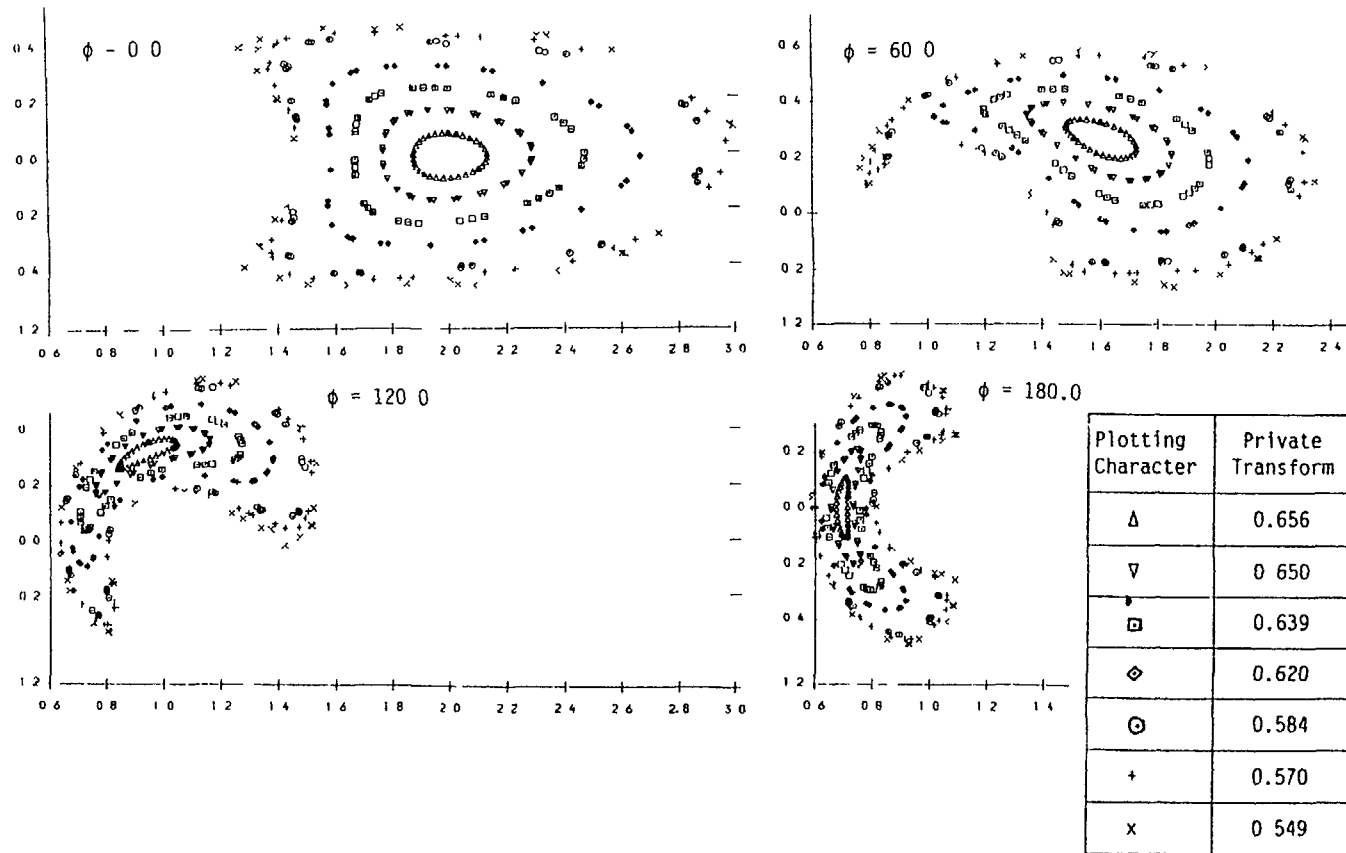


Figure 3 Low aspect ratio, high transform example ( $I_R/I_Z = 0.15$ , tilt =  $0^\circ$ , TFC size =  $7R \times 14R$ ) shown for four toroidal angles  $\phi$ .  $\phi = 180^\circ$  corresponds to the angle of the TFC return limb

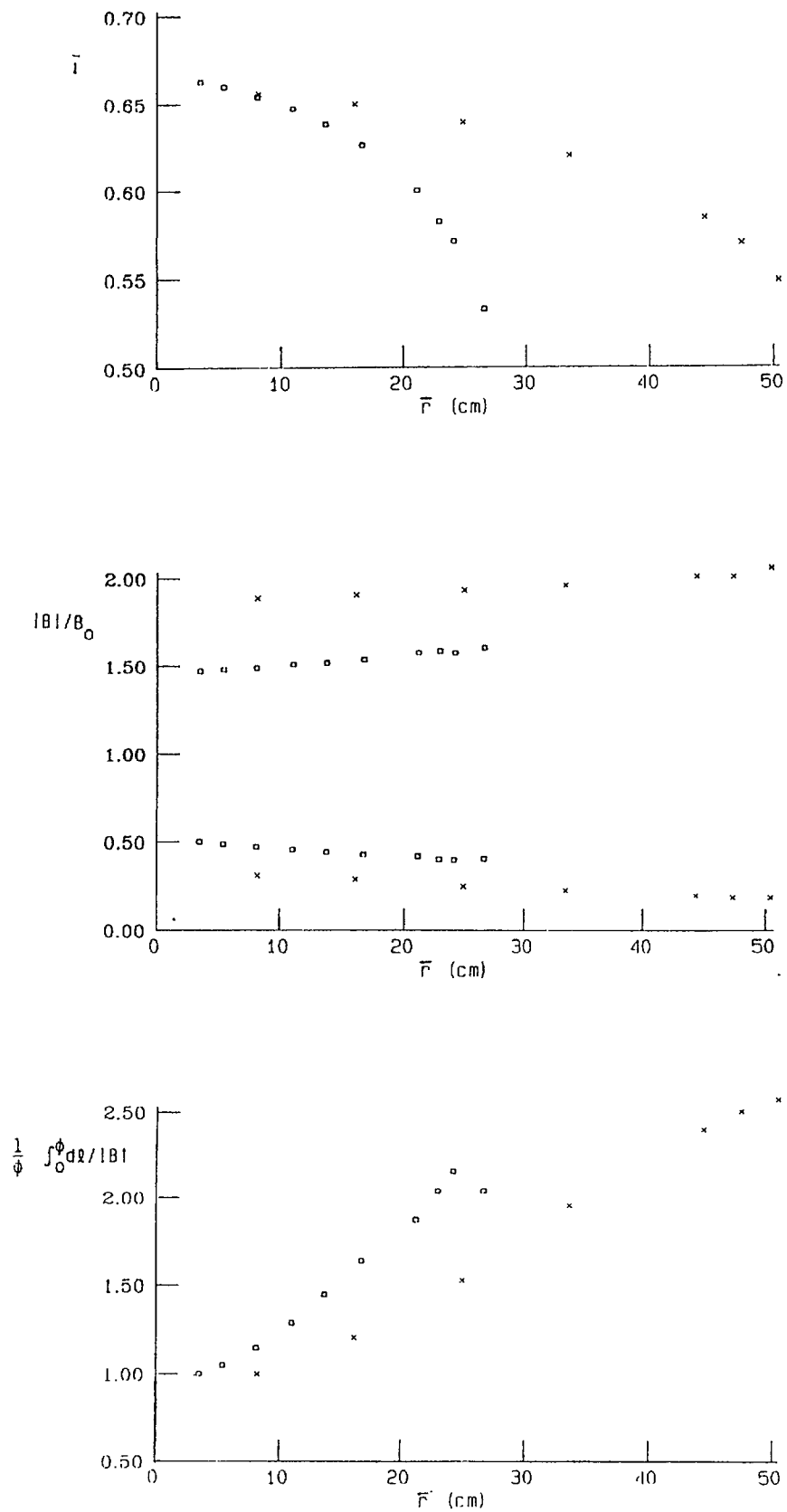


Figure 4 Profiles of (4a) rotational transform ( $\bar{i}$ ) (4b) magnetic field ripple (max and min  $|B|$ ) and (4c) specific volume ( $\frac{1}{\phi} \int_0^\phi \frac{d\ell}{|B|}$ ) for the case of Figure 2,  $I_Z/I_R = 0.05$ , and Figure 3

tion of  $\ell = 2$  fields (i.e. another ring coil, paralleling the plasma) would reduce the hill, but this or any more sophisticated optimisation, e.g. via an implementation of the Cary-Hanson technique [10], may well result in non-planar coil deformations as well as additional coils, complicating the structure.

A potential advantage with a penalty of increased geometrical complexity arises if the coils are formed without interlinking, as favoured for any wound-wire construction. As a demonstration of the robustness of the configuration, two such cases corresponding to case 4 of Fig 2, but with the ring substituted by a “Pacman” shaped coil (modelled by  $\approx 70$  straight filaments specified only to an accuracy of  $10^{-2}$  of the ring radius) were evaluated with and without a compensation loop. Despite the broad spectrum of perturbations these distortions created, the surface splitting was found to be quite modest even in the uncompensated case, Fig 5, and could presumably be nulled by a more subtle optimisation.

The lowest order resonance in this family of configurations ( $0.5 < \bar{\iota} < 0.667$ ) is at  $\bar{\iota} = 0.60$  with  $m = 5, n = 3$ , and small islands were observed here in some of the cases studied. However the effective  $n = 3$  spectrum can be modified by forming the toroidal field coil conductor stack into a triangular or trifoliate cross-section where it passes through the ring, readily producing a null or inverse island phase in the cases examined, and simultaneously improving the outermost surfaces, where the  $m = 6, n = 3$  is marginally resonant.

In conclusion this limited study has shown that there exist classes of tight aspect ratio, high rotational transform heliac stellarators which feature extreme engineering simplicity and very robust magnetic surfaces, capable of providing a suitable basis for the investigation of generic stellarator issues such as magnetic hill and ripple effects. It seems likely that related configurations should exist which would preserve the fundamental simplicity of these examples but improve upon their magnetic properties.

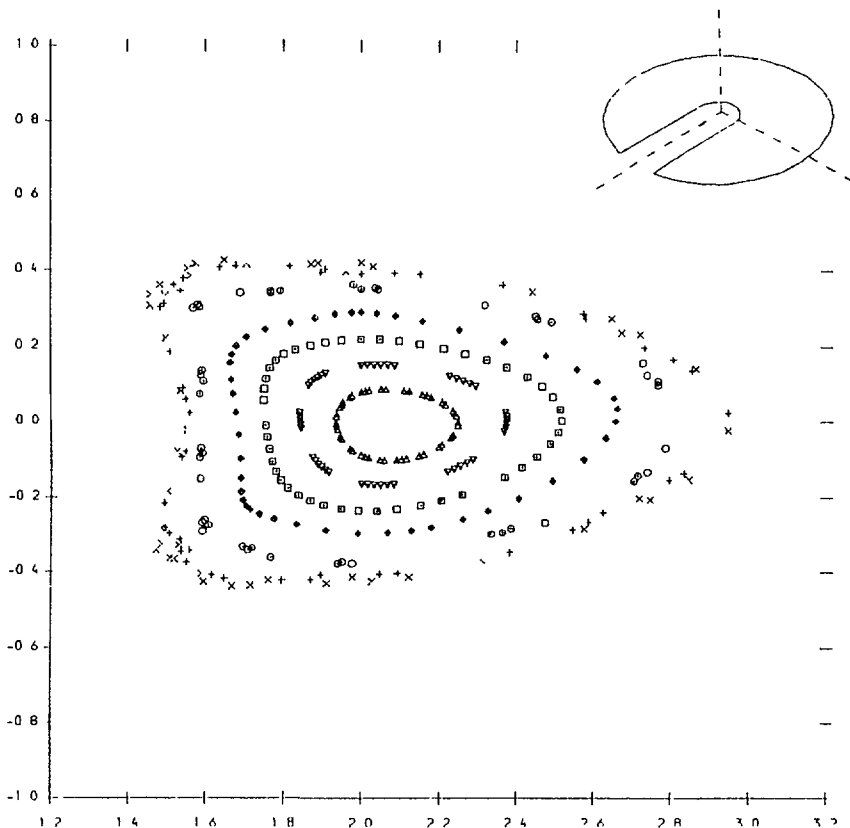


Figure 5 Magnetic surfaces with uncompensated “Pacman” ring coil

## REFERENCES

- [1] Boozer, A et al, Proc of 9th Int Conf on PP and CNFR Baltimore 1982 V3 p129
- [2] Dommaschk, W et al, Proc of Int Stell Workshop Kyoto 1986 V2 p336-357
- [3] Shaing, K and Carreras, B, Phys Flu 1985 V28, p2027
- [4] Funanto, V et al, Jap J of App Ph, 1984 V23 No 10 pp779-781
- [5] Hillis, D L Et al, Phys Flu 1986 V29 N11 pp3706-3806
- [6] Jaeger, E F et al, Nuc Fus 1985 V25 N1 pp71-84
- [7] Ikegami, H et al, Proc of 11th IAEA Conf on PP and CNF, Kyoto 1986, V2 p489
- [8] Riviere, A C et al, proc of 3rd Top Conf on RF Plasma Heating, Pasadena 1978, paper F7-1
- [9] Okabayashi, M and Freeman, R, Phys Flu 1972 V15 N2 pp359-363
- [10] Cary, J R and Hanson J D, Phys Flu 1984 V27 N4 p767-769

## **LARGE NEXT-GENERATION EXPERIMENTS**

## RECENT STATUS OF THE LARGE HELICAL DEVICE PROJECT

A. IYOSHI

Institute of Fusion Plasma Science,  
Nagoya University,  
Nagoya, Japan

### Abstract

The description of the administrative scheme and the scientific programme of the newly established Japanese fusion institute is given. The major objectives of the programme are construction and operation of Large Helical Device with the purpose of physical investigation of the plasma with target parameters close to the burning plasma region.

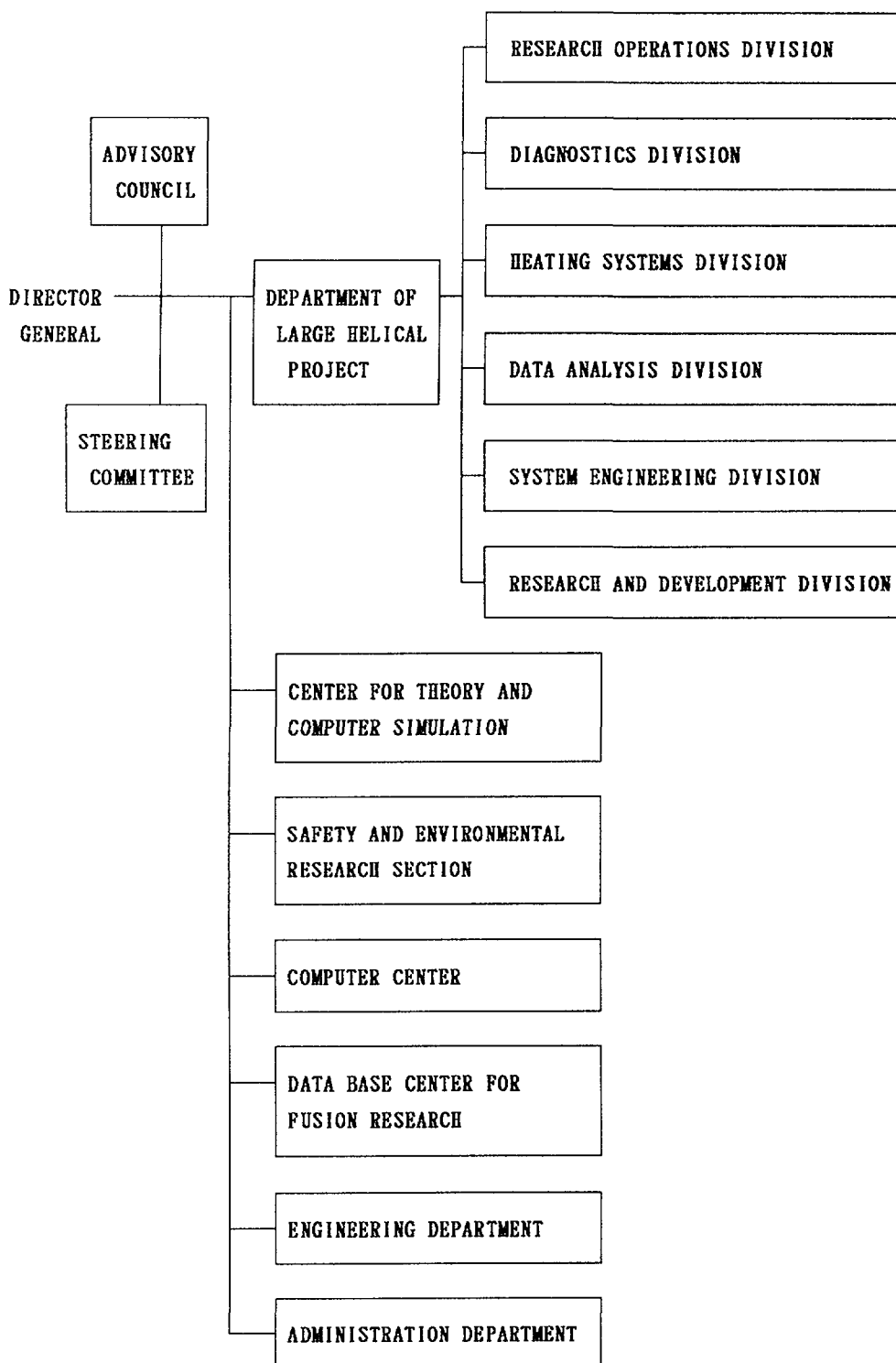
---

Establishment of the new Japanese fusion institute has been approved in the draft of the government fiscal budget 1989, which was disclosed on January, 1989. A total of about 32M\$ (1989 budget) has been approved for operating the new institute, and developing a large helical superconducting coil system and the major component of the large helical device. This new institute will be located at the site of Nagoya University (buildings of Institute of Plasma Physics) for the first several years. Institute of Plasma Physics will be abolished and the majority of the staff will be transferred to the new institute. It will be joined by a group of researchers from Plasma Physics Laboratory (Kyoto University, Heliotron) and Fusion Theory Center (Hiroshima University).

The institute will be the fusion research center (Inter-University Research Institute for Joint Use) under the Ministry of Education, Science and Culture, and many researchers of various Universities will participate in the research activities. The major activity in the first several years will be the design and construction of the Large Helical Device. We will also keep operating the small devices existing such as CHS and Heliotron E (Kyoto University) until the experiment of the new device starts.

The main objectives of the large helical device project are the physical investigations on the plasmas of which target parameter region is set between the present plasma region

INSTITUTE FOR FUSION RESEARCH (TENTATIVE)



attained by helical machines and the future burning plasma region. This helps us to obtain confinement scalings extrapolatable to the reactor plasma and contributes to develop the fusion research. The basic and necessary machine parameters are,  $R = 4$  m,  $B = 4$  T,  $m = 10$ , and  $\bar{a}_p = 50 - 60$  cm. The heating power exceeds 20 MW with ECRH, NBI and ICRF.

In the present plan, we will start the experiment on the Large Helical Device in 1995. For this end, we have to finalize the design specification early 1990, and we also need a year developing the superconducting coil which is the major component of the device. In this fiscal year, we have decided the basic specification of the Large Helical Device and the coil design, particularly m-number of the helical coil. As for the heating systems, we start the research and development program on negative ion source and new gyrotron in 1989.

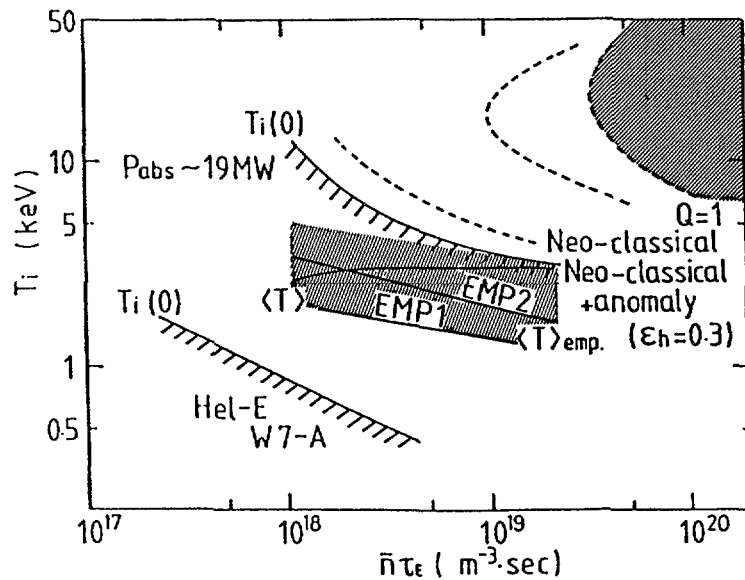


FIG. 1. Target plasma parameters space. Shaded area in the centre is the target of this project.

TABLE 1. THREE PLASMA REGIMES

<p>CASE 1 (high <math>n\tau T</math>) <math>B = 4</math> T  <math>\langle T_i \rangle = 3 - 4</math> keV,  <math>\langle n \rangle = 10^{20} \text{ m}^{-3}</math>,  <math>\tau_E = 0.1 - 0.3</math> sec,</p>
<p>CASE 2 (high <math>T_i</math>) <math>B = 4</math> T  <math>T_i(0) = 10</math> keV,  <math>\langle n \rangle = 2 \times 10^{19} \text{ m}^{-3}</math>,  <math>\tau_E = 0.05 - 0.1</math> sec,</p>
<p>CASE 3 (high <math>\beta</math>) <math>B = 1 \sim 2</math> T  <math>\langle \beta \rangle = 5 \%</math>,</p>

## RECENT DESIGN CONSIDERATIONS FOR THE LARGE HELICAL DEVICE

O. MOTOJIMA

Institute of Fusion Plasma Science,  
Nagoya University,  
Nagoya, Japan

### Abstract

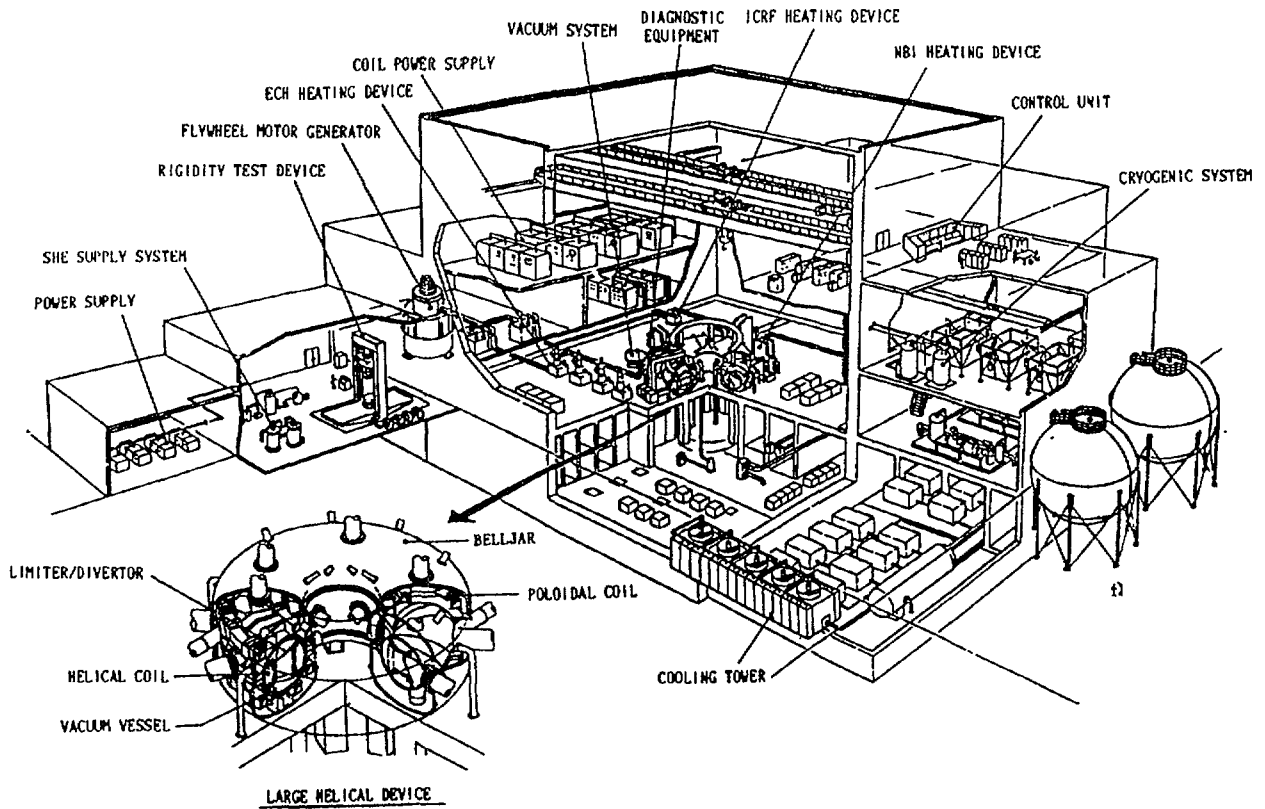
This paper describes the objectives of the new project for large superconducting helical devices at the new Japanese fusion research institute. The basic device parameters as well as the target parameter region are reported.

---

A large superconducting (SC) helical device of Heliotron Type has been designed for two years by Design Team (A Joint University Effort in Japan). This will be a major experimental device for the new Toki Institute (Institute for Fusion Research, Gifu Prefecture, Japan), which will be founded in 1989 by the Ministry of Education, Science and Culture. After intensive design study of both super-conducting (SC) and normal-conducting (NC) systems, the SC design was adopted. This paper describes the objective of this project and the recent design consideration of the SC helical device.

The main objectives of this large helical system project are;

- (a) To carry out transport study in a wide range of plasma condition and to achieve high  $nT$  plasma conditions extrapolatable to reactor plasmas.
- (b) To realize high-beta plasmas with average beta value of 5%, which is required for reactor plasmas, and to understand the related plasma physics.
- (c) To attain quasi-steady state operation and the related data base using helical divertors.
- (d) To study the behavior of high-energy particles in this non-axisymmetric system, and to simulate alpha-particle behaviors.
- (e) To increase the comprehensive understanding of toroidally confined plasmas by carrying out studies complementary to those in tokamaks.

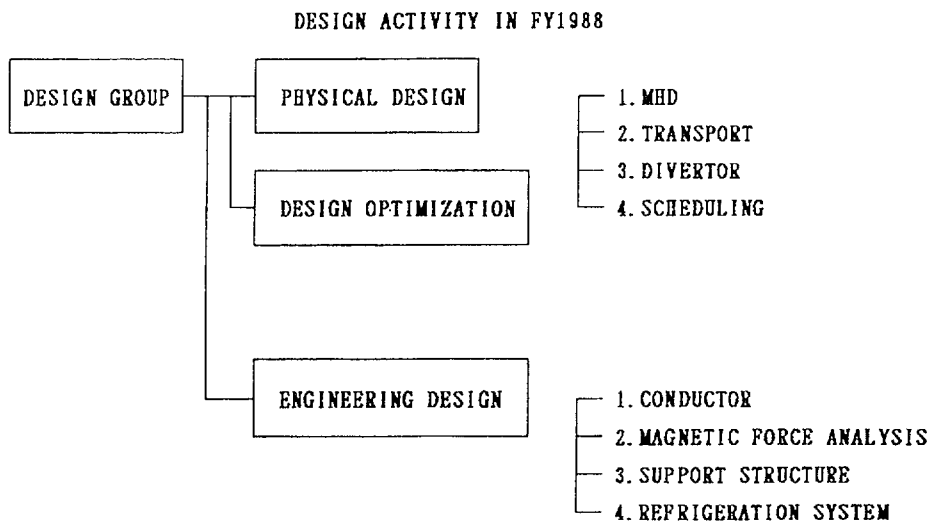


Large helical system device and supporting facilities.

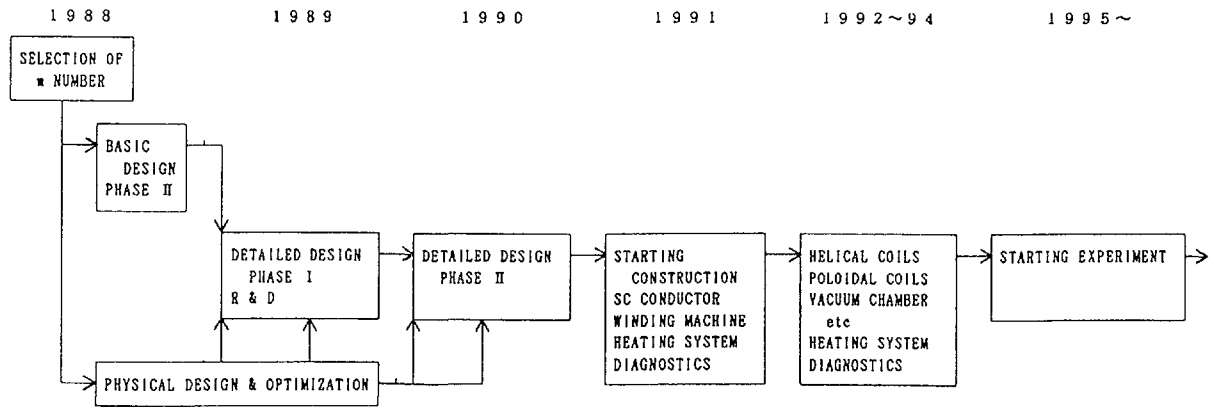
The target parameter region of this project is set between the present plasma region attained by helical machines and the future burning plasma region, which help us obtain confinement scalings extrapolatable to the reactor plasma. This region is estimated by the neoclassical theory and two experimental scalings mainly based on the Heliotron experimental data. It is an important engineering innovation to build a super-conducting helical device of which stored energy is larger than 2 GJ, largest in the world. The construction is scheduled to be completed in 1995. At present, the device parameters have been almost converged to the followings after the intensive design studies.

Major Radius	4	m
Minor Coil Radius	0.96	m
Magnetic Field(plasma center)	4.0	T
(maximum)	8	T
Toroidal Field Period	10	
Helical Coil Current	8	MAT
Coil current Density	4.0	kA/cm <sup>2</sup>
Rotational Transform(center)	0.5	
(surface)	1.0	
Heating Power	20	MW

Basic design of the helical device were carried out in FY 1988 to determine the helical field period and winding law (basic phase-2 design) and to conduct the further optimization. The detailed phase-1 design for the decision of the cooling system will be done in FY 1989. After the decision of the main contractor for the machine construction, detailed phase-2 design will be conducted in FY 1990. The device contraction will be started in FY 1991 and completed in FY 1994. A first plasma is expected in FY 1995.



TIME SCHEDULE



## THEORETICAL STUDY OF THE LARGE HELICAL DEVICE

M. WAKATANI, Y. NAKAMURA, K. HANATANI

Plasma Physics Laboratory,  
Kyoto University,  
Gokasho, Uji, Kyoto

T. KAMIMURA, H. SANUKI, T. AMANO,  
N. NAKAJIMA, M. OKAMOTO

Institute of Plasma Physics,  
Nagoya University,  
Nagoya

T. HAYASHI

Institute of Fusion Theory,  
Hiroshima University,  
Hiroshima

A. FUKUYAMA

Faculty of Engineering,  
Okayama University,  
Okayama

M. OHNISHI

Institute of Atomic Energy,  
Kyoto University,  
Gokasho, Uji, Kyoto

J. TODOROKI

Institute of Fusion Plasma Science,  
Nagoya University,  
Nagoya

Japan

### Abstract

In this paper the general properties of  $l=2$  torsatron/heliotron are discussed from MHD equilibrium and stability, neoclassical transport, particle confinement and auxiliary heating. Compatibility of high beta limit and good confinement is studied for low aspect ratio systems.

---

General properties of  $\ell=2$  heliotron/torsatron are discussed from MHD equilibrium, stability, neoclassical transport, high energy particle confinement and NBI or ICRF heating. Compatibility of high beta limit and good confinement is intensively studied for low aspect ratio systems of  $M=10$  configurations, where  $M$  is a helical period number.<sup>1)</sup>

### M=14 Configuration

Since there is a size limitation,  $R \sim 4$  m, for the Large Helical System (LHS), pitch parameter  $\gamma = a_c/R \cdot M/\ell$  must be less than about 1.3, where  $a_c$  is a coil radius. If  $\gamma$  exceeds this value, the outermost flux surface will get in contact with the finite size helical coils having a current density of (30 - 40) A/mm<sup>2</sup>, which is given technologically to produce B=4 T at the center of vacuum vessel. For  $\gamma < 1.3$ , the rotational transform at the edge,  $\iota(a)$ , always exceeds one, which brings about a severe MHD stability beta limit. It is usually in the range of  $\beta(0) \simeq 3 - 4$  % for the standard pressure profile,  $P=P_o(1-\psi)^2$ . This beta limit is much less than the equilibrium beta limit of  $\beta_{eq}^c(0) > (15 - 20)$  %.

Though particle confinement properties is better than the configuration with M=12 or M=10, it is not easy to enhance the stability to obtain the critical beta of  $\beta^c(0) \sim 15$  %.

### M=12 Configuration

Under the constraints of reserving a space for the divertor region larger than several cm and of the maximum coil current density,  $j_{max} < 40$  A/mm<sup>2</sup>,  $\iota(a)$  still exceeds one even in the case of M=12, R=4 and B=4 T. ATF is optimized from the point of view of the high beta plasma confinement, which requires  $\gamma \sim 1.4$ . For an example where  $\iota(a) \sim 1.4$  and plasma aspect ratio is A=8, the low n mode stability limit is  $\beta(0) \simeq 5$  % for  $P=P_o(1-\psi)^2$ .<sup>2)</sup>

### M=10 Configuration

In this case, configurations with  $\iota(a) \sim 1$  and no contact of the outermost flux surface with the finite size helical coils are realized.

#### (i) Equilibrium beta limit ( $\beta_{eq}^c$ )

When the magnetic axis position exists at the center of the vacuum chamber, which is called standard case, we examined  $\beta_{eq}^c$  for various  $\iota(0)$  with a fixed  $\iota(a) \sim 1$ . When  $\iota(0)$  decreases,  $\beta_{eq}^c$  degrade a little bit; however,  $\beta_{eq}^c$  still keeps  $\beta_{eq}^c(0) \sim 15$  %. In the case that the magnetic axis is shifted inside by the vertical field,  $\beta_{eq}^c$  again degrade a little bit. By applying the quadrupole field additionally, the averaged flux surfaces can be controlled. When they become horizontally elliptic,  $\beta_{eq}^c$  degrades due to an enhancement of P-S current.

#### (ii) Stability beta limit ( $\beta_{st}^c$ )

For the standard case,  $\beta^c(0) > 15$  % limited by  $\beta_{eq}^c$  is obtained for various configurations with  $\iota(0) \sim 0.3, 0.4,$  and  $0.5$  from both the low n mode stability limit and the Mercier criterion. Thus the M=10 configurations satisfy the requirement for LHS. When the magnetic axis is shifted inside, the magnetic hill region expands and there appears a tendency losing MHD stability by the Mercier criterion. However, low n mode stability limit does not decrease significantly for the inward magnetic axis shift of (5 ~ 10) cm. When the inward shift of the magnetic axis exceeds a critical value,  $\beta_{st}^c$  decreases suddenly from  $\beta_{st}^c(0) \simeq (10 - 15)$  % to the level of  $\beta_{st}^c(0) \simeq (3 - 4)$  %.

When the quadrupole field is applied additionally to the standard case for producing the horizontally elongated averaged flux surfaces, the Mercier criterion degrades a little bit due to the enhancement of the geodesic curvature term related to the P-S current. However, the low n mode stability does not change when the quadrupole field is less than a threshold value. In the case that the quadrupole field produces the vertically elongated averaged flux surfaces, the confinement of trapped particles degrades. We have no interest in such a case.

### (iii) Confinement of trapped particles

It is known that the trapped particle loss is increased in the low aspect ratio heliotron/torsatron configurations. We studied two approaches to improve particle confinement properties. One is to shift the magnetic axis inside by the vertical field. However, this is the direction that degrades the MHD stability properties. The velocity space loss region disappears for  $r/a \leq 0.3$  region, when the axis shift is larger than about 10 cm in the vacuum magnetic configuration with  $R=4$  m and  $B=4$  T. When there is no direct loss of high energy particles for the  $r/a \leq 0.3$  region, ICRF heating with  $H_e$  minority works and parallel neutral beam injection heating is shown effective by the Monte Carlo calculations. Thus, if we can control the magnetic axis freely by the vertical field, the configuration is varied from the standard one with good MHD properties to the inwardly shifted case of the magnetic axis with good particle confinement properties.

The other approach to obtain good confinement of trapped particles is the application of the quadrupole field to produce horizontally elongated averaged flux surfaces. When the quadrupole field is chosen suitably, loss of trapped particles from the half radius region becomes less than (20 - 25) %. Here it is assumed that particle density is uniform both in the velocity space and in the real space.

The best way to improve the particle confinement without deteriorating the good MHD properties of the standard case is to combine the inward magnetic axis shift of (5 - 10) cm with the application of the quadrupole field to produce almost circular averaged flux surfaces at  $R=4$  m and  $B=4$  T. It is noted that degradation of the particle confinement due to the Shafranov shift is minimized by taking the best configuration to confine trapped particles at  $\beta=0$ .

### Transport Prediction

Transport code predicts that two interesting regimes exist in LHS experiments. One is the high density regime with the largest  $\bar{n} \tau_E (T_e(0) + T_i(0))$  (ion root case) and the other is the low density regime with the highest  $T_i(0)$  (electron root case).

Our transport model based on the neoclassical ripple transport with an edge anomalous transport for the particle diffusion and the electron thermal transport gave the confinement time scaling  $\tau_E \propto B^{0.33} R^{0.75} a^{1.8}$ . This scaling suggests a little lower B and a little larger R will give a better confinement, which is almost consistent with the empirical LHS scaling result following  $\tau_E \propto B^{0.53} R a^{2.3}$

We acknowledge ORNL theory group particularly B. A. Carreras, and J. Johnson and G. Rewoldt at PPPL for supporting the theoretical studies of LHS design.

## REFERENCES

- 1) J.Todoroki, T.Kamimura, H.Sanuki, T.Amano, T.Hayashi, K.Suzuki, T.Sato, K. Hanatani, Y.Nakamura, M.Wakatani, and A.Iiyoshi, in 12th IAEA Conf. on Plasma Physics and Controlled Nuclear Fusion Research (Nice, 1988) IAEA-CN-50/C-5-4.
- 2) Y.Nakamura, K.Ichiguchi, M.Wakatani, H.Zushi, J.L.Johnson, G.Rewoldt, B.A. Carreras, N.Dominguez, J.N.Leboeuf, J.A.Holmes, and V.E.Lynch, US-Japan Workshop on Kinetic Modifications of MHD Modes, Second Stability, and Alpha Particles in Toroidal Systems (Princeton, 1989)
- 3) S.Sudo, private communication.

## PHYSICS AND ENGINEERING DESIGN FOR WENDELSTEIN VII-X

C. BEIDLER, G. GRIEGER, F. HERRNEGGER,  
E. HARMEYER, J. KISSLINGER, H. MAASSBERG,  
P. MERKEL, J. NÜHRENBERG, F. RAU, J. SAPPER,  
R. SCARDOVELLI, A. SCHLÜTER, H. WOBIG  
Euratom-IPP Association,  
Max-Planck-Institut für Plasmaphysik,  
Garching, Federal Republic of Germany

### Abstract

At IPP Garching, the future experiment *Wendelstein VII-X* is being developed. A Helias configuration ( Helical Advanced Stellarator ) has been chosen because of its confinement and stability properties [1]. The aim of *Wendelstein VII-X* is to demonstrate the reactor capability of this stellarator line, to achieve quasi-steady state operation in a temperature regime above 5 keV and to investigate the merits and limits of the modular stellarator. A heating power of 20 MW will be applied to reach the reactor relevant parameter regime.

The magnetic field in *Wendelstein VII-X* has 5 periods; other basic data are: major radius  $R_0 = 6.5$  m, magnetic induction  $B_0 = 3$  T and a stored magnetic energy of  $W \approx 0.88$  GJ. The average plasma radius is 0.65 m. Studies of superconducting coil systems for Helias configurations have shown that the lateral force components can reach the magnitude of radial force components which exhibit helicity in accordance with the helix-like magnetic axis. Other studies are concerned with the engineering of superconducting non-planar coils and its conductor.

---

### I. Introduction

*Wendelstein VII-X* is a continuation of the Advanced Stellarator line, which has been developed in Garching and successfully realized with the construction of *Wendelstein VII-AS*. *Wendelstein VII-X* will go a step further than *Wendelstein VII-AS*, aiming to reach reactor relevant parameter regimes and to demonstrate the reactor capability of modular stellarators. For this purpose the size of *Wendelstein VII-X* has been chosen large enough to give access to powerful heating methods and to allow quasi-steady state operations. In detail the aims of the *Wendelstein VII-X* experiment are:

- to achieve quasi-steady state operation in a reactor relevant parameter regime with temperatures above 5 keV and densities above  $10^{20} \text{ m}^{-3}$
- to demonstrate stable plasma equilibrium with  $\langle \beta \rangle = 5\%$
- to confine a plasma over a sufficiently long time, allowing extrapolation to reactor parameters
- to control plasma density and impurity content
- to operate the experiment in steady state with a field generated by modular and superconducting coils.

*Wendelstein VII-X* does not aim at ignition and therefore D-T reactions will not occur and provisions for handling radioactive materials need not be made. The parameter regime above 5 keV has been chosen, since in a reactor this regime has to be reached with auxiliary heating only and without assistance of  $\alpha$ -particle heating which becomes important at higher temperatures. The aim of  $\langle\beta\rangle = 5\%$  results from economic requirements of nuclear fusion and not so much from physics requirements. Since fusion power output grows with  $\langle\beta\rangle$ , the limits of  $\langle\beta\rangle$ , set by plasma instabilities have to be pushed as high as possible and explored experimentally.

Since plasma confinement and stability depend mainly on such properties of the magnetic field like rotational transform, shear, magnetic well, local mirrors and the magnitude of Pfirsch-Schlüter currents, it requires a careful optimisation of the magnetic field and the modular coils to extend the desired properties to their limits. The following principles have been taken into account:

- I. High quality of the magnetic surfaces.
- II. Good finite-equilibrium properties.
- III. Good MHD-stability properties.
- IV. Reduced neoclassical transport in the  $1/\nu$ -regime.
- V. Small bootstrap current in the *lmfp*-regime.
- VI. Good modular coil feasibility

Generally, strong geometrical shaping of the plasma boundary will improve confinement and stability properties while it adversely affects coil feasibility. Thus, side conditions on the shaping parameters on the plasma boundary will have to be used to ensure coil feasibility. Important issues for selecting the coil geometry are the minimum distance between coils and plasma and the minimum bending radius of the coils.

A further necessary prerequisite for application to an experimental device is a sufficiently broad accessible range of variable magnetic field parameters, like field strength, rotational transform and axis position.

## II. Basic Data of Wendelstein VII-X

The magnetic field configuration of *Wendelstein VII-X* differs from *Wendelstein VII-AS* mainly in the shape of the magnetic surfaces and the existence of a helical magnetic axis. This Helias-concept, developed by J. Nührenberg et al. [1] (Helias = Helical Advanced Stellarator) extends the principle of minimum Pfirsch-Schlüter currents to its maximum while it preserves MHD-stability by a magnetic well. Helias configurations, which have been investigated for 4,5 and 6 field periods, are characterized by very low Shafranov shift and negligible change of the rotational transform with finite  $\langle\beta\rangle$ . Configurations which are stable up to an average  $\langle\beta\rangle$  of 9% (resistive interchange modes) are found. In the special case of quasi-helically symmetric configurations [2] neoclassical transport is very low and comparable to axisymmetric configurations since trapped particles are on confined orbits. Other Helias configurations are more of the linked-mirror type [3] with poloidally closed mod B-contour lines. Furthermore, Helias configurations with very small bootstrap currents for all plasma radii have been found recently.

For all these reasons a Helias configuration with 5 field periods has been selected for *Wendelstein VII-X*. The choice of 5 field periods is mainly dictated by MHD-ballooning modes, which lead to  $\langle\beta\rangle$ -limits below or equal to 3% in systems with 4 field periods. Otherwise, the 4-period case would be preferable due to its less complex geometrical properties of the coil system.

The number of modular coils per period is determined by the desire of maximum distance between adjacent coils for heating and diagnostics and the necessity to minimize the magnetic field ripple arising from these gaps. A compromise has been found with 12 coils per period [4].

The magnetic field on axis is 3 T. This value is mainly determined by the available space for the modular coils, the maximum current density in the coils and the mechanical stresses. The rotational transform of 5-period Helias configurations can be adjusted in the range between 0.7 and 1.4 with a shear of  $\delta\epsilon/\epsilon < 0.2$ .

For the sake of experimental flexibility provision has to be made to vary the rotational transform. This can be either done by dividing the modular coils in an upper and lower winding pack and feeding each one separately with current or by adding a separate coil system which superimposes a toroidal field parallel or antiparallel to the field of the modular coils. This latter solution has been chosen for *Wendelstein VII-X*; by superimposing a field of 10% the rotational transform can be varied by  $\pm 20\%$  [5]. In addition, these separate coils allow also to shift the magnetic axis by about 1% of the major radius. Vertical field components are introduced by appropriate current polarities.

A heating power of at least 20 MW is necessary to reach a reactor relevant parameter regime in *Wendelstein VII-X*. For this reason the geometric dimensions of the device have to be chosen large enough to give access to heating schemes like neutral beam injection and to allow for heat removal systems. Furthermore, the distance between plasma and wall has to be made as large as possible to keep wall loading and impurity influx low. Collecting all arguments related to the geometrical dimensions of *Wendelstein VII-X*, a major radius of 6.5 m and an average plasma radius of 0.65 m were chosen. The coil system of *Wendelstein VII-X* and a magnetic surface are shown in Fig. 1 (HS-5-8). In this specific version the rotational transform on axis is  $\epsilon = 1.02$  and  $\epsilon = 1.18$  on the boundary. By a slightly different choice of the geometrical parameters another version, HS-5-7, with  $\epsilon(0) = 0.75$  and  $\epsilon(a) = 0.95$  is obtained. Which version will be realized is not yet decided.

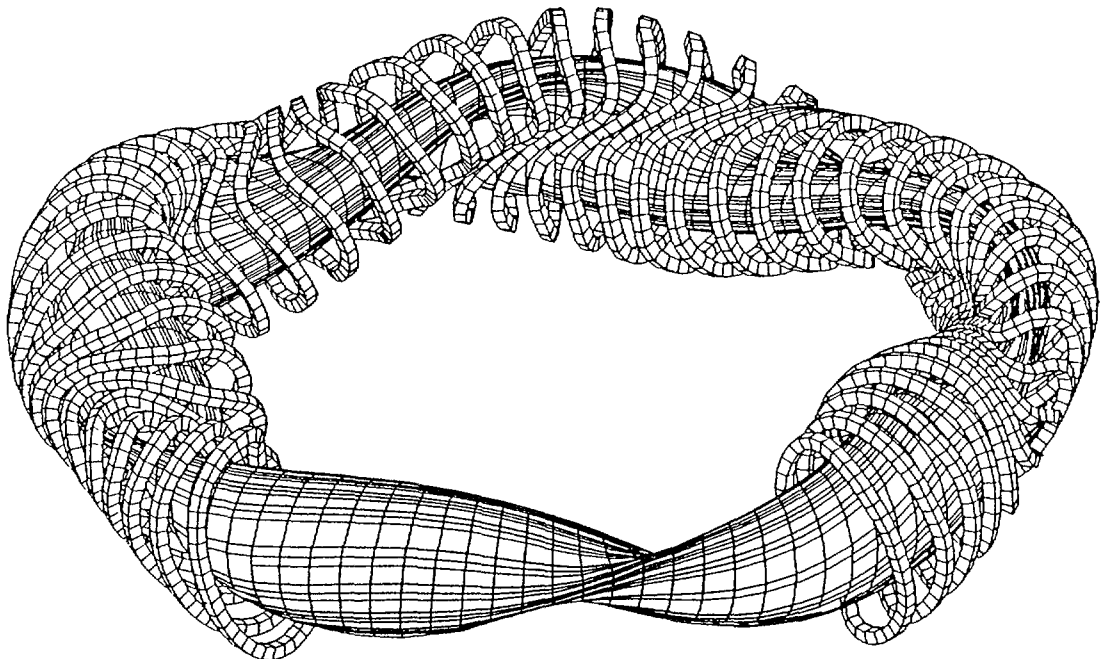


Fig. 1 Coil system of HS-5-8, 5 field periods, 12 coils per period. Geometrical data are listed in Table I.

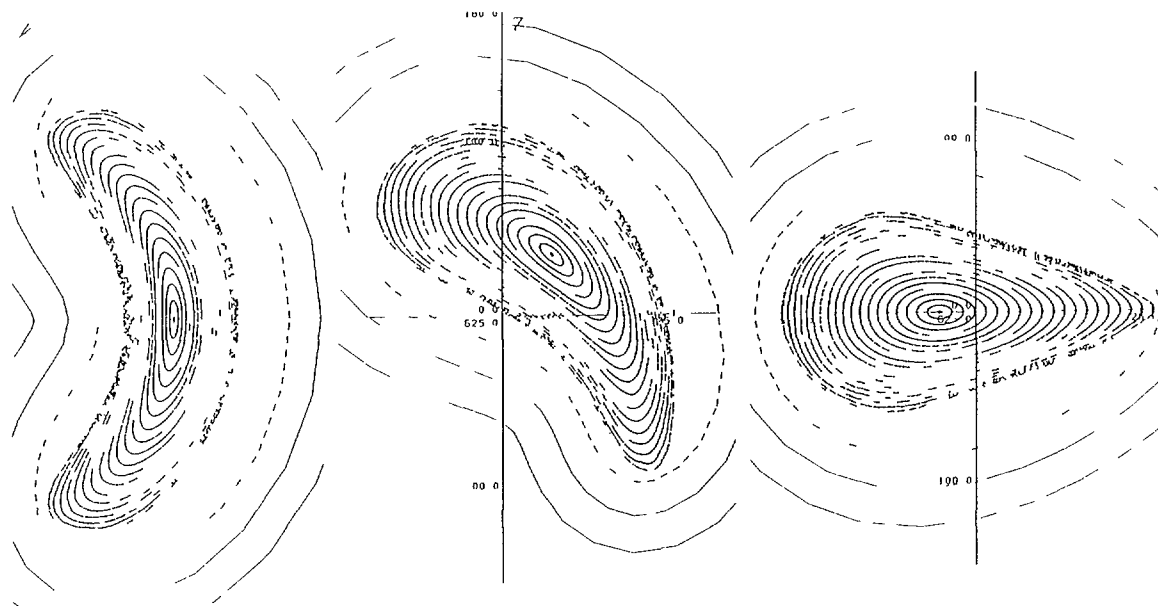


Fig. 2 Cross section of the magnetic surfaces of HS-5-8 at 3 different toroidal angles. Solid lines: coil contours, dashed line: first wall.

HS-5081, which will also be discussed for comparison is a nearly quasi-helically invariant configuration with  $\iota$  around 0.9. A list of all important parameters of *Wendelstein VII-X* is given in Table I.

### III. Physics Studies

Equilibrium in Helias configurations has been investigated using the VMEC-code with fixed boundaries [6]. The results verify the expected small Shafranov shift and the small change of the rotational transform with finite  $\beta$ . Free boundary equilibria of the Helias type have been studied by P. Merkel [7] showing that due to the small Pfirsch-Schlüter currents the plasma pressure has little effect on the shape of the boundary. MHD-stability of Helias configurations depends mainly on resistive interchange modes and ideal ballooning modes. The lowest  $\langle\beta\rangle$ -limit is given by the ideal ballooning mode, which in 4-period Helias configurations yields a  $\langle\beta\rangle$ -limit of  $\approx 3\%$ . In 5-period configurations this limit is  $\langle\beta\rangle_{crit} \leq 5\%$ . Resistive ballooning modes may lower these limits slightly.

Neoclassical transport in Helias configurations has been studied by various methods.

- Monte-Carlo technique
- Analytical solution of the bounce-averaged drift kinetic equation
- Numerical solution of the drift-kinetic equation (DKES-code)

In the *lmfp*-regime a  $1/\nu$ -scaling of the transport coefficients occurs, however, due to the reduced radial drift of trapped particles the equivalent helical ripple  $\epsilon_{eff}$  is below or equal to 0.01 at half minor radius. Ripple losses induced by the modular ripple is kept small by choosing 12 coils per period.

Table I

			HS5-7	HS5-8
Average major radius	$R_0$	[m]	6.5	6.5
Average coil radius	$r_c$	[m]	1.30	1.30
Radial coil height	$t$	[m]	0.20	0.20
Lateral coil width	$w$	[m]	0.18	0.18
Average coil volume	$V_c$	[m <sup>3</sup> ]	0.33	0.33
Total coil volume	$n \cdot V_c$	[m <sup>3</sup> ]	19.7	19.8
Min. radius of curvature	$\rho_c$	[m]	0.27	0.28
Min. distance between coils	$\Delta_c$	[m]	0.06	0.04
Coil number total / per FP	$n/n_p$		60/12	60/12
Total coil current	$I_c$	[MA]	1.73	1.73
Overall current density	$j_c$	[MA/m <sup>2</sup> ]	48.6	48.6
Total inductance (one-turn)	$L$	[μH]	591.	580.
Stored magnetic energy	$W$	[GJ]	0.88	0.87
Induction on axis	$B_o$	[T]	3.0	3.0
Max. induction at coil	$B_m$	[T]	5.7	5.8
Rotat. transform on axis	$t_o$		0.75	1.02
Rotat. transform on boundary	$t_a$		0.95	1.18
Average plasma radius	$r_p$	[m]	0.65	0.70
Average force density	$\langle F' \rangle$	[MN/m <sup>3</sup> ]	76.	75.
Local max. force density	$F'_m$	[MN/m <sup>3</sup> ]	274.	282.
Max. net force (one coil)	$F_{res}$	[MN]	3.8	4.0
Virial stress	$\sigma_V$	[MPa]	44.7	44.0

Neoclassical bootstrap currents in *Wendelstein VII-X* can be kept small by a proper choice of the magnetic field [8]. Evaluation of the geometrical factor  $G_b$  allows to predict total bootstrap currents of less than 50 kA at highest temperatures. The corresponding change of  $\epsilon$  is  $\delta\epsilon \leq 0.1$ .

Plasma parameters in *Wendelstein VII-X* are predicted using an one-dimensional guiding center code with neoclassical transport coefficients and anomalous thermal electron conduction found in *Wendelstein VII-A*. Under these conditions Plasma temperatures above 5 keV are obtained with 10 MW heating power at a confinement time of 0.6 - 1.2 seconds, depending on the ripple loss. At these high temperatures the anomalous transport is concentrated to the boundary region and has only little effect on plasma parameters. Investigation of the boundary region is made by Monte Carlo technique and field line tracing showing "hot spots" on the first wall or limiter plates for field lines starting near the separatrix [9]. The DEGAS code is used to study neutral gas behaviour and a guiding center code to identify the locations of enhanced wall loading by charged particles. On the basis of these results neutralizer plates and pump limiters will be designed.

#### IV. Engineering Studies

The superconducting coils are the main technical components of *Wendelstein VII-X* and for this reason engineering studies have been concentrated on critical issues of these coils. This includes superconducting windings, manufacturing techniques, forces and stress analysis, support system and cryostat. Because of the maximum magnetic field of 6 Tesla NbTi- superconductors can be used. Together with industry a concept has been developed which demonstrates the feasibility of 3-dimensional superconducting coils with the special specifications of *Wendelstein VII-X*. In particular, the small bending radii of 20 - 30 cm require to develop special superconducting cables with currents between 5 and 10 kA.

Another issue are mechanical stresses in the coils which are being analysed by finite element technique. To keep stresses small enough the coils have to be enclosed by a casing and fixed to a structural shell. Taking into account the necessary penetrations for diagnostics and heating systems the support system has to be optimized. The whole coil system will be enclosed by the cryostat. Although a detailed design of the coil system has not yet been made the investigations available so far confirm the feasibility of these modular coils.

#### V. Summary and Conclusions

The optimization of stellarator equilibria has led to the Helias concept which is characterized by very low Shafranov shift and MHD-stability limits up to  $\langle\beta\rangle \approx 5\%$ . Furthermore, neoclassical transport and bootstrap currents were reduced to a tolerable level by properly shaped magnetic surfaces. Based on these theoretical results the *Wendelstein VII-X* experiment is being planned with the aim to achieve reactor relevant parameter regimes and to demonstrate the reactor capability of this stellarator line.

The design of the modular coil system will be based on the experience gained with the construction of *Wendelstein VII-AS* (IPP Garching). The expertise on superconducting coils obtained in the LCT-project is also of great importance and for this reason the cooperation with KfK Karlsruhe has been initiated.

In summary it can be said that the *Wendelstein VII-X* experiment offers the chance of a new and promising stellarator line .

#### REFERENCES

- [1] NÜHRENBERG, J., ZILLE, R., *Phys. Letters* **114A** (1986) 129.
- [2] NÜHRENBERG, J., ZILLE, R., *Phys. Letters* **129A** (1988) 113.
- [3] WOBIG, H. *Proc. 2<sup>nd</sup> Workshop on Wendelstein VII-X* Ringberg, 13-16 June 1988, EUR 11705 EN, p. 3
- [4] BEIDLER, C.D. *Europhys. Conf. Abstracts*, Vol. 13B, Pt II, p. 675, Venice, March 13-17 (1989)
- [5] KISSLINGER, J. et al. *Europhys. Conf. Abstracts*, Vol. 13B, Pt II, p. 595, Venice, March 13-17 (1989)
- [6] NÜHRENBERG, J., ZILLE, R. *Theory of Fusion Plasma*, Varenna, 24-28 August 1987, Int. School on Plasma Phys. Piero Caldirola, EUR 11336 En, p. 3
- [7] MERKEL, P. *Theory of Fusion Plasma*, Varenna, 24-28 August 1987, Int. School on Plasma Phys. Piero Caldirola, EUR 11336 En, p. 25
- [8] WOBIG, H. et al. *Europhys. Conf. Abstracts*, Vol. 13B, Pt II, p. 679, Venice, March 13-17 (1989)
- [9] RAU, F. et al. *Europhys. Conf. Abstracts*, Vol. 13B, Pt II, p. 699, Venice, March 13-17 (1989)

# OPTIMIZATION OF HELIAS FOR W VII-X

W. LOTZ, P. MERKEL, J. NÜHRENBURG,  
A. SCHLÜTER, R. ZILLE  
Euratom-IPP Association,  
Max-Planck-Institut für Plasmaphysik,  
Garching, Federal Republic of Germany

## Abstract

Preliminary theoretical evidence is presented that Helias configurations can simultaneously meet seven stellarator-specific goodness criteria.

## 1. Introduction

Optimization of Helias<sup>1</sup> equilibria at finite- $\beta$  was attempted with respect to the following set of criteria: 1. high quality of vacuum field magnetic surfaces (regular boundary, avoidance of major resonances on the torus, avoidance of medium-order – for example  $\frac{1}{6}$  – resonances per period for low shear or small island widths at these rational values for significant shear, adjustment of the shear), 2. good finite- $\beta$  equilibrium properties (small parallel current density –  $\langle j_{\parallel}^2/j_{\perp}^2 \rangle \lesssim 1$  – which results in small Shafranov shift and small change of rotational transform and shear with  $\beta$  for vanishing net toroidal current), 3. good MHD stability properties (stability with respect to local resistive interchanges and ideal ballooning at  $\langle \beta \rangle \gtrsim 0.05$ ), 4. small neoclassical transport in the  $\frac{1}{\nu}$ -regime (equivalent ripple  $\delta_e \lesssim 0.02$ ), 5. small bootstrap current in the lmf- $\beta$ -regime (ratio of bootstrap current to the bootstrap current in a tokamak with same aspect ratio and rotational transform of  $J_{\text{stell}}/J_{\text{tok}} \lesssim 0.1$ ), 6. good collisionless  $\alpha$ -particle containment (fractional prompt loss of  $\alpha$ -energy  $f_{\alpha} \lesssim 0.1$ ), 7. good modular coil feasibility (sufficient distance of the coils from the plasma and sufficiently small coil curvatures). Criteria 1 and 7 are taken into account by solving Helias boundary value problems with side conditions on the shaping parameters. Criteria 2 and 3 are satisfied by maintaining resistive-interchange and ballooning stability at  $\langle \beta \rangle \approx 0.05$  for configurations with 5 periods and aspect ratio of approximately 10.

While maintaining resistive-interchange stability is directly incorporated into the optimization, ballooning stability is taken into account through its driving terms.<sup>2</sup> Criteria 4, 5, and 6 are taken into account by optimizing the structure of  $B(\theta, \phi)$  in magnetic coordinates.

## 2. Results for a Particular Example

An example (Helias50BINBR), obtained in the way outlined above, is described here. The configuration, whose boundary was obtained by finite- $\beta$  optimization, is shown in Fig. 1. Figure 2 shows the shape of the flux surfaces at  $\beta = 0$ . Both results were obtained with the VMEC code.<sup>3</sup> The small parallel current density of  $\langle j_{\parallel}^2/j_{\perp}^2 \rangle \lesssim 0.5$  leads to a small Shafranov shift as obvious from Figs. 1, 2.

---

<sup>1</sup>Nührenberg, J., R. Zille, Phys. Letters A **114A** (1986) 129; **129** (1988) 113

<sup>2</sup>Nührenberg, J., R. Zille, Sherwood Theory Conf. 1989, San Antonio

<sup>3</sup>Hirshman, S.P., Lee, D.K., Comput. Phys. Comm. **39** (1986) 161; Hirshman, S.P., Van Rij, W.I., Merkel, P., Comput. Phys. Comm. **43** (1986) 143.

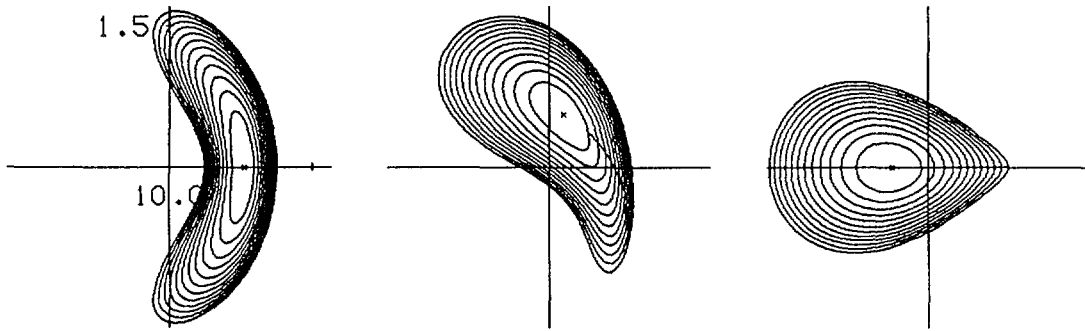


Fig. 1: Cross-sections of magnetic surfaces of the Helias equilibrium 50BINBR at  $\langle\beta\rangle = 0.049$ .

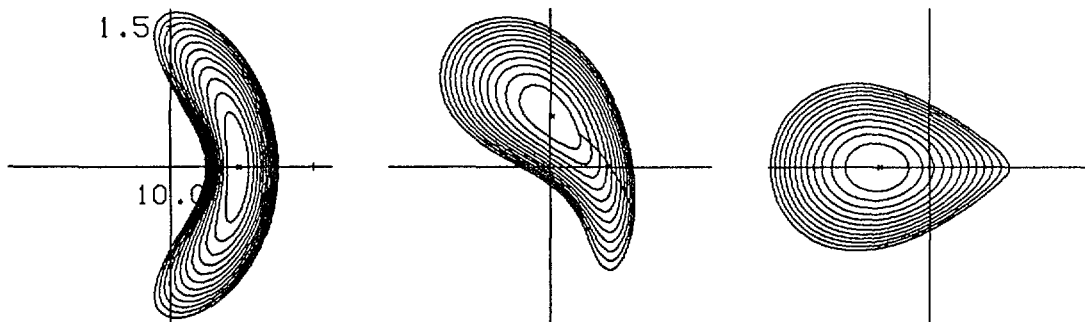


Fig. 2: Cross-sections of magnetic surfaces of the Helias equilibrium 50BINBR at  $\langle\beta\rangle = 0$ .

Further parameters of the configuration are a magnetic well of 0.018,  $\iota(0) \approx 0.83$ ,  $\iota(1) \approx 0.96$  in the vacuum field. Solving a boundary value problem with a regular boundary results in well-behaved magnetic surfaces<sup>4</sup> as is seen from Fig. 3. A further consequence of the small parallel current density is the small change in rotational transform with  $\beta$  as is seen from Fig. 4. The  $\iota$ -profile at  $\langle\beta\rangle = 0.049$  contains the rational values with medium denominator and numerator incommensurable with the number of periods  $\frac{4}{5}$ ,  $\frac{6}{7}$ ,  $\frac{7}{8}$ . By way of example, results of local ballooning mode evaluations<sup>5</sup> are shown in Fig. 5 and indicate the equilibrium shown in Fig. 1 to be ballooning stable.

The structure of  $B(s, \theta, \phi)$  in terms of its Fourier components is shown in Fig. 6 for the finite- $\beta$  case and used for the calculation of the neoclassical transport properties, the bootstrap current, and the  $\alpha$ -particle behaviour.

<sup>4</sup>Merkel, P., Nucl. Fusion **27** (1987) 867.

<sup>5</sup>Nührenberg, J. and R. Zille, Proc. Workshop on Theory of Fusion Plasmas, Varenna, Italy, 1987, EUR 11336 EN; (1988) 3-23.

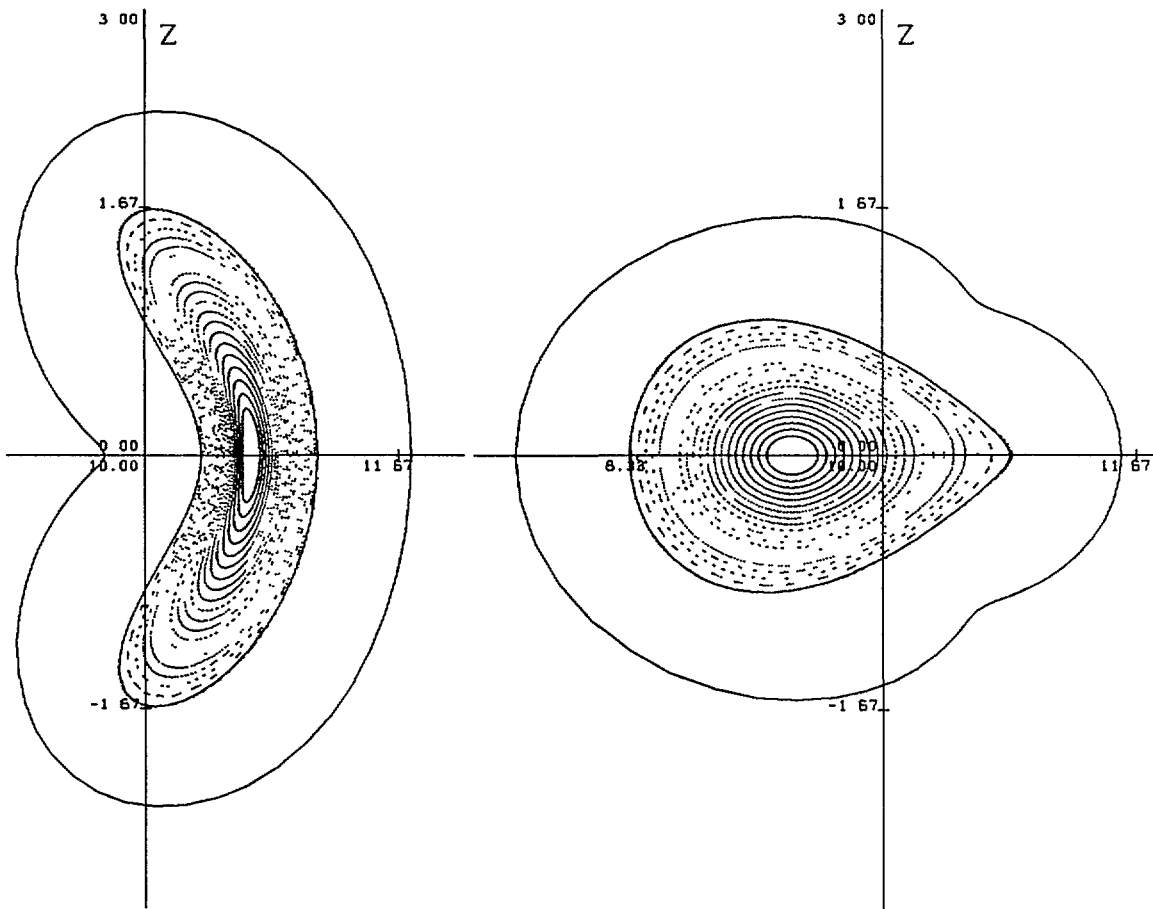


Fig 3 Poincaré plots of the vacuum field of 50BINBR obtained by solving a Neumann problem at the plasma boundary with NESCOIL; the outer surface carries the surface current density which yields the field shown inside the plasma boundary

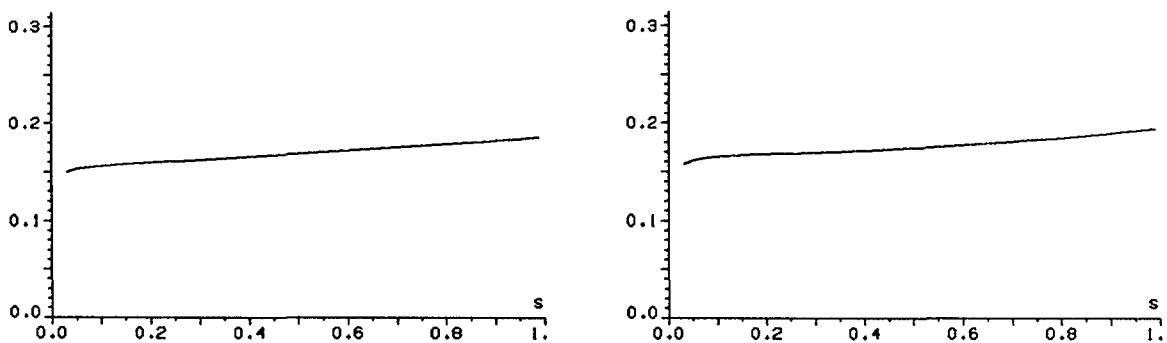


Fig 4 Rotational transform profiles at  $\langle \beta \rangle = 0.049$  (left) and  $\langle \beta \rangle = 0$  (right) Shown is the rotational transform per period versus flux label  $s$

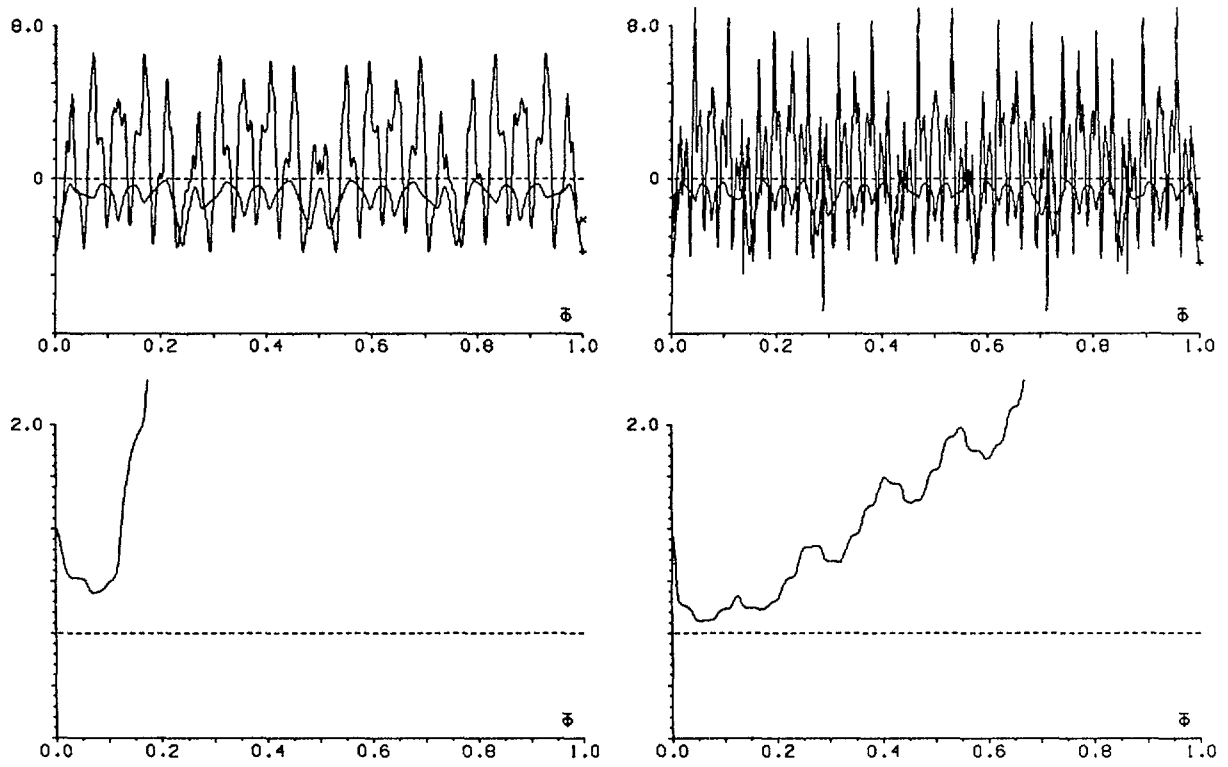


Fig. 5: Upper part: the functions  $a(+)$  and  $\tilde{D}(x)$  (see Ref. 5) at  $\iota = \frac{n_+}{m_+} = \frac{4}{5}$  located at  $s \approx 0.2$  (left) and at  $\iota = \frac{7}{8}$  located at  $s \approx 0.8$  (right).  $\bar{\phi}$  is the contracted variable  $\bar{\phi} = \frac{\phi}{m_+ N}$  where  $N$  is the number of periods. Lower part: the corresponding ballooning solutions.

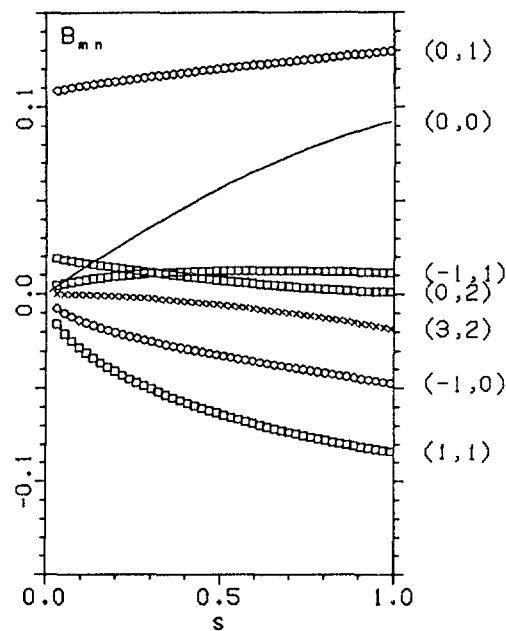


Fig. 6: The largest Fourier coefficients  $B_{m,n}$  of 50BINBR at  $\langle \beta \rangle = 0.049$  versus flux label.  $B = \sum B_{m,n} \cos 2\pi(m\theta - n\phi)$ . For clarity, Fourier coefficients smaller than 0.012 are not shown.  $B_{0,0}(0)$  is subtracted.

Monte Carlo methods for the computation of monoenergetic local transport coefficients and convolution with a Maxwellian energy distribution<sup>6</sup> are used to obtain the results shown in Fig. 7.

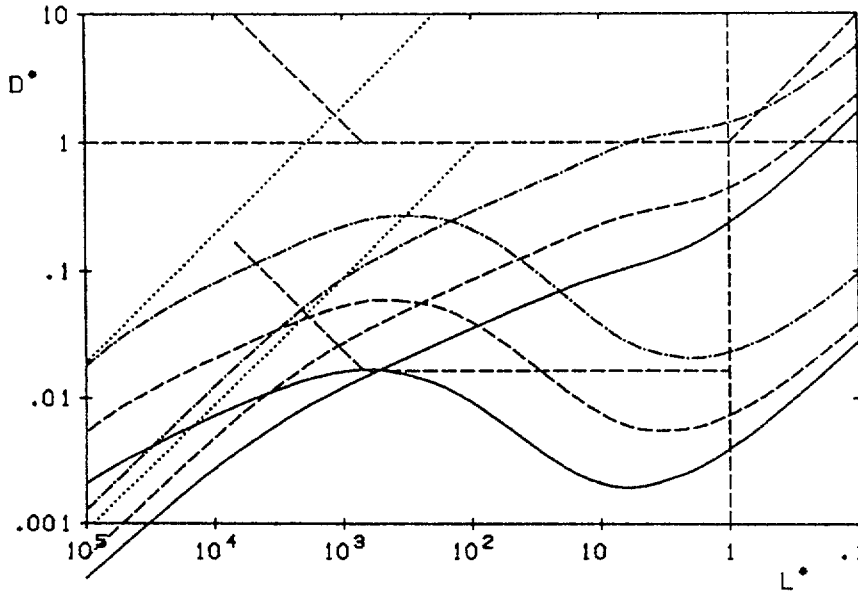


Fig. 7: Transport coefficients  $D_1^*$  (—),  $D_2^*$  (---), and  $D_3^*$  (· · ·) versus normalized mean free path  $L^*$  for deuterons and electrons obtained for 50BINBR ( $\langle\beta\rangle = 0.049$ ) at  $A = 20$  with  $Q_{oq} = 100$  (deuterons),  $Q_{oq} = 6 \cdot 10^3$  (electrons), and  $e\phi_o/E_o = 1$ . Dashed lines represent monoenergetic plateau and ripple transport. Dotted lines represent tokamak banana and ion loss cone (without electric field) transport.

Its main characteristic is that the neoclassical ion and electron heat conductivities stay well below the ion plateau level for all mean free paths of practical interest. With a specification of device parameters these results can also be used to obtain zero-dimensional estimates of confinement times, which are shown in the table; also shown are corresponding estimates for W VII-AS, W VII-AS with W VII-X dimensions and a quasi-helically symmetric stellarator.

In the lmfpl regime the bootstrap current is caused by the deviation of the drifts of trapped particles from magnetic surfaces. These deviations are of opposite sign for axisymmetry as opposed to quasi-helical symmetry; for a visualization of such orbits see for example.<sup>7</sup>

In terms of a global stationary monoenergetic distribution function<sup>8</sup> they lead to nonsymmetric behaviour in  $v_{||}/v$ , see Fig. 8. An appropriate mixture of helical and toroidal field components ( $B_{1,1}$ ,  $B_{1,0}$ ) therefore leads to a symmetric distribution function, i.e. vanishing bootstrap current which is approximately obtained in the configuration discussed here. The collisionless  $\alpha$ -particle confinement is assessed by following guiding centre orbits of a sample of  $\alpha$ -particles started at  $\frac{1}{4}$  of the plasma radius with random values in the angular variables  $\theta$ ,  $\phi$  and pitch angle  $v_{||}/v$ . In a stellarator which is governed by a  $B_{m,n}$  spectrum as complicated as in W VII-AS, all  $\alpha$ -particles that undergo reflections are quickly lost, i.e. for path lengths corresponding to approximately 10 connection lengths.

<sup>6</sup>Lotz, W., J. Nührenberg, Phys. Fluids **31** (1988) 2984

<sup>7</sup>IPP AR/1988

<sup>8</sup>Lotz, W., J. Nührenberg, A. Schlüter, JCP **73** (1987) 73

Table: For assumed device parameters  $R_0$  (major radius),  $a$  (minor radius,  $r_0 = a/2$ ), rotational transform  $\iota$  at half the plasma radius,  $B_0$  (magnetic field at the magnetic axis), temperature at half the radius, and an assumed electric potential difference between the magnetic axis and the plasma boundary of  $\frac{3}{2}$  the temperature, the density is chosen in such a way that  $D_{2e}^* = D_{2i}^*$  (see Fig. 7). The table shows  $\tau_c$  (ion collision time),  $\tau_0$  (plateau value of confinement time), and confinement times  $\tau_1$ ,  $\tau_2$ ,  $\tau_3$  (see Ref. 6) of which  $\tau_3$  represents energy confinement. The last column gives results for a quasi-helically symmetric stellarator.

		W VII AS	W VII AS	IIS-BINBR	HS 61
$R_0$	[m]	2 0	5 0	5 0	5 0
$a$	[m]	0 20	0 50	0 50	0 50
$\iota(r_0)$		0 389	0 389	0 830	1 531
$B_0$	[T]	3 0	4 0	4 0	4 0
$kT(r_0)$	[keV]	2 0	6 4	6 4	6 4
$n_e(r_0)$	[ $10^{19} \text{ m}^{-3}$ ]	2 8	6 2	12 4	9 3
$\beta(r_0)$	[%]	0 5	2 0	4 0	3 0
$\tau_c$	[ms]	3 6	9.2	4 6	6 2
$\tau_0$	[ms]	3 6	17	37	69
$\tau_1$	[ms]	55	160	2200	12000
$\tau_2$	[ms]	19	60	790	3800
$\tau_3$	[ms]	8	27	330	1500

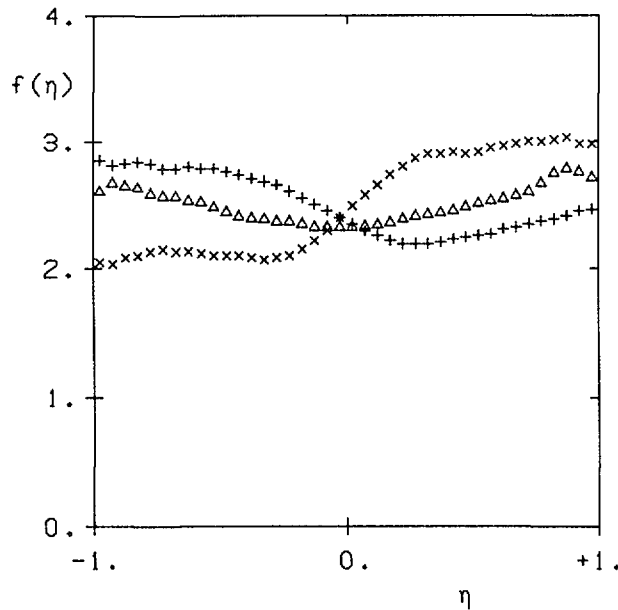


Fig 8 Monoenergetic Monte Carlo distributions averaged over the plasma radius as functions of pitch angle.  $\times$  tokamak  $A = 10$ ,  $\iota = 1$ ,  $+$  quasi-helically symmetric stellarator  $A \approx 14$ ,  $\iota \approx 1.5$ .  $\Delta$  50BINBR at  $\langle \beta \rangle = 0.049$

The other extreme is given by quasi-helically symmetric stellarators<sup>1</sup> in which they are completely confined<sup>7</sup>. As seen in Fig. 9, for the  $B_{m,n}$  spectrum of the configuration considered here, the  $\beta$ -effect at  $\langle\beta\rangle \approx 0.05$  is sufficient to improve the  $\alpha$ -particle confinement so much that the fraction of prompt losses is reduced to approximately 0.1 and can further improve by collisional slowing down on the electrons.

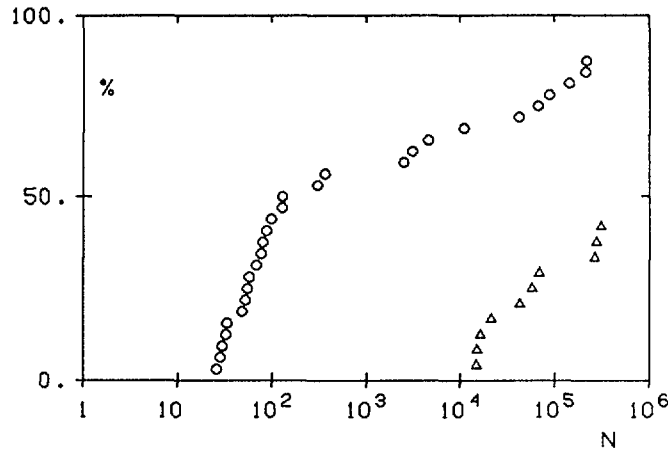


Fig. 9:  $\alpha$ -particle losses as a function of collisionless path length.  $N$  is the number of connection lengths. Shown is the fraction of reflected particles which is lost:  $\Delta$  50BINBR ( $\langle\beta\rangle = 5.5\%$ ),  $\circ$  50BINBR ( $\beta = 0$ ).

### 3. Conclusion

It seems that  $N = 5$ ,  $A \approx 10$  stellarators with good surfaces,  $\langle j_{\parallel}^2/j_{\perp}^2 \rangle \lesssim 1$ ,  $\langle\beta\rangle_{\text{stab}} \gtrsim 0.05$ ,  $\delta_e(r/a = \frac{1}{2}) \lesssim 0.02$ ,  $J_{\text{BS}} \lesssim 0.1 J_{\text{BS,tok}}$ ,  $f_{\alpha} \lesssim 0.1$  (at  $\langle\beta\rangle \approx 0.05$ ) can be found. A study of the coils for such a stellarator<sup>9</sup> is underway.

<sup>9</sup>Merkel, P., Proc. Workshop on Theory of Fusion Plasmas, Villa Cipressi, Varenna, Italy, 1987, EUR 11336 EN; (1988) 25-46.

## LOW-ASPECT-RATIO OPTIMIZATION STUDIES FOR ATF-II\*

S.P. HIRSHMAN, R.N. MORRIS<sup>1</sup>, C.L. HEDRICK,  
J.F. LYON, J.A. ROME, S.L. PAINTER, W.I. VAN RIJ<sup>1</sup>  
Oak Ridge National Laboratory,  
Oak Ridge, Tennessee,  
United States of America

### Abstract

*A numerical procedure for optimizing stellarator MHD and transport properties at finite  $\beta$  is described. This method is applied to finding a low-aspect-ratio ATF-II configuration.*

---

Prompted by the economic and experimental attractiveness of low-aspect-ratio stellarators, we have initiated a study to optimize the plasma physics properties of such configurations. The design goal of this study is to decrease the aspect ratio,  $A = R/a$ , by a factor of two from  $A = 7.8$  for the present ATF device to  $A < 4$ , without sacrificing MHD and transport performance. Stability to Mercier modes for  $\langle \beta \rangle$  values up to 5% is considered essential for an attractive design. Also, a significant fraction of high-energy particles must be confined so that neutral-beam heating will be feasible in the next-generation experiments.

Previous studies at ORNL of the Compact Toratron Sequence (CTS) [1] emphasized optimization of MHD high- $\beta$  performance at low aspect ratios. Ancillary transport optimizations were performed by applications of vertical and quadrupolar magnetic fields. In spite of this, the particle confinement properties of these configurations deteriorated rapidly with increasing beta. In fact, for  $\langle \beta \rangle > 2\%$ , essentially all fast trapped alphas were lost in several poloidal transits. It seemed desirable to relinquish some of the stability margin afforded by the magnetic well in these configurations in order to improve their confinement properties. This observation then formed the impetus for the current study.

In order to extend the CTS studies into a regime of improved transport, it was necessary to broaden the range of allowable configurations. The CTS was restricted to stellarators produced by a single set of modulated current windings on a (prescribed) surface. By adopting an optimization approach that works directly with the shape of the outer plasma flux surface, we can avoid any *a priori* restrictions on the type of coils needed to produce a given magnetic configuration. In this way, the task of optimizing the physics properties of the stellarator is separated from the coil determination process. This division has the advantage that optimization of both MHD and transport can be performed simultaneously. However, unlike the CTS study, in the present method there is no guarantee that an acceptable coil set (from an engineering point of view) will result from the

---

\* Research sponsored by the Office of Fusion Energy, US Department of Energy, under contract DE-AC05-84OR21400 with Martin Marietta Energy Systems, Inc.

<sup>1</sup> Computing and Telecommunications Division, Martin Marietta Energy Systems, Inc., Oak Ridge, TN 37831, USA.

physics optimization. The NESCOIL code [2] can be used, together with a judicious estimate for the coil winding surface(s), to yield a set of helical and/or modular coils with appropriate accessibility and dimensions.

The method described here is therefore similar to the optimization approach used in designing Helias [3], although it is being applied to a distinctly different set of physical criteria. In addition to being a low-aspect-ratio device (compared with  $A = 10$  for Helias), the ATF-II design retains the basic rotational transform profile of ATF, i.e. strong shear in the outer plasma volume to provide interchange stability. Furthermore, whereas Helias has been optimized to reduce Pfirsch-Schlüter currents, the ATF-II design relies on the finite- $\beta$  Shafranov shift arising from these currents to dig a well and hence improve its high- $\beta$  stability. Finally, the ATF-II design does not attempt to generate a quasi-helical  $|B|$  configuration, but rather uses the alignment of the  $B_{\min}$  contours with the flux surfaces (see below) as a measure of the effective alpha-particle confinement. In this way, we can achieve factors of two to five improvement in confinement. This limited transport optimization is of practical significance, since it is probably not necessary to improve the neoclassical confinement beyond the point where it no longer dominates the expected anomalous diffusion.

The present stellarator optimization procedure requires an initial guess for the boundary of the desired configuration. This guess is determined by the large-aspect-ratio ATF and by the requirement that  $A/M$  (aspect ratio per field period  $M$ , or coil pitch for a fixed winding law) be approximately constant to maintain the edge value of  $i$ . The three-dimensional equilibrium code VMEC is then used to process this boundary information (which, together with the requirement for zero net toroidal current and the pressure profile, completely specifies the MHD equilibrium) and to compute the relevant physical parameters required for optimization. For example, the equilibrium solution yields values for the edge and central values of  $i$ , the percentage of the plasma volume that is Mercier stable, and various measures of transport performance. These parameters are passed to a nonlinear Newton optimizer, and an updated guess for the boundary is obtained which is consistent with improving the various optimization criteria. This loop is continued until no further improvement is obtained.

Because this loop may be repeated many times (10 - 30 iterations is typical) before terminating, it is crucial that the analytic optimization criteria be relatively easy to evaluate. This is certainly the case for the Mercier criteria. In the case of transport, however, it is not feasible to perform time-consuming Monte-Carlo simulations for each intermediate configuration. Rather, we opt for an approximate figure of merit for transport, based on the confinement of deeply helically trapped orbits of energetic (collisionless) particles. From  $J^*$  conservation, it can be shown that these particles follow contours of  $B_{\min}(\Phi, \theta) = \text{const}$ , where the minimization of  $B$  is done with respect to the toroidal angle  $\phi$  in a single field period, keeping the poloidal angle  $\theta$  and toroidal flux  $\Phi$  fixed. This criterion is easily evaluated and yields two topological parameters which characterize the confinement of trapped alphas: (i)  $d$ , the fraction of plasma volume enclosed by a  $B_{\min}$  contour not

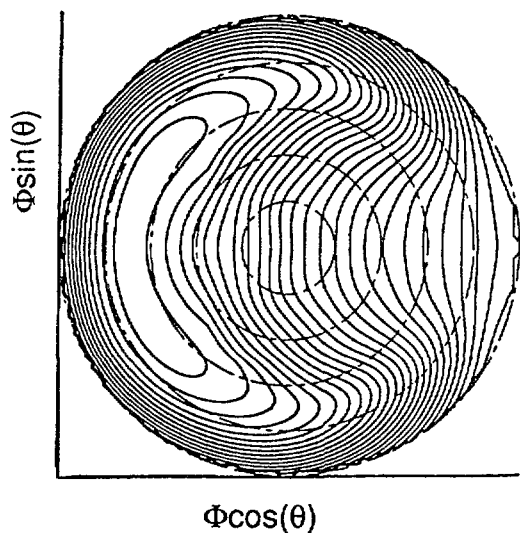


FIG. 1(a).  $B_{\min}$  contours:  
no vertical field.

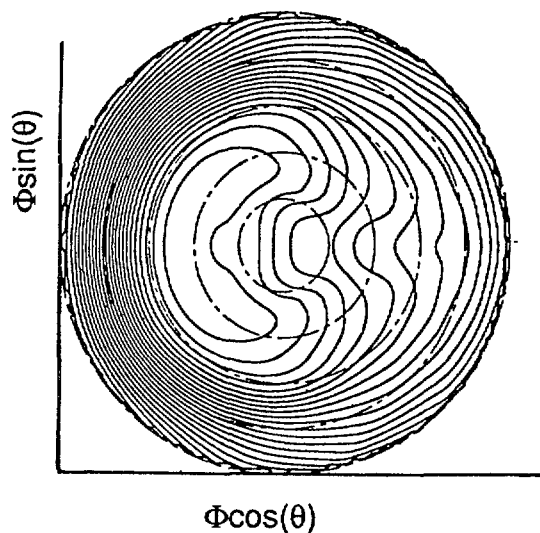


FIG. 1(b).  $B_{\min}$  contours:  
vertical field applied.

intersecting the wall ( $d = 1$  is desirable) and (ii)  $o$ , the offset of  $B_{\min}$  with respect to the flux surfaces ( $o = 0$  is desirable). Figure 1 illustrates the topological effects of these two parameters for an optimized ATF-II design at  $\langle \beta \rangle = 2\%$ . The concentric chain-dashed circles are the flux surfaces, and the solid curves are  $B_{\min}$  contours. The application of a vertical field substantially improves trapped particle confinement in this case by both increasing  $d$  and simultaneously decreasing the offset parameter  $o$ . Indeed, this configuration, with the vertical field applied, has a trapped alpha loss fraction less than 10%. Of course, it is necessary to correlate these simplified confinement criteria with the actual confinement of a distribution (in pitch angle) of high-energy alphas, as calculated from a Monte-Carlo simulation. Figure 2 is a "bubble" plot of the fraction of confined alphas for various values of  $d$  and  $o$ . The biggest dots represent almost no loss, with the dot sizes being proportional to the confined fractions. (All the simulations of alpha particles presented here were performed with reactor scale parameters:  $B = 5T$  and  $\bar{a} = 2m$ ).

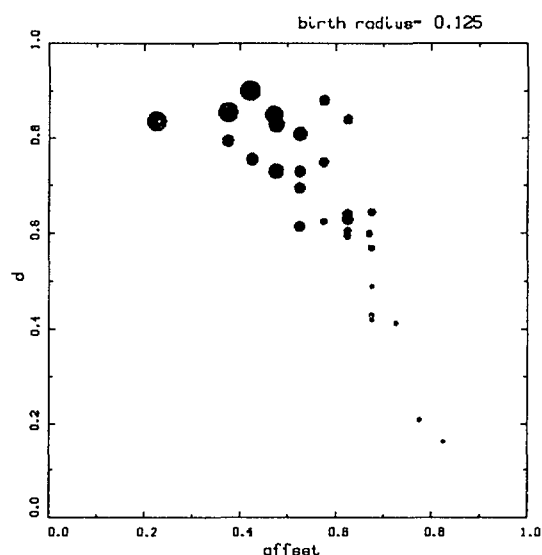


FIG. 2. Correlation of confined fast  
alphas with  $B_{\min}$  parameters.

This figure shows that, in general, configurations with low values of offset ( $o < 0.3$ ) and  $d > 0.75$  also have good confinement properties.

Our numerical computations suggest that there is a relatively narrow range of boundary parameters at finite  $\beta$  that yield acceptable configurations. Therefore, configurations which are optimized at zero  $\beta$  generally do not make a good starting point for finding finite- $\beta$  configurations. Rather, our design philosophy is to perform the optimization directly at finite  $\beta$  (*lowering*  $\beta$  is generally not a problem for maintaining good stability and transport properties). The only difficulty with this approach is that it is not possible to obtain the *exact* discrete coil set with NESCOIL, which requires a vacuum field. However, assuming that the main external contribution at finite  $\beta$  arising from the plasma currents is a vertical magnetic field, it is easy to obtain an *approximate* set of coils using NESCOIL. The vacuum magnetic surfaces obtained by such an optimization at  $\langle\beta\rangle = 2\%$  are shown in Fig. 3 for the two symmetry planes ( $M\phi=0$  and  $M\phi=\pi$ , for  $M=6$ ). Note that the plasma is centered at  $R = 1.00$  (arbitrary units). Raising the  $\langle\beta\rangle$  to 2% yields the configuration shown in Fig. 4. Without a compensating vertical field (VF), the magnetic axis has shifted out to  $R = 1.10$ , while an applied VF recenters the configuration at  $R = 1.00$ . (The magnitude of the VF was determined to optimize the alignment of  $B_{\min}$  contours and produced the results shown previously in Fig. 1.) Note that with the applied VF, the Shafranov shift is reduced. This produces an associated reduction of the magnetic well. Figure 5 shows the magnetic well with and without the VF coils. Not only is the well reduced in depth, but also its spatial extent is contracted from about  $\Phi < 0.65$  with no VF to  $\Phi < 0.45$  with an applied VF ( $\Phi$  is the normalized toroidal flux). In spite of this erosion of the magnetic well, stability to Mercier modes is maintained throughout the discharge, as shown in Fig. 6. (For stability to Mercier modes, the curve marked  $M$  in Fig. 6 must be greater than zero.) The stabilizing contribution from the  $\mathbf{J}\cdot\mathbf{B}$  term in the Mercier criterion (curve marked  $C$  in Fig. 6) increases and

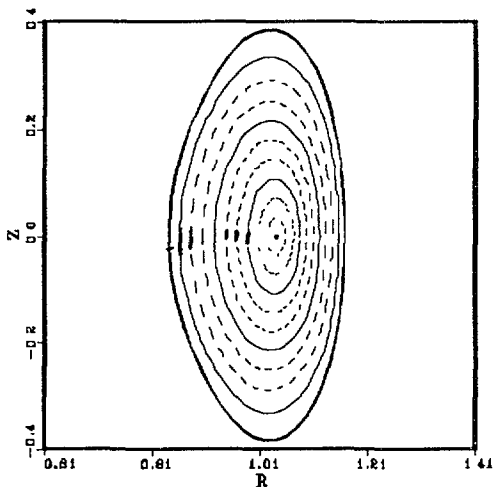


FIG. 3(a). Vacuum flux surfaces for ATF-II prototype,  $M\phi=0$ .

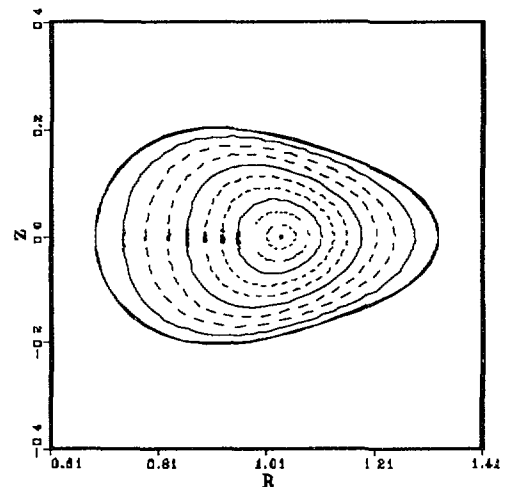


FIG. 3(b). Vacuum flux surfaces for ATF-II prototype,  $M\phi=\pi$ .

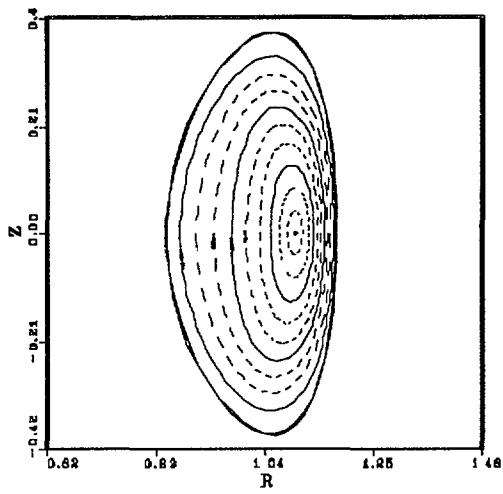


FIG. 4(a).  $\langle \beta \rangle = 0.02, M\phi = 0$ .  
No Vertical Field.

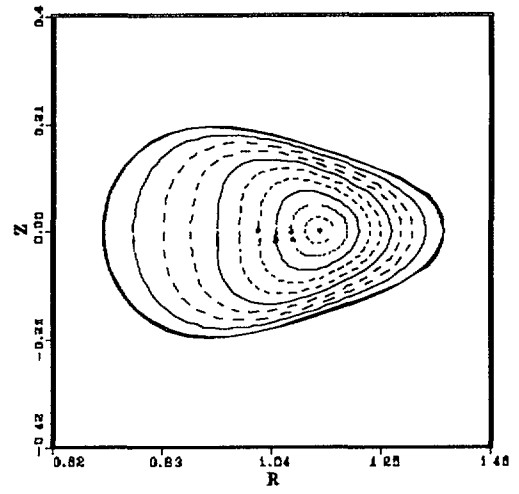


FIG. 4(b).  $\langle \beta \rangle = 0.02, M\phi = \pi$ .  
No vertical field.

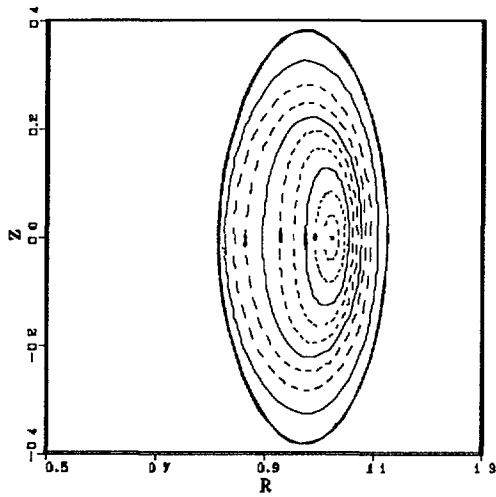


FIG. 4(c). With vertical field.

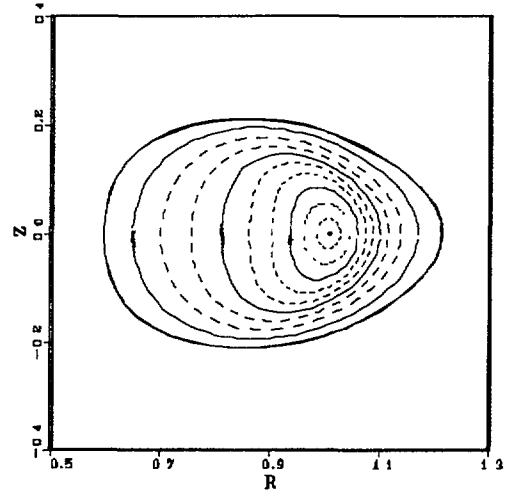


FIG. 4(d). With vertical field.

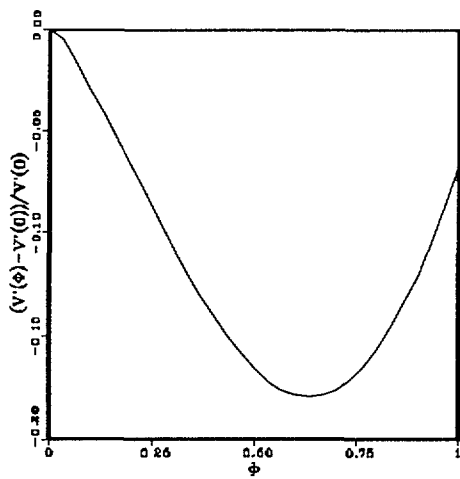


FIG. 5(a). Magnetic well.  
No vertical field.

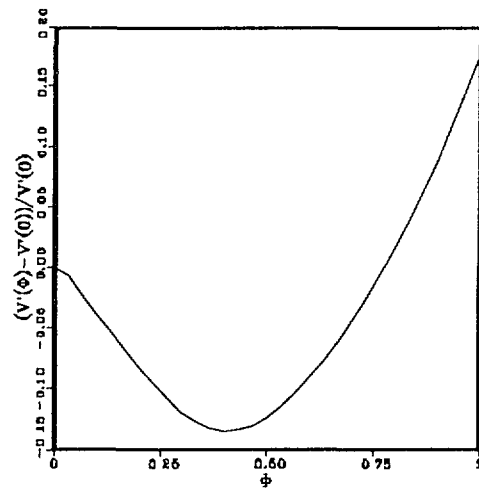


FIG. 5(b). Magnetic well.  
With Applied vertical field.

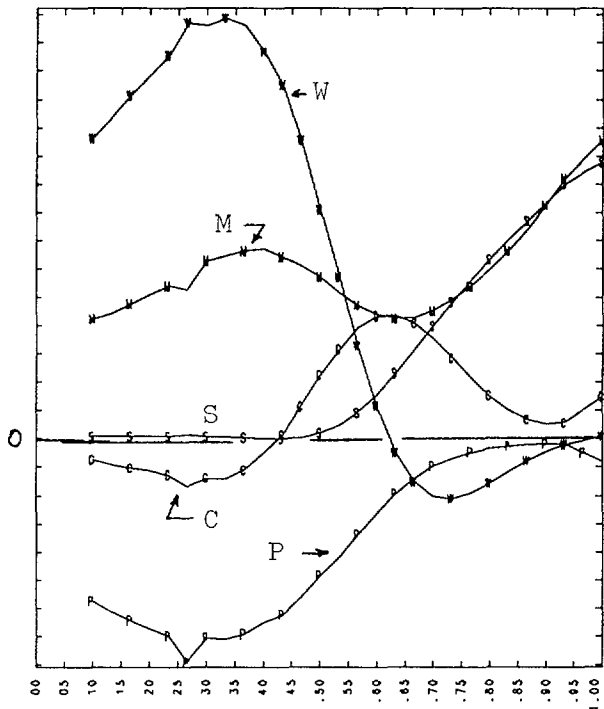


FIG. 6(a). Mercier stability criterion (M), no vertical field.

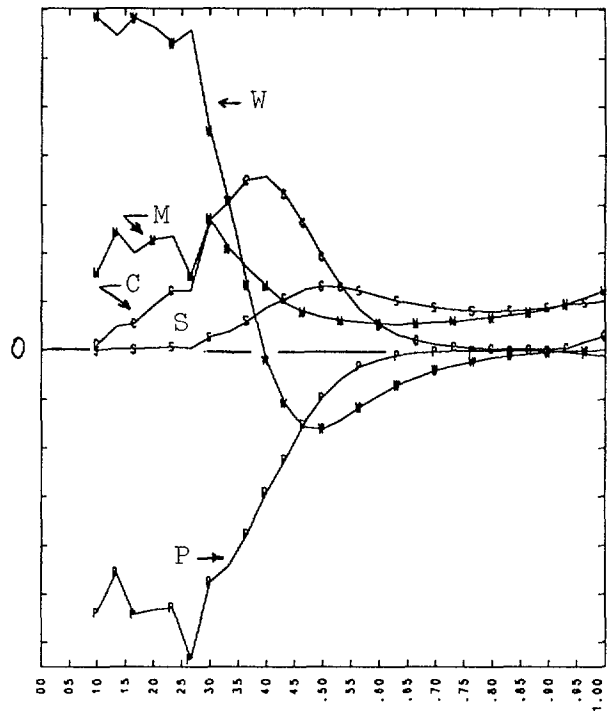


FIG. 6(b). Mercier stability criterion (M), vertical field applied.

moves inward (toward smaller  $\Phi$ ) at the same rate as the well (curve W) disappears, so that global stability is maintained. In this sense, the stability of this configuration differs from the canonical ATF picture, which relies on a deepening, radially expanding well for high- $\beta$  stability. Finally, the iota profile is nearly identical to the usual ATF result, with a small (15%) reduction (0.85 rather than 1.00) at the edge.

It should be noted from Fig. 4 that the effect of the VF coils is not confined to recentering the plasma, but also leads to a significant modification of the outer boundary shape. This change in the outer boundary has been accounted for self-consistently here by a free-boundary computation, and it can influence the confinement and stability properties of the plasma. Previous optimization methods assumed that the plasma boundary was fixed as  $\langle\beta\rangle$  increases, which is clearly not realistic with the addition of only VF coils.

Detailed coil design efforts using NESCOIL are reported in Ref. [4]. The optimized ATF-II configuration discussed here can be created using either modular or helical coils at a plasma-to-coil spacing of 15 cm (normalized to a major radius of 1 m). As this spacing is increased, the coils become increasingly kinked, and local areas of closed currents appear on the winding surface. Studies are under way to simplify these coils by removing selected helical or modular coil components and synthesizing the remaining currents on a different winding surface.

In conclusion, we have shown preliminary results which indicate that a low-aspect-ratio torsatron with adequate transport and MHD stability properties exists for  $\langle\beta\rangle < 2\%$ . It remains a subject of continuing research to extend this

configuration to a regime of increased  $\langle\beta\rangle$ . The use of vertical fields to maintain high-energy particle confinement as  $\langle\beta\rangle$  is raised has been demonstrated. Optimization of a finite- $\beta$  plasma has been shown to be a robust way of accessing new and potentially attractive configurations. Although the exact determination of the vacuum coils is difficult, it is possible to obtain coils with sufficient accuracy so that the  $\langle\beta\rangle$ -optimized parameters are not adversely affected.

## REFERENCES

- [1] CARRERAS, B.A., DOMINGUEZ, N., GARCIA, L., et al., Nucl. Fusion **28** (1988) 1195.
- [2] MERKEL, P., Nucl. Fusion **27** (1987) 867.
- [3] NÜHRENBERG, J., et al., these proceedings.
- [4] ROME, J.A., et al., these proceedings.

**NEXT-GENERATION DEVICES  
AND REACTORS**

## DIVERTOR DESIGN STUDY OF THE LARGE HELICAL DEVICE

N. OHYABU

Institute of Fusion Plasma Science,  
Nagoya University,  
Nagoya, Japan

### Abstract

In this paper the design rationale of the divertor for the proposed Japanese Large Helical Device are discussed. The main objective of the JLHD is to achieve high quality plasma for a long period. This goal could be achieved by the installation of an appropriate divertor in the device.

---

Helical Divertor is one of the major features of the proposed Japanese Large Helical Device ( $l=2$ ,  $m=10$ ,  $B_T \sim 4T$ ,  $R \sim 4m$ ,  $a \geq 0.5m$ ). In this report, we discuss design rationale of the divertor and its conceptual design. The main objective of the Large Helical Device is to achieve high quality plasma for a long period. This necessitates (1) minimization of the impurity contamination, (2) reduction of the heat load on the divertor plate, (3) improvement in energy confinement time. We believe that the above functions could be met by installing a good divertor in the device.

The magnetic field configuration of the helical divertor is rather complicate and thus needs to be studied carefully before designing the divertor system. Fig.1 shows divertor magnetic configurations for the Large Helical Device. As shown in this figure there exists an ergodic region just outside the outermost closed surface, which is created by overlapping of the island layers with toroidal mode number of 10. Field lines escaping from the ergodic region deviates radially from the ergodic region before reaching to the divertor plate. This radial deviation is larger for less helically symmetric configuration (smaller coil pitch modulation( $\alpha$ ) and smaller inward shift of the plasma axis( $-\Delta$ )). This radial deviation aggravates a design problem of clearance between the edge plasma and the wall on the smaller major radius side of the torus. This is one of the main reason for adopting high current density ( $40 A/mm^2$ ) superconducting coil, which leads to smaller helical coil and hence larger clearance between the plasma and the wall. Further minor adjustments of  $B_T$ ,  $R$ , and  $\alpha$  will be made to have a clearance of  $\approx 3$  cm .

We describe a few other features of the divertor magnetic configuration. Axisymmetric field changes the size and position of the outermost closed flux surface, but it alters very little the position of the diverting field lines near the divertor plate, i.e. helical coil current almost determines the

Variation of Divertor Magnetic Configuration  
due to coil pitch modulation ( $\alpha$ ) and shift ( $\Delta$ )

( $l=2, m=10, \gamma=1.2$ )

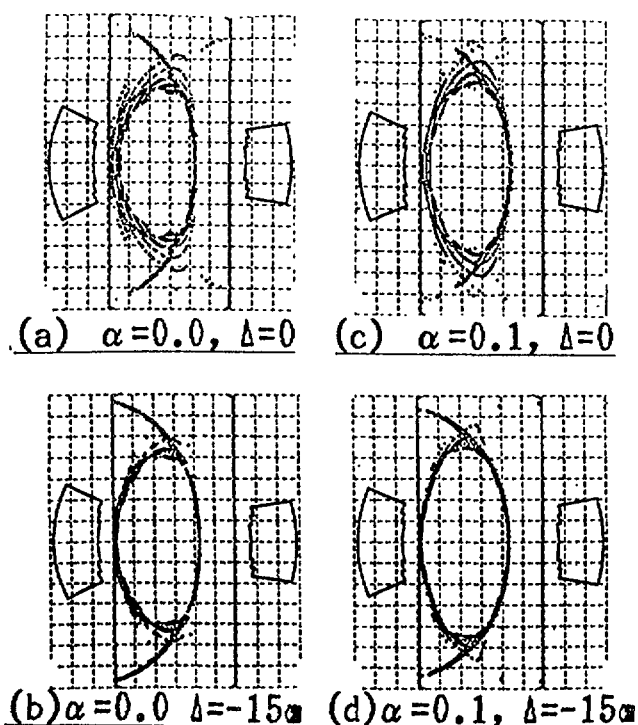


FIG. 1.

position of the divertor channel regardless of plasma shape, position and  $\beta$ . An example of this feature is shown in Fig 1(a),(b) where the divertoring field line intersect the nearly the same position at the divertor plate or wall for two configurations with different axis positions ( $\Delta=0, \Delta=-15\text{cm}$ ). With increasing  $\alpha$ , the closed outermost flux surface becomes larger and the ergodic region becomes narrower, leading to larger clearance between the divertor plasma and the wall ( Fig 1(c),(d)). However, there is a limit on  $\alpha$  above which theoretically achievable  $\beta$  value suddenly drops. In this sense,  $\alpha = 0.1$  is acceptable, but  $\alpha = 0.2$  is not.

The another important feature is that the connection length between the main plasma scrape-off layer and the divertor plate is very short ( $\sim 1\text{m}$ ) compared with that of the comparable size tokamak ( $\sim 10\text{m}$ ). However, unlike a helically symmetric configuration, the field line outside the last closed surface does not always escape when the "X-point" pass and thus the effective connection length becomes longer and the heat-flow pattern may be more complicated than that of the tokamak.

Tokamak divertor experiments have shown that the effective divertor functions require the divertor configuration with high plugging efficiency, i.e. plasma in the divertor channel "plugs" neutrals recycled at the divertor plasma through ionization process, minimizing the neutral flux into the main plasma. This is particularly important for creation of the high density, cold divertor plasma and access to the H-mode regime. The plugging efficiency depends on the divertor geometry and the divertor plasma (particularly density). Compared with the tokamak divertor, the divertor density for the helical divertor channel is lower for a given average main plasma density. For a helical divertor configuration, its shorter connection length causes faster parallel particle transport in the divertor channel, lowering the divertor density. Lower divertor density for helical divertor makes the plasma plugging more difficult and therefore a more elaborate design of the baffle plate is needed.

Fig 2 shows examples of conceptual baffle plate design. With such baffle plates, we expect that high plugging efficiency can be achieved when the average density is above  $\sim 5 \times 10^{13} \text{ cm}^{-3}$ . If so, the following divertor function will help to improve plasma performance in the Large Helical Device.

### Baffle Design

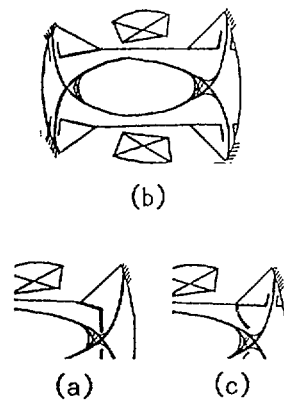


FIG. 2.

- (1) High density, cold divertor plasma is formed just in front of the divertor plate, lowering impurity sputtering from the plate. Even if the impurities are sputtered, they are likely to be ionized in the divertor channel and be swept toward the plate by the plasma flow.
- (2) High Density, Cold Divertor plasma enhances the radiation power, thus lowering the heat flux on the divertor plasma. This is a divertor function which is necessary for a long pulse or steady state operation of the discharge.

- (3) Enhanced recycling at the divertor region makes pumping of the particle and hence the plasma density control easier.
- (4) Particle recycling can be localized within the divertor region. This is an important condition for creation of H-mode tokamak discharge and thus an improved confinement regime may also be obtained even in the helical discharge.

## COIL SYSTEMS, VACUUM FIELDS, AND PARAMETER RANGE FOR WENDELSTEIN VII-X COILS

C. BEIDLER, E. HARMEYER, J. KISSLINGER,  
P. MERKEL, F. RAU, R. SCARDOVELLI, H. WOBIG  
Euratom-IPP Association,  
Max-Planck-Institut für Plasmaphysik,  
Garching, Federal Republic of Germany

### Abstract

Details of a recent modular coil system called HS5-8 are described, along with some properties of the vacuum field. A system of additional planar coils allows the variation of both the rotational transform and the position of the magnetic axis, within reasonable parameter ranges.

---

### INTRODUCTION

At IPP Garching, the stellarator experiment WENDELSTEIN VII-X is being developed [1]. Among stellarators, the Helias configuration [2] ( Helical advanced stellarator ) offers the prospect of stable plasma operation at  $\langle\beta\rangle \approx 5\%$  because of the optimization of confinement, MHD-equilibrium and stability. Considering ballooning modes and resistive interchange instability, Helias configurations with five field periods are preferred to those with four periods [3]. The systems of modular coils are developed from a given finite-beta configuration using the NESCOIL code [4], and subsequent smoothing. The present paper extends a recent publication [5]. Technical details are given elsewhere, including aspects of electromagnetic forces and stresses [6].

### COIL SYSTEM AND VACUUM FIELD, 'STANDARD CASE'

The coil systems labelled HS 5-6 to HS 5-8 and their vacuum field configurations are a series of successively improved data sets, which stem from the finite-beta topology designated HS 5081. In these abbreviations, HS stands for Helias; the number of field periods is  $M = 5$ . In HS 5081, the zero corresponds to an aspect ratio of  $A \approx 10$ , and the last two digits refer to the rotational transform on the axis,  $\iota_0 = 0.8$ , and at the plasma edge,  $\iota_p = 1$ . The vacuum field of HS 5-6 approaches the 'quasi-helical' configuration HS 5081. The Fourier coefficients of  $mod B$  for HS 5-7 and those for HS 5-8 exhibit larger toroidal components, up to about 1/3 of the principal helical ones [5]. This appears to yield lower values for the bootstrap current. In the three cases, typical values of the aspect ratios are  $A_p \approx 10$  and  $A_c \approx 5$ , for the last useful magnetic surface and the modular coils, respectively, at a major radius of 6.5 m.

The NESCOIL code requires two toroidal surfaces as input. One surface,  $S_1$ , is chosen inside and near the plasma edge and a second one,  $S_2$ , at some distance outside. It determines the location of external current lines; see Fig. 1. Both surfaces are given in Fourier series of two periodic variables. The NESCOIL code then determines the Fourier coefficients of a current distribution on  $S_2$ , from which a number of 'current polygons' are derived numerically, i.e. the 'center filaments' of modular coils. A number of engineering constraints is observed, such as limits in current density, local curvature

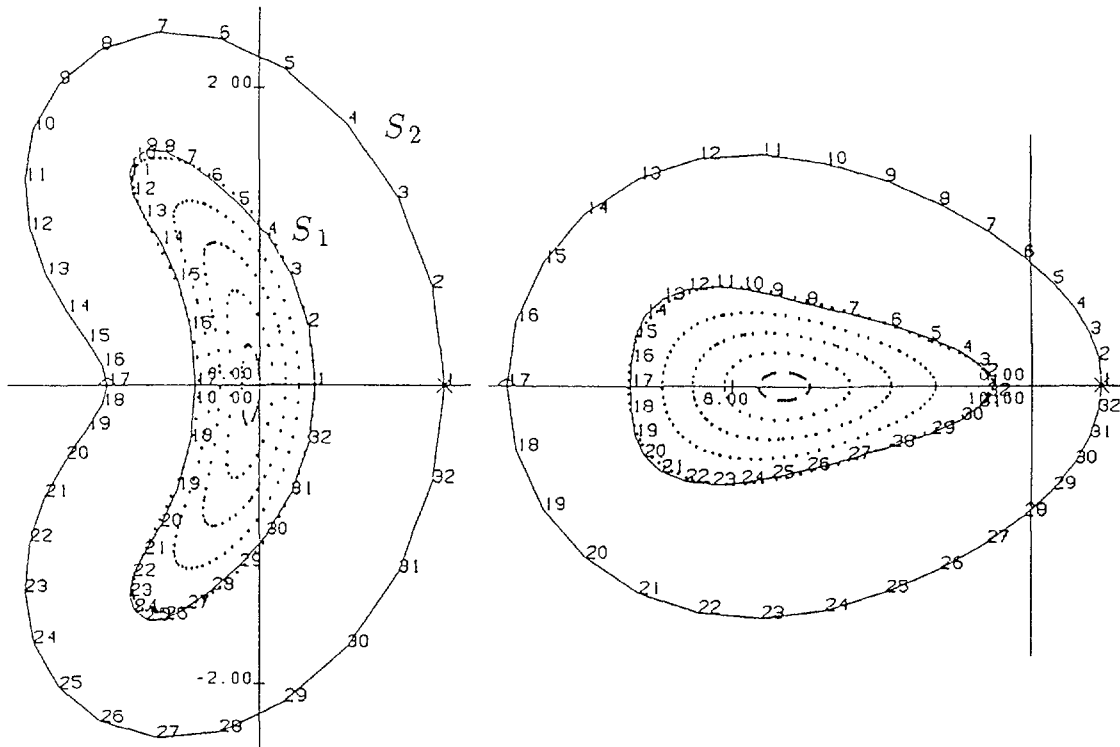


**Fig. 1:** Magnetic surfaces and contours of toroidal surfaces  $S_1$  and  $S_2$  used as input for the NESCOIL code; toroidal positions 0, and  $1/2$  field period.

and toroidal excursion of the modular coils, and the required distance between coils and plasma edge. The coil contours are locally smoothed, and the magnetic fields are compared to those of earlier iterations, in order to maintain the field quality.

**Fig. 2** gives as an example the coil winding packs derived for HS 5–8 ; the upper part is from the direct output of NESCOIL; the lower part is the result after smoothing. There are 12 coils per period, which keep the ‘modular ripple’ sufficiently low. This is important with respect to neoclassical transport, see [7] . Nevertheless, the access between adjacent coils is sufficient for experimental purposes; see **Fig. 3** . A lateral distance of 0.15 m between the port and the winding packs is considered to be adequate for coil casing and cryostat.

An average magnetic field of  $B_o = 3$  T is generated by a total current of 1.75 MA in each modular coil. **Fig. 4** shows the nested magnetic surfaces of the HS 5-8 ‘Standard Case’ vacuum field and with contours  $mod B = const.$ , drawn as thin lines at intervals  $\delta B = 0.1$  T . In the top part of the figure, the combined effect of indentation and toroidal current elements in the coils can be seen; in the lower part the direction of the field gradient is reversed for a considerable area within the magnetic surfaces. Both features are typical for Helias systems. The rotational transform is  $t_a = 1.02$  on axis, and  $t_p = 1.18$  on the surface with an average minor radius of 0.7 m. A magnetic well of 1.6 % exists between the axis and this surface [5] . Low-order rational values of  $t$  such as  $5/6$ ,  $5/5$ , and  $5/4$  are avoided; for  $t = 10/9$  and  $t = 15/13$  small islands exist with an averaged radial extension of 1.5 to 2 cm, at average minor radii  $r = 51$  cm and  $r = 62$  cm, respectively. They are not shown in the figure. A perspective view of an outer magnetic surface is given in the upper part of **Fig. 5** . The lower part of the figure is an unfolding

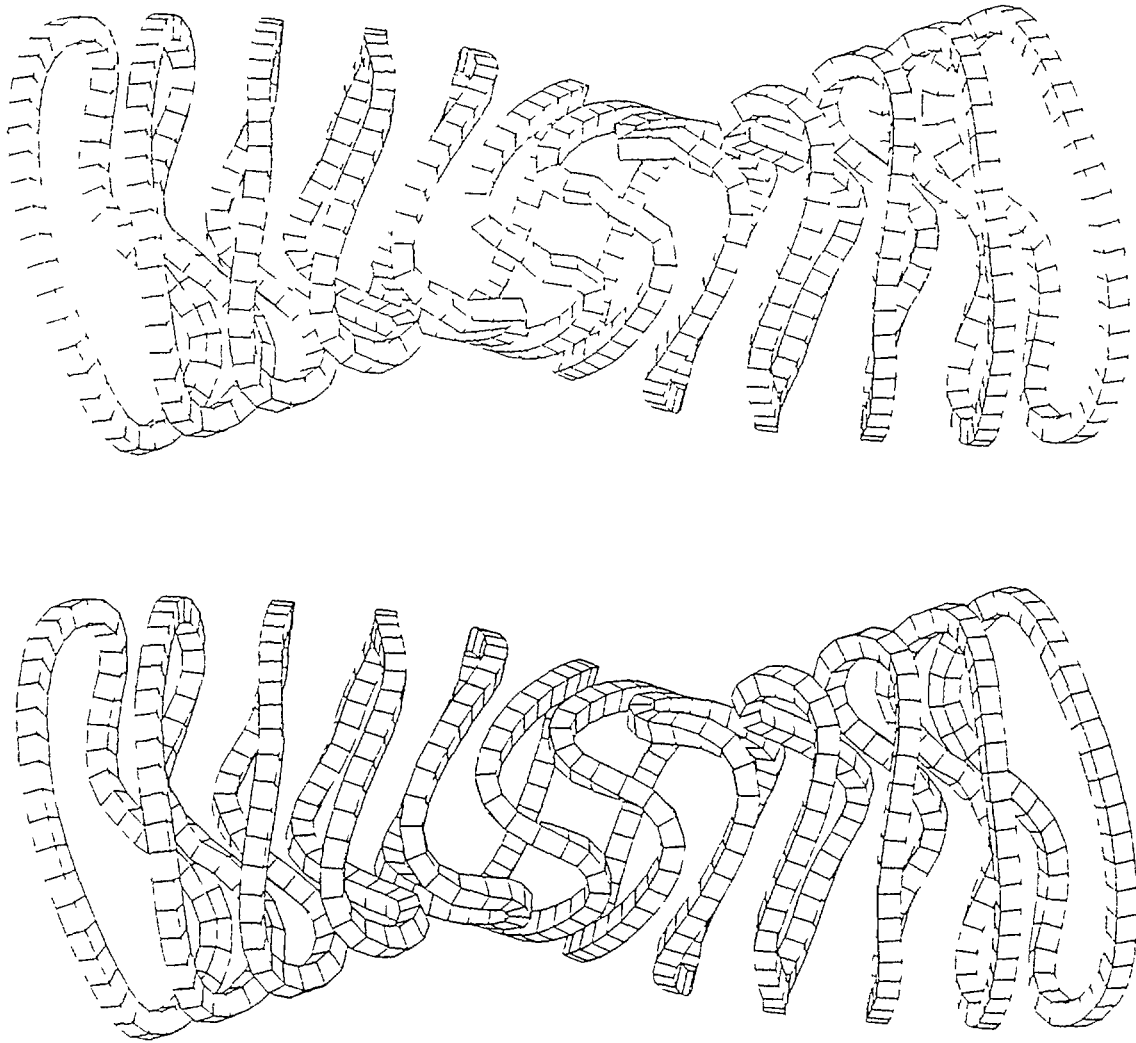
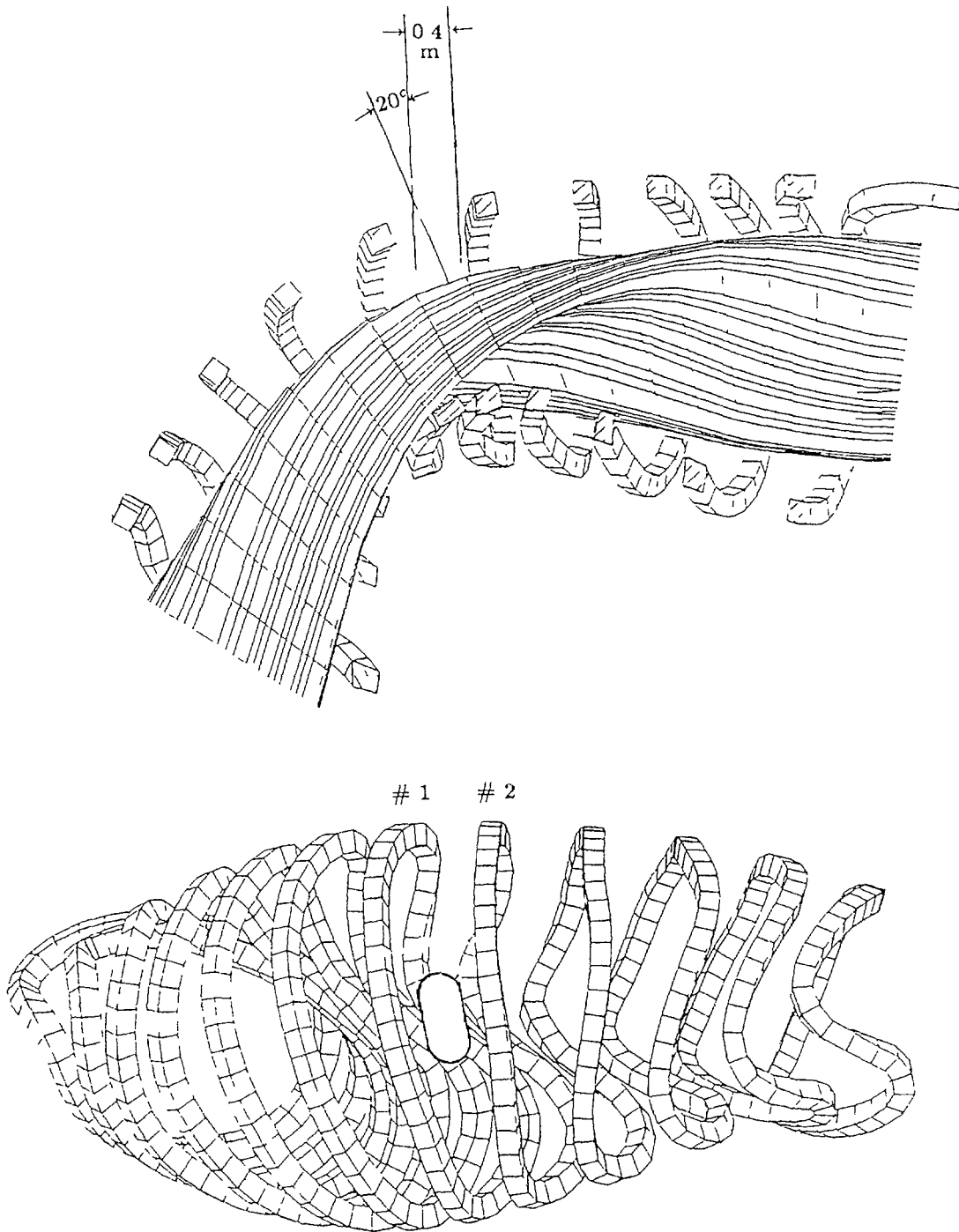
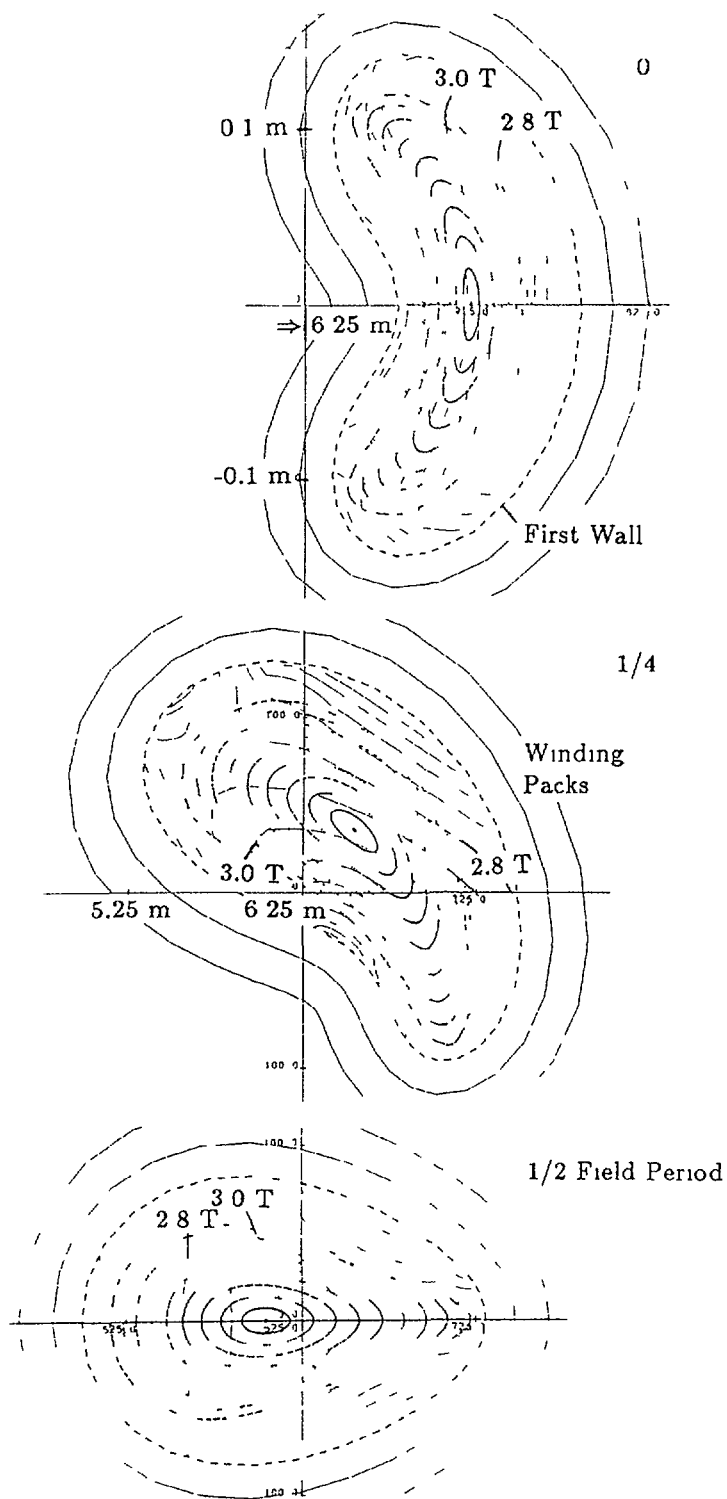


Fig. 2: Coils derived from the surface current lines before and after smoothing, one field period seen from the radial outside



**Fig 3:** Experimental port between coils # 1 and # 2 .  
Tentative dimensions are 0.4 m wide and 0.8 m high.  
Tilt angle of port axis  $20^\circ$  , useful for neutral beam heating.



**Fig. 4** Standard case of HS 5-8 and contours of  $mod B = const$   
 Axis centered at 7.22 and 6.04 m, for 0 and 1/2 field period, resp

HS 5-8  
Standard Case

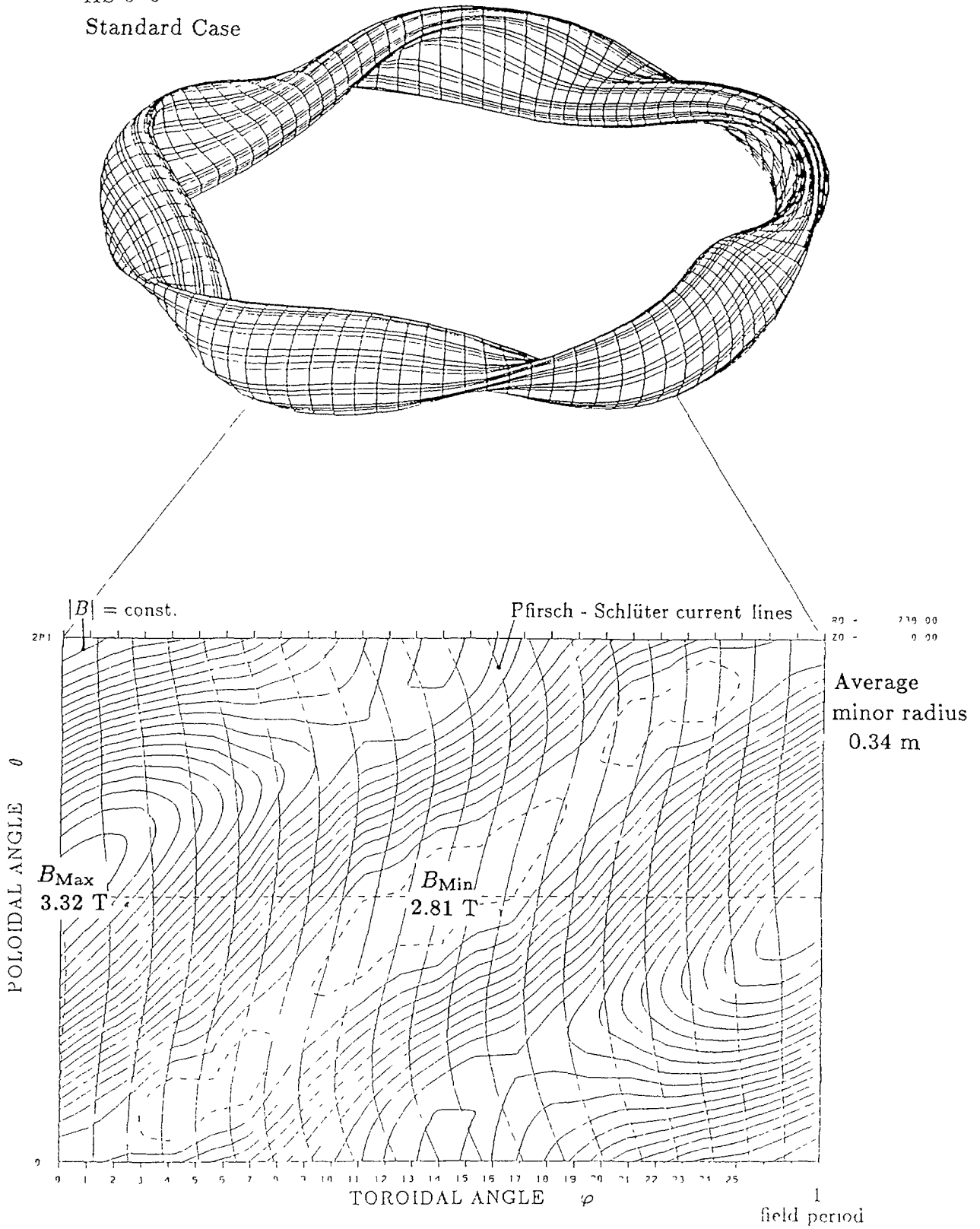


**Fig. 5:** Perspective view on magnetic surface, unfolding of one field period with contours  $\text{mod } B = \text{const.}$  and shape of Pfirsch-Schlüter current lines.

of one field period of the magnetic surface with an average minor radius  $r = 34$  cm, showing the contours of constant magnetic field and a number of Pfirsch-Schlüter current lines. Their toroidal excursions are much smaller than those of a standard stellarator or torsatron with the same aspect ratio and rotational transform,  $\epsilon = 1.06$ . The amplitude of the magnetic ripple is  $\delta B/B = (B_{\text{Max}} - B_{\text{Min}})/(B_{\text{Max}} + B_{\text{Min}}) = 14.2\%$ . The 'effective' ripple is much smaller [5].

Characteristic data for HS 5–8 are compared to those of the two preceding data sets in TABLE I, for the magnetic axis and an outer magnetic surface of the vacuum field. The expression  $\langle |j_{\parallel}/j_{\perp}| \rangle$  is the ratio of parallel and perpendicular current density, averaged over the flux surface. It is derived from the poloidal variation of  $\int dl/B$  taken along one field period. The weighted average  $J^* = \langle (B_o^2/B^2) \cdot (1 + (j_{\parallel}/j_{\perp})^2) \rangle$  enters the stability criterion of resistive interchange modes, and is a direct measure of the reduced secondary currents. The quantities  $C_{pl}$ ,  $C_{b,pl}$ , and  $C_{b,lmfp}$  are geometrical factors derived from the Fourier coefficients of  $mod B$ . They represent, respectively, the plateau diffusion coefficient and quantities which enter the relationships for the bootstrap current in the plateau and lmfp regimes, normalized to axisymmetric values of an equivalent configuration with the same rotational transform and aspect ratio; see [8].

TABLE I: Characteristic data of different Helias configurations.  
'STANDARD CASE'

		HS5-6	HS5-7	HS5-8
AXIS				
Rotat. Transf.	$\epsilon_o$	0.81	0.76	1.02
Current Ratio	$\langle  j_{\parallel}/j_{\perp}  \rangle$	0.71	0.78	0.60
Stabil. Param.	$J_o^*$	1.5	1.6	1.4
Plateau Diffus.	$C_{pl}$	0.47	0.31	0.39
Bootstrap Curr.	$C_{b,pl}$	-2.01	-1.06	-1.2
" "	$C_{b,lmfp}$	-0.1	0.1	0.01
EDGE				
Aver. Radius	$a$ [m]	0.65	0.65	0.70
Rotat. Transf.	$\epsilon_a$	0.97	0.97	1.18
Well Depth	$\delta V'/V_o'$ [%]	-1.6	-0.8	-1.6
Current Ratio	$\langle  j_{\parallel}/j_{\perp}  \rangle$	0.79	0.74	0.63
Stabil. Param.	$J_a^*$	1.7	1.6	1.4
Plateau Diffus.	$C_{pl}$	0.64	0.42	0.55
Bootstrap Curr.	$C_{b,pl}$	-2.01	-0.93	-0.97
" "	$C_{b,lmfp}$	-0.25	0.02	-0.03

## ADJUSTMENT OF ROTATIONAL TRANSFORM AND AXIS POSITION

For experimental flexibility, control of the rotational transform and of the magnetic axis position are required. One should be able to vary the  $\epsilon$ -value for more than the range between two adjacent low-order rational values. Regarding the edge, two cases are considered: keeping the last closed magnetic surface at some irrational value, or conversely, adjusting for low-numbered and comparatively large ‘natural’ magnetic islands near the edge in an attempt to use them for plasma edge control. Such different edge conditions in Helias fields have been studied in [9] for HS 5–8 with a sharp separatrix at  $\epsilon = 5/4$ , and in [10] for HS 5–7 with five islands.

Vertical fields for shifting the magnetic axis are usually introduced by current loops in standard coil systems. For a major radius of 6.5 m as considered in the present investigation, such current loops would be rather large. They can be avoided by the use of four planar coils per period, which allow one to adjust the polarity and magnitude of the coil currents separately, up to maximum values of  $\pm 0.5$  MA . Thus, toroidal and vertical fields can be superimposed as well. The axes of these additional coils follow approximately the magnetic axis; see [Fig. 6](#) .

Superposing about  $\pm 10\%$  of the modular field by use of the external coils changes the rotational transform from about -10 to +15 % of its standard value. The induced local magnetic ripple is compensated to a large extent by slightly different currents in some of the non-planar coils. Magnetic islands within the plasma or at the edge occur at  $\epsilon = 5/5$ ; see top and middle parts of [Fig. 7A](#). The edge structure of the configuration shown in the lower part of the figure has been investigated in [9] . In the upper part of [Fig. 7B](#), a system similar to the standard case of HS 5–8 is given, where the higher-order resonances 15/13 and 25/22 are resolved. These resonances are elements of the ‘Farey-tree’ :  $5/5$  combined with  $5/4 \Rightarrow 10/9$  ,  $10/9$  with  $5/4 \Rightarrow 15/13$ , and  $15/13$  with  $10/9 \Rightarrow 25/22$  . The middle part of the figure is a low- $\epsilon$  case. The transform approaches unity at the separatrix. Outside the separatrix, remnants of five magnetic islands may be

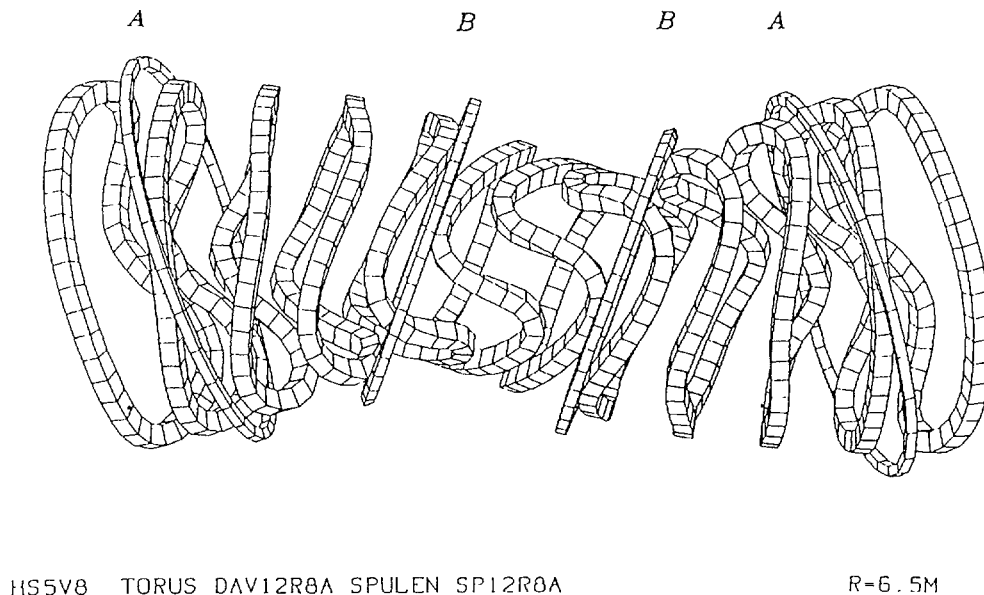


[Fig. 6](#): Coils of HS 5–8, 12 coils per period seen from the radial outside, with additional set of 4 coils per period for experimental flexibility.

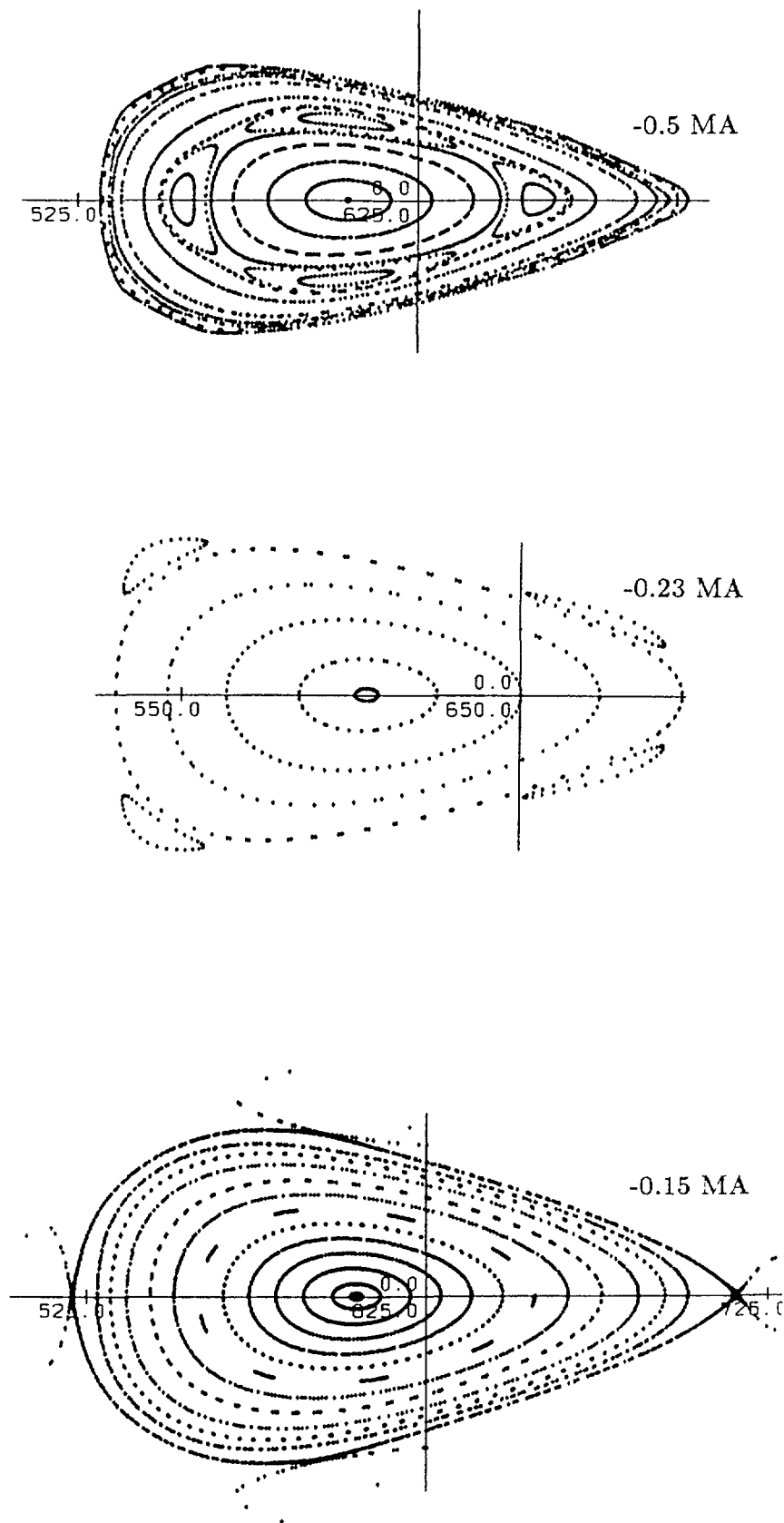


Fig. 7A:  $\epsilon$ -variation in HS 5-8.  
 High- $\epsilon$  cases : outer coils with negative polarity.  
 Toroidal position at  $1/2$  field period.

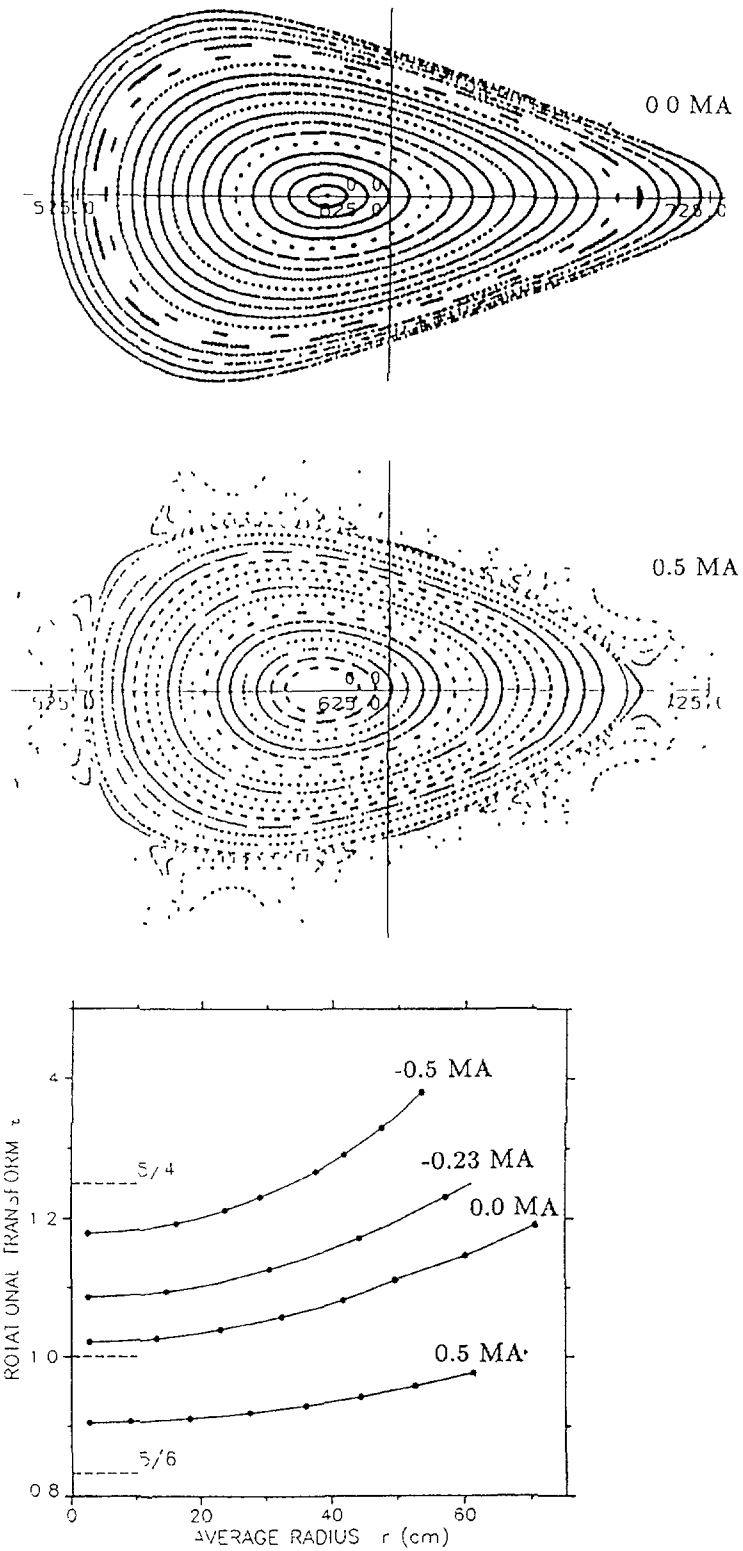


Fig. 7B: Standard case of HS 5-8 and low  $\epsilon$  :  
 outer coils zero current and positive polarity.  
 Radial dependence of  $\epsilon$  shown in lower part of the figure.

present. Such outer field structures have been omitted in the other plots, except for the case with the sharp separatrix at  $\iota = 5/4$ . This configuration has been investigated in [9] in more detail. The lower part in the figure gives the radial profiles of the rotational transform for the other four cases, as identified by the respective current values used in the set of external planar coils. Apart from the two cases with the 5/4-islands inside or at the edge of the closed magnetic surfaces, low-numbered rational values of the rotational transform are avoided in these configurations, but a situation with 5 islands can be attained as well. As seen in the plot, the shear  $\delta\iota/\iota_0$  increases from 10 to 16 % for the configurations shown. The well depth increases with  $\iota$  ; see [5] .

Vertical field components can also be generated by proper polarity of the external coils; this allows one to shift the magnetic axis by about  $\pm 1\%$  of the major radius as seen in the Figures 8 and 9. The respective polarities of the outer coils are given in the figures; simultaneously a 5 % correction of the currents is applied in order to reduce the total modular ripple. For both cases, the outermost field lines are still at distances of more than 10 cm from the first wall, at different toroidal and poloidal positions.

## SUMMARY AND CONCLUSIONS

The configuration HS 5–8, with 5 field periods, a major radius of 6.5 m, an averaged field of 3 T, an  $\iota$ -value between 1.02 and 1.18, is generated by 60 modular coils. The coils are optimized according to technical constraints; they leave sufficient access to the plasma and offer space between plasma and wall. The vacuum field properties, e. g. small Pfirsch-Schlüter currents, deep magnetic well, low ‘effective’ ripple, high quality of flux surfaces, are the basis for good plasma confinement and a sufficiently high stability- $\beta$ . The adjusted combination of the field components reduces the bootstrap current to a tolerable value. A set of external planar coils allows both a variation of the rotational transform between -10 and +15 % of that of the standard case, and also a shift of the magnetic axis by  $\pm 1\%$  of the major radius. Low-order magnetic islands at the edge can either be provided or avoided in the vacuum fields; both situations may be of interest for impurity control, using divertor plates or pump limiters.

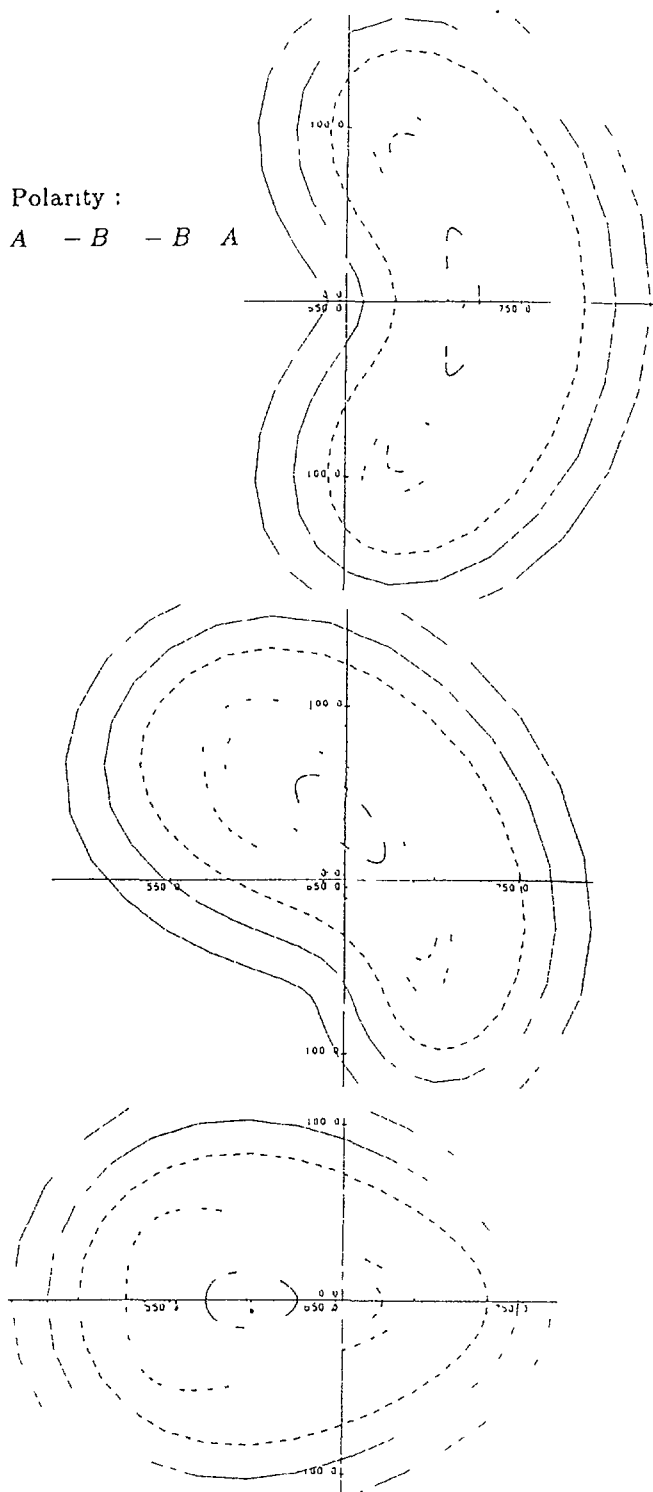


**Fig. 8:**  $B_z$ -variation in HS 5-8.  
 Axis shifted inwards to 7.15 and 5.97 m, at 0 and 1/2 field period.

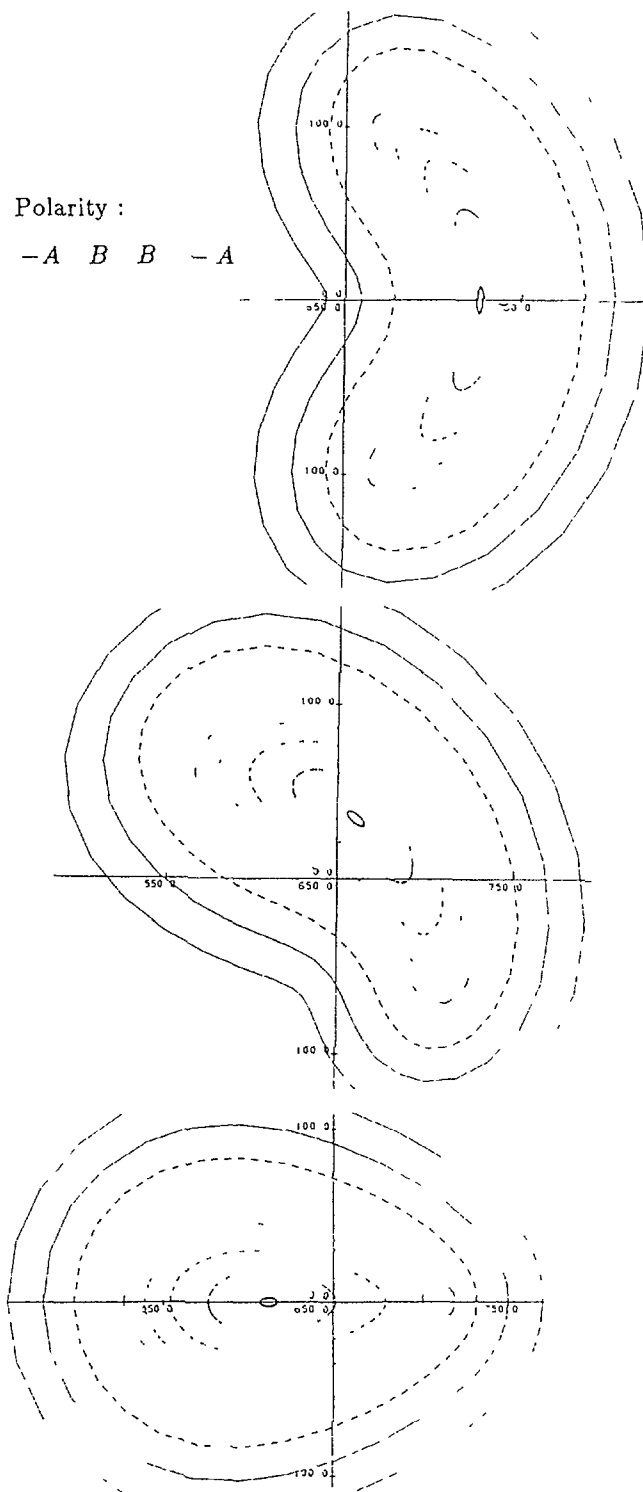


Fig. 9:  $B_z$ -variation in HS 5-8.  
 Axis shifted outwards to 7.26 and 6.13 m, at 0 and 1/2 field period.

## REFERENCES

- [1] WOBIG, H. et al., this conference, paper O 4-4.
- [2] NÜHRENBERG, J. and ZILLE, R., Phys. Letters **114A** (1986) 129.
- [3] GRIEGER, G. et. al., paper IAEA-CN-50/C-I-4, 12<sup>th</sup> Conf. on Plasma Physics and Nuclear Fusion Research, Nice (France), 1988.
- [4] MERKEL, P., Nuclear Fusion **27** (1987) 867.
- [5] BEIDLER, C., et al., Proc. 16<sup>th</sup> Europ. Conf. Venezia (Italy), Vol. 13B Pt.II, 595 (1989).
- [6] BEIDLER, C., et al., submitted for publication in Fusion Technology.
- [7] WOBIG, H., et al., this conference, poster 7 P-5.
- [8] WOBIG, H. et al., this conference, paper O 5-8.
- [9] RAU, F., et al., this conference, poster 7 P-4.
- [10] BEIDLER, C., et al., Proc. 16<sup>th</sup> Europ. Conf. Venezia (Italy), Vol. 13B Pt.II, 699 (1989).

# AN INVERSE METHOD FOR EXPANDING ABOUT A MAGNETIC AXIS

D.A. GARREN, A.H. BOOZER  
College of William and Mary,  
Williamsburg, Virginia,  
United States of America

## Abstract

We found a large class of analytic equilibria in which  $1/B^2$  is a function of only the flux and one helical coordinate. Such quasi-helical equilibria have identical drift orbits and associated transport in magnetic coordinates to that of a symmetric torus.

---

## I. METHOD

The traditional method for expanding about a magnetic axis was used by Mercier<sup>1</sup>, Lortz and Nürhenburg<sup>2,3,4</sup>, and Solov'ev and Shafranov<sup>5</sup>. They used the toroidal flux  $\psi$  Taylor expanded in the minor radius  $r$  and Fourier expanded in the poloidal angle  $\theta$ . We used a similar method but with the transformation equations  $x(\psi, \theta, \phi)$  Taylor expanded in the square root of the toroidal flux  $\psi^{1/2}$  and Fourier expanded in  $\theta$ . Here  $2\pi\psi$  is the toroidal magnetic flux enclosed by a magnetic surface,  $\theta$  is a poloidal angle, and  $\phi$  is a toroidal angle. We require that the B-field satisfy both the contravariant form

$$\mathbf{B} = \nabla\psi \times \nabla\theta + \nabla\phi \times \nabla\chi(\psi)$$

and the covariant form

$$\mathbf{B} = G(\psi)\nabla\phi + I(\psi)\nabla\theta + \beta(\psi, \theta, \phi)\nabla\psi,$$

where  $-2\pi\chi(\psi)$  is the poloidal magnetic flux outside of a magnetic surface,  $2\pi G(\psi)/\mu_0$  is the total poloidal current outside of a constant  $\psi$  surface,  $2\pi I(\psi)/\mu_0$  is the total toroidal current enclosed by a constant  $\psi$  surface, and  $\beta(\psi, \theta, \phi)$  is proportional to the local pressure gradient.

Given  $x(\psi, \theta, \phi)$ , flux surfaces are found by simply holding  $\psi$  constant and allowing  $\theta$  and  $\phi$  to vary. Field line trajectories are given by

$$\theta - \iota(\psi)\varphi = \theta_0 \text{ and } \psi = \psi_0,$$

with  $\iota(\psi) \equiv d\chi/d\psi$  the rotational transform, and  $\theta_0$  and  $\varphi_0$  constants that determine the field line.  $1/[B(\psi, \theta, \varphi)]^2$  is given by

$$\frac{1}{B^2} = \frac{(\partial x/\partial \psi) \cdot (\partial x/\partial \theta) \times (\partial x/\partial \varphi)}{G(\psi) + \iota(\psi)I(\psi)}.$$

We choose our transformation equations to be of the form

$$\mathbf{x}(\psi, \theta, \varphi) = r_0(l) + K(\psi, \theta, \varphi)\hat{\kappa}_0(l) + T(\psi, \theta, \varphi)\hat{\tau}_0(l),$$

with  $r_0(l)$  the magnetic axis, and  $l(\psi, \theta, \varphi)$  the axis distance. The Frenet unit vectors  $(\hat{\kappa}_0(l), \hat{\tau}_0(l), \hat{b}_0(l))$  are given by:

$$\begin{aligned} dr_0/dl &= \hat{b}_0(l), \\ d\hat{b}_0/dl &= \kappa(l)\hat{\kappa}_0(l), \\ d\hat{\kappa}_0/dl &= -\kappa(l)\hat{b}_0(l) - \tau(l)\hat{\tau}_0(l), \\ d\hat{\tau}_0/dl &= \tau(l)\hat{\kappa}_0(l), \\ [\hat{b}_0(l) \times \hat{\kappa}_0(l)] \cdot \hat{\tau}_0(l) &= 1, \end{aligned}$$

where  $\kappa(l)$  is the curvature and  $\tau(l)$  is the torsion. The most general form of  $K(\psi, \theta, \varphi)$  and  $T(\psi, \theta, \varphi)$  to  $\psi^{1/2}$  order is

$$K(\psi, \theta, \varphi) = \psi^{1/2}R(\varphi)\{\cos[\theta - \vartheta(\varphi)] + \epsilon(\varphi)\cos[\theta - \vartheta(\varphi) - \Delta(\varphi)]\},$$

$$T(\psi, \theta, \varphi) = \psi^{1/2}R(\varphi)\{\sin[\theta - \vartheta(\varphi)] + \epsilon(\varphi)\sin[\theta - \vartheta(\varphi) - \Delta(\varphi)]\},$$

with  $R(\varphi)$  the size parameter,  $\epsilon(\varphi)$  the ellipticity magnitude,  $\Delta(\varphi)$  the ellipticity phase, and  $\vartheta(\varphi)$  a phase parameter. The  $\theta=0$  position as a function of  $\varphi$  is chosen so that  $\theta = \vartheta(\varphi)$  is in the  $\hat{\kappa}_0(\varphi)$  direction. The rotational transform on axis (which must be constant) is

$$\iota_0 = d\vartheta/d\varphi + v(\varphi),$$

with

$$v(\varphi) = \{[1 - \epsilon^2][L/2\pi][\tau_0 + (1/2)(dI/d\psi)_0] + \epsilon^2(d\Delta/d\varphi)\}/\{1 + \epsilon^2\},$$

where  $\tau_0(\varphi)$  is the torsion on axis, and  $L$  is the length of the magnetic axis.

This implies that the transform on axis is given by

$$\iota_0 = (1/2\pi) \int_0^{2\pi} d\varphi v(\varphi).$$

## II. QUASI-HELICAL EQUILIBRIA

Quasi-helical equilibria are defined to be those equilibria in which  $1/B^2$  takes the form

$$1/[B(\psi, \theta)]^2 = (1/B_0)^2 [1 - \bar{\kappa} \sqrt{8/B_0} \cos(\theta) \psi^{1/2}] + \dots,$$

with  $B_0$ ,  $\bar{\kappa}$ , etc., all constant. Here  $B_0$  is the field strength on axis, and  $\bar{\kappa}$  is a parameter whose dimensions are inverse length. The following are necessary and sufficient conditions for quasi-helical equilibria:

1) The curvature on axis  $\kappa_0(\psi)$ , the torsion  $\tau_0(\psi)$ , and the length of the axis  $L$  are all arbitrary except

a)  $\kappa_0(\psi)$  can not be zero or infinite; (However, there exists a trivial solution with  $\kappa_0(\psi)$  equal to zero for all  $\psi$ .)

b)  $\kappa_0(\psi)$ ,  $\tau_0(\psi)$ , and  $L$  must be consistent with a closed curve.

2) One other function of  $\psi$  is free, which we take to be  $\alpha(\psi)$ .

For quasi-helical equilibria,  $B_0$ ,  $\bar{\kappa}$ , and  $L$  are free constants, and  $\kappa_0(\psi)$ ,  $\tau_0(\psi)$ , and  $\alpha(\psi)$  are free functions of  $\psi$ .  $R(\psi)$ ,  $\epsilon(\psi)$ , and  $\Delta(\psi)$  are obtained from these six functions by:

$$R(\psi) = \sqrt{2/[1 - [\epsilon(\psi)]^2] B_0},$$

$$\epsilon(\psi) = \sqrt{1 - [u(\psi)]^2},$$

$$u(\psi) = \{2\bar{\kappa}\kappa_0(\psi)\cos[\alpha(\psi)]\}/\{\bar{\kappa}^2 + [\kappa_0(\psi)]^2\},$$

$$d\Delta/d\psi = (dv/d\psi)/\{1 + [v(\psi)]^2\} - d\alpha/d\psi,$$

$$v = \tan[\alpha(\psi)]/\{1 - 2\bar{\kappa}^2/[\bar{\kappa}^2 + [\kappa_0(\psi)]^2]\}.$$

## III. SUMMARY

A large class of quasi-helical non-unique equilibria exist that are isomorphic to the symmetric torus and therefore have identical drift orbits and associated transport in magnetic coordinates<sup>6</sup>. The curvature of the magnetic axis must either remain non-zero for all values of the toroidal angle or it must be precisely zero for all values of the toroidal angle in order for non-trivial

quasi-helical equilibria to exist. In the case that the curvature is non-zero for all values of the toroidal angle, the net parallel current on the magnetic axis must be non-zero or the magnetic axis must have non-zero torsion in order for non-trivial quasi-helical equilibria to exist. The expansion parameter is  $r\bar{\kappa}$  where  $r$  is the minor radius of the outermost flux surface. Quasi-helical equilibria are not unique; further constraints must be given to determine the flux surfaces for each order in the expansion, just as for the symmetric torus. The helical dependence cannot be made to disappear, even in first order in the expansion. The variation in the field strength  $\Delta B$  goes as  $r\bar{\kappa}B_0$ ; the flux surfaces become highly elliptical unless  $\bar{\kappa}$  is chosen to be on the same order as the  $\phi$ -average of  $\kappa_0(\phi)$ . Non-zero bootstrap current, arbitrary rotational transform, and arbitrary magnetic well are consistent with quasi-helical symmetry. Quasi-helical symmetry specifies one half of the available parameters in this formalism as the order of the expansion goes to infinity. Constancy of the rotational transform on all magnetic surface places constraints on both the shape of the flux surfaces and the torsion of the magnetic axis as a function of the toroidal angle. Quasi-helical symmetry may be maintained whether the torsion goes in the same or the opposite direction to that of the rotating ellipse.

#### REFERENCES

1. C. Mercier, *Nucl. Fusion* **4**, 213 (1964).
2. D. Lortz and J. Nührenberg, *Z. Naturforsch* **31a**, 1277 (1976).
3. D. Lortz and J. Nührenberg, *Nucl. Fusion* **17** 1, 125 (1977).
4. D. Lortz and J. Nührenberg, *Z. Naturforsch* **34a**, 167 (1979).
5. L. S. Solov'ev and V. D. Shafranov, *Reviews of Plasma Physics* **5**, 1 (1967).
6. A. H. Boozer, *Phys. Fluids* **26**, 496 (1983).

## ON EDGE STRUCTURE AND PERTURBATIONS IN A HELIAS VACUUM FIELD

C. BEIDLER, E. HARMEYER, F. HERRNEGGER,  
J. KISSLINGER, F. RAU, R. SCARDOVELLI, H. WOBIG  
Euratom-IPP Association,  
Max-Planck-Institut für Plasmaphysik,  
Garching, Federal Republic of Germany

### Abstract

After reviewing earlier and recently published results, data of an improved configuration are presented and compared. Some critical issues are outlined.

---

### INTRODUCTION

The next step in the Garching stellarator programme, WENDELSTEIN VII-X, [1] will use a HELIAS configuration ( = Helical Advanced Stellarator ) with  $M = 5$  field periods. The magnetic field topology, with an aspect ratio around 10 at a major radius of 6.5 m, is produced by modular non-planar coils, and can be varied by superposition of external fields [2] . One of the aims of this experiment is to operate at elevated values of the average beta up to 5%. This calls for a heating power of the order of 20 MW, and poses challenging tasks in its application and removal, especially in order to attain a low level of impurities, which depends on internal transport processes and on various effects at the plasma boundary. Details of the magnetic field near the edge are therefore of interest. Several cases can be discussed: Limiter or separatrix dominated configurations, the latter with low-numbered or with high-numbered rational values of the rotational transform.

### EDGE STRUCTURE OF VACUUM FIELDS

A previous study [3] was concerned with the 'standard case' of the coil system called HS 5-7 . Because of a rational value of the rotational transform near the edge,  $t_s = 5/5 = 1$  , the vacuum field exhibits 5 'natural' magnetic islands. These islands are partially intersected by the first wall, toroidally between 3/8 and 5/8 of the field period. Some ergodicity is seen near the separatrix if this intersection is neglected. An inhomogeneous pattern of the intersection points is found for field lines starting close to the separatrix; comparatively well defined 'fans' are seen to leave the separatrix near the X-points. For more than 750 field lines started in the separatrix region, an average length of about 390 m to the wall is seen, i.e. about 9 times around the machine. The lengths to the wall scatter between less than the length of a field period, and up to more than 100 transits around the system. A total 'hot-spot area' of the order of  $1 \text{ m}^2$  is estimated. Owing to the comparatively low transit numbers of most field lines, the finite radial extent of the ergodic region cannot be utilized to increase this area. Two tentative limiter shapes are also studied. They collect a fraction of the field lines emerging outside the separatrix at differing intersection patterns; see [3] .

The present work is concerned mainly with the edge structure of the vacuum field attainable in HS 5-8 , an improved data set described in more detail in [2] . The vacuum field of its 'high- $t$  case' is shown in Fig. 1. The magnetic axis undulates radially

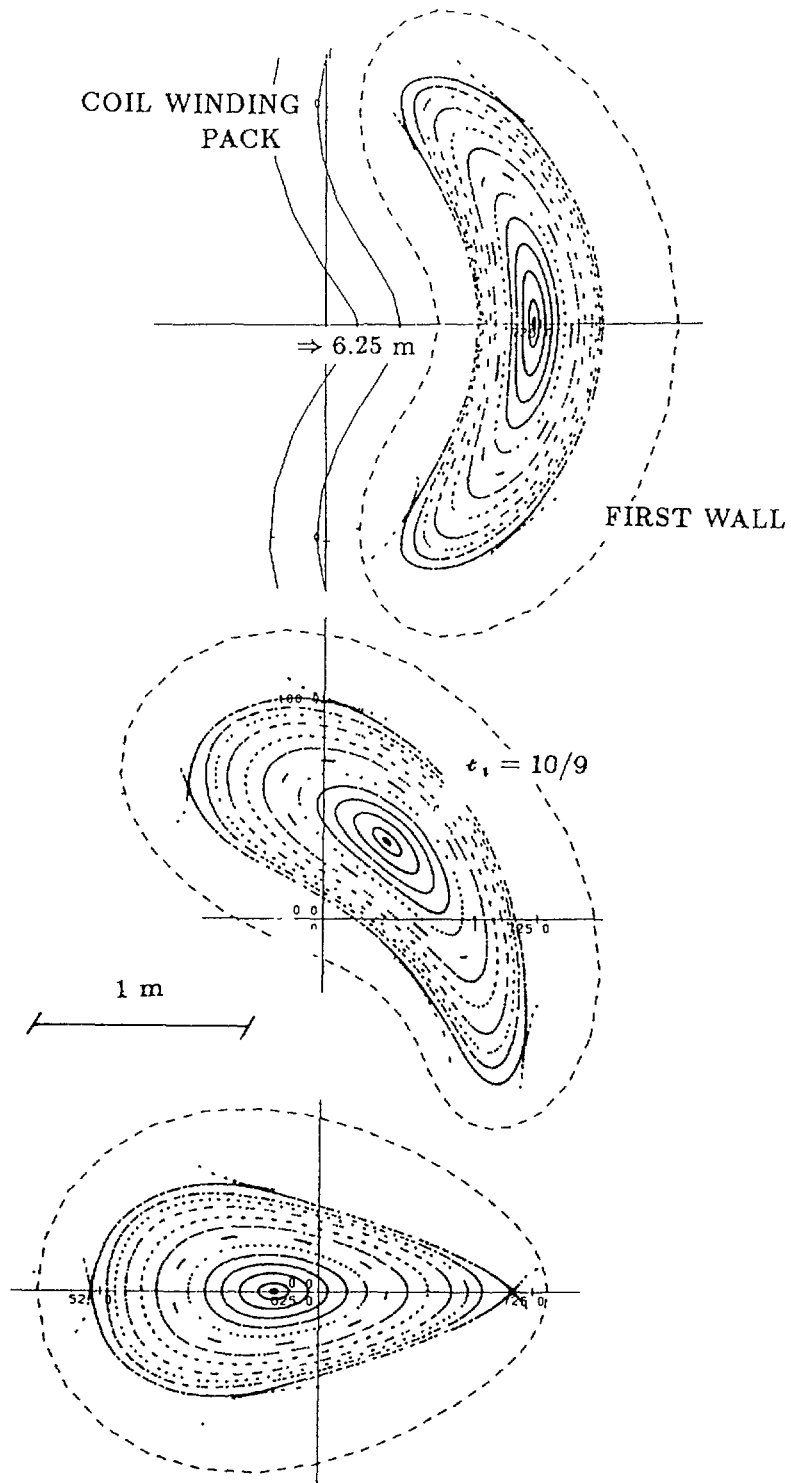


**Fig. 1:** High- $t$  case of HS 5-8.  
 Toroidal positions 0, 1/4, and 1/2 field period,  
 dashed line : contour of first wall, 18 cm within coil bores,  
 lowest-order resonance inside separatrix  $t_1 = 10/9$  .

between 722 and 604 cm; the vertical excursion is considerably smaller. The rotational transform increases from an axis value  $t_a = 1.06$  to  $t_s = 5/4$  at the separatrix. In contrast to the case with  $t_s = 5/5$  of ref. [3] and its 5 large 'natural' islands, edge islands of low order are avoided in the present configuration.

Details of configuration towards the separatrix region are given in Fig. 2 at  $\varphi = 36^\circ$ , i.e. at  $1/2$  field period. A number of high-order resonances is resolved. They are separated by slightly ergodic field lines which have been omitted in the left part of the figure for clarity. The ergodicity appears to increase towards the edge. It is smaller when using lower transit numbers and shorter integration steps. The integration is performed between 180 and 400 toroidal transits; field lines started close to the X-point and at some vertical offset comprise up to 40 transits. They show practically no ergodicity. The field line marked by  $S$  drifts slowly inwards. Reducing the integration step length (from  $9 \times 24$  to  $12 \times 24$  toroidal steps per period) for this field line indicates the possibility of one or more occasional 'offsets' in the computation, presumably occurring near the X-point, and the separatrix is seen to shrink by some small amount.

Effects of the finite grid size (stored field values in a spatial grid with 24 planes per period, and 39 radial and vertical grid points in a helical array) are seen. Fig. 3 is a close-up of the X-point region demonstrated by 2 times 3 field lines parallel and

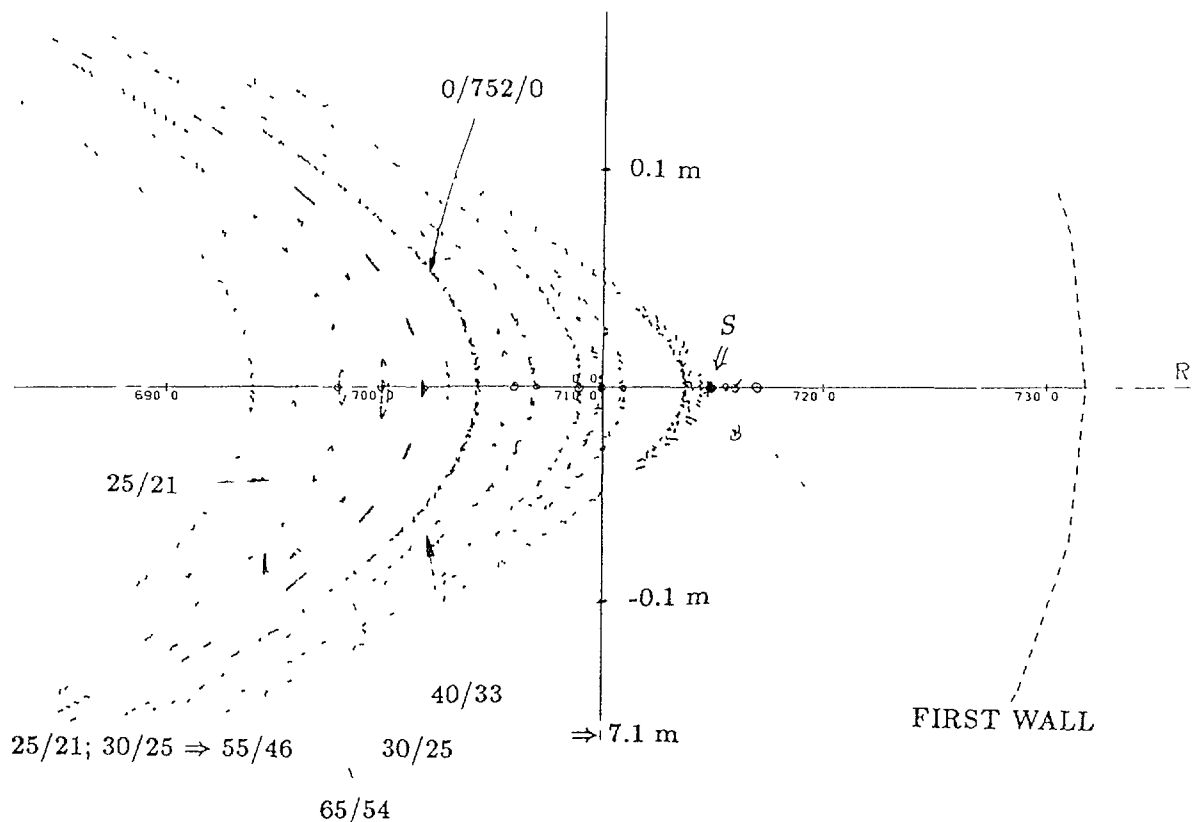
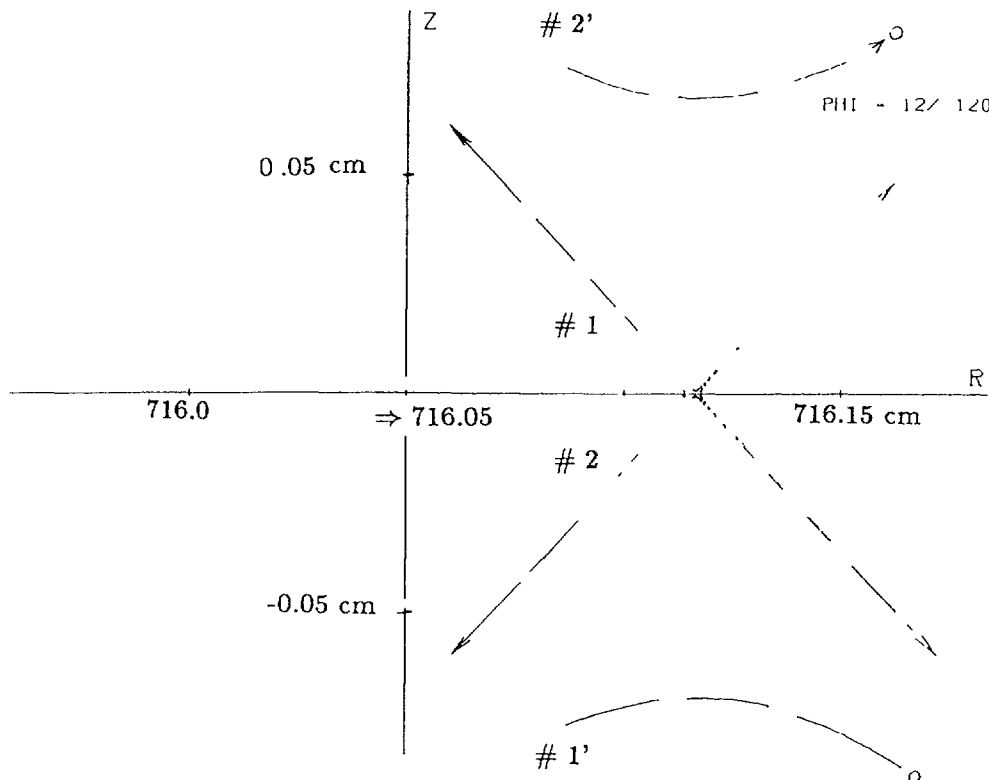


Fig. 2: Edge of configuration.

Fig. 1 enlarged at  $1/2$  field period, scale factor = 10 .

Higher-order resonances of the 'Farey-tree'  $5/5; 5/4 \Rightarrow 10/9$ , etc. ;  
e.g.  $25/21; 30/25 \Rightarrow 55/46$ , largest ratio seen so far :  $65/54$ .



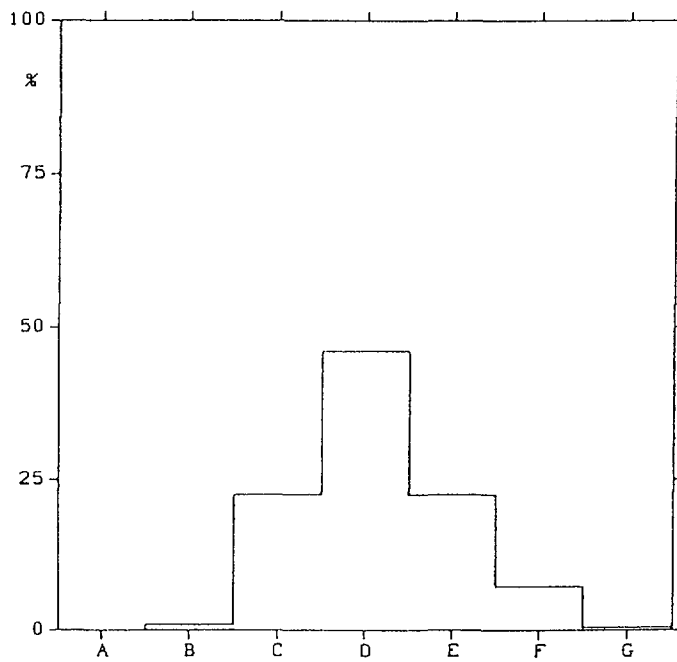
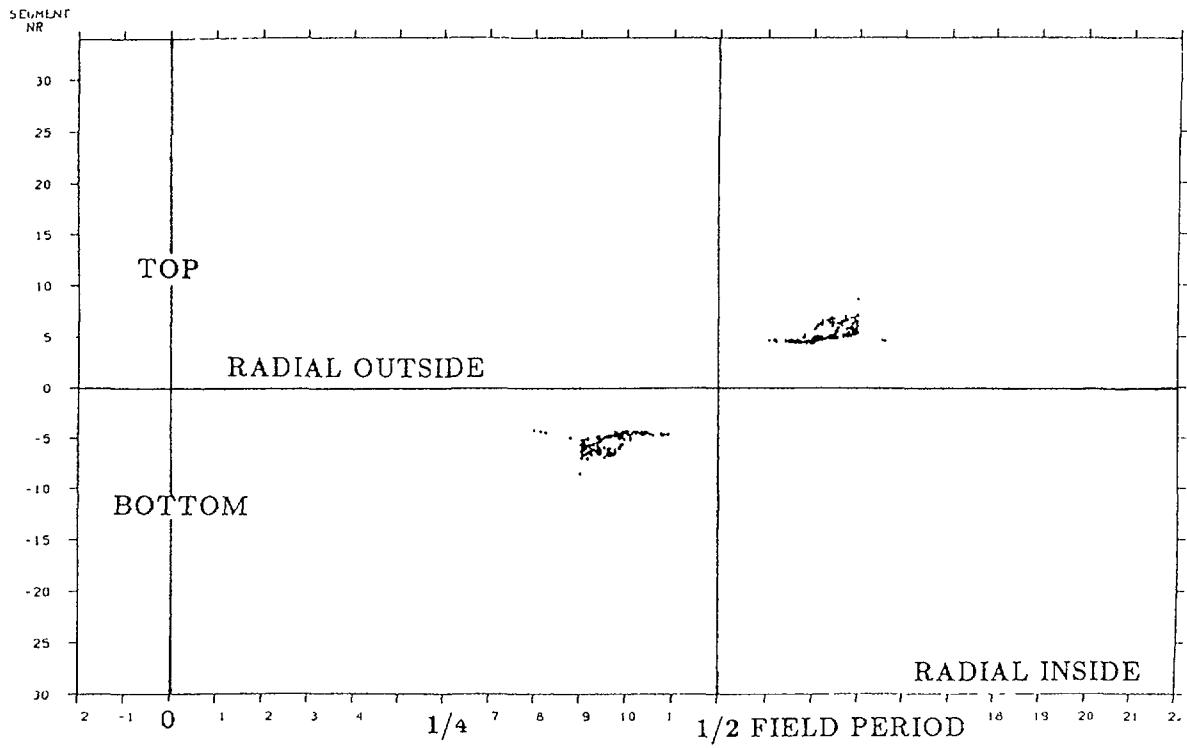
**Fig. 3:** Detail near X-point, 6 field lines:  
the scale is enlarged by another factor of 200 compared to that of Fig 2 .

opposite to the magnetic field, in 'direct' integration without stored field values. The two inner field lines # 1 and # 2 perform many transits and are then seen as upper and lower arc segments # 1' and # 2' in the figure. These lines are offset to the outside of the separatrix, despite a short step length of 1 cm . All field lines shown in the picture leave the system. Using stored field values for the integration yields a slightly blurred picture, and the X-point is shifted by  $\approx 0.14$  cm inwards.

#### INTERSECTION WITH FIRST WALL AND/OR LIMITER

The pattern of intersection points with the first wall in HS 5-8 is plotted in Fig. 4 . A number of field lines is started at some radial value, toroidally at 13, and poloidally at 10 or 20 positions; other field lines are started near the X-point at 1/2 field period. The pattern is similar to that shown in Fig. 4 of ref. [3] for the HS 5-7 configuration, but has a smaller size of the 'hot spots'. This may be partially due to the fact that up to now only one radial position of start points has been used in HS 5-8 . The statistics of the lengths to the wall are given in the lower part of the figure. About 400 data points yield an average of about 11 transits, with a scatter shown in the histogram. Four lines are shorter than 43.4 m which is the length of one transit. A group of 126 field lines started near the X-point yields more than 20 transits on average; no line is shorter than three, and two lines exceed 100 transits.

In each of the 5 field periods two plates are considered as a tentative limiter, with a radial dimension of 0.3 m, following roughly the apex of the magnetic surfaces, and



AVER LENGTH OF FIELD LINES

LQ (M) 475 10

AVER LENGTH OF 1 TRANSIT

L1 (M) 43 37

TOTAL 399

A  $L < L1/M$  0

B  $L < 1 * L1$  4

C  $L < 3 * L1$  90

D  $L < 10 * L1$  184

E  $L < 30 * L1$  90

F  $L < 100 * L1$  29

G  $L > 100 * L1$  2

Fig. 4: Intersection with First Wall.

Upper part:

angular plot of one field period (abscissa),  
the ordinate is one poloidal transit.

Lower part: statistics of intersection lengths.

extended at  $Z = \pm 1.2$  m between  $\varphi = \mp 3$  and  $\pm 12^\circ$ , respectively. The field line integration is stopped at these plates. In addition, a possible intersection with the torus is monitored. As a first test, field lines are started near the X-point at  $\varphi = 36^\circ$ ; see Fig. 5. For vertical plate positions at 1.22 m, the limiter system is not effective, and the field lines cut the torus. Shifting the limiter plates to 1.18 m causes intersection with the limiter after typically 0.7 to 3.4 km; for one start point a maximum value of 7.8 km is seen. The average length of 18 lines is 1.85 km, corresponding to more than 40 transits.

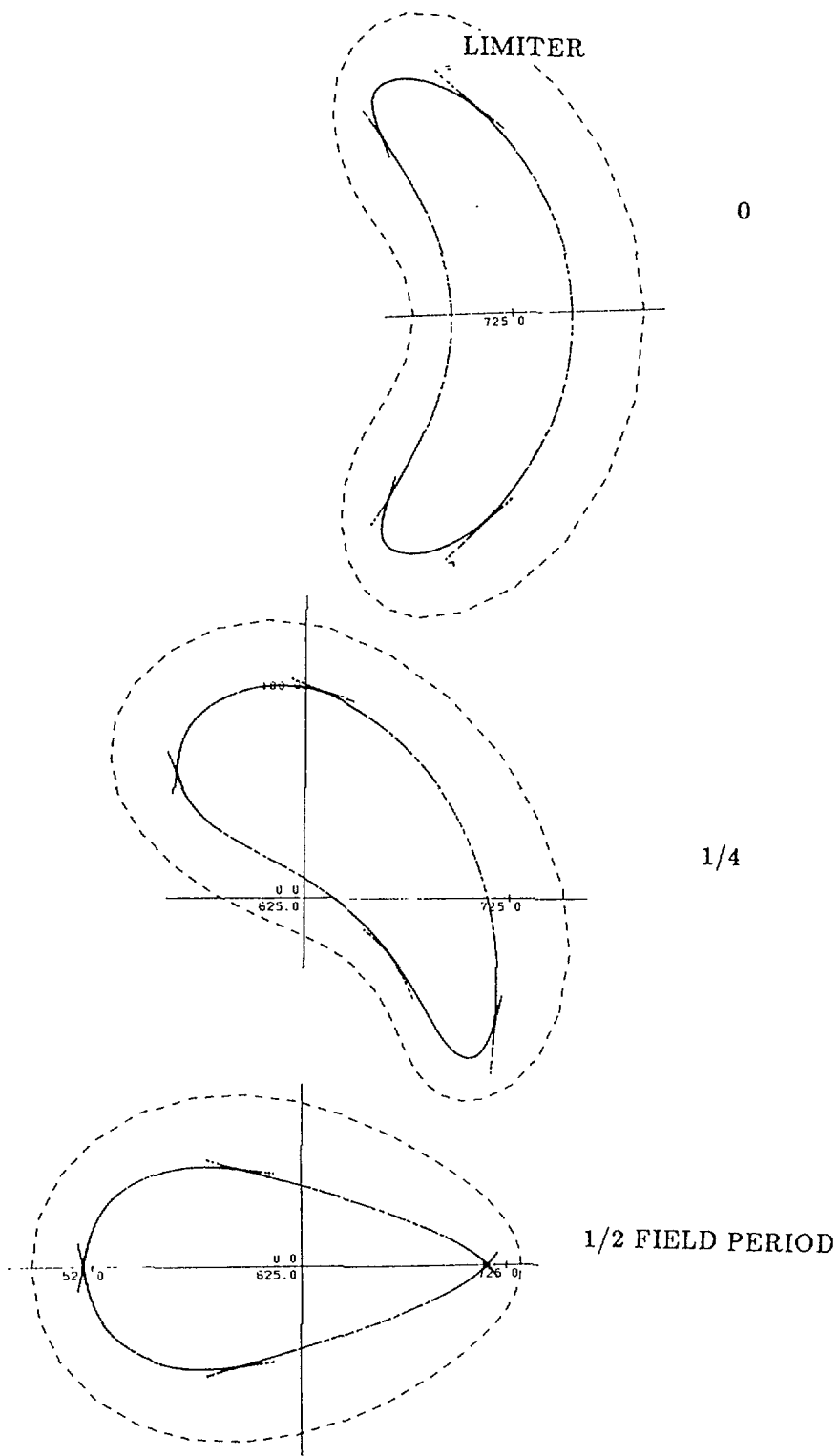
## PERTURBATIONS

Fig. 6 demonstrates in the upper half the effect on the HS 5-8 configuration, generated by perturbing fields with  $M = 1$  periodicity: the effective minor separatrix radius shrinks to a lower value than that without perturbation, see lower part of the figure. A number of new islands occurs, such as  $\iota = 6/5, 7/6$ , and  $8/7$  with low order, and also a resonance at  $\iota = 20/17$ . The denominator is equal to the number of islands. The first of these ratios corresponds to the high-order element of the Farey-tree  $\iota = 30/25$ , shown in Fig. 2 in the unperturbed system. The island at  $\iota = 6/5$  and the magnetic surfaces near the edge region show some enhanced ergodicity.

Similar islands have been obtained for the HS 5-8 configuration for various perturbations (orientation, field amplitude and structure). Corresponding to the lower  $\iota$ -value, the new islands are at  $\iota = 7/8$  and  $6/7$ . The resonance  $\iota = 5/6$  has nearly the same island size as in the unperturbed system. The poloidal position of the islands and an over-all tilt of the magnetic axis depend on the orientation of the perturbation in space.

## SUMMARY AND CONCLUSIONS

The proximity of the first wall in the Helias systems investigated so far dominates the edge field structure of unperturbed configurations in HS 5-7, and is of importance in those of HS 5-8. There, a rather close distance of a tentative plate limiter array to the last closed magnetic surface is required. Some ergodicity is seen in both systems for field lines at large transit numbers, increasing towards the separatrix. Without limiter, inhomogeneous patterns of the intersection points of field lines with the first wall are seen, when starting close to the separatrix. For HS 5-7 a total 'hot spot' area of the order of  $1 \text{ m}^2$  is estimated. Due to the comparatively low transit numbers of most field lines the finite radial extension of the ergodic region cannot be utilized to increase this area. For HS 5-8 the 'hot spot' area is even smaller. This calls for an improved (pump) limiter system or a divertor for edge control of the plasma, to be optimized for various  $\iota$ -values, also when considering possible perturbation fields. They introduce new magnetic islands; large perturbation fields increase the island size, the ergodicity, and the aspect ratio of the system. In general it is felt that the confinement properties are reduced by the ergodicity of field lines and the presence of magnetic islands. In model fields a considerable reduction of the effective minor radius has been seen [4], when increasing the perturbation. For future investigations it is necessary to study the trajectories of charged particles as well, including collisions. Trapped particles are likely to introduce 'hot spots' at areas differing from those studied so far.



**Fig. 5:** Intersection with limiter.  
Field lines started near the X-point.

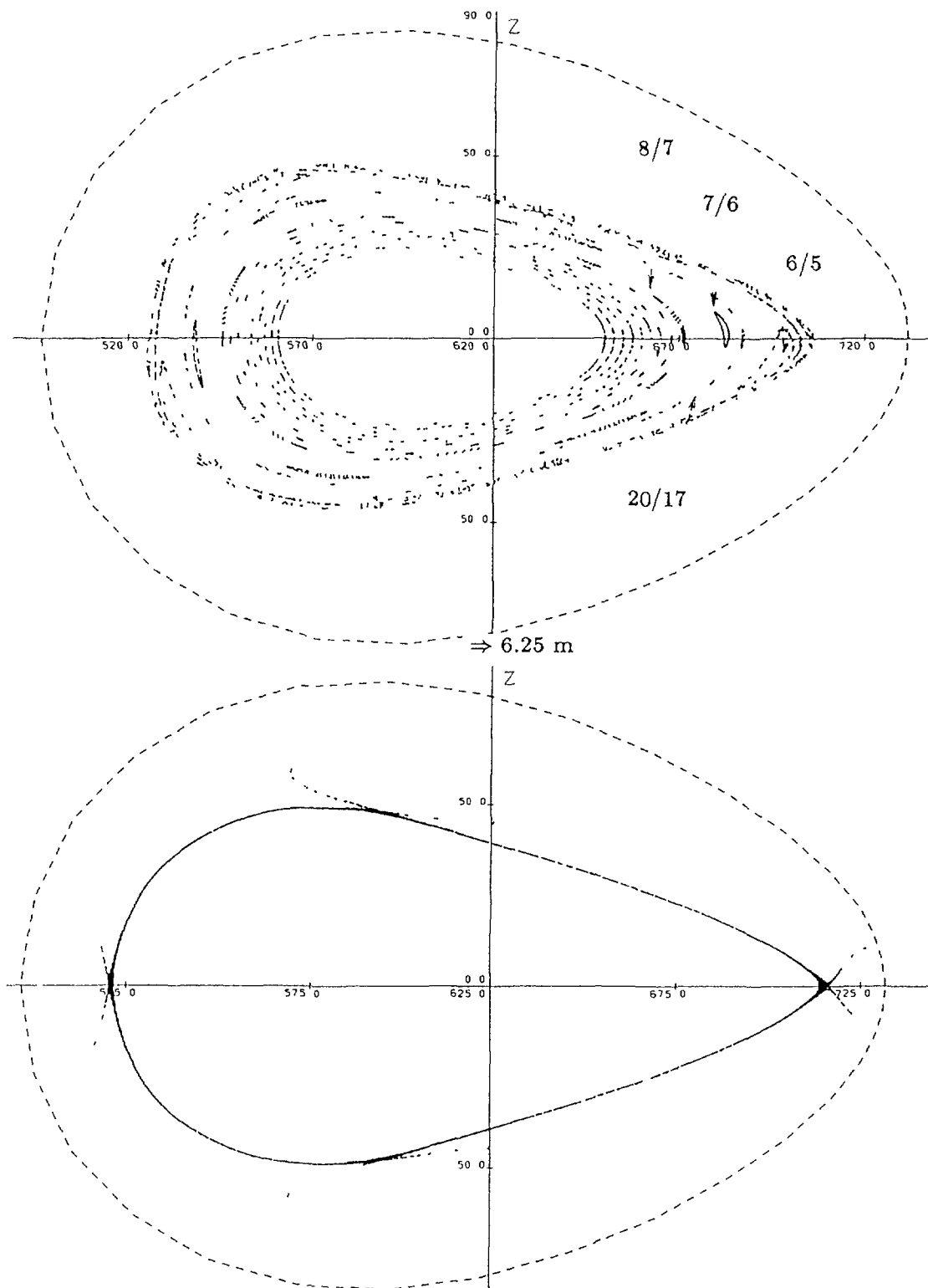


Fig. 6:

Upper part: Perturbed configuration.

Lower part. Separatrix region without perturbation.

## REFERENCES

- [1] WOBIG, H. et al., this conference, paper O 4-4.
- [2] RAU, F., et al., this conference, poster 7 P-2.
- [3] BEIDLER, C., et al., Proc. 16<sup>th</sup> Europ. Conf. Venezia (Italy),  
Vol. 13B Pt.II, 699 (1989).
- [4] WOBIG, H., et al., Proc. Int. Stellarator/Heliotron Workshop Kyoto (Japan),  
Vol. II, 422 (1986), Report PPLK-6.

## NEOCLASSICAL TRANSPORT IN A MODULAR HELIAS

C.D. BEIDLER, E. HARMEYER, J. KISSLINGER,  
F. RAU, R. SCARDOVELLI, H. WOBIG  
Euratom-IPP Association,  
Max-Planck-Institut für Plasmaphysik,  
Garching, Federal Republic of Germany

### Abstract

Neoclassical transport rates are determined for Helical-Axis Advanced Stellarators (Helias). Special emphasis is given to Wendelstein VII-X candidates, for which the magnetic field is produced by a large number of discrete non-planar coils. The investigation is concentrated on the long-mean-free-path regime where particles trapped in local *ripple* wells of the magnetic field make the dominant contribution to transport. For Wendelstein VII-X, such particles fall into two classes; those localized in the *helical* ripple common to all stellarator-type devices and those very-localized particles which are trapped in the *modular* ripples existing between the individual coils. Using analytical techniques it is shown that helical-ripple transport rates are substantially reduced for Wendelstein VII-X candidates relative to classical stellarator/torsatron configurations. This reduction is most pronounced in the  $\nu^{-1}$  regime — equivalent helical ripples of less than 1% lead to reduction factors of more than an order of magnitude — but is significant throughout the entire long-mean-free-path regime. Modular ripple transport in Wendelstein VII-X is calculated by analytically solving the bounce-averaged kinetic equation. This solution assumes a general magnetic field model and fully accounts for the deformation of modular ripples due to the presence of the other magnetic-field harmonics. Results indicate that 12 coils per field period are necessary if modular-ripple losses are to remain smaller than helical-ripple losses over the entire plasma cross section.

---

### INTRODUCTION

The future stellarator experiment, Wendelstein VII-X, will be the first to employ the Helical-Axis Advanced Stellarator (Helias) concept. One of the expected advantages of the Helias relative to conventional stellarator/torsatron devices is a much smaller rate of neoclassical transport in the long-mean-free-path (*lmfp*) regime where particles trapped in the *helical* ripple of the stellarator's magnetic field provide the dominant transport mechanism.

Unlike the conventional stellarator/torsatron, however, the magnetic field of Wendelstein VII-X will be produced by a large number of discrete, non-planar, current-carrying coils. These *modular* coils introduce a further ripple in the magnetic field and thereby provide an additional transport mechanism. Clearly, it is of no value to optimize the Helias magnetic field for reduction of helical-ripple transport if the resulting level of modular-ripple transport is far in excess. There is, however, some freedom of choice in the number of modular coils which make up each field period; a large number of coils reduces the magnitude of the modular ripple but also increases fabrication costs of the machine and decreases plasma access.

In the current paper, the neoclassical transport levels resulting from both the helical and modular ripples will be estimated for Wendelstein VII-X candidates using analytic theories. Results will be used to find the optimum number of coils per field period insuring that modular-ripple losses are tolerable over the entire plasma cross section.

## HELICAL-RIPPLE TRANSPORT

Throughout this paper the set of magnetic coordinates  $(r, \theta_0, \phi)$  [1] will be used to represent physical space. In this system, a general model for the magnitude of the magnetic field is given by

$$\frac{B}{B_0} = \sum_{m,\ell} C_{m,\ell}(r) \cos \ell\theta \cos m\phi + \sum_{m,\ell} S_{m,\ell}(r) \sin \ell\theta \sin m\phi. \quad (1)$$

Along a field line the poloidal angle is related to the toroidal angle through the rotational transform,  $\theta = \theta_0 + \iota\phi$ . In this section, only the principal harmonics of Wendelstein VII-X candidates will be considered, namely  $C_{0,1}$ ,  $C_{1,0}$ ,  $C_{1,1}$  and  $S_{1,1}$ . Using the method of reference [2], this simplified model magnetic field may be cast in the form

$$B = B_0(1 + C_{0,1} \cos \theta + \epsilon_h(1 + \sigma \cos \theta) \cos(\eta - \chi)), \quad (2)$$

where

$$\begin{aligned} \epsilon_h &= \left( C_{1,0}^2 + \frac{C_{1,1}^2 + S_{1,1}^2}{2} \right)^{1/2}, & \sigma &= \frac{C_{1,0}C_{1,1}}{\epsilon_h^2}, \\ \eta &= p\phi, & \sin \chi &= \frac{S_{1,1} \sin \theta}{\epsilon_h(1 + \sigma \cos \theta)}, & \cos \chi &= \frac{C_{1,0} + C_{1,1} \cos \theta}{\epsilon_h(1 + \sigma \cos \theta)}. \end{aligned}$$

A general theory of *lmfp* transport in the model field of equation (2) was presented in reference [3]. This theory has been used to predict neoclassical transport coefficients in a pair of Wendelstein VII-X candidates; results obtained were shown to be in good agreement with those of a numerical Monte Carlo simulation [4]. For these two configurations, transport levels in the  $\nu^{-1}$  regime were reduced by as much as a factor of 50 relative to those expected in the equivalent classical stellarator. (The equivalent classical stellarator is defined to have the same value of  $\epsilon_h$  but to have  $C_{0,1} = \epsilon_t$  and  $\sigma = 0$ .) At lower collision frequencies the reduction was not as dramatic but was still significant.

This favorable result may be most easily understood in the  $\nu^{-1}$  regime where it is possible to obtain a solution for the particle flux,  $\Gamma$ , in which the magnetic field quantities  $C_{0,1}$ ,  $\epsilon_h$  and  $\sigma$  appear explicitly [2]. This solution may be written in the form  $\Gamma = A_h W(\kappa)$ , where  $W$  is a function only of energy and

$$A_h \approx \frac{64}{9} \epsilon_h^{3/2} \left( \frac{C_{0,1}}{\epsilon_t} \right)^2 \left\{ 1 - \frac{6}{5} \frac{\sigma \epsilon_h}{C_{0,1}} + 0.385 \left( \frac{\sigma \epsilon_h}{C_{0,1}} \right)^2 \right\} \quad (3)$$

contains all information relating to the magnetic field. Clearly, for the equivalent classical stellarator,  $A_h = A_h^{(ecs)} = (64/9) \epsilon_h^{3/2}$ .

Equation (3) offers Helias configurations two routes for significant reduction of  $A_h$ . The first is to make the ratio  $C_{0,1}/\epsilon_t$  as small as possible while the second is to have  $\sigma \epsilon_h / C_{0,1} \approx 1.56$  as this minimizes the bracketed term in equation (3). Various Wendelstein VII-X candidates utilize both of these routes to different degrees as illustrated in the table below. The configurations designated HS4-8 and HS5-6 are those which were investigated in reference [4]; the results obtained here confirm those of the earlier analytical/numerical calculations. The configuration HS5-7, one of the leading candidates for Wendelstein VII-X, is particularly well optimized; a decrease of

neoclassical transport rates in the  $\nu^{-1}$  regime of almost two orders of magnitude is predicted by equation (3).

	$\epsilon_h$	$\sigma$	$C_{0,1}/\epsilon_t$	$\sigma\epsilon_h/C_{0,1}$	$A_h/A_h^{(ecs)}$	$\bar{\epsilon}_h$
HS4-8	0.0502	0.4775	0.5178	1.0284	0.0464	0.0065
HS5-6	0.0666	0.0525	0.1848	0.4112	0.0195	0.0048
HS5-7	0.0626	0.4852	0.4004	1.6429	0.0109	0.0031

Note: The values given above are taken at half the plasma radius ( $r/a = 1/2$ ). The "equivalent helical ripple",  $\bar{\epsilon}_h$ , is defined by the equation  $A_h = (64/9)\bar{\epsilon}_h^{3/2}$ .

## MODULAR-RIPPLE TRANSPORT

For Wendelstein VII-X candidates, the high-order magnetic field harmonics which are identified with the modular ripple are generally of much smaller amplitude than those associated with the helical ripple. Thus, in regions of significant helical-ripple gradient, it is not always possible for modular ripple wells to form; even in regions where this gradient is small, the depth and extent of individual modular wells are often strongly influenced by the presence of the low-order magnetic field harmonics. This deformation of local wells is an effect which is well-known in the case of non-axisymmetric "rippled" tokamaks [5,6]. Given these considerations, a simplified model field similar to that of equation (2) is not an appropriate starting point if one wishes to obtain a realistic estimate of modular-ripple transport in a general Helias magnetic field. Instead, in the theory outlined below, the general form of  $B$  given in equation (1) is adopted, insuring that the results may be applied with equal accuracy regardless of the complexity of the magnetic field configuration.

In the *lmfp* regime the longitudinal adiabatic invariant,  $J = \oint mv_{\parallel} dl$ , is a constant of a trapped particle's motion and the guiding-center drift-kinetic equation may be simplified by application of the operator,  $\oint dl/v_{\parallel}$ . The resulting *bounce-averaged* kinetic equation is then solved in lowest non-trivial order by expanding the distribution function in terms of a local Maxwellian,  $F_M$ , and a perturbation term,  $f$ , yielding

$$\frac{1}{qB_0 r} \frac{\partial B}{\partial \theta_0} \frac{\partial F_M}{\partial r} \frac{\partial}{\partial \mu} (\mu J) = \nu \frac{\partial}{\partial \mu} \left( \mu J \frac{\partial f}{\partial \mu} \right), \quad (4)$$

where  $\mu = mv_{\perp}^2/2B$  is the magnetic moment,  $q$  is the particle charge and  $\nu$  is the 90 degree deflection frequency. The solution of equation (4) is sought in the region of phase space where local modular ripple wells exist (i.e. the range of  $\mu$  values which satisfy  $\kappa/B_{max} < \mu < \kappa/B_{min}$ , with  $\kappa = mv^2/2$  and  $B_{min}, B_{max}$  the local minimum and maximum values of  $B$  which define the ripple well) with the boundary conditions that  $\partial f/\partial \mu$  be finite in the region of solution and that  $f = 0$  for non-ripple-trapped particles. The solution for  $f$  is

$$f = \frac{1}{qB_0 r} \frac{\partial B}{\partial \theta_0} \frac{\partial F_M}{\partial r} \frac{(\mu - \kappa/B_{max})}{\nu}. \quad (5)$$

The particle flux due to localized particles may once again be written in the form  $\Gamma_{\delta} = A_{\delta}(\theta_0, \phi)W(\kappa)$ , where

$$A_{\delta}(\theta_0, \phi) = \frac{2\sqrt{2}}{15\pi} \int_0^{2\pi} d\theta_0 \int_0^{2\pi} d\phi \left( \frac{1}{B\epsilon_t} \frac{\partial B}{\partial \theta_0} \right)^2 (1 - B/B_{max})^{3/2} (4 + B/B_{max}). \quad (6)$$

In principal this completes the solution, although further simplification of equation (6) is impossible given the very complicated magnetic field geometry introduced by equation (1). Difficulties appear not only in the expression for  $B$  itself, but also in the accompanying deformation of individual modular ripples, greatly complicating any analytic expression for  $B_{max}$ . Instead, equation (6) is integrated numerically; at each point that the integrand is evaluated, the condition  $\partial B/\partial\phi = 0$  (along the field line passing through that point) is *numerically* solved to determine whether a modular ripple well exists at that point, and if so, what the local value of  $B_{max}$  is.

The method described above makes it possible to determine to what degree the optimization of neoclassical transport, given in the previous section, is degraded by modular-ripple transport. As an example, the ratio  $A_\delta/A_h$  will be evaluated on various flux surfaces for the Wendelstein VII-X candidate HS5-7, a five field period Helias with rotational transform varying from  $\iota = .76$  on axis to  $\iota = .96$  at the plasma edge.

It is possible to realize the magnetic field of HS5-7 (or any other Helias) through a number of different modular coil configurations, differing in the number of discrete coils per field period,  $N$ . The principal magnetic-field harmonics are essentially identical in these various cases, only the magnitude of the modular ripple,  $\delta$ , and its periodicity are effected. Large values of  $N$  reduce  $\delta$  significantly but also greatly limit experimental access to the plasma. Ideally, the value of  $N$  should be as small as possible to maximize access, but also large enough to insure that  $A_\delta/A_h$  remains small over the entire plasma cross section.

Coil sets for the HS5-7 configuration exist in both  $N = 10$  and  $N = 12$  versions. The ratio of  $A_\delta/A_h$  has been calculated in these two cases for several flux surfaces; results are presented below. The  $N = 10$  version shows values of this ratio considerably in excess of one near the plasma edge. On the other hand, the ratio of  $A_\delta/A_h < 1$  at all radii for the  $N = 12$  version of HS5-7. As this latter version also allows sufficient plasma access, 12 coils per field period is deemed to be the optimum value for HS5-7.

	Ratio of $A_\delta/A_h$ at				
	$\rho = 0.2$	$\rho = 0.4$	$\rho = 0.6$	$\rho = 0.8$	$\rho = 1.0$
HS5-7 ( $N = 10$ )	0.0125	0.1372	1.1452	3.2496	8.1374
HS5-7 ( $N = 12$ )	0.0035	0.0230	0.0833	0.2990	0.5308

## REFERENCES

- [1] BOOZER, A.H., KUO-PETRAVIC, G., Phys. Fluids, **24**, (1981) 851.
- [2] SHAIN, K.C., HOKIN, S.A., Phys. Fluids, **26**, (1983) 2136.
- [3] BEIDLER, C.D., HITCHON, W.N.G., VAN RIJ, W.I., HIRSHMAN, S.P., SHOJET, J.L., Phys. Rev. Lett., **58**, (1987) 1745.
- [4] BEIDLER, C.D., in Proceedings of the Second Workshop on WENDELSTEIN VII-X, (Proc. Second WVII-X Workshop, Schloss Ringberg, 1988, RAU, F., LEOTTA, G.G., Ed.), Commission of the European Communities, EUR 11705 EN, (1988) 121.
- [5] STRINGER, T.E., Nuclear Fusion, **12**, (1972) 689.
- [6] CONNOR, J.W., HASTIE, R.J., Nuclear Fusion, **13**, (1973) 221.

## NUMERICAL METHODS FOR STELLARATOR OPTIMIZATION\*

R.N. MORRIS, C.L. HEDRICK, S.P. HIRSHMAN,  
J.F. LYON, J.A. ROME  
Oak Ridge National Laboratory,  
Oak Ridge, Tennessee,  
United States of America

### Abstract

A numerical optimization procedure utilizing an inverse 3-D equilibrium solver, a Mercier stability assessment, a deeply-trapped-particle loss assessment, and a nonlinear optimization package has been used to produce low aspect ratio ( $A = 4$ ) stellarator designs. These designs combine good stability and improved transport with a compact configuration.

---

The development of 3-D plasma analysis tools for the optimization of stellarator designs is important for the current ATF-II studies and beyond. The subject of this work, low aspect ratio studies, presents the challenge of reconciling MHD stability with favorable neoclassical transport in a single compact device. Toroidal effects, which are enhanced at low aspect ratios, often tend to influence MHD and transport properties in opposing ways and this work will present a numerical procedure that seeks an optimal balance between the two. The parameter space over which the optimization is carried out is defined by a set of Fourier harmonic coefficients describing the boundary of the plasma. The basis of the nonlinear optimal search scheme is formed by varying the boundary around a tentative design and assessing the changes in Mercier stability and the transport of deeply trapped particles in the altered configuration. The success of this procedure depends on the proper evaluation of the plasma parameters as well as the existence of an adequate initial configuration. The rapid computations of inverse equilibria, stability, and confinement criteria are also crucial. Plasma parameters of interest include iota profile, magnetic well profile, MHD stability, particle transport, and configuration complexity.

Because of the complexity and time-consuming nature of most plasma physics calculations, the MHD stability and transport evaluations have to be limited in scope. The Mercier criterion [1] has been chosen for the MHD stability calculation and the "B minimum" ( $B_{\min}$ ) contours [2] have been selected for calculation of the transport criterion. In both cases the figure of merit used for the optimization is a percentage of the appropriate maximum as measured in normalized flux space,  $\psi$ . The Mercier stability module returns the percentage of the plasma that is unstable to high order localized ideal MHD modes outside of the central ( $0.1 < \psi$ ) plasma region. The transport module concentrates only on deeply trapped particles and returns the width, in flux space, of the last closed  $B_{\min}$  contour. Also available is an option to determine the offset of the  $B_{\min}$  contours from the magnetic axis.

---

\* Research sponsored by the Office of Fusion Energy, US Department of Energy, under contract DE-AC05-84OR21400 with Martin Marietta Energy Systems, Inc.

It is useful for the boundary Fourier expansions of the three-dimensional inverse MHD equilibria to have a unique poloidal angle, in order to prevent the problems of an ill defined convergence path in Fourier space. To this end we have chosen to use the following form to represent the boundary [3]:

$$\begin{aligned}
R &= \sum_{n=0}^N R_{0n} \cos n\phi + \sum_{n=-N}^N R_{1n} \cos(\theta - n\phi) + \bar{r} \cos \theta \\
Z &= \sum_{n=0}^N Z_{0n} \sin n\phi - \sum_{n=-N}^N R_{1n} \sin(\theta - n\phi) + \bar{r} \sin \theta \\
\bar{r} &= \sum_{n=0}^N r_{0n} \cos n\phi + \sum_{m=3,n}^N r_{mn} \cos(m\theta - n\phi)
\end{aligned}$$

where  $\phi$  is the toroidal angle and  $\theta$  is the poloidal angle. Seven of these coefficients are allowed to vary during the course of the optimization. They are:  $R_{0N_p}$ ,  $Z_{0N_p}$ ,  $R_{10}$ ,  $R_{1N_p}$ ,  $r_{30}$ ,  $r_{0N_p}$ , and  $r_{3N_p}$ , with  $r_{00} = 1 - R_{10}$  to keep the aspect ratio fixed during the iterations. The remainder of the harmonics, 20-30 total, are zero at the boundary and are chosen to provide numerical accuracy. The number of field periods,  $N_p$ , also remains fixed during the course of the optimization. Finally, the varying coefficients are scaled to order 1 before being used in the numerical process to insure numerical stability.

The optimization process is implemented by forming a loop composed of a multi-dimensional nonlinear optimization routine (MNOR), a three dimensional inverse plasma equilibrium solver [4], a routine for assessing Mercier stability [5], an analysis of plasma transport, and finally, a function that combines this information into a single numerical value for use by the MNOR. A typical iteration proceeds by the MNOR package providing the plasma equilibrium solver with the Fourier coefficients of a trial boundary. The equilibrium solver then computes the plasma profiles of iota, flux, magnetic well, etc. for use by the Mercier and transport modules. These modules return figures of merit and the computed criteria are combined in a function of the form,

$$\begin{aligned}
F &= x_a \text{TANH}(\gamma x_a) + x_e \text{TANH}(\gamma x_e) + \alpha L_M - \delta L_B; \\
x_a &= (\tau_a - \tau_{a0})/\tau_{a0}, \quad x_e = (\tau_e - \tau_{e0})/\tau_{e0}
\end{aligned}$$

where  $\tau_a$  and  $\tau_e$  are the computed rotational transform at the magnetic axis and plasma edge, respectively, and  $\tau_{a0}$  and  $\tau_{e0}$  are the corresponding desired transform values;  $L_M$  is the percentage of the plasma that is Mercier unstable,  $L_B$  is the percentage width of the last closed  $B_{\min}$  contour, and  $\alpha$ ,  $\gamma$ ,  $\delta$  are constants chosen to steer the optimization in the desired direction. The  $\text{TANH}$  function prevents the optimization function from increasing too rapidly when the iota values differ greatly while providing a sum-of-squares behavior near the optimum. Experience has shown that this form provides the most reliable results. The constants  $\delta$  and  $\alpha$  fall in the ranges,  $1 < \delta < 10$  and  $3 < \alpha < 30$  with  $\gamma \sim 10.0$ . Unfortunately these values can only be determined empirically and require many computer runs to estimate the best values.

The MNOR is a quasi-newton method using finite differences; it is the E04JBF subroutine contained in the NAG library [6,7]. Since subroutines of this nature can find only local minima, the path from large aspect ratio devices to small ones is

best located by an incremental process. In this work an approximate representation of the current ATF device was used as the starting point and the aspect ratio and number of field periods were reduced by small steps until the goal of  $A = 4$  was reached. At each converged step small perturbations were made in the boundary to examine the local parameter space. This process does not require that all the optimization modules be used; one may wish to focus on only a couple of the criteria to conserve effort until the desired aspect ratio/field period region is reached.

The results of this process at  $\langle\beta\rangle = 0$  are shown in Table I. In these cases the optimization included only  $\tau_a(\tau_{ao} = 0.35)$ ,  $\tau_e(\tau_{eo} = 1.0)$ ,  $L_B$  and the magnetic well; rather than employ the complete Mercier criterion, the entries in Table I were only required to have a magnetic well with a finite width. Note that by keeping the ratio of field periods to aspect ratio in the range of 1.5-1.6 the iota and  $L_B$  values are preserved as the aspect ratio is reduced.

TABLE I

Aspect Ratio	Field Period	$\tau$ Axis	$\tau$ Edge	$L_B$	Magnetic Well
7.8 (8)	12	0.42	1.0	0.61	2%
5.13 (5.33)	8	0.36	0.95	0.59	2.3%
3.9 (4.0)	6	0.36	0.94	0.58	3.2%
3.3 (3.33)	5	0.35	0.92	0.57	3.5%
3.9 (4.0)	6	0.33	0.98	0.87	1.9%

The aspect ratio is defined as  $A = \pi R_a \sqrt{2R_a/V}$ , where  $V$  is the plasma volume and  $R_a$  is the radius of the plasma center which is approximately the edge value of the  $R_{00}$  harmonic. For the cases shown in Table I, the aspect ratio may be very closely approximated as the edge value of the  $R_{00}$  harmonic because of the selected normalization. This value is shown in parentheses in Table I.

The last case in Table I was obtained by examining the parameters locally around the previous 6 field period case. Note that a large improvement in  $L_B$  came at the expense of the well depth. This compromise also appears in calculations that use the Mercier stability criterion instead of finite well width and underlines the conflict between stability and transport.

Currently the optimization can be performed only at a fixed plasma pressure. Fortunately, our calculations show that if the plasma is stable at a given average beta,  $\langle\beta\rangle$ , it will also be stable at lower  $\langle\beta\rangle$  with the same pressure profile. Selection of the plasma pressure profile is somewhat difficult, but a modestly peaked profile with weak edge gradients appears to give the most useful results. The present work uses a pressure profile of the form

$$p(\psi) = p_0(1 - \psi)^2(1 + \psi^2)$$

where  $\psi$  is the normalized toroidal flux and  $p_0$  can be adjusted to provide the necessary  $\langle \beta \rangle$ .

The results of an optimization on a  $N_p = 6$ ,  $A = 4$  device at  $\langle \beta \rangle = 5\%$  is shown in Figs. 1 and 2. The  $\langle \beta \rangle = 0$  fixed boundary result, obtained by using the optimized  $\langle \beta \rangle = 5\%$  boundary with  $p_0 \sim 0$ , is shown in Fig. 1. Starting at the

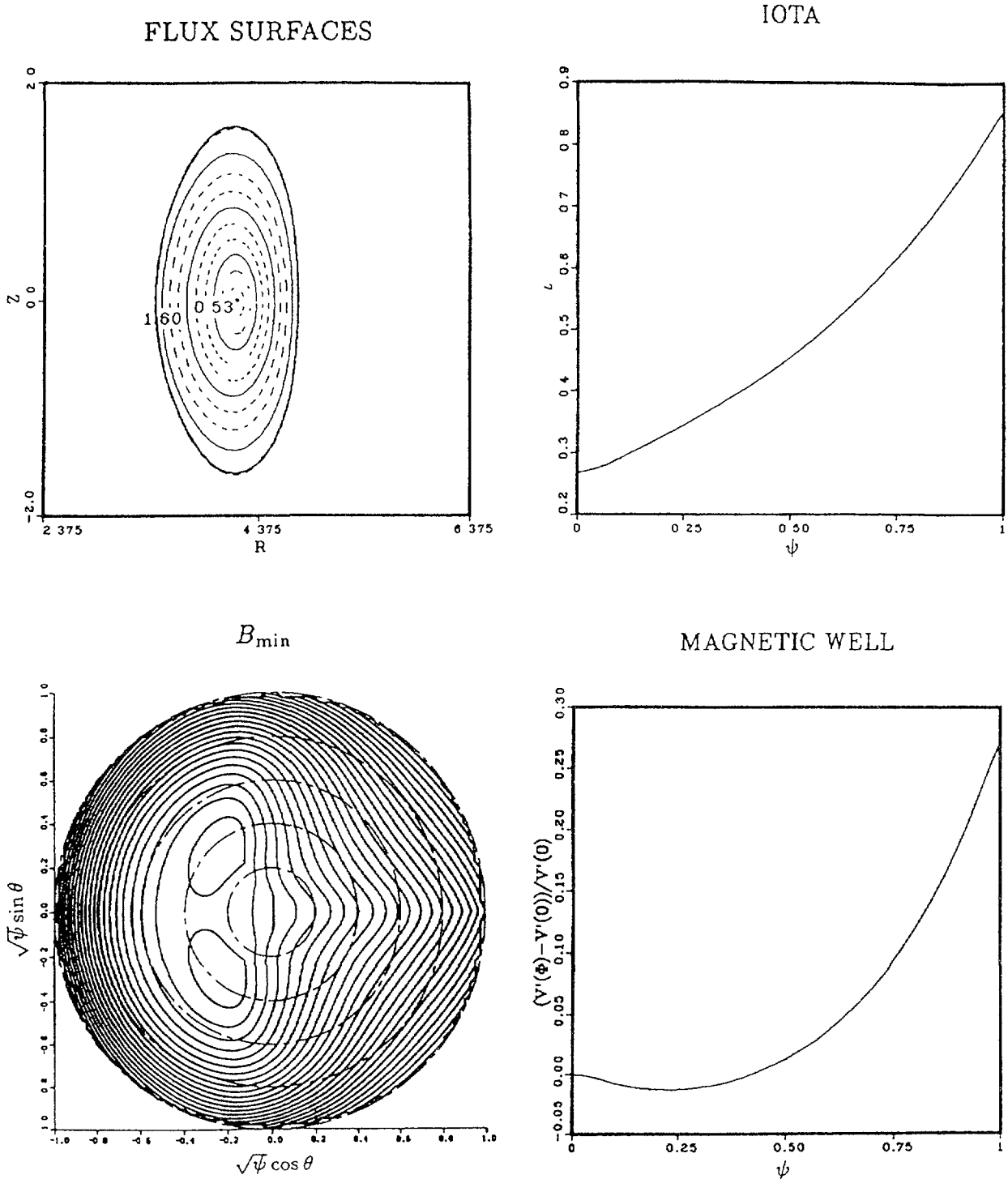
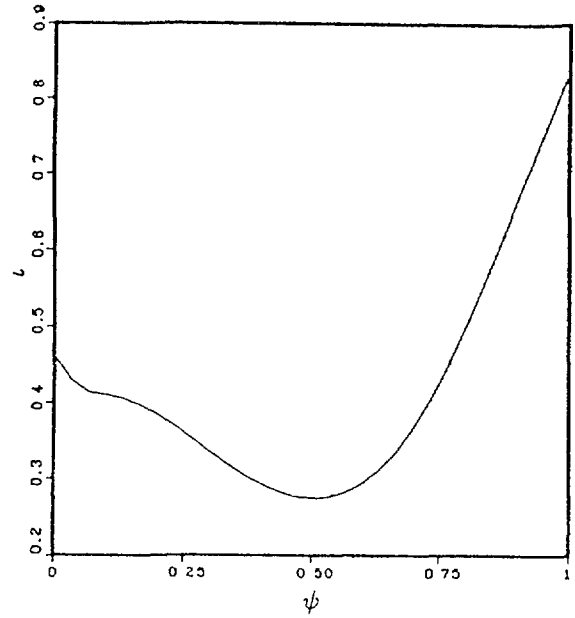
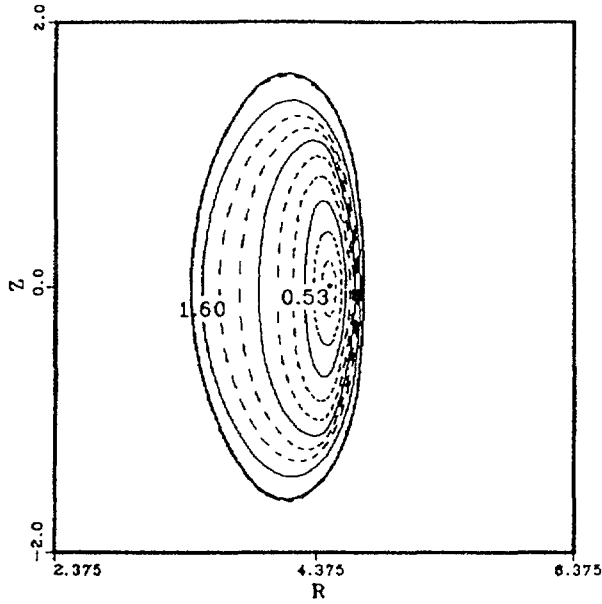


FIG. 1.

FLUX SURFACES

IOTA



$B_{\min}$

$D_M$

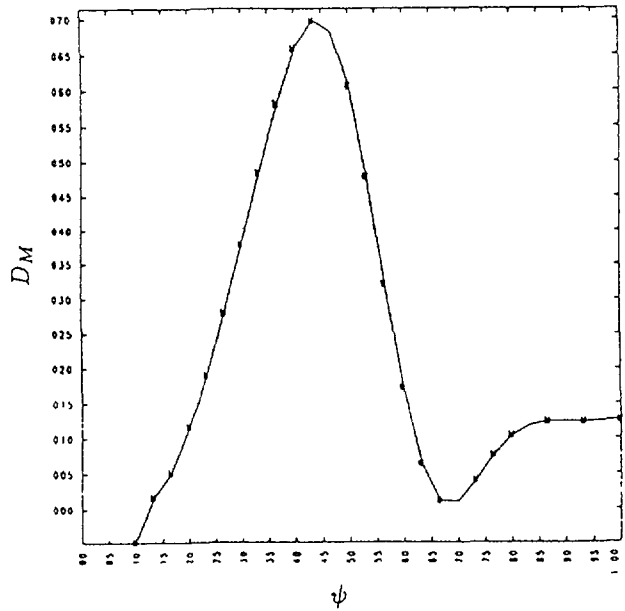
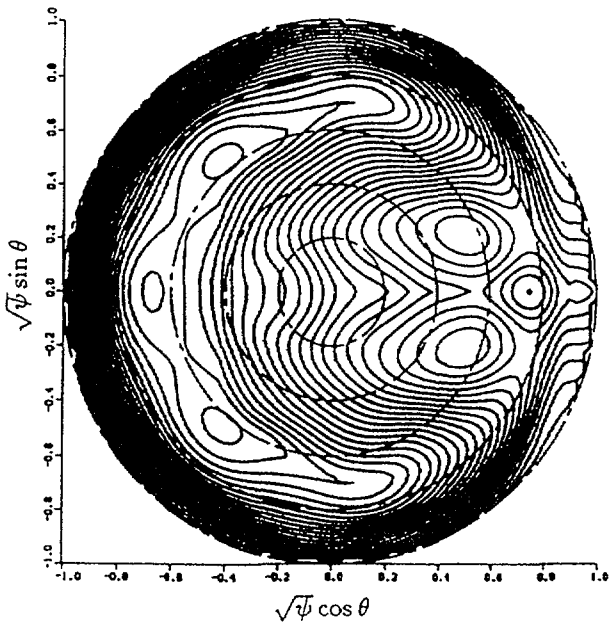


FIG. 2.

top left and moving clockwise, one has the flux surfaces at  $\phi = 0$ , the iota profile vs  $\psi$ , the magnetic well vs  $\psi$ , and the  $B_{\min}$  contours ( $L_B = 0.9$ ). The  $\langle \beta \rangle = 5\%$  case is shown in Fig. 2. Starting at the top left and moving clockwise, one has the flux surfaces at  $\phi = 0$  (note the shift), the iota profile vs  $\psi$ , the Mercier criterion vs  $\psi$ , and the  $B_{\min}$  contours ( $L_B = 0.8$ ). The minimum in the Mercier value takes place at the  $\tau = 1/3$  surface. The  $B_{\min}$  contours become increasingly shifted as  $\langle \beta \rangle$  increases, a factor that adversely affects transport.

We conclude that promising low aspect ratio stellarator designs may exist and that the described numerical process is a useful tool for locating them. Further work remains to be done to examine the parameter space and numerical sensitivity issues.

## REFERENCES

- [1] BAUER, F., BETANCOURT, O., GARABEDIAN, P. A., "Magnetohydrodynamic Equilibrium and Stability of Stellarators," Springer-Verlag, New York (1984).
- [2] HEDRICK, C. L., CARY, J. R., TOLLIVER, J. S., "Adiabatic and Full Guiding Center Motion in 3-D Toroidal Systems," to be published.
- [3] HIRSHMAN, S. P., WEITZNER, H., Phys. Fluids **28**, 1207 (1985).
- [4] HIRSHMAN, S. P., WHITSON, J. C., Phys. Fluids **26**, 3553 (1983).
- [5] DOMINGUEZ, N., private communication.
- [6] Numerical Algorithms Group, Inc., Downers Grove, Illinois 60515-1263.
- [7] GILL, P. E., MURRAY, W., Journal of the Institute of Mathematics and Its Applications, **9** 91 (1972).

## COIL CONFIGURATIONS FOR LOW ASPECT RATIO STELLARATORS\*

J.A. ROME, R.N. MORRIS,  
S.P. HIRSHMAN, R.H. FOWLER  
Oak Ridge National Laboratory,  
Oak Ridge, Tennessee  
United States of America

P. MERKEL  
Max-Planck-Institut für Plasmaphysik,  
Garching, Federal Republic of Germany

### Abstract

Using the NESCOIL code [1], it is possible to find a surface current distribution which can create a given last closed flux surface. Thus, almost any stellarator configuration can be created with either helical or modular currents. In particular, we have succeeded in finding current distributions which generate the optimized ATF-II configuration described in Hirshman's paper [2].

As the aspect ratio of the configuration is decreased, or the plasma-to-coil distance is increased, the harmonic content of the surface currents is increased. This makes it a challenge to cut the distribution into either discrete helical or modular coils which are attractive from an engineering point of view. Several approaches to this problem are discussed. There have been some hints of promising configurations, but to date, none of them are satisfactory.

---

### INTRODUCTION:

In the past three or four years, it has been realized that the coil configuration for a particular stellarator is not immutable; in principle, there exist a large number of different current distributions that can make a given set of flux surfaces. Moreover, a stellarator can be designed to optimize physical properties (equilibrium, stability and transport) without reference to the coil set.

These facts are a consequence of the fact that for a currentless stellarator, there exists a scalar potential ( $\mathbf{B} = \nabla\chi$ ) that satisfies Laplace's equation. Thus, if one specifies the shape of the last closed flux surface on which the normal component of  $\mathbf{B}$  is zero, the solution is unique inside this surface. Both the Garching and Oak Ridge groups (see papers this conference) have been using this approach to find the shape of the outer flux surface that yields optimal goodness criteria. The Fourier harmonics of these surfaces are then given to the coil designer who must determine a set of coils that creates the required magnetic fields.

The tool used to find these coils is the NESCOIL code. To use NESCOIL, the cylindrical coordinates  $R$  and  $Z$  of the toroidal current surface must be expressed as double Fourier

---

\* Research sponsored by the Office of Fusion Energy, US Department of Energy, under contract DE-AC05-84OR21400 with Martin Marietta Energy Systems, Inc.

series in  $\theta$  and  $\phi$ . This surface must enclose the outer flux surface, and have the same periodicity and symmetry properties as the outer flux surface. The shape of this surface can itself be determined by a computerized search which can optimize some of the resulting coil properties (such as kinkiness, access, etc.).

NESCOIL solves the Neumann problem for the current stream function on the surface. For a fixed number of harmonics, and in the presence of any fields due to external coils, the amplitude of each harmonic is varied to minimize the normal component of  $\mathbf{B}$  on the outer flux surface. The equipotentials of the current stream function corresponds to the surface current, and the current density is determined by the spacing between the equipotentials. In general, the currents can be closed either poloidally (modular coils) or helically.

### GOODNESS CRITERIA:

For the purposes of this paper, we assume a major radius of 1.0 m. A real device such as ATF-II might be scaled up by a factor of two, and a reactor might be scaled up by a factor of 6 or so. The driving dimension in these designs is the plasma-to-coil spacing which must be at least 15cm (scaled up by the appropriate factors). Since this is a minimum criteria, we have chosen to make the plasma-to-coil spacing uniform at all places on the torus. This is easiest to do by increasing the  $n=0, m=1$  harmonic of the outer flux surface by the plasma-to-coil spacing. Here,  $n$  is the toroidal harmonic number, and  $m$  is the poloidal harmonic number. The surface is given by

$$R = \sum_{n,m} R_{nm} \cos(n\phi + m\theta)$$

$$Z = \sum_{n,m} Z_{nm} \sin(n\phi + m\theta)$$

We also limit our scope to the problem of trying to synthesize coils for the OT-7 M4 configuration which has an aspect ratio of 4. This example was optimized at  $\beta=4\%$  using the free-boundary VMEC code. Although NESCOIL assumes that the equilibrium is current-free, it turns out that if we find the coils using the finite  $\beta$  outer flux surface, the configuration that results has good properties at zero  $\beta$  and at finite  $\beta$  (with the addition of some vertical field).

Then, our goal is to determine a set of coils which do not have extreme kinks and which allow access to the plasma for experimental purposes.

### RESULTS:

OT7 can be synthesized with currents at 15 cm using either modular or helical coils (Figs. 1-3).

In either case, the underlying helical nature of the configuration can be seen in the concentrated current density regions. To improve the configuration, we would like to pull out one or two discrete coils, and then hope that the high current density regions disappear from the potential plots. The remaining currents can be synthesized on a surface that is either inside or outside the discrete coils.

From Fig. 2, we can see that there are two fairly straight coils. We removed them at a 15 cm spacing, and synthesized the remaining currents as modular coils at 20 cm. This did not yield a noticeable improvement in the configuration.

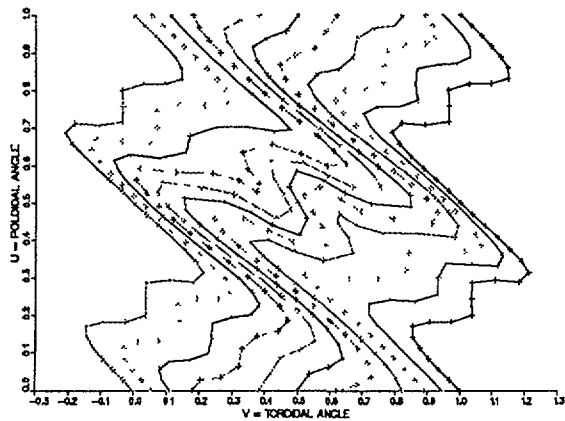


Fig. 1: Synthesis using modular coils at 15 cm

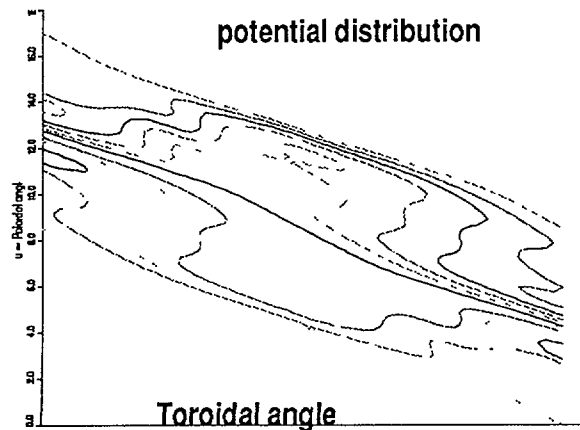


Fig. 2: Synthesis using helical coils at 15 cm



Figure 3: Top view and side view of a set of base case modular coils that can produce the OT7-M4 configuration. Only the front coils are shown in the side view. These coils are clearly too complicated, are too kinky, and offer little access to the plasma, and are only used to generate the external fields for the free-boundary VMEC code.

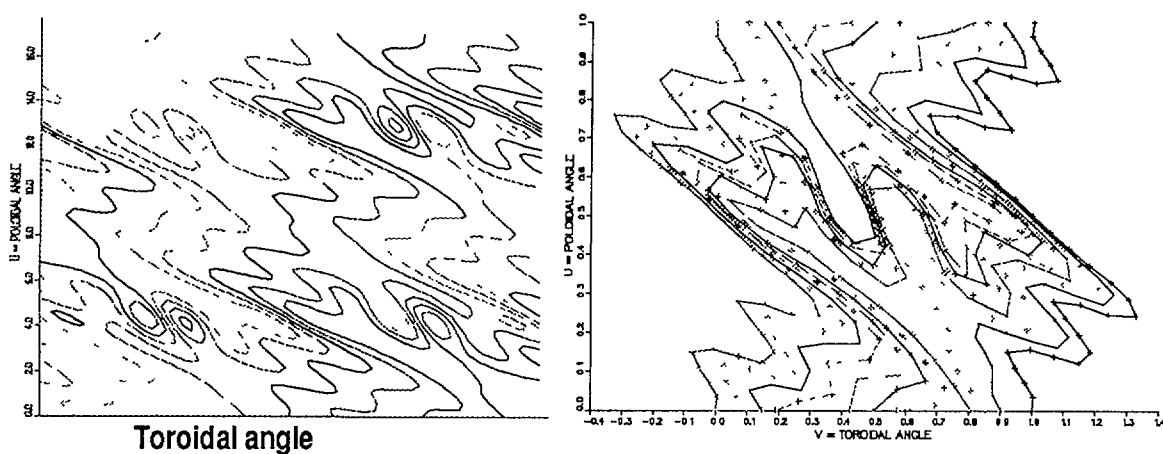


Fig. 4: The potential (left) and resulting modular coils when two helical coils are removed at 15 cm, and the remaining fields are synthesized using modular coils at 20 cm. The potential plot covers two field periods in each direction. We required that there be 10 modular coils per field period, which may be excessive.

More examination of this figure reveals that the current density along these helices varies considerably. In fact, at any given toroidal cross-section, there is only one region of high current density, like  $l=1$ , but the pitch is still that of an  $l=2$  system. We call this an  $l=1.5$  system. A model for these currents made with continuous coils is shown below:

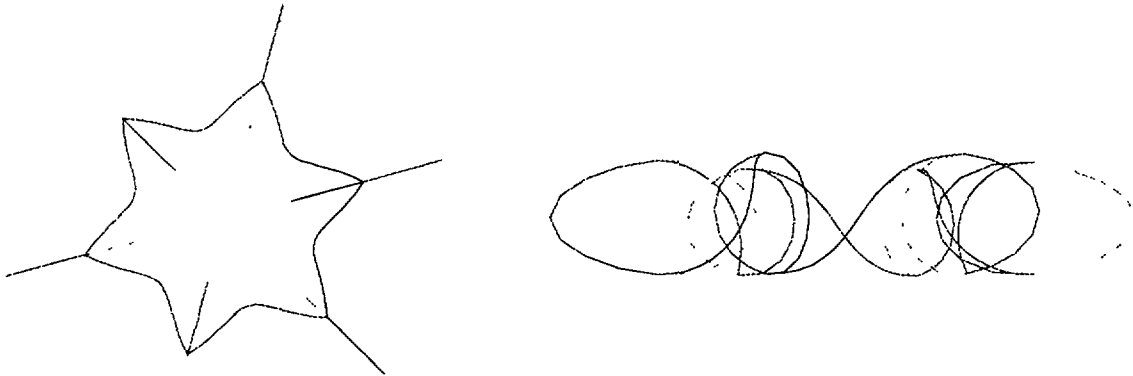


Fig. 5: Top view and side view of the  $l=1.5$  coils. The two helices merge on the inside half of the torus.

Removal of these coils at 20 cm, and synthesis of the remainder of the field using helical coils at 15 cm yielded the following results:

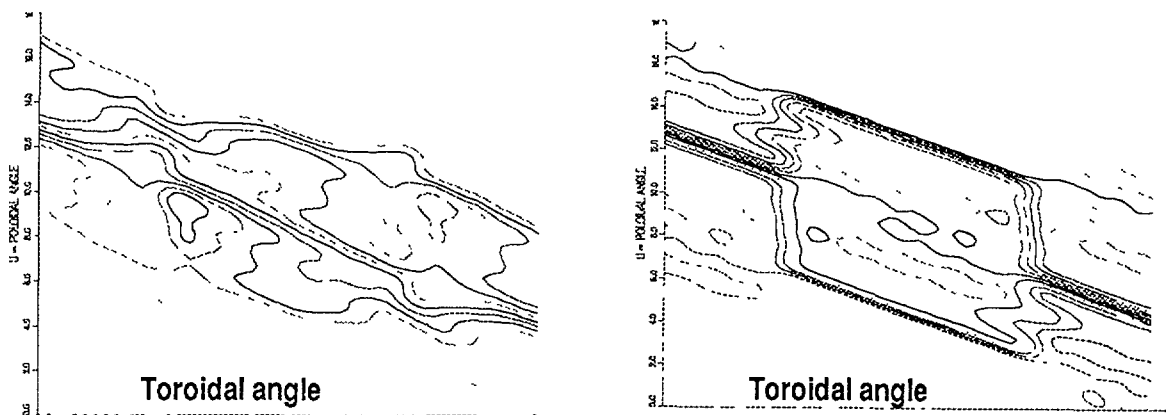


Fig. 6: Removal of the  $l=1.5$  coils does change the current distribution (left). If they are added instead (right), the  $l=1.5$  coil current is clearly visible. However, in this case, the result is not much simpler than the original case in Fig. 2.

Finally, we removed one modular coil (at 15 cm) in each field period and synthesized the remaining field from modular coils at 20 cm.

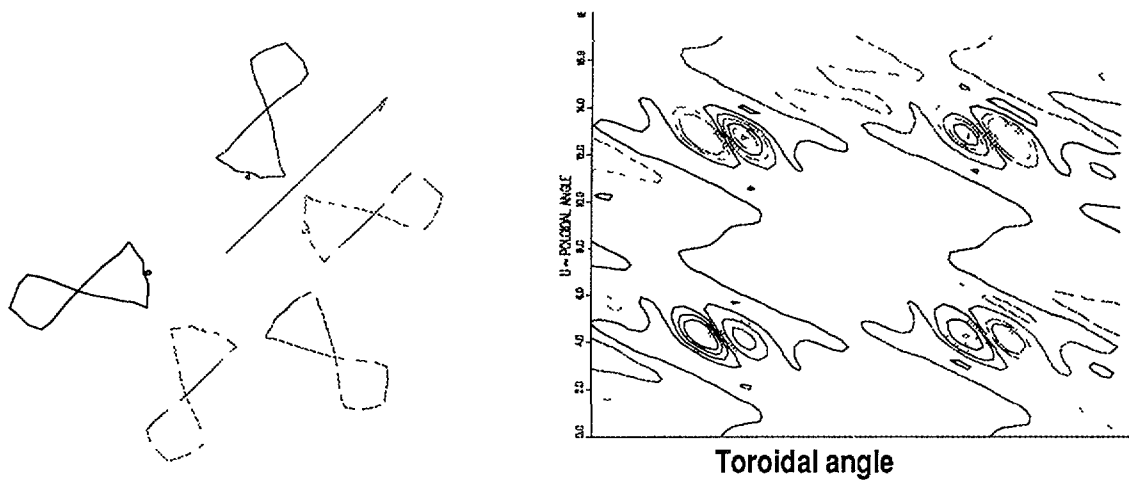


Fig. 7: Top view of the modular coils removed at 15 cm. The arrow is the x-axis. The resulting potential has reduced current densities everywhere except in the whorls which occur on the midplane on the inside of the torus. The modular coils can probably be simplified without losing the configuration.

## CONCLUSIONS:

This is still very much work in progress. The codes seem to work properly, and coils can be removed or added to the configuration. If the coil winding surface is moved out much beyond 20 cm, the coils become very kinky, and whorls (regions of closed current) appear. The high frequency spatial oscillations of the currents are probably artifices of the Fourier representation since the fields due to them decay rapidly away from the coils.

Removal of discrete or modular coils does not work as successfully as one might like. If the discrete coil current cancels a piece of the continuous surface current, the cancelled current does not disappear from the resulting current distribution. This may be due to the high Fourier harmonics introduced by the discrete coil.

It does seem possible (Fig. 7) to reduce the current density of the current distribution. The question remains whether a lower current density can be modeled using a few discrete coils, or whether many coils of lower current density are required.

The next step in this project is to create data sets for each of the current filaments (in the cases with whorls) and see how many filaments are required to reproduce the flux surfaces. Then we can smooth the contours of these coils and eliminate the high frequency spatial oscillations. Finally, Cary-Hanson techniques can be used to rebuild any lost flux surfaces.

## REFERENCES

- [1] P. Merkel, *Nuclear Fusion* **27** (1987) 867.
- [2] S.P. Hirshman et al, *Low Aspect Ratio Optimization Studies for ATF-II*, this conference.

# HIGH-FIELD, HIGH-CURRENT-DENSITY, STABLE SUPERCONDUCTING MAGNETS FOR FUSION MACHINES\*

J.W. LUE, L. DRESNER, M.S. LUBELL  
Oak Ridge National Laboratory,  
Oak Ridge, Tennessee,  
United States of America

## Abstract

Designs for large fusion machines require high-performance superconducting magnets to reduce cost or increase machine performance. By employing force-flow cooling, cable-in-conduit conductor configuration, and NbTi superconductor, it is now possible to design superconducting magnets that operate at high fields (8–12 T) with high current densities (5–15 kA/cm<sup>2</sup> over the winding pack) in a stable manner. High current density leads to smaller, lighter, and thus less expensive coils. The force-flow cooling provides confined helium, full conductor insulation, and a rigid winding pack for better load distribution. The cable-in-conduit conductor configuration ensures a high stability margin for the magnet. The NbTi superconductor has reached a good engineering material standard. Its strain-insensitive critical parameters are particularly suitable for complex coil windings of a stellarator machine. The optimization procedure for such a conductor design, developed over the past decade, is summarized here. If desired, a magnet built on the principles outlined in this paper can be extended to a field higher than the design value without degrading its stability by simply lowering the operating temperature below 4.2 K.

---

## INTRODUCTION

High-performance superconducting magnets that run at high current densities and produce high fields are in constant demand in fusion machine design as well as other physics applications. The large next-generation stellarators under design—the Large Helical Device (LHD) [1], Wendelstein VII-X (W VII-X) [2], and the Advanced Toroidal Facility (ATF-II) [3]—all call for a magnetic field on plasma axis of 3–4 T, or a maximum field on the winding of 6–8 T. Current density requirements for both LHD and W VII-X have increased from 2.5 kA/cm<sup>2</sup> to 4 kA/cm<sup>2</sup> over the winding pack in their latest design changes [1,2]. This is because higher current density will lead to a smaller, lighter winding pack and smaller machine. Thus, a less expensive machine or a better performance machine can be realized at a given cost.

The superconducting magnet development efforts over the past decade have led to a conclusion that force-flow cooling magnets based on cable-in-conduit NbTi superconductor will best fulfill these demands. A force-flow-cooled conductor can be fully insulated to provide high-voltage integrity, and the winding can be potted to form a rigid structure. The cable-in-conduit conductor configuration further provides a large cooling surface for the superconducting strands and ensures good stability margin for the coil. NbTi superconductor has proven to be a good engineering material, suitable for large fusion magnets.

---

\* Research sponsored by the Office of Fusion Energy, US Department of Energy, under contract DE-AC05-84OR21400 with Martin Marietta Energy Systems, Inc.

## FORCE-FLOW COOLING

A force-flow-cooled magnet is built with conductor that has the cooling channel embedded within it or on the perimeter of the winding. Supercritical or two-phase helium is forced through the channel for direct or indirect cooling. The conductor outer surface is not wetted with helium for heat transfer. It can be fully wrapped with multiple layers of insulation. Thus, high-voltage integrity (10 kV or more) can be maintained.

The winding of a force-cooled magnet is usually potted in an epoxy compound suitable for cryogenic service. Thus, it forms a rigid structure and limits conductor motion (excessive conductor motion can generate enough heat to quench the coil). The potting also helps to distribute the electromagnetic load throughout the winding and transmit it to an external case. This helps to prevent local stress buildup on the conductor. Force and stress calculations can be performed for potted coils with higher reliability than for pool-boiling coils.

Since the helium is not boiling and is well confined in a force-cooled magnet, its temperature can easily be changed by either the refrigerator or an outside heat exchanger. The heat transfer coefficient stays essentially the same. Thus, a magnet can be operated at higher current and higher field without losing its stability margin by lowering the operating temperature below 4.2 K, provided enough structure has been built into the magnet. Or it can be operated at higher temperatures to save on refrigeration load. This is particularly true with cable-in-conduit conductors, as discussed later. Another advantage that may be worth mentioning is that, for a force-cooled magnet, a relatively small-scale segment test may suffice to extrapolate to a full-size magnet. This makes the R&D program for a large system less expensive and faster to carry out.

## CABLE-IN-CONDUIT CONDUCTOR CONFIGURATION

In a superconducting magnet, it is generally believed that conductor motion under electromagnetic forces can generate enough local heating to drive the conductor normal. If the heat is not transferred away by the coolant, the normal zone will grow and the whole magnet will quench. As mentioned above, the potting of a force-cooled magnet can minimize the motion-induced heat source. But the conventional force-cooled conductors do not provide a heat barrier to the superconductor and do not have large enough cooled surfaces. Thus, they do not have good stability margins as a whole.

An internally cooled cable-in-conduit conductor configuration was proposed, first by Hoenig [4] of the Massachusetts Institute of Technology (MIT), to increase the stability of a force-cooled magnet. The superconductor is contained in a braided cable of fine strands enclosed in a protective (steel) conduit. Helium, usually supercritical, is forced through the interstices of the cable. The fine division of the conductor into cable form provides large surfaces wetted by the helium. The consequent excellent heat transfer allows a cable-in-conduit conductor to operate stably at quite high current densities.

### Engineering Equations for Optimization

Experiments performed on small-scale cable-in-conduit conductors have shown that, because of the tight confinement of helium in the conduit, heat from the conductor induces transient local flow of the helium. This local flow greatly enhances heat transfer from the conductor to the helium. The combination of enhanced heat transfer and the transient conductive heat transfer causes the multiple stability phenomena observed in some cable-in-conduit conductors [5]. The important engineering outcome of these investigations is that there is a limiting current, below which the stability margin of the conductor is very high and is limited only by the available helium enthalpy. The limiting current density over the cable space is found to be [6]

$$J_{\text{lim}} = f(F, F_{co}) [(T_c - T_b) \rho^{-1}]^{1/2} d^{-1} (l^2/\tau)^{1/15} \quad (1)$$

where  $f(F, F_{co})$  is a function of the fraction of conductor in the cable space,  $F_{co}$ , and the fraction of copper in the cable,  $F$ ,  $T_c$  is the critical temperature of the superconductor,  $T_b$  is the temperature of the helium (bath),  $\rho$  is the copper resistivity,  $d$  is the diameter of the cable strand, and  $l$  and  $\tau$  are the local heating length and duration. Because of the very small power (1/15), Eq. (1) is insensitive to the uncertain factor  $l^2/\tau$ .

In addition to stability, protection of a coil when it quenches should be carefully considered. Since a force-cooled magnet can have very good voltage withstand capability, it can be dumped rapidly and prevented from having damaging hot spots. However, the hydraulic length can still be long enough to produce very high helium pressures. The worst case is when the conductor of a whole hydraulic length goes normal all at once. An equation to estimate the ensuing maximum quench pressure,  $P_{\text{max}}$ , has also been derived and tested experimentally [7]. It has the form

$$P_{\text{max}} = g(F, F_{co}) (\rho^2 J_{cs}^4 l^3 d^{-1})^{0.36} \quad (2)$$

where  $g(F, F_{co})$  is another function of  $F$  and  $F_{co}$ ,  $J_{cs}$  is the current density over the cable space, and  $l$  is now the hydraulic length.

Based on Eqs. (1) and (2) and the available helium enthalpy, one can calculate the stability margin,  $\Delta H$ , and maximum quench pressure for different values of  $F$  and  $F_{co}$ . The results can then be plotted as contours of constant  $\Delta H$  and constant  $P_{\text{max}}$  in the  $(F_{co}, F)$  plane. As an example, a NbTi conductor operating at 8 T and 4.0 K, with a current density over the cable space of 20 kA/cm<sup>2</sup>, would have the contours shown in Fig. 1. In this figure, the upper boundary of the contours is cut off by  $i = 1$ , when the operating current would equal the critical current of the conductor. The left boundary is the limiting current density given by Eq. (1). The right boundary is a safe engineering choice of limiting  $P_{\text{max}}$  to 500 atm. From this plot, one finds that for the given operating conditions a conductor with  $F_{co} = 0.8$  (20% void in the cable space) and  $F = 0.62$  (Cu/SC = 1.6) would be an optimum choice. Such a conductor operates at 49% of its critical current and has a stability margin of about 100 mJ/cm<sup>3</sup>.

### Variations

During the studies of cable-in-conduit conductor that led to these scaling equations, it was also found that forced helium flow would push the limiting current to a higher value [6]. However, if a conductor is already in the high-stability regime, the flow has no effect on stability. Thus, helium flow is needed only for steady-state heat removal. In a large magnet with long hydraulic length, the plain cable-in-conduit conductor may present too big a pressure drop to have enough helium flow through the conductor. It is prudent to provide additional cooling paths for a big cable-in-conduit magnet. Figure 2 shows two possible variations to the plain cable-in-conduit configuration. The tube in the conduit variation adds a central cooling tube in the cable space. This is a straightforward modification of the plain configuration. The cable-in-double conduit variation adds another conduit inside the steel conduit. The inner conduit would be more or less round and create additional, larger cooling channels between the two conduits. The inner conduit can be made of a material, such as copper, that would aid in the quench protection of the coil. It would also serve as an additional thermal barrier for the friction heating generated between the conductors and as a magnetic barrier for field perturbations.

The helium in the additional cooling channel and the (possible) copper in the additional conduit (or tube) would probably not aid in the stability margin of the conductor. Thus, the

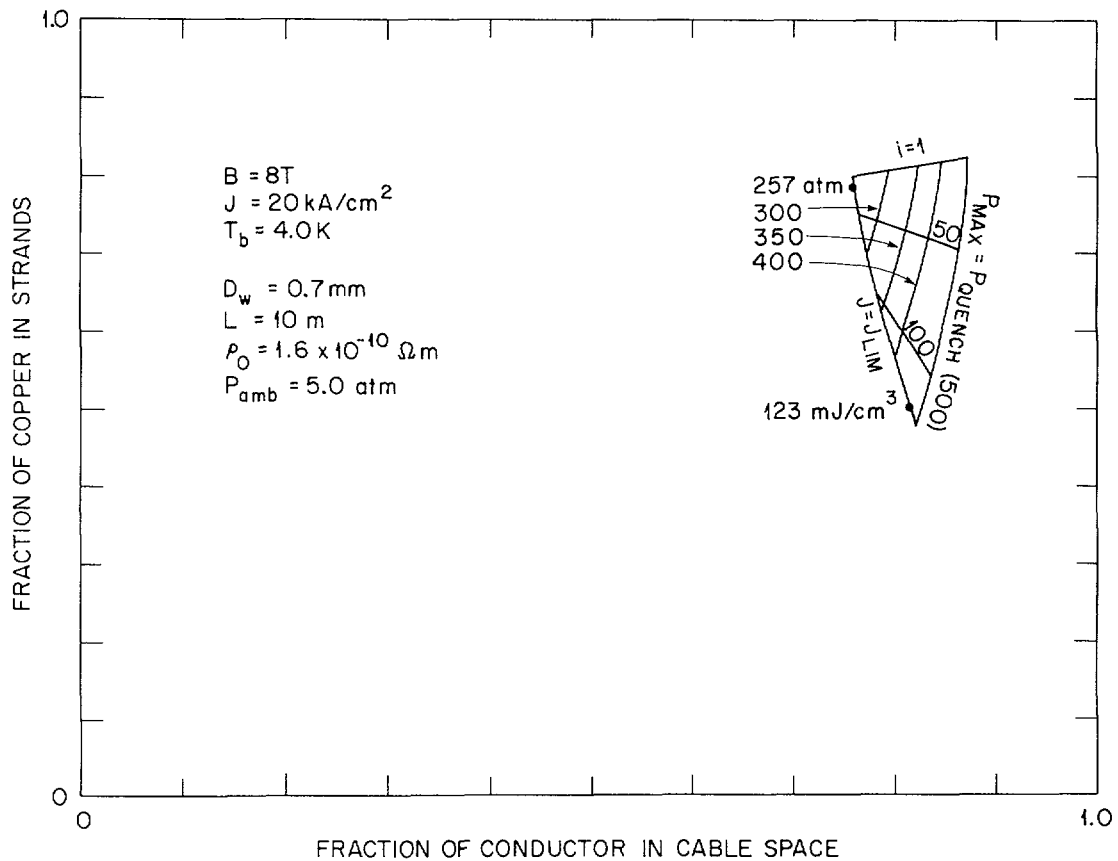


FIG. 1. Contour plots of stability margins and maximum quench pressures for a NbTi cable-in-conduit conductor operating at 8 T and 4.0 K with  $J_w = 20 \text{ kA/cm}^2$ .

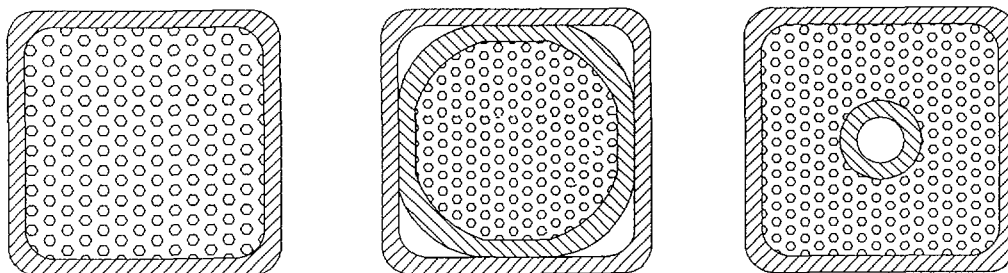


FIG. 2. Possible variations from the plain cable-in-conduit conductor configuration.

current density used in optimization studies such as those shown in Fig. 1 should refer to that over the cable space only. The current density over the conductor would be lowered by adding the conduits and any additional cooling channel cross sections. The current density over the winding would further be reduced by adding insulation thickness and packing factor. Depending on the conductor size, configuration, shape, and voltage withstand requirement, the current density over the winding could be 35–65% of that over the cable space.

## NbTi SUPERCONDUCTOR

The field requirement of 8 T or less on the winding of the next-generation stellarator machine is well within the capability of NbTi superconductor. This material has reached an engineering standard such that all coils built with NbTi in the Large Coil Task operated to 9 T [8]. This superconductor is also preferable for the complex and non-planar helical or modular winding of a stellarator. The strain-sensitive Nb<sub>3</sub>Sn superconductor is more liable to damage in such a complex winding.

Even if a field as high as 10–12 T is required, NbTi can still be used by lowering the helium temperature. Optimization studies similar to those discussed in Eqs. (1) and (2) can also be done with superfluid helium [9]. The limiting current density is replaced by a Kapitza limit. Contour plots of stability margin and maximum pressure for a NbTi cable-in-conduit conductor operating at 10 T and 1.8 K with current density of 30 kA/cm<sup>2</sup> are shown in Fig. 3. It is clear from such a plot that higher stability margin, higher field, or higher current density can be achieved with 1.8 K superfluid helium.

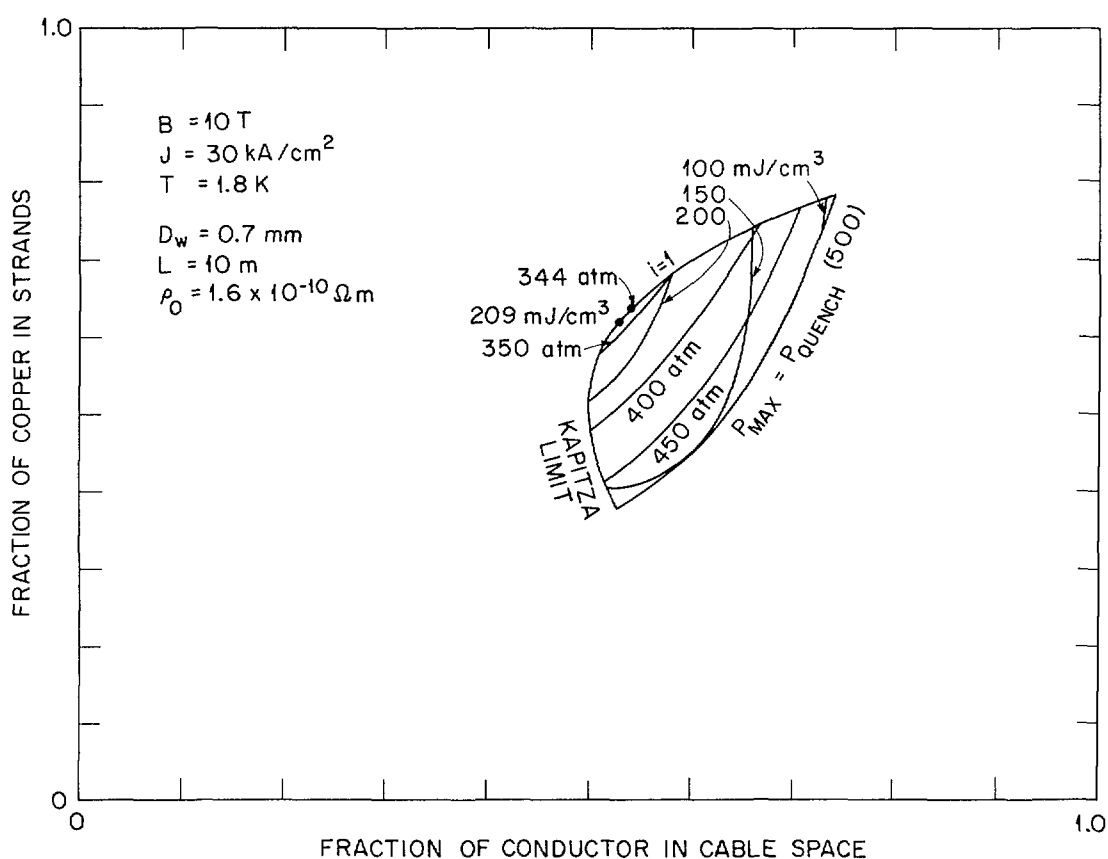


FIG. 3. Contour plots of stability margins and maximum quench pressures for a NbTi cable-in-conduit conductor operating in 1.8 K superfluid helium at 10 T with  $J_c = 30 \text{ kA/cm}^2$ .

## CONCLUSION

On the basis of superconducting magnet development efforts over the past decade, it can be shown that by employing force-flow cooling, cable-in-conduit conductor configuration, and NbTi superconductor, a superconducting magnet system can be built to operate at high fields (8–12 T) and high current densities (5–15 kA/cm<sup>2</sup> over the winding pack) in a stable manner. It would thus lead to a less expensive and higher performance next-generation stellarator machine.

It should, however, be pointed out that the database for such coils is still very sparse. A NbTi cable-in-conduit coil [10] was built and tested at Oak Ridge National Laboratory (ORNL) to 7.7 T at 4.2 K and 8.1 T at 3.9 K. It never quenched spontaneously, although the stability margin was measured to be less than 50 mJ/cm<sup>3</sup> above 7 T. Some Nb<sub>3</sub>Sn pancakes were built and tested to 12 T by Hoenig of MIT [11]. The largest cable-in-conduit coil built to date is the Nb<sub>3</sub>Sn coil built by Westinghouse for the Large Coil Task. The test results showed that it performed well and in good agreement with the small-scale experiments as far as the cable-in-conduit stability properties were concerned.

Finally, in addition to the need for a larger database, a few remaining unresolved issues should be addressed. The cable form of this type of conductor is subjected to strand motion and severe stress at the point of contact under electromagnetic load. It is not clear how much cyclic loading it could take before fatigue would start to degrade the conductor performance. Normal-zone propagation in a cable-in-conduit conductor has not been investigated carefully, and its behavior under different operating conditions is not clear. Systematic studies of this issue may shed light on what the real maximum quench pressure is and on whether the ensuing helium expulsion can be used for quench detection.

#### REFERENCES

- [1] IYOSHI, A., et al., Recent status of the Large Helical Device project," paper O4-1 presented at this workshop; MOTOJIMA, O., et al., Recent design considerations for the Large Helical Device," paper O4-2 presented at this workshop.
- [2] WOBIG, H., et al., The Wendelstein VII-X project, paper O4-4 presented at this workshop.
- [3] LYON, J.F., et al., Overview of the ATF program," paper O1-2 presented at this workshop.
- [4] HOENIG, M.O., MONTGOMERY, D.B., IEEE Trans. Magn. **MAG-11** (1975) 569.
- [5] LUE, J.W., MILLER, J.R., DRESNER, L., J. Appl. Phys. **51** (1980) 772.
- [6] DRESNER, L., IEEE Trans. Magn. **MAG-17** (1981) 753; LUE, J.W., MILLER, J.R., IEEE Trans. Magn. **MAG-17** (1981) 757.
- [7] MILLER, J.R., DRESNER, L., LUE, J.W., SHEN, S.S., Yeh, H.T., in Proc. 8th Int. Cryogenic Engineering Conf. (Genova, 1980) (RIZZUTO, C., Ed.), IPC Science and Technology Press, Surrey (1980) 321.
- [8] BEARD, D.S., KLOSE, W., SHIMAMOTO, S., VÉCSEY, G. (Eds), Fusion Eng. Des. **7** (1988) 1.
- [9] DRESNER, L., IEEE Trans. Magn. **MAG-23** (1987) 918.
- [10] MILLER, J.R., LUE, J.W., BROWN, R.L., KENNEY, W.J., IEEE Trans. Magn. **MAG-17** (1981) 2250.
- [11] HOENIG, M.O., STEEVES, M.M., IEEE Trans. Magn. **MAG-21** (1985) 1052.

## ALPHA-PARTICLE LOSSES IN COMPACT TORSATRON REACTORS\*

S.L. PAINTER<sup>1</sup>, J.F. LYON  
Fusion Energy Division,  
Oak Ridge National Laboratory,  
Oak Ridge, Tennessee,  
United States of America

### Abstract

*Loss of alpha particles in compact torsatron reactors is studied. For 6, 9, and 12 field period reactors, the direct loss is a relatively weak function of radius and energy and varies from  $\simeq 33\%$  for  $M = 6$  to  $\simeq 18\%$  for  $M = 12$ . Loss of alpha particles through scattering into the loss region is calculated using the Fokker-Plank equation for fast ions and found to contribute an additional alpha-particle energy loss of  $\simeq 15\%$ . The consequences of these relatively large losses for torsatron reactor design are discussed.*

*The relationship between the direct particle losses and the magnetic field structure is also studied. Orbit losses from a variety of stellarator configurations are calculated and a figure-of-merit that characterizes the orbit confinement of a magnetic configuration is deduced from these calculations. This figure-of-merit is used to show how the direct losses might be reduced at low aspect-ratio. Effects of finite beta on the direct particle losses are also addressed, and are shown to significantly increase the direct losses in some configurations.*

---

The compact torsatron sequence<sup>1</sup> is a family of low aspect-ratio  $l = 2$  torsatron configurations optimized for high-beta operation. These configurations make interesting reactor candidates because they have the capability for high-beta operation in the second stability regime, possess natural divertors, and have relatively open coil geometry for access to the plasma. Compact torsatrons are, however, optimized for MHD properties, not orbit confinement. A large fraction ( $\approx \frac{1}{3}$ ) of particles in these devices are trapped in the relatively large helical ripple in the magnetic field strength  $B$ . Toroidal effects at low aspect ratio cause orbits of these trapped particles to deviate significantly from flux surfaces leading to increased transport and in some cases to loss of the particles from the confinement region. Radial electric fields which develop to maintain quasineutrality of the plasma can reduce the deviation of the trapped particles from the flux surface through  $E \times B$  orbit rotation, but only for those particles which have kinetic energies less than their potential energies

---

\* Research sponsored by the Office of Fusion Energy, US Department of Energy, under contract DE-AC05-84OR21400 with Martin Marietta Energy Systems, Inc.

<sup>1</sup> Research performed to meet the requirements for the degree of PhD in nuclear engineering, University of Tennessee.

in the electric field. Energetic particles created by fusion reactions or through external plasma heating will not be affected by radial electric fields and many of these energetic particles may be lost from the plasma region. The confinement of energetic alpha particles in compact torsatron reactor configurations is addressed in this paper.

## CALCULATION OF ALPHA-PARTICLE LOSSES

The complicated magnetic field structure at low aspect ratio and the large particle energies of interest here make a numerical treatment of the particle loss fraction necessary. Direct particle losses were calculated by computing collisionless guiding center orbits<sup>2-5</sup> for a distribution of alpha particles launched randomly from a given flux surface. Details of the calculation can be found in reference 6. Each particle was followed until it left the plasma volume, made two poloidal revolutions, or exceeded a preset time cutoff (several hundred helical bounce periods). Magnetic coordinates<sup>2</sup> were used so that only the magnitude of the magnetic field and not its vector components was needed in the calculation. The magnetic field strength was represented by a double Fourier expansion in the poloidal ( $\theta$ ) and toroidal ( $\phi$ ) angles

$$B(\rho, \theta, \phi) = \sum B_{n,m}(\rho) \cos(n\phi - m\theta) \quad (1)$$

using 12 to 25 terms. Here the normalized radial coordinate ( $\rho$ ) is proportional to the square root of the toroidal flux.

## ALPHA-PARTICLE LOSSES FOR REFERENCE REACTORS

The fraction of alpha particles confined is shown versus the radial coordinate  $\rho$  in Fig. 1 for three minimum radius reference reactors<sup>7</sup>, ATR-1, ATR-2 and ATR-3. ATR-3 is the ATF<sup>8</sup> configuration scaled up to reactor size (aspect ratio 7.78, 11.1 meters major radius) while ATR-1 and ATR-2 are lower-aspect-ratio configurations (aspect ratio 3.87, 8.4 meters major radius for ATR-1; aspect ratio 4.66, major radius 10.5 meters for ATR-2). The magnetic field strength at the magnetic axis is 5 T in all cases and the particle energy is 3.5 MeV. The alpha-particle gyroradius is 2-3% of the plasma radius. The direct particle loss fraction is a relatively weak function of radius and is smaller for the higher aspect ratio ATR-3. The difference in the alpha-particle loss fraction is due to a smaller trapped particle fraction for ATR-3 and to better confinement of the trapped particles. ATR-3 confines 60% of the trapped particles that start at  $\rho = 0.25$  while ATR-1 and ATR-2 lose nearly 100%

of trapped particles starting from the same radius. This can be seen in Fig. 2 where the fraction of trapped particles lost is shown versus the pitch-angle parameter for ATR-3 and ATR-1. Deeply-trapped particles (those having small pitch angles) are confined in ATR-3 but not in ATR-1.

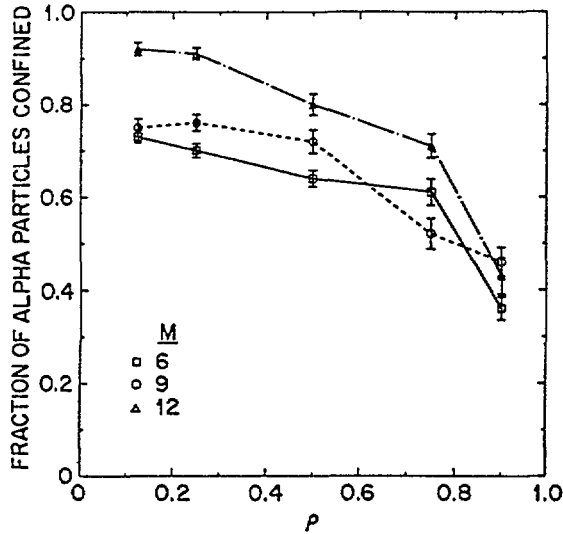


Fig. 1. Fraction of alpha particles confined versus radial coordinate for three reference reactors.

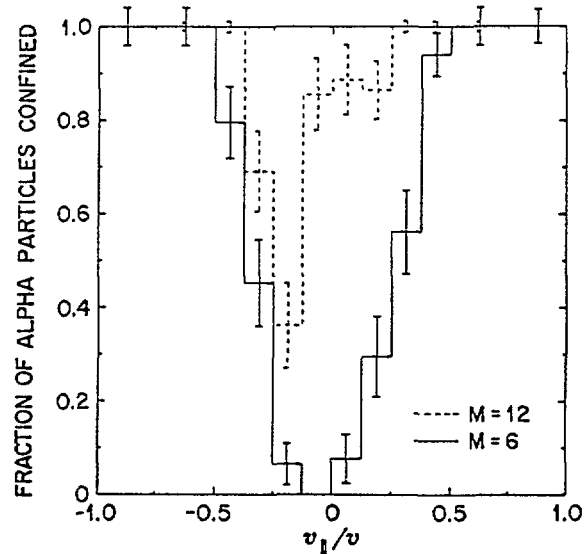


Fig. 2. Fraction of alpha particles lost versus pitch angle parameter for ATR-1 and ATR-3.

Alpha particles and energy are also lost when particles scatter into the direct loss region. Energetic alpha particles slow down and give up their energy to the background electrons without undergoing significant pitch-angle scattering until they reach energy  $E_{crit} \approx 32T_e$ . Below  $E_{crit}$  pitch-angle scattering on the background ions becomes important and most alpha particles find their way into the loss region before they can slow down enough to become confined by the radial electric field, thus preventing the accumulation of helium ash. The additional energy and particle losses due to alpha particles scattering into the loss region can be estimated from known solutions to the Fokker-Plank equation for fast ions<sup>9-11</sup>. The additional energy losses estimated this way are  $\approx 15\%$ , but  $\approx 80\%$  of the alpha particles are lost before thermalizing.

The total (direct plus indirect) loss of alpha heating power is 32 % for ATR-3 and 46 % for ATR-1 for alpha source profiles of the form  $(1 - \rho^2)^4$  which corresponds to parabolic density and temperature profiles. The main implications of this loss are to increase the plasma temperature at ignition and the external heating power required to reach ignition. Once ignition is reached, the alpha-particle loss region is beneficial; it aids in burn control by reducing the amount of heat available to the

thermal excursion, prevents thermalized alpha particles from accumulating in the plasma, and channels the particle energy into narrow helical stripes on the outside of the torus where it can be recovered efficiently.

## DEPENDENCE ON THE MAGNETIC FIELD STRUCTURE

In order to understand how the direct particle losses depend on the structure of the magnetic field and possibly how they might be reduced, the orbit confinement characteristics of a number of idealized stellarator configurations and a number of variant compact torsatron configurations were also investigated. In this section, the plasma radius is 2 m, the magnetic field strength on axis is 5 T, and the alpha-particle energy is 3.5 MeV. The idealized stellarator configurations have  $B$  of the form

$$B(\rho, \theta, \phi) = B_0[1 - \epsilon_{ta}\rho\cos(\theta) + \epsilon_{ha}\rho^2\cos(6\phi - 2\theta)] \quad (2)$$

were  $\epsilon_{ha}$  is the helical ripple at the plasma edge and  $\epsilon_{ta}$  is the inverse plasma aspect ratio. The fraction of trapped alpha particles lost versus the ratio  $p_2 = \epsilon_{ha}/\epsilon_{ta}$  is shown in Fig. 3 for aspect ratios 5 and 10. The fraction of trapped particles lost is approximately independent of aspect ratio for a given value of  $p_2$ , is nearly unity when  $p_2 = 1$ , and decreases on either side of  $p_2 = 1$ .

The results shown in Fig. 3 can be understood on the basis of the  $B_{min}$  model.  $B_{min}$  surfaces are surfaces of constant

$$B_{min}(\rho, \theta) = \min_{\phi}[B(\rho, \theta, \phi)]$$

and in the absence of radial electric fields are good approximations to deeply-trapped particle orbits. Particles that are not deeply trapped also tend to drift along B-min contours so the confinement of a distribution of alpha particles (not all deeply-trapped) is correlated with the closing of these contours. When  $p_2 = 1$ ,  $B_{min}$  contours are not closed in the plasma region and helically-trapped particles drift out of the confinement region. When  $p_2 \gg 1$ , the configuration appears nearly helically symmetric,  $B_{min}$  contours coincide approximately with flux surfaces, and helically-trapped particles are confined. In the case  $p_2 \ll 1$  the alpha-particle confinement is not correlated with closing of the  $B_{min}$  contours because the majority of trapped particles are trapped by the toroidal  $\frac{1}{R}$  variation in  $B$  and not by the helical variation. In this case the dominant loss mechanism is stochastic drift<sup>12</sup> of the banana orbits.

The confinement of trapped particles in more complicated magnetic fields can also be explained with the  $B_{min}$  model. To illustrate this, trapped particle loss fractions were computed for a variety of torsatron configurations. These configurations differ from the reference reactors in that they have different vertical fields, different helical coil winding trajectories, or  $l = 1$  coils in addition to the primary  $l = 2$  coil set. Aspect ratios ranging from 3 to 8 and helical ripples ranging from 0.1 to 0.4 were considered. The results of these calculations are summarized in Fig. 4. The vertical axis is the fraction of trapped particles lost; the horizontal axis is the fractional area  $f$  of closed  $B_{min}$  contours. The fraction of trapped particles confined can be fitted by

$$f_c = 1.61f^2 \quad , \quad f < 0.79 \quad (3a)$$

$$f_c = 1.0 \quad f > 0.79 \quad (3b)$$

with an rms error of only 8% for the wide variety of vacuum configurations considered.

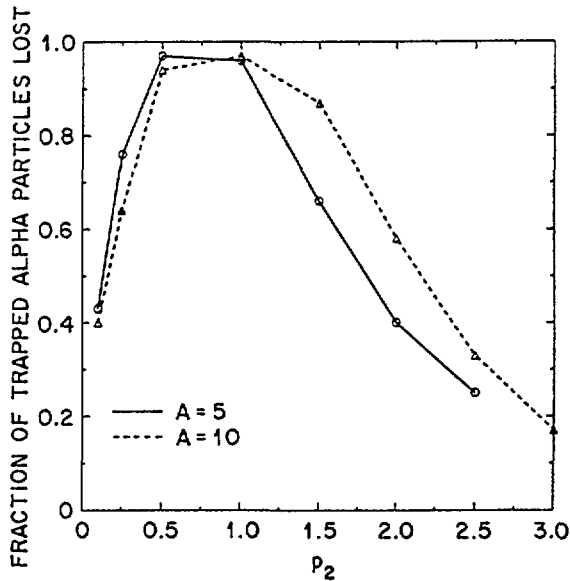


Fig. 3. Fraction of trapped alpha particles lost versus the ratio of helical ripple to toroidal ripple.

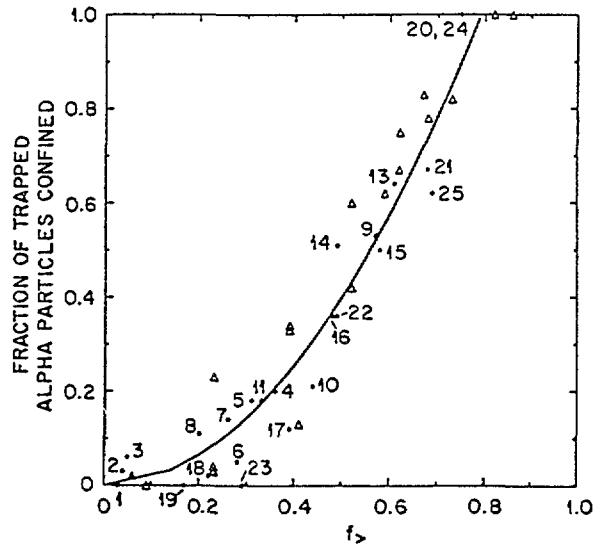


Fig. 4. Fraction of trapped alpha particles confined versus the normalized area of closed  $B_{min}$  contours.

## REDUCTION OF DIRECT LOSS FRACTION

The correlation between the area of closed  $B_{min}$  contours and the direct loss fraction can be used to study how additional helical harmonics might be added to the single helicity idealized configuration of (Eq. 2) in order to reduce the loss fractions. Flux surfaces are not guaranteed to exist for these model configurations; the results presented here are, however, useful for understanding the tradeoffs available to the stellarator reactor designer.

Mynick<sup>14</sup> proposed poloidal modulation of the helical ripple

$$B(\rho, \theta, \phi) = B_0 \{ 1 - \epsilon_{ta} \rho \cos(\theta) + [1 - \sigma \cos(\theta)] \epsilon_{ha} \rho^2 \cos(6\phi - 2\theta) \} \quad (4)$$

which is the same as (Eq. 2) with  $\epsilon_{ha}$  replaced by  $[1 - \sigma \cos(\theta)] \epsilon_{ha}$ . Here  $\sigma$  is an optimization parameter which is chosen to make trapped particle orbits coincide approximately with flux surfaces. Mynick took  $p_2 = 1$  and found optimized configurations with  $\sigma = 1$ . Using the correlation between the  $B_{min}$  area and losses, it can be shown that this configuration is a member of a family of zero loss configurations having  $\sigma \approx 1/p_2$ .

If (Eq. 4) is rewritten in terms of the Fourier expansion (Eq. 1), a spectrum of helical harmonics results. Perhaps a more straightforward way of improving orbit confinement is to add only  $l = 1$  and  $l = 3$  satellite harmonics to the single helicity configuration. Contours of constant particle loss fraction found with the correlation (Eq. 3) for a configuration having  $p_2 = 1$  are shown in Fig. 5. Here  $p_1$  and  $p_3$  are  $l = 1$  and  $l = 3$  ripple amplitudes normalized to the inverse plasma aspect ratio similar to the definition of  $p_2$ . For single helicity configurations having  $p_2 = 1$ , the trapped particle loss fraction is unity. Additional  $l = 1$  and  $l = 3$  terms reduce the loss fraction to zero in a manner similar to Mynick's  $\sigma$ -optimized configuration. In these configurations, the  $B_{min}$  contours coincide approximately with flux surfaces and the configuration appears helically symmetric to helically-trapped particles.

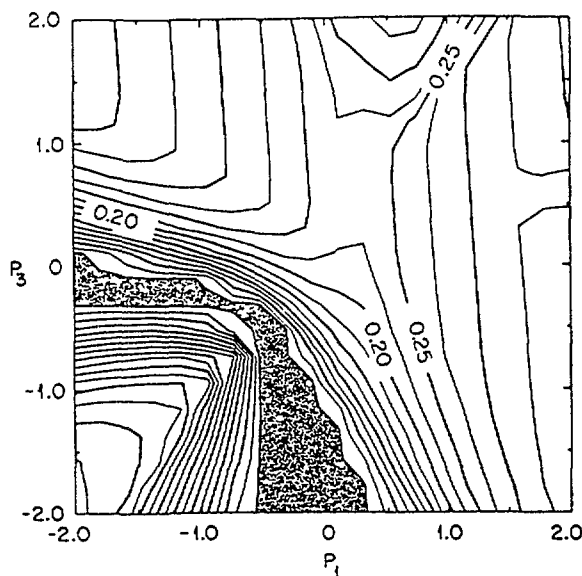


Fig. 5. Contours of constant alpha particle losses for vacuum field stellarator having aspect ratio 5 and helical ripple of 0.2.  $p_1$  and  $p_3$  are  $l = 1$  and  $l = 3$  ripple amplitudes normalized to the inverse aspect ratio.

## EFFECTS OF FINITE BETA

Vacuum field configurations which approximate the zero loss configurations discussed above can be produced by the ATR-3 coil set by including additional vertical fields to change the shape of the vacuum flux surfaces or shift the magnetic axis inward in major radius. Trapped particle loss fractions can then be reduced to zero. However, Pfirsch-Schluter currents which flow in nonzero-beta plasmas can alter the  $B$  spectrum and change particle orbits. To study this effect, three sequences of fixed-boundary zero net current equilibria were obtained with the 3-D code VMEC<sup>14</sup>. The initial vacuum field configurations for the three sequences are the standard ATR-3, ATR-3 shifted inward, and ATR-3 with increased central transform. The latter two vacuum configurations have zero losses. The fraction of trapped particles lost versus volume averaged beta is shown in Fig. 6 for the three sequences. The loss fraction increases toward unity with increasing plasma beta. At volume-averaged beta of a few percent, the reduction in losses gained by shifting or shaping the vacuum field flux surfaces has disappeared. This behaviour can also be understood within the context of the  $B_{min}$  model. As beta increases and the magnetic axis shifts outward relative to the fixed helical coil set, the  $B_{min}$  contours become distorted and noncircular. Even though the area of closed  $B_{min}$  contours

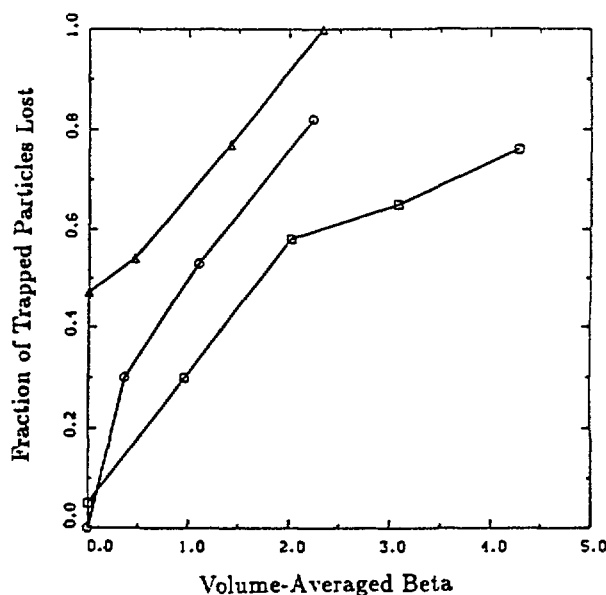


Fig. 6. Fraction of trapped alpha particle lost versus volume-averaged beta for three variants of ATR-3. Triangles represent the standard configuration, squares are for a configuration shifted inward in major radius, and circles are for a configuration with increased central transform.

does not decrease substantially, the center of the  $B_{min}$  contours shifts relative to the magnetic axis (Fig. 7). This causes deeply-trapped particle orbits to pass close to the plasma boundary and particles which are not deeply-trapped leave the confinement region.  $B_{min}$  contours for two values of plasma beta are shown in Fig. 8 for the inward shifted ATR-3.

The sequence of finite beta equilibria used here are intended to illustrate how finite beta can undo orbit optimization; they are not intended to represent a reactor startup scenario. Current studies seek to identify startup sequences for ATR-3 which have improved orbit confinement. This ancillary optimization with vertical fields is not effective at improving orbit confinement in the lower aspect ratio ATR-1 and ATR-2 however. In order to find low aspect-ratio configurations with good orbit confinement, it will be necessary to introduce transport considerations directly into the primary configuration optimization procedure<sup>15</sup>.

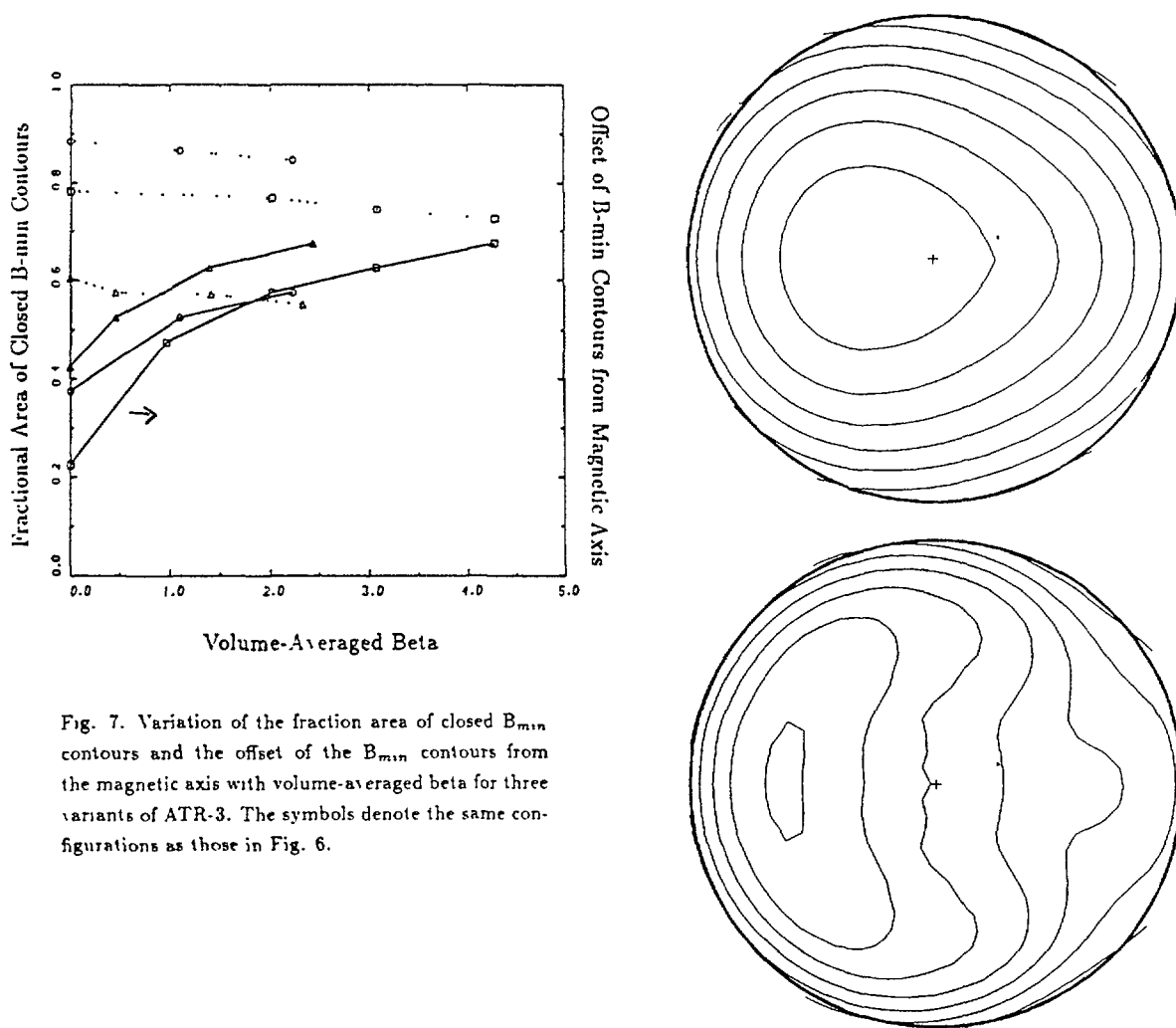


Fig. 7. Variation of the fraction area of closed  $B_{min}$  contours and the offset of the  $B_{min}$  contours from the magnetic axis with volume-averaged beta for three variants of ATR-3. The symbols denote the same configurations as those in Fig. 6.

Fig. 8.  $B_{min}$  contours at  $\beta = 0$  and  $\beta = 3\%$  for the shifted-in ATR-3 configuration. The radial coordinate is proportional to the square root of toroidal flux and the angle variable is Boozer's poloidal angle

## ACKNOWLEDGEMENTS

The authors acknowledge C. L. Hedrick and B. A. Carreras for suggesting the correlation between alpha-particle losses and the area of closed  $B_{min}$  contours and the addition of  $l = 1$  and  $l = 3$  components. They also thank V. E. Lynch for providing Fourier components of  $B$  for the configurations studied, R. H. Fowler for providing the orbit-following code, and N. Dominguez for providing the finite-beta equilibria. One author (SLP) also thanks P. N. Stevens for his encouragement.

## REFERENCES

1. B. A. CARRERAS, N. DOMINGUEZ, L. GARCIA, V. E. LYNCH, J. F. LYON, J. R. CARY, J. D. HANSON, and A. P. NAVARRO, "Low-Aspect-Ratio Torsatron Configurations," *Nucl. Fusion*, **28**, 1195 (1988); see also ORNL/TM-10030, Oak Ridge National Laboratory (1987).
2. A. H. BOOZER, "Guiding Center Drift Equations," *Phys. Fluids*, **23**, 904 (1980).
3. G. KUO-PETRAVIC, A. H. BOOZER, J. A. ROME, and R. H. FOWLER, "Numerical Evaluation of Magnetic Coordinates for Particle Transport Studies in Asymmetric Plasmas," *J. Comput. Phys.*, **51**, 261 (1983).
4. A. H. BOOZER and G. KUO-PETRAVIC, "Monte Carlo Evaluation of Transport Coefficients," *Phys. Fluids*, **24**, 851 (1981).
5. R. H. FOWLER, J. A. ROME, and J. F. LYON, "Monte-Carlo Studies of Transport in Stellarators," *Phys. Fluids*, **28**, 338 (1985).
6. S. L. PAINTER, J. F. LYON, "Alpha Particle Losses in Compact Torsatron Reactors," *Fusion Technol.*, accepted for publication; see also ORNL/TM-10792, Oak Ridge National Laboratory (Oct. 1988).
7. J. F. LYON, B. A. CARRERAS, V. E. LYNCH, J. S. TOLLIVER, and I. N. SVI-ATOSLAVSKY, "Compact Torsatron Reactors," *Fusion Technol.*, **15**, 1401 (1989).
8. J. F. LYON, B. A. CARRERAS, K. K. CHIPLEY, M. J. COLE, J. H. HARRIS, T. C. JERNIGAN, R. L. JOHNSON, V. E. LYNCH, B. E. NELSON, J. A. ROME, J. SHEFFIELD, and P. B. THOMPSON, "The Advanced Toroidal Facility," *Fusion Technol.*, **10**, 179 (1986).
9. J. G. CORDEY and W. G. F. CORE, "Energetic Particle Distribution in a Toroidal Plasma with Neutral Injection Heating," *Phys. Fluids*, **17**, 1626 (1974).

10. J. A. ROME, D. G. McALEES, J. D. CALLEN, and R. H. FOWLER, "Particle-Orbit Loss Regions and Their Effects on Neutral-Injection Heating in Tokamaks," *Nucl. Fusion*, **16**, 55 (1976).
11. D. ANDERSON, H. HAMNÉN, and M. LISAK, " $\alpha$ -Particle Ripple Losses During Slow Down in a Tokamak Reactor," *Phys. Fluids*, **25**, 353 (1982).
12. R. J. GOLDSTON, R. B. WHITE, and A. H. BOOZER, "Confinement of High-Energy Trapped Particles in Tokamaks," *Phys. Rev. Lett.*, **47**, 647 (1981).
13. H. E. MYNICK, T. K. CHU, and A. H. BOOZER, "Class of Model Stellarator Fields with Enhanced Confinement," *Phys. Rev. Lett.*, **48**, 322 (1982).
14. S. P. HIRSHMAN and J. C. WHITSON, "A Steepest-Descent Moment Method for Three-Dimensional Magnetohydrodynamic Equilibria," *Phys. Fluids*, **26**, 3553 (1983).
15. S. P. HIRSHMAN, R. N. MORRIS, C. L. HEDRICK, J. F. LYON, R. H. FOWLER, J. A. ROME, S. L. PAINTER, W. L. VAN RIJ, "Low-Aspect-Ratio Optimization Studies for ATF-II," these proceedings.

## TRANSPORT SURVEY CALCULATIONS USING THE SPECTRAL COLLOCATION METHOD\*

S.L. PAINTER<sup>1</sup>, J.F. LYON  
Fusion Energy Division,  
Oak Ridge National Laboratory,  
Oak Ridge, Tennessee,  
United States of America

### Abstract

*A novel transport survey code has been developed and is being used to study the sensitivity of stellarator reactor performance to various transport assumptions. Instead of following one of the usual approaches (0-D model or 1-D time-dependent solution to the energy transport equations), the steady-state transport equations are solved in integral form using the spectral collocation method. This approach effectively combines the computational efficiency of global models with the general nature of 1-D solutions.*

*A compact toratron reactor test case was used to study the convergence properties and flexibility of the new method. The heat transport model combined Shaing's model for ripple-induced neoclassical transport, the Chang-Hinton model for axisymmetric neoclassical transport, and neoclassical scaling for anomalous electron heat flux. Alpha particle heating, radiation losses, classical electron-ion heat flow, and external heating were included. For the test problem, the method exhibited some remarkable convergence properties. As the number of basis functions was increased, the maximum pointwise error in the integrated power balance decayed exponentially until the numerical noise level was reached ( $\approx 25$  basis functions). Better than 10% accuracy in the globally-averaged quantities was achieved with only 5 basis functions; better than 1% accuracy was achieved with 10 basis functions. The numerical method was also found to be very general. Extreme temperature gradients at the plasma edge which sometimes arise from the neoclassical models and are difficult to resolve with finite-difference methods were easily resolved. Constraints on the temperature gradients were also introduced without causing any numerical instabilities.*

---

Transport survey calculations such as those used in studies of fusion reactors or new experiments have traditionally employed one of two basic approaches: global (0-D) models or one-dimensional (1-D) solutions to the transport equations. In the global approach (e.g. Ref. 1), the differential equations which describe local energy transport are integrated over the plasma volume with the assumption of fixed temperature and density profile shapes. The resulting algebraic equations are then solved for average temperatures and densities. This is an efficient approach; a large number of cases can be examined quickly so that the underlying sensitivities can be easily identified.

---

\* Research sponsored by the Office of Fusion Energy, US Department of Energy, under contract DE-AC05-84OR21400 with Martin Marietta Energy Systems, Inc.

<sup>1</sup> Research performed to meet the requirements for the degree of PhD in nuclear engineering, University of Tennessee.

The disadvantage of the global approach is that it requires an *a priori* assumption about the profile shape. This is not a serious disadvantage for tokamaks since the experimental data base indicates that the range of accessible profile shapes is limited (profile consistency). For stellarators however, the experimental data base of confinement results is smaller, and a larger variety of profile shapes are possible. In this case, 1-D solutions to the energy transport equations are necessary. Although sophisticated time-dependent codes<sup>2,3,4</sup> exist for solving these equations, these codes are computationally intensive and require long computing times on large computers.

An accurate and computationally efficient transport survey code is being developed. This code solves the 1-D steady-state transport equations in integral form using the spectral collocation method<sup>5</sup>. This approach combines the computational efficiency of the global approach with the general nature of 1-D solutions.

## THE TRANSPORT EQUATIONS

A self-consistent treatment of the transport problem requires solutions to the particle and power balance equations for both electrons and ions with the ambipolarity constraint to determine the radial electric field. The numerical approach described in this paper is, in principle, capable of treating the self-consistent problem. However, the density and electric field profiles are determined by transport processes that are not well understood. To avoid this uncertainty, the particle density and radial electric field profiles are fixed while the electron and ion power balance equations are solved. Sensitivity to the profile assumptions will be addressed.

With these assumptions the steady-state energy transport equations in integral form are

$$\rho q_a(\rho) = \int_0^\rho S_a(\rho) \rho d\rho, \quad (1)$$

where  $a = e(i)$  for electrons (ions),  $\rho$  is the normalized radial variable, and  $S$  is the total (external plus internal) heat source including alpha particle heating, radiation losses, inter-species coupling, and external heating. For stellarators the heat flux  $q(\rho)$  can be written as

$$q_a = -n_a \chi_a^T \frac{dT_a}{d\rho} - T_a \chi_a^n \frac{dn_a}{d\rho} - Z_a e n_a \chi_a^\Phi \frac{d\Phi}{d\rho},$$

where  $n_a$  is the density of species  $a$ ,  $T_a$  is the temperature of species  $a$ ,  $\Phi$  is the electric potential, and the  $\chi$ 's are the various heat diffusivities. Shaing's model is used for the neoclassical ripple contribution to the diagonal and off-diagonal diffusion coefficients for electrons and ions, the Chang-Hinton model is used for the axisymmetric neoclassical

contribution to  $\chi_i$  (diagonal term only), and the neoculator scaling is used for the anomalous contribution to  $\chi_e^T$ . The integrals in Shaing's model are approximated by 10 point Gauss-Laguerre quadrature.

The integral form of the equations is used for two reasons. The heat flux  $q$  is in general a complicated function of temperature, may not be available in closed-form, and is more expensive to compute than the total heat source  $S$ . Also, global quantities such as the average temperature are of most interest here; using the integral form causes these global quantities to converge faster.

## THE CHEBYSHEV COLLOCATION METHOD

Although the assumption of fixed density and electric field profiles simplifies the system (Eq. 1) compared to the self-consistent problem, the equations are in general severely non-linear since the source depends non-linearly on the dependent variables (electron and ion temperature) and the heat flux can depend non-linearly on the temperatures and the temperature gradients. The usual solution approach would be to apply the finite-difference approximation to the spatial derivatives and evolve the time-dependent equations until the steady-state is reached. This approach is inefficient, especially since only steady-state quantities are of interest here.

The Chebyshev collocation method is a more efficient approach. In this method the dependent variable (temperature in this case) is expressed as a series expansion in Chebyshev polynomials ( $T_j$ )

$$T(\rho) = \sum A_j T_j(y),$$

where  $y = 2\rho - 1$ . The expansion coefficients  $A_j$  are determined by requiring the original system of equations to be satisfied on a discrete set of points ( $\rho_j$ ), the collocation points, which are the interior extrema of the highest order basis function

$$\rho_j = \frac{1 - \cos(\frac{\pi j}{N})}{2}, \quad 1 \leq j \leq N - 1$$

Applying this method to the integrodifferential system (Eq. 1) and rearranging yields the following algebraic system

$$\rho_j q_a(\rho_j) - \rho_{j-1} q_a(\rho_{j-1}) = \int_{\rho_{j-1}}^{\rho_j} S_a(\rho) \rho d\rho, \quad 1 \leq j \leq N - 1$$

These equations plus equations coming from boundary conditions and auxiliary conditions on the solution are solved by iteration.

This method resembles the finite element method but is more efficient since the continuity conditions at the element interfaces are intrinsically satisfied. The collocation method is significantly more accurate (for a given grid size) than the finite difference method particularly when the solution is changing rapidly near one of the boundaries. Boundary layers are treated efficiently since the collocation points are more closely spaced near the boundary (grid spacing near the boundary is  $\approx \frac{1}{N^2}$  where  $N$  is the truncation order).

## CONVERGENCE STUDIES

An ignited compact torsatron reactor<sup>6</sup> test case was used to determine the convergence properties of the collocation method. This is a single-helicity stellarator with aspect ratio 5, helical ripple 0.2, and major radius 10 m. The density and electric potential  $\Phi$  profiles are both parabolic squared with a central density of  $3 \times 10^{20} \text{ m}^{-3}$  and  $e\phi_0/T_{e0} = -2$ .

Profiles of electron temperature and ion temperature obtained for the test case are shown in Fig. 1. The residual power (error in the integrated power balance) normalized to the total alpha-particle heating is shown versus radius  $\rho$  in Fig. 2 for  $N = 25$ .

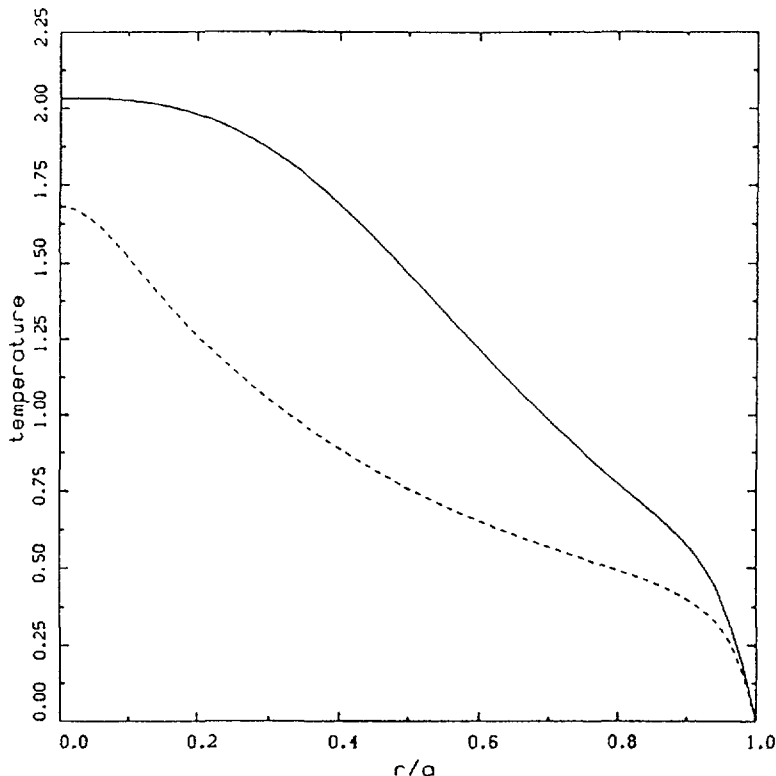


FIG. 1. Profiles of electron temperature (dashed line) and ion temperature (solid line) for the ignited compact torsatron test case. Temperatures are in units of 10 keV.

The residual power is small over most of the plasma region but peaks near the plasma boundary. This peak is due to interpolation errors in the temperature gradients between collocation points. However, the nature of the collocation method prevents this type of error from propagating away from the offending point.

If the spike in the residual power near the plasma boundary is excluded, the residual power decreases rapidly with increasing number of basis functions. The maximum error in the integrated power balance defined as

$$R_{xa} = \max_{0 \leq \rho \leq .4} \left| \rho q_a(\rho) - \int_0^\rho S_a(\rho_*) \rho_* d\rho_* \right|$$

is shown versus the number of basis functions in Fig. 3. The nearly straight line on the log-linear plot indicates that the convergence is essentially exponential. Only 25 basis functions are required before the residual error reaches the level of numerical noise in this single precision calculation. The average quantities converge even more rapidly. In Fig. 4 the average electron and ion temperatures at ignition are shown versus the number of basis functions. One percent accuracy is obtained with 10 basis functions, and ten percent accuracy is obtained with only 5 basis functions. The rapid convergence of the global quantities is a direct consequence of solving the equations in integral form.

The computational time required is shown versus the number of basis functions in Fig. 5. By comparing Fig. 4 and Fig. 5 one can see that less than 2 CPU seconds on a Digital Equipment VAX 8700 are required for 1% accuracy in the average quantities.

## NUMERICAL EXAMPLES

In order to illustrate the versatility of the collocation method for this problem, some example profiles of electron and ion temperatures are shown in Fig. 6. These profiles are for the same compact torsatron reactor discussed earlier, but here the average temperature is fixed at 10 keV and the amount of external heating power required to maintain the steady-state is solved for. The profile of the external heating power  $P_x$  is parabolic in all cases, with one-half of the power going to electrons and one-half going to ions. The cases on the left-hand side have  $e\Phi_0/T_{e0} = -2$ . Those on the right-hand side have  $e\Phi_0/T_{e0} = +2$ .

In Fig. 6a and Fig. 6b, the  $\Phi$  profiles are parabolic squared. Positive values of  $\Phi$  (electric field vector pointing outward) leads to broader ion temperature profiles and larger values of  $P_x$  to maintain the steady-state (19 MW for  $e\Phi_0/T_{e0} = -2$ , 385 MW for  $e\Phi_0/T_{e0} = +2$ ). Electron temperatures remain peaked in both cases due to the

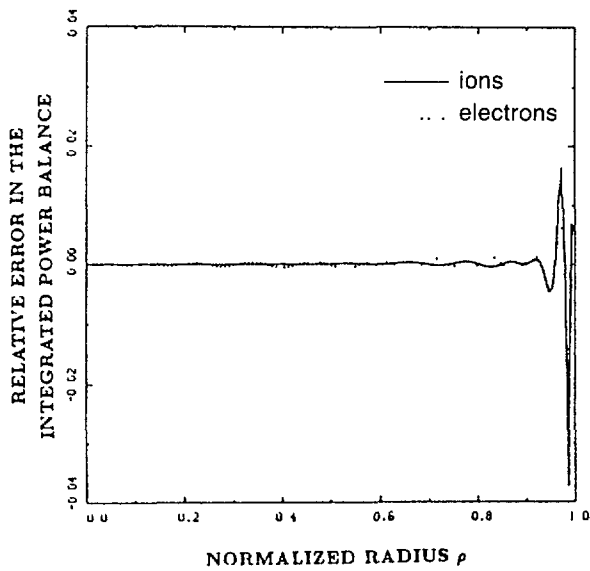


FIG. 2. Error in the integrated power balance normalized to the total alpha particle heating power for the compact torsatron test case.

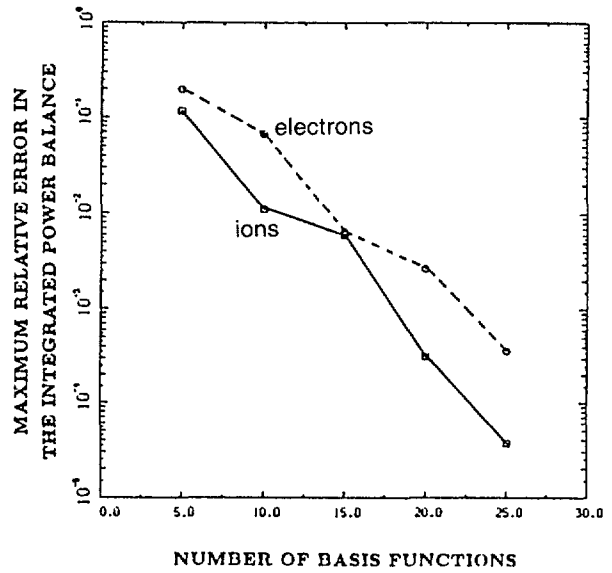


FIG. 3. Maximum relative error in the integrated power balance for the compact torsatron test case.

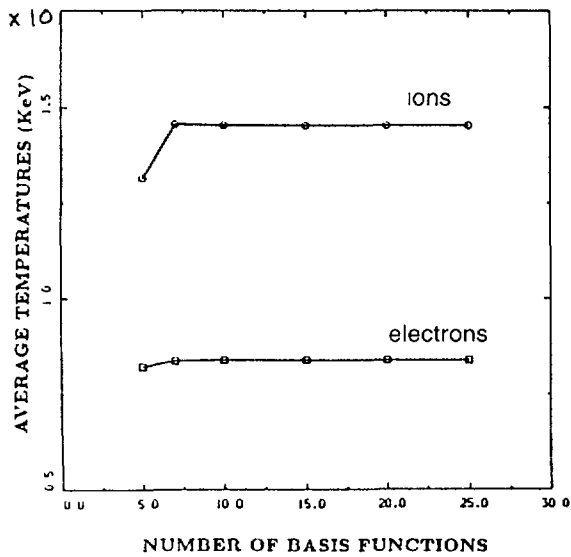


FIG. 4. Average temperature at ignition for the compact torsatron test case.

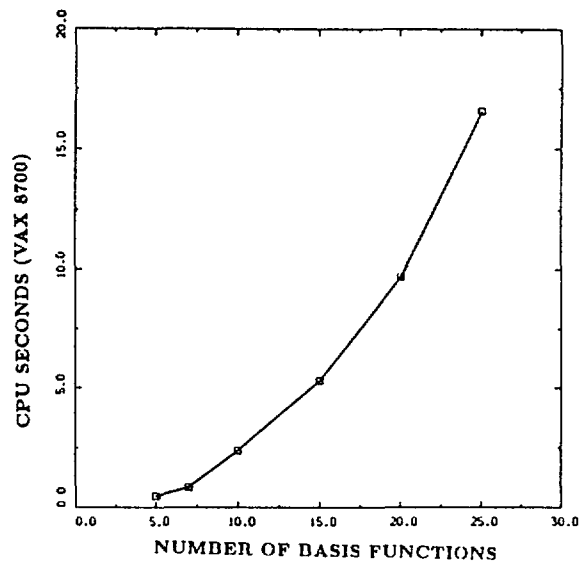


FIG. 5. Computation time for the compact torsatron test case.

influence of the neoalcatraz term. In Fig. 6c and Fig. 6d, the  $\Phi$  profiles are parabolic so that the radial electric field is largest at the plasma edge. In both cases the ion temperature profile is hollow with extremely steep gradients near the plasma edge. 38 MW's are required to maintain steady-state in the case represented in Fig. 6c, 263 MW's are required in Fig. 6d.

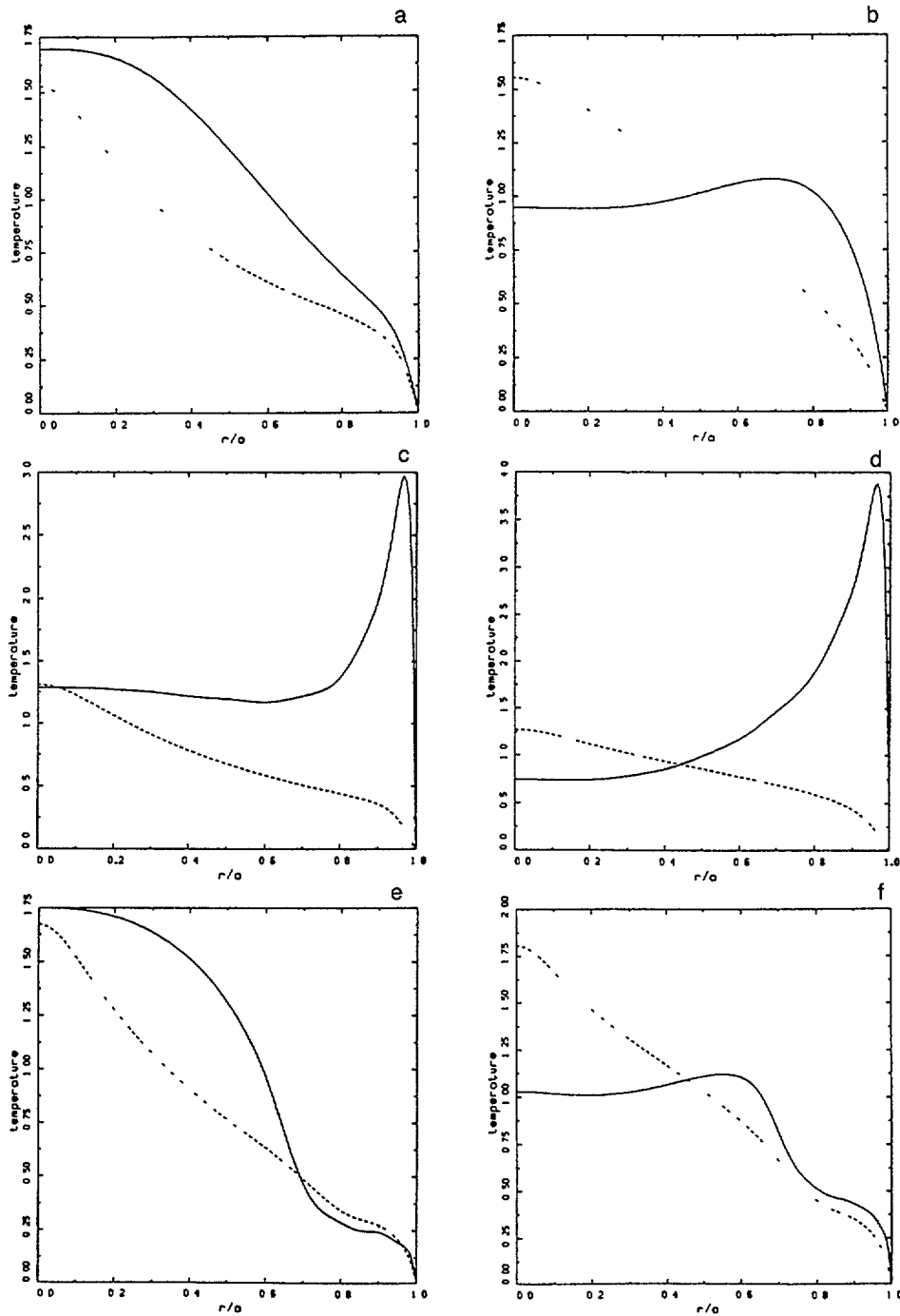


FIG. 6 Example profiles of electron temperature (dashed lines) and ion temperature (solid lines) for the compact torsatron reactor test case. Temperatures are in units of 10 keV. The various cases are explained in the text.

The pressure profiles associated with the profiles in Fig. 6c and 6d would probably be unstable to ideal MHD modes. Unstable profiles can be prevented by defining a gradient-limiting-diffusivity

$$\chi_{GL} = \chi_{Bohm} \left\{ 1 + \exp\left[\frac{p'_{crt} - p'}{\epsilon p}\right] \right\}^{-1}$$

where  $p$  refers to the plasma pressure, the prime indicates the derivative with respect to the radial variable,  $\chi_{Bohm}$  is the Bohm value for the diffusivity, and  $\epsilon$  is a small number. The critical pressure gradient  $p'_{crit}$  should be determined from MHD stability considerations; simple expressions for  $p'_{crit}$  are being investigated. A constant value,  $\frac{p'_{crit}}{p} = 10$ , is used in Fig. 6e and 6f to illustrate the effect of introducing this constraint. The amount of external heating power required increases dramatically compared to the unconstrained cases. 198 MW are required in Fig. 6e and 755 MW are required in Fig. 6f.

The numerical method described in this paper provides an accurate and efficient means for obtaining steady-state solutions to the fluid-equations describing energy transport in fusion plasmas. The collocation method could also be extended to treat the time-dependent problem with self-consistent determination of the density profiles and the radial electric-field. The efficiency of detailed time-dependent transport simulations could also be improved by the use of this method.

**ACKNOWLEDGEMENTS** The authors acknowledge Steven Hirshman and Paul Stevens for useful discussions about the numerical method.

## REFERENCES

1. N. A. UCKAN and J. SHEFFIELD, in Fusion Engineering (Proc. 11th Symp. Auxtin, TX, 1985) Vol. 1 IEEE, New York (1986) 89.
2. W. A. HOULBERG, S. E. ATTENBERGER, and L. M. HIVELY, "Contour Analysis of Fusion Reactor Plasma Performance," *Nucl. Fusion*, **22**, 935 (1982).
3. H. C. HOWE, Oak Ridge National Laboratory Report ORNL/TM-9537 (1985).
4. C. E. SINGER, D. E. POST, D. R. MIKKELSEN, M. H. REDI, A. MCKENNEY, A. SILVERMAN, F. G. P. SEIDL, P. H. RUTHERFORD, R. J. HAWRYLUK, W. D. LANGER, L. FOOTE, D. B. HEIFETZ, W. A. HOULBERG, M. H. HUGHES, R. V. JENSEN, G. LISTER, and J. OGDEN, "BALDUR: A One-Dimensional Plasma Transport Code," *Comput. Phys. Commun.*, **49**, 275 (1988).
5. D. GOTTLIEB and S. A. ORSZAG, *Numerical Analysis of Spectral Methods: Theory and Applications* (Soc. Indus. and Appl. Math., Philadelphia 1977).

6. J. F. LYON, B. A. CARRERAS, V. E. LYNCH, J. S. TOLLIVER, and I. N. SVIATOSLAVSKY, "Compact Torsatron Reactors," *Fusion Technol.*, **15**, 1401 (1989).
7. K. C. SHAINING, "Stability of the Radial Electric Field in a Nonaxisymmetric Torus," *Phys. Fluids*, **27**, 1567 (1984).
8. C. S. CHANG and F. L. HINTON, "Effect of Finite Aspect Ratio on the Neoclassical Ion Thermal Conductivity in the Banana Regime," *Phys. Fluids*, **25**, 1493 (1982).

## **IMPURITIES, DIVERTORS**

## OPTICAL MEASUREMENTS OF ECRH HELIUM PLASMA IN THE L-2 STELLARATOR

N.P. DONSKAYA, N.F. LARIONOVA, V.I. ROSHCHIN,  
A.D. SMIRNOVA, G.S. VORONOV  
General Physics Institute,  
Moscow, Union of Soviet Socialist Republics

### Abstract

This paper describes in detail the optical measurements of the main parameters ECR-heated helium plasma in L-2 stellarator.

---

Experiments on ECR-heating of helium plasma in the L-2 stellarator were fulfilled with the ordinary wave fundamental harmonic in 1988 [1]. This report describes in more detail optical measurements of the plasma parameters.

Microwave beam ( $f=37.5\text{GHz}$ ) was launched into the chamber through the external horizontal window from the low-field side. The lens beam-guide was used to transfer the beam to the machine. Microwave beam power at the window was about 100 kW, beam diameter as measured at the level of .1 of central power was about 6cm, beam divergency was .02.

Helium was chosen as working gas in order to decrease radiation losses and to prevent the effect of wall conditions on the discharge parameters. In fact, the radiation losses dropped to .7 of those in hydrogen, less than 20% of plasma absorbed power was lost with radiation. The increase of plasma density during the heating pulse was also smaller than in hydrogen.

Optical diagnostics used were: 1) Thomson scattering at the second harmonic of neodim-glass laser (wavelength 5300 Å), 2) multichannel submillimeter interferometer at the wavelength .337mm for measurements of plasma density radial distributions, 3) spectral measurements in both quartz and vacuum-ultraviolet wavelength regions.

Gas breakdown and plasma formation was due to microwave field, considerable role in this phenomenon could be played by X-polarised wave obtained in the course of multiple beam reflections from metal walls of the chamber. The breakdown power  $F$  was noticeably smaller than heating power  $W$  (Fig.1). Rather small time of .5-1ms was needed for gas breakdown and plasma formation, the slow density increase due to impurities followed (Fig.2). As could be concluded from absolute spectral-line intensity measurements, density increase was due to increase in concentration of oxygen and carbon which were 4% and 1.5% correspondingly, at the end of the heating pulse.

Radiation loss power  $P_{\text{rad}}=12-15\text{kW}$  was considerably less than absorbed power  $P_{\text{abs}}$  and was approximately equal to power emitted by oxygen and carbon ions.

Electron temperature evolution measured with Thomson scattering and spectral-line localisation evolution studies [2] had shown that the ECR plasma heating in the L-2 stellarator could

develop in two different ways. Fast increase and subsequent stabilization at the level of 600 eV of the central electron temperature was characteristic of one of these "A" regimes (Fig.3). In "B" regime central electron temperature was growing during the whole heating pulse to get .9-1.1keV at the end of it (Fig.4). Sometimes, a transition could be observed from "A" to "B" regime during the heating process (Fig.5).

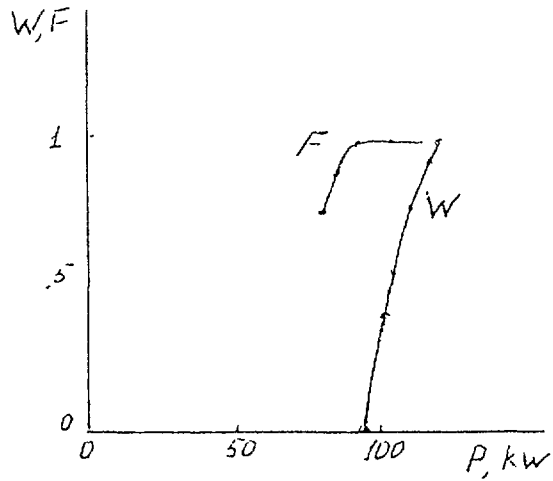


FIG 1

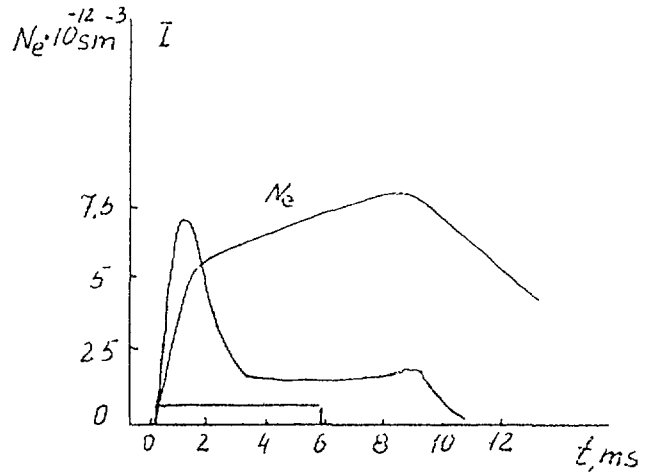


FIG. 2.

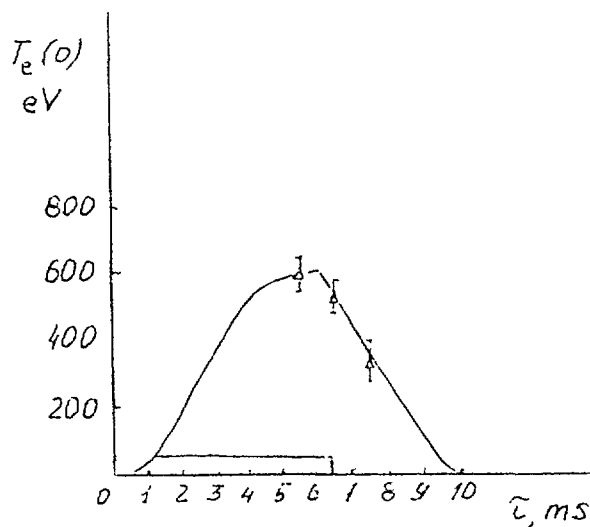


FIG 3

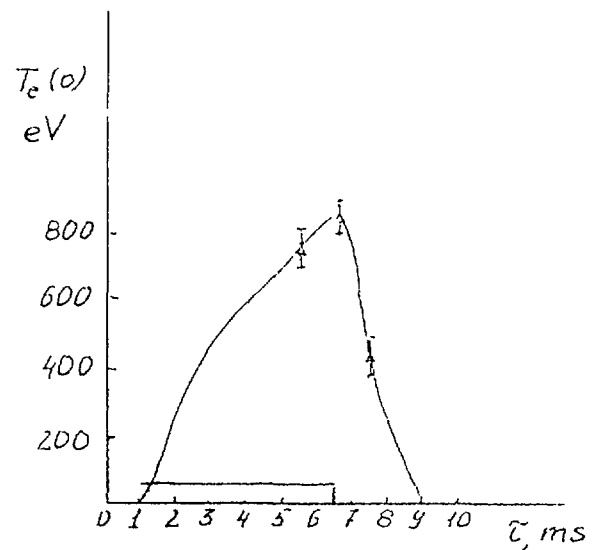


FIG 4

"B" regime could be obtained in very narrow region of the magnetic field values :  $E/B \approx .5\%$ . B value corresponded approximately to central location of the ECR resonance but was also affected by some other parameters difficult to be controlled such as profile and plasma density magnitude, microwave beam direction at the chamber entrance, etc. This B uncertainty could be due to beam refraction in plasma and, therefore, power absorption region changing its localization.

Shown in Fig.6 and Fig.7 is  $T_e$  profile evolution in "A" and "B" regimes. In "A" regime  $T_e(r)$  widened to the end of the heating pulse while  $T_e(0)$  remained the same. In "B" regime  $T_e(r)$  profile had been keeping its peaked form during all the heating time. Difference in these  $T_e$  profiles can be easily seen in Fig.8 where a transition is shown from "A" to "B" regime.

Density profile measured with HCN-laser interferometer is parabolic for the most part. Sometimes more peaked profiles were observed during the heating, any correlation to heating regime, however, had not been observed.

Energy containment of the plasma electron component obtained with integration over the profiles  $T_e(r)$  and  $N_e(r)$  was (140-150)J in "A" regime and (180-190)J in "B" regime in good agreement with diamagnetic measurements results. Absorbed power was 60W and (60-70)W in "A" and "B" regimes correspondingly as measured with diamagnetic signal derivative at the time when heating power had been switched off. Energy confinement time was calculated to be 2.4ms ("A" regime) and 2.8ms ("B" regime) with radiation losses having been neglected.

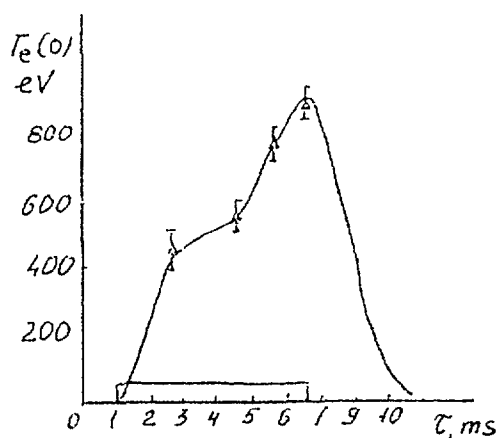


FIG 5

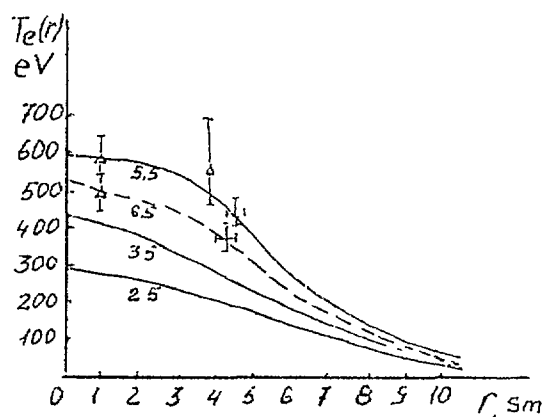


FIG. 6.

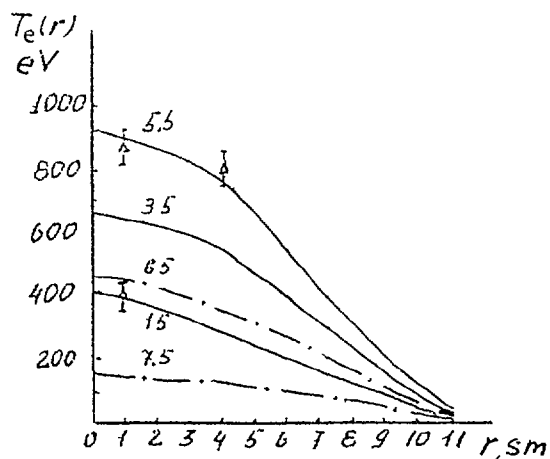


FIG. 7.

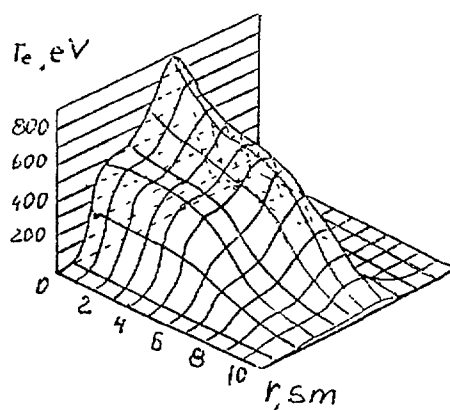


FIG. 8

At present, there is no any possibility to measure space distribution of the absorbed power  $Q(r)$ . An attempt was made to calculate it with help of plasma energy derivative at the time moment when heating power had been switched off.

Spectral line localization followed the electron temperature evolution with some delay .5ms due to finite velocities of impurity ionization and diffusion processes.  $T_e(r)$  profile, meantime, changed because of heat conduction. Nevertheless, qualitative difference in  $T_e(r)$  profiles for the abovesaid regimes, are quite obvious (Fig.9). As it can be seen, narrow profile  $T_e(r)$  with high central temperature  $T_e(0)$  11'ev ("B" regime) was obtained when power absorption maximum was located at the centre while more flat profile with central temperature  $T_e(0)$  6000ev ("A" regime) corresponded to peripheral heating.

Magnetic surface structure is complex in L-2 stellarator. Slight change in the magnetic field amplitude and beam refraction on plasma inhomogeneities can make absorption region to move to the saddle point of the magnetic field structure. Ray tracing calculation results [2] are in agreement with this supposition.

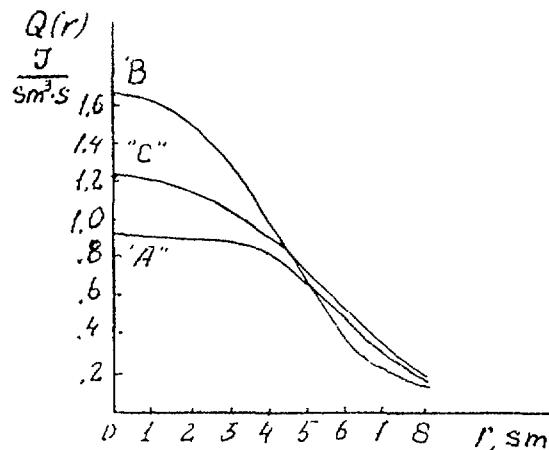


FIG 9

#### REFERENCES

- [1] Andryukhina E. D. et al. in Europhysics Conf. Abs. 120 (Proc. 15th Eur. Conf. Contr. Fusion and Plasma Phys., Dubrovnik, 1988) Part 2, p.447.
- [2] Liliin F. M. et al. ibid, Part 2, p.451.
- [3] Voronov G.S., Donskaya N. P., Roshchin V. I. Preprint U.S., 265, 1987 (in Russian).

# INVESTIGATIONS OF IMPURITY RADIATION DURING THE INITIAL PHASE OF W VII-AS OPERATION

R. BRAKEL, R. BURHENN, H. HACKER,  
H.J. JÄCKEL, A. WELLER, W VII-AS TEAM<sup>1</sup>,  
ECRH GROUP<sup>1</sup>, NBI GROUP<sup>1</sup>  
Euratom-IPP Association,  
Max-Planck-Institut für Plasmaphysik,  
Garching, Federal Republic of Germany

## Abstract

The impurity measurements at WENDELSTEIN WVII-AS and the calculations used to analyze the data are described. The initial experiments were performed mainly at low densities ( $n_e \lesssim 2 \times 10^{13} \text{ cm}^{-3}$ ) due to 2<sup>nd</sup> harmonic ECF - heating at 1.25 Tesla. Steady state conditions are obtained with low radiation powers ( $\approx 20\%$  of absorbed ECRH power). However, this radiation level corresponds to rather high impurity concentrations and  $Z_{eff}$  can reach values of 5. At the highest densities (fundamental ECRH at 2.5 T),  $Z_{eff} \approx 2.5$ . Carbon, oxygen and iron are the main impurities in the plasma. The relative abundances C:O  $\sim 3:1$  were derived from CX-excited lines of fully stripped impurity ions during first neutral beam injection experiments. The Bragg spectrometer yields typical values of  $\sim 2\%$  of oxygen and up to  $\sim 0.03\%$  of iron but usually a factor of 2 more is required to fit the total radiation as well as the X-Ray intensities. In order to investigate impurity transport effects, a Ne-puff experiment was performed. The X-ray emission from plasma impurities was also used to probe the electron temperature profile using the absorber foil method.

## 1. INTRODUCTION

Most of the experiments in WENDELSTEIN VII-AS were performed by generating and heating the plasma with 2<sup>nd</sup> harmonic ECF (X-mode) at 1.25 T [1]. With up to 3 gyrotrons (70 GHz) central temperatures of  $\sim 1.7 \text{ keV}$  at densities of  $\sim 1.5 \times 10^{13} \text{ cm}^{-3}$  have been achieved. Few experiments were performed at 2.5 T (O-mode ECRH) and with neutral beam injection (NBI). Glow discharge conditioning in He was necessary to control the plasma density. The operational range included configurations with the last closed magnetic surface defined by the two Ti-C coated graphite limiters (which can be moved radially) or by a magnetic separatrix inside.

## 2. DIAGNOSTICS

The X-ray spectrum is investigated by a flat crystal Bragg-spectrometer viewing the plasma along a fixed, almost central line of sight. The range 0.8 – 87 Å can be assessed by 3 crystals (KAP, Pb-stearate, Si) with provision for energy filtering by absorber foils. The spectrometer was calibrated absolutely by an X-ray tube using a proportional counter and a microchannel plate as detectors.

The VUV spectral range is monitored by a grazing incidence monochromator, which will be upgraded by a rotating mirror. A second identical system is prepared in order to analyze radial emission profiles and poloidal asymmetries. In addition, a multichannel SPRED-spectrometer is being installed. The spectrometers can view the interaction volume of the plasma with one of the neutral beams allowing to monitor fully stripped light impurity ions via CX-excited lines [2,3].

---

\* The members of the W VII-AS Team, ECRH Group and NBI Group are identified in the paper entitled 'Status of the advanced stellarator Wendelstein W 7AS: first results and further programme', these proceedings, p. 25.

Total radiation power profiles are measured using the WVII-A 10-channel bolometer system. The detector head can be rotated in order to increase the radial resolution by using several similar shots. Radial X-ray emission profiles have been recorded using a 12-diode-pair camera system, which mainly serves to determine electron temperature profiles according to the X-ray absorber foil method [4,5]. For the central chords Be-foils with thicknesses between 0.1 – 1 mm can be used in addition to a fixed 25  $\mu\text{m}$  Be-foil.

Owing to the particular 3-dimensional structure of the magnetic surfaces and the possible changes of the configuration in WVII-AS [6], a transformation procedure is applied in order to relate all measurements to equivalent flux coordinates. For line of sight integrated measurements an effective impact radius is used. The lengths of the lines of sight through the plasma are renormalized to circular geometry in order to apply usual Abel-inversion techniques.

### 3. IMPURITY MODELLING

The impurity radiation modelling codes IONEQ [7], SITAR [8] and STRAHL [9] are used, which use the datasets for ionization- and recombination- (rad., diel. and CX) rate calculations originating from the 1-dim. transport code STRAHL. SITAR is the impurity transport code used in WVII-A with a different transport- and radiation-calculation approach and a particular source term for neutral beam injected impurities. Both transport codes use anomalous and/or neoclassical (tokamak) transport coefficients. For the simulation of X-ray emission the coronal equilibrium code IONEQ is used, which also serves to test the radiation calculations for SITAR. IONEQ provides calculations of the total radiation power and for specific lines, with or without continuum radiation and also takes the attenuation by absorber foils into account. Radiation spectra and radial emission profiles are calculated either locally or line of sight integrated in order to compare directly with measurements. Finally, also the tabulated radiative cooling rates according to the average ion model in coronal equilibrium [10] are used for first impurity content estimates from total radiation power profiles.

### 4. RESULTS

The VUV radiation spectra are dominated by lines of C (limiter, protection tiles), O and Fe (wall). The attempt to detect carbon by the Bragg-spectrometer using the Pb-stearate crystal failed due to the low reflectivity and the high background radiation level, but O- and Fe-lines are clearly seen (fig. 1). The data were obtained during different discharge conditions but are normalized to equal line density. Comparing the observed intensities with simulated spectra from IONEQ based on measured  $T_e$ -,  $n_e$ - profiles yield typical concentrations  $n_O/n_e \approx 2\%$  and  $n_{Fe}/n_e \approx 0.02\%$ . The iron contamination is reduced beyond the detection limit, when the limiters are moved in and their heat load is raised to  $\sim 30\%$  of the input energy. The ratio between C and O is difficult to obtain from the low ionization states, but during the onset of NBI CX-excited lines (fig. 2) are used to derive typical ratios of  $n_C : n_O \approx 3 : 1$  with effective rate coefficients given in refs. 2,3 and the known fractions of beam neutrals with full, 1/2 and 1/3 energy.

The total radiation power loss in ECF heated plasmas is  $\sim 20 - 40 \text{ kW}$  corresponding to  $\sim 15 - 30\%$  of the absorbed heating power. A typical evolution of the total radiation is shown in fig. 3. An Abel-inverted profile is also given, which is compared with cooling rate predictions using 6% C, 4% O and 0.05% Fe for the impurity concentrations and assuming the same (typically hollow) profile shape for the impurities as derived for  $n_e(r)$ . With the same parameters also the X-ray profiles for the case of two filters are calculated and compared with X-ray camera data. The rather high impurity content ( $Z_{eff} \simeq 5$ ) can almost explain the observed intensities. In the lowest density plasmas the impurity level seems to be even higher, particularly in the plasma centre (peaked total radiation profiles can occur). The best cases correspond to  $Z_{eff}$ -values of  $\sim 2.5$  at higher densities obtained during 2.5 T field experiments. The influence of impurity transport effects and CX-recombination using neutral density profiles consistent with  $H_\alpha$ -measurements and

DEGAS-calculations [11] was investigated. The inclusion of these effects tend to improve the agreement between the observed total radiation profiles and the calculations, but some ambiguities in the derivation of the impurity density profiles remain. In particular, by a factor of  $\sim 2$  higher concentrations than derived with the Bragg-spectrometer calibration factor are required to model the observed total radiation and X-ray intensity.

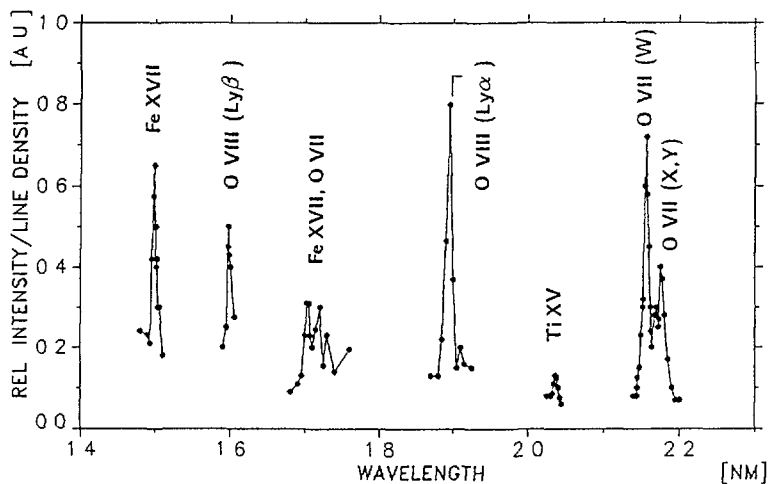


Fig. 1 Survey spectrum from Bragg spectrometer (KAP). The wavelength was scanned shot by shot.

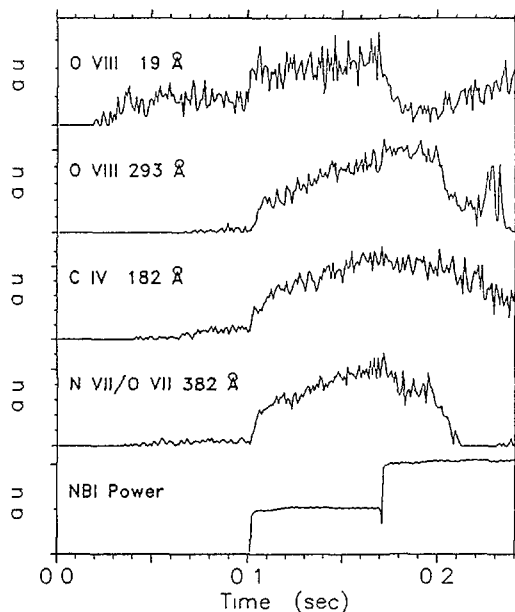


Fig. 2 CX-excited lines show a marked step, when the NBI starts.

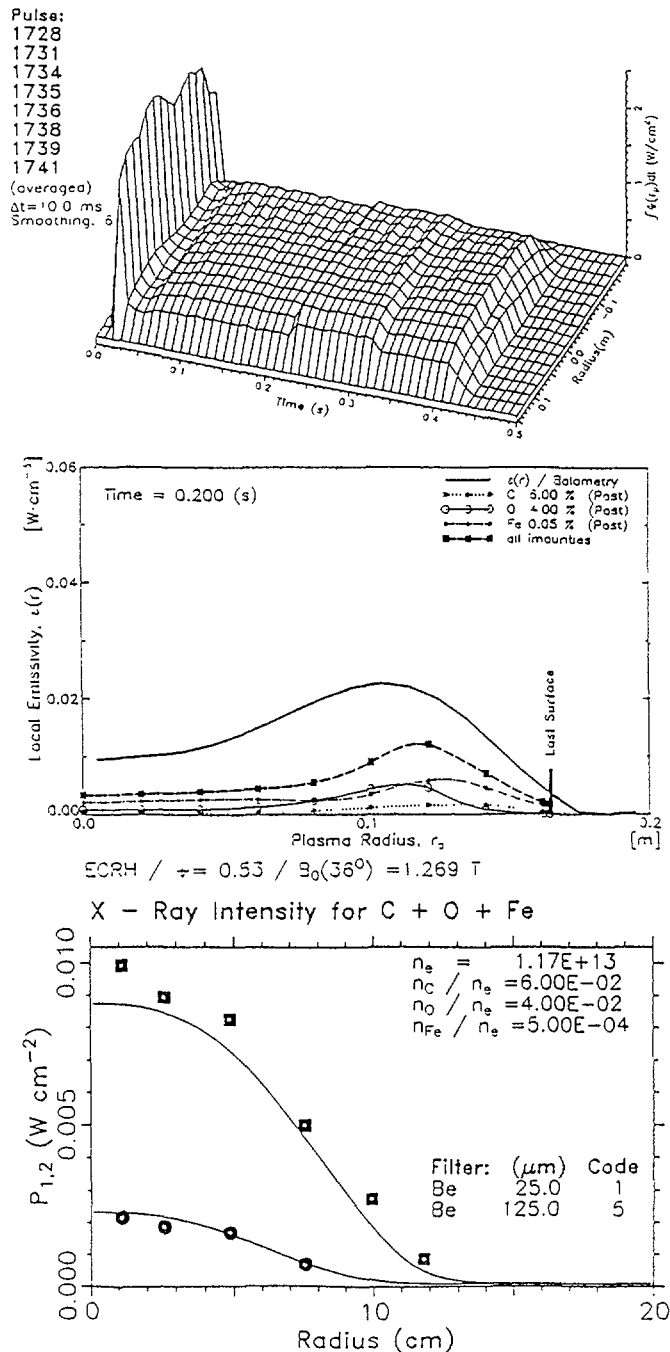


Fig. 3 Evolution of the total radiation (top) during ECRH, Abel inverted radiation profile compared with cooling rate calculations (middle) and X-ray intensities for 2 filters (symbols) compared with calculations (IONEQ).

In order to get a first estimate of the magnitude of the impurity transport and in order to see, whether the high total radiation level often seen in the plasma centre might be due to impurity density peaking, Ne was puffed into a ECRH target plasma. Observed line intensities of different Ne ionization-states are plotted in fig. 4 together with a soft X-ray signal, which serves as a monitor for He- and H-like neon radiation. A first transport calculation using a diffusion coefficient  $D = 1000 \text{ cm}^2 \text{ s}^{-1}$  approximately fits the observed time evolution. The steady state radiation profiles after Ne-injection indicate Ne density peaking, but more elaborate studies are required.

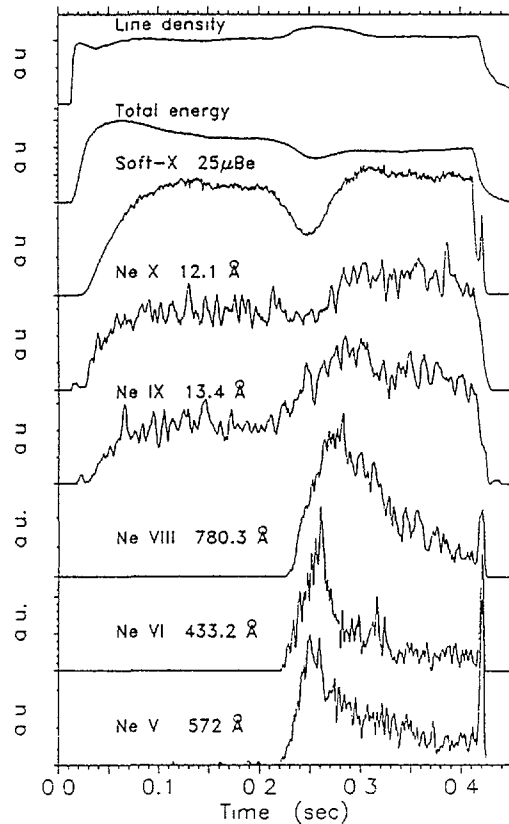


Fig. 4 Behaviour of Ne lines and X-radiation after a short Ne gas puff at 0.22 s. The effect on the line density and the plasma energy are also shown.

## 5. ELECTRON TEMPERATURE FROM X-RAY INTENSITY RATIO

The X-ray emission from the plasma sensitively depends on the electron temperature, which can be determined from intensity ratios obtained using pairs of absorber foils. The temperatures follow from comparison with the calculated  $T_e$ -dependence provided by IONEQ. In the case of light impurities the filtered radiation is mainly due to continuum radiation, which leads to the same results for O and C. If metal impurities (Fe) contribute significantly, the ratios are expected to deviate for  $T_e \gtrsim 0.7 \text{ keV}$  due to strong K-line radiation. This effect can be included in the calculations if the metal concentration is known. An example of the analysis is given in fig. 5, in which the temporal evolution of the  $T_e$ -profiles for on-axis ECF heating are compared with off-axis heating, which leads to broad and even hollow  $T_e$ -profiles. Generally the agreement with  $T_e$ -profiles from Thomson scattering is good, but at low densities and high ECF heating powers errors of the filter method can occur due to suprathermal electrons. These are generated by the ECF and their fraction can be estimated by using different filter pairs.

## SUMMARY

By using different code calculations an integrated analysis of the spectroscopic, total radiation and soft X-ray data gives first results of the impurity content in ECF and NBI heated plasmas in WVII-AS. The radiated power is not a significant loss channel due to low density operation. The impurity concentrations can be high at low densities ( $Z_{eff} \simeq 5$  typically). The agreement between measured and calculated total radiation

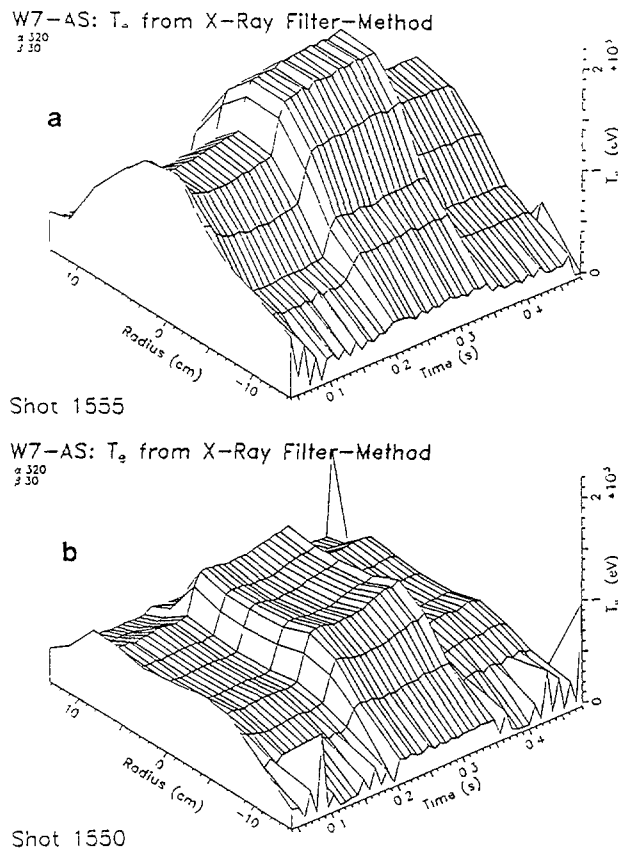


Fig. 5 Evolution of the electron temperature derived by the X-ray filter-method. Top: on-axis heating, bottom: off-axis ECF heating.

profiles is improved, if diffusive spreading, impurity density peaking and CX-recombination effects are included. First conclusions on the impurity transport have been obtained by a Ne-puff experiment. Electron temperature profiles derived from the X-ray filter method can provide additional information about the plasma dynamics, but suprathreshold electron radiation can lead to limitations of this method.

## REFERENCES

- [1] RENNER, H., WVII-AS TEAM, NBI GROUP, ICF GROUP, ECRH GROUP, Initial Operation of the Advanced Stellarator WENDELSTEIN WVII-AS, in Controlled Fusion and Plasma Physics (Proc. 16th Europ. Conf. Venice, 1989), invited talk
- [2] FONCK, R.J., DARROW, D.S., JAEHNIG, K.P., Determination of plasma ion velocity distribution via charge-exchange recombination spectroscopy, PPL Report PPPL-2067 (1983).
- [3] ISLER, R.C., Nucl. Instr. and Meth. B9 (1985) 673.
- [4] SMEULDERS, P., Soft X-ray fluxes as a diagnostic for hot plasmas, Max-Planck-Institut für Plasma-physik Garching, Rep. IPP 2/233 (1979).
- [5] KIRALY, J., BITTER, M., EFTHIMION, P., GREK, B., HILL, K.W. et al., Nucl. Fusion 27 (1987) 397
- [6] JAENICKE, R., SCHWÖRER, K., ASCASIBAR, E., GRIGULL, P., HAILER, H. et al., in Controlled Fusion and Plasma Physics (Proc. 16th Europ. Conf. Venice, 1989), Vol. 13B, Part II(1989) 627-630.
- [7] WELLER, A., PASINI, D., EDWARDS, A.W., GILL, R.D., GRANETZ, R., Modelling of Soft X - Ray emission from JET plasmas, JET Joint Undertaking internal Report JET-IR-(87)10 (1987).
- [8] WVII-A TEAM, NI-GROUP, Nucl. Fusion 25 (1985) 1593
- [9] BEHRINGER, K., Description of the impurity transport code 'STRAHL', JET Joint Undertaking Report JET-R-(87)08 (1987).
- [10] POST, D.E., JENSEN, R.V., TARTER, C.B., GRASBERGER, W.H., LOKKE, W.A., Atomic Data and Nuclear Data Tables, Vol. 20 (1977) 397.
- [11] SARDEI, F., RINGLER, H., DODHY, A., KÜHNER, G., WVII-AS TEAM, ECRH GROUP, in Controlled Fusion and Plasma Physics (Proc. 16th Europ. Conf. Venice, 1989), Vol. 13B, Part II(1989) 639-642.

## IMPURITY STUDIES AND TRANSPORT IN ATF

L.D. HORTON, E.C. CRUME, H.C. HOWE, R.C. ISLER  
Oak Ridge National Laboratory,  
Oak Ridge, Tennessee,  
United States of America

### Abstract

Impurities and impurity radiation have played important roles in the operation of ATF. Despite reducing  $Z_{eff}$  to approximately 2 by applying a variety of wall conditioning techniques, radiative collapses have not yet been avoided in neutral-beam-heated discharges. These discharges have been modeled with a transport code which solves the multi-charge-state impurity equations for flux-surface-averaged densities. The simulations reproduce the basic features of the experimentally observed line radiation and predict a collapse of the plasma temperature and density that is driven by light impurity radiation. In contrast to the one-dimensional description in the model, it appears that this collapse is initiated by a strong, poloidally asymmetric plasma-wall interaction. Specifically, strong emission is observed on the inboard side of the plasma near the helical field coil troughs.

---

## 1. INTRODUCTION

Early operation of ATF was dominated by an uncontrolled increase of the electron density followed by a rapid collapse to a low density, low temperature plasma. Attempts to improve the vessel wall conditions using electron cyclotron resonance discharge cleaning resulted in only gradual improvement of this problem. Only after the implementation of combined glow discharge cleaning in hydrogen and baking of the vessel to 150°C were essentially steady-state plasmas obtained with electron cyclotron heating (ECH). Despite these improved wall conditions, it has not yet been possible to avoid collapses in the plasma stored energy and density during heating using neutral beam injection (NBI). After the beginning of NBI the energy content of the plasma increases for typically 50–60 ms and then decreases gradually until both the energy and the electron density suddenly collapse with a simultaneous flash of light from the light impurity lines.

## 2. PLASMA AND IMPURITY MODELING

Because of the transient nature of the discharge during NBI we have incorporated our impurity models into a time-dependent transport code (PROCTR) [1]. The full

multi-charge-state impurity equations are solved in PROCTR:

$$\begin{aligned} \frac{\partial n_{Ij}^q}{\partial t} &= -\frac{1}{V_\rho'} \frac{\partial}{\partial \rho} \left( V_\rho' \Gamma_{Ij}^q \right) - \frac{n_{Ij}^q}{\tau_{\parallel Ij}} \\ &\quad + n_e n_{Ij}^{q-1} \langle \sigma v \rangle_i^{q-1} + n_e n_{Ij}^{q+1} \langle \sigma v \rangle_r^q - n_e n_{Ij}^q \langle \sigma v \rangle_i^q - n_e n_{Ij}^q \langle \sigma v \rangle_r^{q-1} \\ \Gamma_{Ij}^q &= -\langle (\nabla \rho)^2 \rangle_\psi D_{AI} \frac{\partial n_{Ij}^q}{\partial \rho} + \langle |\nabla \rho| \rangle_\psi n_{Ij}^q v_{AI} \\ n_{Ij}^{q=0} &= \frac{S_{Ij}}{n_e \langle \sigma v \rangle_i^{q=0}} \end{aligned}$$

where  $q = 1 \rightarrow Z$  for charged states of an impurity with total nuclear charge  $Z$  and  $q = 0$  for the neutral impurity density,  $\langle \sigma v \rangle_i^q$  is the rate of ionization of impurities in charge state  $q$  into charge state  $q + 1$ ,  $\langle \sigma v \rangle_r^q$  is the rate of recombination of impurities in charge state  $q + 1$  into charge state  $q$ ,  $S_{Ij}$  is the impurity source arising from ionization of wall- and limiter-evolved neutral impurities, and the  $\tau_{\parallel}$  term accounts for parallel loss of impurities to the limiter or divertor in the scrape-off layer.

Plasmas from the 1988 operating period, which are described in this paper, had significant magnetic islands outside the  $\iota = 1/2$  surface [2,3]. The modeling of these discharges is accomplished by taking  $\chi_e$  and  $\chi_i$  to be neoclassical in the plasma center and greatly enhanced in the outer part of the plasma so as to simulate the large transport due to these islands. The solutions of the individual charge state densities are then used to predict measured line strengths and the total radiated power from the plasma. The influx of impurities from the wall is found empirically by matching the predicted and measured line strengths from a sequence of similar discharges. In practice, we find that a constant impurity influx models the ECH phase of ATF plasmas quite well, while it is necessary to assume a linearly increasing influx during neutral beam heating in order to reproduce the observed emission. Figure 1 shows a comparison between model and experiment for two strong lines. The agreement is reasonable, with all of the qualitative behavior reproduced by the model. With the impurity influxes chosen to give this agreement the transport code

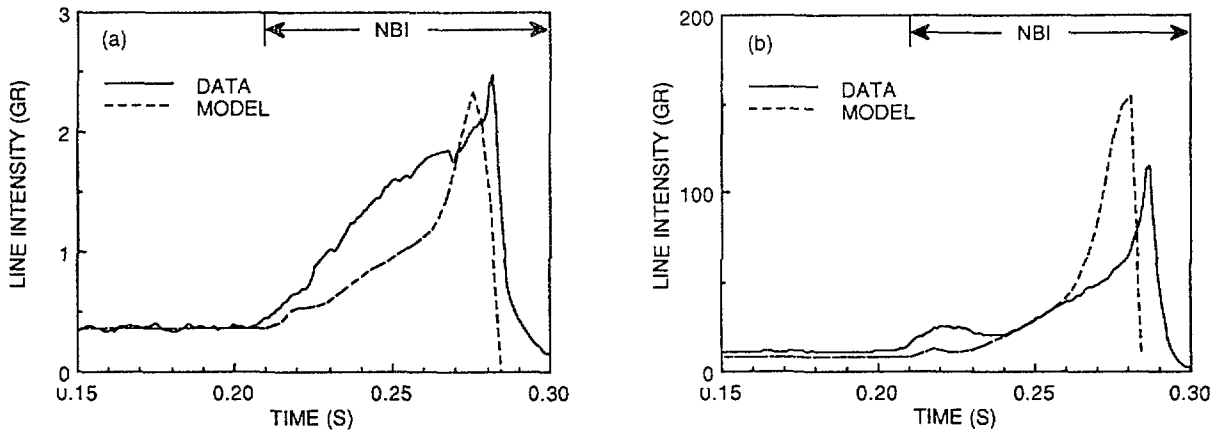


FIG. 1: Comparison between model predictions and experimentally measured line strengths of (a) C IV at 312 Å, and (b) O V at 630 Å.

also reproduces the global plasma behavior as shown in Fig. 2. The plasma stored energy initially increases with the beam heating and fueling but, after about 50 ms, the increased radiation due to the rising impurity influx begins to dominate and the stored energy slowly decreases. After the plasma reaches about 100 eV it becomes thermally unstable and collapses to a low temperature in a few milliseconds. Spectroscopic estimates of radiated power, made assuming poloidal symmetry of all emissions, agree quite well with the model predictions, at least until the final collapse of the plasma.

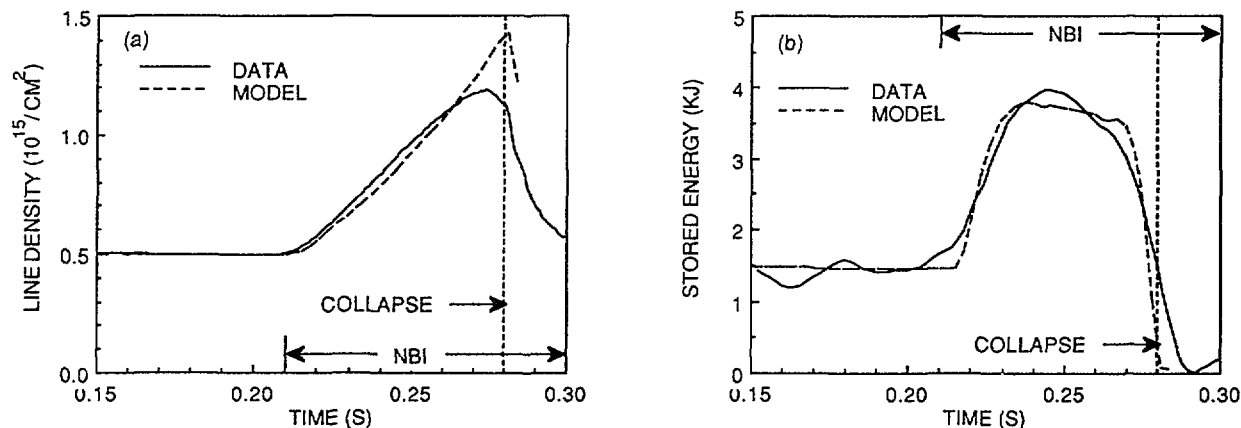


FIG. 2: Comparison between model predictions and experimentally measured global plasma parameters. (a) The line-integrated electron density is feedback controlled so as to match experiment due to uncertainties in the wall hydrogen source. (b) The model reproduces the global plasma evolution with an increase in stored energy at the onset of NBI followed by a cooling towards a radiative collapse.

### 3. ASYMMETRIES IN PLASMA EMISSIONS AND RADIATED POWER

The modeling done in PROCTR is necessarily one-dimensional and flux-surface-averaged. There is growing evidence that this assumption of symmetry is not valid just before the plasma collapse. Figure 3 shows profiles of C IV emission taken at different times during an ATF discharge. The solid curves are experimental, chord-integrated data and the dashed curves are Abel inversions of the data assuming poloidal symmetry of the emission. The first two frames, one taken during the ECH phase of the discharge and one before the peak of the plasma stored energy during NBI, are what is expected for a peripheral ion such as C IV. The inverted profiles show a strong shell near the plasma edge with the ionization stage being completely burnt out of the interior. As the plasma approaches collapse, increased signal is seen in the chords which pass through the plasma center, as shown in the third frame. If the signal were assumed to be poloidally symmetric, then the inverted profiles would indicate a substantial buildup of C IV in the plasma core. We know of no reasonable explanation for such an increase in the central C IV density and, in fact, expect the collapse of the plasma to start at the outside and propagate inward. This central signal is believed

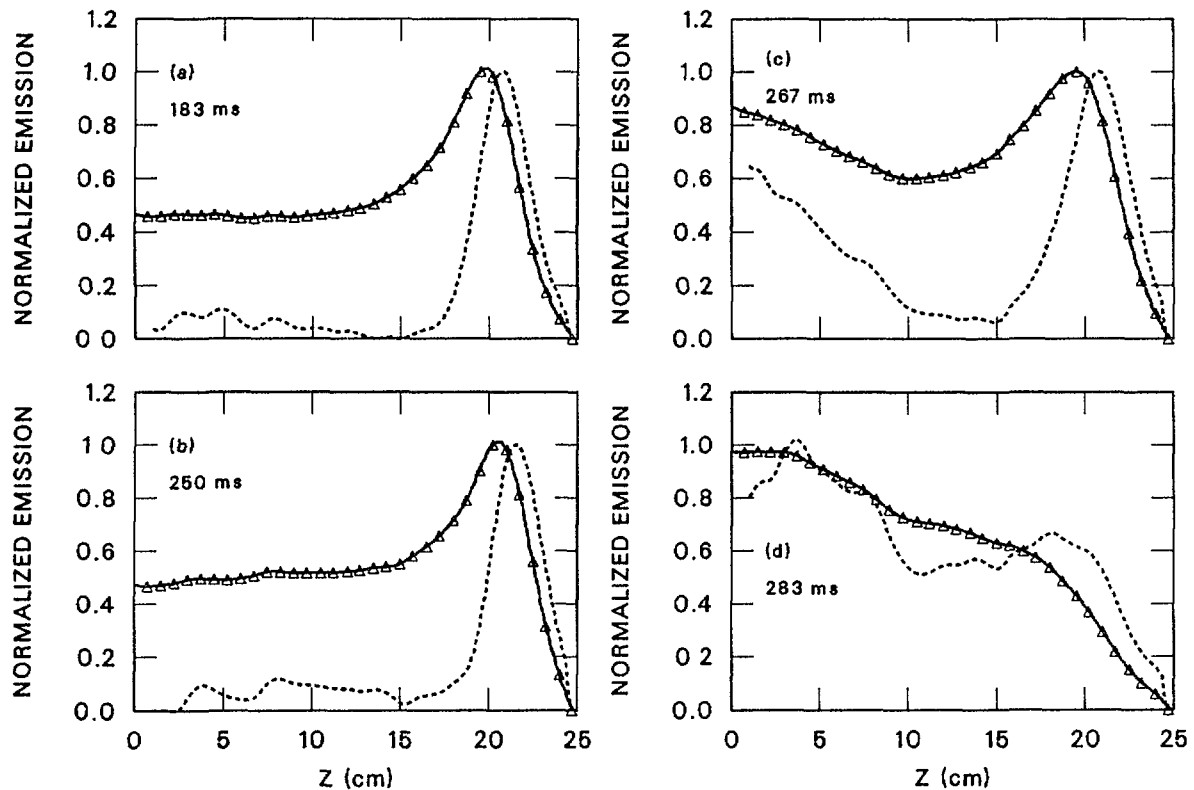


FIG 3 Experimentally measured profiles of emission from C IV. The solid curves are chord-integrated data as a function of  $Z$ , the height of the chord as it crosses  $R = 210\text{cm}$ , the nominal major radius of ATF. The dashed curves are Abel inversions of the experimental data made assuming poloidal symmetry of the emission. The increased signal in the central chords of frame (c) is interpreted as indicating strong, local emission from the inner wall of the vacuum vessel.

to be evidence of a strong increase of C IV emission on the inner wall of the vessel, possibly near one of the helical field coil troughs. This is significant because C IV is a major contributor to the total radiated power in ATF, and thus the radiated power must become strongly asymmetric around the time of the collapse. The influence of this asymmetry on the global plasma evolution is not yet clear, but it is obvious that the simple one-dimensional model in PROCTR is insufficient to model this type of plasma.

#### ACKNOWLEDGEMENTS

Work sponsored by the Office of Fusion Energy, U. S. Department of Energy, under contract DE-AC05-84OR21400 with Martin Marietta Energy Systems, Inc

#### REFERENCES

- [1] HOWE, H C., Physics Models in the Tokamak Transport Code PROCTR, Technical Memo ORNL/TM-9537, Oak Ridge National Laboratory (1985)
- [2] COLCHIN, R J., et al., in these proceedings (1989).
- [3] ANDERSON, F.S.B., et al., in these proceedings (1989).

# NEUTRAL TRANSPORT AND PLASMA BEHAVIOR IN HELIOTRON E DIVERTOR

T. OBIKI, T. MIZUUCHI, F. SANO, S. SUDO,  
H. ZUSHI, M. SATO, H. KANEKO, M. NAKASUGA,  
K. HANATANI, H. OKADA, M. IIMA, T. KAWABATA,  
H. MATSUURA, M. HARADA, M. WAKATANI, A. IYOSHI,  
K. MURAOKA<sup>1</sup>, K. UCHINO<sup>1</sup>

Plasma Physics Laboratory,  
Kyoto University,  
Gokasho, Uji, Kyoto,  
Japan

## Abstract

This paper contains the results of comparison between the experimentally measured plasma parameters at the divertor region of the Heliotron E device and the theoretical predictions based on 1D fluid model linked with 2D DEGAS code. The agreement between the observation and the simulation implies that plasma behaviour seems to be not so largely affected by a 3D helical geometry.

---

## Introduction

An intrinsic or natural divertor field configuration exists in helical systems with no additional poloidal coils. The measurement of the plasma parameters in the edge region in Heliotron E has shown that the plasma diffused from the confinement region flowed along the divertor field line, and that the plasma density and heat flux distribution at the edge region has shown good agreement with the magnetic field structure [1]. These observations suggest that the basic condition necessary to utilize the field structure as a divertor are satisfied.

The neutral transport in the divertor plasma is most essential to achieve the divertor action or to produce dense and cold divertor plasmas. The baffle plate of 1/5 toroidal length (4 helical pitches) is installed to enhance the ionization of recycling neutrals. The effect of the baffle on the neutral transport is investigated by comparing the measured plasma parameters with the results of the divertor plasma simulation code.

## Edge plasma behavior

The plasma parameters near the wall such as the plasma density,  $n_d$ , temperature,  $T_{ed}$ , and heat flux are measured using poloidal arrays of Langmuir probes and calorimeters and found to be  $n_{ed} = 10^{16} - 5 \times 10^{18} m^{-3}$ ,  $T_{ed} = 10 \sim 40 eV$  for ECH/NBI currentless bulk plasma parameters of  $\bar{n}_e = 5 \times 10^{18} \sim 2 \times 10^{20} m^{-3}$ ,  $T_{i,e} = 0.3 \sim 1.3 keV$ . The

---

<sup>1</sup> Interdisciplinary Graduate School of Engineering Sciences, Kyushu University, Kyushu, Japan.

dependences of the edge electron temperature (a) and the edge density (b) at the baffle (●) and no-baffle (○) sections on the line averaged bulk electron density are shown in Fig.1. The heating power is not constant in this figure. In general, higher power is required for higher density plasma. The edge density increases with the bulk plasma density while the edge temperature stays almost constant for  $\bar{n}_e \gtrsim 3 \times 10^{19} \text{cm}^{-3}$ . In these figures, it is shown that the edge temperature in both the baffled and non-baffled section is almost the same and the density in the baffled section is slightly higher than that in the non-baffled

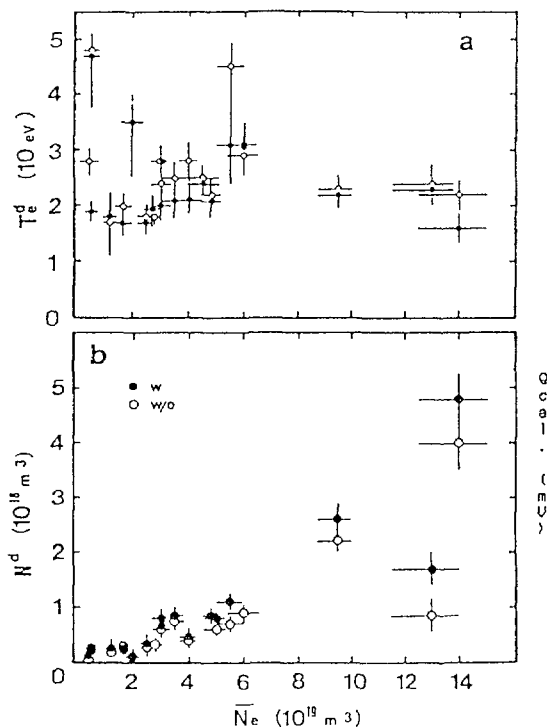


Fig 1 Edge electron temperature (a) and edge density (b) at the baffled (●) and non-baffled (○) sections as a function of the average bulk plasma density

section at higher bulk densities. The weak dependence of the edge temperature on the bulk density seems to be resulted from the selection of optimum plasma operation condition under which a good plasma confinement has been obtained. In other words, the constant edge temperature yields  $P_m/\bar{n}_e \sim \text{constant}$ , which is partly correspond to the confinement scaling of the heliotron E plasma.

Figure 2 shows the dependence of a calorimeter signal ( $\propto \int q s dt$ , q: heat flux, s: effective area of the calorimeter probe) on the port-through input energy. The signal represent approximately a total heat flux flow to the outside divertor region (fish tail region), where ▲ and □ indicate the signal at the baffled and non-baffled section, respectively. The integrated heat flux near the wall is slightly lower in the baffled section than that in the non-baffled section. The heat flux at the inside wall (fish mouth region), however, is higher for NBI-heated plasmas, especially in the perpendicular injection case.

The cord-integrated  $H_\alpha$  intensity is measured to observe the effect of the baffle plate on the neutral density at the baffled and non-baffled section. In the case of low density ECH-only plasmas, the ratio of the  $H_\alpha$  intensity in the baffled section to that in the non-baffled section is around 2, while in the case of medium density ECH/NBI plasmas, the

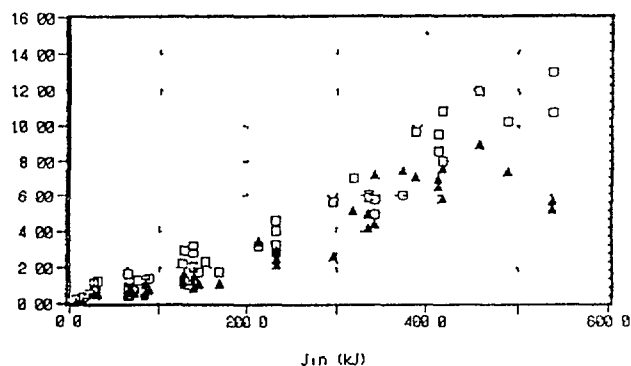


Fig 2 Time integrated heat flux at the baffled ( $\blacktriangle$ ) and non-baffled ( $\square$ ) sections as a function of the input energy

ratio is nearly 1. As mentioned above, the electron density is not largely different in both sections, this result implies that the neutral densities in the baffled and non-baffled section are different due to the effect of the baffle under some plasma conditions

### Divertor plasma simulation

In order to understand the experimental observations, the divertor plasma is calculated with use of the 1-D fluid model linked with the 2-D DEGAS code [2] for the Heliotron-E geometry in which the toroidal symmetry is assumed

The experimental set up (the baffled and non-baffled section exists together) imposes such constraint on the boundary plasma parameters at the divertor throat as to be the same because the field lines in the vicinity of the outermost magnetic surface connect the plasma in both sections. Although the simulation code assumes a fully baffled or fully non-baffled geometry, we can deduce approximately the effective behavior of the partially baffled torus with taking into account the temperature and the density to be almost constant and to be the same in both sections. It should be noted that the temperature drop or density rise in the divertor region is not so large since the ionization rate of recycling neutrals is low due to the small size geometry and the short connection length (0.5 ~ 1 m) of the field line of the Heliotron E divertor configuration

Under these conditions, the simulation analysis can well reproduce the observed edge plasma parameters and its dependences on the bulk plasma parameters. Using the plasma parameter dependence, we can estimate the input power and the particle influx into the divertor. These values can also yield the particle confinement time of the bulk plasma. Figure 3 shows an example of the particle confinement time deduced from the experimental values and calculated results as a function of the average electron density of the bulk plasma. The absolute value agrees with other measurement [3] within a factor of 2. More data will be necessary to obtain a density dependence

The heat flux on the wall can also be calculated by the simulation and it is found that the heat flux is reduced in the baffled section around 10 ~ 20 % than in the non-baffled section. This result also explain the experimental observation shown in Fig.2.

In Fig.4, the ratio of the volume integrated  $H_\alpha$  intensity in the baffled section to the non-baffled section is shown as a function of the density in the divertor region. It is shown that the ratio of the  $H_\alpha$  intensity becomes maximum of about 2 at some density and decreases as the density deviates from this density and as the power increases. The calculated property of the  $H_\alpha$  intensity ratio agrees with the observation mentioned before, and this specific feature may be attributed to the increase of the neutral density in the baffled section due to a choking effect of the baffle.

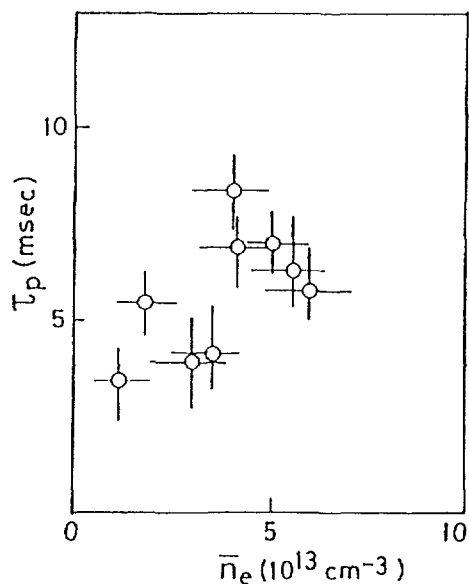


Fig.3 Particle confinement time estimated from the experimental and the simulation results as a function of the averaged bulk plasma density.

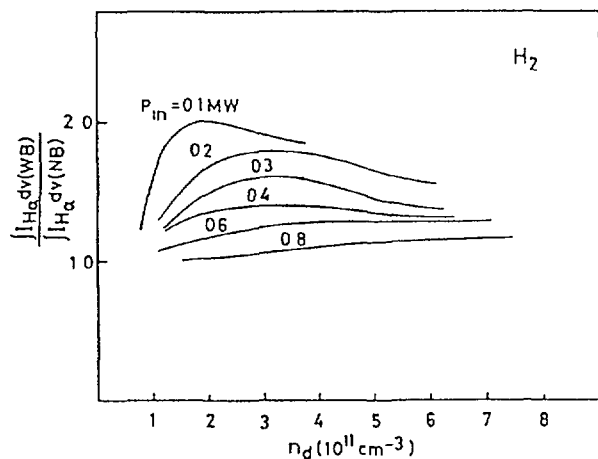


Fig.4 Intensity ratio of  $H_\alpha$  emission at the baffled and the non-baffled section as a function of the edge plasma density for several input power into the throat of the divertor.

## Discussion

The plasma parameters at the divertor region and its dependences on the bulk plasma parameters are found to be described qualitatively by a simple divertor plasma model. The divertor field structure, however, is not symmetric in the toroidal direction as adopted in the simulation. The agreement between the observation and the simulation within a factor of 2 implies that the neutral transport and the plasma behavior seems to be not so largely affected by a 3-D helical geometry in the experimental conditions, and that the essential effect of the baffle can be represented by this model. The quantitative agreement will be improved if the experimental conditions such as the asymmetric geometry in the toroidal direction and the surface condition (T; gettering etc.) be considered in the simulation.

A numerical calculation of the orbit of high energy particles corresponding to the perpendicular injection of the neutral beam shows that the loss-particle also flows toward the wall along the divertor field line[4]. The amount of the loss particle hitting the wall is larger and localized at the torus inside. This result also can explain the heat flux measurement.

In conclusion, it can be said that the natural divertor structure in helical systems can be used as a divertor if a proper choice of the field configuration and the divertor chamber design be made in large scale devices.

## References

- [1] T.Obiki, *et al.*, IAEA-CN-50/C-1-1, NICE 1988.
- [2] Physics of Plasma-Wall Interaction in Controlled Fusion, edited by D.E.Post, Plenum Publishing CO., (1986).
- [3] K.Uchino, *et al.*, J. Phys. Soc. Japan, 57, 909(1988).
- [4] T.Watanabe, private communication.

# IMPURITY STUDIES FOR THE RF HEATED PLASMA IN THE URAGAN-3 TORSATRON

V.V. VASIL'EV, V.S. VOJTSENYA, E.D. VOLKOV,  
O.S. PAVLICHENKO, G.N. POLYAKOVA,  
V.G. KONOVALOV, V.D. KOTSUBANOV, V.V. CHECHKIN,  
L.I. GRIGOR'EVA, I.K. NIKOLSKIJ  
Institute of Physics and Technology,  
Ukrainian Academy of Sciences,  
Khar'kov, Union of Soviet Socialist Republics

## Abstract

Light and heavy impurity role in the radiative losses and the metal impurity sources have studied for RF Q-discharges in the Uragan-3 torsatron. It is shown that metal impurities are responsible for radiative losses and helical winding casing are main source of metal impurities. Carbon injection experiment allowed to estimate the diffusion and flow velocity coefficients of carbon impurity in the plasma.

## 1. Introduction.

Studies of plasma produced by the RF power absorption in the region of  $\omega \simeq \omega_{ci}$  for the Uragan-3 torsatron showed that non-degrading plasmas (Q-discharges [1]) can be obtained with TiN antierrosion antenna coating only. This fact pointed out the important role of antenna generated impurities in a plasma power balance due to impurity radiation. Thus it was necessary to clear out the light and heavy impurity and antenna and helical winding impurity fluxes contribution for radiative power losses. This studies has been performed for the Q-discharges ( $B=0,45T$ ,  $n_e = 2 \cdot 10^{22} \text{ cm}^{-3}$ ,  $T_i(0) = 350 \text{ eV}$ ,  $T_e(0) = 250 \text{ eV}$ ) described in report [2].

## 2. The role of light and heavy impurities in radiative losses.

Q-discharges in the Uragan-3 torsatron are characterized by a low level of plasma radiative losses ( $P_{rad} = 6 \text{ KW}$ ) [2]. Spectroscopic measurements showed that the light (O, C) and heavy (Cr, Ni, Fe, Ti) impurity lines were observed along a line-of-sight intersecting the plasma core, ergodic magnetic layer and diverting magnetic fluxes.

The relative role of light impurities (C, O) in a plasma radiative losses was studied by the observation of plasma parameters change after injection of additional carbon flux from a massive carbon target placed at the helical winding casings surface and irradiated by a ruby laser light ( $E = 4J$ ,  $\tau = 30 \text{ ns}$ ).

The amount of injected carbon  $\Delta N_C$  was chosen to produce the measurable electron density change  $\Delta n_e$  but didn't give a visible change of the plasma energy content  $W(\frac{\Delta n_e}{n_e} \simeq 0.2$  at  $\Delta N_C \simeq 2 \cdot 10^{16}$ ). At such amount of injected carbon the 10-fold CV line intensity increase was observed but the pyroelectric detector signal

increased of 10 ± 15% only (Fig.1). It meant that the carbon radiation played no noticeable role in the radiation losses of plasma.

Measurements of the  $C\bar{V}$  line intensity increment  $\Delta I_{C\bar{V}}$ , the electron density increment  $\Delta \bar{n}_e$  and account of the fact that for the electron temperature in the discharge ( $T_e(0) \simeq 250\text{eV}$ ) helium-like carbon ions are the most representative ones ( $Z=4$ )

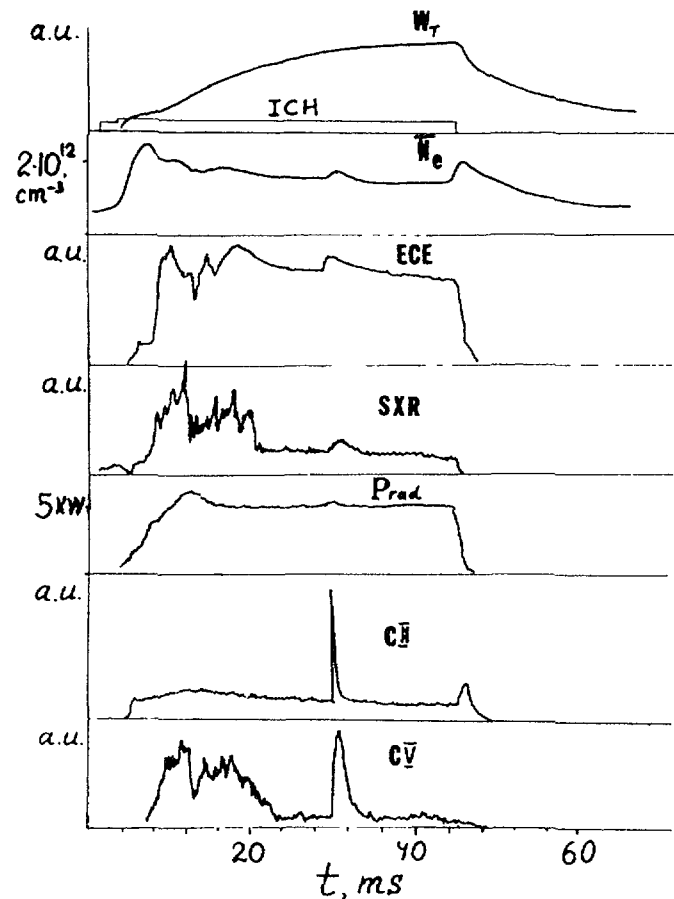


Fig. 1 Time history of plasma parameters in Q-discharge with carbon injection ( $t = 30$  ms).

allowed to obtain the upper estimate for carbon density  $\bar{n}_c$  before the injection:

$$\bar{n}_c \simeq \frac{\Delta \bar{n}_e}{Z \cdot \frac{\Delta I_{C\bar{V}}}{I_{C\bar{V}}}} \simeq 1 \cdot 10 \text{ cm}^{-3} \quad (1)$$

( $\bar{n}_e, I_{C\bar{V}}$  - electron density and  $C\bar{V}$  intensity before injection correspondingly).

Estimates of carbon ion density obtained from  $C\bar{V}$  line absolute intensity measurements agreed with estimates of (1) within an error of 50%.

Carbon radiation power calculations using data on the carbon density proved the conclusion that the carbon radiative losses didn't account for the total radiation loss power. Preliminary

estimates of the oxygen role in the radiation loss power using the OVI line absolute intensity measurements allowed to conclude that the light impurities play no noticeable role in the plasma radiative losses for Q-discharges in the URAGAN-3 toratron.

Studies of correlation between plasma radiative losses  $P_{rad}$  and spectral lines of metals from plasma periphery pointed out qualitatively (Fig.2) that helical winding casings were most probable sources of metal impurities (Cr, Ni, Fe) responsible for plasma radiative losses.

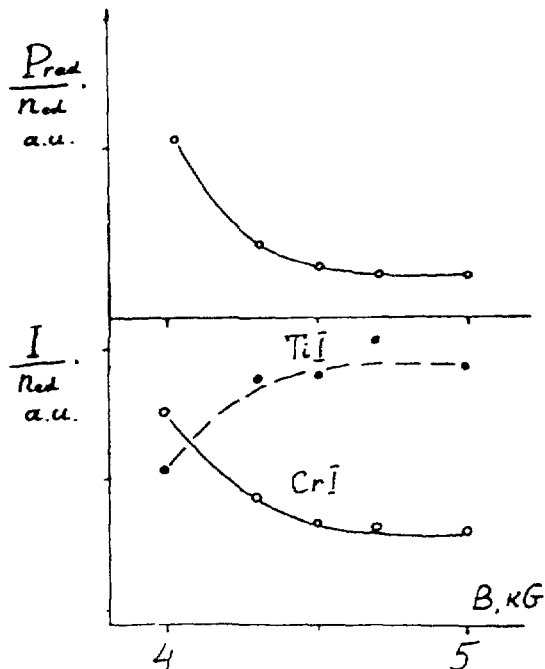


Fig.2 Normalized radiation power  $P_{rad}$  and spectral line intensities  $I$  versus magnetic field  $B$  ( $n_e$  - electron density in divertor magnetic flux).

### 3. Metal impurity release from surfaces.

To clarify the processes responsible for the metal impurity release the spectral line emission of Ti (RF antenna) and Cr I (Helical winding casing) and plasma fluxes on antenna and casing surfaces have been studied. The plasma fluxes were measured by a plane electric probes put on casings or into diverting plasma fluxes intersecting RF antenna. Plasma potential oscillations  $\phi$  ( $\omega = n \cdot \omega_{ci}$ ,  $n = 1, 2$ ) near the casing surface were studied by a capacitive probe also.

Besides 9 surface probes were placed on helical winding casing around the major circumference and the content of metal atoms (Ti, Ni, Cr, Fe) in probe sediment were measured by means of RFA and RBS technics.

Mesurements of Cr I and Ti I spectral line intensities during the hydrogen pressure scan (Fig.3) and confining field scan (fig.4) showed that intensity of Ti I was well correlated with plasma ion current in diverting flux and intensity of Cr I - with the RF oscillation amplitude  $\phi$ . The increase of RF potential oscillation amplitude was accompanied by plasma flux at helical winding casing increase.

These data allowed to make a conclusion that the metal atom release is the result of plasma ion interaction with the surfaces and that RF potential oscillations played the important role in a cross-magnetic field movement of plasma on helical winding.

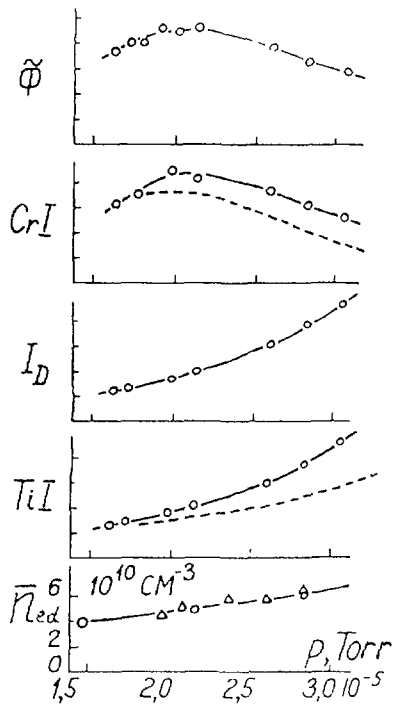


Fig.3 Potential oscillation amplitude  $\tilde{\phi}$ , spectral line intensities (Cr I and TiI), diverting plasma flux  $I_D$ , electron density in diverting flux  $\bar{n}_{ed}$  versus gas pressure P. Dashed lines-intensities normalized on  $\bar{n}_{ed}$ .

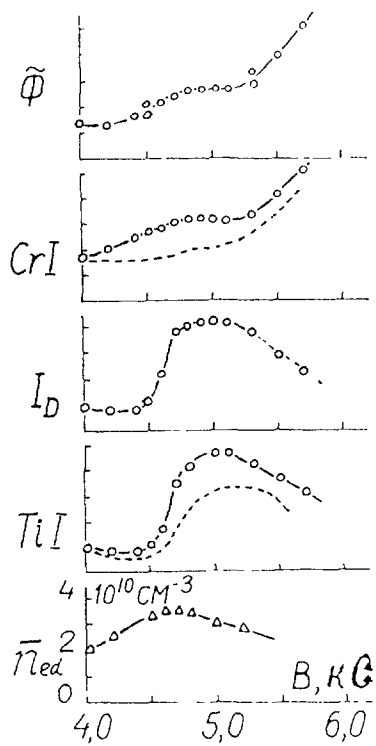


Fig.4 Potential oscillation amplitude  $\tilde{\phi}$ , spectral line intensities (Cr I and TiI), diverting plasma flux  $I_D$ , electron density in diverting flux  $\bar{n}_{ed}$  versus magnetic field B. Dashed lines-intensities normalized on  $\bar{n}_{ed}$ .

Titanium atoms distribution on surface probes was strongly inhomogeneous with a maximum near RF antenna location. This means that the atom flux from antenna surface is captured mostly by a surrounding ergodic magnetic layer plasma and transferred outside by a diverting magnetic fluxes.

#### 4. Injected carbon behaviour in a plasma core.

The injected carbon didn't accumulate in a plasma core (Fig.1). To understand this result the computer modelling of carbon impurity transport in a frame of diffusion-ionization model was performed [2]. The impurity ion flux  $\Gamma_z$  was described as  $\Gamma_z = -D \cdot \frac{dn_z}{dz} - V \cdot \frac{r}{a} \cdot n_z$  with diffusion coefficient and flow velocity  $V$  independent on  $z, r, t$ . Electron temperature and density profiles were taken from our previous experiments [2]. The computer modelling indicated that CV line time history can be accounted for only by simultaneous inclusion of the effects of diffusion and convective flow (Fig.5, dashed line). In this particular case the impurity diffusion coefficient and flow velocity  $V$  used to match the time history of CV line and to give a realistic carbon density value (for a known injected carbon amount) are of  $1.4 \cdot 10^4 \text{ cm}^2 \cdot \text{s}^{-1}$  and  $+4.5 \cdot 10^3 \text{ cm} \cdot \text{s}^{-1}$  correspondingly.\* The carbon ion density profiles  $n_z(z)$  obtained by computer calculation with available data on  $n_e, \text{Ti}$ -profiles were used for the calculation of neoclassical impurity flux at  $z = 0,5 \cdot a$ . These data were in a fairly good agreement with the flux calculations using above mentioned values of  $D$  and  $V$ .

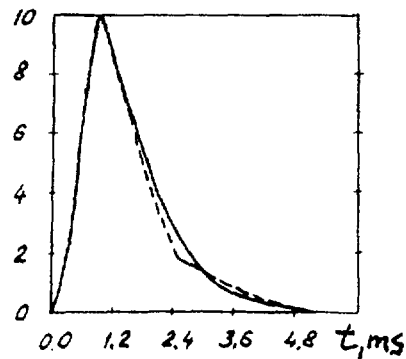


Fig. 5 Time history of CV line intensity during carbon injection (--- experiment, — calculation)

\* Our previous conclusion on existence of outward impurity flow in URAGAN-3 [3] was erroneous. These previous calculations well described the time history of CV line but gave a non-realistic low ( $\sim 10^7 \text{ cm}^{-3}$ ) carbon density.

## 5. Conclusion.

Studies of the impurity role in the Q-discharge radiation power give an indication that the light impurities played a minor role in the power loss balance and the metal impurities released from the helical winding casing rather from RF antenna are the most probable candidates for an explanation of the radiative losses. The lack of spatial distribution of radiative losses leaves this conclusion as tentative and needs additional experimental efforts.

The evaluation of the carbon injection experiment data showed that the light impurity transport in Q-discharges does not contradict to the neoclassical impurity transport predictions. The comparison of experimental data with the full neoclassical impurity transport theory calculations will allow to make more solid conclusion.

## REFERENCES

1. V.L.Berezhnyi, N.T.Besedin, M.P.Vasil'ev et al., Plasma Physics and Controlled Nuclear Fusion Research, 1986, v.2, 497(1987).
2. V.L.Berezhnyi, M.P.Vasil'ev, V.S.Voitsenya et al., Power balance studies for RF heated plasma in the Uragan-3 torsatron, this conference.
3. S.P.Bondarenko, M.P.Vasil'ev, V.S. Voitsenya et al., XII Internat.Conf.on Plasma Physics and Control.Nucl.Fus. Research, Nice (1988) CN-50/C-V-1.

## **BOOTSTRAP CURRENTS**

# BOOTSTRAP CURRENT IN STELLARATORS\*

A.H. BOOZER

College of William and Mary,  
Williamsburg, Virginia,  
United States of America

H. GARDNER

Max-Planck-Institut für Plasmaphysik,  
Garching, Federal Republic of Germany

## Abstract

The bootstrap current is the surface-averaged parallel current that is driven by the pressure gradient. It is determined by the variation of the magnetic field strength in the magnetic surface; the shape of the magnetic surfaces is irrelevant. The device dependence of the bootstrap current comes through a single quantity  $\Delta_0$ , which can be determined by a set of field line integrations.  $\Delta_0$  can also be determined using a Monte Carlo code, and it is not necessary in such a code to make the collision operator momentum conserving.

---

## Fundamental Equations

The bootstrap current is calculated using the drift-kinetic equation,  $\mathbf{v}_g \cdot \nabla f = C(f)$  with  $\mathbf{v}_g$  the guiding-center velocity of the particles and  $C(f)$  the collision operator. The most convenient form for the guiding center velocity is

$$\mathbf{v}_g = (v_{\parallel}/B) [\mathbf{B} + \nabla X(\rho_{\parallel} B)] \quad (1)$$

with the parallel gyroradius,  $\rho_{\parallel} \equiv v_{\parallel}/(eB/m)$ , taken as function of the energy  $\epsilon = mv_{\parallel}^2/2 + \mu B$ , the magnetic moment  $\mu = mv_{\perp}^2/2B$ , and position  $\mathbf{x}$ . When the fraction of trapped particles is small, which we assume in this calculation, the collision operator can be approximated by a momentum conserving Lorentz operator,

$$C(f) = \nu \frac{m}{B} v_{\parallel} \frac{\partial}{\partial \mu} \left[ \mu \left[ v_{\parallel} \frac{\partial f}{\partial \mu} + Wf \right] \right] \quad (2)$$

with  $W(\mathbf{x})$  chosen so that the parallel momentum  $mv_{\parallel}$  is conserved at each spatial location  $\mathbf{x}$ , which means that  $\int mv_{\parallel} C(f) d^3v = 0$ .

---

\* This work was partially supported by the US Department of Energy under grant DE-FG05-84ER53176.

The spatial coordinates  $\psi, \alpha, \zeta$  that simplify the calculation give a simple contravariant representation of the magnetic field,  $\mathbf{B} = \nabla\psi \times \nabla\alpha$  as well as a simple covariant representation,  $\mathbf{B} = g(\psi)\nabla\zeta + \beta_*\nabla\psi$ . The toroidal magnetic flux is  $\psi$ ,  $\alpha = \theta - \iota\phi$  with  $\theta$  a poloidal angle,  $\iota(\psi)$  the rotational transform, and  $\phi$  a toroidal angle, and

$$\zeta = [G(\psi)\phi + I(\psi)\theta]/(G + \iota I) \quad (3)$$

with  $G$  the total poloidal current outside of a pressure surface and  $I$  the toroidal current inside of a pressure surface. The quantity  $g(\psi) = \mu_0(G + \iota I)$  with  $\mu_0$  the permeability of free space. If the stellarator has no net current,  $I(\psi)$  is zero, and  $\zeta = \phi$ . The quantity  $\beta_*(\psi, \theta, \phi)$  is proportional to the pressure gradient but is essentially irrelevant in the calculation of the bootstrap current.

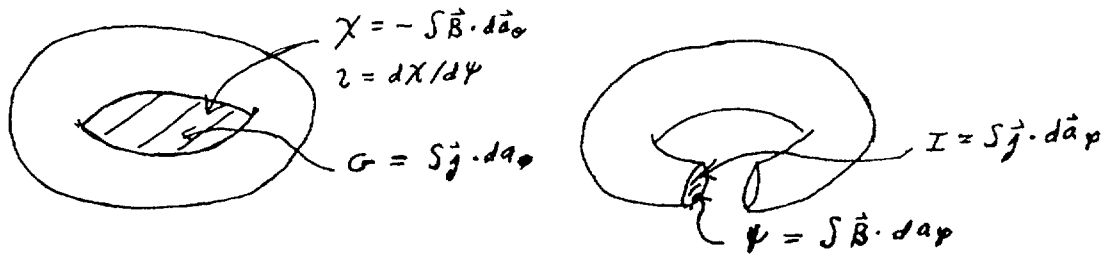


FIG. 1.

It is convenient to write the distribution function  $f(x, \epsilon, \mu)$  in terms of the displacement  $\delta$  of a particle from its home pressure surface,

$$f = f_M(\epsilon, \psi) - \delta(x, \epsilon, \mu) \partial f_M / \partial \psi, \quad (4)$$

with  $f_M$  a local Maxwellian. To leading order in  $\rho_{||}$  and  $\delta$ , one finds that

$$\frac{v_{||} B}{g} \frac{\partial f_M}{\partial \psi} \left[ - \frac{\partial \delta}{\partial \zeta} + g \frac{\partial \rho_{||}}{\partial \alpha} \right] = C(f). \quad (5)$$

The bootstrap current  $j_{bs}$  is defined in the absence of a loop voltage as

$$j_{bs}/B = \int q (v_{||}/B) \delta (\partial f_M / \partial \psi) d^3 v d\theta d\phi. \quad (6)$$

The quantity  $j_{bs}/B$  is a function of  $\psi$  alone. The factor of  $B$  is included in the definition to make the bootstrap current divergence-free,  $\nabla \cdot (j_{bs} B/B) = 0$ .

## Qualitative Solution

The salient features of the calculation of the bootstrap current can be understood from the properties of the deviation  $\delta$  of particles from their home flux surfaces. The effect of the collision operator is to make  $\delta$  independent of the pitch  $\xi \equiv \mu B_0 / \epsilon$  with  $B_0(\psi)$  the maximum value of the field on a pressure surface. The effect of the drift motion is to make  $\delta$  constant along the drift trajectory. In the long mean free path limit  $\delta$  will be as constant in pitch as it can be, consistent with being constant along the drift trajectories. As implied by equation (5), the drift trajectories, which satisfy  $\mathbf{v}_g \cdot \nabla \delta = 0$ , are given by

$$\partial \delta / \partial \zeta = g \partial \rho_{\parallel} / \partial \alpha. \quad (7)$$

If the magnetic field strength in the constant  $\psi$  surfaces depends on a single angular variable  $\Theta = \ell \theta - M \phi$  with  $\ell$  and  $M$  integers, then  $\delta$  depends on the angular coordinates only through  $\Theta$  and

$$\delta = \delta_C(\epsilon, \mu, \psi) - \mu_0 (\ell G + M I) \rho_{\parallel} / (\ell \ell - M). \quad (8)$$

The two most important cases of this symmetry are the tokamak,  $\ell=1$  and  $M=0$ , and quasi-helical symmetry,  $\ell=1$  and  $M$  equal to the number of periods. For a trapped particle,  $v_{\parallel} \approx \pm \sqrt{2\epsilon_0} v$  with  $v$  its velocity and with  $\epsilon_0$  the fractional variation in the field strength while for passing particles  $v_{\parallel}$  changes little over a surface. The displacement at the trapped-passing boundary is  $\delta_b = \sqrt{2\epsilon_0} \mu_0 (\ell G + M I) \rho / (\ell \ell - M)$ . The quantity  $\delta$ , therefore, has the form of figure (2).

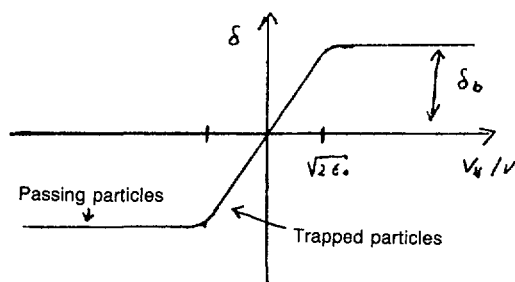


FIG. 2.

It should be noted that  $\ell - M$  is of the opposite sign for quasi-helical symmetry to that of a tokamak. This change of sign causes the bootstrap current to flow in the opposite direction in these two cases.

If the magnetic configuration is asymmetric, which means the field strength can not be expressed in terms of a single angle  $\Theta$ , the trapped particle trajectories do not close but drift across the surfaces with a step per bounce

$$\delta_s = (g/2) \int \left[ \frac{\partial \rho_{\parallel}}{\partial \alpha} \right] d\zeta \quad (9)$$

$\int \left[ \frac{\partial \rho_{\parallel}}{\partial \alpha} \right] d\zeta$ ; the loop integral is performed with  $v_{\parallel} > 0$  while integrating along the field lines from the first turning point to the second and with  $v_{\parallel} < 0$  while integrating back from the second turning point to the first. This stepping of the trapped particles dominates the transport of heat and particles in an asymmetric device, but it makes no contribution to the bootstrap current since the steps are in the same direction for either sign of  $v_{\parallel}$ . The odd part (in  $v_{\parallel}$ ) of the displacement  $\delta_0$ , which is the part that contributes to the bootstrap current, is somewhat messy for the deeply trapped particles, but for the barely trapped particles

$$\delta_b = \int_{\zeta_1}^{\zeta_2} \left\{ g \left( \frac{\partial \rho_{\parallel}}{\partial \alpha} \right) - \frac{v_{\parallel}}{[v_{\parallel}]} \left[ \left[ g \frac{\partial \rho_{\parallel}}{\partial \alpha} \right] \right] \right\} d\zeta \quad (10)$$

with  $\zeta_1$  and  $\zeta_2$  the two turning points. For passing particles,  $\delta_0 = \delta_c(\epsilon, \mu) + g \int \left( \frac{\partial \rho_{\parallel}}{\partial \alpha} \right) d\zeta$ . A plot of the odd part of the displacement  $\delta_0$  looks qualitatively like Figure (2) but the displacement of the barely trapped particles,  $\delta_b(\epsilon, \zeta)$  is not simply related to the fraction of trapped particles as it is in symmetric configurations.

The quantity  $\Delta_0$ , which characterizes the bootstrap current, is given by  $\Delta_0 = \Delta(\xi=0)$ , remember  $\xi = \mu B_0 / \epsilon$ . There is a complicated expression for  $d\Delta/d\xi$  in the passing particle region  $1 > \xi > 0$ , but the actual change in  $\Delta$  is small compared to  $\Delta_b = \Delta(\xi=1)$ , which is a field line average of  $\delta_b$ ,  $\Delta_b = (3eB_0/2gmv) \int \left[ \delta_b \right] / (\zeta_2 - \zeta_1)$ .

The bootstrap current is then

$$j_{bs} = - \Delta_0 \frac{g}{B_0} \left[ 1.67 (T_e + T_i) \frac{dn}{d\psi} + 0.47 n \frac{dT_e}{d\psi} - 0.29 n \frac{dT_i}{d\psi} \right]. \quad (11)$$

Numerical calculations have been made for a number of field configurations.

# BOOTSTRAP CURRENT CONTROL AND THE EFFECTS OF THE RADIAL ELECTRIC FIELD IN STELLARATORS\*

K.C. SHAING, B.A. CARRERAS, E.C. CRUME,  
N. DOMINGUEZ, S.P. HIRSHMAN  
Oak Ridge National Laboratory

V.E. LYNCH, J.S. TOLLIVER, W.I. VAN RIJ  
Computing and Telecommunications Division,  
Martin Marietta Energy Systems, Inc.

Oak Ridge, Tennessee,  
United States of America

## Abstract

The effects of the radial electric field  $E_r$  on the bootstrap current in ATF-type configurations are studied with the Drift Kinetic Equation Solver (DKES). It is found that there is a range of  $E_r$  values over which the bootstrap current does not depend on  $E_r$ . The effects of  $E_r$  on the bootstrap current are due to the resonance between the parallel velocity and the poloidal  $\mathbf{E} \times \mathbf{B}$  drift.

The poloidal coil system of a stellarator can be used to modify the  $|\mathbf{B}|$  spectrum and, as a consequence, change the magnitude of the bootstrap current. The addition of a small  $\ell = 1$  field component to a stellarator field can cancel or reverse the direction of the bootstrap current. It is shown that currentless operation in the collisionless regime is not impaired by the bootstrap current, because the effects of the bootstrap current can be eliminated by an appropriate external coil system. These results can be tested in ATF.

---

## 1. INTRODUCTION

The magnitude of the bootstrap current is an important issue for stellarator reactors. Because stellarator reactors are ideally operated in the currentless mode, it is desirable to minimize the magnitude of the bootstrap current. Bootstrap currents have been measured in a levitated toroidal octupole [1] and in several stellarator/heliotron devices, including Heliotron-E, Wendelstein VII-A, and Proto-Cleo [2-4]. Recently, it was reported that bootstrap currents also exist in the Tokamak Fusion Test Reactor (TFTR) [5]. In these experiments, bootstrap currents were identified indirectly.

Very few experiments have been performed to establish the scalings of these inferred bootstrap currents with plasma parameters, especially with geometric factors such as aspect ratio. One purpose of this paper is to demonstrate that such experiments could be performed in stellarator devices by controlling the externally imposed magnetic fields. These experiments could provide direct evidence for the existence of bootstrap currents in toroidal plasmas and test the origin of the current (i.e., whether it is neoclassical or induced by instabilities [6]). The Advanced Toroidal Facility (ATF) configuration [7] is used here as a specific example. We find that, with appropriately adjusted currents in the ATF vertical magnetic field coils, we can change the magnitude and even the direction of the bootstrap current by unbalancing the currents in the helical magnetic field coils.

The bootstrap current does not change the equilibrium flux surfaces very much. However, if it is large enough, it can modify the radial profile of the rotational transform  $\iota$  and thus affect the stability of the equilibrium. This effect can be remedied by choosing a configuration that either gives rise to an appropriate  $\iota$  profile when the bootstrap current is included or has no bootstrap current at all. The feasibility of these approaches is demonstrated here.

---

\* Research sponsored by the Office of Fusion Energy, US Department of Energy, under contract DE-AC05-84OR21400 with Martin Marietta Energy Systems, Inc.

The effects of the radial electric field  $E_r$  on the bootstrap current in stellarators are also discussed. It is shown that for  $e\Phi/T$  of the order of unity, the bootstrap current in ATF is not affected by  $E_r$ . Here,  $\Phi$  is the equilibrium potential and  $T$  is plasma temperature. However, such effects could become important in stellarators with aspect ratio larger than that of ATF.

## 2. ANALYTIC EXPRESSION FOR BOOTSTRAP CURRENTS

An approximate analytic formula for the bootstrap current in a stellarator can be written as [8]

$$\begin{aligned} \langle BJ_{\parallel} \rangle_b &= -\sigma_{\text{eff}} (M_e \nu_e / N e^2) (f_t / f_c) c \tilde{G}_b \mu_{1e} \\ &\times \left[ \left( 1 + \frac{\ell_{12}^{eb} \mu_{2e}}{\ell_{22}^{eb} \mu_{1e}} \right) \left( P' + N T'_i \frac{\ell_{22}^i \mu_{2i}}{|\mu_{1i} \nu_i N M_i f_i / f_c + \ell_{22}^i \mu_{1i}} \right) \right. \\ &\left. + \frac{\mu_{2e}}{\mu_{1e}} \left( 1 + \frac{\ell_{12}^{eb} \mu_{3e}}{\ell_{22}^{eb} \mu_{2e}} \right) N T'_e \right] \end{aligned} \quad (1)$$

where  $P' = P'_e + P'_i$ , the geometric factor

$$\begin{aligned} \tilde{G}_b &= \langle H_1 \rangle + \frac{H_2}{2} \langle B^2 \rangle \frac{G + \iota I}{B_0^2 \iota} - \frac{f_c}{f_t} q \frac{G + \iota I}{B_0^2 \iota} \langle g_{\gamma} B^2 \rangle \\ &- \frac{3}{4} \frac{q}{f_t} \frac{G + \iota I}{B_0^2 \iota} \int_0^1 d\lambda \frac{\lambda W(\lambda)}{\langle |v_{\parallel}| / v \rangle} \end{aligned} \quad (2)$$

and the effective plasma conductivity is

$$\sigma_{\text{eff}} = (N e)^2 \frac{\ell_{22}^{eb}}{\ell_{11}^{eb} \ell_{22}^{eb} - (\ell_{12}^{eb})^2} \quad (3)$$

The various symbols are defined in Ref. [8].

In the limit where  $f_t/f_c \ll 1$ , we can approximate  $\ell_{11}^{eb} \simeq \ell_{11}^e$ ,  $\ell_{12}^{eb} \simeq \ell_{12}^e$ ,  $\ell_{22}^{eb} \simeq \ell_{22}^e$ , and  $\sigma_{\text{eff}} \simeq \sigma_s$ , the Spitzer conductivity, and obtain the previous expression of  $\langle BJ_{\parallel} \rangle_b$  for large-aspect-ratio toroidal systems. In the opposite limit, where  $f_t/f_c \gg 1$ , we have

$$\sigma_{\text{eff}}|_{f_t/f_c \gg 1} = \frac{\mu_{3e}}{\mu_{1e} \mu_{3e} - \mu_{2e}^2} \frac{N e^2 f_c}{M_e \nu_e f_t} \quad (4)$$

and

$$\langle BJ_{\parallel} \rangle_b|_{f_t/f_c \gg 1} = -c \tilde{G}_b P' \quad (5)$$

We see that in the low-aspect-ratio limit the plasma conductivity  $\sigma_{\text{eff}}$  is linearly proportional to  $f_c/f_t$  and vanishes as  $f_c \rightarrow 0$ . The bootstrap current is simply the difference between the electron and ion diamagnetic flows, weighted by the appropriate geometric factor  $\tilde{G}_b$ .

In the axisymmetric limit, both  $\langle g_{\gamma} B^2 \rangle$  and the term involving  $W(\lambda)$  in the expression of  $\tilde{G}_b$  are zero, and we have

$$\tilde{G}_b|_{\text{symmetric}} = \langle H_1 \rangle + \frac{H_2}{2} \langle B^2 \rangle \frac{G + \iota I}{B_0^2 \iota} \quad (6)$$

Equation (6) is valid for all finite-aspect-ratio systems, including axisymmetric tokamaks and helically symmetric stellarators. We note, however, that the finite-aspect-ratio effects discussed here are not complete for nonaxisymmetric systems because the collisionless detrapping/retrapping effects are not taken into account.

### 3. BOOTSTRAP CURRENT CONTROL IN STELLARATORS

In a nonaxisymmetric device, the geometrical factor  $\tilde{G}_b$  depends sensitively on the magnetic field spectrum. In a stellarator, the magnetic field is created externally; thus, the spectrum can be modified by the use of an external coil system. With external control of the  $\tilde{G}_b$  factor, one can test the theory of the bootstrap current and determine if the neoclassical mechanism is the only cause for the bootstrap current.<sup>6</sup>

We first consider the effect of the bootstrap current on  $\epsilon$ . As shown in Ref. [8], the bootstrap current in a stellarator is smaller than that in the equivalent tokamak (axisymmetric limit of the  $|\vec{B}|$  expansion) because the geometrical factor  $|(\tilde{G}_b)_{\text{stellarator}}| < |(\tilde{G}_b)_{\text{tokamak}}|$ . Thus, any change in  $\epsilon$  caused by the bootstrap current is expected to be less important in a stellarator. However, Ohkawa and Chu [9] pointed out that the difference in aspect ratio between typical tokamaks and stellarators could compensate for the effect of the geometrical factor  $\tilde{G}_b$ . Their estimate does not consider other differences between tokamaks and stellarators: the two types of devices have different  $\epsilon$  scalings in the sense that  $\epsilon$  scales as the aspect ratio in a stellarator while it is practically constant in tokamaks, and, more importantly, they have different  $\epsilon$  profiles. When all of these factors are taken into account, one concludes that the effect of the bootstrap current on  $\epsilon$  is larger in a tokamak than in a stellarator. This is illustrated in Fig. 1, where we compare  $\Delta\epsilon/\epsilon$  for the standard ATF configuration [7] and for a "classical" tokamak (with an aspect ratio of 4,  $q(0) = 1$ , and  $q$  at the edge of 3.5). For both cases, the pressure profile is the same,  $\langle\beta\rangle = 3\%$ , and the plasma has been assumed to be in the collisionless regime over the whole cross section.

In ATF, the change in  $\epsilon$  can be compensated for by using the poloidal coil system [10]. Several 3-D free-boundary equilibria have been calculated with the VMEC code [11] for different values of the quadrupole field of the poloidal coil system. The equilibria were calculated for a pressure profile  $p \sim \psi^2$  and  $\beta_0 = 6\%$ , with the corresponding current profile given by the bootstrap current. These equilibria thus have a net current. Figure 2 shows the transform profile for three different cases: a case without bootstrap current, a case with bootstrap current, and a case with bootstrap current and an added quadrupole field that approximately cancels the change in the transform due to the bootstrap current. This shows a way of compensating for the effects of bootstrap current on the transform. In Fig. 3, the flux surfaces corresponding to the three equilibria are shown. The effect of the bootstrap current on the magnetic surfaces is weak.

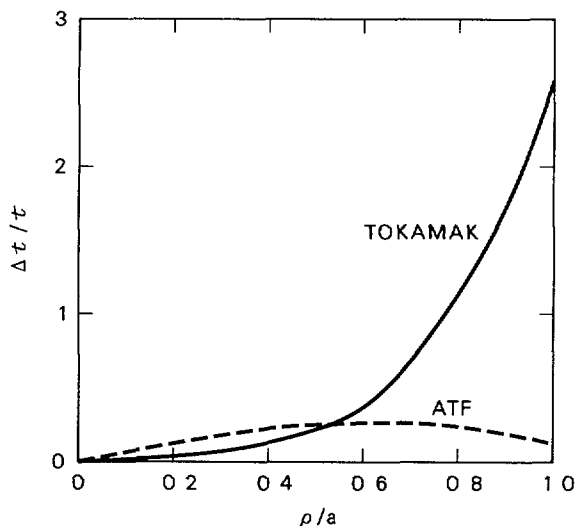


FIG. 1. Relative change of rotational transform in a tokamak and in a stellarator. The pressure profile is the same for both configurations with  $\langle\beta\rangle = 3\%$

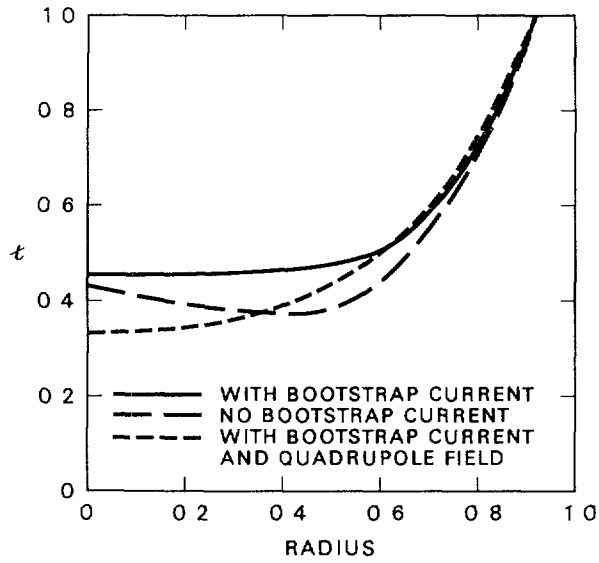


FIG 2 Rotational transform profile for  $\beta_0 = 6\%$ , zero-current equilibria with and without bootstrap current for ATF

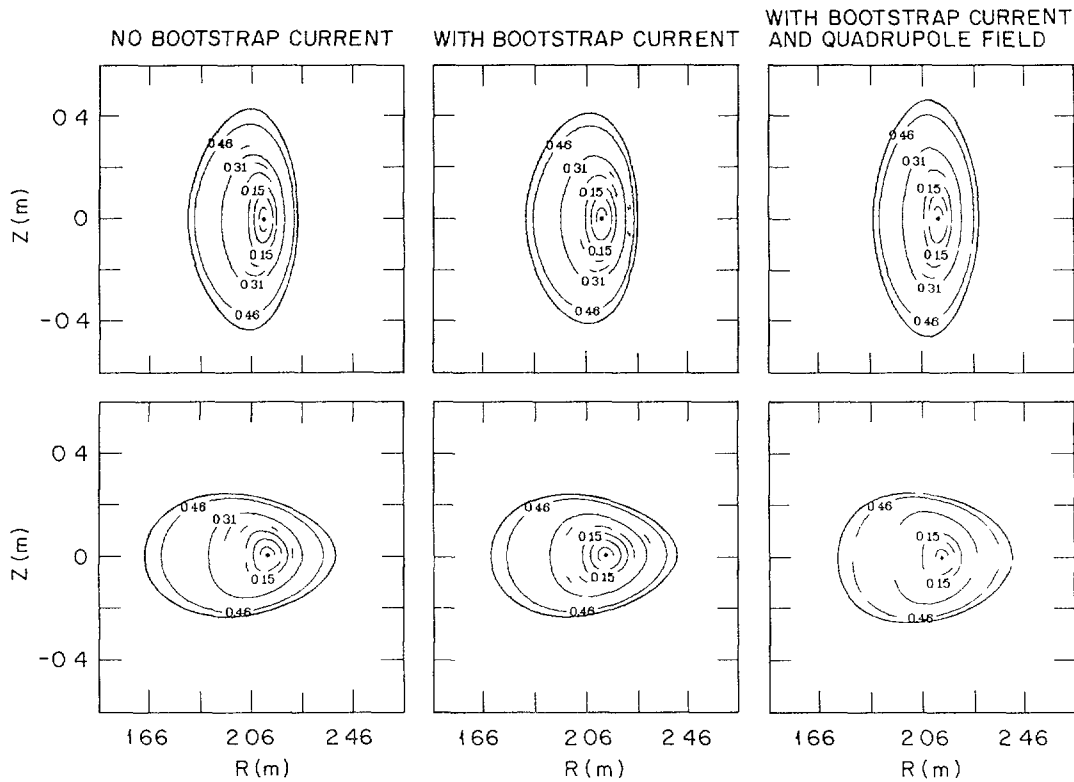


FIG 3 Flux surfaces for the equilibria in Fig 2

An  $\ell = 2$  torsatron coil system with an even number of toroidal field periods has three main external “knobs” to change the confining magnetic field: the dipole and quadrupole moments of the poloidal coil system and the currents in the two helical coils. The first two add an axisymmetric field; the third, an  $\ell = 1$  helical field that has half the number of field periods of the coil system. However, because of nonlinear couplings,

changing these “knobs” alters the spectrum of  $|\vec{B}|$  and, thus, the value of the  $\tilde{G}_b$  factor. The effect of changing these fields on  $\tilde{G}_b$  is considered for ATF parameters. In these calculations, the geometrical factor  $\tilde{G}_b$  is normalized to its axisymmetric limit, that is,  $G_b \equiv \tilde{G}_b/(\tilde{G}_b)_{\text{axisymmetric}}$ . To calculate the induced current once the  $G_b$  profile is known, we assume that the plasma is in the collisionless regime and the pressure profile is  $p = p_0[1 - (r/\bar{a})^2]^2$ .

The effect on  $G_b$  of changing the quadrupole moment of the poloidal coils is shown in Fig. 4(a). In this figure,  $I$  is the current in the poloidal coils, normalized to the current in the helical coils, which controls the quadrupole moment of the coil system. The range of values for  $I$  is compatible with design values of ATF. For the standard ATF configuration ( $I = 0$ ),  $G_b \sim 0.4$ . This value can be increased up to  $G_b \sim 0.5$  or reduced to practically zero by changing  $I$ . The sign of quadrupole moment required to reduce the bootstrap current is the same as that required to achieve approximate flux conservation and zero current for high- $\beta$  operation [10]. Thus, at high  $\beta$ , zero-current operation can be approximately maintained even in the presence of bootstrap current. In Fig. 4(b), the induced plasma current for  $\langle\beta\rangle = 1\%$  is plotted for the different values of the quadrupole moment.

Unbalancing the currents in the helical coils induces an  $\ell = 1$ ,  $M = 6$  magnetic field component in ATF. This causes a helical excursion of the magnetic axis. Using the radius of the helical excursion of the magnetic axis  $r_h$  as a measure of this  $\ell = 1$  component, we plot  $G_b$  as a function of  $r_h$  in Fig. 5(a). With a helical axis radius of the order of 10% of the plasma radius,  $G_b$  (and the bootstrap current) can be reduced to practically zero, Fig. 5(b). With a larger helical axis radius, the bootstrap current reverses direction. This offers one of the best ways to experimentally test the properties of the bootstrap current. However, it is not the easiest way. The results in Fig. 5 correspond to a case in which a quadrupole field with  $I = 0.13$  has been applied to minimize the helical excursion of the magnetic axis in cancelling the bootstrap current.

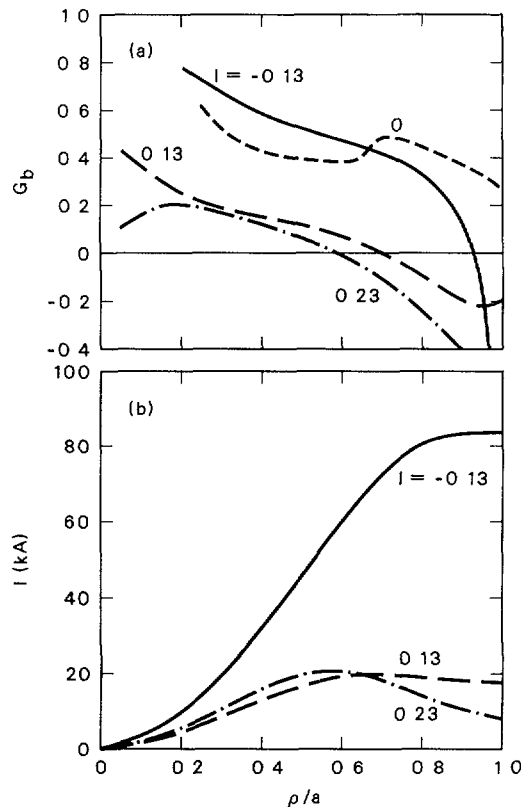


FIG. 4. Effect of a quadrupole field on (a) the geometrical factor of the bootstrap current and (b) the integrated bootstrap current as a function of the average minor radius.

The magnitude of the bootstrap current can also be changed by changing the dipole moment of the poloidal field coils. This change manifests itself in a shift of the vacuum magnetic axis,  $\Delta$ . Figure 6 shows the change of  $G_b$  when the magnetic axis is shifted 5 cm inward or outward in ATF. This offers the simplest experimental test of the theory.

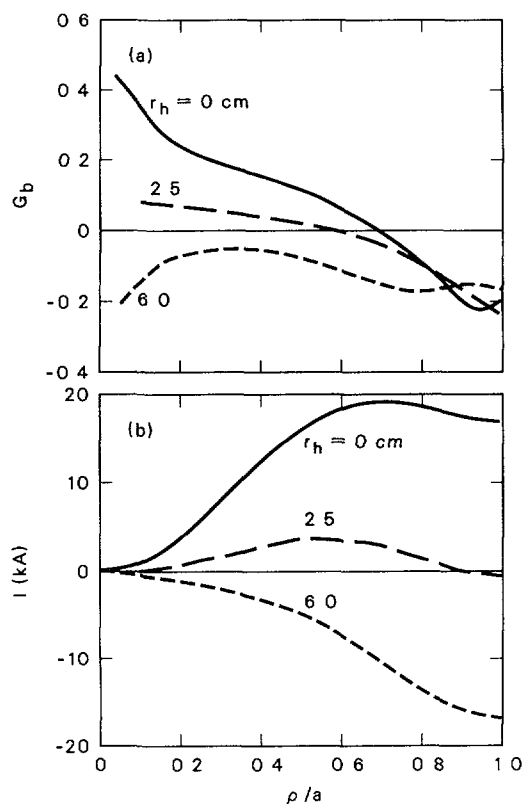


FIG. 5. Effect of a helical excursion of the magnetic axis on (a) the geometrical factor of the bootstrap current and (b) the integrated bootstrap current as a function of the average minor radius.

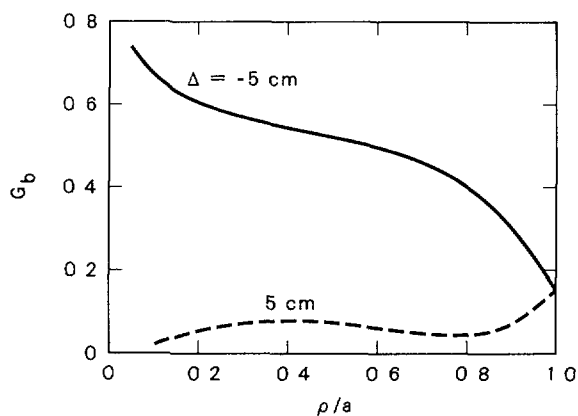


FIG. 6. Effect of a dipole field on the geometrical factor of the bootstrap current.

#### 4. NUMERICAL COMPARISON WITH DKES RESULTS

For a given magnetic field spectrum

$$\frac{B}{B_0} = 1 + \sum_{\substack{n,m \\ \neq 0}} \epsilon_{nm} \cos(n\theta - m\zeta) \quad (7)$$

we can evaluate Eq. (1) to obtain the bootstrap current of the corresponding toroidal magnetic confinement system. These analytic expressions can be shown to reproduce all known results for symmetric systems such as tokamaks and straight stellarators [1,3,7]. To investigate the validity of these expressions for nonaxisymmetric systems, we evaluate them numerically for a model stellarator magnetic field spectrum,

$$\frac{B}{B_0} = 1 - \epsilon_t \cos \theta - \epsilon_h \cos(2\theta - 12\zeta) \quad (8)$$

and compare the results with those obtained using DKES [13].

In Fig. 7, we show the collision frequency dependence of the stellarator bootstrap current  $(j_b)_s$  for the magnetic field spectrum of Eq. (8). Also shown in Fig. 7 is the bootstrap current  $(j_b)_{\text{ESD}}$  for an equivalent symmetric device (ESD), which has a magnetic field spectrum

$$B/B_0 = 1 - \epsilon_t \cos \theta, \quad (9)$$

where  $\epsilon_t$  and the safety factor  $q$  are the same as those of the model stellarator. As can be seen in Fig. 7, the directions of  $j_b$  for the stellarator  $(j_b)_s$  and its ESD  $(j_b)_{\text{ESD}}$  are opposite to each other in the high collision frequency (plateau) regime, in agreement with the results obtained in Ref. [14]. In the low collisionality regime where  $\nu_{\text{eff}} \simeq \nu/\epsilon_h \ll \Omega_E$ , the poloidal  $\mathbf{E} \times \mathbf{B}$  frequency, the value of  $(j_b)_s$  is insensitive to the values of the radial electric field. It is this "saturated state" for which the analytic expressions given in Eq. (2) are valid. Between the saturated state and the plateau regime there is a transition regime in which  $(j_b)_s$  is sensitive to the value of the radial electric field. In this regime, the bootstrap current is likely to be dominated by the contribution from the boundary layer solution discussed in Ref. [15]. The range of the transition regime becomes smaller as the magnitude of  $\mathbf{E}$  increases. The sensitivity of  $(j_b)_s$  around  $\nu/\omega_t \sim 2 \times 10^{-3}$  results mainly from the fact that the magnitude of  $\mathbf{E}$ , and therefore the range of the transition regime, differs for the three cases shown. Also shown in Fig. 7, the transition from the plateau regime to the saturated state begins near  $\nu_{\text{eff}}/\Omega_E \simeq 1$ .

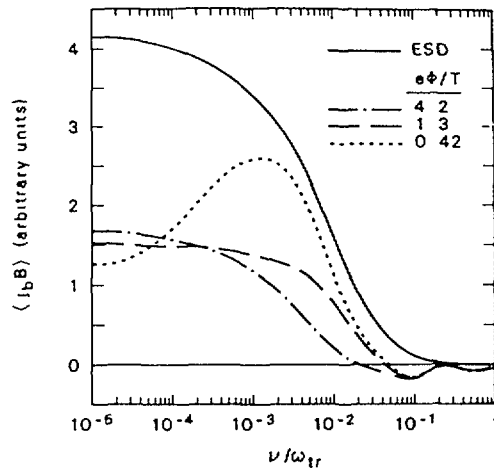


FIG. 7.  $(j_b B)$  versus collision frequency for several values of  $e\phi/T$ , where  $\bar{a}$ , the electric field scale length, is 0.3 m, representative of the Advanced Toroidal Facility (ATF). Model magnetic field spectrum with  $\epsilon_t = 0.11$ ,  $\epsilon_h = 0.14$ , and  $q = 1.5$ . For the ESD,  $\epsilon_t = 0.11$  and  $q = 1.5$ .  $\omega_t$  is the transit frequency.  $T_e = T_i = 1$  keV.

The profile of the ratio  $(j_b)_s/(j_b)_{\text{ESD}}$  calculated from Eq. (1) is shown in Fig. 8 for the  $\epsilon_t$ ,  $\epsilon_h$ , and  $q$  profiles of Fig. 9. Also shown in Fig. 8 are DKES results for several selected radial points. As can be seen from the figure, the results agree qualitatively. We note that, since only a pitch-angle scattering operator is employed in DKES, the absolute magnitude of the bootstrap current obtained using DKES is accurate only to order unity. However, the effects of collisionless detrapping/retrapping and some finite-aspect-ratio corrections are included in DKES but not in the analytic formula. The quantitative agreement seen in Fig. 8 should be regarded as to within a factor of order unity only.

We examine the effects of the radial electric field  $E_r$  on the bootstrap current with the model magnetic field given in Eq. (8) and the  $\epsilon_t$ ,  $\epsilon_h$ , and  $q$  profiles shown in Fig. 9. The bootstrap currents at various radii are evaluated with DKES for several values of  $E_r$ . The results are shown in Fig. 10. At a given radius, there is a plateau regime over which the bootstrap current is not sensitive to  $E_r$ . In this plateau regime, the analytic theory is approximately applicable. At large values of  $E_r$ , the bootstrap current becomes dependent on  $E_r$ . The effects of  $E_r$  on the bootstrap current are caused by the resonance between particle parallel speed  $v_{\parallel}$  and poloidal  $\mathbf{E} \times \mathbf{B}$  drift. When the bootstrap current becomes dependent on  $E_r$ , the particle flux also deviates from its normal  $E_r^{-2}$  dependence, as shown in Fig. 11. We note that the range of  $e\Phi/T$  over which the bootstrap current does not depend on  $E_r$  becomes smaller at a smaller radius. This indicates that, in a large-aspect-ratio stellarator, bootstrap current is more sensitive to  $E_r$ . In ATF, for  $e\Phi/T$  in the range between 1 and 3, the bootstrap current is not sensitive to  $E_r$ .

## 5. DISCUSSION AND CONCLUSION

The stellarator configuration is a convenient toroidal confinement system in which to test predictions from neoclassical theory about the bootstrap current. The coil system of the ATF device is flexible enough to perform such tests. The main problem in doing these tests is the amount of heating power required to operate at a relevant  $\beta$  value in the collisionless regime. Estimates based on experimental results from Wendelstein VII-A indicate that it should be possible to produce the appropriate conditions by operating at low density in plasmas with electron cyclotron heating. In addition, calculations using Heliotron-E parameters for neutral beam injection and operation at 2 T give bootstrap current levels above 5 kA. In plasmas with neutral beam injection, beam-driven currents could obscure the measurements. However, the different density scalings of the bootstrap current and the beam-driven current permit the separation of these current components if measurements are made at different densities.

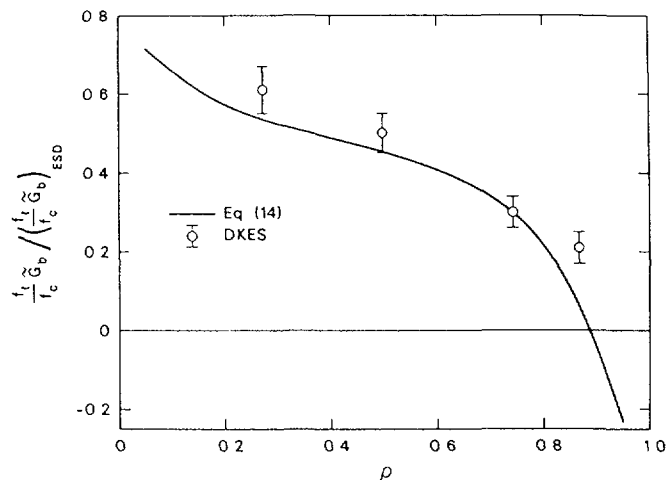


FIG. 8. Profile of the ratio of the stellarator bootstrap current  $(j_b)_s$  to the ESD bootstrap current  $(j_b)_{\text{ESD}}$  for the model magnetic field spectrum for the profiles of  $\epsilon_t$ ,  $\epsilon_h$ , and  $q$  given in Fig. 3. The normalized radial coordinate is  $\rho$ . For  $\rho \gtrsim 0.89$ ,  $q \lesssim 1$ , the results have questionable relevance.

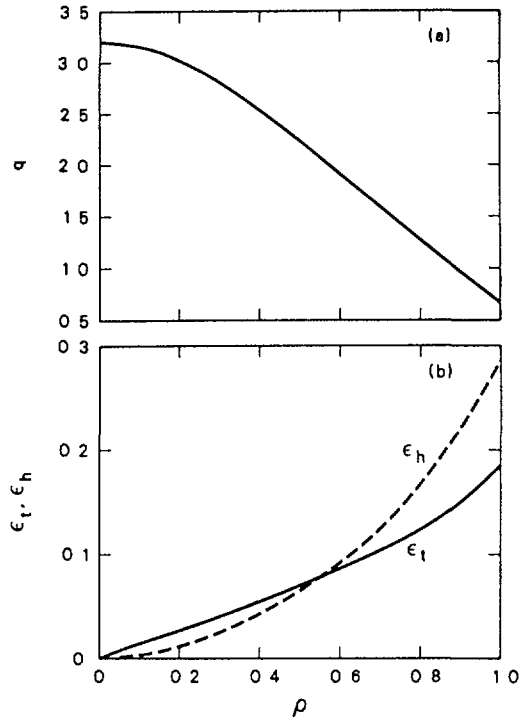


FIG. 9. (a) Profile of  $q$  for model calculations (b) Profiles of  $\epsilon_t$  and  $\epsilon_h$  for model magnetic field spectrum.

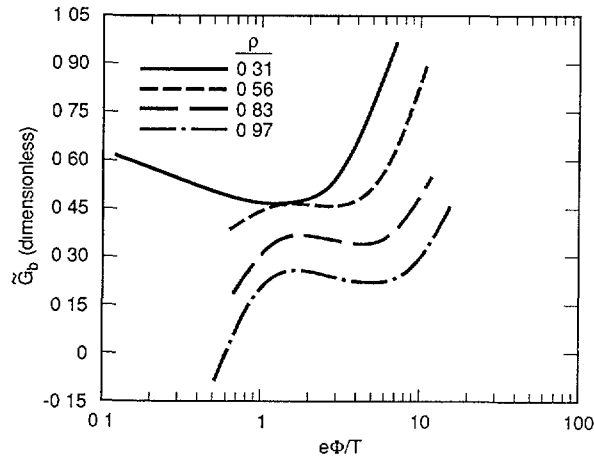


FIG 10 Bootstrap current versus radial electric field for four different radii

If the neoclassical viscosities are the dominant mechanism driving the bootstrap current, we can use external fields in stellarators to control that current. Appropriate external field controls can also be employed to reduce the bootstrap current to zero. Therefore, currentless operation of stellarators in a low collisionality regime should not be impaired.

The effect of the radial field on the bootstrap current is very weak in the  $\nu_{eff}/\Omega_E \ll 1$  regime, as long as the resonance between  $v_{\parallel}$  and poloidal  $\mathbf{E} \times \mathbf{B}$  rotation is avoided. We show that in ATF this resonance behaviour does not exist for  $e\Phi/T \sim 1-3$ . Under this condition, the results of analytic expressions are in good agreement with those of DKES. One can therefore evaluate the analytic expressions to obtain the bootstrap current in ATF, using DKES when necessary to perform occasional checks.

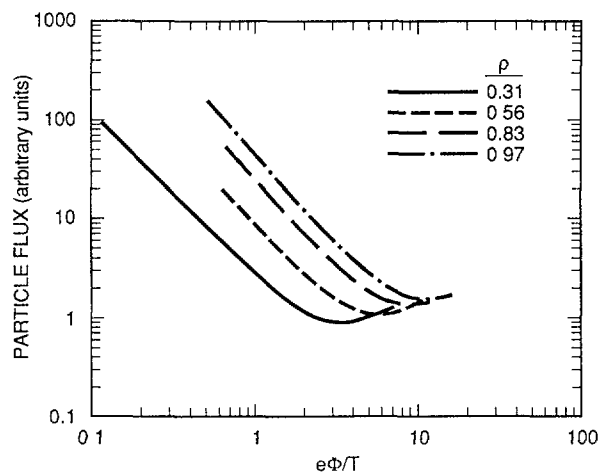


FIG. 11. Particle flux versus radial electric field for four different radii.

### REFERENCES

- [1] ZARNSTORFF, M., PRAGER, S.C., *Phys. Rev. Lett.* **53** (1984) 454.
- [2] BESSHOU, S., MOTOJIMA, O., SATO, M., et al., *Plasma Phys. Controlled Fusion* **26** (1984) 565.
- [3] GASPARINO, U., MAASSBERG, H., TUTTER, M., W VII-A TEAM, RÄUCHLE, E., ECRH GROUP, in *Controlled Fusion and Plasma Physics*, (Proc. 14th Eur. Conf. Madrid, 1987), Vol. 11D, Part II, European Physical Society (1987) 818.
- [4] TREFFERT, J.D., SHOHEIT, J.L., BERK, H.L., *Phys. Rev. Lett.* **53** (1984) 2409.
- [5] ZARNSTORFF, M., BELL, M.C., BITTER, M., et al., *Phys. Rev. Lett.* **60** (1988) 1306.
- [6] SHAING, K.C., *Phys. Fluids* **31** (1988) 8.
- [7] LYON, J.F., CARRERAS, B.A., CHIPLEY, K.K., et al., *Fusion Technol.* **10** (1986) 179.
- [8] SHAING, K.C., CALLEN, J.D., *Phys. Fluids* **26** (1983) 1526; SHAING, K.C., CRUME, E.C., TOLLIVER, J.S., HIRSHMAN, S.P., van RIJ, W.I., *Phys. Fluids B* **1** (1989) 148.
- [9] OHKAWA, T., CHU, M.S., in *Sixth International Stellarator/Heliotron Workshop* (Proc. IAEA Technical Committee Meeting, Kyoto, 1986), Vol. 1, Plasma Physics Laboratory, Kyoto University (1987) 305.
- [10] CARRERAS, B.A., HICKS, H.R., HOLMES, J.A., LYNCH, V.E., NEILSON, G.H., *Nucl. Fusion* **24** (1984) 1347.
- [11] HIRSHMAN, S.P., van RIJ, W.I., MERKEL, P., *Comput. Phys. Commun.* **43** (1986) 143.
- [12] PYTTE, A., BOOZER, A.H., *Phys. Fluids* **24** (1981) 88.
- [13] HIRSHMAN, S.P., SHAING, K.C., van RIJ, W.I., BEASLEY, C.O., CRUME, E.C., *Phys. Fluids* **29** (1986) 2951.
- [14] RODRIGUEZ-SOLANO RIBEIRO, E., SHAING, K.C., *Phys. Fluids* **30** (1987) 462.
- [15] HAZELTINE, R.D., ROSENBLUTH, M.N., *Phys. Fluids* **15** (1972) 2211.

## BOOTSTRAP CURRENTS IN HELIAS CONFIGURATIONS

C. BEIDLER, E. HARMEYER, F. HERRNEGGER,  
J. KISSLINGER, H. MAASSBERG, A. MONTVAI<sup>1</sup>,  
F. RAU, R. SCARDOVELLI, H. WOBIG  
Euratom-IPP Association,  
Max-Planck-Institut für Plasmaphysik,  
Garching, Federal Republic of Germany

### Abstract

Neoclassical bootstrap currents cause severe problems in stellarators since the profile of the rotational transform is modified with increasing plasma pressure. Therefore, in future stellarators neoclassical bootstrap currents should be avoided by proper shaping of the magnetic surfaces. As has been shown by Shaing and Callen [1] bootstrap currents in stellarators can be made small by the counteracting effect of toroidal curvature and helical stellarator fields. In Helias configurations [2] this effect can be verified. In quasi-helically symmetric stellarators [3] bootstrap currents flow opposite to those in axisymmetric configurations, however, they are smaller than these. A certain deviation from symmetry is necessary for achieving small bootstrap currents. The present paper discusses analytic theory relating bootstrap currents to neoclassical radial losses and presents some results of numerical calculations based on the DKES-code [4]. Numerical evaluation of the geometrical factor  $G_b$  shows the effect of various Fourier harmonics in  $B(\theta, \phi)$  on each magnetic surface.

---

**A Analytic theory** Bootstrap currents are the result of parallel momentum balance on every magnetic surface. Particle drifts in the magnetic field lead to a distortion of the distribution function  $f(v_{\parallel})$  and a deviation from the Maxwellian which is balanced by collisions. In the macroscopic picture this leads to tangential forces in the magnetic surface described by the anisotropic part of the pressure tensor. The momentum balance and the resulting flux-friction relations [5] have been widely used in literature to express the bootstrap current in terms of these tangential forces or so-called parallel viscosity. The flux-friction relations also contain radial plasma losses consisting of Pfirsch-Schlüter fluxes and neoclassical fluxes and therefore these equations provide a correlation between bootstrap currents and neoclassical radial losses. Such a relation has already been found by Bickerton et al. [6] for tokamaks. In [7] this proportionality between currents and fluxes has been extended to helically symmetric and quasi-helically symmetric stellarator configurations and yields

$$\eta \langle B^2 \rangle I'(\psi) = C(\psi) (\tau - \gamma_{\omega}) \left\{ \frac{\Gamma_{neo}}{N} + 0.32 \frac{q_{e,neo}}{NT_e} \right\}. \quad (1)$$

$I'(\psi) d\psi$  is the differential toroidal current on a magnetic surface  $\psi = \text{const}$ ,  $\eta$  = Spitzer resistivity,  $\tau$  = rotational transform,  $\gamma_{\omega}$  = slope of the invariant direction.  $\Gamma_{neo}$ ,  $q_{e,neo}$  = neoclassical particle flux and electron thermal flux.  $C(\psi)$  is a positive constant on

---

<sup>1</sup> Guest from the Central Research Institute for Physics, Budapest, Hungary.

the magnetic surface. Tokamak results are obtained by setting  $\gamma_\omega = 0$ . Equation (1) can be generalized to an arbitrary non-symmetric stellarator, in that case the coefficient  $C(\psi)$  can be of either sign and the exact value has to be found from kinetic theory. Details are given in [7].

**B Quasi-helically invariant configurations** These are characterized by the magnetic field being a function of one variable  $\theta - \gamma_\omega \phi$  alone ( $\theta, \phi =$  poloidal and toroidal magnetic coordinates). Since particle orbits in magnetic coordinates and consequently neoclassical effects are only determined by  $B(\theta, \phi)$  and not by the shape of the magnetic surfaces, this implies, that neoclassical tokamak theory can easily be transferred to helically symmetric or quasi-helically symmetric configurations. This isomorphism has been pointed out in [8]. Based on this similarity and Eq.(1) the bootstrap current and the resulting shift of  $t$  are evaluated for helically invariant configurations. The neoclassical fluxes are taken from ref. [8]. In the long-mean-free-path regime, where bootstrap current is largest, this leads to a total current

$$I \approx I_o \beta(0) (R/a)^2 \sqrt{\epsilon} \frac{0.3}{t - \gamma_\omega}. \quad (2)$$

$I_o = 2\pi a^2 B / \mu_o R$  is a reference current with  $t = 1$ ,  $a =$  av. plasma radius,  $\sqrt{\epsilon} =$  number of trapped particles. In extrapolating this to a quasi-helically invariant Helias configuration with  $R = 6.5$  m,  $a = 0.6$  m,  $B = 2.5$  T,  $t = 0.85$ ,  $\gamma_\omega = 5$  and  $n(0) = 10^{20} \text{m}^{-3}$  the bootstrap current is 300 kA at  $T_e(0) = 8$  keV. The corresponding shift of the rotational transform is  $\delta t = -(0.25 - 0.3)$  depending on the plasma profiles. Eq. (2) says that the bootstrap current in helically invariant stellarators is negative and smaller than the current in a tokamak with the same aspect ratio, the factor is  $t/(t - \gamma_\omega)$ .

**C Non-symmetric stellarators** The shift of  $t$  in helically invariant stellarators is still too large to be tolerable and therefore a superposition of several helical harmonics, leading to a small deviation from helical symmetry, may be necessary to reduce the bootstrap current further. In realistic Helias configurations ( see [10] ) the magnetic field

$$B = B_o \left\{ \sum_{m,n=0} C_{n,m} \cos(n\phi) \cos(m\theta) + S_{n,m} \sin(n\phi) \sin(m\theta) \right\} \quad (3)$$

not only contains the dominating helical harmonic  $C_{1,1}$  and  $S_{1,1}$ , but also the toroidal term  $C_{0,1}$  and higher harmonics. In [10] an example of a five-period Helias configuration and the spectrum of  $B$  is given. The geometrical bootstrap factor  $G_b f_f / f_c$  [11], which determines the bootstrap factor in the  $lmfp$ -regime has been computed for various Helias configurations. For comparison, this factor is normalized to an axisymmetric configuration with the same rotational transform and the same aspect ratio. Fig. 1 shows the bootstrap factor for various Helias configurations with the magnetic field generated by coils. The case HS-5-8A is described in [10]. As can be seen, the bootstrap factor ranges between -0.1 and +0.1, which means that the bootstrap current is smaller than 1/10 of the current in an equivalent tokamak. The dominant terms in  $B(\theta, \phi)$  responsible for the bootstrap current are  $C_{1,1}$ ,  $S_{1,1}$  and  $C_{0,1}$ . The value of  $C_{0,1}$  needed to compensate for the current of the helical harmonics  $C_{1,1}$  and  $S_{1,1}$  is roughly  $|C_{0,1}| \approx 0.3 \cdot |S_{1,1}|$  or  $|C_{1,1}|$ . The case HS-5081 is nearly quasi-helically invariant, symmetry-breaking terms are  $C_{0,1}$  and  $C_{2,2}$ . Here, a toroidal term  $|C_{0,1}| \approx 0.18 \cdot |C_{1,1}|$  is sufficient to reduce  $G_b f_t / f_c$  to -0.1, without these term we find  $C_b f_t / f_c = -(0.24 - 0.3)$ .

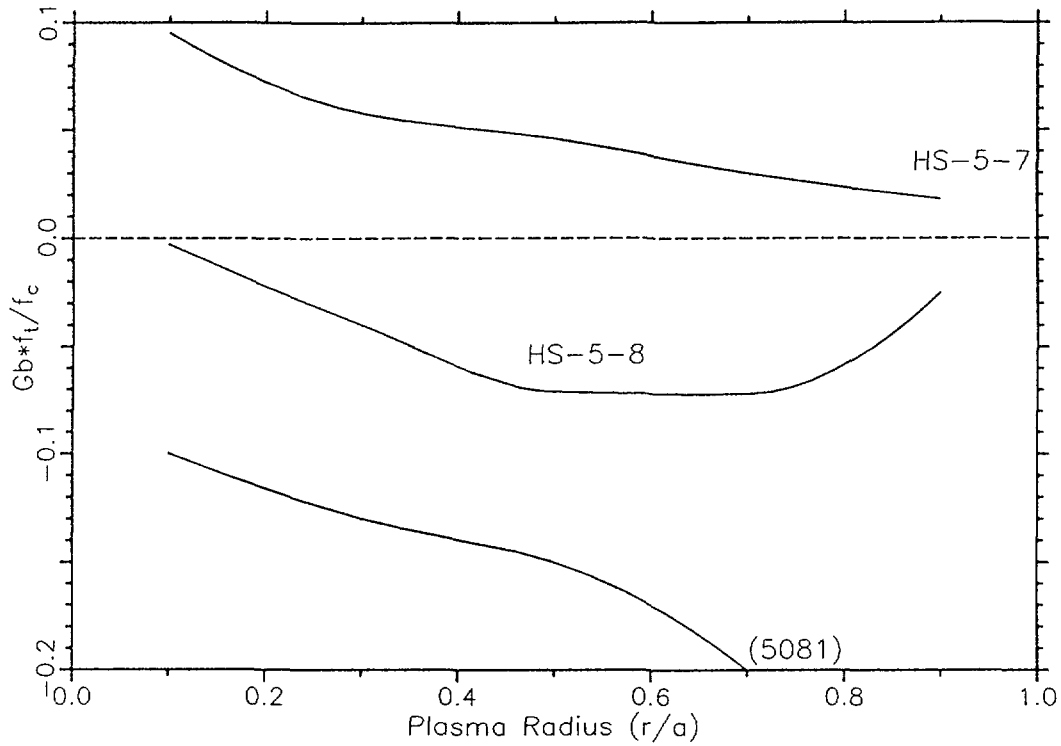


Fig. 1 Normalized bootstrap factor  $G_b f_t/f_c$  vs plasma radius for several 5-period Helias configurations. The configuration HS-5-8 is described in ref. [10]

**D Results of numerical calculations.** Using the DKES-code [4] the coefficient of the bootstrap current can be calculated for all regimes of collisionality. This code solves the drift-kinetic equation and yields the whole transport matrix  $D_{ik}$  with the non-diagonal term  $D_{31}$  being the relevant coefficient. Numerical results of Helias configurations show negative bootstrap currents in nearly quasi-helically invariant cases (HS-5081, Fig. 2). Fig. 3 shows the result in comparison with the coefficient of the equivalent axisymmetric case. The factor  $D_{31}$  is smaller than in the axisymmetric case, however it exhibits a strong dependence on the collisionality  $\nu^*$  and the radial electric field. In the *lmfp*-regime the coefficient  $D_{31}$  changes from negative to positive, this cross-over point, however, depends on the particular magnetic surface and on the radial electric field. This feature complicates the comparison with the *lmfp*-limit  $G_b$ . A similar behaviour was also found in the other configurations listed in Fig. 1.

**E Summary and conclusions.** Bootstrap currents in optimized Helias configurations have been computed by various methods. In 5-period configurations the current is about a factor 10 smaller than in the equivalent axisymmetric case. This low value may be acceptable in stellarator experiments, however, it is found that bootstrap currents depend sensitively on the Fourier spectrum of the magnetic field and therefore accurate calculations are required. Evaluation of the  $G_b$ -factor shows that a toroidal  $C_{0,1}$ -term of the order  $0.3 \cdot |C_{1,1}|$  is needed for sufficiently small bootstrap currents, however, results from the DKES-code show that the size of the current also depends critically on the radial electric field and the collisionality.

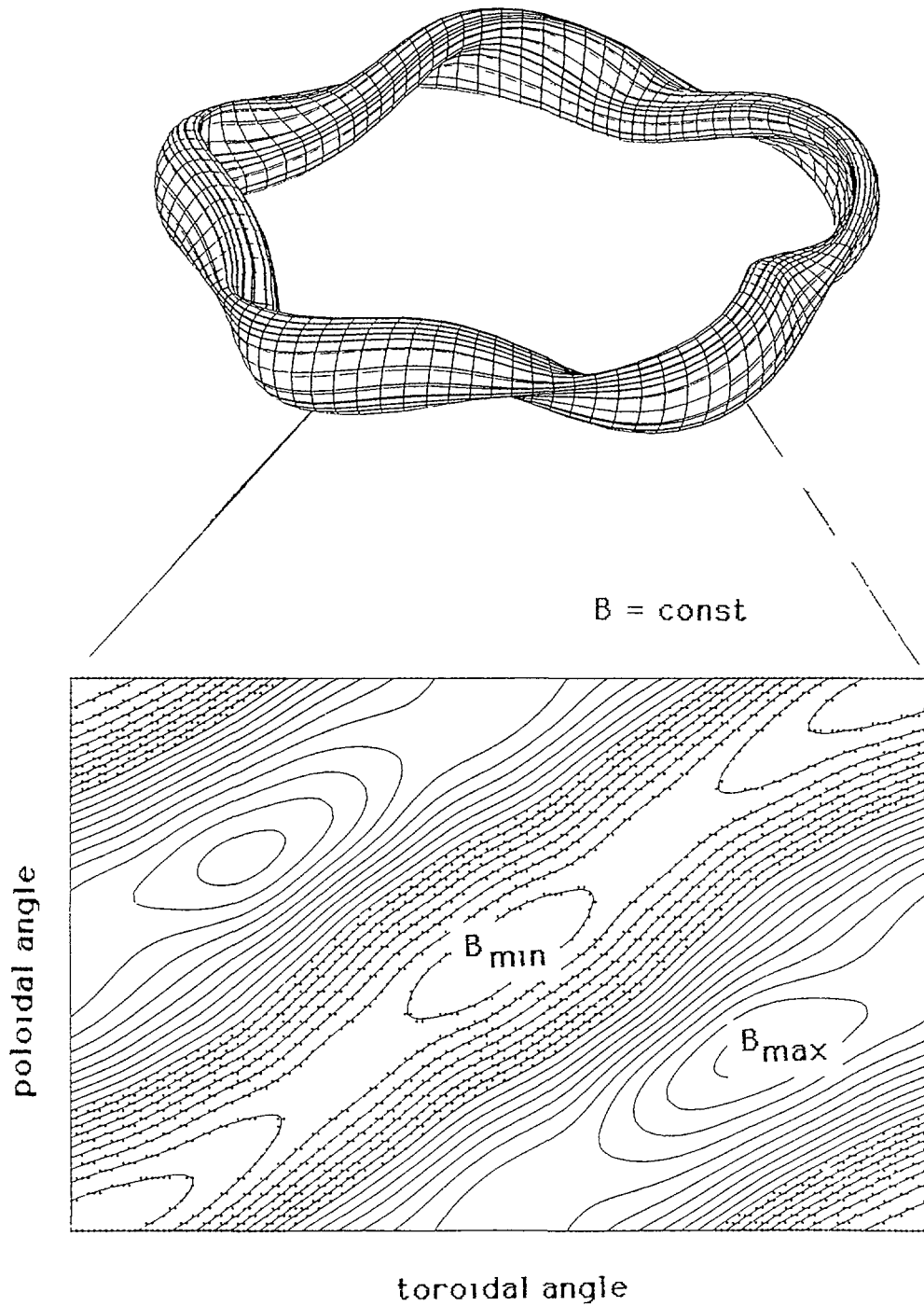


Fig. 2 Helias configuration HS-5081. Top: Magnetic surface, 5 field periods. Bottom:  $B(\theta, \phi) = \text{const.}$  on magnetic surface,  $\bar{r}/a = 0.6$ ,  $B_{\text{max}}/B_0 = 1.1$ ,  $B_{\text{min}}/B_0 = 0.92$ . Shaded area:  $B/B_0 \leq 1$ .

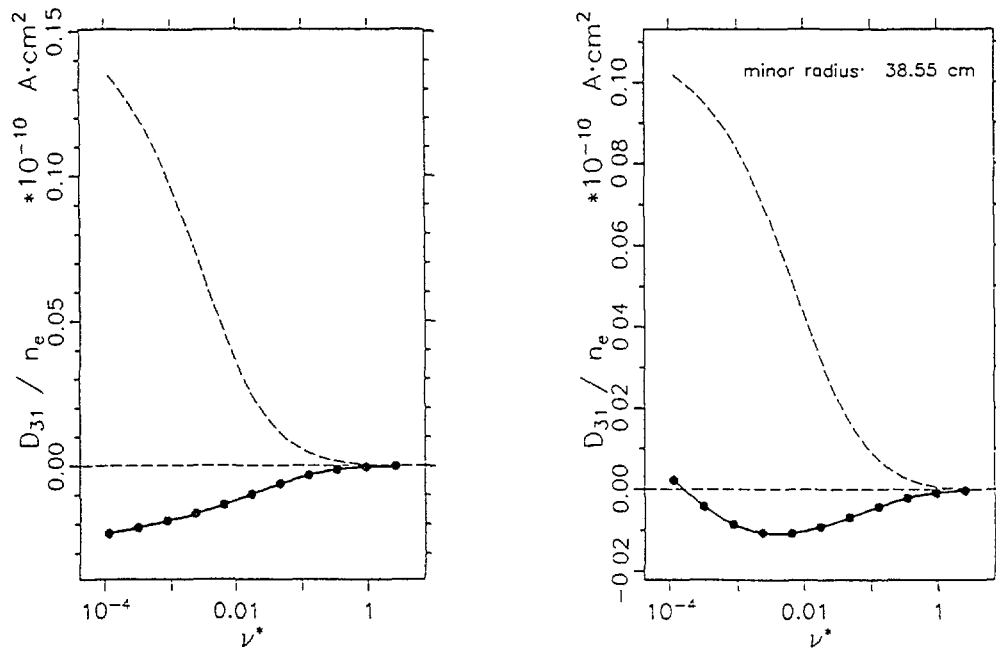


Fig. 3 Bootstrap coefficient  $D_{31}/n$  of the Helias configuration HS-5081 vs collisionality (solid line). Broken line: equivalent axisymmetric configuration. Electric field  $E=0$ . Plasma parameter:  $B=3$  T,  $T_e=2$  keV,  $t=0.89$ .

#### REFERENCES

- [1] J. Nührenberg, R. Zille, *Phys. Letters A* **114** (1986), 129
- [2] K.C. Shaing, J.D. Callen *Phys. Fluids* **26** (1983) 3315
- [3] J. Nührenberg, R. Zille, *Phys. Letters A* **129**(1988) 113
- [4] S.P. Hirshman et al. *Report ORNL/TM-9925*, April 1986
- [5] S.P. Hirshman, D.J. Sigmar *Nucl. Fusion* **21** (1981) 1079
- [6] R.J. Bickerton, J.W. Connor and J.B. Taylor *Nat. Phys. Sci.* **225** 110 (1971)
- [7] H. Wobig, *Report IPP 2/297*, October 1988
- [8] A.H. Boozer, *Phys. Fluids* **26**(1983) 496
- [9] M.N. Rosenbluth, R.D. Hazeltine and F.L. Hinton, *Phys. Fluids* **15** (1972), 116
- [10] C. Beidler et al. *paper P2B5 of this conference*
- [11] T.S. Ohkawa, M.S. Shu, *Report GA-A18688* Nov. 1986

# QUASI-STATIONARY CURRENTS IN THE RF HEATED PLASMA OF THE URAGAN-3 TORSATRON

Yu.V. GUTAREV, Yu.K. KUZNETSOV, O.S. PAVLICHENKO,  
V.K. PASHNEV, O.M. SHVETS  
Institute of Physics and Technology,  
Ukrainian Academy of Sciences,  
Khar'kov, Union of Soviet Socialist Republics

## Abstract

Quasistationary plasma currents in the RF heated plasma of the URAGAN-3 torsatron has been studied for a wide range of electron collision frequencies ( $7 \cdot 10^{-1} \leq \nu_e / \nu_e^* \leq 10^3$ ). Data are compared with the neoclassical theory predictions.

## 1. INTRODUCTION

The quasistationary currents are one of the essential features of plasma produced and heated by RF power absorption in the frequency range of  $\omega \lesssim \omega_{ci}$  in the URAGAN-3 torsatron [1]. These currents are observed by means of magnetic field measurements [2] and exist in all RF heating regimes. In these experiments the magnetic coils have measured the toroidal flux  $\Phi_p$  (diamagnetic coil), the poloidal flux  $\Delta\psi_p$  (saddle-type  $\psi$  - coil) and the plasma current  $I_p$  (Rogovsky coil).

In this report the analysis of experimental data on the quasistationary currents in the URAGAN-3 torsatron and currents predicted by the plasma equilibrium theory in the stellarator is presented.

## 2. THEORY

In the equation describing the plasma equilibrium in stellarator [3-5]

$$R^2 \operatorname{div} [R^{-2} \nabla(\Psi - \Psi^*)] = - \frac{8\pi^2}{c} R j_\varphi \quad (1)$$

a toroidal current

$$j_\varphi = 2\pi c R \frac{dP}{d\Psi} + \frac{2(F+F^*)}{cR} \frac{dF}{d\Psi} \quad (2)$$

can be presented in a form

$$j_\varphi = \frac{2\pi c}{R} \frac{dP}{d\Psi} [R^2 - \bar{R}(\bar{R}^{-1}) + \bar{R}(\bar{R}^{-1})^{-1} \left( \frac{\bar{B}_\varphi^*}{R_0 B_0 R^{-1}} - \frac{B_\varphi^* R}{B_0 R_0} \right)] + \frac{\bar{j}_\varphi}{R R^{-1}} \quad (3)$$

Here the universally adopted symbols are used, the line over the symbols means the averaging over the magnetic surface. In the right hand of equation (3) the first term describe a dipole Pfirsch-Schluter currents, the second term describes an uni-directional current.

In general the plasma configuration which is satisfying to external magnetic field measurements finds out by solving of equation (1). In our calculations the simplified analytical terms applicable for large aspect ratio, low- $\beta$  and circular flux surfaces were used.

In the coordinate system  $r, \theta, \varphi$  ( $R=R_0 + z \cos \theta, z = r \sin \theta$ ) the measurable quantities derived from the equation (1-3) are presented in a form

$$\Phi_p = -4\pi S_0 \frac{\bar{P}}{B_0} + \frac{S_0}{z} \frac{B_j^2(a)}{B_0} + \frac{4\pi^2}{cR_0} \int_0^a \bar{j}_\varphi(\bar{z}) [\bar{z}^3 t_h + 2\bar{z} \int_0^{\bar{z}} \rho t_h d\rho] d\bar{z} \quad (4)$$

$$\Delta \Psi_p(z_0) = 4\pi z_0 R_0 [B_\beta(z_0) + B_{1_0}^j(z_0) + B_j(a) \frac{a \Delta_j}{z_0^2}], \quad z_0 \geq a \quad (5)$$

$$I_p = 2\pi \int_0^a \bar{j}_\varphi \cdot \bar{z} d\bar{z} \quad (6)$$

where

$$B_\beta(z_0) = -\frac{4\pi}{B_0 z_0^2} \int_0^a \frac{\bar{z}^2 \rho'}{t} (1 + \Delta m t_h R_0^{-1}) d\bar{z} \quad (7)$$

$$B_{1_0}^j(z_0) = \frac{I_p}{cR_0} \left( \ln \frac{8R_0}{z_0} - 1 \right), \quad B_j(a) = \frac{2 I_p}{c a} \quad (8)$$

A plasma border ( $\bar{z} = a$ ) displacement is

$$\Delta_a = a (B_\beta^*(a) + B_j(a))^{-1} \left[ \left( \frac{\Delta \Psi_p}{4\pi z_0 R_0} - B_{1_0}^j(z_0) \right) \frac{z_0^2}{a^2} + B_{1_0}^j(a) + B_1^e \right] \quad (9)$$

and a quantity  $\Delta_j$  entering in the relation of (5) for quasihomogeneous current distribution  $\bar{j}_\varphi(\bar{z}) = \text{Const}$  are defined as

$$\Delta_a = a \cdot B_\beta^{*-1} (B_\beta(a) + B_{1_0}^j(a) + B_1^e) \quad (10)$$

$$\Delta_j = \Delta_a - \frac{a^2}{8R_0} \quad (11)$$

$$\text{where } B_{1_0}^j(a) = \frac{I_p}{cR_0} \left( \ln \frac{8R_0}{a} - \frac{5}{4} \right) \quad (12)$$

In these terms  $z_0$  is the distance from the axis  $R = R_0$  to  $\Psi$ -coil poles ( $\theta_1 = 0; \theta_2 = \pi$ ),  $S_0 = \pi a^2$ ,  $\bar{P} = 2 \cdot a^{-2} \int_0^a \bar{z} \rho(\bar{z}) d\bar{z}$ ,  $t_h$  and  $t$  - vacuum and total field rotational transform angles,  $B_{1_0}^e$  - external vertical field,  $\Delta(\bar{z})$  - flux surface displacement,  $\Delta_j$  - current effective displacement depending on current density distribution.<sup>x</sup>

At least three mechanisms of unidirectional current generation in the RF produced plasma are possible. These are the bootstrap, RF driven and inductive currents.

<sup>x</sup> The terms (10) -(12) are more precise than those described in [2] where it was supposed that  $\Delta_j \approx \Delta_a$  and  $B_{1_0}^j(a) \approx B_{1_0}^j(a)$ . More careful analysis is presented in papers [6 - 8].

The bootstrap current can be evaluated as

$$j_b = -K \cdot \frac{c P_i}{\varepsilon^{1/2} \cdot t B} \quad (13)$$

where quantity  $K$  depends mostly on electron collision frequency:

$$K \left( \frac{\nu}{\nu^*} < 1 \right) \sim 1, \quad K \left( 1 < \frac{\nu}{\nu^*} < \varepsilon^{-3/2} \right) \sim \frac{\nu^*}{\nu}, \quad K \left( \frac{\nu}{\nu^*} > \varepsilon^{-3/2} \right) \sim \left( \frac{\nu^*}{\nu} \right)^2 \quad (14)$$

$$\text{and } \nu^* = v_{Te} \cdot t \cdot \varepsilon^{3/2} / R \quad (15)$$

A diminution of  $K$  due to helical ripple [9] for the URAGAN-3 configuration is less pronounced than for  $\ell = 2$  torsatrons like ATF.

Evaluation of RF driven current in our case is difficult. Although the frame RF antenna generates plasma waves which are symmetric along  $\varphi$ , the current drive can't be excluded completely.

The inductive current  $j_i$  is generated due to time variation of magnetic flux:

$$\frac{\partial \Psi_i}{\partial t} + 2\pi R_0 \cdot c \cdot j_i \cdot \sigma^{-1} = \frac{\partial (\Psi_e + \Psi_o + \Psi_\beta)}{\partial t} \quad (16)$$

where  $\sigma$  - plasma electroconductivity. The value  $\frac{\partial \Psi_e}{\partial t}$  is produced by nonstationarity of magnetic field coils currents,  $\frac{\partial \Psi_o}{\partial t}$  by bootstrap and RF driven currents and  $\frac{\partial \Psi_\beta}{\partial t}$  by equilibrium plasma configuration change [4].

The inductive current  $j_i$  can be evaluated from a solution of an electrical field diffusion equation in cylindrical geometry:

$$\frac{\partial}{\partial t} (\sigma E + j_o + j_\beta) = \frac{c^2}{4\pi} \cdot \frac{\partial}{\partial z} \left( z \frac{\partial E}{\partial z} \right) \quad (17)$$

where  $j_i = \sigma E$ ,  $j_o$  and  $j_\beta$  correspond to  $\Psi_o$  and  $\Psi_\beta$  and  $\Psi_e$  is taken into account in the boundary condition for electric field  $E$ .

### 3. EXPERIMENT

Most described results were obtained for quasistationary  $Q$  - discharges in the URAGAN-3 torsatron [1].

#### Diamagnetic and dipole equilibrium currents.

Measured  $\Phi_p$  and  $\Delta \Psi_p$  fluxes are in good quantitative correspondence with those calculated from (4) and (5). This conclusion is illustrated by Fig.1 where average values of plasma pressure obtained from magnetic measurements and from  $n_e, T_e, T_i$  profile measurements are presented. In the calculations plasma current profile was supposed to be homogeneous. This simplification did not produce noticeable errors due to small value of plasma current  $I_p$ . Notice that in the regimes with higher plasma pressure the diamagnetic loop intersecting the divertor fluxes in the plasma edge neighbourhood has been removed.

Unidirectional current. This current increased with plasma pressure  $\bar{p}$  increase and reached a value of  $I = 2$  kA at  $\bar{p} = 2,5 \cdot 10^{15}$  eV.cm<sup>-3</sup>. Time behavior of current  $I_p$  and plasma pressure  $\bar{p}$  for different values of electron collision frequency  $\nu_e$  is shown in Fig.2. Plasma parameters for these cases are presented in table :

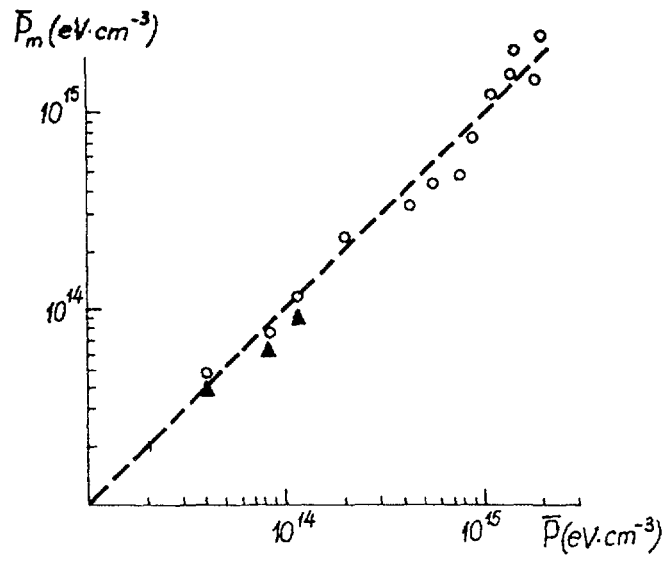


Fig. 1 Comparison between plasma pressure data obtained by magnetic loops ( $\Delta$  -diamagnetic loop),  $\circ$  -  $\psi$  - loop) and data obtained from measurements of  $n_e$ ,  $T_i$ ,  $T_e$  ( $B_0 = 4,5$  kG).

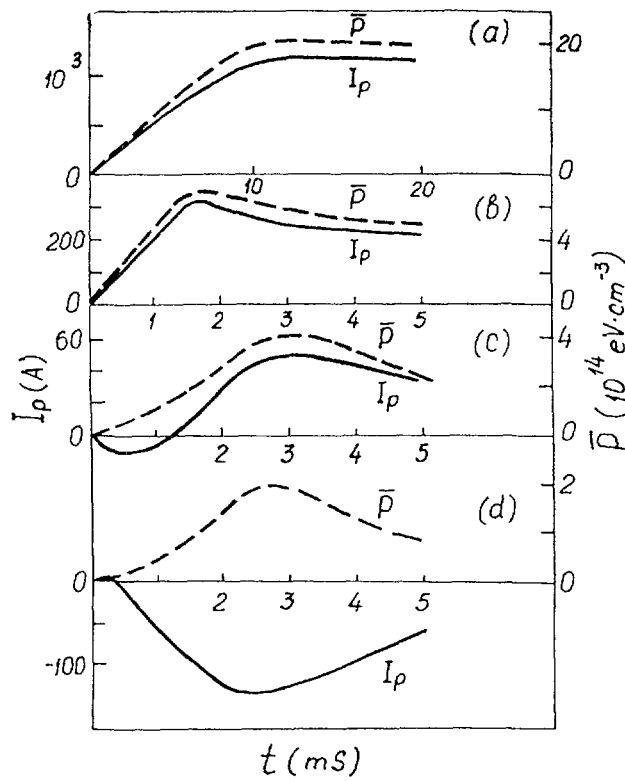


Fig. 2 Time traces of plasma current and pressure for different RF- heating regimes. ( $B_0 = 4,5$  KG).

Regime	$\bar{p}(\text{cm}^{-3}\text{eV})$	$\bar{n}(\text{cm}^{-3})$	$T_e(\text{eV})$	$I_p(\text{A})$	$(\bar{\nu}_e/\bar{\nu}_e^*) _{\bar{r}=0,7\cdot a}$
(a)	$2 \cdot 10^{15}$	$3 \cdot 10^{12}$	120	1200	4,6
(b)	$5 \cdot 10^{14}$	$4 \cdot 10^{12}$	55	250	21,5
(c)	$4 \cdot 10^{14}$	$4,9 \cdot 10^{12}$	40	45	50
(d)	$2 \cdot 10^{14}$	$6,5 \cdot 10^{12}$	15	-150	470

Regime (a) is a principal one (Q-regime). In the Q-regime the diminishment of plasma pressure  $\bar{p}$  at  $\bar{n}_e = \text{const}$  by the diminishment of RF power was possible only in limited range due to gas breakdown difficulties.

Further diminishment of plasma pressure  $\bar{p}$  was realized by the electron density increase (Fig.3). At the electron density of  $\bar{n}_e \approx 3 \cdot 10^{12} \text{cm}^{-3}$  the discharge became the D-type discharge [1] (degrading discharge).

Fig.3 shows that  $I_p \sim \bar{p}$  in the plasma pressure range of  $\bar{p} \approx (0,6 \div 2,5) \cdot 10^{15} \text{eV} \cdot \text{cm}^{-3}$ . The  $I_p$  current direction was changing with the magnetic field  $B_0$  direction and corresponded to  $t_c > 0$  (positive current).

For comparison of experimental data with the theory predictions we normalized the current measurement data  $I_p$  on the banana-regime bootstrap current

$$I_{b0} = \frac{2\pi c \sqrt{aR} \cdot \bar{p}}{t(a) \cdot B_0} \quad (17)$$

calculated for homogeneous plasma pressure and  $\epsilon_h \ll \epsilon_t$ . Thus parameter  $A = I_p/I_{b0}$  includes dependence of bootstrap current on collision frequency of  $\bar{\nu}_e$ ,  $\epsilon_h$  and plasma parameters radial distribution [9].

Fig.4 shows the dependence of A on the normalized electron collision frequency  $\bar{\nu}_e/\bar{\nu}_e^*$  at the radius of  $\bar{r} = 0,7 \cdot a$ . The parameter  $\bar{\nu}_e/\bar{\nu}_e^*$  is nearly constant at  $\bar{r} \geq 0,5 \cdot a$  and increasing for smaller radii. As one can see from Fig.4, most data were obtained for plateau regime of collisions, minimum value of  $(\bar{\nu}_e/\bar{\nu}_e^*)_{\text{min}} = 0,7$  was reached for Q-discharge with  $\bar{p} = 2,5 \cdot 10^{15} \text{eV} \cdot \text{cm}^{-3}$  and  $\bar{n}_e = 2 \cdot 10^{12} \text{cm}^{-3}$ . The theory prediction for A in banana regime gives a value  $A = 2 \div 3$  which is 6  $\div$  9 times higher than experimental value of  $A \approx 0,3$ .

With the increase of collision frequency the value of A decreases, but dependence of A ( $\bar{\nu}_e/\bar{\nu}_e^*$ ) is weaker than the theory predicted behaviour of  $A \sim \bar{\nu}_e^{-1}$ .

Strong diminishment of A at large value of  $\bar{\nu}_e/\bar{\nu}_e^*$  and a current direction change correlates with a transition of discharges in the D-regime. This fact is in a strong contradiction with the bootstrap current generation ideology.

The inductive current calculations predict a negative current with the value of 20 - 30 % of the observed one.

#### 4. CONCLUSION

The quasistationary diamagnetic and dipole currents observed for RF produced and heated plasma in the URAGAN-3 torsatron are well describe by a plasma equilibrium theory in stellarator and are used for measurement of plasma pressure in a wide range of plasma parameters.

The toroidal current  $I_p$  could be explained as the bootstrap current only for regimes with a low collision frequency of electrons ( $\nu_e/\nu_e^* \approx 1$ ). Possible explanation of observed dependence of plasma current on collision frequency can be the influence of RF driven current. This explanation needs new experimental data.

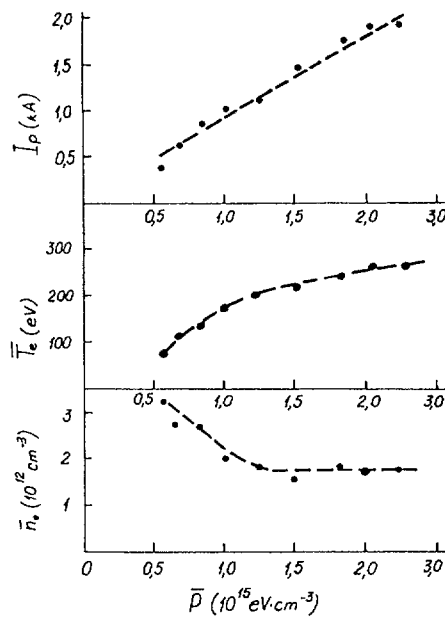


Fig.3 Variation of  $I_p, T_e$  and  $\bar{n}_e$  with  $\bar{\nu}$  ( $B_0=4,5\text{kG}$ ).

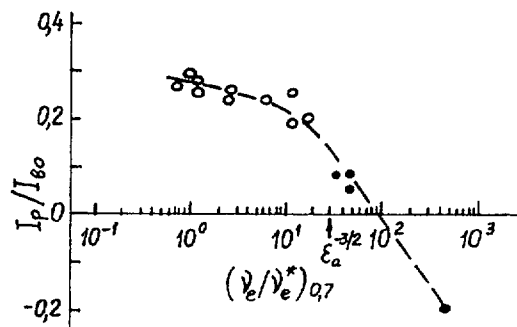


Fig. 4 Variation of ratio  $I_p/I_{Bo}$  with normalized collision frequency  $\bar{\nu}/\bar{\nu}^*$  ( $B_0=4,5\text{kG}$ ,  $\circ$  - Q - regimes,  $\bullet$  - D - regimes).

#### REFERENCES

1. V.L. Berezhnyi, N.T. Besedin, M.P. Vasil'ev et al., Plasma Physics and Controlled Nuclear Fusion Research, 1986, v.2, 497 (1987).
2. Ю.К. Гутарев, Ю.К. Кузнецов, В.К. Пашнев, Н.П. Пономаренко, Физика плазмы, 14, 286 (1988).
3. J.M. Greene, J.L. Johnson, Phys. Fluids, 4, 875 (1961).
4. В.Д. Пустовитов, В.Д. Шафранов, Равновесие и устойчивость плазмы в стеллараторах. В со.: Вопросы теории плазмы, вып. II, М., Энергоатомиздат (1987), стр. 146.
5. Л.М. Коврижных, С.В. Щепетов, УФН, 148, 637 (1986).
6. В.Д. Пустовитов, Физика плазмы, 14, 522 (1988).
7. В.Д. Пустовитов, Физика плазмы, 14, 1436 (1988).
8. В.Д. Пустовитов, Препринт ИАЭ 4752/6 (1989).
9. K.S. Shaing, and J.D. Callen. Phys. Fluids, 26, 3315 (1983).

## LIST OF PARTICIPANTS

Aceto, S. A.	RPI
Alejaldre, C. L.	CIEMAT
Alladio, Franco	EURATOM-ENEA, Italy
Amano, T.	Nagoya IPP
Anabitarte, Ernesto C.	CIEMAT
Anderson, D. T.	University of Wisconsin
Anderson, F.S.B.	University of Wisconsin
Ascasibar, Enrique	CIEMAT
Bell, G. L.	Auburn University
Betancourt, Octavio Labarca	City College - CUNY
Bhattacharjee, A.	Columbia University
Blackwell, Boyd Douglas	Australian National University
Blanken, Ronald	DOE-OFE
Boozer, Allen H.	College of William and Mary
Cary, John	U. Colorado
Conner, K. A.	RPI
Crisanti, Flavio	EURATOM-ENEA, Italy
Diebold, Daniel	DOE-OFE
Fedyanin, O. I.	IGP, Moscow
Gandy, Rex	Auburn University
Garabedian, Paul R.	New York University
Garcia, L.	U. Complutense
Garren, David	College of William and Mary
Grau Malonda, A.	CIEMAT
Grieger, G.	IPP Garching
Haas, G.	DOE-OFE
Hartwell, Greg	Auburn University
Hegna, Chris	Columbia University
Henderson, Mark	Auburn University
Hidalgo Vera, Carlos	CIEMAT
Hamberger, Sydney Maxwell	Australian National University
Hitchon, W.N.G.	University of Wisconsin
Iguchi, Harukazu	Nagoya IPP

Johnson, J. L.	PPPL
Kitajima, S.	Tohoku U.
Knowlton, Steve	Auburn University
Kuznetsov, Yu. K.	Kharkov PTI
Leiser, Manfred	IAEA
Maassberg, H.	IPP Garching
Matsuoka, Keisuke	Nagoya IPP
Matthews, P.	University of Wisconsin
Motojima, Osamu	Nagoya IPP
Müller, Günter A. K.	IPF Stuttgart
Navarro, A. P.	CIEMAT
Nelson, B. A.	University of Washington
Niedermeyer, Helmut	IPP Garching
Nührenberg, J.	IPP Garching
Obiki, Tokuhiko	Kyoto PPL
Obysov, N. A.	USSR SCUAE
Ochando, Maria A.	CIEMAT
Ohyabu, N.	Nagoya IPP
Pavlichenko, O. S.	Kharkov PTI
Peranich, Larry S.	General Atomics
Rau, Fritz	IPP Garching
Ribe, F. L.	University of Washington
Renner, H.	IPP Garching
Ringler, H.	IPP Garching
Sano, Fumimichi	Kyoto PPL
Schneider, Todd	Auburn University
Shohet, J. L.	University of Wisconsin
Swanson, D. Gary	Auburn University
Takeuchi, N.	Tohoku U.
Talmadge, J. N.	University of Wisconsin
Thomas, C. E.	Georgia Tech
Todd, T. N.	Culham
Voronov, G. S.	IGP, Moscow

Wagner, Friedrich  
Wakatani, M.  
Watanabe, H.  
Weller, Arthur  
Wobig, H.

Yoshikawa, Shoichi

Zielinski, J. J.  
Zushi, Hideki

IPP Garching  
Kyoto PPL  
Tohoku U.  
IPP Garching  
IPP Garching

PPPL

RPI  
Kyoto PPL

## ORNL PARTICIPANTS

Batchelor, D. B.  
Berry, L. A.  
Bigelow, T. S.  
Carreras, B. A.  
Carter, M. D.  
Charlton, L. A.  
Colchin, R. J.  
Crume, E. C.  
Dominguez, N.  
Dory, R. A.  
Dunlap, J. L.  
England, A. C.  
Fowler, R. H.  
Glowienka, J. C.  
Goulding, R. H.  
Harris, J. H.  
Haste, G. R.  
Hedrick, C. L.  
Hillis, D. L.  
Hiroe, S.  
Hirshman, S. P.  
Hogan, J. T.  
Horton, L. D.  
Houlberg, W. A.  
Howe, H. C.  
Isler, R. C.

Jernigan, T. C.  
Langley, R. A.  
Leboeuf, J. N.  
Lee, D. K.  
Lee, G. S.  
Lubell, M. S.  
Lue, J. W.  
Lynch, V. E.  
Lyon, J. F.  
Ma, C. H.  
Menon, M. M.  
Mioduszewski, P. K.  
Morris, R. N.  
Murakami, M.  
Neilson, G. H.  
Painter, S. L.  
Rasmussen, D. A.  
Rome, J. A.  
Saltmarsh, M. J.  
Shaing, K. C.  
Sheffield, J.  
Shepard, T. D.  
Trivelpiece, A. W.  
Uckan, T.  
Van Rij, W. I.  
Wilgen, J. B.  
Wing, W. R.

# HOW TO ORDER IAEA PUBLICATIONS

**An exclusive sales agent for IAEA publications, to whom all orders and inquiries should be addressed, has been appointed in the following country:**

UNITED STATES OF AMERICA UNIPUB, 4611-F Assembly Drive, Lanham, MD 20706-4391

---

**In the following countries IAEA publications may be purchased from the sales agents or booksellers listed or through major local booksellers. Payment can be made in local currency or with UNESCO coupons.**

ARGENTINA	Comisión Nacional de Energía Atómica, Avenida del Libertador 8250, RA-1429 Buenos Aires
AUSTRALIA	Hunter Publications, 58 A Gipps Street, Collingwood, Victoria 3066
BELGIUM	Service Courrier UNESCO, 202, Avenue du Roi, B-1060 Brussels
CHILE	Comisión Chilena de Energía Nuclear, Venta de Publicaciones, Amunategui 95, Casilla 188-D, Santiago
CHINA	IAEA Publications in Chinese China Nuclear Energy Industry Corporation, Translation Section, P.O. Box 2103, Beijing IAEA Publications other than in Chinese China National Publications Import & Export Corporation, Deutsche Abteilung, P.O. Box 88, Beijing
CZECHOSLOVAKIA	S.N.T.L., Mikulandska 4, CS-116 86 Prague 1 Alfa, Publishers, Hurbanovo námestie 3, CS-815 89 Bratislava
FRANCE	Office International de Documentation et Librairie, 48, rue Gay-Lussac, F-75240 Paris Cedex 05
HUNGARY	Kultura, Hungarian Foreign Trading Company, P.O. Box 149, H-1389 Budapest 62
INDIA	Oxford Book and Stationery Co., 17, Park Street, Calcutta-700 016 Oxford Book and Stationery Co., Scindia House, New Delhi-110 001
ISRAEL	Heiliger & Co Ltd 23 Keren Hayesod Street, Jerusalem 94188
ITALY	Libreria Scientifica, Dott. Lucio de Biasio "aeiou", Via Meravigli 16, I-20123 Milan
JAPAN	Maruzen Company, Ltd, P.O. Box 5050, 100-31 Tokyo International
PAKISTAN	Mirza Book Agency, 65, Shahrah Quaid-e-Azam, P O Box 729, Lahore 3
POLAND	Ars Polona-Ruch, Centrala Handlu Zagranicznego, Krakowskie Przedmiescie 7, PL-00-068 Warsaw
ROMANIA	Illexim, P.O. Box 136-137, Bucharest
SOUTH AFRICA	Van Schaik Bookstore (Pty) Ltd, P O Box 724, Pretoria 0001
SPAIN	Díaz de Santos, Lagasca 95, E-28006 Madrid Díaz de Santos, Balmes 417, E-08022 Barcelona
SWEDEN	AB Fritzes Kungl. Hovbokhandel, Fredsgatan 2, P O Box 16356, S-103 27 Stockholm
UNITED KINGDOM	Her Majesty's Stationery Office, Publications Centre, Agency Section, 51 Nine Elms Lane, London SW8 5DR
USSR	Mezhdunarodnaya Kniga, Smolenskaya-Sennaya 32-34, Moscow G-200
YUGOSLAVIA	Jugoslovenska Knjiga, Terazije 27, P O Box 36, YU-11001 Belgrade

**Orders from countries where sales agents have not yet been appointed and requests for information should be addressed directly to:**



**Division of Publications  
International Atomic Energy Agency  
Wagramerstrasse 5, P.O. Box 100, A-1400 Vienna, Austria**